Fundamentals of Hybrid Rocket Combustion and Propulsion

Edited by
Martin J. Chiaverini
Kenneth K. Kuo

PROGRESS IN ASTRONAUTICS AND AERONAUTICS

Frank K. Lu, Editor-in-Chief
Volume 218

Fundamentals of Hybrid Rocket Combustion and Propulsion

This page intentionally left blank

Fundamentals of Hybrid Rocket Combustion and Propulsion

Edited by

Martin J. Chiaverini
Orbital Technologies Corporation (ORBITEC)
Madison, Wisconsin

Kenneth K. Kuo
Pennsylvania State University
University Park, Pennsylvania

Volume 218
PROGRESS IN
ASTRONAUTICS AND AERONAUTICS

Frank K. Lu, Editor-in-Chief
University of Texas at Arlington
Arlington, Texas

Published by the
American Institute of Aeronautics and Astronautics, Inc.
1801 Alexander Bell Drive, Reston, Virginia 20191-4344

American Institute of Aeronautics and Astronautics, Inc., Reston, Virginia

1 2 3 4 5

ISBN-13: 978-1-56347-703-4
ISBN-10: 1-56347-703-3/07 $2.50 + .50

Progress in Astronautics and Aeronautics

This page intentionally left blank

Preface

Hybrid rocket propulsion systems have inherent safety and operational features that make them attractive choices for a broad range of applications, including primary propulsion for launch vehicles, upper stage propulsion, tactical and strategic missile systems, and the emerging field of commercial space transportation. Though hybrid rocket motors as we know them today have been investigated for more than six decades, their development and maturation have not been as actively pursued as that of liquid bi-propellant engines or solid rocket motors. Historically, military applications in the United States favored the storability and launch-readiness capabilities of solid rocket motors, while high specific impulse and controllability made liquid engines the system of choice for civil applications. Nevertheless, recent and growing emphasis on greater propulsion safety, reduced development and recurring costs, insensitive munitions, environmentally-benign propellants, propulsion system robustness and reliability, and a high degree of operability have heightened interest in hybrid propulsion systems for commercial space applications and military propulsion programs. In response, a number of government laboratories, large industrial companies, academic research institutions, and small businesses have implemented hybrid rocket research and development efforts that have, within the past decade, led to significant state-of-the-art advancements in hybrid rocket propulsion. Equally important is the ongoing international interests in hybrids in France, Germany, Italy, Israel, Turkey, India, China, Japan, and other countries. It is also very significant that the recent historic flight of SpaceShipOne, the first privately-developed manned vehicle to successfully reach the edge of space, was powered by a hybrid rocket motor with very reasonable cost of development.

While many exceptional researchers have contributed to the hybrid literature over the years, no major text, devoted solely to hybrid rocket combustion and propulsion, had been prepared prior to this volume. In 2001, at the AIAA Hybrid Rocket Technical Committee summer meeting in Salt Lake City, Utah, during the 37th AIAA/ASME/SAE/ASEE Joint Propulsion Conference, the need for a professional text to organize and present the fundamentals of hybrid rocket combustion, as well as to collect and promote more recent advancements, was identified. During subsequent Joint Propulsion Conferences, the desired content of the text was established and experts in various aspects of hybrid rockets were invited to contribute, resulting in the current volume.

Fundamentals of Hybrid Rocket Combustion and Propulsion is designed as a reference text for industrial designers, propulsion system analysts, test engineers, academic researchers, and graduate/undergraduate students studying chemical propulsion. The contents are organized to cover broad aspects of hybrid rocket combustion, including: theoretical and experimental approaches to solid-fuel regression rate characterization, both analytic and numerical modeling of hybrid rocket internal flow fields, transient hybrid combustion phenomena, various fuels and oxidizers used in hybrid rocket combustion, scaling effects

relevant to hybrid motors, practical applications, and challenges for continued advancements in the hybrid rocket field. Fifteen chapters, all peer-reviewed by experts in this area, comprise this volume. While it is by no means comprehensive, we hope that this text will serve as a useful springboard for future research and development efforts by industrial, government, and academic scientists and engineers so that the outstanding features of hybrid rockets will be fully realized.

Martin J. Chiaverini
Kenneth K. Kuo
December 2006

Acknowledgements

The publication of this volume would not have been possible without the contributions of a large number of individuals. First, we sincerely thank all the chapter authors for their great efforts in preparing and revising their manuscripts. In an effort to create synergy among the chapters, many authors also volunteered to review chapters that fell within the range of their expertise. These efforts are greatly appreciated. In addition, many other individuals deserve recognition for contributing their time and talents in providing chapter reviews, including Timothy Barber, Joshua Batterson, Grégoire Casalis, Millicent Coil, Eric Dauenhauer, Paul Gloyer, Erin Halpenny, Dale Jackson, Darren Kearney, Tim Knowles, Peter Kostka, William Knuth, Brian Maicke, Charles Martin, Erin Muldoon, Arie Peretz, Marvin Rocker, Tony Saad, Arthur Sauer, Kim Story, Prem Venugopal, Anand Vyas, and Brian Wygle.

Many members of the hybrid propulsion community and AIAA Hybrid Rocket Technical Committee offered valuable suggestions for developing the content of this volume. These individuals include Terry Abel, Brian Cantwell, Scott Claflin, Robert Frederick, Steve Frolik, Robert Geisler, George Hating, Benveniste Natan, Andrew Prince, John Remen, Eric Rohrbaugh, and Brett Williams.

We also wish to thank Rodger S. Williams, Alex McCray, and Janice Saylor of the AIAA for their invaluable assistance and support in the preparation of this volume.

Martin Chiaverini would also like to thank his wife, Jennifer, and sons, Nicholas and Michael, for their love and support during this endeavor.

Kenneth Kuo would also like to thank his wife, Olivia, and daughters, Phyllis and Angela, for their caring and encouragement during this book preparation.

This page intentionally left blank

Table of Contents

This page intentionally left blank

Chapter 1

Overview and History of Hybrid Rocket Propulsion

David Altman*
Space Propulsion Group, Inc., Menlo Park, California 94025
and
Allen Holzman**
Cupertino, California 95014

I. Introduction

A HYBRID rocket uses both a liquid and a solid as propellants. In the typical classical hybrid, the fuel is a solid and the oxidizer is a liquid (Fig. 1). Although there are many components that are common to the liquid and the solid rocket, the operation of a hybrid is distinctly different. In the solid rocket, the oxidizer and fuel are intimately mixed in the single solid phase and combustion occurs when the exposed surface is heated by the combustion flame to the ignition temperature. In the liquid rocket, both oxidizer and fuel are intimately mixed in the vicinity of the injector to form a combustible mixture. In both cases, therefore, everywhere in the combustion chamber there is a uniform mixture of both oxidizer and fuel. The hybrid, however, burns as a macroscopic turbulent diffusion flame where the oxidizer-to-fuel ratio (O/F) varies down the length of the chamber, ending at a composition that determines the motor performance.

Why has the hybrid provided an attractive alternative to the conventional liquid or solid rockets? Although the liquid rocket is an efficient high-performance system, it is quite complex and costly with all of the required plumbing. The solid motor avoids this problem by premixing the fuel and oxidizer in a solid form that is dense and compact. The major disadvantages, however, are the explosive danger and the lack of thrust control or termination. Although the propulsion system per se may be cheaper, these latter disadvantages translate to a more costly vehicle design to accommodate such requirements as acceleration, atmospheric heating, and shutdown. The hybrid rocket, with half the plumbing of the liquid

*Chairman.
**Aerospace Consultant.

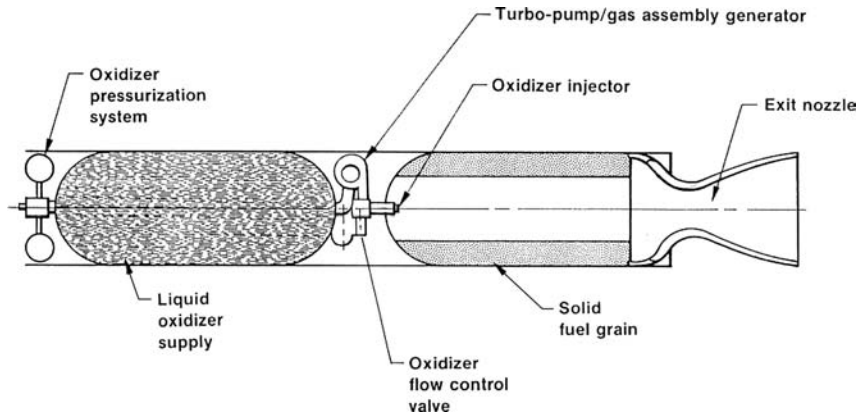

Fig. 1 Hybrid rocket schematic.

but retaining its operational flexibility and avoiding the explosiveness of the solid, therefore, provides an attractive alternative option. Because of its simplicity of operation, safety, nonexplosiveness, and low cost, the hybrid motor has been the favorite for amateur academic groups.

A. Classifications

There are many classifications of hybrid combustion systems. The classical system combines a solid fuel with a liquid or gaseous oxidizer. The classical system has been the most evaluated type, and all of the other concepts are variations on this design. The advantage of the classical concept is that there are many solid fuels such as hydrocarbons (rubbers and plastics) and metals and a wide variety of liquid oxidizers such as oxygen, F_2/O_2 (FLOX), hydrogen peroxide, nitric acid, nitrogen tetroxide, and nitrous oxide.

In the 1950s, reverse hybrids were evaluated. This concept uses a solid oxidizer and liquid fuel. It was not as practical as the classical system, because the solid oxidizer was difficult to fabricate and had to be mixed either with an inert filler or with a small percentage of fuel to press or mold the grains. The inert filler reduced the attainable performance, and the small amount of fuel mixed with the solid oxidizer produced a potentially hazardous mixture.

There is another variation in the hybrid combustion concept that utilizes bipropellant combustion with a third component such as a metallized fuel. This configuration, called a tribrid, uses an oxygen/hydrogen central core within either a cast beryllium-loaded polybutadiene (PB) fuel grain or pressed Be powder mixed with a small amount of Teflon as a binder. That propellant system has the highest known specific impulse together with a very high combustion temperature, over 5000 K. The tribrid is a convenient way of getting Be in the combustion zone, thus avoiding the problems of a slurry with liquid hydrogen.

There is also the solid-fuel ramjet that employs a solid fuel and ram air as the oxidizer. In contrast to the classical liquid-fuel ramjet, it has no liquid piping, but the fuel has a low burn rate due to the dilution of the oxygen in the air. This deficiency can, of course, be lessened by the addition of a solid oxidizer to the fuel.

A further version of the hybrid ramjet is the ducted rocket where a fuel rich solid propellant is burned to produce a flame that then flows through a nozzle and mixes with ram air to generate a roughly stoichiometric flame of optimum performance.

B. Advantages and Disadvantages

The fundamental difference between a classical hybrid and the liquid or solid rocket leads to a number of distinguishing characteristics. The advantages are as follows:

1) Safety. The fuel is inert and can be manufactured, transported, and handled safely in accordance with standard commercial practice. The system is nonexplosive because an intimate mixture of oxidizer and fuel is not possible.

2) Simplified throttling and shutdown. The engine can be throttled by modulating the liquid flow rate, which is simpler than in a liquid rocket where two flow rates must be synchronized while being modulated. In the hybrid rocket, the fuel flow rate, which results from vaporization from the solid surface, automatically adjusts to the change in oxidizer flow rate. Consequently, thrust termination is simply accomplished by turning off the liquid flow rate, a feature of considerable significance in an abort procedure.

3) Grain Robustness. Unlike solid rockets, fuel-grain cracks are not catastrophic because burning only occurs down the port where it encounters the oxidizer flow.

4) Propellant versatility. The selection of propellants is much greater than with either liquids or solids. In contrast to liquids, solid constituents, such as dense energetic metals, can be added to the fuel to enhance both performance and density without resorting to slurries. Also, in contrast to solids, the liquid oxidizers provide much higher energy levels.

5) Temperature Sensitivity. Because the temperature effect on burn rate is small (as in liquids), ambient launch temperature variations have little effect on operating chamber pressure. Thus, the concern in solid rockets in designing for a maximum expected operating pressure (MEOP) is greatly reduced.

6) Low Cost. The total operational cost for hybrid systems benefits greatly from the safety features and inert propellant. Manufacture of the fuel can be done in a commercial facility that does not require the large acreage and many buildings for solid-propellant manufacture. As a consequence, the fuel plant can be located at or near the launch site. Furthermore, the system can tolerate larger design margins, resulting in a lower fabrication cost.

These advantages, however, are not enjoyed without some disadvantages, such as:

1) Low Regression rate. The small resulting fuel web means that most combustion chambers over a foot in diameter require multiple ports to provide adequate burning surface to meet the required thrust. This characteristic, however, is desirable for long-duration applications with a low-thrust requirement such as target drones, hovering vehicles, and gas generators.

2) Low bulk density. A consequence of the low regression rate is that a large grain surface area must be provided to supply the required thrust. This is generally

done with multiple ports that lead to a relatively low volumetric fuel loading or bulk density. The number of sharp corners in a multiport dual grain also leads to a moderate amount of unburned fuel slivers. However, recent efforts to increase the regression rate have reduced this disadvantage.

3) Combustion efficiency. The nature of the large diffusion flame results in a lower degree of mixing and, hence, a lower impulse efficiency. This loss is generally 1–2% greater than in either liquids or solids. In comparison with solids, however, the delivered vehicle performance is greater because of the higher theoretical I_{sp}.

4) O/F shift. The opening of the port during burning causes an O/F shift with burning time, which can lower theoretical performance. However, with proper design of the initial O/F, this loss is usually minimal, and ballistic calculations show that it can be held to less than 1% for a typical hybrid.

5) Slower transients. The ignition transient is slower, as well as the thrust response to throttling. In most practical applications, where reproducibility is more important than speed of response, this aspect is not very significant.

C. Potential Applications

The hybrid rocket can be used in practically all of the applications where rockets are employed. This is because of the versatility of propellants available, the large range of performance capability, and the thrust flexibility including shutdown. There are certain applications, however, where the hybrid is superior. The following listing shows examples of applications:

1) Sounding Rockets. The high-altitude, or sounding rocket, represents one of the most extensive uses to date. Because of its low cost, safety of operation, and wide range of easily available propellants, it continues to be a favorite for amateurs and academics.

2) Auxiliary Power Units. These units are gas generators for various applications such as powering turbines, hot-gas generation (which can be either fuel- or oxidizer-rich), torches, etc.

3) Tactical Rockets. If a compact envelope is not too restrictive, the hybrid is ideal because its throttling (energy management) capability is a significant advantage. Throttling involving boost and sustain capability on demand are desirable features not easily attainable with solid motors.

4) Space Engines. The hybrid features of throttling and stop/restart are particularly desirable to provide either a coasting phase or thrust termination for exact final velocity in orbit insertion. This allows the hybrid to perform the dual function for both velocity increment and orbit insertion.

5) Thrust Augmentation. This is an ideal application for the hybrid because the throttling feature can be used to shape the exoatmospheric trajectory for maximum performance. It also allows for the possibility for steering by differential throttling of side-mounted thrusters.

6) Large Launch Boosters. The largest hybrid engine that has been test fired to date is in the 110-kN (250,000-lb) thrust class. This was done by two organizations, by American Company Rocket (AMROC) in the early 1990s and by the Lockheed, Chemical Systems Division (CSD), and Thiokol (ATK) consortium during 2000–2002. These engines used liquid oxygen (LOX) hydroxy-terminated

polybutadiene (HTPB) as propellants. The incentive for this development was to provide a throttling and thrust termination capability for both vehicle performance improvement and abort capability in the event of a system failure. This interest was partially stimulated by the Space Shuttle *Challenger* failure in 1986.

II. Early History, 1933–1960

The early history of hybrid rocket development dates back to the early 1930s, during which time the initial developments of both liquid and solid rockets occurred. Actually, solid motors were first used because of the early gunpowder history several centuries earlier. The solid rockets, which were investigated by such well-known figures as Robert Goddard, fell into early disrepute because of their explosive hazard. Germany's professor, Hermann Oberth, one of the pioneers in rocketry, warned experimenters, "Powder believes it must explode all at once; from the old use in shells and guns, it is too well-trained always to destroy." Within a few years of this ominous dictum, there occurred in 1933 a tragic demonstration of it. The early rocket engineer, Reinhold Tiling, and three of his assistants were killed in a detonation of 40 lb of powder fuel. Meanwhile, Goddard, who had started his work with powder fuels, decided to avoid the explosive hazard of a large quantity of solid fuel in one container by injecting small quantities of the powder into a small combustion chamber. His objectives were to control burning rate, achieve stop and restart, and to avoid exposing the complete fuel to the heat of combustion. Because of the complexity of feeding powder into the combustion chamber, Goddard eventually turned to liquid propulsion. It took him nearly 22 years of propulsion research, until 1935, before he was able to achieve his most successful flight of a liquid rocket, which attained an altitude of 1.9 km.

The first recorded effort, as a forerunner to the hybrid rocket, was reported by Sergei P. Korolev and Mikhail K. Tikhonravov within the scope of the Russian GIRD.[†] A flight was made of the GIRD-09 on 17 August 1933. It was approximately 7 in. in diameter by 8 ft long, had a thrust of 500 N for 15 s and attained an altitude of 1500 m. The propellants were gasoline/collophonium (gelled gasoline) suspended on a metal mesh and LOX under its own pressure. Although this is not a hybrid as we currently classify it, the literature listed as such.

Shortly afterward in 1937, serious efforts to experiment with hybrid motors were initiated. These included motor tests conducted at I. G. Farben by Leonid Andrussow, O. Lutz, and W. Noeggerath. They tested a 10-kN hybrid motor using coal and gaseous nitrous oxide. These tests shared the same unsuccessful results as Oberth's experiments with LOX and graphite. Their lack of success was due to carbon's very high heat of sublimation, which results in a negligible burning rate.

The earliest significant effort of a flightworthy hybrid rocket was conducted in the mid-1940s by the Pacific Rocket Society that employed LOX in conjunction with such fuels as wood (Douglas fir), a wax loaded with carbon black, and, finally, a rubber-based fuel [1, 2]. The Douglas fir rockets that were tested in 1947 were designated as experimental Douglas fir (XDF-#). The initial recorded configuration

[†]Data available on-line at http://www.hybridracketen.de/Homepage/Old/Antares/Hybridracketen/history.htm.

(XDF-3) used a nozzle made out of Douglas fir, which was soaked in a solution of zinc and ammonium chlorides, apparently based on a notion that this would provide a heat-resistant quality. The XDF-3 nozzle design was quickly eliminated when only 15 s of low-pressure combustion effectively demolished the nozzle. The next experiment, XDF-4, was essentially the same general configuration, but the wood nozzle now contained a thick molded lining of calcium sulfate. An accurate evaluation of the design could not be made because, after 2 s of firing time, the static test motor broke away from the test stand (because the motor reached a thrust of 40–60 lb, which was in excess of the design capability of the stand) and flew over the heads of the observers landing under a Jeep parked nearby. The Society went through 19 more designs before finally arriving at XDF-23, which used a more practical configuration, containing a LOX rubber-base fuel and an aluminum alloy nozzle. It successfully flew in June 1951, reaching an altitude estimated to be about 30,000 ft.

Although the Society apparently did not report any ballistic analyses, they did have an accurate concept of hybrid burning as evidenced by the following statement: "The chamber pressure of a solid–liquid rocket engine is proportional to oxidizer flow and not to the internal surface area exposed to the flame. Thus, there is no danger of explosions due to cracks and fissures in the charge as with solid propellant rockets commonly used for boosters" [3].

The first analytical investigation of the combustion process of a solid-fuel ramjet with laboratory tests was done by H. Bartel and W. Rannie in 1946 at the Jet Propulsion Laboratory (JPL). The propellants were graphite and air, and the purpose was to investigate its performance as a solid-fuel ramjet. Solid-fuel ramjets are hybrids where the air is the oxidizer that is scooped up by inlets from the atmosphere. This effort was abandoned when it was realized that because of the high sublimation heat of carbon, combustion would be extremely slow leading to impractical low-thrust levels. While at JPL, Rannie approached me (Altman) at that time regarding his inability to get any useful thrust from his ramjet. (He jokingly referred to this simple concept as the witches' means of flight on a broomstick.) I was following the controversy on the proper heat of sublimation of carbon in that period, which ranged from values of 124 kcal/mol (Pauling) to over 200. The settled value from spectroscopy was 173 kcal/mol (Brewer, Gilles and Jenkins), and this high value explained the lack of success in using carbon as a hybrid fuel.

An early analytical and experimental investigation in hybrids was made by George Moore and Kurt Berman at General Electric Company in Schenectady, New York, initiated in the late 1940s and continued to 1956. Their engine was based on the use of a hypergolic hybrid rocket propulsion system using 90% hydrogen peroxide as the oxidizer and polyethylene as the fuel [4]. The peroxide was decomposed in a silver screen catalyst bed, and the fuel grain was composed of a tubular or rod and tube configuration as shown in Fig. 2. The early motivation for this approach was to augment the performance of peroxide as a monopropellant. They observed that when a relatively small amount of fuel was added, about 15% of the propellant weight, the I_{sp} increased 70% from 136 to 230 s. This was accomplished by a relatively small extension of the combustion chamber between the catalyst bed and the nozzle. Over 300 tests were made, 100 of which were made with the rod and tube configuration. In this early work, the authors concluded that 1) longitudinal uniformity of burning was remarkable, 2) grain cracks had no

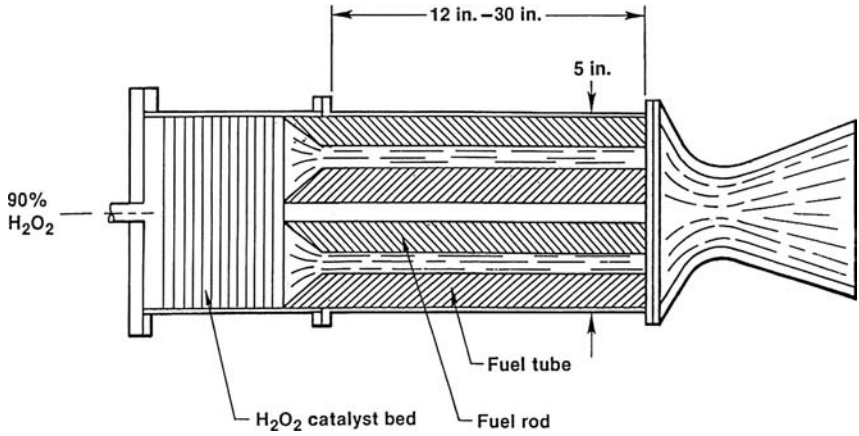

Fig. 2 H_2O_2-polyethylene hybrid rocket (General Electric).

effect on combustion, 3) hard starts were never observed, 4) combustion was stable because the fuel surface acted as its own flameholder, 5) throttling was easily accomplished by a single valve, and 6) a high liquid-to-solid ratio was desirable to simplify uniform burning in the combustion chamber. On the negative side, the investigators noted that the inherent thermal instability of peroxide was a problem and that it was very difficult to vary the burning rate by more than a factor of two. The authors' observations and conclusions were largely substantiated in later years.

In 1952, William Avery and coworkers at the Applied Physics Laboratory of John Hopkins University conducted burning tests with a reverse hybrid rocket propellant system [4]. The propellants tested were benzene and jet propellant (JP) fuel, with potassium perchlorate, ammonium nitrate, and ammonium perchlorate as oxidizers. They concentrated on JP ammonium nitrate because it represented perhaps the lowest cost propellants available, which was the primary motivation for the investigation. Unfortunately, this propellant combination was difficult to burn. The major problems encountered in their work were rough burning and rather poor performance. Note that the liquid-to-solid ratio (F/O) of this propellant combination is in the range of 0.035, which is about 200 times smaller than that used by Moore and Berman.

Other versions of the reverse hybrid were studied by both Thiokol and United Technology Center (UTC) (renamed CSD ~1974) in the mid-1960s using hydrazine-based liquid fuels and such solid oxidizers as ammonium perchlorate, hydrazinium diperchlorate, and nitronium perchlorate. These solid charges were pressed, usually with a non-reactive fluorocarbon as a binder. Efforts were abandoned because of poor combustion behavior and insufficient performance improvement to justify the difficulties experienced in compressing the charges.

III. Typical Fuels and Oxidizers

Because of the characteristics of a hybrid rocket, the fuels and oxidizers that have been tested far exceeds those used in liquid and solid rockets combined. The vista

of available propellants is greatly expanded because two phases are available. The classical hybrid containing an inert solid fuel and liquid oxidizer has the largest inventory of propellants, whereas the reverse hybrid is more restricted. This is because suitable solid oxidizers are limited in number, are usually crystalline, and are difficult to cast in moderate-to-large sizes because of mechanical property limitations.

Aside from the natural rubbers, the largest class of suitable fuels, based on performance and mechanical properties, is the polymeric synthetic rubbers based on the polybutadiene monomer, (PB with the formula C_4H_6). Typical polymers based on PB PB–acrylonitrile (PBAN), PB–acrylic acid (PBAA), HTPB, and carbon-terminated PB (CTPB). The most popular of this group, based on cost and commercial availability, is HTPB. As with all of these polymers, they require curatives to polymerize, the favorite ones being the diisocyanates (DI) such as TDI, DDI, and IPDI. Thus, each propulsion company has its own version of the polymer based on its purity specification to the supplier, the selected curative, and other additives to impart special properties. A good working composition for the PBs is $C_4H_6O_{0.1}$. Other hydrocarbons that have been used, mostly in smaller motors to date, are the paraffin waxes, polyethylene (a higher molecular weight version of paraffin), Plexiglas (Lucite), metatoluene diamine/nylon, and, in earlier small-scale testing, the common fuels, coal and wood.

The formulated fuels, PB polymers, and paraffin waxes, have the virtue of allowing performance additives. A partial list of these additives include Al, AlH_3, Li, LiH, $LiAlH_4$, Li_3AlH_6, B, $B_{10}H_{14}$, $LiBH_4$, aromatic amines, anthracene, etc. These additives can enhance either motor performance through I_{sp} improvement or vehicle performance through increased density and, hence, mass fraction. In some cases, as with Al, for instance, optimum performance results in a shift to a lower O/F that can be beneficial in reducing the gas corrosivity. Other additives, such as amine compounds, have been added to impart hypergolicity when used with HNO_3 or N_2O_4.

Another class of fuels is the cryogenic solids, including pentane, methane, CO, O_2, and H_2. The original stimulus for this research was to obtain hybrid-propellant combinations that are competitive with the high-performance liquid cryogenic propellants. Despite these virtues, the expense, insulating weight penalty, and inconvenience of handling these cryogens in the solid state overshadow the advantages.

The hybrid liquid oxidizers and those used in the liquid rocket engines are essentially the same. These include O_2, N_2O, N_2O_4, HNO_3, inhibited red fuming nitric acid (IRFNA), FLOX ($\frac{2}{3}$ F_2 + $\frac{1}{3}$ O_2), H_2O_2, CTF (ClF_3) and hydroxyl amine nitrate (HAN). Of this group, the most energetic are O_2 and FLOX. Although F_2 is very energetic, it has not reached operational status because of its toxicity and corrosivity. FLOX, on the other hand, is much less corrosive, can be used with conventional carbonaceous fuels, and is much less hazardous to use.

Table 1 shows a list of some propellant combinations, nearly all of which have been tested at some time or other. The high-performing solid cryogenic propellants have I_{sp} values only slightly less than the noncryogenic liquid counterparts because the heat of fusion is small relative to the combustion heat. The reverse hybrids are low performing except for nitronium perchlorate (NP), which, however, is thermally sensitive and potentially explosive. The combination

Table 1 Performance of hybrid propellants, $Pc = 500$ psia and $Pe = 14.7$ psia

Fuel	Oxidizer	Optimum O/F	Sea level I_{sp}, s	c^*, ft/s
HTPB	LOX	1.9	280	5972
PMM($C_5H_8O_2$)	LOX	1.5	259	5449
HTPB	N_2O	7.1	247	5264
HTPB	N_2O_4	3.5	258	5456
HTPB	RFNA	4.3	247	5219
HTPB	FLOX(OF_2)	3.3	314	6701
Li/LiH/HTPB	FLOX(OF_2)	2.8	326	6950
PE	LOX	2.5	279	5877
PE	N_2O	8.0	247	5248
Paraffin	LOX	2.5	281	5920
Paraffin	N_2O	8.0	248	5268
Paraffin	N_2O_4	4.0	259	5469
HTPB/Al(40%)	LOX	1.1	274	5766
HTPB/Al(40%)	N_2O	3.5	252	5370
HTPB/Al(40%)	N_2O_4	1.7	261	5509
HTPB/Al(60%)	FLOX(OF_2)	2.5	312	6582
Cellulose ($C_6H_{10}O_5$)	GOX	1.0	247	5159
Carbon	Air	11.3	184	4017
Carbon	LOX	1.9	249	5245
Carbon	N_2O	6.3	236	4992
	Cryogenic hybrids			
Pentane(s)	LOX	2.7	279	5870
CH_4(s)	LOX	3.0	291	6140
CH_4(s)/Be(36%)	LOX	1.3	306	6292
NH_3(s)/Be(26%)	LOX	0.47	307	6452
	Reverse hybrids			
JP-4	AN	17.0	216	4651
JP-4	AP	9.1	235	5007
JP-4	NP	3.6	259	5476

that most closely resembles the LOX/JP-4 (or kerosene) liquid propellant is the LOX/paraffin hybrid followed closely by LOX/HTPB. Wood, which is approximated by cellulose, shows a fair performance with gaseous oxygen (GOX). As expected, the lowest-performing combination is carbon/air due to the dilution of the oxygen by nitrogen.

A. High-Energy Combinations

In the mid-1960s, a series of NASA-sponsored studies was begun at UTC devoted to high-energy space engines. One concept was based on the use of the very energetic reaction between lithium and hydrogen with fluorine, elements at opposite ends of the Mendeleev periodic table. With the use of the fundamental versatility of the hybrid, the lithium was incorporated in an HTPB binder and

the fluorine was mixed with oxygen to create FLOX, a fluorine/oxygen mixture containing about 70% fluorine. This solution optimizes the performance of a typical hydrocarbon system because it allows most of the oxygen to combine with the carbon to form CO, whereas the fluorine combines both with the hydrogen and lithium. To satisfy conductivity restrictions of the binder and avoid melting of the lithium, a combination of lithium and lithium hydride was finally developed for the propulsion system [5]. The motor diameter was 35 in. (1.07 m) and had an 11 port wagon-wheel grain configuration. The propellant was hypergolic, even on a refire six days later. This throttleable system burned smoothly and exhibited high performance with an I_{sp} efficiency of 93%, corresponding to a delivered vacuum impulse of about 380 s at an area ratio of 40/1. This firing is shown in Fig. 3 as it appeared on the cover of the 26 January 1970 issue of *Aviation Week and Space Technology*.

Another approach to high-performance space engines, also under a NASA contract, was based on the beryllium/oxygen/hydrogen system. The concept is analogous to the nuclear rocket where an intense energy source is used to heat H_2, a low molecular weight gas. The specific heat of combustion of beryllium is more than 40% greater than aluminum, a common energetic additive. As a consequence, this combination yields the highest calculated performance in a chemical rocket with readily available chemically stable ingredients. The plan was to incorporate beryllium into a binder that would act as the structure for a low-conductivity fuel

Fig. 3 High energy upper stage hybrid-fuel: Li/LiH/PBAN oxidizer: F_2/O_2.

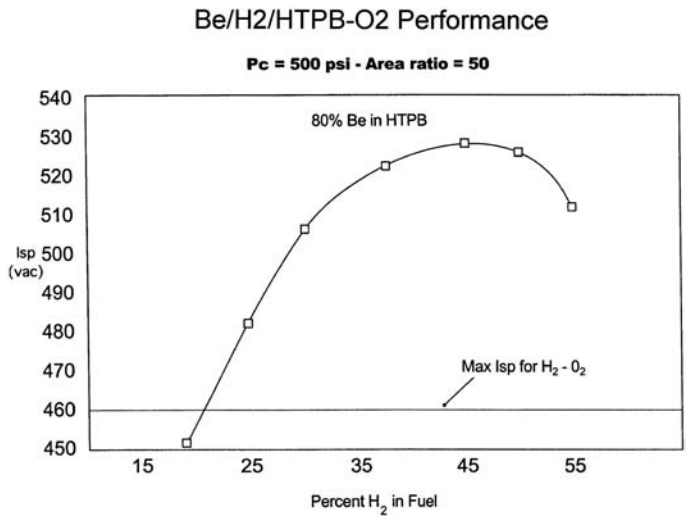

Fig. 4 Be/H_2/HTPB-O_2 tribrid.

grain, a requirement for satisfactory hybrid operation. Calculated I_{sp} values for 80% Be in HTPB are shown in Fig. 4, where a 65-s improvement over H_2/O_2 is observed. This investigation was initiated with aluminum for testing convenience, but the project was later abandoned because of the anticipated toxicity problems that would be associated with the handling and development testing of Be.

IV. Flight Programs

A. Target Drones

In the mid-1960s, a requirement arose for target drones that could fly at high altitudes for durations up to 5 min. The unit was to be launched at an altitude of about 12 km and accelerated to 30 km at Mach values between 2 and 4 attaining a range up to 90 km. This clearly called for a boost and low-thrust sustain unit that the hybrid motor could easily satisfy. UTC and Beech Aircraft began work on the Sandpiper, using a storable propellant combination composed of mixed oxides of nitrogen (MON-25) as an oxidizer (25% NO, 75% N_2O_4) and a polymethyl methacrylate (PMM)/Mg fuel. The first of six flights occurred in January 1968 at the Eglin Air Force Base missile range, 18 months after start of the program. Throttleability over a range of 8:1 was required after launch at about 40,000 ft to attain speeds up to Mach 4 at an altitude of 100,000 ft. The flight duration was in excess of 300 s.

Two more drone programs followed the Sandpiper (Table 2). A second U.S. Air Force program, which required a heavier payload, was the High Altitude Supersonic Target (HAST). In contrast to the Sandpiper, the thrust chamber diameter was increased from 10 to 13 in., the propellant changed to IRFNA/PB/PMM (PB/plexiglass), and the oxidizer was pressurized by a ram air turbine instead of N_2. The thrust range on command was controlled by a throttle valve providing

Table 2 Hybrid drone programs

Program	Description
Sandpiper	NO/N_2O_4 oxidizer, PMM/Mg fuel 13-in. outside case diameter 6 flights in 1968 Burn times to 300 s Throttleable over 8:1 range
HAST	IRFNA oxidizer, PMM/PB fuel 13-in. outside case diameter 38 built in 1970s Ram-air pressurization of oxidizer Recoverable Throttleable over 10:1 range
Firebolt	40 built, early 1980s Launch at 40,000 ft, $M = 1.5$ Ram-air pressurization Cruise at 100,000 ft, $M = 4.0$ Recoverable Throttleable over 10:1 range

a 10/1 range. The grain configuration was also changed from a single cylindrical port to a cruciform using four liquid injectors. Unlike the Sandpiper, which was expendable, the HAST was recoverable by use of an onboard drogue chute and retrieved in midair by helicopter. A later version of this target missile was initiated in 1980 with CSD and Teledyne Ryan Aircraft as the airframe contractor. The propulsion configuration and performance was the same as for HAST. In this program, 48 thrust chamber assemblies were delivered. The program was successfully completed in the mid-1980s. These drones were the only hybrid flight programs built to military specifications.

B. High-Altitude Sounding Rockets

During the 1960s, two European countries engaged in hybrid studies leading to flight tests of sounding rockets. The organizations were ONERA [in conjunction with SNECMA and Société Européenne de Propulsion (SEP)] in France and Volvo-Flygmotor in Sweden. The ONERA development [7] was centered on a hypergolic propellant combination based on nitric acid (or RFNA) and an amine fuel consisting of metatoluene diamine/nylon. It constituted the Lithergol experimental (LEX) series. The motor was throttleable over a 5/1 range to optimize flight performance. The first flight of this vehicle occurred in April 1964, followed by three flights in June 1965, and four flights of an improved version in November 1967. All eight flights were successful, reaching altitudes in excess of 100 km, which was a record for that time period. They then embarked on a larger, more complicated version, the LEX 04, and conducted 12 successful ground tests. No flights, however, were conducted with this motor.

The Swedish program was initiated by Volvo Flygmotor in 1962 and was also based on a hypergolic combination using nitric acid and Tagaform (PB plus an aromatic amine). This propellant was used in the HR-3 hybrid vehicles, which had a diameter of 125 mm, a length of 2.86 m, a propellant mass of 5.6 kg, and an average thrust at 35 bar of 2.3 kN. There were two successful flight trials with the HR-3 rocket probe using this fuel, one on 30 September 1965 and the other 1 October 1965. Because of the softening point of 65°C of the fuel, no further testing occurred. An improved version of this fuel was later developed (Sagaform A) with better physical properties, such as a softening point of 143°C, a specific gravity of 1.18, and an ignition delay of 8 ms. Two sounding rockets were planned using Sagaform A, the SR-1 and SR-2. The SR-1 design listed a payload of 25 kg, a launch weight of 361 kg, a propellant weight of 264 kg, and a calculated altitude of 200 km, whereas the SR-2 design called for a capability about four times greater. These vehicles were scheduled for flight in the early 1970s but there does not appear to be any published record that this took place (private communication from G. Broman, 7 October 1970, and S. Bjornholt, March 1971 included plans for flights in the 1971–1975 time period).

Note that these early European hybrid programs utilized hypergolic propellants based on nitric acid and a solid amine-containing fuel. It appears probable that this choice was based on the German experiments during the early 1940s on hypergolic liquid propellants based on nitric acid and hydrazine. These experiments also influenced the choice of the hypergolic nitric acid/aniline/furfuryl alcohol propellant subsequently employed by the Jet Propulsion Laboratory (JPL) in the Corporal vehicle in the late 1940s. It was natural, therefore, that the early hybrid propellants chosen used a solid amine compound with nitric acid as propellants.

There were two significant sounding rocket programs after 1995 in the United States. One was the Hyperion Sounding Rocket by the Environmental Aeroscience Corp (eAc) using N_2O and HTPB as propellants ([7] and private communication with K. Kline of eAc). They employed a single-port slotted grain to provide an increased burning surface area. The vehicle height was 18 ft 8 in. (5.7 m) with a 6 in. (152 mm) diameter. The propellant mass fraction was 50% and the delivered I_{sp} was 205 s. Four rail-launched flights took place, two on 18 November 1996 (within 90 min of each other), the third on 8 January 1997, and the fourth on 25 April 1997. The first two flights were planned for low altitude of ~25,000 ft, which was achieved by off-loading the oxidizer and adding ballast. The next two flights carried the full propellant load of 103 lb and achieved altitudes of 36.5 and 33.8 km, respectively. These flights represent the first time a self-pressurized oxidizer was successfully employed in flight.

A few years later on 18 December 2002, the Lockheed Martin Corporation flew a larger hybrid rocket based on LOX and HTPB [8]. This was a multiport motor with a height of 57 ft (17.4 m) and a diameter of 2 ft (61 cm). It had an initial thrust of 60,000 lb (267 kN) and achieved an altitude of 44 miles (~71 km). Although the altitude was somewhat less than the predicted 62 miles, this flight represented the largest hybrid sounding rocket successfully flown to that date. The two previous attempts at larger sounding rockets by Starstruck and AMROC failed to complete their missions due to stuck oxidizer valves (cf., later section on large-scale hybrids).

V. Fundamental Studies

In the decade of the 1960s, there was a great increase of interest in hybrid propulsion in the United States. Among the U.S. Army, Navy, Air Force, and Advanced Research Projects Agency (ARPA), there were over 40 sponsored studies covering a wide area of activities [9]. In addition, several industries pursued research with their own funds. The U.S. companies involved at that time included UTC, Aerojet, Marquardt, Rocketdyne, Thiokol, Atlantic Research, and several of the government agencies including the U.S. Naval Ordnance Test Station (NOTS). Of this group, a major contributor was UTC, and a summary of its activities follows.

In late 1959, shortly after UTC was formed, Altman began assembling a technical group to investigate the fundamentals of hybrid rockets and their potential as alternates to both solids and liquids. (UTC developed the large solid boosters for the Titan vehicle, and as a consequence of its success, many of its design elements were subsequently used in the shuttle and the Ariane 5.) This group contained over 12 professionals exploring the fundamental science of ballistic behavior and engineering development. Within the decade of the 1960s, in addition to basic ballistic studies, they experimented with a wide variety of fuels and oxidizers. These included IRFNA, N_2O_4, MON, FLOX, O_2, and air as oxidizers and the various PBs with such additives as Al, Mg, Li, AP, and AN.

A. Hybrid Demonstrator

A rather simple device that accelerated the analytical and experimental analysis of hybrids was the hybrid demonstrator [10] (Fig. 5). This small combustor used several types of igniters including a short pulse of propane or butane with a high-voltage spark plug in parallel with the oxygen flow to ignite the fuel grain. Also used was an electrically heated steel wool in an oxygen flow. This device proved to be safe, inexpensive, and an excellent laboratory tool for investigating interior ballistic

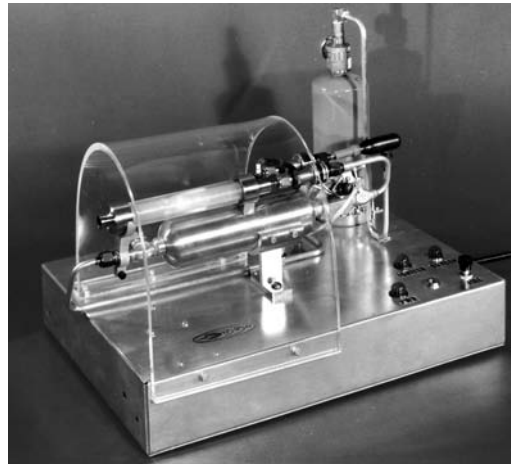

Fig. 5 Hybrid demonstrator.

behavior. It was used to obtain the schlieren photographs of the hybrid combustion process that formed the basis for developing the hybrid regression rate equations by Marxman and Gilbert [11]. One specific example of its application occurred in the study of oxygen dilution effects where it was found that, with a proper flameholding device, operation was successful with an 80% N_2 dilution. This observation, made by Holzman in 1962, subsequently led to the development of the solid-fuel ramjet. Because of the smooth and reliable burning of the demonstrator unit, a lunar lander module was designed using it. Figure 6 shows this system operating in 1969 at the Alabama Space and Rocket Museum in Huntsville as witnessed by Werner Von Braun and E. Buckbee, the Museum Director. Over a period of more than 10 years, over 10,000 tests were performed with dozens of fuels and many oxidizers such as oxygen, 90% hydrogen peroxide, and dilutions of oxygen with nitrogen, argon, and helium.

By 1962, a considerable amount of work had been accomplished, a good portion with the help of the subscale testing [12]. A listing of some of the concepts divulged during that period is as follows:

1) Justification was found for the practical use of a simplified space average regression rate expression, that is, $\dot{r} = a\, Go^n\, L^m$, where Go is the oxidizer flux, L the port length, and a, n, and m are determined empirically.

Fig. 6 Hybrid demonstrator as lunar lander model.

2) Engine design studies were conducted. Equations were developed for the thrust and O/F shift with time, port L/D based on Go and regression rate, stoichiometric length, and thrust-time decay for circular ports. These relations were later used in the design of the drone vehicles.

3) Pressure effect on regression rate was determined. Theoretical studies of hybrid combustion indicate that the regression rates should be independent of pressure except for the case where radiation is significant or where combustion kinetics is dominant. These effects were initially evaluated with PMM and later with PBAN showing little variation for pressures over 90 psia with PMM or between 40 and 715 psia for PBAN. However, for 45% metallized PBAN, a regression rate increase with pressure was noted.

4) Impact of aft chamber L^* and mixers on combustion, c^*, efficiency were determined. For the PMM/O_2 system, c^* was measured for various aft chamber lengths. Data using aft end chamber L^* exhibit a humpback curve when c^* efficiency is plotted vs L^*. This behavior results from the competing effects of additional length to increase residence time but also increases heat loss. In experiments using a perforated mixer plate at the aft chamber entrance, the efficiency was considerably improved. Adding L^* in this case led to a decrease in c^* due to heat loss. The mixer concept was scaled up and tested in a 12-in.-diam hybrid motor using a 45% aluminized grain. The delivered I_{sp} achieved a respectable 92% of theoretical,

5) Use of a plug nozzle for c^* enhancement was investigated. It was found that this restriction upstream of the throat can create a recirculation region where mixing of the oxygen-rich core and the fuel-rich annulus is improved before entering the nozzle. This configuration increased c^* from 85% efficiency in conical nozzles to 95% in a plug nozzle. (Note that the reentrant nozzle partially accomplishes the same purpose.)

6) Temperature sensitivity of regression rate was explored. An expression for the variation of regression rate with ambient temperature was derived, and it was shown to be many times smaller than for typical solid propellants. Experiments validated this conclusion, which means that, in contrast to solid motors, the concern over MEOP in hybrid motor design is insignificant.

7) Efforts were made to increase regression rate. Techniques investigated were solid oxidizer added to the fuel, aluminum addition, and surface roughening by use of screens. These techniques will be discussed further in the section on high regression rate fuels.

8) Oxidizer flooding was studied. The main liquid oxidizer used during this period was N_2O_4. It was found that with a given injector, there was a given maximum value above which flooding occurred in the upstream region of the port. The flooding could be reduced by improved atomization and provision of a heat source in the vicinity of the injector, such as use of a hypergolic agent. To quote the report [12], "This situation is attributable to insufficient heat being generated by the reaction at the point of principal contact to effectively vaporize the liquid." This observation has been confirmed years later where the large motor developments using LOX (AMROC and HPDP programs) were plagued by instabilities.

B. Regression Rate Modeling

A significant accomplishment during that period was the development of a regression rate model by Marxman and coworkers [mainly Muzzy and Wooldridge (see Bibliography)]. It was more complete and versatile than any proposed at that time (cf., Green, Price, and Smoot in the Bibliography). With the schlieren photographs taken by Muzzy as a guide (Fig. 7), a combustion model was established (Fig. 8). The treatment employed turbulent boundary-layer theory showing both a combustion and a momentum layer. It is interesting that the concept of a combustion zone standing off from the fuel surface was successfully treated 10 years earlier by Godsave [at the National Gas-Turbine Establishment (NGTE) in the United Kingdom] to explain droplet burning in a turbine combustion chamber. That expression was also used by Altman at JPL in the late 1940s to calculate the L^* of the Corporal liquid motor assuming that the vaporization time lag was longer than the gas-phase combustion kinetics. The application of this model to hybrid burning was more complex, of course, because it had to consider burning in a high-velocity turbulent flowfield with boundary-layer growth and heat-transfer blockage from the issuing fuel vapor. The first of several papers [11] during this period by Marxman and Gilbert on the boundary-layer combustion was delivered in 1962. (Additional references are listed in the Bibliography.) The resulting regression rate expression took into account the two boundary layers (combustion and momentum), the impact of blowing on reducing the heat flux, the use of a total effective heat of vaporization to account for various thermal reactions at the

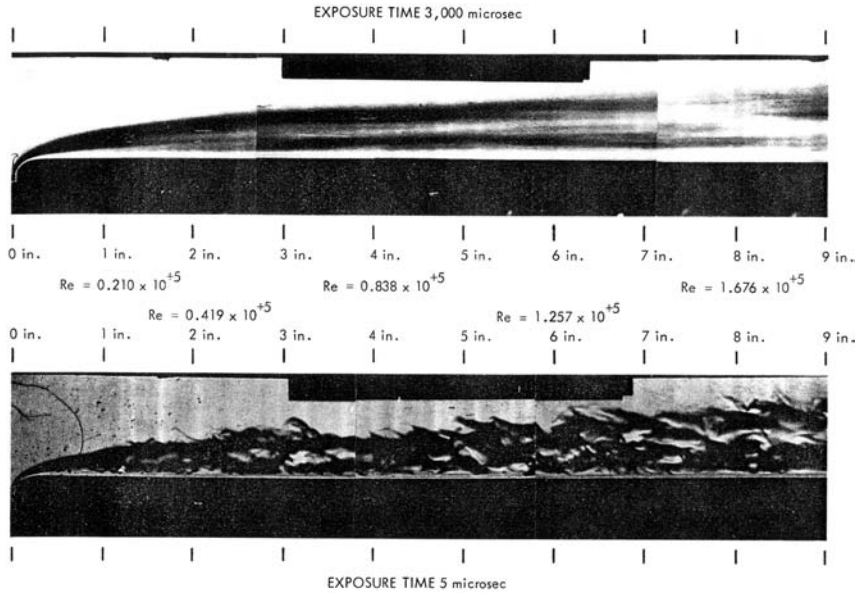

Fig. 7 Hybrid combustion boundary layer Schlieren photographs.

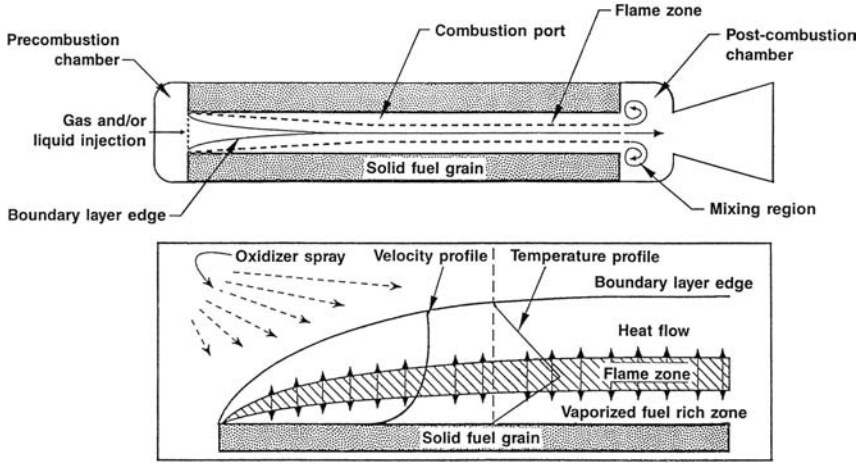

Fig. 8 Hybrid combustion boundary layer.

surface, and the contribution of radiation when coupled with convection. It is still widely used today.

An interesting set of laboratory experiments was conducted by Houser and Peck [13] during this period on the PMM/O_2 system in which they measured the regression rate down the port as a function of the axial length. The grain consisted of a stacked series of cubical blocks, 5 cm on a side, with cylindrical holes 2.5 cm in diameter. There were 12 of these stacked to form a 60-cm-long grain. At two different oxygen flow rates, they measured the weight loss every 15 s for a duration of 180 s. From these measurements, they calculated the port diameters and regression rates as a function both of time and of axial distance. The diameter–time plots were quite smooth, and they fell on the curve predicted by the regression rate expression

$$\dot{r} = aG^n/x^m$$

where $G = Go + Gf(x)$. In particular, although not mentioned by the authors, it may be observed that the measurements further showed the minimum in $\dot{r}$ vs x as predicted in the preceding equation (discussed by Ordahl and Altman [10]). That was the first time such detailed measurements were reported.

Fundamental programs continued for the remainder of the decade at a slower pace, where major attention was paid to motor development. The basic studies included 1) further refinement of the regression rate equations including better understanding of the blowing phenomenon, radiation effects, and its coupling with conductive heat transfer; 2) startup and throttling transients in motors; 3) deep throttling (used in the drone programs) and associated performance loss due to the O/F change, 4) studies on hypergolic fuels that can be used with either N_2O_4 or IRFNA; and 5) studies on propellants to yield high performance (Li, LiH, Be, as fuel additives with LOX and FLOX as oxidizers).

VI. Large-Scale Hybrids

It has always been envisioned that a major advantage for hybrids can potentially be realized in large boosters due to their inherent operational safety, potentially lower cost, throttleability, and shutdown capability. These are features that the solid cannot claim, and although the liquid can, it does so at greater complexity and cost. The challenge has been to demonstrate acceptable grain fabrication and efficient motor operation as the motor dimensions increased. The low regression rate required multiport designs to provide sufficient burning surface for the necessary fuel flow. The further problem had to do with efficient mixing of oxidizer and fuel, which is scale dependent because it results from a macroscopic diffusion process. These problems were addressed by several organizations over a three decade period as discussed next.

The prospect of scaling the hybrid motor to large boosters was first investigated by UTC in the mid-1960s with the hybrid test motor (HTM) series. Under U.S. Air Force sponsorship, the HTM-38 motor (38 in. diam) was built using N_2O_4 as oxidizer and aluminized PB as the fuel. Because of the low regression rate, a 12-port wagon-wheel grain was designed and tested at a thrust level of 40,000 lb. Ignition was provided by a hydrazine injection, which is hypergolic with the oxidizer. The uniformity of burning was quite remarkable, an important observation confirming the practicality of multiport fuel grains as shown in Figs. 9a and 9b [15]. Encouraged by these results, CSD researchers subsequently proposed very large motor designs in which the fuel could be separately cast in convenient segments and bonded together in the motor at the launch site. This manufacturing method was believed to be possible with the hybrid because of the insensitivity of operation

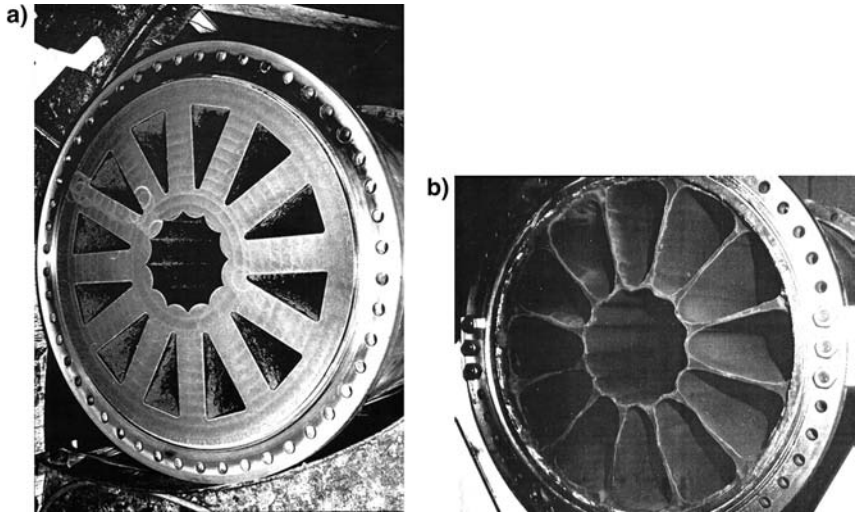

Fig. 9 a) 38 in. dia hybrid fuel grain—as cast. b) 38 in. dia hybrid fuel grain—after test firing.

to internal cracks. This approach, however, was not pursued because it required regression rates much higher than those available at that time.

In the mid-1980s, there were two situations that created a stimulus for reviving interest in the large hybrid rocket. One was the recognition of the growing business worldwide in commercial satellites, which stimulated many industrialized nations to build their own versions of a space vehicle capable of placing communication satellites in orbit. This caused a price competition and a search for a low-cost approach to launch space vehicles. Although many of these vehicle programs were government supported, private ventures, principally in the United States, led to a search for a low-cost space vehicle that could be profitable in the growing commercial market. Both liquid rockets, and more particularly solid rockets based on assembling existing developed units in Tinkertoy fashion, became candidates. An alternative to this approach was made by two companies in the 1980s employing hybrid motors.

The company STARSTRUCK was created in March 1981 to develop a large 50-ft-long sounding rocket (the Dolphin) weighing 16,500 lbs. The propellants were LOX and a PB fuel developing a thrust of 35,000 lb in a 42-in.-diam motor. After six full-scale static tests, a sea launch of this vehicle was attempted on 3 August 1984 off the coast of San Clemente Island in the Pacific Ocean. The flight was a partial success where at 3 s into the flight, a thrust vector LOX valve froze in the closed position causing a pitch over and a subsequent command termination [16]. Except for the component failure, the motor performance was as predicted for the initial period and was the largest hybrid vehicle flown, despite its short duration.

The company was subsequently reorganized in 1985 and renamed AMROC under a new sponsor. The company was founded on the belief that a nonexplosive, throttleable and low-cost manufacturing system could translate to a profitable, competitive commercial launch vehicle. With private funding, AMROC proceeded to build a series of motors at vacuum thrust levels between 5000 lb and 260,000 lb based on LOX/HTPB propellants. During the period 1985–1992, 124 static test firings were made at various subscale levels. There were more than a dozen successful firings with the 75,000-lb thrust motor, which represented the largest hybrid motor fired to that time. Scaling the motor to this size presented few problems because the grain configuration was patterned after the UTC HTM-38 motor fired some 20 years earlier. Based on these successful firings, a 51-in.-diam sounding rocket was built that was a factor of two greater than the Dolphin vehicle. The 75,000-lb thrust motor was incorporated in the single engine test (SET-1) Koopman Express sounding rocket. (Koopman was the president of AMROC at that time.) A flight was attempted from the Pacific coast in 1989. It unfortunately suffered a fate similar the Dolphin in that a LOX valve froze in a partially open position resulting in insufficient thrust for liftoff. Undaunted, the company proceeded with its plan to use this motor as a subscale version of a 250,000 lbf (1.1 MN) 6-ft-diam motor to become the basic booster in a three- or four-stage AQUILA vehicle for satellite missions. The individual motor is shown in Fig. 10. Many versions of the AQUILA vehicle were studied in which the first two stages were the basic 1.1-MN motor. Four firings of this motor took place between 22 January 1993 and 24 March 1993. Figure 11 shows the second firing on 17 February 1993, which developed a thrust of 272,000 lb during a 10-s burn time.

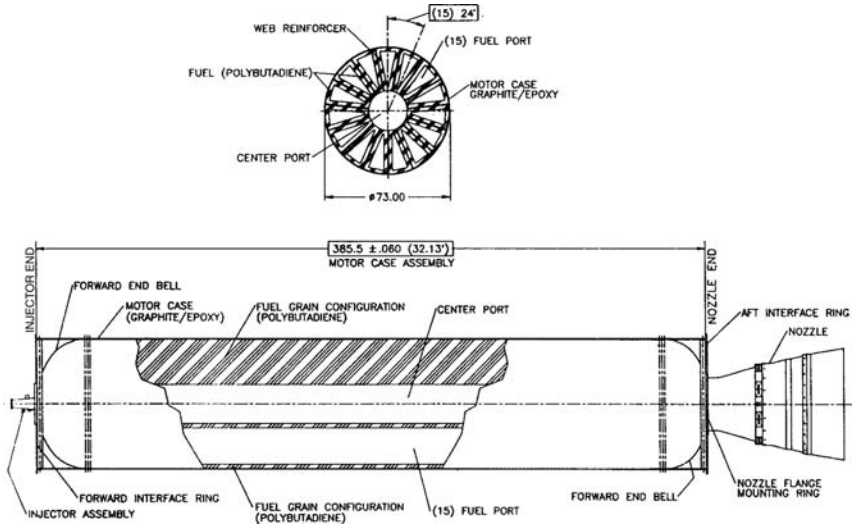

Fig. 10 AMROC DM-01 motor assembly-250 Klb thrust.

Fig. 11 AMROC 250 Klb thrust firing.

To prove its flightworthiness, the HyFlyer sounding rocket program was initiated with a mission of carrying a 1420-lb payload into a high altitude of about 295 n miles (545 km), which would provide a 10-min, gravity-free trajectory. Because AMROC had insufficient funding to pursue this program on their own, a new group was formed, with the partial support from NASA, to participate in the development of the vehicle. The project was renamed the Hybrid Technology Option Project (HyTOP) program and included the companies AMROC, Martin Marietta, and CSD as the dominant participants. Static tests of the basic large motor occurred during 1993 and 1994. After a short period of stable burning, the tests encountered a period of low-frequency instability. Resolution of the problem in this large motor with proposed fixes was very expensive, and in 1995, AMROC lost its sponsor. Because of the continued interest of the remaining members of the group, a new program was generated, called the Hybrid Propulsion Demonstration Program (HPDP) with a new member (Thiokol) replacing AMROC in the consortium. The objective of a flight vehicle was abandoned, and the focus was placed on the motor development itself. This motor design continued from the AMROC design with several improvements. The principal changes were in the grain design, where the 15-port wagon-wheel grain with a blocked centerport was replaced with a thicker web 7-port grain and an active center circular port. Several 11-in.-subscale motor tests were made to obtain regression rate data followed by 24-in.-subscale tests with a single quadrilateral fuel port of the same size as those planned in the full-scale motor [16]. Four tests were conducted at NASA Stennis Space Center of the 250,000-lb-thrust hybrid rocket motor. The internal configuration of this motor is shown in Fig. 12. A firing of the third test of motor 2 is shown in Fig. 13. A major problem appeared in both the subscale and full-scale tests using LOX. The vaporization of the LOX did not happen fast enough in the precombustion chamber, with the result that liquid droplets of oxygen entered the eight ports. As a consequence, relatively low-frequency, high-amplitude pressure oscillations appeared as the oxidizer flow tried to balance out in the eight ports between the upstream and downstream plenums. In the earlier UTC HTM-38 motor tests, these oscillations were not a problem because each of the fuel-grain ports had its own oxidizer injector, which inhibited any backflow. In summary, the experience

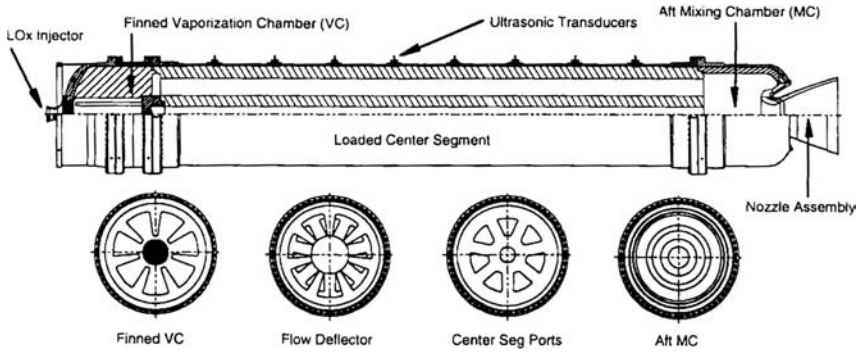

Fig. 12 HPDP 250 Klb motor component schematic.

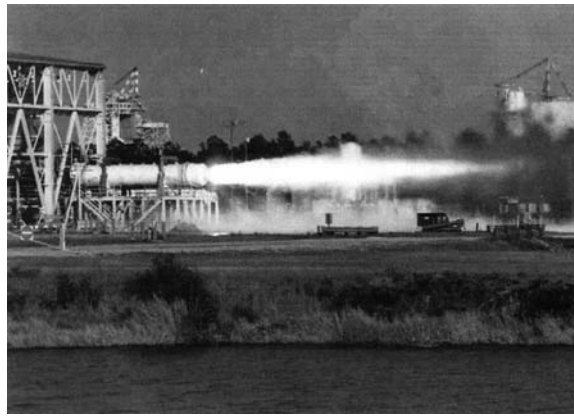

Fig. 13 HPDP 250 Klb motor firing.

of over 10 years of testing large LOX hybrid motors, at two organizations, has emphasized the need to provide adequate head end heating to vaporize the LOX before entrance into the fuel ports.

VII. High Regression Rates

A major deficiency of the hybrid when scaled to larger units is the low regression rate. This defect was brought home after the *Challenger* disaster when NASA-sponsored studies for a hybrid replacement of the solid booster strapons. Many companies participated in this effort with basically two design approaches. One involved the use of a low-grade solid propellant that required liquid oxidizer to sustain burning. The oxidizer was fed into the thrust chamber either at the head end or aft of the grain to achieve a roughly stoichometric proportion for maximum I_{sp}. The regression rate now had a modest dependence on pressure because it basically was a gas-generator-type solid propellant. This design showed good performance and was throttleable. However, it suffered from two basic uncertainties: 1) Because of the oxidizer addition, the fuel would be classified as a low-grade solid propellant, that is, potentially explosive, which would add costly restrictions on manufacture, assembly, and shipping. 2) The shutoff requirement of the new motor could not confidently be demonstrated in a large booster. In small motors, shutting off the oxidizer flow would terminate combustion if the additive were below a critical concentration. However, this process follows the similar principle as dp/dt extinguishment in solid propellants, where a rapid pressure drop causes flame blowoff. In a given motor configuration, each oxidizing additive has a critical concentration above which sustained burning will persist. This critical concentration, which is scale dependent, posed a rather uncomfortable uncertainty in large-scale applications.

The second approach involved the use of a conventional hybrid that retains the advantage of low cost; safety in manufacture, shipping, and assembly; is throttleable; and can be shut off with no uncertainty. However, the design suffered from the low burning rate that now required a grain design with many ports. One design

showed 32 ports arranged in two rings around a centerport. This design posed the disadvantage of requiring web supports that would degrade the volumetric loading efficiency of the grain and, therefore, performance. The web supports plus the remaining slivers would now add considerably to the inert weight of the motor. This design emphasized the basic deficiency that had been recognized for many years, namely, the low regression rate and its impact on grain design, motor envelope, and performance.

A. Energetic Fuel Additives

Early efforts to increase regression rates started in the 1960s when both NH_4ClO_4 [ammonium perchlorate (AP)] and NH_4NO_3 [ammonium nitrate (AN)] were employed as fuel additives. In an earlier period, these systems were described as liquid-augmented solid propellants, where the incentive was to improve the performance and impart throttleability. As discussed in the preceding section, each additive has a critical concentration above which the fuel performs as a low-grade gas generator and shutoff is not possible. This critical concentration is also motor size dependent because of extinguishment requirements in solid rockets. Various other energetic additives such as nitroorganic compounds, RDX $(CH_2N_2O_2)_3$ and HMX $(CH_2N_2O_2)_4$ have been added to conventional PB fuels to lower the heat of vaporization effectively by generating an exothermic reaction in the vicinity of the propellant surface. The regression rates of these propellants are typically both pressure and mass flux dependent. Although this approach is effective, its main deterrent is that manufacturing, handling, and shipping costs can be increased due to an increased hazard classification.

B. Turbulence Generators

Another favorite approach has been designs that generate a high degree of turbulence at the burning surface, thereby increasing the heat-transfer coefficient. An early design, tested at UTC, was based on inserting wire screens periodically in the grain normal to the axis. During burning, the ragged edges of the screens acted as turbulence trippers, and an increased overall burn rate was indeed observed (Fig. 14). The burned surface showed periodic troughs just downstream of the screens due to the localized turbulence. The approach was not pursued at that time due to the perceived increased cost in fabrication. The principle of increasing the local heat-transfer coefficient has also been explored with other techniques. One is by adding an easily vaporized component that on vaporization creates vacuoles to roughen the surface. This technique can be enhanced by the use of crystalline additives to further roughen the exposed surface [17].

Another technique found to be highly effective is the generation of a vortex in a circular fuel port, driven by the tangential injection of oxidizer [18]. The oxidizer is injected at the aft end and travels forward to the head end where a smaller counterflowing coaxial vortex travels aft through the nozzle. With conventional polymeric substances, such as HTPB and PMMA, substantial regression rates averaging about a fourfold increase over a standard injection pattern were observed. In this approach, the magnification of the local mass flux is sufficient to override the inhibiting blowing effect of the classical hybrid. The challenge in using this

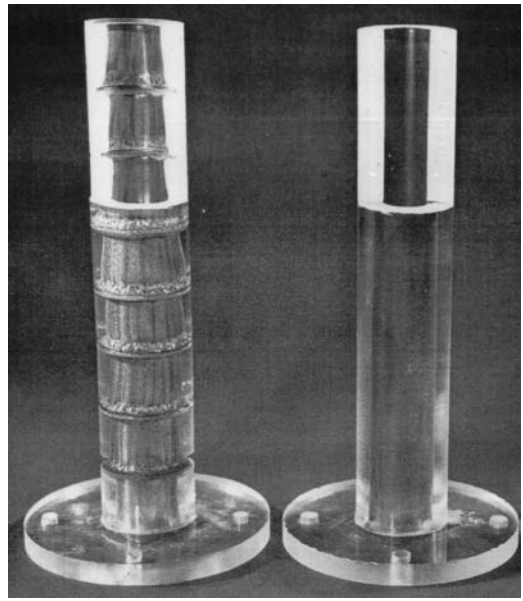

Fig. 14 Metal screen turbulence generators.

technique is the scaling to larger sizes and the maintenance of consistent vortex intensity during burning for practical thicker webs.

C. Entrainment

In U.S. Air Force investigation of solid pentane as a hybrid fuel with GOX, it was found that the regression rates were 3–5 times higher than with a conventional fuel. This increase could not be accounted for with the regression rate equation [20]. In an analysis made at Stanford University [21], it was conjectured that fuels that develop a melt layer of low viscosity could entrain liquid droplets under the influence of the shear stress of the gas flow in the port. It has been shown that if the melt layer is sufficiently fluid, that is, with low viscosity and surface tension, then under a high gas flux environment, an instability is created in the liquid layer, resulting in the formation of liquid droplets that are expelled from the surface. This behavior is typical of cryogenic compounds that crystallize on solidification and exhibit high fluidity on melting. Also included are a class of non-polymerizable fuels, such as the alkanes, whose melt layers are quite fluid. When liquid entrainment occurs, the resulting propellant flow from the surface is composed of a mixture of vapor and liquid droplets. This occurrence can have a profound effect on the regression rate, increasing it by many factors. There are two reasons for this effectiveness:

1) The droplets that are formed do not require a heat of vaporization, but only a heat of fusion, which is generally several times less than vaporization.

2) Because the gas flow from the surface is reduced, the blowing term B is diminished, resulting in a reduced blocking of the convective heat transfer.

The effect of blowing on heat transfer when entrainment occurs is shown graphically in Fig. 15. The range for classical polymeric hybrid fuels ($5 < B < 20$) shows a heat-transfer reduction by a factor of about 3–6, whereas, with entrainment, the value of B is estimated to be <2, showing a much reduced heat-transfer blockage. This effect explains the effectiveness of porous wall cooling in combustion chambers, where, on the other hand, blocking is desired. The higher alkanes, including many of the paraffins, can also form liquid layers of sufficiently low viscosity to exhibit entrainment of liquid droplets. A similar result was obtained at ORBITEC [22] in studies to produce high-performance with solid O_2, CH_4, C_2H_2, and H_2. The results showed even higher regression rates approaching a factor of 20 over HTPB for solid H_2. A concern with liquid entrainment has been whether the droplets have sufficient residence time for complete burning. This concern has been addressed by providing an aft combustion chamber, typically one-half diameter in length to provide enhanced mixing.

To test the entrainment concept with a noncryogenic fuel that satisfies the viscosity and surface tension requirement in the liquid phase, the Space Propulsion Group and Stanford University developed a paraffin-based fuel suitably modified to satisfy the structural requirements for motor testing. Some 200 tests were initially conducted in a laboratory burner at a thrust level of 230 N. These tests verified that the increased burning rate observed with pentane was obtained with GOX after calibrating the equipment with a standard fuel [20]. As a consequence, under support from both the Defense Advanced Research Projects Agency (DARPA) and NASA, scaled-up tests were performed at thrust levels between 4 and 9 kN with

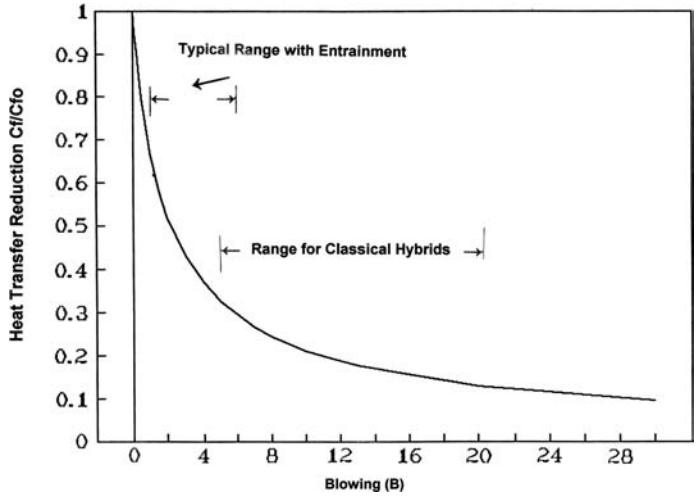

Fig. 15 Blowing effect as a function of entrainment.

a) Facility Stanford University

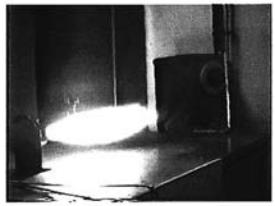

Thrust – approximately 50 lbs
Oxidizer – gaseous oxygen
Grain diameter – 2 3/8 inches
Nozzle type – simple convergent
Number of tests to date - 200

b) Facility Environmental Aerosciences Corp, Miami, FL

Thrust – approximately 900 lbs
Oxidizer – Nitrous oxide
Grain diameter – 5.25 inches
Nozzle type – 5:1 converging-diverging
Number of tests to date - 15

c) Hybrid Combustion Facility, NASA Ames Research Center

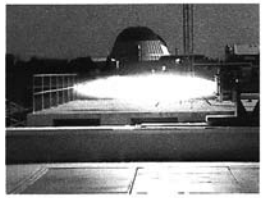

Thrust – approximately 2500 lbs
Oxidizer – gaseous Oxygen
Grain diameter – 7.5 inches
Nozzle type – simple convergent
Number of tests to date - 15

d) Facility Spath Engineering, Albequerque, New Mexico

Thrust – approximately 2000 lbs
Oxidizer – liquid Oxygen
Grain diameter – 8.40 inches
Nozzle type – 5:1 converging-diverging
Number of tests to date - 5

Fig. 16 Single port paraffin at four facilities.

three different oxidizers (GOX, N_2O, and LOX). All tests indicated a regression rate amplification of 200–300% for the given oxidizer. Figure 16 shows a group of firings of a single-port, paraffin-based fuel with three different oxidizers and four different facilities. The significant conclusion from these scaled tests is that larger motors in the 100–1000 kN class can be designed with simple one- or two-port grain configurations. This capability with its reduced grain complexity would greatly enhance the acceptability of hybrids in the larger motor class such as space engines, thrust augmenters, and boosters.

VIII. Survey of University Work

It was natural for universities to select the hybrid rocket for both fundamental ballistic studies and flight projects because of the inherent safety with the use of hybrid propellants and the ability to use common fuels and oxidizers in a laboratory environment. Many schools have done regression rate and configuration evaluations with minimal safety problems outside of those associated with pressurized systems and high-temperature exhaust flames.

Some of the colleges and universities that have generated technical papers on hybrids include the University of Alabama, University of Arizona, University of Arkansas, the U.S. Air Force Academy in Colorado Springs, John Hopkins University, Pennsylvania State University, University of New Orleans, Purdue University, Stanford University, and Utah State University. These are some of the facilities using the hybrid rocket concept as a teaching, research, static testing, and flight-testing tool. Hybrid rocket activities are also being conducted in Germany, The Netherlands, India, Japan, Korea, Italy, Sweden, Israel, and Russia at a minimum.

A. Universities

1. John Hopkins University

The earliest university hybrid studies occurred in 1952 where burning tests with a reverse hybrid rocket propellant system were conducted at the Applied Physics Laboratory of John Hopkins University. The propellants tested were benzene and JP fuel as liquids with potassium perchlorate, AN, and AP. Because of the significance of this research in opening the door to reverse hybrids, it was discussed in more detail earlier in Sec. II, "Early History."

2. University of Alabama in Huntsville

The University of Alabama in Huntsville (UAH) Propulsion Research Center in Huntsville, Alabama, has been doing hybrid work since the late 1980s. They have worked closely with NASA Marshall Space Flight Center (MSFC) and industry on a laboratory-scale hybrid rocket motor on combustion stability, ballistics of mixed-oxidizer propellants, water-tunnel studies of head end flowfields design and testing of microporous LOX injectors, test-facility design, and uncertainty analysis of burning rates and thrust.

3. University of Arizona/Arizona State University

Both schools have done significant research on hybrid fuels and regression rate determination. The University of Arizona has done work with HAN and AN mixtures. They have also worked with metallized fuels in addition to PMM, the standard initial tool of most investigators. At Arizona State University, testing was done in such areas as swirl injector design and its effects on increasing regression rate and combustion stability.

4. University of Arkansas/Hendrix College

The test facilities used are located at the University of Arkansas at Little Rock (UALR) Hybrid Rocket Facility. There is some collaboration with Hendrix College

at Conway, Arkansas. Early test work was done on glycidyl azide polymer added to HTPB for increased performance and regression rate. Many of their published papers involve optical evaluation on the test stand. These included spectral studies, plume flicker, opacity studies, and UV spectroscopic monitoring of the combustion process.

5. Pennsylvania State University

At Pennsylvania State University, the activities included regression rate studies of the standard GOX/HTPB hybrid and pyrolysis and combustion of solid fuels in oxidizing atmospheres. They have also done performance comparisons of HTPB-based solid fuels containing nanosized energetic powders, principally aluminum, and scaleup studies of hybrid rocket motors.

6. University of New Orleans

At the University of New Orleans, they have done the mathematical modeling of regression rate of ablating hybrid solid fuels and the study of flame propagation in hybrid rocket motors.

7. University of Tennessee Space Institute

The published papers from Tullahoma, Tennessee, are on inviscid modeling of classical and vortex injection hybrids.

8. Purdue University

Much of Purdue University's hybrid activities have involved the use of 85% hydrogen peroxide as the oxidizer of choice with PE and PMM. They have also evaluated higher strength peroxide and high-energy additives. Additional studies were made on the basic combustion phenomena in hybrids.

9. Stanford University

The Aeronautics and Astronautics Department has been involved with ballistic studies where they developed the theory for high regression rate fuels by way of liquid entrainment. The principal fuel is paraffin based with stabilizing additives. Three flight tests were conducted at Black Rock in Nevada in October 1999 with both a cellulose fuel and a paraffin fuel using N_2O as the oxidizer. The motor hardware was a commercial purchase from Aerotech RMS/Hybrid 54 that normally comes with a cellulose fuel. It was 45.5 in. long with a diameter of $2\frac{1}{4}$ in. The cellulose-fueled rocket achieved an altitude of 5360 ft, whereas the first paraffin flight flew to 5800 ft. The third paraffin flight had a damaged fuselage from a previous recovery and achieved a lower altitude of 4460 ft. The difference in altitudes of the cellulose- and paraffin-fueled rockets can be largely explained by the difference in I_{sp} values as seen in Table 1.

10. Hybrid Rocket Activities at Utah Universities

In 1991–1992, R. Gilbert Moore of Utah State University initiated the Unity IV university hybrid rocket program. The name was derived from the four universities involved: Brigham Young University, University of Utah, Utah State University,

and Weber State University. The goal was to collaboratively build and launch a hybrid rocket to an altitude over 100,000 ft and carry an atmospheric density measuring instrument. The initial rocket used GOX and HTPB in a 50-in.-long aluminum motor. After several launch attempts, a successful flight was achieved in November 1995 at the Utah Test and Training Range reaching an altitude of approximately 3800 ft. The second-generation rocket was based on the use of liquid nitrous oxide for the oxidizer due to its relative safety as compared to other oxidizers. This vehicle had an 8-in.-diam motor with a 2-in. nozzle throat developing 2500 lb of initial thrust. This vehicle had a successful launch in December 2003 reaching an altitude of 4100 ft.

B. International Universities

1. Germany

A discussion of the early work on the BARBARELLA rocket in the 1970 time period at the Technical University of Munich was given at the beginning of this section. In the subsequent period, from 1974 to 1987, storable hybrid propellants were experimentally investigated at DLR German Aerospace Center Lampolshausen. The purpose was to demonstrate the technical feasibility of storable hybrid motors for missile propulsion and fuel-rich gas generators for ram rockets. The effects of different fuel additives on fuel regression rate were determined, and most of the experiments were done with RFNA and N_2O_4, some with hydrogen peroxide as oxidizer. Investigations on a hybrid gas generator with metal- (Mg, Al, B) containing fuels at low O/F mixture ratios producing a fuel-rich exhaust. A suitable concept for manufacturing fuels with up to 80% of boron was developed. These compositions were analytically shown to be suitable for ram rocket applications in the late 1970s.

2. Institute of Space Propulsion Technology at Technical University of Munich

Somewhat later between 1968 and 1974, a group of students of the Institute developed a hybrid rocket, the BARBARELLA [23]. It used HNO_3 and a mixture of toluidine and aminophenole as the fuel. The rocket had a length of 1.6 m and diameter of 10 cm, with an initial mass of 10.6 kg. It had a thrust of 370 N and burned for 22 s. A flight took place in 1974 off the coast of the Baltic Sea.

3. The Netherlands

The TNO Prins Maurits Laboratory at Rijswijk, The Netherlands, has been involved in hybrid studies for a number of years. They have developed system analysis models of complete hybrid systems with optimized grain designs with the associated liquid components.

4. Indian Efforts

Hybrid rocket research has taken place mostly in the academic institutions: Gorakhpur University, Birla Institute of Technology, Indian Institute of Science, and Indian Institute of Technology Madras. The first two institutions initiated studies to establish regression rate equations. At the Indian Institute of Science, the study was mainly devoted to understand the combustion mechanism in hybrid

rockets. The Indian Institute of Technology Madras focused on the issue of finding methods to enhance fuel regression rates.

Rastogi and his coworkers at the Gorakhpur University studied experimentally the regression rates of different kinds of polymers (polystyrene, polystyrene containing B–O and B–C linkage, and oxygen styrene copolymers) with GOX at atmospheric pressure. They measured the regression rates at different GOX mass fluxes by two methods: 1) from the loss of fuel mass and 2) from the measurements of the port diameters at the grain ends for a known burn time.

Paul et al. at the Indian Institute of Science conducted experiments on rubber/oxygen/nitrogen system and explored the effect of the mass transfer number B on regression rate. He found it to be more sensitive than predicted by the theoretical expression given by Marxman and coworkers. They further experimentally obtained the fuel regression rates in a hypergolic combination (difurfurylidene cyclo-hexanone plus RFNA) for different mass fluxes and found them to be pressure independent.

George et al. at the Indian Institute of Technology Madras conducted a systematic experimental investigation on the methods of enhancing the regression rate in GOX/HTPB hybrid rocket motor. They showed that the addition of AP or aluminum in the fuel, and the reduction of grain port diameter enhanced the regression rate.

IX. Space Tourism

It has always been the dream of amateur rocketeers to fly into space commercially. Inspired by the Lindbergh transatlantic solo flight in the Spirit of St. Louis aircraft in 1927, a group of space enthusiasts led by Peter Diamandis, founder of the X Prize Foundation, proposed a new Spirit of St. Louis in 1996. The goal was for a commercially sponsored flight to transport three people safely to an altitude of 100 km and to repeat this feat within two weeks. It was envisioned that, because the Orteig Prize in 1927 stimulated the commercial aviation industry we have today, a similar stimulus might have a corresponding result for rocket travel in space. The New Spirit of St. Louis organization met in May 1996 to announce the X Prize contest. In attendance were Lindbergh's two grandsons, NASA administrator Dan Goldin, Richard Fleming, astronaut Buzz Aldrin, and Burt Rutan, president of Scaled Composites. This group was able to attract several million dollars of support, and in May 2004, the Ansari family contributed the additional funds to create the $10 million Ansari X Prize.

This challenge attracted 26 teams from 7 countries. A leading contender and eventual winner was Burt Rutan, who received his financial support largely from retired Microsoft executive Paul Allen. He had a running start because his own personal goal had been to show the feasibility of privately developed manned space flight. In this pursuit, his group had developed several safety related concepts. His approach was to use an aircraft to carry a rocket ship to an altitude of 46,000 ft (14 km), at which point the rocket would be launched from a horizontal position. While in a descending glide to clear the mother ship, the rocket engine is fired using the ship's wings to reorient to a near-vertical trajectory. The rocket thrust would then provide the velocity to achieve the apogee of 100 km. He actually realized this goal in a publicly attended flight on 21 June 2004. After this successful flight,

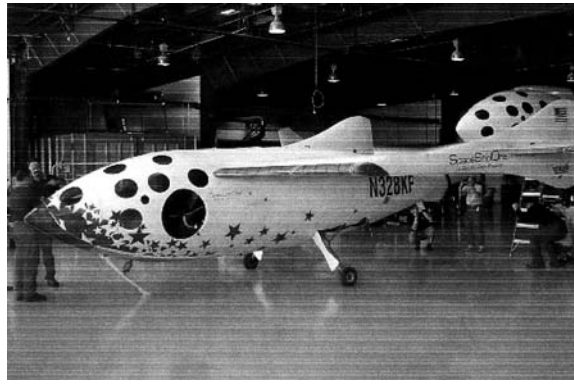

Fig. 17 SpaceShipOne vehicle.

he set out to fly the heavier payload of the X Prize requiring two flights within two weeks. Rutan officially accomplished this feat on 29 September 2004 and on 4 October 2004, ahead of all other competitors, thus claiming the $10 million reward. The second flight reached an altitude of 112 km exceeding the goal by 12 km [24–27]. The SpaceShipOne vehicle is shown in Fig. 17.

After the evaluation of the various types of rocket motors for the second portion of the flight, it is significant that Rutan chose a hybrid motor. The important considerations were safety of operation, good performance, system cost, quick turnaround, and thrust termination. The propellant system selected was nitrous oxide (N_2O) and HTPB, a PB fuel. To satisfy their required burning time of 80 s with the relatively low burn rate, the grain design contained four longitudinal ports to increase the burning surface area. The N_2O with its ambient vapor pressure in the 600–700 psi range allowed self-pressurization, a weight-saving feature.

The success of the Rutan flight has inspired other more ambitious contests including the X Prize Cup and Bigelow's $50 million America's X Prize with a goal to launch a crew of five to an altitude of 400 km. This must be accomplished twice before 10 January 2010. The ultimate goal, of course, is to provide a satellite capability so tourists can view the entire planet for indefinite periods of time [27]. This would require an energy of 5–10 times that of the X Prize involving a multistage rocket vehicle probably in the meganewton thrust class.

X. Highlights in Perspective

When viewed in perspective, some of the highlighted events retained their significance in later years. The following events were chosen because either they were the first in which significant experiments were conducted, they divulged a new concept, or they provided an expanded insight into a useful technology.

A. Pacific Rocket Society Experiments

This activity, which covered an early period from the mid-1940s to the 1950s involved both static and flight tests. In contrast to earlier work, investigations

were conducted of a wide variety of fuels and ended with practical propellants, such as LOX and rubber, which are common to this day. A successful flight was accomplished in June 1951 reaching an altitude of 30,000 ft (9100 m).

B. 180-Kilonewton Thrust Motor, Tested by UTC in 1967

This early version of a multiport grain paved the way to the later developments by STARSTRUCK, AMROC, and the HPDP consortium two decades later. The wagon-wheel grain design was used as the basis for these subsequent motors.

C. Drone Programs Sponsored by U.S. Air Force

These vehicles, which used UTC hybrids, lasted for 15 years. They demonstrated the practicality of the hybrid motor in a mission requiring a wide 8/1 throttling ratio. Several versions of the hybrid motors were employed, including two oxidizers, three fuels, and a stacked disk approach to fuel fabrication. No hybrid flight program has ever persisted for such a long period of time and satisfied military specifications. It also demonstrated the versatility of the hybrid in that several system concepts were employed with different propellants, all performing successfully.

D. Burning Rate Expression Developed by Marxman and Coworkers

In the early 1960s, this was the most complete treatment up to that time and is a basic relation used to this day. The expression incorporates the effect of blowing on heat transfer, the two boundary layers of momentum and combustion, and the radiation correction, taking into account coupling with convection. Because of its versatility, it has served as a starting point for interpreting various burning rate concepts, such as entrainment, and provided the basis for engine design.

E. Large Boosters in >1 Meganewton Thrust Motor Class

Using the principles learned in earlier scaling programs, AMROC, and subsequently the HPDP consortium, were able to design and test large hybrid engines in the meganewton thrust class. Although these motors did not reach operational status, they elucidated the problems facing large booster development, such as grain fabrication, fuel utilization, and combustion stability.

F. SpaceShipOne Suborbital Manned Flight by Scaled Composites

This privately funded event in 2004 opened the door to space tourism in suborbital flights with the future potential for tourist flights into orbit. It has also stimulated venture capitalists to sponsor future space flights.

XI. Conclusions

In viewing the past history of hybrid motor development in perspective, it is clear that most, but not all, of the claimed advantages have been realized. Most important, the units are safe and there has never been a reported chemical explosion. The failures that have occurred have been relatively few and benign in nature,

resulting in occasional damage to the motor but nothing significant to the test facility. Throttling and shutoff capability have been demonstrated, features that are of importance in manned flight applications. Because of the safety and reduced manufacturing tolerances, the hybrid motor has been the rocket of choice by both universities and amateur rocket enthusiasts. Furthermore, the versatility of propellant selection has been amply demonstrated in that it has outstripped the available candidates in both solid- and liquid-propulsion systems.

Problems have arisen, however, in the development of motors whose diameters are roughly in excess of 1 m. This approximate diameter limitation, due to the low regression rate of the classical hybrid, has led to multiport grain designs that have partially compromised motor mass fractions and created an uncertainty in grain behavior at burnout, particularly in flight. Some of the current efforts on investigating burning rate increase appear promising and need further verification for larger size motors. An additional area of considerable importance is combustion instability, particularly with LOX as an oxidizer. In contrast to both liquids and solids, the hybrid does not exhibit severe high-frequency acoustic modes. However, it does experience a low-frequency chugging-type behavior that can be aggravated by inadequate vaporization of a liquid oxidizer in the precombustion chamber. This is not a fundamental objection because all rocket and airbreathing engines have experienced instability at some time in their development, but it does need more research for acceptable resolution. In contrast to the solid and liquid rocket development programs, the hybrid has received only a fraction of the investment made with the other engines. It is reasonable to expect that, with a more substantial funding, the hybrid motor can play a significant role in major space applications envisioned today.

References

[1] *World Aerospace Systems*, May 1968, p. 5.
[2] Herrick, J. W., and Burgess, E. *Rocket Encyclopedia*, 1959, p. 320.
[3] Ewing, E. G. *Journal of the Pacific Rocket Society*, 1947.
[4] Moore, G. E., and Berman, K. "A Solid Liquid Rocket Propellant System," *Jet Propulsion*, Vol. 26, No. 11, 1956.
[5] U.S. Patent No. 3,136,119, 9 June 1964.
[6] La Force, P. D., and Wolff, H. "Demonstration of an Upper Stage High Energy Hybrid Rocket," 12th Annual Liquid Propulsion Meeting, 24 Aug. 1970.
[7] Salmon, M. "An ONERA Hybrid Rocket for Scientific Probes," *World Aerospace Systems*, May 1968, p. 5.
[8] *Aviation Week and Space Technology*, 12 May 1997.
[9] *Aviation Week and Space Technology*, 3 Feb. 2003, p. 50.
[10] Schuler, A. L. "U. S. History of Hybrid Propulsion," 29th Aerospace Sciences Meeting, Jan. 1991.
[11] Holzman, A. "Hybrid Demonstrator," U. S. Patent No. 3,156,092, 10 Nov. 1964.
[12] Marxman, G., and Gilbert, M. "Turbulent Boundary Layer Combustion and the Hybrid Rocket," *9th Symposium on Combustion*, Academic Press, 1962, p. 371.
[13] Ordahl, D. D., and Altman, D. "Hybrid Propellant Combustion Characteristics and Engine Design," 3rd Symposium on Advanced Propulsion Concepts, 1962.

[14] Houser, T. J., and Peck, M. V. "Research in Hybrid Combustion," *Heterogeneous Combustion*, 1963, p. 554.
[15] Feemster, J. R. "Demonstration of a High-Thrust Hybrid Thrust Chamber Assembly," Pt. **1**, Technical Rept., UTC AFRPL-TR-68-56, United Technology Center, Sunnyvale, CA, April 1968.
[16] *Aviation Week and Space Technology*, 13, Aug. 1984.
[17] Boardman, T. A., Ael, T. M., Clafin, S. E., and Shaeffer, C. W. "Design and Test Planning for a 250klbf Thrust Hybrid Motor under the HPDP," AIAA Paper 97-2804, July 1997.
[18] Stickler, D. B., U.S. Patent No. 5,529,648, 25 June 1996.
[19] Knuth, W. H., Chiaverini, M. J., Sauer, J. A., and Gramer, D. J. "Solid Fuel Regression Rate Behavior of Vortex Hybrid Rocket Engines," *Journal of Propulsion and Power*, Vol. 18, No. 3, 2002, p. 600.
[20] Larson, C. W., DeRose, M. E., Pheil, K. L., and Carrick, P. G. "High Pressure Combustion of Cryogenic Hybrid Fuels in a Lab-Scale Burner," *1995 JANNAF Joint Propulsion Conference*, Combustion Propulsion Information Agency, Johns Hopkins Univ., Columbia, MD, 1997, pp. 117–128.
[21] Karabeyoglu, M. A., Altman, D., and Cantwell, B. J. "Combustion of Liquefying Hybrid Propellants: Part I General Theory," *Journal of Propulsion and Power*, Vol. 18, No. 3, 2002, p. 610.
[22] St. Clair, C., Rice, E., Knuth, W., and Gramer, D. "Advanced Cryogenic Solid Hybrid Rocket Engine Developments: Concept and Testing," AIAA Paper 98-3508, July 1998.
[23] Lengelle, G., "Hybrid Propulsion, Historical Aspect. Context. International Activities," Energetics Dept., ONERA, France, Jan. 2003.
[24] *Aviation Week and Space Technology*, 9 Aug. 2004.
[25] *Aviation Week and Space Technology*, 27 Sept. 2004.
[26] *Aviation Week and Space Technology*, 11 Oct. 2004.
[27] *Aviation Week and Space Technology*, 18 Oct. 2004.
[28] *Aerospace America*, Aug. 2005, p. 37.

Bibliography

Altman, D., "Hybrid Rocket Development History," AIAA Paper 91-2515, June 1991.

Altman, D., and Humble, R., "Hybrid Rocket Propulsion Systems," *Space Propulsion Analysis and Design*, edited by R. Humble, G. Henry, and W. Larson, McGraw-Hill, New York, pp. 365–441.

Calabro, M., "European Hybrid Propulsion History," AIAA Hybrid Propulsion Lecture Series, Jan. 1991.

"Demonstration of a High-Thrust Hybrid Thrust Chamber Assembly," Vol. 1, UTC Technical Proposal 65-129, United Technology Center, Sunnyvale, CA, 18 Nov. 1965.

Godsave, G. A. E., NGTE (UK) Rept. R-66, (1950) and Rept. R-87, National Gas-Turbine Establishment, U.K. 1951.

Godsave, G. A. E., "Study of Combustion of Drops in a Fuel Spray—The Burning of Single Drops of Fuel," *Sixteenth Symposium (International) on Combustion*, 1952, p. 818.

Green, L., "Introductory Considerations on Hybrid Rocket Combustion," *Heterogeneous Combustion*, Progress in Astronautics and Aeronautics, edited by H. G. Wolfhard, I. Glassman, and L. Green Jr., Academic Press, New York, 1964, p. 451.

"Hybrid Propulsion Technology Program," Final Rept. Contract NAS8-37776, Atlantic Research Corp., Alexandria, VA, Jan. 1990.

"Hybrid Propulsion Technology Program," Space Systems Div., Final Rept., Contract NAS8-37777, General Dynamics Corp., San Diego, CA, Nov. 1989.

"Hybrid Propulsion Technology Program," Chemical Systems Div., Final Rept., Contract NAS8-37778, United Technologies Corp., Sunnyvale, CA, Jan. 1990.

Kniffen, R. J., "The Development Status of the 260,000 lbf Thrust Hybrid Rocket Booster," Paper IAF-92-0631, 43rd International Astronautical Federation Congress, Aug. 1992.

Kuentzmann, P., and Sternfeld, H. J., "What Future for Hybrid Propulsion?," *Symposium on Launcher Propulsion Towards the Year 2010*, 1991, pp. 159–168.

Marxman, G. A., and Wooldridge, C. E., "Research on the Combustion Mechanism of Hybrid Rockets," UTC Contract Now 64-0659-c, United Technology Center, Sunnyvale, CA, May 1965.

Marxman, G. A., Wooldridge, C. E., and Muzzy, R. J., "Fundamentals of Hybrid Boundary Layer Combustion," *Heterogeneous Combustion*, Progress in Astronautics and Aeronautics, Vol. 15, Academic Press, New York, 1964, pp. 485–521.

Mead, F., "Sandpiper: A Hybrid Rocket History," AIAA Paper No. 95-2946, July 1995.

Miller, E., "Hybrid Rocket Combustion Regression Rate Model," *AIAA Journal*, Vol. 4, No. 4, 1965, pp. 1408–1413.

Muzzy, R. J., "Applied Hybrid Combustion Theory," AIAA Paper 72-1143, 1972.

Netzer, D. W., *Hybrid Rocket Internal Ballistics*, CPIA Publ. 22, Chemical Propulsion Information Agency, Laurel, MD, Jan. 1972.

Ramohali, K., and Yi, J., "Hybrids Revisited," AIAA Paper 90-1962, July 1990.

Rastogi, R. P., and Deepak, D., "Pressure Dependence of Hybrid Fuel Burning Rate," *AIAA Journal*, Vol. 14, No. 7, 1976, pp. 988–990.

Smoot, I. D., and Price, C. F., "Pressure Dependence of Hybrid Fuel Regression Rates," *AIAA Journal*, Vol. 5, No. 1, 1967, pp. 102–106.

Smoot, I. D., and Price, C. F., "Regression Rates of Metalized Hybrid Fuel Systems," *AIAA Journal*, Vol. 4, No. 5, 1966, pp. 910–915.

Spalding, D. B., "The Combustion of Liquid Fuels," *Fourth Symposium (International) on Combustion*, Wm and Wilkins, 1953, p. 847.

Sutton, G., *Rocket Propulsion Elements: An Introduction to the Engineering of Rockets*, 6th ed., Wiley, 1992.

Chapter 2

Review of Solid-Fuel Regression Rate Behavior in Classical and Nonclassical Hybrid Rocket Motors

Martin Chiaverini*

Orbital Technologies Corporation, Madison, Wisconsin 53717

Nomenclature

A = Arrhenius preexponential constant, mm/s
B = blowing parameter, $\rho_f r/(Gc_f/2)$
B_{mod} = modified blowing parameter, $B\exp(q''_r/q''_c)$
c_s = fuel specific heat, J/kg · K
c_f = skin-friction coefficient
c_p = gas isobaric specific heat, J/kg · K
C^* = characteristic exhaust velocity, m/s
D = diameter, cm
$\boldsymbol{D}$ = mass diffusivity, m^2/s
Da = Damköhler number
D_h = hydraulic diameter, cm
E_a = activation energy, kcal/mole
G = local, bulk mass flux, $kg/m^2 \cdot s$
h = enthalpy, J/kg; port height, mm
I_{sp} = specific impulse, s
k = absorption coefficient, kinetic rate constant
K = concentration
L = length of fuel slab, cm
Le = Lewis number
N_p = particle number density
Nu = Nusselt number
O/F = oxidizer to fuel mass mixture ratio
Pr = Prandtl number
p = pressure, atm or MPa
q'' = heat flux, W/m^2

*Principal Propulsion Engineer. AIAA Senior Member.

Re = Reynolds number
R_u = universal gas constant, kcal/kg · K
r = regression rate, mm/s
Sc = Schmidt number
S_g = geometric swirl number defined in Eq. (69)
St = Stanton number
Sw = swirl number
T = temperature, K
t = time, s
u = streamwise velocity component, m/s
w = fuel web thickness, mm
X = mole fraction
x = axial location, cm
Y = mass fraction
α = absorptivity
α_p = particle weight fraction
ΔH_f^o = heat of formation, J/kg
ΔH_r = heat of reaction per unit mass reactants, J/kg
ΔH_v = heat of vaporization, J/kg
ε = emissivity, or turbulence dissipation rate, m^2/s^3
κ = thermal conductivity
μ = viscosity, $N \cdot s/m^2$
ρ = density, g/cm^3
ρ_f = fuel density, g/cm^3
σ = Stefan–Boltzmann constant
θ = temperature ratio, $T_{\text{fl,av}}/T_s$
λ = weight fraction of gas in decomposed fuel products at fuel surface

Subscripts

av = average
c = convective
d = hydraulic diameter
e = boundary layer edge
eff = effective
f = fuel
fl = flame
g = gas phase
i = initial
o = oxidizer, or reference
rad = radiant
s = surface or soot
sw = swirl
t = turbulent
tot = total
v = vortex
w = wall

x = local, axial
$+$ = just above fuel surface
$-$ = just below fuel surface

I. Introduction

LIKE liquid- or gelled-bipropellant propulsion systems, monopropellant thrusters, and solid rocket motors, hybrid rocket propulsion systems use energy liberated from the combustion of fuel and oxidizer to generate thrust. In hybrid rockets, however, the propellants are both physically separated and stored in different phases. For example, conventional (sometimes called classical or typical) hybrid motors use a solid-fuel grain and a liquid oxidizer. The liquid oxidizer is injected into the head end of the solid-fuel grain, sometimes first through a precombustion chamber that serves to vaporize the oxidizer and allows it to enter the combustion port in a nonpreferential manner. The pyrolyzed gaseous fuel and oxidizer mix and react along the length of the fuel grain and undergo final mixing in the aft combustion chamber. The hot product gases are then expelled out the nozzle to generate thrust. Figure 1 illustrates the main features of a classical hybrid rocket propulsion system.

The key parameter influencing the design of hybrid fuel grains, and, therefore, the overall hybrid-motor design, is the solid-fuel regression rate. The regression rate, a velocity, is defined as the rate at which the solid-phase fuel is converted to a gas. Though the term burning rate is sometimes used to describe hybrid solid-fuel regression, this term is more appropriately applied to solid propellants, which typically undergo combustion reactions on the propellant surface. In hybrid motors, combustion usually occurs in the boundary layer above the fuel surface rather than at the fuel surface itself. Sometimes, the terms erosion rate or ablation rate are also used and are essentially equivalent to the more favored regression rate. Two other terms of interest in the literature are the *pyrolysis* rate and *sublimation* rate of the fuel. The term sublimation is used in the usual sense of phase change from a solid to gas without first passing through the liquid phase. The term pyrolysis refers to a solid-to-gas phase change that is accompanied by a chemical change, such as the polymer chain breaking, cyclization, and re-organization that occurs in the in-depth near-surface region when polymer-based fuels degrade and regress. However, note that some specialized fuels, such as solid cryogens (for example, frozen methane) and paraffin waxes, appear to regress. Solid cryogens seem to melt or sublimate without a chemical change, whereas paraffins have been proposed to melt and form wavelets on the fuel melt-layer surface that spray droplets into the gas flow. However, these fuels are exceptions to the general behavior and are discussed later.

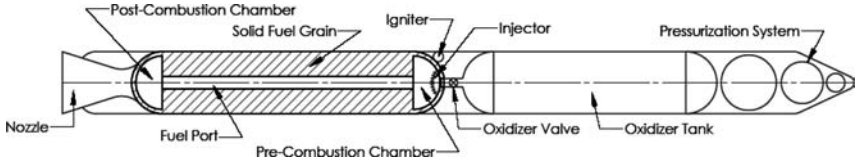

Fig. 1 Typical classical hybrid propulsion system.

The main objective of this chapter is to survey broadly some of the more significant theories and analyses that have been developed to explain the solid-fuel regression rate behavior of various types of hybrid motors and solid fuels under different operation conditions. Both classical and nonclassical hybrid motor configurations, as well as traditional and nontraditional fuels, will be examined. In Sec. II, a brief introduction to hybrid motors is provided and particular advantages, disadvantages, and performance characteristics compared to liquid-bipropellant rocket engines and solid-propellant motors, are discussed. In Sec. III, physical processes involved in hybrid solid-fuel regression are described and a review of relevant literature is presented. This review focuses primarily on theoretical and semi-empirical approaches to developing regression rate laws. The effects of turbulent heat transfer, radiant heat transfer, gas-phase kinetics, heterogeneous reactions on the solid-fuel surface via oxidizer attack, oxidizer injector design, and fuel additives are described and discussed. A few investigations of scaling and geometry effects are also discussed. In Sec. IV, regression rate characteristics of nonclassical hybrid motor configurations are discussed, including swirl-injected hybrids, vortex hybrids, and end-burning hybrids, as well as regression rate behavior of nontraditional fuels such as paraffins and cryogenic solid fuels. Other types of nonclassical hybrid concepts are also briefly reviewed and discussed. Conclusions and recommendations for future research are also presented. The reader is referred to Chapters 3 and 4 for additional discussions of regression rate mechanisms and measurement techniques, Chapter 10 for solid fuel characteristics, and Chapter 12 for scaling effects. We will not here address the very important subject of transients or unsteady combustion in hybrid rocket motor as this subject is discussed in Chapter 9.

II. Hybrid Motor Characteristics

Because they store fuel and oxidizer in separate phases, conventional hybrid systems offer several important advantages over their liquid and solid rocket counterparts that potentially make them attractive for a variety of applications. Characteristic hybrid benefits include those listed in the following paragraphs:

1) *Safety*—Enhanced safety compared to liquid bipropellant and all-solid systems often represents the most desirable and distinguishing characteristic of conventional hybrid-propulsion systems. Because the fuel and oxidizer are separated by distance and phase, hybrids have almost no explosion hazard and very few failure modes. Moreover, solid fuels are not hazardous for storage and transportation, unlike solid propellants and volatile liquid fuels such as hydrogen, methane, and kerosene.

2) *Insensitivity*—Unlike solid-propellant grains where the fuel and oxidizer are intimately mixed, hybrid-fuel grains are insensitive to cracks and imperfections because they are inert. In conventional hybrids, heterogeneous reactions due to oxidizer attacking the fuel surface generally do not come into play because the diffusion flame zone shields the fuel surface from the oxidizer-rich core flow. Therefore, potential cracks and fuel imperfections that may increase the fuel surface area do not have a significant effect on the internal ballistics of the fuel grain. The inert solid-fuel grain is ideally suited for tactical systems that require "wooden round" insensitivity to small arms fire and case penetration. Solid-propellant

cracks, on the other hand, can have a catastrophic effect on the motor because they increase the burning surface area, which in turn increases the motor pressure beyond the design conditions. Finally, solid-fuel regression rates are typically not sensitive to ambient temperature effects, providing for reliable and consistent motor operations over a broad range of conditions. Solid-propellant motors, however, must incorporate design margins to allow for chamber pressure variations that result from burning rate temperature sensitivity.

3) *Reliability*—Because only the oxidizer is stored in liquid form, hybrid rockets require only half as much feed-system hardware as liquid-propellant rockets. This arrangement provides advantages in terms of improved reliability, lower feed system weight, and less complex mechanical design.

4) *Energy management*—Hybrid rockets can be throttled for thrust control, maneuvering, motor shutdown, and restart by adjusting only the oxidizer flow rate while avoiding the necessity of matching hydraulic characteristics with the fuel, as must be done for liquid-propellant rockets. Throttling is attractive for various tactical applications such as missile-intercept and air-to-air missions. Hybrid rocket designs can also include a non-destructive mission abort mode.

5) *Fuel versatility*—The solid-phase fuel provides a convenient matrix for introducing a variety of additives for purposes such as plume signature tailoring for military applications, metal particles for high-energy missions, and simulating solid-propellant exhaust products or other chemically reacting flows for research purposes.

6) *Design flexibility*—Though most hybrid developmental efforts have focused on large boosters or upper stages using the conventional configuration, additional concepts described later in this chapter have been proposed for a variety of missions including in-space propulsion, satellite maneuvering, orbit maintenance, waste generators, and even an underwater welding torch. In Chapter 14, the historic flight of Space Ship One, the first privately developed spacecraft, which used an N_2O/hydroxyl-terminated polybutadiene (HTPB) hybrid motor, is described. Hybrids are also a very safe and effective educational tool for demonstrating rocket propulsion concepts to a broad audience. Overall, hybrids possess a great range of design flexibility to meet a wide variety of missions.

7) *Environmental friendliness*—Hybrid rockets using typical propellants such as liquid oxygen (LOX) and rubber-based fuel such as HTPB, have environmentally clean exhaust without hydrogen chloride or aluminum oxide, which can be ecologically damaging.

8) *Low cost*—Hybrid rockets pose almost no explosion hazard during manufacture, transport, ground test, and storage because the fuel and oxidizer are separated both physically and by phase. This arrangement also allows for easier and safer clean up in the event of an oxidizer spill. Hybrids should be very economical to both manufacture and launch because of their inherent safety and minimal failure modes.

Classical hybrid rockets also display several disadvantages with respect to other chemical-propulsion systems, including the following:

1) *Slow regression rate*—Polymeric hybrid fuels, such HTPB, regress rather slowly, generally at least an order of magnitude slower than solid propellants.

To produce the necessary mass flow rate of pyrolyzed vapor from the fuel grain consistent with a desired thrust level, multiport grains with large wetted surface areas must often be employed. Such grains require proportionally large pressure cases and can display poor volumetric loading. Also note that low regression rates are also a disadvantage when small grain L/D ratios may be desirable, such as for upper stages. Fuel-rich gas-generator grains with some oxidizer content, such as glycyl azide polymer (GAP) or HTPB with small amounts of ammonium perchlorate (AP), can be used to increase regression rates, but are not as insensitive as pure fuels. However, as described later, advanced solid fuels and innovative injection methods have recently shown great promise for overcoming the design difficulties associated with low fuel regression rates.

2) *Low volumetric loading*—In addition to slow regression rates leading to poor volumetric loading, the use of aft combustion chambers downstream of the fuel grain to complete the mixing and combustion of fuel and oxidizer further exacerbates the mass fraction disadvantage compared to liquid and solid systems. Conventional hybrid propulsion systems therefore, typically require a larger installation envelope.

3) *Fuel residuals*—Conventional hybrids with multiple ports cannot be burned to completion because portions of the fuel web between the ports would dislodge from the host grain and potentially block the nozzle. Therefore, a few percent of the fuel must be left intact at the end of the mission. These so-called fuel slivers subtract from the overall propulsion system mass fraction.

4) *Mixture ratio shift*—Because of the strong coupling between the oxidizer flow through the fuel port and the grain ballistic behavior, the overall mixture ratio during the burn displays a time variation due to the increase in the port size. As will be discussed in detail later in this chapter, the increase in port cross section increases the fuel burning surface area but decreases the fuel regression rate. These two effects are in general not balanced, leading to a change (usually a decrease) in the overall fuel production rate. This variation in turn affects the propulsion system performance. However, use of secondary oxidizer injectors and innovative grain designs can offset or eliminate the mixture ratio shift.

5) *Mixing/combustion inefficiencies*—Hybrids have fundamentally different mixing and combustion processes than either liquid-bipropellants or all-solid systems. In liquid engines, propellant mixing occurs on a droplet-size scale, whereas in solids the fuel and oxidizer are intimately mixed during the grain casting process. In hybrids, however, propellant mixing and combustion occur in a macroscopic diffusion (nonpremixed) flame zone that has a length scale of the same order as the fuel grain length. This mode of mixing and combustion may result in slightly lower overall combustion efficiency than competing chemical systems.

Whereas this chapter primarily addresses solid-fuel regression rate behavior in both classical and nonclassical hybrid motor configurations, it is worthwhile reviewing some of the basic performance characteristics and applications of hybrid motors to place the importance of the regression rate in proper context. The early days of hybrid combustion research and development often saw use of wood, wax, and carbon for fuels. Though polymethylmethacrylate (PMM) and polyethylene (PE) are sometimes used for laboratory experiments, the most commonly employed modern solid fuels for hybrid motor propulsion are the butadiene-based

fuels, such as HTPB. HTPB is safe and easy to formulate using a two-part polymer mixture of resin and curing agent. Additives may include cross-linking agents for enhanced mechanical strength, densifying agents such as polycyclopentadiene, carbon powder to opacify the grain to thermal radiation penetration, and metal powders for increased energy density. In Chapter 10 hybrid solid fuels are discussed in much more detail.

When combined with various oxidizers, HTPB-powered hybrids typically display specific impulse greater than that of solid propellants, such as AP/HTPB heterogeneous solids, but lower than that of high-energy liquid-bipropellant combinations such as hydrogen–oxygen systems. However, HTPB/LOX is quite similar in performance to kerosene/LOX. On the other hand, HTPB hybrids have higher density impulse than liquid-bipropellants, but lower than that of solid propellants. Figure 2 shows the theoretical specific impulse and density impulse performance of HTPB as a function of mixture ratio for several oxidizers at a chamber pressure of 1000 psia and a nozzle area expansion ratio of 10:1. Notice that LOX provides the highest specific impulse because of high oxidation potential, whereas hydrogen peroxide (H_2O_2) provides the larger density impulse due to its high mass density. In Chapter 9, hybrid oxidizers, especially the use of hydrogen peroxide, are discussed in more detail. Figure 3 provides additional comparisons of the performance of various hybrid-, solid-, and liquid-bipropellant systems.

The fuel mass for a given mission may be determined from an analysis of the specific impulse for the selected propellant combination. However, the shape of the fuel grain and design of the combustion port(s) depends on the internal ballistic characteristics of the motor, which in turn are set by the fuel regression rate behavior. Therefore, a thorough understanding of the physical processes that govern solid-fuel regression under various conditions is essential for optimizing the design of high-performance hybrid motors. In the next section, we turn our attention to the main focus of this chapter, a review and discussion of the fundamental processes governing solid-fuel regression phenomena in various types of hybrid motors. To set the stage, the salient features of boundary-layer combustion and solid-fuel regression in hybrid motors are presented.

Figure 4 shows in a qualitative manner, many of the physical processes involved in hybrid combustion. Shortly after ignition, a chemically reacting boundary layer develops over the solid-fuel surface due to the injection of oxidizer at the head end of the motor. Though the oxidizer could be introduced in either gaseous or liquid form, liquid droplet and spray physics are not represented in Fig. 4 for clarity. In addition, the boundary layer is assumed to be turbulent due to the typically high injection Reynolds numbers for hybrid motors; however, laminar and transition flow regimes could also be present near the leading edge of the fuel grain under some circumstances. The turbulent boundary layer is characterized by strong velocity, temperature, and species gradients normal to the surface, and mass, momentum, and energy transport are dominated by the turbulent flow processes.

Shortly after ignition, a diffusion flame region forms in the boundary layer. According to Marxman and Gilbert [2], the flame resides at a location approximately 10–20% of the boundary-layer thickness above the surface. Heat from the flame is convected and radiated to the fuel surface. This energy flux causes the solid fuel to pyrolyze (undergo a physical change accompanied by chemical changes).

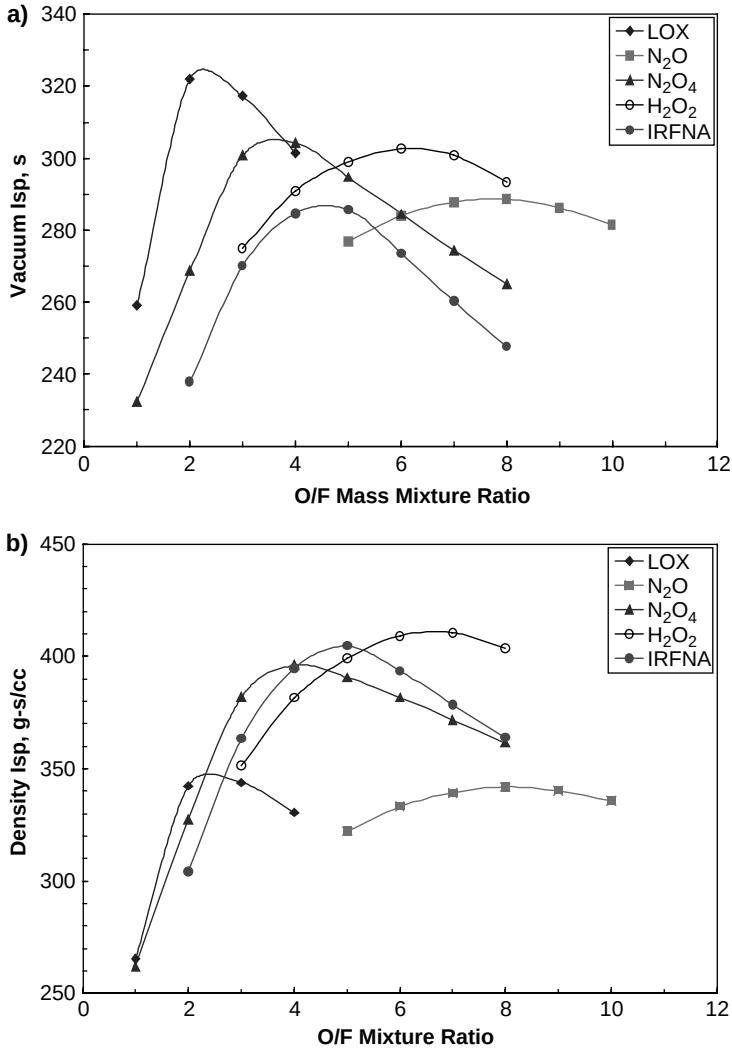

Fig. 2 Specific impulse vs mixture ratio for several oxidizers with HTPB at $P_C = 1000$ psia and 10:1 nozzle expansion area ratio: a) vacuum I_{sp} and b) density I_{sp}.

The pyrolyzed fuel vapor is then transported to the flame zone by convection and diffusion, where it mixes with the gaseous oxidizer, which has been transported through the boundary layer from the core flow region via turbulent diffusion. The two components react in the diffusion flame, a process that provides heat to sustain further fuel pyrolysis. The fuel mass flux due to pyrolysis, however, blocks some of the heat transfer to the surface, which causes a decrease in the regression rate

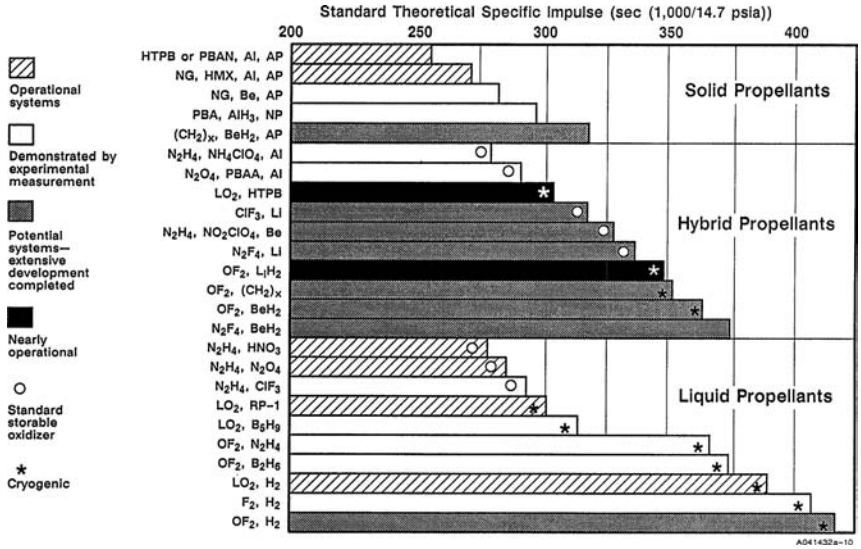

Fig. 3 Theoretical I_{sp} for various solid, liquid, and hybrid rocket propellants [1].

and corresponding strength of the wall blowing effect and, in turn, a weakening of the blocking action, which in turns means that more heat can reach the surface, and so on. This tendency toward a self-regulating interaction between heat flux, mass blowing, and heat flux blockage is a distinguishing characteristic of hybrid combustion.

The hybrid boundary layer is also characterized by several different spatial zones normal to the fuel surface. A fuel-rich region exists below the diffusion flame and an oxidizer-rich region resides above the flame. Under some conditions, oxidizer gas may be able to pass through the flame zone and participate in heterogeneous reactions with the fuel on the pyrolyzing surface. The importance of this phenomena was the subject of much investigation during the 1960s and 1970s and will be discussed further in Sec. III.

Additional fuel surface phenomena include polymer degradation and fragment desorption (for polymeric fuels) as discussed by Arisawa and Brill [3, 4], surface roughness effects that can affect heat transfer, mechanical deformation of the solid fuel by chamber pressure excursions, and the effects of solid-fuel additives, such as metal particles, on modifying (usually lowering) the bulk fuel enthalpy of gasification and the heat-transfer blocking effect. A liquid-melt layer may also form on the fuel surface in the absence of sufficient heat flux to cause direct gasification of the solid fuel. As discussed later in the chapter, Karabeyoglu [5–7] have proposed that cryogenic solid fuels, for example, frozen methane, and certain paraffin fuels regress quickly compared to conventional fuels because, in addition to gasification, they also undergo a surface melt-layer/fuel droplet entrainment process that does not contribute to the blocking effect. These fuels will be discussed later in this chapter as well as in Chapter 10.

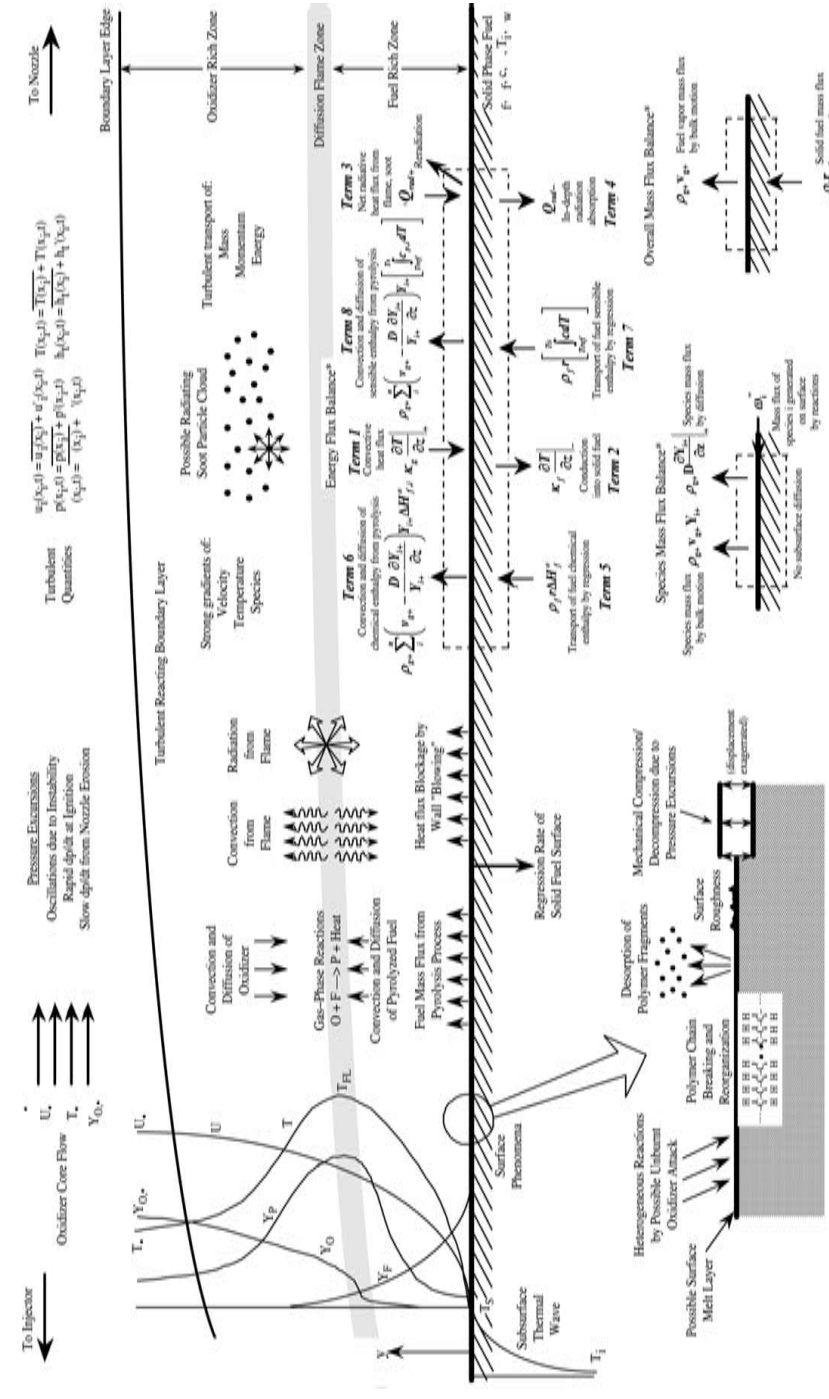

Fig. 4 Physical processes involved in hybrid rocket combustion.

In all practical hybrid rocket fuel grains, the gas-phase flow is confined between the fuel surfaces. Thus, a true freestream does not really exist, and the flow is more similar to an internal pipe flow than the flat plate-type flow shown in Fig. 4. The core flow may, therefore, undergo axial acceleration along the fuel grain, caused by accumulation of fuel mass and combustion enthalpy in the downstream direction, as well as by boundary-layer growth. Axial temperature, enthalpy, pressure, and mixture ratio gradients can also affect the character of the boundary layer above the solid-fuel surface. In addition, the boundary layers may grow to the point where they merge at some location along the fuel port.

The interfacial energy, species, and overall mass flux balances are also shown in Fig. 4, for a surface fixed in space. With respect to the fuel surface, one may imagine the solid fuel feeding into the pyrolyzing surface at the regression velocity r. The energy balance is the most complex boundary condition and consists of conductive, radiative, and enthalpy changes across the interface. Term 1 represents the heat flux convected from the flame to the fuel surface, whereas term 2 is the heat lost by conduction into the solid fuel. The analogous radiant fluxes are given by terms 3 and 4. Term 3 represents the net radiant flux to the surface from the flame and possible soot particles. The fuel-rich gases between the flame and surface may absorb some portion of the radiation, and reradiation from the surface to the gas phase is also possible. For fuels containing metal additives, such as aluminum, an additional term must be included in the energy flux balance to account for the radiant flux due to metallic particles. Terms 5 and 7 represent the chemical enthalpy and sensible enthalpy, respectively, delivered to the pyrolyzing surface by fuel regression. Notice that these terms both contain the solid-fuel regression rate as a variable. Term 6 indicates the chemical enthalpy carried away from the surface by the pyrolyzed species via bulk motion and diffusion, and term 8 accounts for the corresponding sensible enthalpy flux. This energy flux balance can serves as a useful starting point for an analytic regression rate approach based on heat transfer from the flame to the fuel surface and is given by

$$Q_{\text{tot}} = \rho_f r \left[\left(\sum_i^n Y_{i+} \Delta H^o_{f,i} \right) - \Delta H^o_{f,\text{HTPB}} \right] + \rho_f r \sum_i^n Y_{i+} \left[\int_{T_{\text{ref}}}^{T_s} c_{p,i}\, \mathrm{d}T \right]$$

The Appendix provides the derivation for this equation. The chemical species mass flux boundary condition represents a balance between species generated on the surface by decomposition reactions and species carried away from the surface by bulk motion and diffusion. Here, terms due to subsurface diffusion and species accumulation on the surface are assumed negligible. The overall mass flux balance has been used to show that the pyrolyzed-fuel mass flux must equal the product of solid-fuel density and regression rate.

At this point, note that most empirical, semi-empirical, or theoretical investigations have shown that the fuel regression rate depends very strongly on the local mass flux along the fuel port. However, the "normal" regression rate regime of practical interest is bound between two extreme mass flux regimes: the upper limit, often called the "flooding" limit, and the lower limit, referred to here as the "cooking" limit. Flooding corresponds to a situation wherein the oxidizer flux is high enough to prevent burning in the fuel port, or is increased to the point where

the flame is extinguished, presumably due to finite reaction rates that can not keep pace with fluid dynamic mixing rates at high flux levels or to the development of very oxidizer-rich conditions in the fuel port. Flooding has not received much attention in the open literature, although Muzzy [8] has described it briefly. According to him, in the transition region between steady-state combustion and the onset of flooding, the combustion process appears to be controlled by kinetics and not by diffusion. Flooding limits also appear to depend on the specific fuel/oxidizer combination and the motor pressure. Highly reactive fuels and oxidizers, such as lithium hydride and fluorinated oxidizers, have higher flooding limits, that is, can operate in classical hybrid mode at a relatively high G_o threshold, than less reactive propellants, such as hydrocarbon fuels with N_2O. Establishing particular flooding limits may be important for some volume-limited, high-energy applications, such as tactical systems.

On the other hand, at very low mass fluxes, the convective heat-transfer rates to the fuel surface, and, therefore, the fuel regression rates, are low and the thermal wave penetrates deep into the solid-fuel grain. Depending on the specific type of fuel, this situation can lead to melting or charring and subsurface cooking reactions that may cause the virgin fuel to undergo depolymerization reactions well below the surface. According to Marxman et al. [9] this situation may lead to undesirable modifications to the fuel properties, poor combustion efficiency, and unreliable operation. For Plexiglas/oxygen, Marxman et al. [9] showed that the minimum regression rate before these phenomena become important is about 0.1 mm/s, which is probably lower than any practical application of interest. For the remainder of this chapter, we will concern ourselves with systems that operate between these two extrema of flooding and cooking.

This brief, qualitative description of some hybrid rocket combustion phenomena serves as an appropriate point of departure for a review of the relevant literature. Probably the most influential theory so far for explaining regression rate behavior was developed by Marxman and Gilbert [2], Marxman et al. [9], and Marxman [10, 11]. They based their approach on turbulent combustion over a flat-fuel surface. According to their study, the solid-fuel regression rate is governed primarily by convective heat transfer from the flame to the fuel surface. The local mass flux G is the primary operating parameter governing regression rate in this theory. Both Marxman and Paul et al. [12] later attempted to modify Marxman and Gilbert's original approach to account for density variations across the boundary layer. Marxman et al. [9] and Marxman [10, 11] also made allowances for radiant heat flux due to gas-phase combustion products, but concluded that only a strong source of thermal radiation would significantly alter the regression rate behavior.

Several more recent investigations have furthered the study of thermal radiation effects in hybrid combustion. Estey et al. [13] found that including a term to account for thermal radiation improved empirical correlations for metal-loaded fuels, whereas convective heat-transfer theory worked best for pure hydrocarbon fuels. Strand et al. [14] measured the total radiant heat flux to the fuel surface in a slab-geometry, laboratory-scale motor. In contrast to Estey's findings and the earlier conclusions of Marxman, they found that radiation from soot may significantly influence the regression rate of pure HTPB, especially at lower O/F ratios. They also suggested that future experiments consider the variations in thermal radiation with motor pressure and O/F ratio. Chiaverini et al. [15, 16] drew on

Strand's work [14] to semi-empirically characterize radiant heat fluxes from both gas-phase combustion products and soot for a large amount of hot-fire data under practical operating conditions for oxygen and HTPB.

At about the same time Marxman and his coworkers performed their work, Smoot and Price [17–19] conducted a large number of experiments which indicated that, at relatively low pressures and high mass fluxes, the solid-fuel regression rates in hybrids employing fluorinated oxidizers displayed a strong dependency on chamber pressure, but only a weak dependence on mass flux. After an extensive investigation, they concluded that oxidizer transport to the fuel surface and subsequent first-order heterogeneous reactions were responsible for the observed pressure dependence. Their correlation predicted the experimental regression rates to within $\pm 40\%$. However, both Kosdon and Williams [20] and Muzzy [8] attributed the pressure dependence to finite-rate gas-phase chemical kinetics, whereas Rastogi and Deepak [21] suggested that heterogeneous reactions at the fuel surface could be responsible for this phenomenon. Citing a mismatch between pyrolysis data obtained in a hybrid motor and from various thermal pyrolysis studies, Kumar and Stickler [22] also considered the possibility of fuel surface attack by unburnt oxidizer passing through the boundary layer. Miller [23] derived an expression, based on both chemical kinetic and gasdynamic variables, that successfully correlated Smoot and Price's data to within the accuracy of their experiments. However, Wooldridge et al. [24] and Kosdon and Williams [20] pointed out potentially significant limitations of Miller's approach. Chiaverini et al. [16] did not find any significant effects of chamber pressure on regression rate and concluded that, under typical hybrid motor conditions for oxygen and HTPB, neither gas-phase chemical kinetics nor heterogeneous surface reactions play a significant role in regression rate behavior. In support of this result, they subsequently conducted thermal pyrolysis experiments at atmospheric pressure in an inert environment and showed that the resulting pyrolysis law matched their motor firing data to within the accuracy of the experimental measurement [25]. These various works, as well as those of others, will be examined in more detail later.

The results for the classical hybrid configuration provide a strong basis for the analysis of non-classical hybrids, which include swirl-injected hybrids, vortex hybrids, end-burning hybrids, radial-flow hybrids, and hybrids employing cryogenic solid fuels or paraffin-based solid fuels. These concepts will be reviewed in Sec. IV.

III. Regression Rate Behavior of Classical Hybrids

Here, we will examine regression rate characteristics of classical hybrid configurations in the following manner: First, a few early investigations that laid the groundwork for future efforts are discussed. This section is followed by a more thorough discussion of the very important classical diffusion-limited theory, as developed by Marxman and his coworkers in the early 1960s. The accuracy of heat-transfer diffusion-limited theory has largely been borne out in the intervening years since Marxman's original work, especially for modern fuels such as HTPB and HTPB-based fuel blends. Modifications to classical diffusion-limited theory to account for the effects of thermal radiation and variable fluid and transport properties across the boundary layer are also presented. This section is followed by a

discussion of the effects of chemical kinetics on regression rate behavior. It should be stated from the outset that the role of chemical kinetics, whether for gas-phase reactions in the boundary layer, heterogeneous reactions due to oxidizer attacking the fuel surface, or polymer degradation in the condensed phase, appears to have been the most controversial aspect of hybrid regression rate analyses and experimentation during the 1960s and early part of the 1970s. For an example of this, the interested reader is invited to review the Comments section at the end of [11] where Marxman responds to various inquiries from other hybrid researchers such as F. A. Williams, L. D. Smoot, and R. J. Muzzy.

A. Early Investigations

Early investigations into hybrid solid-fuel regression rate behavior were conducted by Bartel and Rannie [26], Emmons [27], and Houser and Peck [28]. Green [29] presented an early summary of hybrid research that included work by additional investigators. Bartel and Rannie considered the one-dimensional axial flow of air through a tube of carbon. The turbulent airstream entered the tube of diameter D with assumed known inlet velocity, density, pressure, and total temperature. Bartel and Rannie theorized that the diffusion of oxygen to the fuel surface controlled the fuel regression process. They also assumed that the mass addition due to fuel burning was negligible in comparison to the air mass flux down the tube length and that fuel and air were completely mixed at each station along the tube. By examining the rate of heat added to the gas flowing through an elemental cross sectional area, they obtained the following expression:

$$\rho_f r = \frac{1}{2} c_f G f_m \exp(-2c_f x/D) \tag{1}$$

where $\rho_f r$ is the mass burning rate of fuel per unit area, c_f the friction coefficient on the fuel surface, G the average mass flux down the tube, f_m the fuel/air ratio of the reaction, x the distance along the tube from the entrance, and D the tube inner diameter. According to this expression, the fuel burning rate decreases exponentially with axial position along the tube. Bartel and Rannie also used the well-known pipe flow correlation of friction coefficient with Reynolds number, $c_f = 0.046 Re_D^{-0.2}$. When this expression is substituted into Eq. (1), a $G^{0.8}$ dependency is obtained because Re_D can be written as GD/μ. Although Bartel and Rannie correctly obtained the classical $G^{0.8}$ dependence for the regression rate, the exponential decay of the regression rate with respect to length has not been empirically verified. In fact, most empirical results show an increase in regression rate with respect to increasing distance from the head end of the fuel grain, a behavior that is usually attributed to accumulation of fuel and corresponding increase in turbulence intensity and heat transfer in the downstream direction.

Emmons [27] also obtained a solution for the boundary-layer combustion of a gaseous oxidizer flowing over a fuel surface, although he did not necessarily have in mind hybrid rocket propulsion as an application of the problem. Emmons assumed a laminar flame zone of finite thickness in the boundary layer and then transformed the energy, momentum, and species equations into Blasius-type equations by assuming unity Prandtl, Lewis, and Schmidt numbers. His exact numerical

solution was

$$\rho_f r = \rho_e u_e Y(B)/Re_x^{1/2} \tag{2}$$

where $Y(B)$ is a function of the blowing number B (which Emmons calls the heat ratio). The blowing number is a very important parameter for hybrid regression rate investigations and can be defined as the ratio of the thermal energy per unit mass of the core flow to the thermal energy required at the surface to gasify a unit mass of fuel

$$B = \frac{[(K_{O_e} - K_{O_s})(H/n_O) + c_p(T_e - T_s)]}{[\Delta H_v + c_s(T_s - T_i)]} \tag{3}$$

In Eq. (3) K_O is the oxidizer concentration, H the heat of reaction per mass of fuel, and n_O the O/F ratio. Subscript e indicates the outer edge of the boundary layer, and subscripts s and i represent the surface and initial conditions, respectively. For the range of $0.5 < B < 5$, Emmons found

$$\rho_f r = \rho_e u_e[0.18 + \log_{10}(B + 0.7)]/Re_x^{1/2} \tag{4}$$

where $\rho_e u_e = G$. Notice from this expression that $\rho_f r$ is proportional to $G^{0.5}$ due to the assumed laminar nature of the flow. The boundary layer involved in practical hybrid systems is probably mostly turbulent due to the destabilizing influence of mass injection at the solid surface, as well as the high Reynolds number of the oxidizer flow. However, the significance of Emmons work is the inclusion of the boundary layer-blowing parameter B, which later investigators have found central to hybrid regression analysis.

Houser and Peck made a useful contribution to the hybrid literature with their measurement of quasi-real-time regression rate of a cylindrical hybrid-fuel grain of several polymeric fuels burning with gaseous oxygen [28]. They burned cylindrical blocks of varying total length having an initial inner diameter of 1 in. Most tests were conducted with polymethylmethacrylate (PMMA) as the solid fuel. They also used embedded chromel–alumel thermocouples of either 25 or 15 μm diameter to measure the fuel surface temperature. The regression rates were deduced at several axial positions at various flow rates, using an interrupted burning technique wherein the combustion is stopped, fuel thickness measured, and the test restarted. The main disadvantage of this method is that it is difficult to estimate the cumulative error generated by the startup and shutdown transients. Houser and Peck found that the inner radius of the combustion port followed a power-law function of time of the form

$$\text{rad}(t) = A + Bt^{0.8} + Ct^{0.3} \tag{5}$$

so that the instantaneous regression rate r at a particular axial location can be found by taking the time derivative of Eq. (5),

$$r(t) = 0.8B/t^{0.2} + 0.3C/t^{0.7} \tag{6}$$

where A, B, and C are empirical constants. Houser and Peck did not provide any theoretical significance for this equation. Notice that the best-fit equation

given by Eq. (6) does not apply at time zero, where the regression rate goes to infinity. In addition, Houser and Peck were unable to obtain accurate data for times less than 10 s after ignition. Despite these shortcomings, they were possibly the first to recognize the importance of obtaining the regression rates as a function of both axial position and time. Houser and Peck also showed experimentally that the regression rate decreases with time due to an increase in port area (and corresponding decrease in port mass flux) and increases with axial distance due to an increase in mass flux from fuel addition. (Note that this experimental finding contradicted Bartel and Rannie's earlier theoretical treatment [26].) Furthermore, Houser and Peck showed that the measured fuel surface temperatures were the same for both translucent fuel grains and opaque fuel grains processed with carbon black. Chiaverini et al. [14, 15] drew upon their method to determine instantaneous regression rates from x-ray radiography videos of hybrid rocket fuel ports and found similar qualitative results concerning the time and spatial dependence of the solid-fuel regression rates.

B. Marxman's Diffusion-Limited Analysis

The most influential heat-transfer-limited theory of hybrid combustion was developed by Marxman, Gilbert, Wooldridge, and Muzzy at the United Technology Center in Sunnyvale, California during the early-to-mid 1960s. Marxman and Gilbert [2] and Marxman et al. [9] discuss their initial analysis and experiments in detail. According to their theory, a flame sheet separates the boundary layer into two zones: one zone above the flame, where the temperature and velocity gradients are opposite in direction, and one zone below the flame, where the gradients are in the same direction, as shown in Fig. 4. The upper zone is oxidizer rich, while the lower zone is fuel rich. The flame occurs at a position where the concentrations of each are sufficient for combustion to occur [2], but not necessarily at a stoichiometric condition, according to their analysis. In as much as Marxman and Gilbert [2] conjectured that heat transfer from the flame to the fuel surface was the controlling mechanism of hybrid combustion, they applied a simplified energy flux balance at the fuel surface to obtain an expression for the fuel regression rate, as follows:

$$\rho_f r \Delta H_{v,\text{eff}} = Q_{\text{tot}} \tag{7}$$

where ρ_f is the solid-fuel density, r the regression rate, Q_{tot} the heat transfer per unit area to the fuel surface (which may include both convective and radiant components), and $\Delta H_{v,\text{eff}}$ the total energy required to heat a unit mass of the solid fuel from its initial temperature to the surface temperature and then to vaporize it. Physically, Eq. (7) states that the enthalpy delivered to the fuel surface via solid-fuel regression equals the total heat flux incident on the fuel surface.

To derive a useful equation for the regression rate from Eq. (7), Marxman and Gilbert assumed that the boundary-layer flow was turbulent over the entire fuel slab length due to the destabilizing effect of fuel injection at the surface. Second, they reasoned that the Reynolds analogy (which states that the transport of energy and momentum in a boundary layer are similar) and unity Lewis and Prandtl numbers hold in both the upper and lower boundary-layer zones, but not necessarily in the flame sheet itself. Third, they assumed that the velocity profile in the boundary layer is unaffected or only slightly affected by the presence of wall blowing

and combustion, so that the standard friction coefficient for a turbulent boundary layer remains valid. (Note that later numerical and semi-empirical analyzes by Venketeswaran et al. and Chiaverini et al. have found that the hot, low-density reaction zone in the boundary layer may actually have a quite significant effect on the velocity profile. These analyses and effects are discussed later in this chapter and in Chapter 8.) By employing these assumptions, Marxman and Gilbert [2] developed an equation for the local solid-fuel regression rate given by

$$\rho_f r = CGRe_x^{-0.2}(St/St_o)(u_e/u_{\text{fl}})[(h_{\text{fl}} - h_w)/\Delta H_{v,\text{eff}}] \tag{8}$$

where C is a function of the mainstream Mach number (about 0.03 for the low Mach numbers encountered in hybrids), G the local mass flux due to both oxidizer injection and all upstream fuel addition, St the Stanton number, St_o the Stanton number in the absence of blowing for turbulent flow over a flat plate, u_e the velocity at the edge of the boundary layer, u_c the velocity at the flame, h_{fl} the stagnation enthalpy at the flame temperature, h_w the enthalpy at the wall in the gas phase, and $\Delta H_{v,\text{eff}}$ the total heat of gasification, as in Eq. (7). The ratio of Stanton numbers, St/St_o, represents the fraction of heat transferred to the surface by convection when compared to the case with no wall blowing. According to Marxman and Gilbert, this ratio may be lower than 0.2 for typical hybrid combustion conditions [2]. The velocity ratio u_e/u_{fl} is determined by the flame position in the boundary layer through an analysis discussed in [9]. If radiant heat transfer is also important, as may be the case with metallized or sooty fuels [9], an additional term is added to the right side of Eq. (8),

$$\rho_f r_{\text{rad}} = \sigma\varepsilon_w(\varepsilon_g T_{\text{fl}}^4 - \alpha_g T_w^4)/\Delta H_{v,\text{eff}} \tag{9}$$

where σ is the Stefan–Boltzmann constant, ε_w the emissivity of the wall, ε_g the emissivity of the gas at the flame temperature T_{fl}, and α_g the absorptivity of the gas at the wall temperature T_w.

Marxman et al. [9] present methods to obtain some of the factors comprising the right side of Eq. (8), which are not known *a priori* for a given hybrid system. Using the integral technique of boundary-layer theory, they showed that the velocity ratio between the combustion zone and boundary-layer edge may be obtained from

$$\frac{u_{\text{fl}}}{u_e} = \frac{[O/F(h_{\text{fl}} - h_w)/\Delta H]}{K_{\text{ox}_e} + (O/F + K_{\text{ox}_e})[(h_{\text{fl}} - h_w)/\Delta H_{v,\text{eff}}]} \tag{10}$$

where O/F is the oxidizer-to-fuel mass ratio and K_{ox_e} is the mass fraction of oxidizer in the freestream core flow, which, for a hybrid motor using oxygen as the oxidizer, would equal unity. Marxman et al. assumed that the O/F ratio and the $(h_{\text{fl}} - h_w)/\Delta H_{v,\text{eff}}$ factor are independent of axial location along the fuel port and constant for a given oxidizer/fuel combination. Marxman approximated the Stanton number ratio as a function of B as [9]

$$St/St_o = 1.2B^{-0.77} \tag{11}$$

for $5 < B < 100$, where

$$B = \frac{\rho v|_w}{\rho_e u_e(c_f/2)} = u_e/u_{\text{fl}}[(h_{\text{fl}} - h_w)/\Delta H_{v,\text{eff}}] \tag{12}$$

is the mass transfer, or blowing, number. (Altman [30] has recently shown that the power of -0.77 originally determined by Marxman is actually closer to -0.68.) When the Prandtl number is equal to unity, indicating similar transfer of momentum and energy, and the radiation term in Eq. (9) is negligible, the value of B can be approximated by the last expression given on the right side of Eq. (12), knowing the velocity ratio from Eq. (11). The blowing number B represents both the similarity parameter for a boundary layer with wall injection and a thermodynamic parameter of the system that describes the enthalpy driving force between the flame and the wall that causes fuel regression. When $B =$ constant and $Le = 1$, the velocity, species concentration, and enthalpy profiles are similar everywhere in the turbulent boundary layer [9].

Combining Equations (8), (11), and (12) yields a useful, simplified regression rate expression for hybrid combustion with no radiant heat transfer,

$$\rho_f r = 0.036 G B^{0.23} Re_x^{-0.2} \propto B^{0.23} G^{0.8} x^{-0.2} \tag{13a}$$

or, with Altman's refit of the data,

$$\rho_f r \propto B^{0.32} G^{0.8} x^{-0.2} \tag{13b}$$

Note that specifying the oxidizer/fuel combination essentially fixes B in this analysis. Marxman noted that because B is raised to a small power, even large changes in $(h_{\mathrm{fl}} - h_w)$ or $\Delta H_{v,\mathrm{eff}}$ produce only minor changes in the regression rate. This phenomenon reflects the tight coupling between the solid-fuel regression rate and the aerodynamics of the reacting boundary-layer flow. Increasing $(h_{\mathrm{fl}} - h_w)$, for example, tends to increase the regression rate. However, the increase in fuel mass injection into the boundary layer creates stronger blockage of the convective heat transfer to the surface, which tends to decrease the regression rate. Paul et al. [12] later attempted to modify Marxman's analysis to account for the effect of the molecular weight of the pyrolyzed species on the blocking effect, which, according to Paul et al. [11], may explain why hydrocarbon fuels often display significantly different regression rates under the same operating conditions. This will be discussed later in more detail.

In Marxman's analysis, the fuel regression rate depends primarily on G, the total mass flux. Because G at some location x depends on both the oxidizer flow entering the combustion port as well as all fuel injected upstream of location x, the local regression rate depends on the regression rate at all upstream locations. In addition, G decreases as the port area increases during burning. Therefore, one expects the regression generally to increase with axial position along the fuel grain, while decreasing with time, as Houser and Peck [28] showed experimentally. However, recall from Eq. (13a) that the regression rate also exhibits a weak negative dependence on axial position x, which reflects the effects of boundary-layer growth on heat transfer. As the boundary layer increases in the downstream direction, the boundary-layer temperature and velocity gradients normal to the fuel surface become less severe, all other things being equal, so that the convective heat flux decreases. As predicted by Marxman and Gilbert [2], the competing effects of increasing mass flux and increasing boundary-layer thickness in the downstream direction suggest that a location of minimum regression rate exists somewhere along the fuel port.

Several researchers have reported empirical evidence of this phenomenon, including Chiaverini et al. [15] and Yuasa et al. [31]. Figure 5 shows typical data Chiaverini et al. observed during their empirical investigation of hybrid motor internal ballistics using a real-time x-ray radiography system to interrogate local, instantaneous regression rates in a slab-geometry hybrid burning gaseous oxygen (GOX) and HTPB [15]. The lower portion of the graph shows several instantaneous regression rate profiles from test 13, with an initial G_o of 215 $kg/m^2 \cdot s$, and from test 15, with an initial G_o of 320 $kg/m^2 \cdot s$. For test 13, the x-ray system was set up to view the upstream portion of the fuel slabs, whereas for test 15, the x-ray images were taken from the downstream region of the fuel slabs. The instantaneous profiles are 0.5 s apart for test 13 and 0.4 s apart for test 15.

The test 13 data show that the regression rate is relatively high near the leading edge of the fuel slabs, but decreases with axial location for a certain interval until reaching a minimum, beyond which the regression rate increases with increasing axial distance from the leading edge. This point of minimum regression rate corresponds to the crossover of the two competing effects of boundary-layer growth, as represented by the local Reynolds number, and increasing local mass

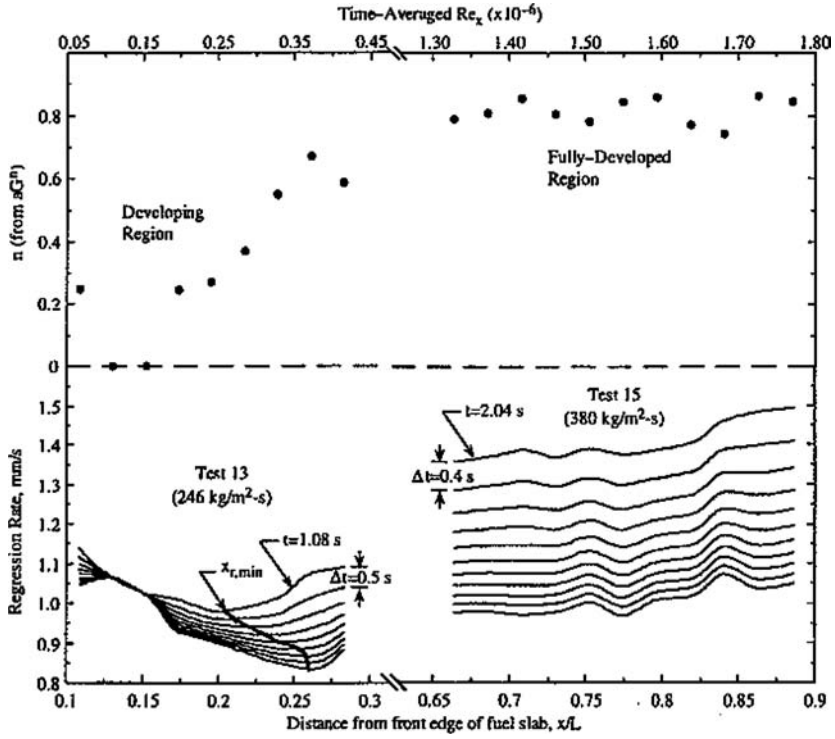

Fig. 5 Internal ballistic behavior in a laboratory-scale, slab-geometry hybrid motor. (From Chiaverini et al. [15].)

flux. Near the fuel slab leading edge, the effect of boundary-layer growth (increasing Reynolds number Re_x) dominates the solid-fuel regression rate, but farther downstream, the effect of mass flux becomes more important, thus, causing the bowl-shaped regression rate profiles shown in Fig. 5. In addition, the location of the minimum regression rate $x_{r_{\min}}$ moved downstream slightly during the test, as indicated by the heavy line passing through the locus of minimums. It is believed that because the regression rate is more sensitive to G than to x, the decrease of mass flux with time tends to favor the boundary-layer growth effect, thus, causing the location of minimum regression to move downstream with time. The regression rates also vary with position in the downstream region, but generally tend to increase in the downstream direction due to fuel mass accumulation. The nonuniform regression behavior of the fuel slabs in the downstream region was assumed by the researchers [15] to be caused by local increases in turbulence generated by several embedded thermocouple extension wires.

The upper portion of Fig. 5 shows the variation of the power n on G, that is, $r \sim G^n$, with time-averaged axial Reynolds number (as measured from the fuel slab leading edge), which has a one-to-one correspondence with the x/L axis. The deduced value of n, obtained by curve fitting a set of instantaneous r with the corresponding G values at a given axial station, gives an indication of the boundary-layer characteristics. In the downstream region (test 15 data), the particular n at individual axial locations did not vary significantly from the expected value of 0.8 for fully turbulent flow. In the upstream entrance flow region, however, the local n varies signficantly. Near the fuel slab leading edge, for x/L between 0.125 and 0.15, the deduced instantaneous regression rates were found to be independent of G, that is, $n = 0$, and also constant with time. Chiaverini et al. [15] conjectured that this behavior may have been caused by a vortical recirculation zone, due to the axial GOX injector, standing in the port entrance. As discussed later in Sec. IIIF, recent results from injector studies suggest that this type of regression rate behavior may also be related to a similar phenomena of oxidizer jet impingement.

Downstream of this initial region, the value of n increases approximately linearly until reaching the end of the viewing window at $x/L = 0.28$. This behavior suggests that entrance effects or recirculating flow structures due to the aerodynamics of the injector influence the flow behavior in this region. Although it is tempting to suggest the existence of a laminar flow regime in the vicinity of the $n \sim 0.5$ region, it is difficult to see how a laminar boundary layer could exist in the aggressive environment present in the hybrid motor, especially considering the destabilizing influences of wall blowing (fuel pyrolysis) and temperature inversion due to the presence of the flame zone. More likely, this behavior is also a consequence of entrance effects and the particular GOX injection method.

C. Effects of Thermal Radiation on Convective Heat-Transfer-Limited Models

For systems wherein radiant heat transfer to the fuel surface may be important, such as in the case of a solid-fuel grain with a high metal loading or a heavily sooting fuel, the diffusion-limited analysis must be modified to account for the additional surface heat flux due to radiation. Marxman et al. [9] showed that the

regression rate for combined convective and radiant heat transfer can be estimated from

$$\rho_f r = [Q_c \exp(-Q_{\text{rad}}/Q_c) + Q_{\text{rad}}]/\Delta H_{v,\text{eff}} \tag{14}$$

where

$$Q_c = 0.036 G \Delta H_{v,\text{eff}} (Gx/\mu)^{-0.2} B^{0.23} \tag{15}$$

$$Q_{\text{rad}} = \sigma \varepsilon_w (\varepsilon_g T_{\text{fl}}^4 - \alpha_g T_w^4) \tag{16}$$

whereas B remains as defined earlier. Note that Eq. (14) reduces to Eq. (8) in the absence of radiant heat transfer. Equation (16) results from a radiation exchange between the fuel surface and the flame zone. The first term in parentheses represents the radiant flux emitted by the flame zone to the surface, whereas the second is the radiant flux absorbed by the flame from the surface. Note that because the flame temperature typically has a value of about 3000 K or greater for practical hybrids, while the surface temperature is on the order of 1000 K, the second term in parentheses is negligible due to the T^4 dependence and because the emissivity and absorptivity of the gas-phase reaction zone are typically of the same order. Marxman et al. stated that for a Plexiglas/oxygen system, the gas-phase emissivity is about 0.02 [9]. Their experiments indicated that the radiant transfer to the solid-fuel surface amounted to about 5–10% of the convective heat transfer for nonmetallized fuels.

From the preceding analysis, Marxman noted that small amounts of radiant heat flux should not affect the regression rate to a significant degree because the radiant flux causes additional mass transfer into the boundary layer, which in turn acts to block more of the convective heat flux. Marxman et al. [9], and later Muzzy [8], suggested that only strong radiation sources are likely to significant affect solid-fuel regression rate behavior in hybrid motors. Marxman's analysis in [10] indicates that weak radiant transfer on the order of one-half the convective heat transfer, results in a small (about 10%) net increase in regression rate.

Several other researchers have constructed heat-transfer models that include the effects of thermal radiation on regression rate behavior, and it should be noted that a fair amount of disagreement appears in the literature regarding the importance this effect.

In a more recent publication, Estey et al. also considered radiant heat transfer [13]. They employed a radiant flux term of the form

$$Q_{\text{rad}} = \sigma T_g^4 (1 - e^{-k_g p D}) \tag{17}$$

which is similar to that suggested by Muzzy [8]. Here, the parameter k_g is the gas-phase absorption coefficient and the term in parentheses is the emissivity of the gas phase, which increases as the product of pressure and diameter (or hydraulic diameter) increases. Note that Eq. (17) is equivalent to Eq. (16) if one ignores the (small) second term on the right side of Eq. (16). From their correlation of both small- and large-scale data obtained from other researchers, Estey et al. concluded that the addition of a radiant transfer term for metal-loaded fuels improves

empirical correlations, whereas for pure hydrocarbon fuels, classical convective heat-transfer theory worked best [13].

Strand et al. [14] provided a empirical treatment of radiant heat transfer in a laboratory hybrid slab-burning motor. They used a calorimeter, radiometer, and infrared thermometer to measure the total heat flux to the fuel surface, radiant heat flux to the fuel surface, and flame temperature, respectively. The operating pressure, average regression rate, and average O/F ratio were also measured and reported. Based on observations of the combustion zone through optical windows and of the exhaust plume, Strand et al. suggested that the measured radiant heat flux incident to the fuel surface originated from both combustion product gases, such as CO_2 and H_2O, and soot particles [14]. For the gas-phase radiation, Strand used Eq. (17), but also included an empirical expression for k_g as a function of pressure

$$k_g = 9.33 \times 10^{-4} - 6.19 \times 10^{-6} p + 1.79 \times 10^{-8} p^2 \tag{18}$$

which was obtained from thermal radiation measurements of a high-energy, nonmetalized solid propellant, where p was measured in pounds per square inch gauge. They represented the radiant heat flux from soot by

$$Q_{r,s} = \sigma T_g^4 (1 - e^{-a_p N p}) \tag{19}$$

where N_p is the particle number density and a_p is a constant. Note the similarity to Eq. (17). The term $a_p N_p$ depends on the weight fraction of the radiating particles and may be evaluated from [14]

$$a_p N_p = 0.134[\alpha_p p/(1 + O/F - \alpha_p)] \tag{20}$$

where α_p is the soot particle weight fraction. Notice that the exponential term in Eq. (19) depends on the pressure and O/F ratio through Eq. (20). Strand et al. found a reference particle weight fraction α_p by solving Eqs (19) and (20) using the measured radiant surface heat flux at a test condition of 158 psi and an assumed O/F ratio of 2.0. They calculated a value of 0.045 for α_p at these conditions, but also suggested that, at higher pressures and higher O/F ratios, α_p could decrease to about 0.01.

Implicit in the Strand et al. development is the assumption that the soot particles have the same temperature as the flame zone. Because soot particles generally have sizes in the range of 0.1–0.005 μm, they should come to equilibrium with the surrounding gas very quickly and emit thermal radiation over the entire infrared spectrum [32]. In contrast to previous researchers, Strand et al., thus, concluded that particle radiation from powdery soot was a significant source of energy driving solid-fuel regression in their experiments. They found that the total radiant heat flux, from both gas-phase products and soot, often accounted for more than 50% of the total heat flux, which represents a much larger fraction than that postulated by earlier researchers. They also emphasized the importance of including variations in gas radiation with pressure and O/F ratio in future works.

As part of their investigation, Chiaverini et al. [15, 16, 33] used a semi-empirical approach to investigate radiant heat-transfer phenomena in hybrid motors burning

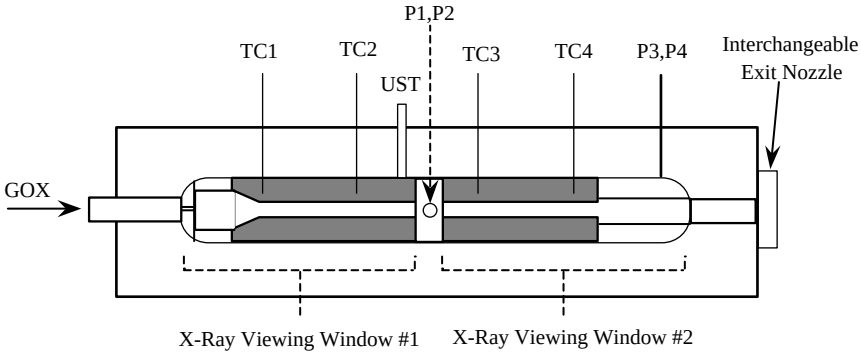

Fig. 6 Schematic of Pennsylvania State University slab-geometry motor instrumentation: ultrasonic transducer (UST), pressure tap (P), and thermocouple (TC).

HTPB and GOX. As described earlier, they employed an x-ray radiography system to interrogate the internal ballistics of a slab-burning hybrid motor as a function of both time and local position. They also used an ultrasonic pulse–echo system to verify the regression rate results from the x-ray radiography system [34]. Shown in Fig. 6, the laboratory-scale hybrid motor had fuel slabs located at the top and bottom of the motor and reinforced graphite windows to accommodate the x-ray radiography system along the motor side walls. The motor utilized two opposing fuel slabs each 58.4 cm long and 7.62 cm wide with a uniform initial web thickness of either 4.28 or 4.45 cm, corresponding to port heights of 1.27 or 0.89 cm, respectively. The motor operated at pressures of 13.5–68 atm, GOX mass fluxes of 100–530 $\mathrm{kg/m^2 \cdot s}$, initial fuel port length-to-hydraulic diameter ratios of 25–37, and average O/F ratios of 1.6–2.5.

During the early portion of the investigation, Chiaverini et al. found indications of the potential influence of radiant heat transfer by examining behavior of the instantaneous regression rate traces vs the total mass flux [15]. As shown in Fig. 7, the chamber pressure (in terms of megapascal at various locations) seemed to affect the regression rate in the low-mass-flux regime, with higher pressures causing higher regression due to larger overall heat flux to the fuel surface. If turbulent heat transfer alone governed the regression rate the data would tend to follow a straight line on this log–log plot of r vs G. Notice also that the influence of radiation tends to decrease the effective slope of the regression rate vs oxidizer mass flux curve in the low-mass-flux regime. The power n of a simple aG^n correlation would be lower under the influence of radiation than in the absence of radiation because of the reduced importance of convection (represented by G). Strand et al. also recognized this effect at low flux levels [35]. In addition, Muzzy presented regression rate data for polybutadiene/PMMA fuel burning with inhibited red fuming nitric acid (IRFNA) from the High-Altitude Supersonic Target (HAST) II program that indicated a similar pressure dependence due to radiation [8], shown here as Fig. 8. Note the similarity with Fig. 7.

Using the interfacial energy flux balance shown in Fig. 4 and described in the Appendix, Chiaverini et al. coupled their local, instantaneous regression rate data

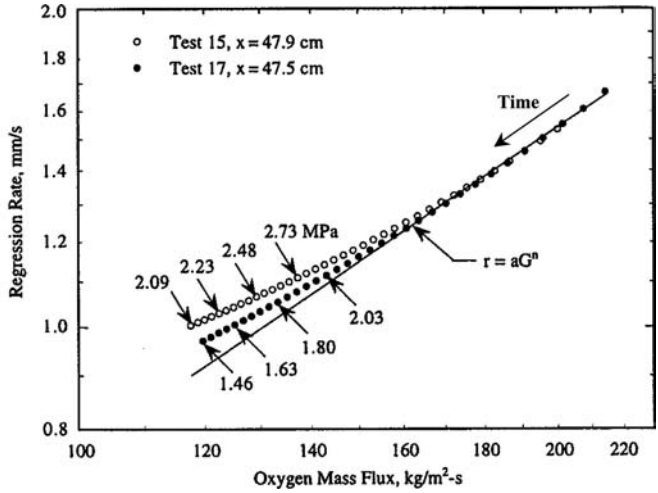

Fig. 7 Effect of pressure via radiant heat flux on regression rate for HTPB/GOX. (From Chiaverini et al. [15].)

with their empirical fuel pyrolysis law [25] (shown later) to calculate the local total heat flux to the fuel surface. The total heat flux was assumed to be the sum of the convective heat flux, the radiant heat flux due to soot particles, and the radiant heat flux due to gas-phase combustion products. To determine these component heat

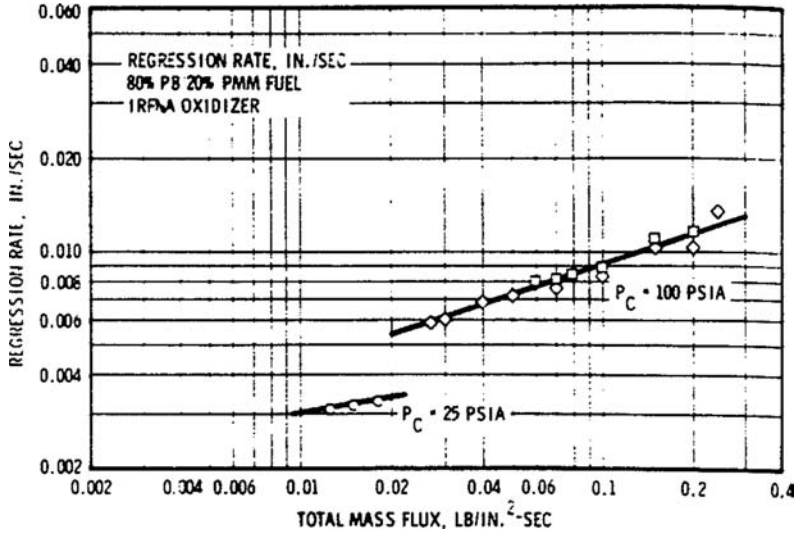

Fig. 8 Effect of pressure via radiant heat flux on regression rate for 80% PB/20% PMMA fuel and IRFNA oxidizer. (From Muzzy [8].)

fluxes, the Strand et al. data were used to develop an appropriate soot radiation model. To distinguish the relative amounts of radiation from soot and gas-phase products in the Strand et al. [14] experiments, Chiaverini et al. employed chemical equilibrium calculations coupled with Leckner's method to estimate the heat flux due to CO_2 and H_2O and Edward's exponential wide-band model to calculate the contribution from CO [32]. The amount of radiation due to these gas-phase products was then subtracted from the Strand et al. total radiation measurements to yield the estimated amount of net radiation due to soot particles reaching the solid-fuel surface. The results of this analysis indicated that radiation from the gas-phase products actually contributed a relatively small amount to the total radiant heat flux. Soot was found to account for about 80% of the total radiant heat flux measured by Strand et al. [14].

The soot absorption coefficient k_s was found by assuming that the soot particles were in thermal equilibrium with the surrounding gas and that the deduced values of $Q_{r,s}$ at the operating conditions provided by Strand et al. had the following form:

$$Q_{r,s} = \sigma T_g^4 (1 - e^{-k_s}) \tag{21}$$

where $Q_{r,s}$ is the net radiative heat flux due to soot shown in Table 1 and the term in parentheses is the effective soot emissivity. The gas temperature T_g was estimated to be 95% of the equilibrium flame temperature because Strand et al. provided the measured flame temperature only for one particular case. Chiaverini

Table 1 Empirical data from Strand et al. [14] and estimated quantities from Chiaverini et al. [16] used to determine radiant characteristics of HTPB/GOX

	Case						
Quantity	1	2	3	4	5	6	7
Pressure, psia	150	313	158	158	217	320	240
Global O/F	2	3	2	2	2	3	2
G, $lb_m/in.^2 \cdot s$	0.125	0.072	0.074	0.080	0.107	0.125	0.087
$T_{fl,eq}$, K	3419.2	3614.2	3425.9	3425.9	3468.9	3616.6	3482.9
Total heat flux, $cal/cm^2 \cdot s$	94	69	80	84	107	111	80
Convective heat flux, $cal/cm^2 \cdot s$	60	35	35.5	40	60	74	42
Total radial heat flux, $cal/cm^2 \cdot s$	34	34	44.5	44	47	37	38
Gas radiant heat flux $cal/cm^2 \cdot s$[a]	1.78	5.67	1.89	1.89	2.57	5.72	2.85
Gas-phase emissivity[a]	0.0128	0.0321	0.0134	0.0134	0.0174	0.0326	0.0188
Soot radial heat flux, $cal/cm^2 \cdot s$[a]	32.22	28.33	42.61	42.61	44.43	31.28	35.16
Effective soot emissivity[a]	0.174	0.123	0.228	0.226	0.227	0.135	0.176

[a]Estimated quantities from Chiaverini et al. [16].

et al. [16] noted that use of a reference gas temperature does not imply that all of the soot particles are at this temperature. In general, the soot in the motor should have a temperature distribution. Nevertheless, the reference gas temperature T_g was used to relate the absorption coefficient to the motor operating conditions. They then correlated the absorption coefficients k_s calculated using Eq. (21) with the experimental chamber pressures and O/F ratios for the different cases given by Strand et al. Table 1 summarizes the data given by Strand et al. and the quantities estimated by Chiaverini using the procedure described earlier. Notice that the calculated soot emissivites ($\sim$0.12–0.23) are much larger than the gas-phase emmisivities ($\sim$0.013–0.033), which include the combined contributions of CO_2, H_2O, and CO, especially at the lower O/F ratio. According to the data, k_s exhibited no obvious pressure dependence, but depended strongly on the measured O/F ratio, in a linear fashion, such that

$$k_s = 0.51 - 0.113O/F \tag{22}$$

Though Strand et al. measured average O/F ratios between 2 and 3, Chiaverini et al. assumed that Eq. (22) remained valid for the mixture ratios in their experiments, which ranged from about 1.5 to 3.5. Equation (22) indicates that higher O/F ratios lead to lower soot emissivities because more oxidizer is available to react with the pyrolysis products. With regard to the weak pressure dependency of the soot emissivity, Glassman [36] stated that the soot concentration should depend primarily on temperature and only weakly on pressure, which supports the described finding. Also note that Eq. (22) probably applies only for the combustion of oxygen and HTPB. Other solid-fuel and oxidizer combinations may display different sooting tendencies.

Chiaverini et al. subsequently used Eqs. (21) and (22) to determine the radiant heat flux due to soot particles and the Lecker and Edwards as given in [31] correlations to determine the gas-phase radiant heat flux. These quantities were then subtracted from the total heat flux given by the interfacial energy flux balance equation given in Sec. II along with the empirical regression rates and pyrolysis law (which relates regression rate to surface temperature) to provide the local convective heat fluxes. As described fully by Chiaverini et al. [16] and Chiaverini [37] they then developed semi-empirical correlations to relate the regression rate to heat transfer and fluid dynamic parameters, as follows:

$$\frac{\rho_f r}{G} = aStB\theta^b \left\{ c\left(\frac{Q_{\text{rad}}}{Q_c}\right)^d + \exp\left[-c\left(\frac{Q_{\text{rad}}}{Q_c}\right)^d\right]\right\} = aStB\theta^b\left[F\left(\frac{Q_{\text{rad}}}{Q_c}\right)\right] \tag{23}$$

where *a–d* are empirical parameters. In Eq. (24), the ratio of heat fluxes in the term in square brackets represents the ratio of the total radiant heat flux (sum of soot and gas-phase products) to the convective heat flux. The blowing parameter *B* and Stanton number *St* were defined as

$$St \equiv Q_c/G[\Delta H_r + (h_{\text{bulk}} - h_{\text{w}})] \tag{24}$$

$$B \equiv [\Delta H_r + (h_{\text{bulk}} - h_{\text{w}})]/(\Delta H_v)_{\text{eff}} \tag{25}$$

The term θ in Eq. (23) represents the ratio of the average flame temperature to the surface temperature and, as will be discussed further in the following section, was included to account for the effects of variable fluid and transport properties across the boundary layer.

Whereas Marxman suggested that c and d were both unity for hybrid systems with $B > 5$, Chiaverini et al. allowed these two parameters to vary to fit the data because the local, instantaneous values of B were sometimes found to be less than 5. Using a least-squares analysis to minimize error, they found that $a = 0.524$, $b = 0.6$, $c = 1.3$, and $d = 0.75$. Figure 9 shows that Eq. (23) predicted their experimental results to within $\pm 3\%$, which is about the same as the estimated measurement error [16]. Chiaverini noted that although Eq. (23) does not have a particularly simple form, each of the factors has a definite physical significance: Stanton number St and B account for turbulent heat transfer to the fuel surface in the presence of wall blowing, the term in brackets accounts for the additional driving force of thermal radiation, and θ accounts for effects of fluid and transport property variations in the shear layer below the reaction zone. When the intricate aerothermodynamics and combustion phenomena in the chemically reacting boundary-layer flow that govern the solid-fuel regression rate behavior are considered, the complex nature of Eq. (23) is not surprising. Figure 10 shows the results of a simple $r = aG^n$ Chiaverini et al. developed from their global (time- and space-averaged) data applied to both their instantaneous and average regression rate data. The correlation fairly accurately describes the average regression rate data. However, the local, real-time data does not fit nearly as well and frequently displays errors up to $\pm 20\%$.

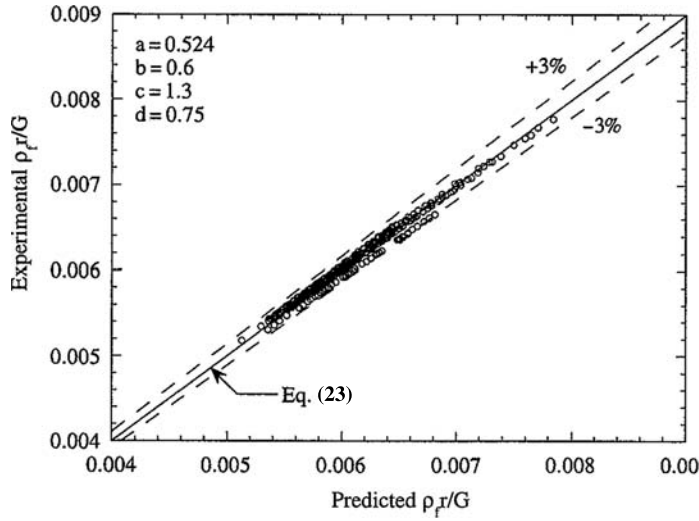

Fig. 9 Regression rate correlation using Eq. (23) with empirical constants $a = 0.524$, $b = 0.6$, $c = 1.3$, and $d = 0.75$ [16].

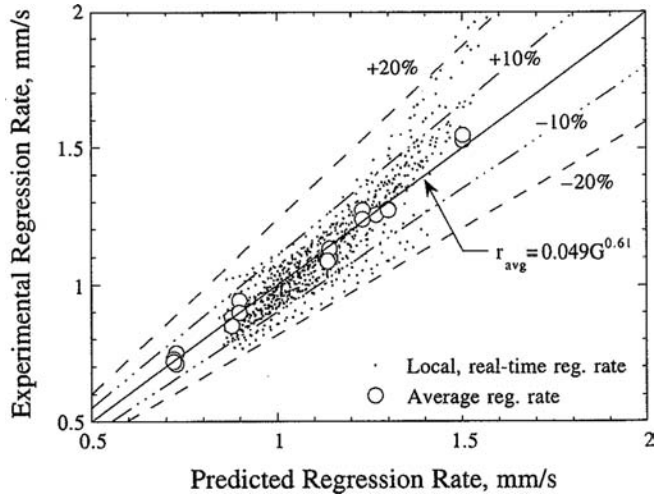

Fig. 10 Inadequacy of using power law expression generated from average regression rates to correlate instantaneous regression rates [16].

Figure 11 shows the behavior of the radiant term in Eq. (23) and the corresponding term suggested by Marxman et al. [9] and Marxman [10]. Up to a radiant-to-convective heat flux ratio of 2.86, the function $F(Q_{\text{rad}}/Q_c)$ shown in Eq. (23) is larger than Marxman's term. When $Q_{\text{rad}}/Q_c = 1.0$, $F(Q_{\text{rad}}/Q_c)$ is about 15% larger than Marxman's. Above 2.86, Marxman's term becomes larger.

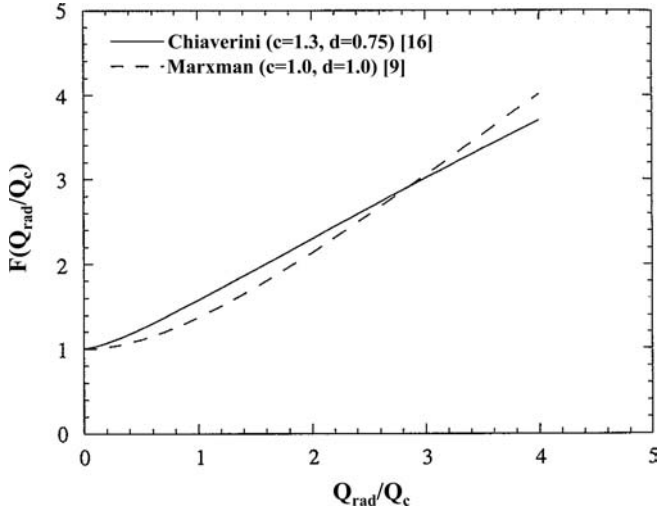

Fig. 11 Comparison of the Marxman et al. [9] and Marxman [10] and the Chiaverini et al. [16] radiation correction terms.

For the Chiaverini et al. tests, the calculated values of Q_{rad}/Q_c were most typically between 0.5 and 1.0, indicating that the radiant heat flux was generally on the same order as convective heat flux. As already noted, Strand et al. found similar results for the combustion of HTPB and GOX. Though Chiaverini [16] and Strand's [14] results may represent a reasonable approximation for other butadiene-based fuels burning with oxygen, they would not necessarily be expected to apply directly to other fuel/oxidizer combinations. In addition, systems employing fuels containing metal additives, such as those described in Chapter 10, would most likely behave in a different manner due to the additional effects of radiant heat flux resulting from the metallic combustion products.

D. Effects of Variable Fluid Properties

Although not often discussed in the more recent literature, variable fluid properties across the boundary layer has been found by several researchers to have a significant effect on the local regression rate. In 1965, Wooldridge and Muzzy [38] presented the results of a detailed and well-designed set of experiments to understand the structure of reacting, turbulent boundary layers with mass addition from the sidewalls. To simulate hybrid boundary-layer combustion processes, they conducted wind-tunnel experiments in an apparatus with sectional porous walls through which they injected mixtures of hydrogen and nitrogen. They controlled the blowing parameter B over a wide range of values, 2.2–54, and set the mixture of H_2/N_2 to react with the crossflow air at a temperature of about 1000°C. They also used a combined pressure, temperature, and gas-sampling probe to interrogate the boundary-layer profiles. They showed that for $B = 2.2$, a value representative of typical hybrid combustion situations, the flame resides at a position about 20% of the boundary-layer thickness above the fuel surface. This result confirmed the earlier theoretical work of Marxman and Gilbert [2]. In addition, the temperature profiles indicated a flame thickness of only about 10% of the boundary-layer thickness, suggesting that the thin-flame approximation invoked by Marxman and Gibert [2] and Marxman et al. [9] was valid, at least for this set of test conditions. Interestingly, gas sampling measurements indicated small, but finite concentrations of oxidizer at the wall surface and of fuel above the flame, indicating that unburnt reactants can cross the finite-rate reaction zone.

Interestingly, Wooldridge and Muzzy [38] also found a significant static pressure gradient normal to the wall beneath the flame, which they attributed to the interaction of a strong density gradient and the gradient of the vertical velocity. Above the flame, they found only a negligible pressure gradient. In addition, no pressure gradient normal to the wall was detected for noncombusting flow.

Another significant result was that the presence of the flame zone in the boundary layer distorted the profile of the axial velocity in the direction normal to the wall (represented in Fig. 4 by the u velocity), causing an inflection near the reaction zone location. However, similar inflections were also found for the sensible enthalpy and species concentrations profiles, suggesting that the generalized Reynolds analogy assumption (equal coefficients for energy, mass, and momentum transfer) is valid, even in turbulent combusting boundary layers. This result is important because use of Reynolds analogy greatly simplifies analytic approaches, such as Marxman's.

Marxman also analyzed the effects of variable fluid properties across the boundary layer on the mass transfer number B and the regression rate [10]. He reasoned that, even for low Mach numbers, flows with chemical reactions should be treated as compressible to account for the effects of large temperature and density gradients on heat transfer. Marxman used a Howarth–Dorodnitsyn transformation to show that his previous regression rate law

$$\rho_f r = (\rho v)_w = 0.03 G Re_x^{-0.2} (St/St_o) B \tag{26}$$

with

$$B = (u_e/u_{fl})(h_{fl} - h_w)/\Delta H_{v,\text{eff}} \tag{27}$$

and derived under incompressible assumptions, becomes

$$\rho_f r = 0.036 G (\bar{\rho}/\rho_e)^{0.6} B^{0.23} Re_x^{-0.2} \tag{28}$$

for compressible flow situations with $5 \leq B \leq 100$ where $\bar{\rho}$ is the average gas density. In deriving Eq. (28), Marxman assumed that

$$(St_o/St) = 1.2 B^{-0.77} \tag{29}$$

again for $5 \leq B \leq 100$. [However, as already mentioned, Altman [30] has noted that a more accurate expression over this range of blowing parameters is given by $(St_o/St) = 1.2B^{-0.68}$, so that in Eq. (28) B should be raised to the 0.32 power rather than the 0.23 power originally determined by Marxman.] Marxman then assumed that the gas density variations are linear both above and below the flame and showed that the density-ratio term in Eq. (28) can be calculated from a closed-form but rather complex function of the flame density, gas density at the wall, gas density at the edge of the boundary-layer, blowing number B, local Reynolds number, and boundary-layer thickness (see Eq. (16) in [10]). However, most of these quantities are not conveniently known, and the boundary thickness must be measured at some reference state. Marxman presented typical values for PMMA/oxygen systems indicating that the density ratio factor is about 1.38. When used to predict the variation of local flame height above the fuel surface, the theory based on Eq. (28) was shown to be in good agreement with schlieren measurements by Wooldridge and Muzzy [38].

Paul et al. [12] also studied the effects of variable fluid properties on regression rate behavior of rubber-based fuel/oxygen systems. They discussed discrepancies between Marxman's diffusion-limited theory (Marxman and Gilbert [2], Marxman et al. [9], and Marxman [10]) and experiments by Wooldridge et al. [24] that, according to Paul et al., reportedly showed significant pressure effects on regression rate, as well as the inability of Marxman's theory, even with his density ratio term shown earlier, to account for the significant differences in regression rates among different polymeric fuels. Citing earlier literature by Lees [39] on the reduction of the heat-transfer blocking effect when dense gas is injected from the wall (dense as compared to the core flow), Paul et al. then developed a modified theory that relies

on correction factors based on density ratios between the flame and core flow and the wall and core flow. Their resulting regression rate equation was

$$\rho_f r = 0.033 G Re_x^{-0.2} (St/St_o)^{0.8} [B/(1+B)^{0.2}] \tag{30}$$

where Reynolds analogy was used to substitute S_t/S_{to} for C_f/C_{fo}. In the Paul et al. derivation, the evaluation of C_f/C_{fo}, or equivalently S_t/S_{to}, is complicated. Therefore, they obtained a simplified regression rate expression by empirically curve fitting C_f/C_{fo} (or, equivalently, S_t/S_{to}) as a function of ρ_{fl}/ρ_e, ρ_w/ρ_e, and B to obtain

$$\rho_f r = 0.056 G Re_x^{-0.2} (\rho_{fl}/\rho_e)^{0.71} (\rho_w/\rho_e)^{0.14} B(1+B)^{-(0.73-0.002\rho_w/\rho_e)} \tag{31}$$

where the densities correspond to those at the flame, ρ_{fl}, the wall, ρ_w, and the core flow, ρ_e. Paul et al. do not show the correlation that gives C_f/C_{f0} vs ρ_{fl}/ρ_e and ρ_w/ρ_e in [12], nor do they provide a physical interpretation of the peculiar variable power on the $(1+B)$ term. However, they state that Eq. (31) matches Eq. (30) to within 5% over the range of interest for hybrid motors. Furthermore, they note that the density variations across the boundary layer are affected by both the gas temperature and the molecular weight of the injected species, with the molecular weight having the stronger influence [12]. They note that the molecular weights of typical pyrolyzed species at the fuel surface are on the order of 100–400 g/mole, compared to about 24–28 g/mole in the core flow. According to Paul et al., this large difference can cause a significant reduction in the blocking effect, which is not accounted for in earlier theories. Consequently, they note that the significantly different regression rates empirically measured for polymeric fuels may be explained by the different molecular weights of their respective decomposition gases near the fuel surface. For example, Paul et al. [12] note that PMMA, which generates near-wall gases with a molecular weight of about 90–100 g/mole, regresses slowly compared to fuels such as polybutadiene–acrylic acid–acrylonitrile terpolymer (PBAN) and polyurethane (PU), whose decomposition gases are roughly 250 g/mole. The heavier decomposition gases of the latter fuels reduce the blocking effect caused by mass injection into the boundary layer, and, therefore, regress relatively faster than fuels with lower molecular weight decomposition gases because the fuel surface is subject to a relatively higher heat flux.

Paul et al. also made an interesting, but not conclusive, observation related to the dependence of regression rates with chamber pressure measured by Wooldridge et al. (albeit at fairly low pressures of about 50–250 psia) [24], which would presumably apply to similar results by other researchers. According to their hypothesis, the pressure dependence is due not to chemical kinetics or heterogeneous reactions at the fuel surface, but instead to a variation of core temperature with pressure. This temperature variation in turn affects the density ratios used in the Paul et al. regression rate expression. However, note that flame temperatures are typically not strongly influenced by pressure. For example, chemical equilibrium calculations show that at a mixture ratio of 2.5 the combustion temperature of HTPB and GOX increase from about 3450 K at 100 psia to about 3800 K at 1000 psia, an increase of only about 10% for an order of magnitude increase in pressure. Therefore, the validity of the Paul et al. hypothesis that pressure effects arise due to gas temperature variations with pressure is open to question and requires further investigation.

Further note that the Paul et al. experiments were conducted at fairly low pressure (75–270 psia) and low mass flux (initial oxidizer flux of 0.045 lbm/in.$^2 \cdot$ s) with an unusual fuel composed of 1 part poly isoprene and 3 parts difurfurylidiene cyclo hexanone (DFCH) and a mixed oxidizer composed of oxygen and nitrogen. Although it may be difficult to ascertain the applicability of the Paul et al. results to other propellant combinations, the potential significance of the boundary-layer fluid property variations they elucidated should not be overlooked.

Following the property ratio method suggested by Kays and Crawford for flows with chemical reactions and/or high speeds [40], Chiaverini et al. [16], therefore, used a temperature factor θ representing the ratio of the flame temperature to the local surface temperature, to account for the effects of variable fluid properties across the boundary layer on heat transfer to the fuel surface where

$$\theta(t,x) \equiv \bar{T}_{\text{fl}}(t,x)/T_s(t,x) \tag{32}$$

These particular temperatures were chosen because the reaction zone represents the effective "boundary" for heat transfer to the fuel surface. (Note that this assumes that the near-wall gas temperature was in thermal equilibrium with the fuel surface temperature.) More recent research efforts have employed a similar approach to account for fluid property variations (personal communication with Greg Zilliac, NASA/AMES, July 2006). In the Chiaverini et al. semi-empirical analysis, the surface temperature T_s was treated as a local, instantaneous quantity and calculated by combining the measured local, instantaneous regression rates with an empirical pyrolysis law that relates $r(t,x)$ to $T_s(t,x)$ [25]. The flame zone temperature was calculated using a procedure described fully by Chiaverini [37] and summarized in [16]. Here, it is worth noting that they did not make a thin-flame approximation, but instead estimated the local, instantaneous flame zone thickness using an approximate method described in [16]. The T_{fl} used in Eq. (32) (as well as in the Chiaverini et al. gas-phase radiant heat flux calculations described earlier) is actually a local, instantaneous quantity that represents the average temperature across the finite-thickness reaction zone. However, as noted in [16], these average values were quite close to 95% of the theoretical adiabatic flame temperature.

The Chiaverini et al. regression rate equation has already been introduced in Eq. (23), where it was shown that parameterization yielded a value of 0.6 for the empirical power on θ. For typical values of surface temperature and average flame temperature in their tests, Chiaverini et al. determined that $\theta^{0.6}$ ranged from 1.7 to 2.0. Note that this correction factor does not explicitly account for effects of gas molecular weight variations, as do those of Paul et al. [12]. However, according to the results of the Chiaverini et al. thermal pyrolysis experiments in a gas chromatograph mass spectrometer [25] shown in Fig. 12 and listed in Table 2, the molecular weights of the pyrolysis gases do not vary much with respect to pyrolysis temperature and have typical values of around 60 g/mole. If similar behavior is assumed in hybrid motor firings, it may be expected that the influence of the pyrolyzed-fuel gas molecular weight on the blocking effect in the boundary layer may not be readily apparent during a given test, or even from test to test for a given fuel/oxidizer combination. This result may explain why the Chiaverini et al. data correlated well with the flame-to-surface temperature ratio: In the absence of significant changes in pyrolysis gas composition or mixture molecular weight, the gas density effects

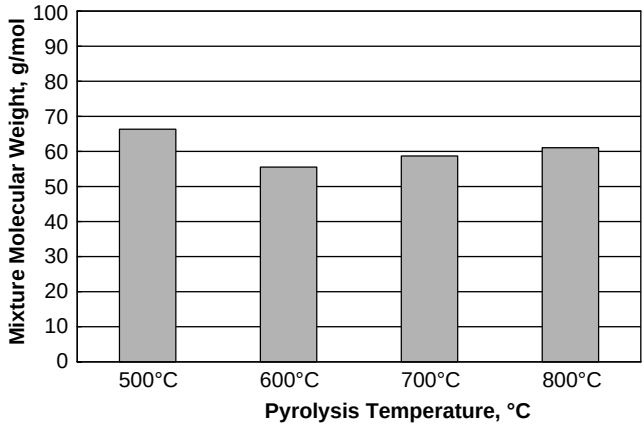

Fig. 12 HTPB pyrolysis product mixture molecular weight vs. temperature.

Table 2 HTPB pyrolysis product mass fraction vs. temperature

Major pyrolysis product species M_i, chemical formula	Heat of formation ΔH_f^o, J/g	Mass fractions of pyrolysis products at various temperatures, K			
		773	873	973	1073
Ethene, C_2H_4	1865.69	——	5.59	3.05	6.58
Propene, C_3H_6	485.49	——	——	4.90	10.99
1,3–Butadiene, C_4H_6	2037.27	77.4	89.06	66.1	41.07
3–Pentene–1–Yne, C_5H_6	2119.82	——	——	9.20	10.28
Benzene, C_6H_6	1062.29	——	——	10.3	22.02
Toluene, C_7H_8	542.97	——	——	6.41	9.06
4-Vinyl–cyclohexene, C_8H_{12}	280.78	22.6	5.35	——	——

represented by the density ratios in Eq. (31) are due primarily to variations in gas temperature. However, the role of potential boundary-layer pressure gradients below the flame, such as those measured by Wooldridge and Muzzy [38], must also be considered because these can also affect the boundary-layer density profiles. Our understanding of fuel regression rate and boundary-layer combustion processes would benefit from a more thorough treatment of these various effects in future investigations.

E. Effects of Chemical Kinetics

This section focuses on various theories proposed to explain the regression rate pressure-sensitivity observed by several researchers, most notably Smoot and Price in the 1960s, over certain ranges of hybrid operating conditions for various fuel/oxidizer combinations. In general, the approaches fall into one of three

categories: 1) pressure dependence due to gas-phase chemical reaction kinetics, 2) pressure dependence due to heterogeneous reaction kinetics, and 3) theories where both gas-phase and heterogeneous reaction kinetics play important roles. After a review of Smoot and Price's experiments and subsequent analysis (which focused on heterogeneous reactions at the solid-fuel surface) each of these categories is discussed.

1. *Smoot and Price's Analysis*

Besides Marxman and his associates, several other groups were actively pursuing hybrid combustion research during the 1960s. Smoot and Price [17–19] performed over 150 experiments with a laboratory-scale slab burner at what was then the Lockheed Propulsion Company in Redlands, California. They initially developed a theory of solid-fuel regression by extending the work of earlier researchers to include the effects of condensed-phase species in the near-wall region. Like previous researchers, Smoot and Price also found that the local regression rate should theoretically vary with $G^{0.8}$ such that [17]

$$\rho_f r = 0.03 G Re_x^{-0.2} \{\ln[1 + (\lambda B/\mathrm{Pr}^{2/3})]/\lambda\} \tag{33}$$

for turbulent boundary-layer flow and

$$\rho_f r = 0.023 G Re_D^{-0.2} \{\ln[1 + (\lambda B/\mathrm{Pr}^{2/3})]/\lambda\} \tag{34}$$

for fully developed turbulent flow in circular tubes. In Eqs. (33) and (34), the Reynolds numbers are defined in the usual way of $Re_x = Gx/\mu$ and $Re_D = GD/\mu$, so that in both cases the overall regression rate variation with $G^{0.8}$ is evident. Note that Eq. (33) is similar to Marxman's expression given in Eq. (13a) except that Smoot and Price used a different definition for B and also included the term λ, the weight fraction of gas in the decomposed fuel grain at the fuel surface, to account for the possibility of condensed-phase decomposition products that tend to reduce the heat-transfer blocking effects of wall blowing. Smoot and Price defined B as

$$B = (h_{fl} - h_w)/\Delta H_{v,\mathrm{eff}} \tag{35}$$

where the numerator represents the enthalpy difference between the combustion gases at the theoretical flame temperature and the pyrolyzed fuel gases at the wall temperature and the denominator is the effective heat of gasification of the solid fuel.

Smoot and Price performed initial experiments using solid fuels of butyl rubber, polybutadiene–acrylic acid (PBAA) copolymer, and PU. They varied the oxidizer composition from 100% fluorine to 100% oxygen. They found that average regression rates were higher when a larger ratio of fluorine to oxygen was used for the oxidizer. They also discovered that at low total mass fluxes (G less than about $0.07\,\mathrm{lbm/in.}^2 \cdot \mathrm{s}$) the average regression rates of the butyl rubber solid-fuel slabs followed the diffusion-limited $G^{0.8}$ law. However, at higher G levels the regression rate became essentially independent of mass flux, but appeared to be strongly dependent on total operating pressure. The threshold value of G where this occurred seemed to depend strongly on the oxidize composition and the chamber pressure.

For the relatively low operating pressures involved (<170 psia), the regression rates always fell below that predicted by the $G^{0.8}$ theory, but increases in pressure pushed the regression rate toward the value predicted by diffusion-limited theory. They predicted that at 1000 psi the regression rates should reach the diffusion-limited values predicted by the $G^{0.8}$ relationship [17].

Smoot and Price defined three regimes of regression rate dependency [17]. In the low-mass-flux regime, the regression rate was controlled entirely by heat transfer and depended on $G^{0.8}$. For intermediate mass fluxes, the regression rate depended on both flux rate and pressure, with higher pressures causing increasing regression rate for a constant mass flux. In this region, Smoot and Price postulated an empirical equation of the form

$$r = (aG^{0.8}bp^n)/(aG^{0.8} + bp^n) \tag{36}$$

where p is the motor pressure and a, b, and n are empirical constants, which were not determined in the investigation. In the "high-" mass-flux regime, Smoot and Price suggested that the regression rates depended solely on operating pressure, such that $r = ap^n$, similar to a solid-propellant grain [17].

Smoot and Price also studied the regression rate behavior of solid-fuel grains loaded with metal particles [17]. They varied the solid-fuel composition from 100% butyl rubber to 90% LiH (lithium hydride) and the oxidizer composition from 100% fluorine to 100% oxygen. They found that in the low-mass-flux regime ($G < 0.04\,\text{lbm/in.}^2 \cdot \text{s}$) the average regression rate increased significantly with respect to %LiH only if the amount of LiH in the grain was greater than about 50% [17]. This is the same region where they found 100% butyl rubber grains to regress according to the $G^{0.8}$ law, as already discussed. At higher mass flux levels, where the operating pressure was found to influence the regression rate, the solid-fuel regression rates displayed much more sensitivity to the LiH mass fraction. Smoot and Price postulated that the observed change in regression rate sensitivity to LiH mass fraction resulted from the transition from one controlling mechanism to the other, that is, from a diffusion-controlled to a kinetics-controlled regression rate. They also found that increasing the percentage of LiH reduced the sensitivity to pressure in the high-mass-flux region.

Smoot and Price suggested that either gas-phase reactions between the oxidizer and the pyrolyzed fuel vapor or heterogeneous reactions between oxidizer and fuel at the fuel surface were responsible for the observed dependence of regression rate on operating pressure [18]. However, after performing a series of experiments wherein they varied the fluorine partial pressure independently of the total pressure by using oxygen and nitrogen as diluents, they found that the solid-fuel regression rates depended significantly on the partial pressure of fluorine, but not on the total pressure. Based on these results, they concluded that oxidizer transport to the fuel surface and subsequent first-order heterogeneous reactions were responsible for the pressure dependence and derived the following equation:

$$p_{o_\infty}/\rho_f r = \{33p_\infty(x/\mu)^{0.2}Sc^{2/3}[\exp(B\lambda) - 1]/G^{0.8}B\lambda\} + (1/k) \tag{37}$$

where P_{o_∞} is the partial oxidizer pressure in the freestream (pounds per square inch absolute), P_∞ the total freestream pressure, and k a kinetic rate constant.

Recall that Wooldridge and Muzzy [38] measured a small but finite concentration of oxidizer at the porous injection surface in their experiments, a result which tends to support Smoot and Price's hypothesis. Equation (37) correlated most of Smoot and Prices's data to within about 30–40% error. It is worth emphasizing that the experiments described in [17–19] were conducted at relatively low pressures of about 20 to 165 psia. This range may lie below the practical operating pressures of many applications. Next, we shall discuss various theories presented by different researchers to explain the phenomena observed by Smoot and Price.

2. *Approaches Based on Analysis of Gas-Phase Chemical Reaction Kinetics*

The effect of gas-phase kinetics on regression rate has been studied by several researchers, including Miller [23] and Kosdon and Williams [20]. Miller derived an analytical expression to describe the solid-fuel regression rate as a function of both chemical kinetic and gasdynamic parameters. He estimated the thickness of the reaction zone by considering molecular diffusion of the fuel to the flame and the rate of chemical reactions within the flame zone and derived the following expression:

$$p_{o_\infty}/\rho_f r = (pB^{0.8}x^{0.2}/aG^{0.8})O/F|_{st} + (X_o^*/K) \tag{38}$$

which relates regression rate to both gasdynamic and kinetic variables. In Eq. (38), $O/F|_{st}$ is the stoichiometric propellant mixture ratio, X_o^* is the oxidizer mole function at the flame, and p_o is the oxidizer partial pressure in the core flow. Miller used Eq. (38) to correlate Smoot and Price's data successfully to within the accuracy of their measurement. Note that Miller's expression bears some similarities to Smoot and Price's in that for both equations the regression rate varies linearly with oxidizer partial pressure and is proportional to $G^{0.8}/x^{0.2}$. However, the expressions differ in the functional dependency on B. Miller does not define B specifically, but it may be inferred that he used Smoot and Price's definition from [17] because he correlates their data from this reference.

Kosdon and Williams [20], who also attributed the pressure dependence to finite-rate, gas-phase chemical reactions, noted potential weaknesses in Miller's analysis due to limitations of his formula for reaction zone thickness [23]. They suggest that Miller's analysis is probably applicable only to weakly pressure-dependent systems at flow rates that are not "too large." Kosdon and Williams used a perturbation analysis to develop a regression rate law valid for small departures from the flux-dependent, pressure-independent regime. To account for a flame zone of finite thickness (as opposed to the flame-sheet, infinite-reaction rate approximation of Marxman), they defined the blowing number as

$$B = [c_p(T_e - T_w) + Q(Y_{oe} - Y_{ow})]/(\Delta H_{v,\text{eff}} + QY_{ow}) \tag{39}$$

where the term QY_{ow} in both the numerator and denominator is absent for the flame-sheet approximation and Q represents the combustion heat release per unit mass of oxidizer. As discussed by Kosdon and Williams [20], they derived an expression for Y_{ow}, the mass fraction of oxidizer at the wall, to obtain a closed-form solution for their regression rate formula, assuming a second-order gas-phase

combustion reaction,

$$(r_o - r)/r_o = [K_1 G(Q/\Delta H_{v,\text{eff}})^{-\varepsilon}]/xp^2 Y_{oe}^{\varepsilon} \tag{40}$$

where the value of ε is either zero or a small positive number compared to unity, K_1 is a constant and r_o is the reference regression rate obtained for flame-sheet approximations, such as that given by Eq. (13a). Therefore, the right side of Eq. (40) may be interpreted as a correction for the regression rate to account for a finite-thickness reaction zone for the range of operation where the regression rate is weakly pressure dependent. In the limit of high pressure, Eq. (40) correctly shows that r becomes r_o. However, Kosdon and Williams point out that their expression given for Y_{ow} in [20] (but not repeated here) may not apply well for hybrid combustion situations. Note also that Eq. (40), due to the assumption of a second-order reaction, shows that the regression rate depends on p^2, whereas Miller, who also assumed second-order combustion reactions, found that r was dependent on p. Therefore, as noted by Kosdon and Williams, the results of perturbation analysis applied to the regression rate's dependency to finite-rate reactions appear to be sensitive to the model employed.

Kosdon and Williams compared their regression rate expression to Smoot and Price's data for nonmetallized fuels from [17]. Though it is not clear from their analytic description, they appear to set $\varepsilon = 0$ for this purpose. They also compared the accuracy of their regression rate law given by Eq. (40) to that of Miller's. Kosdon and William's regression rate expression predicted Smoot and Price's data for butyl rubber with oxygen to a reasonable accuracy, but apparently did not correlate the fluorine oxidizer data to any extent. They concluded that their regression rate equation and Miller's give very similar results when applied to predict Smoot and Price's nonmetallized regression rate data, though Miller's correlation was slightly more accurate.

For the kinetically controlled regime with *strong* pressure dependence, Kosdon and Williams showed theoretically that [20]

$$r \sim p^{1/2} \tag{41}$$

independent of G. An empirical fit of Smoot and Price's data in [20] to a simple $r = ap^n$ correlation indicated a pressure exponent of 0.52 for fluorine and 0.61 for oxygen, empirical values very similar to their theoretical value of 0.5 for the kinetically controlled Eq. (41).

3. *Approaches Based on Analysis of Heterogeneous Surface Reaction Kinetics*

Marxman analyzed the role of chemical kinetics by examining the subtle, yet important, relationship between the gas-phase reaction zone and potential heterogeneous reactions on the fuel surface due to oxidizer attack [11]. Based on the experimental results produced by Smoot and Price [17, 18], Marxman postulated the existence of a threshold pressure below which the gas-phase chemical reaction rates become sufficiently slow, in some phase of the overall combustion process, to approach the rates of mass and heat transfer in the turbulent boundary layer. He then reasoned as follows to derive regression rate expressions for two limiting cases:

1) When gas-phase reaction rates are **high** (fast reactions in the flame zone), the fraction of mainstream oxidizer gas that (potentially) passes through the flame zone is small and any heterogeneous reactions that occur are diffusion (transport) limited.

2) When gas-phase reaction rates are **low** (slow reaction in the flame zone), a large portion of the mainstream oxidizer can pass through the flame zone and participate in heterogeneous reactions on the fuel surface. In this case, the heterogeneous reactions will be primarily **kinetically limited**.

Therefore, Marxman concluded that kinetics are likely to play an important role in heterogeneous reactions only if the gas-phase reaction rates are slow (on the order of the turbulent transport rates). On the other hand, if the gas-phase reactions are fast such that combustion is transport limited, then any heterogeneous reactions will also be transport limited. For the transport-limited case 1 scenario, Marxman derived a modified regression rate law using an approach analogous to that for the radiant heat flux situation, but with Q_r replaced by Q_h, the heat flux due to heterogeneous reactions:

$$\rho_f r = 0.036 G \left(\frac{\bar{\rho}}{\rho_e}\right)^{0.6} (B')^{0.23} Re_x^{-0.2} \left[\exp\left(\frac{-Q_h}{Q_c}\right)\left(1 + \frac{\Delta H_{r,h}}{\Delta H_{v,\text{eff}}} \frac{Y_{o,w}}{\phi_{\text{fl}} B}\right)\right] \quad (42)$$

where $B' = BPr^{-0.67}$, $\Delta H_{r,h}$ is the heat of heterogeneous reaction per unit mass, $Y_{o,w}$ the oxidizer mass fraction that reaches the fuel surface, and $\phi_{\text{fl}} = u_{\text{fl}}/u_e$ is the velocity ratio between the gas-phase flame and the freestream velocity. Notice that Eq. (42) includes Marxman's density correction factor discussed earlier.

Eq. (42) becomes

$$\rho_f r = 0.036 G (\bar{\rho}/\rho_e)^{0.6} (B')^{0.23} Re_x^{-0.2} [\exp(-Q_h/Q_c) + (Q_h/Q_c)] \quad (43)$$

because, according to Marxman [11],

$$\frac{Q_h}{Q_c} \approx \left(\frac{\Delta H_{r,h}}{\Delta H_{v,\text{eff}}} \frac{Y_{o,w}}{\phi_{\text{fl}} B}\right) \exp\left(\frac{-Q_h}{Q_c}\right) \quad (44)$$

Note the similarity between Eq. (43) and Eq. (14) for radiant heat flux. Notice also that Eq. (43) does not depend explicitly on the chamber pressure p. Marxman therefore notes that when gas-phase reactions are high, potential heterogeneous reactions at the fuel surface do not offer an explanation for pressure dependency. The bracketed term in Eq. (43) represents a correction factor that accounts for the additional driving force of heterogeneous reactions on fuel regression, though Marxman states that this term generally does not differ from unity by more than about 10%.

With regard to the kinetically-limited case 2, Marxman reasoned that in many cases only a small fraction of the solid fuel may participate in the heterogeneous reactions so the heterogeneous reaction rate may often depend on the rate of delivery of the solid fuel to the reacting surface. He then derived a second set of equations that did show a pressure dependence to describe the regression rate behavior in this regime [11]. As noted by Marxman, this equation was not particularly useful in a

quantitative sense. However, in a later work, Wooldridge and Marxman continued to analyze kinetic effects by considering the effects of both finite-rate gas-phase reactions and heterogeneous reactions. Muzzy discussed their analysis in some detail [8], and the results of these efforts strongly suggested that heterogeneous reactions alone could not account for the pressure effects observed by Smoot and Price in their experiments [17]. Wooldridge and Marxman derived a normalized regression rate law based on a characteristic Damköhler number that describes the ratio of the reaction time to the mixing time for the turbulent boundary-layer reaction zone,

$$r/r_o = (2t_m/t_c)^{0.5}\,\{1 - (t_m/t_c)[1 - \exp(-t_c/t_m)]\}^{0.5} \tag{45}$$

where t_m and t_c are the characteristic mixing and chemical reaction times, respectively. As in Kosdon and William's analysis, the reference state regression rate in Eq. (45) corresponds to that of the flux-dependent, pressure-independent regime. Figure 13 shows the behavior of r/r_o vs t_c/t_m as described by Eq. (45). Equation (45) predicts that the regression rate will be about 1% lower than the flux-limited value when the chemical reaction time is about 20 times faster than the mixing time ($Da = 0.05$). When Damköhler number Da is unity, indicating equal reaction and mixing times, the regression rate is about 86% of its flux-limited value. The regression rates drops to about 50% of the flux-limited value when the characteristic mixing reaction time is seven times faster than the chemical reaction time ($Da = 7$).

For large values of t_c/t_m, which occur for either low chamber pressures P or high mass flux G levels, the term in braces in Eq. (45) approaches unity and Eq. (45) reduces to

$$r/r_o = (2t_m/t_c)^{0.5} \tag{46}$$

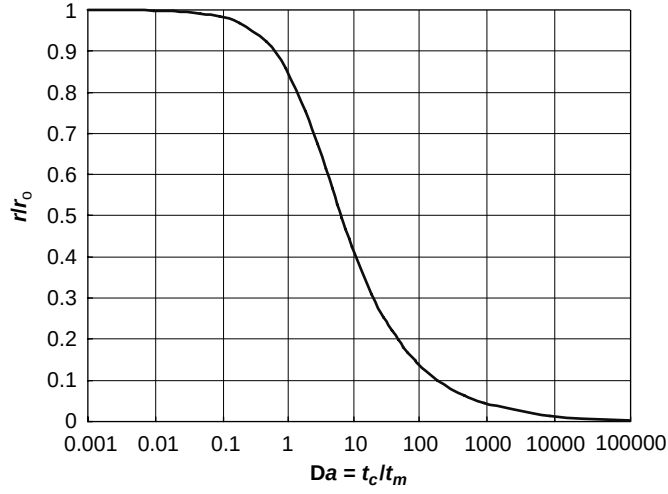

Fig. 13 Effect of Damköhler number on regression rate from Eq. (45).

which describes the kinetically controlled regime. Muzzy made some simplifying assumptions to show that, for a second-order reaction, the value of t_c/t_m can be approximated by

$$t_c/t_m = C_1(G^{0.8}x^{-0.2})/p \tag{47}$$

where the constant C_1 includes effects of blowing parameter, gas viscosity, and flame temperature and will in general be different for each fuel/oxidizer combination. Combining Eqs. (46) and (47) yields

$$r/r_o = C_2(p^{0.5}x^{0.1}/G^{0.4}) \tag{48}$$

Substituting Eq. (13a) while absorbing the blowing parameter function into C_2, one obtains

$$r = C_3p^{0.5}G^{0.4}x^{-0.1} \tag{49}$$

for the kinetically-controlled regime. As expected, Eq. (49) shows a weaker dependence than does Eq. (13a) on both G and x, which represent convective transfer parameters, and a significant dependence on the chamber pressure p. Muzzy suggested that in the transition region between the flux-controlled and the kinetically-controlled regimes, the power on G would be expected to vary between 0.4 and 0.8 and the power on p would be lower than 0.5. He also points out that the functional form of Eq. (49) seemed to agree with Smoot and Price's high G data for lithium fuels and fluorinated oxidizer. Note that Kosdon and Williams [20] found similar results in Eq. (41).

Working independently and from a different perspective, Kumar and Stickler [22] developed a very similar expression to describe the regression rate in the kinetically controlled region. They suggested that the regression rates of typical hybrids were too fast to be governed purely by thermal degradation resulting from heat transfer via convection and radiation. They cited PMMA pyrolysis data that indicated a mismatch in the regression rate-vs-fuel surface temperature correlations between 1) laboratory experiments conducted with a hot plate in an inert environment and 2) hot-fire hybrid motor data. In other words, the regression rate dependency on fuel surface temperature was different in inert and noninert environments, according to Kumar and Stickler's assessment. They also noted that the r vs T_s correlations for the two data sets in the inert environment and the hybrid motor data intersected in the region where pressure sensitivity begins to appear [22]. Citing data generated by Wooldridge and Muzzy in their simulated hybrid experiments discussed earlier [38] (wherein a small, but finite amount of oxidizer was measured in the near-wall region beneath the diffusion flame), Kumar and Stickler conjectured that either oxidation-driven polymer degradation or catalytic effects attributed to the oxidizer at the fuel surface contribute to the regression rate by enhancing depolymerization, leading to higher regression rates for motor testing compared to inert pyrolysis at the same surface temperature. They suggested that this depolymerization mechanism could also explain the observed pressure dependency. They also conducted an order-of-magnitude analysis of the gas-phase transport mechanisms in a hybrid

turbulent reacting boundary layer and suggested that gas-phase chemical kinetics are not slow enough to account for the pressure-sensitive regression rate regime.

Kumar and Stickler [22] then developed a regression rate analysis that considered the kinetics of polymer fuel degradation by specifying the size of the vaporized fuel fragments in relation to their particular vapor pressure. They found that the experimental PMMA regression rates could be correlated by normalizing the regression rate with the flux-limited value, resulting in the following expression:

$$\frac{r}{r_\infty} \cdot \frac{G_\infty^n}{G^n}\left[\frac{\ln(p_{\text{ref}}/p_\infty)}{\ln(p_{\text{ref}}/p)}\right] = f_1\left[\frac{G}{G_\infty} \cdot \frac{p_\infty}{p_{\text{ox}}}\right] \tag{50}$$

where the reference state denoted by subscript ref was selected to correspond to the condition at which pressure sensitivity first appears. In Eq. (50), subscript ∞ denotes the standard state, p_{ox} is the oxidizer partial pressure, G is the total mass flux, and G_∞ is the total mass flux in the standard state. Though Kumar and Stickler did not provide it, the function form on the right side of Eq. (50) could presumably be determined using the data in Fig. 6 of [22] or in Fig. 14 here.

When the term $(G/G_0)(p_0/p_{\text{ox}}) < 1$, their analysis indicated that the kinetics of polymer degradation are rate limiting and the regression rate is only weakly dependent on pressure. In this regime, the regression rate is limited by polymer bond breaking and the left side of Eq. (50) equals unity (see Fig. 14).

On the other hand, for values of $(G/G_\infty)(p_\infty/p_{\text{ox}}) > 1$, the regression rate is pressure dependent. In this regime, Kumar and Stickler postulated that the regression rate for a given surface temperature is limited by the turbulent transport of unburnt oxidizer across the flame zone and to the wall. For these conditions Muzzy [8] has noted, under the assumption that the oxidizer concentration at the wall does not change significantly with mass flux G, that the normalized regression rate can

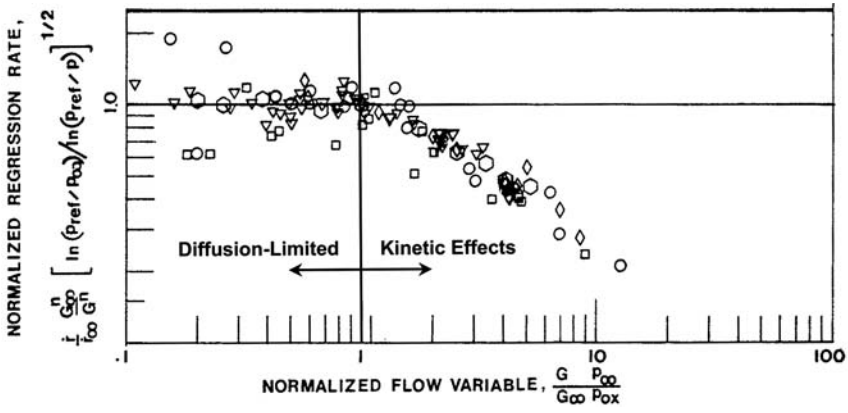

Fig. 14 Kumar and Stickler's [22] correlation of nonmetallized hybrid data showing departure from diffusion-limited behavior and corresponding kinetic effects for normalized flow variable >1.

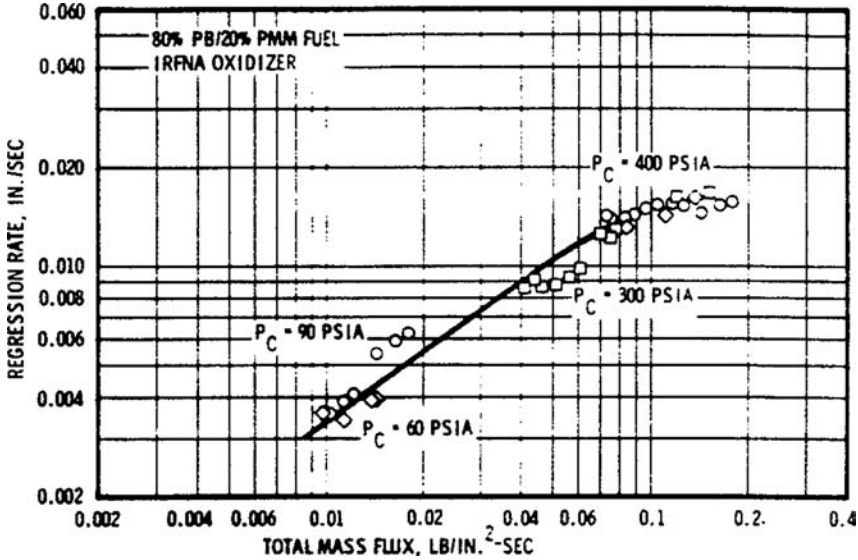

Fig. 15 Effect of pressure via chemical kinetics on regression rate for 80% PB/20% PMMA fuel and IRFNA oxidizer. (From Kosdon and Williams [19].)

be expressed by

$$r/r_\infty = [C_4(p/G)]^{0.5} \tag{51}$$

In which case, for a nonradiating system with no significant effects from variable fluid properties in the boundary layer, we obtain, again by substitution of Eq. (13a),

$$r = C_5 p^{0.5} G^{0.3} x^{-0.2} \tag{52}$$

which is very similar to Eq. (49). As shown in Fig. 15, Muzzy then favorably compared the general trends of Eqs. (49) and (52) to empirical data from the HAST I program, which employed IRFNA and a fuel consisting of 80% polybutadiene (PB) and 20% PMMA, that appeared to display a pressure dependency in the upper G regime [8].

4. Effects of Chemical Kinetics on Regression Rate Behavior of HTPB-Based Fuels

Although Smoot and Price's regression rate data and the HAST I regression rate data do appear to display a pressure dependency over certain ranges, note that modern hybrid rocket propellants such as HTPB and oxygen have not, in general, displayed these same trends. Here, we cite the data of several researchers, including Strand et al. [35], Chiaverini et al. [16], and Boardman et al. [41], none of whom found any significant pressure dependency for the regression rate of HTPB with oxygen. Chiaverini et al. and Strand et al. tested HTPB with GOX in laboratory-scale hybrid motors. Strand et al. conducted hot firings with total mass flux levels

of up to $\sim$0.16 lbm/in.$^2 \cdot$ s at chamber pressures of between 130 and 185 psia. As shown in Fig. 4 of [35] both the lower pressure and higher pressure data matched well over the entire mass flux range to a single regression rate correlation. Strand et al. stated that "No clear effect of pressure is indicated over the pressure range tested" [35]. Similarly, Chiaverini tested HTPB/GOX over a range of mass flux and chamber pressure conditions. No explicit kinetic effects were noted even at the highest flux/lowest pressure condition of 0.4 lbm/in.$^2 \cdot$ s and 270 psia. However, as already noted, Strand et al. and Chiaverini et al. did find strong evidence suggesting a significant radiant heat flux, which leads to a pressure, but not a kinetic, dependency.

Boardman et al. [41] tested GOX and UTF-29901, a 40% by weight/60% by weight blend of HTPB and polycyclopentadiene, in an 11-in. hybrid motor as part of the Joint Government/Industry Research and Development (JIRAD) hybrid program. The oxygen flux ranged from 0.14 to 0.80 lbm/in.$^2 \cdot$ s, the port diameter from 3.4 to 6.1 in., the motor pressure from 145 to 790 psig, and the resulting regression rates from 0.021 to 0.059 in./s. Table 4 in [41] lists the particular data for each test. At relatively low pressures (about 324 psia), the data showed no significant pressure effects, even at GOX flux levels of up to 0.67 lbm/in.$^2 \cdot$ s (Note that the total mass flux is even higher due to fuel addition.) In fact, the initial correlation derived by Boardman et al. [41] indicated a slight negative pressure dependence, such that

$$\bar{r} = 0.064\bar{G}_o^{0.73}(\bar{D}_p/3)^{0.59}(\bar{p}/500)^{-0.08}; \qquad R^2 = 0.99 \tag{53}$$

where the overbars designate time- and space-averaged quantities. In Eq. (53), the regression rate is in inches per second, the oxygen flux in pounds mass per square inch per second, the port diameter in inches, and the pressure in pounds per square inch gauge. Eliminating the pressure term did not significantly degrade the accuracy of the correlation, but did increase the resulting dependency on the chamber diameter,

$$\bar{r} = 0.065\bar{G}_o^{0.77}(\bar{D}_p/3)^{0.71}; \qquad R^2 = 0.98 \tag{54}$$

Eliminating the chamber diameter, however, degraded the accuracy of the fit and also reduced the empirical power on the oxygen mass flux by a significant degree,

$$\bar{r} = 0.070\bar{G}_o^{0.57}; \qquad R^2 = 0.91 \tag{55}$$

suggesting that thermal radiation may be an important driver for fuel pyrolysis in this system. The large power on diameter in Eq. (54) also implies that this correlation should not be used outside the range of operating conditions for which it was derived without caution and further investigation.

Chiaverini et al. conducted solid-fuel thermal pyrolysis experiments with HTPB (and other fuels), compared them to the results of laboratory hybrid motor tests, and obtained indirect evidence relating to the effects of potential heterogeneous reactions due to surface oxidizer attack, as well as effects of chamber pressure, on regression rate [25]. These thermal pyrolysis tests are described fully elsewhere [25, 37]. Briefly, a solid-fuel strand with embedded 25-μm thermocouples was

placed in a purge chamber filled with nitrogen gas at atmospheric pressure and then subjected to direct conductive heating from a copper block. The copper block was heated to a selected bulk temperature in a tube furnace, then placed on top of the fuel strand using a pneumatic system. The fuel regression rate was measured using a video camera and post-test image analysis. The surface temperature and thermal wave thickness were determined from the embedded microthermocouples. The results of these tests were also compared to the aforementioned measurements from a laboratory hybrid motor outfitted with an x-ray radiography imaging system and fuel with embedded microthermocouples. Arrhenius-type pyrolysis laws were obtained for each of the fuel formulations tested. Figure 16 shows the Arrhenius plot for HTPB in terms of regression rate (in millimeters per second) vs the reciprocal surface temperature $1/T_s$ (in degrees Kelvin). The top axis shows the corresponding surface temperature [25].

Both atmospheric pressure data from the conductive heating pyrolysis tests (open circles) and high-pressure (25.5–40.8 atm) data from the hybrid-slab motor tests (closed circles) were used to deduce the pyrolysis law. At surface temperatures above 722 K, both sets of data follow the same trend and fit quite well to a single straight line on the semilog plot represented by the Arrhenius-type expression

$$r = A \exp(-E_a/R_u T_s) \tag{56}$$

or

$$\ln(r) = \ln(A) - E_a/R_u T_s \tag{57}$$

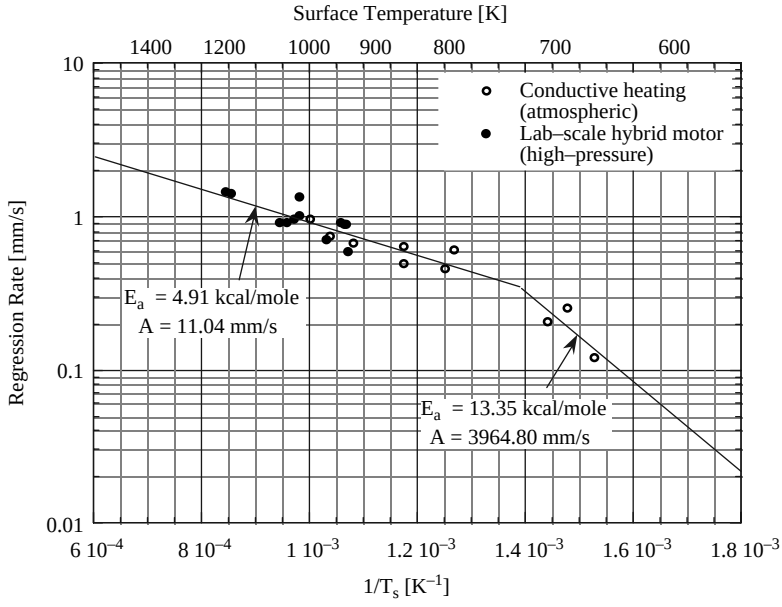

Fig. 16 Regression rate vs fuel surface temperature for HTPB pyrolysis [25].

where $E_a = 4.91$ kcal/mole and $A = 11.04$ mm/s represent the empirically determined Arrhenius parameters and R_u is the universal gas constant. At temperatures below 722 K, the data follow another trend with $E_a = 13.35$ kcal/mole and $A = 3.96 \times 10^3$ mm/s. Note that Eq. (56) is given strictly in the Arrhenius form instead of the pyrolysis law based on bulk kinetics,

$$r = A \exp(-E_{\text{py}}/2R_u T_s) \tag{58}$$

where E_{py} has twice the value of E_a. The bulk pyrolysis rate usually corresponds to the activation energy based on E_{py} instead of E_a. Arisawa and Brill [3, 4] obtained a relatively low activation energy E_{py} of 12 kcal/mole for HTPB under high heating rates (about 600°C/s) at a pressure of 11 atm and temperature range of 460–600°C. They stated that low activation energies (such as those cited here) indicate that the overall pyrolysis is limited by the physical process of desorption of pyrolyzed fuel molecules from the solid-fuel surface and not by chemical processes, such as polymer chain scission and cyclization, in the solid-fuel decomposition zone just below the surface [3, 4]. The latter are characterized by higher activation energies E_{py} on the order of 40–50 kcal/mole and dominate the pyrolysis process at low heating rates or low temperatures. This difference in mechanisms may explain why Lengellé et al. obtained a comparitively high E_{py} of 48.6 kcal/mole at low heating rates [42].

The very favorable comparison of high-pressure and atmospheric-pressure test data in Fig. 16 suggests there is no significant effect of pressure on the HTPB Arrhenius parameters for the surface temperature range tested, which, it should be stated, covers the expected range of practical operation for hybrid motors. Furthermore, given that the conductive heating tests were performed in an inert nitrogen environment and that the two data sets from the independent testing methods followed the same trend with respect to surface temperature, it appears that fuel surface attack by unburnt oxidizer, which should tend to increase the regression rate via catalytic reactions as suggested by Kumar and Stickler [22], played little role in the fuel pyrolysis processes of the laboratory-scale hybrid motor. These results contradict the conclusions drawn by Kumar and Stickler [22] for PMMA solid fuel, which indicated a mismatch in data between hot-fire and pyrolysis regression rate data. The Chiaverini et al. results for HTPB [25], on the other hand, showed that their laboratory-scale hybrid motor test results matched very well with those of the conductive-heating induced thermal pyrolysis tests, suggesting that heterogeneous surface reactions probably did not play an important role in the motor firings. This conclusion supports the previous empirical results of Strand [35], Boardman [41], and Chiaverini [15, 16] that showed no significant pressure dependence of the regression rates from hybrid motor testing.

F. Injector Effects

Compared to the effects reviewed in the preceding sections, detailed injector studies for classical hybrids have in general been somewhat lacking in the hybrid propulsion literature. However, Boardman et al. [43], Carmicino and Sorge [44], and Pucci [45] have reported the effects of different types of oxidizer injectors on

fuel regression rate, combustion efficiency, and combustion instability in various hybrid motors. Carmicino and Sorge's laboratory-scale motor burned PE solid-fuel tubes with GOX injected using either an axial or a radial injector. They found that the axial injector had several advantages over the radial injector, including stable combustion, higher average regression rates, lower mass flux dependence, and higher combustion efficiency. The radial injector, however, was found to contribute to more uniform regression rate profiles [44].

Based on earlier work in solid-fuel ramjets, Carmicino and Sorge identified three distinct flow regions associated with their injectors [44]. Zone 1, closest to the injector, consisted of a recirculation region that extends part of the way into the fuel port. In zone 2, deeper into the fuel port, the expanding oxidizer jet impinges on the fuel surface and contributes to heterogeneous reactions. Downstream of this location, in zone 3, the turbulent boundary layer begins to develop. Carmicino and Sorge found that their empirical regression rates displayed a small mass-flux power of about 0.37, presumably due to the effects of the injection methods and the attendant large, three-dimensional flow structures that prevail in the fuel port and reduce the dependence on mass flux. However, they were careful to note that the regression rates were *not* pressure dependent, even though the mass flux power of 0.37 is very close to the values of 0.3 and 0.4 discussed by Muzzy [8] and shown in Eqs. (49) and (52). Recall that Chiaverini et al. found similar effects in their regression rate data near the leading edge of the fuel slab [15]. Carmicino and Sorge further note that Boardman et al. [43] tested similar injectors at a much larger scale and found that the radial injector produced a clockwise rotating vortex ring (for injected flow from left to right) that did not enter the fuel port from its location in the precombustion chamber, but the axial injector produced a counterclockwise vortex that extended into the fuel port. Both Boardman et al. [43] and Carmicino and Sorge [44] suggested that this second type of vortex zone allows for stable combustion by providing a flameholder for the diffusion flame at the head end of the fuel grain. In fact, Boardman et al. noted that any injector configuration or oxidizer plenum that generates strong recirculation, such that the oxidizer is preheated before entering the fuel port, produces stable combustion [43]. In addition, Boardman et al. showed empirically that a secondary heat source at the leading edge of the fuel grain, such as an oxidizer-rich hydrogen/oxygen torch also produced stable combustion. In Chapter 9, an additional discussion of hybrid motor combustion instabilities, is provided.

Drawing on the Boardman et al. earlier work, Pucci [46] conducted laboratory-scale testing with a 250-lb_f thrust N_2O/PE motor to study the effects of axial, radial, and swirl oxidizer injection on combustion instability. Similar to Carmicino and Sorge, he found that the axial injection method produced stable combustion and the radial injector produced unstable combustion. However, he also found that weak swirl produced unstable combustion, whereas strongly swirling injection produced combustion only slightly less stable than the axial injector, but increased regression rates by 182% compared to axial injection. He surmised that the combustion instability resulted from a flameholding instability in all cases of unstable combustion. Note that Knuth's work on vortex-injection hybrids, discussed in Sec. IV.A.1, has also indicated that strongly swirling injection produces stable combustion and high regression rates in hybrid motors.

G. Effects of Solid-Fuel Additives

As described more fully in Chapter 10 several researchers, including Strand et al. [46], George et al. [47] and Risha et al. [48] have considered the effects of fuel additives for enhancing regression rates. Dean [49] investigated the use of amine-containing additives, such as hexamine and melamine, to HTPB to increase bulk fuel density and tailor the flux dependence to a power of 0.5 to achieve neutrally regressing fuel grains with circular ports. Muzzy [8] noted that for a fuel containing additives, such as powdered aluminum, the presence of the metal increases the regression rate by reducing the effective heat of gasification of the bulk fuel because, to regress, the binder must pyrolyze but the additive is only heated to the fuel surface temperature. Because the surface temperature of regressing hydrocarbon fuels is on the order of 1000 K, it is clear that metal additives, such as aluminum with a boiling temperature of 2793 K, will not vaporize on the surface (though the surface temperature could exceed the melting temperature of 933 K). In addition, the presence of nonpyrolyzing additives can reduce the blocking effect of mass blowing because only gasified products will shield the fuel surface from convective heat transfer. Note that the Karabeyoglu et al. theory of liquifying solid fuels that regress quickly via a surface melting and droplet entrainment process [5–7] is qualitatively similar to this phenomenon because the liquid droplets ejected from the surface melt layer do not contribute to blocking.

Strand et al. [46] tested and analyzed fuels consisting of 40% Al, 30% coal, and 30% HTPB to investigate how a reduction in fuel heat of gasification and addition of radiating metal combustion products would affect regression rate behavior. The particulate-loaded fuel of Strand et al. had a higher density of 1.64 g/cm^3 and lower enthalpy of gasification of 166 cal/g compared to pure HTPB (0.92 g/cm^3 and 433 cal/g). They found that the metallized-fuel blend regressed about 17% faster than pure HTPB due to stronger radiation from the aluminum oxide combustion products, potential soot radiation, and the lower enthalpy of vaporization. The addition of aluminum will also raise the theoretical combustion flame temperature, which may also increase the regression rate. However, because the flame temperature (or enthalpy) enters the diffusion-limited regression rate equation [such as Eq. (13a)] through the blowing parameter B, which is raised to a small power, slight increases in flame temperature probably do not have a very significant effect on regression rate. Also, metal additives or other fillers that reduce the blocking effect will only increase the overall motor performance if they burn efficiently. High fuel regression rates are not attractive if they are accompanied by low combustion efficiency.

It should be emphasized that the exact nature of a specific binder/additive combination should be investigated before making generalizations about how additives will modify the effective heat of gasification and, therefore, the regression rate. It is possible that the sensible energy increase of the additive may be larger than the binder gasification enthalpy in some cases (as testing of cryogenic solid fuels loaded with aluminum described in Sec. IV.B.1 have suggested). The binder properties, additive properties, and mass fraction of additive should be carefully evaluated in analyzing the test data from such experiments. In addition, the effect of additives on the mechanical properties of the resulting bulk fuel must be evaluated so that structurally sound fuel grains can be produced.

H. Scaling and Geometry Effects

We conclude this section with a discussion of scaling effects and the effects of fuel port geometry on regression rates. Size scale-up is a very important consideration for the development of large-scale operational hybrid propulsion systems, especially when larger-scale designs are based on subscale or laboratory-scale experimental data. Note that empirical scaling (and geometry) effects reported in the literature often appear to conflict. For example, the Boardman et al. correlations for the circular-port, 11-in. JIRAD motor [41] in Eqs. (53) and (54) show a significant positive power on chamber diameter, indicating a strong increase of regression rate with port size presumably due to more intense radiation that accompanies larger gas volumes. On the other hand, George et al. [47] have recently shown that data from their laboratory-scale testing indicates a decrease of regression rate with increasing port size possibly due to boundary layer growth and less severe temperature gradients. These results suggest that different combustion phenomena, such as thermal radiation and boundary-layer growth, may be more or less significant at different motor scales and that empirical scaling laws may apply only over a limited range of motor sizes. Furthermore, scaling effects may be highly nonlinear, given the complex phenomena that may influence regression rate behavior. In Chapter 12, a detailed treatment of this subject is presented; however, we here review several approaches and results for the sake of completeness.

During the mid-to-late 1990s, Venkateswaran and Merkle conducted an analysis of scaling and geometry effects using a computational fluid dynamics (CFD) code [50]. Their model employed the three-dimensional, unsteady Navier–Stokes equations coupled with a solid-fuel pyrolyis model based on Arisawa and Brill's results [3], a two-step chemical kinetics model, a $\kappa-\varepsilon$ turbulence model, and a radiation model based on testing conducted in a parallel experimental effort with a laboratory-scale, slab-geometry HTPB/GOX motor [15]. Venkateswaran and Merkle first validated their model against laboratory-scale results. As shown in Fig. 17, good agreement was obtained between the numerical simulations and empirical data. They then analyzed geometric effects by simulating the slab-geometry motor and axisymmetric analogs of this motor for two cases: case A, where the initial cross-sectional area of the axisymmetric and slab motor fuel ports were equal, and case B, where the initial diameter of the axisymmetric port had the same value as the initial gap between the two fuel slabs. All three simulations used a common value of initial G_o at the inlet. The simulations indicated markedly different regression rate profiles for all three cases, differing by as much as 50%, prompting the authors to note that classical hybrid theory developed by Marxman and Gilbert [1], Marxman et al. [8], and Marxman [9, 10], does not account for differences in port shape and the particulars of internal flow, such as acceleration along the port and merging boundary layers.

Venkateswaran and Merkle then conducted additional simulations on axisymmetric and geometrically similar laboratory-scale (23-in. fuel grain), intermediate-scale (100-in. fuel grain), and full-scale (350-in. fuel grain) hybrid motors to examine scaling issues [50]. All three simulations were conducted at a fixed grain initial L/D (35), initial GOX mass flux ($0.8\,\mathrm{lb_m/in.^2 \cdot s}$), and chamber pressure (900 psia). The fuel was HTPB in all cases. The results of the simulations indicated that the regression rates varied significantly among the different scales, with

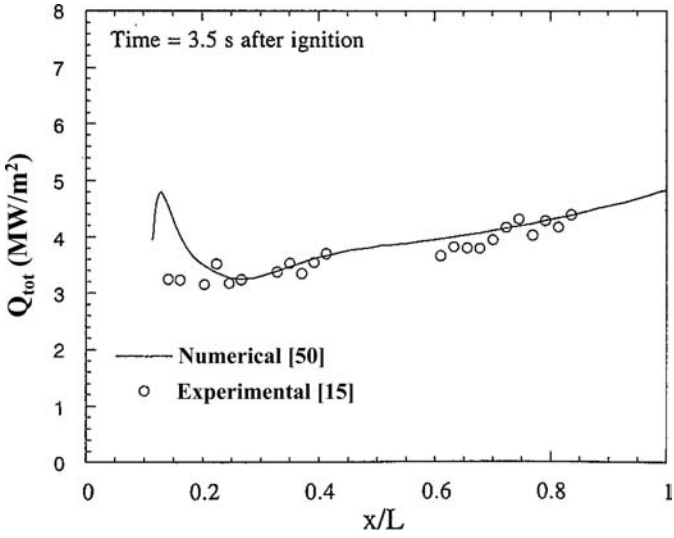

Fig. 17 Comparison of experimental [15] and numerical [50] total heat flux profiles to the fuel surface.

the laboratory-scale motor having the highest regression rate (about 3 mm/s at the midpoint of the fuel grain) and the full scale the lowest (about 2.2 mm/s at the same nondimensional location). After investigating the flame zone location and attendant heat fluxes for all three cases, Venkateswaran and Merkle concluded that the relative contribution of convective heat flux decreases at larger scales because the physical height of the flame zone above the fuel surface increases dramatically, causing a more shallow temperature gradient between the flame and fuel surface and, correspondingly, less convective heating. On the other hand, due to the increasing gas volume-to-fuel surface area at larger scales, radiant heating becomes relatively more important as size increases. However, this increase in radiant heat transfer does not offset the decrease in convective heat transfer, and the overall regression rate decreases with motor size. They also noted that their radiation model might overpredict the magnitude of the radiant heat flux at larger scales [50].

Estey et al. [13] examined scaling effects from an empirical standpoint by using various regression rate equations to predict experimental regression rates from two different fuels and two different motor sizes. They developed nine different regression rate equations that included various combinations of either oxidizer or total mass flux, chamber length, chamber pressure (to account for chemical kinetic effects), and combination of chamber diameter and pressure (to account for radiation effects). The regression rate data sets included HTPB/LOX and HTPB/GOX motors ranging in size from 300 to 73,000 lb_f (a thrust scale-up factor of 240) and data from NASA's Solid Rocket Combustion Simulator (SRCS) program. The SRCS motor used a metallized-fuel formulation consisting of HTPB, Al, and NH_4Cl. The SRCS data analyzed by Estey et al. consisted of 43 motors firings ranging in size from 1.7 to 7.9 in. port diameters [13]. Estey et al. noted that the

results of the analysis indicated that classical regression rate theory worked best for the pure HTPB/O_2 data, such that

$$r \sim G^{0.75} L^{-0.12} \tag{59}$$

which is quite close the classical $G^{0.8} x^{-0.2}$ dependence predicted by Marxman [9]. The metallized SRCS data were best predicted by

$$r \sim G_o^{0.54} L^{-0.04} [1 - \exp(-D/D_{\text{ref}})][1 - \exp(-p/p_{\text{ref}})] \tag{60}$$

which accounts for radiant effects. As discussed earlier, these additional effects reduce the dependence on convective heating evidenced by the lower values of the powers on G_o and L.

Estey et al. also found that fairly large errors resulted when extrapolating empirical regression rate correlations developed using small-scale data to motors of larger scales [13] suggesting the importance of scaling effects in regression rate prediction. For the HTPB motors, the minimum extrapolation error was about 11%, whereas for the metallized SRCS motors, the most accurate correlation gave a 17.7% error. Note that Estey et al. made no attempt to develop nondimensional correlations based on physically meaningful dimensionless parameters. Such an approach may potentially yield improved results for extrapolating to large scales.

Chiaverini et al. [16] also conducted an empirical investigation of both scaling and geometry effects by applying their semi-empirical correlation

$$\rho_f r/G = 0.524 StB\theta^{0.6} \left\{ 1.3(Q_r/Q_c)^{0.75} + \exp[-1.3(Q_r/Q_c)^{0.75}] \right\} \tag{61}$$

to data from the literature. As described fully by Chiaverini et al., they developed Stanton number correlations from their data and analysis to make Eq. (61) useful. Similar to Marxman's approach [9], they defined a modified blowing number to account for thermal radiation effects,

$$B_{\text{rad}} = B \exp(Q_r/Q_c) \tag{62}$$

and attempted to correlate the Stanton number ratio St/St_o with B_{rad} to eliminate St from Eq. (61). However, to develop reasonably accurate St/St_o vs B_{rad} correlations, they found that it was necessary to distinguish between the data in the upstream and downstream portions of the motor because the upstream Stanton numbers were typically higher at the same value of B_{rad} than those in the downstream region (see Fig. 12 of [15]). They attributed this to differences in convective heat transfer in the developing and fully developed boundary-layer region which they defined as the location where the momentum boundary layers were estimated to merge. (Because the boundary layer in hybrid combustion is subject to continuous addition of fuel and combustion enthalpy, the term "fully developed" has questionable meaning. In addition, a distinction should be made between the thermal, momentum, and species boundary layers in chemically reacting boundary-layer flow because they may all have different local thickness due to the specific values of the Prandlt, Lewis, and Schmidt numbers.) They also noted that in both regions the value of St/St_o, where St_o is the Stanton number for reference turbulent pipe

flow, exceeded unity for low values of B_{rad} (less than about 3). Chiaverini referenced Venkateswaran and Merkle's CFD results [50] to suggest that this behavior resulted from the significant distortion of the local mass flux profile at the reaction zone caused by the presence of the flame. They then developed separate St/St_o correlations as a function of B_{rad} and D_h, local hydraulic diameter, for the developing and fully-developed regions of the motor. However, for the developed (supposedly merged boundary layers) region, Chiaverini found that

$$St/St_o = 2B_{\text{rad}}^{-0.73} \tag{63}$$

for values of $B_{\text{rad}} > 5$. It is interesting that the empirical power of -0.73 is mid-way between that of Marxman's [11] original empirical constant of -0.77 and Altman's [30] correction of -0.68, although these earlier correlations were developed for B rather than B_{rad}. The results of their empirical heat-transfer calculations, coupled with both Venkateswaran and Merkle's [50] and Chiaverini's [37] earlier semi-empirical finding that the ratio of the local flame-to-core axial velocity exceeded unity for their experiments (as opposed to Marxman's assumption that this velocity ratio is about 0.5), prompted Chiaverini et al. [16] to suggest that the shear flow in a practical hybrid motor is quite different than that of flat-plate boundary-layer flow due to the effects of developing boundary layers, axial acceleration of the core flow, and variable fluid properties across the boundary layer. Green reached a similar conclusion in a much earlier work [29]. As with Venkateswaran and Merkle's findings, these effects suggest that different regression rates will most likely result for different scales and port shapes, all other conditions being equal.

To check the applicability of their analysis to independent data of different scale and geometry, Chiaverini et al. attempted to correlate the empirical results of Shanks and Hudson [51] and Boardman et al. [41]. Shanks and Hudson presented a set of results from a series of HTPB/GOX test firings in a tube-geometry, laboratory-scale hybrid motor. They reported experimental values G_o, O/F, p, D, and L, which Chiaverini et al. used to predict their regression rate with their semi-empirical model [16]. Boardman et al. [41] presented results from the 11-in. JIRAD motor that burned a fuel consisting of about 40% HTPB and 60% Escorez (polycyclopentadiene). Chiaverini et al. used their empirical pyrolysis model for the JIRAD fuel [25] for analyzing the Boardman et al. data. However, they used the soot model for pure HTPB, as described in Sec. III.D because no soot data were available for the JIRAD fuel [16].

The results of the analysis are shown in Fig. 18, and indicated that Eq. (61) slightly over-predicted the Shanks and Hudson tube-geometry data by $+3.9\%$, whereas the Boardman et al. data from the larger-scale testing were slightly under-predicted by -5.7%. For comparison, Chiaverini et al. also developed a simplified G^n correlation based on their empirical data such that

$$r = 0.049G^{0.61} \tag{64}$$

with r in mm/s and G in kg/m$^2 \cdot$ s and used it to also predict Shanks and Hudson's tube-burner data, which resulted in a much larger average error of 35%. They did not attempt to correlate the JIRAD data with Eq. (64) because of the difference in fuel formulation. Note that whereas both Shanks and Hudson's motor and the

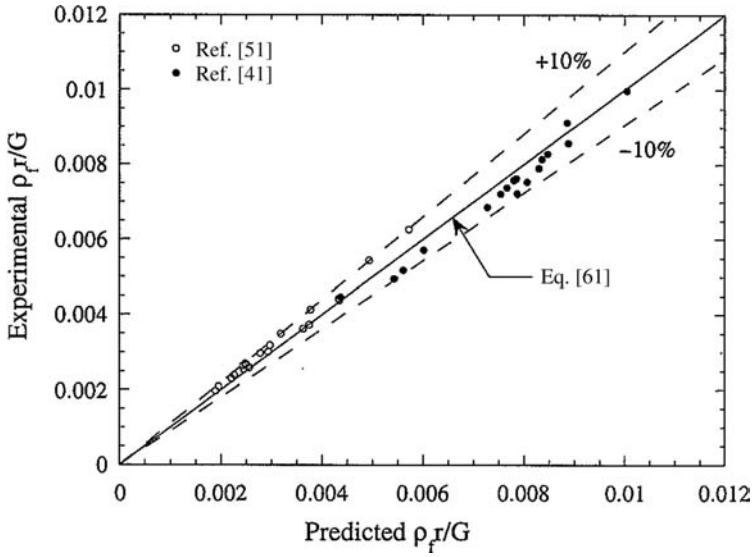

Fig. 18 Prediction of literature data using Eq. (61) showing close agreement with larger-scale and alternate-geometry motors.

Table 3 Example of scaling and geometry effects on regression rate prediction

	Case	
Parameter	1	2
Reference	Shanks and Hudson [51]	Boardman et al. [41]
Scale	Laboratory-scale	Subscale
Fuel port geometry	Circular	Circular
Propellants	HTPB/GOX	40%HTPB + 60% Escorez/GOX
Average error using Eq. (61)	3.9%	−5.7%
Average error using Eq. (64)	35%	——

JIRAD motor used circular ports and Shanks and Hudson's and Chiaverini's motor had a similar scale, the JIRAD motor was approximately five times larger. Thus, as summarized in Table 3, Eq. (61), obtained using data from a laboratory-scale, slab-geometry motor, gave quite reasonable results for a circular-port motor of substantially larger scale, with no explicit changes to the correlation to account for scaling or geometry effects. Note that these results are qualitatively in contrast to the previous findings of Estey et al. [13], who found substantial differences in the regression rate behavior when extrapolating to larger scales. Though preliminary, these results suggest that properly accounting for the salient features of boundary-layer processes in hybrid motors using physically relevant dimensionless parameters may provide for reasonably accurate extrapolations to larger

scales and/or alternate geometries (at least for a given fuel/oxidizer combination). However, note that correlations developed for hydrocarbon fuels, for instance, would not be expected to apply accurately to highly metallized fuels, and vice versa, due to the different radiative properties of the combustion gases. For a similar reason, we would not expect a correlation such as that given in Eq. (61) to apply to paraffin fuels (discussed in the next section), which appear to regress via a surface melt-layer process.

Table 4 summarizes the major regression rate expressions from the investigations already discussed, and Fig. 19 qualitatively illustrates some of the regression rate phenomena elucidated by the results of the various research. At "intermediate" mass fluxes, the regression behavior is be dominated by turbulent heat transfer, and theoretically follows, for example, Eq. (13a) or Eq. (13b). In this regime, neither radiation nor kinetics significantly influence the *behavior* of the regression rate with respect to mass flux. However, it is possible that such effects are present to some extent and may influence the overall *magnitude* of the regression rate. At high mass fluxes and low pressures conditions, the dependency of heterogeneous and/or gas-phase reaction rates on chamber pressure could have a significant effect on the regression rate behavior. When the chamber pressure is lower than a threshold value determined by the particular mass flux and fuel/oxidizer combination, the regression rate can be lower than that predicted by classical hybrid boundary layer theory due to finite-rate kinetic effects (gas-phase reactions, heterogeneous reactions, or polymer decomposition). As pressure or propellant reactivity increases, the reaction rates increase, and the regression rate approaches the classically-predicted value. Regression rate expressions given by Smoot and Price [17–19], Miller [23], Kosdon and Williams [20], Kumar and Stickler [22], and Wooldridge and Marxman [24], attempted to capture these effects. It is interesting to note that Marxman [11] suggested that chemical kinetic effects may become important at a pressure threshold of about 200 psia and lower for many types of propellant combinations and port sizes at "typical" flow rates. Though more recent investigations by researchers such as Strand et al. [14, 35], Boardman et al. [43], and Chiaverini et al. [16] has not uncovered significant kinetic influences, even in this range or relatively low-pressure operation, it should be kept in mind that such effects may be difficult to characterize without careful interpretation of detailed empirical data from well-designed experiments and test matrices.

The flooding limit is eventually reached as mass flux increases to still higher values. However, the flooding limit also depends on the pressure and propellant reactivity of the system. Highly-reactive combinations such as lithium hydride and fluorine, for example, would therefore be expected to flood at higher mass fluxes than a less reactive system such as hydrocarbon fuels with nitrous oxide.

Pressure has the opposite effect on the other end of the mass flux spectrum. In the low mass-flux regime, the effect of thermal radiation becomes important because the heat flux due to turbulent convection is relatively small. As the product of pressure and motor inner diameter (pD) increases, the effect of radiation becomes more prominent at a given mass flux. The pD term gives a measure of the gas optical density as described by Incropera and Dewitt [52]. When pD is high, the gas emits thermal radiation more efficiently and the regression rate increases to higher values than predicted by classical theory. Marxman [9–11], Estey et al. [13], Strand et al. [14], and Chiaverini et al. [15, 16] investigated this behavior. Similar

Table 4 Summary of classical hybrid regression rate equations

Investigators	Reference	Regression rate equations/correlations	Equation number	Comments/ significance
Bartel and Rannie	[26]	$\rho_f r = \frac{1}{2} c_f G f_m \exp(-2c_f x/D)$	(1)	Assumed diffusion of oxidizer to fuel surface was rate limiting
Emmons	[27]	$\rho_f r = \rho_e u_e [0.18 + \log_{10}(B + 0.7)]/Re_x^{1/2}$	(4)	For laminar flow
Houser and Peck	[28]	$r(t) = 0.8B/t^{0.2} + 0.3C/t^{0.7}$	(6)	Empirical expression for instantaneous data
Marxman, Gilbert, Wooldridge, Muzzy, and Altman	[2, 9]	$\rho_f r = CGRe_x^{-0.2}(St/St_o)(u_e/u_{\mathrm{fl}})(h_{\mathrm{fl}} - h_w/\Delta H_{v,\mathrm{eff}})$	(8) and subsequent equations	Very significant analysis and results for diffusion-limited regression rate behavior. Altman later provided the more accurate power on B of 0.32 rather than Marxman's orginal 0.23. The assumption that the flame does not affect the local axial velocity profile across the port is probably not completely accurate.
		$B = \dfrac{\rho v\|_w}{\rho_e u_e (c_f/2)} = \dfrac{u_e}{u_{\mathrm{fl}}} \dfrac{(h_{\mathrm{fl}} - h_w)}{\Delta H_{v,\mathrm{eff}}}$		
	[30]	$St/St_o = 1.2B^{-0.77}$		
		$\rho_f r = 0.036 G B^{0.23} Re_x^{-0.2} \propto B^{0.23} G^{0.8} x^{-0.2}$		
		$\rho_f r \propto B^{0.32} G^{0.8} x^{-0.2}$		
Marxman et al.	[9]	$\rho_f r = [Q_c \exp(-Q_{\mathrm{rad}}/Q_c) + Q_{\mathrm{rad}}]/\Delta H_{v,\mathrm{eff}}$	(14)	Correction for thermal radiation effects
Chiaverini et al.	[16]	$\dfrac{\rho_f r}{G} = aStB\theta^b \left\{ c\left(\dfrac{Q_{\mathrm{rad}}}{Q_c}\right)^d + \exp\left[-c\left(\dfrac{Q_{\mathrm{rad}}}{Q_c}\right)^d\right]\right\} = aStB\theta^b \left[F\left(\dfrac{Q_{\mathrm{rad}}}{Q_c}\right)\right]$	(23)	Includes four empirical constants and correction factors for thermal radiation and variable fluid properties
		$a = 0.524; \quad b = 0.6; \quad c = 1.3; \quad d = 0.75$		
		$B \equiv \dfrac{\Delta H_r + (h_{\mathrm{bulk}} - h_{\mathrm{w}})}{(\Delta H_v)_{\mathrm{eff}}}, \quad B_{\mathrm{rad}} = B \exp\left(\dfrac{Q_{\mathrm{rad}}}{Q_c}\right),$		
		$St/St_o = 2B_{\mathrm{rad}}^{-0.73}$ for $B_{\mathrm{rad}} > 5$ in developed region		

Marxman	[10]	$\rho_f r = 0.036 G \left(\frac{\bar{\rho}}{\rho_e}\right)^{0.6} B^{0.23} Re_x^{-0.2}$	(28)	Correction for variable fluid properties; Altman's correction for $B^{0.32}$ could be applied
Paul et al.	[12]	$\rho_f r = 0.056 G Re_x^{-0.2} \left(\frac{\rho_{fl}}{\rho_e}\right)^{0.71} \left(\frac{\rho_w}{\rho_e}\right)^{0.14} B(1+B)^{-(0.73-0.002\rho_w/\rho_e)}$	(31)	Correction for variable fluid properties and molecular weight of pyrolyzed gases at fuel surface
Smoot and Price	[17]	$\rho_f r = 0.03 G Re_x^{-0.2} \frac{\ln[1+(\lambda B/Pr^{2/3})]}{\lambda}, \qquad B = \frac{h_{fl} - h_w}{\Delta H_{v,\text{eff}}}$	[33]	Diffusion-limited expression that includes effects of condensed-phase products at wall on blowing effect
Smoot and Price	[19]	$\frac{p_{o_\infty}}{\rho_f r} = \left\{ 33 P_\infty \left(\frac{x}{\mu}\right)^{0.2} Sc^{2/3} \frac{[\exp(B\lambda) - 1]}{G^{0.8} B\lambda} \right\} + \frac{1}{k}$	(37)	Kinetic-limited; assumes turbulent transport of oxidizer to wall and subsequent heterogeneous reactions are rate-limiting
Miller	[23]	$\frac{p_o}{\rho_f r} = \frac{p B^{0.8} x^{0.2}}{a G^{0.8}} O/F\|_{st} + \frac{X_o^*}{K}$	(38)	Includes effects of gas-phase kinetics and convective heat transfer
Kosdon and Williams	[20]	$\frac{(r_o - r)}{r_o} = \frac{K_1 G (Q/\Delta H_{v,\text{eff}})^{-\varepsilon}}{x p^2 Y_{Oe}^{\varepsilon}}$	(40)	Includes effects of gas-phase kinetics and convection for weak pressure-dependence
Kosdon and Williams	[20]	$r \sim p^{1/2}$	(41)	Includes effects of gas-phase kinetics for strong pressure-dependence

(*Continued*)

Table 4 Summary of classical hybrid regression rate equations (Continued)

Investigators	Reference	Regression rate equations/correlations	Equation number	Comments/ significance
Marxman	[11]	$\rho_f r = 0.036 G \left(\frac{\bar{\rho}}{\rho_e}\right)^{0.6} (B')^{0.23} \times Re_x^{-0.2} \left[\exp\left(\frac{-Q_h}{Q_c}\right) + \frac{Q_h}{Q_c}\right]$	(43)	Correction for potential heterogeneous reactions in diffusion-limited range, also includes variable fluid property correction; no explicit pressure dependency
Wooldridge and Marxman	[24]	$\frac{r}{r_o} = \left(2\frac{t_m}{t_c}\right)^{0.5} \left[1 - \frac{t_m}{t_c}(1 - (\exp - t_c/t_m))\right]^{0.5}$	(45)	Accounts for chemical kinetic effects due to both gas-phase and heterogeneous reactions
Muzzy	[8]	$r = C_3 P^{0.5} G^{0.4} x^{-0.1}$	(49)	Simplified version of Eq. (45) for kinetically influenced regime
Kumar and Stickler	[22]	$\left(\frac{r}{r_o}\right)\left(\frac{G_\infty^n}{G^n}\right)\left[\frac{\ln(p_{\text{ref}}/p_\infty)}{\ln(p_{\text{ref}}/p)}\right] = f_1\left(\frac{G}{G_\infty}\frac{p_\infty}{p_{\text{ox}}}\right)$	(50)	Accounts for pressure effects due to kinetics of polymer fuel decomposition
Muzzy	[8]	$r = C_5 P^{0.5} G^{0.3} x^{-0.2}$	(52)	Simplified version of Eq. (50) for kinetically influenced regime; note similarity to Eq. (49)
Boardman et al.	[43]	$\bar{r} = 0.064 \bar{G}_o^{0.73} (\bar{D}_p/3)^{0.59} (\bar{P}_c/500)^{-0.08}$	(53)	Empirical fit for UTF-29901 and GOX; note significant dependence on diameter, insignificant pressure dependence
Chiaverini et al.	[25]	$r = A\exp(-E_a/R_u T_s)$; $A = 11$ mm/s, $E_a = 4.91$ kcal/mol for $T_s > 722$ k	(56)	Pyrolysis law that relates regression rate to surface temperature in absence of significant heterogeneous surface reactions

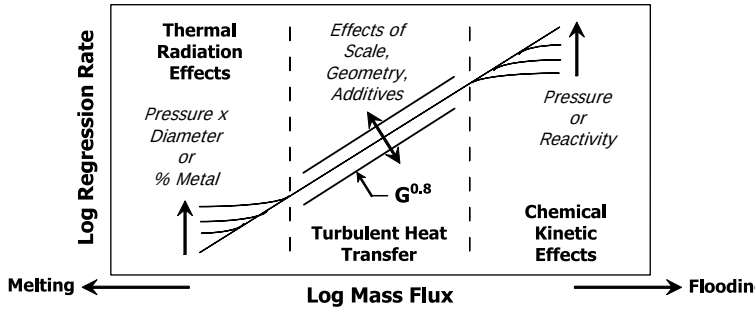

Fig. 19 Regimes of regression rate dependency.

behavior is expected as the amount of metal loading is increased for metallized fuels. As mass flux decreases further, the "cooking" limit is reached and steady-state combustion is no longer sustainable. Here, the fuel is expected to melt, char, or undergo subsurface decomposition as the thermal wave penetrates deep into subsurface region.

Finally, as discussed earlier in this chapter, it should be emphasized that the solid-fuel regression rate behavior in the low, intermediate, and high mass flux regimes may also be influenced by effects of fuel port size (scaling effects), fuel port geometry, oxidizer injector design and associated flow structures in the fuel port, solid fuel additives, and boundary layer fluid property variations.

IV. Regression Rate Behavior in Nonclassical Hybrids

We now turn our attention to the fuel regression rate behavior of various types of non-classical hybrid motors, including swirl-injected hybrids, vortex hybrids, end-burning hybrids, radial-flow hybrids, and hybrids employing cryogenic solid fuels or paraffin-based solid fuels. In most cases, these hybrids have been introduced fairly recently (circa mid-1990s) with the objective of either increasing fuel regression rates to improve overall performance and design flexibility or of developing a unique motor geometry for a particular application. We will first examine various types of hybrids that employ unique injection methods and grain geometries, such as swirl-injected hybrids and end-burning hybrids. Afterward, high-regression rate solid fuels such as paraffin-based fuels and cryogenic solid fuels will be discussed. For completeness, the regression rate behavior of metallized solid fuels will be reviewed briefly, although in Chapter 10 this topic is discussed in more detail.

A. Hybrid Motors with Unique Injectors and Fuel Grain Geometries

Several researchers have attempted to enhance fuel regression rates by using various types of swirl injectors to increase local fuel surface heat flux. Most notably, these have included efforts by Knuth et al. [53, 54], Yuasa et al. [31], Lee et al. [55], Rice et al. [56], and Haag et al. [57]. Caravella et al. [58] tested an end-burning hybrid motor that used radial-flow injectors to burn PE fuel disks with decomposed hydrogen peroxide, whereas Nagata et al. developed and tested a unique axial-flow

end-burning hybrid called the “dry towel” configuration [59, 60]. These motors and investigations are discussed next.

1. *Vortex Hybrids*

Motivated by the desire to increase fuel regression rates for obtaining volumetrically efficient fuel grain designs, Knuth et al. at Orbital Technologies Corporation [ORBITEC] experimented during the mid-1990s with laboratory-scale vortex hybrids wherein the swirl oxidizer injector was located at the aft end of the fuel grain just upstream of the converging portion of the exit nozzle. Figure 20 is a schematic of one of their test motors. Knuth et al. discovered that this arrangement generated a pair of coaxial, bidirection vortices in the combustion port. The outer vortex spiraled toward the head end of the motor across the fuel surface, mixing and burning with the pyrolyzed fuel. At the head end, the vortex flowed inward toward the motor axis and formed an inner vortex that spiralled downward and out the nozzle [53]. Figure 21 shows a velocity vector field in the meridonal plane generated from numerical simulations of a 500-lbf thrust vortex hybrid burning GOX and HTPB using the Finite Difference Navier Stokes (FDNS) code [54]. The numerical simulation captured the salient features of the bidirectional vortex flowfield including the upward-flowing outer vortex and the downward-flowing inner vortex. Note that the swirl velocity is not apparent in this sectional view of the grain chamber. Vortex hybrid flowfield characteristics are further discussed in Chapter 6.

Knuth et al. initially investigated the regression rate behavior of HTPB fuels burning with gaseous oxygen, then later tested several proprietary fuel blends

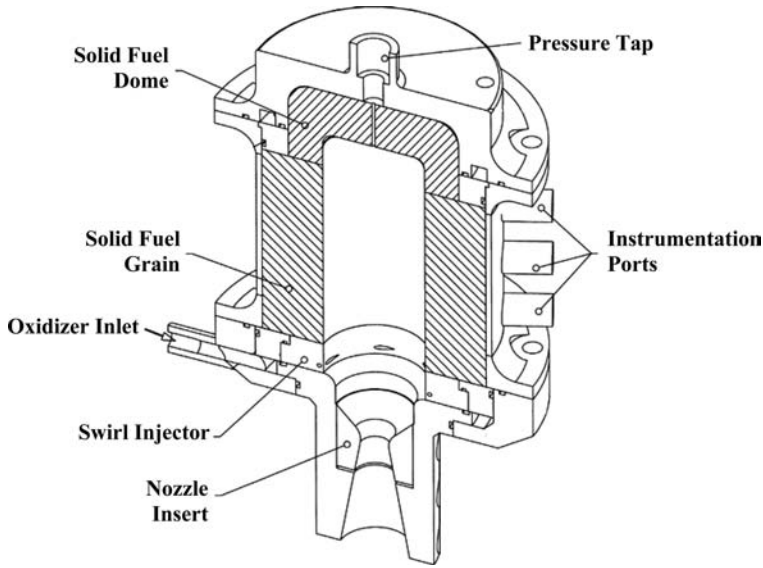

Fig. 20 ORBITEC laboratory-scale vortex hybrid motor.

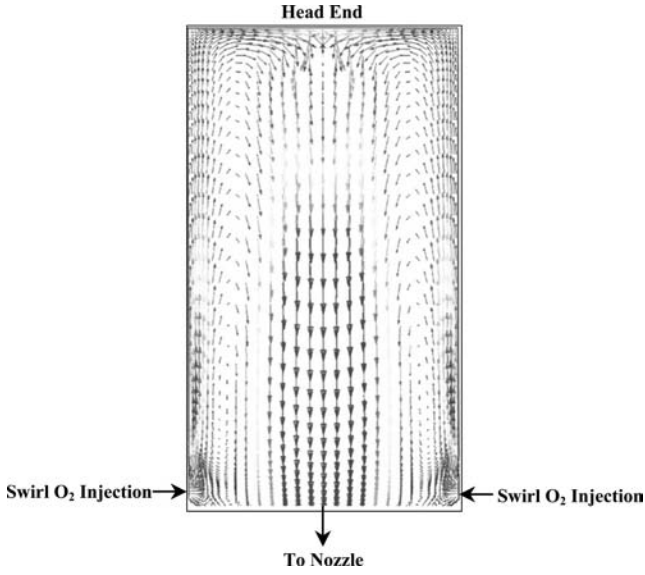

Fig. 21 Results of numerical simulation of 500-lbf thrust vortex hybrid flowfield. (From Knuth et al. [54].)

in a vortex hybrid to further increase regression rates. One of these, "Fuel A," had regression rates similar to frozen methane (personal communications with William Knuth at ORBITEC, July 2005). They examined the effects of swirl injector design and fuel port geometry on regression rate, developed empirical and semi-empirical regression rate and heat-transfer correlations, and also performed additional numerical simulations of the coaxial vortex flowfield. Similar to the vortex hybrid schematic shown in Fig. 20, motors up to about 300-lbf thrust were tested. HTPB solid-fuel regression rates up to 6 times faster than those in classic hybrids operating at the same mass flux conditions were measured [53]. An empirical regression rate correlation was developed to describe regression rate as a function of mass flux,

$$r = 0.193G^{0.54} \tag{65}$$

with r in mm/s and G in $\mathrm{kg/m^2 \cdot s}$.

Even at modest mass fluxes of about $100\,\mathrm{kg/m^2 \cdot s}$ ($0.14\,\mathrm{lbm/in.^2 \cdot s}$), the vortex hybrid displayed regression rates of about 2.3 mm/s. In contrast, classical hybrids burning HTPB and GOX have typically been found to regress at about 0.4–0.6 mm/s at this same mass flux. As shown in Fig. 22, uniform regression rates with respect to axial distribution were also obtained.

Also note that the empirical power of 0.54 on mass flux suggests that vortex hybrids should produce a nearly neutral burn where the decrease in regression rate over time is almost balanced by the increase in fuel surface area such that the overall fuel production rate, and therefore the O/F mixture ratio, remain nearly constant over the course of the burn. As noted by Knuth et al. [53], the relatively

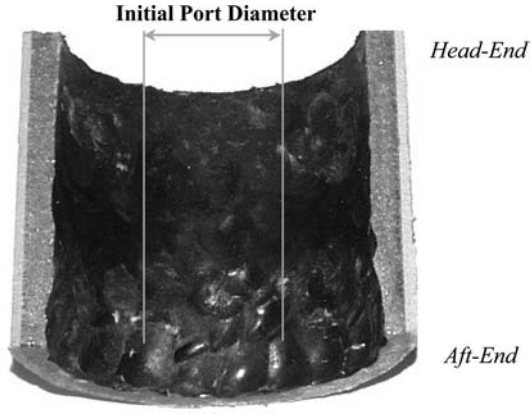

Fig. 22 Vortex hybrid recovered fuel grain showing uniform axial regression rate profile.

low dependence on G also suggests that other factors influence the regression rate. More detailed empirical correlation development showed that the regression rate had a significant dependence on injection velocity and fuel port geometry. Higher injection velocities, which induce stronger swirl in the combustion port appeared to cause higher regression rates [53]. Employing the Chiaverini et al. semi-empirical methods [16] and pyrolysis model [25], Knuth et al. developed semi-empirical regression rate and heat-transfer correlations to show that the highly swirling flow in the near-wall region was responsible for large increases in the convective heat transfer rates. They did not find any explicit pressure effects from either chemical kinetics or radiant heat transfer. Their nondimensional regression rate correlation was

$$\rho_f r/G = 0.082 Re_D^{-0.33} (St_{\mathrm{sw}}/St_o)(St_v/St_{\mathrm{sw}})B, \qquad R^2 = 0.99 \qquad (66)$$

where the dimensionless regression rate, $\rho_f r/G$, is a function of the Reynolds number based on average port diameter, two Stanton number ratios, and the blowing parameter B defined as in Eq. (25). This correlation fit the data to within a $+/-$ 10% error band, even though the thrust level varied by a factor of 10 (from 20 to over 200 $\mathrm{lb_f}$). Figure 23 shows the results of the correlation given by Eq. (66). The power of -0.33 on the Reynolds number implies that the boundary-layer processes in the vortex hybrid engine differ from those in conventional pipe flow, as might be expected. The reaction zone in the hybrid boundary layer may cause the shape of the velocity profile to differ from that of ordinary turbulent flow, which could lead to the particular Reynolds number dependency indicated by Eq. (66). Except for the use of two Stanton number ratios, Eq. (66) is similar in form to Marxman's original expression given in Eq. (13a). The term St_{sw}/St_o accounted for the enhanced local heat transfer due to tangential injection and was calculated from Dhir and Chang's analysis of enhanced heat transfer in pipes using (noncombusting) swirl flow [61]. The ratio of St_v to St_{sw} accounted for the

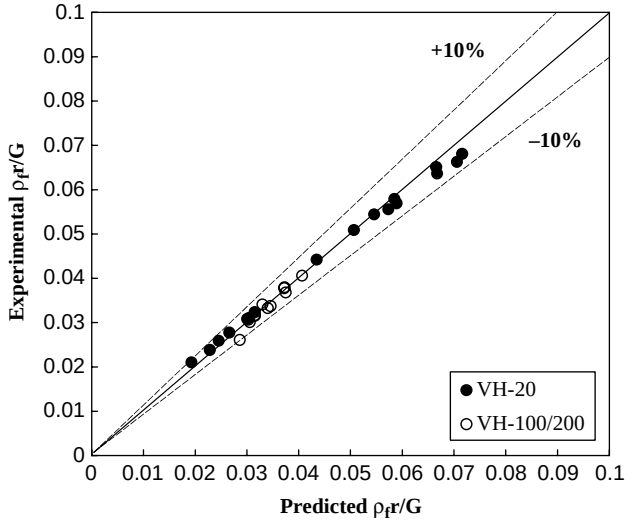

Fig. 23 Vortex hybrid semi-empirical regression rate correlation using $\rho_f r/G = 0.082 Re_D^{-0.33} (St_{sw}/St_o)(St_v/St_{sw})B$.

additional effects of wall blowing, combustion, and the presence of the inner vortex field that were not considered in Dhir and Chang's swirling pipe flow analysis.

Knuth et al. also developed an empirical heat-transfer correlation for this Stanton number ratio vs B. As for classical hybrids, the data showed a reciprocal relationship between B and St_v/St_{sw} due to the blocking effect, such that

$$St_v/St_{sw} = 0.55B^{-0.97}, \qquad R^2 = 0.868 \tag{67}$$

Note that Eq. (67) shows a higher dependence on blowing parameter than for classical hybrids where the power is -0.68, according to Altman [30]. Combining Eqs. (66) and (67) shows that the vortex hybrid regression rates were approximately independent of B, at least for the range of blowing parameters tested [53]. Knuth et al. also noted that at smaller values of B, Stanton number ratio St_v/St_{sw} exceeded unity by about 15%. This result again suggests that the shear effects in the hybrid boundary layer differ from the reference case of noncombusting flow due to the presence of the diffusion flame. As also indicated by the power of -0.33 on the Reynolds number in Eq. (66), the flame zone may alter the velocity profile, allowing the vortex hybrid to sometimes display larger heat transfer rates than the reference swirling flow, even in the presence of wall blowing. Venkateswaran and Merkle found from numerical analysis that the diffusion flame zone caused a steeper velocity gradient near the fuel surface than would normally occur for noncombusting turbulent flow [50]. In addition, recall that Chiaverini et al. also found evidence of this effect in experimental regression rate data obtained in a large laboratory-scale hybrid engine [16].

The vortex hybrid has been shown to produce high regression rates at relatively low mass fluxes because the nature of the bidirectional vortex flowfield seems to

compress the injected oxidizer to a layer near the fuel surface that is relatively thin compared to the port diameter. Thus, the fuel surface experiences an effectively high mass flux compared to the overall port size. However, it is not yet known how the regression rates will behave at even higher mass flux conditions, for example, in the range of interest to classical hybrids of 500 $\mathrm{kg/m^2 \cdot s}$ or greater, or at much larger motor scales. Despite these issues, it appears that the vortex hybrid may offer a good deal of design flexibility due to its unique injection method.

2. *Swirl-Flow Hybrids*

Yuasa et al. [31] also experimented with swirl-oxidizer hybrid motors wherein the swirl injector was located at the head end of the grain case. Using GOX and PMMA, they obtained regression rate increases about 2.7 times greater than that for axial flow hybrids (similar to Pucci's findings discussed earlier [45]), eventually flying a small (1.8-m, 15.4-kg) rocket using the same method. Yuasa et al. ran several series of experiments to determine the effects of swirl strength and oxidizer mass flux on fuel regression rate. Use of various fuel injector designs allowed them to vary these two effects independently [31]. Swirl injectors with geometric swirl numbers S_g of 19.4 and 9.7 were employed, where S_g is defined as

$$S_g = (R_{\mathrm{inj}} - R_{\mathrm{port}})R_{\mathrm{inj}}/NR_{\mathrm{port}}^2 \tag{68}$$

based on conservation of momentum following Beer and Chigier's convention [62]. In Eq. (68), R_{inj} is the radius of the injector exit (into the fuel port), R_{port} the individual injection port radii, and N the number of injection ports feeding the oxidizer into the swirl injector. A no-swirl injector was also used to obtain a baseline regression rate correlation. The effect of fuel grain length on average regression rate was also examined using two different fuel grain designs of 150 and 500 mm. Average oxidizer mass fluxes ranged from about 10 to 20 $\mathrm{kg/m^2 \cdot s}$ (0.014 to 0.028 $\mathrm{lbm/in.^2 \cdot s}$) for the shorter (150-mm) fuel grains and from about 40–60 $\mathrm{kg/m^2 \cdot s}$ (0.057 to 0.085 $\mathrm{lbm/in.^2 \cdot s}$) for the longer (500-mm) fuel grains.

Yuasa et al. [31] correlated the regression rates with the GOX mass flux using an $r = aG_o^n$ expression for the various cases and found the empirical parameters shown in Fig. 24 and Table 5. When it is kept in mind that the tests with shorter grain length correspond to a lower G_o level and tests with the longer grain length correspond to a higher G_o, several interesting observations follow from these data. First, notice that for both sets of data the parameter a varies approximately linearly with the swirl number (Fig. 24) over the range tested, with larger swirl numbers leading to higher values of a consistent with the observed increases in regression rate with larger swirl intensity (see Fig. 4 of [31]). However, the empirical constant n does not change significantly with swirl number variations within a given set of data, suggesting that the strength of swirl in the oxidizer stream does not fundamentally alter the nature of the heat flux heat transfer in the turbulent, reacting boundary layer, but mainly affects its magnitude. Also note that the n value for data set 1 is quite close to the theoretical turbulent value of 0.8 for all three S_g values, whereas data set 2, the lower mass flux range, displayed corresponding values closer to 0.6 (Table 5). This finding agrees with earlier results (Figs 7 and 8), which indicated that for lower mass fluxes solid-fuel regression rates are often influenced by thermal radiation, leading to weaker dependency on turbulent heat

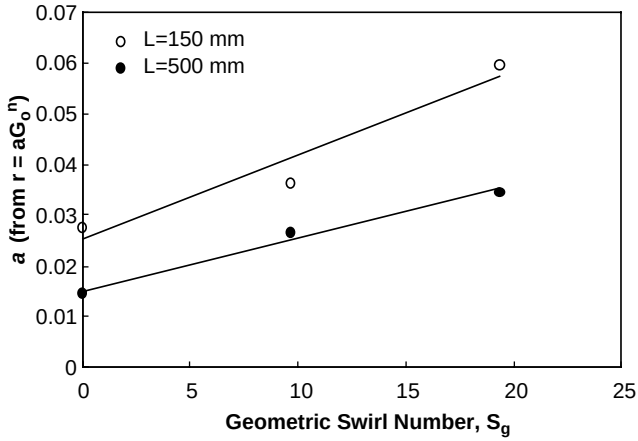

Fig. 24 Variation in preexponential constant a with S_g for the Yuasa et al. experiments [30].

Table 5 Variation in preexponential constant a with S_g for the Yuasa et al. experiment [31]

	Grain length, mm	G_o range, kg/m$^2 \cdot$ s	S_g	a	n
Data set 1	500	40–60	19.4	0.0345	0.778
	500	40–60	9.7	0.0266	0.790
	500	40–60	0	0.0145	0.749
Data set 2	150	10–20	19.4	0.0596	0.641
	150	10–20	9.7	0.0362	0.587
	150	10–20	0	0.0276	0.581

transfer (represented by $n \sim 0.8$). However, the data presented by Yuasa et al. [31] do not permit one to separate the effects of grain length and G_o level, and so it is premature to attempt definite conclusions concerning this behavior. Possibly, the lower n value on data set 2 may also be influenced by other effects such as a relatively long portion of the grain subject to entrance or injector effects.

Yuasa et al. also investigated how the axial regression rate profiles of the PMMA tubes were influenced by the different swirl strengths. They noted that, in addition to increasing the magnitude of the regression rates, the dependency of the local regression rate on axial location was significantly weakened as a function of increasing S_g. In other words, the fuel grain tended to regress more uniformly as swirl intensity was increased. For the no-swirl case, the local regression rates were high near the forward edge of the grain, then decreased with increasing distance to a minimum, then began increasing again as a function of axial location. Yuasa et al. noted the similarity between this result and that of Chiaverini et al. [15] for HTPB burning with GOX in a slab-geometry hybrid and explained the existence of a local minimum regression rate as the tradeoff between boundary-layer

growth in the streamwise direction (which decreases the thermal gradient and corresponding convective heat transfer) and fuel mass addition, which increases the local mass flux, turbulence intensity, and heat transfer. Recall that Knuth et al. [53] also found that swirl flow in the vortex motor configuration could produce very uniform regression rate profiles. It appears that swirl momentum in the boundary layer causes enhanced heat transfer by reducing the boundary-layer thickness and also retards the growth of the boundary layer in the downstream direction, thus producing more uniform heat transfer and corresponding fuel regression rates.

Lee et al. have recently described an approach similar to that of Yuasa et al., but one that employs fore-end swirl injection into a helical fuel grain configuration [55]. They tested a laboratory-scale hybrid using PMMA and GOX over a mass flux range of 30–80 $kg/m^2 \cdot s$ at about 300 psi. The fuel grains were 200 mm long. These conditions were very similar to that of Yuasa et al., and as shown by Lee et al., the regression rate results for the two sets of data for the no-swirl conditions agreed very well (see Fig. 3 of [55]).

Lee et al. conducted several series of tests to determine how fuel regression rates were affected by 1) spiral grooves of various pitch cut into the PMMA fuel tubes, 2) swirl imposed on the injected oxidizer at the fuel port inlet, and 3) various combinations of spiral grooves and swirl injection. For the spiral groove testing, pitches of 3, 6, 12, and 18 were examined, where the pitch was defined as the distance in millimeters between the troughs of adjacent grooves. The pitch depth was fixed for all of the fuel grain configurations tested and grooves were machined into only the aft-half of the fuel tubes. Although Lee et al. suggested that this method allowed for a direct observation of regression rate enhancement by comparing the fore and aft portions of the fuel grain, it most likely has the benefit of minimizing entrance effects on regression rate behavior in the grooved portion. Lee et al. recognized that the presence of the spiral grooves affected both the wetted fuel surface area (the burning surface area) and the fuel volumetric efficiency [55]. For the smallest pitch of 3 mm (where the grooves were arranged nearly perpendicular to the flow direction) the fuel volumetric efficiency was reduced by about 1%, but the fuel surface area was increased by almost 50% over the baseline case of no grooves. For the largest pitch of 18 mm, the corresponding values were 0.4 and 112%. Testing indicated that, compared to the baseline fuel grain, the grains with grooves regressed somewhat faster, with smaller pitch leading to larger increases of up to 35%. However, the 18-mm pitch appeared to have almost no effect on regression rate magnitude. Lee et al. surmised that the regression rate increase resulted from enhanced turbulence in the near-surface region due to the presence of the grooves and the resistance to axial flow [55].

Lee et al. also conducted additional experiments to examine the behavior of swirl GOX injection from two types of head-end swirl injectors both with and without helical grooves. Whereas both types of injectors were designed with the inlet holes tangential to the inside surface of the injector, and had a geometric swirl number of 5 as defined by Eq. (68), the inlet holes had different orientations with respect to the longitudinal axis of the motor. The first design, designated type I by Lee et al., employed inlet holes aligned tangential to the inner surface of the injector but perpendicular to the grain axis. The second injector (type II) was similar, but had inlet holes canted 30 deg in the downstream direction. Lee et al. found that this second design caused more uniform regression enhancement

than the first design, which resulted in only localized regression enhancement near the injector [55]. However, no correlations or regression rate profiles were provided.

Lee et al. also investigated the combined effects of flow rotation and spiral grooves on regression rate behavior. For this testing, 6- and 100-mm-pitch helical groove grains were used in conjunction with the type II swirl injector. The internal surface areas of the two grains were maintained to be the same. As explained by Lee et al., the motivation for the 100-mm-pitch grain is that it may induce flow rotation, but does not necessarily enhance turbulence in the near-wall region to any significant degree, thereby allowing the two effects to be evaluated independently by comparing the empirical results to the 6-mm-pitch grain. The results of the testing indicated that the 6-mm-pitch grain regressed slightly faster when no swirl was imposed on the oxidizer stream, but that the 100-mm-pitch grain displayed a slightly higher regression rate with a swirl oxidizer injector. These results imply that an optimum regression behavior for a given application may be obtained using a proper combination of grooves and swirl strength. However, note that according to the Lee et al. data [55] swirl oxidizer injection increased the regression rate by about a factor of two over the baseline axial flow case, whereas the use of the helical grooves had a much smaller effect on enhancing the regression rate when used independently of swirl injection. For a given application, the potential performance benefits of helically grooved fuel grains would need to be weighed against the increased complexity and cost associated with grain manufacture. In addition, although plastic fuels such as PMMA may be readily machined, it may not be practical to fabricate helical grooves in the higher regression rate rubbery fuels such as HTPB. However, it may be possible to use fuel additives to increase the fuel surface roughness in order to achieve similar results, as noted in Chapter 1.

3. Swirl-Injection End-Burning Hybrids

Haag et al. [57] also employed tangential oxidizer injection in an end-burning vortex hybrid configuration for a spacecraft maneuvering application. In the so-called vortex flow pancake (VFP) configuration, the swirl oxidizer injector was sandwiched between two fuel disks that end burn in opposite directions during combustion. The top disk regressed toward the motor face, whereas the lower disk regressed toward the nozzle backplate. The lower disk also had a central port to allow the combustion products to escape out the nozzle. Haag et al. tested PMMA fuel disks with hydrogen peroxide, nitrous oxide, and GOX. They examined the effects of oxidizer mass flow rate, injection velocity, number of injectors, chamber pressure, and initial fuel grain separation distance. The chamber diameter was not varied. The motor was 120 mm in diameter and 50 mm tall [57]. Haag et al. used the fuel mass flow rate as the performance metric of interest rather than the regression rate, making direct comparisons to other types of hybrid difficult.

As expected, the fuel mass flow rate was found to vary strongly with oxidizer mass flow rate. In addition, the oxidizer injection velocity had a very significant effect on fuel flow rate, prompting Haag et al. to note that this behavior provides additional leverage to optimize the design for a given application [57]. Though the authors did not provide a fundamental explanation for this result, it seems

apparent that higher injection velocities would decrease the end-wall boundary-layer thickness, in turn increasing shear stress and heat transfer across the fuel disk surface.

Haag et al. found that varying the initial separation distance between the fuel disks had no noticeable effect on fuel flow rate over the range tested (14–45 mm). In addition, chamber pressure was not found to have a significant effect, probably because the high convective heat fluxes associated with the swirling flowfield completely dominate any radiant heat transfer. Haag et al. also performed cold-flow experiments to show that swirl oxidizer injection did not impart significant residual torque to the motor [53]. Though the researchers did not provide a typical swirl number for their motor, they did note from C^* calculations that the throat size did not appear to be significantly affected by swirl flow. Anderson et al. [63] reached a similar conclusions for vortex chambers applied to liquid and gaseous rocket engine applications. The reason for this appears to be that, compared to the swirl injection velocity of the cold oxidizer, the axial velocity through the nozzle throat is quite high due to the acceleration of the hot combustion products to Mach 1 conditions. The resulting flow streamlines at the throat are, thus, aligned nearly parallel with the chamber axis, as in conventional rocket engines, with only a very small twist angle due to the angular momentum of the swirl injection [63].

Rice et al. [56] tested a similar configuration using GOX and HTPB for a planetary ascent vehicle application. Though their end-burning hybrid motor had only a single fuel disk located at the face plate, they designed conceptual chambers with two fuel disks arranged in a manner similar to that of Haag et al. [55]. They experimentally investigated the effects of chamber (fuel disk) inner diameter, oxidizer mass flux, oxidizer injection velocity, and separation distance between the initial fuel surface and swirl injector on regression rate behavior. Experimental results demonstrated that the regression rate was sensitive to both injection velocity and separation distance, but not chamber diameter over the range tested (4–8 in.) [56].

Rice et al. initially tested a 4-in. inner diameter end-burning hybrid to obtain a baseline regression rate law for GOX and HTPB. This laboratory-scale motor, designated as the vortex end-burning hybrid (VEBH) by Rice et al., operated at a chamber pressure of about 50–60 psia with GOX flow rates of about 19–36 g/s. The resulting oxidizer mass fluxes based on the chamber diameter were quite small, on the order of 2–4 $\mathrm{kg/m^2 \cdot s}$. Based on the results of about a dozen firings, Rice et al. developed the following empirical regression rate correlation [56]:

$$r = 0.40\, G_o^{0.62} \tag{69}$$

with r in mm/s and G_o in $\mathrm{kg/m^2 \cdot s}$. In comparison to conventional hybrid HTPB/GOX correlations, such as

$$r = 0.03\, G_o^{0.68} \tag{70}$$

given by Sutton [64], the Rice et al. VEBH motor appears to have regression rates more than an order of magnitude greater than those of conventional hybrid motors operating under similar conditions, presumably due very strong boundary-layer gradients across the fuel surface that result from the strong swirl injection. However, because conventional hybrids typically operate at much higher mass

fluxes than the range over which Eq. (69) was derived, it is difficult to make direct comparisons because large extrapolations of regression rate laws, such as that given by Eq. (70), to lower mass flux regimes would be required. Equation (70) was developed for a small-scale classical hybrid burning GOX and HTPB over an oxidizer mass flux range of about 35–280 $\mathrm{kg/m^2 \cdot s}$, which is far higher than that for Eq. (69). However, when Eqs. (69) and (70) are compared over the limited range of conditions Rice et al. tested, it can be said that to produce the same regression rate in a classical hybrid as in the end-burning hybrid G_o must be on the order of 30–40 greater in the classical hybrid given the classical definition of mass flux (which may have little meaning for this particular geometry). As Haag et al. also noted, this result implies that the vortex end-burning hybrid may provide a great deal of design flexibility, especially for applications where short length-to-diameter motors are desirable, such as for upper-stage propulsion systems. The ability to achieve classical-hybrid-like regression rates in an alternate geometry for packaging optimization may be the most beneficial aspect of end-burning hybrids because is not clear at present how the regression rate would behave at the much higher oxidizer mass flux levels typical of classical hybrids. Like the swirl and vortex hybrids discussed earlier, the oxidizer injection method in the swirl end-burner hybrid configuration appears to cause local mass fluxes in the near-surface region that are effectively much higher than indicated by the standard definition of G, where G is the port mass flow rate normalized by the port cross-sectional area. Therefore, regression rates are much higher than those that would be expected from classical hybrids at the same flux condition. This behavior implies that an alternate definition of G for swirl-flow hybrids may be useful in developing theoretical and empirical correlations of the regression rate behavior.

Figure 25 is a photograph of one of the Rice et al. recovered fuel disks [56]. Note the swirl pattern evident on the fuel surface. Rice et al. found that a region of very high regression rates existed near the center of the fuel disks such that the recovered fuel samples were bowl-shaped about the chamber axis. In addition, an intermediate zone of apparent counter-rotation was evident from the recovered fuel disks. The researchers postulated that this patterning actually resulted from a corotating, but radial *outflow* zone of toroidal recirculation about the chamber axis, as illustrated in the qualitative streamline plot shown in the lower portion of Fig. 25. Though they considered nonreacting situations, Georgantas et al. [65] have found that such recirculation zones are likely to exist in confined swirling flows when the swirl strength exceeds a threshold value of about 0.6, where the swirl strength is defined as

$$Sw = \frac{\dot{m}_{\mathrm{sw}} V_{\mathrm{inj}} R_c}{\dot{m}_{\mathrm{tot}} V^* R^*} = \frac{\text{input} \cdot \text{angular} \cdot \text{momentum}}{\text{exit} \cdot \text{linear} \cdot \text{momentum} \times \text{exit} \cdot \text{radius}} \tag{71}$$

In Eq. (71) $\dot{m}_{\mathrm{sw}}$ represents the oxidizer flow rate through the swirl injector, $\dot{m}_{\mathrm{tot}}$ is the total flow rate (oxidizer plus fuel) exiting the nozzle, V_{inj} the swirl oxidizer injection velocity, V^* the sonic velocity at the throat, R_c the chamber radius (assumed to be equal to the injector radius) and R^* the throat radius.

Based on the operating conditions and chamber geometry, the Sw for the Rice et al. tests correspond to an approximate range of 0.7–1.2, so that recirculation seems likely. Note the similarity between this phenomena and that suggested by

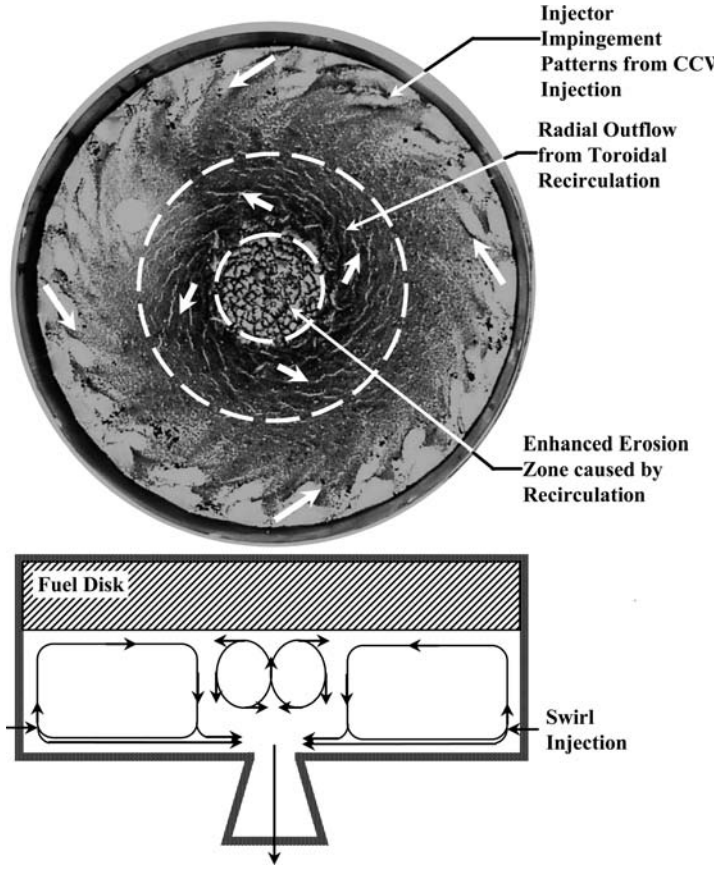

Fig. 25 Recovered 8-in. fuel disk (from outer to inner radius): counter clockwise (CCW) swirl with radial inflow, CCW swirl with radial outflow, and toroidal recirculation zone. Note that inner vortex appears to swirl in a clockwise (CW) direction, but that this sculpting actually indicates a CCW swirl with radial outflow.

Pucci in his study of swirl-stabilized flows in classical hybrid motors discussed earlier [45]. The recovered fuel disk profile in Fig. 25 further suggests that, to reduce fuel residuals and to obtain good volumetric loading, the optimum fuel shape for this type of motor may be a domed or hemispherical grain. However, such a configuration may have a variable fuel surface area through the burn so that a mixture ratio shift would be anticipated. In addition, it should be kept in mind that use of a lower fuel disk, as in the Haag et al. geometry, may affect the behavior of the recirculation zone.

Rice et al. also performed a parametric investigation of the VEBH regression rate behavior as affected by the chamber inner diameter (which is identical to the fuel disk diameter), the injection velocity, and the initial spacing between the swirl injectors and the fuel disk surface area [56]. For each diameter size tested (4 to

8 in.), the G_o level and target chamber pressure were held constant at 1.3 $kg/m^2 \cdot s$ and 10 atm, respectively, by controlling both the GOX mass flow rate into the chamber and the exit nozzle throat diameter. This particular value of G_o was chosen based on the flow-rate limitations of the test facility limitations. A total of 18 test conditions were examined. Similar to the Haag et al. results [57], Rice et al. found that the injection velocity had a significant influence on the regression rates. However, in contrast to the Haag et al. findings, Rice et al. also showed that the initial separation distance had a significant effect on regression rate. In fact, statistical analysis showed that, for the conditions tested, the regression rates were about two times more sensitive to the separation distance than to the injection velocity. The contrast between these two results may lie in the different motor geometries: The Haag et al. motor employed upper and lower fuel disks, whereas the Rice et al. motor used a single fuel disk attached to the face plate. Interestingly, Rice et al. found that the chamber diameter itself did not affect the regression rate significantly, suggesting that the vortex end-burning hybrid may scale predictably with respect to chamber size [56]. As already noted, Haag et al. also reached this conclusion from their experiments. However, additional work in this area is needed before further conclusions about scaling effects can be confidently made. In addition, future vortex end-burning hybrid investigations would benefit from a theoretical or semi-empirical analysis of the convective heating characteristics of end-wall boundary layers in swirl chambers, such as that given by Volchkov et al. [66].

4. Radial-Injection End-Burning Hybrids

With the objective of reducing fuel grain complexity and improving volumetric efficiency, Caravella et al. tested a unique radial-flow hybrid motor, which used PE fuel and hydrogen peroxide [58]. They identified several radial-flow hybrid concepts, as shown in Fig. 1 of [58], but reported experimental results only on their center-injection/annular nozzle configuration. In this configuration, the oxidizer was injected through a central port in the top fuel disk, impinged on the lower disk, and flowed outward between the gap between the two disks, exiting the motor through a series of nozzles located at equal intervals around the periphery of the lower fuel disk. This arrangement provided an approximation of an annular nozzle that would be used in practical applications. Note that the Caravella et al. alternative annular-flow/conventional nozzle configuration, wherein oxidizer flows from an annular injector into the gap between the two fuel disks and then out through a nozzle situated below a central port in the lower disk, is very similar to the end-burning hybrids tested by Haag et al. and Rice et al. except for the specific injection method. Both designs are end-burning configurations wherein the normal direction of the regressing fuel surfaces is oriented parallel to the thrust axis.

Caravella et al. tested a laboratory-scale device that had a fuel disk diameter of approximately 6 in. and operated at chamber pressures of 118–238 psia. Their test apparatus precluded measurement of the motor thrust; however, combustion efficiencies calculated using standard methods ranged from 83 to 95% [58]. Regression rates were measured across the top and bottom fuel disks at various radial and circumferential stations using a digital caliper. The hydrogen peroxide was decomposed in a catalyst bed and flowed into the chamber through a central port

in the upper fuel disk, then impinged on the lower fuel disk. Tests were conducted to determine the effects of initial fuel port and grain geometry, mass flux, and chamber pressure. The initial spacing between the disks ranged from 0.2 to 0.4 in., and the oxidizer mass flux ranged from 23 to 67 $\mathrm{kg/m^2 \cdot s}$. Test times were on the order of 5–13 s. Chamber pressure oscillations were on the order of $\pm 5\%$ P_c. The researchers noted that the radial regression rate profiles across the upper fuel disk were more uniform than the corresponding lower disk profiles, presumably due to stagnation point heat transfer near the edge of the impinging oxidizer jet. In general, higher regression rates were measured for the lower disk. Additionally, the researchers noted that regression rates showed a much weaker dependence on radial location than would be expected from classical aG^n behavior, which for this geometry predicts a decrease in regression rate moving outward toward the disk periphery due to the increase in flow area at larger radii. In fact, some of the testing indicated increasing regression rates with respect to increasing radial location. The authors also note that the average regression rates were significantly larger by about a factor of three than those measured by Wernimont and Heister in classical hybrids using the same fuel/oxidizer combination [67] at the same conditions. (See Chapter 11 of this text for additional details.) According to Caravella et al. [58], this behavior suggests that the flow in the channel is strongly influenced by three-dimensional flow structures that arise due to the unique injection method. The authors further note that Prata et al. [68] predicted streamline patterns in a similar geometry and found a region of separated flow and associated recirculation zone attached to the corner of the upper plate. Though the hybrid rocket situation differs due to Reynolds number, fuel addition, and time-varying surface geometry effects, this type of flow structure, along with the radial variation of heat transfer associated with jet flow impinging on a surface, may be responsible for the regression rate behavior noted in the radial flow hybrid. As already noted, several other researchers, such as Carmicino and Sorge [44], have encountered unusual regression rate behavior in the presence of recirculation zones and entrance effects.

The authors did not find any significant regression rate dependence on the initial disk spacing, and their attempt to investigate pressure effects by isolating the effect of chamber pressure from mass flux proved inconclusive [58].

Caravella et al. fit the average regression rate data to the average total mass flux for both the upper and lower disks using a correlation of the form $r = aG^n$, where $a = 0.092$ and $n = 0.57$ for the lower disk and $a = 0.10$ and $n = 0.70$ for the upper disk. For a G value of 0.1 $\mathrm{lb_m/in.^2 \cdot s}$, representing the approximate upper limit of the mass flux range tested, these correlations predict that the lower disk regressed about 25% faster than the upper disk, whereas at the lower end of the mass flux range represented by 0.04 $\mathrm{lb_m/in.^2 \cdot s}$, the lower disk regressed about 40% faster. These significant differences are presumably due to the unusual oxidizer injection technique and the attendant flow structure that prevails between the fuel disks.

5. *Axial-Injection End-Burning Hybrids*

Nagata et al. introduced two types of end-burning hybrids that employed axial oxidizer injection [59, 60, 69]. In the so-called "dry-towel" configuration, the oxidizer is injected through a cluster of thin fuel tubes. The oxidizer passes through the tube cluster without burning, exits the downstream end of the tubes, then

participates in diffusion-flame combustion on the downstream face of the fuel tube cluster. The fuel tube cluster end burns and regresses from the downstream toward the upstream face. As with other types of end-burning hybrids, the dry-towel configuration has the advantage of nearly constant burning surface area and, therefore, fixed mixture ratio.

Nagata et al. initially tested the combustion characteristics of a single polyethylene tube, either 2-mm i.d. and 4-mm o.d. or 0.5-mm i.d. and 3.1-mm o.d., burning with GOX over a range of GOX velocities from about 8 to 80 m/s and a range of ambient pressures [59]. Regression rates ranged from about 0.5 to 10 mm/s, a very high value for hybrids. Interestingly, the GOX velocity through the tube (in meters per second, not to be confused with the mass flux) had little effect on the regression rate, although in some cases the regression rates appeared to decrease slightly with increasing velocity, possibly due to increasing the flame standoff distance from the end of the tube. However, the regression rates showed a strong dependence on ambient pressure and increased significantly at elevated pressures. Nagata et al. later tested alternate hydrocarbon fuels [60] and developed solid-propellant like regression rate correlations of the form $r = ap^n$. Interestingly, the regression rates showed no significant dependence on GOX flow rate for these cases. As noted by Nagata et al., these results imply that the diffusion flame forms immediately above the fuel surface, as in a heterogeneous solid propellant such as AP/HPTB.

Nagata et al. also identified a range of oxygen flow velocities over which the dry-towel configuration would burn on the downstream face of the tube. The high end of this range was bound by what Nagata et al. call the "upper critical velocity" and corresponds to the blowoff limit. Beyond this velocity, the diffusion flame is not established. Below the corresponding lower critical velocity, the flame flows back upstream into the fuel tube and burns like a classical hybrid. The value of these critical oxygen velocities depend on the ambient pressure, with higher pressures allowing for both higher upper and lower critical velocities (see Fig. 5 of [60]). As noted by Nagata et al., the upper critical velocity is probably also highly dependent on the tube geometry and whether a single or cluster of tubes is used. Furthermore, at higher pressures, they suggest that it may be possible to prevent flashback into the fuel tubes by reducing the port diameters so that they are smaller than the thickness of the diffusion flame, which become thinner as pressure increases [60]. Although this configuration displayed high regression rates during the single-tube tests presented by Nagata et al. [59, 60], it is not yet clear how the concept can be scaled to large clusters for practical thrust ranges.

Note that the desired operating range of the Nagata et al. dry-towel fuel grain, that is, burning on the rearward face rather than in the port itself, may be related to the classical hybrid motor phenomena of flooding, discussed at the beginning of this chapter. Flooding corresponds to a situation wherein the oxidizer flux is high enough to prevent burning in the fuel port, or is increased to the point where the flame is extinguished, presumably due to finite reaction rates that can not keep pace with fluid dynamic mixing rates at very high flux levels or to the development of very oxidizer-rich conditions in the fuel port. For the Nagata et al. dry-towel concept, it appears that the oxidizer flow along the fuel tubes must be high enough to prevent burning within the fuel ports.

Nagata et al. also developed a second type of axial flow end-burning hybrid that consisted of a series of stacked, cylindrical blocks confined in a motor case

with a small space between each block [69]. Each block had several fuel ports to allow for combustion gas to pass into the next block in the downstream direction, although the fuel ports of consecutive blocks were deliberately not aligned. In this configuration, the fuel regresses on both the block faces and in the fuel ports. Nagata et al. tested PMMA fuel with GOX and found that the fuel faces regressed about twice as fast as the ports and that combustion efficiency was about 90%. They also state that this particular type of hybrid may provide for short L/D motors. However, it appears from the descriptions given by Nagata et al. [69] that this configuration may be subject to large fuel slivers and open volumes that reduce the overall volumetric efficiency of the fuel grain.

B. Motors with High Regression Rate Solid Fuels

Here we review approaches to enhancing regression rate via unique fuel formulations, including cryogenic solid fuels, paraffin fuels, and metal additives.

1. Cryogenic Solid Fuels

During the early 1990s, several research groups began investigating the regression rate and combustion characteristics of hybrid motors that employed cryogenic solid fuels such as solid ethylene and solid methane. The initial motivation for these studies was to develop a method to stabilize and combust high-energy density matter (HEDM), such as solid hydrogen (not to be confused with metallic hydrogen) at 4 K seeded with 8% atomic hydrogen [70]. At the U.S. Air Force Phillips Laboratory (now U.S. Air Force Research Laboratory) Carrick and Larson developed a laboratory demonstration burner for testing solid ethylene and solid pentane with GOX to demonstrate the feasibility of this approach. As discussed by Carrick and Larson [70], they examined several methods to prepare solid-cryogenic-fuel tubes using liquid nitrogen as a refrigerant. Hot-fire testing demonstrated that solid pentane and solid ethylene regressed about 3 and 10 times faster than PMMA, respectively, all other conditions being equal. Later, DeRose et al. [71], working in the same laboratory, experimented with eight additional cryogenic solid hydrocarbons, including quadracyclane, RP-1, acetone, and isopropyl alcohol. The regression rates for the cryogenic fuels investigated ranged from 2 to 10 times faster than HTPB operating at the same conditions [71]. Though thrust was not measured directly, the specific impulse efficiency was estimated at about 92–94% for the solid pentane experiments after correcting for heat loss to the chamber surfaces. The authors did not provide a comprehensive theory or explanation for the relatively high regression rates, but indicated that the energy required to gasify a unit mass of fuel is much smaller for cryogenic solids than conventional solid fuels by about a factor of 10–20. Based on this, Carrick and Larson estimated a thermodynamic blowing parameter of about 85 for ethylene [70].

By assuming a liquid–vapor equilibrium at the vaporizing fuel surface, Carrick and Larson estimated the fuel surface temperature using the Clausius–Clapeyron equation and calculated, for example, that the fuel surface temperature for ethylene in their experiments was about 114–117 K, depending on oxidizer mass flux, and corresponding values of pentane were about 202–206 K. Based on the significant differences in regression rates (inferred from chamber pressure measurements) at

these deduced fuel temperatures, they concluded that the cryogenic fuel regression rates were very sensitive to surface temperature [70].

Motivated to achieve fast regression rates in combination with high specific impulse propellants, as well as the by the HEDM objective noted earlier, Rice et al. [72], St. Clair et al. [73], and Gramer and Rice [74] conducted similar research at Orbital Technologies Corporation (ORBITEC), but on different fuels in a larger motor. They noted an additional benefit of cryogenic solid fuels in that they tend to have higher mass density than their liquid counterparts, for example, solid CO has a density about 20% larger than liquid CO and solid methane is about 15% more dense than liquid methane [72]. The ORBITEC group conducted several projects into the early 2000s and tested a large number of cryogenic solid fuels. With use of a reverse hybrid configuration, solid oxygen (SOX) was also investigated in combination with gaseous hydrogen for a high-energy upper-stage/in-space propulsion application [73]. Figure 26a shows the conceptual approach for their cryogenic solid hybrid test engines and Fig. 26b a photograph of the experimental apparatus that was used during the 1990s and early 2000s. The combustion chamber was encased in a vacuum chamber to reduce heat transfer from the environment. A refrigerant [liquid helium (LHe) or liquid nitrogen (LN_2)] filled the cooling jacket surrounding the combustion chamber. The fuel gas (or oxygen gas), admitted to the combustion chamber at a pressure below its triple-point pressure, sublimated on the cold inner wall of the chamber, forming a tube of solid fuel. During firing operations, the gaseous component of the propellant combination was injected at the head end of the grain and the igniter torch activated. Because the fuel grains could not be physically examined or weighed before and after testing, an alternate method was employed to determine regression rates. A camera was used to make visual observations of the fuel grain during the freezing process to estimate the initial fuel port diameter. The flow rate of the gaseous fuel entering the chamber during the freezing process was also measured and integrated to determine the fuel grain weight, and the burn time was determined from engine pressure traces to yield the regression rate.

Early feasibility and engine checkout testing was conducted with cryogenically frozen paraffin wax and kerosene using LN_2 refrigerant in a prototype version of the chamber shown in Fig. 26 [74]. A portion of this testing focused on how the regression rate of paraffin fuel was affected by the type of aluminum loaded into the grain (powder, foam, wool, and platelets) and the amount of aluminum loading with a selected type of aluminum (powder). Loadings of up to 40% by weight were successfully ignited and burned.

A significant amount of testing was then conducted using solid methane and aluminized solid methane burning with GOX. In addition to the effects of GOX flux, the dependency of the regression rate on fuel grain size, oxidizer injector geometry, and initial fuel grain temperature (by freezing with LHe vs freezing with LN_2) was investigated. Aluminized solid methane was formulated by loading tubes of aluminum wool or foam into the combustion chamber, then freezing the methane from the vapor state into the aluminum matrix. Hot-fire testing demonstrated very high regression rates on the order of 10–20 times faster than HTPB under similar conditions. Empirical correlations indicated a power on G_o of about 0.8. In addition, the authors stated that lower initial grain temperature (where freezing with LHe rather than LN_2 produced methane at 10 K instead of 80 K) caused

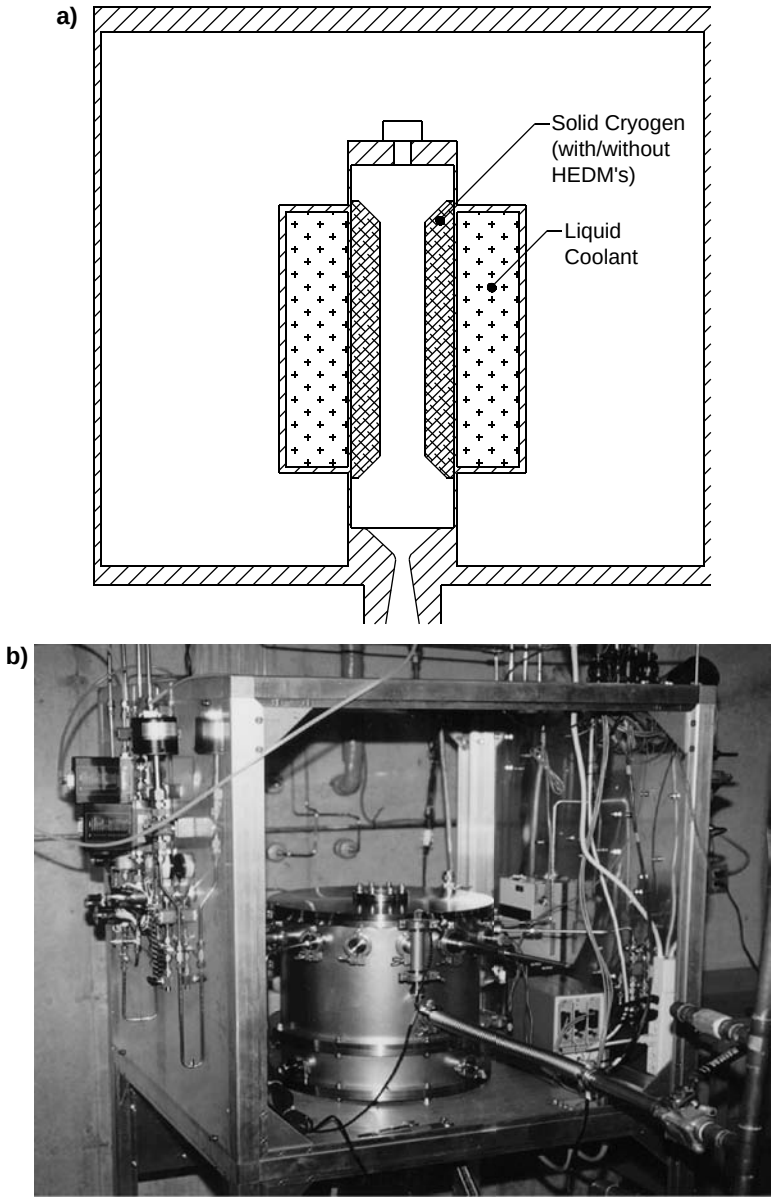

Fig. 26 ORBITEC's cryogenic solid hybrid a) conceptual schematic and b) hybrid motor hardware in vacuum chamber.

reductions in regression rates, as did higher percentages of aluminum in the fuel grain [74]. Both of these conditions imply that the cryogenic fuels with higher effective heats of vaporization regressed more slowly. Freezing temperature and aluminum loading were both suggested as a means of controlling mixture ratio.

Combustion efficiencies of up to 95% were obtained with aluminum loadings of 15% by weight of the total grain [74].

A reverse hybrid configuration using SOX grains and gaseous hydrogen (GH_2) as the injectant was also tested to pave the way for formulating high-energy cryogenic oxidizer grains consisting of ozone embedded in a matrix of solid oxygen. Though this type of oxidizer was never implemented, a significant amount of testing was conducted with SOX/GH_2. In general, solid methane burning with GOX was found to exhibit more predictable and steadier burning behavior than did SOX with GH_2 [73].

Rice et al. later investigated the regression rate behavior of solid carbon monoxide (SCO) burning with GOX for a Mars indigenous propellant production application [72]. An analysis of the SCO regression rates indicated an empirical mass flux power of 0.38, which, for circular port fuel grains, corresponds to a progressive burn wherein the overall fuel production rate increases with burn time [72]. This behavior was consistent with the measured chamber pressures, which increased with time during the main stage portion of the test. However, it is not clear what type of phenomena was responsible for this weak dependency on G_o and only a few tests were conducted during the program.

Most of the ORBITEC cryogenic solid hybrid tests were conducted at a relatively low mass flux range of less than 20 $kg/m^2 \cdot s$. However, even at this level, the methane testing indicated that regression rates of nearly 8 mm/s were achieved. In addition, the testing demonstrated that the cryogenic fuels can operate at very low mass flux regimes, where classical hydrocarbon fuels would most likely only melt and soften, though the usefulness of this trait is not immediately evident. The range of applications of this technology would appear to be most suited to in-space propulsion systems because the solid grain and the liquid component must be maintained in a manner similar to that of cryogenic liquid bi-propellants. It is also important to recognize that, although the cryogenic solid hybrid concept appears to offer the high performance of liquid bipropellant engines (depending on the specific propellant choice) with the safety and operational advantages of classical hybrids, these desirable traits must be balanced against the potential complications of cryogenic solid storage. In addition, it is not readily apparent how to scale the grain formation process to larger sizes.

2. Paraffin Solid Fuels

The cryogenic solid fuel investigations discussed above did not present a model or theory to explain the governing physics underlying the fast regression rates of these cryogens. However, Karabeyoglu later developed his regression rate theory for liquefying solid fuels to explain the cryogenic solid-fuel behavior and the behavior of some paraffin fuels. For completeness, we briefly review this theory next. For additional details, the interested reader is referred to the Karabeyoglu et al. thorough treatment of this subject [5–7, 75].

According to Karabeyoglu et al. the very high regression rates of cryogenic solid fuels and SOX cannot be explained simply by their characteristically low heats of vaporization [5]. Recall that in the Marxman et al. classical regression rate expression [9] the heat of vaporization appears in the blowing parameter B raised to a power 0.32 [see Eq. (13b)]. Thus, reducing the effective heat of

vaporization would only cause a modest increase in the regression rate (30–50%) over conventional systems rather than the observed increases of 300–400% or more. An alternative mechanism must, therefore, be responsible for the very high regression rates observed during cryogenic solid-propellant firings.

In addition to the classical gasification process, Karabeyoglu postulated a mass transfer mechanism involving the entrainment of liquid droplets from the surface melt layer (Karabeyoglu et al. [5] and Karabeyoglu and Cantwell [6]). As Karabeyoglu demonstrated, droplet formation is due to liquid-layer instabilities, which result from the high-velocity gas flow in the port. Figure 27 shows a schematic of the entrainment model. Because of the complex nature of the problem, the modeling was performed in three stages. Initially, the requirements for the formation of a melt layer on the fuel grain were investigated. In the second stage, the linear stability of a thin melt layer under the strong shear of a gas flow was considered. Later, the linear stability results were linked to the entrainment of liquid droplets with use of some experimental results and some semi-empirical relations developed in the nuclear engineering and film cooling literature. In the final stage, Karabeyoglu extended classical theory to the case of liquid-droplet entrainment. Karabeyoglu showed that the formation of the liquid-layer instabilities and entrainment of liquid droplets required three major modifications in the classical hybrid combustion theory:

1) The effective heat of gasification is reduced because the evaporation energy required for the fuel mass transfer from the surface is partly avoided by the mechanical entrainment of the liquid. The enthalpy difference between the flame and the surface is also reduced because some of the reactants are now in the liquid phase. Karabeyoglu estimated that the reduction in the effective heat of gasification is more dominant than the change in the enthalpy difference.

2) The blocking factor St/St_o that modifies the convective heat flux to the surface is also altered due to the presence of the two-phase flow. As a first approximation, the effect of liquid droplets on the momentum and energy transfer can be

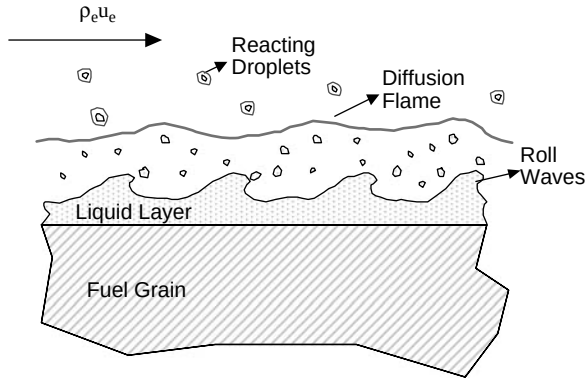

Fig. 27 Karabeyoglu's schematic of entrainment process in hybrid rocket combustion.

ignored. Under this assumption, the blocking factor can be expressed as a function of an evaporation blowing parameter,

$$St/St_o = f(B_g) \tag{72}$$

The evaporation blowing parameter B_g includes only the gas-phase mass transfer from the fuel surface and not the liquid droplets. One can also assume that evaporation of the droplets released from the liquid surface into the gas stream does not take place beneath the flame sheet. This assumption is consistent with the standard flame sheet approximation. Moreover, it is a reasonable approximation for typical hybrid operating conditions that are characterized by high blowing rates and, thus, low residence time of droplets between the liquid surface and the diffusion flame.

3) The ripples formed on the liquid-layer surface increase the surface roughness and the heat transfer from the flame front to the surface, similar to Lee's helical grooves [55]. Karabeyoglu predicted this effect had a smaller influence on the total regression rate compared to the first two factors.

In general, the total regression rate of a hybrid motor can then be written as a sum of the evaporation regression rate that is generated by the vaporization of the liquid into the gas stream (or first thermal decomposition and later volatilization into the gas stream in the case of supercritical operation) and the entrainment regression rate, which is related to the fuel mass mechanically extracted from the liquid surface.

Karabeyoglu used his liquid-layer hybrid combustion theory to formulate various non-cryogenic paraffin-based fuels that have demonstrated burn rates several times faster than HTPB at the same operating conditions. A specific formulation, SP-1a, with the baseline paraffin wax FR 5560 (melting temperature of approximately 70°C) was tested extensively with various oxidizers, that is, GOX, LOX, and N_2O, in several different facilities, using motors up to 6000 lb_f of nominal thrust [7]. The regression rates established from the motor test data for the paraffin-based formulations confirmed the improvement factors of 2.5–3.5 as predicted by the theory.

The liquid layer combustion theory was refined and expanded by Karabeyoglu et al. [75] to include the case of supercritical conditions under which most of the paraffin-based fuel systems operate. To test its accuracy, the enhanced model was applied to predict the regression rates for the entire homologous series of normal alkanes (a group of fully saturated, straight-chain hydrocarbons with the chemical formula C_nH_{2n+2}). Each member of the series is identified by the carbon number n, which ranges from 1 (methane) all of the way up to high-density PE (HDPE) polymer with carbon numbers in the range of tens of thousands. A large fraction of the fast-burning liquefying hybrid fuels tested to date are either pure normal alkanes such as pentane or mixtures of *n*-alkanes such as paraffin waxes. HDPE polymer is also commonly used as a hybrid fuel. In general, good agreement between the theory and the test results over a wide range of carbon numbers was found. The results of the liquid-layer theory show that, for most applications, the paraffin waxes have the best properties as hybrid rocket fuels among the series of *n*-alkanes due to their fast regression rates at relatively high melting temperatures.

The theory can also be applied to the other candidate liquefying materials (or other homologous series such as normal alcohols or normal acids) to establish their burn rate capability.

3. *Metal Additives*

Effects of solid-fuel additives have already been discussed briefly in Sec. III.G. Risha et al. investigated the effects of various metal powders on the regression rate characteristics of HTPB-based solid fuels [48]. They conducted a large number of tests in a laboratory-scale classical motor to examine the influence of 10 different solid-fuel formulations, including 3 types of nanoaluminum particles, both coated (with a fluorine-containing material) and uncoated aluminum flakes, boron particles, and boron carbide particles. Most of the fuel formulations consisted of 13% by weight metal additive and 87% by weight HTPB. As discussed by Risha et al. [48], a few of the metal additives had a 6.5% by weight concentration. In Chapter 10, these results are discussed in detail, and only the main results will be presented here for completeness.

First, the different types of nanoaluminum powders produced significantly different results depending on their respective active aluminum content. Not surprisingly, the powder with the highest active aluminum content (84.8% by weight) produced the largest increase in mass burning rate $\rho_f r$ of 62% with respect to neat HTPB. This formulation had an estimated C^*_{eff} of 88–92%. The fuel formulation containing boron and the fuel formulation containing the coated aluminum flakes also provided significant mass burning rate increases of about 42%, but only slight increases in linear regression rate. The uncoated aluminum flakes produced only about one-half the mass burning rate enhancement as the coated flakes. The authors attribute this to enhanced aluminum ignition and combustion caused by the fluorine and fluorinated compounds produced from the dissociation of the aluminum coating. These formulations had lower calculated C^*_{eff} of about 75–83%.

The metallized fuel regression rates may have been influenced by a reduced blocking effect due to the ejection of metal particulates, an increased blowing parameter due to a reduction of the effective enthalpy of vaporization from that of the binder (pure HTPB), and an increase in flame temperature due to metal burning, and radiant heat flux from metal combustion products. These various influences would need to be evaluated to obtain a more thorough understanding of the effects of metal and nano-metal additives on solid-fuel regression rates. It should also be noted that Evans et al. [76] have recently investigated fuel formulations consisting of paraffin and nano aluminum. These tests produced very high solid fuel regression rates up to 7 mm/s in a classical hybrid configuration.

Figure 28 shows a comparison of the regression rate vs G_o trends of some of the nonclassical concepts discussed earlier and Table 6 is a summary of the correlations. Several correlations for conventional fuels of HTPB and HDPE in classical motors are also shown for comparison. In general, the nonclassical concepts show significantly higher regression rates at similar operating conditions, which could provide future benefits for hybrid motor volumetric loading, design flexibility, operation, and overall performance. However, in most cases, much additional testing and detailed analysis must be conducted to explore fully the potential range of operating conditions before practical designs can be developed for specific

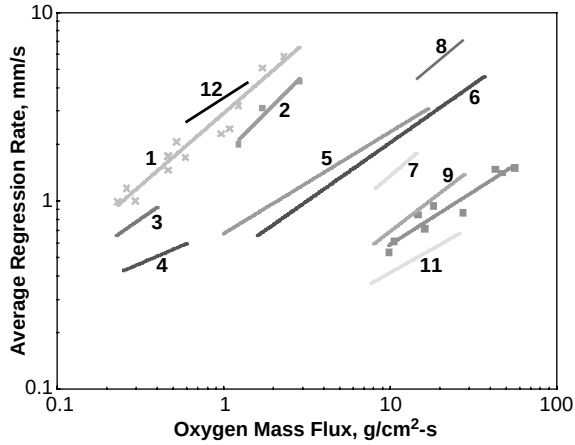

Fig. 28 Empirical $r = aG_o^n$ correlations for selected classical and non-classical hybrid motors and fuels.

Table 6 Summary of empirical $r = aG_o^n$ correlations for various nonclassical hybrids

System	Solid fuel	Motor type	a	n	Ref.
1	Methane	Classical	2.91	0.77	74
2	85% Methane + 15% Al	Classical	1.75	0.89	74
3	HTPB	Swirl End-Burner	1.62	0.61	56
4	Solid CO	Classical	0.72	0.38	72
5	HTPB	Vortex	0.67	0.54	53
6	FR5560 Paraffin	Classical	0.49	0.62	7
7	87% HTPB + 13% nano Al	Classical	0.24	0.76	48
8	87% FR5560 Paraffin + 13% nano Al	Classical	0.60	0.73	76
9	HTPB	Classical	0.14	0.68	64
10	40% HTPB + 60% Escorez	Classical	0.16	0.56	41
11	HDPE	Classical	0.13	0.50	77
12	"Fuel A"	Vortex	3.51	0.59	—

applications. For example, it would be highly beneficial to test approaches such as the swirl and vortex hybrids and paraffin fuels to higher mass fluxes to probe for threshold levels where kinetic effects potentially become important, or flooding limits are reached, to determine maximum regression rate levels compared to classical motors. In addition, any of the concepts employing swirl oxidizer injection discussed in Secs. IV.A.1–IV.A.3 must adequately address the effects of swirl flow on reducing the effective nozzle throat area, on thrust losses due to non-axial flow out the nozzle exit, and on residual toque acting on the motor before practical operation can be realized. High regression rate concepts that use single-port fuel grains for improved volumetric efficiency will undergo large changes in fuel port geometry over the course of the burn, so that regression rate correlations must cover a broad range of operating conditions. Advanced hybrid fuels must be able to meet

mechanical and thermal property requirements for given applications to ensure adequate grain strength and integrity. In addition, the nonclassical motors and fuels discussed here must also be able to produce high specific impulse efficiency for their advantages to be fully realized.

V. Summary

The main purpose of this chapter has been to provide a review and comparison of some of the more significant models that have been developed to explain various phenomena that can affect solid-fuel regression rates in hybrid motors so that the rocket designer, industrial engineer, or academic researcher can further the development of these promising propulsion systems. Toward this end, the interested reader is strongly encouraged to consult the sources referenced, as well as additional hybrid rocket literature, as this chapter is by no means exhaustive and no attempt has been made to capture all of the interesting subtleties of the particular works.

We have reviewed a number of approaches to regression rate analysis in classical hybrids, including diffusion- or flux-limited theory, effects of radiation from gas-phase combustion products and potential soot, effects of both gas-phase and heterogeneous reaction kinetics, and effects of variable fluid and transport properties across the turbulent, chemically reacting boundary layer. The influence of different oxidizer injector designs on classical hybrid regression rate behavior and combustion instability was also briefly reviewed. Scaling analyses for classical motors have been introduced and are discussed further by Gany in Chapter 12.

Several nonclassical hybrid configurations, including swirl-injected hybrids, vortex hybrids, and various types of end-burning hybrids were described. In addition, high regression rate hybrid fuels, such as paraffins and cryogenic solid fuels have been discussed. In Chapter 10, a more detailed discussion of hybrid rocket fuels is presented.

With regard to classical hybrids, diffusion-limited regression rate theory has in general been quite successful in explaining regression rate behavior, particularly for more modern hydrocarbon fuels, such as HTPB and HTPB-based fules, that typically have not shown much sensitivity to chemical kinetics. However, the potential effects of radiation from soot and the effects of variable properties across the boundary layer should be kept in mind when making detailed analyses of empirical data, for developing regression rate correlations, and for advanced theoretical treatments. Radiation from gas-phase reaction products such as CO_2, H_2O, and CO do not appear to contribute significantly to the total heat flux incident on the fuel surface, at least under practical operating conditions.

Future research on classical hybrid regression rate behavior would benefit from 1) theoretical and semi-empirical investigations of the effects of radiation for highly metallized fuels; 2) additional measurements and analysis of radiation effects for nonmetallized fuels; 3) development of detailed chemical kinetic models to understand the dependence of the gas-phase reaction rates and potential heterogeneous reaction rates on chamber pressure and fuel/oxidizer combination ratio to determine threshold operating conditions where kinetic processes become rate limiting, or at least important; 4) additional analysis of the role of

pyrolyzed-species molecular weight on the blowing effect to potentially understand the differences in regression rate characteristics among various hydrocarbon fuels; 5) further investigations to elucidate scaling, port geometry, and injector effects; and 6) more investigations that combine detailed regression rate and combustion property measurements with companion numerical simulations to obtain a broader understanding of the complete injection/regression rate/combustion process in hybrid motors.

The nonclassical hybrid configurations and alternate fuels discussed in this chapter show potential for improving overall performance for a range of applications by providing either higher solid-fuel regression rates or greater design flexibility than classical hybrids. However, except for the paraffin-based fuels and, to a lesser extent, the vortex and swirl hybrids, most of these concepts have not been thoroughly investigated or tested beyond the laboratory scale. Theoretical treatments of these concepts have tended toward engineering-type analysis to explain empirical data. The development and maturation of these motor configurations would benefit from larger scale development and testing, numerical simulations, and fundamental analytic approaches similar to those employed during the early days of classical hybrid motor research.

As noted at the beginning of this chapter, hybrid rockets have not yet enjoyed the widespread popularity of liquid bi-propellant engines or solid rocket motors. However, it is clear that hybrids have been investigated by a large number of excellent researchers, scientists, and engineers over the decades since the 1950s. And, as evidenced by the historic flight to Space Ship One, hybrids have definitely moved beyond the laboratory curiosity stage into the full-scale development arena. While hybrid propulsion systems will continue to benefit from additional research, the same can be said of almost all areas of chemical rocket propulsion. However, it can no longer be said that one of the disadvantages of hybrid motors is a lack of sufficient technology base. Hybrid rockets are a true contender for safe, high-performance 21st century propulsion systems.

Appendix

The energy flux, species mass flux, and overall mass flux balances on the gas/solid interface are shown in Fig. 4. The energy flux balance is used to calculate the total heat flux to the solid-fuel surface and, for a surface fixed in space, can be written as

$$\begin{aligned}\rho_f r \Delta H_f^o + \cdot \rho_f r \int_{T_i}^{T} c_s \mathrm{d}T \cdot - \cdot \kappa_g \left.\frac{\partial T}{\partial y}\right|_+ + Q_{\mathrm{rad}+} \\ = \rho_{g+} \sum_i^n \left(v_{g+} - \frac{D}{Y_{i+}} \frac{\partial Y_{i+}}{\partial z} \right) Y_{i+} \Delta H_{f,i}^o \cdot - \cdot \kappa_f \left.\frac{\partial T}{\partial z}\right|_- \\ + \cdot \rho_{g+} \sum_i^n \left(v_{g+} - \frac{D}{Y_{i+}} \frac{\partial Y_{i+}}{\partial z} \right) Y_{i+} \int_{T_i}^{T} c_{p,i}\, \mathrm{d}T + Q_{\mathrm{rad}-}\end{aligned} \tag{A1}$$

where the terms on the left side of the equation represent the various energy fluxes entering the pyrolyzing surface and the terms on the right side represent the fluxes

leaving the surface. The first two terms on the left side of Eq. (A1) represent the chemical enthalpy and sensible enthalpy, respectively, being fed into the pyrolyzing surface via the regression process. The third and fourth terms on the left side are the convective and radiant heat fluxes driving the regression process. The first and third terms on the right hand side of Eq. (A1) represent the chemical and sensible enthalpy, respectively, leaving the surface due to bulk flow and diffusion of the n pyrolyzed species. The second and fourth terms represent energy leaving the surface due to subsurface conduction and radiation.

Equation (A1) can be rearranged to solve for the total energy flux reaching the surface due to both convection and radiation,

$$-\kappa_g \left.\frac{\partial T}{\partial z}\right|_+ + Q_{\text{rad}+} = -\kappa_f \left.\frac{\partial T}{\partial z}\right|_- + Q_{\text{rad}-} - \rho_f r \left(\Delta H_f^o + \int_{T_{\text{ref}}}^{T} c_s \mathrm{d}T\right) + \rho_{g+} \sum_i^n \left(v_{g+} - \frac{D}{Y_{i+}} \frac{\partial Y_{i+}}{\partial z}\right) Y_{i+} \left(\Delta H_{f,i}^o + \int_{T_{\text{ref}}}^{T} c_{p,i}\, \mathrm{d}T\right) \tag{A2}$$

The first term on the left side of Eq. (A2) represents the heat flux due to convection from the flame to the pyrolyzing surface, whereas the second term represents the corresponding radiant heat flux. Because the x component of velocity becomes zero at the fuel surface, the convective heat flux, which, in the boundary layer is due to both bulk flow and diffusion, can be written in the gradient form shown in Eq. (A2). Once the total heat flux is known, one can employ a model to estimate the radiant heat flux to isolate and solve for the convective heat flux alone, as described in Sec. III.C. An experimental Stanton number can then be found using the convective heat flux and other quantities. It is first necessary to analyze the individual terms on the right side of the equality in Eq. (A2) to make appropriate substitutions and approximations for the unknown quantities.

The first term on the right side of Eq. (A2) is due to thermal energy leaving the pyrolyzing surface via conduction into the subsurface region of the fuel due to the solid fuel's nonzero thermal conductivity. This term can be determined by considering the energy equation for the solid phase with bulk motion and diffusion only in the z (regression) direction,

$$\kappa_f \frac{\mathrm{d}^2 T}{\mathrm{d}z^2} - \rho_f r c_s \frac{\mathrm{d}T}{\mathrm{d}z} = 0 \tag{A3}$$

with boundary conditions

$$z = 0: \quad T = T_s \tag{A4}$$

$$z = -: \quad T = T_o \tag{A5}$$

where T_s is the fuel surface temperature, T_o the initial fuel temperature deep below the pyrolyzing surface, and κ_f the thermal conductivity of the fuel. In Eq. (A3), it was assumed that the thermal conductivity and specific heat are independent of temperature. Also, the overall mass flux balance on the solid-fuel surface was used

to replace ρv with $\rho_f r$. Assuming an exponential solution for temperature, such as $T = e^{mz}$, yields the characteristic equation for Eq. (A3),

$$m^2 - [(\rho_f c_s/\kappa_f)r]m = 0 \tag{A6}$$

which has solutions

$$m = 0$$
$$m = (\rho_f c_s/\kappa_f)r \tag{A7}$$

The general solution for $T(z)$ is, therefore,

$$T(z) = C_1 + C_2 \exp[(\rho_f c_s/\kappa_f)rz] \tag{A8}$$

Applying Eqs. (A4) and (A5) to Eq. (A8) yields the final expression for the subsurface temperature profile,

$$T(z) = T_o + (T_s - T_o) \exp[(\rho_f c_s/\kappa_f)rz] \tag{A9}$$

Equation (A9) indicates that the subsurface temperature profile varies exponentially with respect to the depth coordinate z.

The first derivative of Eq. (A9) is

$$\frac{\mathrm{d}T}{\mathrm{d}z} = (T_s - T_o)\frac{\rho_f c_s}{\kappa_f} r \cdot \exp\left(\frac{\rho_f c_s}{\kappa_f} rz\right) \tag{A10}$$

At the fuel surface, where $z = 0$, the temperature profile becomes

$$\left.\frac{\mathrm{d}T}{\mathrm{d}z}\right|_o = (T_s - T_o)\frac{\rho_f c_s}{\kappa_f} r \tag{A11}$$

Rearranging Eq. (A11) yields the heat flux leaving the fuel surface via subsurface conduction,

$$\kappa_f \left.\frac{\mathrm{d}T}{\mathrm{d}z}\right|_o = \rho_f c_s r (T_s - T_o) \tag{A12}$$

which can readily be determined because both the regression rate and surface temperature represent known quantities.

The second term on the right side of Eq. (A2) represents the heat flux leaving the pyrolyzing surface because of thermal radiation absorbed beneath the fuel surface. This term can typically be assumed negligibly small because most fuels are opaque to thermal radiation or are manufactured with opacifying agents, such as 1% or so carbon powder. Radiation reaching the surface should be absorbed on the surface and not transmitted into the interior region of the fuel slabs.

The third term in Eq. (A2) represents the total enthalpy delivered to the fixed pyrolyzing surface via the solid-fuel regression process. When an average specific

heat for the solid fuel across the thin, in-depth thermal wave is assumed, the energy flux of total enthalpy delivered to the surface by regression becomes

$$\rho_f r\left(\Delta H_f^o + \int_{T_{\text{ref}}}^{T} c_s \mathrm{d}T\right) = \rho_f r[\Delta H_f^o + c_s(T_s - T_{\text{ref}})] \tag{A13}$$

where T_{ref} is a reference temperature. The solid-fuel specific heat c_s, density ρ_f, and enthalpy of formation, ΔH_f^o, are 1630 J/kg · K, 920 kg/m^3, and −124.32 kJ/kg, respectively, for HTPB.

The final term on the right side of Eq. (A2) represents the total enthalpy leaving the surface due to bulk motion and diffusion of the pyrolyzed species. To determine this term, the identities and mass fractions of the products of pyrolysis must be known, for example, see Fig. 12 for HTPB pyrolysis data. Assuming that the diffusion velocities are negligible compared to the bulk velocity above the surface and again invoking the overall mass flux balance yields

$$\begin{aligned}\rho_{g+} \sum_i^n \left(v_{g+} - \frac{D}{Y_{i+}} \frac{\partial Y_{i+}}{\partial z}\right) Y_{i+} \left(\Delta H_{f,i}^o + \int_{T\text{ref}}^{Ts} c_{p,i}\, \mathrm{d}T\right) \\ \approx \rho_f r \sum_i^n Y_{i+} \left[\Delta H_{f,i}^o + \int_{T\text{ref}}^{Ts} c_{p,i}\, \mathrm{d}T\right]\end{aligned} \tag{A14}$$

for the last term on the right side of Eq. (A2). A polynomial expression for the species specific heats can be used in Eq. (A14) and integrated to obtain numerical values for the total species enthalpy flux.

Equation (A2) can now be reorganized by substituting in Eqs. (A12–A14) and ignoring in-depth radiation absorption,

$$\begin{aligned}Q_{\text{tot}} = \rho_f c_s r(T_s - T_o) - \rho_f r[\Delta H_{f,\text{HTPB}}^o + c_s(T_s - T_{\text{ref}})] \\ + \rho_f r \sum_i^n Y_{i+} \left[\Delta H_{f,i}^o + \int_{T\text{ref}}^{Ts} c_{p,i}\, \mathrm{d}T\right]\end{aligned} \tag{A15}$$

where the left side represents the total heat flux received by the fuel surface as a consequence of both convective and radiant heat flux in the boundary layer. If one assumes that $T_o = T_{\text{ref}} = 298$ K, then the energy flux leaving the surface by conduction into the solid phase cancels the sensible enthalpy flux delivered to the surface by the regression process, and the following simplified form results:

$$Q_{\text{tot}} = \rho_f r \left[\left(\sum_i^n Y_{i+} \Delta H_{f,i}^o\right) - \Delta H_{f,\text{HTPB}}^o\right] + \rho_f r \sum_i^n Y_{i+} \left[\int_{T\text{ref}}^{Ts} c_{p,i}\, \mathrm{d}T\right] \tag{A16}$$

where the first term on the right side represents the heat of decomposition, or the heat evolved in converting the solid-phase fuel to the gas-phase pyrolyzed species.

A pyrolysis law can be used to relate the measured regression rate to the corresponding surface temperature to obtain Q_{tot} from Eq. (A16). An Arrhenius-type expression relates the two quantities,

$$r = A \exp[-(E_a/R_u T_s)] \tag{A17}$$

where R_u, the universal gas constant, equals 1.9872×10^{-3} kcal/mole. If the regression rate represents an experimentally measured quantity, Eq. (A17) can be inverted to solve for the surface temperature for a given regression rate,

$$T_s = E_a/R_u \ln(A/r) \tag{A18}$$

Together, Eqs. (A16) and (A18) allow one to solve for the total surface heat flux, knowing the regression rate, Arrhenius parameters, and thermophysical constants.

Acknowledgement

The valuable suggestions and support of E. E. Rice, W. H. Knuth, R. R. Teeter, C. P. St. Clair, J. A. Sauer, and D. J. Gramer, all of ORBITEC, in the preparation of Sec. IV.A.1, Sec. IV.A.3, and Sec. IV.B.2 is very much appreciated. The assistance of N. B. Knoke in preparing Figure 1 of this chapter is gratefully acknowledged. The discussion in Sec. IV.B.2 and Fig. 27 were graciously provided by M. A. Karabeyoglu. His assistance in summarizing liquefying hybrid combustion theory for this chapter is highly appreciated.

References

[1] AIAA Hybrid Rocket Technical Committee, "A Short Course on the Concept, Systems, Applications, and Operating Principles of Hybrid Rockets," presented at the 31st Joint Propulsion Conference and Exhibit, San Diego, CA, July 1995.

[2] Marxman, G. A., and Gilbert, M., "Turbulent Boundary Layer Combustion in the Hybrid Rocket," *Ninth International Symposium on Combustion*, Academic Press, New York, 1963, pp. 371–383.

[3] Arisawa, H., and Brill, T. B., "Flash Pyrolysis of Hydroxyl–Terminated Polybutadiene (HTPB) I: Analysis and Implications of the Gaseous Products," *Combustion and Flame*, Vol. 106, 1996, pp. 131–143.

[4] Arisawa, H., and Brill, T. B., "Flash Pyrolysis of Hydroxyl–Terminated Polybutadiene (HTPB) II: Implications of the Kinetics to Combustion of Organic Polymers," *Combustion and Flame*, Vol. 106, 1996, pp. 144–154.

[5] Karabeyoglu, M. A., Altman, D., and Cantwell, B. J., "Combustion of Liquefying Hybrid Propellants: Part 1, General Theory," *Journal of Propulsion and Power*, Vol. 18, No. 3, 2002, pp. 610–620.

[6] Karabeyoglu, M. A., and Cantwell B. J., "Combustion of Liquefying Hybrid Propellants: Part 2, Stability of Liquid Films," *Journal of Propulsion and Power*, Vol. 18, No. 3, 2002, pp. 621–630.

[7] Karabeyoglu, M. A., Zilliac, G., Cantwell, B. J., DeZilwa, S., and Castellucci, P., "Scale-Up Tests of High Regression Rate Paraffin-Based Hybrid Rocket Fuels," *Journal of Propulsion and Power*, Vol. 20, No. 6, 2004, pp. 1037–1045.

[8] Muzzy, R. J., "Applied Hybrid Combustion Theory," AIAA Paper 72-1143, 1972.

[9] Marxman, G. A., Wooldridge, C. E., and Muzzy, R. J., "Fundamentals of Hybrid Boundary Layer Combustion," *Heterogeneous Combustion*, edited by H. G. Wolfhard, I. Glassman, and L. Green, Jr., Vol. 15, AIAA Progress in Astronautics and Aeronautics, Academic Press, New York, 1964, pp. 485–521.

[10] Marxman, G. A., "Combustion in the Turbulent Boundary Layer on a Vaporizing Surface," *Tenth Symposium (International) on Combustion*, Combustion Inst., Pittsburgh, PA, 1965, pp. 1337–1349.

[11] Marxman, G. A., "Boundary-Layer Combustion in Propulsion," *Eleventh Symposium (International) on Combustion*, Combustion Inst., Pittsburgh, PA, 1966, pp. 269–289.

[12] Paul, P. J., Mukunda, H. S., and Jain, V. K., "Regression Rates in Boundary Layer Combustion," *Nineteenth Symposium (International) on Combustion*, Combustion Inst., Pittsburgh, PA, 1982, pp. 717–729.

[13] Estey, P. N., Altman, D., and McFarlane, J. S., "An Evaluation of Scaling Effects for Hybrid Rocket Motors," AIAA Paper 91-2517, 1991.

[14] Strand, L. D., Jones, M. D., Ray, R. L., and Cohen, N. S., "Characterization of Hybrid Rocket Internal Heat Flux and HTPB Fuel Pyrolysis," AIAA Paper 94-2876, 1994.

[15] Chiaverini, M. J., Serin, N., Johnson, D. K., Lu, Y.-C., Kuo, K. K., and Risha, G. A., "Regression Rate Behavior of Hybrid Rocket Solid Fuels," *Journal of Propulsion and Power*, Vol. 16, No. 1, 2000, pp. 125–132.

[16] Chiaverini, M. J., Kuo, K. K., Peretz, A., and Harting, G. C., "Regression-Rate and Heat-Transfer Correlations for Hybrid Rocket Combustion," *Journal of Propulsion and Power*, Vol. 17, No. 1, 2001, pp. 99–110.

[17] Smoot, L. D., and Price, C. F., "Regression Rates of Nonmetalized Hybrid Fuel Systems," *AIAA Journal*, Vol. 3, No. 8, 1965, pp. 1408–1413.

[18] Smoot, L. D., and Price, C. F., "Regression Rates of Metalized Hybrid Fuel Systems," *AIAA Journal*, Vol. 4, No. 5, 1965, pp. 910–915.

[19] Smoot, L. D., and Price, C. F., "Pressure Dependence of Hybrid Fuel Regression Rates," *AIAA Journal*, Vol. 5, No. 1, 1966.

[20] Kosdon, F. J., and Williams, F. A., "Pressure Dependence of Nonmetalized Hybrid Fuel Regression Rate," *AIAA Journal*, Vol. 5, No. 4, 1967, pp. 774–777.

[21] Rastogi, R. P. and Deepak, D., "Pressure Dependence of Hybrid Fuel Burning Rate," *AIAA Journal*, Vol. 14, No. 7, 1976, pp. 988–990.

[22] Kumar, R. N., and Stickler, D. B., "Polymer-Degradation Theory of Pressure-Sensitive Hybrid Combustion," *Thirteenth Symposium (International) on Combustion*, Combustion Inst., Pittsburgh, PA, 1971, pp. 1059–1072.

[23] Miller, E., "Hybrid Rocket Combustion Regression Rate Model," *AIAA Journal*, Vol. 4, No. 4, 1966, pp. 752–753.

[24] Wooldridge, C. E., Marxman, G. A., and Kier, R. J., *Investigation of Combustion Instability in Hybrid Rockets*, NASA CR-66812, 1969.

[25] Chiaverini, M. J., Harting, G. C., Lu, Y. C., Kuo, K. K., Peretz, A., Jones, S., Wygle, B., and Arves, J. P., "Pyrolysis Behavior of Hybrid Rocket Solid Fuels Under Rapid Heating Conditions," *Journal of Propulsion and Power*, Vol. 15, No. 6, 1999, pp. 888–895.

[26] Bartel H. R., and Rannie, W. D., "Solid Fuel Combustion as Applied to Ramjets," Jet Propulsion Lab., Progress Rep. 3-12, California Inst. of Technology, Pasadena, CA, Sept. 1946.

[27] Emmons, H. W., "Film Combustion of a Liquid Fuel," Combustion Aerodynamics Lab., Interim Technical Rep. 6, Harvard Univ., Cambridge, MA, June 1953.
[28] Houser, T. J., and Peck, M. V., "Research in Hybrid Combustion," *Heterogeneous Combustion*, 1963, pp. 559–581.
[29] Green, L., "Introductory Considerations on Hybrid Rocket Combustion," *Heterogeneous Combustion*, edited by H. G. Wolfhard, I. Glassman, and L. Green, Jr., Vol. 15, AIAA Progress in Astronautics and Aeronautics, Academic Press, New York, 1964, pp. 451–484.
[30] Altman, D., and Humble, R., "Hybrid Rocket Propulsion Systems," *Space Propulsion Analysis and Design*, edited by Humble, R. W., Henry, G. N., and Larson, W. J., The McGraw-Hill Companies, Inc., Primis Custom Publishing, New York, 1995, p. 379.
[31] Yuasa, S., Yamamoto, K., Hachiya, H., Kitagawa, K., and Oowada, Y., "Development of a Small Sounding Hybrid Rocket with a Swirling-Oxidizer-Type Engine," AIAA Paper 2001-3537, July 2001.
[32] Modest, M. F., *Radiative Heat Transfer*, McGraw-Hill, New York, 1993, pp. 349–369.
[33] Chiaverini, M. J., Serin, N., Johnson, D. K., Lu, Y. C., and Kuo, K. K., "Instantaneous Regression Behavior of HTPB Solid Fuels Burning with GOX in a Simulated Hybrid Rocket Motor," *Challenges in Propellants and Combustion 100 Years After Nobel*, edited by K. K. Kuo et al., Begell House, New York, 1997, pp. 719–733.
[34] Serin, N., Chiaverini, M. J., Harting, G. C., and Kuo, K. K., "Pressure Correction of Ultrasonic Regression Rate Measurements of a Hybrid Slab Motor," 35th Joint Propulsion Conf., 20–24 June 1999.
[35] Strand, L., Ray, R., Anderson, F., and Cohen, N., "Hybrid Rocket Fuel Combustion and Regression Rate Study," AIAA Paper 92-3302, 1992.
[36] Glassman, I., *Combustion*, 2nd ed., Academic Press, San Diego, CA, 1987, pp. 360–375.
[37] Chiaverini, M. J., "Regression Rate and Pyrolysis Behavior of HTPB-Based Solid Fuels in a Hybrid Rocket Motor," Ph.D. Dissertation, Pennsylvania State University Park, PA, 1997.
[38] Wooldridge, C. E., and Muzzy, R. J., "Measurements in a Turbulent Boundary Layer with Porous Wall Injection and Combustion," *Tenth Symposium (International) on Combustion*, Combustion Inst., Pittsburgh, PA, 1965, pp. 1351–1362.
[39] Lees, L., *Combustion and Propulsion*, Third AGARD Colloquium, Pergamon Press, 1958, p. 451.
[40] Kays, W. M., and Crawford, M. E., *Convective Heat and Mass Transfer*, 2nd ed., McGraw–Hill, New York, 1980.
[41] Boardman, T. A., Carpenter, R. L., Goldberg, B. E., and Shaeffer, C. W., "Development and Testing of 11- and 24-Inch Hybrid Motors Under the Joint Government/Industry IR&D Program," AIAA Paper 93-2552, 1993.
[42] Lengellé, G., Fourest, B., Godon, J. C., and Guin, C., "Condensed Phase Behavior and Ablation Rate of Fuels for Hybrid Propulsion," AIAA Paper 93-2413, 1993.
[43] Boardman, T. A., Brinton, D. H., Carpenter, R. L., and Zoladz, T. F., "An Experimental Investigation of Pressure Oscillations and Their Suppression in Subscale Hybrid Rocket Motors," AIAA Paper 95-2689, July 1995.
[44] Carmicino, C., and Sorge, A. R., "Influence of a Conical Axial Injector on Hybrid Rockets Performance."
[45] Pucci, J. M., "The Effects of Swirl Injector Design on Hybrid Flame-Holding Combustion Instability," AIAA Paper 2002-3578, July 2002.

[46] Strand, L. D., Ray, R. L., and Cohen, N. S., "Hybrid Rocket Combustion Study," AIAA Paper 93-2412, June 1993.
[47] George, P., Krishnan, S., Varkey, P. M., Ravindran, M., and Ramachandran, L., "Fuel Regression Rate in Hydroxyl-Terminated-Polybutadiene/Gaseous-Oxygen Hybrid Rocket Motors," *Journal of Propulsion and Power*, Vol. 17, No. 1, 2001, pp. 35–42.
[48] Risha, G. A., Boyer, E., Wehrman, R. B., and Kuo, K. K., "Performance Comparison of HTPB-Based Solid Fuels Containing Nano-Sized Energetic Powder in a Cylindrical Hybrid Rocket Motor," AIAA Paper 2002-3576, July 2002.
[49] Dean, D. L., "Effect of Fuel Formulation on Regression Performance in Hybrid Motors," AIAA Paper 96-0648, Jan. 1996.
[50] Venkateswaran, S., and Merkle, C. L., "Size Scale-up in Hybrid Rocket Motors," AIAA Paper 96-0647, Jan., 1996.
[51] Shanks, R. B., and Hudson, M. K., "The Design and Control of a Labscale Hybrid Rocket Facility for Spectroscopy Studies," AIAA Paper 94-3016, 1994.
[52] Incropera, F. P., and DeWitt, D. P., *Fundamentals of Heat and Mass Transfer*, 3rd ed., Wiley, New York, 1990.
[53] Knuth, W. K., Chiaverini, M. J., Sauer, J. A., and Gramer, D. J., "Solid-Fuel Regression Rate Behavior of Vortex Hybrid Rocket Engines," *Journal of Propulsion and Power*, Vol. 18, No. 3, pp. 600–609.
[54] Knuth, W. H., Chiaverini, M. J., Gramer, D. J., and Sauer, J. A., "Numerical Simulation of Vortex-Driven, Hybrid Rocket Engines," AIAA Paper 98-3351, July 1998.
[55] Lee, C., Na, Y., and Lee, G., "The Enhancement of Regression Rate of Hybrid Rocket Fuel by Helical Grain Configuration and Swirl Flow," AIAA Paper 2005-3906, July 2005.
[56] Rice, E. E., Gramer, D. J., St. Clair, C. P., and Chiaverini, M. J., "Mars ISRU CO/O_2 Rocket Engine Development and Testing," 7th NASA International Microgravity Combustion Symposium, June 2003.
[57] Haag, G., Sweeting, M., and Richardson, G., "An Alternative Geometry Hybrid Rocket for Spacecraft Orbit Transfer Manoeuvers," 51st International Astronautical Congress, IAF Paper 00-W.2.07, 2–6 Oct. 2000.
[58] Caravella, J. R., Heister, S. D., and Wernimont, E. J., "Characterization of Fuel Regression in a Radial Flow Hybrid Rocket," *Journal of Propulsion and Power*, Vol. 14, No. 1, 1998.
[59] Nagata, H., Aikawa, N., Akiba, R., Kudo, I., Ito, K., and Tanatsugu, N., "Combustion Characteristics of Propellants for Dry Towel Hybrid Rocket Motor," 48th International Astronautical Congress, Paper IAF-97-S.2.08, 6–10 Oct. 1997.
[60] Nagata, H., Okada, K., San'da, T., Kato, T., Akiba, R., Satori, S., and Kudo, I., "Combustion Characteristics of Fibrous Fuels for Dry Towel Hybrid Motor," *JSTS*, Vol. 13, No. 1, pp. 11–16.
[61] Dhir, V. K., and Chang, F., "Heat Transfer Enhancement Using Tangential Injection," *ASHRAE Transactions*, Vol. 98, P. 2, 1992, pp. 383–390.
[62] Beer, J. M., and Chigier, N. A., *Combustion Aerodynamics*, Applied Science, London, 1972.
[63] Anderson, M., Rom, C., Bonazza, R., and Chiaverini, M. J., "Vortex Chamber Flow Field Characterization Using Laser Diagnostics," 52nd JANNAF Propulsion Meeting/1st Liquid Propulsion Subcommittee Meeting, 10–13 May 2004.
[64] Sutton, G., *Rocket Propulsion Elements: An Introduction to the Engineering of Rockets*, 6th ed., Wiley, New York, 1992, pp. 512–513.

[65] Georgantas, A. I., Krepec, T., and Kwok, C. K., "Vortex Flow Patterns in a Cylindrical Chamber," AIAA Paper 86-1098, 1986.

[66] Volchkov, E. P., Semenov, S. V., and Tereknov, V. I., "Turbulent Heat Transfer at the Forward Face Surface of a Vortex Chamber," *Inzhenerno-Fizicheskii Zhurnal*, Vol. 56, No. 2, pp. 181–188, Feb. 1989 (Translation published by Plenum).

[67] Wernimont, E. J., and Heister, S. D., "Progress in Hydrogen Peroxide Oxidized Hybrid Rocket Experiments," AIAA Paper 96-2696, 1996.

[68] Prata, A. T., Pilichi, C. D. M., and Ferreira, R. T. S., "Local Heat Transfer in Axially Feeding Radial Flow Between Parallel Disks," *Journal of Heat Transfer*, Vol. 117, Feb. 1995, pp. 47–53.

[69] Nagata, H., Okada, K., San'da, T., Akiba, R., Satori, S., and Kudo, I., "New Fuel Configurations for Advanced Hybrid Rockets," 49th International Astronautical Congress, Paper IAF-98-S.3.09, 28 Sept.–6 Oct. 1998.

[70] Carrick, P. G., and Larson, W. C., "Lab Scale Test and Evaluation of Cryogenic Solid Hybrid Rocket Fuels," AIAA Paper 95-2948, July 1995.

[71] DeRose, M. E., Pfeil, K. L., Carrick, P. G., and Larson, W. C., "Tube Burner Studies of Cryogenic Solid Combustion," AIAA Paper 97-3076, July 1997.

[72] Rice, E. E., Chiaverini, M. J., St. Clair, C. P., Knuth, W. H., and Gustafson, R. J., "Mars ISRU CO/O_2 Hybrid Engine Development Status," AIAA Paper 2000-1066, Jan. 2000.

[73] St. Clair, C. P., Rice, E. E., Knuth, W. H., and Gramer, D. J., "Advanced Cryogenic Solid Hybrid Rocket Engine Developments: Concept and Testing," AIAA Paper 98-3508, July 1998.

[74] Gramer, D. J., and Rice, E. E., "Experimental Investigation of a Metallized Cryogenic Hybrid Rocket Engine," AIAA Paper 98-3509, July 1998.

[75] Karabeyoglu, A., Cantwell, B., and Stevens, J., "Evaluation of Homologous Series of Normal-Alkanes as Hybrid Rocket Fuels," AIAA Paper 2005-3908, 2005.

[76] Evans, B., Favorito, A., and Kuo, K., "Study of Solid Fuel Burning-Rate Enhancement Behavior in an X-ray Translucent Hybrid Rocket Motor," AIAA Paper 2005-3909, July 2005.

[77] Zilliac, G., and Karabeyoglu, M. A., "Hybrid Rocket Fuel Regression Rate Data and Modeling," AIAA Paper 2006-4504, July 2006.

This page intentionally left blank

Chapter 3

Solid-Fuel Pyrolysis Phenomena and Regression Rate, Part 1: Mechanisms

Guy Lengellé*
ONERA, Châtillon, France 92322

Nomenclature

A = preexponential factor
B = transfer coefficient
c_f = friction coefficient
d_p = thermal diffusivity of the material
E = activation energy
$\mathcal{J}$ = nondimensional activation energy
h_{abl} = heat of ablation
h_D = heat of degradation
m = molar mass, g/mole
n = velocity profile exponent, Eq. (12)
$\dot{r}$ = regression rate
T = temperature
Y = mass fraction
δ = boundary-layer thickness
δ^* = boundary-layer displacement thickness
ε = gas/particles emissivity
θ = momentum thickness
λ = thermal conductivity
ρ = specific mass
ρu = specific mass flow rate

Subscript

c = condensed phase or center of channel for flow

*Research Director, Energetics Department. Associate Fellow AIAA.

Parts of this document were initially presented as Paper 93-2413 at the AIAA/ASME/SAE/ASEE 29th Joint Propulsion Conference and Exhibit, Monterey, CA, June 28–30, 1993. They have been extensively revised and completed since then.

I. Introduction

IN the last 10 years, interest has grown again for hybrid propulsion for space launchers, small satellites, and missiles, in which a gaseous oxidizer, initially liquid, flows over a solid fuel and ablates it with the heat flux issuing from the resulting gases, which react in the main flow with the oxidizer. There are also a number of missile applications in which air is ingested in a ram rocket and burns with the pyrolysis gases from a solid fuel lining the chamber walls.

Altman [1] and Calabro [2] present the history of hybrid propulsion, starting in the 1940s with various liquid oxidizers (HNO_3, H_2O_2, N_2O_4, etc.) and various solid fuels (commercial polymers, amines). The work of ONERA, which, for experimental sounding rockets, was conducted in the early 1970s, is described in particular by Kuentzmann and Sternfeld [3].

Interest for hybrid propulsion results from the advantages it could offer for 1) reduced cost, 2) safety of utilization, 3) improved reliability, 4) improved performances as compared to solid propulsion, 5) tailorability, and 6) reduced impact on the environment. Arguments about these points may be found elsewhere [3–6]. The American Rocket Corporation (AMROC), before it disappeared in 1995, devoted its activity to hybrid propulsion [7], whereas NASA has coordinated a demonstration program that resulted in firings at the 100 ton (250,000 lbf) thrust level [8].

The present chapter aims to enhance understanding of the combined processes of the fuel condensed-phase degradation and of its ablation, under the influence of the diffusion-limited flame between the gaseous oxidizer and fuel pyrolysis gases.

The physical description of the diffusion flame and the resulting heat flux to the surface of the material was established in the 1960s. An attempt is made to use it for correlating results obtained on small laboratory motors, in particular at ONERA (with the use of an ultrasonic technique for measuring the regression rates), with a very wide range of stream parameter values (specific mass flow rate, temperature, oxidizer content). The ablation rate results from the coupling with the condensed-phase process, which is described by an approach proposed in the early 1970s and which has been used successfully for a number of polymers as well as various solid propellants. This approach extrapolates the results of bulk degradation experiments to the regression regime for which temperatures higher by about 300°C are reached.

II. Condensed-Phase Behavior

Under the effect of an external heat flux, the solid fuel undergoes a sharp temperature profile and, very close to the surface, decomposes into gases (Fig. 1). The kinetics and energetics of thermal degradation can be investigated, under much lower heating rates and under bulk degradation conditions, with various thermal analysis techniques, such as thermogravimetry (TG) and differential scanning calorimetry (DSC), and the gases produced can be sampled and analyzed. In particular, these techniques have been applied to hydroxyl-terminated polybutadiene (HTPB), a fuel often considered for application to large hybrid motors, polyethylene (PE), which can be considered as a reference material for laboratory testing and also can be used for small motors with simple perforations, and glycidyl azide polymer (GAP), a fuel which is of interest because of its potential for high regression rates due to its exothermic decomposition.

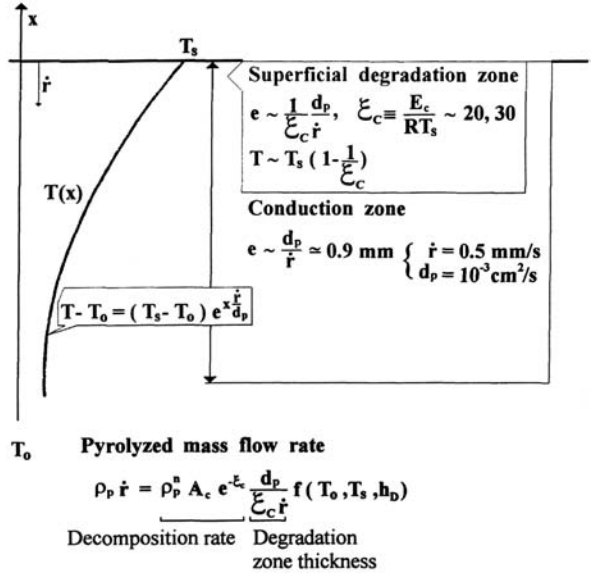

Fig. 1 Principle of the modeling of the condensed-phase behavior.

Much information has been acquired over the years (for fuels, as well as for propellants [9–11]) on the validity of extrapolating the test results to the regression regime. Surface regression, so-called linear pyrolysis, experiments have been performed by different authors by utilizing the various methods shown in Fig. 2. From these experiments, measurements of the regression rate and of the surface temperature T_s are obtained, as well as of the heat of ablation of the material, h_{abl}, under conditions close to those of hybrid propulsion.

A. Pyrolysis Law of Fuels

The temperature profile within the condensed fuel is given by the relation, where $x > 0$ is outward into the gas phase (Fig. 1),

$$(T - T_0)/(T_s - T_0) = \exp(x\dot{r}/\mathrm{d}_p) \tag{1}$$

with $d_p = \lambda_p/\rho_p c_p$ (thermal diffusivity of the material) always close to $1 \times 10^{-3}\,\text{cm}^2/\text{s}$. From this law, an estimation of the thickness of the conduction zone can be extracted (where the temperature $T - T_0$ is 10^{-2} the value at the surface)

$$e_{\text{cond}} = (\mathrm{d}_p/\dot{r})\ell n 10^2 \tag{2}$$

For example, at $\dot{r} = 1\,\text{mm/s}$, a thickness of 0.45 mm, with an associated residence time of about $\frac{1}{2}$s, is attained.

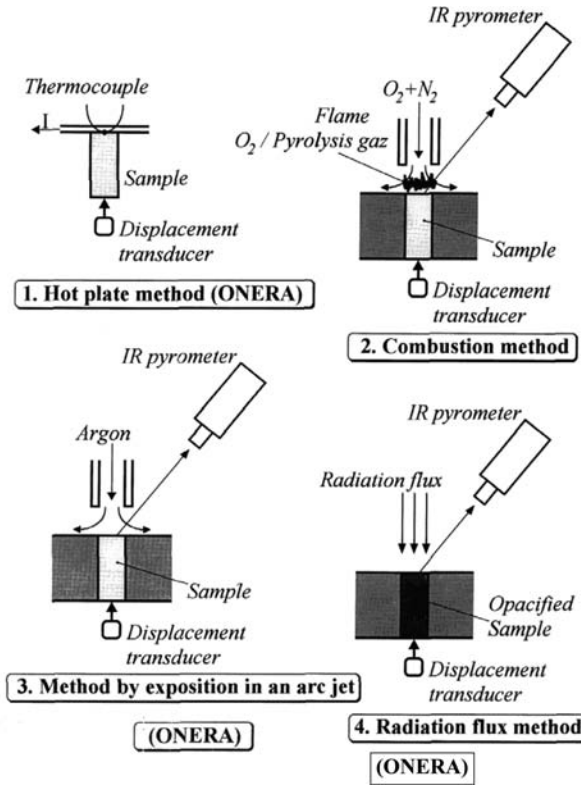

Fig. 2 Various means for linear pyrolysis experiments.

The superficial degradation zone is described by the conservation of the nondegraded material (for a first-order reaction)

$$\rho_p \dot{r} \frac{\mathrm{d}Y_p}{\mathrm{d}x} = -\rho_p Y_p A_c \exp\left(-\frac{E_c}{RT}\right) \tag{3}$$

The thickness of the degradation layer is ruled by the very fast drop in the degradation rate. Conventionally the end of this degradation layer can be considered to be reached when the temperature drop is such that

$$\exp[-\mathcal{J}_c/(1-\Delta T/T_s)] = 10^{-2}\exp(-\mathcal{J}_c)$$

with $\mathcal{J}_c = E_c/RT_s$. This temperature drop is then

$$\Delta T/T_s = 1/(1+\mathcal{J}_c/\ell n 10^2)$$

A typical value (for $T_s = 1000\,\mathrm{K}$, $E_c = 50\,\mathrm{kcal/mole}$, and $\mathcal{J}_c \approx 25$) is $\Delta T \approx 150\,\mathrm{K}$. This temperature drop inserted in Eq. (1) results in an estimate of the

degradation zone thickness,

$$e_{\text{reaction}} = -(d_p/\dot{r})\ell n[1 - \Delta T/(T_s - T_0)] \tag{4}$$

For the values already taken, $e_{\text{reaction}} \approx 25\,\mu\text{m}$, a thickness through which the initial material is transformed into gases, with an associated residence time of 25 ms, that is, a temperature rise rate of 6000 K/s. This should be compared to bulk degradation conditions, such as in DSC, where the temperature rise rate is more like 0.1 K/s.

The summimg of Eq. (3) through the degradation zone results in

$$\rho_p \dot{r}(Y_{ps} - Y_{p0}) = -\int \rho_p Y_p A_c \exp(-E_c/RT)\,\mathrm{d}x$$

$$\dot{r} \approx A_c \exp(-E_c/RT_s) e_{\text{reaction}}$$

where from Eq. (4)

$$e_{\text{reaction}} \approx e_{\text{cond}} T_s/\mathcal{J}_c(T_s - T_0)$$

Finally, with the details of the complete explicit calculation given by Lengellé [9], the relation between regression rate and surface temperature, which expresses that as the regression rate increases the surface temperature has to increase and accelerate the degradation to allow for the complete pyrolysis of the material into gases, is obtained,

$$\dot{r}^2 = A_c \exp(-\mathcal{J}_c)(1/\mathcal{J}_c) d_p \mathcal{R}^2 \tag{5}$$

with

$$\mathcal{R}^2 = 1/[-\ell n(Y_{ps})(1 - T_0/T_s + h_D/c_p T_s) - h_D/c_p T_s]$$

It can be seen in Fig. 3 that this expression is a very good approximation of a complete numerical calculation. In this approach, the mass fraction of the

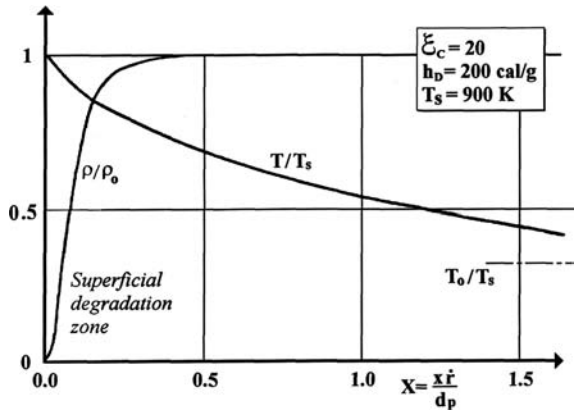

Fig. 3 Profiles in the condensed phase: numerical calculation $R^2 = 0.17$ and explicit calculation $R^2 = 0.173$.

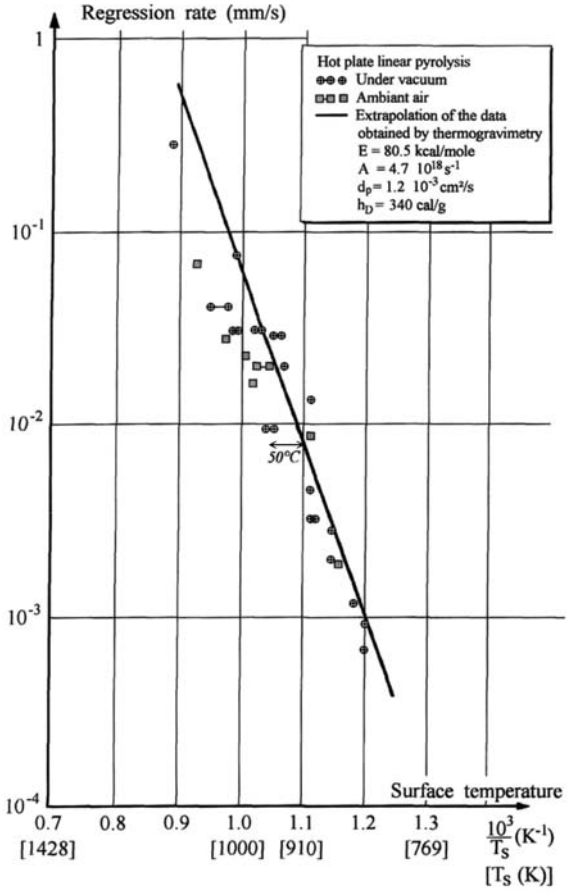

Fig. 4 Pyrolysis law for Teflon, a reference material.

remaining polymer, Y_{ps}, is set to 0.01, a sufficiently small quantity for the end of the degradation. (The rate of a first-order reaction never goes to zero.)

This approach has been applied very successfully to Teflon as a reference material (Fig. 4). It is seen that the extrapolated pyrolysis law fits the experimental results under linear pyrolysis conditions. These experiments, run under either vacuum or ambient air, show the same trend. This confirms the idea that the condensed-phase degradation is a thermally induced (nonpressure influenced) irreversible process.

B. Results for PE

The degradation kinetics for PE, $(C_2H_4)_n$, is reaction order $n = 1$, $E_c = 60$ kcal/mole, and $A_c = 2 \times 10^{16}\ s^{-1}$, as obtained from TG measurements around 650 K ($\approx$400°C) and using the Coats and Redfern method.

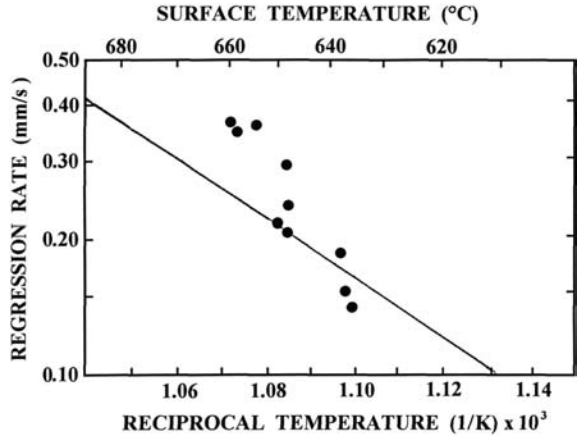

Fig. 5 Pyrolysis law for polyethylene: •, IR pyrometer measurement and —, extrapolated law ($E_c = 60$ kcal/mole, $A_c = 2 \times 10^{16}$ s^{-1}).

The averaged physical and thermal characteristics used for PE are $\rho_p = 0.95\,\mathrm{g/cm^3}$, $c_p = 0.3\,\mathrm{cal/g \cdot K}$, $\lambda_p = 3.7 \times 10^{-4}\,\mathrm{cal/cm \cdot s \cdot K}$, and $d_p = 1.3 \times 10^{-3}\,\mathrm{cm^2/s}$.

From these elements, the law relating the ablation rate $\dot{r}$ to the surface temperature can be obtained from Eq. (5). The result is indicated in Fig. 5 and compared to the data of Blazowski et al. [12]. [The regression was obtained by exposing the sample to the heat flux issuing from the flame between the material degradation gases and an impinging oxygen jet (Fig. 2).] When it is considered that surface temperature measurements are very imprecise [here with an infrared (IR) pyrometer] and that the kinetics is extrapolated from 650 K (for the TG measurements) to about 950 K (linear pyrolysis measurements), the agreement is thought to be very good. The extrapolated law will be the one used later for the evaluation of the ablation of PE.

The heat of ablation of PE can be obtained from experiments [13], in which samples were exposed in the stagnation point in an arc-heated stream. The value obtained is (for an estimated $T_s \approx 950$ K)

$$h_{\mathrm{abl}} = c_p(T_s - T_0) + h_D \approx 850\,\mathrm{cal/g} \tag{6}$$

resulting in a value of $h_D \approx 650\,\mathrm{cal/g}$, the heat of degradation of the material.

C. Results for HTPB

The characteristics of the degradation of HTPB [$(C_4H_6)_n$ cross linked by an isocyanate agent] as measured from DSC experiments, at temperatures around 450°C, are reaction order $n = 1$, $E_C = 48.6$ kcal/mole, and $A_c = 2.63 \times 10^{12}\,\mathrm{s^{-1}}$.

The averaged physical and thermal characteristics used for HTPB are $\rho_p = 0.92\,\mathrm{g/cm^3}$, $c_p = 0.39\,\mathrm{cal/g \cdot K}$, $\lambda_p = 3.6 \times 10^{-4}\,\mathrm{cal/cm \cdot s \cdot K}$, and $d_p = 1.0 \times 10^{-3}\,\mathrm{cm^2/s}$.

The resulting law for $\dot{r}$ vs T_s, as obtained from Eq. (5) and using degradation kinetics, is shown in Fig. 6, where it is compared to results measured by IR pyrometry in a hybrid (with gaseous oxygen) slab motor [14]. One measurement with IR pyrometry is shown in a setup in which the regression of the material is obtained by exposition to the heat flux of CO_2 laser. Results obtained by Cohen et al. [15], who used a similar technique, are shown with an estimation of the scatter as was done by Lengellé et al. [11]. Also shown are more recent results by Chiaverini [16]. In this work, the HTPB is set as slabs in a laboratory hybrid motor working with gaseous oxygen. The surface temperature is measured from the profile obtained by an imbedded small thermocouple (made with 25 μm wires). Examination of the profiles given by Chiaverini [16] seems to show (and this might be open to argument) that only the profiles obtained at locations far downstream are "clean" enough to produce a surface temperature measurement. (More precisely these are the results at locations farther than 30 cm in Table 5.8 of [16].)

The agreement is quite interesting when it is known that the kinetics is extrapolated from ≈700 K for DSC to ≈1100 K for linear pyrolysis, with a corresponding vast increase in degradation rate of 0.35×10^6. Again this tends to show that the pyrolysis of the material is conditioned by the initial thermal degradation of the bonds of the polymer.

The heat of ablation of HTPB was obtained [15] by relating the mass ablated to the radiation heat flux received by the sample. For a regression rate of 0.4 mm/s (and, from Fig. 6, $T_s \approx 1060$ K),

$$h_{\text{abl}} = c_p(T_s - T_o) + h_D = 750\,\text{cal/g} \tag{7}$$

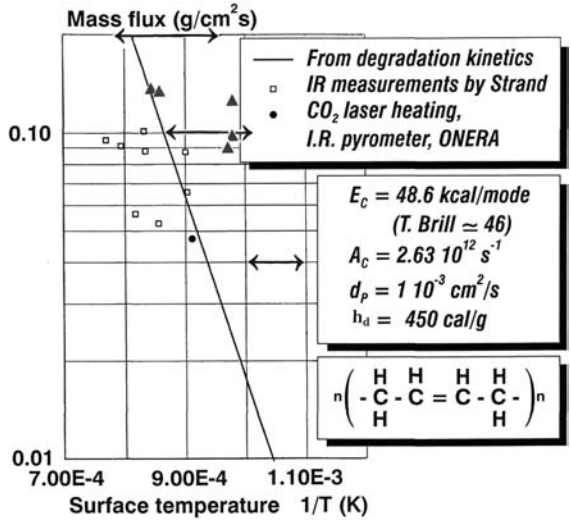

Fig. 6 Surface temperature for HTPB: ⟷, measurements by Cohen and ▲, measurements by Chiaverini.

was obtained and, thus,

$$h_D = 450\,\text{cal/g}$$

It was stated by Lengellé et al. [11] that this value is compatible with the production of mostly C_4H_6 as pyrolysis gas. (This conclusion is also found elsewhere [16–18].) Gas analysis at low temperature reveals a complex set of gases (≈45% in mass butadiene, ethylene, propene, etc.) resulting from the degradation of HTPB. If one evaluates the difference in heats of formation between the initial material and butadiene the following is found:

$$\Delta h = h^0(C_4H_6) - h^0(\text{HTPB}) = 496\,\text{cal/g} - 5\,\text{cal/g} \approx 490\,\text{cal/g}$$

sufficiently close to the measured heat of degradation. At high heating rates, butadiene is probably the major degradation gas.

D. Results for GAP

GAP is a particular material because it has an exothermic heat of degradation due to its N_3 group,

$$-[-CH_2-CH(CH_2N_3)-O-]_n-$$

Its heat of ablation is then particularly low, as will be seen. Although it has the characteristics of a polymer fuel, for example, the combustion of 50% in mass GAP with 50% gaseous O_2 will reach 3675 K, a value very close to what is obtained with HTPB, it can undergo self-sustaining combustion under an inert gas pressure, with a burning rate $r_b = 0.13p^{0.55}$ (in centimeters per second and p in bar), reaching 1 cm/s at 40 bars. Frankel et al. [19] is an interesting source of information on GAP.

Once cross linked, the overall elemental composition of GAP is

$$C_{3.3}H_{5.6}O_{1.1}N_{2.6}$$

The decomposition of GAP under DSC conditions (at about 250°C, which is 200°C lower than for HTPB or any other inert polymers) has been carried out resulting in a reaction order $n = 1$, $E_c = 43$ kcal/mole, and $A_c = 7.5 \times 10^{15}\,\text{s}^{-1}$.

The averaged physicothermal characteristics of GAP thought to be representative are $\rho_p = 1.28\,\text{g/cm}^3$, $c_p = 0.45\,\text{cal/g}\cdot\text{K}$, $\lambda_p = 5.8 \times 10^{-4}\,\text{cal/cm}\cdot\text{s}\cdot\text{K}$, and $d_p \approx 1.0 \times 10^{-3}\,\text{cm}^2/\text{s}$.

As were the preceding materials, the degradation kinetics was extrapolated to the regression regime (here obtained under self-burning), according to Eq. (5) (Also taken into account is an earlier measurement of the degradation kinetics.) The results are shown in Fig. 7, where they are compared to measurements at ONERA and by Kubota and Sonobe [20], obtained by inserting thermocouples of a few micrometers. (To follow the sharp temperature rise, the thermal wave thickness is about 90 μm at $r_b = 0.5$ cm/s.)

Again, in view of the difficulty in measuring the surface temperature (where, in particular, the abundant carbon residue produced on the surface perturbs the

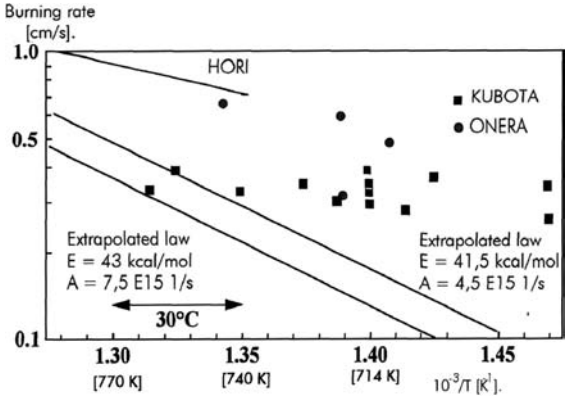

Fig. 7 Surface temperature of GAP.

thermocouple reading) and taking into consideration the long extrapolation from ≈520 K for DSC experiments to ≈770 K for regression conditions, the agreement is considered to be reasonable.

From the thermocouple profiles in the regressing GAP samples, by using the energy balance at the surface, an estimation can be obtained of the heat evolved near the surface by the degradation into gases of GAP [21]. The result obtained is

$$h_D = -150\,\text{cal/g}$$

which is exothermic, as already mentioned. The heat of ablation is then, for example at $\dot{r} = 0.5\,\text{cm/s}$,

$$h_{\text{abl}} = c_p(T_s - T_0) + h_D = 70\,\text{cal/g} \tag{8}$$

an order of magnitude lower than for HTPB.

III. Ablation Rate

The ablation behavior of solid fuels has been investigated at ONERA, in particular, under small-scale conditions. In most of the experiments, an ultrasonic technique [22] often used for solid-propellant motors was applied with success. Results were, thus, obtained on a wide range of specific mass flow rates, of stream temperature, and of oxygen content. An engineering type of approach, taking into account the diffusion-controlled flame between oxidizer gas and degradation gases, will be shown to correlate the results obtained at ONERA as well as the literature for PE and HTPB. Considerations about the ablation regime and a model for the regression of GAP are then presented.

A. Laboratory Setups Used at ONERA

Over several years, for various purposes, and within different contexts, sometimes other than that of hybrid propulsion, that is, for the experimentation of

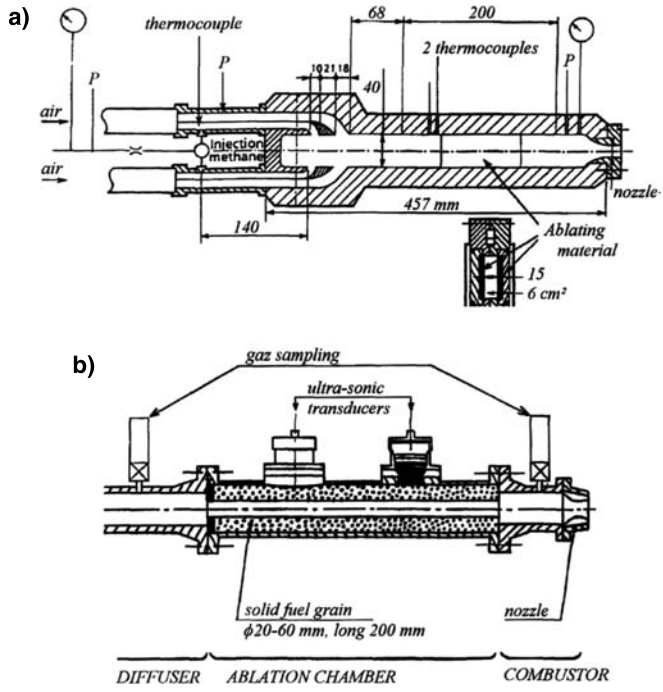

Fig. 8 Setups with air injection: a) 2-D setup, air from resistance heater ($\rho u \leq 500\,\mathrm{kg/m^2 \cdot s}$, $P \leq 1.5\,\mathrm{MPa}$) and b) axisymmetric setup, air from chemical heater ($\rho u \leq 3000\,\mathrm{kg/m^2 \cdot s}$, $P \leq 5\,\mathrm{MPa}$).

solid-fuel ramjets, three setups were used (Figs 8 and 9). The first one is a two-dimensional channel fed with air preheated up to 625 K through an electric resistance heater. A small methane torch allows the ignition of the polymer slabs. The firings last a few seconds, and the specific mass flow rates are at most around $500\,\mathrm{kg/m^2 \cdot s}$. The ablation rate is obtained on this older device both through visualization and primarily through dimensional control after firing.

Measurements were performed in the two-dimensional planar setup for the heat flux received by the surface from the preheated air and compared to estimates based on a thin boundary-layer approach. Results are given in Fig. 10. The measurements were made with thin copper fluxmeters with imbedded thermocouples. The estimates of the heat flux coefficient result from the following considerations. The thin boundary-layer heat-transfer coefficient is

$$c_{ho} = 0.03/(Re_x)^{0.2}$$

and the exchange coefficient is

$$h_o = \rho u|_e c_{ho} c_g$$

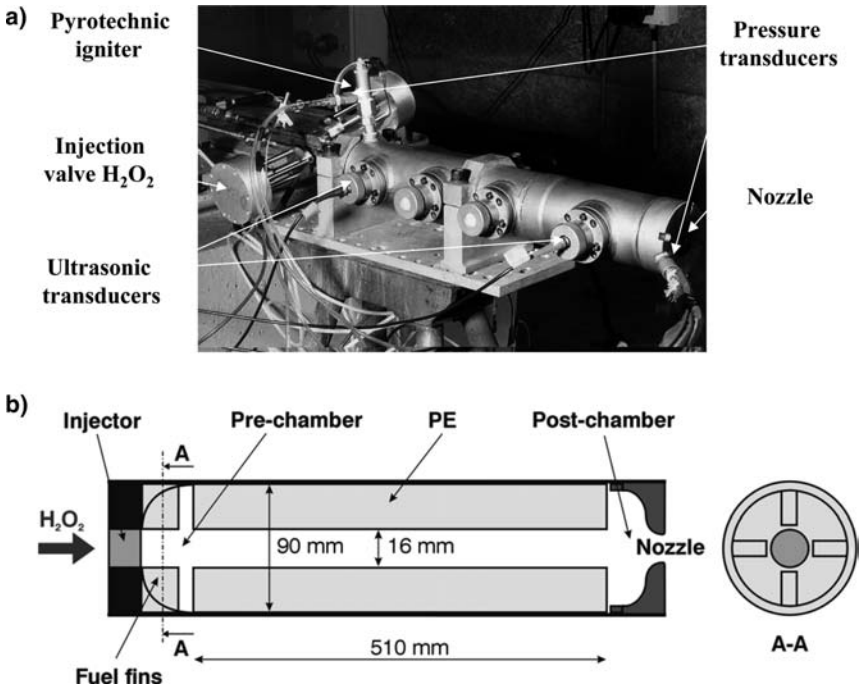

Fig. 9 Small-scale hybrid motor: a) experimental application and b) schematic.

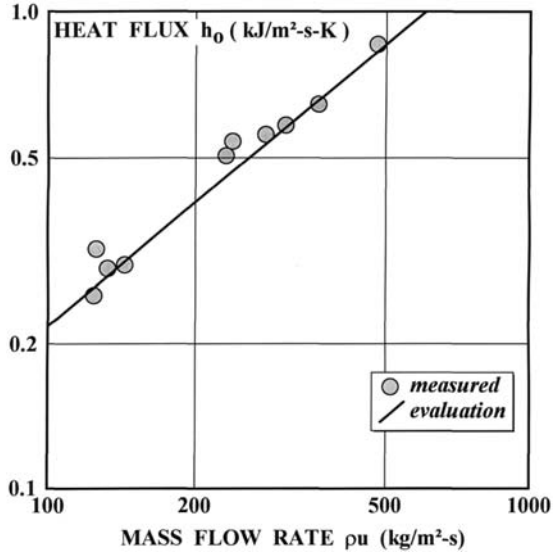

Fig. 10 Heat flux coefficient measurement.

The specific mass flux outside of the boundary layers is obtained from the measured mass flux after taking into account the displacement thicknesses on the walls (with x taken as the distance from the beginning of the channel to half-way of the polymer slab, $x = 168$ mm),

$$\delta^* = \delta/(n+1); \qquad \delta = 0.4x/(Re_x)^{0.2}$$

where $n = 7$ from the classical turbulent profile correlation and the thickness lost from the boundary layer is about 0.5 mm. The properties of air were evaluated at an average temperature between the stream and surface with

$$\mu = 4 \times 10^{-4}(T/1000)^{0.7} \text{ g/cm} \cdot \text{s};$$
$$c_g = 0.28 + 30.7 \times 10^{-5}(T - 1000) \text{ cal/g} \cdot \text{K}$$

The good agreement between the evaluation and measurements supports the idea that the flow in the setup is best described with a boundary-layer approach.

The second setup in Fig. 8 is an axisymmetric channel, again fed with air. The airstream is heated to high temperatures through the use of combustion between added oxidizer/fuel flows, with extra oxygen fed to keep the mass fraction of oxygen at 0.23.

The third setup is shown in Fig. 9, in this case with an H_2O_2 feed system. The measurement of the local, instantaneous regression rate is obtained by an ultrasonic technique. In this technique, the emitting–receiving transducer, separated from the ablating material by a coupling element, sends, 5000 times per second, a mechanical wave that propagates through the material (at a velocity in the vicinity of 2000 m/s), reflects on the surface, and comes back. An instantaneous material thickness is, thus, obtained (limited to about 50 mm, due to the strong damping of the mechanical wave) once the propagation velocity is known. The propagation velocity is somewhat modified by pressure (requiring a calibration) and by temperature,

$$c_{\text{ref}}/c = [1 - k_p(p - p_{\text{ref}})][1 + k_T(T - T_{\text{ref}})]$$

This technique and others will be described later.

As was seen earlier, the thermal penetration depth in the regressing material is a few hundreds of micrometers and, thus, of no consequence when compared to the total thickness.

B. Description of Ablation Behavior

The physical basis for describing the ablation behavior of polymer solid fuels was established in the 1960s, most notably by Marxman [23] and Marxman and Wooldridge [24], who contributed a long list of pioneering works. Also worth mentioning is the, probably little known, work by Williams [25]. Figure 11, from

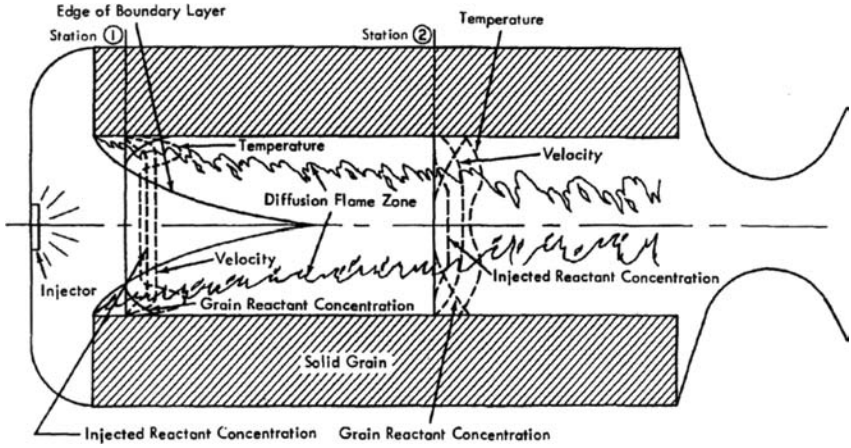

Fig. 11 Flow development in a hybrid motor; axial and radial scales not the same, e.g., boundary layers merge roughly 50 port diameters downstream: - - -, qualitative radial variation of properties indicated.

Williams [25], shows the main features of the hybrid system. The flow from the oxidizer feeding system should transition rapidly to a fully turbulent configuration. For illustration, let us assume a small-scale research motor,

$$L = 400\,\text{mm}; \qquad \Phi_{\text{int}} = 40\,\text{mm}(\approx 1.6\,\text{in.})$$

$$\rho u = 200\,\text{kg/m}^2 \cdot \text{s}(\approx 0.3\,\text{lb/in.}^2 \cdot \text{s})$$

Under typical wall injection conditions, Marxman indicates transition to occur at $Re_x \approx 10^4$, corresponding (for $\mu = 6 \times 10^{-4}\,\text{g/cm} \cdot \text{s}$, a representative value) to x transition $= 3\,\text{mm}$. The first part of the flow will correspond to thin boundary layers as compared to the motor internal diameter; indeed, as seen before, the displacement thickness is at midlength

$$\delta^* \approx 0.4x/(n+1)(Re_x)^{0.2} = 0.7\,\text{mm}$$

Williams indicates a length approximately 50 times the diameter for the boundary layers to fill up the channel to obtain fully developed flow. In our example, this is a length of 2 m.

From these considerations, it appears that small-scale devices can be best treated by a boundary-layer approach with parameters evolving with x, the length covered by the flow. This is indeed the approach adopted by Salita [26]. In large motors, the dimensions should be such that fully developed flow can be reached.

Under the approximation of equal turbulent transport properties ($P_r \approx 1$, $Le \approx 1$), the equations of conservation for momentum, chemical species, and energy, with the boundary-layer approximation (and neglecting the effect of $\text{d}p/\text{d}x$, the longitudinal pressure gradient), reveal the similarity between velocity, mass

fractions, and temperature profiles,

$$\frac{\partial(\rho uu)}{\partial x}+\frac{\partial(\rho vu)}{\partial y}=\frac{\partial(\mu_{\text{eff}}\partial u/\partial y)}{\partial y}$$

$$\frac{\partial(\rho u\alpha_i)}{\partial x}+\frac{\partial(\rho v\alpha_i)}{\partial y}=\frac{\partial(\mu_{\text{eff}}\partial\alpha_i/\partial y)}{\partial y}-\mathring{\Omega}$$

$$\frac{\partial(\rho u\beta)}{\partial x}+\frac{\partial(\rho v\beta)}{\partial y}=\frac{\partial(\mu_{\text{eff}}\partial\beta/\partial y)}{\partial y}+\mathring{\Omega}$$

with $\alpha_i = Y_i/(n_i - n_i')m_i$, $\beta = c_gT/\Delta Q_g$, where c_g is an average value for the heat capacity. These relations hold for an overall chemical reaction,

$$n_iA_i \rightarrow n_i'A_i; \qquad \mathring{\Omega}_i = (n_i - n_i')m_i\mathring{\Omega}$$

$$\Delta Q_g = \sum h_i^\circ(n_i - n_i')m_i$$

in calories per mole, is the heat evolved in the reaction, positive if exothermic, $\mathring{\Omega}$ is the overall rate of reaction in moles per cubic centimeters per second. A combined variable,

$$\alpha = \alpha_{\text{ox}} + \beta$$

obeys the same equation as the u component of the velocity and, thus,

$$\alpha = \beta_s + (u/u_e)(\beta_e - \beta_s + \alpha_{\text{ox},e})$$

with the assumption that the oxidizer is consumed in the diffusion flame and does not reach the surface. (It seems that the approximation of an infinitely thin flame does not have to be made.)

The ablation of the solid fuel is due to the heat flux from the gas phase,

$$\rho_p\dot{r}h_{\text{abl}} = \left.\frac{\lambda\partial T}{\partial y}\right|_s = \left(\frac{\lambda}{c_g}\right)\frac{\Delta Q_g\partial\beta}{\partial y}$$

$$= \mu\left(\frac{\partial u}{\partial y}\right)\Bigg|_s\left(\frac{1}{u_e}\right)\left[c_g(T_e - T_s) + Y_{\text{ox},e}\frac{\Delta Q_g}{n_{\text{ox}}m_{\text{ox}}}\right]$$

resulting in

$$\rho_p\dot{r} = (1/2)c_f\rho_eu_eB \tag{9}$$

with $\tau_s = (1/2)c_f\rho_eu_e^2$ and where

$$B = [c_g(T_e - T_s) + Y_{\text{ox},e}\Delta Q_g/n_{\text{ox}}m_{\text{ox}}]/h_{\text{abl}} \tag{10}$$

These relations were developed long ago by Marxman. However, it is worth underlining the approximations that are used to establish them.

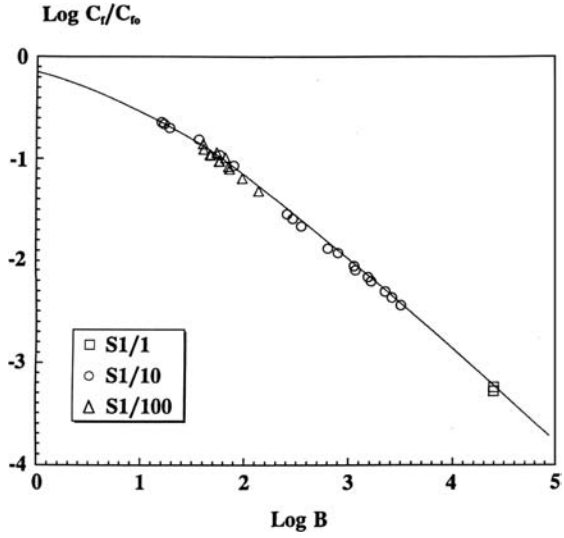

Fig. 12 Blocking effect; $\tau_p = (1/2C_f \cdot \overline{\rho u^2})$ and $B = \dot{m}_p/(1/2C_f \cdot \overline{\rho u})$: —, correlation law.

In the relation for the ablation rate, the friction coefficient is taken from correlation laws for turbulent boundary-layer flows, modified to account for the blocking effect of the injected surface flow. From work on the erosive burning of solid propellants [27, 28], a number of numerical computations of flows with surface injection were performed and the results were correlated with the relation

$$c_f/c_{fo} = \{1 + 0.5[1 - \exp(-0.05B)]\}\ell n(1 + B)/B \tag{11}$$

shown in Fig. 12, which can be seen to recover the standard formula for low values of B. The numerical computations that lead to Eq. (11) take into account measurements on flows with injection [27].

C. Development of Shearing Flow

In the case of a small-scale motor with L/Φ_{int} around 10, the growing boundary-layer approach yields interesting relationships that reveal the essential features of hybrid motor operation. As was already shown, because of the similarity of the momentum, chemical species, and energy equations (under the assumption that the oxidizer from the core flow is consumed in the diffusion flame with the fuel pyrolysis gases), an explicit law results for the regression rate: This is Eq. (9).

When the length of the motor increases (L/Φ_{int} larger than 10), the boundary layers thicken and end up merging. At this point, the pure oxidizer core disappears. The treatment as a boundary layer with an external known state does not apply any longer.

An integral method that allows the treatment of both regions of the flow (with a lack of complication in tune with designing methods in which the flow computation

needs to be repeated many times) has been developed and used. The starting point is the assumption of a velocity profile

$$u(y)/u_c = \eta^{1/n} \tag{12}$$

In zone 1, before merging of the boundary layers, and zone 2 beyond,

$$\eta = y/\delta$$
$$\eta = y/R$$

At $y = \delta$ $u = u_c$ all of the way to the axis for zone 1, and for zone 2 at $y = R$ $u = u_c$, with u_c the velocity at the axis.

Recall now a few results from turbulent inert incompressible flows. It is known from developed turbulent pipe flow that

$$\tau_s = \rho\bar{u}^2 0.04(Re_D)^{-1/4}$$
$$Re_D = \rho\bar{u}D/\mu$$

where $\bar{u}$ is the mean velocity in the section of the pipe, with $\bar{u}/u_c \approx 0.8$ (for $n = 7$ in the velocity profile). Then

$$\tau_s = 0.0225\rho u_c^2 (Re_R)^{-1/4} \tag{13}$$
$$Re_R = \rho u_c R/\mu$$

is obtained. As shown in a textbook approach (such as Schlichting's) this relationship can be applied to a surface boundary layer

$$\tau_s = 0.0225\rho u_\infty^2 (\rho u_\infty \delta/\mu)^{-1/4}$$

with δ the boundary-layer thickness. In a standard boundary-layer approach, the summed conservation equations through the thickness yield

$$\frac{\tau_s}{\rho u_\infty^2} = \frac{\mathrm{d}(u_\infty \theta)}{\mathrm{d}x}$$

with

$$\delta^* u_\infty = \int (u_\infty - u)\,\mathrm{d}y$$

with y from 0 to ∞, displacement thickness,

$$\theta u_\infty^2 = \int u(u_\infty - u)\,\mathrm{d}y$$

y from 0 to ∞, momentum thickness, and

$$\delta * /\delta = 1/(1+n), \theta/\delta = n/(1+n)(2+n)$$

This results in

$$\delta = 0.37x/(Re_x)^{0.2}$$
$$Re_x = \rho u_\infty x/\mu$$

a relationship used earlier and

$$\tau_s = 0.03\rho u_\infty^2/(Re_x)^{0.2} \tag{14}$$

an alternate form of Eq. (13).

As applied to the problem of growing boundary layers in a circular perforation with a core at oxygen concentration and temperature at entrance conditions in zone 1, then of fully developed pipe flow in zone 2, the following approach is used: From the integration of the conservation of mass and momentum through the boundary layer, the differential equation for the momentum thickness in zone 1 is

$$\frac{\mathrm{d}\theta}{\mathrm{d}x} = \frac{\tau_s}{\rho_c u_c^2} + \frac{\rho_s v_s}{\rho_c u_c} \tag{15}$$

(plus terms related to the longitudinal evolution of u_c and p, obtained from the core flow treatment of the conservation equations)

$$\theta/\delta = (\rho_{\mathrm{av}}/\rho)n/(2+n)(1+n)$$

where ρ_{av} is average specific mass. The exchange coefficient is from

$$c_{fo}/2 = 0.0225(\rho_c u_c \delta/\mu_{\mathrm{av}})^{-1/4} \tag{16}$$

$$\tau_s = \rho_c u_c^2 (c_f/c_{fo}) c_{fo}/2 \tag{17}$$

From the cited work [27, 28] on the erosive burning of solid propellants, a number of numerical computations of flows with surface injection were performed and the results were correlated to express the reduction in exchange coefficient as Eq. (11).

In zone 2 after merging of the boundary layers, the conservation equations are integrated over the radius of the pipe, the velocity profile of Eq. (12) is used, and the temperature is linearly related to u (due to the similarity of the corresponding conservation equations), as well as the species profiles. Differential equations result for $\bar{u}$ (or u_c), T_{av} (or T_c), $Y_{\mathrm{ox,av}}$ (or $Y_{\mathrm{ox},c}$), etc.

The friction coefficient is given by Eqs. (16) and (11) with δ replaced by R in zone 2, and finally, the fuel regression rate is from

$$\rho_p \dot{r} = 1/2 c_f \rho_c u_c B$$

this relationship applying throughout the fuel perforation.

D. Results from Simplified Approach

A first illustration of the results obtained from the simplified integral method is given (in the case of the O_2 HTPB system) in Fig. 13. After the entrance region where the boundary layer is very thin and the flame close to the surface, the regression rate flattens to around 1 mm/s for the parameter values indicated. Notice that a rough radiation flux model with $\varepsilon = 0.1$ at T flame is used. (Some elements will be presented later.) In Fig. 14, a computation is carried out much further to the point where the oxidizer mass fraction goes down to zero. By the interruption of the channel at about two-thirds of the maximum length, average values of $Y_{ox,av} \approx 0.11$ and $Y_{fuel,av} \approx 0.04$ are obtained, or a ratio of ≈ 3, a proper level (for O_2/HTPB) to enter the postcombustion chamber and combust to maximum

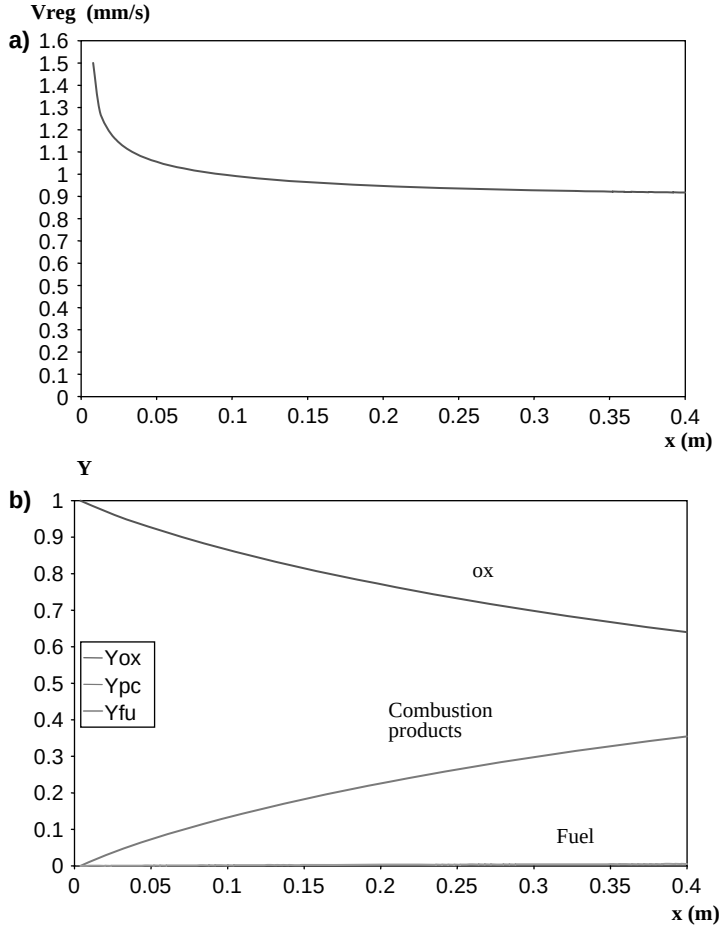

Fig. 13 Evolution of values for a specific mass flow rate 300 kg/m^2 · s $\Phi_{int} = 40$ mm: a) regression rate and b) average values.

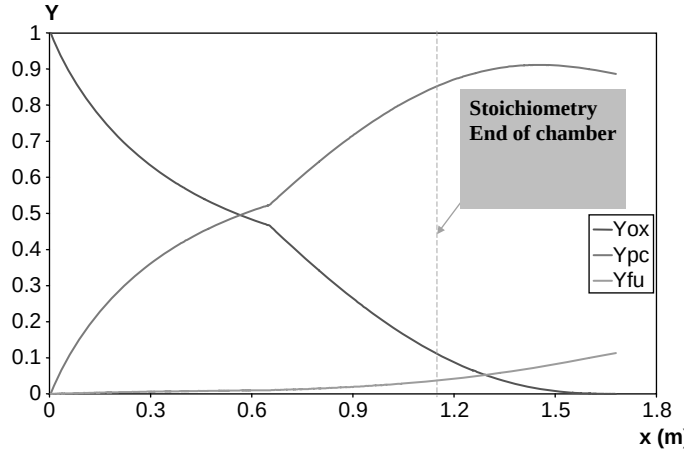

Fig. 14 Evolution of values for a specific mass flow rate 100 kg/m^2 · s; $\Phi_{int} = 40$ mm, average values.

efficiency. Thus, it is not useful to extend the length to the point where all of the oxidizer has disappeared.

The results of the simplified approach are compared to experimental results from Strand et al. [14] and NASA contract report [29] or from work at ONERA in Figs. 15 and 16. It is seen that the results for pure HTPB, which always produces some soot or carbon residues, are represented by taking into account an emissivity

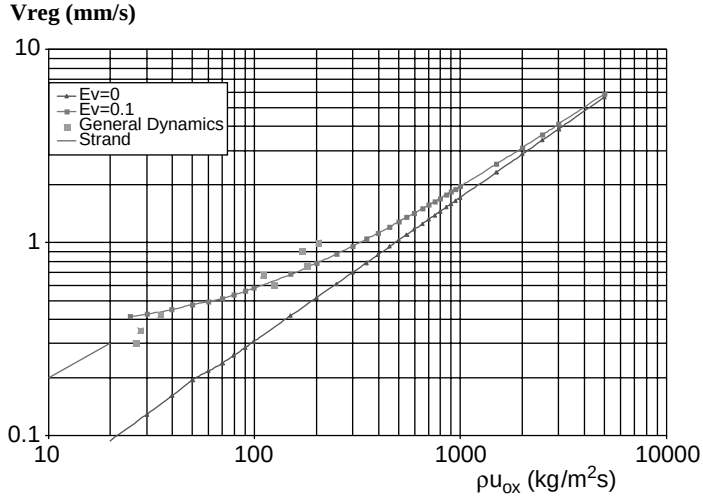

Fig. 15 Testing of the modeling of the solid fuel ablation; O_2 on HTPB, $L = 400$ mm, $\Phi_{in} = 40$ mm, regression rate.

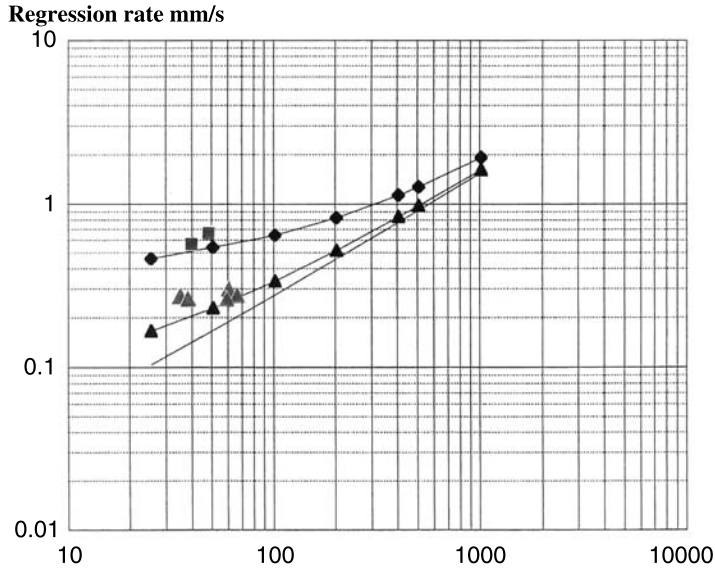

Fig. 16 Regression rate enhancement, specific mass flow rate $\rho u|_{ox}$ kg/m^2 · s, N_2O_4 on HTPB: —, $\varepsilon = 0.02$ computation; ▲, $\varepsilon = 0.1$ computation; ♦, $\varepsilon = 0.5$ computation; △, pure HTPB testing; and ■, HTPB + 4% carbon black testing.

of 0.1. When adding 4% carbon black in the HTPB, the results are represented with an emissivity of 0.5.

In Fig. 17, the effect of pressure, that is, no influence according to the model, is seen. (On this graph, at a given initial diameter of 40 mm and for given initial

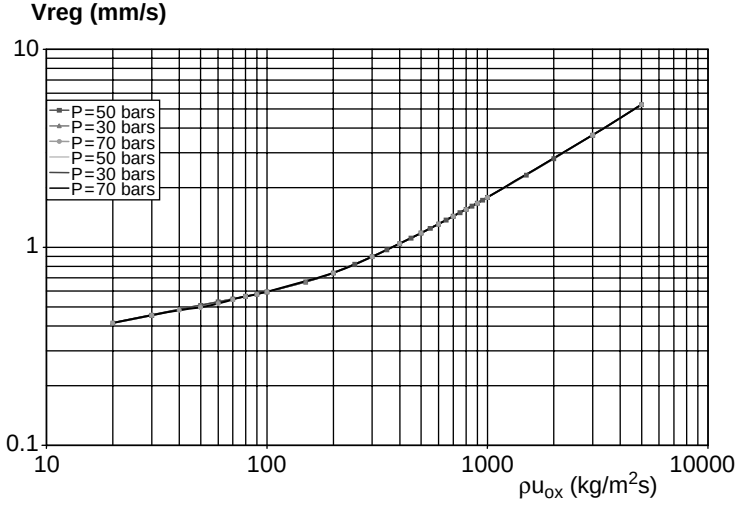

Fig. 17 Influence of pressure.

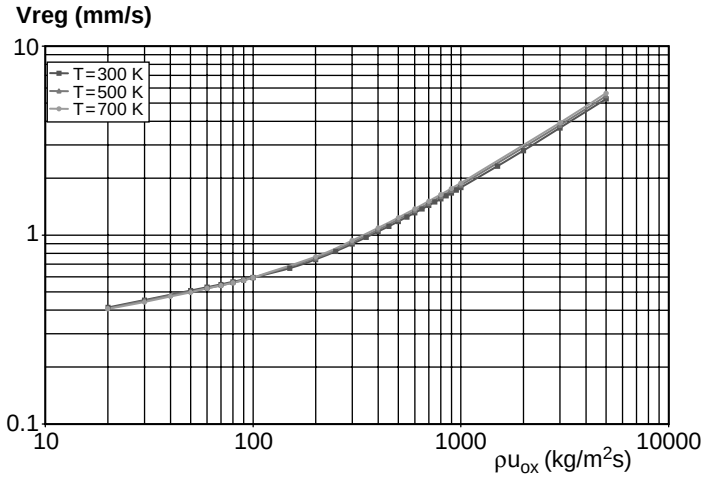

Fig. 18 Influence of injection temperature.

mass flow rates, the results are shown of computations following the evolution for 5 s of regression rate, with ρu_{ox} changing slightly due to the opening of the channel.) Notice that the experimental results of the NASA report [29] (Fig. 15) were obtained for a range of pressures from 88 to 425 psi (6 to 30 bars), with no visible impact. In Fig. 18, the effect of the initial temperature, reached in the weak precombustion that takes place in the forward dome, is also found to be very slight.

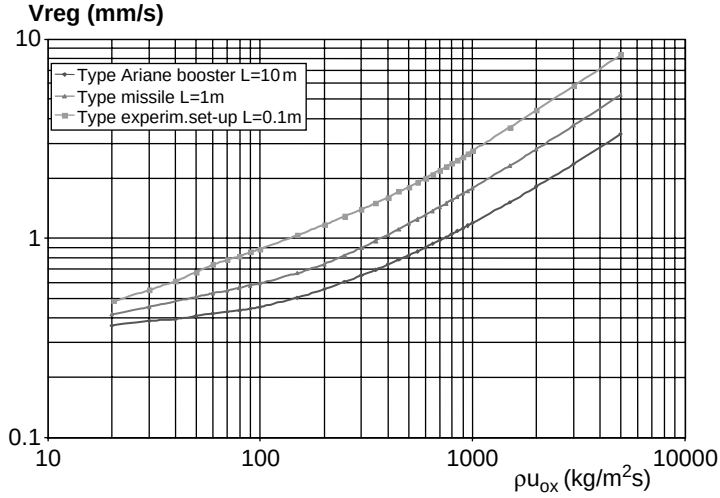

Fig. 19 Effect of scale.

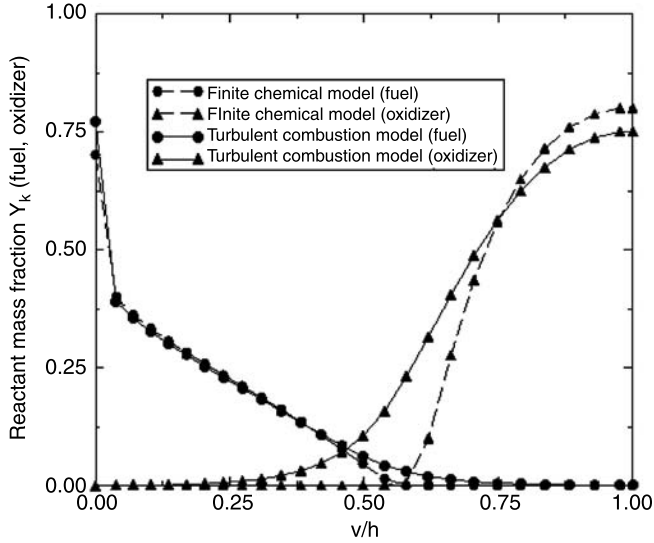

Fig. 20 Effect of distributed flame kinetics.

Finally, in Fig. 19, at a given specific mass flow rate ρu_{ox}, the effect of scale is shown to be fairly strong. A similar result was found in the full Navier–Stokes approach [18]. This effect is due to the change in shear-layer thickness, at a given mass flow rate, as the scale of the setup considered varies.

In Fig. 20, through the use of a two-dimensional approach obtained by parabolyzing the conservation equations [30], an option reveals the thickening of the flame due to the effect of turbulent combustion (here by using a simplified eddy breakup model), whereas taking into account finite chemical kinetics does not lead to any visible interpenetration of the reactants into each other. In any case, the fluxes at the surface are not affected by either of these phenomena, indicating that the simplifying option of a flame totally limited by the diffusion of the oxidizer and fuel gas is quite sufficient. The transverse profiles for the mass

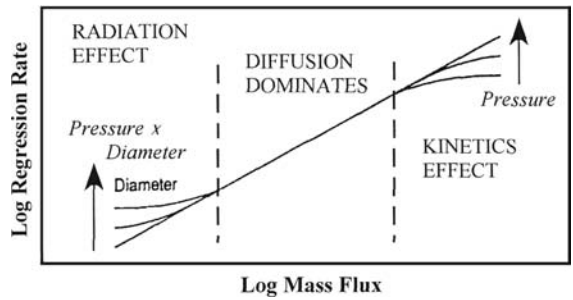

Fig. 21 Influence of parameters on the regression rate.

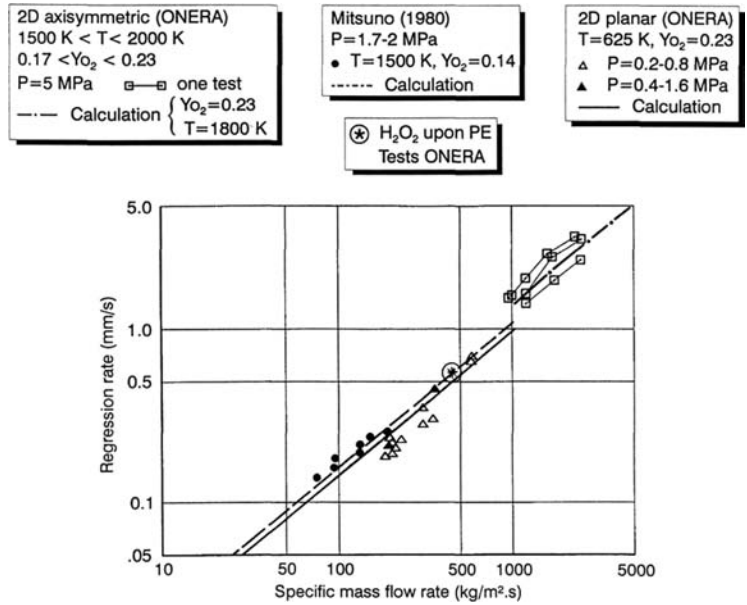

Fig. 22 Regression rate for PE, including at high oxidizer fluxes.

fractions ($x/L = 0.5$) shown in Fig. 20 lead to two conclusions: 1) The heat flux at the surface is not affected. 2) The transfer process is the limiting step.

In Fig. 21, tendencies that can be thought to be observed are indicated. At low mass fluxes, an effect of pressure could be observed via the influence of radiation. It was seen earlier that the effect of radiation, due essentially to the soot and carbon residues produced by the pyrolysis of the solid fuel, is taken into account by using an overall emissivity (which might depend on the nature of the fuel and is affected by the, frequently used, introduction of carbon black). At high mass flow rates, the diffusion of species toward each other becomes less limiting, and the kinetics of the reaction might become in part limiting. This effect would result in an impact of pressure on the ablation rate and a deviation from the $(\rho u)_{\text{ox}}^{0.8}$ trend. Results in Fig. 22 obtained at very high mass flow rates (in excess of $1000\,\text{kg/m}^2 \cdot \text{s}$) do not corroborate that this effect takes place.

IV. Ablation of Various Solid Fuels

A. Application to Polyethylene

PE has been used frequently in laboratory motors to understand the mechanisms of ablation. It can also be used in small motors. Its condensed-phase properties are presented in another chapter. Measurements were carried out at ONERA on both air-fed setups described earlier, as well as in the small hybrid motor. It was seen that the relation for the ablation rate [Eq. (9)] is obtained with the approximation of an overall reaction corresponding to full combustion; oxidizer and fuel do not go through the (possibly not thin) flame. In the case of PE with air, this overall

reaction is taken to be

$$C_2H_4 + 3O_2 \longrightarrow 2H_2O + 2CO_2 \tag{18}$$

$\Delta Q_g = 316 \times 10^3$ cal/mole of ethylene (or 11.3×10^3 cal/g of ethylene).

The first set of experimental results comes from the ONERA two-dimensional channel (Fig. 8) with air preheated at 625 K (Fig. 22) at different pressure levels. The calculation results shown take into account the values of the various parameters presented earlier. They also take into account the boundary-layer displacement thickness midlength of the slab.

Mitsuno [31] has obtained results in an axisymmetric grain, $L = 200$ mm and $\Phi_{\text{int}} = 40$ mm, fed with solid-propellant gases, with oxygen added, under conditions indicated in Fig. 22. The calculation agrees well with the experiments.

Results were also obtained on the ONERA axisymmetric setup (Fig. 8) for which high mass flow rates are produced. In this setup, the displacement thickness at $x = 100$ mm can be evaluated to be 0.2 mm, fully justifying a boundary-layer approach with initial conditions in the core flow. The ablation rate is measured with the ultrasonic transducers, producing a continuous curve $\dot{r}/\rho u$ as the channel opens up (Fig. 22). Calculations take into account the high surface temperature, $\approx$1000 K, predicted by the pyrolysis law as show in Fig. 5. They fall within the experimental results.

Results obtained with H_2O_2 as the oxidizer are shown in Fig. 23. The hydrogen peroxide used is 85% H_2O_2, 15% H_2O. Rusek [32] is an interesting source of information on the oxidizer and on candidate catalysts. Hydrogen peroxide at 85% has a specific mass of 1.36 g/cm^3. It has good propulsive properties, and it is an inexpensive propellant that can be used as a monopropellant to realize small impulses. The pure product is unstable and corrosive, but nontoxic. The introduction of stabilizers makes its use very safe, but there is somewhat of a risk of poisoning the catalytic bed, thus decreasing its decomposition efficiency. The main decomposition catalyst is silver. Among the different usable metals, aluminum is convenient for prolonged contacts; it can be used for tanks. Piping can be in aluminum or polyvinyl chloride.

The characteristics of the solution of hydrogen peroxide at 85% are as follows: specific mass (25°C), 1.36 g/cm^3; T fusion (°C), -17.2 (255.8 K); T boiling (°C), 137 (410 K); and heat of vaporization (kcal/mole H_2O_2), 16.08. The H_2O_2 at 85% decomposes in the catalytic bed according to

$$3H_2O_2 + H_2O \rightarrow 3H_2O + H_2O + 3/2O_2$$

reaching 600°C ($\approx$870 K) due to a heat of reaction of 2.9 MJ/kg of H_2O_2. The temperature at the exit of the catalytic bed is high enough to heat the PE to ignition. In the diffusion flame between oxidizer gases and decomposition gases, the reaction is stoichiometric according to

$$1/2C_2H_4 + 3/2O_2 + 4H_2O \rightarrow CO_2 + H_2O + 4H_2O$$

reaching about 2500 K and with a heat of reaction of 47.3 MJ/kg of C_2H_4 or 42.7 MJ/kg if equilibrium is reached, deviating somewhat from complete combustion. The stoichiometric ratio for complete combustion is 8.57. In the actual

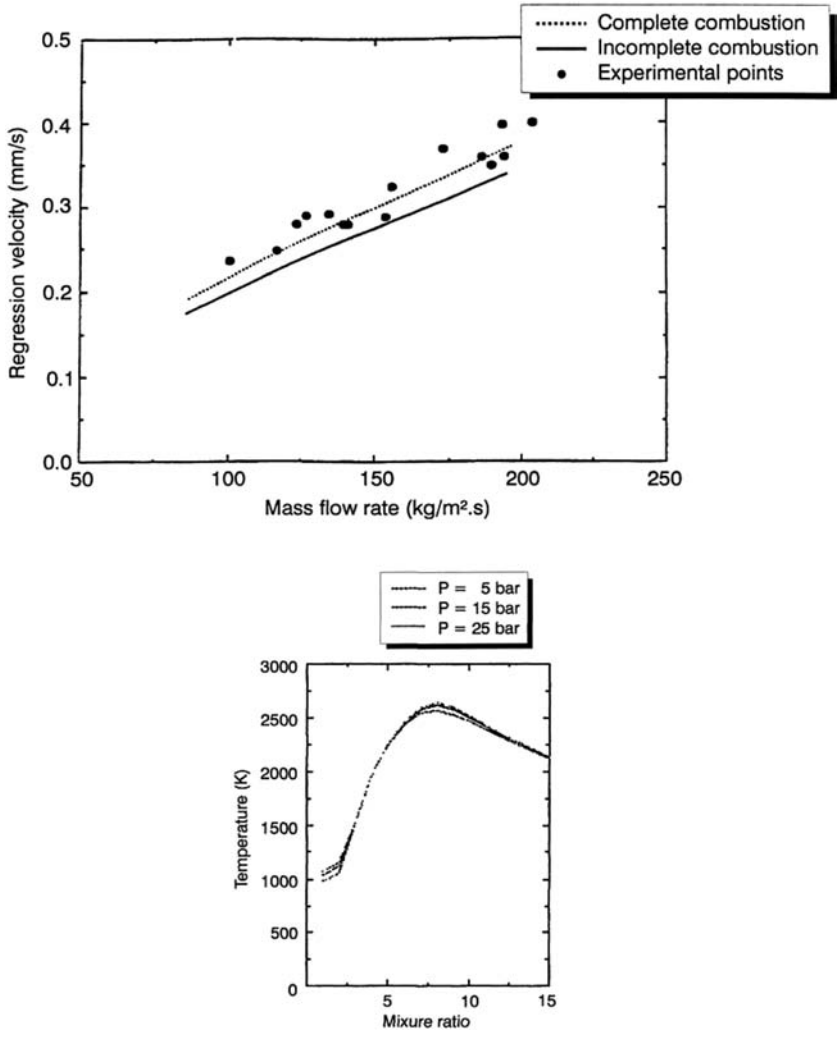

Fig. 23 Ablation rate for polyethylene with H_2O_2.

motor, the dimensioning has to be carried out so that, for a given oxidizer mass flow rate, the mass flow rate of combustible ablated from the inner surface of the grain is in the right proportion. The evolution of the flame temperature with the mixture ratio oxidizer/combustible is indicated in Fig. 23, where it is seen that the pressure level has an almost invisible effect, indicating a low level of dissociation.

The approach was applied to the firings carried out at Purdue University with H_2O_2 [33, 34].

Initial conditions (inputs for the code) are as follows: The loading geometry is 1 port axisymmetrical, length of the canal, and $L = 400$ mm; internal radius

$R_{\text{int}} = 13.3\,\text{mm}$; the initial temperature $T_i = 873\,\text{K}$; and the chamber pressure $P_c = 6.44 \times 10^5$ Pa. The evolution of the regression rate with the total mass flow rate is plotted. Calculations are undertaken in the case of incomplete and complete combustion (Fig. 23). Note that numerical and experimental results are very close, validating the code for the parameters of this study. Also note that these results for H_2O_2 (which in fact give O_2 after decomposition) are totally compatible with those of Fig. 22. Actually the curve of Fig. 23 is almost superimposed on the results of Mitsuno [31]. Also in Fig. 22 is a result from the setup of Fig. 9.

It is seen that there is a good agreement between the evaluation from the simplified approach and the results obtained under a wide range of pressure and specific mass flow rates. Pressure has no visible effect, whereas the specific mass flow rate is the controlling factor, as expressed by the diffusion-limited-flame mechanism.

B. Application to HTPB

As mentioned earlier, HTPB is a likely candidate for hybrid motors for space launchers. The overall reaction of gaseous products of HTPB with oxygen is taken as

$$C_4H_6 + 11/2O_2 \longrightarrow 3H_2O + 4CO_2 \tag{19}$$

The flame is assumed to be limited by diffusion; oxygen and gaseous fuel consume each other instantaneously. It has been assumed that the reaction corresponds to the stoichiometric proportions $C_4H_6 + 11/2O_2$, giving potentially complete combustion to CO_2 and H_2O. However, due to the high temperature reached in the flame (up to 3500 K), these gases can dissociate and the heat evolved is computed for the resulting equilibrium. For example, at 50 atm

$$\Delta Q_g = 367 \times 10^3\,\text{cal/mole of } C_4H_6 = 6.8 \times 10^3\,\text{cal/g}$$

(as compared to 576×10^3 cal/mole for the production of CO_2, H_2O without equilibrium, a ratio of 0.64).

A number of experiments have been carried out to better determine the mechanism of hybrid combustion of HTPB. Results are shown in Fig. 15 for O_2 on HTPB and in Fig. 16 from the ONERA experimental setup shown in Fig. 9, equipped with ultrasonic transducers, which in some instances used N_2O_4 as oxidizer. As already stated, in this setup, two types of HTPB were used, regular material and material with a few percent of additive, carbon black, which has been found to increase the radiation flux.

More recent measurements obtained at Pennsylvania State University [35], on a two-dimensional slab motor are considered (Figs 24 and 25). The geometry was symmetric, plane two-dimensional setup, $L \approx 585\,\text{mm}$ and $h \approx 12.8\,\text{mm}$, with the system fuel/oxidizer HTPB/O_2, and initial operating conditions at $Re = 3.5 \times 10^6$. An interesting feature of these experiments are the regression rate measurements vs time at a given location, with the ultrasonic technique or with x-ray radiography (which are seen to agree very well). Both this evolution and the regression rate (averaged over the firing sequence) along the length are compared against the integral method model. Also shown in Fig. 24 is a field of temperatures as obtained with the parabolyzed approach already mentioned. (This

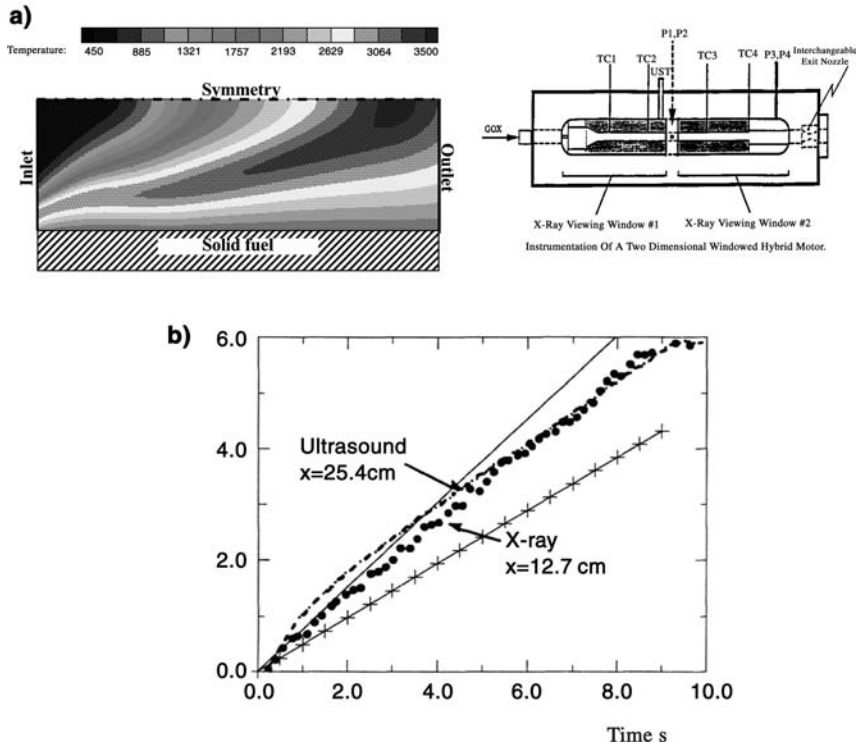

Fig. 24 Experiments at Pennsylvania State University: a) setup and b) regression rate model: —, emissivity 0.2 and +, emissivity 0.1.

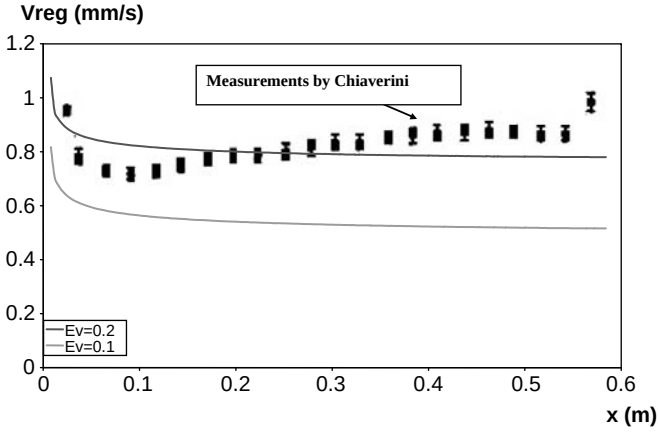

Fig. 25 Local regression rate model compared to experimental results.

approach generated Fig. 20.) The development of the flame reaching about 3500 K can be seen in Fig. 24. Reasonable agreement with the simplified model is found for an emissivity of 0.2. The fairly complete modelization by Venkateswaran and Merkle [18] leads to the conclusion that for this small device the radiation flux can be up to 30% of the total heat flux for oxidizer flux up to about 150 $\mathrm{kg/m^2 \cdot s}$. The problem is that the radiation comes from soot particles and carbon residues from the pyrolysis of the sold fuel and is hard to model. Large boosters, however, are likely to operate at oxidizer fluxes around 1000 $\mathrm{kg/m^2 \cdot s}$ where the radiative contribution has less impact (see Fig. 15).

At low specific mass flowrates, the measured results can be explained by the influence of radiation from the combustion gases. When the convective induced ablation rate is $\approx$1 mm/s at $\rho u = 300\ \mathrm{kg/m^2 \cdot s}$, the radiative component is very small. At $\rho u = 30\ \mathrm{kg/m^2 \cdot s}$, the convective ablation rate $\approx$0.2 mm/s, and the radiative component becomes more visible.

C. Considerations and Model for Ablation Mechanism of GAP

1. *Introductory Considerations*

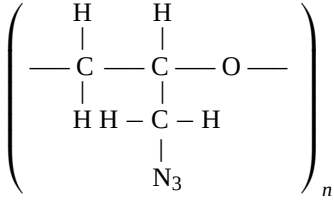

$n = 20$

The other considered fuel is GAP. As already stated, some information about the origins of this polymer may be found in by Frankel et al. [19]. Results on the behavior under pyrolysis or combustion were presented earlier. Because of the N_3 group, it has an exothermic decomposition of -150 cal/g. The heat of ablation is about 70 cal/g, from $c_p(T_s - T_0)$ evaluated at about 220 cal/g (for a surface temperature of about 780 K, for example, at 0.5 cm/s). This should be compared to the high endothermic heat of ablation of HTPB. Ablation gases resulting from this degradation, although weakly oxidizer containing, are able to sustain a premixed flame probably reaching 1350 K. GAP will then possess an autonomous burning rate,

$$\dot{r} = 0.13P^{0.55}$$

(with the $\dot{r}$ in centimeters per second for P in bars) such that at 40 bars it reaches about 1 cm/s. At the end of this premixed flame, the mole fractions of the gases indicated in Table 1 (according to equilibrium computations) are obtained [20]. These still combustible gases can participate in a final flame, after diffusion toward the oxidizing gases from the main flow.

The various mechanisms involved in inducing the regression of condensed materials are presented in Fig. 26. Here the regression mechanism is

$$\Phi_{\text{external}} = \rho_p \dot{r} \underbrace{[c_p(T_s - T_0) + h_D]}_{\sim 250\ \mathrm{cal/g}}$$

Table 1 Gases at the end of the premixed flame

Gas	X_i
N_2	19
C(s)	30
CO	14
CO_2	0.35
CH_4	3.7
H_2	31.5
H_2O	1.6

where a negative h_D is exothermic. A solid propellant regresses under the influence of its own flame, which is sensitive to pressure. When a strong mass flow rate sweeps the surface, turbulence enters into the flame zone (a few tens of micrometers) and enhances the exchange with the surface and, thus, the regression rate (the propellant burning rate), resulting in erosive burning [27, 28]. In the case of a pure fuel such as HTPB, the degradation is endothermic and the heat of ablation is around 700–800 cal/g. The heat flux comes from the diffusion flame between pyrolysis gases and oxidizing gas, as described earlier. GAP has an exothermic heat of degradation and, therefore, a low heat of ablation. Its flame is fairly weak, raising the temperature from 800 K at the surface to a rough estimate of 1350 K at the end of combustion, but nevertheless keeps the material regressing at ≈10 mm/s. When GAP is exposed to an oxidizing flow, two modes of regression could operate: a hybrid mode in which the weak flame is swept away and canceled by the flow and the heat flux comes entirely from the diffusion flame, or a complex mode in which the flux received by the surface is from the autonomous flame as well as from the diffusion flame with the oxidizing stream.

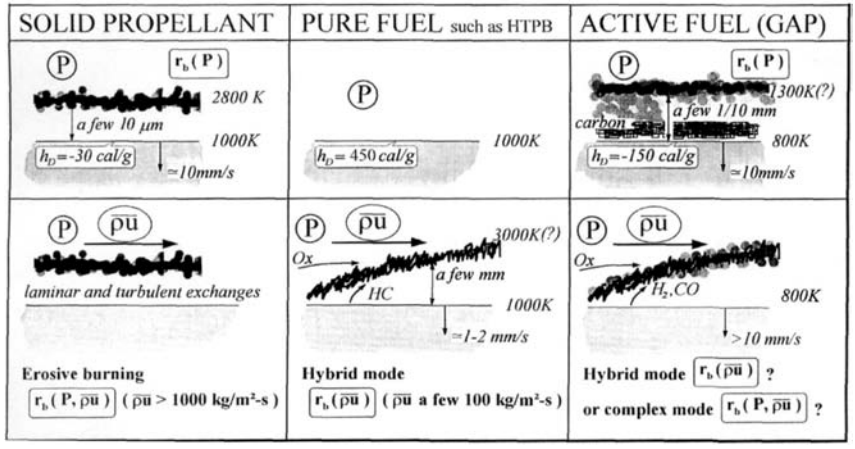

Fig. 26 Mechanisms of regression of condensed materials.

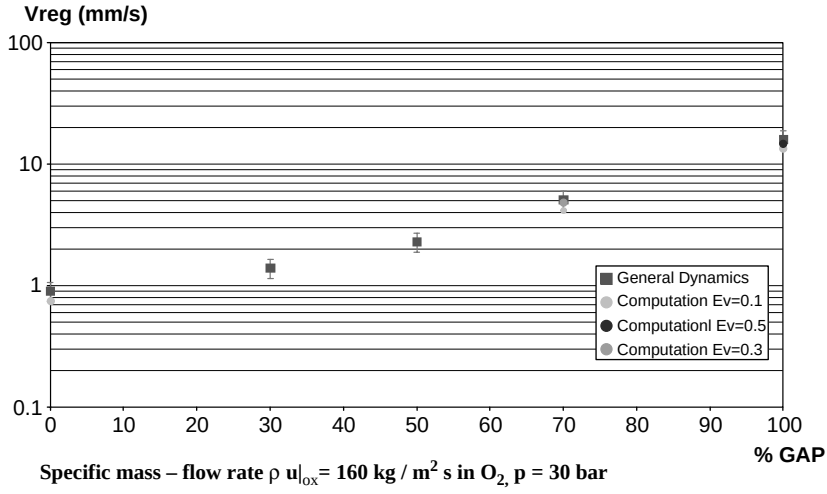

Fig. 27 Burning rate of GAP in an oxidizer flow.

In the case of the hybrid mode, the description of Eq. (9) can be applied. One has to evaluate ΔQ_g, the heat evolved in the combustion of the gaseous decomposition products of GAP with oxygen. The equivalent heat from the solid material is obtained from the reaction

$$C_{3.3}H_{5.6}O_{1.1}N_{2.6} + (3.3 + 5.6/4 - 1.1/2)O_2 \longrightarrow$$
$$(5.6/2)H_2O + 3.3CO_2 + (2.6/2)N_2$$
$$\Delta Q_g \text{ (from solid)} = 500 \times 10^3 \text{ cal/mole of GAP}$$

(taking into account the heat of formation of GAP of $+280$ cal/g). With the heat of degradation of solid GAP into gases being -150 cal/g (exothermic),

$$\Delta Q_g \text{ (from gaseous products of GAP)} = 485 \times 10^3 \text{ cal/mole}$$
$$(4.85 \times 10^3 \text{ cal/g of gaseous GAP})$$

Compared to HTPB for $\rho u = 160\,\text{kg/m}^2 \cdot \text{s}$ (to compare to the results of Fig. 27 [29]) the results for GAP (with $T_e = 1000$ K) are in Table 2.

Table 2 HTPB and GAP comparison

Fuel	T_s, K	h_{abl}, cal/g	B	$\dot{r}$, mm/s
HTPB	1100	745	4.3	0.7
GAP	725	45	83	1.9

Although the ablation parameter B is much larger than for HTPB, it is seen that the increase in ablation rate is moderate. This is due to the regulation mechanism of the blocking effect: When the injection rate at the surface increases, consequently, it tends to reduce the heat flux. [This is expressed by the term $\ell n(1 + B)$ in Eq. (11)]. It is also found that the regression rate resulting from pure hybrid behavior falls very short of the measured rate in Fig. 27. Thus, it appears that when GAP is used as a hybrid fuel it behaves mostly like a solid propellant with its self-burning and essential sensitivily to pressure, with an added effect of the final diffusion flame. The modeling of the regression of GAP when exposed in a hybrid flow amounts to the superimposition of the heat flux from its premixed flame and the heat flux from the main flame (such as that taken into account for pure combustible materials).

2. *Model for Ablation of GAP*

The combustion mode of GAP can be divided in three zones (Fig. 28):

1) Zone 1, zone of nonreactive heat conduction, $T_0 = 293\,\text{K}$.

2) Zone 2, zone of condensed-phase reaction zone, $T_s \approx 700\,\text{K}$.

3) Zone 3, zone of gaseous-phase reaction where the combustion products are formed, $T_g = 1365\,\text{K}$ (at 50 bar).

Observe that the combustion of GAP produces a large amount of carbon residues. This will be taken into account when evaluating the radiation component to the heat flux.

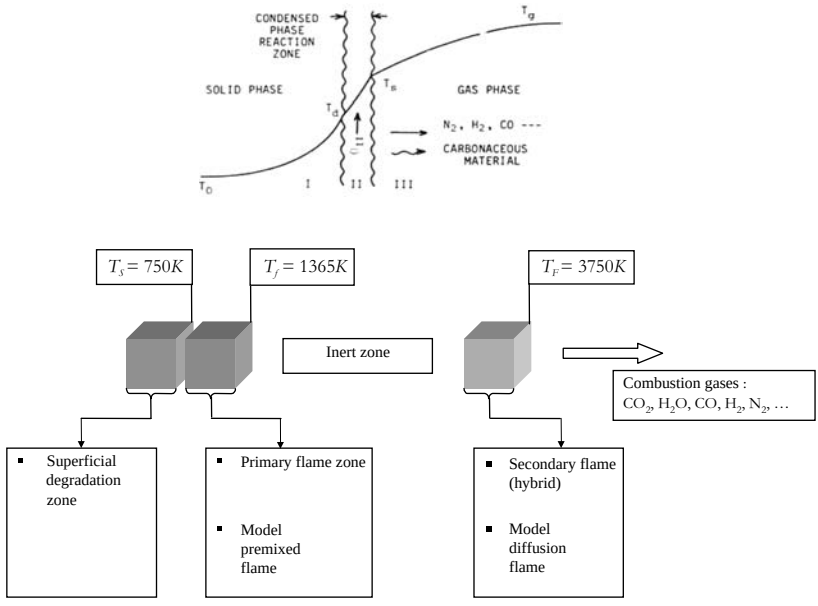

Fig. 28 Combustion mechanism of GAP; abundant carbon residue should enhance the emissivity.

As shown, preliminary computations show that a combined regime occurs for GAP. The aim of the present approach is twofold: a model of the diffusion flame, as already demonstrated, and a model of an autonomous flame (Fig. 28). The autonomous flame of the GAP is modeled similarly to that of homogeneous propellants, following Williams [36]. This approach takes into account a reaction rate following an Arrhenius law $\exp(-E_g/RT)$, with a high activation energy. Thus, there is an induction zone where the reaction rate is low and a thin-flame zone.

Two cases are considered: GAP at 100% and mixture at 70% GAP/30% HTPB. This second composition is interesting because such a composition, while maintaining high regression rates, will extinguish when the oxidizer flow is interrupted [29]. This can be interesting for operations with start-and-go pulses.

The conservation of energy in the flow expressed in a frame tied to the surface regressing at $\dot{r}$, with $x > 0$ in the gaseous phase, is

$$\dot{m}c_g \frac{\mathrm{d}T}{\mathrm{d}x} = \lambda_g \frac{\mathrm{d}^2T}{\mathrm{d}x^2} + Q_g \left(\frac{P}{T}\right)^{\mathrm{m}} B \exp\left(\frac{-E_g}{RT}\right) \tag{20}$$

The last term is the energy released by the reaction, $Q_g > 0$ in calories per gram. The terms c_g and λ_g are the specific heat capacity and the conductivity of the gases (estimated at an average temperature). The specific mass flow rate of the gases $\dot{m}$ in grams per square centimeter per second, due to mass conservation, is constant and equal to $\dot{m} = \rho_p \dot{r}$. The exponent m is the order of the reaction.

In the nonreactive zone, the temperature evolution results from the balance,

$$\dot{m}c_g \frac{\mathrm{d}T}{\mathrm{d}x} = \lambda_g \frac{\mathrm{d}^2T}{\mathrm{d}x^2} \tag{21}$$

with the limiting conditions

$$T = T_s; \qquad x = 0 \tag{22}$$

$$\lambda_g \left.\frac{\mathrm{d}T}{\mathrm{d}x}\right|_{x=0} = \dot{m}Q_c = \dot{m}\left(c_g T_s - c_p T_0 - Q_s\right) \tag{23}$$

The heat flux from the flame to the surface maintains the heat rise from T_0 to T_s, the heat evolved from the decomposition being taken into account.

The temperature profile from Eq. (21) is

$$T = T_s + (Q_c/c_g)\left[\exp(\dot{m}xc_g/\lambda_g) - 1\right] \tag{24}$$

This solution satisfies the boundary conditions. The temperature at the end of the flame T_f is reached at a height x_f (flame standoff distance) given by Eq. (24) with $T = T_f$,

$$x_f = (\lambda_g/c_g\dot{m})\ell n\left[1 + c_g\left(T_f - T_s\right)/Q_c\right] \tag{25}$$

The overall conservation of energy between initial material and end of flame at T_f can be added to relation (25),

$$\dot{m}\left(c_g T_f - Q_g\right) = \dot{m}\left(c_p T_0 + Q_s\right) \tag{26}$$

This relation can also be written as

$$Q_c + c_g\left(T_f - T_s\right) = Q_g \tag{27}$$

When relations (27) and (25) are combined,

$$x_f = (\lambda_g / c_g \dot{m})\, \ell n\, \left(Q_g / Q_c\right) \tag{28}$$

is obtained. The flame height has been obtained with a simplified assumption of a thin flame. This is applicable for a high activation energy. In this case, the order of magnitude of the flame thickness with $\xi_g = E_g / RT_f$ is given by

$$e_{\text{reaction}} \propto (\lambda_g / c_g \mathring{m}) \left[\xi_g (Q_g / c_g T_f)\right]^{-1} \tag{29}$$

When $\xi_g \gg 1$, then $e_{\text{reaction}} \propto x_f / \xi_g$. The reaction zone is much smaller than the flame height.

In this zone of active chemical reactions, the temperature is close to the flame temperature T_f [36],

$$\left[(T_f - T)/T_f\right] \propto (1/\xi_g) \ll 1 \tag{30}$$

It can be stated that for activation energies high enough ($\approx$40 kcal/mole) the approximation of a thin flame is sufficient. For GAP, $1/\xi_g$ is equal to 0.07, and the estimation of x_f is considered to be adequate. The flame having been characterized by Eq. (28), the heat flux to the surface of the solid fuel can now be evaluated.

Conservation equation (20) can be written in terms of the heat flux $q = \lambda_g (\mathrm{d}T/\mathrm{d}x)$ as

$$\dot{m} \frac{c_g}{\lambda_g} q = \frac{\mathrm{d}}{\mathrm{d}x}\,(q) + Q_g \left(\frac{p}{T}\right)^m B \exp\left(\frac{-E_g}{RT}\right) \tag{31}$$

This equation can be written as

$$\frac{\mathrm{d}}{\mathrm{d}x}\left[q \exp\left(\frac{-\dot{m} c_g x}{\lambda_g}\right)\right] = -Q_g \left(\frac{p}{T}\right)^m B \exp\left(\frac{-E_g}{RT}\right) \exp\left(\frac{-\dot{m} c_g x}{\lambda_g}\right) \tag{32}$$

When this equation is summed from surface to the end of flame (where downstream of the flame the flux, under conditions of autonomous combustion, is $q \to 0$)

$$q(0) = \int_0^\infty Q_g \left(\frac{p}{T}\right)^m B \exp\left(\frac{-E_g}{RT}\right) \exp\left(\frac{-\dot{m} c_g x}{\lambda_g}\right) \mathrm{d}x \tag{33}$$

is obtained. This relation shows that the heat flux to the surface results from the heat evolved in the flame zone.

If the approximation $\xi_g \gg 1$ is used, which amounts to taking Eq. (29) into account, a simplified expression is obtained,

$$q(0) \approx Q_g \left(\frac{p}{T}\right)^m B \exp\left(\frac{-E_g}{RT_f}\right) \exp\left(\frac{-\dot{m} c_g x_f}{\lambda_g}\right) \frac{\lambda_g}{c_g \dot{m}} \left[\xi_g \frac{Q_g}{c_g T_f}\right]^{-1} \tag{34}$$

The heat flux maintains the mass flux,

$$q(0) = \lambda_g \left.\frac{\mathrm{d}T}{\mathrm{d}x}\right|_0 = \dot{m}Q_c \equiv \rho_p v_c \left[c_g T_s - c_p T_0 - Q_s\right] \tag{35}$$

After Eq. (28) is taken into account for the flame height, the flux $q(0)$ is written as

$$q(0) \approx \left(p/T_f\right)^{m/2} \exp\left(\frac{-\xi_g}{2}\right) Q_c \left[B\lambda_g (T_f/\xi_g Q_g)\right]^{1/2} \tag{36}$$

The mass flux from the material surface, or the burning rate, is then

$$\overset{\circ}{m} = \rho_p \dot{r} = q(0)/Q_c \tag{37}$$

The decomposition of GAP produces a large amount of carbon residues, which has to be taken into account by adding a radiation component

$$\overset{\circ}{m} = \rho_p \dot{r} = [q(0) + \varphi_{\mathrm{ray}}]/Q_c \tag{38}$$

3. Application to 100% GAP Case

This is to be adjusted to the experimental burning rate,

$$\dot{r} = 0.13P^{0.55} \tag{39}$$

An expression for the heat flux is obtained with respect to the known parameters,

$$q(0) = P_p 0.13P^{0.55} \tag{40}$$

The gas heat capacity c_g is taken as equal to that of nitrogen as a representative average gas between the temperatures $T = 500\,\mathrm{K}$ and $T = 1500\,\mathrm{K}$. The value of the heat flux $q(0)$ is evaluated along the length of the canals at each step dx because T_s and Q_c vary with the local regression rate.

4. Application to 70% GAP/30% HTPB Composition Case

The mixing of the two components does not allow the regression rate as influenced by pressure to be known. First, the activation energy of the gas-phase reaction is needed, which has a strong impact in Eq. (36). The measured sensitivity of the pure GAP burning rate to the initial temperature can be used for this determination,

$$\sigma_p = \left.\frac{\partial \ell n \dot{m}}{\partial T_0}\right|_P \tag{41}$$

where σ_p characterizes the influence of T_0 on T_f and the burning rate is under the influence of the flame temperature. For pure GAP, $\sigma_p = 0.01\,\mathrm{K}^{-1}$ [20].

With $\dot{m}$ from Eqs. (36) and (37) and with the experimental value of σ_p, the activation energy in the gas-phase reaction E_g is obtained from

$$\sigma_p = \frac{\partial \ell n \dot{m}}{\partial T_0} = \frac{1}{\dot{m}} \frac{\partial \dot{m}}{\partial T_0} = \frac{1}{\dot{m}} \frac{\partial \dot{m}}{\partial T_f} \frac{\partial T_f}{\partial T_0}$$

When the overall energy balance is taken into account,

$$h_i^0 + c_p T_0 = h_f^0 + c_g T_f; \qquad \frac{\partial T_f}{\partial T_0} = \frac{c_p}{c_g}$$

$$\sigma_p = \tfrac{1}{2} c_p / c_g \left\{ E_g / R T_f^2 \right\}$$

and finally

$$E_g = \left\{ 2\sigma_p c_g R T_f^2 / c_p \right\} \tag{42}$$

Thus, the activation energy is obtained from known parameters. For $c_p = 0.45\,\text{cal/g} \cdot \text{K}$ and $c_g = 0.28\,\text{cal/g} \cdot \text{K}$, the likely value $E_g = 45 \times 10^3\,\text{cal/mole} \cdot \text{K}$, is found.

The burning rate of the GAP/HTPB mixture under the influence of pressure can now be computed as compared to that of pure GAP,

$$\frac{\dot{m}_{\%}}{\dot{m}_{\text{PAG}}} = \exp\left\{ \frac{E_g}{2R} \left(\frac{1}{T_f|_{\text{PAG}}} - \frac{1}{T_f|_{\%}} \right) \right\} \left\{ \frac{Q_g|_{\text{PAG}}}{Q_g|_{\%}} \right\}^{1/2} \tag{43}$$

In this expression, the heat of reaction in the gas phase depends on the flame and surface temperatures,

$$Q_g = c_g (T_f - T_s) + Q_c$$

5. Comparison of Results [29]

In the NASA contract report [29], measurements were carried out under hybrid combustion conditions, with O_2/GAP or GAP/HTPB mixtures, with the following characteristics: $L_c = 0.4\,\text{m}$, $P_0 = 30\,\text{bars}$, and $D_{cc} = 4\,\text{cm}$. The effect of the final flame between pyrolysis gases and oxidizer gas is computed following the method established for pure fuel materials.

It is assumed that only hydrogen and methane are reacting in the diffusion flame.

$$\text{100\%GAP} \qquad 44.97\text{H}_2 + 5.25\text{CH}_4 + 32.98\text{O}_2 \longrightarrow 5.25\text{CO}_2 + 55.47\text{H}_2\text{O} \tag{44}$$

$$\text{70\%GAP} \qquad 31.5\text{H}_2 + 3.7\text{CH}_4 + 0.3\text{C}_4\text{H}_6 + 24.8\text{O}_2 \rightarrow 4.9\text{CO}_2 + 39.8\text{H}_2\text{O} \tag{45}$$

The reaction between GAP and oxygen creates a heat of reaction of $Q_r = 2.14\,\text{MJ/mole}$ (510,000 cal/mole) or 21.6 MJ/kg (GAP) (5200 cal/g of GAP).

The General Dynamics measurements [29] were carried out twice around $160\,\text{kg/m}^2 \cdot \text{s}$: It is then possible to evaluate a bar of dispersion as indicated on Fig. 27. The results of the modelization are compared in Fig. 27 to the measurements [29] (The results [29] for pure HTPB are also in Fig. 15.) Although most of the regression comes from the conduction flux (and within that to a large extent from the autonomous flame of the GAP, which creates a regression rate of about

8.5 mm/s), when an emissivity of 0.5 is taken into account (justified by the large amount of carbon material ejected from the combustion of GAP) the match to the measurement is quite good. Also indicated in Fig. 27 are the results for the mixture of 70% GAP and 30% HTPB, which responds to the (weakened) autonomous flame and to the final flame with the oxidizer gases. (The less abundant carbon production is reflected by the emissivity of 0.3 required to reproduce the experiment.) In practical application, if extinction of the propulsion by closing the flow of the oxidizer is requested, without doubt pure GAP cannot be used because it would probably maintain its autonomous burning. It is stated in the final report [29] that mixtures below 70% GAP are self-extinguishing, an interesting feature to keep in mind.

V. Conclusion

The aim of this work is to understand the process of ablation of fuels for hybrid propulsion applications. This process involves the condensed phase and the heat flux from the reacting flow. The condensed-phase process is a thermal degradation (nonpressure sensitive), which can be described from the knowledge of the degradation kinetics as obtained by DSC or TGA (thermo-gravimetric analysis). This approach is applied to PE, HTPB, and GAP. Values for the heat of ablation of these three materials are given, about 800 cal/g for the two inert polymers and about 70 cal/g for the active polymer GAP.

The heat flux from the diffusion flame is described from simple concepts. It is shown to represent adequately the results for PE and HTPB on small laboratory or demonstration motors (at ONERA, with the use of an ultrasonic technique for measuring the regression rate, or in the literature [29, 35]). The measured ablation rates of GAP are much too high to be accounted for by a pure hybrid mode. Although exposed to external mass flow rates, GAP keeps its flame, which allows for high regression rates, $\approx$15 mm/s as compared to $\approx$1 mm/s for PE and HTPB.

Acknowledgments

Partial support from (the then) Direction de la Recherche et de la Technologie of Délégation Générale à l'Armement was obtained. Early contributions by B. Fourest and C. Guin as well as participation in the experiments by Y. Maisonneuve and P. Prevot are recognized.

References

[1] Altman, D., "Hybrid Rocket Development History," AIAA Paper 91-2515, June 1991.

[2] Calabro, M., "European Hybrid Propulsion History," AIAA Hybrid Propulsion Lecture Series, 29th AIAA Aerospace Sciences Meeting, Jan. 1990.

[3] Kuentzmann, P., and Sternfeld, H. J., "What Future for Hybrid Propulsion," ESA Colloquium, Bordeaux, June 1991.

[4] Goldberg, B. E., and Wiley, D. R., "Hybrids: Best of Both Worlds," *Aerospace America*, pp. 28–31, June 1991.

[5] Cook, J. R., Goldberg, B. E., Estey, P. N., and Wiley, D. R., "Hybrid Rockets: Combining the Best of Liquids and Solids," *Aerospace America*, July 1992.

[6] Estey, P. N., "Hybrid Rockets," *Aerospace America*, Dec. 1992.

[7] "Amroc Hybrid Motor Tests Aimed at 1995 Flight," *Aviation Week and Space Technology*, 1 March 1993.
[8] Story, G., Zoladz, T., Arves, J., Kearny, D., Abel, T., and Park, O., "Hybrid Propulsion Demonstration Program 250 K Hybrid Motor," AIAA Paper 2003-5198, July 2003.
[9] Lengellé, G., "Thermal Degradation Kinetics and Surface Pyrolysis of Polymers," *AIAA Journal*, Vol. 8, No. 11, 1970, pp. 1989–1996.
[10] Lengellé, G., Duterque, J., and Trubert, J. F., "Physico-Chemical Mechanisms of Solid Propellant Combustion," *Solid Propellant Chemistry, Combustion, and Motor Interior Ballistics*, Vol. 185, Progress in Astronautics and Aeronautics, AIAA, Reston, VA, 2000, pp. 287–332.
[11] Lengellé, G., Fourest, B., Godon, J. C., and Guin, C., "Condensed Phase Behavior and Ablation Rate of Fuels for Hybrid Propulsion," AIAA Paper 93-2413, June 1993.
[12] Blazowski, W. S., Cole, R. B., and Mc Alevy, R. F., "An Investigation of the Combustion Characteristics of Some Polymers Using the Diffusion-Flame Technique," Stevens Inst. of Technology, Technical Rept. TR ME-RT 71004, June 1971.
[13] Compton, D. L., et al., "Measurements of the Effective Heats of Ablation of Teflon and Polyethylene," NASA TN D1332, Aug. 1962.
[14] Strand, L. D., Jones, M. D., and Ray, R. L., "Characterization of Hybrid Rocket Internal Flux and HTPB Fuel Pyrolysis," AIAA Paper 94-2876, June 1994.
[15] Cohen, N. S., Fleming, R. W., and Derr, R. L., "Role of Binders in Solid Propellant Combustion," *AIAA Journal*, Vol. 12, No. 2, 1974, pp. 212–218.
[16] Chiaverini, M. J., "Regression Rate and Pyrolysis Behavior of HTPB-Based Solid Fuels in a Hybrid Rocket Motor," Ph.D. Dissertation, Dept. of Mechanical Engineering, Pennsylvania State Univ., University Park, PA, Dec. 1997.
[17] Cheng, G. C., Farmer, R. C., Jones, H. S., and Mc Farlane, J. S., "Numerical Simulation of the Internal Ballistics of a Hybrid Rocket Motor," AIAA Paper 94-0554, Jan. 1994.
[18] Venkateswaran, S., and Merkle, C. L., "Size Scale-up in Hybrid Rocket Motors," AIAA Paper 96-0647, Jan. 1996.
[19] Frankel, M. B., et al., "Historical Development of Glycidyl Azide Polymer," *Journal of Propulsion and Power*, Vol. 8, No. 3, 1992, pp. 560–563.
[20] Kubota, N., and Sonobe, T., "Combustion Mechanism of Azide Polymer," *Propellants, Explosives and Pyrotechnics*, Vol. 13, 1988, pp. 172–177.
[21] Trubert, J. F., Duterque, J., and Lengellé, G., "Study of the Condensed Phase Degradation and Combustion of Glycidyl Azide Polymer (GAP)," 30th International Annual Conf. of ICT, Karlsruke, June 1999.
[22] Cauty, F., "Non-Intrusive Measurement Methods Applied to Energetic Material Regression Rate and Determination," 2nd International High Energy Materials Conf., Chennai, India, 8–10 Dec. 1998.
[23] Marxman, G. A., "Boundary Layer Combustion in Propulsion," *Eleventh Symposium International on Combustion*, Combustion Inst., Pittsburgh, PA, 1966.
[24] Marxman, G. A., and Wooldridge, C. E., "Research on the Combustion Mechanism of Hybrid Rockets," *Advances in Tactical Rocket Propulsion*, 25th Meeting AGARD Combustion and Propulsion Panel, April 1965.
[25] Williams, F. A., "Grain Design and Throttling of Hybrid Rocket Motors," Inst. for Defense Analysis, Research Paper P. 119, March 1964.
[26] Salita, M., "Comparison of Four Boundary Layer Solutions for Fuel Regression Rate in Classical Hybrid Rocket Motors," AIAA Paper 91-2520, June 1991.

[27] Godon, J. C., Duterque, J., and Lengellé, G., "Solid Propellant Erosive Burning," *Journal of Propulsion and Power*, Vol. 8, No. 4, 1992.

[28] Godon, J. C., Duterque, J., and Lengellé, G., "Erosive Burning in Solid Propellant Motors," *Journal of Propulsion and Power*, Vol. 9, No. 6, 1993.

[29] "Hybrid Propulsion Technology," Final Rep. NASA CR 183972-183973-183974-183975, General Dynamics–Thiokol–Rocketdyne, Nov. 1989.

[30] Wang, H. Y., Most, J. M., Simon, P., and Lengellé, G., "Prediction of Fuel Regression Rate in Confined Turbulent Boundary Layer Combustion," *5th International Symposium in Chemical Propulsion*, Begell House, New York, 2002.

[31] Mitsuno, M., et al., "Experimental Study on Solid Fuel Ram Rocket," International Astronautical Federation 31st Congress, IAF Paper 80-269, Sept. 1980.

[32] Rusek, J. J., "New Decomposition Catalysts and Characterization Techniques for Rocket Grade Hydrogen Peroxide," *Journal of Propulsion and Power*, Vol. 12, No. 3, 1996, pp. 574–579.

[33] Wernimont, E. J., and Meyer, S. E., "Hydrogen Peroxide Hybrid Rocket Engine Performance Investigation," AIAA Paper 94-3147, June 1994.

[34] Wernimont, E. J., and Heister, S. D., "Progress in Hydrogen Peroxide-Oxidized Hybrid Rocket Experiments," AIAA Paper 96-2696, July 1996.

[35] Chiaverini, M. J., Harting, G. C., Lu, Y. C., Kuo, K. K, Serin, N., and Johnson, D. K., "Fuel Decomposition and Boundary Layer Combustion Processes of Hybrid Rocket, Motors," AIAA Paper 95-2686, July 1995.

[36] Williams, F. A., "Quasi Steady Flame Theory in Unsteady Burning of Homogeneous Solid Propellants," *AIAA Journal*, Vol. 11, No. 9, 1973.

This page intentionally left blank

Chapter 4

Solid-Fuel Pyrolysis Phenomena and Regression Rate, Part 2: Measurement Techniques

Franck Cauty*

ONERA, Office National d'Études et de Recherches Aérospatiales, Châtillon, France 92230

Nadir Serýn†

Tubitak Sage, Scientific and Technical Research Council of Turkey, Ankara, Turkey

Daniel Gramer‡

Orbital Technologies Corporation, Madison, Wisconsin 53717

Nomenclature

A = Plasma capacitance gauge area, m^2
A_p = instantaneous grain port cross-sectional area, Eq. (4), cm^2
a = classical regression law constant, Eq. (1)
b = curve-fit exponent
C = mechanical wave velocity, m/s
C = general constant, Eq. (6)
dP/dt = pressure gradient, MPa/s
G_0 = oxidizer mass flux, Eq. (1), $kg/cm^2 \cdot s$
$I_{(\theta)}$ = x-ray intensity arriving at the input screen of the image intensifier at an angle of θ, R/s
I_0 = initial x-ray intensity, R/s
k = wave number
k_P = wave velocity variation coefficient with respect to pressure, MPa^{-1}
k_T = wave velocity variation coefficient with respect to temperature, K^{-1}

*Research Engineer, Fundamental and Applied Energetics Department. Member AIAA.
†Chief Research Engineer. Member AIAA.
‡Principal Mechanical Engineer. Senior Member AIAA.

$L_{(\theta)}$ = interaction length of x ray and material, m
ℓ_0 = initial thickness, m
m = linear attenuation coefficient of photoelectric absorption, m^{-1}
m_0 = oxidizer mass flow rate, Eq. (3), kg/s
n = classical regression law exponent, Eq. (1)
P = pressure, MPa
R_f = cumulative web regression at time t_f, Eq. (8), cm
R_p = initial grain port radius at $t = 0$, Eq. (4), cm
R_t = cumulative web regression at time t, Eq. (2), cm
r = instantaneous surface regression rate, Eq. (1), cm/s
r_b, R_b = burning rate, mm/s
T = temperature, K
t = time, Eq. (6), s
t_f = elapsed time between first and last data point, s
ΔC = capacitance change
ε = permittivity or dielectric constant
λ = wavelength, m
σ_P = initial temperature sensitivity of the burning rate at constant pressure, K^{-1}
τ = propagation time, μs

Subscripts

ϕ = phase shift, deg
b = burning
c = cutoff
G = grain
P = pressure
ref = reference conditions
T = temperature
0 = initial conditions

I. Introduction

AN accurate determination of the quasi-steady state and transient burning rate of solid propellants (which will be mentioned several times because they have been the object of more applications than solid fuels), solid fuels, and other materials is required for validating the design of any propulsion device.

For hybrid propulsion, the solid-fuel regression rate is of course an important parameter for performance prediction. Early studies on hybrid rocket motor regression characteristics generally employed average values of the regression rate based on measuring the fuel geometry or mass before and after motor firing. These data were utilized in developing correlations that contain the mass flux raised to an empirical power. Even though such correlations fit reasonably well to the experimental data for a particular motor configuration, one difficulty lies in whether such regression rate correlations can be scaled to other motor sizes. Additionally, this approach requires a relatively large number of tests to be performed under varying conditions to develop the regression correlation. It also does not allow transient phenomenon and anomalies to be characterized.

A more accurate description of the dependence of the solid-fuel regression rate on the fuel duct mass flux can be obtained using the instantaneous values of the regression rate and mass flux. Having the capability to continuously measure instantaneous surface regression increases data reliability and substantially reduces the required number of developmental tests. As such, a large body of research has been dedicated to developing regression instrumentation. Resistance-based, ultrasonic pulse–echo, x-ray radiography, and other methods have been used.

The steady-state regression rate is always determined from the time variation of the material thickness, for a period of time, which should be as short as possible, depending on the spatial resolution of the method. An error of less than 1% on the regression rate data is the challenge for measurement methods. This chapter describes a set of novel techniques in terms of their principles of operation, examples of applications, results, and merits. One can also refer to Zarko and Kuo [1] for a general review of a portion of these measurement methods.

II. Ultrasound Measurement Method

A. Principle of Method

The principle of this method is well known: It is similar to the sonar technique. An ultrasound transducer emits a mechanical wave that travels through the tested materials (Fig. 1). The wave reflects on the regressing surface and comes back to the transducer. Thus, this measurement technique is named the pulse–echo

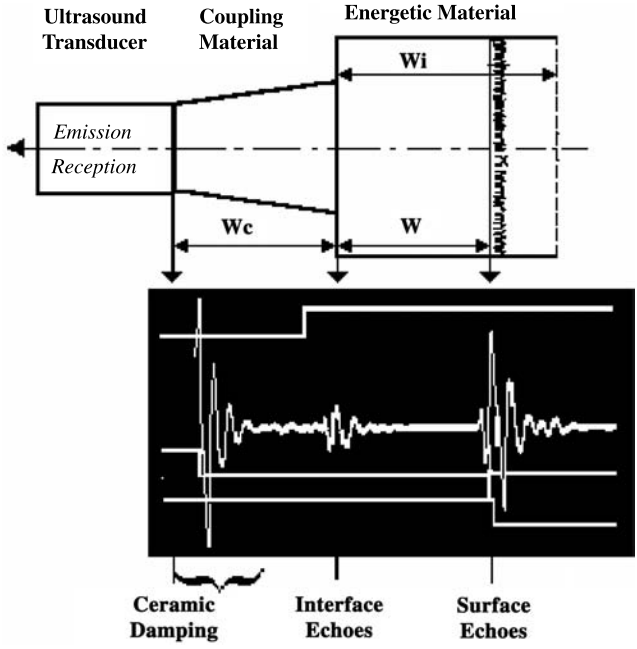

Fig. 1 Principle of ultrasonic measurement.

method. The ultrasound transducer is rarely mounted in direct contact with the tested material. A coupling material is inserted between the transducer and the material, corresponding to a delay line that allows a measurement up to zero thickness and isolates the transducer from the severe conditions of temperature and pressure inside the motor.

The coupling material is made of a hardening resin acoustically adapted, cast into a hole drilled through the steel cases of the setups or, for the carbon or Kevlar cases, bound on their external surfaces. The measurement of the return propagation time of the mechanical wave is related to the material thickness via the mechanical wave velocities. If the wave velocity C were constant, the thickness of the sample, W, would be straightly proportional to the transit time $\tau = 2W/C$. Unfortunately, the wave velocity varies according to the temperature (initial value and thermal profile), the stress field due to the internal pressure, and the geometries. The method of analysis allows the establishment of a relationship that takes into account all of the physical parameters that have an effect on the propagation time variation [2, 3],

$$C_{\text{ref}}/C = [1 + k_T(T - T_{\text{ref}})]\,[1 - k_P(P - P_{\text{ref}})]$$

The overview presented here is extracted from ONERA publications, where the details of the analyses can be found. Generally speaking, the effect of the temperature and pressure will be stronger under unsteady conditions, which means with pressure and incident heat flux variations. One finds two types of behaviors, which can be defined depending on the regression rate level. The boundary stands roughly around 1 mm/s of regression rate. First, above this value (the case for almost all of the solid propellants), the thermal profile does not have any significant influence on the burned thickness and the burning rate, but the pressure effect must be included into the analysis of the measurement [3–5]. Second, for slower regression rates, although the pressure effect always has an influence, the main parameter becomes the thermal profile variation. The ultrasound echo position will be modified by the heat quantity accumulated into the material. When the temperature rises, the wave velocity decreases, yielding a propagation time increase. Examples will show that the heat flux can have as pronounced an effect as, but opposite to, that of the degradation itself.

B. Solid Propellant Combustion

This section deals with solid-propellant combustion to illustrate the benefit of the method. Remember that glycidyl azide polymer (GAP) is a fuel of interest for hybrid applications. It behaves much like a solid propellant. The ultrasound technique widely used in France, at ONERA and at Société Nationale des Poudres et Explosifs (SNPE), the French-solid propellant manufacturer, aims at determining the quasi-steady-state burning rate law [5,6]. To establish the classical burning rate law as a function of the pressure $r_b = aP^n$, a very simple setup is used with an end-burning grain and an ablative nozzle with which the pressure varies during the test while measuring the propagation time. In this way, the number of tests is reduced. An example of the result obtained from seven tests (Fig. 2) shows that the scattering of the measurement is around ± 0.3 mm/s for this high burning rate solid propellant. One has to adapt the coupling material to the solid-propellant acoustic impedance to minimize interface echos, to determine the sensitivity of

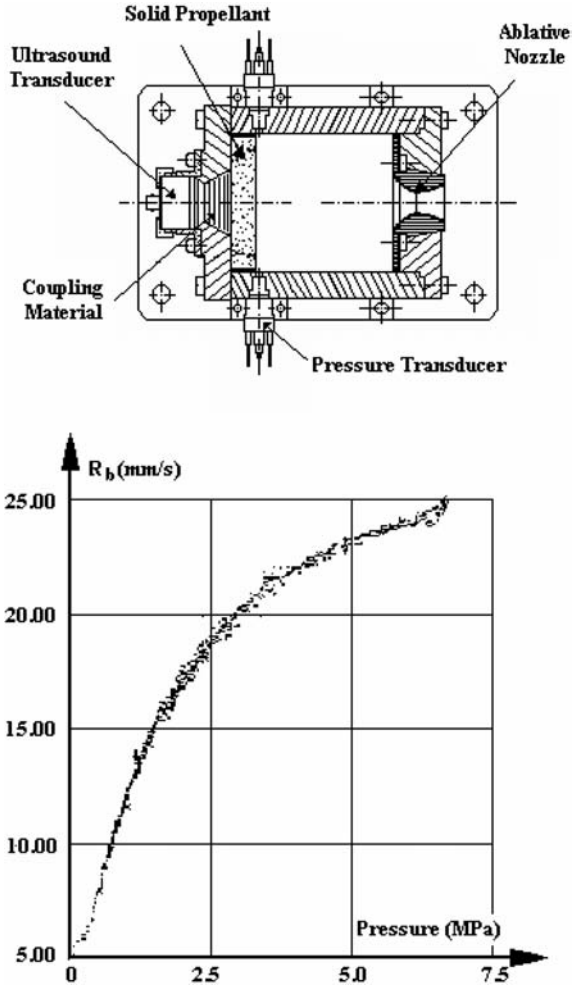

Fig. 2 Quasi-steady-state regression rate measurement.

the wave velocity of the materials, and to take into account these parameters with a data processing code. Once known by the user, this method is more precise and competitive than more commonly used techniques.

A solid-propellant rocket motor can be subject to a large variation of temperature: hot desert, sea level, or high-altitude during the flight. Thus, the temperature sensitivity of the burning rate, σ_P, is an important parameter the missile designer and the propellant manufacturer have to know to predict the performances. The ultrasound method allows such a measurement (from -50 to 80°C), but many difficulties have had to be overcome before acquiring precise data. With respect to the coupling material matching, there is no unique solution for every different

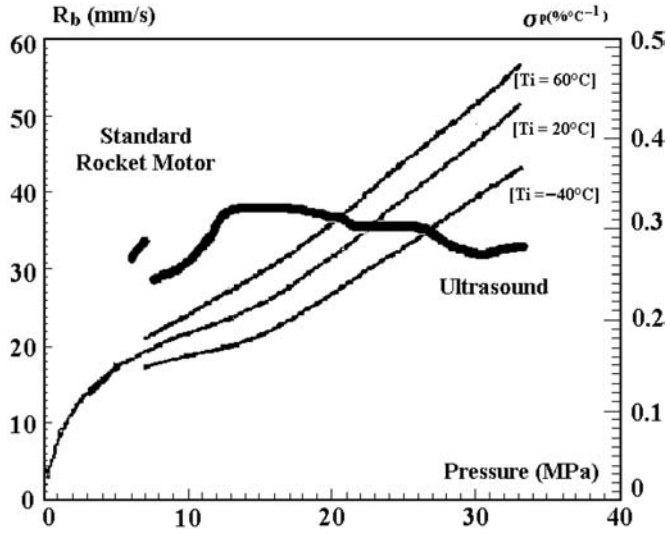

Fig. 3 Sensitivity of burning rate to initial temperature (aluminized ammonium perchlorate propellant).

temperature. Mechanical properties, bonding qualities, and dilatation coefficients have a pronounced effect on the measurement for cold as well as hot temperatures [5]. Firing tests in a thermally regulated closed bomb of a small volume, pressurized by the combustion gases themselves, can determine the burning rate over a very large pressure range. The smaller the bomb internal volume is, the thinner the sample becomes and the higher the dP/dt level becomes. This leads to a larger scattering, mainly due to the electronic device. The evolution obtained in these experimental conditions should be considered as a first draft and be confirmed using a larger volume bomb (and smaller dP/dt level).

The influence of the initial temperature on the burning rate is represented by the curves in Fig. 3 for a metallized composite propellant. In Fig. 3, the temperature sensitivity coefficient is shown, deduced from these three smoothed evolution curves, which in turn is compared to the results of a classical standard rocket motor test method. The σ_P level is the same, but the determination range is improved and much larger: One can see a slope variation for the pressure level that corresponds to an increase of the pressure exponent (13–14 MPa).

C. Energetic Materials Degradation: Ablation

Year after year, the application field of the ultrasound measurement method has been spreading into new domains such as the study of the degradation of various energetic materials: hydroxyl-terminated polybutadiene (HTPB), polyethylene (PE), polymethylmethacrylate (PMMA, Plexiglas®) and polytetrafluoroethylene (PTFE, Teflon®), or internal thermal insulators. The degradation rate is usually slow, and the heat fluxes are not constant: The tracking of the ultrasound echos'

displacement and the analysis of the measurement become more difficult compared to the solid-propellant burning rate determination.

1. Hybrid Propulsion

In hybrid propulsion, the oxidizer is initially liquid, such as liquid oxygen (LOX) for launch vehicle systems, or is brought by the air, for ramjet missiles. The control of the degradation process of the fuels is mainly related to the heat flux coming into the material; this heat flux results from the chemical reactions between the pyrolysis gases and the oxidizer. Many studies have been carried out on this topic in France [7], in The Netherlands [8], and in the United States [9, 10] using the ultrasound measurement method to characterize the behavior of HTPB fuel.

One of the ONERA experimental setups is presented in Fig. 4. An ablation chamber is mounted downstream of a diffuser in which is flowing the hot air from a chemical heater (H_2/O_2). The results obtained from the ultrasound measurements highlight the thermal phenomenon that modifies the conditions of the wave propagation: The initial preheating phase turns into an apparent thickness variation due to the slowing down of the wave velocity with the temperature (Fig. 5). During the quasi steady combustion phase, the ablation rate is fairly well evaluated from the time derivative function of the propagation time variation without calculating in detail the thermal profile effect, but the accuracy will depend on the mean wave velocity that one defines with respect to this initial deviation. The higher the heat flux is, the smaller the initial deviation and the better the accuracy of the result will be. The degradation of the fuels considered in hybrid propulsion does not produce any char or residue on their surfaces, except in the case of GAP, which produces a large amount of carbon residue. A few of them exhibit a change of "state" before they are totally degraded: a semiliquid layer (PMMA and HTPB) or a semigel (PTFE) covers the sample surface. In these cases, the ultrasound propagation can be modified. The change of state leads to an acoustic impedance variation large enough to reflect a part of the acoustic energy at the transition section. Thus, one extra echo appears at this location combined with the external surface echo. Tracking these echoes variations can only be performed via the digital acquisition of the

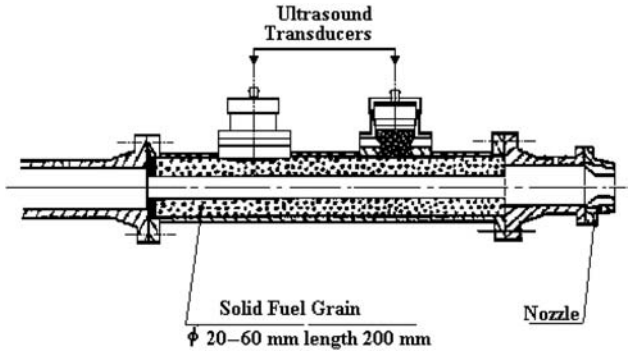

Fig. 4 Ablation setup.

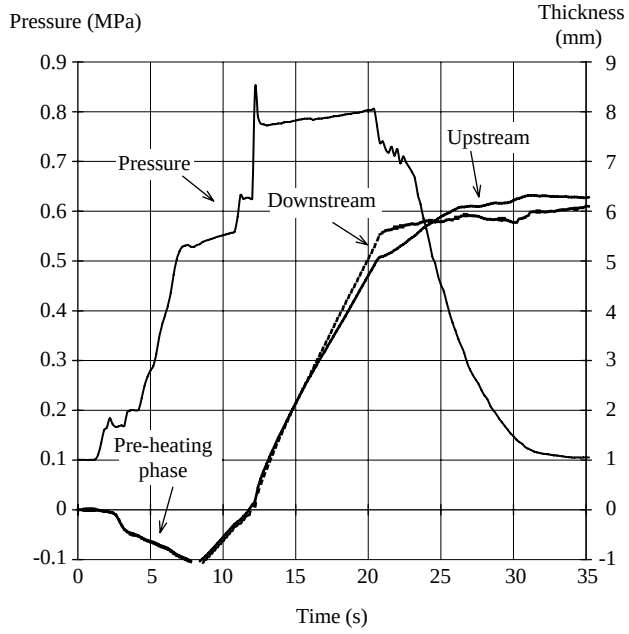

Fig. 5 Ablation, ultrasound measurement with thermal effects.

ultrasound windows coupled with a postrun processing. This is also true for the materials developing a char on their surface. The char will induce modifications of the thermal exchange on the surface and, consequently, have an effect on the wave propagation.

A set of results obtained with the ultrasonic technique is shown in Fig. 6, showing the evolution of the regression rate with the evolving specific mass flow rate during the testing, as realized with the setup of Fig. 4.

2. Method for Correcting Effect of Pressure

The work at Pennsylvania State University addressed in detail the impact of the correction due to the pressure effect on the ultrasonic measurement. These results were obtained on the slab motor [10, 11], shown in Fig. 7. Also shown is a block diagram of the major components of the ultrasonic pulse–echo system. Solid-fuel slabs are inside the two-dimensional windowed hybrid motor. A 1-MHz, 19-mm ($\frac{3}{4}$-in.) Panametrics Videoscan ultrasonic transducer (Model V114-RM) is placed behind the fuel slab in a fuel sample holder. The transducer is connected directly to the electronic device for ultrasonic measurement (EDUM). The EDUM is connected to an oscilloscope to provide a real-time video camera record and to a data acquisition unit (Nicolet Multipro Transient Analyzer). Through a pretest calibration procedure, the voltage signal is converted to the propagation time.

Hybrid rocket motor experiments were conducted at the Pennsylvania State University High Pressure Combustion Laboratory (PSU–HPCL). The axial

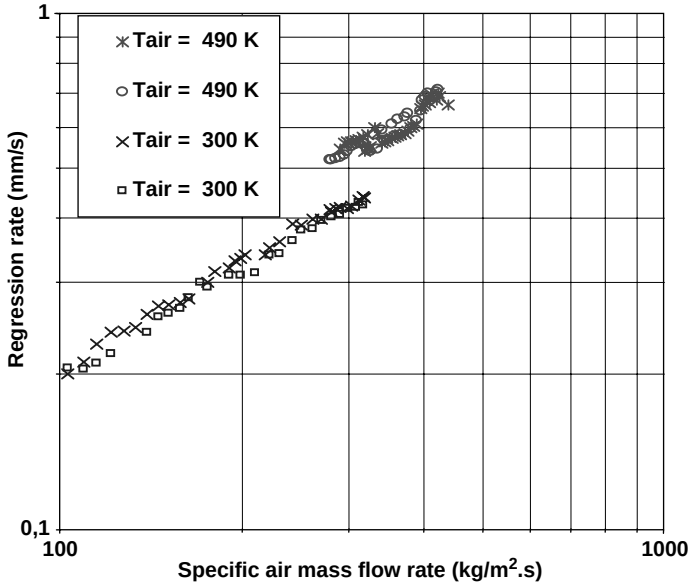

Fig. 6 Continuous upstream and downstream HTPB measurement during test, ramjet setup.

position of the transducer was selected from one of four locations on the upper fuel slab (Fig. 7). The ultrasonic measurement was possible at only one location because only one EDUM unit was available. One of the thermocouple ports was used for the coaxial cable connection. The solid fuel was not totally burned in these hybrid tests. Hence, a coupling material between fuel and transducer was not needed; they contacted each other directly. A smooth contact surface was obtained in the fuel casting. The fuel was cured under vacuum to get rid of any nonhomogeneity, such as bubbles. The transducer was placed inside the fuel holder in such a way that the fuel and transducer contact was tight. Moreover, oil was applied between the transducer and fuel to improve the contact.

The output voltage of the EDUM is an indication of the measured propagation time in microseconds. The propagation time and voltage are indirectly proportional, and the proportionality constant mainly depends on the output voltage gain setting. Consequently, the EDUM has to be calibrated before each test to find this proportionality constant. During the data processing, a computer program uses this proportionality constant to convert the voltage input into the propagation time.

Because of the chamber pressure evolution during burning, the measured propagation time needs a correction. Conventional theory assumes the fuel as incompressible. However, some hybrid fuels can be compressible (or deformable) under operating chamber pressures as in the case of the HTPB fuel ($\sim$40 Shore A), which is used in hybrid rocket motor analog tests. Closed-bomb compression tests showed that the fuel is compressible, and special care was needed to be applied. Hence, the lumped pressure correction method for ultrasonic measurement was

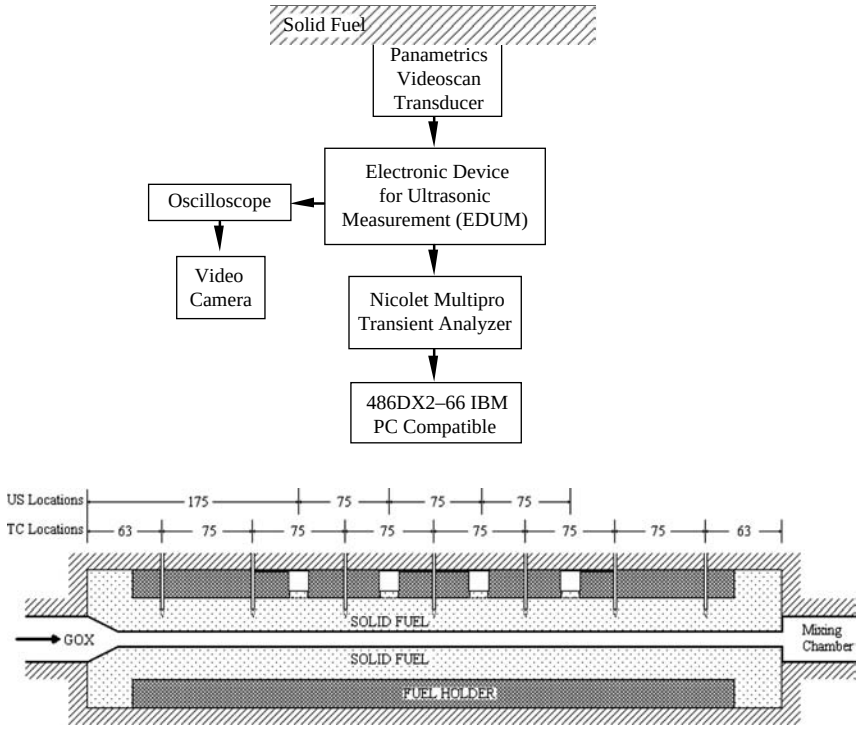

Fig. 7 Block diagram for ultrasonic pulse-echo system and slab setup.

developed to reduce inaccuracy, instead of the conventional method. This method is described in the Chapter 3. The effect of the corrections thus realized is shown in Fig. 8.

3. Internal Thermal Insulator

The internal thermal insulators (ITI) are widely used in solid-propellant rocket motors. They are usually made of an EPDM polymer loaded with various compounds (silica, Kevlar fibers, etc.). For silica/EPDM insulators, the control of the degradation process driven by the incident heat flux depends on the char layer over the surface. If the wall shear stresses induced by the core flow are too weak to stripp away the char layer, the pyrolysis rate will be of a low level and thermally unstable. The ultrasound measurement follows this process with, of course, some difficulty in interpreting what is seen because the thermal effects on the propagation are of the order of the effect of the surface regression. When the char layers are ejected as soon as created, a steady ablation regime occurs. Here, the ultrasound measurement behavior is similar to that obtained for a solid propellant: The thermal effects are negligible. Between these two regimes (pure pyrolysis or pure ablation), the layers of residue of a thin thickness are ejected one by one like the tiles of a roof. The alternating of pyrolysis phase and thermal effect can be interpreted with

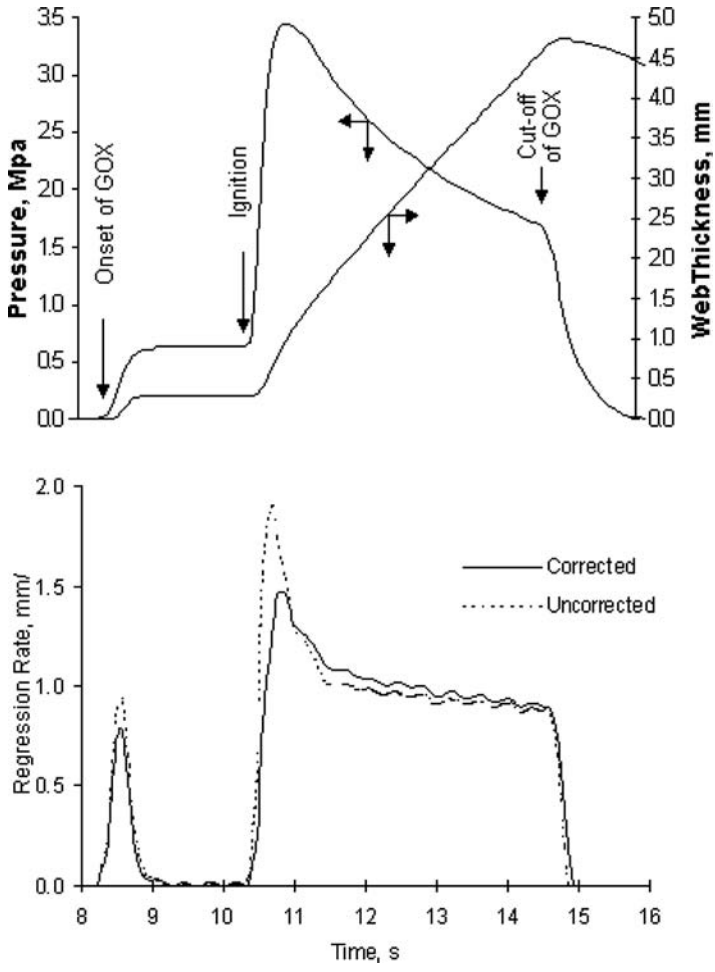

Fig. 8 Ablation rate at PSU-HPCL with ultrasound.

the help of the modelization of the thermoablative behavior of the ITI, giving the thermal profile inside the material during its degradation. These internal thermal insulator materials are of interest because their behavior is somewhat similar to that of GAP. As mentioned, GAP leaves an appreciable carbon residue layer that is probably stripped away progressively by the flow of oxidizer gas.

With knowledge of the wave velocity variation with respect to the temperature and with a criterion defining the reflection of the wave with the porosity through the degraded zone, the propagation time variation (that is, what is measured with the ultrasound method) is computed from expected thermal exchange conditions. This computed result is compared to the measurement (Fig. 9). Once this fitting has been obtained, the heat flux history is determined and the effects due to the

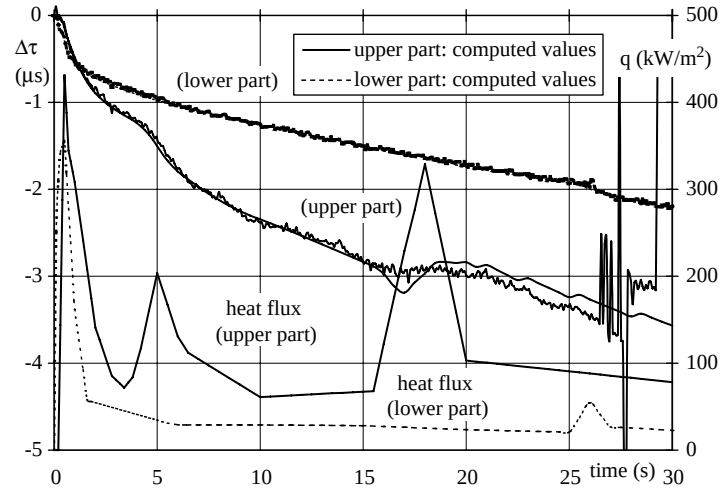

Fig. 9 Heat flux evaluation from ultrasound measurement, full-scale motor.

heating and the degradation can be separated [12]. These results are obtained on an horizontally fired axisymmetric motor in which the gravity effect is felt differently on the upper and lower ITI.

The SNECMA Propulsion Solide (SPS) thermoablative code allows carry out very reasonable calculations when the char stays on the surface, is ejected periodically layer by layer, and when there is no residue. This technique is helpful for having a good estimation of the thermal loads at full scale, and, on small scale set-ups, for validating the data set of the material input code. The main shortcoming is that the thermal quantities, the pyrolysis characteristics, and the wave propagation conditions have to be known in detail. The advantage of the ultrasound measurement and the degradation code working together rests in the computation of the heat flux evolution, the starting point of the preheating and the degradation. The ultrasound transducer becomes a flux sensor. The degraded thickness and the regression rate are not deduced from the ultrasonic measurement but calculated with the code. When the measurement locations are multiplied on a full-scale rocket motor, a map of the degradation of the internal insulator can be drawn. The results obtained during a ground test will supply a data set, which is very important for the sizing of the ITI. The severity of the flight/ground difference could be estimated if a flight ultrasound electronic device were developed.

D. Merits

The ultrasound measurement method has been an industrial tool operating on many setups or rocket motors as well as a pressure or temperature sensor. As opposed to the microwave technique, the implementation of the transducer does not require any special device. It can be integrated on previously machined setups. The only difficulty is the fitting of the suitable coupling material, the delay line through the case, which must be chemically and acoustically adapted to the tested

material and have good mechanical strength and good bonding qualities. The wave propagation is mastered in the case of solid propellant, although a little less so for materials with a low regression rate.

The precision of the final result, the regression rate, depends on the experimental conditions (dP/dt), the numerical acquisition conditions (from 25 to 20,000 data per second), the derivative function computation conditions (smoothing procedure, mean square method, etc.), and the operator (who has to be experienced). Estimating the accuracy of the method is not easy: The measurement is local but not on a tiny surface and the ONERA background shows that the combustion itself is not totally stable under fixed conditions (P and T).

The ultrasound technique is an excellent research tool, the study of the erosive burning being the best example of what can be obtained, as well as a tool for controlling manufacturing with a lower cost with better accuracy. Measurements of full-scale rocket motors with composite wraparound cases are being used more often; thus, the reduction of the ground-test program cost is expected.

Of course, the investment in time and money could be considered heavy: The measurement electronic devices are not inexpensive, but it is the experience that the user has to accumulate that is the main burden before the return on investment can be collected.

III. Real-Time X-Ray Radiography

A. Description of Method

X-ray radiation is attenuated in proportion to the thickness and physicochemical properties of the material by $I_{(\theta)} = I_0 \exp(-mL_{(\theta)})$. This model assumes a linear attenuation coefficient that is a function of both the radiation source energy level and the particular composition of the materials through which the beam passes. Because the change in transmitted radiation can be related to the web thickness variation, with the beam perpendicular to the burning surface, after a pretest calibration, one can determine the burning rate. The most commonly used technique is, however, another one: real time radiography (RTR). The profile of transmitted radiation has a sharp gradient at the position corresponding to the solid/gas interface. The basic configuration of an RTR system is shown in Fig. 10. The x-ray source consists of a control unit, a pulse-forming network, an RF power source (magnetron), and a linear accelerator (or a flash). The RTR imaging system consists of an x-ray screen that converts x rays to visible light, a first-surface mirror, and one or two low-light-level silicon-intensified target (SIT) cameras to convert the visible light to video signals. The images produced by the x-ray systems must be interpreted to determine the solid material surface position. Image processing has become a powerful tool in analyzing radiography: mapping techniques, noise removal, image segmentation, gray-scale morphology, frame-by-frame processing, film digitization, etc. The determination of the location of the regressing surface is highly subjective. The operator or the digital image processing software could select the position within two video pixels. The value of this error is then dependent on the magnification of the x-ray image from the test configuration.

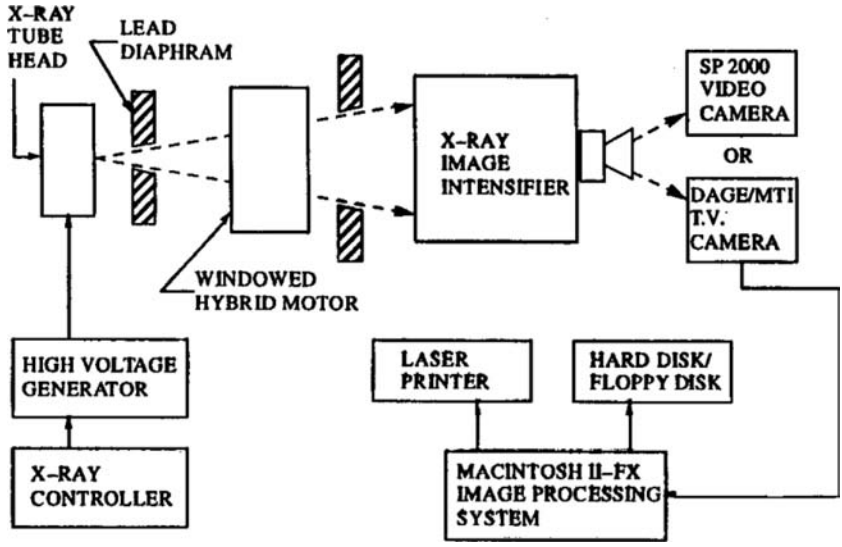

Fig. 10 RTR layout at PSU-HPCL.

B. Examples of Applications and Results

A two-dimensional image of the internal structure of a rocket motor can be obtained during the firing. This technique has been used successfully at Arnold Engineering Development Center (AEDC), SNPE, and other locations [13–16] to image a variety of dynamic events in solid rocket motor firings and to investigate areas such as deformations, case/insulator separation, insulator erosion, combustion surface evolution (Fig. 11) [14], propellant burning rate, propellant cracks, and slag accumulation. X-ray sources are available to image through up to 27-in. of propellant. The images can be large enough to view an entire tactical rocket motor or the entire section of a large booster tangent to tangent. This has been a successful technique in use at China Lake for over 25 years.

X rays have been used in a wide variety of configurations to study the behavior of solid propellants or energetic materials. The motivation has generally been to look at dynamic events inside the motor in a qualitative way. Burning rate data can

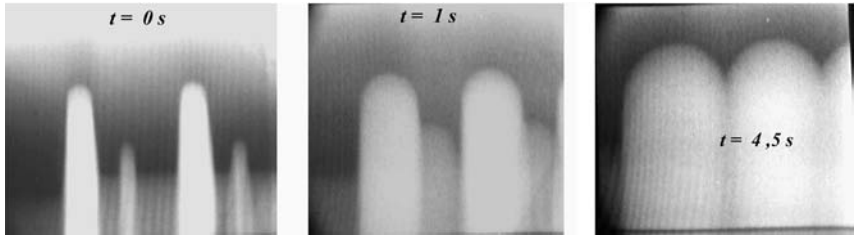

Fig. 11 Grain evolution by RTR in an axisymmetrical motor.

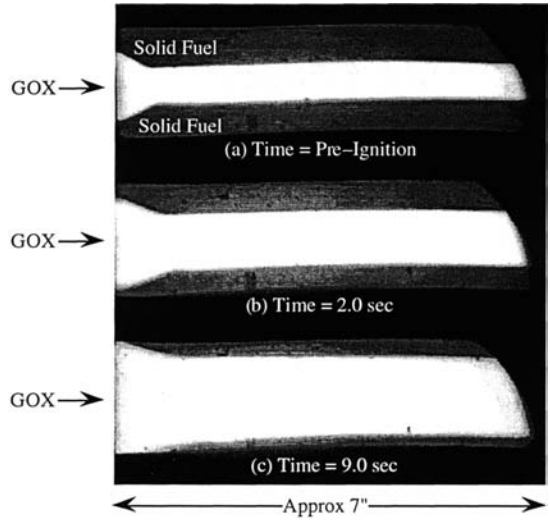

Fig. 12 Solid-fuel regression measured by x rays at PSU-HPCL.

be deduced, but the acquisition is relatively expensive and data interpretation is labor intensive. However the results are quite good. Figure 12 shows a set of typical images of a portion of HTPB slabs at different burning times [17]. The viewing window is approximately 17 cm long. These images were used to determine the instantaneous web thickness and port cross-sectional area along the fuel slabs. Chiaverini [17] indicates that the time resolution between two images was around 33.3 ms, whereas the web thickness measurements were made at about 12.5-mm

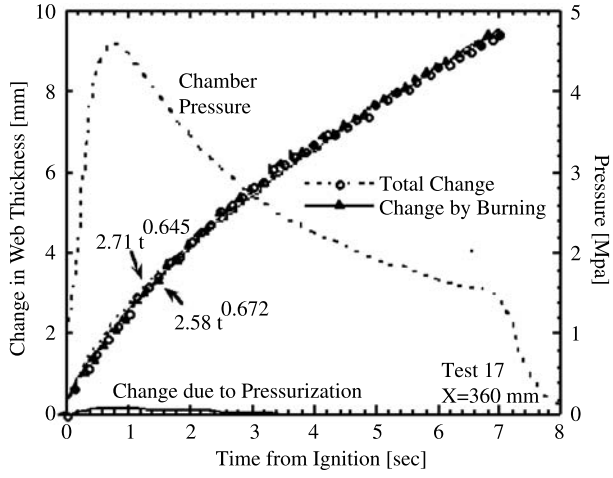

Fig. 13 Changes in solid-fuel thickness from RTR.

spatial increments. Figure 13 shows the change in web thickness obtained for one location along the slab; the change due to compression was subtracted from the overall change measured from the x-ray images. The real-time x-ray radiography system allows the instantaneous regression rate to be measured not only at a single location, as does the ultrasonic method, but over a finite region along the grain.

C. Merits

The examples given underline the value of RTR, which is a nonintrusive technique. It is a real-time data recording system. Pictures captured in the test event can be played back immediately after the test firing at a lower speed for visualization and analysis. It covers a portion of the grain with a correlation between magnitude and reliability. The technique can be applied to either two-dimensional or axisymmetric propellant or solid-fuel grain geometries, giving a general visual presentation of the rocket motor. Disadvantages include the complexity and high-power requirements of the x-ray equipment used, personnel hazards associated with x rays of high intensity, and the high cost of the technique.

IV. Microwave Technique

A. Description of Method

This method is based on the propagation of electromagnetic waves (at some 10 GHz) in absorbing materials. This technique has been investigated for local burning rate measurement over 30 years. At the end of the 1960s, the purpose for its use was the determination of the solid-propellant burning rate [18–20].

A microwave source creates the electromagnetic waves that are injected through the propellant sample. A reflection occurs at the regressing surface, and the phase of the reflected signal changes. The microwaves are transmitted into the motor using a microwave horn antenna, which also acts as a receiver (Fig. 14). The reflected signal is then compared with a portion of the transmitted signal to obtain regression rate information. The phase angle ϕ between the incident and reflected signals shifts with the reduction in length of the regressing sample. The regression rate is directly proportional to the rate of change of this phase shift, where the proportionality constant is the microwave-phase constant in the propellant, a function of the geometry of the waveguide and the dielectric constant of the propellant. Whatever the electronic device used, the measured quantity is the rate of change

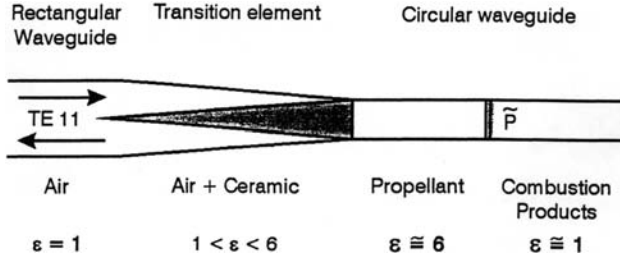

Fig. 14 Microwave waveguide.

of this phase shift,

$$W_b = (l_0/\varphi_0)\varphi = (\lambda_G/4\pi)\,\varphi$$

then

$$r_b = (\lambda_G/4\pi)\,(\mathrm{d}\varphi/\mathrm{d}t)$$

with $\lambda_G = \lambda/\sqrt{1-(\lambda/\lambda_c)^2}$ and $\lambda = \frac{c}{f\sqrt{\varepsilon}}$ where λ represents the wavelength in the solid material, which depends on the frequency of the microwaves and the permittivity of the propellant. The cutoff wavelength $\lambda_c = ka$ is related to the characteristics and geometry of the waveguide. With $f = 10\,\mathrm{GHz}$, $\varepsilon = 4.23$, and a cylindrical waveguide TE11 ($k = 3.142$ and radius $a = 7.95\,\mathrm{mm}$), then $\lambda_c = 2.713\,\mathrm{cm}$ and $\lambda_G = 1.731\,\mathrm{cm}$. This means that an uncertainty of 1 deg in the phase shift gives an error of $24\,\mu\mathrm{m}$ in the material thickness.

B. Examples of Applications and Results

The microwave propagation can be compared to a grid applied over the cross section of the sample. The microwave signal is seen to complete one full cycle for each one-half wavelength of motion of the propellant burning surface. Because the wavelength of the radiation in the propellant is assumed constant, the one-half cycle-time measurements represents the average burning rate during that half-cycle. The higher the microwave frequency is, the finer the grid will be, but the stronger the damping of the microwaves. From the time-interval values, one can deduce the mean burning rate. Such results were obtained in 1967 on an end-burning grain test rocket motor, with a correlation of the burning rate level with the results from thermocouples implemented in the grain [20].

ONERA developed a small burner using the microwave technique for pressure-coupled response function measurement in the 1980s [21, 22]. A schematic of the setup is given in Fig. 15. A specific homodyne transmitter–receiver associated to a reflectometer bridge was designed to give access to the steady (and unsteady) components of the phase shift between the incident and reflective waves. Cold-flow calibration was found to be mandatory to avoid the nonperfect matching of the transition element to the propellant. An ad hoc software was also developed and upgraded during several years of work. Although this technique was used only for unsteady measurements, an interesting spinoff was found in the determination of the steady-state burning rate of a propellant sample. Figure 16 shows the results obtained on a test performed under steady pressure conditions and during the tailoff part of the test. The agreement with the standard burning rate law is quite good.

C. Merits

The microwave technique has been applied mostly to unsteady combustion measurement in the United States and in France. For steady-state measurement, this method is underexploited. It continues to show promise in many applications, but it requires a costly device and a long training period for users before being fully operational. Thus, it is far from being applicable as an industrial control tool.

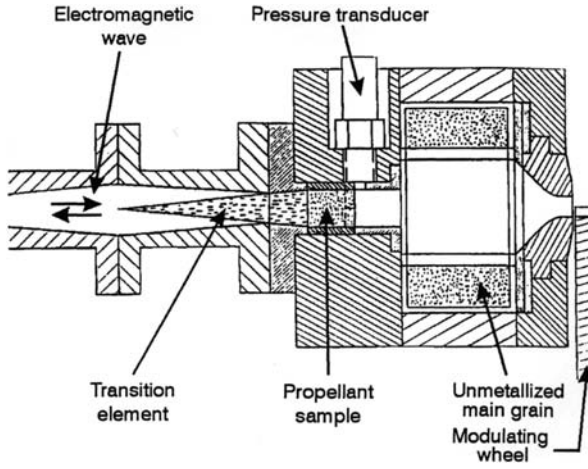

Fig. 15 Microwave experimental setup.

Regarding the great amount of work done in the United States in the 1960s–1970s without modern data acquisition and digital data reduction instruments, it seems that the possibilities for applications of the microwave technique should now be enhanced.

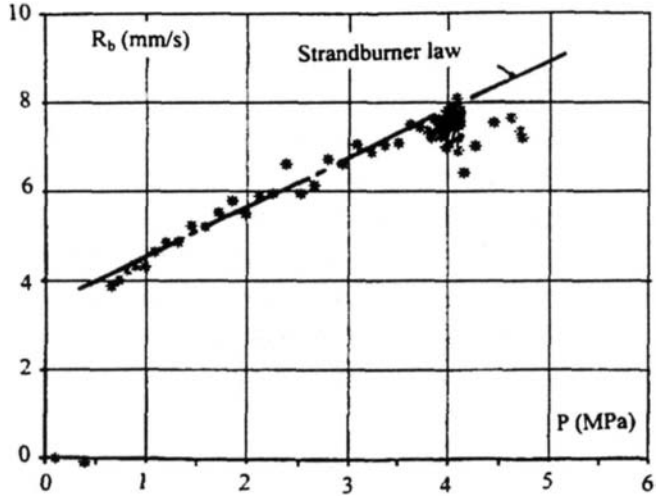

Fig. 16 Steady burning rate with the microwave device.

V. Plasma Capacitance Gauge

A. Description of Method

The plasma capacitance gauge (PCG) technique was developed in the United States during the 1980s at TRW, Inc., and in France at ONERA in the 1990s, mostly to measure internal insulator erosion. This technique is based on the variation of the electrical capacity with time, which is (should be) directly related to the thickness of the material between two electrodes. The first electrode is located along the case of the solid rocket motor, and the second electrode is formed by the plasma generated by the combustion gases. The capacitance increases as the thickness of insulator decreases, and these data yield real-time information on the insulation thickness, behavior, and possibly, on the flame arrival time.

Measurements of internal thermal insulator erosion on subscale and full-scale motors (ground test and flight tests) have been made [23]. The fundamental advantage of this technique is that it can measure through materials that x rays and ultrasonic waves have difficulty in penetrating.

B. Examples of Applications and Results

The principle of operation in a solid rocket motor is shown in Fig. 17. Electrodes are located along the outside envelope of the motor. The strong ionization of the combustion products or the conductive char of the insulator forms the second electrode. Adjusting the polarization frequency on the electrodes can provide information on both propellant and insulation degradation or on insulation degradation only. The diameter of the PCG is adjusted depending on the thickness range for which the measurement is performed. The relationship between the thickness and the output voltage is not linear. A pretest calibration is required on various tested material samples of different heights.

The application of the PCG technique to solid-propellant burning rate measurement was done on a small motor using a sample of propellant (10 mm thick) fitted to an insulator layer (4 mm thick) and a main grain for pressurization [24]. Typical

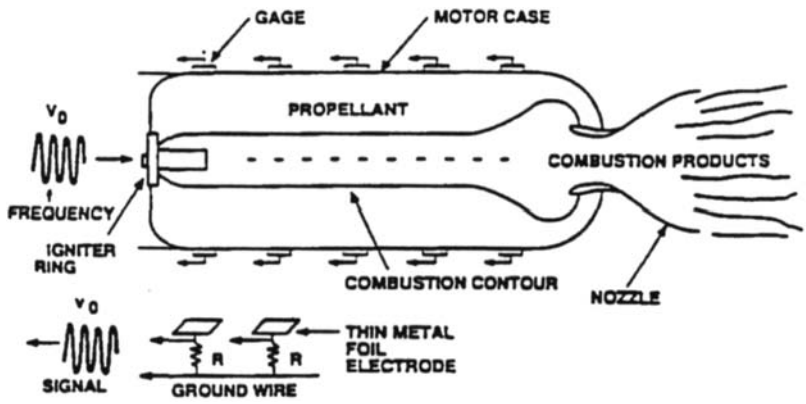

Fig. 17 Principle of operation.

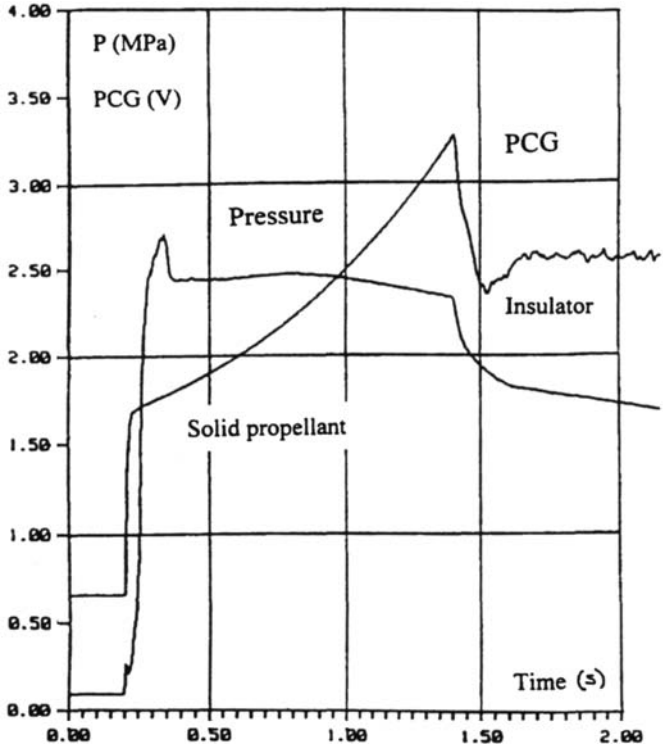

Fig. 18 Typical output of PCG measurement for solid-propellant burning.

pressure and PCG voltage time histories are presented in Fig. 18. The burning of the propellant sample ends at 1.4 s, and then the PCG voltage shows the degradation of the insulator layer. The evolution of the PCG voltage during the propellant burning follows an exponential feature. When an in situ calibration of the gauge is used, an accurate measurement of the burning rate was found in relatively good agreement with the standard burning rate of the propellant. The behavior of the PCG output changes drastically when the insulator is reached due to the char layer growing on its surface.

The technique was also used to measure insulation erosion on subscale motors [24]. During the development phase of this technique, PCGs were tested on an internal insulator axisymmetric grain fitted in a specific rocket motor. The conditions of test were adjusted by changing the solid-propellant grain size and the internal initial diameter of the insulator grain. The degradation process was observed by PCGs and also by ultrasound transducers mounted at the same location as the PCGs, with the acoustic waves traveling through the thin PCG. As discussed earlier in the ultrasound technique presentation, the variation of the propagation time of the ultrasound waves is modified by the heat coming into the material. The ultrasound measurement is affected by the pyrolysis process inside the solid phase. For the PCGs, the measurement is more or less outside information. In Fig. 19,

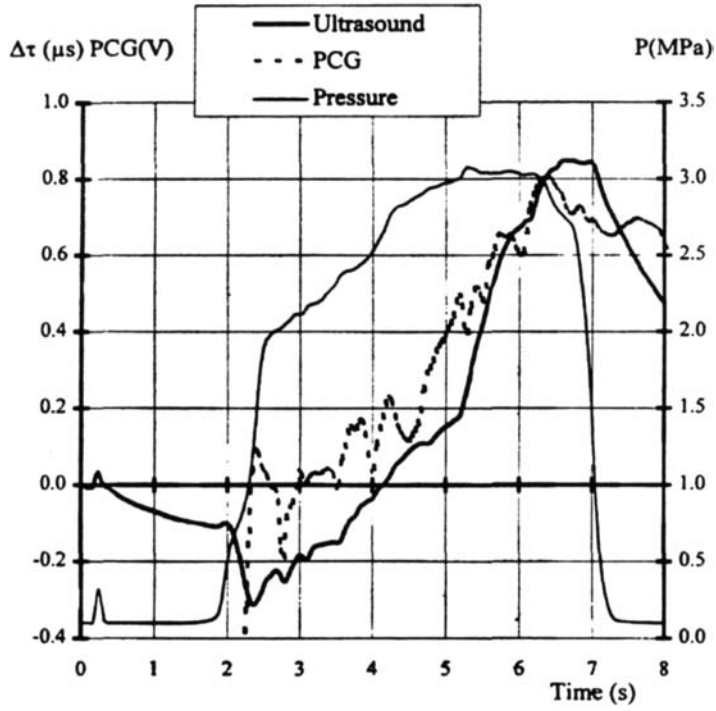

Fig. 19 PCG and ultrasound signals on insulator grain obtained at the same location.

the char behavior can be observed: The spikes on the PCG trace correspond to the ejection of a portion of the char layer. The ultrasound trace shows slope variations due to heat-transfer changes that occur at the same time that a char layer is ejected. Understanding of the insulator degradation process could be studied in detail and improved using both techniques: The PCG is helpful for the effect of the core flow on the char, and the ultrasound measurement indicates the heat flux history.

C. Merits

The PCG technique has demonstrated its ability to measure the thickness of a solid-propellant sample in a way similar to that which can be obtained from an ultrasonic transducer. The first attempt carried out at the research level in France seems to be very promising, even if some work still has to be done to better understand the real influence of the plasma location near the propellant surface (height of flame and boundary layer) and the temperature sensitivity of the propellant electrical property. When applied on an insulator or more generally on a material developing a residue on its surface, understanding of the PCG behavior is not complete yet. However, it is expected that this method could be very inexpensive and less restrictive than the ultrasonic method. The capability of application to flight measurement has been proved.

VI. Resistance-Based Regression Measurement Technologies

A. Principle of Method

At least two different resistance-based regression measurement technologies have been implemented [25, 26]. These sensors are designed to be embedded in the material of interest and regress along with it. During this process, the resistance of the sensor is related to its instantaneous length, allowing the instantaneous thickness of the host material to be recorded. The time derivative of these data reveals the instantaneous surface regression rate as a function of time. A reliable resistance-based regression sensor must exhibit the following characteristics: 1) regresses at the same rate as the host material, 2) does not affect the regression of the host material or adversely disrupt the process under study, and 3) exhibits a resistance that can be accurately correlated to the instantaneous sensor length.

Extensive development and testing of a resistance-based sensor applied to hybrid rockets, the miniature resistive regressions and ablation sensor (MIRRAS), has been conducted [27] and patented [28] by Orbital Technologies Corporation (ORBITEC^{TM}). ORBITEC began this work in 1996 and has produced several hundred MIRRAS sensors in a variety of designs and sizes. This section will focus on the basic MIRRAS technology to illustrate the fundamental approaches and considerations involved in the design, installation, operation, and signal conditioning and transmission of resistance-based regression sensors. Several derivatives and advancements of this basic approach are deemed possible and likely [27].

B. MIRRAS Design and Operation

Two general versions of the MIRRAS technology are shown in Fig. 20. The MIRRAS continuous sensor has one continuous strip of resistive material across two parallel conductive legs. When it is assumed that this strip has spatially uniform thickness and resistivity, and that the electrical resistance of the legs is much lower than that of the strip, the electrical resistance of the sensor is inversely proportional to the remaining length of the sensor. Because this version of the sensor operates on the basis of an absolute resistance reading, it could be sensitive to external noise factors, such as heat, pressure, and vibration, that impact the sensor resistance.

The MIRRAS ladder sensor consists of two conductive legs, bridged by several perpendicular resistive elements, or "rungs," of approximately equal resistance on a flat polymer substrate. As the surface of the host material and sensor tip regress together, the sensor rungs are consumed, causing the sensor resistance to increase. Electrically, the sensor is equivalent to several tiny resistors in parallel, where each rung of the sensor is an individual resistor. The resulting idealized sensor length vs resistance and conductance trends are shown in Fig. 21. A mechanical connector is secured to lead attachment pads, allowing the sensor's resistance to be monitored via two wires. Correlating the step changes in the sensor's electrical properties with the rung spacing indicates the time-dependant thickness and regression rate of the solid fuel. A MIRRAS ladder sensor is shown in Fig. 22.

There are several potential sources of sensor disturbance during typical MIRRAS applications including heat conduction, combustion of the sensor tip, momentary charring and shorting across the sensor tip, and electrical noise derived from the combustion process. The sensor step changes in resistance are designed to

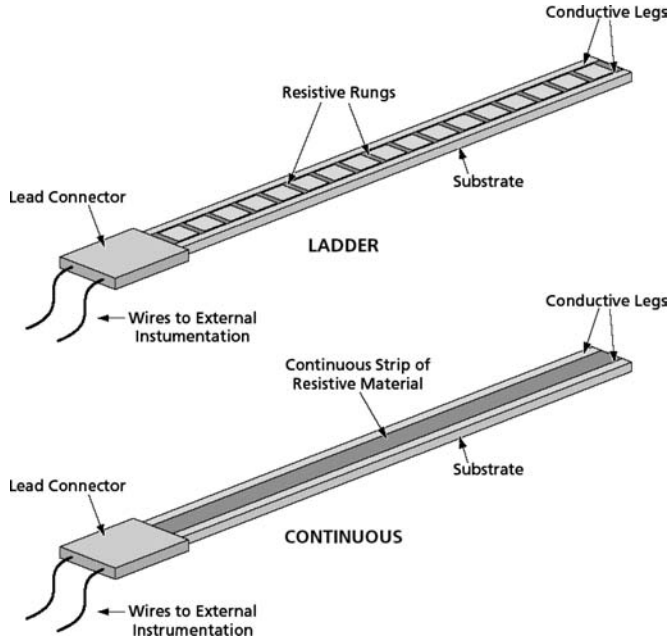

Fig. 20 Two versions of MIRRAS sensor.

provide discrete steps that can be distinguished from background noise. Figure 23 displays raw MIRRAS ladder sensor data collected during an HTPB/gaseous oxygen (GOX) hybrid rocket test. Although the absolute value of the sensor resistance may slightly vary due to noise factors, step changes in the signal can be discerned

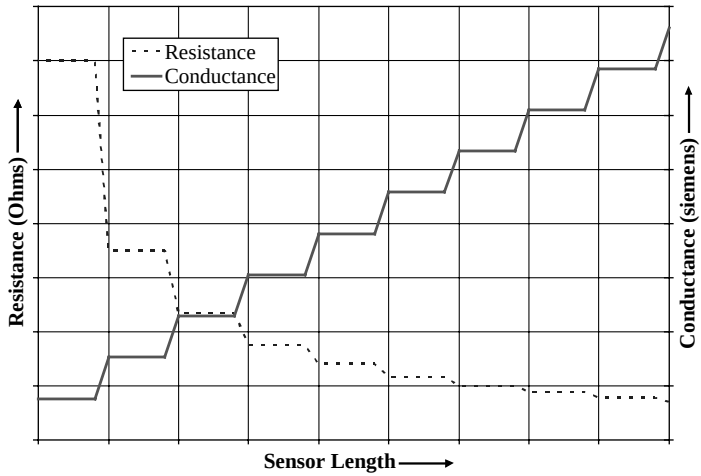

Fig. 21 Sensor length vs resistance and conductance.

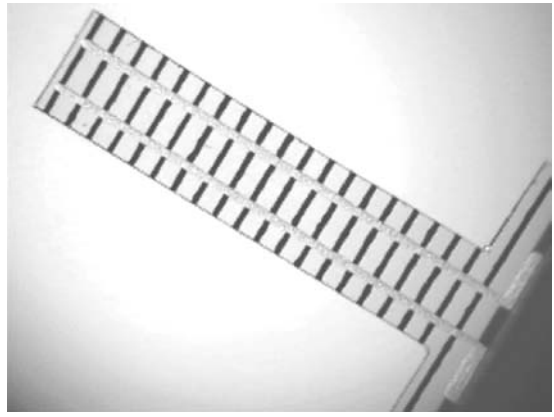

Fig. 22 MIRRAS ladder sensor.

when a rung is consumed. There is also a spike in the output voltage near the end of the test. This is a result of an electrical short across the tip of the sensor caused by momentary conductive char buildup.

The closest rung spacing that has been experimentally demonstrated to date is 0.0125 in., and closer rung spacing is deemed possible though the use of advanced sensor production techniques [27]. Sensor lengths have varied from a fraction of an inch up to 1.5 in., and substantially longer sensors are expected to be readily achievable. The maximum number of initial (equal resistance) rungs that can be resolved is estimated to be approximately 40, independent of the sensor length. More advanced designs, such as those implementing a higher resistance for the

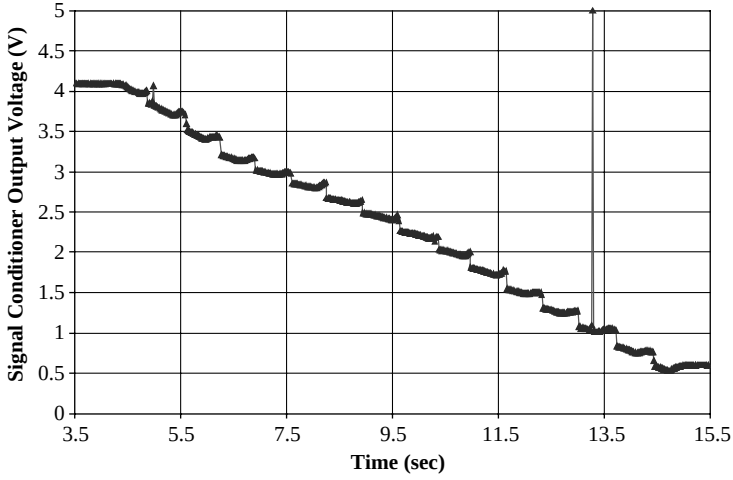

Fig. 23 Raw MIRRAS data collected during hybrid rocket firing.

first rungs that are consumed, could enable this number to be increased. The application of resistance-based regression technology to very large motors appears to be relatively straightforward if it has already been proven at laboratory scale.

C. MIRRAS Installation

MIRRAS sensors have been installed into hybrid fuels, solid propellants, and ablative materials. Two general sensor installation approaches have been successfully demonstrated [26]. The first is to cast sensors directly into the host material (in situ), and the second is to insert them after the material has been formed or cured (postcure).

The MIRRAS sensor and sensor lead wires are rigid enough to allow the assembly to be suspended in a host material mold without any additional support. The sensor can be positioned by placing its tip in contact with a known datum, such as the combustion port casting mandrel in a hybrid-fuel grain mold. Figure 24 shows this approach, where several MIRRAS sensors are positioned for casting in a 6-in. hybrid motor assembly. The uncured fuel can then be poured around the suspended sensors and allowed to cure. A slightly different approach has been implemented when host materials are too viscous for pouring or injection. In this instance, the host material has been packed around the sensor. The in situ sensor installation method has been found to be relatively straightforward by several first-time users. Over 100 MIRRAS sensors have been installed using this approach, and grain dissections have demonstrated reliable and accurate positioning of the sensors [27].

The second installation approach is to insert the sensor into a material after it has cured or been formed (postcure). This could include sandwiching a sensor in between two host material sections or generating a slot in the host material to house the sensor. In both cases, the sensor must be secured in place with a pressure-tight sealant to prevent hot gasses from penetrating along the sensor installation seam.

Fig. 24 MIRRAS sensors positioned for casting inside 6-in. hybrid motor assembly.

This concept has been successfully demonstrated in both acrylic and HTPB hybrid-fuel grains [27]. The postcure installation method is generally more complicated than the in situ method.

A third installation approach is a hybrid of the first two, where the sensor is cast into a small section of the host material and then that assembly is bonded/cast into position within the parent host material. This method may be the most practical approach for very large grains.

D. MIRRAS Signal Conditioning and Transmission

Two senor lead wires are crimped to the MIRRAS sensor body and attached to a signal conditioner. The signal conditioning circuit is based on conductance to provide a constant voltage resolution output with respect to sensor length. The sensor signal has been transmitted from inside a high-pressure chamber to the ambient environment using commercially available feedthrough connectors. Gland-type feedthroughs enable the sensor to be moved independently of the connector to facilitate sensor positioning within the chamber/casting mold and affect a pressure-tight seal around the wires. ORBITEC developed a multi-channel signal conditioner that can accommodate up to six sensors at a time over a wide range of initial sensor lengths (Fig. 25).

Another data acquisition approach is to install a miniature signal conditioner and data logger inside the chamber, possibly embedded in the motor case lining. Preliminary designs indicate this system would be about the size of a nickel for a MIRRAS sensor. Alternatively, a miniature transmitter could be implemented to send sensor data to an external receiver in real time. These two approaches eliminate the need to produce any motor case penetrations or other modifications and are particularly well suited for flight-type motor testing or onboard flight systems [26].

Fig. 25 MIRRAS multichannel signal conditioner.

E. Examples of Applications and Results

The accuracy of the MIRRAS sensor was assessed by carefully dissecting over 50 sensor installations after hybrid-grain and ablative material hot firings [27]. After a test firing, a rectangular section of the host material containing the remaining portion of the sensor was sectioned from the bulk material. Inspection of the dissections indicated proper sensor positioning in the host material. Detailed measurements were taken, using a miniature ruler with a resolution of 0.0025 cm, under a microscope. The sensor tip was found to reside in the thin-surface char layer. Collectively, the dissections verified that the sensors were working properly. A brief description of the sensor test results from hybrid-fuel, solid-propellant, and ablative materials testing is given subsequently.

1. Solid-Fuel Applications

Extensive subscale MIRRAS sensor development was completed in a 25 lbf water-cooled HTPB/GOX hybrid motor [26]. These tests shaped the general sensor design and signal conditioning approach. The sensor was then tested in a 15-cm (grain outside diameter) HTPB/GOX hybrid motor fired at 200 lbf of thrust (Table 1). The resulting regression data from two sensors were reduced using the hybrid regression curve-fit approach discussed in Sec. VIII of this chapter. Both sensors were positioned 48 cm from the head end of the grain. The initial and final grain thickness measurements were used as the boundary conditions for the curve-fit approach. The average value of b (see Sec. VIII) was independently calculated for each sensor and found to be 1.77 for both of them, resulting in the following identical curve fit for both sensors:

$$R_t = (0.381 \cdot t + 3.13)^{0.564} - 1.91 \text{ (cm)}$$

A second shorter firing, which lasted for 7.7 s, was conducted with the same oxygen flow rate and initial port diameter as the first. The chamber pressure traces for the two tests from $t = 0$ to 7.7 s were nearly indistinguishable. The total material regression at the end of the second test was measured at the same axial location where the two sensors had been installed for the first test. The regression predicted by the curve-fit equation at $t = 7.7$ s was found to be in good agreement with these measurements, indicating that the sensors overpredicted the total web regression at this time by 0.01 cm out of 0.85-cm total regression.

Table 1 Conditions of 15-cm hybrid test

Parameter	Value
Initial grain port diameter	3.81 cm
Final local grain port diameter	7.58 cm
Singlet GOX injector diameter	0.95 cm
Grain length	56 cm
Oxygen flow rate	0.22 kg/s
Firing duration	19.6 s

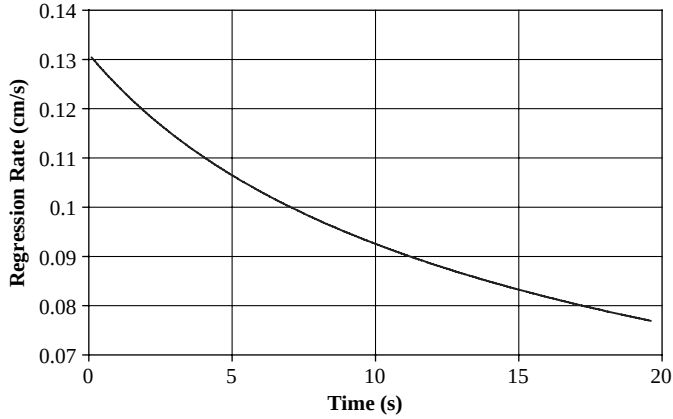

Fig. 26 Regression rate vs time.

Differentiating the curve-fit equation with respect to time yields the instantaneous regression rate in Fig. 26. With use of the curve-fit equation to calculate the time-dependant port area, the instantaneous regression rate is plotted against the instantaneous oxidizer port mass flux in Fig. 27. The resulting regression law, also shown in Fig. 27, has a relatively low-mass-flux exponent. However, there are several indications that this accurately represents the physical nature of the grain regression. The chamber pressure gradually increased during the firings, suggesting that the fuel mass flow rate was increasing. In accordance with the hybrid regression law, this will only occur if the hybrid exponent is less than 0.5. Plotting the average regression rate against the average oxygen mass flux for the two tests,

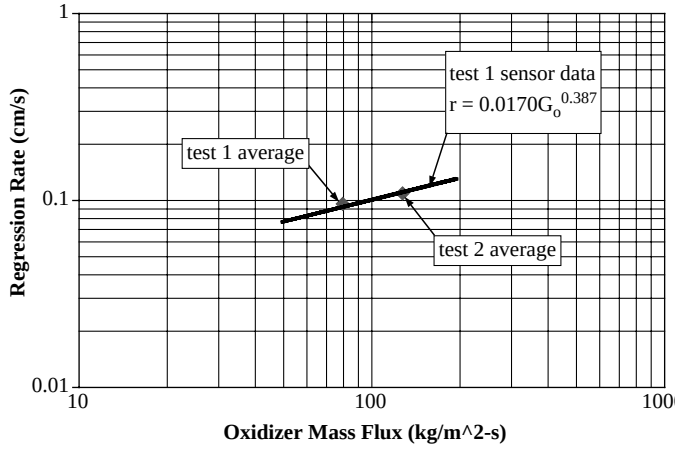

Fig. 27 Reduced MIRRAS data: regression rate vs oxidizer mass flux.

shown in Fig. 27, is further verification of a low flux exponent. The strongest evidence for the low exponent is the agreement between the sensor reading at $t = 7.7$ s and the measurements taken after the second test.

The hybrid regression law in Fig. 27 is shown only over the range of experimental data collected by the sensors. The ability to characterize a motor/fuel combination over such a large range of mass flux with only one firing is a prime motivator for the use of instantaneous regression instrumentation. The MIRRAS sensor is expected to be applicable to other hybrid fuels, such as paraffin, PE, and acrylic.

2. Solid Propellant Applications

Limited testing of the MIRRAS sensor has been conducted in solid propellants. The sensor has not been observed to affect the localized burning rate or create any other anomalies. The occurrence of electrical shorts across the sensor tip has been found to more pronounced in solid propellants, increasing in frequency and duration with the amount of metallization. Direct verification of the sensor accuracy is more difficult to obtain with solid propellant because the grain is completely consumed and does not allow postfiring dissection of the sensor installation. Performance of the sensors in solid propellants has been mixed. In some applications, the sensors have appeared to function properly and the burning rate trends they measured were consistent with chamber pressure trends. In other instances, the sensors have experienced extensive shorting that has rendered the data unreliable. There are several theories as to the cause of and resolution of these phenomena that need to be pursued to create a more generally applicable MIRRAS sensor for solid propellants.

3. Ablative Material Applications

Limited testing of the MIRRAS sensor has also been conducted in ablative materials [26]. The top three-quarters of a hybrid motor was cast with HTPB, and two MIRRAS sensors were cast into a silicone ablative in the bottom one-quarter of the motor. The approach was to burn the HTPB with GOX and produce a hot flow of combusting gasses across the ablative material. The test conditions were as follows: a constant oxygen flow rate of 27 g/s, an initial port diameter of 1.91 cm, and a test duration of 15 s. The data from the sensors were reduced to predict the ablative material thickness vs time, shown in Fig. 28. As expected, the ablation rate decreases as the port area increases. The two sensors are in good agreement, and the slightly faster ablation recorded by sensor 1 is consistent with postfiring measurements. Dissection of the material after the test, along with the sensor data, indicates that the sensors regressed flush with the surface of the ablative. Higher-temperature versions of the standard MIRRAS sensor design may be required for some ablative materials, depending on the magnitude and depth of the surface thermal wave.

F. Merits

Resistance-based and other embedded regression sensor technologies offer unique advantages. For example, their small size and low mass give rise to potential use onboard flight systems [26]. Their generally simple signal conditioning

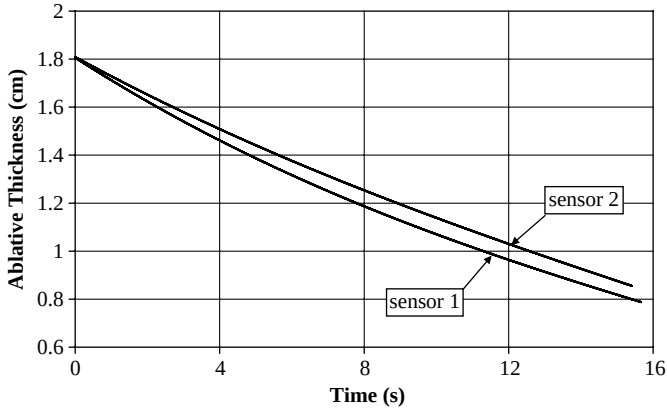

Fig. 28 Reduced MIRRAS data: ablative thickness vs time.

can be readily miniaturized, and the sensors themselves are inherently small by necessity. This enables systems that can measure and transmit real-time regression and solid-fuel mass quantity gauging data from a vehicle in flight. In this role, the embedded sensor technology could both serve as a health monitoring instrument and be used to obtain actual flight data.

As new host materials emerge (such as solid fuels, solid propellants, and ablatives), the proper operation of embedded sensors must be verified to ensure that they continue to regress at the same rate as the host material and are not adversely influenced by its ablation/pyrolysis characteristics. Once mature, embedded regression technologies are generally much less expensive to implement from both an equipment and personnel training standpoint. However, if a large number of tests are to be conducted with a given motor assembly by the same test team, the higher initial cost of nonintrusive technologies (equipment, installation, training, and calibration) must be weighed against the reoccurring installation and sensor expense of embedded technologies to determine the most cost-effective approach.

Another advantage of embedded sensors is the ability for localized regression measurements in complex grain geometries, including those with multiple ports [26]. This is enabled by their ability to be installed at nearly any orientation and location in the grain, provided that the signal transmission wires are properly routed. Nonintrusive line-of-sight or global sampling technologies can have difficulty resolving the spatial location of several surfaces because they regress at potentially different rates and in different directions.

VII. Additional Regression Measurement Technologies

A number of tests have been performed [29] with various devices embedded in solid fuel. An example of application to the regression of a hybrid fuel is shown in Fig. 29 taken from Russo Sorge and Quaranta [29]. Thermocouples are inserted in the solid fuel at set spacings, and when the surface regresses, it is possible to detect the progression of the temperature profile attached to the surface and, thus, obtain the regression rate. In Fig. 30 the use of a condenser consisting in a dielectric

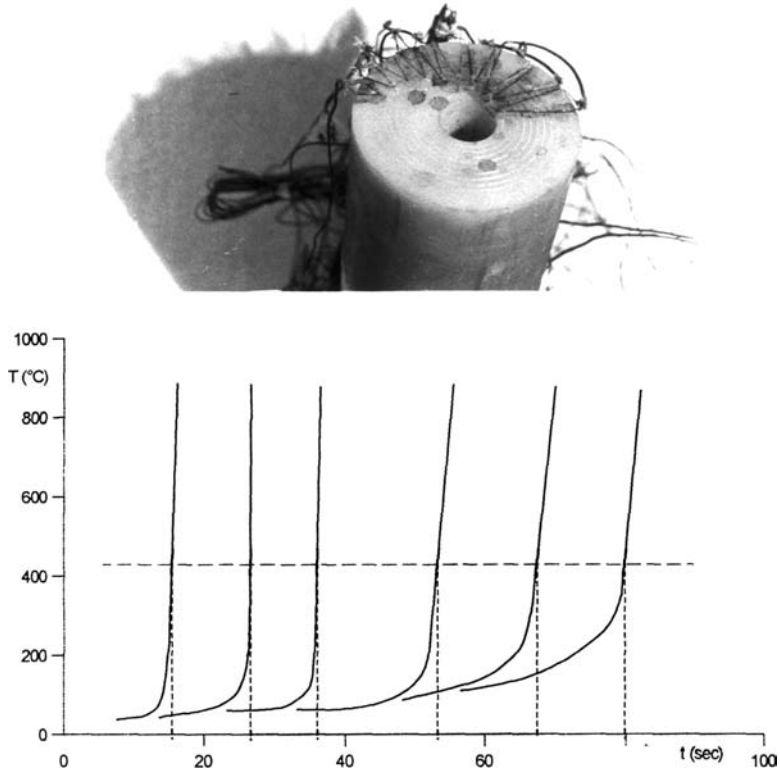

Fig. 29 Measurement with inserted thermocouples.

deposited on a cut in a central bore fuel grain (either from a conductive paint or from a PE sheet covered in aluminum) is shown. When the surface regresses, the capacitor is consumed progressively, allowing the measurement of the regression.

VIII. General Technique for Regression Data Reduction

Regardless of the regression measurement approach used, the raw length vs time data must be reduced to arrive at the instantaneous regression rate. One method is to differentiate numerically between individual data points. However, noise and/or error in the data frequently renders this approach impractical for many regression measurement technologies/applications. Another technique is to fit a curve to the thickness vs time data, and then to differentiate numerically or directly the curve fit with respect to time, yielding an expression for the instantaneous regression rate. Several curve-fit methods have been implemented, including polynomial, logarithmic, and power fits. Comparing the predicted length vs time of these different curve-fit approaches has demonstrated that they can be in good agreement for the prediction of instantaneous length. However, taking the derivative of these curve fits can yield very different regression trends for the same experimental data

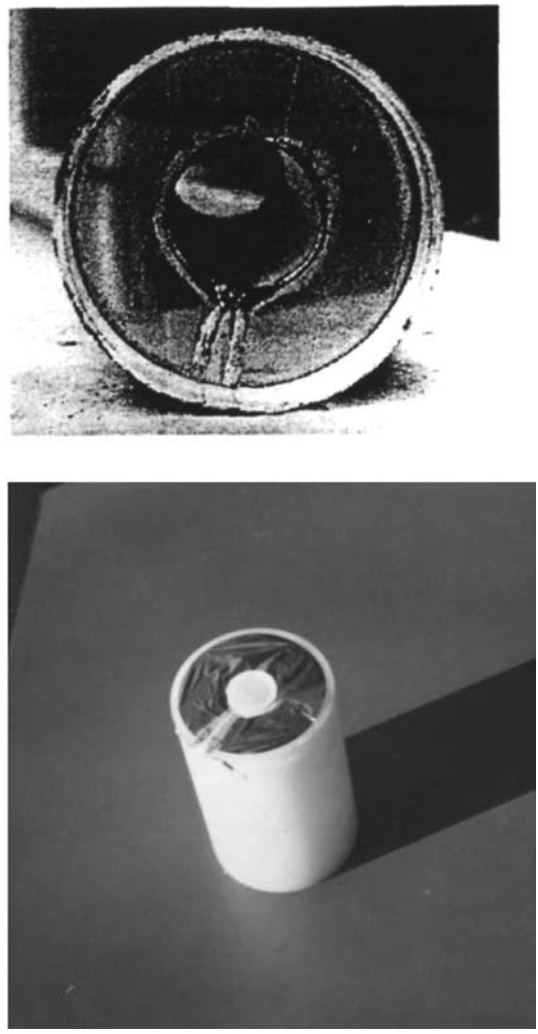

Fig. 30 Varying capacity condenser.

set [26]. The main issue is that a curve fit of a given form presupposes the general regression trend vs time, independent of the experimental regression data. For example, using a third-order polynomial for the length curve fit forces the resulting time-dependant regression to be of a quadratic form.

This issue was recognized by Gramer and Taagen, which prompted them to develop an approach for fitting the raw regression data to a curve fit that has physical meaning to the process under study [26]. A further motivation was to provide a method for consistently analyzing instantaneous regression data (for example, among different researchers and hardware designs). The derivation and

application of this approach for hybrid motors is discussed next, where the data are fit to an expression dictated by the classical hybrid regression law, Eq. (1). A similar technique can be used for the analysis of solid-propellant regression data, beginning with the burning rate power law.

Equations (2) and (3) are definitions of the hybrid regression law, and Eq. (4) assumes a circular grain port. The approach is generally applicable to other grain port geometries if Eq. (4) is replaced by an appropriate relation. Similarly, if the oxidizer flow rate varies over time, the relation can be substituted into Eq. (3). If there is a discontinuity in the oxidizer flow rate, such as a throttling step change, the analysis can be separated into multiple curve-fit equations. Assuming the oxidizer flow is constant and substituting Eqs. (2–4) into Eq. (1) yields the differential equation (5). Thus,

$$r = a \cdot G_0^n \tag{1}$$

$$r = \frac{\mathrm{d}R_t}{\mathrm{d}t} \tag{2}$$

$$G_0 = \frac{m_0}{A_p} \tag{3}$$

$$A_p = \pi \cdot (R_p + R_t)^2 \tag{4}$$

$$\frac{\mathrm{d}R_t}{\mathrm{d}t} = a \cdot \left[\frac{m_o}{\left(R_p + R_t\right)^2 \cdot \pi} \right]^n \tag{5}$$

Separating the variables of Eq. (5) and integrating both sides as an indefinite integral from the limits of 0 to R_t, and 0 to t, yields Eq. (6), where C_1 and C_2 are constants of integration. Recognizing that π, a, and m_0 are constants, defining the relationship $b = 2n + 1$, combining constants, and solving for the two constants of integration by introducing the boundary conditions (7) and (8) results in expression (9):

$$t + C_1 = a \cdot \left[\frac{\pi}{m_0} \right]^n \cdot \left[\frac{\left(R_t + R_p\right)(2 \cdot n + 1)}{2 \cdot n + 1} + C_2 \right] \tag{6}$$

At $t = 0$,

$$R_t = 0 \tag{7}$$

At $t = t_f$,

$$R_t = R_f \tag{8}$$

$$R_t = [b \cdot (t + Z)/X]^{[1/b]} - R_p \tag{9}$$

where the constants Z and X are defined as

$$Z = X \cdot R_p^b / b \tag{10}$$

$$X = t_f \cdot b / [(R_f + R_p)^b - R_p^b] \tag{11}$$

When it is assumed that the instantaneous regression follows the classical hybrid regression law, Eq. (9) is the theoretical form for the total web regression as a function of time.

The sensor data are then fit to Eq. (9). The time at the first data point is set as $t = 0$, and the elapsed time between this point and the last point in the data set is defined as t_f. The initial port radius R_p is the actual instantaneous value of the port radius at $t = 0$. The total amount of web regression at t_f is defined as R_f. Depending on the experimental setup and the goals of the test, different approaches might be taken to define these constants. For example, the definition of the initial port radius can be taken as the actual port radius before the firing began. However, if there is a large start transient in the firing, it may be more accurate to define $t = 0$ at a sensor data point taken after the start transient. Similarly, the total amount of web regression R_f can be assigned as that measured by the last sensor data point or as the actual total web regression measured after the firing.

The last constant to solve for is the curve-fit exponent b. This is accomplished by using each sensor data point to solve for the constant b and then using the average value of b in the curve fit. Thus, for each data point, the time and total amount of regression at that time, R_t, is plugged into the curve fit, where the elapsed time is referenced to $t = 0$. An iterative approach or an equation solver is then used to find the value of b that makes the expression true. When it is assumed that the actual initial and final grain thickness measurements are used in the curve-fit equation, this effectively forces the curve fit to the actual initial and final web thickness. In this case, the sensor data are used to find the path between the two endpoints: the constant b.

This approach also serves as a check to determine if the regression data obey the hybrid regression law, or if there are any anomalies during the test. The curve fits produced using this approach have been reported to fit the data very well [26].

The Instantaneous regression rate vs time can be arrived at by differentiating Eq. (9) with respect to time. Plotting these data against the instantaneous mass flux and using the curve fit to determine the time-dependant port geometry allow the hybrid regression law to be determined from a single hot-fire test.

IX. Comparison of Nonintrusive Measurement Methods

A classification of the nonintrusive techniques briefly described in this chapter can be done depending on their spatial and time resolution [1]. Measurement methods such as microwave and PCG yield a continuous output signal that can be digitized without any repetition rate limitation. For x rays, a compromise has to be found between the spatial resolution (magnitude of the image) and the time resolution (frame per second) due to the digitization rate. The emission repetition rate of the ultrasonic pulse can be fitted from a few tens of hertz for ultrasonic signal window digitization to 20,000 Hz for high-burning-rate propellants with a thickness of the sample adapted to the two successive pulses time interval.

The spatial resolution in depth can be estimated as done by Zarko and Kuo and compared to condensed-phase and thermal-layer thicknesses [1]. The external

surface of the energetic material, on which the ultrasonic or microwaves reflect, or which contributes to form the active electrode of the capacitance technique, should be considered as of high importance. Solid propellants, solid fuels, or insulators are viscoelastic materials: Internal damping and scattering are high. The ultrasonic field is likewise focused by the material; the diameter of the reflective surface is about one-third of the ultrasonic transducer diameter. The smaller the transducer is, the more local the measurement becomes, but, also, the smaller the sample thickness through which the measurement can be performed. The reflective surface can also be shrunken by the grain shape, the curvature radius of an axisymmetrical grain, for instance. Nevertheless, the first-arrival echo will correspond to the shortest propagation time, thus, the shortest distance between the transducer and the reflective surface. For microwaves, the sample diameter is fitted at the transition size. The material sample acts as a waveguide. The question is of interest for a larger propellant grain. For PCGs, one can estimate, by computation, the part of the material section that contributes to the capacitance measurement. The combustion surface has the same feature as the probe electrode due to the guard electrode.

Common limitations or uncertainties should be underlined. The damping and the reflection coefficient of the waves through tested materials change the accuracy and, sometimes, the ability to obtain data for the microwave and ultrasound methods. The microwave transition horn has to be adapted to the dielectric constant of the propellant, as well as for the coupling material, the delay line between the transducer and the material sample, in the ultrasonic technique.

The high conductivity of the flame is of great importance in the high-frequency (140-GHz) microwave propagation and capacitance measurement. The metallized solid propellant makes the measurement difficult to operate. As opposed to these techniques, PCG benefits by this property of the combustion gases.

Notice the effect of the parameters (pressure, temperature, etc.) on the wave propagation characteristics and capacitance values. For the ultrasonic method, the stress–strain field created by the internal pressure has to be taken into account in the measurement analysis (the isovolume deformation as well). The temperature profile will affect the wave velocity. Temperature sensitivity coefficients and phase-change effect on damping (porosity, etc.) are very difficult to determine precisely, but in the framework of the insulator degradation studies, understanding of these phenomena has been improved and the ultrasonic transducer could be considered as a fluxmeter. For microwaves and capacitance techniques, the variation of the dielectric properties in the preheated zone should be considered. Dielectric properties may change due to variation of density, component composition, etc.

It is only through the combined information concerning the substance properties and/or physical principles of the measurement that one can reliably estimate and substantiate the accuracy of a given method [1]. There is no perfect method. They each have their own advantages and disadvantages, which should be evaluated for each test program considering a variety of factors. A summary of some of the methods has been presented by Fry [30] (also see [29]). A summary similar to the one presented in Table 2 was included in the analysis done by the AGARD/Research and Technology Organisation WG27 participants [6], restricted to quasi-steady-state combustion measurement on full-scale rocket motor.

Table 2 Summary of advanced methods for regression-rate measurements

Technique	Purpose	Limitations	Accuracy	Cost	Maturity	Advantages, remarks
Microwave	Burning rate	Complex	Good	High	Medium	Direct measurement
X ray	Failure diagnostics	Metallic case possible depending on source	Medium	Very high	Medium	Large motor, visual data
	Burning rate	Metallic case needs special set-up and analysis	Fair	High	Medium	Laboratory setup
	High transient	Same remark	Good	High	High	Laboratory setup
PCG	Burning rate	Physical understanding	Good	Low	Medium	Flight integration Local measurement
	Ablation	Physical understanding	Fair	Low	Medium	Small size, local measurement
Ultrasonic	Burning rate for propellants	Coupling material	Very good	Low	Medium	Cost time, local measurement
	Ablation	Variation in speed of sound	Fair	Low	Medium	Flight integration
	Fluxmeter	Variation in speed of sound	Good	Low	Fair	
	De bonding		Good	Low	Low	Local measurement
Resistance	Burning rate for solid fuels	May require additional development for exotic fuels	Very good	Very low	High	Very low total cost, local measurements, small size, simple and small flight design
	Burning rate for solid propellants	Not yet mature, shorting problem	Fair	Very low	Low	Very low total cost, local measurements, small size, simple and small flight design
	Ablation	Not yet mature, limited experimental database	Good (with very limited data set)	Very low	Low	Very low total cost, local measurements, small size, simple and small flight design

X. Conclusions

From the point of view of the program manager, a measurement method should be a low-cost method (with respect to implementation and analysis) yielding high-accuracy data and on both local and large sections. The best compromise could be obtained by two methods operating at the same time on a rocket motor, much like what ONERA is doing with PCGs and ultrasonic transducers for insulator studies. The correlation of the two measurements should increase the accuracy of the results and the understanding of what happens inside the material, taking advantages of each method. For example, the ultrasound or resistance method could be helpful for scaling x-ray images. Flight measurements have been done using PCG; resistance, and ultrasound measurements could be used as well. There are certain applications where an embedded sensor is the only feasible type of technology for obtaining localized regression data in very large and/or complex grains.

Results relative to solid propellants were presented because it is in this domain that much work has been performed for the nonintrusive technologies. Much of the embedded regression sensor technology development to date has primarily focused on hybrid rocket applications. Microwaves are too delicate to be used outside of the laboratory, similarly, x rays are also quite heavy.

A generalized data reduction technique developed by Gramer [26] was presented, which could be implemented as a common means of reducing and comparing regression data across several different regression measurement technologies, propellant combinations, and motors. The approach may also offer increased overall measurement accuracy for select applications.

Acknowledgment

The authors thank Guy Lengellé (retired, ONERA, France) for his highly appreciated contribution to this chapter.

References

[1] Zarko, V., and Kuo, K. K., "Critical Review of Methods for Regression Rate Measurements of Condensed Phase Systems," *Non Intrusive Combustion Diagnostics*, edited by K. K. Kuo and T. P. Parr, Begell House, New York, 1994, pp. 600–623.

[2] Kuentzmann, P., Démarais, J. C., and Cauty, F., "Mesure de la vitesse de combustion des propergols solides par ultrasons," *La Recherche Aérospatiale*, 1979, pp. 55–79.

[3] Cauty, F., "Mesure par ultrasons de la vitesse de combustion des propergols solides," ONERA Technical Internal Rep. 5/3173 EY, Chatillon, France, July 1983.

[4] Cauty, F., and Traineau, J. C., "Mesure par ultrasons de la vitesse de combustion d'un propergol solide: perfectionnement et applications à divers régimes de fonctionnement," *Proceedings of the 19th International Congress of Institute für Chemische Technologie*, Karlsruhe, Germany, June 1988, pp. 54–113.

[5] Cauty, F., Démarais, J. C., and Éradès, C., "Determination of Solid Propellant Burning Rate Sensitivity to the Initial Temperature by the Ultrasonic Method," *Non Intrusive Combustion Diagnostics*, edited by K. K. Kuo and T. P. Parr, Begell House, New York, 1994, pp. 642–653.

[6] NATO PEP Working Group 27, "Evaluation of Methods for Solid Propellant Burning Rate Measurements. Chap. 4.0: Non-Intrusive Burning Rate Measurement Technologies," NATO Rept. RTO-TR-043, AGARD, Feb. 2002; CD edited by Research and Technology Organisation, Neuilly, France.

[7] Lengellé, G., Fourest, B., Godon, J. C., and Guin, C., "Condensed Phase Behavior and Ablation Rate of Fuels for Hybrid Propulsion," AIAA Paper 93-2413, June 1993.

[8] Dijkstra, R., Korting, P., and van den Berg, R., "Ultrasonic Regression Rate Measurement in Solid Fuel Ramjets," AIAA Paper 90-1963, July 1990.

[9] Boardman, T. A., Porter, L. G., Brasfield, F. W., and Abel, T. M., "An Ultrasonic Fuel Regression Rate Measurement Technique for Mixture Ratio Control of a Hybrid Motor," AIAA Paper 95-3081, July 1995.

[10] Chiaverini, M., Harting, G., Lu, Y. C., Kuo, K. K., Serin, N., and Johnson, D., "Fuel Decomposition and Boundary-Layer Combustion Processes of Hybrid Rocket Motors," AIAA Paper 95-2686, July 1995.

[11] Serin, N., Chiaverini, M., Harting, G., and Kuo, K. K., "Pressure Correction of Ultrasonic Regression Rate Measurements of a Hybrid Slab Motor," AIAA Paper 99-2319, June 1999.

[12] Cauty, F., Démarais, J. C., Eradès, C., and Caugant, C., "Internal Insulation and Solid Propellant Behavior Measured by Ultrasonic Method on Solid Rocket Motors," AIAA Paper 97–2994, July 1997.

[13] Anderson, M. G., "Real-Time Radiography Support for Titan LAM," AIAA Paper 92-3823, July 1992.

[14] Tauzia, J. M., and Lamarque, P., "Solid Rocket Propellant Behavior During Static Firing Test Using Real Time X Ray Radiography," *AGARD 598*, May 1998, p. 35.

[15] Rogerson, D., "Dynamic Real-Time Radioscopy," Solid Rocket Motor Test and Test Techniques, *AIAA Solid Rocket Technical Committee Lecture Series*, Jan. 1998.

[16] Thépenier, J., "Solid Rocket Motor Behavior During Static Firing Test Using Real Time X-Ray Radioscopy," *AIAA Solid Rocket Technical Committee Lectuire Series*, Jan. 1998.

[17] Chiaverini, M., "Regression Rate and Pyrolysis Behavior of HTPB-Based Solid Fuels in a Hybrid Rocket Motor," Ph.D. Dissertation, Dept. of Mechanical Engineering, Pennsylvania State Univ., University Park, PA, Dec. 1997.

[18] Ho, P. H., "Feasibility Study of the Microwave and the Ultrasonic Techniques on the Continuous Measurement of Solid Propellant Burning Rates," M. S. Thesis, Purdue Univ., Lafayette, IN., Aug. 1965.

[19] Johnson, D. L., "Microwave Measurements of Solid Propellant Burning Rates," Giannini Controls Corp., Technical Note, Duarte, CA, July 1962.

[20] O'Brien, W. F., "A Study of the Application of Microwave Techniques to the Measurement of Solid Rocket Propellant Burning Rates," Ph.D. Dissertation, Virginia Polytechnic Insti. and State Univ., Dept. of Mechanical Engineering, Blackburg, VA, Sept. 1967.

[21] Kuentzmann, P., and Traineau, J. C., "Advances in Solid Propellant Pressure Coupled Response Function Measurement via a Microwave Technique," International Workshop Transient Combustion and Stability of Solid Propellants, Nov. 1990.

[22] Traineau, J. C., Prévost, M., and Tarrin, P., "Experimental Low and Medium Frequency Determination of Solid Propellants Pressure-Coupled Response Function," AIAA Paper 94-3034, July 1994.

[23] Yang, L. C., Miner, E. L., and Romanos, T. C., "Application of Plasma Capacitance Gage (PCG) for Real Time Measurements of Solid Rocket Motor Internal Insulation Erosion," AIAA Paper 90-2327, July 1990.

[24] Seret, J., Démarais, J. C., Cauty, F., and Dupont, M., "Application des techniques de mesure d'épaisseur à la détermination de la vitesse de régression d'une protection thermique," Colloque Centre National d'Etudes Spatiales/ONERA *Fonctionnement des moteurs à propergol solide segmentés pour lanceurs spatiaux*, Paris, Dec. 1992.

[25] McWhorter, B. B., Johnson, M. A., Bryner, B. B., and Ewing, M. E., "An Instrument for Real-Time Measurement of Solid Rocket Motor Insulation Erosion," AIAA Paper 99-2136, June 1999.

[26] Gramer, D. J., and Taagen, J. T., "Low-Cost Surface Regression Sensor for Hybrid Fuels, Solid Propellants, and Ablatives," AIAA Paper 2001-3529, July 2001.

[27] Gramer, D. J., Taagen, T. T., Vermaak, A. G., Harris, J. D., Peissig, D. E., Evans, B. J., Selig, C. J., Mitten, M., and Chiaverini, M. J., "Final Report on Miniature Resistive Regression and Ablation Sensor," OTC-GS-0073-FR-2001-1, Orbital Technologies Corp., NASA Small Business Innovative Research Phase II Rep., Madison, WI, Jan. 2001.

[28] Gramer, D. J., and Taagen, T. J., "Material Regression Sensor," U.S. Patent 6,590,403, 8 July 2003.

[29] Russo Sorge, A., and Quaranta, G., "Regression Rate Measurement Methods in Hybrid Motors," International Workshop on Measurement of Thermophysical and Ballistic Properties of Energetic Materials, June 1998.

[30] Fry, R., "Solid Rocket Motor Test and Test Techniques," *AIAA Solid Rocket Technical Committee Lecture Series*, Jan. 1998.

This page intentionally left blank

Chapter 5

Analytical Models for Hybrid Rockets

Joseph Majdalani*
University of Tennessee Space Institute, Tullahoma, Tennessee 37388

Nomenclature

a = chamber radius
F = mean flow characteristic function
p = normalized pressure, $\bar{p}/(\rho U_w^2)$
Re = wall injection Reynolds number, $U_w a/\nu$
r = normalized radial coordinate, $\bar{r}/a$
U_c = headwall injection velocity, $\bar{u}_z(0,0)$
U_w = sidewall injection velocity, $-\bar{u}_r(a,\bar{z})$
$\boldsymbol{u}$ = normalized velocity, $(\bar{u}_r,\ \bar{u}_z)/U_w$
u_c = normalized injection velocity, U_c/U_w
u_h = headwall injection constant, $U_c/(\pi U_w)$
z = normalized axial coordinate, $\bar{z}/a$
ε = viscous parameter, $1/Re = \nu/(U_w a)$
η = action variable, $\frac{1}{2}\pi r^2$ or $\frac{1}{2}\pi y$
ν = kinematic viscosity, μ/ρ
ρ = density
ψ = normalized stream function

Subscripts and Superscript

c = centerline property
h = headwall property
r, z = radial/axial component or partial derivative
w = sidewall property
$\bar{}$ = dimensional variables

*Jack D. Whitfield Professor of High Speed Flows, Department of Mechanical, Aerospace and Biomedical Engineering. Member AIAA.

I. Introduction

THIS chapter devotes itself to the analytical modeling of the basic flowfield in hybrid rockets with arbitrary headwall injection. Specific solutions pertaining to vortex injection hybrid rockets are covered separately in Chapter 6, whereas the effect of compressibility on the internal gasdynamics is examined in Chapter 7.

In the first part of this trilogy, we focus on the conventional flow configuration assuming a full length, internal burning cylinder. The solution is sought in a non-reactive, rotational, non-swirling, incompressible, and frictionless environment. After the presentation of the basic approximation using Berman's half-cosine headwall injection profile, viscous corrections are added. The analysis is then extended to encompass arbitrary headwall injection. For thoroughness, the formulation is also applied to the slab hybrid rocket chamber. The main results are verified using computational fluid dynamics (CFD) under inviscid and turbulent flow conditions. In addition to the mathematical models that this chapter seeks to advance, several fundamental questions are brought into perspective. These include the following: 1) the purpose of analyzing a hybrid rocket core flow; 2) the difference between a hybrid model and that of a solid or a liquid, and the dissimilarities in boundary conditions and how these differences stand to affect the analysis; 3) the benefits of analytical solutions and how they can aid in understanding the functionality, operability and limitations of hybrid engines; and 4) the experiences inherited from modeling solid rocket motors and how generalizations secured for hybrids may encompass both systems.

A. Background and Relevance

When different methods of propulsion are considered, it must be borne in mind that there is an overall hierarchy of engines depending on the application at hand. Among rocket engines, one may cite two general types, electrical and chemical. Whereas electrical motors are efficient with regard to fuel economy, they provide such little thrust that they are primarily employed in supraorbital missions. For heavy payload launches, one resorts to chemical rockets, the most common being solid and liquid systems.

It is well known that, in chemical rockets, at least two substances, a fuel and an oxidizer, must be mixed in a specific manner depending on the propellant type and category. The chemical energy associated with combining these two substances is transferred to the gaseous products, which, in turn, are expanded through a nozzle; the expansion process produces the desired thrust for the attached vehicle. Three options are available depending on mission requirements: These are 1) solid, 2) liquid, and 3) hybrid rockets. In this chapter, we focus on idealized representations of full-length hybrid rockets with circular or rectangular bores.

To review and compare differences, briefly, liquid rockets utilize liquid fuel and oxidizer stored in separate tanks, except in the case of a monopropellant. By either gas-pressure feeding or mechanically pumping the propellants from their respective tanks, they are sprayed into a mixing chamber where they are combusted and consumed. Liquid rocket engines provide high-thrust capability and can be throttled at will. Additionally, they tend to be the most efficient of high-thrust engines. Their main drawback however is the complexity of their multiple components, specifically, their stop-valves, pressure regulators, injectors, baffles,

turbopump machinery, and other plumbing accessories. In fact, to secure a certain degree of reliability, the need for system redundancies on most components often imposes excessive cost and weight penalties.

Solid rocket motors (SRMs) are somewhat different, having a specific set of advantages and drawbacks. In SRMs, the fuel and oxidizer are chemically premixed to form the solid-propellant grain. By the simple ignition of this rubbery, soap-like substance, the oxidizer and fuel in the solid matrix react to produce the high-energy propulsive gases. Because the propellant grain lines the inner wall of the combustion chamber, the cross section can be tailored to prescribe the desired thrust performance. In fact, a variety of designs for the central burning port are available. SRMs are simple to build and operate. On the downside, they are less efficient fuel burners, and their combustion cannot be regulated. They are more hazardous to handle and possess limited shelf lives due to degradation with aging.

B. Characteristic Features of Hybrids

As we have seen in earlier chapters, hybrid rockets seem to offer a compromising solution in their ability to combine some of the simplistic features of solids and the performance of liquids. In a hybrid, a gaseous or liquid oxidizer (or fuel) is stored in an insulated tank. The fuel grain (or less commonly, the oxidizer) is placed inside a thrust chamber extending between an injector faceplate and a nozzle (Fig. 1). The typical fuel grain is hollowed out to produce a combustion port in a fashion similar to that of an SRM. When the oxidizer is injected into the chamber at high mass flow rate and pressure, reactions are initiated in a thin boundary layer just above the fuel surface. The ensuing high combustion temperature helps to sustain solid-fuel vaporization. The resulting diffusion flame resembles that of a household candle: As the hot combustion gases cause a thin layer of fuel to pyrolyze and vaporize, the oxidizer and fuel particles react along the exposed port areas in several zones of decreasing fuel concentration. This process is shown in Fig. 2, where stacked layers of decreasing fuel fraction are shown to separate the oxidizer from the solid-fuel grain. The reaction gases cross the combustion port and expand through the nozzle. By the metering of the oxidizer, the production of exhaust gases and corresponding thrust can be modulated. This gives hybrid rockets throttling and start–stop–restart capabilities.

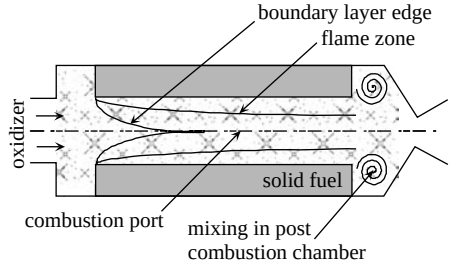

Fig. 1 Schematic of circular-port hybrid rocket.

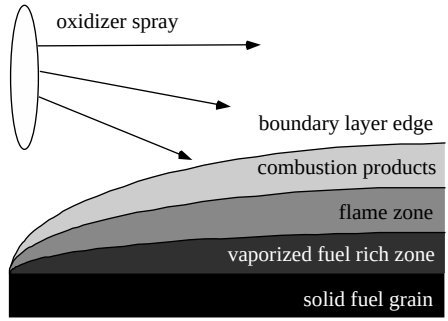

Fig. 2 Decreasing fuel concentration zones above solid surface during hybrid grain pyrolysis.

On the downside, hybrids exhibit lower combustion efficiencies and are susceptible to fluctuations in specific impulse. These setbacks can be chiefly attributed to incomplete mixing in the active combustion zone and the presence of residual slivers at propellant burnout. Despite these relative drawbacks, the specific impulse is only weakly compromised. In practice, conventional hybrids sit on the median between liquid and solid rockets. Their typical performance numbers are available in the open literature: For liquid systems, specific impulse can range between 300 and 400 s; most SRMs operate at an impulse of 200–270 s; yet experimental tests put hybrid engines in the 275–350 s range, directly above SRMs.

Several advantages of hybrids are easy to enumerate. Although they are more complex than SRMs, they compare in performance to liquid systems while requiring one-half of the usual plumbing. This appreciable reduction in overall engine weight and cost is accompanied by a marked increase in reliability. By comparison with solids, hybrids are safer to produce and store, ecologically less hazardous, and the fuel grain, being inert, is more resilient and, therefore, more reliable than solid propellants. By comparison with liquid systems, the partly solid-fuel grain of the hybrid grants volumetric loading advantages over the tankage required for liquids. Clearly, hybrid rocket engines offer several distinct benefits at a reasonable price, especially when technological measures are taken to alleviate their combustion inefficiencies and boost their performance figures. It is in light of these prospects that dedicated teams have been formed at several research laboratories to design and test increasingly more promising models of hybrid rockets [1–7].

C. Flow Modeling Technique

In 1966, a simple analytical solution was proposed by Culick [8] for describing the mean gaseous motion in SRMs. His solution was derived under the contingencies of steady, incompressible, rotational, axisymmetric, and inviscid (high Reynolds number) flow. It coincided with Taylor's 1956 solution obtained in a different context [9]. The resulting profile was scrutinized in subsequent studies, including computational [10–12], experimental [12–15], and theoretical investigations [16–18]; in all cases, it was found to be quite adequate for modeling the mean

flow in a full-length cylindrical motor. To this date, Culick's profile remains at the foundation of several theoretical studies, especially, those concerned with combustion instability. Despite its simplicity and dismissal of SRM physicochemistry, it has proven to be quite helpful in investigating several performance-related mechanisms that are germane to rocket motor internal ballistics. Inspired by Culick's model, other analytical solutions have since been advanced; these include both planar [17, 18] and axisymmetric [16] approximations for the viscous flow in a rocket chamber with regressing walls. The oscillatory wave motion that often accompanies unsteady disturbances in SRMs has also been described by Majdalani [19], Majdalani and Flandro [20], Griffond [21], and others.

Despite the relative complexity of the fluid structures that lie directly above the fuel surface, the trajectory followed by gases ejected into a hybrid chamber can be assumed to be normal to the surface, as in the case of an SRM. In fact, a closed-form analytical approximation, namely, one that will be furnished here, can be used to describe the gas motion corresponding to this idealized representation of a hybrid engine. The interactions within the flame zone must be ignored lest an intractable problem is reached at leading order. Instead, the burning surface will be modeled, as in the case of a solid propellant, by assuming a porous surface [8]. The difference here lies in the mass injection rate across the sidewall, which will be (an order of magnitude) smaller than in the case of a solid propellant. To the author's knowledge, no analytical solution for the hybrid has yet been advanced. The technique we choose relies on a conventional similarity approach; this will be employed in conjunction with Euler's equations, whose application is justified in view of the (still) appreciable injection Reynolds number that accompanies this problem. This will result in a steady, incompressible mean flow solution for a full-length circular-port hybrid engine. The same methodology will be applied to the slab hybrid rocket configuration. In both cases, viscous corrections are added *a posteriori* using asymptotics. Naturally, the solutions suggested in the past for SRMs with similar conditions will have to be modified to include oxidizer inflow stemming from the headwall. Until more refined models become available, these approximations will provide simplistic idealizations owing to the following reasons and limitations:

1) The burning rate of hybrid rocket fuel is very sensitive to the flowfield in the chamber. Hence, many standard assumptions, such as uniform burning rate, which can be justified in SRMs, become less suitable in hybrids. The regression rate is strongly controlled by the pyrolyzing fluid and flow conditions; it is prescribed by complex fluid dynamics and interactions with heat transfer from the hot core to the solid-fuel surface. The heat flux is related, in turn, to turbulent conditions, multiphase effects, and radiation. These factors are not considered here.

2) The validity of the inviscid solution for SRMs has been shown to be adequate at high wall injection Reynolds numbers (generally, exceeding 500) [12–15]. This is easily satisfied in SRMs where large burning rates produce wall injection Reynolds numbers in excess of 1000. In hybrid rockets, the fuel burning rate is an order of magnitude smaller, albeit sufficiently large to justify an asymptotic treatment in which viscosity can be accounted for. The construction of a viscous solution appears to be more essential here than in the case of an SRM, especially because viscous effects will have a more pronounced impact on pressure than

velocity. With this in mind, a viscous rotational approximation will be provided as a more accurate alternative.

3) The real challenge of hybrid propulsion is in the mixing and burning of the two streams. However, in seeking a basic description, no attempts will be made to capture the mixing patterns of oxidizer and fuel or to model the burning of the two streams. These desirable pursuits must await studies in which nonuniform burning, mixing, and the effect of particle-mean flow interactions may be separately addressed. This delicate interplay of underpinning core flow mechanisms is hoped to inspire capable theoreticians to seek higher-order physical idealizations.

II. Basic Hybrid Model

The basic hybrid engine can be modeled as a cylindrical chamber of porous length L_0 and radius a with both a permeable head end and a fully-open downstream end. The permeable headwall permits the injection of a fluid at a prescribed velocity profile $\bar{u}_0$. The chamber is shown in Fig. 3, where $\bar{r}$ and $\bar{z}$ are the radial and axial coordinates. The field of interest extends from the headwall to the typical nozzle attachment point at the aft end.

At the headwall, an oxidizer stream may be injected into the chamber at a maximum centerline speed equal to U_c. This incoming stream must be assimilated with the lateral crossflow sustained by uniform mass addition along the porous sidewall. Naturally, the sidewall velocity U_w is commensurate with the fuel regression rate and can be appreciably smaller than U_c due to typical rates of fuel pyrolysis. This condition can be later exploited in seeking an asymptotic approximation of higher

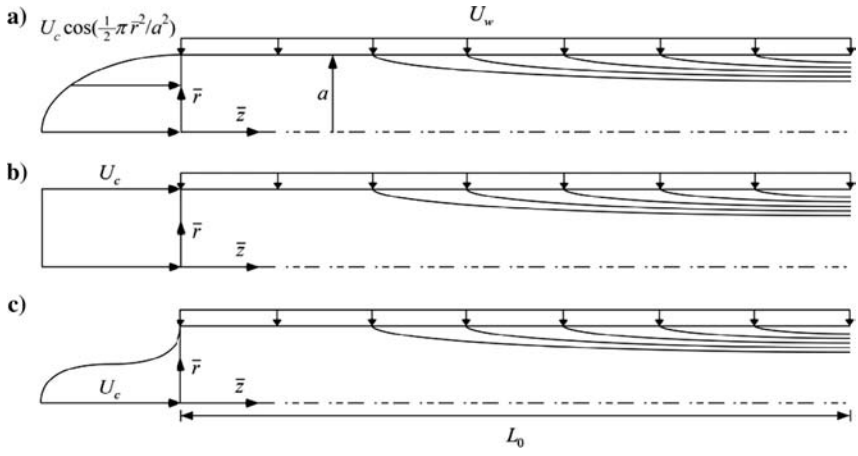

Fig. 3 Full-length hybrid chamber with mass addition from both sidewall and headwall boundaries; oxidizer injection profile at the headwall a) sinusoidal, b) uniform, and c) arbitrary distribution.

order. The present analysis seeks to capture the essential features of the ensuing flowfield using several headwall injection profiles. These correspond to

$$\bar{u}_0(\bar{r}) = \bar{u}_z(\bar{r}, 0) = \begin{cases} U_c = \text{const}; & \text{uniform} \\ U_c \cos\left(\frac{1}{2}\pi \bar{r}^2/a^2\right); & \text{sinusoidal} \\ U_c[1 - (\bar{r}/a)^m]; & \text{laminar and turbulent} \\ U_c(1 - \bar{r}/a)^{1/m}; & \text{turbulent} \end{cases} \tag{1}$$

In addition to providing a generic solution, the focus will be devoted to the realistic profiles that may be used in the context of a rotational flow with sidewall mass addition.

A. Equations

A non-reactive 'outer' flow may be considered, prompted by the weak reactions that accompany diffusion flames. Furthermore, the basic flow may be assumed to be 1) steady, 2) inviscid, 3) incompressible, 4) rotational, 5) axisymmetric, and 6) nonswirling ($\bar{u}_\theta = 0$). Based on these assumptions, Euler's equations become

$$\frac{1}{\bar{r}} \frac{\partial(\bar{r}\bar{u}_r)}{\partial \bar{r}} + \frac{\partial \bar{u}_z}{\partial \bar{z}} = 0 \tag{2}$$

$$\bar{u}_r \frac{\partial \bar{u}_r}{\partial \bar{r}} + \bar{u}_z \frac{\partial \bar{u}_r}{\partial \bar{z}} = -\frac{1}{\rho} \frac{\partial \bar{p}}{\partial \bar{r}} \tag{3}$$

$$\bar{u}_r \frac{\partial \bar{u}_z}{\partial \bar{r}} + \bar{u}_z \frac{\partial \bar{u}_z}{\partial \bar{z}} = -\frac{1}{\rho} \frac{\partial \bar{p}}{\partial \bar{z}} \tag{4}$$

B. Boundary Conditions

The boundary conditions are due to symmetry, no-slip at the sidewall, and both headwall and sidewall injection. Specifically, one may assume 1) axial symmetry and, therefore, no flow across the centerline; 2) vanishing axial flow in fulfillment of the no-slip boundary condition at the sidewall; 3) uniform injection along the cylindrical sidewall, and 4) a prescribed injection pattern at the headwall. These particulars may be written as

$$\begin{aligned} &\bar{r} = 0,\ 0 \le \bar{z} < L_0; && \bar{u}_r = 0 && \text{(no flow across centerline)} \\ &\bar{r} = a,\ 0 \le \bar{z} < L_0; && \bar{u}_z = 0 && \text{(no-slip at the wall)} \\ &\bar{r} = a,\ 0 \le \bar{z} < L_0; && \bar{u}_r = -U_w && \text{(sidewall mass addition)} \\ &\bar{z} = 0,\ 0 \le \bar{r} < a; && \bar{u}_z = \bar{u}_0(\bar{r}) && \text{(variable headwall injection)} \end{aligned} \tag{5}$$

C. Normalization

In seeking a similarity solution using the vorticity-stream function approach, it is helpful to normalize all variables and operators. This can follow

$$z = \bar{z}/a; \qquad r = \bar{r}/a; \qquad \nabla = a\bar{\nabla}; \qquad p = \bar{p}/(\rho U_w^2); \qquad \psi = \bar{\psi}/(a^2 U_w) \tag{6}$$

$$u_r = \bar{u}_r/U_w; \qquad u_z = \bar{u}_z/U_w; \qquad u_c = U_c/U_w \tag{7}$$

Here $U_c = \bar{u}_z(0,0)$ and $U_w = -\bar{u}_r(a,\bar{z})$ are the characteristic fluid injection velocity at the headwall and the uniform wall injection velocity at the sidewall, respectively. As usual, ψ is the Stokes stream function.

Pursuant to Eqs. (6) and (7), motion is prescribed by

$$\nabla \cdot \boldsymbol{u} = 0; \qquad \boldsymbol{u} \cdot \nabla \boldsymbol{u} = -\nabla p \tag{8}$$

Using $\boldsymbol{u} \cdot \nabla \boldsymbol{u} = \frac{1}{2}\nabla(\boldsymbol{u} \cdot \boldsymbol{u}) - \boldsymbol{u} \times \nabla \times \boldsymbol{u}$ and taking the curl of the momentum equation, one obtains the steady inviscid vorticity transport equation. This is

$$\nabla \times \boldsymbol{u} \times \boldsymbol{\Omega} = 0; \quad \boldsymbol{\Omega} \equiv \nabla \times \boldsymbol{u} \tag{9}$$

The corresponding boundary conditions reduce to

$$\begin{aligned} &u_r(0,z) = 0; && \text{(no flow across centerline)} \\ &u_z(1,z) = 0; && \text{(no slip at sidewall);} \\ &u_r(1,z) = -1; && \text{(constant radial inflow at sidewall);} \\ &u_z(r,0) = u_0; && \text{(arbitrary inflow at headwall);} \\ &u_0(r) = \begin{cases} u_c = \text{const} \\ u_c \cos\left(\frac{1}{2}\pi r^2\right) \\ u_c(1 - r^m) \\ u_c(1 - r)^{1/m} \end{cases} \end{aligned} \tag{10}$$

Equation (9) must be solved in conjunction with the constraints granted by Eq. (10).

D. Sinusoidal Headwall Injection

We begin the analysis by presenting the rotational solution corresponding to a sinusoidal headwall injection velocity, $u_0 = u_c \cos\left(\frac{1}{2}\pi r^2\right)$. This half-cosine was shown by Berman to provide a similarity-conforming solution [22]. To start, we consider the vorticity equation, namely,

$$\boldsymbol{\Omega} = \Omega_\theta \boldsymbol{e}_\theta = \left(\frac{\partial u_r}{\partial z} - \frac{\partial u_z}{\partial r}\right)\boldsymbol{e}_\theta \tag{11}$$

The vorticity–stream function approach can be applied by introducing the standard

$$u_r = -\frac{1}{r}\frac{\partial \psi}{\partial z}; \qquad u_z = \frac{1}{r}\frac{\partial \psi}{\partial r} \tag{12}$$

Substitution into the vorticity transport Eq. (9) yields

$$\frac{\partial(u_r\Omega_\theta)}{\partial r} + \frac{\partial(u_z\Omega_\theta)}{\partial z} = 0 \tag{13}$$

and so

$$\frac{\partial\psi}{\partial z}\frac{\partial}{\partial r}\left(\frac{\Omega_\theta}{r}\right) = \frac{\partial\psi}{\partial r}\frac{\partial}{\partial z}\left(\frac{\Omega_\theta}{r}\right) \tag{14}$$

This will be satisfied when

$$\Omega_\theta/r = F(\psi) \tag{15}$$

In seeking a closed-form solution, we choose

$$\Omega_\theta = C^2 r\psi \tag{16}$$

It must be borne in mind that this linear choice is not unique; other possible forms exist, including the case of $\Omega_\theta = C^2 = 0$ for which an irrotational solution is realized. However, when Eq. (16) is inserted into the vorticity equation, one obtains the classic partial differential equation (PDE),

$$\frac{\partial^2\psi}{\partial z^2} + \frac{\partial^2\psi}{\partial r^2} - \frac{1}{r}\frac{\partial\psi}{\partial r} + C^2 r^2\psi = 0 \tag{17}$$

At this juncture, the boundary conditions may be written for the stream function. Based on Eq. (10), these become

$$\lim_{r\to 0}\frac{1}{r}\frac{\partial\psi(r,z)}{\partial z} = 0 \tag{18a}$$

$$\frac{\partial\,\psi(1,z)}{\partial r} = 0 \tag{18b}$$

$$\frac{1}{r}\frac{\partial\psi(1,z)}{\partial z} = 1 \tag{18c}$$

$$\frac{1}{r}\frac{\partial\,\psi(r,0)}{\partial r} = u_0 \tag{18d}$$

By virtue of L'Hôpital's rule, removing the singularity in Eq. (18a) a requires that both

$$\frac{\partial\psi(0,z)}{\partial z} = 0 \tag{19a}$$

and

$$\frac{\partial^2\psi(0,z)}{\partial r\partial z} = 0 \tag{19b}$$

Using separation of variables, one sets

$$\psi(r,z) = f(r)g(z) \tag{20}$$

This reduces Eq. (17) into

$$-(g''/g) = (f''/f) - (1/r)(f'/f) + C^2r^2 = \pm\lambda^2 \tag{21}$$

The physically meaningful case corresponds to $\lambda = 0$. At the outset, one collects

$$g(z) = C_1z + C_2 \tag{22}$$

$$f'' - (1/r)f' + C^2r^2f = 0 \tag{23}$$

The latter can be rearranged into

$$\frac{1}{r}\frac{\mathrm{d}}{\mathrm{d}r}\left(\frac{1}{r}\frac{\mathrm{d}f}{\mathrm{d}r}\right) + C^2f = 0 \tag{24}$$

Using the transformation, $\eta = \frac{1}{2}\pi r^2$, one finds

$$\frac{\mathrm{d}^2f}{\mathrm{d}\eta^2} + \frac{C^2}{\pi^2}f = 0 \tag{25}$$

hence,

$$f(\eta) = A\cos(C\eta/\pi) + B\sin(C\eta/\pi) \tag{26}$$

or

$$f(r) = A\cos\left(\tfrac{1}{2}Cr^2\right) + B\sin\left(\tfrac{1}{2}Cr^2\right) \tag{27}$$

The stream function becomes

$$\psi = (C_1z + C_2)\left[A\cos\left(\tfrac{1}{2}Cr^2\right) + B\sin\left(\tfrac{1}{2}Cr^2\right)\right] \tag{28}$$

At the outset, one derives

$$u_z = (C_1z + C_2)\left[-AC\sin\left(\tfrac{1}{2}Cr^2\right) + BC\cos\left(\tfrac{1}{2}Cr^2\right)\right] \tag{29}$$

and

$$u_r = -(C_1/r)\left[-A\cos\left(\tfrac{1}{2}Cr^2\right) + B\sin\left(\tfrac{1}{2}Cr^2\right)\right] \tag{30}$$

Now, the boundary conditions may be utilized to extract the unknown coefficients.

From $u_r(0,z) = 0$, one finds $A = 0$. Hence,

$$u_z = (C_1 z + C_2)\left[BC\cos\left(\tfrac{1}{2}Cr^2\right)\right] \tag{31}$$

$$u_r = -(C_1/r)\left[B\sin\left(\tfrac{1}{2}Cr^2\right)\right] \tag{32}$$

Then, based on $u_z(1,z) = 0$, one gets $\cos\left(\frac{1}{2}C\right) = 0$ or $C = \pi$. At this point, one is left with

$$\begin{aligned} u_z &= (C_1 z + C_2)\left[B\pi\cos\left(\tfrac{1}{2}\pi r^2\right)\right] \\ u_r &= -(C_1/r)\,B\sin\left(\tfrac{1}{2}\pi r^2\right) \end{aligned} \tag{33}$$

The key boundary condition at the headwall may now be applied. By putting

$$u_z(r,0) = u_c\cos\left(\tfrac{1}{2}\pi r^2\right) \tag{34}$$

one deduces $C_2 = u_c/(B\pi)$; the last constant can be obtained by writing

$$u_z = (C_1 B\pi z + u_c)\cos\left(\tfrac{1}{2}\pi r^2\right) \tag{35}$$

and imposing $u_r(1,z) = -1$. One reaps $C_1 = B^{-1}$. The solution we seek can finally be expressed as

$$\psi = (z + u_h)\sin\left(\tfrac{1}{2}\pi r^2\right); \qquad u_h \equiv u_c/\pi \tag{36}$$

As shown in Fig. 4, increasing the headwall injection parameter increases the flow turning severity near the sidewall. Specifically, as u_h is increased from 50 to 200, the streamlines, which otherwise resemble those of an SRM, become dominated by axial (parallel-flow) motion everywhere except in the neighborhood of the sidewall. This can be clearly attributed to the increased propensity of the axial stream bursting into the chamber. At larger u_h, the sidewall originating stream is met by an overwhelmingly larger axial flow that forces it to rapidly turn and assimilate with it. In practice, the values of U_c and U_w can be calibrated to reproduce the patterns associated with a prototypical hybrid engine. Note that the inviscid solution was verified numerically (despite being exact), using a general purpose finite element code for simulating the axisymmetric equations of incompressible fluid flow. The numerical streamlines were overlaid on the analytical curves and found to be imperceptible. A more detailed comparison with Navier–Stokes computations will be described in a later section.

Based on Eq. (36) other pertinent variables may be evaluated. For example, one finds

$$u_r = -(1/r)\sin\left(\tfrac{1}{2}\pi r^2\right) \tag{37}$$

$$u_z = \pi(z + u_h)\cos\left(\tfrac{1}{2}\pi r^2\right) \tag{38}$$

$$\Omega_\theta = \pi^2(z + u_h)r\sin\left(\tfrac{1}{2}\pi r^2\right) \tag{39}$$

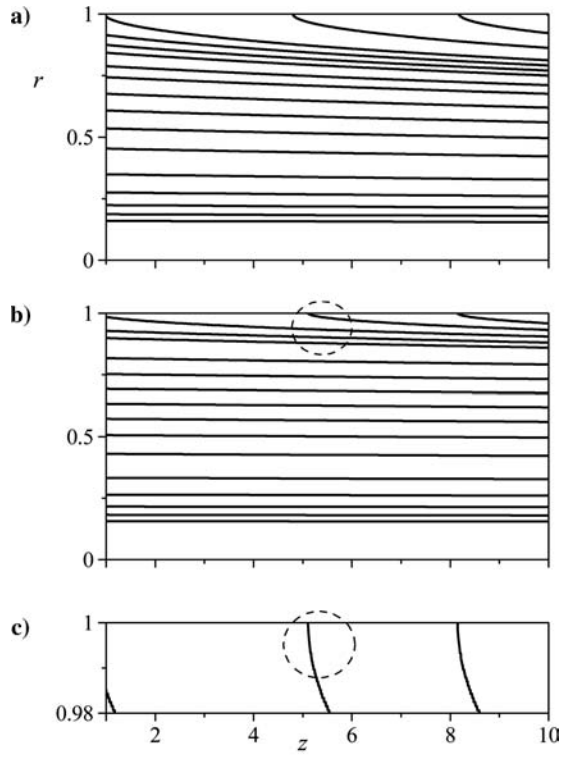

Fig. 4 Rotational streamlines for two increasing headwall injection parameters: a) $u_h = 50$ and b) $u_h = 200$; by magnifying the scale in c) for $u_h = 200$, the wall-normal injection feature is illustrated.

$$\frac{\partial p}{\partial r} = -\frac{-1 + \pi r^2 \sin(\pi r^2) + \cos(\pi r^2)}{2r^3} \tag{40}$$

$$\frac{\partial p}{\partial z} = -\pi^2 (u_h + z) \tag{41}$$

where the pressure gradient is evaluated from Eq. (8). The pressure drop from the headwall becomes

$$\Delta p = \frac{-1 - 2\pi^2 r^2 z(2u_h + z) + \cos(\pi r^2)}{4r^2} \tag{42}$$

In Fig. 5, the two velocity components, vorticity and the radial pressure drop at the headwall, are plotted. Whereas the axial velocity increases linearly with the headwall injection parameter, the radial velocity remains unaffected. In fact, the radial component is seen to be identical to its counterpart in SRMs, namely, that of Culick [8]. In Fig. 5c, the vorticity is seen to be largest near the sidewall, where flow is entering perpendicularly to the fuel surface. Away from the wall, vorticity

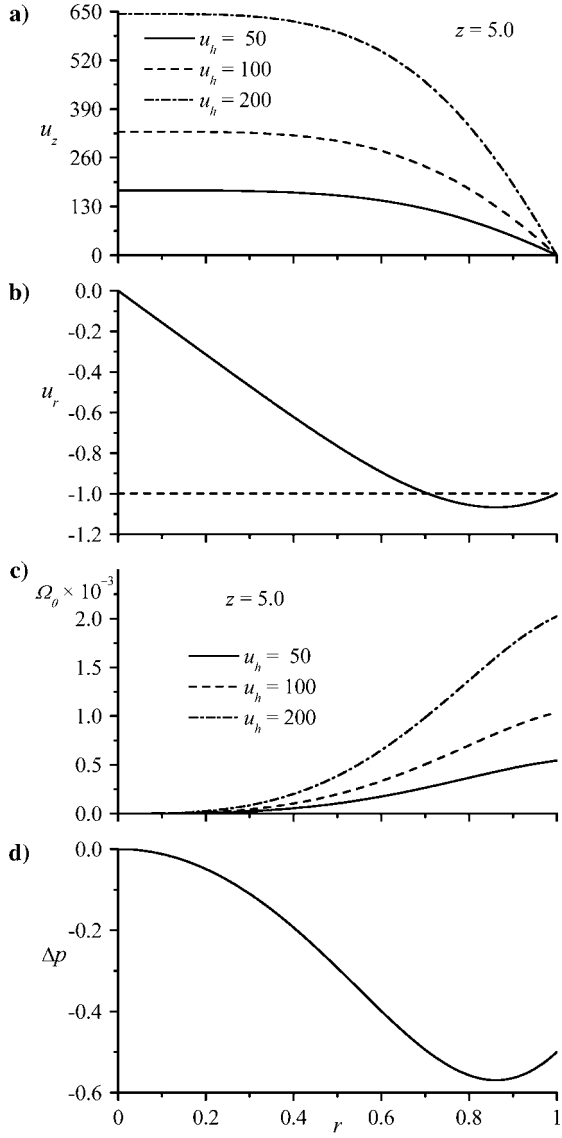

Fig. 5 Axial velocity and vorticity at fixed axial postion: a) axial velocity, b) radial velocity, c) vorticity, and d) pressure drop at chamber's headwall.

decays rapidly; it approaches zero near the centerline, where the flow becomes nearly uniform. As for the pressure drop, Fig. 5d illustrates how $\Delta p(r, 0)$ in the headwall plane can surpass its wall value when

$$\tfrac{1}{2}\sqrt{2} < r < 1 \tag{43}$$

In this range, the largest magnitude corresponds to $\Delta p = -0.569108$. This extremum can be obtained by differentiating Eq. (42) at fixed z. For example, by letting

$$\frac{-1 + \pi r_m^2 \sin(\pi r_m^2) + \cos(\pi r_m^2)}{2r_m^3} = 0 \tag{44}$$

one may expand the numerator using a Taylor series about $\frac{1}{2}\sqrt{3}$; forthwith, a quadratic equation of the form $ax^2 + bx + c = 0$ is obtained where

$$\begin{aligned} a &= -36\pi^2 (\pi + 2)\sqrt{2}\, r_m^2 \\ b &= 12\pi^2 (3\pi + 4)\sqrt{6}\, r_m \\ c &= -64 - 32\sqrt{2} + 24\pi\sqrt{2} - 18\pi^2\sqrt{2} - 27\pi^3\sqrt{2} \simeq -1437.8012 \end{aligned} \tag{45}$$

The extrema of Δp correspond to the two possible roots, one of which being $r_m = 0.861405$. Note that the radial pressure variation is strongly connected with the radial velocity shown in Fig. 5b; both experience an unexpected surge in magnitude immediately after injection (thus exceeding their absolute value at the wall). This behavior is due to the decrease in surface area open to radial flow near $r = 1$.

Equations (36–42) constitute the most basic rotational model that can be used to describe the streamtube motion in a circular hybrid chamber. Despite being inviscid and incompressible, it satisfies no-slip at the sidewall and its headwall injection constant may be adjusted to mimic the bulk gasified motion in an actual system. Furthermore, its simplicity permits the straightforward addition of viscous effects as we shall illustrate next.

E. Axisymmetric Viscous Correction

Viscous effects may be accommodated as formerly performed in the context of SRM internal ballistics [16]. For example, one can start with the reduced Navier–Stokes equation incorporating both viscosity and wall regression speed, namely,

$$\begin{aligned} 2\varepsilon \left[\eta \frac{\mathrm{d}^4 F}{\mathrm{d}\eta^4} + \left(2 + \frac{\alpha}{\pi}\eta\right) \frac{\mathrm{d}^3 F}{\mathrm{d}\eta^3} + 2\frac{\alpha}{\pi} \frac{\mathrm{d}^2 F}{\mathrm{d}\eta^2} \right] \\ + F \frac{\mathrm{d}^3 F}{\mathrm{d}\eta^3} - \frac{\mathrm{d}F}{\mathrm{d}\eta} \frac{\mathrm{d}^2 F}{\mathrm{d}\eta^2} = 0; \quad \eta = \tfrac{1}{2}\pi r^2 \end{aligned} \tag{46}$$

where $F = \psi/(z + u_h)$ is the mean flow characteristic function and $\alpha = a\dot{a}/\nu$ is the Reynolds number based on the speed of regression. In the present case, wall regression may be suppressed by setting $\alpha = 0$ [16]. Subsequently, one is left with

$$2\varepsilon \left(\eta \frac{\mathrm{d}^4 F}{\mathrm{d}\eta^4} + 2\frac{\mathrm{d}^3 F}{\mathrm{d}\eta^3} \right) + F \frac{\mathrm{d}^3 F}{\mathrm{d}\eta^3} - \frac{\mathrm{d}F}{\mathrm{d}\eta} \frac{\mathrm{d}^2 F}{\mathrm{d}\eta^2} = 0 \tag{47}$$

The corresponding boundary conditions are

$$\frac{\mathrm{d}F\left(\frac{1}{2}\pi\right)}{\mathrm{d}\eta} = 0; \qquad F\left(\tfrac{1}{2}\pi\right) = 1; \qquad F(0) = 0; \qquad \lim_{\eta \to 0} \sqrt{\eta} \frac{\mathrm{d}^2 F}{\mathrm{d}\eta^2} = 0 \tag{48}$$

Note that $\varepsilon \equiv \nu/(aU_w)$ is the inverted Reynolds number based on the sidewall injection velocity. A regular perturbation solution to Eqs. (47) and (48) can be readily obtained and verified. The result is

$$\begin{aligned} F = \sin\eta + \varepsilon\{&-3 + (\eta\cos\eta - \sin\eta)S(\eta) - S_1(\eta)\cos\eta \\ &+ \left[3 + S\left(\tfrac{1}{2}\pi\right)\right]\sin\eta - \left[6/\pi + 1 + S\left(\tfrac{1}{2}\pi\right)\right. \\ &\left. - (2/\pi)S_1\left(\tfrac{1}{2}\pi\right)\right]\eta\cos\eta + 2\cos\eta\} \end{aligned} \tag{49}$$

where

$$S(\eta) = \int_0^\eta \phi\csc\phi\,\mathrm{d}\phi = \eta + \sum_{k=1}^{\infty}\frac{2}{\pi^{2k}}\left(\sum_{n=1}^{\infty}\frac{1}{n^{2k}}\right)\frac{\left(1-2^{1-2k}\right)}{(2k+1)}\eta^{2k+1} \tag{50}$$

$$S_1(\eta) = \int_0^\eta \phi^2\csc\phi\,\mathrm{d}\phi = \frac{1}{2}\eta^2 + \sum_{k=1}^{\infty}\left(\sum_{n=1}^{\infty}n^{-2k}\right)\frac{\left(1-2^{1-2k}\right)}{(k+1)\,\pi^{2k}}\eta^{2k+2} \tag{51}$$

The primary dependent variables of interest, namely, the streamline and velocity components, may be calculated from

$$\psi = (z+u_h)F; \qquad u_r = -\frac{F}{r}; \qquad u_z = \frac{(z+u_h)}{r}\frac{\mathrm{d}F}{\mathrm{d}r} \tag{52}$$

By inspection, it can be seen that if viscosity is set to zero in Eq. (49), the inviscid form given by Eqs. (36–38) will be recovered. In summary, the viscous approximation for the rotational model comprises

$$\begin{aligned} \psi = (z+u_h)\Big[\sin\eta + \varepsilon\Big(&-3 + \left[3 + S\left(\tfrac{1}{2}\pi\right) - S(\eta)\right]\sin\eta \\ &- \cos\eta\left\{S_1(\eta) - 3 + \eta\left[1 + 6\pi^{-1} + S\left(\tfrac{1}{2}\pi\right)\right.\right. \\ &\left.\left. - S(\eta) - 2\pi^{-1}S_1\left(\tfrac{1}{2}\pi\right)\right]\right\}\Big)\Big] + \mathcal{O}(\varepsilon^2) \end{aligned} \tag{53}$$

$$\begin{aligned} u_r = -\sqrt{\pi/(2\eta)}\Big[\sin\eta + \varepsilon\Big(&-3 + \left[3 + S\left(\tfrac{1}{2}\pi\right) - S(\eta)\right]\sin\eta \\ &- \cos\eta\left\{S_1(\eta) - 3 + \eta\left[1 + 6\pi^{-1} + S\left(\tfrac{1}{2}\pi\right)\right.\right. \\ &\left.\left. - S(\eta) - 2\pi^{-1}S_1\left(\tfrac{1}{2}\pi\right)\right]\right\}\Big)\Big] + \mathcal{O}(\varepsilon^2) \end{aligned} \tag{54}$$

$$\begin{aligned} u_z = \pi\,(z+u_h)\Big[\cos\eta + \varepsilon\Big(&-\eta + 2\left[1 - 3\pi^{-1} + \pi^{-1}S_1\left(\tfrac{1}{2}\pi\right)\right]\cos\eta \\ &+ \left\{S_1(\eta) - 3 + \eta\left[1 + 6\pi^{-1} + S\left(\tfrac{1}{2}\pi\right) - S(\eta)\right.\right. \\ &\left.\left. - 2\pi^{-1}S_1\left(\tfrac{1}{2}\pi\right)\right]\right\}\sin\eta\Big)\Big] + \mathcal{O}(\varepsilon^2) \end{aligned} \tag{55}$$

As for the corrected pressure drop, it may be obtained by integrating from the centerline to any radius. One gets

$$\begin{aligned}\Delta p_\perp \equiv p(0,z) - p(\eta,z) &= \pi\left[\varepsilon F_\eta + \tfrac{1}{4}\eta^{-1}F^2 - \varepsilon F_\eta(0)\right] \\ &= \tfrac{1}{4}\pi\eta^{-1}\sin^2\eta + \varepsilon\pi\Big(\cos\eta - 1 - \tfrac{3}{2}\eta^{-1}\sin\eta \\ &\quad + \tfrac{1}{4}\eta^{-1}\left\{3 + S\left(\tfrac{1}{2}\pi\right) - S(\eta) + \cos(2\eta)\left[S(\eta) - S\left(\tfrac{1}{2}\pi\right) - 3\right]\right\} \\ &\quad + \tfrac{1}{4}\sin(2\eta)\Big\{S(\eta) - S\left(\tfrac{1}{2}\pi\right) - 1 - 6\pi^{-1} \\ &\quad + 2\pi^{-1}S_1\left(\tfrac{1}{2}\pi\right) + \eta^{-1}\left[3 - S_1(\eta)\right]\Big\}\Big) + \mathcal{O}(\varepsilon^2) \end{aligned} \tag{56}$$

In like fashion, the pressure drop in the flow direction can be estimated from

$$\begin{aligned}\Delta p_\parallel \equiv p(\eta,0) - p(\eta,z) &= -\pi^2 z\left(\tfrac{1}{2}z + u_h\right)\left[2\varepsilon(\eta F_{\eta\eta\eta} + F_{\eta\eta}) - (F_\eta)^2 + FF_{\eta\eta}\right] \\ &= \pi^2 z\left(\tfrac{1}{2}z + u_h\right)\{1 + (2\varepsilon/\pi)[2\pi - 6 + 4\pi\mathcal{C} - 7\zeta(3)]\} \\ &\quad + \mathcal{O}(\varepsilon^2) \end{aligned} \tag{57}$$

where $\mathcal{C} = \frac{1}{2}S\left(\frac{1}{2}\pi\right) \simeq 0.91596559$ is Catalan's constant, and $\zeta(3) \simeq 1.2020569$ is the Riemann zeta function defined by

$$\zeta(x) = \sum_{k=1}^{\infty} k^{-x}$$

Note that the final expression in Eq. (57) is evaluated along the axis of the chamber in the flow direction. Hence, one can put $\Delta p_\parallel \simeq \pi^2 z\left(\frac{1}{2}z + u_h\right)(1 + 2.15123\varepsilon) + \mathcal{O}(\varepsilon^2)$. Finally, the shear stress (or vorticity) can be calculated from

$$\begin{aligned}\tau = \bar{\tau}/(\rho U_w^2) &= -\varepsilon\Omega = \varepsilon(z + u_h)\sqrt{2}\,\pi^{\frac{3}{2}}\sqrt{\eta}F_{\eta\eta} \\ &= -\varepsilon(z + u_h)\pi\sqrt{2\pi\eta}\sin\eta + \mathcal{O}(\varepsilon^2) \end{aligned} \tag{58}$$

At the sidewall, one is left with $\tau_w = -\varepsilon\pi^2(z + u_h) + \mathcal{O}(\varepsilon^2)$. This approximation illustrates the method by which one may obtain the small viscous corrections. These can be appreciable in hybrids wherein the sidewall injection Reynolds number is roughly an order of magnitude smaller than in SRMs. The resulting mean flow can, thus, be used as a seed in the modeling of internal burning hybrids.

III. General Headwall Injection

One may seek to generalize by first recognizing that solutions to Eq. (17) are of the form

$$\psi(r,z) = (\alpha z + \beta)\left[A\cos\left(\tfrac{1}{2}Cr^2\right) + B\sin\left(\tfrac{1}{2}Cr^2\right)\right] \tag{59}$$

This expression satisfies Eq. (19b) identically. Therefore, from this point forward, Eq. (18a) a may be superseded by Eq. (19a).

A. Solution by General Eigenfunction Expansions

Application of the boundary conditions must be carefully carried out, preferably, in the order in which they appear. For example, Eq. (19a) gives:

$$\frac{\partial \psi(0,z)}{\partial z} = \alpha A \cos\left(\tfrac{1}{2}Cr^2\right) + \alpha B \sin\left(\tfrac{1}{2}Cr^2\right)\Big|_{r=0} = 0 \tag{60}$$

or $A = 0$. Without loss in generality, we set $B = 1$ and rewrite Eq. (18b) as

$$rC(\alpha z + \beta)\, \cos\left(\tfrac{1}{2}Cr^2\right)\Big|_{r=1} = 0; \qquad \forall z \tag{61}$$

and so $\cos\left(\frac{1}{2}C\right) = 0$; this is satisfied by

$$C = C_n = (2n+1)\pi; \qquad n = \{0, 1, 2, \ldots, \infty\} \in \mathbb{N} \tag{62}$$

Using $C_n = (2n+1)\pi$ enables us to sum over eigenfunctions corresponding to both wall suction and injection. Whereas even integers yield injection-driven eigenfunctions, odd integers correspond to suction driven solutions. When combined, one can put

$$\psi_n(r,z) = (\alpha_n z + \beta_n) \sin\left[\left(n + \tfrac{1}{2}\right)\pi r^2\right]$$

or

$$\psi(r,z) = \sum_{n=0}^{\infty} (\alpha_n z + \beta_n) \sin\left[\left(n + \tfrac{1}{2}\right)\pi r^2\right] \tag{63}$$

The third condition becomes

$$\frac{\partial \psi(1,z)}{\partial z} = \sum_{n=0}^{\infty} \alpha_n \sin\left[\left(n + \tfrac{1}{2}\right)\pi\right] = 1 \qquad \text{or} \qquad \sum_{n=0}^{\infty} (-1)^n \alpha_n = 1 \tag{64}$$

which may exhibit several outcomes depending on the behavior of α_n. Finally, the headwall condition may be satisfied by evoking the idea of orthogonality. Starting with

$$\frac{1}{r}\frac{\partial \psi(r,0)}{\partial r} = \pi \sum_{n=0}^{\infty} (2n+1)\beta_n \cos\left[\left(n + \tfrac{1}{2}\right)\pi r^2\right] = u_0(r) \tag{65}$$

one can apply orthogonality to secure

$$\beta_n \int_0^1 (2n+1) \cos^2\left[\left(n + \tfrac{1}{2}\right)\pi r^2\right] r\, \mathrm{d}r = \frac{1}{\pi}\int_0^1 u_0(r) \cos\left[\left(n + \tfrac{1}{2}\right)\pi r^2\right] r\, \mathrm{d}r \tag{66}$$

or

$$\beta_n = \frac{\displaystyle\int_0^1 u_0(r)\cos\left[\left(n+\tfrac{1}{2}\right)\pi r^2\right] r\,\mathrm{d}r}{\displaystyle\pi\int_0^1 (2n+1)\cos^2\left[\left(n+\tfrac{1}{2}\right)\pi r^2\right] r\mathrm{d}r}$$

$$= \frac{4}{\pi(2n+1)}\int_0^1 u_0(r)\cos\left[\left(n+\tfrac{1}{2}\right)\pi r^2\right] r\mathrm{d}r \tag{67}$$

For uniform headwall injection, $u_0(r) = u_c$, so one recovers

$$\beta_n = \frac{4(-1)^n u_c}{\pi^2(2n+1)^2} = \frac{4(-1)^n u_h}{\pi(2n+1)^2} \tag{68}$$

Backward substitution into Eq. (63) enables us to extract, for the general case,

$$\psi(r,z) = \sum_{n=0}^{\infty}(\alpha_n z + \beta_n)\sin\left[\left(n+\tfrac{1}{2}\right)\pi r^2\right] \tag{69}$$

and for the particular case of uniform headwall injection,

$$\psi(r,z) = \sum_{n=0}^{\infty}\left[\alpha_n z + \frac{4(-1)^n u_c}{\pi^2(2n+1)^2}\right]\sin\left[\left(n+\tfrac{1}{2}\right)\pi r^2\right] \tag{70}$$

Note that many solutions may be arrived at depending on the choice of α_n that properly fulfills Eq. (64). One such case corresponds to Taylor's classic solution for which

$$\alpha_0 = 1 \qquad \alpha_n = 0; \qquad \forall n \neq 0 \tag{71}$$

At the outset, Eq. (69) reduces to

$$\psi(r,z) = z\sin\left(\tfrac{1}{2}\pi r^2\right) + \frac{4u_c}{\pi^2}\sum_{n=0}^{\infty}\frac{(-1)^n}{(2n+1)^2}\sin\left[\left(n+\tfrac{1}{2}\right)\pi r^2\right]$$

(uniform headwall injection) (72)

In all cases, one may obtain the solution from

$$\psi = z\sin\left(\tfrac{1}{2}\pi r^2\right) + \sum_{n=0}^{\infty}\beta_n\sin\left[\left(n+\tfrac{1}{2}\right)\pi r^2\right];$$

$$u_z = \pi z\cos\left(\tfrac{1}{2}\pi r^2\right) + \pi\sum_{n=0}^{\infty}(2n+1)\beta_n\cos\left[\left(n+\tfrac{1}{2}\right)\pi r^2\right] \tag{73}$$

For Berman's half-cosine, Eq. (67) may be evaluated to give $\beta_0 = u_c/\pi$ and $\beta_n = 0,\ \forall n \neq 0$. Equation (73) becomes

$$u_z = \pi z \cos\left(\tfrac{1}{2}\pi r^2\right) + u_c \cos\left(\tfrac{1}{2}\pi r^2\right) = \pi (z + u_h) \cos\left(\tfrac{1}{2}\pi r^2\right) \tag{74}$$

This reproduces the special case caused by harmonic headwall injection leading to Eq. (38) [23].

Equation (72) is deliberately left as an infinite series, albeit collapsible into closed form when put in terms of special functions. The character of this expression is shown in Fig. 6 for a headwall injection rate appropriate for SRMs with reactive headend (or T-burners). With use of $u_c = 1$, a balance between sidewall and headwall injection causes the streamline originating at the corner (1,0) to bisect the flowfield at an angle of $\frac{1}{4}\pi$. When one concentrates on specific areas, it may be seen that the solution conforms to the stated boundary conditions. Whereas Fig. 6b shows the corner streamlines, Figs. 6c–6f confirm the satisfaction of the no-slip condition by reproducing the expected behavior in different sectors.

When the same analysis is repeated in Fig. 7 for $u_c = 1000$, a streamtube motion akin to that of hybrid rocket core flow is seen to dominate. This is true everywhere except in the close vicinity of the sidewall. Whereas Fig. 7a offers an overview of the streamtube motion, magnification near the sidewall enables us to reaffirm that the gas enters the chamber perpendicularly to the grain surface. By approaching the headwall, the presence of parallel flow in Figs. 7e and 7f lends support to the local orthogonality.

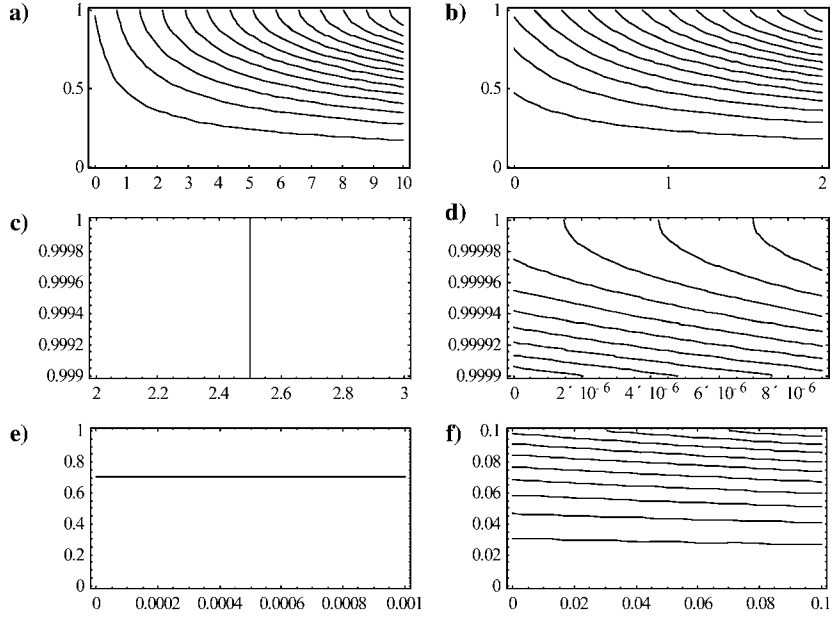

Fig. 6 Streamlines for $u_c = 1$ in $r - z$ plane, in different localities.

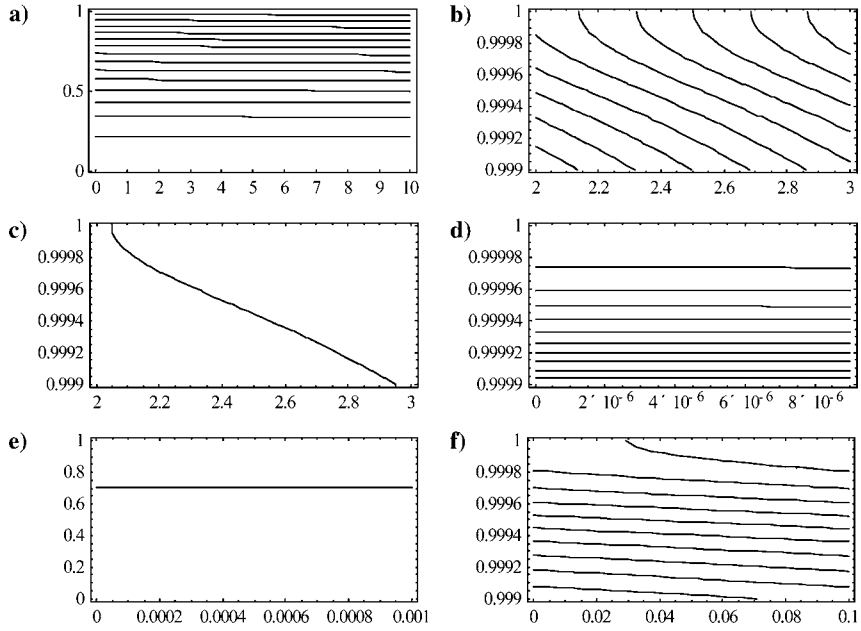

Fig. 7 Streamlines for $u_c = 1{,}000$ in $r - z$ plane, in different localities.

Once ψ is determined, the velocity and vorticity components may be recovered from Eqs. (12) and (16). One obtains

$$
\begin{aligned}
u_r(r) &= -r^{-1}\sin\left(\tfrac{1}{2}\pi r^2\right)\\
\Omega(r,z) &= \pi^2 rz\sin\left(\tfrac{1}{2}\pi r^2\right)\\
u_z(r,z) &= \pi z\cos\left(\tfrac{1}{2}\pi r^2\right) + 4u_h\sum_{n=0}^{\infty}\frac{(-1)^n}{(2n+1)}\cos\left[\left(n+\tfrac{1}{2}\right)\pi r^2\right]
\end{aligned}
\tag{75}
$$

Note that uniform headwall injection does not introduce any mean flow vorticity and that $u_z(1,z) = 0$ because each $\cos[(n+\frac{1}{2})\pi]$ term vanishes at the sidewall. This behavior is shown in Figs. 8a and 8b at the headwall and, using $L_0 = 2$, at six equally spaced axial stations corresponding to 0, 0.4, 0.8, 1.2, 1.6, and 2. Note that the streamwise velocity is also collapsible into closed form by recognizing that

$$
4u_h\sum_{n=0}^{\infty}\frac{(-1)^n}{(2n+1)}\cos\left[\left(n+\tfrac{1}{2}\right)\pi r^2\right] = 2u_h q(r) = u_c\left[1-\delta_k(1-r)\right] \tag{76}
$$

where δ_k is the Kronecker delta and $q(r) = \tan^{-1}(e^{\frac{1}{2}i\pi r^2}) + \tan^{-1}(e^{-\frac{1}{2}i\pi r^2})$.

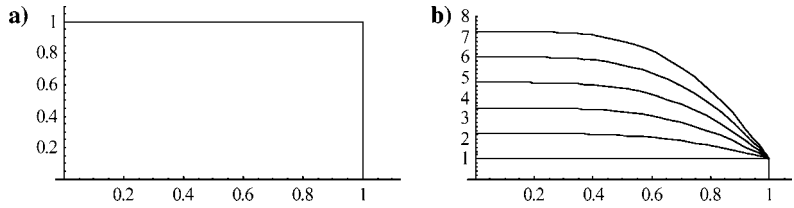

Fig. 8 Radial evolution of the streamwise velocity corresponding to $u_c = 1$: a) $z = 0$ and b) six equidistant positions at $z = 0$, 0.4, 0.8, 1.2, 1.6, and 2.

B. Solution by Injection-Driven Eigenfunctions

The same analysis may be repeated by retaining only the even eigenvalues associated with an injection-driven wall contribution. This can be seen by reconsidering Eq. (61) and writing

$$C = C_n = (4n+1)\pi; \qquad n \in \mathbb{Z} \tag{77}$$

This choice enables us to skip every other multiple of $\frac{1}{2}\pi$, thus producing a series of injection-based solutions. At the outset, the third condition becomes

$$\sum_{n=-\infty}^{\infty} \alpha_n \sin\left[\left(2n+\tfrac{1}{2}\right)\pi\right] = 1 \quad \text{or} \quad \sum_{n=-\infty}^{\infty} \alpha_n = 1 \tag{78}$$

Note that we start our sum at negative infinity lest we capture half of the headwall injection velocity. As we pursue this route, the headwall requirement reduces to

$$\pi \sum_{n=-\infty}^{\infty} (4n+1)\beta_n \cos\left[\left(2n+\tfrac{1}{2}\right)\pi r^2\right] = u_0 \tag{79}$$

and so, by use of orthogonality, we put

$$\beta_n \int_0^1 (4n+1)\cos^2\left[\left(2n+\tfrac{1}{2}\right)\pi r^2\right] r\,\mathrm{d}r = \frac{1}{\pi}\int_0^1 u_0 \cos\left[\left(2n+\tfrac{1}{2}\right)\pi r^2\right] r\,\mathrm{d}r \tag{80}$$

or

$$\beta_n = \frac{4}{\pi(4n+1)}\int_0^1 u_0 \cos\left[\left(2n+\tfrac{1}{2}\right)\pi r^2\right] r\,\mathrm{d}r \tag{81}$$

When $u_0 = u_c$, the direct result is

$$\beta_n = \frac{4u_c}{\pi^2(4n+1)^2} = \frac{4u_h}{\pi(4n+1)^2} \quad \text{(uniform headwall injection)} \tag{82}$$

The injection-based stream function becomes

$$\psi_{inj}(r,z) = \sum_{n=-\infty}^{\infty}\left[\alpha_n z + \frac{4u_c}{\pi^2(4n+1)^2}\right]\sin\left[\left(2n+\tfrac{1}{2}\right)\pi r^2\right] \tag{83}$$

A special case of Eq. (83) corresponds to $\alpha_0 = 1$ and $\alpha_n = 0;\ \forall n \neq 0$. The injection-driven solution becomes

$$\psi_{inj}(r,z) = z\sin\left(\tfrac{1}{2}\pi r^2\right) + \frac{4u_c}{\pi^2}\sum_{n=-\infty}^{\infty}(4n+1)^{-2}\sin\left[\left(2n+\tfrac{1}{2}\right)\pi r^2\right] \tag{84}$$

Although bearing a slightly different appearance, Eq. (84) is identical to Eq. (72). The seemingly dissimilar part corresponds to the streamwise velocity, which can be readily identified as

$$u_z(r,z) = \pi z\cos\left(\tfrac{1}{2}\pi r^2\right) + 4u_h\sum_{n=-\infty}^{\infty}\frac{1}{(4n+1)}\cos\left[\left(2n+\tfrac{1}{2}\right)\pi r^2\right] \tag{85}$$

This result merely duplicates the behavior of Eq. (75) especially that, at $r = 0$, one may use the convergent series

$$\sum_{n=-\infty}^{\infty}\frac{1}{(4n+1)} = \frac{\pi}{4} \tag{86}$$

to write $u_z(0,z) = \pi z + u_c$. Similarly, at the sidewall, no-slip is observed by virtue of $\cos[(2n+\frac{1}{2})\pi] = 0, \forall n \in \mathbb{Z}$. In hindsight, had we limited our sum to $n \in \mathbb{Z}$, the orthogonality condition would have yielded half of the headwall contribution, namely, $u_z(r,0) = \frac{1}{2}u_c$ and $u_z(0,z) = \pi z + \frac{1}{2}u_c$.

C. Nonlinear Residual in the Vorticity Transport Equation

Based on Eq. (9), the residual Q of the vorticity transport equation may be calculated from

$$\nabla\times\boldsymbol{u}\times\boldsymbol{\Omega} = -\left[\frac{\partial}{\partial r}(u_r\Omega) + \frac{\partial}{\partial z}(u_z\Omega)\right]\boldsymbol{e}_\theta = Q(r,z)\boldsymbol{e}_\theta \tag{87}$$

In terms of the stream function, we, therefore, have

$$Q = -\frac{\Omega}{r^2}\frac{\partial\psi}{\partial z} + \frac{1}{r}\frac{\partial\psi}{\partial z}\frac{\partial\Omega}{\partial r} - \frac{1}{r}\frac{\partial\psi}{\partial r}\frac{\partial\Omega}{\partial z} \tag{88}$$

For each eigensolution given by Eq. (69), the vorticity transport equation vanishes on substitution. When $\Omega = \Omega_n = C_n^2 r\psi_n$ is used, Eq. (88) becomes

$$\begin{aligned} Q_n &= -\frac{C_n^2\psi_n}{r}\frac{\partial\psi_n}{\partial z} + \frac{1}{r}\frac{\partial\psi_n}{\partial z}\frac{\partial}{\partial r}(C_n^2 r\psi_n) - \frac{1}{r}\frac{\partial\psi_n}{\partial r}\frac{\partial}{\partial z}(C_n^2 r\psi_n) \\ &= -\frac{C_n^2\psi_n}{r}\frac{\partial\psi_n}{\partial z} + \frac{1}{r}\frac{\partial\psi_n}{\partial z}C_n^2\psi_n + C_n^2\frac{\partial\psi_n}{\partial z}\frac{\partial\psi_n}{\partial r} - C_n^2\frac{\partial\psi_n}{\partial r}\frac{\partial\psi_n}{\partial z} \\ &= 0 \end{aligned} \tag{89}$$

The summation of Eq. (89) over all eigenmodes is identically zero if a hypothetical case may be considered for which all eigensolutions coexist independently. However, when coupling between eigenmodes is considered, the total vorticity and stream function must be accounted for in the vorticity transport equation. Substitution into Eq. (88) requires evaluating

$$Q = -\frac{1}{r^2}\sum_{n=0}^{m}\Omega_n\sum_{n=0}^{m}\frac{\partial\psi_n}{\partial z} + \frac{1}{r}\sum_{n=0}^{m}\frac{\partial\psi_n}{\partial z}\sum_{n=0}^{m}\frac{\partial\Omega_n}{\partial r} - \frac{1}{r}\sum_{n=0}^{m}\frac{\partial\psi_n}{\partial r}\sum_{n=0}^{m}\frac{\partial\Omega_n}{\partial z} \tag{90}$$

Now, by taking into account that

$$\begin{aligned}
&\psi_n(r,z) = (\alpha_n z + \beta_n)\sin\left(\tfrac{1}{2}C_n r^2\right); \qquad &&\frac{\partial\psi_n}{\partial z}(r) = \alpha_n \sin\left(\tfrac{1}{2}C_n r^2\right)\\
&\frac{\partial\psi_n}{\partial r}(r,z) = rC_n(\alpha_n z + \beta_n)\cos\left(\tfrac{1}{2}C_n r^2\right); \qquad &&\frac{\partial\Omega_n}{\partial z}(r) = rC_n^2\alpha_n \sin\left(\tfrac{1}{2}C_n r^2\right)
\end{aligned} \tag{91}$$

and, for the Taylor–Culick class of solutions, $\alpha_0 = 1$ and $\alpha_n = 0; \forall n \neq 0$, one is left with

$$\begin{aligned}
\frac{\partial\psi_n}{\partial z}(r) &= \begin{cases} \alpha_0 \sin\left(\tfrac{1}{2}C_0 r^2\right); & n = 0 \\ 0; & \forall n \neq 0 \end{cases}\\
\frac{\partial\Omega_n}{\partial z}(r) &= \begin{cases} C_0^2 r\alpha_0 \sin\left(\tfrac{1}{2}C_0 r^2\right) = C_0^2 r\dfrac{\partial\psi_0}{\partial z}; & n = 0 \\ 0; & \forall n \neq 0 \end{cases}
\end{aligned} \tag{92}$$

where the axial derivatives are solely due to the zeroth eigenmode. This reduces Eq. (90) to

$$Q = \frac{\partial\psi_0}{\partial z}\left(-\frac{1}{r^2}\sum_{n=0}^{m}\Omega_n + \frac{1}{r}\sum_{n=0}^{m}\frac{\partial\Omega_n}{\partial r} - C_0^2\sum_{n=0}^{m}\frac{\partial\psi_n}{\partial r}\right) \tag{93}$$

We may skip the $n = 0$ case for which the residual vanishes. Finally, noting that

$$\frac{\partial\Omega_n}{\partial r} = C_n^2\psi_n + C_n^2 r\frac{\partial\psi_n}{\partial r} \tag{94}$$

we retrieve

$$Q(r) = \frac{\partial\psi_0}{\partial z}\sum_{n=0}^{m}\left(C_n^2 - C_0^2\right)\frac{\partial\psi_n}{\partial r} \tag{95}$$

Equation (95) represents the net residual of the vorticity transport equation due to nonlinear coupling; it is not necessarily zero except for inert or sinusoidal headwall

injection profiles. Based on Eq. (73), one recovers

$$Q(r) = r\sin\left(\tfrac{1}{2}\pi r^2\right)\sum_{n=0}^{m}\left(C_n^2 - C_0^2\right)C_n\beta_n\cos\left(\tfrac{1}{2}C_n r^2\right)$$

$$\sim \tfrac{1}{2}\pi r^3\sum_{n=0}^{m}\left(C_n^2 - C_0^2\right)C_n\beta_n + \mathcal{O}(r^5) \tag{96}$$

Clearly, solutions with modes for which $C_n^2 - C_0^2 \neq 0$ entail a residual and become, at the outset, non-exact. However, as much as it is independent of z, the residual becomes relatively smaller as we move away from the headwall. Further, it becomes more accurate near the centerline and the sidewall where the approximation becomes exact. The diminution in the streamwise direction makes the approximation appropriate for long SRM chambers. The behavior is also consistent with the Taylor–Culick model, which is known for its subtle discontinuity at $z = 0$. In all cases, the core flow approximations become increasingly more accurate away from the headwall.

D. Pressure Analysis

The steady momentum equation may be readily solved for the pressure distribution. By ignoring the viscous diffusion of vorticity, one may start with $\boldsymbol{u}\cdot\nabla\boldsymbol{u} = -\nabla p$ and integrate in two spatial directions to retrieve, at length,

$$p = p_0 - \tfrac{1}{2}\boldsymbol{u}\cdot\boldsymbol{u} - \int u_r\frac{\partial u_z}{\partial r}\,\mathrm{d}z \tag{97}$$

where $p_0 = p(0,0)$ represents the headwall pressure. Immediate integration and substitution based on Eqs. (75) and (76) lead to

$$\begin{aligned} p &= p_0 - \tfrac{1}{2}\pi^2 z^2 - \tfrac{1}{2}r^{-2}\sin^2\left(\tfrac{1}{2}\pi r^2\right) + \tfrac{1}{2}u_c^2 \\ &\quad - 2\pi^{-2}u_c q(r)\left[u_c q(r) + \pi^2 z\cos\left(\tfrac{1}{2}\pi r^2\right)\right] \\ &= p_0 - \tfrac{1}{2}\pi^2 z^2 - \tfrac{1}{2}r^{-2}\sin^2\left(\tfrac{1}{2}\pi r^2\right) + \tfrac{1}{2}u_c^2\delta_k(1-r) \\ &\quad - \pi u_c z\cos\left(\tfrac{1}{2}\pi r^2\right)[1 - \delta_k(1-r)] \end{aligned} \tag{98}$$

At the centerline, we recover $p(0,z) = p_0 - \frac{1}{2}\pi^2 z^2 - \pi u_c z$. To put this in Culick's traditional form, we first write the dimensional pressure, $\bar{p} = \bar{p}_0 - \frac{1}{2}\rho U_w^2\pi z\times(\pi z + 2u_c)$, and then renormalize by $\bar{p}_0 = \rho a_0^2/\gamma$. Using $M_w = U_w/a_0$ for the wall Mach number, we obtain

$$\begin{aligned} p* = \bar{p}/\bar{p}_0 = 1 - \tfrac{1}{2}\gamma M_w^2\Big\{&\pi^2 z^2 + r^{-2}\sin^2\left(\tfrac{1}{2}\pi r^2\right) - u_c^2 \\ &+4\pi^{-2}u_c q(r)\left[u_c q(r) + \pi^2 z\cos\left(\tfrac{1}{2}\pi r^2\right)\right]\Big\} \end{aligned}$$

$$= 1 - \tfrac{1}{2}\gamma M_w^2 \left\{ \pi^2 z^2 + r^{-2} \sin^2\left(\tfrac{1}{2}\pi r^2\right) - u_c^2 \delta_k (1-r) \right.$$
$$\left. + 2\pi u_c z \cos\left(\tfrac{1}{2}\pi r^2\right)[1 - \delta_k(1-r)] \right\} \tag{99}$$

with $p^*(0,z) = 1 - \frac{1}{2}\gamma M_w^2 \pi z(\pi z + 2u_c)$.

E. Other Variable Headwall Injection Profiles

The analysis may be repeated using an arbitrary headwall injection profile. To be specific, one may use

$$u_0(r) = u_c(1 - r^m) \tag{100a}$$

$$u_0(r) = u_c(1 - r)^{1/m} \tag{100b}$$

These are prescribed by classic profiles used by Poiseuille, Darcy, and others. For the parabolic Poiseuille profile, one may use $u_0(r) = u_c(1 - r^2)$ and extract

$$\beta_n = 8u_c/\lambda_n^3; \qquad \lambda_n \equiv (2n+1)\pi \tag{101}$$

Both Berman's and Poiseuille's headwall injection velocities are shown in Fig. 9 using the same representative parameters of Fig. 8 and fixed $u_c = 1$. As evidenced by Figs. 9a, 9c, 9e, and 9f, the effect of varying the headwall injection profile in SRMs becomes negligible as the chamber length is increased. However, it remains important near the headwall and, therefore, in short chambers such as upper stage SRMs and T-burners. In contrast, the headwall injection profile plays a pivotal role in hybrid rocket analysis (recall Fig. 7). As for the turbulent profiles corresponding to Eq. (100a), three commonly examined cases may be connected with $m = 6, 8, 10$. These lead to

$$\frac{\lambda_n^{2+m/2}\beta_n}{u_c} = \begin{cases} 96[(-1)^n\lambda_n - 2]; & m = 6 \\ 192(-1)^n(\lambda_n^2 - 8); & m = 8 \\ 320\left[(-1)^n\lambda_n(\lambda_n^2 - 24) + 48\right]; & m = 10 \end{cases} \tag{102}$$

Finally, for the turbulent model associated with Eq. (100b), one may resort to symbolic programming and obtain a recursive relation in terms of the generalized hypergeometric function ${}_pF_q(a;b;z)$; this is

$$\beta_n = \frac{4m^2 u_c}{(1+m)(1+2m)\lambda_n} {}_3F_4$$
$$\times \left(\left\{ \frac{3}{4}, 1, \frac{5}{4} \right\}, \left\{ \frac{3}{4} + \frac{1}{4m}, 1 + \frac{1}{4m}, \frac{5}{4} + \frac{1}{4m}, \frac{3}{2} + \frac{1}{4m} \right\}, -\frac{1}{16}\lambda_n^2 \right) \tag{103}$$

The commonly employed (middle) values in Eqs. (102) and (103) are shown in Figs. 9e– 9h using a fixed $u_c = 1$.

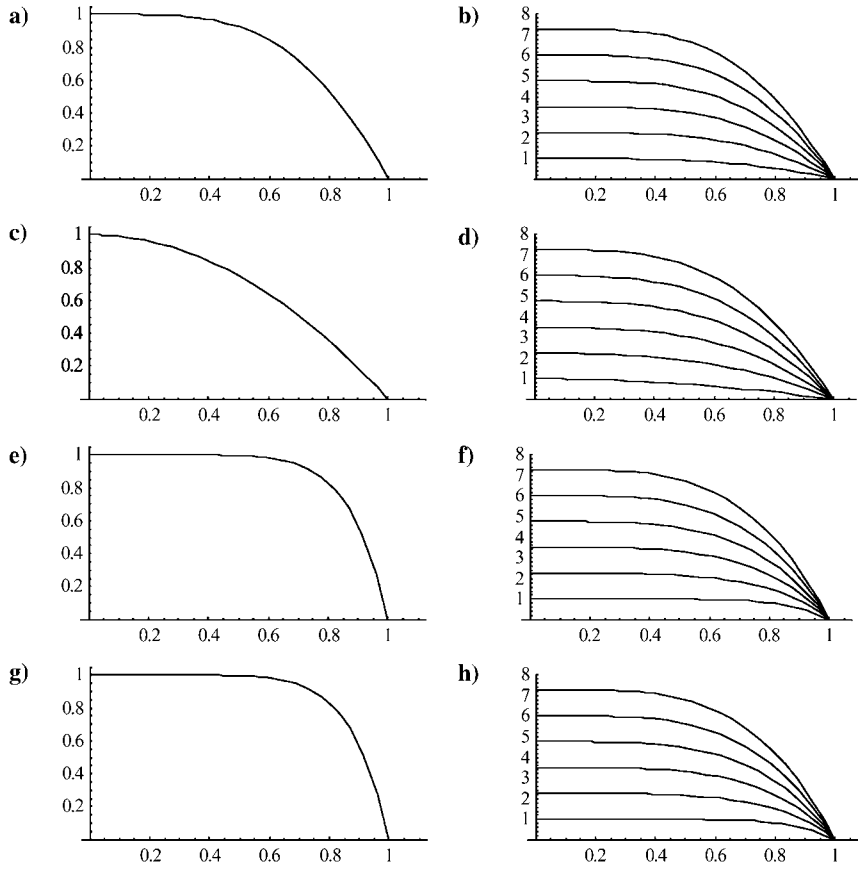

Fig. 9 Radial evolution of the streamwise velocity for $u_c = 1$ and several headwall inlet profiles associated with a–b) Berman's half-cosine, c–d) Poiseuille, $1 - r^2$, e–f) $1 - r^8$, and g–h) $(1 - r)^{1/7}$. Profiles are shown at headwall (left) and six equidistant positions corresponding to $z = 0$, 0.4, 0.8, 1.2, 1.6 and 2 (right).

The formulation for variable headwall injection permits the analytical modeling of complicated injection patterns in real hybrid systems. In later sections, these solutions are compared to CFD results and shown to provide adequate approximations.

F. Non-Series Approximation

According to Prandtl's boundary-layer theory, the no-slip condition at the sidewall need not be satisfied by a standard outer solution due to the absence of friction. If we were to relax this constraint by permitting the streamwise velocity to be finite at the sidewall, the solution will, of course, relinquish its quasi-viscous character. Under these auspices, a simple solution may be obtained in the form of an

outer approximation that would later demand a boundary-layer treatment along the sidewall. Bearing this in mind, we may choose to ignore the second boundary condition in Eq. (10) and only require that

$$\begin{aligned} u_r(0,z) &= 0 \\ u_r(1,z) &= -1 \\ u_z(r,0) &= u_c \end{aligned} \tag{104}$$

In searching for an exact outer solution, we may follow Terrill and Colgan [24] and superimpose on Taylor's profile (with impervious headwall) a uniform field of zero dimensionality. The resultant is $\psi = \psi_0 + \psi_w$, where $\psi_w = z\sin(\frac{1}{2}\pi r^2)$ is the sidewall-driven Taylor–Culick stream function. At the headwall, one may introduce a uniform, axially independent plug flow exhibiting the classic form $\psi_0 = \frac{1}{2}u_c r^2$ with $u = u_z = u_c$. Note that ψ_0 represents a plain irrotational field that still satisfies the vorticity equation by substitution of $C = 0$ in Eq. (17). It also observes three of the original boundary conditions. Overall, ψ_0 and ψ_w satisfy, respectively,

$$\begin{aligned} &u_r(0,z) = 0; \qquad u_r(1,z) = 0; \qquad u_z(r,0) = u_c \\ &u_r(0,z) = 0; \qquad u_r(1,z) = -1; \qquad u_z(r,0) = 0 \end{aligned} \tag{105}$$

Note that the sum of the separate boundary conditions reproduces Eq. (104). Because of linearity, the composite solution will, hence, observe the chief requirements, albeit at the expense of carrying $u_z(1,z) = u_c, \forall z$. The composite outer solution is, hence, expressible by

$$\psi = \tfrac{1}{2}u_c r^2 + z\sin\left(\tfrac{1}{2}\pi r^2\right); \qquad u_r(r) = -r^{-1}\sin\left(\tfrac{1}{2}\pi r^2\right);$$

$$u_z(r,z) = u_c + \pi z\cos\left(\tfrac{1}{2}\pi r^2\right); \qquad \Omega(r,z) = \pi^2 rz\sin\left(\tfrac{1}{2}\pi r^2\right) \tag{106}$$

Equation (106) is similar to Eq. (75) except for the inability to vanish at the sidewall. A viscous boundary-layer treatment will be needed to restore Eq. (72).

G. Slab Burner Geometry

The same analysis can be repeated for the slab burner configuration. This can be modeled using Cartesian coordinates and a porous channel with arbitrary headwall injection. The advantage of retrieving the solution for the planar hybrid chamber is that it provides an avenue for comparison with experimental and numerical investigations of slab rocket grains. These are becoming increasingly more popular in academic circles [25].

The slab rocket can be idealized as a two-dimensional channel of porous length L_0 and height $2a$. The fluid stream enters the headwall at an axial speed $\bar{u}_0$. The lateral cross flow is driven at a sidewall velocity U_w. As shown in Fig. 10, $\bar{x}$ and $\bar{y}$ stay for the axial and normal coordinates. As usual, we set

$$x = \bar{x}/a; \quad y = \bar{y}/a; \quad \nabla = a\bar{\nabla}; \quad p = \bar{p}/(\rho U_w^2); \quad \psi = \bar{\psi}/(aU_w) \tag{107}$$

$$u_x = \bar{u}_x/U_w; \quad u_y = \bar{u}_y/U_w; \quad u_c = U_c/U_w; \quad L = L_0/a \tag{108}$$

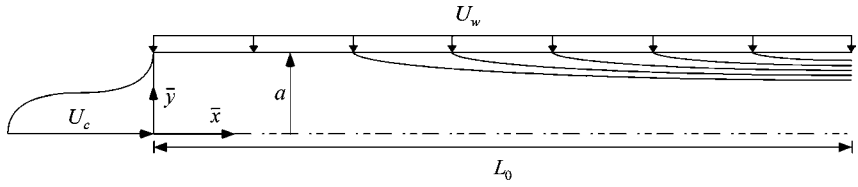

Fig. 10 Slab burner with arbitrary headwall injection.

To reduce redundant boundary conditions, we consider half of the channel and use symmetry about the midsection plane. This enables us to write

$$\begin{aligned} &u_y(x,0) = 0 && \text{(no flow across midsection plane)} \\ &u_x(0,y) = u_0(y) && \text{(headwall injection profile)} \\ &u_y(x,1) = -1 && \text{(constant sidewall mass addition)} \\ &u_x(x,1) = 0 && \text{(no-slip)} \end{aligned} \tag{109}$$

Subsequently, we introduce the Cartesian stream function via $u_x = \partial\psi/\partial y$ and $u_y = -\partial\psi/\partial x$; the vorticity transport equation is then fulfilled by any field exhibiting $\Omega = \Omega_z = F(\psi)$ including $\Omega = C^2\psi$. The latter transforms the vorticity equation into

$$\nabla^2\psi + C^2\psi = 0 \tag{110}$$

The general solution is straightforward and can be expressed with

$$\psi(x,y) = (\alpha x + \beta)[A\cos(Cy) + B\sin(Cy)] \tag{111}$$

Application of the four boundary conditions parallels our earlier work; we recover

$$\psi(x,y) = x\sin\left(\tfrac{1}{2}\pi y\right) + \sum_{n=0}^{\infty}\beta_n \sin\left[\left(n+\tfrac{1}{2}\right)\pi y\right] \tag{112}$$

For a variable injection profile, the eigencoefficients may be calculated from

$$\beta_n = \frac{4}{(2n+1)\pi}\int_0^1 u_0(y)\cos\left[\left(n+\tfrac{1}{2}\right)\pi y\right]\mathrm{d}y \tag{113}$$

These clearly depend on the prescribed headwall velocity $u_0(y)$. Despite possible exceptions, an arbitrary inlet velocity profile can be assimilated using Eq. (113). Table 1 summarizes the solution for three commonly employed headwall injection models. Note that the solutions in general accrue a non-zero residual in the vorticity

Table 1 Sample solutions for slab burner with arbitrary headwall injection, $\eta = \frac{1}{2}\pi y$

$u_0(y)$	$\psi(x,y)$	$u_x(x,y)$	$u_y(x,y)$
u_C	$x \sin\eta + u_C \sum_{n=0}^{\infty} \frac{8(-1)^n}{\pi^2(2n+1)^2} \sin[(2n+1)\eta]$	$\frac{1}{2}\pi x \cos\eta + u_C \sum_{n=0}^{\infty} \frac{4(-1)^n}{\pi(2n+1)} \cos[(2n+1)\eta]$	$-\sin\eta$
$u_C \cos\eta$	$(x + 2u_h)\sin\eta$	$\frac{1}{2}\pi(x + 2u_h)\cos\eta$	$-\sin\eta$
$u_C(1-y^2)$	$x \sin\eta + u_C \sum_{n=0}^{\infty} \frac{64(-1)^n}{\pi^4(2n+1)^4} \sin[(2n+1)\eta]$	$\frac{1}{2}\pi x \cos\eta + u_C \sum_{n=0}^{\infty} \frac{32(-1)^n}{\pi^3(2n+1)^3} \cos[(2n+1)\eta]$	$-\sin\eta$

transport equation. This can be obtained from

$$Q(y) = \frac{\partial \psi}{\partial x}\frac{\partial \Omega}{\partial y} - \frac{\partial \psi}{\partial y}\frac{\partial \Omega}{\partial x} = \frac{\partial \psi_0}{\partial x}\sum_{n=0}^{m}\left(C_n^2 - C_0^2\right)\frac{\partial \psi_n}{\partial y}$$

$$= \sin\left(\frac{1}{2}\pi y\right)\sum_{n=0}^{m}\left(C_n^2 - C_0^2\right)C_n\beta_n\cos\left(C_n y\right)$$

$$\sim \frac{1}{2}\pi y\sum_{n=0}^{m}\left(C_n^2 - C_0^2\right)C_n\beta_n + \mathcal{O}(y^3) \tag{114}$$

where

$$\Omega_n = C_n^2\psi_n; \quad C_n = (n+\tfrac{1}{2})\pi$$
$$\psi_n(x,y) = (\alpha_n x + \beta_n)\sin\left(C_n y\right) \tag{115}$$

As before, we note that the residual always vanishes at the walls and in the midsection plane; being independent of x, it becomes proportionally smaller in the downstream direction. For $C_n^2 \neq C_0^2$, the solutions are only approximate but become increasingly more accurate away from the headwall.

H. Two-Dimensional Viscous Correction

Viscous effects can be estimated for the slab rocket engine. As already performed in the cylindrical geometry, one may start with the reduced Navier–Stokes equation incorporating both viscosity and wall regression. As shown by Zhou and Majdalani [17], this is given by

$$\varepsilon\frac{\mathrm{d}^4F}{\mathrm{d}y^4} + \alpha\varepsilon\left(y\frac{\mathrm{d}^3F}{\mathrm{d}y^3} + 3\frac{\mathrm{d}^2F}{\mathrm{d}y^2}\right) + F\frac{\mathrm{d}^3F}{\mathrm{d}y^3} - \frac{\mathrm{d}F}{\mathrm{d}y}\frac{\mathrm{d}^2F}{\mathrm{d}y^2} = 0; \quad \varepsilon \equiv \nu/(aU_w) \tag{116}$$

where $F = \psi/(x + 2u_h)$ is the two-dimensional characteristic function for the mean flowfield. In as much as it is inconsequential, wall regression may be ignored by putting $\alpha = 0$ [17]. Berman's equation is instantly regained with its standard assortment of boundary conditions,

$$\varepsilon\frac{\mathrm{d}^4F}{\mathrm{d}y^4} + F\frac{\mathrm{d}^3F}{\mathrm{d}y^3} - \frac{\mathrm{d}F}{\mathrm{d}y}\frac{\mathrm{d}^2F}{\mathrm{d}y^2} = 0 \tag{117}$$

$$\frac{\mathrm{d}^2F}{\mathrm{d}y^2}(0) = 0; \qquad F(0) = 0; \qquad \frac{\mathrm{d}F}{\mathrm{d}y} = 0; \qquad F(1) = 1 \tag{118}$$

A regular perturbation solution complemented by variation of parameters may be applied to Eq. (116–118) [17]. The result is

$$F(\eta) = \sin\eta + \varepsilon\left\{\tfrac{1}{4}\pi\left[(\eta\cos\eta - \sin\eta)\ln\tan\tfrac{1}{2}\eta + \cos\eta S(\eta)\right]\right.$$
$$\left. + \left[\tfrac{1}{2}S\left(\tfrac{1}{2}\pi\right) - \tfrac{1}{2}\right]\eta\cos\eta\right\} \tag{119}$$

where $\eta = \frac{1}{2}\pi y$ for the Cartesian case and $S(\eta)$ is defined in Eq. (50). The velocity and stream function may be obtained directly from

$$\psi = (x + 2u_h)F; \qquad u_x = (x + 2u_h)\frac{\mathrm{d}F}{\mathrm{d}y}; \qquad u_y = -F \tag{120}$$

The normal pressure distribution can be determined by substituting the velocity components into the y-momentum equation and then integrating from the midsection plane to any position y. This operation yields

$$\Delta p_{\perp} = \varepsilon F_y(0) - \left(\varepsilon F_y + \tfrac{1}{2}F^2\right) \tag{121}$$

The axial pressure drop may also be obtained from the x-momentum equation. One gets

$$\Delta p_{\parallel} = x\left(\tfrac{1}{2}x + 2u_h\right)\left[\varepsilon F_{yyy} + FF_{yy} - \left(F_y\right)^2\right] \tag{122}$$

Finally, the shear stress (or vorticity) can be estimated from

$$\tau = \bar{\tau}/(\rho U_w^2) = \varepsilon(x + 2u_h)F_{yy} = -\varepsilon\Omega \tag{123}$$

At the sidewall, one calculates $\tau_{\mathrm{w}} = \varepsilon(x + 2u_h)F_{yy}(1) = -\varepsilon\Omega(1)$.

IV. CFD Verification

To assess judiciously the validity of analytical solutions, laboratory measurements are often employed. However, with the increased reliability of CFD, an acceptable level of trust may be derived from numerical simulations, particularly, in the absence of experimental data. In this vein, we present a point-by-point CFD solution for the mean flowfield in an idealized hybrid engine with three different headwall injection profiles. Because our results equally apply to SRMs with reactive headwalls, the SRM case will also be considered despite the two orders of magnitude difference in headwall-to-sidewall velocity ratio.

Here a pressure-based, finite volume, unstructured, two-dimensional code is used to perform the simulations. The targeted flow is that corresponding to a hybrid rocket engine with an average inlet Mach number of 0.3 and a sidewall Mach number of 0.003. The exaggerated sidewall Mach number is purposefully chosen to draw attention to the flow behavior near the sidewall. The aspect ratio of the domain is set at $L = 16$. The boundary conditions at the sidewalls are specified as velocity inlets to closely mimic the mathematical model, where injection is imposed uniformly along the grain surface. The headwall is also specified as an inlet. On the right-hand side of the domain, a pressure outlet boundary condition is selected. Although an outflow boundary condition can also be imposed at the downstream section, it is discounted here to avoid the possible case of a partially developed flow. Despite the length of the chamber, the presence of sidewall mass addition can delay the onset of fully developed conditions. The domain

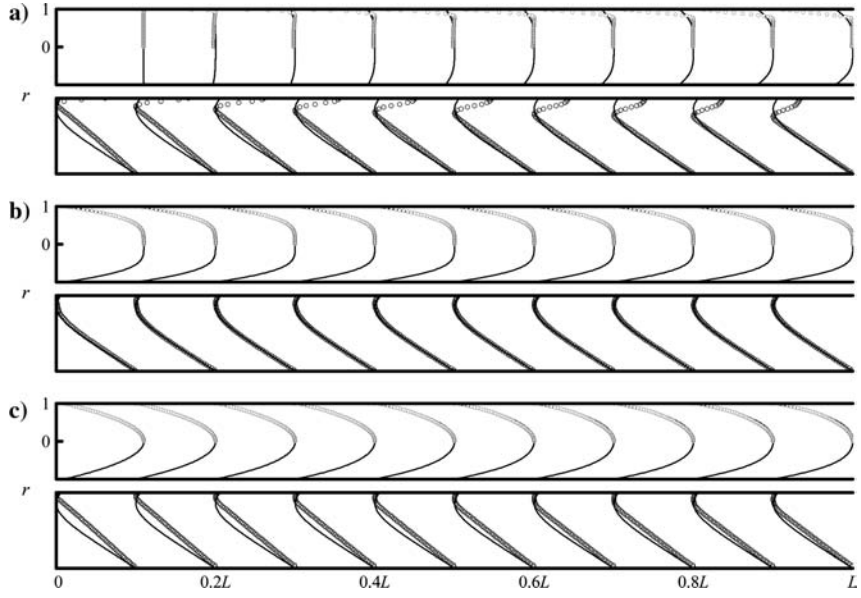

Fig. 11 Inviscid analytical and turbulent k–ε simulations for a) uniform, b) half-cosine, and c) Poiseuille injection profiles in a cylindrical chamber for $u_c = 100$: ∘, computational results.

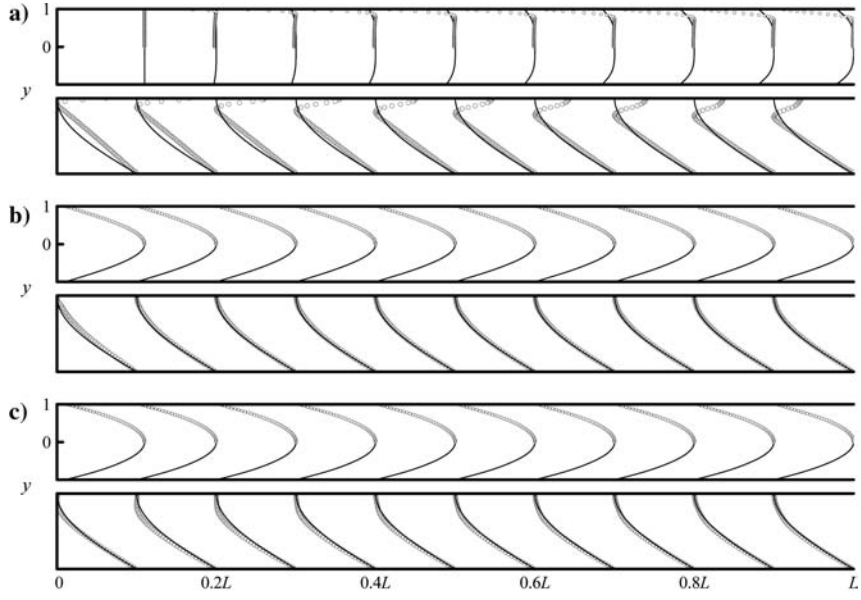

Fig. 12 Inviscid analytical and turbulent k–ε simulations for a) uniform, b) half-cosine, and c) Poiseuille injection profiles in a rectangular slab chamber for $u_c = 100$.

is meshed into 51,200 square cells (640×80) to maintain the aspect ratio of the chamber.

Results for the inviscid simulations are shown in Figs. 11 and 12 for the cylindrical and slab burners, respectively. These calculations are conducted for $u_c = 100$ and show the streamwise evolution of the axial and transverse velocities at $z/L = 0.01, 0.1, 0.2, 0.3, \ldots, 0.9$. Everywhere, the working fluid is taken to be ambient air. It may be seen that the agreement with numerics is satisfactory, especially in the cylindrical chamber with Berman's half-cosine and the rectangular chamber with both Berman's and Poiseuille's parabolic profiles. When it is recalled that Berman's solutions are exact representations, the improved agreement that they exhibit is unsurprising. Overall, the limited discrepancies may be attributed to our models being only quasi viscous. Another factor could be linked

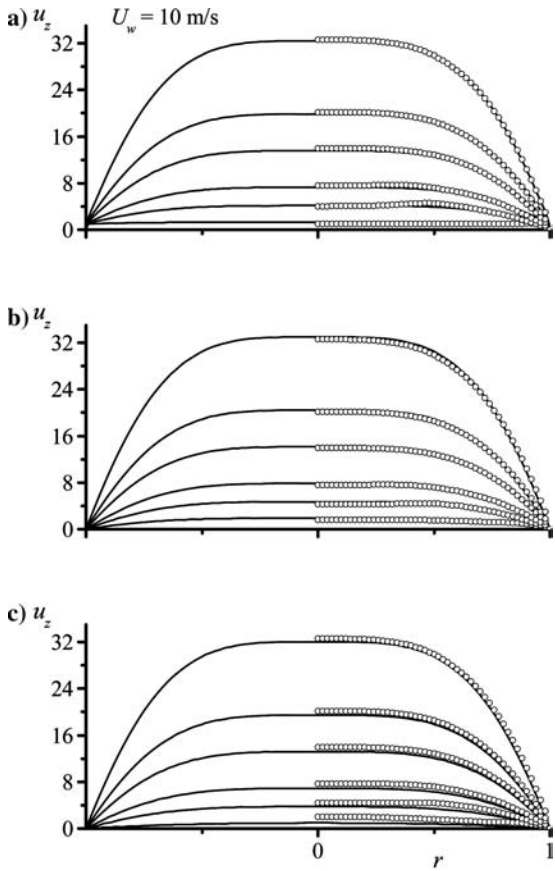

Fig. 13 Inviscid analytical and numerical simulations for a) uniform, b) half-cosine, and c) Poiseuille injection profiles in a cylindrical (SRM) chamber for $u_c = 1, \frac{1}{2}\pi$, and 2, respectively: —, analytic and ∘, numeric.

to the finite volume method in which the transverse velocity is evaluated at the centroid of each square cell. This enables us to circumvent the need to evaluate the transverse velocity right at the headwall and, thereby, avoid the Taylor–Culick discontinuity at $z = 0$. Instead, the transverse velocity is computed at a small distance from the wall (the centroid of the leading cell) that is sufficient to suppress the attendant singularity.

Similar results are given in Figs. 13 and 14 for the case of a SRM with noninert head end. Here, the k–ε turbulence model is used and compared to the axial velocity predictions at six streamwise positions corresponding to $z = 0.1, 1, 2, 4, 6$, and 10. These numerical experiments lend support to the viability of the analytical solutions.

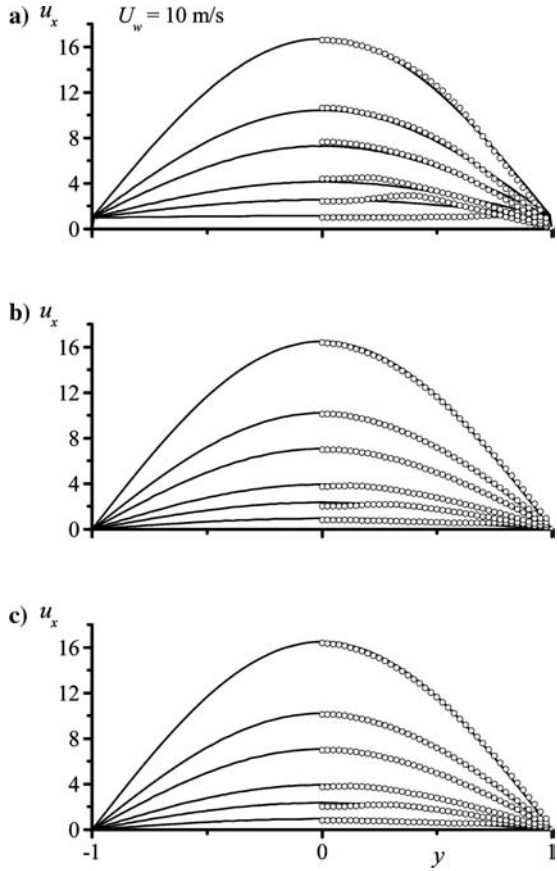

Fig. 14 Inviscid analytical and numerical simulations for a) uniform, b) half-cosine, and c) Poiseuille injection profiles in a slab (SRM) chamber for $u_c = 1, \frac{1}{2}\pi$, and $\frac{3}{2}$, respectively; —, analytic and ∘, numeric.

V. Practicality and Significance

Given that burning surfaces in hybrid chambers are rough, heterogeneous, and pliable, one may question the role of an idealized model as a vehicle for physical understanding. Could a core flow that does not account for all conceivable features, such as surface vibrations and complex boundary conditions, be relied on? To answer this question, one must explore the physical benefits of mathematical models and recognize the scope, objectives, and recent successes of core flow idealizations. These have been motivated by important technological applications despite their limitations to simplistic geometry and physical properties.

First, in justifying the need to pursue an analytical side to any full-scale investigation, a plethora of convincing arguments may be offered. The use of idealized boundary conditions should not be viewed as a debilitating feature because it is not limited to theoretical models alone. Many numerical and experimental simulations of rockets are in effect based on simplified geometric configurations and smooth porous walls.

One example may be derived from a propulsion-related study. In the investigation of aeroacoustic technologies to reduce the excess noise of Concorde jet engines, the elegant use of applied mathematics by Crighton as cited by Williams [26, 27] has proven invaluable to the comprehensive Anglo–French endeavor. Despite the obvious dissimilarities between turbulent shear layers surrounding the propulsive Rolls–Royce jets and the simplistic laminar models based on acoustic analogies, the use of powerful mathematical techniques has unraveled the means to suppress the ensuing sound and vibration. When the jet was seeded with sound upstream of the nozzle, a coherent turbulent structure could be promoted in a manner to reduce jet noise without impairing thrust and the aircraft's ability to climb. Thus, when an aeroacoustic source whose troughs coincided with the pressure peaks of an existing acoustic environment was deliberately superimposed, a quieter combination could be obtained. The degree of suppression depended on the accuracy of the active cancellation models that were suggested analytically and then refined via numerical and experimental tests. Similar analyses have recently provided multiple-scale solutions for modal sound transmission through turbofan aircraft engines with both hard and acoustically treated inlet walls [28, 29]. These solutions by Rienstra [28] and Rienstra and Eversman [29] have closely agreed with output data gathered from finite element codes.

Another propulsion-related example concerns the acoustic instability problem, which has appeared at the forefront of rocket development programs. Attempts at predicting these instabilities have invariably pointed to the importance of providing accurate assessments of rocket core flow detail [30–34]. The desire for explicit models has also been motivated by the need to physically understand the intricate interplay between unsteady pressure waves and gas motions [35–38].

In support of theoretical approximations, equally appreciable laminar and turbulent segments have been identified in a series of studies conducted by Apte and Yang [39, 40], Liou and Lien [41], and Beddini and Roberts [42, 43]. These teams have simultaneously concurred that turbulent simulations in the downstream sections of long SRMs tended to exhibit convincing similarities with corresponding laminar flow results. In consequence, the unsteady flow solutions derived by Majdalani [19] or Majdalani and Flandro [20] have been used to approximate the

basic deterministic features associated with turbulent flow theory (Griffond [21]) and simulation (Lee and Beddini [44, 45]), respectively. Additionally, they have been used to provide accurate predictions along the forward-half of SRMs where laminar conditions may prevail.

Aside from these sequential contributions, we note that recent efforts have been successful in producing analytical core-flow solutions that are sensitive to the movement of transpiring boundaries. The reader is referred, in that regard, to the planar and axisymmetric solutions presented by Majdalani et al. [16], Zhou and Majdalani [17, 46], and Majdalani et al. [47]. Therein, wall regression is accounted for alongside viscous and rotational features. By the application of a mass balance across the receding interface, the dependence of thrust on propellant morphology and density variation is captured. The effect of grain taper is also examined [48]. These incremental advancements in theoretical models continue to bring us closer to an idealized chamber with varying cross section and grain shape (see Kurdyumov [49] and Saad et al. [50]). Incorporation of swirling effects has also been accomplished by Vyas et al. [51–53]. In some of these applications, analytical solutions are seen to be functional in providing limiting-process case studies against which detailed numerical simulations or collections of experimental data could be compared (private communication from F. M. Najjar, Center for Simulation of Advanced Rockets, University of Illinois at Urbana–Champaign, Urbana, Illinois, 2001).

Regarding the role of chemical reactions and their omission in cold-flow simulations, the reader may find particularly interesting the numerical simulations of the burning zone by Chu et al. [54]. These computations have confirmed the presence of a virtually non-reactive, isothermal region above the flame edge where analytical approximations, such as the ones presented here, become very effective in describing the gasdynamics. Because the outer region constitutes nearly 98% of the chamber volume, the practicality of analytical solutions is evident. This conclusion is reached independently by several investigators, including Avalone et al. [55], Casalis et al. [56], Griffond et al. [57], Ugurtas et al. [58], and Chedevergne and Casalis [59]; these researchers have invested considerable effort in modeling the Ariane-class of rockets.

VI. Summary

In this chapter, incompressible mean flow approximations are presented for axisymmetric and planar representations of a hybrid rocket chamber. Several quasi-viscous solutions are obtained that attempt to observe, for the hybrid model, the principal surface requirements including the orthonormal injection condition on both headwall and sidewall. Their behavior is illustrated for the cases of small and large headwall injection in solid and hybrid rocket chambers. The analysis is further extended to account not only for uniform but also variable inlet patterns that can be potentially used to mimic more realistic systems. With use of Berman's similarity-conforming sinusoidal injection profile, viscous corrections are evaluated and appended to the inviscid solution using asymptotics. In the hybrid configuration, our models are seen to properly capture the fundamental streamtube motion. Overall, these formulations increase our repertoire of engineering approximations for injection-driven porous tubes, particularly, those representing

the core flow in solid and hybrid rockets. Their existence enables us to study hydrodynamic and aeroacoustic instability characteristics of the mean flow with and without particle interactions [60]. They also offer user-friendly benchmarks for testing large-scale numerical simulations.

Acknowledgments

This project is sponsored by the National Science Foundation through Grant CMS-0353518. I wish to thank Tony Saad, Doctoral Research Assistant at the University of Tennessee Space Institute, for numerically verifying the analytical solutions and for deriving the residuals. His untiring support has made this composition truly enjoyable. Tony has also treated and completed the Cartesian flow analog. I am deeply grateful for the assistance of Anand B. Vyas, Visiting Assistant Professor, Department of Mathematical Sciences, University of Delaware. Last, but certainly not least, I wish to acknowledge valuable discussions with Grégoire Casalis, Professor and Director of the Doctoral School of Aeronautics and Astronautics, SUPAERO, and Research Director, Department of Aerodynamics and Energetics, ONERA, Toulouse, France.

References

[1] Chiaverini, M. J., Johnson, D. K., Serin, N., Lu, Y. C., Kuo, K. K., and Risha, G. A., "Regression Rate Behavior of Hybrid Rocket Solid Fuels," *Journal of Propulsion and Power*, Vol. 16, No. 1, 2000, pp. 125–132.

[2] Chiaverini, M. J., Kuo, K. K., Peretz, A., and Harting, G. C., "Regression Rate and Heat Transfer Correlations for Hybrid Rocket Combustion," *Journal of Propulsion and Power*, Vol. 17, No. 1, 2001, pp. 99–110.

[3] Jenkins, R. M., and Cook, J. R., "A Preliminary Analysis of Low Frequency Pressure Oscillations in Hybrid Rocket Motors," AIAA Paper 95-2690, July 1995.

[4] Krier, H., and Kerzner, H., "Analysis of the Chemically Reacting Boundary Layer during Hybrid Combustion," *AIAA Journal*, Vol. 11, No. 12, 1973, pp. 1691–1698.

[5] Knuth, W. H., Chiaverini, M. J., Sauer, J. A., and Gramer, D. J., "Solid-Fuel Regression Rate Behavior of Vortex Hybrid Rocket Engines," *Journal of Propulsion and Power*, Vol. 18, No. 3, 2002, pp. 600–609.

[6] Karabeyoglu, M. A., Altman, D., and Cantwell, B. J., "Combustion of Liquifying Hybrid Propellants: Part 1, General Theory," *Journal of Propulsion and Power*, Vol. 18, No. 3, 2002, pp. 600–609.

[7] Karabeyoglu, M. A., and Cantwell, B. J., "Combustion of Liquifying Hybrid Propellants: Part 2, Stability of Liquid Films," *Journal of Propulsion and Power*, Vol. 18, No. 3, 2002, pp. 621–630.

[8] Culick, F. E. C., "Rotational Axisymmetric Mean Flow and Damping of Acoustic Waves in a Solid Propellant Rocket," *AIAA Journal*, Vol. 4, No. 8, 1966, pp. 1462–1464.

[9] Taylor, G. I., "Fluid Flow in Regions Bounded by Porous Surfaces," *Proceedings of the Royal Society of London, Series A: Mathematical and Physical Sciences*, Vol. 234, No. 1199, 1956, pp. 456–475.

[10] Baum, J. D., Levine, J. N., and Lovine, R. L., "Pulsed Instabilities in Rocket Motors: A Comparison Between Predictions and Experiments," *Journal of Propulsion and Power*, Vol. 4, No. 4, 1988, pp. 308–316.

[11] Sabnis, J. S., Gibeling, H. J., and McDonald, H., "Navier–Stokes Analysis of Solid Propellant Rocket Motor Internal Flows," *Journal of Propulsion and Power*, Vol. 5, No. 6, 1989, pp. 657–664.

[12] Dunlap, R., Willoughby, P. G., and Hermsen, R. W., "Flowfield in the Combustion Chamber of a Solid Propellant Rocket Motor," *AIAA Journal*, Vol. 12, No. 10, 1974, pp. 1440–1445.

[13] Dunlap, R., Blackner, A. M., Waugh, R. C., Brown, R. S., and Willoughby, P. G., "Internal Flowfield Studies in a Simulated Cylindrical Port Rocket Chamber," *Journal of Propulsion and Power*, Vol. 6, No. 6, 1990, pp. 690–704.

[14] Yamada, K., Goto, M., and Ishikawa, N., "Simulative Study of the Erosive Burning of Solid Rocket Motors," *AIAA Journal*, Vol. 14, No. 9, 1976, pp. 1170–1176.

[15] Brown, R. S., Blackner, A. M., Willoughby, P. G., and Dunlap, R., "Coupling Between Acoustic Velocity Oscillations and Solid Propellant Combustion," *Journal of Propulsion and Power*, Vol. 2, No. 5, 1986, pp. 428–437.

[16] Majdalani, J., Vyas, A. B., and Flandro, G. A., "Higher Mean-Flow Approximation for a Solid Rocket Motor with Radially Regressing Walls," *AIAA Journal*, Vol. 40, No. 9, 2002, pp. 1780–1788.

[17] Zhou, C., and Majdalani, J., "Improved Mean Flow Solution for Slab Rocket Motors with Regressing Walls," *Journal of Propulsion and Power*, Vol. 18, No. 3, 2002, pp. 703–711.

[18] Zhou, C., and Majdalani, J., "Inner and Outer Solutions for the Injection Driven Channel Flow with Retractable Walls," AIAA Paper 2003-3728, June 2003.

[19] Majdalani, J., "The Oscillatory Channel Flow with Arbitrary Wall Injection," *Journal of Applied Mathematics and Physics*, Vol. 52, No. 1, 2001, pp. 33–61.

[20] Majdalani, J., and Flandro, G. A., "The Oscillatory Pipe Flow with Arbitrary Wall Injection," *Proceedings of the Royal Society of London, Series A: Mathematical and Physical Sciences*, Vol. 458, No. 2022, 2002, pp. 1621–1651.

[21] Griffond, J., "Receptivity and Aeroacoustic Resonance in Channels with Blowing Walls," *Physics of Fluids*, Vol. 14, No. 11, 2002, pp. 3946–3962.

[22] Berman, A. S., "Laminar Flow in Channels with Porous Walls," *Journal of Applied Physics*, Vol. 24, No. 9, 1953, pp. 1232–1235.

[23] Majdalani, J., and Vyas, A. B., "Inviscid Models of the Classic Hybrid Rocket," AIAA Paper 2004-3474, July 2004.

[24] Terrill, R. M., and Colgan, T., "Some Simple Analytic Solutions of the Navier–Stokes Equations," *International Journal of Engineering Science*, Vol. 29, No. 1, 1991, pp. 55–68.

[25] Chiaverini, M. J., "Regression Rate and Pyrolysis Behavior of HTPB-Based Solid Fuels in a Hybrid Rocket Motor," Ph.D. Dissertation, Dept. of Mechanical Engineering, The Pennsylvania State Univ., Dec. 1998.

[26] Williams, J. E. F., "Aeroacoustics, "*Aeronautical Journal*, Vol. 100, No. 1000, 1996, pp. 531–537.

[27] Williams, J. E. F., "David Crighton 1942–2000: A Commentary on His Career and His Influence on Aeroacoustic Theory," *Journal of Fluid Mechanics*, Vol. 437, 2001, pp. 1–11.

[28] Rienstra, S. W., "Sound Transmission in Slowly Varying Circular and Annular Lined Ducts with Flow," *Journal of Fluid Mechanics*, Vol. 380, 1999, pp. 279–296.

[29] Rienstra, S. W., and Eversman, W., "A Numerical Comparison between the Multiple-Scales and Finite-Element Solution for Sound Propagation in Lined Flow Ducts," *Journal of Fluid Mechanics*, Vol. 2001, No. 437, 2001, pp. 367–384.

[30] Majdalani, J., Fischbach, S. R., and Flandro, G. A., "Improved Energy Normalization Function in Rocket Motor Stability Calculations," *Journal of Aerospace Science and Technology*, Vol. 10, No. 6, 2006, pp. 495–500.

[31] Fischbach, S. R., Majdalani, J., and Flandro, G. A., "Acoustic Instability of the Slab Rocket Motor," *Journal of Propulsion and Power*, Vol. 23, No. 1, 2007, pp. 146–157.

[32] Majdalani, J., Flandro, G. A., and Fischbach, S. R., "Some Rotational Corrections to the Acoustic Energy Equation in Injection-Driven Enclosures," *Physics of Fluids*, Vol. 17, No. 7, 2005, pp. 0741021-20.

[33] Fischbach, S. R., Majdalani, J., and Flandro, G. A., "Verification and Validation of Rocket Stability Integral Transformations," AIAA Paper 2005-4001, July 2005.

[34] Abu-Irshaid, E. M., Majdalani, J., and Casalis, G., "Hydrodynamic Stability of Rockets with Headwall Injection," *Physics of Fluids*, Vol. 19, No. 2, 2007, pp. 024101–11.

[35] Majdalani, J., Flandro, G. A., and Roh, T. S., "Implications of Unsteady Analytical Flowfields on Rocket Combustion Instability," AIAA Paper 98-3698, July 1998.

[36] Majdalani, J., and Van Moorhem, W. K., "Improved Time-Dependent Flowfield Solution for Solid Rocket Motors," *AIAA Journal*, Vol. 36, No. 2, 1998, pp. 241–248.

[37] Majdalani, J., "Boundary-Layer Structure in Cylindrical Rocket Motors," *AIAA Journal*, Vol. 37, No. 4, 1999, pp. 505–508.

[38] Majdalani, J., Flandro, G. A., and Roh, T. S., "Convergence of Two Flowfield Models Predicting a Destabilizing Agent in Rocket Combustion," *Journal of Propulsion and Power*, Vol. 16, No. 3, 2000, pp. 492–497.

[39] Apte, S., and Yang, V., "Unsteady Flow Evolution in a Porous Chamber with Surface Mass Injection. Part 1: Free Oscillation," *AIAA Journal*, Vol. 39, No. 8, 2001, pp. 1577–1586.

[40] Apte, S., and Yang, V., "Effect of Acoustic Oscillation on Flow Development in a Simulated Nozzleless Rocket Motor," *Solid Propellant Chemistry, Combustion, and Motor Interior Ballistics*, Vol. 185, edited by V. Yang, T. B. Brill, and W.-Z. Ren, Progress in Astronautics and Aeronautics, AIAA, Reston, VA, Washington, DC, 2000, pp. 791–822.

[41] Liou, T.-M., and Lien, W.-Y., "Numerical Simulations of Injection-Driven Flows in a Two-Dimensional Nozzleless Solid-Rocket Motor," *Journal of Propulsion and Power*, Vol. 11, No. 4, 1995, pp. 600–606.

[42] Beddini, R. A., and Roberts, T. A., "Turbularization of an Acoustic Boundary Layer on a Transpiring Surface," *AIAA Journal*, Vol. 26, No. 8, 1988, pp. 917–923.

[43] Beddini, R. A., and Roberts, T. A., "Response of Propellant Combustion to a Turbulent Acoustic Boundary Layer," *Journal of Propulsion and Power*, Vol. 8, No. 2, 1992, pp. 290–296.

[44] Lee, Y., and Beddini, R. A., "Acoustically-Induced Turbulent Transition in Solid Propellant Rocket Chamber Flowfields," AIAA Paper 99-2508, June 1999.

[45] Lee, Y., and Beddini, R. A., "Effect of Solid Rocket Chamber Pressure on Acoustically-Induced Turbulent Transition," AIAA Paper 2000-3802, July 2000.

[46] Zhou, C., and Majdalani, J., "Improved Mean Flow Solution for Slab Rocket Motors with Regressing Walls," AIAA Paper 2000-3191, July 2000.

[47] Majdalani, J., Vyas, A. B., and Flandro, G. A., "Higher Mean-Flow Approximation for a Solid Rocket Motor with Radially Regressing Walls," AIAA Paper 2001-3870, July 2001.

[48] Clayton, C. D., "Flowfields in Solid Rocket Motors with Tapered Bores," AIAA Paper 96-2643, July 1996.

[49] Kurdyumov, V. N., "Steady Flows in the Slender, Noncircular, Combustion Chambers of Solid Propellants Rockets," *AIAA Journal*, Vol. 44, No. 12, 2006, pp. 2979–2986.
[50] Saad, T., Sams, O. C., and Majdalani, J., "Rotational Flow in Tapered Slab Rocket Motors," *Physics of Fluids*, Vol. 18, No. 1, 2006, pp. 103601–13.
[51] Vyas, A. B., Majdalani, J., and Chiaverini, M. J., "The Bidirectional Vortex. Part 1: An Exact Inviscid Solution," AIAA Paper 2003-5052, July 2003.
[52] Vyas, A. B., Majdalani, J., and Chiaverini, M. J., "The Bidirectional Vortex. Part 2: Viscous Core Corrections," AIAA Paper 2003-5053, July 2003.
[53] Vyas, A. B., Majdalani, J., and Chiaverini, M. J., "The Bidirectional Vortex. Part 3: Multiple Solutions," AIAA Paper 2003-5054, July 2003.
[54] Chu, W.-W., Yang, V., and Majdalani, J., "Premixed Flame Response to Acoustic Waves in a Porous-Walled Chamber with Surface Mass Injection," Combustion and Flame, Vol. 133, No. 6129, 2003, pp. 359–370.
[55] Avalon, G., Casalis, G., and Griffond, J., "Flow Instabilities and Acoustic Resonance of Channels with Wall Injection," AIAA Paper 98-3218, July 1998.
[56] Casalis, G., Avalon, G., and Pineau, J.-P., "Spatial Instability of Planar Channel Flow with Fluid Injection through Porous Walls," *Physics of Fluids*, Vol. 10, No. 10, 1998, pp. 2558–2568.
[57] Griffond, J., Casalis, G., and Pineau, J.-P., "Spatial Instability of Flow in a Semi-infinite Cylinder with Fluid Injection through Its Porous Walls," *European Journal of Mechanics B/Fluids*, Vol. 19, No. 1, 2000, pp. 69–87.
[58] Ugurtas, B., Avalon, G., Lupoglazoff, N., Vuillot, F., and Casalis, G., "Stability and Acoustic Resonance of Internal Flows Generated by Side Injection," *Solid Propellant Chemistry, Combustion, and Motor Interior Ballistics*, Vol. 185, edited by V. Yang, T. B. Brill, and W.-Z. Ren, Progress in Astronautics and Aeronautics, AIAA, Reston, VA, 2000, pp. 823–836.
[59] Chedevergne, F., and Casalis, G., "Thrust Oscillations in Reduced Scale Solid Rocket Motors, Part II : A New Theoretical Approach," AIAA Paper 2005-4000, July 2005.
[60] Féraille, T., Casalis, G., and Dupays, J., "Particle Effects on Solid-Propellant Motors Flow Stability," AIAA Paper 2002-3611, July 2002.

Chapter 6

Vortex Injection Hybrid Rockets

Joseph Majdalani*
University of Tennessee Space Institute, Tullahoma, Tennessee 37388

Nomenclature

A_i = inlet area of incoming swirl flow
a = chamber radius
b = chamber discharge radius, βa
L = chamber aspect ratio, L_0/a
p = normalized pressure, $\bar{p}/(\rho U^2)$
Q_i = normalized flow rate, $\sigma^{-1} = \bar{Q}_i/(Ua^2) = A_i/a^2$
$\bar{Q}_i$ = inlet volumetric flow rate at the base
$\bar{Q}_{\text{in}}$ = total incoming flow rate, $\bar{Q}_i + \bar{Q}_w$
$\bar{Q}_w$ = wall-injected flow rate, $2\pi aLU_w$
Re = injection Reynolds number, Ua/ν
Re_w = sidewall injection Reynolds number, $U_w a/\nu$
r = normalized radial coordinate, $\bar{r}/a$
S = unidirectional swirl number, $\pi ab/A_i = \pi\beta\sigma$
U = tangential injection velocity, $\bar{u}_\theta(a, L)$
U_w = sidewall injection velocity, $-\bar{u}_r(a, \bar{z}) = \bar{Q}_w/(2\pi aL)$
$\boldsymbol{u}$ = normalized velocity, $(\bar{u}_r, \bar{u}_z, \bar{u}_\theta)/U$
z = normalized axial coordinate, $\bar{z}/a$
β = normalized discharge radius, b/a
δ = reciprocal of the Reynolds number, $\nu/(Ua)$
ε = sidewall injection parameter, U_w/U
η = action variable, πr^2
κ = tangential inflow parameter, $(2\pi\sigma L)^{-1}$

*Jack D. Whitfield Professor of High Speed Flows, Department of Mechanical, Aerospace and Biomedical Engineering. Member AIAA.

$\tilde{\kappa}$ = modified inflow parameter, $\kappa \csc(\pi\beta^2)$
μ = dynamic viscosity
ν = kinematic viscosity, μ/ρ
ρ = density
σ = modified swirl number, $Q_i^{-1} = S/(\pi\beta) = Ua^2/\bar{Q}_i$
$\boldsymbol{\Omega}$ = mean flow vorticity, $\nabla \times \boldsymbol{u}$

Subscripts

i = inlet property at the base, $\bar{z} = L_0$
r = radial component or partial derivative
w = sidewall property
z = axial component or partial derivative
θ = azimuthal component or partial derivative
$\bar{}$ = dimensional variable

I. Introduction

BECAUSE of recent advancements in propellant composition, injection technology, auxiliary equipment, and chamber design, it may be speculated that the dawn of hybrid rocket commercialization is drawing near. In past years, propulsion industries have refrained from seriously considering hybrid propellants as viable alternatives to liquids or solids because of three principal deficiencies for which hybrids have been noted. These include low combustion efficiency, low regression rate, and low volumetric loading. All three deficiencies may be attributed to the slow diffusion flames that are typically sustained along the interface between solid fuel and gaseous oxidizer. As a result, polymeric fuels used in hybrids are known to display weak burning characteristics because they regress at about one order of magnitude more slowly than solids. To compensate for the sluggish mass flow rate of pyrolyzed fuel, large and expensive pressure cases are required. These cases are needed to hold complex grain shapes comprising wide ports and wet surface areas that are sufficiently large to produce the desired thrust distribution. The gist: diffusion flames are no match to premixed flames unless a mechanism can be conceived to overcome their adverse characteristics.

Despite these long-standing and well-defined impediments, the three-pronged problem affecting hybrids may not be too difficult to solve. As shown recently by Casillas et al. [1], cost effectiveness of hybrids may be achieved if only a three-to-fourfold increase in their fuel regression rate can be accomplished. Such an increase will obviate the need for sophisticated grain designs by promoting major reductions in inert mass.

With these perspectives in mind, an innovative vortex injection hybrid rocket engine (VIHRE) has been developed based on a cyclonic flow concept [2]. It is hoped to find widespread use for this engine in both commercial and military applications due to the favorable features that it offers. One advantage of VIHRE is its ability to produce a sevenfold increase in regression rates by comparison to a classic hybrid [3–6]. According to the criteria furnished by Casillas et al. [1], it stands as a feasible propulsion alternative.

The improved performance granted by VIHRE can be attributed to its unique internal flowfield that is dominated by swirling bidirectional motion (Fig. 1a). The

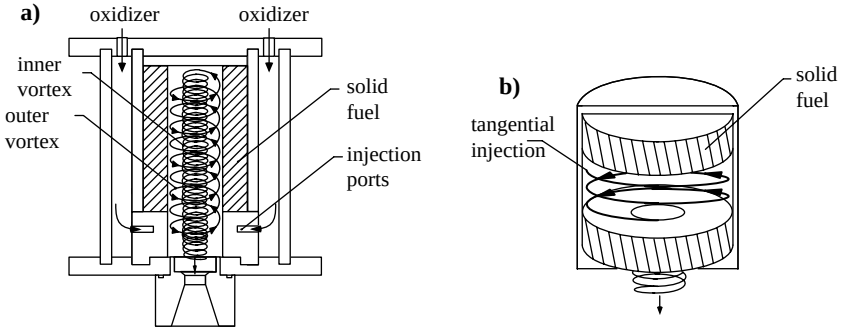

Fig. 1 Schematics: a) bidirectional [2] and b) dual end-burning, unidirectional VIHRE.

corresponding coaxial, counter-flowing vortex pair increases surface erosion while promoting mixing and turbulence [3–6].

Another feature in VIHRE that constitutes a departure from conventional hybrid conceptualization is the aft-end injection of gaseous oxidizer just upstream of the nozzle (between the aft edge of the fuel grain and the inlet to the nozzle). By the alignment of the injector ports tangentially to the inner circumference, a strong vortex is produced that can travel helically along the fuel-grain surface. Fuel particles swept in this manner are compelled to spiral around the chamber axis, thereby crossing the chamber length twice before exiting. Naturally, combustion efficiency is considerably ameliorated due to the markedly increased residence time and the intense mixing between fuel and oxidizer. The injected oxidizer is prevented from short circuiting and draining out the nozzle by the swirl-induced radial pressure gradients that press the incoming stream against the sidewall; the induced centrifugal forces cause this outer stream to cling to and climb the chamber's cylindrical wall. Other feasible injection configurations employ fore end and distributed tangential injectors. A dual-end-burning hybrid grain that is driven by unidirectional vortex motion is also possible (Fig. 1b). In this case, two cylindrically shaped fuel cartridges are placed a small distance apart on both ends of the chamber. Forward swirl injectors are then employed to produce a spiraling stream that sweeps across the exposed fuel surfaces before wheeling its way out of the chamber: Gas expulsion is achieved through the central orifice perforated in the aft cartridge. In this configuration, the fully facing circular surfaces burn and regress axially.

In addition to the improved regression rate and combustion efficiency, the hybrid vortex engines utilize hollow, cylindrical grain cartridges that are simple to mass manufacture. The corresponding web perforation reduces volumetric loading and precludes the need for large and, therefore, expensive case housing. Another advantage is the increased effective length of the chamber owing to the convoluted path traced by fuel and oxidizer particles. For a given thrust level, the increased effective length permits an appreciable reduction in overall size and unused weight.

As in the case of classic hybrids, VIHRE-type engines will provide a more reliable alternative than liquid bipropellants by requiring only half of the feed

system hardware while permitting the same start–stop, mission abort, and throttling capabilities. Furthermore, the nontoxicity of the solid fuel that can be loaded into VIHRE is less hazardous to store and transport than liquid fuels, less degradable than solids, and more environmentally friendly than either of the two. Because of these safety and operational advantages, the upcoming family of hybrid vortex engines stands to offer an attractive propulsion alternative that combines the advantages of both liquids and solids while reducing their undesirable characteristics.

In this chapter, we present theoretical tools that can be applied to model the core flow in hybrid vortex engines; the work culminates in the construction of an analytical solution that can be used to describe the bulk gas motion observed in an idealized representation of VIHRE. To the author's knowledge, no other analytical models have yet been advanced for the treatment of hybrid vortex engines. For this reason, perturbation tools will be employed in conjunction with Euler's inviscid equations, whose application is justified in view of the large Reynolds numbers that characterize this problem. The plan is to first obtain steady, inviscid, incompressible mean flow approximations that can be readily augmented by viscous corrections.

II. Mathematical Model

The bidirectional vortex engine is modeled as a cylindrical chamber of porous length L_0 and radius a with both a closed head end and a partially open downstream end. The latter is attached to a tubular nozzle of radius b. The vortex engine is shown in Fig. 2, where $\bar{r}$ and $\bar{z}$ denote the radial and axial coordinates. The field of interest stretches from the headwall to the base plane in the extent that it remains incompressible. Downstream of the base, the flow may accelerate by expanding through a nozzle.

At the base, the fraction of the radius that permits an outflow is given by $\beta = b/a$. Along the remaining portion of the base, an incompressible fluid is assumed to enter the chamber tangentially to the inner circumference at a prescribed volumetric rate $Q_i = \bar{Q}_i/(Ua^2)$. The corresponding tangential injection velocity U is considered to be sufficiently large to prevent the flow from short circuiting, a condition by which the flow will drift toward and out of the nozzle. Instead, a bidirectional vortex is formed as in the case of cyclonic separators and furnaces [7, 8]. This bidirectional motion is augmented by a secondary wall influx caused by the radial and uniformly distributed sidewall mass addition. The sidewall injection velocity U_w is used to capture the solid-fuel regression rate. Clearly, U_w is appreciably smaller than U due to typical rates of fuel pyrolysis. This condition will be employed in seeking a closed-form asymptotic approximation.

The strong angular momentum borne by the incoming stream causes the formation of a cyclone. This phenomenon subdivides the chamber into two vortex zones: an outer annular section that is separated from the inner core region by virtue of a spinning and nontranslating cylindrical layer termed "mantle." In the outer vortex, the spiraling fluid sweeps up the propellant surface while mixing with the wall transpiring mass. At the chamber head end, the outer vortex switches axial polarity, reverses inwardly, and continues spiraling toward and out of the nozzle. Our analysis focuses on the essential features of the ensuing flowfield, namely, the bidirectional vortex in this idealized rocket chamber.

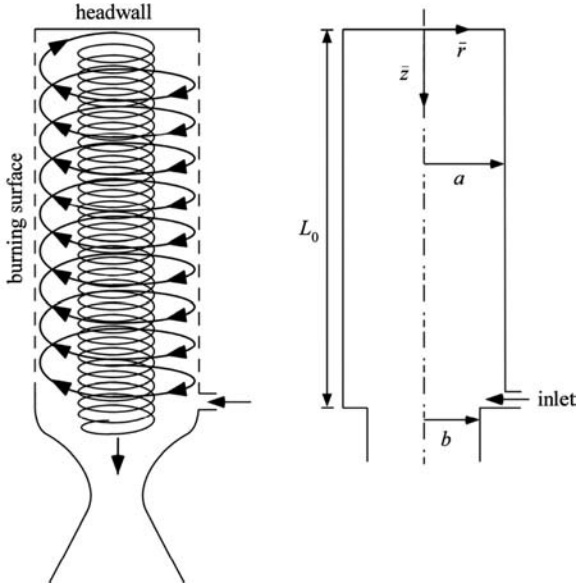

Fig. 2 Hybrid vortex chamber noted by presence of bidirectional vortex in addition to sidewall mass addition.

A. Equations

To characterize the bulk gas motion, a nonreactive model is used. This may be justified by the weak effects of diffusion flames in typical hybrids. In solid rocket motors, ignoring the effect of chemical reactions has led to several models that suitably represent the bulk gas motion. Along similar lines, the flow is assumed to be 1) steady, 2) inviscid, 3) incompressible, 4) rotational, and 5) axisymmetric. Axisymmetry is warranted by the strong swirl velocity and the absence of friction to decelerate the flow in the tangential direction. In fact, this assumption recurs so often in the literature that it is generally adopted without scrutiny (Leibovich [9]). The combination of axisymmetry and frictionless motion leads to another flow attribute of the swirl velocity, namely, axial independence. The weak sensitivity of the swirl velocity to axial variations is corroborated by the work of Leibovich [9, 10], Beran and Culick [11], Bloor and Ingham [7, 8], Vatistas et al. [12, 13], Szeri and Holmes [14], and others. Physically, it is granted by the absence of friction between fluid layers and along both headwall and sidewall. Based on these assumptions, Euler's equations become

$$\frac{1}{\bar{r}}\frac{\partial\,(\bar{r}\bar{u}_r)}{\partial\bar{r}} + \frac{\partial\bar{u}_z}{\partial\bar{z}} = 0 \tag{1}$$

$$\bar{u}_r\frac{\partial\bar{u}_r}{\partial\bar{r}} + \bar{u}_z\frac{\partial\bar{u}_r}{\partial\bar{z}} - \frac{\bar{u}_\theta^2}{\bar{r}} = -\frac{1}{\rho}\frac{\partial\bar{p}}{\partial\bar{r}} \tag{2}$$

$$\bar{u}_r \frac{\partial \bar{u}_\theta}{\partial \bar{r}} + \frac{\bar{u}_\theta \bar{u}_r}{\bar{r}} = 0 \tag{3}$$

$$\bar{u}_r \frac{\partial \bar{u}_z}{\partial \bar{r}} + \bar{u}_z \frac{\partial \bar{u}_z}{\partial \bar{z}} = -\frac{1}{\rho} \frac{\partial \bar{p}}{\partial \bar{z}} \tag{4}$$

B. Boundary Conditions

The first set of boundary conditions is linked to axisymmetry and headwall impermeability. The second set is due to the inlet configuration and bulk mass conservation. Specifically, one can assume 1) a fully tangential inflow, 2) a zero axial flow at the headwall, 3) a zero radial flow at the centerline, 4) a prescribed radial inflow at the sidewall, and 5) an inflow that matches the outflow at the base.

These particular conditions translate into

$$\begin{array}{llll} \bar{r} = a, & \bar{z} = L_0; & \bar{u}_\theta = U & \text{(tangential injection)} \\ \bar{z} = 0, & \forall \bar{r}; & \bar{u}_z = 0 & \text{(inert head end)} \\ \bar{r} = 0, & \forall \bar{z}; & \bar{u}_r = 0 & \text{(no radial flow across the centerline)} \\ \bar{r} = a, & 0 \le \bar{z} < L_0; & \bar{u}_r = -U_w & \text{(sidewall injection)} \\ \bar{z} = L, & 0 \le \bar{r} < b; & \bar{Q}_i = UA_i & \text{(inflow at the base)} \end{array} \tag{5}$$

C. Normalization

When a similarity solution is sought, it is helpful to normalize the principal variables and operators. This can be accomplished by setting

$$z = \bar{z}/a; \qquad r = \bar{r}/a; \qquad \nabla = a\bar{\nabla}; \qquad \beta = b/a \tag{6}$$

$$u_r = \bar{u}_r/U; \qquad u_\theta = \bar{u}_\theta/U; \qquad u_z = \bar{u}_z/U; \qquad \varepsilon = U_w/U \tag{7}$$

$$p = \bar{p}/(\rho U^2); \qquad Q_i = \bar{Q}_i/(Ua^2) = A_i/a^2; \qquad Q_w = \bar{Q}_w/(Ua^2) = 2\pi\varepsilon L \tag{8}$$

Here $U = \bar{u}_\theta(a, L_0)$ and $U_w = -\bar{u}_r(a, \bar{z})$ represent the average fluid injection velocity at the base and the uniform wall injection velocity along the sidewall, respectively.

At this juncture, it may be instructive to mark the relation that exists between the normalized volumetric flow rate Q_i and the unidirectional swirl number S used in the literature [15]. In many studies, such as the one by Hoekstra et al. [16], the swirl number for cyclonic flow is presented by

$$S \equiv \pi ab/A_i = \pi\beta\sigma \tag{9}$$

where $\sigma \equiv Q_i^{-1}$ refers to the modified swirl number that appears in the analytical solution. Clearly, our modified $\sigma \equiv Q_i^{-1}$ is directly proportional to the classic swirl number S. When $\beta = 1/\sqrt{2}$, $S = \frac{1}{2}\pi\sqrt{2}\sigma \simeq 2.22\sigma$.

D. Basic Formulation

Pursuant to Eqs. (6–8), rotational axisymmetric mean flow motion is prescribed by

$$\nabla \cdot \boldsymbol{u} = 0; \qquad \boldsymbol{u} \cdot \nabla \boldsymbol{u} = -\nabla p \tag{10}$$

After substituting $\boldsymbol{u}\cdot\nabla\boldsymbol{u}=\frac{1}{2}\nabla(\boldsymbol{u}\cdot\boldsymbol{u})-\boldsymbol{u}\times\nabla\times\boldsymbol{u}$ into Eq. (10), one can take the curl of the momentum equation to obtain, as usual, the steady and inviscid vorticity transport equation

$$\nabla\times\boldsymbol{u}\times\boldsymbol{\Omega}=0; \qquad \boldsymbol{\Omega}\equiv\nabla\times\boldsymbol{u} \tag{11}$$

The corresponding boundary conditions become

$$\begin{aligned} &u_\theta(1,L)=1; \qquad u_z(r,0)=0; \qquad u_r(1,z)=-\varepsilon \\ &u_r(0,z)=0; \qquad Q_{\text{out}}=\int_0^{2\pi}\int_0^{\beta}\boldsymbol{u}(r,L)\cdot\hat{\boldsymbol{n}}r\,\mathrm{d}r\,\mathrm{d}\theta=Q_{\text{in}} \end{aligned} \tag{12}$$

where $\boldsymbol{u}\cdot\hat{\boldsymbol{n}}=u_z$ represents the outflow velocity at the base whereas $Q_{\text{in}}=Q_i+Q_w$ accounts for the injected flow at the base augmented by the wall-injected fluid.

The presence of a small parameter ε in Eq. (12) suggests the possibility of an asymptotic treatment. Specifically, a regular perturbation expansion may be applied to the velocity and its vorticity companion. This can be implemented by letting

$$\boldsymbol{u}=\boldsymbol{u}^{(0)}+\varepsilon\boldsymbol{u}^{(1)}+\mathcal{O}(\varepsilon^2); \qquad \boldsymbol{\Omega}=\boldsymbol{\Omega}^{(0)}+\varepsilon\boldsymbol{\Omega}^{(1)}+\mathcal{O}(\varepsilon^2) \tag{13}$$

These expressions can be substituted into Eq. (11). Forthwith, the perturbed vorticity transport equation turns into

$$\nabla\times\boldsymbol{u}^{(0)}\times\boldsymbol{\Omega}^{(0)}+\varepsilon\left[\nabla\times\boldsymbol{u}^{(1)}\times\boldsymbol{\Omega}^{(0)}+\nabla\times\boldsymbol{u}^{(0)}\times\boldsymbol{\Omega}^{(1)}\right]+\mathcal{O}(\varepsilon^2)=0 \tag{14}$$

The solution to this set will be described next.

III. Inviscid Solution

Before the asymptotic treatment is carried out, it may be helpful to consider the state of the swirl velocity in light of the foregoing assumptions. Specifically, it may be useful to show that, at leading order, the swirl velocity decouples from the momentum equation and reduces the complexity of Eqs. (13) and (14).

A. Free Outer Vortex

From the θ-momentum equation given by Eq. (3) one can put

$$u_r\left(\frac{\partial u_\theta}{\partial r}+\frac{u_\theta}{r}\right)=0 \tag{15}$$

where $u_\theta(1,L)=1$. Subsequently, one finds

$$u_\theta=1/r \tag{16}$$

As usual, Eq. (16) confirms the presence of a free-vortex motion that is characteristic of swirling inviscid flow. We find that, at leading order, both radial and axial components of vorticity vanish identically.

B. Leading-Order Approximation

At this point, both radial and axial velocity components remain to be determined from the reduced set given by

$$\frac{1}{r}\frac{\partial[ru_r^{(0)}]}{\partial r} + \frac{\partial u_z^{(0)}}{\partial z} = 0 \qquad \text{(continuity)} \tag{17}$$

$$\frac{\partial[u_r^{(0)}\Omega_\theta^{(0)}]}{\partial r} + \frac{\partial[u_z^{(0)}\Omega_\theta^{(0)}]}{\partial z} = 0 \qquad \text{(vorticity transport)} \tag{18}$$

$$\frac{\partial u_r^{(0)}}{\partial z} - \frac{\partial u_z^{(0)}}{\partial r} = \Omega_\theta^{(0)} \qquad \text{(vorticity)} \tag{19}$$

With the realization that the swirl velocity is decoupled from the remaining set (due to axisymmetry), the introduction of the Stokes stream function becomes a possibility. Thus, we let

$$u_r^{(0)} = -\frac{1}{r}\frac{\partial\psi^{(0)}}{\partial z}; \qquad u_z^{(0)} = \frac{1}{r}\frac{\partial\psi^{(0)}}{\partial r} \tag{20}$$

where $\psi = \psi^{(0)} + \varepsilon\psi^{(1)} + \mathcal{O}(\varepsilon^2)$ is a series of diminishing terms. When this transformation is used in the vorticity transport equation given by Eq. (18), one obtains, at leading order,

$$-\frac{\partial\psi^{(0)}}{\partial z}\frac{\partial}{\partial r}\left[\frac{\Omega_\theta^{(0)}}{r}\right] + \frac{\partial\psi^{(0)}}{\partial r}\frac{\partial}{\partial z}\left[\frac{\Omega_\theta^{(0)}}{r}\right] = 0 \tag{21}$$

and so

$$\frac{\left[\Omega_\theta^{(0)}/r\right]_z}{\left[\Omega_\theta^{(0)}/r\right]_r} = \frac{\left[\psi^{(0)}\right]_z}{\left[\psi^{(0)}\right]_r} \tag{22}$$

The resulting equality holds for any

$$\Omega_\theta^{(0)} = rF[\psi^{(0)}(r,z)] \tag{23}$$

When this standard form is substituted into Eq. (22), it can be promptly seen that

$$\frac{\left[\Omega_\theta^{(0)}/r\right]_z}{\left[\Omega_\theta^{(0)}/r\right]_r} = \frac{\left\{F[\psi^{(0)}]\right\}_z}{\left\{F[\psi^{(0)}]\right\}_r} = \frac{F_{\psi^{(0)}}[\psi^{(0)}]_z}{F_{\psi^{(0)}}[\psi^{(0)}]_r} = \frac{[\psi^{(0)}]_z}{[\psi^{(0)}]_r} \tag{24}$$

According to Eq. (23), F can be a general function of $\psi^{(0)}$. The two simplest cases correspond to $F = C^2$ and $F = C^2\psi^{(0)}$, where C is some constant. Although it is a trivial exercise to check that the first choice is incongruent with the boundary

conditions, the linear relation, as will be shown, is quite suitable. Thus, one can put

$$\Omega_\theta^{(0)} = C^2 r \psi^{(0)} \tag{25}$$

It must be borne in mind that this linear choice may not be unique, although no other alternatives could be identified with the potential of yielding a closed-form solution. When Eq. (25) is inserted into the vorticity equation, one obtains the classic result [17]

$$\frac{\partial^2 \psi^{(0)}}{\partial z^2} + \frac{\partial^2 \psi^{(0)}}{\partial r^2} - \frac{1}{r}\frac{\partial \psi^{(0)}}{\partial r} + C^2 r^2 \psi^{(0)} = 0 \tag{26}$$

At this juncture, three of the boundary conditions may be written for the stream function. Based on Eq. (12), one has

$$\begin{aligned} z = 0; \qquad & u_z^{(0)} = 0; \qquad & \frac{\partial \psi^{(0)}}{\partial r} = 0 \\ r = 0; \qquad & u_r^{(0)} = 0; \qquad & \frac{\partial \psi^{(0)}}{\partial z} = 0 \\ r = 1; \qquad & u_r^{(0)} = 0; \qquad & \frac{\partial \psi^{(0)}}{\partial z} = 0 \end{aligned} \tag{27}$$

C. General Solution

Clearly, Eq. (26) is separable. One can proceed by setting

$$\psi^{(0)}(r, z) = f(r)g(z) \tag{28}$$

This decomposes Eq. (26) into

$$-\frac{1}{g}\frac{\mathrm{d}^2 g}{\mathrm{d}z^2} = \frac{1}{f}\left(\frac{\mathrm{d}^2 f}{\mathrm{d}r^2} - \frac{1}{r}\frac{\mathrm{d}f}{\mathrm{d}r} + C^2 r^2 f\right) = \pm\lambda^2 \tag{29}$$

where λ is a separation constant.

For a nonzero λ, the stream function exhibits either trigonometric or hyperbolic variations in the axial direction. In a cyclone, such behavior is unlikely to occur. The possibility of a nonzero separation constant is, hence, ruled out. The only plausible choice is attendant on $\lambda = 0$. On the one hand, this value leads to a linear axial variation of the form $g(z) = C_1 z + C_2$. On the other, it permits retrieving the radial variation of the stream function from the Bessel equation

$$\frac{\mathrm{d}^2 f}{\mathrm{d}r^2} - \frac{1}{r}\frac{\mathrm{d}f}{\mathrm{d}r} + C^2 r^2 f = 0 \tag{30}$$

such that

$$f(r) = rD_3 J_{\frac{1}{2}}\left(\tfrac{1}{2}Cr^2\right) + rD_4 J_{-\frac{1}{2}}\left(\tfrac{1}{2}Cr^2\right) \tag{31}$$

Then using the known identities,

$$J_{\frac{1}{2}}(x) = \sqrt{2/(\pi x)}\sin(x); \qquad J_{-\frac{1}{2}}(x) = \sqrt{2/(\pi x)}\cos(x) \tag{32}$$

one can put

$$f(r) = A\cos\left(\tfrac{1}{2}Cr^2\right) + B\sin\left(\tfrac{1}{2}Cr^2\right) \tag{33}$$

and so

$$\psi^{(0)} = (C_1 z + C_2)\left[A\cos\left(\tfrac{1}{2}Cr^2\right) + B\sin\left(\tfrac{1}{2}Cr^2\right)\right] \tag{34}$$

Except for the unknown constants, which must be prescribed by the boundary conditions, Eqs. (26) and (34) are identical to those invoked by Culick to derive a mean flow approximation for solid rocket motors [17].

D. Particular Solution

Using the constraints associated with Eq. (27), one can evaluate the general constants. First, because of the vanishing axial velocity at the head end, one deduces that $C_2 = 0$. This leaves

$$\psi^{(0)} = C_1 z\left[A\cos\left(\tfrac{1}{2}Cr^2\right) + B\sin\left(\tfrac{1}{2}Cr^2\right)\right] \tag{35}$$

Second, $u_r^{(0)}(0,z) = 0$ implies that $A = 0$. Third, as $u_r^{(0)}$ vanishes along the sidewall, one must have

$$C_1 B\sin\left(\tfrac{1}{2}C\right) = 0 \tag{36}$$

Realizing that neither $C_1 = 0$ nor $B = 0$ are acceptable outcomes, one is left with $\sin\left(\frac{1}{2}C\right) = 0$; forthwith, a fundamental solution may be conceived with $C = 2\pi$. Without sacrificing generality, one may set $C_1 = 1$ and write

$$\psi^{(0)} = Bz\sin(\pi r^2) \tag{37}$$

The velocity field corresponding to Eq. (37) becomes

$$\boldsymbol{u}^{(0)} = -Br^{-1}\sin(\pi r^2)\boldsymbol{e}_r + r^{-1}\boldsymbol{e}_\theta + 2B\pi z\cos(\pi r^2)\boldsymbol{e}_z \tag{38}$$

To calculate the last constant, mass balance must be globally applied to account for the radial inflow along the sidewall. Given that

$$Q_{\text{in}} = Q_{\text{out}} = Q_i + Q_w \tag{39}$$

one calculates

$$Q_i = \frac{A_i}{a^2}; \qquad Q_w = \frac{U_w(2\pi aL)}{Ua^2} = 2\pi\varepsilon L \tag{40}$$

to obtain

$$Q_{\text{in}} = Q_i + Q_w = (A_i/a^2) + 2\pi\varepsilon L = Q_{\text{out}} \tag{41}$$

At leading order ($\varepsilon = 0$), mass conservation requires that

$$2\pi\int_0^{\beta} \boldsymbol{u}^{(0)} \cdot \hat{\boldsymbol{n}}\, r\mathrm{d}r = 2\pi\int_0^{\beta} u_z^{(0)} r\, \mathrm{d}r = Q_i \tag{42}$$

and so

$$B = Q_i \csc(\pi\beta^2)/(2\pi L) \tag{43}$$

It follows that the leading-order velocity field may be expressed by

$$\boldsymbol{u}^{(0)} = -\frac{Q_i \sin(\pi r^2)}{2\pi L \sin(\pi\beta^2) r}\boldsymbol{e}_r + \frac{1}{r}\boldsymbol{e}_\theta + \frac{Q_i z}{L\sin(\pi\beta^2)}\cos(\pi r^2)\boldsymbol{e}_z \tag{44}$$

Thus, by letting

$$\tilde{\kappa} \equiv \frac{Q_i}{2\pi L \sin(\pi\beta^2)} = \kappa \csc(\pi\beta^2) \tag{45}$$

one can put

$$\psi^{(0)} = \tilde{\kappa} z \sin(\pi r^2); \qquad \Omega_\theta^{(0)} = 4\pi^2 \tilde{\kappa} r z \sin(\pi r^2) \tag{46}$$

$$\boldsymbol{u}^{(0)} = -\tilde{\kappa} r^{-1}\sin(\pi r^2)\boldsymbol{e}_r + r^{-1}\boldsymbol{e}_\theta + 2\pi\tilde{\kappa} z \cos(\pi r^2)\boldsymbol{e}_z \tag{47}$$

Other important flow characteristics at leading order include

$$\frac{\partial p^{(0)}}{\partial r} = \frac{1 + \tilde{\kappa}^2\left[\sin^2(\pi r^2) - \pi r^2 \sin(2\pi r^2)\right]}{r^3} \tag{48}$$

$$\frac{\partial p^{(0)}}{\partial z} = -4\pi^2\tilde{\kappa}^2 z \tag{49}$$

$$\Delta p^{(0)} = -\tfrac{1}{2} r^{-2}\left\{1 + \tfrac{1}{2}\tilde{\kappa}^2\left[8\pi^2 r^2 z^2 + 1 - \cos(2\pi r^2)\right]\right\} \tag{50}$$

E. First-Order Equation with Sidewall Mass Addition

Before the first-order solution is set up, we note that the swirl velocity is not perturbed and, as such, the angular momentum equation remains uncoupled from the axial and radial momentum equations. At $\mathcal{O}(\varepsilon)$, the perturbed mass conservation and vorticity transport equations appear as

$$\nabla \cdot \boldsymbol{u}^{(1)} = 0; \qquad \nabla \times \boldsymbol{u}^{(1)} \times \boldsymbol{\Omega}^{(0)} + \nabla \times \boldsymbol{u}^{(0)} \times \boldsymbol{\Omega}^{(1)} = 0 \tag{51}$$

The corresponding boundary conditions become

$$\begin{aligned} u_z^{(1)}(r,0) &= 0; \qquad u_r^{(1)}(1,z) = -1 \\ u_r^{(1)}(0,z) &= 0; \qquad Q_w = \int_0^{2\pi}\int_0^{\beta} \boldsymbol{u}^{(1)}(r,L)\cdot\hat{\boldsymbol{n}}\, r\,\mathrm{d}r\,\mathrm{d}\theta \end{aligned} \tag{52}$$

As before, one may let

$$\boldsymbol{u}^{(1)} = -\frac{1}{r}\frac{\partial\psi^{(1)}}{\partial z}\boldsymbol{e}_r + \frac{1}{r}\frac{\partial\psi^{(1)}}{\partial r}\boldsymbol{e}_z \tag{53}$$

At $\mathcal{O}(\varepsilon)$, the first and second terms in the linearized vorticity transport equation give

$$\nabla\times\boldsymbol{u}^{(0)}\times\boldsymbol{\Omega}^{(1)} = -\left\{\frac{\partial[u_r^{(0)}\Omega_\theta^{(1)}]}{\partial r} + \frac{\partial(u_z^{(0)}\Omega_\theta^{(1)})}{\partial z}\right\}\boldsymbol{e}_\theta \tag{54}$$

$$\nabla\times\boldsymbol{u}^{(1)}\times\boldsymbol{\Omega}^{(0)} = -\left\{\frac{\partial[u_r^{(1)}\Omega_\theta^{(0)}]}{\partial r} + \frac{\partial[u_z^{(1)}\Omega_\theta^{(0)}]}{\partial z}\right\}\boldsymbol{e}_\theta \tag{55}$$

Substitution of Eqs. (54) and (55) into the linearized vorticity transport equation given by Eq. (51) leads to

$$\frac{\partial}{\partial r}\left[u_r^{(0)}\Omega_\theta^{(1)} + u_r^{(1)}\Omega_\theta^{(0)}\right] + \frac{\partial}{\partial z}\left[u_z^{(0)}\Omega_\theta^{(1)} + u_z^{(1)}\Omega_\theta^{(0)}\right] = 0 \tag{56}$$

where

$$\Omega_\theta^{(1)} = \frac{\partial u_r^{(1)}}{\partial z} - \frac{\partial u_z^{(1)}}{\partial r} = \frac{\partial}{\partial z}\left[-\frac{1}{r}\frac{\partial\psi^{(1)}}{\partial z}\right] - \frac{\partial}{\partial r}\left[\frac{1}{r}\frac{\partial\psi^{(1)}}{\partial r}\right] \tag{57}$$

To be consistent with the similarity transformation of the velocity at the zeroth order, the radial velocity must be taken to be dependent on the radial coordinate. On the one hand, this requires a stream function of the form $\psi^{(1)} = z\,h(r)$. On the other hand, one may let $u_r^{(1)} = u_r^{(1)}(r)$ so that Eq. (57) reduces to

$$\Omega_\theta^{(1)} = -\frac{\partial u_z^{(1)}}{\partial r} = -\frac{\partial}{\partial r}\left[\frac{1}{r}\frac{\partial\psi^{(1)}}{\partial r}\right] \tag{58}$$

After inserting $\psi^{(1)} = z\,h(r)$ and Eqs. (47–58) into Eq. (56), we collect

$$\begin{aligned} &\frac{1}{r}\frac{\mathrm{d}}{\mathrm{d}r}\left[\frac{\sin(\pi r^2)}{r}\frac{\mathrm{d}}{\mathrm{d}r}\left(\frac{1}{r}\frac{\mathrm{d}h}{\mathrm{d}r}\right) - 4\pi^2\sin(\pi r^2)h\right] \\ &\quad - 4\pi\cos(\pi r^2)\frac{1}{r}\frac{\mathrm{d}}{\mathrm{d}r}\left(\frac{1}{r}\frac{\mathrm{d}h}{\mathrm{d}r}\right) + 8\pi^2\frac{1}{r}\frac{\mathrm{d}h}{\mathrm{d}r}\sin(\pi r^2) = 0 \end{aligned} \tag{59}$$

It is now appropriate to employ $\eta \equiv \pi r^2$. After some algebra, Eq. (59) collapses into

$$\frac{\mathrm{d}^3 h}{\mathrm{d}\eta^3}\sin\eta - \frac{\mathrm{d}^2 h}{\mathrm{d}\eta^2}\cos\eta + \frac{\mathrm{d}h}{\mathrm{d}\eta}\sin\eta - h\cos\eta = 0 \tag{60}$$

F. Solution by Variation of Parameters

To make headway, one solution to Eq. (60) may be guessed to be $h(\eta) = C\sin\eta$. By the use of the method of variation of parameters (Zhou and Majdalani [18]) the total solution $h(\eta)$ may be compiled by allowing C to vary. Starting with the derivatives,

$$h' = C'\sin\eta + C\cos\eta \tag{61}$$

$$h'' = C''\sin\eta + 2C'\cos\eta - C\sin\eta \tag{62}$$

$$h''' = C'''\sin\eta + 3C''\cos\eta - 3C'\sin\eta - C\cos\eta \tag{63}$$

one may substitute Eqs. (61–63) into Eq. (60); many terms cancel while making room for

$$C'''\sin^2\eta + C''\sin(2\eta) - 2C' = 0 \tag{64}$$

Equation (64) can be readily solved [19]; the result is

$$C(\eta) = C_1 - \left(C_2 + \tfrac{1}{2}C_3\eta\right)\cot\eta \tag{65}$$

where C_1, C_2, and C_3 are pure constants. Recalling that $h = C(\eta)\sin\eta$, one may put

$$h = C_1\sin\eta - \tfrac{1}{2}(C_2 + C_3\eta)\cos\eta \tag{66}$$

When one reverts back to the radial coordinate, the total solution may be represented by

$$h(r) = C_1\sin(\pi r^2) - \tfrac{1}{2}C_2\cos(\pi r^2) - \tfrac{1}{4}\pi C_3 r^2\cos(\pi r^2) \tag{67}$$

and so

$$\psi^{(1)} = C_1 z\sin(\pi r^2) - \tfrac{1}{2}C_2 z\cos(\pi r^2) - \tfrac{1}{4}\pi C_3 r^2 z\cos(\pi r^2) \tag{68}$$

Similarly, one finds

$$u_r^{(1)} = -C_1 r^{-1}\sin(\pi r^2) + \tfrac{1}{2}C_2 r^{-1}\cos(\pi r^2) + \tfrac{1}{4}\pi C_3 r\cos(\pi r^2) \tag{69}$$

To observe the underlying assumption of symmetry about the longitudinal axis, C_2 must vanish. Moreover, to comply with the wall injection boundary condition in Eq. (52), one must have $C_3 = 4/\pi$. It must be realized that the hardwall boundary condition at $z = 0$ is automatically satisfied having employed the proper

ansatz, $\psi^{(1)} = z\,h(r) = C_1 z \sin(\pi r^2) - r^2 z \cos(\pi r^2)$. Only one constant remains undetermined, namely, C_1. This appears in the axial term

$$u_z^{(1)} = 2\pi C_1 z \cos(\pi r^2) - 2z \cos(\pi r^2) + 2\pi z r^2 \sin(\pi r^2) \tag{70}$$

To fix C_1, the global mass balance at the first order must be secured. Starting with

$$Q_w = 2\pi L = 2\pi \int_0^\beta u_z^{(1)}(r, L)\, r\, \mathrm{d}r \tag{71}$$

one finds $C_1 = [1 + \beta^2 \cos(\pi\beta^2)] \csc(\pi\beta^2)$. Forthwith, the first-order streamfunction and its velocity components may be updated, namely,

$$\psi^{(1)} = [1 + \beta^2 \cos(\pi\beta^2)] \csc(\pi\beta^2)\; z \sin(\pi r^2) - z\, r^2 \cos(\pi r^2) \tag{72}$$

$$u_r^{(1)} = -[1 + \beta^2 \cos(\pi\beta^2)] \csc(\pi\beta^2) \sin(\pi r^2)/r + r \cos(\pi r^2) \tag{73}$$

$$u_z^{(1)} = 2\pi [1 + \beta^2 \cos(\pi\beta^2)] \csc(\pi\beta^2) z \cos(\pi r^2) - 2z \cos(\pi r^2) + 2\pi z r^2 \sin(\pi r^2) \tag{74}$$

IV. Flowfield Characteristics

A. Sidewall Velocity Estimates

The wall injection velocity may be estimated from experiments yielding correlations for r_s, the solid-fuel regression rate [3]. A thorough coverage of regression rate measurements and formulations is furnished in earlier chapters. The estimates are generally based on the assumption of steady-state regression of propellant grain. To that end, one must recall that simple mass conservation along the pyrolyzing grain surface requires that

$$\rho_s r_s = \rho_g U_w \tag{75}$$

where subscripts s and g refer to the solid and gas phases, respectively. The gas density at the regressing surface may be estimated using the ideal gas equation of state. Based on empirical studies by Chiaverini et al. [20], the average surface temperature may be taken to be 1000 K. The solid phase may be specified to be, for example, hydroxyl-terminated polybutadiene (HTPB) fuel, and the corresponding density may be calculated accordingly. In the same vein, the regression rate r_s may be obtained from available literature [3].

For the typical hybrid vortex, the wall injection velocity U_w may vary between 0.3 and 2.5 m/s, whereas the average oxidizer injection velocity U is held at 260 m/s. The wall injection parameter ε may, hence, vary between 0.001 and 0.01.

B. Mantle Sensitivity to Sidewall Velocity

The fluid layer that separates the outer vortex from the inner one, the so-called mantle (or spinning wheel), can rotate about the chamber axis. However, it cannot

axially translate. Defined by the surface along which the axial velocity vanishes, the mantle can be located by solving for the root of

$$u_z = u_z^{(0)} + \varepsilon u_z^{(1)} = 0 \tag{76}$$

and so

$$2z\cos(\pi r^2)\{\pi\tilde{\kappa} + \pi\varepsilon[1 + \beta^2\cos(\pi\beta^2)]\csc(\pi\beta^2) - \varepsilon\} + 2\pi\varepsilon z r^2\sin(\pi r^2) = 0 \tag{77}$$

When $r = \beta^*$ is used to denote the radius of the mantle, this root can be determined from Eq. (77) for an arbitrary chamber opening β. We are especially interested in the ideal flow that can be achieved when the nozzle radius is coincident with the mantle radius. Thus, by setting $\beta = \beta^*$, the radius of the inner vortex (exiting the chamber) will match the radius of the chamber opening. This ideal condition leads to a smooth outflow, mitigating the formation of corner vortices that could be caused by wall collisions in the exit plane. Granted this idealization, Eq. (77) reduces to

$$\begin{aligned} &2z\cos(\pi\beta^{*2})\{\pi\tilde{\kappa} + \pi\varepsilon[1 + \beta^{*2}\cos(\pi\beta^{*2})]\csc(\pi\beta^{*2}) - \varepsilon\} \\ &\quad + 2\pi\varepsilon z\beta^{*2}\sin(\pi\beta^{*2}) = 0 \end{aligned} \tag{78}$$

For $\kappa = 0.01$ and $\varepsilon = 0.001$, the mantle location obtained via Eq. (78) is 0.717888. Increasing the wall injection to $\varepsilon = 0.005$ pushes the mantle closer to the wall as β^* shifts to 0.753472.

Explicit roots may be obtained asymptotically using a quadratic polynomial retrieved from Taylor's series of Eq. (78) about the point $\beta^* = 1/\sqrt{2}$; this particular root corresponds to the limiting physical process for which the solution approaches the case of insignificant injection ($\varepsilon \to 0$). After some algebra, one gets

$$\beta^* = (A - \sqrt{C})/B \tag{79}$$

where

$$\begin{aligned} A &= \pi^2\varepsilon/\sqrt{2}; \qquad B = 4\varepsilon - 2\pi\varepsilon + \pi^2\varepsilon - 2\pi\kappa \\ C &= 4\varepsilon^2 - 6\pi\varepsilon^2 + \pi^2\varepsilon^2 - 6\pi\varepsilon\kappa + 4\pi^2\varepsilon\kappa + 2\pi^2\kappa^2 \end{aligned} \tag{80}$$

The roots determined using Eq. (79) are 0.717896, 0.754199, and 0.790398 corresponding to $\kappa = 0.01$ and ε values of 0.001, 0.005, and 0.01, respectively.

Unsurprisingly, both the swirl parameter κ and the wall injection parameter ε affect the mantle location β^*. This is contrary to the behavior observed in the case of bidirectional flow in an idealized liquid rocket engine [21].

To assess the mantle sensitivity to wall injection, ε can be varied at constant κ or vice versa. Results are shown in Table 1 where κ is held at 0.01 while ε is varied from 0 to 0.01. The limiting case of $\varepsilon = 0$ may be used to describe the flowfield in the liquid vortex engine [21]. When wall injection is increased, the mantle is pushed closer to the sidewall. This trend can be attributed to the increased secondary mass flowing into the inner vortex at higher regression rates; the increased mass flux causes the inner vortex to expand by pressing the outer annular region against the sidewall.

Table 1 Mantle location

No.	κ	ε	β^*	$\beta^* - 1/\sqrt{2}$
1	0.01	0.000	0.707	0.000
2	0.01	0.001	0.718	0.011
3	0.01	0.005	0.752	0.045
4	0.01	0.010	0.786	0.079

C. Streamlines

To better visualize the bidirectional motion, streamlines are shown in Fig. 3 for $\kappa = 0.01$ and an order of magnitude increase in wall injection. For steady flow, one recalls that streamlines, pathlines, and streaklines coincide in describing the trajectory of fluid particles throughout the chamber. Figures 3a–c confirm that the mantle location does not vary in the axial direction and that the turning point in the axial velocity approaches the sidewall at higher values of ε. The full asymptotic expression for ψ may be written as

$$\psi = \psi^{(0)} + \varepsilon\psi^{(1)} + \mathcal{O}(\varepsilon^2) = \kappa \csc(\pi\beta^2) z \sin(\pi r^2) + \varepsilon\{[1 + \beta^2 \cos(\pi\beta^2)] \times \csc(\pi\beta^2) z \sin(\pi r^2) - z\, r^2 \cos(\pi r^2)\} + \mathcal{O}(\varepsilon^2) \tag{81}$$

D. Axial Velocity Distribution

The axial velocity is shown in Fig. 4. There it can be seen that as ε is increased from 0 to 0.01, the centerline velocity is nearly doubled. This appreciable velocity increase can be once more attributed to the role of sidewall mass injection; in this case, it causes the axial velocity magnitude to increase throughout the inner

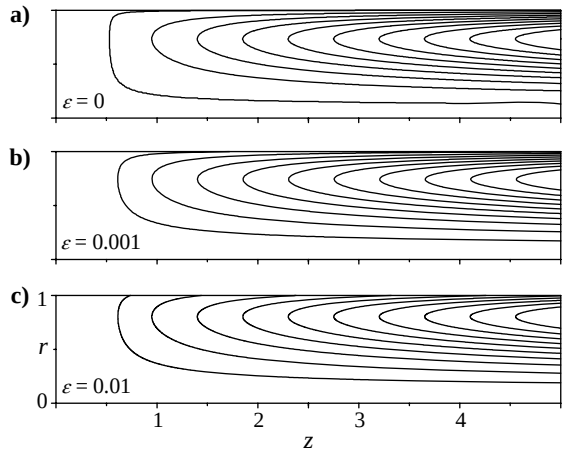

Fig. 3 Swirling bidirectional flow streamlines with increasing sidewall injection, $\kappa = 0.01$.

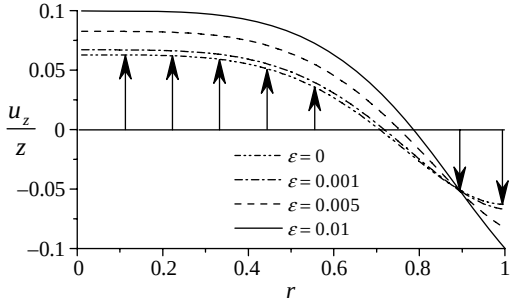

Fig. 4 Axial velocity distribution for $\kappa = 0.01$ and several wall injection rates.

vortex, a trend that supports the streamline behavior described earlier. The total axial velocity becomes

$$\begin{aligned} u_z &= u_z^{(0)} + \varepsilon u_z^{(1)} + \mathcal{O}(\varepsilon^2) \\ &= 2z\cos(\pi r^2)\{\pi\kappa\csc(\pi\beta^2) + \pi\varepsilon[1 + \beta^2\cos(\pi\beta^2)]\csc(\pi\beta^2) - \varepsilon\} \\ &\quad + 2\pi\varepsilon z r^2\sin(\pi r^2) + \mathcal{O}(\varepsilon^2) \end{aligned} \tag{82}$$

E. Radial Velocity Distribution

The radial velocity is shown in Fig. 5 for $\kappa = 0.01$ and the usual values of the perturbation parameter. Note the shift in maximum u_r in the direction of the wall with successive increases in sidewall mass addition. This trend is consistent with the movement of the mantle. The radial velocity for the hybrid model may be expressed by

$$\begin{aligned} u_r &= u_r^{(0)} + \varepsilon u_r^{(1)} + \mathcal{O}(\varepsilon^2) \\ &= -\kappa\csc(\pi\beta^2)r^{-1}\sin(\pi r^2) - \varepsilon\{r^{-1}\sin(\pi r^2)\csc(\pi\beta^2) \\ &\quad \times [1 + \beta^2\cos(\pi\beta^2)] - r\cos(\pi r^2)\} + \mathcal{O}(\varepsilon^2) \end{aligned} \tag{83}$$

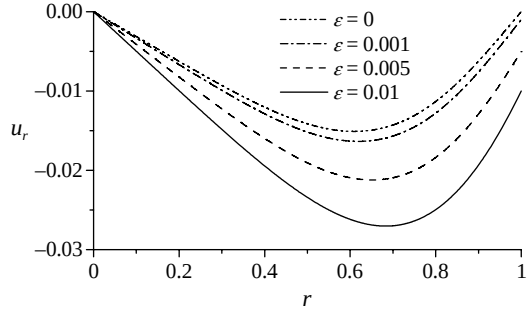

Fig. 5 Radial velocity distribution for $\kappa = 0.01$ and several wall injection rates.

To predict the maximum radial velocity and its locus accurately, one can set $\mathrm{d}u_r/\mathrm{d}r = 0$ and solve for $r = r_m$. The outcome is

$$\begin{aligned}&\kappa \csc(\pi\beta^2)\sin(\pi r_m^2) - 2\pi\kappa r_m^2 \csc(\pi\beta^2)\cos(\pi r_m^2)\\ &\quad + \varepsilon[r_m^2\cos(\pi r_m^2) - 2\pi\beta^2\cot(\pi\beta^2)r_m^2\cos(\pi r_m^2)\\ &\quad - 2\pi\csc(\pi\beta^2)r_m^2\cos(\pi r_m^2) - 2\pi r_m^4\sin(\pi r_m^2) + \beta^2\cot(\pi\beta^2)\sin(\pi r_m^2)\\ &\quad + \csc(\pi\beta^2)\sin(\pi r_m^2)] = 0\end{aligned} \tag{84}$$

When the transcendental nature of Eq. (84) is considered, a numerical root finding technique may be employed. Results are cataloged in Table 2 where κ is kept fixed while ε is varied. One finds that the radial velocity maxima occur at the normalized radii of 0.61, 0.62, 0.65, and 0.68 for $\varepsilon = 0$, 0.001, 0.005, and 0.01, respectively. At these locations, $|(u_r)_{\max}|$ is rendered equal to 0.015, 0.016, 0.021, and 0.027.

Alternatively, an asymptotic expression for the radial velocity maximum and its location may be determined using the same series expansion approach attempted for the mantle location. One finds

$$r_m = (A - \sqrt{C})/B \tag{85}$$

where

$$A = \sqrt{2}\begin{bmatrix}-\pi^3\varepsilon - \cot(\pi\beta^2)(16\varepsilon\beta^2 - 2\varepsilon\beta^2\pi^2)\\ +\csc(\pi\beta^2)(16\varepsilon + 2\pi^2\varepsilon - 16\kappa - 2\pi^2\kappa)\end{bmatrix} \tag{86}$$

$$B = \begin{bmatrix}6\pi\varepsilon - 2\pi^3\varepsilon - 24\beta^2\varepsilon\cot(\pi\beta^2)\\ -24\csc(\pi\beta^2)(\varepsilon + \kappa)\end{bmatrix} \tag{87}$$

$$\begin{aligned}C = A^2 &- \begin{bmatrix}6\pi\varepsilon + 2\pi^3\varepsilon + 24\beta^2\varepsilon\cot(\pi\beta^2)\\ +24\csc(\pi\beta^2)(\varepsilon + \kappa)\end{bmatrix}\\ &\times\begin{bmatrix}\pi\varepsilon + \pi^3\varepsilon + \cot(\pi\beta^2)(24\beta^2\varepsilon - 4\pi^2\beta^2)\\ +\csc(\pi\beta^2)(24\varepsilon - 4\pi^2\varepsilon + 24\kappa - 4\pi^2\kappa)\end{bmatrix}\end{aligned} \tag{88}$$

The radial velocity maxima for ε values of 0.001, 0.005, and 0.01 are approximated at 0.620972, 0.651096, and 0.68322, respectively. Their corresponding radial velocities are −0.016346, −0.021214, and −0.027028.

Table 2 Radial velocity maxima

No.	κ	ε	$r_{\max}$	$(u_r)_{\max}$
1	0.01	0.000	0.609	−0.015
2	0.01	0.001	0.618	−0.016
3	0.01	0.005	0.650	−0.021
4	0.01	0.010	0.683	−0.027

F. Pressure Distribution

The pressure gradients in the radial and axial directions can be determined using Eqs. (10), (13), (47), (73), and (74); after some algebra, one finds

$$\frac{\partial p}{\partial r} = \frac{1+\kappa^2 \csc^2(\pi\beta^2)[\sin^2(\pi r^2) - \pi r^2 \sin(2\pi r^2)]}{r^3} + \varepsilon \frac{2\kappa \csc(\pi\beta^2)}{r^3} \times \{[-\pi r^4 + \beta^2 \cot(\pi\beta^2) + \csc(\pi\beta^2)] \sin^2(\pi r^2) + \pi r^4 \cos^2(\pi r^2) - \pi r^2[\beta^2 \cot(\pi\beta^2) + \csc(\pi\beta^2)] \sin(2\pi r^2)\} \tag{89}$$

$$\frac{\partial p}{\partial z} = -4\pi^2 \kappa \csc^2(\pi\beta^2) z - 8\varepsilon\pi\kappa z \csc(\pi\beta^2) \left[\cot(\pi\beta^2) - \pi \csc(\pi\beta^2) - 1\right] \tag{90}$$

Integrating Eqs. (89) and (90) partially with respect to r and z enables us to calculate the total pressure drop. One finds

$$\Delta p = -\frac{\csc^2(\pi\beta^2)}{4r^2}\left[1 + \kappa^2\left(1 + 8\pi^2 r^2 z^2\right) + \kappa^2 \cos(2\pi r^2) + \cos(2\pi\beta^2)\right] - \varepsilon \frac{\kappa \csc(\pi\beta^2)}{2r^2}\left\{\left[\beta^2 \cot(\pi\beta^2) + \csc(\pi\beta^2)\right] \times \left[1 + 8\pi^2 r^2 z^2 - \cos(2\pi r^2)\right] - r^2\left[8\pi z^2 + \sin(2\pi r^2)\right]\right\} \tag{91}$$

In practice, it must be noted that Eqs. (89) and (91) are virtually insensitive to ε. Being nearly independent of ε , they are well represented by their corresponding curves described by Vyas et al. [21] for the no wall injection case. Specifically, they support the presence of an upward flowing outer vortex. Only the axial pressure gradient is affected by sidewall mass addition as shown in Fig. 6, where $\partial p/\partial z$ is shown along the chamber centerline. Clearly, the pressure drop in the axial direction is more pronounced when the mass to be driven out of the chamber is increased.

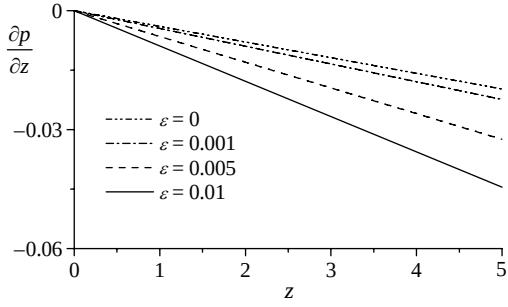

Fig. 6 Axial pressure gradient along the centerline for $\kappa = 0.01$ and several wall injection rates.

So far an exact closed-form analytical expression for the hybrid vortex has been presented. The solution emerges from the inviscid Navier–Stokes equations and corroborates the existence of a bipolar, coaxial vortex pair inside a hybrid chamber model. The present formulation, albeit approximate, exhibits most of the known features of the bidirectional vortex, specifically, those that have been reported in numerical simulations [3, 4] and laboratory tests [5, 6]. In addition to its ability to predict pressure, velocity, and vorticity distributions throughout the chamber domain, the present solution captures the movement of the mantle due to variations in regression rate. The inviscid formulation for the hybrid vortex engine supports the existence of a cyclonic flow formation based on the fundamental equations of motion and a judicious set of boundary conditions.

V. Viscous Corrections

It has become well established that the free-vortex solution presented earlier for the swirl velocity is a suitable approximation only when sufficiently removed from the chamber axis. As the centerline is approached, transition to forced-vortex motion must be entertained en route to suppressing the blatant singularity at $r = 0$. Physically, the forced vortex is induced by viscous forces; these dominate near the chamber axis to the extent of mitigating further growth in the swirl velocity. The inability of inviscid solutions to display the forced-vortex behavior is a known feature of swirling flows [8, 9]. At the sidewall, another boundary layer emerges as a consequence of the no-slip requirement in the wall-tangential direction. This is needed to bring the swirl velocity to zero at the sidewall. The treatment of these boundary layers will be discussed next.

A. Boundary-Layer Equation

From Eq. (83), one can express the radial velocity as

$$u_r = -\kappa A r^{-1} \sin(\pi r^2) - \varepsilon[B r^{-1} \sin(\pi r^2) - r \cos(\pi r^2)] \tag{92}$$

where

$$A = \csc(\pi\beta^2); \quad B = \csc(\pi\beta^2)[1 + \beta^2 \cos(\pi\beta^2)] \tag{93}$$

By retaining the dominant viscous term in the swirl momentum equation, one can put

$$\frac{u_r}{r}\frac{\mathrm{d}(ru_\theta)}{\mathrm{d}r} = \delta \frac{\mathrm{d}}{\mathrm{d}r}\left[\frac{1}{r}\frac{\mathrm{d}\,(ru_\theta)}{\mathrm{d}r}\right]; \qquad \delta \equiv \frac{1}{Re} = \frac{\nu}{Ua} \tag{94}$$

where $\delta \equiv \nu/(Ua)$ is small, being the reciprocal of the tangential-injection Reynolds number. The regularized momentum equation can be recast in the form

$$u_r \frac{\mathrm{d}X}{\mathrm{d}\eta} = 2\delta\sqrt{\pi\eta}\frac{\mathrm{d}^2X}{\mathrm{d}\eta^2} \tag{95}$$

where

$$\eta = \pi r^2 \quad \text{and} \quad X \equiv ru_\theta \tag{96}$$

When this variable transformation is used, Eq. (92) can be converted into

$$u_r = -(\kappa A + \varepsilon B)\sin\eta\sqrt{\pi/\eta} + \varepsilon\sqrt{\eta/\pi}\cos\eta \tag{97}$$

then, by substitution into Eq. (95), one gets

$$\delta\frac{\mathrm{d}^2X}{\mathrm{d}\eta^2} + \frac{1}{2\pi}\left[\pi(\kappa A + \varepsilon B)\frac{\sin\eta}{\eta} - \varepsilon\cos\eta\right]\frac{\mathrm{d}X}{\mathrm{d}\eta} = 0 \tag{98}$$

The ensuing relation represents the key boundary-layer equation that must be asymptotically manipulated to capture the forced vortex behavior near the centerline and the boundary layer near the sidewall. The corresponding regions of nonuniformity are shown in Fig. 7.

B. Inner and Outer Expansions

The outer expansion of Eq. (98) can be swiftly initiated. Using a regularly perturbed series of the form $X_o = X_o^{(0)} + \delta X_o^{(1)} + \cdots$, one collects

$$\frac{1}{2\pi}\left[\pi(\kappa A + \varepsilon B)\frac{\sin\eta}{\eta} - \varepsilon\cos\eta\right]\frac{\mathrm{d}X_o^{(0)}}{\mathrm{d}\eta} = 0; \quad X_o^{(0)} = \text{constant} = C_0 \tag{99}$$

where the subscript o denotes an outer expansion. Note that the leading-order outer solution is a mere duplication of the earlier assumed free-vortex expression, $X_o^{(0)} = ru_\theta^{(0)} = C_0$.

The inner equation that underscores the role of viscous stresses may be arrived at by introducing a spatially magnified scale proportionate to the forced-vortex region (Fig. 7). This may be accomplished by stretching the outer variable by means of

$$s = \eta/\delta^m \tag{100}$$

where s is the inner scale. The exponent m may be determined from the distinguished limit for which consistency in asymptotic orders is achieved. Substitution into Eq. (98) yields

$$\frac{\delta}{\delta^{2m}}\frac{\mathrm{d}^2X_i}{\mathrm{d}s^2} + \frac{1}{2\pi}\left[\frac{\pi(\kappa A + \varepsilon B)}{s\delta^m}\sin(s\delta^m) - \varepsilon\cos(s\delta^m)\right]\frac{1}{\delta^m}\frac{\mathrm{d}X_i}{\mathrm{d}s} = 0 \tag{101}$$

where the subscript i denotes an inner expansion.

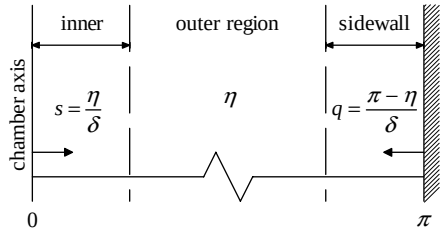

Fig. 7 Inner and wall-tangential boundary layers and corresponding coordinate transformations.

Because we are interested in studying the effects near the chamber axis, we can proceed by linearizing all functions near $\eta = 0$. This operation entails no loss in generality. Using McLaurin series expansions for the sine and cosine, we put

$$\frac{\delta}{\delta^{2m}}\frac{\mathrm{d}^2 X_i}{\mathrm{d}s^2} + \frac{1}{2\pi}\left\{\frac{\pi(\kappa A + \varepsilon B)}{s\delta^m}\left[s\delta^m - \frac{1}{3!}(s\delta^m)^3 + \cdots\right] - \varepsilon\left[1 - \frac{1}{2!}(s\delta^m)^2 + \cdots\right]\right\}\frac{1}{\delta^m}\frac{\mathrm{d}X_i}{\mathrm{d}s} = 0 \tag{102}$$

which, by virtue of some cancellations, begets

$$\delta^{1-m}\frac{\mathrm{d}^2 X_i}{\mathrm{d}s^2} + \frac{1}{2\pi}\left\{(\kappa A + \varepsilon B)\pi\left[1 - \frac{1}{6}(s\delta^m)^2 + \cdots\right] - \varepsilon\left[1 - \frac{1}{2}(s\delta^m)^2 + \cdots\right]\right\}\frac{\mathrm{d}X_i}{\mathrm{d}s} = 0 \tag{103}$$

To achieve a balance between diffusive and convective terms, one must have $m = 1$. This enables us to collapse Eq. (103) into

$$\frac{\mathrm{d}^2 X_i}{\mathrm{d}s^2} + \frac{1}{2\pi}\left[\pi(\kappa A + \varepsilon B) - \varepsilon\right]\frac{\mathrm{d}X_i}{\mathrm{d}s} + \mathcal{O}(\delta^2) = 0 \tag{104}$$

Then using an inner expansion of the form $X_i = X_i^{(0)} + \delta X_i^{(1)} + \cdots$, one collects, at leading order,

$$\frac{\mathrm{d}^2 X_i^{(0)}}{\mathrm{d}s^2} + \frac{1}{2\pi}\left[\pi(\kappa A + \varepsilon B) - \varepsilon\right]\frac{\mathrm{d}X_i^{(0)}}{\mathrm{d}s} = 0 \tag{105}$$

The solution is simple, namely,

$$X_i^{(0)} = A_0 - (A_1/\chi)\exp(-\chi s); \qquad \chi \equiv \frac{1}{2}(\kappa A + \varepsilon B - \varepsilon/\pi) \tag{106}$$

The emerging integration constants can be related to the outer solution using Prandtl's matching principle. Accordingly, the outer limit of the inner solution must equal the inner limit of the outer expansion. Thus, by placing

$$\lim_{s\to\infty} X_i^{(0)} = \lim_{\eta\to 0} X_o^{(0)} \qquad \text{or} \qquad \lim_{s\to\infty} A_0 - (A_1/\chi)\exp(-\chi s) = \lim_{\eta\to 0} C_0 \tag{107}$$

one deduces the common part to both inner and outer approximations, namely, $[X_i^{(0)}]_o = C_0 = A_0$. The composite inner ($ci$) solution can be constructed by way of superposition from

$$X_{ci} = X_o + X_i - \left[X_i^{(0)}\right]_o = A_0 - (A_1/\chi)\exp(-\chi\eta/\delta) \tag{108}$$

C. Nonsingular Swirl Component

At this juncture, we may return to the radial coordinate and express the composite inner swirl velocity as

$$u_\theta^{(ci)} = \frac{A_0}{r}\left[1 - \frac{A_1}{A_0\chi}\exp\left(-\frac{\chi}{\delta}\pi r^2\right)\right] \tag{109}$$

The two remaining unknowns may be secured from the problem's physical constraints. On the one hand, knowing that the azimuthal velocity must vanish along the chamber axis, one must set $u_\theta^{(ci)}(0) = 0$, thereby retrieving $A_0 = A_1/\chi$. On the other hand, one must equate $u_\theta^{(ci)}$ (1) to the wall-tangential speed at which the oxidizer is injected into the chamber. This condition requires that

$$\left(\frac{A_1}{\chi}\right)[1 - \exp(-\pi\chi/\delta)] = 1 \qquad \text{or} \qquad A_1 = \frac{\chi}{1 - \exp(-\pi\chi/\delta)} \tag{110}$$

The nonsecular approximation for the swirl velocity is now at hand. We find and define

$$\begin{aligned} u_\theta^{(ci)} &= \frac{1}{r}\left[\frac{1 - \exp(-\pi r^2\chi/\delta)}{1 - \exp(-\pi\chi/\delta)}\right] = \frac{1 - \exp\left(-\frac{1}{4}Vr^2\right)}{r\left[1 - \exp\left(-\frac{1}{4}V\right)\right]} \\ &\simeq \frac{1 - \exp\left(-\frac{1}{4}Vr^2\right)}{r}; \quad V \equiv \frac{4\pi\chi}{\delta} \end{aligned} \tag{111}$$

where the hybrid form of the vortex injection Reynolds number V surfaces [22]. When sidewall mass addition is present, this important parameter takes the form

$$\begin{aligned} V &= [2(\kappa A + \varepsilon B)\pi - 2\varepsilon]/\delta \\ &= (2\{\kappa\csc(\pi\beta^2) + \varepsilon\csc(\pi\beta^2)[1 + \beta^2\cos(\pi\beta^2)]\}\pi - 2\varepsilon)/\delta \\ &= \left\{\frac{A_i}{aL_0}\csc(\pi\beta^2) + \frac{2U_w}{U}\pi\csc(\pi\beta^2)[1 + \beta^2\cos(\pi\beta^2)] - \frac{2U_w}{U}\right\}Re \\ &= \frac{\bar{Q}_i}{\nu L_0}\csc(\pi\beta^2) + 2\pi Re_w\csc(\pi\beta^2)[1 + \beta^2\cos(\pi\beta^2)] - 2Re_w \end{aligned} \tag{112}$$

where $Re_w = U_w a/\nu$ is the sidewall injection Reynolds number.

D. Sidewall Expansion

To capture the rapid changes near the sidewall, we note that, by virtue of $0 \leq \eta \leq \pi$, we may introduce the slow coordinate

$$q = (\pi - \eta)/\delta^m \tag{113}$$

Here δ^m refers to the thickness of the wall-tangential boundary-layer region in the η variable. When w is used to denote a wall expansion, Eq. (98) may be written as

$$\frac{\delta}{\delta^{2m}}\frac{\mathrm{d}^2X_w}{\mathrm{d}q^2}-\frac{1}{2\pi}\left[\frac{\pi(\kappa A+\varepsilon B)}{\pi-q\delta^m}\sin(\pi-q\delta^m)-\varepsilon\cos(\pi-q\delta^m)\right]\frac{1}{\delta^m}\frac{\mathrm{d}X_w}{\mathrm{d}q}=0 \tag{114}$$

Taylor-series expansions of the trigonometric terms yield

$$\delta^{1-m}\frac{\mathrm{d}^2X_w}{\mathrm{d}q^2}-\frac{1}{2\pi}\left[\pi(\kappa A+\varepsilon B)\left(1-\frac{1}{6}\pi^2\right)-\varepsilon\right]\frac{\mathrm{d}X_w}{\mathrm{d}q}+\mathcal{O}(\delta^m)=0 \tag{115}$$

It may be seen that a balance between diffusion and convection may be achieved for $m=1$. This distinguished limit enables us to write a wall expansion in the form $X_w=X_w^{(0)}+\delta X_w^{(1)}+\cdots$. At leading order, we collect

$$\frac{\mathrm{d}^2X_w^{(0)}}{\mathrm{d}q^2}+\frac{1}{2\pi}\left[\pi(\kappa A+\varepsilon B)\left(\frac{1}{6}\pi^2-1\right)+\varepsilon\right]\frac{\mathrm{d}X_w^{(0)}}{\mathrm{d}q}=0 \tag{116}$$

The solution is nearly at hand. Integration readily gives

$$X_w^{(0)}=B_0-\frac{B_1}{\varphi}\exp(-\varphi q);\qquad \varphi\equiv\frac{1}{2}\left[(\kappa A+\varepsilon B)\left(\frac{1}{6}\pi^2-1\right)+\frac{\varepsilon}{\pi}\right] \tag{117}$$

The two required auxiliary conditions may be established from the no-slip at the sidewall and matching with the composite inner solution. These are

$$\begin{aligned} X_w^{(0)}(0)&=0\\ \lim_{r\to 0}X_w^{(0)}&=\lim_{r\to 1}X_{ci}^{(0)}\end{aligned} \tag{118}$$

The first condition gives $B_1=\varphi B_0$. Thus, we have

$$B_0=1/[1-\exp(-\pi\varphi/\delta)] \tag{119}$$

Through backward substitution, the sidewall approximation emerges. This is

$$X_w^{(0)}=\frac{1-\exp\left[-\frac{1}{4}V_w(1-r^2)\right]}{1-\exp\left(-\frac{1}{4}V_w\right)}$$

or

$$u_\theta^{(w)}=\frac{1}{r}\left\{\frac{1-\exp\left[-\frac{1}{4}V_w(1-r^2)\right]}{1-\exp\left(-\frac{1}{4}V_w\right)}\right\} \tag{120}$$

where the wall-characteristic vortex Reynolds number is given by

$$
\begin{aligned}
V_w &= 2/\delta\left[\pi\left(\tfrac{1}{6}\pi^2-1\right)(\kappa A+\varepsilon B)+\varepsilon\right] \\
&= \left(2\pi\left(\tfrac{1}{6}\pi^2-1\right)\{\kappa\csc(\pi\beta^2)+\varepsilon\csc(\pi\beta^2)[1+\beta^2\cos(\pi\beta^2)]\}+2\varepsilon\right)\Big/\delta \\
&= \left\{\frac{A_i}{aL_0}\left(\tfrac{1}{6}\pi^2-1\right)\csc(\pi\beta^2)\right. \\
&\quad \left.+\frac{2U_w}{U}\pi\left(\tfrac{1}{6}\pi^2-1\right)\csc(\pi\beta^2)[1+\beta^2\cos(\pi\beta^2)]+\frac{2U_w}{U}\right\}Re \\
&= \left[\bar{Q}_i/(\nu L_0)\right]\left(\tfrac{1}{6}\pi^2-1\right)\csc(\pi\beta^2) \\
&\quad +2\pi\left(\tfrac{1}{6}\pi^2-1\right)Re_w\csc(\pi\beta^2)[1+\beta^2\cos(\pi\beta^2)]+2Re_w
\end{aligned}
\tag{121}
$$

Whereas the near-wall approximation vanishes at $r=1$, it exhibits the free-vortex aspect away from the wall.

E. Uniformly Valid Swirl Velocity

When the composite inner and wall expansions are properly combined, a solution may be constructed in a manner to incorporate the problem's key constraints. Although cognizant of free-vortex motion in the outer region, this composite solution stands to capture the velocity adherence condition at the wall and the forced-vortex behavior at the centerline. This can be achieved by superimposing

$$
\begin{aligned}
X_c = X_{ci}+X_w-\left[X_{ci}^{(0)}\right]_w &= \frac{1-\exp\left(-\frac{1}{4}Vr^2\right)}{1-\exp\left(-\frac{1}{4}V\right)} \\
&\quad +\frac{1-\exp\left[-\frac{1}{4}V_w(1-r^2)\right]}{1-\exp\left(-\frac{1}{4}V_w\right)}-1
\end{aligned}
\tag{122}
$$

Recalling that wall-tangential injection is permitted at $z=L$, one can express the swirl velocity in the piecewise form

$$
u_\theta = u_\theta^{(c)} = \begin{cases}
\dfrac{1}{r}\left[\dfrac{1-e^{-\frac{1}{4}Vr^2}}{1-e^{-\frac{1}{4}V}}+\dfrac{1-e^{-\frac{1}{4}V_w(1-r^2)}}{1-e^{-\frac{1}{4}V_w}}-1\right] & \\
\quad\sim\dfrac{1}{r}\left[1-e^{-\frac{1}{4}Vr^2}-e^{-\frac{1}{4}V_w(1-r^2)}\right]; & 0<z<L \\
\dfrac{1}{r}\left(\dfrac{1-e^{-\frac{1}{4}Vr^2}}{1-e^{-\frac{1}{4}V}}\right)\sim\dfrac{1}{r}\left(1-e^{-\frac{1}{4}Vr^2}\right); & z=L \\
\qquad\qquad\text{(tangential injection)} &
\end{cases}
\tag{123}
$$

Note that, in both cases, an asymptotically equivalent representation is provided by ignoring transcendentally small terms. Also note that, at $z = 0$, the presence of an Ekman-type boundary layer may be expected to suppress the swirl velocity at the headwall. However, the attendant analysis is beyond the scope of this work. With the advent of a uniformly valid swirl velocity over $0 < z \leq L$, our presentation of a basic solution for the hybrid vortex chamber is concluded. In the interest of clarity, the final solution is summarized in Table 3 for the general case of a nozzle whose diameter matches that of the outflow; it is also listed in Table 4 for a fixed nozzle diameter corresponding to the no-injection case ($\beta = 1/\sqrt{2}$).

Table 3 Hybrid model for outlet matching inner vortex, $\beta = \beta^*$

Variable	Two-term approximation
u_r	$-\kappa\ \csc(\pi\beta^2) r^{-1} \sin(\pi r^2) - \varepsilon \left\{ r^{-1} \sin(\pi r^2)\ \csc(\pi\beta^2) \times [1 + \beta^2 \cos(\pi\beta^2)] - r \cos(\pi r^2) \right\}$
u_θ	$\left\{ \left(1 - e^{-\frac{1}{4}Vr^2}\right) \left(1 - e^{-\frac{1}{4}V}\right)^{-1} + \left[1 - e^{-\frac{1}{4}V_w(1-r^2)}\right] \times \left(1 - e^{-\frac{1}{4}V_w}\right)^{-1} - 1 \right\} r^{-1}$
u_z	$2z \cos(\pi r^2)\{\pi\kappa \csc(\pi\beta^2) + \pi\varepsilon[1 + \beta^2 \cos(\pi\beta^2)] \csc(\pi\beta^2) - \varepsilon\} + 2\pi\varepsilon z r^2 \sin(\pi r^2)$
Ω_θ	$4\pi^2 \kappa r z \sin(\pi r^2) \csc(\pi\beta^2) - 4\pi r z \varepsilon \left\{ \pi r^2 \cos(\pi r^2) + \sin(\pi r^2) \times \left[2 - \pi\beta^2 \cot(\pi\beta^2) - \pi \csc(\pi\beta^2) \right] \right\}$
ψ	$\kappa \csc(\pi\beta^2)\, z \sin(\pi r^2) + \varepsilon \{[1 + \beta^2 \cos(\pi\beta^2)] \times \csc(\pi\beta^2) z \sin(\pi r^2) - z\, r^2 \cos(\pi r^2)\}$
ε	U_w/U
κ	$1/(2\pi\sigma L) = \bar{Q}_i/(2\pi U a L_0) = A_i/(2\pi a L_0)$
σ	$S/(\pi\beta) = Ua^2/\bar{Q}_i$
Re_w	$U_w a/\nu$
V	$[\bar{Q}_i/(\nu L_0)] \csc(\pi\beta^2) + 2\pi Re_w \csc(\pi\beta^2) \times [1 + \beta^2 \cos(\pi\beta^2)] - 2Re_w$
V_w	$[\bar{Q}_i/(\nu L_0)] \left(\frac{1}{6}\pi^2 - 1\right) \csc(\pi\beta^2) + 2\pi \left(\frac{1}{6}\pi^2 - 1\right) Re_w \csc(\pi\beta^2)[1 + \beta^2 \cos(\pi\beta^2)] + 2Re_w$

Table 4 Hybrid model for fixed outlet radius, $\beta = 1/\sqrt{2}$

Variable	Two-term approximation
u_r	$-\kappa \sin(\pi r^2)/r + \varepsilon \left[r\cos(\pi r^2) - \sin(\pi r^2)/r \right]$
u_θ	$\left\{ \left(1 - e^{-\frac{1}{4}Vr^2}\right)\left(1 - e^{-\frac{1}{4}V}\right)^{-1} + \left[1 - e^{-\frac{1}{4}V_w(1-r^2)}\right] \times \left(1 - e^{-\frac{1}{4}V_w}\right)^{-1} - 1 \right\} r^{-1}$
u_z	$2\pi\kappa z\cos(\pi r^2) + 2\varepsilon z\left[(\pi - 1)\cos(\pi r^2) + \pi r^2 \sin(\pi r^2)\right]$
Ω_θ	$4\pi^2\kappa r z \sin(\pi r^2) + 4\pi r z\varepsilon \left[(\pi - 2)\sin(\pi r^2) - \pi r^2 \cos(\pi r^2)\right]$
ψ	$\kappa z \sin(\pi r^2) + \varepsilon z\left[\sin(\pi r^2) - r^2\cos(\pi r^2)\right]$
σ	$(\sqrt{2}/\pi)\, S \simeq 0.45S$
V	$\bar{Q}_i/(\nu L_0) + 2(\pi - 1)Re_w$
V_w	$\left(\frac{1}{6}\pi^2 - 1\right)[\bar{Q}_i/(\nu L_0)] + 2\left[\pi\left(\frac{1}{6}\pi^2 - 1\right) + 1\right] Re_w$

When considering the latter, the vortex Reynolds numbers reduce to

$$V = 2[(\kappa + \varepsilon)\pi - \varepsilon]Re = 2\pi\kappa Re + 2\varepsilon(\pi - 1)Re = V_0 + 2(\pi - 1)Re_w \tag{124}$$

$$V_w = 2\left[\pi\left(\tfrac{1}{6}\pi^2 - 1\right)(\kappa + \varepsilon) + \varepsilon\right] Re = 2\pi\alpha\kappa Re + 2\varepsilon(\alpha\pi + 1)Re$$
$$= \alpha V_0 + 2(\pi\alpha + 1)Re_w \tag{125}$$

where $\alpha \equiv \frac{1}{6}\pi^2 - 1 \simeq 0.644934$ and V_0 is the vortex Reynolds number for the baseline case of $\varepsilon = 0$ (for a non-injecting sidewall). The sensitivity of the tangential velocity to the sidewall injection and vortex Reynolds numbers is illustrated in Fig. 8. This is accomplished by displaying a one-order-of-magnitude variation in V_0 at constant Re_w or, conversely, a one-order-of-magnitude variation in Re_w at constant V_0. For the range under consideration, the maximum tangential speed is seen to exceed, in some cases, twelve times the average circumferential injection value at entry. Clearly, increasing the vortex Reynolds number has the largest influence on increasing the maximum tangential speed and decreasing the diameter of the forced vortex core. Increasing the blowing Reynolds number has a similar, albeit less pronounced effect. In the same vein, the sensitivity of the solution to the blowing Reynolds number appears to diminish at higher vortex Reynolds numbers.

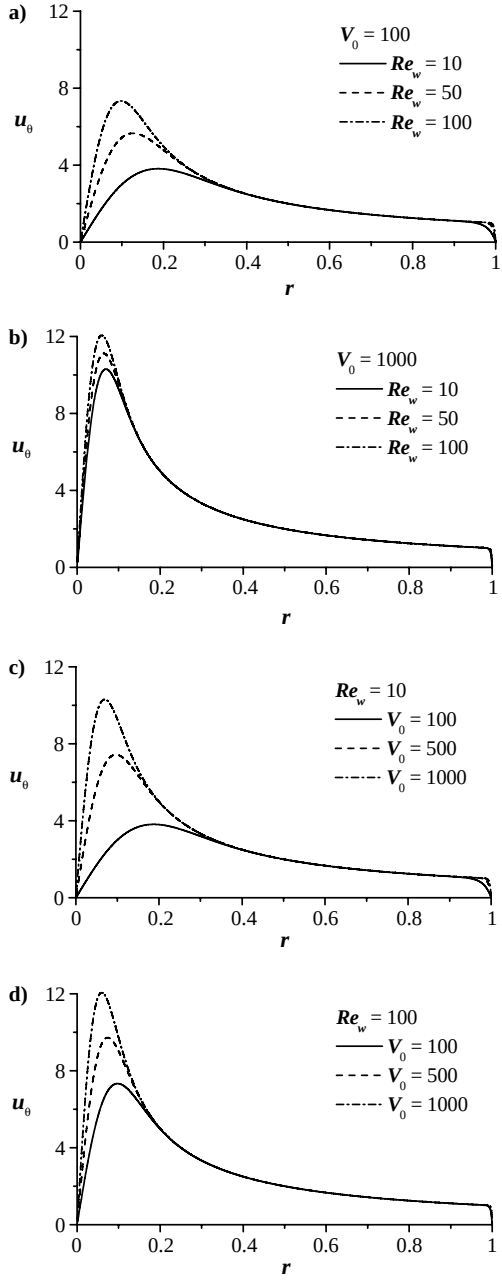

Fig. 8 Variation of the tangential velocity with the sidewall blowing and vortex Reynolds numbers.

VI. Summary

In this chapter, an incompressible mean flow approximation is derived to describe the bidirectional coaxial motion in the VIHRE. The solution is obtained incrementally by first devising an inviscid axisymmetric model in which the vorticity–stream function approach can be applied after decoupling the azimuthal momentum equation from Euler's equations. This fundamental decoupling is promoted by axisymmetry. It is enhanced by the presence of an axially independent azimuthal velocity representation, specifically, a free vortex that appears in the absence of shear or deceleration in both axial and azimuthal directions. Then with use of regular perturbations, the small sidewall-to-headwall injection ratio is employed to derive an asymptotic solution for the bulk flow. This enables us to correlate the location of the mantle as a function of the wall regression speed. Other essential flow ingredients are also obtained and discussed. To overcome the swirl-based singularity along the axis, a boundary-layer treatment is applied to the chamber core. Matched asymptotic expansions are subsequently used to capture the effect of viscous forces along the axis as well as the sidewall. The ensuing analysis yields a uniformly valid approximation that observes the forced-vortex behavior near the core and the no-slip requirement at the sidewall. Whereas the analysis is far from complete, the present work may be used as a springboard for constructing higher-order models that seek to accommodate, for example, the flow dynamics near the headwall, the effects of compressibility, exothermic reactions, multiple species, and radiation heat transfer.

Acknowledgments

This project is sponsored by the National Science Foundation Grant CMS-0353518. I am deeply grateful for assistance received from Anand B. Vyas, Visiting Assistant Professor, Department of Mathematical Sciences, University of Delaware.

References

[1] Casillas, E. D., Shaeffer, C. W., and Trowbridge, J. C., "Cost and Performance Payoffs Inherent in Increased Fuel Regression Rates," AIAA Paper 97-3081, July 1997.

[2] Knuth, W. H., Bemowski, P. A., Gramer, D. J., Majdalani, J., and Rothbauer, W. J., "Gas-Fed, Vortex Injection Hybrid Rocket Engine," NASA Marshall Space Flight Center, Small Business Innovative Research Phase I Final Technical Rept. NASA/MSFC Contract NAS8-40679, Huntsville, AL, Aug. 1996.

[3] Knuth, W. H., Chiaverini, M. J., Sauer, J. A., and Gramer, D. J., "Solid-Fuel Regression Rate Behavior of Vortex Hybrid Rocket Engines," *Journal of Propulsion and Power*, Vol. 18, No. 3, 2002, pp. 600–609.

[4] Knuth, W. H., Chiaverini, M. J., Gramer, D. J., Sauer, J. A., St. Clair, C. P., Whitesides, R. H., and Dill, R. A., "Preliminary Computational Fluid Dynamics Analysis of the Vortex Hybrid Rocket Chamber and Nozzle Flowfield," AIAA Paper 98-3351, July 1998.

[5] Knuth, W. H., Gramer, D. J., Chiaverini, M. J., and Sauer, J. A., "Development and Testing of Vortex Driven, High Regression Rate Hybrid Rocket Engines," AIAA Paper 98-3507, July 1998.

[6] Knuth, W. H., Chiaverini, M. J., Gramer, D. J., and Sauer, J. A., "Experimental Investigation of a Vortex-Driven High-Regression Rate Hybrid Rocket Engine," AIAA Paper 98-3348, July 1998.

[7] Bloor, M. I. G., and Ingham, D. B., "Theoretical Investigation of the Flow in a Conical Hydrocyclone," *Transactions of the Institution of Chemical Engineers*, Vol. 51, No. 1, 1973, pp. 36–41.

[8] Bloor, M. I. G., and Ingham, D. B., "The Flow in Industrial Cyclones," *Journal of Fluid Mechanics*, Vol. 178, 1987, pp. 507–519.

[9] Leibovich, S., "Vortex Stability and Breakdown: Survey and Extension," *AIAA Journal*, Vol. 22, No. 9, 1984, pp. 1192–1206.

[10] Leibovich, S., "The Structure of Vortex Breakdown," *Annual Review of Fluid Mechanics*, Vol. 10, 1978, pp. 221–246.

[11] Beran, P. S., and Culick, F. E. C., "The Role of Non-Uniqueness in the Development of Vortex Breakdown in Tubes," *Journal of Fluid Mechanics*, Vol. 242, 1992, pp. 491–527.

[12] Vatistas, G. H., Lin, S., and Kwok, C. K., "Reverse Flow Radius in Vortex Chambers," *AIAA Journal*, Vol. 24, No. 11, 1986, pp. 1872–1873.

[13] Vatistas, G. H., Lin, S., and Kwok, C. K., "Theoretical and Experimental Studies on Vortex Chamber Flows," *AIAA Journal*, Vol. 24, No. 4, 1986, pp. 635–642.

[14] Szeri, A., and Holmes, P., "Nonlinear Stability of Axisymmetric Swirling Flows," *Philosophical Transactions of the Royal Society of London, Series A: Mathematical and Physical Sciences*, Vol. 326, No. 1590, 1988, pp. 327–354.

[15] Gupta, A. K., Lilley, D. G., and Syred, N., *Swirl Flows*, Abacus, London, 1984, pp. 314–349.

[16] Hoekstra, A. J., Derksen, J. J., and Van den Akker, H. E. A., "An Experimental and Numerical Study of Turbulent Swirling Flow in Gas Cyclones," *Chemical Engineering Science*, Vol. 54, No. 13, 1999, pp. 2055–2065.

[17] Culick, F. E. C., "Rotational Axisymmetric Mean Flow and Damping of Acoustic Waves in a Solid Propellant Rocket," *AIAA Journal*, Vol. 4, No. 8, 1966, pp. 1462–1464.

[18] Zhou, C., and Majdalani, J., "Improved Mean Flow Solution for Slab Rocket Motors with Regressing Walls," *Journal of Propulsion and Power*, Vol. 18, No. 3, 2002, pp. 703–711.

[19] Wolfram, S., Mathematica. A System for Doing Mathematics on Computer, Version 5.0, Addison–Wesley, Reading, MA, 1988.

[20] Chiaverini, M. J., Serin, N., Johnson, D. K., Lu, Y.-C., Kuo, K. K., and Risha, G. A., "Regression Rate Behavior of Hybrid Rocket Solid Fuels," *Journal of Propulsion and Power*, Vol. 16, No. 1, 2000, pp. 125–132.

[21] Vyas, A. B., Majdalani, J., and Chiaverini, M. J., "The Bidirectional Vortex. Part 1: An Exact Inviscid Solution," AIAA Paper 2003-5052, July 2003.

[22] Vyas, A. B., Majdalani, J., and Chiaverini, M. J., "The Bidirectional Vortex. Part 2: Viscous Core Corrections," AIAA Paper 2003-5053, July 2003.

Chapter 7

High-Speed Flow Effects in Hybrid Rockets

Joseph Majdalani*
University of Tennessee Space Institute, Tullahoma, Tennessee 37388

Nomenclature

a = chamber radius
a_0 = sonic speed at chamber origin, $a_0 = \sqrt{\gamma p_0/\rho_0}$
p = pressure normalized by headwall condition, $\bar{p}/p_0$
r, z = normalized radial and streamwise coordinates, $\bar{r}/a$, $\bar{z}/a$
U_c, u_c = centerline speed at headwall, $\bar{u}_z(0,0)$, U_c/U_w
U_w = sidewall injection velocity, $-\bar{u}_r(a,\bar{z})$
$\boldsymbol{u}$ = normalized velocity, $(\bar{u}_r, \bar{u}_z)/a_0$
u_h = headwall injection constant, $u_c/\pi = U_c/(\pi U_w)$
α, β, σ = pure constants defined in text
δ, λ = functions of γ defined via Eqs. (68) and (69)
η = action variable, $\frac{1}{2}\pi r^2$ (cylindrical) or $\frac{1}{2}\pi y$ (Cartesian)
ρ_0 = density

Subscripts and Superscripts

c = centerline property or net correction
h = headwall property
m = area-averaged mean value
r = radial component or partial derivative
s = sonic condition
w = sidewall property
z = axial component or partial derivative
$\bar{}$, $\sim$ = dimensional or approximate variable

*Jack D. Whitfield Professor of High Speed Flows, Department of Mechanical, Aerospace and Biomedical Engineering. Member AIAA.

I. Introduction

IN Chapters 5 and 6, we have presented a combination of exact and asymptotic techniques that enable us to capture the nonreactive, incompressible mean flow motion in both traditional and vortex injection hybrid chambers. As we complete this trilogy, we turn our attention to the role of high-speed flows and the compressibility effects that they engender.

The chapter proceeds as follows. First we consider the compressible flow analog in a solid rocket motor (SRM), namely, the Taylor–Culick profile. We present the compressible Euler equations for steady, axisymmetric, isentropic flow assuming uniform injection of a calorically perfect gas in a porous chamber. We then apply a Rayleigh–Janzen expansion in powers of M_w^2, where M_w is the wall Mach number. We solve the ensuing equations to order M_w^4 and apply the results up to the sonic point in a nozzleless chamber. Area averaging is also performed to reconcile with one-dimensional theory. We show that our compressible solution agrees with existing theory to the extent that it faithfully captures the steepening of the Taylor–Culick profile with downstream development. Based on the closed-form expressions that we obtain, the main flow attributes are quantified parametrically and compared to existing incompressible and quasi-one-dimensional theories. Verification by computational fluid dynamics (CFD) is also undertaken. Comparison with two turbulent flow models is used to confirm the agreement, particularly, in retracing the streamwise evolution of the velocity. Regardless of the Mach number, we identify nearly identical trends in chambers that are rescaled by the critical sonic length L_S. Using a suitable transformation, we prove the attendant similarity and provide universal criteria that can be used to assess the relative importance of gas compression in solid and hybrid rockets with sinusoidal headwall injection. Finally, we repeat the analysis for the slab hybrid.

The key questions that this chapter seeks to answer and the principal findings that we obtain may be summarized in 1) the role of high-speed flows in altering the fundamental flowfield, 2) the advent of simple solutions that enable us to capture the effects of compressibility, 3) the close agreement between our inviscid solution and turbulent Navier–Stokes simulations, 4) the explicit criteria that establish whether high-speed flow effects must be accounted for, 5) the critical geometric length that can be used to rescale the problem and unravel a nearly universal solution, and 6) the general mathematical procedure needed to derive the compressible flow corrections in two dimensional and axisymmetric configurations.

A. Background and Relevance

The injection-driven flow of an incompressible fluid was first described by Taylor [1], who not only resolved this problem in porous tubes, but also in channels, wedges, and cones. In lieu of using Taylor's integral equation, other investigators, such as Yuan [2], Yuan and Finkelstein [3], Wageman and Guevara [4], Terrill [5, 6], and Culick [7] used different routes and recovered, in the inviscid limit, the same cosine-shaped profile found by Taylor. Some of these studies relied on the vorticity–stream function approach or asymptotic tools to perturb the similarity-reduced equation derived by Berman [8] for steady laminar flow in porous channels.

In addition to its sheer simplicity, the Taylor–Culick solution would later prove surprisingly accurate in modeling the drainage of watery suspensions across porous sheets, in surface ablation and sweat cooling [9, 10], and in simulating the mean flow in SRMs. This could be attributed, in part, to its streamlines being observant of the no slip requirement at the sidewall, a feature that has inspired a few to coin it quasi viscous. It quickly resembled the viscous solution with successive increases in the injection Reynolds number.

Following the inventive experiments by Taylor [1] under laminar conditions, Wageman and Guevara [4] and Yamada et al. [11] confirmed the same behavior under Reynolds numbers that were sufficiently high to induce turbulence. Turbulence appeared to have little bearing on altering the mean flow structure except in the downstream segment of the chamber where flow steepening was observed. In this part of the domain, compressibility intensified to the extent that it became difficult to discern which of the two mechanisms was more responsible for the steepening effect. The flattened shape was further reported in cold-flow experiments by Dunlap et al. [12]; and Traineau et al. [13], which employed nitrogen and air injection, respectively. The spatial evolution was also parametrically substantiated via numerical simulations by Beddini [14], Baum et al. [15], Sabnis et al. [16], Liou and Lien [17], and Apte and Yang [18, 19]. In summary, these studies confirmed the existence of a laminar segment that could stretch over the entire length of the chamber depending on the injection Reynolds number. They also suggested that, in sufficiently long chambers, transition from the classic solution typically occurred past the midsection plane, although transition of the mean velocity was delayed to the fully developed section where the axial profile became fuller. Both compressibility and turbulence were posited as plausible candidates for causing these departures.

The ability of the Taylor–Culick equation to imitate faithfully the motion of reactive gases ejected from the regressing wall of a solid-propellant rocket has vast implications and, as such, has been the subject of much scrutiny. In one study, it has been shown that, unless the burning rate is exceedingly high, the slow expansion of the sidewall may be discounted in favor of a quasi-steady model [20]. Moreover, the idea of a uniform burning rate along the grain and the attendant assumption of constant mass addition at the sidewall have been reiterated in both nozzle-adapted and nozzleless configurations. In the latter case, Gany and Aharon [21] have pointed out that the axially accentuated erosive-burning effects on the regression rate are generally offset by the decreasing pressure in the downstream direction. In the same vein, the nearly nonreactive environment outside of the thin-propellant flame zone has been repeatedly simulated and shown to be appropriately treatable by cold-flow models [22]. This can be ascribed to the weak coupling with the energy equation where the temperature is almost uniform [23]. Such factors have placed Taylor's mean flow formula at the epicenter of a large body of theoretical investigations focused on modeling rocket performance, flame zone analysis, particle–mean flow interactions, and the ever-daunting task of predicting aeroacoustic instability. Relevance to internal ballistics and performance prediction in rockets is briefly reviewed by Majdalani [24]. By way of example, the accuracy of Taylor's formula has given Varapaev and Yagodkin [25] the impetus to use it at the basis of their investigation of hydrodynamic instability. In the same context, it has been employed by Griffond et al. [26] and, subsequently, by Abu-Irshaid et al. [27] to investigate the evolution

of turbulence in straight porous cylinders. It has been essential to the evaluation of particle–mean flow interactions as demonstrated by Féraille and Casalis [28].

B. Technical Motivation

The need for refined analytical solutions has since continued to grow hand-in-hand with computing power for two fundamental reasons. First, to gain deeper physical insight into an "eternally complex problem" [43] and, second, to provide the much needed limiting process validations for numerical simulations of chemically reactive rocket chambers. As argued by Wasistho et al. [29], a team of researchers at the University of Illinois Center for Simulation of Advanced Rockets (CSAR) has determined that analytical models often present the only valuable resource for checking numerical results; this is partly caused by the difficulty of acquiring specific experimental data and, partly, due to the harsh environment erupting in rocket chambers, particularly, one that is hostile to proper instrumentation. In the same study [29], Wasistho et al. have suggested the need to employ a compressible mean flow model to promote better agreement with their full-scale computations. Their steady and unsteady flow results were compared, respectively, to the numerical solution of the integral equation obtained by Balakrishnan et al. [30] and to the time-dependent expression for wave motion by Majdalani and Flandro [31]. Favorable agreement was noted on both counts. Today, as regulatory requirements for validation and verification continue to mount in the propulsion industry, so do the demands for improved analytical tools. In this chapter, we focus on the compressible Taylor flow analog and its extension to hybrid rocket core gasdynamics.

C. Specific Targets and Benefits

The quest for a compressible mean flow expression serves multiple objectives. First, it is needed to ameliorate our representation of the undisturbed inviscid field and its impact on the ensuing acoustic wave motion and flame zone analysis. For instance, it will help to obtain a more consistent solution for the total internal flowfield by insisting that both mean and unsteady components retain a compressible ingredient. Existing expressions for the time-dependent flowfield are based on an incompressible steady flow representation in both planar and axisymmetric chambers (cf. Majdalani and Roh [32], Majdalani [33], and Majdalani and Flandro [31]). By the same token, a compressible outer solution can be indispensable in analyzing the thin-flame zone that forms above the surface of a solid propellant or a hybrid fuel where pyrolysis and vaporization must be carefully modeled. It has often been reported that the exothermic viscous-layer treatment cannot be completed without a compressible outer approximation [34]. The second, objective is to upgrade our analysis of hydrodynamic instability, which so far has been limited to incompressible equations. The use of a compressible formula at the baseline of such development can markedly improve the actual methodology and its potential outcome. Venugopal [35] shows that a minor increase in mean flow velocity caused by density variations along the wall can engender large excursions in the growth of disturbances in a simulated SRM. The third objective is to provide a more precise

platform for calculating the acoustic growth rate factors inherited from volume integrals of internal flow components [36]. The fourth objective is to facilitate the characterization of nozzleless rocket motors, whose increased volumetric efficiency has made them prime candidates for ramjet-boosting applications. The absence of a nozzle has enabled investigators to focus on specific features of the flow, thus providing an attractive vehicle for academic studies that employ either experimentation or computation. The operation of such motors has been examined from one- and two-dimensional perspectives by Traineau et al. [13], Gany and Aharon [37], and King [21]. It has been recently considered by Balakrishnan et al. [30], who followed Traineau et al. [13] in presenting an inviscid, rotational, and compressible integral equation that can be solved numerically in two dimensions. With use of scaling arguments, their radial momentum equation was discarded and a perturbation expansion was implemented using the reciprocal of the aspect ratio. In the process, pressure and grain regression were related by the Saint-Robert power law. The resulting pseudo-two-dimensional approximation has proven adequate in treating long motors with arbitrary cross section and wall injection rate.

In this chapter, we reconsider Taylor's original problem in an axisymmetric, constant-area chamber with uniform wall injection. We also permit the imposition of sinusoidal injection at the headwall to model hybrid rockets. Using a Janzen–Rayleigh expansion in the wall Mach number, we expand the system of equations up to fourth order and extract the compressible Taylor flow solution.

II. Mathematical Model

A. Geometry

We consider the steady, inviscid, and non-heat-conducting flow of an ideal gas in the domain bounded by the porous sidewall of a tube with radius a and finite length L_0. We assume that the speed of the gas at the wall U_w is uniform and that L_0 can reach the critical length. In solid and hybrid rockets, the sidewall velocity $U_w = \rho_P \dot{r}_P/\rho$ is commensurate with the solid- or fuel-propellant regression rate $\dot{r}_P$. To justify a constant U_w, we recall that the streamwise depreciation in pressure and its wall-coupling effect can nearly offset the axial decrease in density. As shown in Fig. 1, $\bar{r}$ and $\bar{z}$ stand for the radial and streamwise coordinates (with the overbar denoting a dimensional quantity). We normalize these variables by a and select a curvilinear coordinate system whose origin is centered at the headwall. Axial symmetry reduces the field investigation to the region $0 \le r \le 1$ and $0 \le z \le L$, where $L = L_0/a$. The tube can be either closed at $z = 0$, corresponding to a zero inlet profile in Berman's equation (Fig. 1a), or open, permitting the classic similarity-conforming profile with characteristic speed U_c (Fig. 1b) [3]. Hence, the streamlines can be either induced by the injection process or by the two converging streams. The latter is useful in modeling the flow in hybrid rockets, where U_w can be appreciably smaller than U_c due to slow fuel pyrolysis and fast oxidizer injection. Typical hybrids exhibit values of $U_c/U_w \sim \mathcal{O}(10^2$–$10^3)$ and $M_w = U_w/a_0 \sim \mathcal{O}(10^{-4})$, where a_0 is the speed of sound at the origin. Although we concentrate on the interesting case of choked flow at $z = L_s$, our solution will still apply to an isobaric opening when $z < L_s$. In rocketry, the wall Mach number can be as high as 0.02.

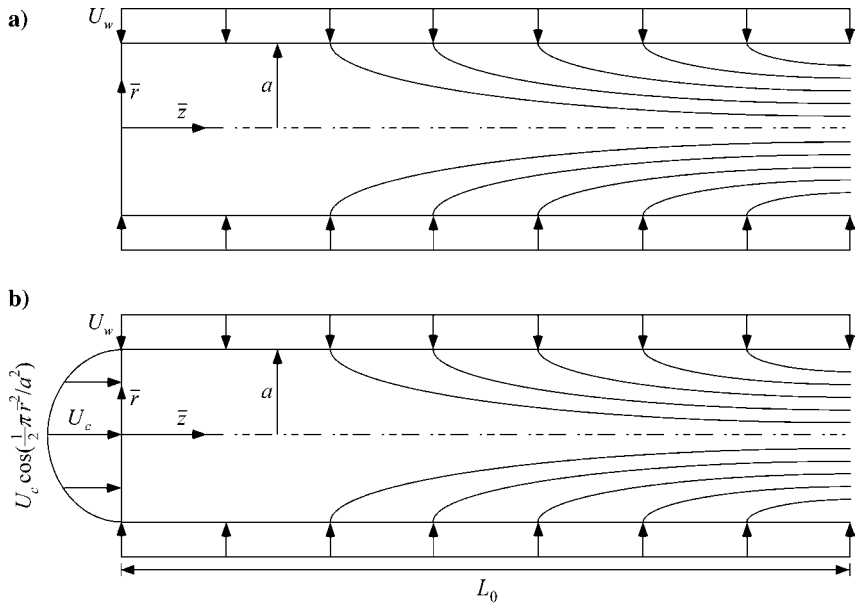

Fig. 1 Porous tube accommodating inlet profile corresponding to a) inert headwall conditions and b) Berman's similarity-conforming cosine distribution.

B. Formulation

We begin by normalizing all remaining variables and operators using standard axisymmetric descriptors. This can be done by setting

$$u_r = \bar{u}_r/a_0; \qquad u_z = \bar{u}_z/a_0; \qquad u_c = U_c/U_w; \qquad p = \bar{p}/p_0; \qquad T = \bar{T}/T_0;$$
$$\rho = \bar{\rho}/\rho_0; \qquad \psi = \bar{\psi}/(\rho_0 a_0 a^2); \qquad \boldsymbol{\Omega} = \bar{\boldsymbol{\Omega}} a/a_0; \qquad \nabla = a\bar{\nabla}; \qquad \mathrm{D}^2 = a^2\bar{\mathrm{D}}^2 \tag{1}$$

where the subscript 0 refers to conditions at the origin; meanwhile $U_c = \bar{u}_z(0,0)$ and $U_w = -\bar{u}_r(a,\bar{z})$ allude to the injection constants along the headwall and sidewall, respectively. Because of its frequent recurrence, we define the second-order linear operate D^2 as

$$\mathrm{D}^2 \equiv \frac{\partial}{\partial r^2} - \frac{1}{r}\frac{\partial}{\partial r} + \frac{\partial^2}{\partial z^2} = r\frac{\partial}{\partial r}\left(\frac{1}{r}\frac{\partial}{\partial r}\right) + \frac{\partial^2}{\partial z^2} \tag{2}$$

As usual, the velocity, Stokes stream-function, and the vorticity are related by

$$\boldsymbol{u} = u_r\boldsymbol{e}_r + u_z\boldsymbol{e}_z = -\frac{1}{\rho r}\frac{\partial \psi}{\partial z}\boldsymbol{e}_r + \frac{1}{\rho r}\frac{\partial \psi}{\partial r}\boldsymbol{e}_z;$$
$$\Omega = \Omega_\theta = -\frac{1}{r}\frac{\partial}{\partial z}\left(\frac{1}{\rho}\frac{\partial \psi}{\partial z}\right) - \frac{\partial}{\partial r}\left(\frac{1}{\rho r}\frac{\partial \psi}{\partial r}\right) \tag{3}$$

Moreover, for steady inviscid motion, the momentum equation can be manipulated and reduced to

$$\tfrac{1}{2}\nabla(\boldsymbol{u}\cdot\boldsymbol{u}) - \boldsymbol{u}\times\boldsymbol{\Omega} = -\nabla p/(\rho\gamma)$$
$$\text{or } \tfrac{1}{2}\rho\nabla\left[\nabla\psi\cdot\nabla\psi/(\rho r)^2\right] + (\Omega/r)\nabla\psi = -\nabla p/\gamma \tag{4}$$

where $\gamma \equiv c_p/c_v$. At this stage, the curl of Eq. (4) may be taken to eliminate the pressure and obtain the vorticity transport equation. After grouping and rearranging, one identifies the set of equations that must be solved. These are

$$\nabla\times(\boldsymbol{u}\times\boldsymbol{\Omega}) = -\nabla\rho\times\nabla p/(\gamma\rho^2) \quad \text{(vorticity transport equation)} \tag{5}$$

$$\mathrm{D}^2\psi + \rho r\Omega = \nabla\rho\cdot\nabla\psi/\rho \quad \text{(vorticity equation)} \tag{6}$$

$$\nabla p/\gamma = -\tfrac{1}{2}\rho\nabla\left[\nabla\psi\cdot\nabla\psi/(\rho^2 r^2)\right] - (\Omega/r)\nabla\psi \quad \text{(momentum equation)} \tag{7}$$

Given an isentropic flow of a calorically perfect gas, one also has

$$\rho = p^{1/\gamma}; \qquad T = p^{1-1/\gamma} \tag{8}$$

Our auxiliary conditions are prescribed by the continuity of the flow across the centerline and the radial inflow at the sidewall where the streamwise component of the velocity must vanish. Headwall injection can be imposed on the streamwise component in the event of an open boundary. In adherence to the Taylor–Culick model, we begin by considering the case of no flow at $z = 0$. This assortment can be expressed by

$$\begin{aligned}
&\bar{r} = 0; \quad \forall\bar{z}; && \bar{u}_r = 0 && \text{(no flow across centerline)}\\
&\bar{r} = a; \quad 0 \le \bar{z} < L_0; && \bar{u}_z = 0 && \text{(no-slip at sidewall)}\\
&\bar{r} = a; \quad 0 \le \bar{z} < L_0; && \bar{u}_r = -U_w && \text{(uniform sidewall injection)}\\
&\bar{z} = 0; \quad \forall\bar{r}; && \bar{u}_z = 0 && \text{(no headwall injection)}
\end{aligned}$$

$$\text{and so} \begin{cases} u_r(0,z) = 0 \\ u_z(1,z) = 0 \\ u_r(1,z) = -M_w \\ u_z(r,0) = 0 \end{cases} \tag{9}$$

Equations (5–8) must be solved sequentially according to the following strategy. To satisfy the vorticity transport equation, a relation between Ω and ψ must first be determined. This relation is needed in the vorticity equation to eliminate Ω and render a second-order partial differental equation (PDE) in ψ. A solution that satisfies Eq. (9) may then be obtained and returned to the momentum equation so that the pressure distribution can be deduced. Isentropic relations can then be invoked to calculate the density and temperature. This procedure must be applied after perturbing the system.

C. Perturbation Expansion

Using a Rayleigh–Janzen series in powers of M_w^2, we expand each variable according to

$$\begin{aligned}
u_r(r,z) &= M_w u_r^{(0)} + M_w^3 u_r^{(1)} + \mathcal{O}(M_w^5)\\
u_z(r,z) &= M_w u_z^{(0)} + M_w^3 u_z^{(1)} + \mathcal{O}(M_w^5)\\
\psi(r,z) &= M_w \psi^{(0)} + M_w^3 \psi^{(1)} + \mathcal{O}(M_w^5)\\
\Omega(r,z) &= M_w \Omega^{(0)} + M_w^3 \Omega^{(1)} + \mathcal{O}(M_w^5)\\
\rho(r,z) &= 1 + M_w^2 \rho^{(1)} + M_w^4 \rho^{(2)} + \mathcal{O}(M_w^6)\\
p(r,z) &= 1 + M_w^2 p^{(1)} + M_w^4 p^{(2)} + \mathcal{O}(M_w^6)\\
T(r,z) &= 1 + M_w^2 T^{(1)} + M_w^4 T^{(2)} + \mathcal{O}(M_w^6)
\end{aligned} \tag{10}$$

The leading- and first-order velocity components can be readily obtained at even powers in M_w, specifically,

$$M_w\text{: } u_r^{(0)} = -\frac{1}{r}\frac{\partial \psi^{(0)}}{\partial z}; \qquad u_z^{(0)} = \frac{1}{r}\frac{\partial \psi^{(0)}}{\partial r} \tag{11}$$

$$M_w^3\text{: } u_r^{(1)} = \frac{\rho^{(1)}}{r}\frac{\partial \psi^{(0)}}{\partial z} - \frac{1}{r}\frac{\partial \psi^{(1)}}{\partial z}; \qquad u_z^{(1)} = \frac{1}{r}\frac{\partial \psi^{(1)}}{\partial r} - \frac{\rho^{(1)}}{r}\frac{\partial \psi^{(0)}}{\partial r} \tag{12}$$

On substituting Eq. (10) into Eqs. (5–8), we collect, at $\sigma(M_w)$,

$$M_w^2\text{: } \nabla \times [\boldsymbol{u}^{(0)} \times \boldsymbol{\Omega}^{(0)}] = 0 \tag{13}$$

$$M_w\text{: } \mathrm{D}^2\psi(0) + r\Omega^{(0)} = 0 \tag{14}$$

$$M_w^2\text{: } -\nabla p^{(1)} = \gamma\left\{\tfrac{1}{2}\nabla\left[\nabla\psi^{(0)}\cdot\nabla\psi^{(0)}/r^2\right] + [\Omega^{(0)}/r]\nabla\psi^{(0)}\right\} \tag{15}$$

$$M_w^2\text{: } \rho^{(1)} = p^{(1)}/\gamma \quad T^{(1)} = (\gamma-1)p^{(1)}/\gamma \tag{16}$$

Expansion of Eq. (9) yields, in turn,

$$u_r^{(0)}(0,z) = 0; \qquad \frac{\partial \psi^{(0)}(0,z)}{\partial z} = 0 \left(\text{and } \frac{\partial^2 \psi^{(0)}(0,z)}{\partial r \partial z} = 0\right) \tag{17a}$$

$$u_z^{(0)}(1,z) = 0; \qquad \frac{\partial \psi^{(0)}(1,z)}{\partial r} = 0 \tag{17b}$$

$$u_r^{(0)}(1,z) = -1; \qquad \frac{1}{r}\frac{\partial \psi^{(0)}(1,z)}{\partial z} = 1 \tag{17c}$$

$$u_z^{(0)}(r,0) = 0; \qquad \frac{\partial \psi^{(0)}(r,0)}{\partial r} = 0 \tag{17d}$$

and so on; at $\sigma(M_w^3)$, we segregate the first-order vorticity transport equation, vorticity expression, momentum equation, and isentropic flow relations,

$$M_w^4\text{: } \nabla \times [\boldsymbol{u}^{(0)} \times \boldsymbol{\Omega}^{(1)}] + \nabla \times [\boldsymbol{u}^{(1)} \times \boldsymbol{\Omega}^{(0)}] = -\nabla\rho^{(1)} \times \nabla p^{(1)}/\gamma \tag{18}$$

$$M_w^3\text{: } \mathrm{D}^2\psi^{(1)} + r\Omega^{(1)} = \nabla\rho^{(1)} \cdot \nabla\psi^{(0)} - r\rho^{(1)}\Omega^{(0)} \tag{19}$$

$$M_w^4\text{: } \nabla p^{(2)} = -\gamma\left(\tfrac{1}{2}\rho^{(1)}\nabla[\nabla\psi^{(0)} \cdot \nabla\psi^{(0)}/r^2] + \nabla[\nabla\psi^{(0)} \cdot \nabla\psi^{(1)}/r^2] - \nabla\{\rho^{(1)}[\nabla\psi^{(0)} \cdot \nabla\psi^{(0)}/r^2]\} + [\Omega^{(0)}\nabla\psi^{(1)} + \Omega^{(1)}\nabla\psi^{(0)}]/r\right) \tag{20}$$

$$M_w^4\text{: } \rho^{(2)} = \{2\gamma p^{(2)} + (1-\gamma)[p^{(1)}]^2\}/(2\gamma^2) \text{ and } T^{(2)} = (\gamma - 1) \times \{2\gamma p^{(2)} - [p^{(1)}]^2\}/(2\gamma^2) \tag{21}$$

For this system, we invoke homogenous boundary conditions to avoid disturbing the leading-order approximation, which alone must bear the four chief requirements.

III. Axisymmetric Solution

A. Basic Analysis

Equations (13–17) can be solved consecutively to yield the classic Taylor–Culick solution. To illustrate this, we first recall that the vorticity transport relation may be satisfied by $\Omega^{(0)} = C^2 r\psi^{(0)}$. This expression is then fed into Eq. (14) to obtain $\mathrm{D}^2\psi^{(0)} + C^2r^2\psi^{(0)} = 0$. An incompressible solution that fulfills the problem's constraints ensues for $C = \pi$, namely, $\psi^{(0)} = z\sin(\frac{1}{2}\pi r^2)$. With the replacement of $\psi^{(0)}\nabla\psi^{(0)}$ by $\frac{1}{2}\nabla[\psi^{(0)}]^2$ in the last member of Eq. (15), the basic momentum equation can be integrated into

$$p^{(1)} = -\tfrac{1}{2}\gamma\left\{\nabla\psi^{(0)} \cdot \nabla\psi^{(0)}/r^2 + [\pi\psi^{(0)}]^2\right\} = -\tfrac{1}{2}\gamma\left(\pi^2z^2 + r^{-2}\sin^2\eta\right); \quad \eta = \tfrac{1}{2}\pi r^2 \tag{22}$$

The companion density and temperature are tenable directly from Eq. (16). A simple division by γ yields, for example, $\rho^{(1)} = -\frac{1}{2}(\pi^2z^2 + r^{-2}\sin^2\eta)$.

B. First-Order Vorticity Stream Function Relation

We begin by determining a pivotal relation between $\Omega^{(1)}$ and $\psi^{(1)}$ that satisfies the vorticity transport equation. Because the momentum equation is only used to solve for the pressure, it is vital that Eq. (18) be first secured. In view of the isentropic relation given by Eq. (16), the baroclinic term $\nabla\rho^{(1)} \times \nabla p^{(1)}$ vanishes. We are left with

$$\nabla \times [\boldsymbol{u}^{(0)} \times \boldsymbol{\Omega}^{(1)}] + \nabla \times [\boldsymbol{u}^{(1)} \times \boldsymbol{\Omega}^{(0)}] = 0 \tag{23}$$

The scalar projection of this vector yields a single component, namely,

$$\frac{\partial[u_r^{(0)}\Omega^{(1)}]}{\partial r} + \frac{\partial[u_z^{(0)}\Omega^{(1)}]}{\partial z} + \frac{\partial[u_r^{(1)}\Omega^{(0)}]}{\partial r} + \frac{\partial[u_z^{(1)}\Omega^{(0)}]}{\partial z} = 0 \tag{24}$$

We now insert Eqs. (11) and (12) into Eq. (24) and use $\Omega^{(0)} = \pi^2 r \psi^{(0)}$. After expanding and simplifying, we collect

$$\frac{\partial \psi^{(0)}}{\partial z}\left(\frac{\Omega^{(1)}}{r} - \frac{\partial \Omega^{(1)}}{\partial r}\right) + \frac{\partial \psi^{(0)}}{\partial r}\frac{\partial \Omega^{(1)}}{\partial z} = -\pi^2 r\left\{\psi^{(0)}\left[\frac{\partial \rho^{(1)}}{\partial r}\frac{\partial \psi^{(0)}}{\partial z} - \frac{\partial \rho^{(1)}}{\partial z}\frac{\partial \psi^{(0)}}{\partial r}\right] + \frac{\partial \psi^{(1)}}{\partial r}\frac{\partial \psi^{(0)}}{\partial z} - \frac{\partial \psi^{(1)}}{\partial z}\frac{\partial \psi^{(0)}}{\partial r}\right\} \tag{25}$$

At first glance, Eq. (25) appears to be staggeringly complex, thereby intractable by known methods. However, taking a cue from the leading-order relation for the vorticity, we realize that a solution may mirror the incompressible form within a linear correction. Thus, we let

$$\Omega^{(1)} = \pi^2 r \psi^{(1)} + \Omega_c^{(1)} \tag{26}$$

We find that the first-order vorticity transport equation will indeed be satisfied by eliminating the residual

$$\frac{\partial \psi^{(0)}}{\partial z}\left[\frac{\Omega_c^{(1)}}{r} - \frac{\partial \Omega_c^{(1)}}{\partial r}\right] + \frac{\partial \psi^{(0)}}{\partial r}\frac{\partial \Omega_c^{(1)}}{\partial z} = -\pi^2 r \psi^{(0)}\left[\frac{\partial \rho^{(1)}}{\partial r}\frac{\partial \psi^{(0)}}{\partial z} - \frac{\partial \rho^{(1)}}{\partial z}\frac{\partial \psi^{(0)}}{\partial r}\right] \tag{27}$$

or

$$\sin\eta\left[\frac{\Omega_c^{(1)}}{r} - \frac{\partial \Omega_c^{(1)}}{\partial r}\right] + \pi r z \cos\eta \frac{\partial \Omega_c^{(1)}}{\partial z} = -\pi^2 r^{-2} z \sin\eta\left[\sin^3\eta + \pi r^2 \cos\eta\left(\pi^2 r^2 z^2 - \sin^2\eta\right)\right] \tag{28}$$

Equation (28) represents a first-order PDE in $\Omega_c^{(1)}$ that can be suitably integrated. After some effort, we recoup the general form

$$\Omega_c^{(1)} = -\tfrac{1}{2}\pi^2 r^{-1}(\sin^2\eta + \pi^2 r^2 z^2)\psi^{(0)} + rG[\psi^{(0)}] \tag{29}$$

where $G[\psi^{(0)}]$ is arbitrary.

C. First-Order Vorticity Equation

With $\Omega^{(1)}$ at hand, we turn our attention to Eq. (19). With appropriate substitutions, we extract

$$\begin{aligned}\mathrm{D}^2\psi^{(1)} + \pi^2 r^2 \psi^{(1)} &= \tfrac{1}{4}\pi r^{-2}\psi^{(0)}\{-4\pi r^2 + 2\sin(2\eta) - 4\pi r^2\cos(2\eta) \\ &\quad + 4\pi^3 r^4 z^2 - (4/\pi) r^4 G[\psi^{(0)}]/\psi^{(0)}\} \\ &= \tfrac{1}{4}\pi^2 z \sin\eta\{-4 + \sin(2\eta)/\eta - 4\cos(2\eta) + 8\pi\eta z^2 \\ &\quad - (8/\pi^3)\eta G(z\sin\eta)/(z\sin\eta)\} \end{aligned} \tag{30}$$

To make further headway, it is expedient to apply the transformation $\psi^{(1)} = F(\eta, z)\sin\eta$. After some algebra, we hold

$$\eta^2 \frac{\partial^2 F}{\partial \eta^2} + 2\eta^2 \cot\eta \frac{\partial F}{\partial \eta} + \frac{\eta}{2\pi}\frac{\partial^2 F}{\partial z^2} = q(\eta, z) \tag{31}$$

where

$$\begin{aligned} q(\eta, z) &= \tfrac{1}{8}\pi\eta z\{-4 + \sin(2\eta)/\eta - 4\cos(2\eta) + 8\pi\eta z^2 \\ &\quad - (8/\pi^3)\eta G(z\sin\eta)/(z\sin\eta)\} \end{aligned} \tag{32}$$

The difficulty in solving Eq. (31) is not only in the need to guess the proper particular solution, but also, in selecting a suitable form of G that is congruent with the problem's boundary conditions. Assuming G to be some polynomial, we let

$$G = \pi^3\left(A_0 + A_1 z\sin\eta + A_2 z^2\sin^2\eta + \pi A_3 z^3\sin^3\eta\right) \tag{33}$$

and so

$$\begin{aligned} q = \tfrac{1}{8}\pi\eta z\{&-4 + \sin(2\eta)/\eta - 4\cos(2\eta) - 8A_0\eta\csc\eta/z - 8A_1\eta - 8A_2\eta z\sin\eta \\ &+ 4\pi\eta z^2[2 - A_3 + A_3\cos(2\eta)]\} \end{aligned} \tag{34}$$

The problem is now ready to be handled. The next step is to introduce a general solution of the form

$$F(\eta, z) = z^3 f(\eta) + z g(\eta) \tag{35}$$

Substitution into Eq. (31) reveals that solvability is possible when $A_0 = A_2 = 0$. We recover two simultaneous ordinary differential equations (ODEs)

$$\eta^2 f'' + 2\eta^2\cot\eta f' = \tfrac{1}{2}\pi^2\eta^2[2 - A_3 + A_3\cos(2\eta)] \tag{36}$$

$$\eta^2 g'' + 2\eta^2\cot\eta g' = \pi\eta\left\{\tfrac{1}{8}\sin(2\eta)/\eta - \tfrac{1}{2}[\cos(2\eta) + 1] - A_1\eta - 3f/\pi^2\right\} \tag{37}$$

where the prime denotes differentiation with respect to η. In as much as it is linear, the resulting set is straightforward to manage. We obtain

$$f = \tfrac{1}{8}\cot\eta[\pi^2\eta(3A_3-4)-8C_1]+C_2-\tfrac{1}{16}A_3\pi^2\cos(2\eta) \tag{38}$$

$$\begin{aligned} g = {} & \tfrac{1}{64}\pi^{-1}(3A_3\pi^2\mathrm{Ci}(4\eta)\cot\eta+\mathrm{Ci}(2\eta)\{96C_1-2[(4+3A_3)\pi^2+48C_2]\cot\eta\} \\ & +2\pi\{6(4-3A_3)\pi\eta+32C_4+[\pi(12-9A_3+16A_1\eta)-32C_3]\cot\eta\} \\ & +\{96C_1+[(8+3A_3)\pi^2+96C_2]\cot\eta\}\ln\eta \\ & -16(\pi^2+6C_2+6C_1\cot\eta)\mathrm{Si}(2\eta)+3A_3\pi^2\mathrm{Si}(4\eta)) \end{aligned} \tag{39}$$

Here Si and Ci are the fast converging sine integral and cosine integral functions. They are given by

$$\mathrm{Si}(x)=\int_0^x t^{-1}\sin t\,\mathrm{d}t = x-\frac{1}{18}x^3+\frac{1}{600}x^5-\frac{1}{35,280}x^7+\mathcal{O}(x^9) \tag{40}$$

$$\begin{aligned} \mathrm{Ci}(x) &= \int_\infty^x t^{-1}\cos t\,\mathrm{d}t = \mathfrak{E}+\ln x-\frac{1}{4}x^2+\frac{1}{96}x^4-\frac{1}{4320}x^6+\mathcal{O}(x^8) \\ \mathfrak{E} &\simeq 0.577216 \text{ (Euler's gamma constant)} \end{aligned} \tag{41}$$

D. Undetermined Constants and Vital Boundary Conditions

Our general solution $\psi^{(1)} = z(z^2f+g)\sin\eta$ contains a set of six unknown constants, A_1, A_3, C_1, C_2, C_3, and C_4. This is not an overly determined system but, rather, one consistent with Eq. (9). Out of the four existing boundary conditions,

$$u_r^{(1)}(0,z)=0 \tag{42a}$$

$$u_z^{(1)}(1,z)=0 \tag{42b}$$

$$u_r^{(1)}(1,z)=0 \tag{42c}$$

$$u_z^{(1)}(r,0)=0 \tag{42d}$$

only three are useful. The fourth, $u_z^{(1)}(r,0)=0$, is identically satisfied by $\psi^{(1)}$ at $z=0$. The three remaining statements (42a–42c) yield six constraints in integer powers of z that must vanish independently. The two additional constants (one could have expected four) are, therefore, essential. As noted by Balakrishnan et al. [30] this problem is quasi parabolic. To illustrate this behavior, we first consider Eq. (42a) which conveys

$$r=0,\forall z:\ \frac{\partial\psi^{(1)}}{\partial z}-\rho^{(1)}\frac{\partial\psi^{(0)}}{\partial z}=0; \qquad \frac{\partial}{\partial r}\left[\frac{\partial\psi^{(1)}}{\partial z}-\rho^{(1)}\frac{\partial\psi^{(0)}}{\partial z}\right]=0 \tag{43}$$

Its evaluation begets two equations at $\mathcal{O}(1)$ and $\mathcal{O}(z^2)$ that must cancel simultaneously. The first one reads

$$64\pi C_3+96C_2(\ln 2+\mathfrak{E})+\pi^2[8\ln 2-24+8\mathfrak{E}+3A_3(6+\mathfrak{E})]=0 \tag{44}$$

whereas the second leads to $C_1=0$.

To ensure no slippage and uniform inflow along the sidewall, we must enforce $u_z^{(1)}(1,z) = u_r^{(1)}(1,z) = 0$. In terms of the stream function, we now write

$$r = 1, \forall z: \quad \frac{\partial \psi^{(1)}}{\partial r} - \rho^{(1)} \frac{\partial \psi^{(0)}}{\partial r} = 0; \qquad \frac{\partial \psi^{(1)}}{\partial z} - \rho^{(1)} \frac{\partial \psi^{(0)}}{\partial z} = 0 \tag{45}$$

This set engenders four equations in descending orders of z. By canceling the $\mathcal{O}(z^3)$, $\mathcal{O}(z^2)$, and $\mathcal{O}(1)$ terms, we retrieve $A_3 = 4/3$, $C_2 = -\frac{1}{4}\pi^2$, and $C_4 = -\frac{1}{2} - \frac{1}{16}\pi[\mathrm{Si}(2\pi) + 2\mathrm{Si}(\pi)] = -1.50571$. Finally, at $\mathcal{O}(z)$ we reap

$$4A_1\pi - 16C_3/\pi - 3\ln\left(\tfrac{1}{2}\pi\right) + \mathrm{Ci}(2\pi) + 2\mathrm{Ci}(\pi) = 0 \tag{46}$$

Equation (44) may be revisited to pick $C_3 = \frac{1}{16}\pi(4\ln 2 + 3\mathfrak{E}) \simeq 0.884405$. This enables us to calculate the last constant from Eq. (46), namely, $A_1 = [\ln(2\pi^3) + 3\mathfrak{E} - \mathrm{Ci}(2\pi) - 2\mathrm{Ci}(\pi)]/(4\pi) \simeq 0.456314$. Thus, we conclude our derivation of a fully axisymmetric solution that exactly satisfies Eqs. (18) and (19).

IV. Flowfield Characteristics

The compressible correction may be rearranged and simplified with the net product taking the form of a rather straightforward expression. It collapses into

$$\psi^{(1)} = \tfrac{1}{4}\pi z \sin\eta \left(-\pi z^2\left[1 + \tfrac{1}{3}\cos(2\eta)\right] + \tfrac{1}{4}\{\mathrm{Si}(4\eta) + 2\mathrm{Si}(2\eta) - \alpha + [\beta r^2 - 3\mathfrak{E} + \mathrm{Ci}(4\eta) + 2\mathrm{Ci}(2\eta) - \ln(2\pi^3 r^6)]\cot\eta\right\}\right) \tag{47}$$

where $\alpha = 8/\pi + \mathrm{Si}(2\pi) + 2\mathrm{Si}(\pi) \simeq 7.6685048$ and $\beta = \ln(2\pi^3) + 3\mathfrak{E} - \mathrm{Ci}(2\pi) - 2\mathrm{Ci}(\pi) \simeq 5.7342087$. Equation (47) will be referred to as the exact solution. On closer scrutiny, we identify an approximate form $\tilde{\psi}^{(1)}$ that is practically equivalent in spatial behavior due to the dominance of the third power in z; thus, we propose

$$\tilde{\psi}^{(1)} = -\tfrac{1}{4}\psi^{(0)}\left\{\pi^2 z^2\left[1 + \tfrac{1}{3}\cos(2\eta)\right] + 2\right\}$$

or

$$\tilde{\psi} = M_w\psi^{(0)}\left(1 - \tfrac{1}{4}M_w^2\left\{\pi^2 z^2\left[1 + \tfrac{1}{3}\cos(\pi r^2)\right] + 2\right\}\right) \tag{48}$$

Equation (48) represents the simplest axisymmetric form that satisfies the problem's four boundary conditions while exhibiting a high degree of precision in observing first principles. It accrues a negligible error in comparison with $\psi^{(1)}$ to the extent of being graphically indiscernible from Eq. (47). Furthermore, the error continues to diminish with the distance from the headwall. Hence, it is ideally suited to model long porous tubes such as those used to simulate rocket chambers. In making our choice, the exact solution will be utilized in graphical depictions although, for added confirmation, $\tilde{\psi}^{(1)}$ will be carried alongside $\psi^{(1)}$ during the upcoming development. In actuality, $\tilde{\psi}^{(1)}$ may serve as a crucial replacement in applications where simplicity of the mean flow formula is essential in preventing a purely numerical outcome, for example, those involving integration.

A. Representative Streamlines

Figure 2 shows a comparison of the flow turning behavior with and without compressibility at two wall Mach numbers and chamber lengths. Here we plot the characteristic ψ/M_w. The first observation is that compressibility causes the fluid to turn more sharply at a given location and that the streamline curvature is steepened with successive increases in M_w. This effect has important implications on flow stability [38]. In fact, it appears that fluid expansion in the downstream direction has a similar effect to that of increasing the viscosity. As illustrated previously [20], decreasing the wall Reynolds number has a similar injunction on the flow. Incorporating both density changes and viscosity may, therefore, lead to more pronounced steepening. Viscosity, which has often been neglected in SRM simulations, may become an important factor in hybrid rocket analysis where the wall Reynolds number is considerably smaller. We mention in passing that, for simulated SRMs, wall expansion has been shown to exhibit the reverse effect on curvature, albeit too small to be considered except for extremely large regression rates. A purely hypothetical case occurs when the sidewall regresses at the same speed as that of the fluid entering the tube. Under these auspices, the expansion process can offset the effect of injection to such a degree that streamlines become normal to the sidewall.

The second observation in Fig. 2 concerns the striking similarity between Fig. 2a and Fig. 2b and the connection with the corresponding ratio of Mach numbers and chamber lengths. Because M_w is reduced by one-half in Fig. 2b, it takes the

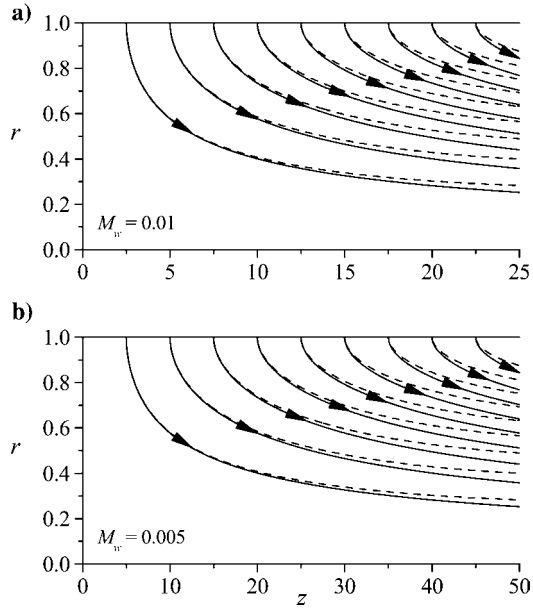

Fig. 2 Effect of compressibility on representative streamlines, $\gamma = 1.4$: —, incompressible solution and - - -, compressible solutions.

streamlines twice the distance to reach the same level of development and disparity with respect to the Taylor solution. This trend insinuates that a direct relation may exist between M_w and the length to reach a level of development. Figure 2b also suggests that compressibility effects may not be large in short chambers unless M_w is sufficiently high, particularly, exceeding a threshold value that may be helpful to determine. Finding the choking distance is another critical requirement for the purpose of delimiting the subsonic domain.

B. Velocity and Vorticity Fields

Velocity corrections can be derived starting from Eq. (12). We obtain

$$u_r^{(1)} = \tfrac{1}{4} r^{-1} \sin\eta \left(\pi^2 z^2 [1 + \cos(2\eta)] - \tfrac{1}{4}\pi \left\{ 2[1 - \cos(2\eta)]/\eta + \mathrm{Si}(4\eta) + 2\mathrm{Si}(2\eta) - \alpha + \cot(\eta)[\mathrm{Ci}(4\eta) + 2\mathrm{Ci}(2\eta) + 2\beta\eta/\pi - 3\mathfrak{E} - \ln(16\eta^3)] \right\} \right); \quad u_r^{(0)} = -r^{-1}\sin\eta \tag{49}$$

$$u_z^{(1)} = \tfrac{1}{4}\pi z \cos\eta \left(\pi^2 z^2 \left[\tfrac{5}{3} - \cos(2\eta) \right] + \tfrac{1}{4}\pi \left\{ \mathrm{Si}(4\eta) + 2\mathrm{Si}(2\eta) - \alpha + 2\beta/\pi + \tan(\eta)[3\mathfrak{E} - 2\beta\eta/\pi - \mathrm{Ci}(4\eta) - 2\mathrm{Ci}(2\eta) + \ln(16\eta^3)] \right\} \right); \quad u_z^{(0)} = \pi z \cos\eta \tag{50}$$

Then, with use of $\Omega^{(0)} = \pi^2 rz \sin\eta$, the first-order vorticity may be expressed by

$$\Omega^{(1)} = \tfrac{1}{16} r^{-2} \Omega^{(0)} \left\{ 2(1 - 6\pi\eta z^2)(3 - 4\sin^2\eta) - 6 + r^2 \left(\tfrac{14}{3}\pi^2 z^2 - \pi\alpha + 4\beta \right) + 2\eta[\mathrm{Si}(4\eta) + 2\mathrm{Si}(2\eta)] + 2\eta\cot\eta[\beta r^2 - 3\mathfrak{E} + \mathrm{Ci}(4\eta) + 2\mathrm{Ci}(2\eta) - \ln(2\pi^3 r^6)] \right\} \tag{51}$$

When the classic solution is recalled, $\boldsymbol{u}^{(0)} = -r^{-1}\sin\eta \boldsymbol{e}_r + \pi z \cos\eta \boldsymbol{e}_z$, the approximate velocity can be assembled into

$$\tilde{\boldsymbol{u}}^{(1)} = -\tfrac{1}{4} u_r^{(0)} \{\pi^2 z^2 [1 + \cos(2\eta)] - r^{-2}[1 - \cos(2\eta)] + 2\} \boldsymbol{e}_r + \tfrac{1}{12} u_z^{(0)} \{\pi^2 z^2 [5 - 3\cos(2\eta)] + 3r^{-2}[1 - \cos(2\eta)] - 6\} \boldsymbol{e}_z \tag{52}$$

and so $\tilde{\Omega}^{(1)} = \frac{1}{6}\psi^{(0)} r^{-3} \{\eta[3\pi - 2(6 + \pi^2 z^2)\eta] - 3\pi\eta(1 + 6\pi z^2\eta)\cos(2\eta) + 3\pi\sin(2\eta)\}$. The total vorticity becomes

$$\tilde{\Omega} = M_w \Omega^{(0)} \left(1 + \tfrac{1}{24} M_w^2 \left\{ 3\pi[1 - \cos(2\eta)]/\eta - 12 - 2\pi^2 z^2 [1 + 9\cos(2\eta)] + 3\pi\sin(2\eta)/\eta^2 \right\} \right) \tag{53}$$

As usual, the vorticity vanishes along the centerline and, by observing surface adherence, is maximum at the sidewall. It can be calculated from

$$\Omega_w = M_w \pi^2 z \left[1 + M_w^2 \left(\tfrac{2}{3}\pi^2 z^2 + \tfrac{1}{4}\beta - 1\right)\right]$$

or

$$\tilde{\Omega}_w = M_w \pi^2 z \left(1 + \tfrac{2}{3} M_w^2 \pi^2 z^2\right) \tag{54}$$

The last two expressions differ by a mere $\pi^2 z M_w^3 (\frac{1}{4}\beta - 1)$. This reflects the inherent accuracy that accompanies our compact formula. As it builds up with successive increases in z, vorticity Ω_w reaches its highest value in the exit plane.

Typical profiles corresponding to Fig. 2a are shown in Fig. 3; here, we plot both streamwise and radial components of velocity at six axial stations, $\gamma = 1.4$, and a characteristic Mach number of 0.01. We choose the latter because of its proximity to $M_w = 0.0095$, a figure that has been fixed in two separate studies; these include Apte and Yang [18, 19] who added much insight to the elegant work of Traineau et al. [13]. Incidentally, both groups have focused on cold-flow compressible simulations and laboratory experiments of the planar, porous channel case with air injection. We hereby select the same values in the interest of uniformity and portability. Lower injection rates from 0.0018 to 0.0036 have also been investigated by Dunlap et al. [39].

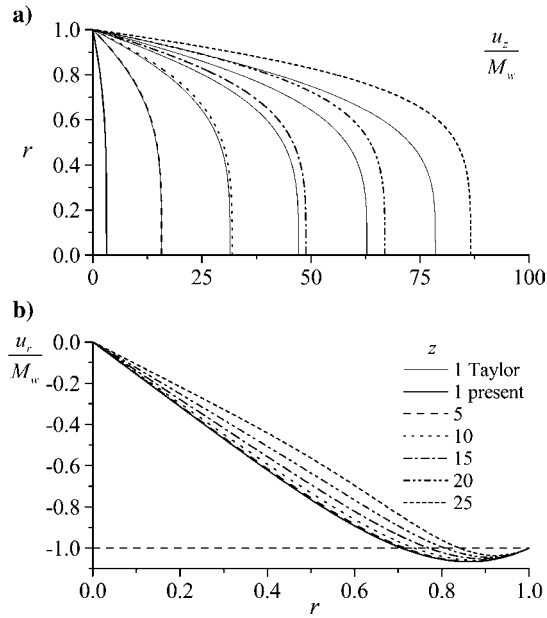

Fig. 3 Spatial evolution of axial and radial velocities for $M_w = 0.01$; compressible solution leads with respect to Taylor–Culick marker lines.

In Fig. 3, it is clear that the discrepancy with respect to the leading-order solution increases with the distance from the headwall. In both Fig. 3a and 3b this difference is hardly noticeable before crossing nearly one-third of the chamber span. Subsequently, the error in the Taylor–Culick model becomes progressively more pronounced, especially after passing $z = 15$. Both streamwise and radial profiles begin to flatten, precisely as predicted by numerical simulations and experimental evidence. By $z = 25$, the error between both models, taken at the centerline, reaches about 10%.

To better understand the factors that influence our solution, we find it imperative to calculate the point where the Mach number reaches unity. To this end, we define the length L_s to be the distance along the centerline to the point where a sonic condition is met. We base our definition on the idea of a local Mach number instead of an area-averaged value. The latter is necessitated by one-dimensional or pseudo-two-dimensional models where information is often lumped at a given cross section. Bearing this in mind, we remark that when $z = L_s$ only the centerline velocity component would have reached the speed of sound. At this junction, the area-averaged Mach number will be smaller than unity. To determine the sonic point precisely, we realize that the temperature correction must be evaluated to estimate the local a_0 accurately. In this vein, the momentum equation must first be solved for the higher-order pressure correction. We do this for the sake of completeness, although higher-order pressures and temperatures are not likely to be large contributors except in long chambers.

C. Higher-Order Pressures and Temperatures

In seeking the higher-order pressure term, we return to Eq. (20), whose right-hand side is now fully determined. We write

$$\nabla p^{(2)} = -\gamma\left(\tfrac{1}{2}\rho^{(1)}\nabla[\nabla\psi^{(0)}\cdot\nabla\psi^{(0)}/r^2] + \nabla[\nabla\psi^{(0)}\cdot\nabla\psi^{(1)}/r^2] - \nabla\{\rho^{(1)}[\nabla\psi^{(0)}\cdot\psi^{(0)}/r^2]\} + [\Omega^{(0)}\nabla\psi^{(1)} + \Omega^{(1)}\nabla\psi^{(0)}]/r\right) \tag{55}$$

Partial integration must be carefully carried out to identify common terms in both radial and streamwise directions. It is expedient to start with the approximate solution because the process can help in verifying the final formulation. After some algebra, we obtain $\tilde{p}^{(2)}/\gamma = -\frac{1}{24}\pi^4 z^4 + \frac{1}{8}\pi^2 z^2(4 - \pi\eta) + \frac{1}{32}\pi\eta \times (8 - 3\pi\eta)$. Backward substitution into the perturbed pressure yields

$$\tilde{p}/\gamma = \gamma^{-1} - \tfrac{1}{2}\pi^2 M_w^2 z^2\left[1 + \left(\tfrac{1}{4}\pi\eta - 1\right)M_w^2\right] - \tfrac{1}{24}\pi^4 M_w^4 z^4 - \tfrac{1}{4}\pi M_w^2 \sin^2\eta/\eta + \tfrac{1}{32}\pi^2 M_w^4\eta(8/\pi - 3\eta) \tag{56}$$

Along similar lines, we find

$$p^{(2)}/\gamma = -\tfrac{1}{24}\pi^4 z^4 + \tfrac{1}{16}\pi^2 z^2(\sigma - 2\pi\eta) + \tfrac{1}{32}\pi^2\eta(\sigma/\pi - 5\eta) \tag{57}$$

where $\sigma = \pi\alpha - 2\beta \simeq 12.6229$. It is clear that the pressure is dominated by $p \sim 1 - \frac{1}{2}\pi^2\gamma M_w^2 z^2 - \frac{1}{24}\pi^4 M_w^4 z^4$. This series can be further confirmed by calculating

the centerline pressure ratio p_c. In fact, we find $\tilde{p}_c = 1 - \frac{1}{2}\pi^2\gamma M_w^2 z^2(1 - M_w^2) - \frac{1}{24}\pi^4\gamma M_w^4 z^4$ to be in perfect union with

$$p_c = 1 - \tfrac{1}{2}\pi^2\gamma M_w^2 z^2\left(1 - \tfrac{1}{8}\sigma M_w^2\right) - \tfrac{1}{24}\pi^4\gamma M_w^4 z^4 \tag{58}$$

The higher-order density and temperature can be evaluated from Eq. (21). The latter may be arranged into

$$T = 1 + \tfrac{1}{8}\pi(\gamma - 1)M_w^2\{-4\pi z^2 + \eta^{-1}[\cos(2\eta) - 1]\} + M_w^4 T^{(2)} \tag{59}$$

where $T^{(2)}$ is given by

$$\begin{aligned}\tilde{T}^{(2)} = &-\tfrac{1}{6}\pi^2(\gamma - 1)\{\pi^2 z^4 + \tfrac{3}{8}\pi\eta^{-1}z^2[1 - \cos(2\eta) - 8\eta/\pi + 2\eta^2] \\ &+ \tfrac{3}{128}\eta^{-2}[3 - 4\cos(2\eta) + \cos(4\eta) - 64\eta^3/\pi + 24\eta^4]\}\end{aligned} \tag{60}$$

or

$$\begin{aligned}T^{(2)} = &-\tfrac{1}{6}\pi^2(\gamma - 1)\left\{\pi^2 z^4 + \tfrac{3}{8}\pi\eta^{-1}z^2\left[1 - \cos(2\eta) - \sigma\eta/\pi + 2\eta^2\right]\right. \\ &\left. + \eta^{-2}\left[\tfrac{9}{128} - \tfrac{3}{32}\cos(2\eta) + \tfrac{3}{128}\cos(4\eta) - \tfrac{3}{16}\sigma\eta^3/\pi + \tfrac{15}{16}\eta^4\right]\right\}\end{aligned} \tag{61}$$

Here, too, the temperature is dominated by $T \sim 1 - \frac{1}{2}\pi^2(\gamma - 1)M_w^2 z^2 - \frac{1}{6}\pi^4(\gamma - 1)M_w^4 z^4$. Centerline temperatures yield, in turn,

$$\begin{aligned}\tilde{T}_c &= 1 - \tfrac{1}{2}\pi^2(\gamma - 1)M_w^2 z^2(1 - M_w^2) - \tfrac{1}{6}\pi^4(\gamma - 1)M_w^4 z^4 \\ T_c &= 1 - \tfrac{1}{2}\pi^2(\gamma - 1)M_w^2 z^2(1 - \tfrac{1}{8}\sigma M_w^2) - \tfrac{1}{6}\pi^4(\gamma - 1)M_w^4 z^4\end{aligned} \tag{62}$$

These variables are crucial for estimating the maximum Mach number at a given cross section. We remark that approximate results at $\eta = 0$ may be deduced from the exact expressions by replacing σ with 8.

D. Critical Chamber Length

With the temperature in hand, we can calculate the centerline Mach number based on the local speed, namely,

$$\begin{aligned}u_c &= u_z(0, z) = \pi M_w z + \tfrac{1}{6}\pi^3 M_w^3 z^3 - \tfrac{1}{16}\sigma\pi M_w^3 z \\ \tilde{u}_c &= \pi M_w z + \tfrac{1}{6}\pi^3 M_w^3 z^3 - \tfrac{1}{2}\pi M_w^3 z\end{aligned} \tag{63}$$

Clearly, $u_c \sim \pi M_w z + \frac{1}{6}\pi^3 M_w^3 z^3$ controls the solution. Using $\bar{u}_c/\sqrt{c_p(\gamma - 1)\bar{T}_c} = 1$ or $u_c/\sqrt{T_c} = 1$, we can solve for the streamwise coordinate z_s at which a sonic condition is first detected. Depending on the level of approximation in the speed and temperature, we obtain estimates of increasing accuracy. At leading order, we have

$$\begin{aligned}\pi M_w z_s &= \sqrt{1 - \tfrac{1}{2}\pi^2(\gamma - 1)M_w^2 z_s^2} + \mathcal{O}(M_w^3 z_s^3) \\ z_s^{(0)} &= \sqrt{2/(1 + \gamma)}\,1/(\pi M_w) + \mathcal{O}(M_w^2 z_s^3)\end{aligned} \tag{64}$$

In like manner, by retaining two terms in the velocity, we can put

$$\pi M_w z_s + \tfrac{1}{6}\pi^3 M_w^3 z_s^3 = \sqrt{1 - \tfrac{1}{2}\pi^2(\gamma - 1)M_w^2 z_s^2} + \mathcal{O}(M_w^4 z_s^4)$$
$$z_s^{(1)} = \sqrt{\varphi - 4 + 2(5 - 3\gamma)/\varphi}/(\pi M_w) + \mathcal{O}(M_w^3 z_s^4) \tag{65}$$

where

$$\varphi = \left(36\gamma - 10 + 6\sqrt{6\gamma^3 + 6\gamma^2 + 30\gamma - 25}\right)^{1/3} \tag{66}$$

An unusually simple expression can be obtained by "borrowing" the well-known critical pressure ratio from one-dimensional nozzle theory. By choosing only two terms in Eq. (58), we can equate, at the sonic point, which stands for the hypothetical nozzle throat, $(p_c)_{\text{sonic}} = 1 - \frac{1}{2}\pi^2\gamma M_w^2 z_s^2 = [\frac{1}{2}(\gamma + 1)]^{\gamma/(1-\gamma)}$ or

$$z_s^{(2)} = \frac{1}{\pi M_w}\sqrt{2\gamma^{-1}\left[1 - \left(\tfrac{1}{2}\gamma + \tfrac{1}{2}\right)^{\gamma/(1-\gamma)}\right]} = \frac{\sqrt{2(1 - e^{-1/2})}}{\pi M_w} \tag{67}$$

for $\gamma = 1$. Note that the spurious singularity as $\gamma \to 1$ can be easily overcome using L'Hôpital's rule. However, it is not simple to render the truncation order of this quantity because of the uncertainty associated with utilizing one-dimensional theory to evaluate the critical pressure ratio. No throat of a nozzle exists here. Whereas Eq. (58) exhibits a truncation error of $\mathcal{O}(M_w^4 z_s^4)$, the global error accrued in crisscrossing with one-dimensional nozzle theory remains an open question. At this point, a comparison with the most precise value of z_s may be illuminating.

The most accurate representation of $\mathcal{O}(M_w^4 z_s^3)$, for example, $z_s^{(5)}$, may be derived by mustering every term that arises in Eqs. (62) and (63). The lengthy formula we obtain is omitted here because it may be relegated to symbolic programming. Instead, we realize that, within four-digit accuracy, an equivalent expression is attainable by employing the dominant members of the temperature and velocity. We find

$$z_s^{(3)} = \delta^{1/2}\sqrt{\cos\{\tfrac{1}{3}\cos^{-1}[16(14 + 6\gamma - 3\gamma^2 - 4\gamma^3)/\delta^3]\} - 2(\gamma + 1)}/(\pi M_w)$$
$$+ \mathcal{O}(M_w^2 z_s);$$
$$\delta = 2\sqrt{2(\gamma + 1)(2\gamma - 1)} \tag{68}$$

or, equivalently,

$$z_s^{(3)} = \sqrt{\lambda - 2\gamma - 2 + 2(2\gamma^2 + \gamma - 1)/\lambda}/(\pi M_w)$$
$$\lambda = \left(28 + 12\gamma - 6\gamma^2 - 8\gamma^3 + 6\sqrt{22 + 18\gamma - 6\gamma^2 - 14\gamma^3 - 3\gamma^4}\right)^{1/3} \tag{69}$$

These supplement the expanded form of $z_s^{(5)}$, namely,

$$z_s^{(4)} = [0.8846222 - 0.17729882(\gamma - 1) + 0.05391187(\gamma - 1)^2 - 0.01806146(\gamma - 1)^3 + 0.50162947M_w^2]/(\pi M_w) \tag{70}$$

As it turns out, Eqs. (67), (68), and (70) are the closest to $z_s^{(5)}$. This trend is illustrated in Tables 1 and 2, where the critical lengths are cataloged at typical Mach numbers and a range of specific heats. We note that the errors we entail are commensurate with the order in which they are introduced. Interestingly, the pseudo-one-dimensional approximation $z_s^{(2)}$ leads to a surprisingly valid estimate that keeps improving at higher M_w. This may explain the ubiquitous acceptance of one-dimensional analyses, which, in some work, have been reported to exceed expectations in predicting compressible flow behavior. This is especially true concerning pressure distributions. Depending on the desired tolerances, we recommend the use of $L_s = z_s^{(4)}$ or $z_s^{(3)}$ for small and large γ, respectively. We post in Table 2 the most precise estimate $z_s^{(5)}$ for six representative values of M_w. In that respect, we note that, for $M_w < 0.005$, L_s becomes so large as to render it impractical in propulsive applications that exclude headwall injection; this may explain why choking through a nozzle is the rule rather than the exception in rocket-based applications.

Past the sonic point, it is uncertain whether our solution will continue to hold. Unless area expansion is permitted, weak shocks are likely to form and these are normally accompanied by irreversibilities; of course, the latter tend to invalidate our underlying assumptions. Barring these ostensible incidences, it may be argued that the solution may continue to hold up to the point where the area-averaged Mach

Table 1 Critical sonic length L_s

	z					
γ	$z_s^{(0)}$	$z_s^{(1)}$	$z_s^{(2)}$	$z_s^{(3)}$	$z_s^{(4)}$	$z_s^{(5)}$
			$M_w = 10^{-2}$			
1.0	31.831	28.158	28.237	28.158	28.160	28.160
1.1	31.064	27.719	27.661	27.611	27.612	27.612
1.2	30.350	27.294	27.119	27.094	27.095	27.096
1.3	29.683	26.884	26.610	26.606	26.606	26.607
1.4	29.058	26.488	26.130	26.143	26.140	26.145
5/3	27.566	25.496	24.972	25.020	24.990	25.022
			$M_w = 5 \times 10^{-3}$			
1.0	63.662	56.317	56.474	56.317	56.318	56.318
1.1	62.128	55.437	55.321	55.221	55.222	55.222
1.2	60.699	54.588	54.239	54.188	54.188	54.189
1.3	59.365	53.768	53.221	53.211	53.209	53.212
1.4	58.115	52.976	52.260	52.286	52.278	52.287
5/3	55.133	50.993	49.943	50.040	49.978	50.041

Table 2 Higher order approximation for $L_s = z_s^{(5)}$

	M_w					
γ	0.0001	0.0005	0.001	0.005	0.01	0.05
1.0	2815.840	563.168	281.584	56.318	28.160	5.640
1.1	2761.064	552.213	276.107	55.222	27.612	5.530
1.2	2709.402	541.880	270.940	54.189	27.096	5.427
1.3	2660.569	532.114	266.057	53.212	26.607	5.329
1.4	2614.318	522.864	261.432	52.287	26.145	5.236
5/3	2502.020	500.402	250.201	50.041	25.022	5.011

number has reached unity. Although we do not wish to venture farther downstream, it may be useful to examine the evolution of the area-averaged Mach number for two main reasons: first, to set an upper bound on the range of validity and, second, to provide supplementary tools that may be needed in sketching a meaningful parallelism with one-dimensional theory.

E. Area Averaging

The local Mach number may be calculated from the total velocity and temperature using $M \equiv u/\sqrt{T}$, where u is the Pythagorean sum of u_r and u_z. Several lines of constant Mach number can thus be produced and shown in Fig. 4a for $\gamma = 1.4$ and $M_w = 0.01$. Also shown in Fig. 4a are a few representative streamlines. What is most intriguing is perhaps our attempt to recreate the same plots using widely dissimilar Mach values of 10^{-3} and 10^{-4}. So long as the streamwise coordinate is rescaled by the appropriate critical length L_s, differences remain indiscernible. The same attempt is repeated using, this time, $\gamma = 1$ and $5/3$; differences are found to be so minor that they do not warrant further attention. Hence, Fig. 4a is characteristic of the expected isocontours. In fact, they bear a striking resemblance to those reported in Fig. 3 of Balakrishnan et al. [30]. We show our streamlines and Mach numbers past the choking distance to illustrate their spatial evolution in the event that a shock is delayed. As mentioned earlier, only the centerline velocity would have reached sonic speed at $z = L_s$ and there is little certainty beyond that point. We recall that, instead of deteriorating past $M = 0.3$, the Taylor model continues to hold farther downstream. The compressible flow analog may exhibit comparable resilience. Furthermore, the area-averaged Mach number at $z = L_s$ may be calculated and shown to vary quite gradually, specifically, between 0.696 and 0.710 as γ is reduced from $5/3$ to 1. This will be expounded next.

The centerline Mach number $M_c \equiv u_c/\sqrt{T_c}$ can be readily obtained from Eqs. (62) and (63) and is plotted in Fig. 4b. Also shown is a crude but compact approximation based on $\tilde{\psi}$ and the first-order temperature. We imply

$$\tilde{M}_c = \pi M_w z \frac{2 + M_w^2(\frac{1}{3}\pi^2 z^2 - 1)}{\sqrt{4 - 2M_w^2\pi^2 z^2(\gamma - 1)}} \tag{71}$$

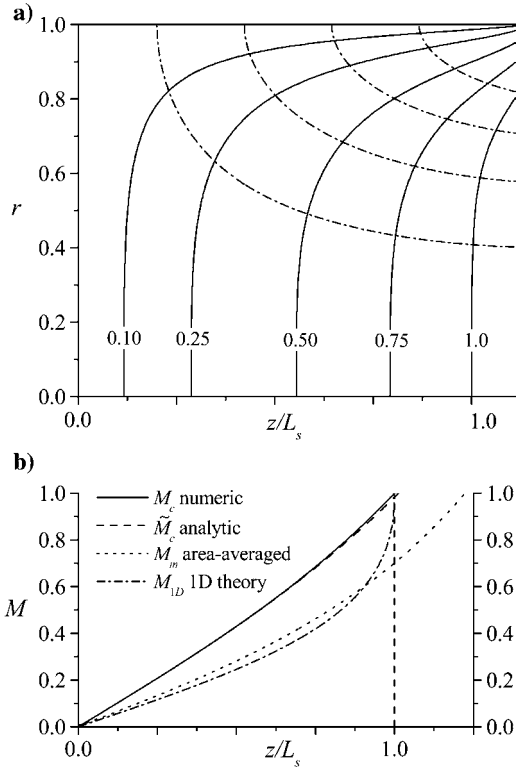

Fig. 4 Evolution of the local Mach number over a range of M_w and $\gamma = 1.4$: a) streamlines extend slightly past the choking distance and b) centerline Mach numbers and area-averaged values are compared to the one-dimensional compressible flow formula by Gany and Aharon [21].

One may infer from Fig. 4b that $\tilde{M}_c$ is an adequate representation except for the slight overshoot that it displays near the aft end. As γ is decreased, this discrepancy becomes less conspicuous and vanishes, eventually, near unity.

To set the stage for comparisons with one-dimensional theory, the area-averaged Mach number M_m can be numerically integrated from

$$M_m = 2\int_0^1 uT^{-1/2} r\,\mathrm{d}r$$

As shown in Fig. 4b, M_m is close to 0.7 and does not reach unity until $z = L_m$. Following a parametric analysis, we find L_m to be a weak function of γ and, practically, independent of M_w. It diminishes from $L_m = 1.257L_s$ to $1.204L_s$ as γ is escorted across its full range. Along this excursion, M_c crawls from 1.341 to 1.390. We suspect that full choking in a straight porous tube may be delayed an extra 20–25% of the critical length. If the opposite were proven true, then

the evaluation of M_m would still serve a useful purpose because it enables us to judiciously compare our results to one-dimensional theory. According to the latter,

$$M_{1D} = \sqrt{\frac{1-\sqrt{1-z^2/L_s^2}}{1+\gamma\sqrt{1-z^2/L_s^2}}} \tag{72}$$

Equation (72) is superimposed as the chained line in Fig. 4b; clearly it follows M_m except for the sudden jump in the last 10% stretch. This result confirms the ability of our solution to mimic one-dimensional analysis except near the sonic point where radial flow variability comes into play. Our results also support the idea of a local Mach number being independent of M_w.

F. Key Geometric Similarity

Inspired by the form of Eq. (72), a more convincing proof of this behavior may be pursued by introducing a rescaled variable, $X = z/L_s$. One may, for example, substitute back into Eq. (71) and rearrange. As confirmed by Eqs. (64–69), the ensuing product $\pi M_w L_s = \Gamma(\gamma) \sim 1$ is a strong function of γ, particularly, one for which several approximations have been unraveled in increasing order of accuracy. It can be seen that

$$\tilde{M}_c = \Gamma X \frac{2+\frac{1}{3}\Gamma^2X^2 - M_w^2}{\sqrt{4-2\Gamma^2X^2(\gamma-1)}} = \frac{\left(1+\frac{1}{6}\Gamma^2X^2\right)\Gamma X}{\sqrt{1-\frac{1}{2}(\gamma-1)\Gamma^2X^2}} \tag{73}$$

The influence of M_w is clearly negligible. Furthermore, the dependence on γ is also feeble in view of the slowly varying filter Γ. The latter shifts by a total of 11%, from 0.8846 to 0.7860, over the full range of γ. In rocketry, γ seldom exceeds 1.2; the corresponding 3.78% deviation in Γ is marginal, decrementing from 88.5 to 85.1% only. Because γ barely changes in a given application, the behavior of our solution with respect to X is nearly frozen. This finding is pivotal because it enables us to render the results in a more universal fashion, namely, independently of the wall Mach number. The same idea applies to the stream function and its derivatives; this can be demonstrated by revisiting

$$\tilde{\Psi} = \tilde{\psi}/M_w = \psi^{(0)}\left(1-\tfrac{1}{4}\Gamma^2(\gamma)\left\{X^2\left[1+\tfrac{1}{3}\cos(\pi r^2)\right]+2\pi^{-2}L_s^{-2}\right\}\right) \tag{74}$$

Note that dependence on M_w disappears in a suitably normalized variable. Because ψ is a parent function, all related family members inherit this property. This also explains and settles our earlier bewilderment regarding the nature of Fig. 3, where, in hindsight, the geometric scaling required to achieve similarity was met (unintentionally). The critical lengths for the two cases were actually 26 and 52, respectively.

G. Critical Pressure and Temperature Ratios

Unlike the local Mach number that can undergo wide excursions at a given cross section, we find the pressures and temperatures to be quasi uniform. This can

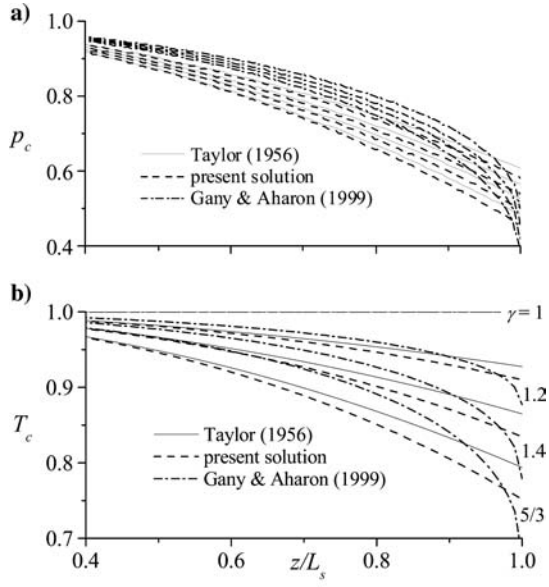

Fig. 5 Streamwise evolution of centerline pressures and temperatures using available theories: from outside moving inward, $\gamma = 1, 1.2, 1.4$, and 1.67.

be quickly inferred from the favorable comparisons that may be drawn between any two of the centerline, sidewall, or area-averaged properties. Because of their similarities, we focus hereafter on centerline behavior (Fig. 5). Our axisymmetric results can also be examined in the context of existing theories. Of those, we choose the oft-cited one dimensional model of Gany and Aharon [37], the pseudo-two-dimensional model of Traineau et al. [13], and the incompressible formula of Taylor [1]. Also, because of the variability that exists among available data, we opt to conduct our own numerical simulations of the porous tube. In the interest of uniformity, we replicate conditions that mimic those implemented by Traineau et al. [13] and subsequently, by Apte and Yang [19].

Our porous tube is chosen to be 28 cm long with a 1 cm radius and a wall Mach number of 0.0095. We apply a constant mass flux of 13 $\text{kg} \cdot \text{m}^{-2} \cdot \text{s}^{-1}$ at an injection temperature of 260 K; the fluid is air with a molecular weight of 29 $\text{kg} \cdot \text{kmol}^{-1}$, $\gamma = 1.4$, and a dynamic viscosity of $\mu = 1.66 \times 10^{-5} \text{kg} \cdot \text{m}^{-1} \cdot \text{s}^{-1}$. Unlike Traineau et al. [13], we do not attach a divergent nozzle at the aft end. Our chief concern is with the faithful replication of the geometry used in the mathematical derivation. We recognize that area expansion can expedite convergence, but we opt to stay with Taylor's model, albeit at a small computational expense.

As shown in Fig. 5a, the streamwise variation of p_c is steeper than that of Taylor's or Gany and Aharon's except in the last 15% stretch. It becomes more pronounced with successive increases in γ. The incremental steepening reflects inevitable departures from the ideal isothermal case for which $\gamma = 1$. The same can be said of the temperature variation in Fig. 5b. In both cases, the one-dimensional

model accrues a smaller drop along a major portion of the chamber. It then briskly accelerates in the aft 15% of the length on its way to reclaiming its choke-point value. Its evolution may be traced from

$$p_{1D} = (1+\gamma)^{-1}\left(1+\gamma\sqrt{1-z^2/L_s^2}\right);$$
$$T_{1D} = (1+\gamma)^{1/\gamma-1}\left(1+\gamma\sqrt{1-z^2/L_s^2}\right)^{1-1/\gamma} \tag{75}$$

Note that Gany and Aharon [21] project a critical pressure ratio of $p_s^{(-)} = (1+\gamma)^{-1}$ (at $z = L_s$), although nozzle theory foresees a critical ratio of $p_s^{(+)} = [\frac{1}{2}(\gamma+1)]^{\gamma/(1-\gamma)}$; ours predicts an intermediate quantity. For example, at the sonic point, Eqs. (58) and (62) reduce to

$$p_s = 1 - \tfrac{1}{2}\gamma\Gamma^2\left(1-\tfrac{1}{8}\sigma M_w^2\right) - \tfrac{1}{24}\gamma\Gamma^4;$$
$$T_s = 1 - \tfrac{1}{2}(\gamma-1)\Gamma^2\left(1-\tfrac{1}{8}\sigma M_w^2\right) - \tfrac{1}{6}(\gamma-1)\Gamma^4 \tag{76}$$

where Γ may be directly extracted from Eqs. (68), (69), or yet Eq. (67) if a blend with one-dimensional theory is to be entertained. The latter yields the simplest, $\Gamma^2 = 2\gamma^{-1}[1-(\frac{1}{2}\gamma+\frac{1}{2})^{\gamma/(1-\gamma)}]$. The most accurate are

$$\Gamma = \sqrt{\delta\cos\left\{\tfrac{1}{3}\cos^{-1}[16(14+6\gamma-3\gamma^2-4\gamma^3)/\delta^3]\right\} - 2(\gamma+1)}$$

or

$$\Gamma = \sqrt{\lambda - 2\gamma - 2 + 2(2\gamma^2+\gamma-1)/\lambda} \tag{77}$$

Both render

$$\Gamma \simeq 0.884622 - 0.177299(\gamma-1) + 0.0539119(\gamma-1)^2 - 0.0180615(\gamma-1)^3 \tag{78}$$

Interestingly, the Taylor series expansion of Γ matches the γ dependence of the highest-order expression for $z_s^{(5)}$ encapsulated by Eq. (70). Furthermore, the M_w^2 term in Eq. (76) may be safely ignored without affecting the three-digit accuracy in the algebraic outcome. For the reader's convenience, a summary of critical pressure and temperature ratios is posted in Table 3.

Over the range of γ, our pressure ratio depreciates from 0.583 to 0.459. This constitutes a 16.6–22.4% increase in pressure recovery with respect to one-dimensional theory. The increased pressure recovery may be attributed to the absence of viscosity in our model. Had viscosity been accounted for, a larger pressure drop would have been entailed. The one-dimensional model appears to be less vulnerable to friction and attendant irreversibilities: It integrates those away in the process of injecting the flow directly along the axis where viscous damping

Table 3 Critical pressure and temperature ratios

γ	$p_s^{(-)a}$	p_s	$p_s^{(+)b}$	$T_s^{(-)a}$	T_s	$T_s^{(+)b}$
1.0	0.500	0.583	0.607	1	1	1
1.1	0.476	0.560	0.585	0.935	0.953	0.952
1.2	0.455	0.539	0.564	0.877	0.910	0.909
1.3	0.435	0.519	0.546	0.825	0.871	0.870
1.4	0.417	0.501	0.528	0.779	0.835	0.833
1.5	0.400	0.484	0.512	0.737	0.802	0.800
1.6	0.385	0.469	0.497	0.699	0.771	0.769
5/3	0.375	0.459	0.487	0.675	0.752	0.750

[a]Gany and Aharon [21]. [b]One-dimensional nozzle theory.

is the least prominent. Had it been viscous, the present model would have been subject to irreversibilities that consume their share of thermal energy and increase both the temperature and internal energy of the flow. The pressure drop, which is partly a measure of these irreversibilities, would have been larger. The accentuated sensitivity of our axisymmetric representation to viscous losses can, therefore, explain the larger pressure recoveries observed relative to viscous simulations or one-dimensional approximations.

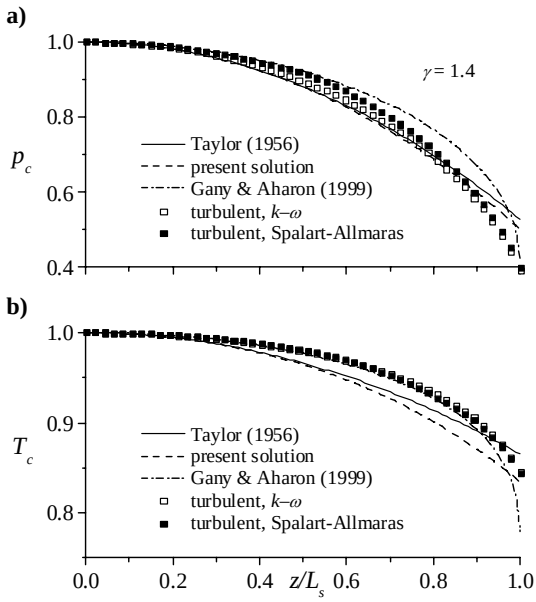

Fig. 6 Comparison of theoretical pressures and temperatures to Navier–Stokes computations obtained from two turbulent flow models.

For example, using $\gamma = 1.4$, our results are compared in Fig. 6a to the CFD pressure curves obtained under two widely accepted turbulent flow models. Whereas the computed k–ω curve nearly coincides with our analytical solution over a significant portion of the chamber, it begins to slightly diverge near the aft end to the extent of closing at 0.400. The Spalart–Allmaras simulation is slightly higher near the headwall but is terminated by the same value. The increased pressure drop compared to ours at 0.501 may be linked to viscous damping. Naturally, the CFD value is nearest to the one-dimensional critical ratio (0.417) proposed by Gany and Aharon [21]. Up until the exit section, however, the present solution adequately performs in matching the k–ω curve.

When temperatures are compared in Fig. 6b, an equally interesting behavior is captured. As predicted, the turbulent-flow computations seem to fall slightly above our theoretical curve; they specifically coincide with the one-dimensional solution over a major portion of the chamber. In contrast to the pressure behavior, a better agreement with our model is seen near the aft end, where the numerical curves terminate at 0.845 and 0.843, respectively; this puts them nearest to our theoretical 0.835. A better accord with numerics would, thus, require the participation of viscosity.

Before leaving this subject, it may be instructive to evaluate the area-averaged quantities because they can provide expeditious estimates. We find

$$T_m^{(0)} = 1 - \tfrac{1}{4}(\gamma - 1)M_w^2[2\pi^2 z^2 + \mathfrak{E} + \ln\pi - \mathrm{Ci}(\pi)];$$

$$p_m^{(0)} = 1 - \tfrac{1}{4}\gamma M_w^2[2\pi^2 z^2 + \mathfrak{E} + \ln\pi - \mathrm{Ci}(\pi)] \qquad \text{(Taylor's)} \qquad (79)$$

$$p_m = p_m^{(0)} - \tfrac{1}{384}\gamma\pi^2 M_w^4[\pi^2(16z^4 + 12z^2 + 5) - 3\sigma(8z^2 + 1)]$$

$$T_m = T_m^{(0)} - \tfrac{1}{384}(\gamma - 1)M_w^4(48 + \pi^4(64z^4 + 12z^2 + 5) - 3\pi^3\alpha(8z^2 + 1) + 6\pi^2\{\beta + 8z^2[\beta + \mathfrak{E} - \mathrm{Ci}(\pi) + \ln(\pi)]\} - 12\pi[\alpha - 4\mathrm{Si}(\pi)]) \qquad (80)$$

Although not shown on the graphs, p_m and T_m vary in concert with their counterparts taken along the axis. This reaffirms the frail pressure and temperature gradients in the radial direction. It also justifies the appropriateness of earlier comparisons between centerline properties and area-averaged one-dimensional projections.

H. Characteristic Effects of Compressibility

Having established the importance of L_s as a geometric scaling parameter, we can use it to delineate the zone of validity for the subsonic region. We show this in Fig. 7 at four representative values of γ. The minute shifts in the sonic curves reflect the weak sensitivity of the solution to the ratio of specific heats. This reinforces the notion of recouping a nearly frozen state after rescaling with respect to L_s.

When a chamber of length L_s is considered as our baseline case, the spatial evolution of the velocity field across the entire domain may be captured independently of the Mach number. This is shown in Fig. 8, where both streamwise and radial components are plotted, respectively, in the upper and lower parts of

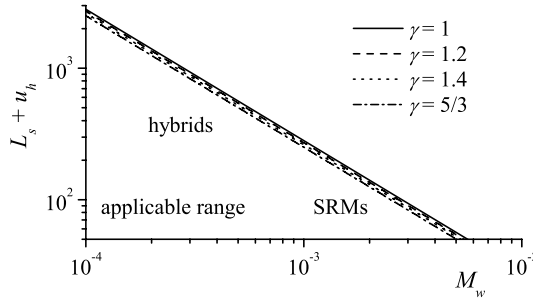

Fig. 7 Sonic distance vs wall Mach number.

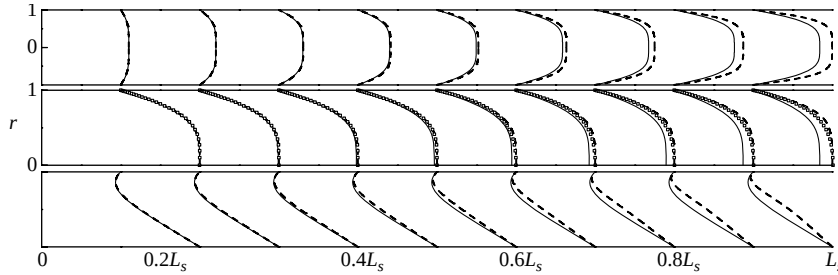

Fig. 8 Spatial evolution of axial and radial velocity profiles up to sonic point. Inset rescales the axial velocity by its centerline value and compares it to CFD data (hollow squares for *k–ω* model).

the graph. These represent scaled-down versions that preserve the relative proportions of actual magnitudes. The former plot is repeated in the middle part where it is magnified for better clarity (using the local centerline speed) and compared to CFD predictions. These are shown at nine equally spaced axial stations corresponding to 0.1, 0.2, 0.3, . . . , $0.9L_S$. Although we use a wall Mach number of 0.01 and $L_S = 28$, which co-tail our computational model, we emphasize the geometric similarity that renders this plot universal. Its response to changing γ is so minor that it may be ignored. This is verified by modifying the Mach number from 0.0001 to 0.01 with no distinct influence on the solution. Changing γ from 1 to $5/3$ has some influence, but it is too small to deserve particular attention. The gradual flattening of the compressible profile past $L_S/2$ is corroborated by both theory and experiment.

As expected, these profiles bear a striking resemblance to the numerical results and to both laboratory and computational experiments obtained by Traineau et al. [13], Balakrishnan et al. [30], Apte and Yang [18, 19], and others. Specifically, we note that the streamwise velocity becomes much fuller than Taylor's sinusoidal profile as choking is approached. This is accompanied by the classic linearization of the radial velocity. The evolution into a blunter, turbulent like, or pseudo-one-dimensional plug flow is conformant to both theory and experiment.

It faithfully captures the increased gradients at the sidewall, and these can have important implications in mean-flow related analyses. To the author's knowledge, this represents the first explicit analog of Taylor's compressible flow that exhibits the correct steepening behavior. Its agreement with CFD predictions is favorable despite the presence of small viscosity in the numerical simulation.

To quantify the steepening effect and magnification caused by compressibility, theoretical and CFD profiles are overlaid in Fig. 9. In Fig. 9a, the streamwise velocity, normalized by $\pi z M_w$, is shown at four evenly spaced distances from the sonic point. Because the leading-order sinusoidal profile varies between 0 and 1, it can be conveniently adopted as a benchmark. The amplification of the streamwise velocity can, thus, be inferred relative to Taylor's model. We note that, below $0.4\,L_s$, the compressible solution and Taylor's overlap (the discrepancy between them being less than 2%). This justifies the use of Taylor's solution in chambers whose actual length is roughly $L \leq 0.4\,L_s$. The precise cutoff point is a matter of conjecture, but we shall attempt to define it based on the relative error with respect to Taylor's. Therefore, first, this relative error must be characterized.

As shown in Fig. 9b, the maximum difference between the axial velocities, which appears at the centerline, can be evaluated. In as much as it is commensurate with the local impact of fluid compression, the ratio $\vartheta_c = u_z(0,z)/u_z^{(0)}(0,z) =$

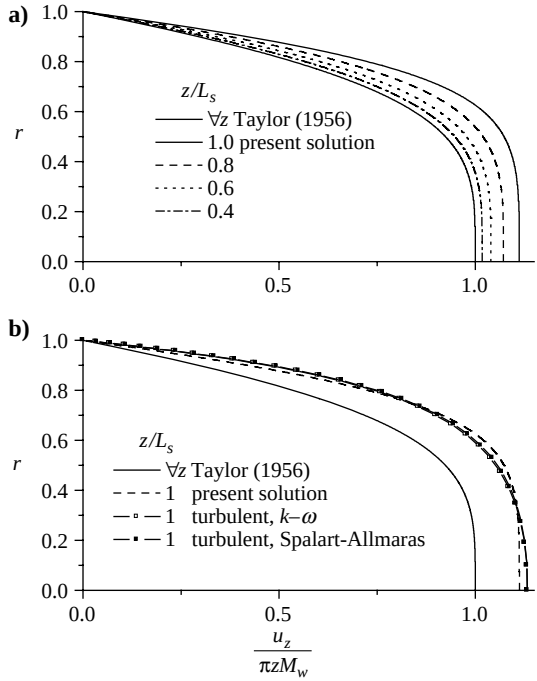

Fig. 9 Streamwise velocity: a) gradual steepening as choking is approached and b) computational curves at critical location. Normalized Taylor profile is axially invariant.

$u_z(0,z)/(\pi z M_w)$ becomes a direct measure of relative amplification. For example, the theoretical amplification at $z = L_s$ can be determined to be 1.112 vs a computed value of 1.133; the CFD limit is converged on by each of the turbulent models. Despite selecting the (most) critical location, a nearly perfect match with the turbulent profiles is realized in both fullness and extent. The turbulent simulations are performed using two standard schemes, namely, the k–ω and Spalart–Allmaras (private communication from B. A. Maicke, 2005). These yield such similar distributions that their differences are graphically imperceptible. The concurrence of the analytical solution with turbulent simulations is gratifying, especially that the model is often applied to problems involving large crossflow Reynolds numbers. The concurrence with turbulent predictions is not an artifact but rather an attribute of inviscid flows.

Overall, the amplification at a radial position can be measured from the ratio of velocities, $\vartheta(r,z) \equiv u_z/u_z^{(0)}$. At any cross section, the maximum local ratio occurs along the centerline where $\vartheta_c(z) \equiv u_c/u_c^{(0)}$. The smallest increase in ϑ_c can have an appreciable impact on core-flow ingredients, including the growth rate of disturbances. As recently shown in a compressible flow simulation of a model rocket motor, a roughly 10% increase in centerline speed (caused by density variations) can lead to a 70% overshoot in the growth of oscillatory wave amplitudes at a streamwise location of 40 (cf. Venugopal [35], pp. 61–65). The evolution of ϑ_c

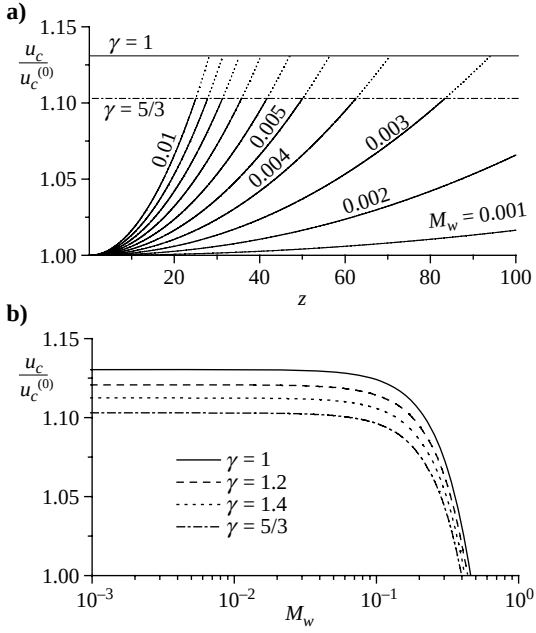

Fig. 10 Evolution of u_c: a) effect of varying M_w on compressible centerline velocity ratio as choking is axially approached and b) maximum velocity ratio at the sonic point.

with distance from the headwall is shown in Fig. 10a over a wide range of operating parameters and up to the sonic point. The latter occurs sooner at higher γ. Because the critical length depends on the gas compression ratio, dotted lines are used in the buffer region that is bracketed by the upper and lower bounds for γ. As M_w is lowered, for the chosen range of Mach numbers, it appears that the relative amplification ratio increases to a pure constant at fixed γ. This observation prompts us to define the maximum overall velocity amplification, $\vartheta_s = u_s/u_c^{(0)}$, based on $u_s = u_c(L_s)$. In Fig. 10b, a plot of ϑ_s confirms our hypothesis. We find that the sonic amplification ratio does indeed asymptote to a constant value in the practical range of Mach numbers. The asymptotic limit varies between $\vartheta_s = 1.130$ for $\gamma = 1$ to $\vartheta_s = 1.103$ for $\gamma = 5/3$. Analytically, the corresponding magnification may be obtained from Eq. (63) such that

$$\vartheta_c = 1 + \tfrac{1}{6}\pi^2 M_w^2 z^2 - \tfrac{1}{16}\sigma M_w^2 \qquad \text{or} \qquad \tilde{\vartheta}_c = 1 + \tfrac{1}{6}\pi^2 M_w^2 z^2 - \tfrac{1}{2}M_w^2 \tag{81}$$

By insertion of Γ, we collect $\vartheta_c = 1 + \frac{1}{6}\Gamma^2 X^2 - \frac{1}{16}\sigma M_w^2 \sim 1 + \frac{1}{6}\Gamma^2 X^2$. The asymptotic amplification for $X = 1$ may be readily estimated from

$$\vartheta_s^* \sim 1 + \tfrac{1}{6}\Gamma^2 \sim 1.13043 - 0.0522808(\gamma - 1) + 0.0211364(\gamma - 1)^2 - 0.00851203(\gamma - 1)^3$$

In applications that feature $M_w > 0.02$, an additional correction is required, specifically,

$$\vartheta_s = \vartheta_s^* - M_w^2[0.641014 + 0.0487504(\gamma - 1) - 0.0186428(\gamma - 1)^2] \tag{82}$$

These quantities enable us to measure directly the propensity of fluid compression and its bearing on the mean flow.

I. Extension to Solid and Hybrid Rockets

One may wonder under what circumstances density variations become important in SRMs. The present study can help to answer this question given a desired level of precision set by the designer. Suppose that an error that exceeds $\varepsilon = 4\%$ over more than $\ell = \frac{1}{4}$ of the chamber length is deemed unacceptable. Our solution enables us to calculate the distance to reach such degree of disparity with respect to Taylor's equation. This is met when $\vartheta_c = 1 + \varepsilon$, or, to good approximation, at

$$z_\varepsilon = \sqrt{6\varepsilon}/(\pi M_w) \tag{83}$$

If $z_\varepsilon a < (1 - \ell)L_0$, then volumetric expansions must be accounted for. By applying this formula in reverse to a chamber with a relatively large aspect ratio, for example, $L = 50$, we find the (minimum) cutoff Mach number M_w^* that must be surpassed for this condition to hold. This is

$$M_w^* = \sqrt{6\varepsilon}/[\pi(1 - \ell)L] \simeq 0.0042 \qquad \text{(no headwall injection, SRMs)} \tag{84}$$

Thus, if this motor has $M_w > M_w^*$, a 4% error will affect more than its aft-quarter length. Otherwise, it may be safely treated using Taylor's formula. When it is

considered that many SRMs operate under $M_w = 0.0042$ and have lengths that are shorter than $L = 50$, the suitability of Taylor's model remains unchallenged in those particular instances. The present solution becomes necessary, however, in applications that exhibit accentuated sensitivity to the mean flow. Examples include the full-scale numerical simulations conducted by CSAR, the treatment of the Stokes acoustic layer with sidewall injection (cf. Wasistho et al. [29]), the investigation of instability (cf. Venugopal et al. [40]), and the analysis of the exothermic boundary layer (cf. Balakrishnan et al. [30]). Surely, when precision is required to mitigate unwanted deviations, the present solution may be invoked. Overall, it increases our arsenal of physical approximations for the treatment of high-speed compressible flow.

If the interest is shifted to the modeling of hybrid rockets, one may repeat the analysis presented here using a nonzero inlet velocity at the headwall. One can use, for example, the similarity-conforming cosine shape proposed by Majdalani and Vyas [41]; this classic profile dating back to Berman [8] was presented in the context of providing an inviscid, outer approximation for the steady streamtube motion in hybrid rockets. Although it does not enforce an inlet condition on u_r, it remains quasi viscous because it fully observes the no-slip condition along the sidewall.

For implementation, the fourth boundary condition in Eq. (9) must be properly altered; as before, we write $u_z(r,0) = M_c \cos(\frac{1}{2}\pi r^2)$, $M_c \equiv U_c/a_0$. Note that only the streamwise velocity is constrained at the headwall. No condition is imposed on the radial inflow component. The notion of an open boundary at $z = 0$ is suitable in hybrid rocket applications where the injection at the headwall is not necessarily orthonormal to the surface. Some injectors are deliberately designed with a nonzero angle of attack.

As shown in a previous study [41], the solution connected with a sinusoidal headwall injection can be recovered by shifting the origin of Taylor's model to a hypothetical station located (upstream of the headwall) at a distance of $z = -u_h$, where $u_h = u_c/\pi$. Hence, a simple translation of the axis will enable us to modify the solution appropriately. One can write, for example,

$$\tilde{\psi} = M_w \psi^{(0)} \left(1 - \tfrac{1}{4} M_w^2 \left\{\pi^2 (z+u_h)^2 \left[1 + \tfrac{1}{3}\cos(\pi r^2)\right] + 2\right\}\right) \tag{85}$$

where $\psi^{(0)} = (z + u_h)\sin\eta$ represents the extended version of Taylor's formula with sinusoidal headwall injection [41]. Most of the foregoing expressions can be modified straightforwardly by replacing the streamwise coordinate by $Z = z + u_h$. At the outset, the critical length must be rectified by subtracting from it the headwall effect. The new effective distance to the sonic point becomes $L_h = L_s - u_h$. This correction has a large bearing on the hybrid model because it suggests that compressibility may be important despite a small M_w so long as u_h is sufficiently large. This all depends on M_w and the relative length of the hybrid chamber with respect to L_h. The criterion given by Eq. (84) translates into

$$M_w^* = \frac{1}{\pi[(1-\ell)L + u_h]}\sqrt{6\varepsilon}$$

(with headwall injection, SRMs, and hybrid rockets) (86)

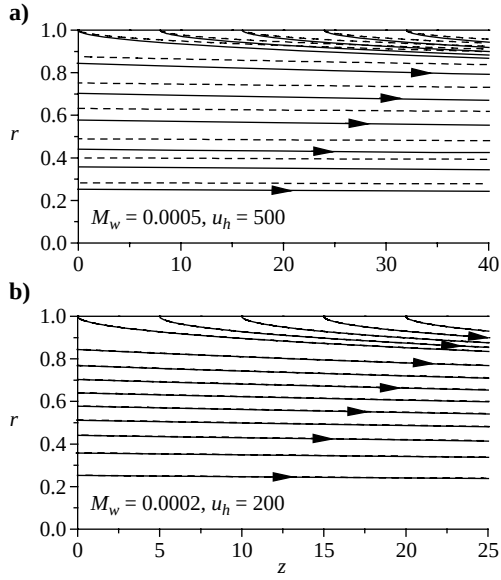

Fig. 11 Streamlines corresponding to hybrid rocket model with sinusoidal headwall injection: a) conditions susceptible to fluid compression and b) flow nearly incompressible.

The effect of fluid compression in hybrids is shown in Fig. 11 at two sets of parameters and $\gamma = 1.2$. These two parameters correspond to circumstances under which the cutoff M_w^* is 0.0003 (Fig. 11a) and 0.0007 (Fig. 11b). Both cases tend to approximate the characteristic streamtube motion reported in hybrid core flow. Because the wall Mach number in Fig. 11a exceeds 0.0003, compressibility effects are seen to permeate the chamber. The converse may be said of Fig. 11b, where no deviations from Taylor's formula are visible. Equation (86) provides a simple but helpful tool for judging whether a compressible or incompressible solution is required in the modeling of solid and hybrid rockets. Note that, in recent years, hybrid rocket development has continued to evolve. The latest data suggest typical aspect ratios ranging from 20 to 80 and headwall Mach numbers reaching 0.3–0.5 (private communication, M. J. Chiaverini, Chair, AIAA Technical Committee on Hybrids, 2005). Using a hybrid wall Mach number of $M_w \simeq 0.0003$, one calculates the headwall injection constant to be upward of 1000. Under such high-speed conditions, compressibility becomes quintessential. The key results for the internal burning hybrid rocket are summarized in Table 4.

V. Solution for Slab Rocket

To model the two-dimensional slab rocket, we change our geometry to that of a rectangular duct of length L_0, where $L_0 \leq L_s$ and L_s is the critical length [42]. As shown in Fig. 12, the origin is set at the center of the headwall and the half-height is taken to be a. Because of symmetry about the midsection plane, the domain is

Table 4 Axisymmetric solution for the internal burning hybrid rocket. Here $\eta = \frac{1}{2}\pi r^2$

Variable	Formula
$\tilde{\psi}$	$M_w z \sin\eta \left(1 - \frac{1}{4}M_w^2 \left\{\pi^2 z^2[1 + \frac{1}{3}\cos(2\eta)] + 2\right\}\right)$
$\tilde{u}_z$	$\pi M_w z \cos\eta \left(1 + \frac{1}{4}M_w^2 \left\{\pi^2 z^2 \left[\frac{5}{3} - \cos(2\eta)\right] + r^{-2}[1 - \cos(2\eta)] - 2\right\}\right)$
$\tilde{u}_r$	$-M_w r^{-1} \sin\eta \left(1 - \frac{1}{4}M_w^2 \left\{\pi^2 z^2[1 + \cos(2\eta)] - r^{-2}[1 - \cos(2\eta)] + 2\right\}\right)$
$\tilde{\Omega}$	$M_w \pi^2 r z \sin\eta \left(1 + \frac{1}{24}M_w^2 \left\{-2\pi^2 z^2[1 + 9\cos(2\eta)] + 3\pi\eta^{-1}[1 - \cos(2\eta)] - 12 + 3\pi\eta^{-2}\sin(2\eta)\right\}\right)$
$\tilde{p}$	$1 - \frac{1}{2}\pi\gamma M_w^2 \left\{\pi z^2 + \frac{1}{4}\eta^{-1}[1 - \cos(2\eta)]\right\} - \frac{1}{8}\pi^2\gamma M_w^4 \left[\frac{1}{3}\pi^2 z^4 + \pi z^2(\eta - 4/\pi) + \frac{1}{4}\eta(3\eta - 8/\pi)\right]$
$\tilde{\rho}$	$1 - \frac{1}{2}\pi M_w^2 \left\{\pi z^2 + \frac{1}{4}\eta^{-1}[1 - \cos(2\eta)]\right\} - \frac{1}{8}\pi^2 M_w^4 \left(\frac{1}{3}\pi^2 z^4(3\gamma - 2) + \pi z^2 \left\{\eta + \frac{1}{2}(\gamma - 1)\eta^{-1}[1 - \cos(2\eta)] - 4/\pi\right\} + \frac{1}{4}\eta(3\eta - 8/\pi) + \frac{1}{32}(\gamma - 1)\eta^{-2}[3 - 4\cos(2\eta) + \cos(4\eta)]\right)$
$\tilde{T}$	$1 - \frac{1}{8}\pi(\gamma - 1)M_w^2 \left\{4\pi z^2 + \eta^{-1}[1 - \cos(2\eta)]\right\} - \frac{1}{6}\pi^2(\gamma - 1)M_w^4 \left\{\pi^2 z^4 + \frac{3}{8}\pi\eta^{-1}z^2[1 - \cos(2\eta) + 2\eta(\eta - 4/\pi)] + \frac{3}{128}\eta^{-2}[3 - 4\cos(2\eta) + \cos(4\eta) - 64\eta^3/\pi + 24\eta^4]\right\}$
Γ	$\begin{cases} \sqrt{2\gamma^{-1}\left[1 - \left(\frac{1}{2}\gamma + \frac{1}{2}\right)^{\gamma/(1-\gamma)}\right]}; \quad \Gamma \equiv \pi M_w L_s \\ \delta^{1/2}\sqrt{\cos\left\{\frac{1}{3}\cos^{-1}[16(14 + 6\gamma - 3\gamma^2 - 4\gamma^3)/\delta^3]\right\} - 2(\gamma + 1)}; \\ \quad \delta \equiv 2\sqrt{2(\gamma + 1)(2\gamma - 1)} \\ \sqrt{\lambda - 2\gamma - 2 + 2(2\gamma^2 + \gamma - 1)/\lambda}; \\ \quad \lambda \equiv \left(28 + 12\gamma - 6\gamma^2 - 8\gamma^3 + 6\sqrt{22 + 18\gamma - 6\gamma^2 - 14\gamma^3 - 3\gamma^4}\right)^{1/3} \\ 0.884622 - 0.177299(\gamma - 1) + 0.0539119(\gamma - 1)^2 - 0.0180615(\gamma - 1)^3 \end{cases}$
$\tilde{M}_c$	$\frac{1 + \frac{1}{6}\Gamma^2 X^2 - \frac{1}{2}M_w^2}{\sqrt{\Gamma^{-2}X^{-2} - \frac{1}{2}(\gamma - 1)}} \simeq \frac{\left(1 + \frac{1}{6}\Gamma^2 X^2\right)\Gamma X}{\sqrt{1 - \frac{1}{2}(\gamma - 1)\Gamma^2 X^2}}; \quad X \equiv z/L_s$

Table 4 Axisymmetric solution for the internal burning hybrid rocket. Here $\eta = \frac{1}{2}\pi r^2$ (Continued)

Variable	Formula
$\tilde{\psi}$	$z \sin\eta \left(1 - \frac{1}{4}\Gamma^2 \left\{X^2 \left[1 + \frac{1}{3}\cos(2\eta)\right] + 2\pi^{-2} L_s^{-2}\right\}\right); \quad X \equiv \tilde{\psi}/M_w$
ϑ_c	$1 + \frac{1}{6}\Gamma^2 X^2; \quad \vartheta_c(z) \equiv u_z(0,z)/u_z^{(0)}(0,z)$
ϑ_s^*	$1 + \frac{1}{6}\Gamma^2 \sim 1.13043 - 0.0522808(\gamma - 1) + 0.0211364(\gamma - 1)^2 - 0.00851203(\gamma - 1)^3$
M_w^*	$\dfrac{\sqrt{6\varepsilon}}{\pi[(1-\ell)L + u_h]}$ to prevent an error ε over more than a fraction ℓ of the chamber length L

truncated to the region bounded by $0 \le y \le 1$ and $0 \le x \le L$, where $L = L_0/a$ is the aspect ratio. At first, we assume closed-headwall conditions. The injection velocity at the opposing sidewalls is uniform and designated by U_w.

A. Cartesian Equations

The first step in our formulation is to nondimensionalize key variables using, as before,

$$u_x = \bar{u}_x/a_0; \qquad u_y = \bar{u}_y/a_0; \qquad p = \bar{p}/p_0; \qquad T = \bar{T}/T_0;$$
$$\rho = \bar{\rho}/\rho_0; \qquad \psi = \bar{\psi}/(\rho_0 a_0 a); \qquad \boldsymbol{\Omega} = \bar{\boldsymbol{\Omega}} a/a_0; \qquad \nabla = a\bar{\nabla} \tag{87}$$

where the subscript 0 denotes a reference condition at the origin. As before, we invoke the two-dimensional stream function approach that is the cornerstone of this analysis; it relates the velocity and vorticity in such a way that the governing

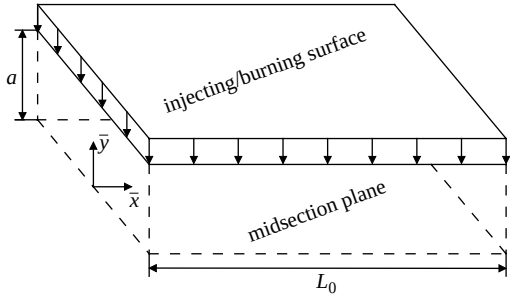

Fig. 12 Planar slab burner with coordinate system shown in half the domain.

equations for the problem reduce to

$$\nabla^2\psi + \rho\Omega = \rho^{-1}\nabla\rho\cdot\nabla\psi \quad \text{(vorticity equation)} \tag{88}$$

$$\nabla\times(\boldsymbol{u}\times\boldsymbol{\Omega}) = -\nabla\rho\times\nabla p/(\gamma\rho^2) \quad \text{(vorticity transport equation)} \tag{89}$$

$$\nabla p/\gamma = -\tfrac{1}{2}\rho\nabla[\rho^{-2}\nabla\psi\cdot\nabla\psi] - (\Omega/r)\nabla\psi \quad \text{(momentum equation)} \tag{90}$$

Finally, given the assumptions of a calorically perfect gas and isentropic flow, one may employ the standard closure equations

$$\rho = p^{1/\gamma}; \qquad T = p^{1-1/\gamma} \tag{91}$$

The boundary conditions imposed on our solution follow directly from the physical interpretation of the velocity inputs. At first (for the SRM analysis), a zero velocity condition is imposed at the headwall of the chamber, a constant velocity injection normal to the sidewall, and no flow is allowed to cross the midsection plane.

B. Cartesian Expansions

Using a Rayleigh–Janzen perturbation, we expand our variables according to

$$\begin{aligned}
\boldsymbol{u}(x,y) &= M_w\boldsymbol{u}^{(0)} + M_w^3\boldsymbol{u}^{(1)} + \mathcal{O}(M_w^5)\\
\rho(x,y) &= 1 + M_w^2\rho^{(1)} + M_w^4\rho^{(2)} + \mathcal{O}(M_w^6)\\
\psi(x,y) &= M_w\psi^{(0)} + M_w^3\psi^{(1)} + \mathcal{O}(M_w^5)\\
p(x,y) &= 1 + M_w^2 p^{(1)} + M_w^4 p^{(2)} + \mathcal{O}(M_w^6)\\
\Omega(x,y) &= M_w\Omega^{(0)} + M_w^3\Omega^{(1)} + \mathcal{O}(M_w^5)\\
T(x,y) &= 1 + M_w^2 T^{(1)} + M_w^4 T^{(2)} + \mathcal{O}(M_w^6)
\end{aligned} \tag{92}$$

When these quantities are substituted into Eqs. (88–91), leading-order terms may be identified. These are

$$\nabla^2\psi^{(0)} + \Omega^{(0)} = 0 \tag{93}$$

$$\nabla\times[\boldsymbol{u}^{(0)}\times\boldsymbol{\Omega}^{(0)}] = 0 \tag{94}$$

$$\nabla p^{(1)} = -\gamma\left\{\tfrac{1}{2}\nabla[\nabla\psi^{(0)}\cdot\nabla\psi^{(0)}] + \Omega^{(0)}\nabla\psi^{(0)}\right\} \tag{95}$$

$$\rho^{(1)} = p^{(1)}/\gamma; \qquad T^{(1)} = (\gamma-1)p^{(1)}/\gamma \tag{96}$$

Corresponding boundary conditions may be retrieved and expressed as

$$\frac{\partial \psi^{(0)}(x,0)}{\partial x} = 0 \tag{97a}$$

$$\frac{\partial \psi^{(0)}(x,1)}{\partial y} = 0 \tag{97b}$$

$$\frac{\partial \psi^{(0)}(x,1)}{\partial x} = 1 \tag{97c}$$

$$\frac{\partial \psi^{(0)}(0,y)}{\partial y} = 0 \tag{97d}$$

Along similar lines, we collect the first order-equations at $\sigma(M_w^3)$;

$$\nabla^2 \psi^{(1)} + \Omega^{(1)} = \nabla \psi^{(0)} \cdot \nabla \rho^{(1)} - \Omega^{(0)} \rho^{(1)} \tag{98}$$

$$\nabla \times [\boldsymbol{u}^{(0)} \times \boldsymbol{\Omega}^{(1)}] + \nabla \times [\boldsymbol{u}^{(1)} \times \boldsymbol{\Omega}^{(0)}] = -\nabla \rho^{(1)} \times \nabla p^{(1)}/\gamma \tag{99}$$

$$\begin{aligned} \nabla p^{(2)} = -\gamma (\nabla \{ &\nabla \psi^{(0)} \cdot \nabla \psi^{(1)} - \rho^{(1)} [\nabla \psi^{(0)} \cdot \nabla \psi^{(0)}] \} \\ &+ \tfrac{1}{2} \rho^{(1)} \nabla [\nabla \psi^{(0)} \cdot \nabla \psi^{(0)}] + \Omega^{(0)} \nabla \psi^{(1)} + \Omega^{(1)} \nabla \psi^{(0)}) \end{aligned} \tag{100}$$

$$\rho^{(2)} = \{2\gamma p^{(2)} + (1-\gamma)[p^{(1)}]^2\}/(2\gamma^2);$$

$$T^{(2)} = (\gamma - 1)\{2\gamma p^{(2)} - [p^{(1)}]^2\}/(2\gamma^2) \tag{101}$$

When it is recalled that the leading-order solution is expected to satisfy the problem's boundary conditions, only homogenous boundary conditions may be associated with Eqs. (98–101).

C. Basic Cartesian Solution

The leading-order approximation can be readily obtained by solving Eqs. (93–96); one recovers the incompressible Taylor solution for an internally burning slab rocket. Characteristic attributes include

$$\Omega^{(0)} = \tfrac{1}{4}\pi^2 \psi^{(0)};\ \psi^{(0)} = x \sin \eta; \qquad \eta = \tfrac{1}{2}\pi y \tag{102}$$

$$p^{(1)} = -\tfrac{1}{2}\gamma \left(\tfrac{1}{4}\pi^2 x^2 + \sin^2 \eta\right) \tag{103}$$

$$\rho^{(1)} = -\tfrac{1}{2}\left(\tfrac{1}{4}\pi^2 x^2 + \sin^2 \eta\right); \qquad T^{(1)} = -\tfrac{1}{2}(\gamma - 1)\left(\tfrac{1}{4}\pi^2 x^2 + \sin^2 \eta\right) \tag{104}$$

D. First-Order Vorticity

To satisfy the vorticity transport equation, a relationship between $\Omega^{(1)}$ and $\psi^{(1)}$ is needed. When the isentropic assumption made earlier is kept in mind, Eq. (99) collapses into

$$\nabla \times [\boldsymbol{u}^{(0)} \times \boldsymbol{\Omega}^{(1)}] + \nabla \times [\boldsymbol{u}^{(1)} \times \boldsymbol{\Omega}^{(0)}] = 0 \tag{105}$$

This renders a single equation in the z direction. It is possible to substitute Eq. (102) and eliminate the leading-order velocity and vorticity terms. Then using the velocity–stream function relation, an expression can be found linking the first-order vorticity, first-order stream function, and other known quantities. The resulting equation can be further simplified by realizing that the first-order vorticity–stream function relation must mirror the incompressible vorticity term $\Omega^{(0)} = \frac{1}{4}\pi^2\psi^{(0)}$, but with an additional term due to compressibility. To capture this correction, we let

$$\Omega^{(1)} = \tfrac{1}{4}\pi^2\psi^{(1)} + \Omega_c^{(1)} \tag{106}$$

This realization takes a complicated first-order vorticity transport relation and simplifies it to the much more tractable

$$\frac{\partial\psi^{(0)}}{\partial x}\frac{\partial\Omega_c^{(1)}}{\partial y} - \frac{\partial\psi^{(0)}}{\partial y}\frac{\partial\Omega_c^{(1)}}{\partial x} = -\frac{\pi^2}{4}\psi^{(0)}\left[\frac{\partial\rho^{(1)}}{\partial x}\frac{\partial\psi^{(0)}}{\partial y} - \frac{\partial\rho^{(1)}}{\partial y}\frac{\partial\psi^{(0)}}{\partial x}\right] \tag{107}$$

where Eqs. (102) and (104) may be inserted. We recover

$$\Omega_c^{(1)} = -\tfrac{1}{32}\left(\pi^4x^3\sin\eta + 4\pi^2x\sin^3\eta\right) + H(x\sin\eta) \tag{108}$$

E. First-Order Stream Function Solution

Armed with the first-order vorticity relation in Eq. (108), we can update Eq. (98) and write

$$\nabla^2\psi^{(1)} + \tfrac{1}{4}\pi^2\psi^{(1)} = \nabla\psi^{(0)}\cdot\nabla\rho^{(1)} - \Omega^{(0)}\rho^{(1)} - \Omega_c^{(1)} \tag{109}$$

Substitution from Eqs. (102), (104), and (108) enables us to express the right side in terms of known quantities, specifically,

$$\nabla^2\psi^{(1)} + \tfrac{1}{4}\pi^2\psi^{(1)} = \tfrac{1}{16}\pi^2x\sin\eta(\pi^2x^2 - 8\cos^2\eta) + H(x\sin\eta) \tag{110}$$

where $H(x\sin\eta)$ is chosen such that the solution to Eq. (110) satisfies the governing equations and all of the requisite boundary conditions. For the planar case, the function takes the form

$$H = A_1x^3\sin^3\eta + A_2x\sin\eta \tag{111}$$

The right side of Eq. (110) is now determined. When $\psi^{(1)}$ is sought, experience suggests the special form

$$\psi^{(1)}(x,\eta) = x^3f(\eta) + xg(\eta) \tag{112}$$

When this expression is returned to Eq. (110), two ODEs are precipitated; these are

$$\tfrac{1}{4}\pi^2(f'' + f) = A_1\sin^3\eta + \tfrac{1}{16}\pi^4\sin\eta \tag{113}$$

$$\tfrac{1}{4}\pi^2(g'' + g) = \sin\eta\left[A_2 + \tfrac{1}{4}\pi^2 + \tfrac{1}{4}\pi^2\cos(2\eta)\right] + 6f \tag{114}$$

where derivatives are with respect to η. Equations (113) and (114) can then be solved simultaneously for f and g to complete Eq. (112). This produces a general stream function relation with six unknown constants. The six undetermined coefficients in the general solution can be determined by judicious use of the first-order boundary conditions. Those refer to the axial and normal velocity terms at the walls, and the normal velocity in the midsection plane. Each of these homogeneous boundary conditions contains two equations to the extent of providing the requisite six equations. Solving the resulting set leads to the surprisingly compact solution for the first-order stream function correction [42],

$$\psi^{(1)} = -\tfrac{1}{16} x \sin\eta \left\{ \pi^2 x^2 \left[1 + \tfrac{1}{3}\cos(2\eta) \right] + 7 - \cos(2\eta) \right\} \tag{115}$$

and so

$$\psi = M_w \psi^{(0)} \left(1 - \tfrac{1}{16} M_w^2 \left\{ \pi^2 x^2 \left[1 + \tfrac{1}{3}\cos(2\eta) \right] + 7 - \cos(2\eta) \right\} \right) + \mathcal{O}(M_w^5) \tag{116}$$

F. Second-Order Pressure, Density, and Temperature

With $\psi^{(1)}$ at hand, the right side of the momentum equation, given by Eq. (100), is now completely determined. This vector equation can be expressed as two scalar equations in the x and y directions; partial integration can then be used to determine the second-order pressure term. By the proper handling of the common terms derived from both integral equations, the solution to the second-order pressure becomes

$$p^{(2)} = -\tfrac{1}{16}\gamma[\cos(\pi y) + \cos^2(\pi y)] + \tfrac{1}{64}\pi^2 x^2 \gamma[7 - \cos^2(\pi y)] - \tfrac{1}{384}\gamma\pi^4 x^4 \tag{117}$$

and so, by virtue of Eq. (101), the second-order density and temperature terms may be obtained via

$$\rho^{(2)} = \tfrac{1}{384}\left\{ 6[1 - 3\gamma + 4(\gamma - 2)\cos(\pi y) - (\gamma + 1)\cos(2\pi y)] + \pi^2 x^2 [51 - 12\gamma + 12(\gamma - 1)\cos(\pi y) - 3\cos(2\pi y)] + \pi^4 x^4 (2 - 3\gamma) \right\} \tag{118}$$

$$T^{(2)} = -\tfrac{1}{384}(\gamma - 1)\left\{ 30 + 18\cos(2\pi y) + 3\pi^2 x^2 [\cos(2\pi y) - 4\cos(\pi y) - 9] + 4\pi^4 x^4 \right\} \tag{119}$$

G. Critical Motor Length

As before, it is possible to determine the critical length of the slab rocket motor by determining where the midsection Mach number approaches unity.

This will occur when $u_c/\sqrt{T_c} = 1$, where $u_c = u_x(x, 0)$. Because the perturbation expansions used in this study are of increasing accuracy up to $\mathcal{O}(M_w^5)$, one can determine the critical length to varying degrees of precision; these estimates present a balance between a compact, closed-form solution and a more accurate but lengthy expression. The leading-order approximation for the critical length is simply

$$x_s^{(0)} = 2\sqrt{2/(\gamma+1)}/(\pi M_w) \tag{120}$$

It is twice that in the cylindrical chamber. By the increasing of the truncation threshold, more accurate yet complex expressions for the critical length may be found. A solution to third-digit accuracy can be obtained from

$$x_s^{(1)} = 2\sqrt{\varphi - 4 + 2(5-3\gamma)/\varphi}/(\pi M_w)$$
$$\varphi = \left(36\gamma - 10 + 6\sqrt{6\gamma^3 + 6\gamma^2 + 30\gamma - 25}\right)^{1/3} \tag{121}$$

Higher-order approximations may be obtained along the lines described in Sec. IV.D. Furthermore, when the analysis of Sec. IV.I is followed, the effects of compressibility are found to be important when the wall Mach number exceeds

$$M_w^* = \frac{2}{\pi[(1-\ell)L + 2u_h]}\sqrt{6\varepsilon}$$

(planar case with headwall injection, solid and hybrid slabs) (122)

A summary of the planar results is given in Table 5. For the hybrid slab, one may replace x by $X = x + 2u_h$ in the streamfunction and its derivatives.

VI. Summary

In this chapter, the compressible flow analog to the Taylor–Culick problem is solved analytically and presented for both cylindrical and slab rocket chambers. In the cylindrical geometry, we offer two closed forms: one exact, satisfying all first principles, and one approximate, retaining the essence of the solution. These key findings lead to a formidable leap in our physical understanding of compressible flow behavior in multidimensional settings. In propulsion-rooted applications, they permit the re-evaluation of many ballistic performance measures that, so far, have been mostly confined to one-dimensional platforms.

The most significant result is perhaps the advent of a compact analytical expression for the streamwise and wall-normal velocity profiles, which, unlike other models, can be calculated easily. It is gratifying that the solution can reproduce up to the sonic point the fullness and extent of Navier–Stokes profiles computed using two reliable models of turbulence. The second significant result is the discovery of the critical length as the appropriate scale leading to nearly frozen behavior irrespective of the wall Mach number; this has enabled us to recast the solution in a more portable, parametric-free form. In the wake of this generalization, simple design criteria that quantify the relative importance of gas compression have been

Table 5 Planar solution for the slab rocket. Here $\eta = \frac{1}{2}\pi y$

Variable	Formula
ψ	$M_w x \sin\eta \left(1 - \frac{1}{16}M_w^2 \left\{\pi^2 x^2 \left[1 + \frac{1}{3}\cos(2\eta)\right] + 7 - \cos(2\eta)\right\}\right)$
u_x	$\frac{1}{2}\pi M_w x \cos\eta \left(1 + \frac{1}{16}M_w^2 \left\{\pi^2 x^2 \left[\frac{5}{3} - \cos(2\eta)\right] - 5 - \cos(2\eta)\right\}\right)$
u_y	$-M_w \sin\eta \left\{1 - \frac{1}{16}M_w^2(\pi^2 x^2 + 3)[1 + \cos(2\eta)]\right\}$
Ω	$\frac{1}{4}\pi^2 M_w x \sin\eta \left\{1 - \frac{1}{48}M_w^2 \left[\pi^2 x^2(1 + 9\cos 2\eta) - 3(1 + 5\cos 2\eta)\right]\right\}$
p	$1 - \frac{1}{4}\gamma M_w^2 \left[\frac{1}{2}\pi^2 x^2 + 1 - \cos(2\eta)\right]$ $-\frac{1}{32}\gamma M_w^4 \left\{\frac{1}{12}\pi^4 x^4 - \frac{1}{4}\pi^2 x^2 [13 - \cos(4\eta)] + 1 + 2\cos(2\eta) + \cos(4\eta)\right\}$
ρ	$1 - \frac{1}{4}M_w^2 \left[\frac{1}{2}\pi^2 x^2 + 1 - \cos(2\eta)\right]$ $+\frac{1}{384}M_w^4 \left\{\pi^4 x^4(2 - 3\gamma) + \pi^2 x^2 \left[51 - 12\gamma + 12(\gamma - 1)\cos(2\eta)\right]\right.$ $\left. -3\cos(4\eta) + 6\left[1 - 3\gamma + 4(\gamma - 2)\cos(2\eta) - (\gamma + 1)\cos(4\eta)\right]\right\}$
T	$1 - \frac{1}{4}(\gamma - 1)M_w^2 \left[\frac{1}{2}\pi^2 x^2 + 1 - \cos(2\eta)\right] - \frac{1}{384}(\gamma - 1)M_w^4 \left\{4\pi^4 x^4\right.$ $\left. -3\pi^2 x^2 [9 + 4\cos(2\eta) - \cos(4\eta)] + 30 + 18\cos(4\eta)\right\}$
$x_s^{(3)}$	$\dfrac{2}{\pi M_w}\Gamma$ twice the critical length in the cylindrical case
$\tilde{M}_c$	$\dfrac{1 + \frac{1}{24}\Gamma^2 X^2 - \dfrac{3}{8}M_w^2}{\sqrt{4\Gamma^{-2}X^{-2} - \frac{1}{2}(\gamma - 1)}} \simeq \dfrac{(1 + \frac{1}{24}\Gamma^2 X^2)\Gamma X}{\sqrt{4 - \frac{1}{2}(\gamma - 1)\Gamma^2 X^2}}; \quad X \equiv x/L_s$
$\tilde{\Psi}$	$x \sin\eta \left(1 - \frac{1}{16}\Gamma^2 \left\{X^2 \left[1 + \frac{1}{3}\cos(2\eta)\right] + [7 - \cos(2\eta)]\pi^{-2}L_s^{-2}\right\}\right)$
ϑ_c	$1 + \frac{1}{24}\Gamma^2 X^2; \quad \vartheta_c(x) \equiv u_x(x, 0)/u_x^{(0)}(x, 0)$
ϑ_s^*	$1 + \frac{1}{24}\Gamma^2 \sim 1.13043 - 0.0522808(\gamma - 1) + 0.0211364(\gamma - 1)^2$ $-0.00851203(\gamma - 1)^3$
M_w^*	$\dfrac{2\sqrt{6\varepsilon}}{\pi[(1 - l)L + 2u_h]}$ to prevent an error ε over more than a fraction l of the chamber length L

deduced and shown to realistically project actual behavior. Because of the particular role that it plays, the critical length has been derived and presented using several approximations of increasing precision. The amplification of the centerline velocity, a key parameter in core flow analysis, has also been characterized and tacitly secured.

By the circumventing of the need to compute the mean flow at each point and set of operating variables, these compact solutions greatly facilitate parametric trade analyses. They may be employed in the investigation of hydrodynamic instability of solid and hybrid rockets. The fact that our streamlines are steepened at higher Mach numbers and fixed length lends support to Griffond's [38] and Venugopal's [35] hypotheses; these ascribe the heightened stability sensitivity to steeper streamline curvatures. In light of this consensus regarding the destabilizing role of fluid dilatation, further exploratory studies may be warranted.

The small differences we find in pressure and temperature estimations may be linked to the absence of viscosity in our model. This motivates the quest for a two-pronged viscous and compressible mean flow solution that follows familiar lines [20]. Incorporating friction may be useful in modeling hybrid rocket core flows in which the wall Reynolds number is small in comparison to SRMs. The use of a refined compressible model is hoped to improve our strategy in analyzing unsteady vorticoacoustic wave propagation and stability in porous enclosures. Repeating the analysis with constant mass flux surface conditions may also provide a more suitable model for some existing experimental and numerical simulations. Finally, with the viability of the present methodology demonstrated, the work may be extended to other geometric settings. It is hoped that the analysis could be extended to non-isentropic flow conditions in which the energy transport equation is used. This would permit characterizing density changes due to temperature variations and chemical reactions.

Acknowledgments

This work is sponsored by the National Science Foundation through Grant CMS-0353518. The author wishes to thank Martin J. Chiaverini, Chair, AIAA Technical Committee on Hybrids, for helpful discussions; Brian A. Maicke, graduate student at the University of Tennessee Space Institute, for providing the computational fluid dynamics results and the Cartesian solution; Prem Venugopal, Research Engineer, Philips Medical Systems, University of California at Los Angeles, for valuable comments; and Anand B. Vyas, Visiting Assistant Professor, Department of Mathematical Sciences, University of Delaware, for verifying the higher-order pressures and temperatures.

References

[1] Taylor, G. I., "Fluid Flow in Regions Bounded by Porous Surfaces," *Proceedings of the Royal Society of London, Series A: Mathematical and Physical Sciences*, Vol. 234, No. 1199, 1956, pp. 456–475.

[2] Yuan, S. W., "Further Investigation of Laminar Flow in Channels with Porous Walls," *Journal of Applied Physics*, Vol. 27, No. 3, 1956, pp. 267–269.

[3] Yuan, S. W., and Finkelstein, A. B., "Laminar Pipe Flow with Injection and Suction through a Porous Wall," *Journal of Applied Mechanics, Series E*, Vol. 78, No. 3, 1956, pp. 719–724.
[4] Wageman, W. E., and Guevara, F. A., "Fluid Flow through a Porous Channel," *Physics of Fluids*, Vol. 3, No. 6, 1960, pp. 878–881.
[5] Terrill, R. M., "Laminar Flow in a Uniformly Porous Channel," *Aeronautical Quarterly*, Vol. 15, 1964, pp. 299–310.
[6] Terrill, R. M., "Laminar Flow in a Uniformly Porous Channel with Large Injection," *Aeronautical Quarterly*, Vol. 16, 1965, pp. 323–332.
[7] Culick, F. E. C., "Rotational Axisymmetric Mean Flow and Damping of Acoustic Waves in a Solid Propellant Rocket," *AIAA Journal*, Vol. 4, No. 8, 1966, pp. 1462–1464.
[8] Berman, A. S., "Laminar Flow in Channels with Porous Walls," *Journal of Applied Physics*, Vol. 24, No. 9, 1953, pp. 1232–1235.
[9] Yuan, S. W., "Cooling by Protective Fluid Films," *Turbulent Flows and Heat Transfer*, Ser. G, Vol. V, edited by C. C. Lin, Princeton Univ. Press, Princeton, NJ, 1959, pp. 428–488.
[10] Peng, Y., and Yuan, S. W., "Laminar Pipe Flow with Mass Transfer Cooling," *Journal of Heat Transfer*, Vol. 87, No. 2, 1965, pp. 252–258.
[11] Yamada, K., Goto, M., and Ishikawa, N., "Simulative Study of the Erosive Burning of Solid Rocket Motors," *AIAA Journal*, Vol. 14, No. 9, 1976, pp. 1170–1176.
[12] Dunlap, R., Willoughby, P. G., and Hermsen, R. W., "Flowfield in the Combustion Chamber of a Solid Propellant Rocket Motor," *AIAA Journal*, Vol. 12, No. 10, 1974, pp. 1440–1445.
[13] Traineau, J. C., Hervat, P., and Kuentzmann, P., "Cold-Flow Simulation of a Two-Dimensional Nozzleless Solid-Rocket Motor," AIAA Paper 86-1447, July 1986.
[14] Beddini, R. A., "Injection-Induced Flows in Porous-Walled Ducts," *AIAA Journal*, Vol. 24, No. 11, 1986, pp. 1766–1773.
[15] Baum, J. D., Levine, J. N., and Lovine, R. L., "Pulsed Instabilities in Rocket Motors: A Comparison between Predictions and Experiments," *Journal of Propulsion and Power*, Vol. 4, No. 4, 1988, pp. 308–316.
[16] Sabnis, J. S., Gibeling, H. J., and McDonald, H., "Navier–Stokes Analysis of Solid Propellant Rocket Motor Internal Flows," *Journal of Propulsion and Power*, Vol. 5, No. 6, 1989, pp. 657–664.
[17] Liou, T.-M., and Lien, W.-Y., "Numerical Simulations of Injection-Driven Flows in a Two-Dimensional Nozzleless Solid-Rocket Motor," *Journal of Propulsion and Power*, Vol. 11, No. 4, 1995, pp. 600–606.
[18] Apte, S., and Yang, V., "Effect of Acoustic Oscillation on Flow Development in a Simulated Nozzleless Rocket Motor," *Solid Propellant Chemistry, Combustion, and Motor Interior Ballistics*, Vol. 185, edited by V. Yang, T. B. Brill, and W.-Z. Ren, Progress in Astronautics and Aeronautics, AIAA, Reston, VA, 2000, pp. 791–822.
[19] Apte, S., and Yang, V., "Unsteady Flow Evolution in a Porous Chamber with Surface Mass Injection Part 1: Free Oscillation," *AIAA Journal*, Vol. 39, No. 8, 2001, pp. 1577–1586.
[20] Majdalani, J., Vyas, A. B., and Flandro, G. A., "Higher Mean-Flow Approximation for a Solid Rocket Motor with Radially Regressing Walls," *AIAA Journal*, Vol. 40, No. 9, 2002, pp. 1780–1788.
[21] Gany, A., and Aharon, I., "Internal Ballistics Considerations of Nozzleless Rocket Motors," *Journal of Propulsion and Power*, Vol. 15, No. 6, 1999, pp. 866–873.

[22] Chu, W.-W., Yang, V., and Majdalani, J., "Premixed Flame Response to Acoustic Waves in a Porous-Walled Chamber with Surface Mass Injection," *Combustion and Flame*, Vol. 133, No. 6129, 2003, pp. 359–370.

[23] Vuillot, F., "Vortex-Shedding Phenomena in Solid Rocket Motors," *Journal of Propulsion and Power*, Vol. 11, No. 4, 1995, pp. 626–639.

[24] Majdalani, J., "Physicality of Core Flow Models in Rocket Motors," *Journal of Propulsion and Power*, Vol. 19, No. 1, 2003, pp. 156–159.

[25] Varapaev, V. N., and Yagodkin, V. I., "Flow Stability in a Channel with Porous Walls," *Fluid Dynamics (Izvestiya Akademii Nauk SSSR, Meckanika Zhidkosti i Gaza)*, Vol. 4, No. 5, 1969, pp. 91–95.

[26] Griffond, J., Casalis, G., and Pineau, J.-P., "Spatial Instability of Flow in a Semiinfinite Cylinder with Fluid Injection through Its Porous Walls," *European Journal of Mechanics B/Fluids*, Vol. 19, No. 1, 2000, pp. 69–87.

[27] Abu-Irshaid, E. M., Majdalani, J., and Casalis, G., "Hydrodynamic Stability of Rockets with Headwall Injection," *Physics of Fluids*, Vol. 19, No. 2, 2007, pp. 024101–11.

[28] Féraille, T., and Casalis, G., "Channel Flow Induced by Wall Injection of Fluid and Particles," *Physics of Fluids*, Vol. 15, No. 2, 2003, pp. 348–360.

[29] Wasistho, B., Balachandar, S., and Moser, R. D., "Compressible Wall-Injection Flows in Laminar, Transitional, and Turbulent Regimes: Numerical Prediction," *Journal of Spacecraft and Rockets*, Vol. 41, No. 6, 2004, pp. 915–924.

[30] Balakrishnan, G., Liñan, A., and Williams, F. A., "Rotational Inviscid Flow in Laterally Burning Solid Propellant Rocket Motors," *Journal of Propulsion and Power*, Vol. 8, No. 6, 1992, pp. 1167–1176.

[31] Majdalani, J., and Flandro, G. A., "The Oscillatory Pipe Flow with Arbitrary Wall Injection," *Proceedings of the Royal Society of London, Series A: Mathematical and Physical Sciences*, Vol. 458, No. 2022, 2002, pp. 1621–1651.

[32] Majdalani, J., and Roh, T. S., "The Oscillatory Channel Flow with Large Wall Injection," *Proceedings of the Royal Society of London, Series A: Mathematical and Physical Sciences*, Vol. 456, No. 1999, 2000, pp. 1625–1657.

[33] Majdalani, J., "The Oscillatory Channel Flow with Arbitrary Wall Injection," *Journal of Applied Mathematics and Physics*, Vol. 52, No. 1, 2001, pp. 33–61.

[34] Balakrishnan, G., Liñan, A., and Williams, F. A., "Compressible Effects in Thin Channels with Injection," *AIAA Journal*, Vol. 29, No. 12, 1991, pp. 2149–2154.

[35] Venugopal, P., "Direct Numerical Simulation of Turbulence in a Model Solid Rocket Motor," Ph.D. Dissertation, Univ. of Illinois at Urbana–Champaign, Urbana, IL, Dec. 2003.

[36] Majdalani, J., Flandro, G. A., and Fischbach, S. R., "Some Rotational Corrections to the Acoustic Energy Equation in Injection-Driven Enclosures," *Physics of Fluids*, Vol. 17, No. 7, 2005, pp. 0741021–20.

[37] Griffond, J., "Receptivity and Aeroacoustic Resonance in Channels with Blowing Walls," *Physics of Fluids*, Vol. 14, No. 11, 2002, pp. 3946–3962.

[38] Dunlap, R., Blackner, A. M., Waugh, R. C., Brown, R. S., and Willoughby, P. G., "Internal Flowfield Studies in a Simulated Cylindrical Port Rocket Chamber," *Journal of Propulsion and Power*, Vol. 6, No. 6, 1990, pp. 690–704.

[39] Venugopal, P., Najjar, F. M., and Moser, R. D., "Numerical Simulations of Model Solid Rocket Motor Flows," AIAA Paper 2001-3950, July 2001.

[40] Majdalani, J., and Vyas, A. B., "Inviscid Models of the Classic Hybrid Rocket," AIAA Paper 2004-3474, July 2004.

[41] Maicke, B. A., and Majdalani, J., "The Compressible Taylor Flow in Slab Rocket Motors," AIAA Paper 2006-4957, July 2006.

[42] Jackson, T. L., and Buckmaster, J., "Heterogeneous Propellant Combustion," *AIAA Journal*, Vol. 40, No. 6, June 2002, pp. 1122–1130.

This page intentionally left blank

Chapter 8

Computational Fluid Dynamics Modeling of Hybrid Rocket Flowfields

Venkateswaran Sankaran*

Purdue University, West Lafayette, Indiana 47907

I. Introduction

THERE has been renewed interest in hybrid rocket propulsion in recent years as a candidate for advanced launch vehicle applications [1–14]. Hybrid motors are attractive because of their potential low cost, ease of fuel handling, reliability, throttling capability, and environmentally friendly emissions characteristics. The design of hybrid motors requires an understanding of the physical phenomena that control the combustion and fluid dynamic processes inside the fuel ports. This, in turn, requires knowledge of the complex interactions between such wide-ranging physical phenomena as fuel surface pyrolysis, oxidizer atomization and vaporization (in the case of a liquid oxidizer), gas-phase combustion and mixing, soot formation, and radiation characteristics. Of particular importance in the design of hybrid motors is the fuel surface regression rate and the manner in which it varies with operating conditions. The regression rate determines the overall sizing, mass fluxes, and geometric configuration of the hybrid fuel ports. Classical analyses of hybrid combustion [1, 2] have relied on boundary-layer assumptions to determine the heat flux to the fuel surface and, hence, the surface regression rate. However, such simplified analyses cannot account for many of the complex physical interactions, and more comprehensive computational fluid dynamic (CFD) models are necessary for design-quality prediction capability. The overall objective of the current chapter is to review and summarize the state of the art in the computational modeling of hybrid rockets with particular emphasis on the fundamental physical phenomena of importance in these flowfields.

In classical hybrid rocket motors, liquid or gaseous oxygen flowing over the solid fuel such as hydroxyl-terminated polybutadiene (HTPB) reacts with the pyrolyzed gases close to the fuel surface and forms a turbulent diffusion flame.

*Senior Researcher, School of Mechanical Engineering.

Convective and radiative heat transfer from the flame, in turn, provide the heat of pyrolysis for the thermal decomposition of the solid fuel. It is evident that the rate of fuel surface regression is governed by the interaction between these different processes, and in general, the regression rate is a function of both the axial position in the grain and the stage in the burn. Typical hybrid fuels regress rather slowly, and a relatively large exposed fuel surface is necessary to ensure adequate fuel generation. This is generally accomplished by employing a large number of ports in the fuel grain, leading to low propellant volume fraction in the rocket engine, and detailed flowfield analyses are necessary to optimize the fuel use with the sizing requirements. Moreover, several innovative concepts have been proposed recently that promise significantly higher regression rates. These include tangential oxidizer injection, which leads to a coaxial vortex flowfield in the combustion chamber [10, 11], and the use of paraffin-based fuels that form a thin liquid "melt" layer on the fuel surface [13, 14]. These novel designs introduce additional physics that are responsible for the enhanced regression rates and must also be properly accounted for in the physical model. Finally, other issues in hybrid rocket motors include combustion stability and transient behavior during ignition, throttling, and shutdown. All of which point to the need for a comprehensive CFD model to analyze and understand parametric trends and eventually to provide the basis for a design and development tool.

Analytical studies of hybrid rocket combustion have usually relied on the classical boundary-layer analysis of Marxman et al. [1], Marxman [2], and Majdalani and Vyas [12], to determine the heat flux to the fuel surface, which is then used to characterize the surface regression rate. Typically, the regression rate is given as $r_b = G_0^n$, where G_0 is the head end specific flow rate of the oxidizer ($G_0 = \dot{m}_{ox}/A_{in}$) and the exponent n is generally between 0.6 and 0.8. Such correlations are, however, too simplistic and cannot account for all of the variations in operating conditions, chamber pressure, radiation, and finite-rate chemical kinetics. Some of these effects were characterized experimentally by Chiaverini et al. [8], who further showed that the measured data cannot be properly represented by a relationship of the form $C_1 G_0^n x^m$. To better match their data, Chiaverini et al. also proposed a more comprehensive model, which includes terms accounting for radiative fluxes, similar to those proposed earlier by Marxman et al. [1]. Such simplified models are, nevertheless, limited to providing qualitative understanding of the trends and are inadequate to provide the kind of quantitative data needed for motor design and optimization.

Cheng et al. [15] developed a full Navier–Stokes model for hybrid rocket flowfields. Their model solved the three-dimensional Reynolds averaged Navier–Stokes (RANS) equations within a Lagrangian–Eulerian framework using the FDNS code [16]. Lagrangian droplet tracking was used to describe the motion and vaporization of the liquid oxygen (LOX) droplets and furnish the source terms for the vaporized fuel in the Eulerian gas-phase equations. Two-equation $k-\epsilon$ closure was used for the turbulence, and finite-rate reaction kinetics were used to describe the gas-phase combustion. Empirical blowing rate data were used to specify the pyrolysis rate at the fuel surface. They successfully computed the three-dimensional flowfield in two practical motor configurations as well as several simplified port configurations [15].

Lin and Chiu [17] developed an Eulerian–Eulerian spray combustion model for hybrid rocket flowfields. Their model focused on the postatomization conditions

prevailing in the downstream portion of the spray, and therefore, only dilute-spray effects were considered. Mass and species conservation were enforced on the fuel surface, and the fuel regression rate was obtained as part of the flowfield solution. They employed a pressure-based method with a modified SIMPLER algorithm for numerical solution of the governing equations [18]. Computational results were validated with experimental data, and parametric effects of droplet size and velocity distributions, as well as oxidizer flow rate on fuel regression and combustion efficiency, were performed.

Sankaran and Merkle developed a two-dimensional RANS model for gaseous oxygen and HTPB flowfields [19] and applied it to the experimental slab-burner configuration that was extensively tested by Chiaverini et al. at Pennsylvania State University [8, 9]. A density-based method with preconditioned time-marching techniques was used as the iterative strategy [20, 21]. Surface pyrolysis was represented in semi-empirical fashion by an Arrhenius-type relationship following the work of Cohen et al. [22] and Arisawa and Brill [23, 24]. The solid- and gas-phase boundaries were treated with detailed mass and energy balances on the interface, and the fuel regression rate was obtained implicitly as part of the flowfield solution. Thermal radiation effects were included through an algebraicthick–thin model. The radiative properties of the flame were calibrated to match the experimental regression rate data of Chiaverini et al. [8] and were then held fixed for performing additional parametric and size scale-up studies.

More recent modeling work include that of Serin and Gogus [25], who used a commercial Navier–Stokes code, CFD–ACE, to simulate hybrid rocket flowfields. Their simulations also focused on the Pennsylvania State University slab-burner experiments with gaseous oxygen and HTPB, and their model included radiative effects and surface pyrolysis. In addition, the same authors have developed a fast design code based on unsteady, quasi-one-dimensional simulations of equilibrium combustion [26]. Knuth et al. have carried out detailed CFD analyses of the vortex-driven hybrid motor with an axisymmetric assumption [27]. They used gaseous oxygen and HTPB fuel and analyzed the vortex flowfield for different swirl velocities and at different stages in the burn.

In the present chapter, we present a comprehensive computational model as well as demonstrative solutions and parametric studies of hybrid rocket flowfields. As just discussed, the model comprises the complete time-dependent Navier–Stokes equations, coupled to auxiliary transport equations and physical submodels. The basic model is similar to the one developed earlier by the present author and includes the effects of finite-rate chemistry, turbulence, gas-phase radiation, and coupling of the gas phase to the solid (fuel) phase [19]. Brief details of the physical model variations, particularly in relation to liquid-phase modeling, are also given. The computational model is then applied to the Pennsylvania State University experimental configuration [8, 9]. Representative flowfield results for quasi steady computations performed at several stages of the burn are presented. Calibration and validation of the computational model are carried out using the measurement data. Finally, parametric results of varying test conditions and scaleup to full-scale geometries are also presented. We conclude by giving an assessment of the state of the art of the CFD modeling of hybrid rocket flowfields and summarize the main challenges facing the modeling community.

II. Physical and Computational Modeling

Hybrid rocket combustion flowfields involve fluid dynamics coupled with combustion, turbulence, radiation, spray atomization, and vaporization (in the case of liquid-phase oxidizers such as LOX), fuel surface pyrolysis (in the case of HTPB and other solid fuels), and liquid fuel films (in the case of paraffin-based fuels). A variety of approaches have been proposed for multiphase flowfields in the literature. These include 1) Eulerian–Eulerian homogeneous mixture formulation, which treats the two-phase flow as a mixture in dynamic equilibrium; 2) Eulerian–Eulerian multifluid formulation, which allows for nonequilibrium kinematics and thermal effects between the two phases; and 3) Eulerian–Lagrangian, which treats the gas phase in Eulerian fashion and the liquid phase in a Lagrangian manner. Here, we briefly describe all three approaches, although the computational results presented in this chapter are restricted to HTPB/gaseous oxygen (GOX) flowfields.

We also point out that the equations are written in the full unsteady form for generality. For hybrid rocket flowfields, the fuel regression rate is typically much smaller than the fluid residence time in the ports, and, therefore, steady (or quasi-steady) solutions are adequate for predicting the fuel regression rate, motor efficiency, and size scaleup effects. On the other hand, time-accurate solutions are necessary to analyze the incidence of combustion instability in hybrid rocket motors. Again, the computational results presented in this chapter are concerned with only steady solutions because the focus is on regression rate characterization and size scale up effects.

A. Equations of Motion

1. *Gas-Phase or Homogeneous-Mixture Model*

The governing equations are the standard Navier–Stokes equations coupled with additional transport equations for combusting species and the equations for the turbulence kinetic energy and dissipation. The coupled set of equations may be written in the following vector form:

$$\frac{\partial \boldsymbol{Q}}{\partial t} + \frac{\partial \boldsymbol{E}_i}{\partial x_i} = \boldsymbol{H} + \frac{\partial \boldsymbol{V}_i}{\partial x_i} \tag{1}$$

where

$$\boldsymbol{Q} = \begin{pmatrix} \rho \\ \rho u_j \\ e \\ \rho\kappa \\ \rho\epsilon \\ \rho Y_m \end{pmatrix}; \qquad \boldsymbol{E}_i = \begin{pmatrix} \rho u_i \\ (\rho u_i u_j + p_t \delta_{ij}) \\ (e + p_t) u_i \\ \rho u_i \kappa \\ \rho u_i \epsilon \\ \rho u_i Y_m \end{pmatrix}; \qquad \boldsymbol{V}_i = \begin{pmatrix} 0 \\ \tau_{ij} \\ u_j \tau_{ij} + K \dfrac{\partial T}{\partial x_i} \\ \mu_\kappa \dfrac{\partial \kappa}{\partial x_i} \\ \mu_\epsilon \dfrac{\partial \epsilon}{\partial x_i} \\ \rho D_m \dfrac{\partial Y_m}{\partial x_i} \end{pmatrix} \tag{2}$$

Here, $m = 1, 2, \ldots, N-1$, where N is the total number of chemical species and Y_m is the mass fraction of the mth species. The pressure $p_t = p + \frac{2}{3}\rho\kappa$. Furthermore,

the viscous stress tensor is given as

$$\tau_{ij} = \mu \left(\frac{\partial u_i}{\partial x_j} + \frac{\partial u_j}{\partial x_i} - \frac{2}{3}\delta_{ij} \frac{\partial u_l}{\partial x_l} \right) \tag{3}$$

The viscosity, thermal conductivity, and diffusion coefficients are written in the traditional manner as the sum of the molecular and turbulent components. The vector $\boldsymbol{H}$ contains the source terms related to combustion, turbulence, and radiation and are described in a later section.

The system is closed with an appropriate equation of state, which for a mixture of arbitrary fluids is given by Amagat's mixture rule

$$\frac{1}{\rho} = \sum_{m=1}^{NS} \frac{Y_m}{\tilde{\rho}_m} \tag{4}$$

where the individual density of each species component is given by $\tilde{\rho}_m = \tilde{\rho}_m(p, T)$. In this manner, arbitrary gaseous and liquid species can be included within the formulation (see Li et al. [21] for details), although the applicability of such a homogeneous-mixture model for multiphase flows depends on the nature of the particular flowfield. More detailed treatments of multiphase effects involve solving separate transport equations to represent the dynamics and thermal effects of the liquid field. Such methods are outlined in the following subsections.

2. *Eulerian–Lagrangian Multiphase Formulation*

The Eulerian–Lagrangian formulation solves the gas-phase equations in an Eulerian framework, similar to that described in the preceding section, and the liquid-phase equations in a Lagrangian framework, which describes the motion and transport of parcels of characteristic droplet groups. Droplet vaporization in the liquid phase introduces source terms in the gas-phase equations, which can be expressed as

$$\boldsymbol{H}_{\text{liq}} = \frac{\sum_l}{\Delta V} \begin{pmatrix} n_l \dot{m}_l \\ n_l \dot{m}_l u_{l,j} - \dfrac{1}{6}\pi \tilde{\rho}_l d_l^3 n_l \dfrac{\mathrm{d}u_{l,j}}{\mathrm{d}t} \\ n_l \dot{m}_l [c_p(T_l - T) - \lambda] \\ 0 \\ 0 \\ n_l \dot{m}_l \text{ or } 0 \end{pmatrix} \tag{5}$$

where $l = 1, 2, \ldots, L$ represents each droplet group and $\dot{m}_l$ represents the rate of vaporization of the lth droplet group. The mass source due to vaporization appears in the corresponding vapor species transport equation and is zero for the other gaseous species.

The Lagrangian equations for the liquid phase can be expressed as

$$\frac{\mathrm{d}\boldsymbol{Q}_l}{\mathrm{d}t} = \boldsymbol{H}_l \tag{6}$$

where

$$\boldsymbol{Q}_l = \begin{pmatrix} \tilde{\rho}_l V_l \\ u_{l,j} \\ T_l \end{pmatrix}; \qquad \boldsymbol{H}_l = \begin{pmatrix} -\dot{m}_l \\ \sum F_j / \tilde{\rho}_l V_l \\ -\dot{E}_l / \tilde{\rho}_l V_l c_{p,l} \end{pmatrix} \tag{7}$$

where $\boldsymbol{F}_j$ is the force on the droplet, $\boldsymbol{V}_l$ is the droplet volume, $\dot{m}_l$ is the vaporization rate, and $\dot{\boldsymbol{E}}_l$ is the thermal heating/cooling of the droplets. The preceding equations can be augmented by submodels for drag forces, collision forces, and so on. Likewise, droplet thermal effects can be accounted for by appropriate correlation terms for droplet heating, latent heat, etc. Cheng et al. [15] used an Eulerian–Lagrangian model in their hybrid rocket analysis, and the interested reader is referred to their paper for specific details. Additional details are also given by Chiu and Oefelein [28] and Grenda et al. [29].

3. *Eulerian–Eulerian Multifluid Formulation*

Eulerian–Eulerian multiphase formulations have also been used for spray combustion applications in general (e.g., see Habiballah and Dubois [30]) and for hybrid rocket flowfields in particular [17]. A general formulation involves solving multidimensional conservation laws for each liquid droplet group,

$$\frac{\partial \boldsymbol{Q}_l}{\partial t} + \frac{\partial \boldsymbol{E}_{l,i}}{\partial x_i} = \boldsymbol{H}_l \tag{8}$$

where

$$\boldsymbol{Q}_l = \begin{pmatrix} \tilde{\rho}_l \alpha_l \\ \tilde{\rho}_l \alpha_l u_{l,j} \\ \tilde{\rho}_l \alpha_l T_l \end{pmatrix}; \qquad \boldsymbol{E}_{l,i} = \begin{pmatrix} \tilde{\rho}_l \alpha_l u_{l,i} \\ \tilde{\rho}_l \alpha_l u_{l,i} u_{l,j} \\ \tilde{\rho}_l \alpha_l u_{l,i} T_l \end{pmatrix}; \qquad \boldsymbol{H}_l = \begin{pmatrix} -\dot{m}_l \\ \sum F_j \\ -\dot{\boldsymbol{E}}_l / c_{p,l} \end{pmatrix} \tag{9}$$

where the source terms have the same interpretations as in the Lagrangian formulation given earlier. The reader is referred to the paper by Lin and Chiu [17] for further details pertaining to hybrid rocket flowfields.

B. Physical Submodels

In addition to the equations of motion, several submodels are required to represent the liquid-droplet motion, thermal effects and vaporization, gas-phase chemistry, turbulence, and radiation transfer, as well as the fuel surface pyrolysis and regression. Because the main focus of the present chapter is on gas-phase hybrid rockets, we describe the gas-phase and fuel surface models in greater detail in the following sections.

1. *Gas-Phase Chemistry Model*

The gas-phase species transport equations contain source terms due to species production and depletion as a result of chemical reactions. The source term is

obtained by summing the species generation contributions from various elemental reactions,

$$H_m = \dot{w}_m = M_m \sum_{k=1}^{NR} (\dot{c}_m)_k \tag{10}$$

where NR is the total number of reactions, $(\dot{c}_m)_k$ is the rate of production of moles of species m by reaction k,

$$(\dot{c}_m)_k = ({\nu_{mk}}'' - \nu'_{mk}) \left(k_{fk} \prod_{n=1}^{N} C_n^{\nu'_{nk}} - k_{bk} \prod_{n=1}^{N} C_n^{\nu''_{nk}} \right) \tag{11}$$

where the kth reaction is written as

$$\sum_{m=1}^{N} \nu'_{mk} M_m \rightleftharpoons \sum_{m=1}^{N} \nu''_{mk} M_m \tag{12}$$

Here, ν'_{mk} and ν''_{mk} are the stoichiometric coefficients for the mth species, k_{fk} and k_{bk} are the forward and backward reaction rates, and M_m is the molecular weight of the mth species. C_m is the molar concentration of the species and is given by $C_m = \rho Y_m / M_m$. Simplified kinetics mechanisms for various hydrocarbon fuels are given by Westbrook and Dryer [31].

The computational model used here treats 1, 3-butadiene (C_4H_6) as the main product of HTPB pyrolysis. Detailed chemical kinetics are extremely complicated, involving over 50 species and hundreds of elementary reaction steps. In the present study we, therefore, use a global combustion model, involving two reaction steps, to represent the combustion of the gaseous products. The first step represents the oxidation of C_4H_6, whereas the second step represents the oxidation of wet CO,

$$\begin{gathered} C_4H_6 + 3.5O_2 \longrightarrow 4CO + 3H_2O \\ CO + 0.5O_2 \longleftrightarrow CO_2 \end{gathered} \tag{13}$$

As already noted, the second reaction can proceed in both directions. The rates of production and destruction of species are given by the following expressions:

$$\begin{gathered} \dot{w}_{C_4H_6} = -M_{C_4H_6} k_{f1} [C_4H_6][O_2] \\ \dot{w}_{O_2} = M_{O_2} [-3.5 k_{f1} [C_4H_6][O_2] - 0.5(k_{f2} [CO][O_2]^{0.5} - k_{b2} [CO_2])] \\ \dot{w}_{CO} = M_{CO} [4 k_{f1} [C_4H_6][O_2] - (k_{f2} [CO][O_2]^{0.5} - k_{b2} [CO_2])] \\ \dot{w}_{H_2O} = 3 M_{H_2O} k_{f1} [C_4H_6][O_2] \\ \dot{w}_{CO_2} = M_{CO_2} (k_{f2} [CO][O_2]^{0.5} - k_{b2} [CO_2]) \end{gathered} \tag{14}$$

The reaction rates k_f and k_b for the two reactions are expressed as Arrhenius functions, and the values of the constants used in this study are tabulated in Table 1.

Table 1 Two-step global chemistry model

Reaction	A_f	E_f	A_b	E_b
1	1.3496*e*10	−1.5108*e*4	0	0
2	2.2387*e*12	−2.10143*e*4	5.e8	−2.0143*e*4

2. Gas-Phase Turbulence Model

The source terms in the κ and ϵ transport equation arise due to the production and destruction of these quantities. For the standard $\kappa-\epsilon$ model [32] along with additional low Reynolds number terms introduced for near-wall effects [33], the source terms may be written as

$$\boldsymbol{H}_\kappa = \mu_t \mathcal{S} - \frac{2}{3}\rho\kappa\mathcal{D} - \rho\epsilon - (2\mu\kappa/n^2) \tag{15}$$

$$\boldsymbol{H}_\epsilon = C_1\mu_t(\epsilon/k)\mathcal{S} - \frac{2}{3}C_1\rho\epsilon\mathcal{D} - C_2 f_2(\rho\epsilon^2/k) - (2f_1\mu\epsilon/n^2) \tag{16}$$

where $\mu_t = C_\mu f_\mu \rho k^2/\epsilon$ and $\mathcal{S}$ and $\mathcal{D}$ are given by

$$\mathcal{S} = \left[\frac{\partial u_i}{\partial x_j} + \frac{\partial u_j}{\partial x_i} - \frac{2}{3}\delta_{ij}\frac{\partial u_k}{\partial x_k}\right]\frac{\partial u_i}{\partial x_j} \tag{17}$$

$$\mathcal{D} = \frac{\partial u_i}{\partial x_i} \tag{18}$$

Standard values are used for the constants in the $\kappa-\epsilon$ model: $C_\mu = 0.09$, $C_1 = 1.35$, and $C_2 = 1.8$. Other turbulence models such as the $\kappa-\omega$ model may also be used [34], although most hybrid studies have employed the $k-\epsilon$ model.

3. Radiative Transfer Model

The experimental studies reported in the Pennsylvania State University work [8, 9], as well as other hybrid tests conducted at the Jet Propulsion Laboratory, California Institute of Technology (JPL) [6] indicate that thermal radiation may be a significant contributor to the energy balance on the fuel surface particularly at low mass fluxes. Estimates of the radiative flux contribution to the total heat flux at the fuel surface range from 10% to 30% depending on the conditions in the combustor. In general, higher GOX flow rates lead to higher convective heat fluxes and lower radiation contributions, whereas lower flow rates lead to greater relative importance of radiation. These observations indicate the need for including a model for radiative transfer for the accurate prediction of the fuel surface regression rate. Moreover, it is necessary to assess the relative importance of radiation in a parametric manner, particularly at higher flow rates and as a sizing issue. Because the detailed modeling of radiative properties and radiative transfer in participating media is extremely difficult, we describe a simple radiative transfer model, which represents the radiative contribution phenomenologically.

In optically thin media, the gas-phase can be treated as a purely emitting medium

$$Q_{\text{rad,thin}} = \sum_{i,j} 4\sigma k_{ij} T_{ij}^4 \mathcal{V}_{ij} \mathcal{F}_{ij\to k} \tag{19}$$

where k_{ij} is the absorption coefficient, $\mathcal{V}_{ij}$ is the volume of the (i, j)th cell, and $\mathcal{F}_{ij\to k}$ is the view factor of that cell with respect to the kth grid location on the fuel-slab surface. Summing up the contributions from all of the cells in the computational domain yields the total radiative flux incident on a given axial location on the fuel surface. This in turn is employed in the interfacial energy balance used to determine the fuel surface regression rate.

In the optically thick limit, it is possible to represent the radiative flux using the diffusion approximation [35],

$$Q_{\text{rad,thick}} = -\lambda_R \frac{\partial T}{\partial y} \tag{20}$$

where $\lambda_R = (4/3)\pi c T^3/k$. In practice, it is likely that the gas is optically thick over some regions of the flowfield (as in very sooty regions of the flame), while it is optically thin in others. In the model, the absorption coefficient of the gaseous mixture is taken to be independent of temperature and of the wavelength of the radiation. The magnitudes are empirically determined by calibrating the results with the regression rate data from the subscale tests reported by Chiaverini et al. [8].

4. HTPB Surface Pyrolysis Model

The pyrolysis of the solid fuel (HTPB in this work) into gaseous products is modeled in semi-empirical fashion. Following the work of Cohen et al. [22] and Arisawa and Brill [23, 24], the rate of pyrolysis is described by means of an Arrhenius-type relationship

$$\rho_s r_b = A_s \exp(-E_a/R_u T_s) \tag{21}$$

where T_s is the fuel surface temperature, E_a is the activation energy, and A_s is the reaction constant. The preceding equation (Eq. 21) has two unknowns, the regression rate and the surface temperature, and we, therefore, require an additional condition to solve for these quantities. This is provided by the interfacial energy balance on the fuel surface as discussed in the following section. The models of Arisawa–Brill and Cohen et al. are summarized in Table 2. Most of the computational results given here were based on the Arisawa–Brill model, although

Table 2 Solid-fuel pyrolysis models

Model	A_s	E_a
Cohen et al. [22]	2.99*e*3	−8.577*e*3
Arisawa–Brill [23, 24]	2.208*e*3	−6.797*e*3

computations have also been performed with the Cohen et al. model to assess sensitivity to these parameters [19].

Note that these models do not explicitly account for pressure effects, which have been shown to be of importance at high mass fluxes [36]. More recently, studies have indicated the significance of heterogeneous surface reactions, which also suggests the need for more comprehensive surface chemistry models [37].

5. Solid–Gas Interface Formulation

The coupling between the solid (fuel) and gaseous phases is introduced through an interfacial boundary condition. The energy balance at the solid–gas interface involves a balance between the convective, diffusive, and radiative fluxes on the gas side and the diffusive and heat of pyrolysis on the solid side and is, thus, given by

$$-\lambda \frac{\partial T}{\partial y} + Q_{\text{rad}} + \rho v h - \sum_{m=1}^{N} \rho \mathcal{D}_m \frac{\partial Y_i}{\partial y} h_m = -\lambda_s \left(\frac{\partial T}{\partial y} \right)_s - \rho_s r_b h_s \tag{22}$$

where the left side of this equation represents the gas-phase quantities and the right side represents the solid-phase quantities. The first term on the left is the convective heat flux to the wall, whereas the second term is the total radiative flux. The convective heat flux is obtained from the gas-phase solution, whereas the radiative flux is modeled as discussed in the preceding section.

The two relations are augmented by a closed-form solution for locally one-dimensional thermal conduction in the solid-fuel slab,

$$T(y) = T_\infty + (T_s - T_\infty), \exp(-r_b/\nu_{ts} y) \tag{23}$$

where T_∞ is the temperature of the unheated fuel, ν_{ts} is the thermal diffusivity of the fuel slab, and r_b is the fuel surface regression rate. The derivative of Eq. (23) may be substituted into the interfacial energy balance equation (22) to obtain the conduction heat loss in the solid phase. When Eqs. (21–23) are combined, both the fuel surface temperature T_s and the surface regression rate r_b may be determined.

Finally, the wall blowing rate is obtained by applying a mass balance at the interface,

$$\rho v = -\rho_s r_b \tag{24}$$

For the gas-phase boundary condition, the preceding set of relations is augmented by the standard no-slip axial velocity, the normal momentum equation (for the interface pressure), and the appropriate species balances (for the species mass fractions Y_m).

C. Computational Methodology

The equations of motion coupled with the physical submodels are typically solved following either the so-called density-based approach or the pressure-based approach. Whereas both classes of methods have some specific strengths and weaknesses, we stress that the approaches are in fact closely related. They differ mainly

in how the discrete system is formulated and how the resulting nonlinear algebraic system is iteratively solved. Both classes of methods are discussed briefly in the following paragraphs.

1. Density-Based Approach

The solution methodology used in our hybrid rocket analysis follows the so-called density based approach [19]. In this method, the unsteady form of the governing equations is used to march the nonlinear equations to a steady-state solution. However, rather than use the physical time derivatives, we employ preconditioned or pseudotime derivatives, which are selected to optimize both the accuracy of the discrete formulation and the convergence rate of the iterations [20, 21]. For time-accurate computations, the so-called dual-time paradigm is invoked. In this framework, the equations are marched in the physical time domain using the standard set of time derivatives. Then, at each physical time step, the equations are solved iteratively using a separate set of pseudotime derivatives. Thus, the pseudotime formulation ensures proper accuracy and convergence properties at each physical time step, whereas temporal accuracy is ensured in the physical time level.

Detailed descriptions of the methodology is beyond the scope of the chapter. We simply note that the equations are discretized using a second-order accurate, second-order upwind, Roe-type flux formulation for the inviscid fluxes and central differences for the viscous fluxes. The resulting algebraic system is solved iteratively within a preconditioned time-marching framework, wherein the time step nominally plays the role of the underrelaxation parameters. The resulting linear system is solved using an approximate factorization strategy that involves a series of block tridiagonal solutions in each coordinate direction. For more details of the methodology, the interested reader is directed to the work of Sankaran and Merkle [20].

2. Pressure-Based Approach

The hybrid modeling analysis of Cheng et al. [15], Lin and Chiu [17], Serin and Gogus [25] as well as Knuth et al. [27] adopt the alternate paradigm of the pressure-based solution methodology. Again, we do not present the details of the methodology here. We note that the governing equations are usually discretized on a staggered grid arrangement or by using a Rhie and Chow form of dissipation [38]. The nonlinear equations are solved iteratively using underrelaxation parameters defined for each of the transport equations. For purposes of solution, the coupled system is further segregated into a series of transport equations and a pressure Poisson equation, which enforces global mass conservation. The segregated approach is generally cast within a predictor–corrector framework, and the constituent equations are solved in a sequential fashion. Fundamental details of the approach are given by Patankar [18].

III. Computational Results

Representative computational predictions of hybrid rocket flowfields are presented in this section. The results correspond to the slab-burner geometry tested at Pennsylvania State University [8, 9]. The experiments used HTPB as the solid fuel and GOX as the oxidizer. Accordingly, the results presented here are

restricted to the gas-phase system. Multi-phase predictions have been reported by other researchers, notably Cheng et al. [15] and Lin and Chiu [17]. The focus of the results shown here are to characterize the fuel regression rate by comparing and calibrating the data against the detailed in situ measurements of Chiaverini et al. [8, 9].

A. Representative Flowfields

We begin by showing representative combustor flowfields for the experimental slab-burner geometry. Note that all of the computational results were two-dimensional and obtained using a quasi-steady assumption. In other words, the fuel port dimensions were held fixed at values corresponding to different stages of the burn, and steady-state solutions were obtained to provide the instantaneous burning rates at that operating condition. We note that the quasi-steady assumption is justifiable because the fuel surface regression rate (typically about 1 mm/s) is extremely small compared to the axial velocity in the port (about 1–100 m/s depending on the operating conditions).

Figure 1 shows the grid geometry used for a typical test run and shows three different-sized ports, which approximately correspond to the start, middle, and end of the burn. In each case, the grid size was 151×61. The length of the HTPB fuel slabs corresponds to the experimental configuration and is about 23 in. (580 mm). The initial port height, that is, the distance between the fuel slabs, is 0.5 in. (12 mm). The fuel port is, therefore, a very high aspect ratio domain and the y coordinate has been exaggerated by a factor of 10 so that the grid and flowfield details are visible.

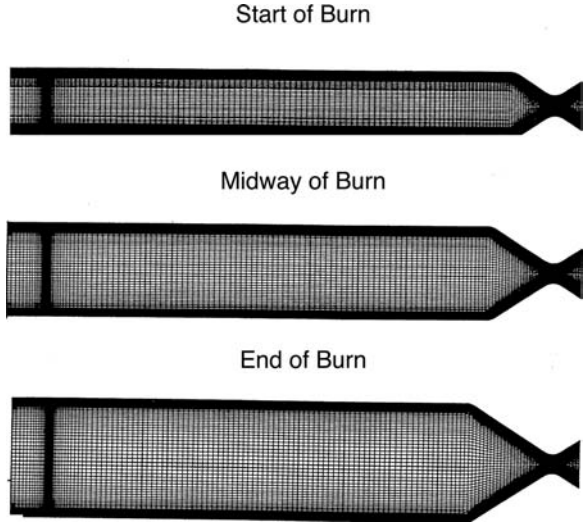

Fig. 1 Grid geometry used in HTPB/GOX two-dimensional slab-burner computations for three different stages in burn.

The fuel slabs are located in the straight section upstream of the converging–diverging nozzle and represent the wall boundary of the gaseous flow in the fuel port. The grid is strongly stretched in the near-wall region to resolve the turbulent boundary layer adjacent to the fuel surface. The axial clustering of grid cells indicates the leading edge of the fuel slab. In the computations, the details of the leading-edge and trailing-edge regions of the fuel slab were omitted because the main purpose was the characterization of the fuel surface regression rate. Furthermore, in many of the calculations, the computational domain included only the straight channel section of the configuration, that is, the nozzle was not included. These simplifications of the geometrical details allowed relatively modest grid sizes to be used, thereby making it economical to perform a larger number of parametric computations.

We first present results for a representative test case (corresponding to test 11 of Chiaverini et al. [9]). The computations were run at a constant GOX mass flow rate, which, for this test, was set at 0.16 kg/s. The specific flow rate G_0 ($= \dot{m}_{\mathrm{GOX}}/A_p$), however, decreases with burn time as a consequence of the surface regression and the corresponding increase in port area A_p. Computational results are shown at three stages during the burn: near the start of the burn, where the port height was 16 mm corresponding to a specific flow rate, $G_0 = 165\,\mathrm{kg/m^2 \cdot s}$; midway through the burn, at a port dimension of 20 mm corresponding to $G_0 = 132\,\mathrm{kg/m^2 \cdot s}$; and near the end of the burn, when the passage height was 26 mm resulting in an oxidizer flow rate of $G_0 = 102\,\mathrm{kg/m^2 \cdot s}$.

Figure 2 shows the temperature contours at the three stages in the burn. In all three situations, the temperature contours in the vicinity of the flame are similar,

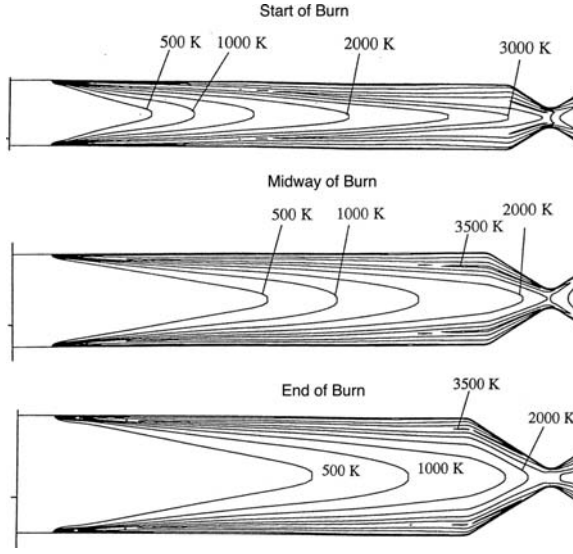

Fig. 2 Temperature contours of two-dimensional slab-burner configuration obtained for three stages in burn.

with a peak temperature of about 3500 K. The temperature contours also reveal that the combustion is most efficient at the start of the burn, which corresponds to the highest GOX specific flow rate and, typically, to the highest fuel regression rate. As the burn progresses, the port opens up and the GOX specific flow rate decreases as do the regression rate and the combustion efficiency. Indeed, near the start of the burn, the flame is observed to extend all of the way to the centerline of the port, whereas at the end of the burn, the temperature contours show that the flame remains close to the fuel surface. This indicates that the incoming GOX is not fully used during the later stages of the burn.

Corresponding contours of gas velocity at the three stages in the burn are shown in Fig. 3. The velocity contours show that the heat addition (due to combustion) and the mass addition (due to fuel regression) lead to dramatic acceleration of the core gases. Again, the acceleration is observed to be strongest near the start of the burn because of the higher regression rate and the smaller port area. As the burn proceeds, the gas acceleration becomes noticeably less pronounced. Figures 3 then clearly demonstrate the relationship between the fluid dynamics and the surface heat fluxes. Higher regression rates lead to faster gas velocities, which consequently results in increased convective heat fluxes. The higher convective fluxes in turn lead to increased pyrolysis rates and increased regression.

Contours of GOX mass fraction are given in Fig. 4. Again, the GOX contours reveal that oxygen consumption in the core gases is more efficient in the early stages in the burn. However, it is apparent that, even in the beginning stages, the GOX is not completely consumed. At this instance, the integrated fuel mass flux at the fuel surface indicates that the O/F ratio in the combustor is about 1.7, indicating that the combustor is fuel rich. (The stoichiometric ratio is about 3.2.) The presence of unburned GOX at the start of the burn is, therefore, an indication of the degree of mixing in the combustor. Toward the end of the burn, the overall O/F ratio in the combustor is 3.2, which is very nearly stoichiometric. Note that

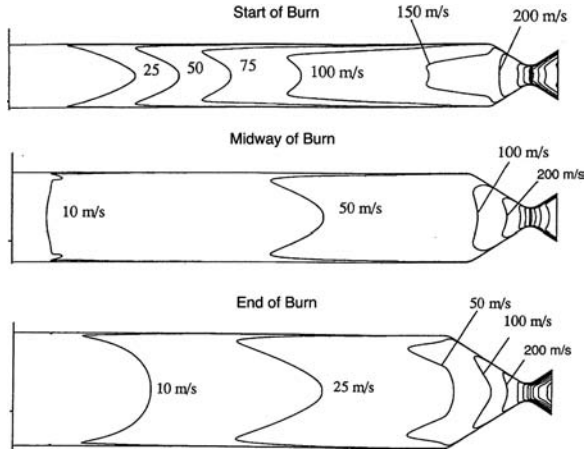

Fig. 3 Velocity contours of two-dimensional slab-burner configuration obtained for three stages in burn.

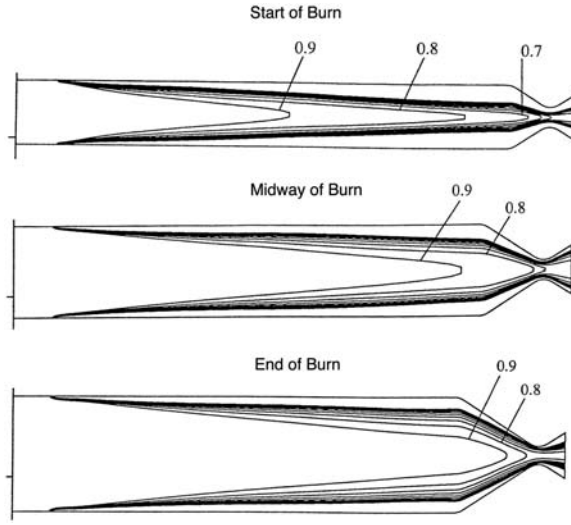

Fig. 4 GOX mass fraction contours of two-dimensional slab-burner configuration obtained for three stages in burn.

the experimental configuration includes a mixing chamber in the aft section of the combustor. The computational geometry is somewhat simplified in this region, and it is likely that the computational results underpredict the aft mixing of the fuel and oxidizer. Because the present study is focused on characterization of the surface regression rate, the details of the aft section are not crucial to the analysis. Clearly, these details should be included for more accurate estimates of overall combustion efficiency.

The fuel surface regression rates at the three times in the burn are shown on Fig. 5. As noted earlier, these predictions confirm that the regression rate is highest during the start of the burn where G_0 is the highest and decreases significantly as the test proceeds. Its nominal magnitude ranges from 0.5 to 1.5 mm/s. The decrease in surface regression rate with time in the burn is related to the decrease in the magnitude of the specific flow rate G_0, which is in qualitative agreement with boundary-layer theory.

The results in Fig. 5 also show that the regression rate varies with axial location for all three surface positions. The large values of surface regression at the leading edge of the fuel slab is due to the singularity in the heat flux computation at this point. Beyond the leading edge, the regression rate is observed to decrease gradually, until it reaches a minimum, and then it increases more or less monotonically. At all three times of burn, the regression rate at the back end is faster than that at the front end. The increase in the regression rate with axial location can be traced to the mass addition effect of the pyrolyzing fuel, which results in an increase in the total specific flow rate as the flow moves downstream. This result is again in qualitative agreement with boundary-layer theory if the local regression rate were expressed in terms of the local specific flow rate (based on the total flow rate in the port).

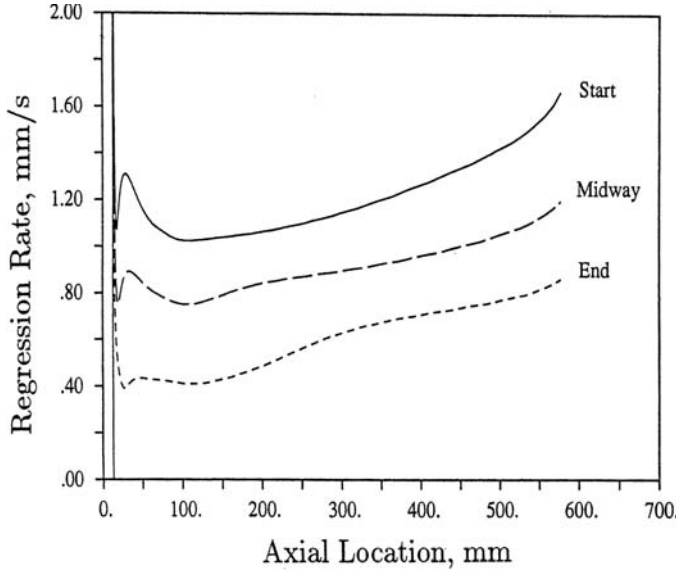

Fig. 5 Fuel surface regression rates of two-dimensional slab-burner configuration for three stages in burn.

B. Model Calibration

Both instantaneous and time-averaged regression rates have been experimentally obtained for the slab-burner configuration under consideration here [8, 9]. The instantaneous results were obtained at several axial stations using two independent techniques: ultrasonic pulse–echo analysis and x-ray radiography. Time-averaged results were obtained by measuring pre- and postfiring fuel-slab web thickness using calipers at several axial stations along the length of the fuel slab. In the computational study, the predictions were compared with both the instantaneous and the averaged data for several of the experimental test runs. In addition to providing a database for validating the computational results and trends, the experimental data were also used to estimate the relative magnitude of radiative flux term in the energy balance at the fuel/gas interface. When these data were used, the absorption coefficient used in the radiative transfer model was calibrated to yield accurate regression rate levels.

The time-averaged regression rate data from test 11 were used to calibrate the radiative transfer model. To obtain an averaged regression rate from the computational data, we performed a simple average of the computed regression rates for five different stages in the burn. The regression rate results obtained midway through the burn proved to be very close to the computed average, and the calibration of the model was done using the midway predictions. Figure 6 shows the computed results with and without radiation along with the time-averaged experimental data for test 11. It is apparent that, for this condition, the regression rate is slightly underpredicted when the radiation effects are ignored. In particular, at

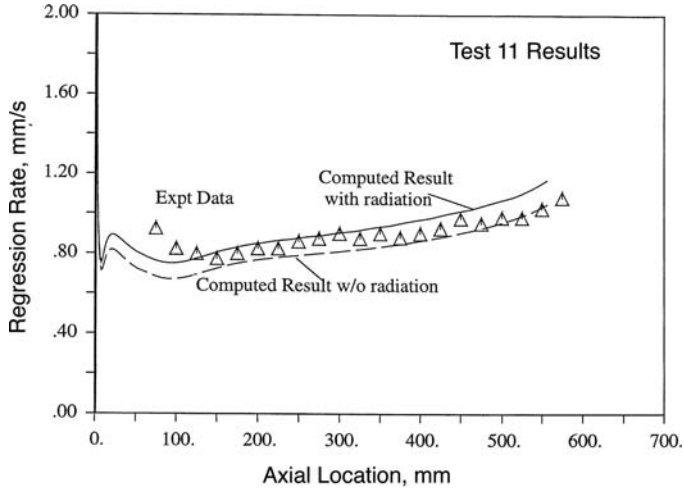

Fig. 6 Experimental (test 11, Chiaverini et al. [8]) and computational regression rates with and without radiation.

the midlocation of the fuel slab, the computed regression rate is about 0.8 mm/s, whereas the experimental rate is 0.9 mm/s, a discrepancy of about 10%. In the calculation with radiation effects included, the radiative absorption coefficient was varied until a close match was obtained with the experimental data at the midlocation on the slab. Once calibrated, the radiative properties were held fixed for all of the parametric studies reported here.

With the calibrated radiative transfer model, the overall agreement with the test 11 data is observed to be reasonably good. The axial variation of the regression rate is qualitatively well predicted. The regression rate decreases initially near the leading edge and then gradually increases. These trends follow from the trends in the convective heat flux, which is discussed later. The computed values are observed to be somewhat under-predicted near the leading edge and overpredicted near the end of the slab. Near the leading edge, the experiments indicate an initial laminar region, which is followed by a transition region, before the flow becomes fully turbulent. In the computational model, because the $\kappa-\epsilon$ model cannot represent transition to turbulence, the leading-edge effects cannot be accurately captured.

C. Model Validation

Detailed comparisons of the fuel surface regression rate have been made between the computational and experimental results for several test runs. Figure 7 shows the comparison of the time-averaged regression rates for three such cases, tests 8, 9, and 11. The GOX flow rate for the tests were 0.1 kg/s (test 8), 0.16 kg/s (test 11), and 0.2 kg/s (test 9). The corresponding specific flow rates were 105, 165, and 210 $\mathrm{kg/m^2 \cdot s}$ (0.15, 0.23, and 0.3 $\mathrm{lb/in.^2 \cdot s}$) respectively. The experimental results are time-averaged regression rate data over the whole test, whereas the computations show the results midway through the burn (representing an approximate

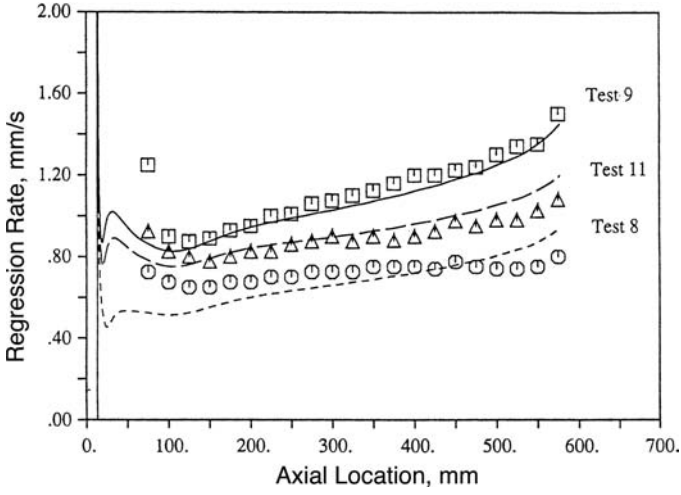

Fig. 7 Experimental and computational regression rates for tests 8, 9, and 11; test conditions from [8].

average regression rate). In all cases, fairly good agreement can be observed over most of the length of the fuel slab. Importantly, the relative change in the regression rate as a function of the GOX flow rate is well predicted. This indicates that the balance between convective and radiative effects are correctly represented over a range of flow rates.

Convective and radiative heat fluxes at the fuel surface for the three test conditions are given in Fig. 8. As noted earlier, the radiation model was calibrated using the experimental data of test 11 ($G_0 = 0.23\,\text{lb/in.}^2 \cdot \text{s}$). For this test case, the radiative fluxes contribute about 10–15% of the total wall heat flux (at the midlocation on the fuel slab). In the cases shown, the convective heat fluxes are observed to decrease steadily with decrease in the specific flow rate G. The radiative fluxes, on the other hand, are more or less invariant to the specific flow rate. Thus, the radiation becomes more of a factor at low specific flow rates. For the conditions in test 8 ($G_0 = 0.15\,\text{lb/in.}^2 \cdot \text{s}$), radiation accounts for almost 25% of the total heat flux. By contrast, at the higher flow rate of test 9 ($G_0 = 0.3\,\text{lb/in.}^2 \cdot \text{s}$), radiation accounts for less than 10% of the total heat flux. Finally, for the even higher flow rate of test 17 ($G_o = 0.56\,\text{lb/in.}^2 \cdot \text{s}$), the radiative contribution (not shown here) is negligibly small and the convective heat flux accounts entirely for the heat flux on the fuel surface. The computational estimates of the relative importance of radiative heat transfer are also in good general agreement with the estimates obtained from the experimental correlations developed by Chiaverini et al. using the same experimental data [8, 9].

Figure 9 shows the predicted fuel surface temperatures for the three test cases. Note that the fuel surface temperature is obtained as part of the flowfield solution and is determined by the energy balance enforced on the solid–gas interface. From the results, it is evident that the surface temperature follows the trends in the

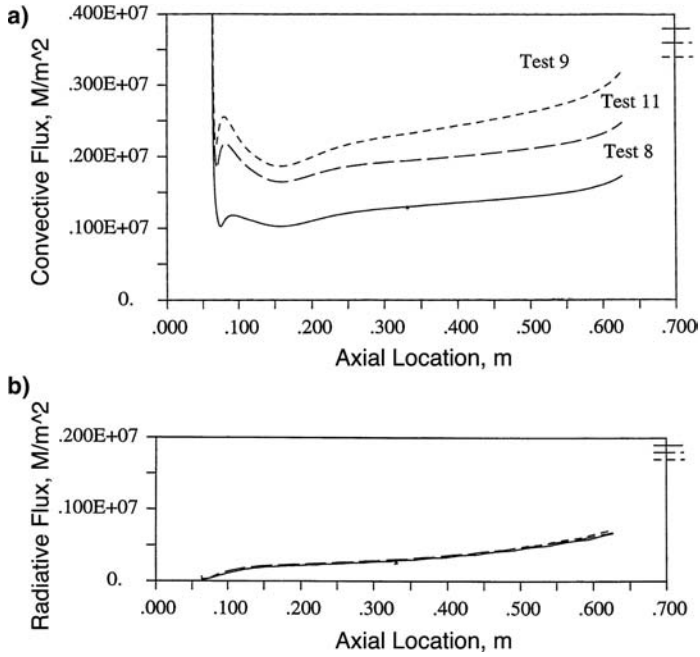

Fig. 8 Computed convective and radiative fluxes at fuel surface for tests 8, 9, and 11; test conditions from Chiaverini et al. [8].

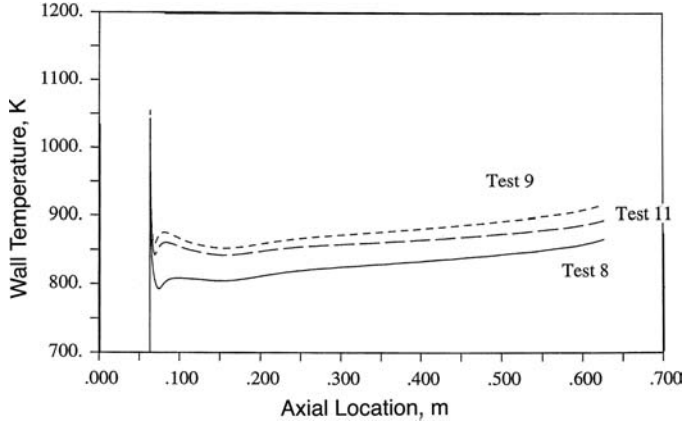

Fig. 9 Computed fuel surface temperatures for tests 8, 9, and 11; test conditions from Chiaverini et al. [8].

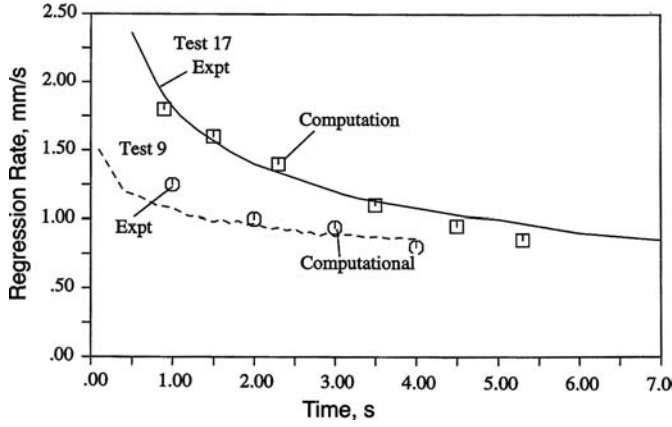

Fig. 10 Instantaneous regression rate comparison at different stages in burn, tests 9 and 17; test conditions from Chiaverini et al. [8].

regression rate. The wall temperatures are observed to be in the range of 800–900 K, which is in reasonable agreement with the experimental estimates of 900–1000 K.

Finally, we show comparisons of the instantaneous regression rate at a given axial location for tests 9 and 17 in Fig. 10. The instantaneous measurements, obtained using the ultrasonic pulse–echo system, show that the regression rate is at its maximum near the start of the test and decreases throughout the burn. The comparisons of the computational predictions with the experimental measurements are again observed to be reasonably good. As noted earlier, the decrease in regression rate is due to the increasing port width caused by the regressing fuel surface, which in turn results in decreasing values of the the specific flow rate G. We note here that test 17 has a GOX mass flow rate of 0.36 kg/s and an initial head end $G = 370\,\text{kg/m}^2 \cdot \text{s}$ ($0.56\,\text{lb/in.}^2 \cdot \text{s}$). This corresponds to the highest flow rate tested in the experimental study. It is encouraging to note that the computational predictions remain in good general agreement with the data even at this much higher value of G. Moreover, the temporal variation of the regression rate is also very well represented by the computational model.

D. Size Scaleup Effects

The effects of chamber sizing on the regression rate is very important in the design of hybrid rocket motors. Once the oxidizer mass flux and the overall O/F ratio of the motor have been set, the regression rate dictates the port dimensions. A reliable understanding of the effect of size scaleup on the regression rate is imperative if experimental and test results are to be used to build larger, full-size motors. The analysis in this section considers the effects of size scale-up between different cylindrical (axisymmetric) port sizes.

Three different motor sizes are considered. For all three configurations, the non-dimensional chamber length was held constant at $L/D = 35$, the oxidizer flow rate was fixed at the value, $G = 565\,\text{kg/m}^2 \cdot \text{s}$ ($0.8\,\text{lb/in.}^2 \cdot \text{s}$), and the chamber pressure was set at 900 psia. We refer to the three sizes as the laboratory-scale, the

intermediate-scale, and the full-scale motors. The respective dimensions of these cases are $L = 23$ in. and $D = 0.66$ in. for the laboratory-scale motor, $L = 100$ in. and $D = 2.86$ in. for the intermediate-scale motor, and $L = 350$ in. and $D = 10$ in. for the full-scale motor. The length chosen for the subscale motor is the same as that used in the planar slab-burner experiments, but unlike the earlier results, the results shown here employ an axisymmetric port configuration. Note that keeping the L/D fixed for the three sizes not only ensures geometric similarity but also maintains the same O/F ratio in the three combustors, provided that the regression rates are independent of the sizing.

The predicted surface regression rates for the three motor sizes are presented in Fig. 11 as a function of the normalized axial distance from the upstream end. The predictions show that the regression rate decreases somewhat as the port dimension is increased. At the midpoint location on the slab ($x/L = 0.5$), the regression rate is about 3 mm/s for the laboratory-scale, 2.5 mm/s for the intermediate geometry, and about 2.2 mm/s for the full-scale configuration.

Temperature contours for the three different sizes are given in Fig. 12. The flame location may be approximately identified from the peak temperature. Note that although the plots are labeled in physical units (meters), they have all been scaled to the same size for comparison. The temperature contours in the laboratory-scale solution show that the flame reaches the centerline before the end of the duct ($x/D = 35$), indicating nearly complete consumption of the oxidizer. By contrast, for the two larger sizes, the flame remains confined to the near-wall region and a portion of the core gas remains unburned. This suggests that the flame is nearer to the wall in nondimensional terms in the larger scale motors, although it is farther from the wall in dimensional terms, as noted later. Additionally, this also indicates that the larger motors do not burn as efficiently as the subscale motor. Both of these observations are consistent with the slower surface regression rates seen in Fig. 11 for the larger motor.

To understand these trends better, we examine the relative contribution between the convective and radiative fluxes to the wall heat flux. These components are

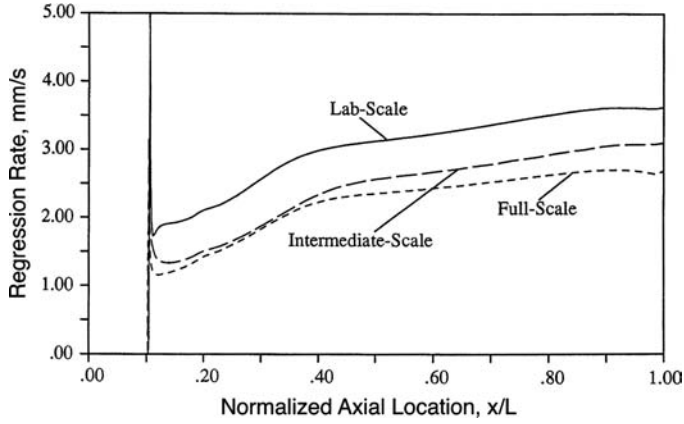

Fig. 11 Fuel regression rates for three hybrid burner configurations.

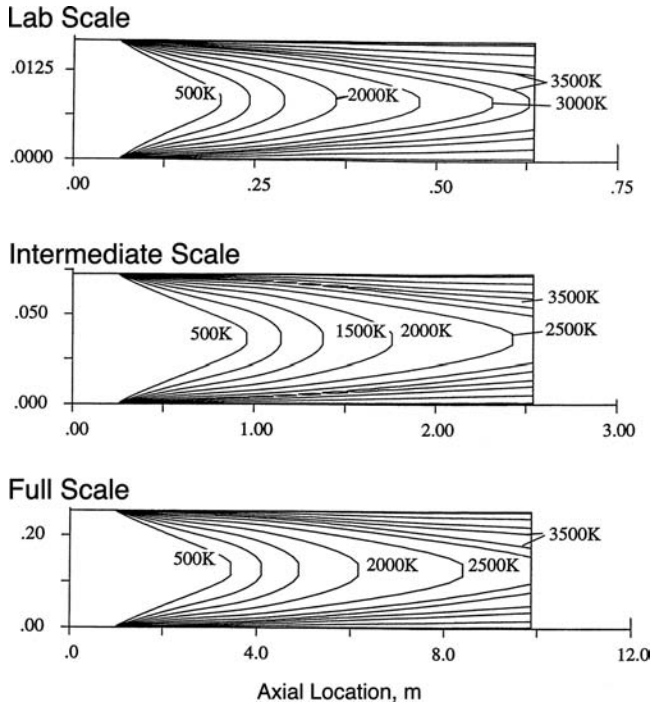

Fig. 12 Temperature contour predictions for three hybrid rocket sizes.

shown in Fig. 13 for the three motor sizes. The qualitative trends are immediately apparent. The convective heat flux decreases with increasing motor size, whereas the radiative flux increases. Specifically, the radiation becomes increasingly more important for larger motor sizes. The decrease in convective flux is, however, larger

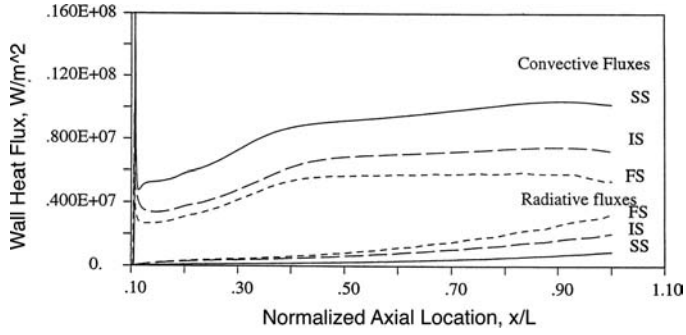

Fig. 13 Predicted convective and radiative fluxes at fuel surface for three hybrid rocket sizes: subscale (SS), intermediate scale (IS), and full scale (FS).

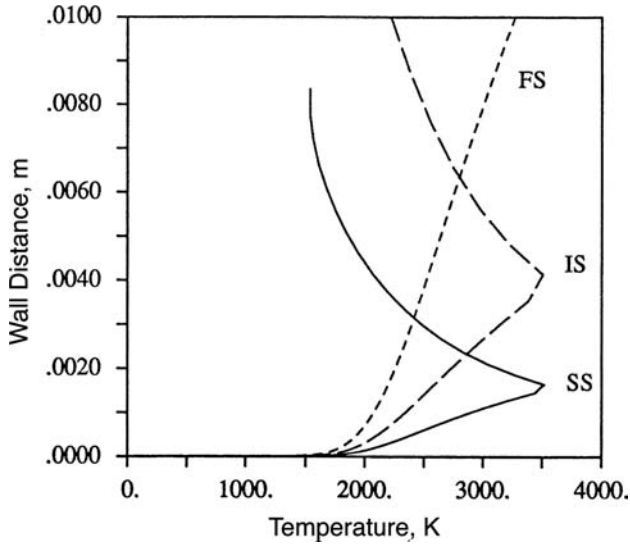

Fig. 14 Predicted near-wall temperature profiles for three hybrid rocket sizes: subscale (SS), intermediate scale (IS), and full scale (FS).

so that the net heat flux, that is, the sum of convection and radiation, decreases with size.

The reason for the decrease in the convective heat flux is evident in Fig. 14, which shows the near-wall temperature profiles as a function of the physical distance from the fuel surface. The full-scale configuration is observed to have a relatively shallow temperature gradient at the wall, that is, the flame is farthest from the wall, whereas the laboratory-scale configuration has the steepest gradient, that is, the flame is closest to the wall. Consequently, the convective heat flux decreases with increasing motor size. On the other hand, the reason that the radiation increases with size is because it is a volumetric source, whose contribution depends on the volume-to-surface ratio. Larger motors possess larger volume-to-surface ratios and, therefore, have higher radiative flux contributions. Furthermore, the radiative flux is also controlled by the temperature field, which we have seen is dependent on the size to a certain extent. We caution that the radiative transfer model used here is considerably simplified and the present sizing results must be treated as preliminary. More detailed radiative transfer models and accurate radiative properties are required to make more substantive predictions.

IV. Summary

Hybrid rocket combustion involves the burning of a solid fuel such as HTPB in a gaseous or liquid oxidizer stream. CFD modeling of these flowfields requires the coupled solution of the Navier–Stokes equations along with turbulence, combustion, multiphase effects, solid-fuel pyrolysis, and radiation. In this chapter, we have described several modeling frameworks, such as the homogeneous-mixture

formulation, the Eulerian–Lagrangian formulation, and the Eulerian–Eulerian multifluid formulation. The homogeneous-mixture approach is an extension of multicomponent gaseous models and assumes that the gases and liquids are in dynamic and thermal equilibrium. The Eulerian–Lagrangian method treats the gas phase in the traditional Eulerian manner, whereas the liquid-phase droplets are tracked using a Lagrangian method. The Eulerian–Eulerian formulation treats both phases within a common framework and involves the solution of coupled sets of conservation laws for each characteristic droplet group. The methods are closed by a generalized equation of state that is valid for arbitrary fluids. All three approaches have been employed in the hybrid modeling literature, although they have specific strengths and shortcomings associated with them.

The fluid dynamic equations must be coupled with other constituent equations to describe the physics involved with combustion, turbulence, pyrolysis, and radiation. We have described appropriate submodels to describe these interactions, focusing on HTPB/GOX flowfields. The governing equations are solved in the Reynolds averaged sense and are coupled to a standard $\kappa-\epsilon$ turbulence model to determine the eddy viscosity. Gas phase combustion is treated with simplified two-step, finite-rate kinetics for the combustion of butadiene (C_4H_6) in oxygen. Radiation is handled in a phenomenological manner with an optically thin/thick model that involves specification of the gaseous absorption coefficient (or opacity). Solid surface pyrolysis is modeled using an Arrhenius expression that is a function of the fuel surface temperature.

The computational results presented are concerned with modeling the Pennsylvania State University slab-burner configuration. Both averaged as well as instantaneous regression rate data are available for HTPB/GOX. The computations were carried out as a series of steady-state solutions at various stages in the burn; in other words, as the burn proceeded, the fuel port dimensions were enlarged to account for the fuel regression. As a first step, the experimental data were used to calibrate the selection of the radiative properties of the gases. This was done to match the predicted and measured average regression rate at the midlocation of the fuel slab for a particular test run. Once calibrated, the model was held fixed for all subsequent parametric computations. Comparisons of the averaged and instantaneous regression rate data indicate reasonable agreement with the trends over a wide range of oxidizer flow rates. In general, increasing the flow rate increases the convective heat fluxes, which leads to faster regression. At lower flow rates, radiative transfer was observed to be a significant contributor to the surface heat flux. Finally, the computations were also employed to study size scaleup trends. In general, convective heat fluxes are reduced for larger sizes (at comparable specific flow rates), whereas radiative transfer is increased. More detailed radiative models may be necessary to make quantitative predictions for full-size motors.

In conclusion, we note that the use of CFD to model hybrid rocket flowfields is still in its infancy. Many challenges remain, such as the modeling of multiphase flows, turbulence, solid- and gas-phase combustion, and radiation. However, given the availability of large-scale computing resources along with recent advances in modeling time-dependent turbulent flows and multiphysics problems such as conjugate heat transfer, one can anticipate that major strides will be made in the modeling of hybrid flowfields in the coming decade.

References

[1] Marxman, G. A., Wooldridge, C. E., and Muzzy, R. J., "Fundamentals of Hybrid Boundary Layer Combustion," *Heterogeneous Combustion*, Progress in Astronautics and Aeronautics, Vol. 15, AIAA, Reston, VA, 1964, pp. 485–521.

[2] Marxman, G. A., "Combustion in the Turbulent Boundary Layer on a Vaporizing Surface," *Proceedings of the Tenth Symposium on Combustion*, Combustion Inst., Pittsburgh, PA, 1965, pp. 1337–1349.

[3] "Hybrid Propulsion Technology," Final Rept. port, General Dynamics–Thiokol–Rocketdyne, NASA CR 183972, 183973, 183974, 183975, Nov. 1989.

[4] Boardman, T. A., Carpenter, R. L., Goldberg, B. E., and Shaeffer, C. W., "Development and Testing of 11- and 24-inch Hybrid Motors Under the Joint Government/Industry IR and D Program," AIAA Paper 93-2552, AIAA/SAE/ASME/ASEE 29th Joint Propulsion Conference and Exhibit, Monterey, CA, June, 1993.

[5] Strand, L. D., Ray, R. L., and Cohen, N. S., "Hybrid Rocket Combustion Study," AIAA Paper 93-2412, AIAA/SAE/ASME/ASEE 29th Joint Propulsion Conference and Exhibit, Monterey, CA, June, 1993.

[6] Strand, L. D., Jones, M. D., Ray, R. L., and Cohen, N. S., "Characterization of Hybrid Rocket Internal Heat Flux and HTPB Fuel Pyrolysis," AIAA Paper 94-2876, AIAA/SAE/ASME/ASEE 30th Joint Propulsion Conference and Exhibit, Indianapolis, IN, June 1994.

[7] Lengelle, G., Fourest, B., Godon, J. C., and Guin, C., "Condensed Phase Behavior and Ablation Rate of Fuels for Hybrid Propulsion," AIAA Paper 93-2413, AIAA/SAE/ASME/ASEE 29th Joint Propulsion Conference and Exhibit, Monterey, CA, June, 1993.

[8] Chiaverini, M. J., Serin, N., Johnson, D. K., Lu, Y., Kuo, K. K., and Risha, G. A., "Regression Rate Behavior of Hybrid Rocket Solid Fuels," *Journal of Propulsion and Power*, Vol. 16, No. 1, 2000, pp. 125–132.

[9] Chiaverini, M. J., Kuo, K. K., Peretz, A., and Harting, G. C., "Regression-Rate and Heat-Transfer Correlations for Hybrid Rocket Combustion," *Journal of Propulsion and Power*, Vol. 17, No. 1, 2001, pp. 99–110.

[10] Knuth, W. H., Chiaverini, M. J., Sauer, A. J., and Gramer, D. J., "Solid Fuel Regression Rate Behavior of Vortex Hybrid Rocket Engines," *Journal of Propulsion and Power*, Vol. 18, No. 3, 2002, pp. 600–609.

[11] Majdalani, J., and Vyas, A. B., Rotational Axisymmetric Mean Flow for the Vortex Injection Hybrid Rocket Engine, AIAA Paper 2004-3475, AIAA/SAE/ASME/ASEE 40th Joint Propulsion Conference and Exhibit, Fort Lauderdale, FL, July 2004.

[12] Majdalani, J., and Vyas, A. B., "Inviscid Models of the Classic Hybrid Rocket," AIAA Paper 2004-3474, AIAA/SAE/ASME/ASEE 40th Joint Propulsion Conference and Exhibit, Fort Lauderdale, FL, July 2004.

[13] Karabeyoglu, M. A., Altman, D., and Cantwell, B. J., "Combustion of Liquefying Hybrid Propellants Part 1: General Theory," *Journal of Propulsion and Power*, Vol. 18, No. 3, 2002, pp. 610–620.

[14] Karabeyoglu, M. A., and Cantwell, B. J., "Combustion of Liquefying Hybrid Propellants," *Journal of Propulsion and Power*, Vol. 18, No. 3, 2002, pp. 621–630.

[15] Cheng, G. C., Farmer, R. C., Jones, H. S., and McFarlane, J. S., "Numerical Simulation of the Internal Ballistics of a Hybrid Rocket Motor," AIAA Paper 94-0554, Aerospace Sciences Meeting and Exhibit, 32nd, Reno, NV, Jan. 1994.

[16] Chen, Y. S., Liaw, P., Shang, H.-M., and Chen, C. P., "Numerical Analysis of Complex Internal and External Viscous Flows with a Second-Order Pressure-Based Method," AIAA Paper 93-2966, 24th Fluid Dynamics Conference, Orlando, FL, July 1993.

[17] Lin, C. L., and Chiu, H. H., "Numerical Analysis of Spray Combustion in Hybrid Rockets," AIAA Paper 95-2687, AIAA/SAE/ASME/ASEE 31st Joint Propulsion Conference and Exhibit, San Diego, CA, July, 1995.

[18] Patankar, S. V., *Numerical Heat Transfer and Fluid Flow*, Series in Computational Methods and Thermal Science, McGraw–Hill, New York, 1980.

[19] Sankaran, V., and Merkle, C. L., "Size Scale-Up in Hybrid Rocket Motors," AIAA Paper 96-0647, 34th Aerospace Sciences Meeting and Exhibit, Reno, NV, Jan. 1996.

[20] Sankaran, V., and Merkle, C. L., "Analysis of Preconditioning Methods for the Euler and Navier–Stokes Equations," von Karman Inst. Lecture Series, VKI LS 1999-03, Rhode Saint-Genese, Belgium, March 1999.

[21] Li, D., Sankaran, V., Lindau, J., and Merkle, C. L., "A Unified Computational Formulation for Multi-Component and Multi-Phase Flows," AIAA Paper 2005-1391, 43rd Aerospace Sciences Meeting and Exhibit, Reno, NV, Jan. 2005.

[22] Cohen, N. S., Fleming, R. W., and Derr, R. L., "Role of Binders in Solid Propellant Combustion," *AIAA Journal*, Vol. 12, No. 2, 1974, pp. 212–218.

[23] Arisawa, H., and Brill, T. B., "Flash Pyrolysis of Hydroxyl Terminated Poly-Butadiene (HTPB). I: Implications of the Kinetics to Combustion of Organic Polymers," *Combustion and Flame*, Vol. 106, No. 1–2, 1996.

[24] Arisawa, H., and Brill, T. B., "Flash Pyrolysis of Hydroxyl Terminated Poly-Butadiene (HTPB). II: Analysis and Implications of the Gaseous Products," *Combustion and Flame*, Vol. 106, No. 1–2, 1996.

[25] Serin, N., and Gogus, Y. A., "Navier–Stokes Investigation on Reacting Flowfield of HTPB/O2 Hybrid Motor and Regression Rate Evaluation," AIAA Paper 2003-4462, AIAA/SAE/ASME/ASEE 39th Joint Propulsion Conference and Exhibit, Huntsville, AL, July 2003.

[26] Serin, N., and Gogus, Y. A., "A Fast Computer Code for Hybrid Motor Design: EULEC, and Results Obtained for HTPB/O2 Combination," AIAA 2003-4747, AIAA/SAE/ASME/ASEE 39th Joint Propulsion Conference and Exhibit, Huntsville, AL, July 2003.

[27] Knuth, W. J., Gramer, D. J., Chiaverini, M. J., Sauer, J. A., Whitesands, R. H., and Dill, R. A., "Preliminary CFD Analysis of the Vortex Hybrid Rocket Chamber and Nozzle Flowfield," AIAA Paper 98-3351, AIAA/SAE/ASME/ASEE 34th Joint Propulsion Conference and Exhibit, Cleveland, OH, July 1998.

[28] Chiu, H. H., and Oefelein, J. C., "Modeling Liquid-Propellant Spray Combustion Processes," *Liquid Rocket Thrust Chambers: Aspects of Modeling, Analysis and Design*, edited by V. Yang, M. Habiballah, J. Hulka, and M. Popp, Progress in Astronautics and Aeronautics, Vol. 200, AIAA, Reston, VA, 2004, pp. 251–290.

[29] Grenda, J. M., Sankaran, V., and Merkle, C. L., "Application of Computational Fluid Dynamics Techniques to Engine Instability Studies," *Liquid Rocket Combustion Instability*, edited by V. Yang and W. Anderson, Progress in Astronautics and Aeronautics, Vol. 169, AIAA, Washington, DC, 1995, pp. 503–528.

[30] Habiballah, M., and Dubois, I., "Numerical Analysis of Engine Stability," *Liquid Rocket Combustion Instability*, edited by V. Yang and W. Anderson, Progress in Astronautics and Aeronautics, Vol. 169, AIAA, Washington, DC, 1995, pp. 475–502.

[31] Westbrook, C. K., and Dryer, F. L., "Simplified Reaction Mechanisms for the Oxidation of Hydrocarbon Fuels in Flames," *Combustion Science and Technology*, Vol. 27, 1981, pp. 31–43.

[32] Jones, W. P., and Launder, B. E., "The Prediction of Laminarization with a Two Equation Model of Turbulence," *International Journal of Heat and Mass Transfer*, Vol. 15, No. 7, 1972, pp. 301–314.

[33] Chien, K., "Predictions of Channel and Boundary Layer Flows with a Low-Reynolds Number Turbulence Model," *AIAA Journal*, Vol. 20, No. 1, 1982, pp. 33–38.

[34] Wilcox, D. C., *Turbulence Modeling for CFD*, 2nd ed., DCW Industries, 1998.

[35] Siegel, R., and Howell, J. R., *Thermal Radiation Heat Transfer*, 4th ed., Taylor and Francis, New York, NY, 2002, pp. 625–659.

[36] Smoot, L. D., and Price, C. F., "Pressure Dependence of Hybrid Fuel Regression Rates," *AIAA Journal*, Vol. 5, No. 1, 1967, pp. 102–106.

[37] Risha, G. A., Harting, G. C., Kuo, K. K., Peretz, A., Koch, D. E., Jones, H. S., and Arves, J. P., "Pyrolysis and Combustion of Solid Fuels in Various Oxidizing Environments," AIAA Paper 98-3184, AIAA/SAE/ASME/ASEE 34th Joint Propulsion Conference and Exhibit, Cleveland, OH, July 1998.

[38] Rhie, C. M., and Chow, W. L., "Numerical Study of the Turbulent Flow Past an Airfoil with Trailing Edge Separation," *AIAA Journal*, Vol. 21, No. 11, 1983, pp. 1525–1532.

This page intentionally left blank

Chapter 9

Combustion Instability and Transient Behavior in Hybrid Rocket Motors

Arif Karabeyoglu*
Space Propulsion Group, Inc., Sunnyvale, California

Nomenclature

A	= preexponential coefficient
A_p, A_n	= port and nozzle throat areas
B	= blowing parameter
B_a, B_t	= aerodynamic and thermal blowing parameters
C	= specific heat of the solid fuel
C_f, C_H	= skin friction coefficient and Stanton number
c^*_{exp}, c^*_{theo}	= measured and calculated characteristic velocities
c'	= boundary-layer delay time coefficient
$\bar{D}$	= average port diameter
E_a	= activation energy
E_L, E_E	= energy parameters
F_T	= thermal system transfer function
F_{TC}	= thermal–combustion coupled system transfer function
f, f_{1-L}	= primary oscillation frequency, first acoustic mode frequency
G_o, G_t	= oxidizer and total mass fluxes
h_v, L_v	= total and latent heats of gasification
k	= blowing parameter exponent
$\hat{I}$	= Laplace transform of oxidizer mass flux perturbation
L, L_m	= length of the fuel port and motor
L^*	= V_m/A_n
$\dot{m}_o$, $\dot{m}_t$	= oxidizer and total mass flow rate
n	= mass flux exponent for hybrids, pressure exponent for solids

*President and CTO.

O/F = oxidizer-to-fuel ratio
P, P_c = chamber pressure and average chamber pressure
$\dot{Q}_c$, $\dot{Q}_w$ = convective and total wall heat fluxes
R = Nondimensional regression rate and specific gas constant
R_c = response coefficient
Re_z = Reynolds number
R_u = Universal gas constants
RT = gas constant temperature product
RT_{av} = average gas constant temperature product
$\dot{r}$ = dimensional regression rate
s = Laplace transform variable
T = temperature
t = time
U^* = diffusion speed in the turbulent boundary layer
u, v = axial and normal velocities
V_p, V_m = port and motor volumes
z = axial distance along the port
α_1, α_2 = thermal profile shape factors
γ = ratio of specific heats
ΔP_{inj} = injector pressure drop
ΔP_{osc} = chamber pressure oscillation amplitude
δ = boundary-layer thickness
κ = thermal diffusivity of fuel
μ = average gas viscosity
ρ_f, ρ = solid fuel and gas densities
τ = combustion time delay/lead
τ_a = acoustic timescale
τ_{bl} = boundary-layer response timescale
τ_c = chamber filling/emptying timescale
τ_f, τ_v = feed system and vaporization timescales
τ_{kg}, τ_{ks} = gas- and solid-phase kinetics timescales
τ_i = pressure insensitive part of the combustion delay
τ_{tl} = thermal lag time in the solid
τ_{o} = shear stress
σ_1, σ_2 = gas-phase response coefficients

Subscripts and Superscripts

a = ambient, port entrance
b = port exit
e = freestream value
qs = quasi-steady
ref = reference quantities
s = surface
1 = first perturbation variable, pre-combustion chamber
2 = post-combustion chamber
- = nondimensional variable
$\hat{}$ = Laplace transform variable

I. Introduction

IN the course of its operation, a hybrid motor undergoes a number of transients. Some of these transients, such as ignition and thrust termination, are inevitable, some are imposed by mission requirements, such as throttling, and the remainder are undesirable events, such as sudden pressure spikes or instabilities. Understanding the transient phenomena that take place in a motor is critical for designing a propulsion system that is capable of delivering the desired performance within the tolerance limits. These may be in terms of the total delivered impulse, in which the thrust termination transient becomes critical, or there could be constraints on the vibrational loads acting on the payload for which the stability character of the motor plays a key role.

Even though relatively extensive theories for explaining transient phenomena in solid and liquid rockets exist, these theories cannot be applied directly to hybrid systems in which the combustion takes place in a unique diffusion-limited turbulent boundary-layer configuration. The purpose of this chapter is to develop a comprehensive transient theory for hybrid rockets and to apply the theory to understand and predict certain important transient events such as the commonly observed low-frequency instabilities. The chapter will be opened with a classification of relevant transient events, which will be followed by an extensive discussion on the characteristics of instabilities commonly observed in hybrid systems.

The modeling of transient combustion in a hybrid rocket motor is a rather complex problem. In this chapter, the approach that is adapted to address this difficult problem is to identify the important physical and chemical phenomena that affect the transient response of the overall system and to isolate the subsystems associated with each phenomenon in the process of developing mathematical models. Eventually the sub-models are integrated to formulate the overall transient response of a hybrid rocket system. The chapter ends with a discussion of the important problem of low-frequency instabilities in the framework of the developed transient theory.

II. Relevant Transient Events

To follow the thrust requirements of a specified mission, a hybrid motor has to operate in a sequence of isolated (or coupled in some instances) transient events, which are classified and briefly discussed in the following paragraphs.

A. Ignition

The techniques used for the ignition of hybrids are based on the heating of the oxidizer flow by virtue of short-duration heat source such as a slug of hypergolic fluid, a solid squib, or spark ignition of a gaseous fuel. During this transient, the first ignition typically takes place in the aft portion of the fuel grain; in time, the flame moves upstream to fill the whole grain length reaching its steady-state configuration. In the ignition process, the combustion gases leaving the motor are oxidizer-rich approaching the steady-state oxidizer-to-fuel ratio (O/F) toward the end of the transient. In contrast, the O/F during a conventional solid-propellant transient is constant. Of the various time elements involved in this process, the longest time lags are those that establish the combustion boundary layer and the

thermal lag in the solid fuel. Thus, the time lag required to establish a steady state in the hybrid motor is observed to be longer than that for the solid rocket.

B. Throttling

In a hybrid, throttling is accomplished by simply changing the oxidizer flow rate. The steady state corresponding to each flow rate sets a new regression rate based on the regression rate law. Although there has been some research work in the early hybrid literature on the quasi-steady-state analysis of the throttling event [1], the full transient phenomenon is not yet studied. During this event, the gas velocity, temperature, and density distributions in the hybrid combustion chamber and the thermal contour in the solid fuel require a lag time to readjust to the new equilibrium. It is clear that a quantitative understanding of this lag is important for predictable impulse management and maneuvering of the vehicle.

C. Instability

Instability of a rocket motor is defined as the operation when the chamber pressure oscillates in a recognizably coherent form with an amplitude of at least 5% of its mean value [2]. Discussion of instabilities is deferred to the next section in this chapter due to their practical importance and complex nature.

D. Thrust Termination

During shutdown, the response time is basically the characteristic emptying time of the motor. During this relaxation, the accumulated heat in the solid is slowly transferred to the surface, leading occasionally to further vaporization or "chuffing," which in the rarefied space environment can contribute a small additional impulse. The relaxation time is generally greater than the emptying time and, therefore, controls the shutdown impulse. An understanding and ability to specify this impulse on shutdown is obviously important for precise control of vehicle velocity.

III. Hybrid Rocket Instabilities

Combustion stability is arguably one of the most important and difficult aspects of developing a new chemical propulsion system. Hybrid rockets certainly are not an exception to this generalization. There exists a host of transient phenomena that take place during the course of motor operation that could potentially couple to result in growing chamber pressure oscillations. Therefore, a through understanding of the transient combustion characteristics of a hybrid rocket is essential to predict its stability behavior. This makes transient modeling a practical necessity because the motor stability is one of the most fundamental problem areas in the development and testing of hybrid propulsion systems.

Presently there are no universally accepted methods to eliminate the problem of oscillatory combustion in hybrid rockets. Fortunately, the combustion chamber pressure oscillations observed in hybrid systems are bounded in amplitude to levels typically less than 50–60% of the mean pressure. In that sense, unlike solid motor instabilities, hybrid instability mechanisms typically are not capable of producing large-amplitude oscillations, limiting the possibility of catastrophic consequences

such as the structural failure of the motor case. This is most likely due to the lack of a strong feedback mechanism that exists in the case of solid-propellant rockets, which is induced by pressure-dependent regression rate. However oscillatory combustion observed in hybrids could still generate unpredictably high burning rates, could introduce excess structural/thermal loading, and also could result in major thrust oscillations. It is well-established that the oscillatory combustion enhances the mean regression rate (through a phenomenon known as the DC shift) [3, 4], and it could result in an unplanned thinning of the fuel web and the insulation material. In fact, an instability-induced increase of the regression of the fuel lining in the precombustion chamber is believed to cause the failure of one of the American Rocket Company (AMROC) DM-01 motors by producing a burn through in the motor casing. The thrust oscillations are potentially harmful to the launch vehicle structure and the payload itself. Therefore, for an operational propulsion system, the combustion oscillations must be kept within acceptable limits that are uniquely defined for each specific system and mission.

Instabilities are generally classified by their frequency range and/or by the suspected driving mechanisms. In this chapter we adopt the following categorization based on the primary oscillation frequency.

1) *Low frequency*—These instabilities are the most common type in hybrid rockets. The chamber pressure oscillates in the bulk mode (almost uniformly in the chamber) with frequencies less than 200 Hz (depending on the size and operational parameters of the rocket motor). These low-frequency instabilities can further be categorized based on their driving mechanisms: a) feed system coupled, b) chuffing due to char-layer formation and breakoff at very low regression rates, and c) intrinsic low frequency instabilities (ILFI) of hybrids associated with the boundary-layer combustion process (successfully outlined by Marxman [5] for the steady case). This last kind of instability with a driving mechanism unique to hybrid systems is observed over a wide range of motors operating with both liquid and also gaseous oxidizers [2, 3, 6, 7]. A more detailed discussion of each mode will be included in the following sections.

2) *Medium frequency*—These are in the range of 200–2000 Hz and are typically associated with the longitudinal acoustic modes of the combustion chamber. Medium-frequency oscillations are also observed in hybrids, and they are generally accompanied by the low-frequency oscillations [3, 6, 7]. Typically the amplitudes of the medium-frequency instabilities are small compared to their low-frequency counterparts.

3) *High frequency*—These are pressure oscillations with even higher frequencies (>2000 Hz), and they are related to the higher longitudinal or transverse acoustic modes of the chamber. The high frequency portion of the chamber pressure spectrum for hybrid systems is generally inactive.

Note that the frequency ranges used in the proceeding classification is somewhat arbitrary, and the quantitative values are included only to give a rough idea of the ranges.

In the following paragraphs, we concentrate our discussions on the low-frequency instabilities because they are the commonly observed mode in hybrid-propulsion systems.

A. Feed System Coupled Instabilities

The feed system coupled instabilities are generally observed in liquid-fed hybrids and are particularly common in systems that utilize cryogenic oxidizers such as liquid oxygen. The gas-fed systems are not as vulnerable to this instability because the feed system can reliably be isolated from the motor by the insertion of sonic orifice/nozzle elements in the line and there is no vaporization lag for a gaseous system. The root cause for this kind of instability is the coupling of the feed system with the combustion processes in the chamber. A combustion lag (such as vaporization lag) along with a feed system/chamber coupling mechanism is needed to produce oscillatory behavior.

The feed system instabilities can easily be recognized due to their distinct characteristics which can be listed as follows.

1) These instabilities are mostly experienced in liquid-fed systems.

2) The pressure oscillations are much more regular in nature compared to the inherent low-frequency instabilities of hybrid rockets. The Fourier transform of the pressure signal shows a reasonably narrow bandwidth peak.

3) The driving force is a simple coupling between the feed system and combustion chamber dynamics. The vaporization delay of the oxidizer in the combustion chamber is the root cause of the positive feedback needed to produce growing pressure oscillations. The injector upstream pressure, generally, participates in the oscillatory behavior.

4) Even feed systems with isolation elements such as cavitating venturis are vulnerable to this kind of coupling due to the finite bulk modulus of the fluid in the feed lines upstream of the injector.

5) The higher modes (at multiples of the fundamental frequency) are typically also evident in the spectra.

Figure 1 shows the pressure–time trace for a small N_2O/paraffin-based motor with a nominal thrust level of 200 lb. Even though Fig. 1 focuses on a short segment of the data (to show the details of the oscillations), the motor had a similar stability character over the course of the entire burn. Figure 2 is a contour plot of the fast Fourier transform (FFT) in the time–frequency plane for the pressure signal from the same test. Note that this particular motor ran in the blowdown mode and no isolation elements were present to decouple the feed system from the chamber.

As indicated in Fig. 1, the chamber pressure oscillates (50–60% peak-to-peak) in a very coherent fashion at its fundamental frequency of approximately 75 Hz. These oscillations are significantly different in nature compared to the inherent ILFI mode of hybrid rockets. Oscillation frequency and the amplitude of the oscillations are fairly uniform, and the frequency level is lower than one would expect for ILFI, that is, predicted to be around 100 Hz for this particular system. Also note that the injector upstream pressure also participates in the coherent oscillations. As shown in Fig. 2, a number of higher harmonics of the fundamental mode are active (up to the sixth mode) with decreasing intensity. The frequency of the fundamental does not shift during the course of the run, and its intensity is almost constant for the entire test. The FFT analysis also indicates that the feed system coupled instability completely dominates the transient behavior and the other low-frequency

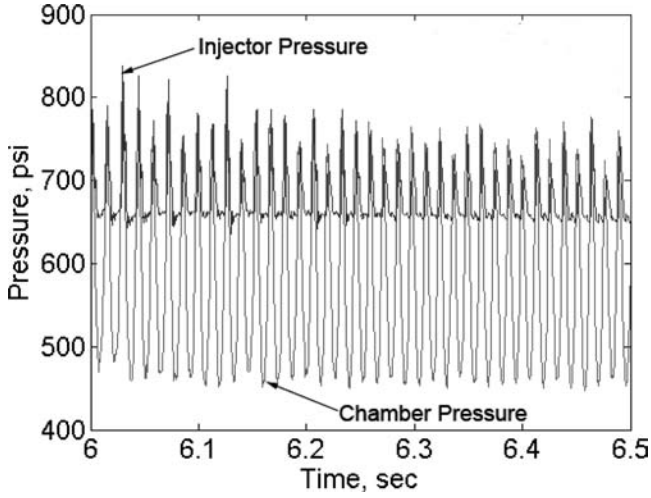

Fig. 1 Pressure–time histories for a small N_2O/paraffin-based motor.

instability modes stay inactive for the entire run. This exclusion phenomenon is commonly observed in hybrid rocket systems.

The existence of a coupling between the feed system and the motor is necessary but not sufficient for the feed system coupled instability. A reasonably long vaporization delay for the oxidizer is also needed to produce the pressure oscillations.

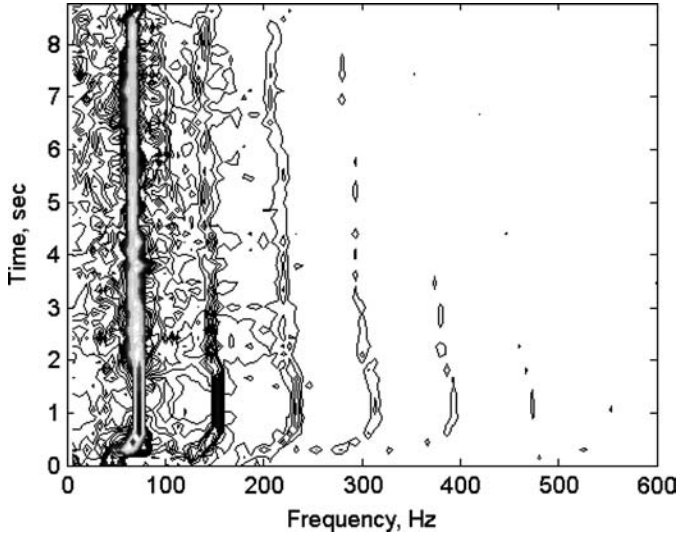

Fig. 2 FFT contour plot of pressure–time trace for test in Fig. 1.

In fact, tests conducted with different injectors running at similar operating conditions, that is, reduced vaporization lag, resulted in stable combustion for the same N_2O/paraffin-based hybrid system.

In this chapter, we will not diverge into the modeling issues for the feed system dynamics and the atomization/vaporization aspects of the hybrid transients. A significant amount of information already exits in the field of liquid rocket combustion instabilities that can be adopted to predict and mitigate the feed system coupled instabilities encountered in hybrid-propulsion systems.

B. Chuffing

Chuffing instability is produced by the char/melt-layer formation and breakoff process that takes place only at very low regression rates. Oscillation frequency for the chuffing instability is dictated by the thermal lag times in the solid fuel and typically is in the range of 1–5 Hz. During operation at very low oxidizer mass fluxes, typically observed toward the end of a slow shutdown transient, the thermal-layer thickness in the solid grows significantly resulting in the "cooking" and/or melting of the solid fuel underneath the port surface. The mechanical removal of this soft layer results in a pressure surge in the chamber. The perpetual repeating of this built-up and removal process results in the chamber oscillations. As stated before, the chuffing frequency scales with the thermal lag time in the solid fuel, $\tau_t = \kappa/\dot{r}$, where κ is the thermal diffusivity, $\dot{r}$ is the regression rate, and τ_t is the thermal lag time.

Because chuffing takes place only during very low mass flux operation, it has limited practical importance, and no modeling for the chuffing instability is addressed in this chapter. However, the thermal lag model that will be outlined in the following sections can be used to quantify this phenomenon.

C. ILFI of Hybrid Rockets

This type of low-frequency instability, which has a driving mechanism unique to hybrid systems, is observed over a wide range of motors operating with both liquid and also gaseous oxidizers [2, 3, 6, 7]. It is instructive to establish qualitatively the nature of these low-frequency pressure oscillations, which have been observed in virtually every hybrid program reported to date. In the following paragraphs, we will discuss results from several of these programs.

The first example is for a fast-burning paraffin-based fuel that has been tested extensively with gaseous oxygen in the Hybrid Combustion Facility (HCF) at NASA Ames Research Center [8]. The pressure–time trace of a typical paraffin-based hybrid motor test is shown in Fig. 3, whereas the Fast Fourier Transform (FFT) for the same test is given in Fig. 4. The pressure–time trace and the spectral signature are typical for a hybrid rocket that does not present a feed coupled instability. As indicated in Fig. 3, the feed system and the chamber are completely decoupled and the activation of the feed system coupled instability mode is not feasible.

The Fourier transform shows three broad peaks corresponding to the inherent low-frequency instability, the Helmholtz mode, and the first longitudinal mode. As discussed earlier, the dominant mode, low-frequency oscillations, are accompanied by lower amplitude, higher frequency acoustic modes.

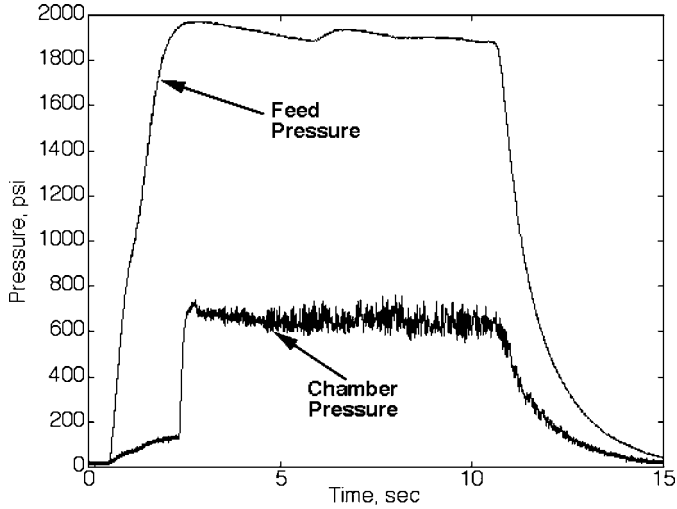

Fig. 3 Pressure–time trace for a GOX/paraffin-based hybrid.

As the next example, we consider various size AMROC motors and 11- and 24-in. Joint Government/Industry Research and Development (JIRAD) motors. These are also of great interest because the data obtained for these tests are reasonably reliable and complete. Note that, in all cases discussed in the following paragraphs, the feed system coupling is not suspected as the root cause for the

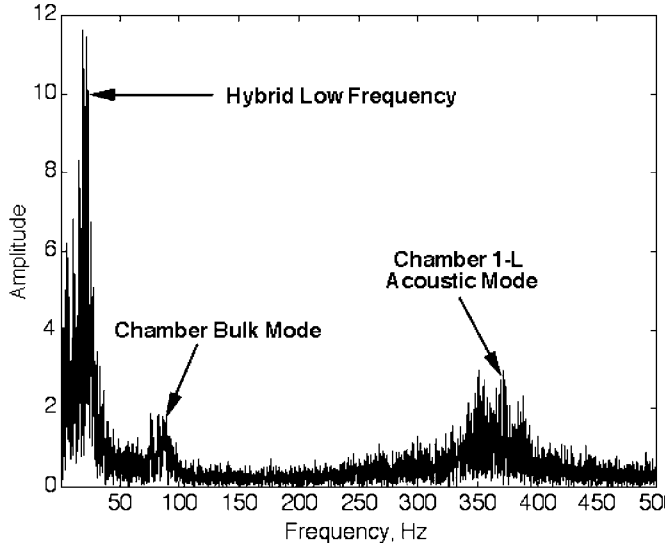

Fig. 4 FFT plot of pressure–time trace for test in Fig. 3.

instability. It is also clear that the regression rates of all of these tests are large enough so that the possibility of chuffing can be ruled out.

For AMROC DM-01 (250,000-lb class motor) tests that showed instability, the observed frequency range was 2–3 Hz and the oscillation amplitudes were about 15–20% of the mean pressure. The JIRAD motors were also susceptible to low-frequency instabilities [3, 6, 7]. Many of these tests showed pressure oscillations in the frequency range of 8–15 Hz and oscillation amplitudes of 5–60% mean pressure. As an example, Fig. 5a represents a typical time history of the chamber pressure during unstable operation for an 11-in. JIRAD motor [3]. Figure 5b shows the high-frequency content of the pressure signal for the same test.

It is commonly observed and generally accepted in the field that the stability level of the motor is controlled by the conditions in the pre-combustion chamber such as the chamber volume/geometry, injector configuration or heating source/distribution. It is reported that the effect of the post-combustion chamber on the instability is not significant [6, 9, 10]. Boardman et al. [3, 6] carefully investigated the effect of the pre-combustion chamber flow conditions on the stability level of the motor. Using 11-in. GOX motors, they have shown that the axial injectors enhanced the stability over the radial and 45-deg inclined injectors. It is also reported by independent researchers that for gaseous systems the volume of the feed system downstream of the sonic choke or venturi adversely influences the stability of the motor. However, a careful experimental investigation of the effect of feed volume on the motor stability has not been reported in the open literature.

As indicated by Figs. 3 and 5, the pressure oscillations are in the nature of a limit-cycle phenomenon. Their amplitude is typically bounded to less than 50% of the mean level. The spectral signature for the inherent low-frequency instability

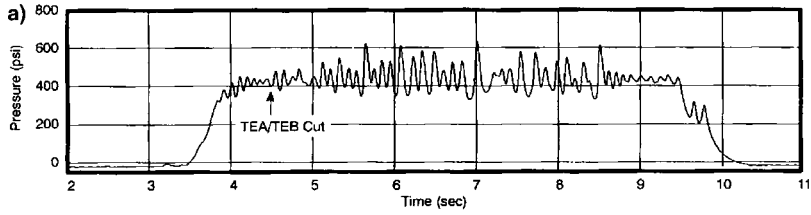

Fig. 5a Chamber pressure–time history of 11-in. JIRAD motor during unstable operation. (From Ref. [3].)

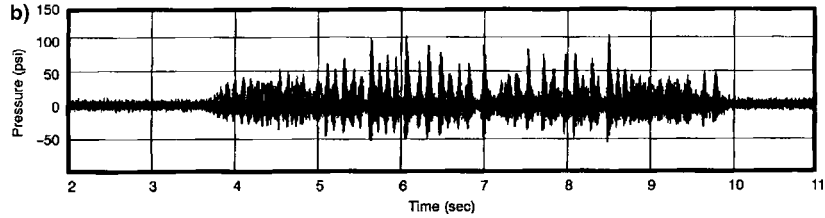

Fig. 5b High-frequency content of signal for same test as Fig. 5a. (From Ref. [3].)

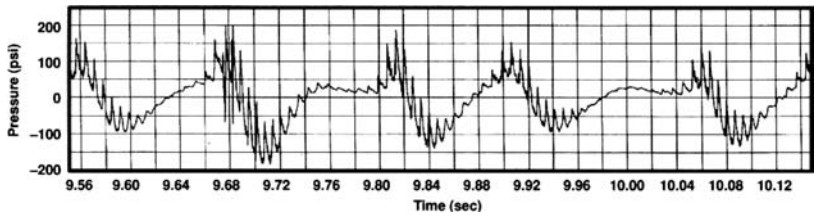

Fig. 6 Pressure–time history for a different JIRAD 11-in. test. (From Ref. [3].)

mode is a relatively broad peak as opposed to the well-defined peaks of the feed coupled instability.

Another interesting observation is that the pressure oscillations may appear or disappear in the middle of a run. Specifically, in AMROC DM-01 tests the low-frequency oscillations started after a pressure spike and decayed rather slowly. This indicates that, at least for this specific case, the hybrid motor as a system possesses natural response components with a small damping coefficient at the low-frequency range of interest. The pressure spike, which may be caused by a brief blockage of nozzle throat or explosion of a fuel oxidizer mixture stored in the pre-combustion chamber, serves as a disturbance to activate the system's natural response.

In both JIRAD and AMROC tests, the low-frequency oscillations are accompanied by higher frequency acoustic activity (as in the case of paraffin-based motor test example in Figs. 2 and 3), mainly the first longitudinal (1-L) mode [6]. The pressure–time history for another JIRAD 11-in. motor test [6], which is shown in Fig. 6, clearly indicates this phenomenon. However, it is not clear from the pressure histories whether the high frequency is driving the low frequency or vise versa. The pressure data show that the shape of the low-frequency oscillations are nonlinear, namely, the pressure plot does not follow sinusoidal waveform. Thus, these nonlinearities in the low-frequency oscillations may very well be exciting the acoustic modes of the combustion chamber.

All of the observations on low-frequency instabilities lead one to believe that, although the instabilities may be generated by a linear mechanism, their amplitudes are controlled by nonlinear effects. In this chapter, we will explore the possible linear couplings that may generate unstable oscillations at the observed frequencies and find the scaling law for the frequency with the operating conditions and the motor internal geometry. We first give a comprehensive list of potential driving mechanisms that could lead to the observed inherent low-frequency instabilities as they have been suggested in the literature.

D. Instability Driving Mechanisms Suggested for Hybrids

1. Atomization/Mixing

It is claimed by some researchers that the atomization/vaporization lags of the liquid oxidizer may couple with the combustion and gasdynamic processes that take place in the chamber to generate the inherent low-frequency instabilities. The researchers also stated that the instability can be suppressed by increasing residence

time of the droplets in the precombustion chamber, for example, by employing vorticity [2] or by providing a rapid means of vaporization as with a hypergolic fluid or igniter. As discussed in the preceding sections, this mechanism is feasible but it is only applicable to a liquid oxidizer system. However, the same types of instabilities are observed in both liquid and also gaseous systems. Thus, this can not be a complete explanation to account for the intrinsic low-frequency instabilities, which are most likely related to phenomena unique to hybrid internal ballistics. On an interesting note, based on motor test data, Boardman et al. [3] concluded that, for systems operating with gaseous oxidizers, the increased precombustion chamber heat release does not improve the stability behavior of the motor.

2. Mass Flux Coupling

Because the hybrid burning rate is mainly mass flux dependent, the flux coupling could potentially provide the energy feeding mechanism in hybrid systems. This is in contrast to solid rockets where pressure coupling is dominant. In the low-frequency regime, where hybrids have shown a particular susceptibility to unstable behavior, there is the distinct possibility of mass flow velocity coupling with the hybrid burning rate. This is because the thermal lag is typically in the range of tenths of seconds rather than milliseconds that are characteristic of gas-phase combustion lags. The feasibility of this type of coupling will be discussed later in this chapter.

3. Chuffing

As discussed earlier, chuffing is the instability that has been associated with the accumulation and breakoff of char or molten layers on the fuel surface. This low-frequency instability (typically, 1–5 Hz) is only possible at very low oxidizer mass flux levels and, thus, cannot explain the widely observed low-frequency oscillations.

4. Pressure Coupling

There are two extreme operating regimes where the hybrid regression rate shows pressure dependency, namely, at high oxidizer mass fluxes where chemical kinetics effects become rate determining and in the low mass flux region where radiation becomes important relative to convection. In these regions, pressure coupling may provide the energy feeding mechanism to create the pressure-coupled combustion instability. Medium-frequency instability, resulted from the coupling between the pressure-dependent combustion and longitudinal acoustic modes, has been reported in the early hybrid literature [10, 11], first by Wooldridge and Marxman [11] for a system with metal loading above a certain critical port diameter. The observed mean frequency of the oscillations was about 600 Hz for a 0.75-m-long motor. The reported frequency corresponds to the first longitudinal acoustic mode of the system. The solid-propellant instability literature on the combustion pressure coupling effect is quite extensive, and a reasonable understanding of this contribution has been demonstrated [12]. It is expected, however, that this type of instability is feasible only in those hybrids showing a distinct pressure effect on the burning rate.

5. Vortex Shedding

This theory presumes that the instability is linked to the vortex shedding in regions of rapid expansion such as the mixing chamber of the motor [9, 13, 14]. These frequencies are generally in the medium range and so may not be a primary driving mechanism for the ILFI of hybrid systems. Moreover, the motor-test experience showed that a change in the aft combustion chamber geometry does not affect the stability character of the motor. Furthermore the observed scaling of the oscillation frequency with motor L^* (or precisely fuel-grain length) cannot be explained by this theory.

6. "DC Shift" Theory

Boardman et al. [6] suggested that the low-frequency instabilities are generated by the high frequency (acoustic) active packages by means of the "DC shift" effect. They claim that the high-frequency pressure oscillations are generated by the back and forth oscillation of the leading edge of the hybrid diffusion flame because it is not stabilized adequately for some hybrid configurations. However, this theory cannot explain why the high-frequency wave packages are modulated at a well-defined low frequency that scales predictably with motor operating conditions. Moreover, it is also possible the cause and effect are reverse, namely, the nonlinear low-frequency wave forms may be driving the high-frequency acoustic modes. The feasibility of this latter alternative is successfully demonstrated by Karabeyoglu [15].

7. L^* Theory

There have been several attempts to develop an L^* instability theory for the hybrids as an analog to the solid rocket L^* model [2, 14]. The feasibility of this model is discussed extensively in the next section in which we compare hybrids with the solid and liquid systems from the perspective of low-frequency instabilities.

E. Comparison of Liquid, Solid, and Hybrid Rocket ILFIs

The low-frequency instability mechanisms for liquid and solid rockets are reasonably well understood. Theories to predict the frequency and the overall nature of these instabilities have been successfully developed and used in the design of rockets for more than four decades. On the contrary, for hybrid rockets a low-frequency theory that explains the widely observed low-frequency oscillations is not yet fully established. This is partly due to the late development of hybrids compared to the other chemical systems. Another important reason is the weak dependency of the combustion process on the chamber pressure in hybrids. It is well known that conventional hybrids operate, unlike the solids and the liquids, in a diffusion-limited combustion regime that makes the regression rate a strong function of the mass flux not the chamber pressure. The lack of explicit dependence of the mass generation rate on the chamber pressure eliminates the possibility of any coupling between the bulk mass balance in the chamber and the combustion through the pressure-dependent regression rate. In this section, we will discuss this issue in detail by considering the relevant solid and liquid rocket low-frequency

instability theories and assessing the applicability of the fundamental principles of these theories to the hybrids.

The low-frequency instability theory (L^* theory) for solid rockets was first developed by Beckstead and Price [16] and Price et al. [17] and improved by many other researchers [18]. The model depends on the bulk mass balance in the rocket chamber, which can be written as Eq. (1) in terms of the normalized pressure $\bar{P}$ and normalized mass generation rate $\bar{\dot{m}}$,

$$\tau_c \frac{\mathrm{d}\bar{P}}{\mathrm{d}t} + \bar{P} = \bar{\dot{m}} \tag{1}$$

where τ_c is the residence time of the fluid particles in the chamber.

The essence of the theory is to represent the mass generation term as an explicit function of the chamber pressure. This can only be done when the fuel generation rate (regression rate) is an explicit function of pressure ($\dot{r} = a\bar{P}^n$), which is a valid approximation for a solid propellant. For pressure-dependent burn rate, Eq. (1) can be reduced to the following linear form

$$\tau_c \frac{\mathrm{d}\bar{P}(t)}{\mathrm{d}t} + \bar{P}(t) = R_c \bar{P}(t+\tau) \tag{2}$$

Here a lead time τ between the pressure and regression rate is applied, and the response coefficient R_c has been introduced. Note that the lead time is induced by the thermal transients in the solid grain. It will be shown later in this chapter that, for a range of frequencies, the regression rate leads the wall heat-transfer input. Also note that the wall heat flux can be expressed in terms of pressure if one assumes quasi-steady gas-phase processes, which is a good assumption in the low-frequency range of interest.

The system dynamic behavior at low frequencies can now be investigated with the use of Eq. (2). We start by taking the Laplace transform of this linear equation,

$$(\tau_c s + 1 - R_c e^{\tau s})\Pi = 0 \tag{3}$$

The term in the parenthesis is the characteristic equation of the system. The roots of this equation determine the time response (natural response) of the system. Because the characteristic equation is an analytic function of s for this particular system, the stability can easily be determined by investigating the location of the poles in the s plane. In short, if the system has any pole in the right half-plane, it is unstable. By dividing this equation into its real and imaginary parts, $s = \alpha + i\omega$, and defining $R' = R_c e^{\tau\alpha}$, one can obtain the stability equations given by Beckstead and Price [16],

$$\tau_c \alpha + 1 = R' \cos(\tau\omega) \tag{4a}$$

$$\tau_c w = R' \sin(\tau\omega) \tag{4b}$$

These equations have been examined carefully by Beckstead and Price [16], and it has been shown that for a range of τ (positive) the amplitude of oscillations grow indefinitely. As an example, the characteristic equation is plotted in Fig. 7 for

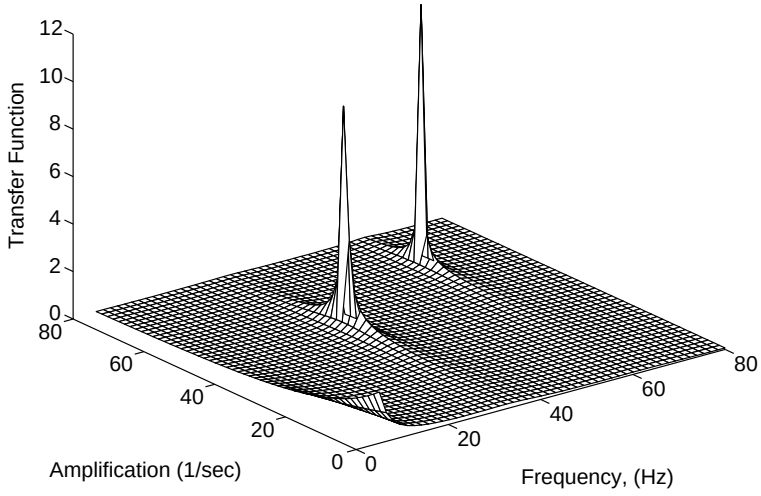

Fig. 7 Poles of L^* instability model transfer function.

the specific case of $\tau_c = 30$ ms, $R_c = 1.3$, and $\tau = 35$ ms. It is obvious from Fig. 7 that the system has at least two poles in the positive real s half-plane. A more careful investigation shows that the equation has, in fact, an infinite number of poles spanning the entire positive s plane. It can be argued that only the pole with the smallest frequency (fundamental mode) has practical significance. This is the case because the higher poles are an artifact of introducing a simple delay instead of the complex dynamics of the combustion process. In fact, numerous T-burner and solid-motor tests conducted by independent researchers have resulted in pressure–time traces that only contained the smallest frequency (fundamental mode) component.

A similar development can also be performed for the low-frequency instabilities of liquid rocket engines [19, 20]. An extensive discussion of the treatment is given by Corocco and Cheng [19]. Here we will only give a brief outline of the model. Similar to the solid rocket case, the bulk mass balance in the liquid engine combustion chamber can be written in the nondimensional form as

$$\tau_c \frac{\mathrm{d}\bar{P}}{\mathrm{d}t} + \bar{P} = \bar{\dot{m}}_b \tag{5}$$

where $\bar{\dot{m}}_b$ is the nondimensionalized mass of burnt gases generated in unit time. Similar to the solid motor, in a liquid engine, the combustion rate (combustion of liquid droplets) will be a function of the chamber pressure. It can be shown [19] that the generation rate of hot gases in the combustion chamber can be expressed to first-order accuracy as

$$\bar{\dot{m}}_b(t) = \bar{\dot{m}}_i(t - \tau_t) + n[\bar{P}(t) - \bar{P}(t - \tau)] \tag{6}$$

Here $\bar{\dot{m}}_i$ is the injection rate of the propellants into the chamber, and n is the pressure sensitivity coefficient. Unlike the solid rocket L^* instability theory, in this model

two types of time delays, τ_i and τ, are introduced. Although both of these delays represent the time lag between the injection of the propellant and the generation of the burned gases, τ is the pressure sensitive contribution, whereas τ_i is the insensitive contribution to the total delay τ_t. The second term in Eq. (6) is available only for the variable-delay case (pressure-sensitive case). Equations (5) and (6) can be combined to obtain the linear response of the system at low frequencies,

$$\tau_c \frac{\mathrm{d}\bar{P}(t)}{\mathrm{d}t} + \bar{P}(t) = \bar{\dot{m}}_i(t - \tau_t) + n[\bar{P}(t) - \bar{P}(t - \tau)] \tag{7}$$

The stability investigations can be performed with the Laplace transformation technique for the system represented with Eq. (7). It is shown [19] that there are at least two types of low-frequency instabilities that can be generated. If the feed system dynamics is very rigid, namely, the injection mass flow rate is constant (decoupled from the chamber pressure), the liquid engine can sustain amplified oscillations of chamber pressure for reasonably high values of the pressure-sensitivity coefficient and for a realistic range of the combustion delays. This kind of feed system independent instability is called the intrinsic instability, and it is due to the existence of variable (sensitive) delay. A second type of instability can occur if the pressure-sensitivity coefficient is zero but the feed system is coupled to the chamber pressure. Note that unlike the solid rocket motors, in general, in liquids the combustion delay (not the lead) generates the instability.

After summarizing the models of low-frequency oscillations for solid and liquid rockets, we can return to the central point of our argument, namely, the applicability of the fundamental principles of these highly accepted theories to hybrid rocket motors. In the literature, there have been several attempts to adapt the L^* analysis developed for solid rockets to hybrid systems [2, 14]. Specifically, a reasonably detailed derivation of the analogous L^* theory has been performed in Ref. [14]. After the bulk mass balance in a hybrid chamber was written (to our knowledge first performed by Wooldridge and Marxman [11]), following the L^* derivation, the investigators introduced a lead time between the combustion and the chamber pressure. We believe that this is not a valid step for hybrids, which, in general, do not possess regression rates with a strong explicit dependence on the chamber pressure. It can be argued that the regression rate for hybrids depends on pressure through the mass flux, which is a product of density and fluid velocity where density is a linear function of the chamber pressure with use of the ideal gas law. However, the response of the chamber thermodynamic properties to the changes in the pressure during these slow transients is not known offhand. For example, an increase in pressure (with a rate that is typical during a low-frequency oscillation) does not necessarily lead to a significant increase in the mass flux because the flow velocity can also arrange (a very likely possibility at the low frequencies of interest) itself to keep the changes in the mass flux small. A quasi-one-dimensional unsteady gasdynamic model of the motor chamber that has been developed in Ref. [15] confirmed this weak dependency of the mass flux on the chamber pressure. In the absence of a coupling between the regression rate and the pressure, the principles used in solid rocket (or liquid rocket) instability modeling cannot generate instabilities. For that reason, one must assume that there is no analog, that

is, analog to L^*, low-frequency* theory for hybrids that will yield the observed unstable behavior.

As will be shown later in this chapter, a complicated coupling mechanism unique to hybrid rockets can be formulated to predict the commonly observed intrinsic low-frequency oscillations.

IV. Subsystems of Hybrid Rocket Motors

As indicated earlier, a reasonable approach to the difficult problem of modeling the dynamic behavior of hybrids is to isolate the subsystems of the motor and consider these subsystem individually. The order of magnitude estimates of the timescales of some of the important processes encountered in a typical hybrid motor are listed in Table 1. Note that in the modeling effort solid and gaseous kinetic times will be assumed to be fast compared to the other relevant timescales. For a reasonably accurate description of motor transients, one has to consider the following subsystems.

A. Feed System

In a hybrid motor, the liquid (or gaseous) oxidizer needs to be fed into the combustion chamber through a feed system. In reality, the feed system response time is finite due to the inherent dynamics of the components in the system. Accurate response depends on the details of the system, which is likely to be significantly different for every motor design. For this reason, we bypass the feed system dynamics in our discussions by assuming the oxidizer mass flow rate as the input parameter. This is a reasonable assumption for most systems because isolating elements decoupling the motor from the feed system, that is, cavitating venture, sonic orifice, are widely used.

Table 1 Transient timescales of various phenomena in typical hybrid rocket

Physical phenomenon	Timescale, s	Explanation
Solid-phase kinetic times	$\tau_{ks} < 10^{-3}$	Degradation mechanisms of the polymer
Gas-phase kinetic times	$\tau_{kg} < 10^{-3}$	Hydrocarbon combustion mechanisms
Feed system response times	τ_f, Varies greatly from system to system	Response time of the feed system
Vaporization times	$\tau_v = f(U_{\text{inj}}, T_1, \Delta P_{\text{inj}})$	Evaporation process of the liquid oxidizer
Thermal lags in solid	$\tau_{\text{tl}} \propto \kappa/\dot{r}^2 \approx 10^{-1}$–1	Thermal profile changes in the solid grain
Boundary-layer diffusion times	$\tau_{\text{bl}} \propto L/u_e \approx 10^{-2}$–$10^{-1}$	Turbulent boundary layer diffusion processes
Acoustic times (longitudinal)	$\tau_a \propto L/c \approx 10^{-4}$–$10^{-2}$	Propagation of the acoustic waves
Gasdynamic filling times	$\tau_c \propto L^*/c^* \approx 10^{-2}$–$10^{-1}$	Global mass flow balance

B. Vaporization of Liquid Oxidizer

Complete vaporization of the oxidizer droplets in the combustion chamber requires a certain characteristic time depending on parameters such as the droplet size, properties of the liquid and the thermal/flow environment of the space where droplet vaporization takes place. Note that this subsystem, too, depends on the specifics of the motor such as oxidizer type, injector design, and precombustion chamber heating scheme. For the purposes of this chapter, we assume that the oxidizer is in gaseous phase when it enters the fuel port.

C. Thermal Response in Solid Grain

A change in the wall heat flux to the hybrid fuel grain cannot be followed immediately by fuel production due to the finite heat capacity of the solid fuel [21]. This is one of the most important transient phenomena that take place in hybrid and will be covered extensively in the following section.

D. Diffusion and Combustion in Boundary Layer

It requires finite time for the hybrid boundary-layer properties to adjust to the changes in the gas velocity in the port or the mass blowing from the fuel surface. The associated dynamics has been discussed in detail elsewhere [15] and will be considered later in this chapter.

E. Chamber Gasdynamics

The chamber pressure responds to the changes in the mass flow with a time-scale proportional to the filling time of the chamber. Acoustic response is also resolved in this subsystem.

In the subsequent sections, the last three of these subsystems (Secs. III.C–III.E) will be modeled and investigated individually. Eventually, these subsystems will be coupled to give the overall system response.

V. Thermal Lags in the Solid

The regression rate of the hybrid-fuel grain cannot respond to changes in the wall heat flux instantaneously due to the finite thermal diffusivity of the solid fuel. The transient heat flow in the solid determines the dynamics of the regression rate response during wall heat flux variations. This phenomenon will be discussed in detail in this section.

The hybrid combustion mechanism differs from the solid rocket in two respects [5, 22]: The flame front is an appreciable distance from the solid surface, and there are no exothermic chemical reactions at the surface. As a consequence, the regression rate is low. The lower regression rate significantly increases the thermal profile response time in the solid. Thus, among the various response times discussed in the preceding paragraphs, the thermal lags in the solid fuel is the rate-limiting (slowest) step during a vast majority of transients. This can be seen from the characteristic thermal lag time $\tau_{\text{tl}} = \kappa/\dot{r}^2$, whose values lie typically in the range of 0.1–1 s.

An early treatment of the thermal lags in hybrids was carried out by Marxman et al. [5]. In the analysis, to obtain a closed-form solution, Marxman et al. assumed

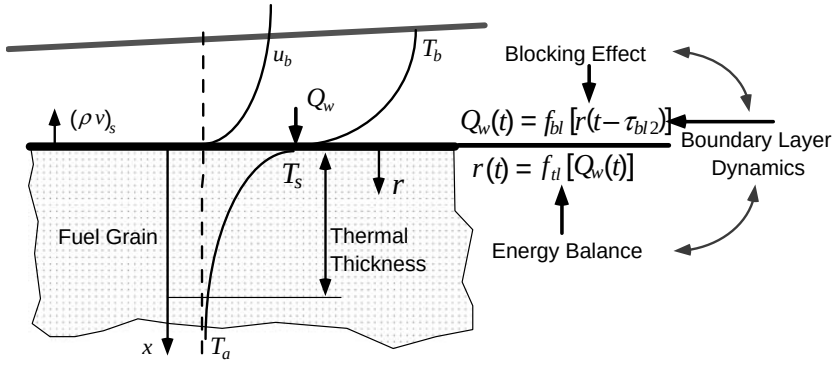

Fig. 8 Schematic of the thermal lag model.

a constant wall temperature and a third-order polynomial shape for the temperature profile. These assumptions limited the applicability of the solution to ignition events with constant heat input. Furthermore, even for this specific case, the solution is inaccurate due to the presumed thermal profile shape, which is far from the actual contour. Other important transient events, such as instabilities or throttling, could not be handled with this approach. In a more comprehensive study of thermal lags in the solid [15], many of these assumptions are relaxed. In the following paragraphs we summarize the findings of this study.

The model for the thermal transients in the solid is shown in Fig. 8. The fundamental assumptions of the model are 1) the penetration depth of the temperature profile is small compared to the web thickness of the fuel; 2) the port radius is large compared to the thermal penetration thickness; 3) all solid-phase reactions accompanying fuel vaporization occur in a thin layer next to the regressing surface, which is a good assumption for large activation energies because the reaction zone thickness in the solid is inversely proportional to the activation energy [15]; 4) the thermophysical properties (such as the thermal diffusivity) of the fuel grain are to be constant; and 5) the temperature gradient in the axial direction is small compared to the gradients in the normal direction. Under these conditions, the suitable heat diffusion equation expressed in the normal x coordinates moving with the regressing surface is

$$\frac{\partial T}{\partial t} = \kappa \frac{\partial^2 T}{\partial x^2} + \dot{r}(t)\frac{\partial T}{\partial x} \tag{8}$$

Landau [23], using Green's theorem, showed that for this kind of a semi-infinite region problem Dirichlet or Neumann types of boundary conditions can be used alternatively, namely,

$$x \longrightarrow \infty; \qquad T = T_a \qquad \text{or} \qquad \frac{\partial T}{\partial x} = 0 \tag{9}$$

The second boundary condition can be derived from the energy balance at the surface, which involves the latent heat of gasification L_v (where the latent heat of

vaporization and solid-phase reaction energies are lumped together to define the latent heat of gasification),

$$x = 0: \qquad \dot{Q}_s(t) = -\lambda\left(\frac{\partial T}{\partial x}\right)_s + \rho_f \dot{r}(t) L_v \tag{10}$$

Note that these boundary conditions, with the appropriate form of the wall heat transfer, are common for all transient events. However, the initial condition that is the temperature distribution at the start of the event is case dependent.

A constitutive relation modeling the surface processes is required to close the set of equations representing the mathematical formulation of thermal lag theory. It is reasonable to use the following distinct models for the surface phenomena.

A. Constant Wall Temperature (CWT) Model

In the case of constant wall temperature (CWT), the surface temperature is independent of the regression rate and is kept fixed to a value that is assumed to be known a priori. Note that the constant specified wall temperature condition replaces the surface boundary condition and Eq. (10) becomes a determining relation for the regression rate.

B. Variable Wall Temperature (VWT) Model

As a more precise approximation, the gasification and pyrolysis reactions at the surface can be represented by an exponential of the Arrhenius type. For chemical reactions, the exponential constant is an activation energy, whereas in vaporization it is the latent heat. To describe this behavior, we assign an average effective activation energy E_a resulting in

$$\begin{aligned} &\dot{r} = A \exp[-(E_a/R_\mu T_s)]; && \text{if} \quad T_s > T_i \\ &\dot{r} = 0; && \text{if} \quad T_s < T_i \end{aligned} \tag{11}$$

where T_i is the temperature below which vaporization is negligible. Here, we inherently assumed that once initiated these reactions are fast compared to thermal diffusion. For typical values of E_a in the range of 5–60 kcal/mole, the percent change in T_s is small, justifying the CWT model as a first approximation.

In the thermal lag model, we represent various transient events with the suitable selection of the initial conditions and the wall heat transfer variations. Our goal is to obtain the response of the regression rate during those simulated events. This requires the solution of the coupled Eqs. (8–11). Note that this moving boundary problem is nonlinear, and because an exact closed-form solution is not available, approximate solutions will be developed. We concentrate on three different methods as described in the following paragraphs.

C. Self-Similar Temperature Profiles Approximation

This approach, which is first introduced by Marxman [5] (in the context of hybrid rockets), is based on assuming a time-invariant functional form for the temperature contour. The wall heat transfer and surface temperature are both assumed to be constant. Thus, the method is only capable of generating solutions for the CWT

Table 2 Shape parameters for various profiles

T–x relation	Shape factor α_1	Shape factor α_2
Exponential	1	1
ierfc	0.443	1.772
Second-order polynomial	0.33	2
Third-order polynomial	0.25	3

model for fixed heat input case and is only good for simulating a special category of ignition events.

Although Marxman's analysis is limited to a third-order polynomial form for the temperature profile, the method has been generalized to arbitrary contours [15, 24]. The final result for the regression rate–time relation can be written as follows:

$$\bar{t} = -\alpha_1\alpha_2\left(\frac{E_L}{E_L+1}\right)\left[\ell n\left(\frac{1-\bar{\delta}}{1-\bar{\delta}}\right)+\bar{\delta}-\bar{\delta}_0\right] \tag{12a}$$

$$R = 1-\frac{1}{E_L}\left(\frac{1-\bar{\delta}}{\bar{\delta}}\right) \tag{12b}$$

where $E_L = L_v/C\Delta T$ and $\bar{\delta} = \delta/\alpha_2\delta_{\text{ref}}$; Here δ is the thickness of the thermal boundary layer in the solid and $\Delta T = T_s - T_a$. The variables of the problem are nondimensionalized with the use of the reference regression rate and the characteristic time and length associated with that reference point in the following way:

$$\bar{t} = t/\tau_{\text{ref}}; \qquad R = \dot{r}/\dot{r}_{\text{ref}} \tag{13a}$$

where

$$\tau_{\text{ref}} = \kappa/\dot{r}_{\text{ref}}^2; \qquad \delta_{\text{ref}} = \kappa/\dot{r}_{\text{ref}} \tag{13b}$$

Note that, for the ignition transient, it is convenient to use the target steady state as the reference point.

The shape factors α_1 and α_2 characterize the capacity and the surface slope of the selected temperature profile, respectively. The values of α_1 and α_2 for various temperature contours including the complementary inverse error function (ierfc), are listed in Table 2.

Equations (12a) and (12b) indicate that $\bar{\delta}$ serves as a free parameter that links the regression rate to the time. Thus, the response of the regression rate only depends on the nondimensional energy parameter E_L and the product of the two shape factors. On the selection of a profile shape and fuel type, Eqs. (12a) and (12b) can be used to generate the solution.

D. Numerical Solutions

The self-similar temperature profiles approximation approach is inadequate to generate solutions for all possible types of transients. Furthermore, in certain cases

this treatment generates significant errors. For this reason, we develop a numerical solution procedure for both of the models for surface phenomena.

We start with normalizing the variables to obtain a nondimensional form of the problem. The nondimensional time and regression rate are defined in Eqs. (13a) and (13b). The remaining variables are normalized in the following way:

$$\bar{T} = (T - T_a)/\Delta T; \qquad \bar{x} = x/\delta_{\text{ref}} \tag{14}$$

The application of the simple stretching transformation defined by Eqs. (13a), (13b), and (14) yields the nondimensional form of the field equation

$$\frac{\partial \bar{T}}{\partial \bar{t}} = \frac{\partial^2 \bar{T}}{\partial \bar{x}^2} + R(\bar{t})\frac{\partial \bar{T}}{\partial \bar{x}} \tag{15}$$

and the boundary conditions

$$\text{for} \quad \bar{x} \longrightarrow \infty: \qquad \bar{T} = 0 \qquad \text{or} \qquad \frac{\partial \bar{T}}{\partial \bar{x}} = 0 \tag{16a}$$

$$\text{for} \quad \bar{x} = 0: \qquad \left(\frac{\partial \bar{T}}{\partial \bar{x}}\right)_s = E_L R(\bar{t}) - \bar{Q}(\bar{t}) \tag{16b}$$

where $\bar{Q}(\bar{t}) = \dot{Q}_w(t)/\dot{r}_{\text{ref}}\rho_f C\Delta T$.

In the process of normalization, we introduce the nondimensional heat loading $\bar{Q}$, which is defined as the ratio of the heat input per unit mass to the energy required to elevate the temperature of the fuel from T_a to $T_s \cdot \bar{Q}$ is, in general, time dependent through the input, and unlike E_L, it is not a property of the fuel alone.

We prefer the following nondimensional form for Eq. (11):

$$\begin{aligned} R &= A\exp\left[-\frac{a}{(\bar{T}_s + b)}\right] \qquad \text{if} \quad \bar{T}_s > \bar{T}_i \\ R &= 0 \qquad\qquad\qquad\qquad\quad \text{if} \quad \bar{T}_s < \bar{T}_i \end{aligned} \tag{17a}$$

where

$$A = \exp(E_a/(\bar{T}_s)_{\text{ref}} R_\mu) \tag{17b}$$

$$a = \frac{E_a}{\Delta \bar{T}_{\text{ref}} R_\mu}; \qquad b = \frac{\bar{T}_a}{\Delta \bar{T}_{\text{ref}}} \tag{17c}$$

A computer program Thermal Lag Code (TLC) has been developed to simulate arbitrary transient events. The TLC is capable of calculating the regression rate for any given initial temperature profile and heat loading. Also, the initial heating period or any such event without regression can be included in the simulated event. A detailed discussion of the numerical solution technique is given in elsewhere [15]. Here some of the important features are summarized.

The finite difference method has been implemented to obtain numerical solutions for the well-posed problem given by Eqs. [15–17]. An exponentially varying space differencing has been used. Because the intention is to generate long-time

solutions for the VWT problem, the global-time error may be significant even for relatively small time steps imposed by the stability condition. For that reason, a fourth order adaptive Runge–Kutta (RK4) scheme, has been implemented for the time integration. The adaptive control of the time-step size has increased the robustness of the solution significantly.

E. Perturbation Solutions

In this section, we develop perturbation solutions for the VWT problem. The results of this perturbation analysis are useful in determining the effects of various parameters on the response, in understanding the system behavior, in verifying the numerical solutions, and in deriving a transfer function to be used in the linear stability investigations. Although this treatment requires small perturbations in the variations of the heat input around a reference point, the functional form of the heat-load perturbation is arbitrary.

We apply a small perturbation, with an arbitrary form in time, to the wall heat flux around the reference steady-state value

$$\bar{Q}(\bar{t}) = (\bar{Q})_{\text{ref}} + \varepsilon \cdot f(\bar{t}) \tag{18}$$

where ε is a small dummy variable ($\varepsilon \ll 1$) introduced to keep track of the orders of various terms.

The linear initial boundary-value problem for the first-order perturbation quantities was formulated and solved with use of the Laplace transformation technique [15, 24]. The transfer function between the regression rate perturbation and the applied heat flux perturbation, which is a result of practical importance, is determined to be [where $R_L(s)$ and $Q_L(s)$ are the Laplace transforms of the regression rate perturbation and the wall heat flux perturbation, respectively]

$$\frac{R_L(s)}{Q_L(s)} = \frac{2E_E s}{(1+\sqrt{4s+1})(s+E_E) - 2E_E + 2E_L E_E s} \tag{19}$$

Here, E_E is another energy parameter that is proportional to the activation energy.

$$E_E = a/(1+b)^2 = E_a(\Delta T)_{\text{ref}}/R_\mu(T_s)^2_{\text{ref}} \tag{20}$$

Note that the derived transfer function is not a simple ratio of two polynomials, as one typically encounters in simple dynamic systems. In fact the denominator is an irrational function of the Laplace transform variable s. From this transfer function, one can deduce that the system has only one zero at $s = 0$ and no poles for the real and positive values of the energy parameters. The consequence of these important features of the linearized thermal lag system will be discussed in the following sections.

F. Discussion of Results

The methods described in the preceding section are applied to generate solutions for various cases. The material properties for hydroxyl-terminated polybutadiene (HTPB) and polymethyl methacrylate (PMMA) used in the calculations are shown in Table 3 (see Karabeyoglu et al. [24]). We follow the classification of the transient events in organizing the discussion of results.

Table 3 Thermophysical properties of fuels used in calculations

Fuel	C, cal/g · K	ρ, g/cm^3	κ, mm^2/s	L_v, cal/g	T_s,[a] K	E_a,[b] kcal/mole	E_E,[c]	E_L
PMMA	0.37	1.1	0.11	231	620	30–40	12.6–14.7	1.94
HTPB	0.57	0.93	0.098	433	820	12–60	4.7–23.4	1.45

[a] Wall temperatures at a specified regression rate, 0.05 cm/s for PMMA and 0.075 cm/s for HTPB.
[b] Range that covers the data in the literature.
[c] Ambient temperature of 300 K in calculations.

1. *Ignition*

The ignition with constant heat transfer case for PMMA fuel for various models is presented in nondimensional form in Fig. 9. For comparison purposes, in each calculation the same value for the constant heat flux is used. The shape parameters of the self-similar temperature profile model are tuned for the best match with the numerical solution of the CWT problem. In the analytical and numerical CWT solutions, the initial heating time is included. (See Karabeyoglu [15] for preheating time formulas). Although the overall shapes of the response curves for the analytical model and numerical CWT cases look similar, the VWT model, which couples the wall temperature to the regression rate, yields a rather different

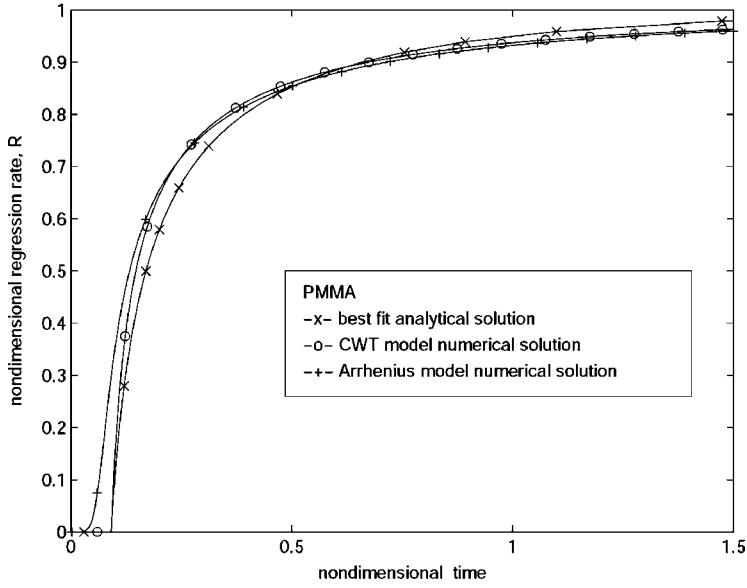

Fig. 9 Effect of temperature profile selection on analytical solution for ignition with constant heat-transfer case; initial heating period neglected, $\dot{r}_{\mathbf{ref}} = 0.05$ cm/s and $\tau_{\mathbf{ref}} = 0.4$ s.

response curve during the early stages of the transient. However, the numerical solutions for the CWT and VWT models match perfectly at large timescales. The nondimensional time $\bar{t}_{90}$ corresponding to the 90% steady-state regression rate is observed to be 0.67. This value is rather different from 0.5, which was predicted by Marxman. This is primarily due to the assumption on the shape of the thermal profile, the exclusion of the initial heating period, and secondarily to differences in material properties. In fact, numerical solutions for the CWT model show that the temperature profile is not self-similar in time because it starts as an ierfc and relaxes to the equilibrium exponential distribution.

Notice that the form of the regression rate curves in the non-dimensional coordinates for the constant heat-transfer case depend only on the energy parameter E_L. This suggests that E_L, which is a property of the fuel, is also a similarity parameter of the thermal lag problem. It can be shown that an increase in E_L reduces the response time. This result is not restricted to the ignition case, and it can be generalized to all types of transients. A possible explanation for this can be deduced from the physical interpretation of E_L, which is defined as the ratio of two possible energy modes for conversion of the total heat input. One mode is associated with the surface processes, which are assumed to be infinitely fast in our model. The other mode is related to a slow process, namely, the heat diffusion in the solid. Thus, E_L can also be treated as a parameter that shows the relative importance of the fast phenomena with respect to the slow phenomena.

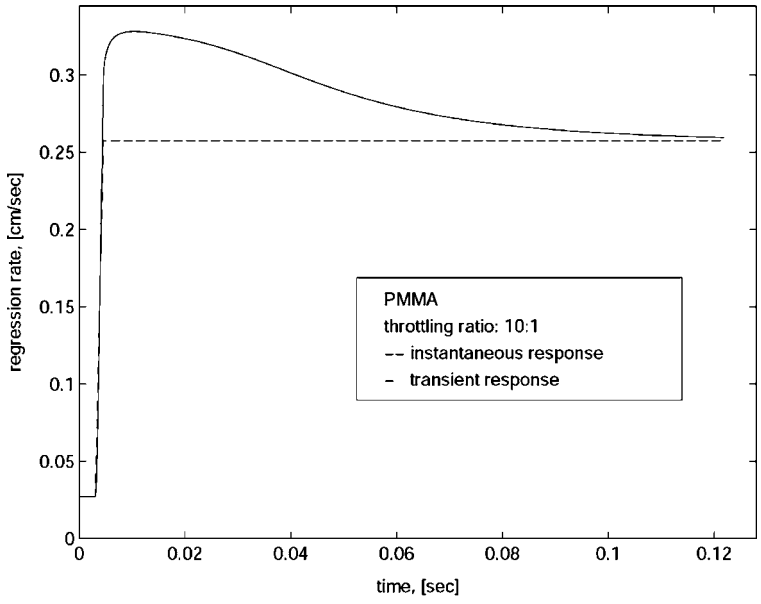

Fig. 10 Overshooting phenomenon for sharp 10:1 throttling; overshooting of regression rate is approximately 25% of its asymptotic value.

2. Throttling

TLC is used to simulate a number of throttling events of interest. We first studied the sharp throttling cases that were modeled by step functions for the heat loading. Figure 10 shows a 10:1 ratio throttle up simulation for PMMA. (In Fig. 10, the instantaneous response curve assume zero thermal lag. Thus, they represent the shape of the heat input.) The response seems to follow the sudden increase perfectly, but it overshoots its asymptotic value by approximately 25% and ultimately relaxes to the target equilibrium, in a relatively long period of time, which appears to be proportional to the characteristic time τ_{tl}.

A careful investigation of the temperature profiles at various stages of the transient is helpful in understanding this interesting phenomenon. The regression rate response and the temperature profiles at certain instants of the transient are plotted in nondimensional parameters for a throttling ratio of 1.5:1 for PMMA in Fig. 11. All of the plots in Fig. 11 are in nondimensional variables as defined in Eqs. (13a, 13b, and 14). In Fig. 11, points A, B, and C correspond to the initial equilibrium, maximum regression rate, and final equilibrium times of the throttling transient, respectively. It is obvious from Fig. 11 that after a short time following the sudden change in the input, only a small region of the temperature profile next

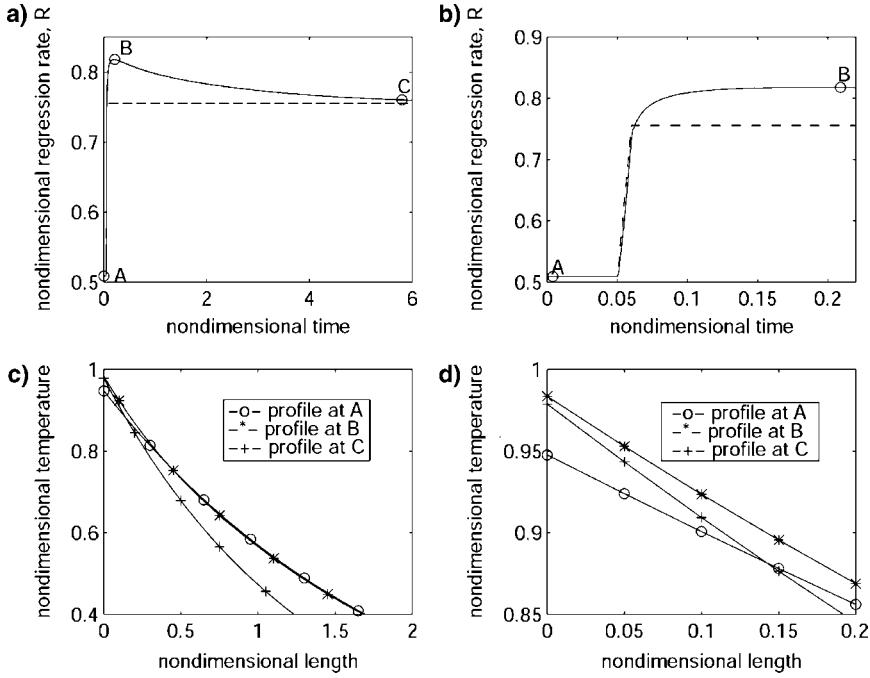

Fig. 11 Overshooting phenomenon, where $\dot{r}_{ref} = 0.106$ cm/s, $\tau_{ref} = 0.091$ s, and $\delta_{ref} = 0.0096$ cm: a) response of regression rate for 1.5:1 ratio sharp throttle up transient for PMMA, b) close up to rapid change region, c) temperature profiles at instants tagged in part a, and d) close up to near-wall region of temperature profiles.

to the wall responds rapidly, whereas the rest of the profile remains unchanged. In fact, the surface temperature and the surface temperature gradient are matched to their correct asymptotic values (point C), at a time between A and B. However at this time, the overall temperature profile is significantly different from the near equilibrium profile corresponding to point C.

These observations indicate that the thermal lag system has two timescales. The surface timescale is related to the sudden adaptation of the temperature profile in a small zone next to the wall. The overshooting phenomenon occurs within this surface timescale. The larger timescale is the well-known relaxation time of the thermal profile in the solid. The thermal timescale governs the relaxation process of the temperature profile and the regression rate to their equilibrium state from the exited state.

As a literature survey will confirm [25–27], reliable data on the activation energy are not available for the fuel types of interest. Thus, the dependence of response on the activation energy is studied parametrically for PMMA and HTPB fuel types. The regression rate response for various activation energies for a throttling ratio of 1.5:1 of PMMA and HTPB fuels are shown in Figs. 12 and 13, respectively.

Observe from Figs. 12 and 13 that the activation energy alters the behavior of the response significantly. The common feature of the transients at different activation energy levels is the overshooting and the relaxation back to the target equilibrium state. However, at high activation energies, the regression rate overshooting, which is defined as $|\dot{r}_{\max} - \dot{r}_f|/\dot{r}_i$, is more apparent and the regression rate reaches its maximum value in a rather short time compared to the thermal relaxation time.

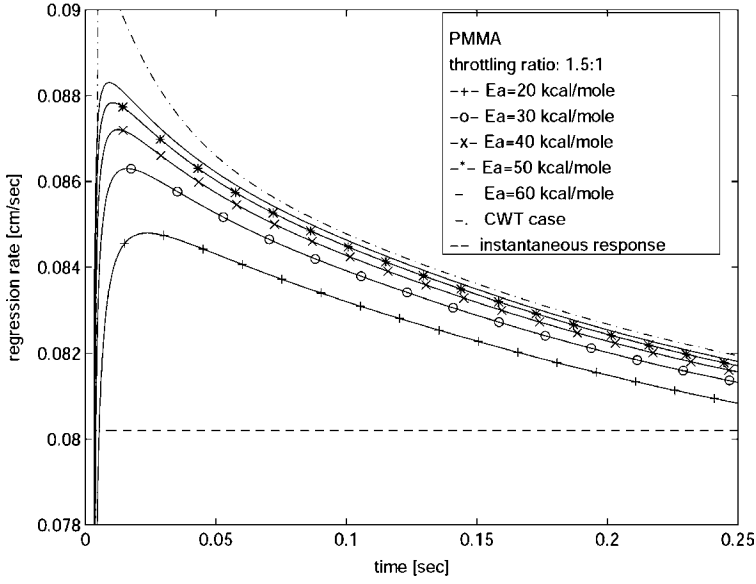

Fig. 12 Effect of activation energy on shape of response for PMMA fuel where CWT case envelopes other solutions.

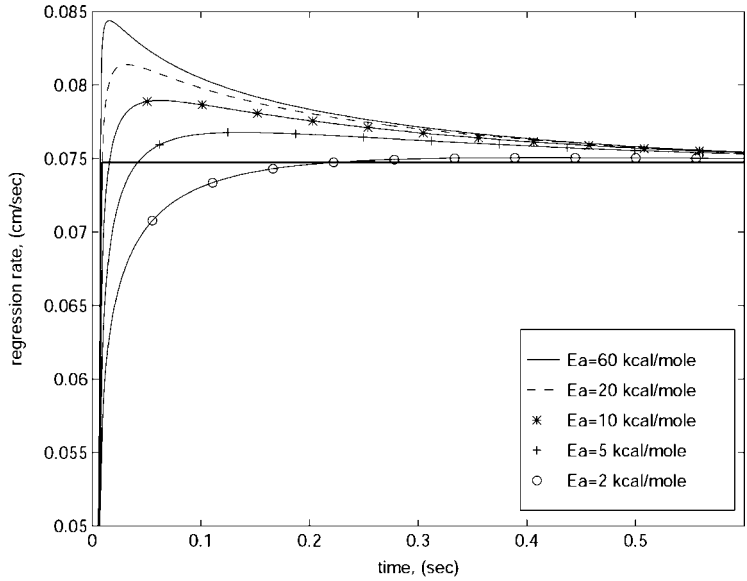

Fig. 13 Effect of activation energy on regression rate response for throttling event for HTPB system with $\tau_{\mathbf{ref}} = 0.4$ s; throttling ratio is 1.5:1.

An interesting observation from Fig. 12 is for infinite activation energy, which represents the constant wall temperature situation. The solution here is singular at the discontinuity of the input. At this point, the regression rate jumps from its initial value to the maximum regression rate, which is approximately 50% higher than the final regression rate for this specific throttling ratio. Thus, the surface timescale is zero. The rest of the response is simply a monotonic relaxation to the second equilibrium in a period on the order of the thermal relaxation time τ_{ref}. As shown in Fig. 12, the constant wall temperature case is an envelope for the family of the response curves generated by the finite activation energies and it determines the upper bound for the overshoot for a specified throttling ratio. In the other extreme of very low activation energies (Fig. 13), the overshooting phenomenon is less significant and the response is similar to the behavior of a first-order system.

The effect of activation energy on these timescales is of fundamental importance. The surface timescale is influenced by the surface phenomenon and must be related to the activation energy. In fact, it is clear from the simulation results that increasing activation energy reduces the surface timescale. However, the thermal timescale is unaffected by the activation energy because it is essentially related to the heat diffusion process in the solid. At high activation energies for which the surface timescale is much smaller than the thermal timescale, very little diffusion takes place over the span of the surface timescale. As a result of this, the overshooting is significant. In the opposite extreme of low activation energies, the surface timescale becomes comparable to the thermal timescale. In this regime the thermal diffusion makes the overshooting less apparent.

To support the preceding argument, we will derive a scaling expression for the surface timescale in terms of the activation energy and the throttling ratio. We start with noting that the instantaneous regression rate response intersects the quasi-steady line at a point between A and B. For simplicity, we arbitrarily define the surface timescale as the time interval from the start of the transient to the intersection point. This definition of the surface timescale simplifies the treatment because at the intersection point the surface temperature is equal to the final equilibrium temperature. Moreover, from the energy balance at the surface, it can be argued that the surface temperature gradient must also be equal to the surface gradient at the final equilibrium state. Thus, at this point of intersection, we can write the following expression for the surface length scale:

$$\delta_s = \frac{T_{sf} - T_{si}}{|\partial T/\partial x|_{sf}}$$

Here the subscripts *si* and *sf* stand for the surface values at the start and the end of the transient.

The gradient term can easily be determined from the final equilibrium profile,

$$\delta_s = [(T_{sf} - T_{si})/(T_{sf} - T_a)]\delta_{\text{tl}}$$

The Arrhenius expression can be used to write this equation in terms of the throttling ratio and the activation energy,

$$\frac{\delta_s}{\delta_{\text{tl}}} = \frac{T_{si}^2 \ell n(\dot{r}_f/\dot{r}_i)}{T_{si}T_a \ell n(\dot{r}_f/\dot{r}_i) + (T_{si} - T_a)E_a/R_u} \tag{21}$$

After noting that $\tau_{\text{tl}} = \delta_{\text{tl}}/\dot{r}$, we can express the ratio of timescales as

$$\frac{\tau_s}{\tau_{\text{tl}}} = \frac{T_{si}^2 \ell n(\dot{r}_f/\dot{r}_i)}{T_{si}T_a \ell n(\dot{r}_f/\dot{r}_i) + (T_{si} - T_a)E_a/R_u} \tag{22}$$

It is clear from Eq. (22) that as the activation energy increases the surface timescale gets smaller with respect to the thermal lag timescale. This result supports the earlier arguments. The scaling expression also predicts that the surface timescale and the thermal lag timescale are on the same order during an ignition event, which serves as an explanation why the overshooting phenomenon is not observed during ignition.

The effect of the throttling ratio $\dot{r}_f/\dot{r}_i$ on the relative overshooting is another issue of practical importance and demonstrated in Fig. 14 for PMMA and $E_a = 30$ kcal/mole. For the throttleup situation, the relative overshooting increases monotonically with the throttling ratio. However, in the throttledown case, the relative excursion increases up to a maximum value and then decreases to zero at zero throttling ratio, $\dot{r}_f/\dot{r}_i = 0$, which represents the thrust termination event. Although, the first-order perturbation analysis indicates that the throttling up response is a mirror image of the throttling down response, the numerical studies show asymmetry (unless the throttling ratio is small). This

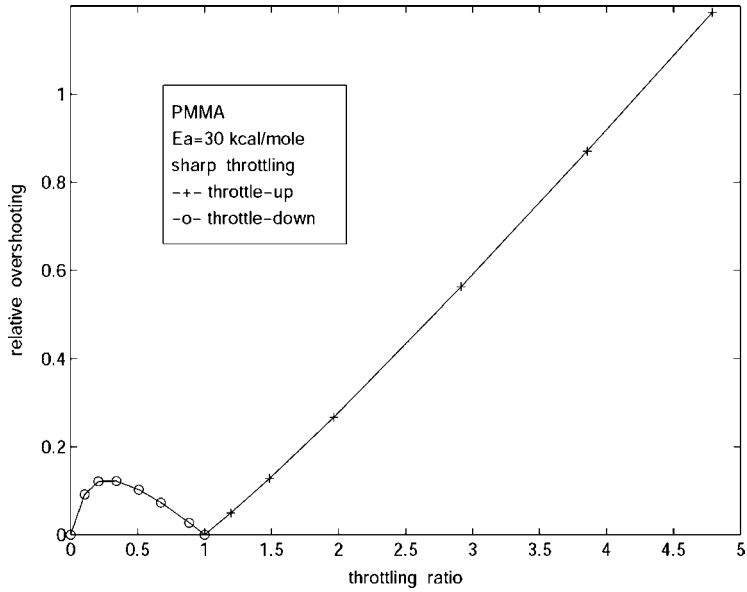

Fig. 14 Effect of the throttling ratio, $\dot{r}_f/\dot{r}_i$, on relative overshooting, $|\dot{r}_{\max} - \dot{r}_f|/\dot{r}_i$; nature of throttleup and throttledown cases are significantly different.

nonlinear effect can be captured with higher-order perturbation solutions. These conclusions can be generalized to other types of polymeric or nonpolymeric fuels.

In the preceding paragraphs, we discussed the instantaneous throttling case, which corresponds to an infinite rate of throttling. It is instructive to consider the more practical case of finite throttling response of the thermal lag system because, in reality, the sudden increase of the heat input cannot be achieved because of the time lags related to the other transient phenomena in the rocket motor. Moreover, finite throttling serves as a bridge to the situation of sinusoidal heat loading, which will be investigated later in this chapter. Figure 15 shows three numerical simulation results for different throttling rates. The important observation is that for low throttling rates the transient response anticipates the heat input. Similar behavior will be observed in the sinusoidal heat loading case. Figure 15b indicates that for all rates there is a finite time range right after the start of the heat loading when the response lags the input. The extent of this lag region increases as the throttling rate increases.

It has been shown [15] that these results are consistent with the perturbation theory predictions.

3. Oscillatory Combustion

In this section, we discuss the frequency response of the thermal lag system. The application of the sinusoidal heat input at a specific frequency simulates regression rate behavior during unstable motor operation. In the calculations, a wall heat flux

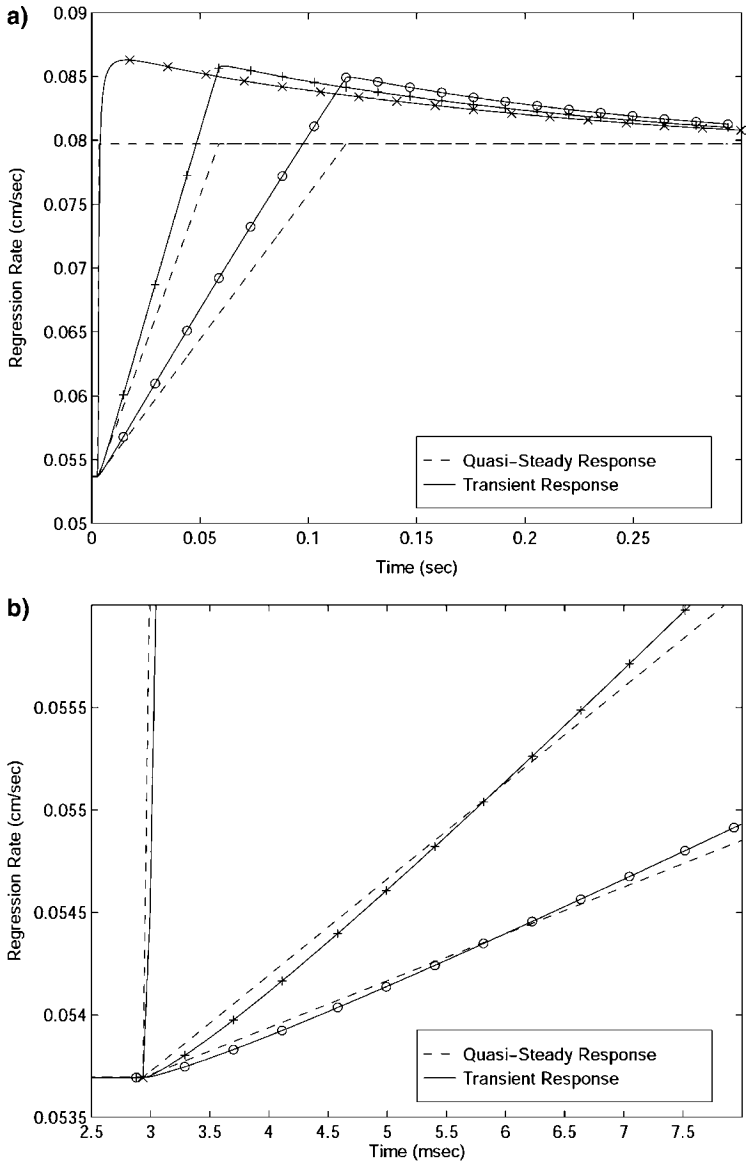

Fig. 15 Effect of throttling rate on regression rate response; PMMA system with $\tau_{\mathbf{ref}} = 0.4$ s, $E_a = 30$ kcal/mole, and throttling ratio of 1.5:1: a) global response and b) initial response.

perturbation of the form of a sine wave with a specified amplitude and frequency is applied. Because the transfer function of the thermal lag system has already been derived, that is, Eq. (19), the response of the regression rate can easily be calculated.

A sinusoidal heat input, $Q_1(\bar{t}) = \sin(\bar{\omega}\bar{t})$, has the Laplace transformation

$$Q_L(s) = \bar{\omega}/(s^2 + \bar{\omega}^2) \tag{23}$$

Note that $\bar{\omega}$ is the nondimensional frequency. The corresponding dimensional angular frequency is $\omega = \bar{\omega}/\tau_{\text{tl}}$, where τ_{tl} is the thermal lag time corresponding to the nominal operating point.

Coupling $Q_L(s)$ with the transfer function yields the response function of the regression rate $R_L(s)$ in the s domain. Inverse transformation back to the time domain can be achieved with the use of the residue theorem [28–30]. In the analysis, we are only interested in the forced response because the influence of the natural response is expected to be confined to a relatively small time period for practically significant applications. This fact is confirmed by the numerical simulations as discussed elsewhere [15].

We will first consider the two limiting behaviors for which the explicit expressions can be obtained relatively easily. The first limit is the low-frequency case, $\bar{\omega} \to 0$, in which the response simplifies to

$$R_1(\bar{t}) = R_1^{\text{qs}} \sin(\bar{\omega}\bar{t}) \tag{24a}$$

where the amplitude can be written as

$$R_1^{\text{qs}} = E_E/(E_L E_E + E_E + 1) \tag{24b}$$

At very low frequencies, the regression follows the variations in the wall heat flux in a quasi-steady manner. Namely, the amplitude of the regression rate is the steady value associated with the heat flux at the time of interest and the phase difference is zero. In dimensional form, the time-dependent component of the regression rate has the form

$$\dot{r}(t) \propto \dot{r}^{\text{qs}} \sin(\omega t)$$

where $\dot{r}^{\text{qs}}$ is the quasi-steady response to the wall heat flux oscillation.

The other limit of interest is the high-frequency one, where the response becomes

$$R_1(\bar{t}) = (E_E/\sqrt{\bar{\omega}}) \sin[\bar{\omega}\bar{t} - (\pi/4)] \tag{25}$$

In the extreme case of very high frequencies, the regression rate lags the wall heat flux with a 45-deg phase angle. The amplitude of the oscillatory component decays with increasing frequency following the functional form $1/\sqrt{\omega}$ as indicated in the dimensional form of the asymptotic formula,

$$\dot{r}(t) - \dot{r}_{\text{ref}} \propto (1/\sqrt{\omega}) \sin[\omega t - (\pi/4)]$$

The response at the intermediate frequencies is quite interesting. As a typical example, we consider the case of a PMMA system with a thermal characteristic time of $\tau_{\text{tl}} = 0.5$ s and $E_a = 30$ kcal/mole. The normalized regression rate amplitudes and phase differences between the regression rate and heat flux are plotted

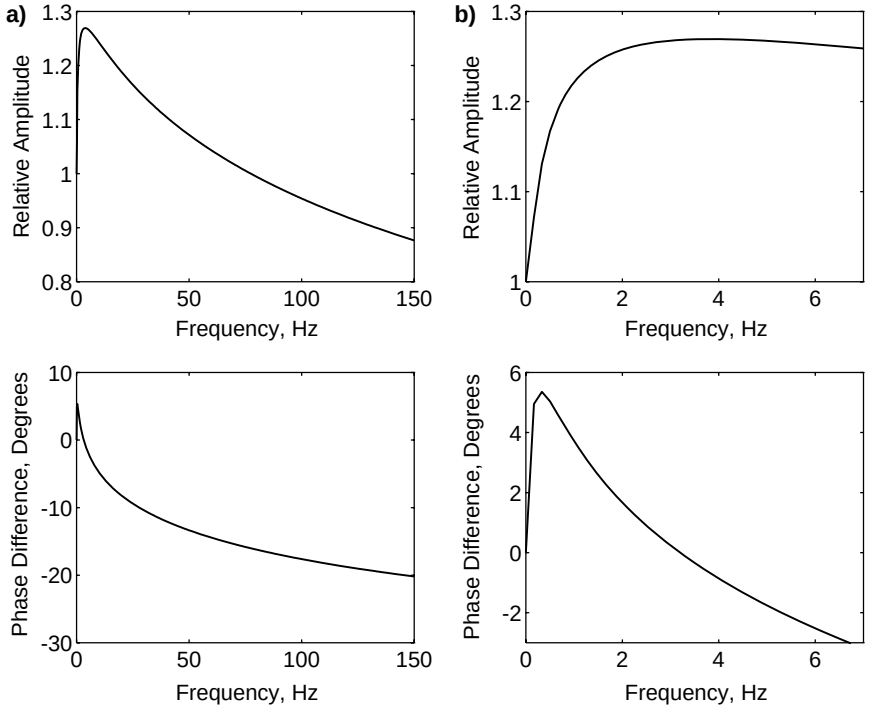

Fig. 16 Frequency response for thermal lag system: a) wide frequency range and b) close up to low-frequency range.

over a range of frequencies in Fig. 16. For convenience, the amplitudes shown in Fig. 16 are normalized with respect to the quasi-steady response [by Eq. (24b)]. It is apparent that for relatively small frequencies, $f < 80$ Hz, the regression rate oscillations are amplified. The amplitude of the regression rate increases from its quasi-steady value and takes a maximum value (at a small frequency close to 4 Hz). For this specific case, the maximum amplitude is approximately 25% larger than R_1^{qs}. At higher frequencies, the amplitude of the response monotonically decreases with increasing frequency. At a moderate frequency, it crosses the quasi-steady amplitude beyond which it is attenuated. Eventually, the amplitude response reaches its asymptotic behavior discussed in the preceding paragraph at very high frequencies.

The nature of phase difference response is also worth noting. In a small range of frequencies close to zero, the regression rate leads the wall heat flux input. Specifically, the phase difference starting from zero at zero frequency increases to a maximum-phase lead, which occurs at a small frequency. Later the phase difference starts decreasing, and it crosses the zero axis (at which the regression rate and the heat flux are in phase again). For the frequencies higher than this crossing value, the regression always lags the heat flux input. Eventually the phase difference asymptotes to $-\pi/4$ monotonically at very high frequencies as already mentioned.

In short, for frequencies smaller than the crossing frequency, the regression rate leads the heat flux input, whereas for higher frequencies it lags. The low-frequency behavior, implying a lower rate of change of heat flux, parallels the $\dot{p}$ extinguishment in solid propellants [31], where the burn rate "anticipates" the steady state leading to a zero burn rate before the steady-state value.

The region of amplitude amplification is much wider than the region of the phase lead in the frequency domain. The amplification of the regression rate is on the order of 20–30% for the practical operating regimes of hybrids. We also note that no resonance behavior is observed for any set of parameters. As an important conclusion, it can be stated that the thermal lag system is inherently stable at least in the linear regime and the thermal lags alone can not generate the low-frequency oscillations observed in hybrids. However, the thermal lag system certainly favors the low-frequency oscillations.

At this point, it is instructive to discuss the relation of these results on the thermal lag response to the solid rocket L^* instabilities. It is clear that the thermal lag model presented here can also be applied to the solid rocket fuel grains. First it is important to note that in solids the combustion is pressure dependent and the wall heat flux is a function of the chamber pressure. A simple analysis of the chamber filling/emptying dynamics indicates [15] that a solid rocket may present bulk mode low-frequency instabilities if the regression rate response leads the pressure oscillations. It has been shown in the preceding paragraphs that this phase-lead behavior is inherent to the thermal lag system. Thus, in solid rockets a coupling between the chamber gasdynamics and the thermal lag system produces the indefinitely growing low-frequency bulk mode chamber pressure oscillations commonly referred as the L^* instabilities. One must realize that the essential ingredient of this type of instability is the explicit dependence of the wall heat flux on the chamber pressure (needed to couple the wall heat flux to the chamber pressure). However, the hybrids do not possess this critical coupling because the combustion is mainly diffusion limited and the wall heat flux fails to have significant dependence on the pressure. In short, even though there may be some combustion leads generated by the thermal lags in the fuel grain, hybrids do not appear to possess low-frequency instabilities in the L^* theory framework.

The different selection of the parameters such as heat of gasification, activation energy, or the characteristic thermal lag time, that is, L_v, E_a, and $\kappa/\dot{r}$, does not alter the qualitative nature of the frequency response. However various quantitative features of the thermal lag response, such as the width of the phase-lead region or the amplification region, that can influence the overall dynamics of the system depend on those parameters. For that reason, an investigation has been performed to explore the effect of each relevant parameter. Some of the important results are summarized in the following paragraphs.

The role of the activation energy is demonstrated in Fig. 17 for an HTPB system operating at a nominal condition corresponding to a characteristic time of $\tau_{\text{tl}} = 0.4\,\text{s}$ [Note that $\tau_{\text{tl}} = \tau_{\text{ref}}$ and the relative amplitude is R_1/R_1^{qs}, where R_1^{qs} is defined by Eq. (24b).] The effect of increasing activation energy is to enlarge the amplification and the phase-lead regions in the frequency domain. As the activation energy increases, the magnitude of the relative amplification and also the value of the maximum phase lead increases. This observation is related to the overshooting phenomenon discussed in the context of throttling. At high activation energies, as

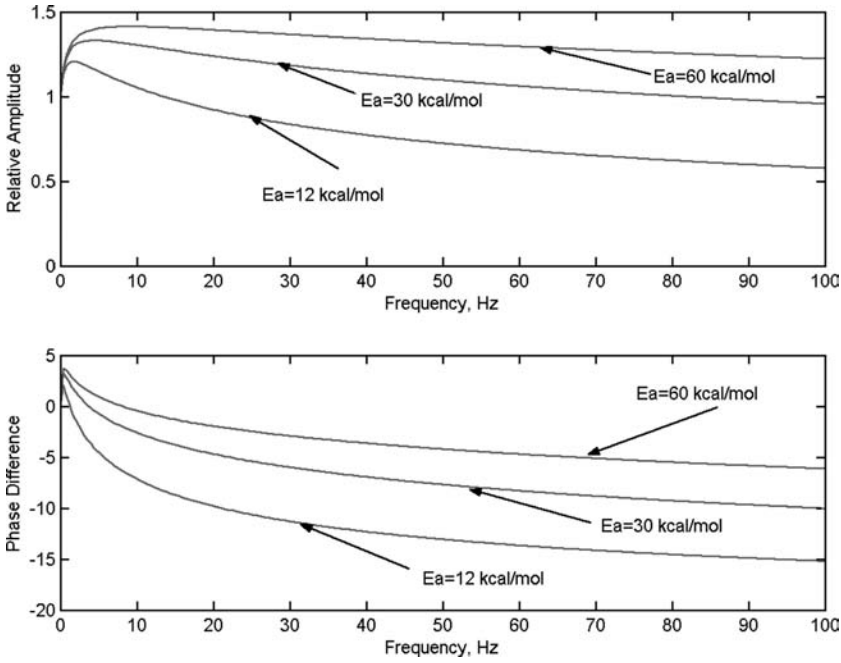

Fig. 17 Effect of activation energy on frequency response of thermal lag system.

described in the preceding section, the surface timescale is small and overshooting is significant. The response can lead and amplify a faster changing input through the overshooting phenomenon. Thus, the phase-lead and amplification domains get larger as the activation energy increases. In the limiting case of infinite activation energy that corresponds to the CWT model, the phase lead and relative amplification covers the whole spectrum. Namely, the relative amplification and phase lead increase to their maximum values at zero frequency and they stay constant for the whole frequency spectrum. For very small activation energies, the frequency response behaves like the response of a first-order system that does not possess any amplification or phase-lead regions.

It is determined that the effect of the energy parameter E_L on the frequency response is secondary for the fuels typically used in hybrid applications. The influence of the thermal lag time is to linearly stretch the frequency axis of the response curves such that a system with smaller thermal lag time will have a broader frequency range of amplification and phase lead.

To explore the possible nonlinear effects on the response and to confirm the perturbation analysis results, we performed some numerical simulations of the sinusoidal heat input case.

We first note that the results of this perturbation analysis are in good agreement with the numerical simulations even for relatively high oscillation amplitudes such as 40% of the mean value. The comparison of the perturbation results with the numerical simulations for various frequencies is given by Karabeyoglu [15]. We

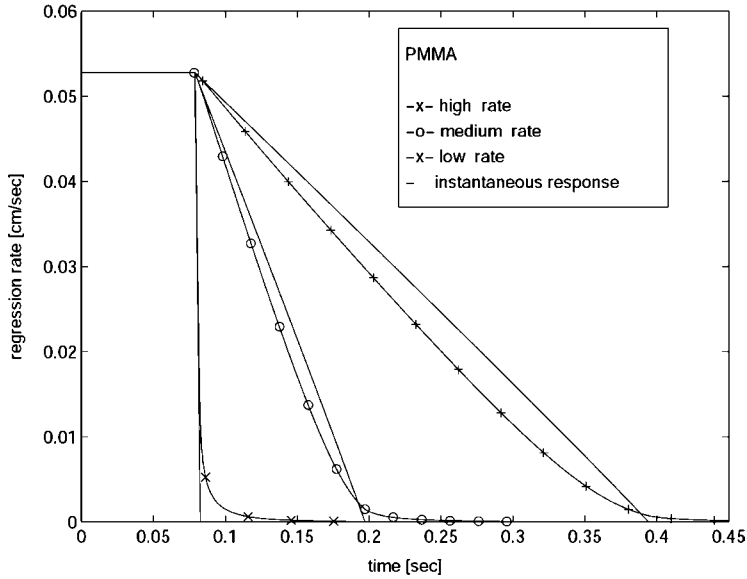

Fig. 18 Thrust termination response for various thrust termination rates.

believe that the larger errors at high-frequency values reported in Ref. [15] are mainly due to the inaccuracies in the amplitude and phase difference calculations made from the numerical simulation data.

Another important observation that is made from the numerical simulation results and also from the second-order perturbation analysis results [15] is the existence of a small shift in the mean regression rate above the mean quasi-steady value. This is consistent with the experimental findings indicating increased mean regression rates during the oscillatory modes of combustion. Note that the thermal lag model only accounts for a fraction of this phenomenon, commonly referred as the "DC shift" [4]. The remainder of the increase in the mean regression rate during oscillatory combustion is induced by the gas-phase dynamics.

4. Thrust Termination

The thrust termination event has been simulated using a heat input model that gradually drops from a constant value to zero. The proper initial condition is the steady-state temperature distribution at the initial heat input. Figure 18 indicates that for sudden thrust termination cases the regression rate closely follows the heat input except in a region next to the zero regression rate point. As the rate decreases, the transient response starts to lead the instantaneous response. This behavior is well documented in solid rockets [31].

VI. Transient Boundary-Layer Combustion

The thermal lag model treats the surface heat flux as a parameter that can be controlled directly. However, in a hybrid motor, the oxidizer mass flow rate

is the primary variable that alters the wall heat flux through other parameters. The actual response of the motor to a change in the oxidizer mass flow is rather complicated during a transient. As the oxidizer mass flow rate of the motor changes, the mass flux at a characteristic point in the port reacts to the change, as does the turbulent boundary layer developed over the fuel surface. In this section, we focus on the modeling of the boundary-layer combustion dynamics and investigate its interactions with the thermal lags in the solid.

A. Quasi-Steady Model for the Boundary Layer Combustion

As a first approximation, we assume that the boundary-layer response is quasi steady, namely, the boundary-layer diffusion lag times are small compared to the thermal lag times in the solid. Under the quasi-steady assumption, one can use the classical approach [32, 33] to calculate the response of the wall heat flux to the changes in mass flux. However, the results of classical hybrid theory cannot be used directly during a transient in the solid because the convective heat transfer to the wall depends explicitly on the instantaneous regression rate through the blocking generated by the blowing of the gaseous fuel from the surface. In the presence of the thermal lags, the blocking generates a coupling mechanism in the gas phase between the regression rate and the heat flow to the surface. For the sake of simplicity, the development will be limited to the case of no radiative heat transfer, $\dot{Q}_w = \dot{Q}_c$. It is expected that the effect of the radiative heat transfer on the results that will be presented in the following paragraphs will be small.

The convective heat flux from the gas to the fuel surface, $\dot{Q}_c$, is given in terms of the heat-transfer coefficient C_H at time t as

$$\dot{Q}_c(t) = C_H \rho_b u_b (h_b - h_w) = C_H \rho_b u_b \Delta h \tag{26}$$

where h_b and h_w are enthalpies at the flame and at the wall, respectively. Note that all variables are functions of time.

We will now assume that the classical assumption of Reynolds analogy is still valid during this quasi-steady operation mode. This allows us to express the heat-transfer coefficient in terms of the skin-friction coefficient as

$$C_H = \tfrac{1}{2} C_f (\rho_e u_e^2 / \rho_b u_b^2) \tag{27}$$

After the elimination of the heat-transfer coefficient, one obtains the following expression for the wall heat flux:

$$\dot{Q}_c(t) = \tfrac{1}{2} C_f G (u_e / u_b) \Delta h \tag{28}$$

where G is the total mass flux $\rho_e u_e$.

At this point, it is useful to define an aerodynamic blowing parameter (also known as the mass transfer number) as

$$B_a = \frac{(\rho v)_w}{\rho_e u_e C_f/2} = \frac{\dot{r}\rho_f}{G C_f/2} \tag{29}$$

The skin-friction coefficient can be written as the skin-friction coefficient for no blowing multiplied by a correction factor, C_f/C_{fo}, for the blocking, which, in general, is a function of the aerodynamic blowing parameter B_a.

For the blowing correction during transient, we assume a similar formula to that proposed by Marxman et al. [5],

$$C_f/C_{fo} = qB_a^{-k} \tag{30}$$

At steady state, Eq. (26) becomes $\dot{Q}_c = \dot{r}\rho_f h_v$, which when combined with Eqs. (27) and (28) gives a steady-state value for the thermochemical blowing parameter

$$B_t = (u_e/u_b)\Delta h/h_v \tag{31}$$

Combining Eqs. (28–31) yields the following expression for convective heat flux at the wall:

$$\dot{Q}_c = \tfrac{1}{2}C_{fo}qh_vGB_a^{-k}B_t = \tfrac{1}{2}C_{fo}qGB_a^{-k}(u_e/u_b)\Delta h \tag{32}$$

It is important to observe the distinction between the two forms of the blowing parameter because during a transient one must use the general form in Eq. (32) because the regression rate is time dependent and must wait for the temperature gradient at the surface, $(\partial T/\partial x)_s$, to adjust.

During a transient, the aerodynamic blowing parameter at a given operating condition of a rocket motor cannot be determined by equating it to the thermochemical blowing parameter. However, B_a can be expressed in terms of regression rate and mass flux with use of Eqs. (29) and (30),

$$B_a = \left(\frac{\dot{r}\rho_f}{qGC_{fo}/2}\right)^{1/(1-k)} \tag{33}$$

Now a general form of the heat conduction expression can be found on the substitution of B_a and the commonly used form of the skin-friction coefficient for the turbulent boundary layers [34], $C_{fo}/2 = 0.03(Gz/\mu)^{-0.2}$ in Eqs. (32) and (33),

$$\dot{Q}_c(t) = (0.03q/\mu^{-0.2})^{1/(1-k)}(B_t h_v/\rho_f^{k/(k-1)})z^{-0.2/(1-k)}G^{0.8/(1-k)}\dot{r}^{-k/(1-k)} \tag{34}$$

Here z is the axial distance from the entrance of the port.

Note that the terms in the parentheses in Eq. (34) are functions of the boundary-layer properties and combustion characteristics. Thus, they can be treated approximately as constants after the propellants are selected, and the expression for the heat flux reduces to the following form where A' is a constant for a given propellant combination.

$$\dot{Q}_c(t) = A'z^{-0.2/(1-k)}G^{0.8/(1-k)}\dot{r}^{-k/(1-k)} \tag{35}$$

So far we have developed a formula that relates the wall heat flux at a specified location of the port to the regression rate and mass flux at that location. However, in practice for a specific propellant combination, the coefficient A' is best determined empirically. Frequently the available data are based on the average regression rate in terms of the oxidizer mass flux [5, 8]. For simplicity we will conduct the

analysis for a propellant combination with the average regression rate expression, $\dot{r} = aG_o^n$. Note that the following analysis can easily be extended to other forms of the regression rate expressions used for hybrids. Similar to the local formulation, a space-averaged expression can be derived as

$$\dot{Q}_c(t) = \bar{A}' G_o^{n/(1-k)} \dot{r}^{-k/(1-k)} \tag{36}$$

where $\bar{A}' = \rho_f h_v a^{1/(1-k)}$. Here G_o replaces G and n replaces 0.8 to conform to typical experimental reporting. Note that the heat flux from the gas to the wall depends on the port mass flux and also the regression rate, by virtue of its blocking effect.

To couple the heat flux expression with the thermal lag formulation, we nondimensionalize with respect to the reference state $(G_o)_{\text{ref}}$, $\dot{Q}_{\text{ref}} (= \dot{r}_{\text{ref}} \rho_f h_v)$, and $\dot{r}_{\text{ref}} [= a(G_o)_{\text{ref}}^n]$, which is selected to be the nominal operating point. In terms of the normalized quantities $\bar{G}_o = G_o/(G_o)_{\text{ref}}$ and $\bar{\dot{Q}}_c = \dot{Q}_c/\dot{Q}_{\text{ref}}$ the heat flux equation takes the form of

$$\bar{\dot{Q}}_c(\bar{t}) = E_h \bar{G}_o^{n/(1-k)} R^{-k/(1-k)} \tag{37}$$

Note that $E_h = h_v/C\Delta T = 1 + E_L$ is another energy parameter.

Next we linearize this equation around the reference point by expanding as follows:

$$\bar{\dot{Q}}_c(\bar{t}) = 1 + \varepsilon Q_1(\bar{t}) + \mathcal{O}(\varepsilon^2) \tag{38a}$$

$$R(\bar{t}) = 1 + \varepsilon R_1(\bar{t}) + \mathcal{O}(\varepsilon^2) \tag{38b}$$

$$\bar{G}_o(\bar{t}) = 1 + \varepsilon G_1(\bar{t}) + \mathcal{O}(\varepsilon^2) \tag{38c}$$

The first-order terms in ε can be collected to give the linear version of the relation to be used in the first-order perturbation analysis,

$$Q_1(\bar{t}) = E_h\{[n/(1-k)]G_1(\bar{t}) - [k/(1-k)]R_1(\bar{t})\} \tag{39}$$

Note that in the absence of the blocking effect, $k = 0$, the heat flux becomes a function of the oxidizer mass flux alone.

B. Combustion Boundary-Layer–Thermal Lag Coupling

In the development of the transient hybrid combustion theory, we assumed that the boundary layer responds rapidly to the changes in the mass flux compared to the other transient timescales in the rocket motor such as the gasdynamic lags or the thermal lags. This assumption fails to be valid especially for large hybrid motors. To develop a realistic model for the dynamics of the hybrid motor, the boundary-layer lags must be considered. There does not appear to be sufficient information in the literature on the response of the turbulent boundary layers with chemical reactions and blowing, that is, hybrid rocket combustion scheme, to the changes in the free-flow conditions. Because this complex dynamic phenomenon is extremely difficult to investigate both theoretically and also experimentally, we consider the

simpler cases reported in the literature of a standard incompressible turbulent boundary layer with no blowing or chemical reactions. The transient response of various kinds of turbulent flowfields are summarized by Karabeyoglu [15]. Here we restrict our discussion to an important set of transient experiments discussed in Ref. [34]. The tests were performed by abruptly changing the freestream velocity over a turbulent boundary layer from one value to another (such as throttling) and by measuring the time-average velocity profile and the fluctuations in the velocity components at various axial locations. The researchers concluded that the time required for transition from the initial equilibrium profile to the final equilibrium profile at any axial location was proportional to the time of flight of a fluid particle from the leading edge of the boundary layer to the specific axial location at the speed of the freestream flow [34]. This very important result can be formulated for hybrid boundary layers as

$$\tau_{\mathrm{bl}} = c'(z/u_e) \tag{40}$$

Here c' is a constant that needs to be determined empirically. We will call this time required for equilibration the characteristic response time of the boundary layer τ_{bl}. Note that the physical nature of the boundary-layer transient time is not related to the propagation of the disturbances with the speed of the port velocity as suggested by Eq. (40). The delay rather depends on the diffusion timescale across the boundary layer, which is proportional to the ratio of the local boundary-layer thickness to the diffusion speed, $\tau_{\mathrm{bl}} \cong \delta/U^*$. The diffusion speed is defined in terms of the shear stress and mean gas density as $U^* = \sqrt{\tau_o/\rho}$. The boundary-layer delay time, after the substitution of the standard (incompressible) turbulent boundary-layer expressions [35] for the shear stress, $\tau_o = 0.0288\rho\, u_e Re_z^{-0.2}$, and the thickness, $\delta = 0.37 z Re_z^{-0.2}$, becomes $\tau_{\mathrm{bl}} = 2.18 Re_z^{-0.1} z/u_e$. Here the local Reynolds number is defined as $Re_z = u_e z\rho/\mu$. Note that the coefficient c' is found to be a weak function of the local Reynolds number for large Reynolds number Re_z values typically observed in hybrids. For simplicity, we assume that c' is constant. For Reynolds numbers corresponding to typical hybrid operation, c' is estimated to be approximately 0.55. In a real hybrid boundary layer with combustion and blowing, c' can be different from this estimation, and for that reason, it is determined empirically.

It is convenient to consider an average boundary-layer delay and replace the local distance z with the length of the grain, L. Note that the empirical constant c' accounts for the correction to the inaccuracies introduced by the selection of the length scale L. However, we recognize that in reality there is a range of boundary-layer delay times that should be considered. Thus, the significant observation here is that erratic or variable low-frequency instability can result. The exact determination of the average delay time is quite difficult because the hybrid boundary layers merge at a point that has been estimated to be at an $L/D \approx 5$ [36]. Note that, after they merge, the diffusion thickness for the oxidizer portion becomes a large fraction of the radius of the port that changes very slowly with the axial distance. However, the diffusion thickness in the fuel side continues to increase due to the increasing distance of the flame from the wall.

The response of the boundary layer to the changes in the mass flux can be approximated by simply inserting time delays in the heat flux expressions derived under the assumption of quasi-steady response. The implementation of this idea

in Eq. (39) yields

$$Q_1(\bar{t}) = E_h\{[n/(1-k)]G_1(\bar{t}-\bar{\tau}_{\text{bl1}}) - [k/(1-k)]R_1(\bar{t}-\bar{\tau}_{\text{bl2}})\} \tag{41}$$

where $\bar{\tau}_{\text{bl1}} = \tau_{\text{bl1}}/\tau_{\text{tl}}$ and $\bar{\tau}_{\text{bl2}} = \tau_{\text{bl2}}/\tau_{\text{tl}}$.

Here τ_{bl1} and τ_{bl2} are the time delays experienced by the wall heat flux $\dot{Q}_c$ to the changes in the oxidizer mass flux and the regression rate, respectively. The scaling of the time delays τ_{bl1} and τ_{bl2} obey the general scaling law given by Eq. (40). However, the c' coefficients for τ_{bl1} and τ_{bl2} are expected to be different because each of these delays represents a different adjustment mechanism for the boundary layer.

The derivation of the transfer function is very similar to the derivation performed for the pure thermal lag case. The only difference is in the energy balance boundary condition at the surface, which must be modified. Substitution of Eq. (41) in the surface boundary condition of the linearized thermal lag problem [Eqs. (15–17)] yields the correct boundary condition for the coupled problem. With this new boundary condition, the linearized thermal lag problem can be solved in a similar way to the case with no delays, with the use of Laplace transformation technique. The transfer function between the regression rate $R_{1L}(s)$ and the mass flux $I(s)$ can be obtained as

$$\frac{R_{1L}(s)}{I(s)} = \frac{2E_E\sigma_2 e^{-\bar{\tau}_{\text{bl1}}s}s}{(1+\sqrt{1+4s})(s+E_E) - 2E_E + 2E_E s(E_L + \sigma_1 e^{-\bar{\tau}_{\text{bl2}}s})} \tag{42}$$

Two new constants are introduced for convenience.

$$\sigma_1 = E_h[k/(1-k)]; \qquad \sigma_2 = E_h[n/(1-k)] \tag{43}$$

This transfer function for the TC coupled system represents the combustion phenomenon includes the dynamics of the thermal processes in the solid and approximates the combustion dynamics in the turbulent boundary layer of the rocket motor. Equation (42) can be used to investigate the stability character of the TC coupled system. The commonly used method for evaluating the stability character of a linear system is to map the poles of the transfer function in the s plane. Particularly, the real component of a certain pole of a transfer function indicates amplification rate associated with that pole. Similarly the imaginary part represents the oscillation frequency.

First a system with zero boundary layer delays, that is, $\tau_{\text{bl1}} = \tau_{\text{bl2}} = 0$, is determined to be always stable. In fact, a plot of the transfer function for a system with typical parameters shows no poles in the s plane [only a zero at (0, 0)] indicating no sign of instability, Fig. 19. If a positive delay is introduced between the regression rate and wall heat flux, a series of unstable poles is generated. The example case with a 38-ms delay is shown in Fig. 20. Note that all of the other parameters are kept identical to the case with no delays. Even though there exists an infinite series of poles generated (at the same amplification rate), we concentrate only on the pole with the lowest frequency (fundamental mode). We believe that the higher-order modes are an artifact of using a simple delay instead of the full dynamics for the boundary-layer transients. Moreover, the higher frequency modes, even if they

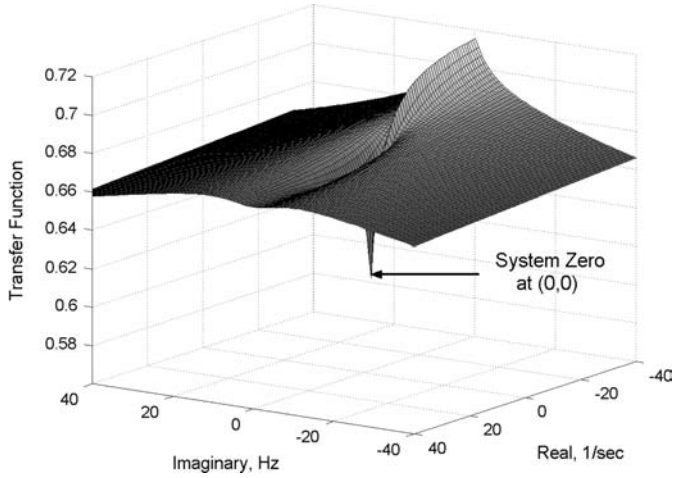

Fig. 19 Transfer function of TC coupled system with no delays ($\tau_{bl1} = \tau_{bl2} = 0$), HTPB system with $E_a = 15$ kcal/mole.

exist in a real system, are likely to be damped more effectively compared to the fundamental mode.

It is important to identify the necessary conditions that must exist for the generation of TC coupled instabilities. A careful examination of the denominator of the transfer function [Eq. (42)], shows that for the instability to exist the blowing exponent k, activation energy E_a, and delay time τ_{bl2} must be nonzero. This indicates

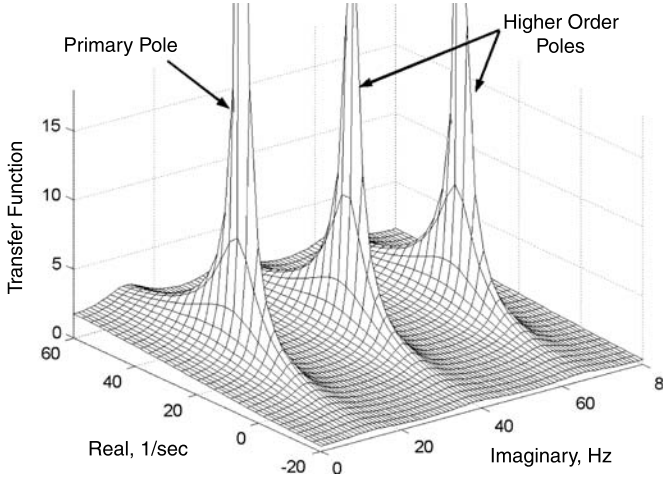

Fig. 20 Unstable poles of TC coupled system in s plane for $\tau_{bl1} = 0$ and $\tau_{bl2} = 38$ ms, HTPB system with $E_a = 15$ kcal/mole.

that the instability is a result of the coupling of three physical phenomena: blocking of heat transfer by radial injection of fuel mass and thermal transients in the solid and the boundary-layer dynamics.

Next we consider the effect of various parameters on the TC coupled instability. It can be shown that the effect of the regression rate mass flux exponent n, heat of vaporization of the fuel, L_v, heat capacity of the solid fuel, C, and surface temperature T_s on the oscillation frequency and amplitude are negligible for the range of these parameters that are commonly found in hybrid systems. Also TC coupled system characteristics are completely independent of the solid density ρ_f and the heat diffusivity in the solid κ.

The effect of the activation energy on the amplification and frequency has been studied in Ref. [37]. It has been shown that for activation energies commonly observed in hybrids, ranging from 5 to 60 kcal/mole, the variation in the oscillation frequency is relatively small. For the specific case considered in the study [37], the systems with activation energies larger than 3 kcal/mole show positive amplification and unstable behavior. Decreased stability at higher activation energies is expected because at high E_a values the surface temperature and regression rate are more closely coupled. As indicated before, this coupling is one of the necessary ingredients for the generation of the instabilities. In fact, in the extreme case of $E_a = 0$, for which the surface temperature is completely independent of the regression rate, oscillation frequency goes to infinity and the amplification asymptotes to negative infinity.

The activation energies for the polymeric systems that are typically used in hybrids range from 5 to 60 kcal/mole. For the nonpolymeric paraffin-based fuel system, the activation energy is equivalent to the latent heat of vaporization [38]. This value for the paraffin-based fuel formulations is estimated to be 17 kcal/mole [39].

Similar results can be obtained for the effect of the blocking exponent. For the range of values reported in the literature for k, that is, 0.68–0.77 [5, 22], the effect of blowing exponent on the frequency is negligible. The amplification increases with increasing k, and systems with k values 0.45 and larger show unstable behavior. Note that for the physically unrealizable case of $k = 0$ the instability disappears because one of the necessary coupling mechanisms is eliminated. We finally note that, even though the blocking effect in paraffin-based systems is somewhat reduced due to the two-phase character of the flowfield, it is still significant enough to establish the coupling between the gas phase and solid phase.

The most influential parameter on the oscillation frequency for the TC coupled system is determined to be the boundary delay time τ_{bl2}. Figure 21 shows the predicted frequency as a function of the delay time for three activation energy values, $E_a = 5$, 15, and 50 kcal/mole. As shown in Fig. 21, the effect of the activation energy on the frequency, especially at longer delay times, is small. For most cases, the effects of activation energy and blowing exponent can be ignored and the frequency can be represented as a function of the boundary delay time alone. The following curve-fit equation is suggested to quantify the inverse relationship between the frequency and the boundary-layer delay time:

$$f = 0.48/\tau_{\text{bl2}} \tag{44}$$

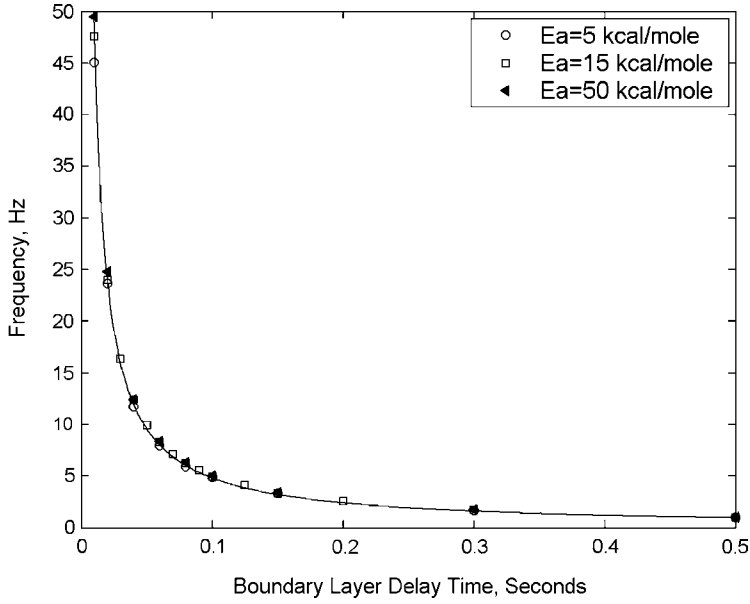

Fig. 21 Effect of boundary-layer delay time on oscillation frequency for various activation energies.

As shown in Fig. 21, this expression represents the predicted frequency to a very high degree of accuracy and will be used for all of the hybrid systems that will be discussed later in this chapter.

VII. Gasdynamics

In the preceding section, the dynamic models for the thermal lags and the hybrid combustion are summarized. In addition, these subsystem models are coupled to obtain the response of the fuel mass generation to the changes in the mass flux in the port. However, practically significant parameters of the rocket operation such as the chamber pressure, specific impulse, and thrust cannot be obtained solely from the TC coupled system. These variables can only be determined after introducing a model for the gasdynamics, which will be discussed in this section. A gasdynamic model, in general, should use the oxidizer mass flow rate and the fuel mass generation rate as the inputs and it should yield the parameters that are more closely related to the performance of the motor such as the chamber pressure and thrust as the outputs.

A specific gas dynamic model (2V-port model) has been developed in Ref. [15]. In this particular model, the motor is divided into four subsections: 1) precombustion chamber, 2) port volume, 3) postcombustion chamber, and 4) nozzle (see Fig. 22 for a schematic). Each component is approximated appropriately with one or zero spatial dimensional models. The subscripts 1 and 2 are used for the physical properties in the pre- and postcombustion chambers, respectively. Various stations of significance are also distinguished by use of subscript notation.

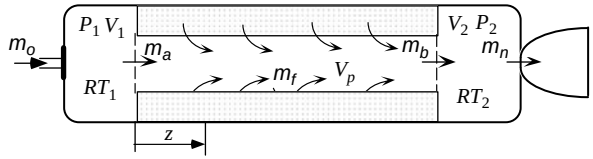

Fig. 22 Schematic of 2V-port gasdynamic model.

Namely, the entrance station of the gaseous oxidizer into the system is represented by a subscript *o*, the nozzle entrance is denoted by *n*, and the port entrance and exit are shown by *a* and *b*, respectively. The specifics of the models for these subsections are discussed in the next section.

A. Precombustion Chamber

A zero-dimensional gasdynamic model for the precombustion chamber has been implemented. Thus, the momentum equation and the energy equations reduce to the mean-state information of the pressure and temperature in this volume. The mass balance equation is nontrivial, and it can be written as

$$V_1 \frac{\mathrm{d}\rho_1}{\mathrm{d}t} = \dot{m}_o - \dot{m}_a \tag{45}$$

Note that the size of the volume is assumed to be constant over the burn time. A constant molar mass and a polytropic process, $P \propto \rho^{n_p}$ (where n_p is the polytropic exponent), approximation is made for this relatively cold chamber. Under these stated conditions and with the use of the ideal gas law, Eq. (45) can be reduced to

$$a_1 \frac{\mathrm{d}P_1}{\mathrm{d}t} = \dot{m}_o - \dot{m}_a \tag{46}$$

where $a_1 = V_1/n_p R_1 T_1$.

B. Port Chamber

The fuel port has been treated as a quasi-one-dimensional tube with continuous mass and heat addition. The conservation of mass can be written as the following differential equation:

$$\frac{\partial \rho}{\partial t} = -\frac{\partial G}{\partial z} + \dot{m}_f \tag{47}$$

Here $\dot{m}_f$ is the mass generated at the axial location z of the port. At this stage, it is preferable to express the mass generation term in the general functional form

$$\dot{m}_f = f(G, z)$$

The momentum equation in the port can be written in terms of the local mass flux G, the local pressure P, and the local density ρ,

$$\frac{\partial G}{\partial t} = -\frac{\partial (G^2/\rho)}{\partial z} - \frac{\partial P}{\partial z} - \left(\frac{C_f C_p}{2A_p}\right)\frac{G^2}{\rho} \tag{48}$$

Note that the last term in this expression is included to capture the effect of the skin friction on the force balance. Here C_f stands for the skin-friction coefficient at location z, A_p for the port area, and the C_p for the circumference of the port. All of the geometrical properties are assumed to be independent of time and axial dimension.

We further assume that the ideal gas law holds locally in the port,

$$P = \rho RT \tag{49}$$

The closure of the system requires the energy equation. For the sake of simplicity, we replace the energy equation with the following linear variation of temperature gas constant product in the port:

$$RT(x) = (RT)_1 + [(RT)_2 - (RT)_1]z/L \tag{50}$$

Note that for the simplicity of notation we treat the gas constant temperature product as a single dependent variable.

Furthermore, we assume that the gas constant temperature product at the exit of the port volume is a fraction of the nozzle entrance value RT_c, which can be calculated from the equilibrium chemistry at the operating O/F ratio of the motor,

$$RT_2 = f_b RT_c \tag{51}$$

In short, we specify the whole temperature field in the motor chamber for a given operating point and we ignore the variations in the temperature field during the transients. In that respect the 2V-port is an isothermal gasdynamic model.

C. Postcombustion Chamber

Similar to the precombustion chamber treatment, we assign uniform thermodynamic properties for the gas in the postcombustion chamber volume. Therefore, the dynamics can be represented with the mass balance that takes the following form after the fixed-volume assumption:

$$V_2 \frac{\mathrm{d}\rho_2}{\mathrm{d}t} = \dot{m}_b - \dot{m}_n \tag{52}$$

Here $\dot{m}_b$ is the mass flow rate entering the hot volume, and $\dot{m}_n$ is the mass flow rate exiting the volume through the nozzle. Note that we have inherently assumed that post-combustion chamber behaves like a well-stirred reactor with the reactions fast compared to the transient rates of concern. Equation (45) can be written as

$$a_2 \frac{\mathrm{d}P_2}{\mathrm{d}t} = \dot{m}_b - \dot{m}_n \tag{53}$$

where $a_2 = V_2/RT_2$. We have approximated the gas constant temperature product in the post-combustion chamber with product at the port exit.

D. Nozzle

We assume that the nozzle flow is quasi steady, which is only valid at relatively slow transients. We also assume that, throughout the operation of the motor, the nozzle is always choked, namely, at any time the ratio of the chamber pressure to the ambient pressure is larger than the critical value associated with the properties of the expending gas. After these simplifying assumptions, the nozzle flow rate can be expressed with use of the classical quasi-one-dimensional gasdynamic formula

$$\dot{m}_n = A_n \Gamma_c P_2 / \sqrt{RT_c} \tag{54}$$

where

$$\Gamma_c = \sqrt{\gamma_c}[2/(\gamma_c + 1)]^{(\gamma_c+1)/2(\gamma_c-1)}$$

Here γ_c is the ratio of the specific heats of the combustion products. An expression for the nozzle dynamics that is more accurate at moderate/high frequencies is given elsewhere [15].

E. Results of the Gasdynamic Model

Small perturbation solutions as well as numerical solutions for the system of equations derived for the 2V-port model are generated by Karabeyoglu [15]. The following conclusions can be drawn from the results of the gasdynamic model.

1) The gasdynamic model captures the filling/emptying dynamics and also the longitudinal acoustic response of the hybrid combustion chamber. As can be seen from the gasdynamic transfer function shown in Fig. 23, acoustic modes are stable (well damped). No unstable oscillation modes are generated by the gasdynamic system by itself.

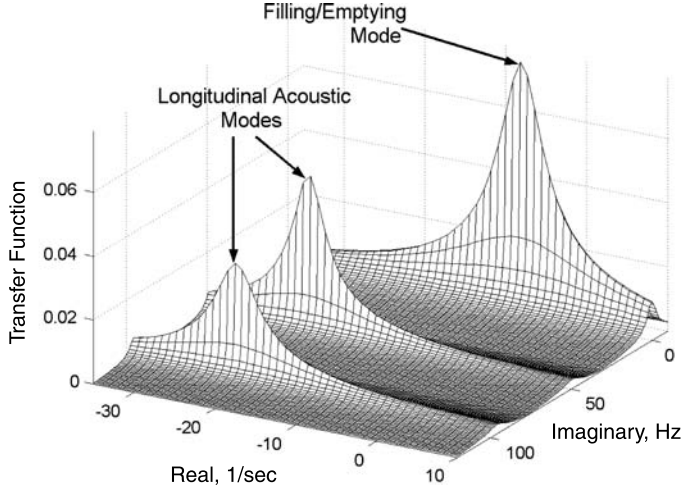

Fig. 23 Transfer function for pure gasdynamic system.

2) The nonlinear disturbances excite the chamber acoustic modes. Simulations showed that a sudden pulse in the oxidizer mass flow rate excites the acoustics modes. These modes decay in a relatively short period. This ringing phenomenon shows that the longitudinal acoustic modes can be driven by nonlinear low-frequency oscillations. Namely, the nonlinear low-frequency pressure waveforms continuously excite the acoustic modes of the chamber. AMROC motor DM-01 showed at least five well-damped longitudinal acoustics modes. The gasdynamic model when corrected for isentropic speed of sound predicts the acoustics frequencies of the DM-01 motor to a high level of accuracy [37].

3) The gasdynamic model coupled with the boundary-layer dynamics ($\tau_{bl1} \neq 0$) does not produce any instabilities. Namely, no extra poles are generated in the s plane. This conclusion is based on transfer function analysis and also numerical simulations. This important result highlights the importance of the thermal lag system, that is, its unique dynamic capability of producing a phase lead, in producing a coupling mechanism to generate low-frequency unstable modes.

VIII. Thermal–Combustion–Gasdynamic (TCG) Coupled System

In this section we integrate the gasdynamic system to the TC coupled system to establish the thermal–combustion–gasdynamic (TCG) coupled response. The TCG coupled system yields the important performance parameters of the rocket (such as chamber pressure) for some given input of oxidizer mass flow rate variation, which is a fundamental control parameter in hybrid rockets. It is fair to state that the TCG-coupled system represents the most fundamental dynamic behavior of a hybrid rocket.

The schematic of the hybrid subsystems and the information flow between the subsystems in the context of TCG coupling are shown in Fig. 24. Note that the lower block in the schematic represents the TC coupled system. The input for the TC coupled system is the local mass flux information, and the output is the mass generation or the regression rate. The upper block shows the 2V-port gasdynamic model. The gasdynamic model takes the oxidizer flow rate and the mass generation rate information and reveals the important performance parameters such as the chamber pressure and specific impulse. The TCG coupled system can be considered as an overall model for the dynamics of a hybrid-propulsion system that utilizes gaseous oxidizer that is delivered by an isolated feed system.

The generalization of the TCG coupled system to a liquid hybrid with significant feed system dynamics can be achieved easily. Namely, two more modules for the liquid droplet evaporation and the feed system dynamics must be added to the front end of the TCG model. We believe that the fundamental phenomenon generating the intrinsic low-frequency instabilities of hybrid systems does not involve either of the evaporation lags or the feed system dynamics.

In the TCG coupled system, the gasdynamic module converts the fuel mass oscillations produced by the TC coupled system into the chamber pressure oscillations. It has been determined that in the process of conversion the oscillations produced by the TC coupled system, that is, frequencies and amplification rates, are not altered. This fact is demonstrated in Fig. 25, which shows the TCG system transfer function for the TC coupled system in Fig. 20. Figure 25 also shows the

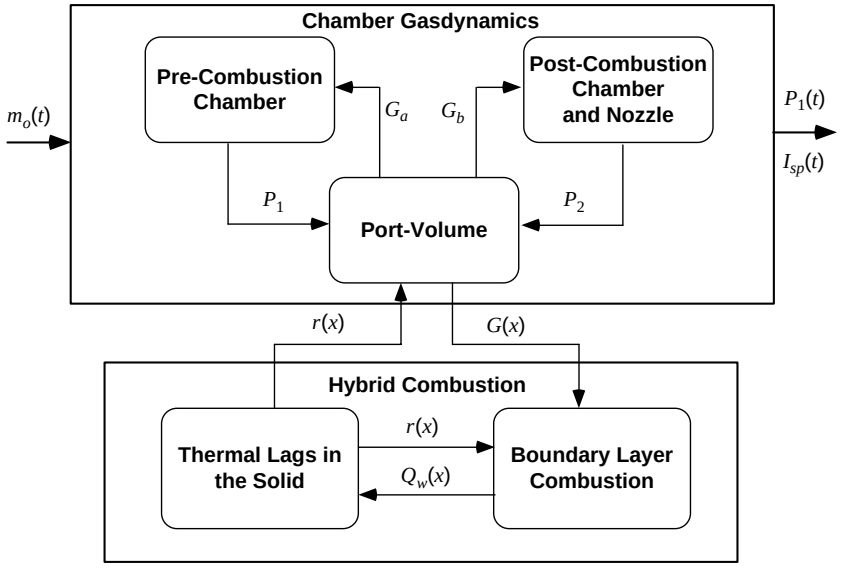

Fig. 24 Schematic of the TCG coupled system.

poles associated with the filling/emptying mode (first order nonoscillatory mode) and the longitudinal acoustic modes with negative real components (damped). The TCG coupled system captures all of the necessary underlying dynamics (linearized version) of a gaseous hybrid with a decoupled feed system.

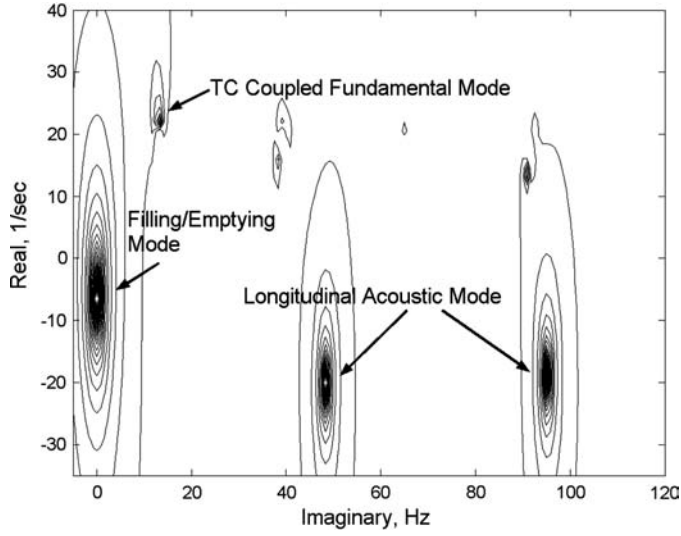

Fig. 25 Contour plot of TCG coupled system with $\tau_{bl2} = 38$ ms; most transient features of hybrid system can be deduced from pole locations.

IX. Application of the Theory to ILFIs

In this section we compare the TC coupled theory oscillation frequency predictions with the chamber pressure oscillation frequencies from hybrid motor test data. To produce a conclusive comparison, we have selected a large number of tests from several hybrid rocket development programs. (The data from these tests are given by Karabeyoglu et al. [37].) The key features of each program is discussed briefly.

1) *AMROC motor tests [2]*—The reported results are for four different thrust class hybrid motors that all used liquid oxygen (LOX)/gaseous oxygen (GOX) as the oxidizer and HTPB as the fuel (see Table 4).

2) *Hybrid Propulsion Demonstration Program (HPDP) 11-in. motor tests [3,6]*—The oxidizer used in these tests is LOX and GOX and the fuel is an HTPB/Escorez formulation. The motor case diameter was 11 in., and the data from five tests are used in this study. Only the tests that exhibit combustion instability and performed with single-port motors are considered. The runs with the rearward-facing steps at the port entrance are also excluded in this study because in these tests the flowfield in the port is significantly altered, which may cause a major change in the boundary-layer delay time coefficient. We also include test 1 of 11-in. LOX motor data in the analysis. We only consider test 1 because it is the only run with a chamber configuration identical to GOX motors used in the calculations (see Table 5).

3) *JIRAD motor tests [7]*—The oxidizer used in these tests is GOX, and the fuel is also an HTPB/Escorez formulation. The motor case diameter was 11 in.

Table 4 Summary of parameters used in the frequency estimations for AMROC motors

AMROC motor (thrust, lb)	O/F	c^*_{theo} (ft/s)	$c^*_{\exp}$(ft/s)	L^* (in.)	f (Hz)	$\tau_{b/2}$ (ms)
S Motor (10 k)	1.45	5584	5361	570	11	40.6
Half-Scale (33 k)	1.45	5584	5361	1305–1430	4.8	97.5
H-500 (75 k)	1.45	5584	5361	1770–2340	4.0	146.3
DM-01 (250 k)	1.55	5700	5472	2168	2–3.5	156.0

Table 5 Summary of parameters used in the frequency estimations for the 11 in. Hybrid motor tests. Grain length is 102 in.

Test no.	$\bar{D}$ (in.)	$\dot{m}_o$ (lb/s)	G_o (lb/in.^{2}-s)	G_t (lb/in.^{2}-s)	P_c (psi)	O/F	f (Hz)	ΔP_{osc} (psi)	$\tau_{b/2}$ (ms)
1 (GOX)	4.25	6.0	0.423	0.571	600	2.85	13	200	49.3
2 (GOX)	4.25	5.7	0.402	0.541	550	2.89	8	300	47.6
7 (GOX)	4.20	4.7	0.339	0.458	440	2.89	15	100	45.1
8 (GOX)	4.22	5.1	0.365	0.492	260/280	2.87	20	400	25.7
1 (LOX)	—	—	0.222	0.31	435	2.51	8	250	66.8

and the data from eight tests are used in this study. Only the tests that exhibit combustion instability and performed with single-port motors are considered here (see Table 6).

4) *Arizona State University [40]*—One test is included in the comparison for a 5-in.-diam nitrous oxide motor. The fuel was HTPB (see Table 7).

5) *Paraffin-based motor tests [8]*—These tests were conducted at NASA Ames Research Center in a 10-in.-diam test facility. The oxidizer was GOX, and the fuel is two separate nonpolymeric paraffin-based formulations (SP-1a and SP-4). The data from 25 motor tests were reported by Karabeyoglu et al. [8] (see Table 8).

The prediction of the frequency requires the estimation of the boundary-layer delay time for each test from the reported data. Because the reported data are somewhat different for each program, different scaling laws for the delay time must be derived.

The first one of these is for the various-size AMROC motors, which operated at different L^* conditions. Because the information on the AMROC motors that can be found in the literature is limited to L^*, c^*, and motor O/F, it is desirable to express the boundary-layer delay time, Eq. (40) (with $z = L/2$) in terms of these variables. The average velocity in the port can be approximated as

$$u_{\text{av}} = \frac{G_t[(1 + 2O/F)/(1 + O/F)]RT_{\text{av}}}{2P_c} \tag{55}$$

where RT_{av} is an average value in the port. Substituting this expression in the delay formula and using the relations for the total mass flow rate $\dot{m}_t = G_t A_p$ and port

Table 6 Summary of parameters used in the frequency estimations for the NASA/MSFC 11 in. Hybrid motor tests

Test no.	$\bar{D}$ (in.)	L (in.)	$\dot{m}_o$ (lb/s)	G_o (lb/in.^{2}-s)	G_t (lb/in.^{2}-s)	P_c (psi)	O/F	f (Hz)	ΔP_{osc} (%)	$\tau_{b/2}$ (ms)
3	3.4	102	3.44	0.38	0.527	745	2.6	6–10	15	67.1
4	4.3	102	3.36	0.23	0.325	325	2.4	10–20	20	47.8
6	3.7	102	8.36	0.78	1.024	750	3.2	10–15	12	34.0
7	5.3	102	3.41	0.15	0.22	335	2.1	6–15	15	73.9
8	5.7	102	3.87	0.15	0.209	850	2.6	2–5	60	193.4
9	6.1	102	6.34	0.28	0.392	215	2.6	6–20	33	26.1
15	5.4	108	10.20	0.45	0.599	1025	3.0	4	10	84.5
10	6.1	102	5.93	0.20	0.278	215	2.6	10–25	5	36.7

Table 7 Summary of parameters used in the frequency estimations for the Arizona State Hybrid motor test

Test no.	$\bar{D}$ (in.)	L (in.)	$\dot{m}_o$ (lb/s)	G_o (lb/in.^{2}-s)	P_c (psi)	O/F	f (Hz)	$\tau_{b/2}$ (ms)
1	2.0	27	3.44	0.29	500	4.0	19	23.7

Table 8 Summary of parameters used in the frequency estimations for the NASA Ames Hybrid motor tests

Test no.	L (in.)	G_o (lb/in.^{2}-s)	P_c (psi)	O/F	f (Hz)	$\tau_{b/2}$ (ms)
4F-4	32	0.44	528.0	3.97	41.6	13.6
4F-5	32	0.49	551.0	3.59	39.9	12.8
4F-1b	32	0.20	561.0	2.72	14.4	30.0
4F1-c	32	0.16	542.0	3.06	13.6	36.4
4P-01	45	0.39	318.0	2.69	40.8	12.4
4P-02	45	0.38	993.8	2.48	13.2	38.9
4P-03	45	0.40	939.1	2.65	14.4	35.9
4L-03	45	0.31	641.6	2.69	12.7	31.2
4L-04	45	0.52	656.7	2.66	23.6	19.0
4L-05	45	0.46	649.3	2.72	19.1	21.4
4L-08	45	0.44	525.0	2.64	23.3	18.0
4I-01	45	0.38	318.7	2.40	39.6	12.5
4P-04	45	0.21	159.1	1.73	42.4	10.8
4L-09	45	0.26	265.3	1.54	20.3	13.8
4L-10	45	0.43	590.0	2.89	27.0	18.4
4L-11	45	0.11	213.0	1.56	17.8	27.5
4L-12	45	0.13	301.0	2.01	15.54	32.5
4NF-01	45	0.39	602.2	2.77	22.60	23.3
4NF-02	45	0.22	600.4	2.34	11.10	40.7
4NF-03	45	0.36	500.8	2.96	23.20	21.6
4NF-04	45	0.48	568.5	3.01	32.75	18.2
4L-14	45	0.43	524.5	2.51	25.15	18.2
4ST-02	45	0.45	540.0	2.71	24.86	18.3
4L-15	45	0.31	555.5	2.09	14.94	26.4
4Rep-02	45	0.45	402.3	2.63	36.49	13.6

volume $V_p = LA_p$ yields

$$\tau_{\text{bl2}} = c' \frac{V_p P_c}{\dot{m}_t[(1+2O/F)/(1+O/F)]RT_{\text{av}}} \tag{56}$$

With the use of the total mass flow relation, $\dot{m}_t = P_c A_n / c^*_{\text{exp}}$, and the definition $L^* = V_m/A_n$, the delay equation can be written as

$$\tau_{\text{bl2}} = c' \frac{V_p}{V_m} \frac{[(1+O/F)/(1+2O/F)]}{RT_{\text{av}}} L^* c^*_{\text{exp}} \tag{57}$$

Here V_p/V_m is the ratio of the port volume to the motor volume, which is estimated to be approximately 0.8 for AMROC DM-01 motor. We assume that all AMROC motors possess the same average gas constant temperature product RT_{av} and volume ratio, V_p/V_m. After noting that all motors operate at very similar O/F and c^*_{exp} values, it can be stated that in these series of tests the boundary-layer characteristic delay time is proportional to L^*.

To reduce data from the rest of the tests, a similar relation for the boundary-layer delay time in terms of the chamber pressure and port flux levels must be derived. The port velocity can be replaced by an average value $(G_o + G_t)/2\rho_{\text{av}}$ with ρ_{av} given by the ideal gas law $P_c = \rho_{\text{av}} RT_{\text{av}}$ to yield, finally, for the boundary-layer lag

$$\tau_{\text{bl2}} = c' \frac{LP_c}{(G_o + G_t)RT_{\text{av}}} \tag{58}$$

Equation (58) gives the scaling law for the boundary-layer delay in terms of the operating conditions of the rocket motor and also with the size of the motor. This states that delay increases with increasing chamber pressure and port length and decreases with increasing mass flux in the port. An important conclusion that can be drawn from those observations is that an increase in the chamber pressure or a decrease in the port mass flux acts to decrease the oscillation frequency of the TC coupled system.

The total mass flux can be eliminated from Eq. (58) by introducing the average oxidizer-to-fuel ratio of the motor,

$$\tau_{\text{bl2}} = c' LP_c \Big/ \left[\left(2 + \frac{1}{O/F} \right) G_o RT_{\text{av}} \right] \tag{59}$$

Equation (59) will be used to reduce the paraffin-based motor data. Note that Eqs. (57–59) are equivalent and the constant multiplier c' is identical for all of these expressions.

The average temperature gas constant product that appears in the denominator of all of the boundary-layer delay time equations is assumed to be constant for all of the LOX/GOX motor tests that are considered in this chapter. This is a fairly good assumption because RT is a weak function of the motor O/F for the practical operating conditions [15]. In fact, the maximum expected variation on the RT values for all of the LOX/GOX tests used for comparison is predicted to be less than 5%. The absolute value of RT_{av} is selected to be 6.38×10^5 $(\text{m/s})^2$ for LOX/GOX motor tests, and because the same value is used for all calculations, any error in RT_{av} will only effect the numerical value of the empirical delay constant c'.

To double check the RT_{av} value used in the calculations, one could use the first acoustic frequency measured from the motor test data and use that to estimate the speed of sound and finally RT_{av} based on the following equation:

$$f_{1-L} = \sqrt{\gamma RT_{\text{av}}}/2L_m \tag{60}$$

Here γ is the ratio of the specific heats averaged over the length of the motor, f_{1-L} is the first longitudinal acoustic mode, and L_m is the effective length of the motor. For a more accurate calculation, the complex gasdynamic model discussed by Karabeyoglu [15] can be used. All of the paraffin-based motor tests with 45-in.-long grains had their first acoustic mode at around 370 Hz. For these tests with use of $\gamma = 1.25$ and $L_m = 1.27$ m, one obtains an RT_{av} of 7.1×10^5 $(\text{m/s})^2$, which is only 10% higher than the assumed value. RT_{av} for the N_2O test is selected to be 4.47×10^5 $(\text{m/s})^2$. This is 30% lower than the RT_{av} for the GOX/LOX system due to the low temperature of the N_2O/hydrocarbon combustion products.

Now Eq. (44) can be coupled with the expressions for the boundary delays time to evaluate the frequencies predicted by the TC coupled model,

$$f = 0.48 \frac{RT_{\text{av}}}{c'(V_p/V_m)[(1+O/F)/(1+2O/F)]L^* c^*_{\text{exp}}} \tag{61a}$$

$$f = 0.48 \frac{(G_o + G_t)RT_{\text{av}}}{c'LP_c} = 0.48 \left(2 + \frac{1}{O/F}\right) \frac{G_o RT_{\text{av}}}{c'LP_c} \tag{61b}$$

The oscillation frequency as a function of the boundary-delay time predicted by the TC coupled theory along with data from the hybrid motor development programs are shown in Fig. 26. Note that we have used a boundary-layer delay constant value c' of 2.05 for all motor tests to obtain the best fit between the theory and test results. Please note that this experimental value for c' is of the same order of magnitude with the rough estimate, that is, ∼0.55, for a boundary layer with no blowing and no combustion.

When the wide range of test conditions is considered, the agreement between the measured pressure oscillation frequencies and the TC coupled model predictions is surprisingly good. Note that the comparison includes a total of 43 motor tests: 1) using results from four different development and research programs; 2) using three separate oxidizers, that is, LOX, GOX, and N_2O; 3) covering a wide range of motor dimensions, that is, from 5 in. o.d. Arizona State University motor up to 72 in. o.d. AMROC motor; 4) using many different fuel compositions, that is, HTPB, HTPB/Escorez, and two paraffin-based formulations; and 5) covering a wide range of operating conditions.

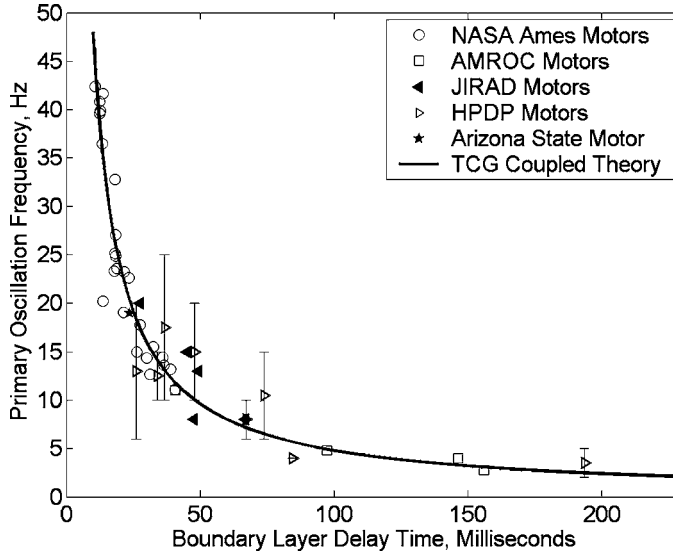

Fig. 26 Comparison of the TCG coupled oscillation frequency prediction with hybrid motor test data available in the literature.

The average error between the frequencies predicted by the TCG coupled theory and the experimentally observed values is 13.94% for all the data shown in Fig. 26 other than the NASA test 4L-09 which clearly is an outlier. The errors associated with individual programs are 8.61% for NASA, 10.03% for AMROC, 19.37% for JIRAD, 29.68% for HPDP and finally 13.94% for the nitrous motor test reported in Ref. [39]. The maximum error is 41.96% which corresponds to one of the HPDP motor tests.

A significant part of the difference between the observed and predicted frequencies is likely due to the inaccuracies associated with the reported frequencies and motor operating conditions in the literature. Note that the error in the operating conditions directly translates into the inaccuracies in the frequency estimation as can be seen from Eqs. (61a and 61b). We believe that the most reliable data set is from the NASA motor tests, since for these tests the low frequency hybrid mode is carefully separated from the other modes of oscillation (i.e., Helmholtz mode). This statement is supported by the fact that NASA set has the least percent error compared to the data reduced from other programs. We believe that the most inaccurate set is from the HPDP motor tests which reports the oscillation frequencies as a wide range as opposed to single peak values (i.e., see Fig. 26). In fact, the combined error without the HPDP data improves to 10.30 percent with a maximum error of 29.04% for one of the JIRAD motor tests.

Equation (61a) indicates that for motors operating at similar O/F, the oscillations frequency is inversely proportional to the L^* of the motor. This conclusion is consistent with previous results reported in the literature. Similarly, Eq. (61b) shows for motors operating at equal oxidizer mass fluxes, chamber pressures, and O/F, the oscillation frequency decreases with increasing fuel-grain length. To prove that motor length plays a critical role setting the oscillation frequency, we have plotted the NASA Ames Research Center motor data, which contains two sets of grain lengths, by removing the length effect from the scaling law. This resulted in an increase in the scatter in the frequency data, thus, indicating the importance of the grain length. A similar check to confirm the importance of length can be conducted by comparing the JIRAD and HPDP motor tests (ran with grains 102 in. long) with the NASA Ames Research Center paraffin tests (ran with grains 32 or 45 in. long) that were conducted under very similar operating conditions. For example, comparing test 8 of the HPDP program to paraffin-based motor test 4P-01 shows that grain length must be included in the scaling law to explain the discrepancy in the oscillation frequencies for these tests. The same conclusion can be drawn by comparing test 2 of HPDP program to the test NASA Ames Research Center test 4L-08.

TC coupled theory predicts oscillations of the regression rate/fuel mass generation rate and would be observed directly in a hybrid motor as the radial oscillations of the diffusion flame within the boundary layer. The gasdynamic model converts the fuel mass generation rate oscillations to the chamber pressure oscillations. It is expected that a system operating at higher O/F ratios would produce weaker chamber pressure oscillations because fuel mass constitutes a smaller fraction of the total mass expelled from the nozzle. This fact is observed in NASA Ames Research Center motor tests, namely, high O/F motors, in general, presented lower amplitude chamber pressure oscillations compared to the mean chamber pressure.

The simple linear model presented in this chapter successfully explains the generation of small-amplitude, intrinsic, low-frequency oscillations and the scaling of the frequency. However, it also falsely predicts an indefinite growth of chamber pressure oscillations. In reality, the nonlinear mechanisms that exist in a hybrid motor would limit the indefinite growth of the oscillations and result in limit-cycle oscillations that are commonly observed in motor tests. Moreover, the simple theory does not explain when these low-frequency instabilities will take place and what their amplitudes would be. It has been shown in the hybrid development programs that the fore end configuration/volume of the motor is of paramount importance in setting the amplitude of the low-frequency instabilities. The motor tests indicate that, at least for gaseous motors, axial injectors result in more stable operation compared to the radial or conical injection of the oxidizer.

A plausible explanation for these observations is that the TC coupled instability mechanism always exists in hybrid systems, but the amplitude of the limit-cycle oscillations will depend on the excitation level by the disturbances in the right frequency range. We believe that the fore end fluid dynamics, that is, vortex shedding, is the primary source of disturbances in a hybrid rocket. For example, changing the injection scheme of the oxidizer from axial to radial may introduce a flow disturbance component that is preferred by the TC coupled system. If one assumes that all of the low-frequency oscillations are developed by the fluid mechanics at the fore end of the motor, one would fail to explain the length effect on the oscillation frequency. Also, all oxidizer injection schemes under identical motor operating conditions seem to produce the same oscillation frequency. This fact is also difficult to explain by the assumptions that all of the oscillations are produced from the fluid dynamic events at the fore end of the motor because the injection scheme should alter the fluid mechanics significantly, that is, vortex shedding frequency.

Note that most of musical instruments also work on the same principle [41]. For example, in a flue organ pipe the column of air inside the pipe is set into vibration, that is, at its natural frequencies, by an edge tone that is produced by a jet of air that impinges on a carefully designed lip. The vortex shedding at the lip sets the edge tone, which itself excites the natural modes in the pipe. Note that in the case of an organ pipe the jet speed and the lip geometry are carefully selected for the pipe length such that the edge tone produced at the lip contains a large component at the natural frequency of the pipe that needs to be excited. In this organ pipe analog, the lip is the fore end of the motor, that is, geometry, injection scheme, velocity, etc., and the organ pipe is the hybrid system modeled by the TC coupled theory.

X. Conclusions

In this chapter the development of a transient combustion theory for hybrid rockets has been outlined. The approach taken to address this difficult problem has been to identify and model the important phenomena that establish the overall transient behavior. Three subsystems that have been determined to be important and fundamental to most hybrids are the thermal lags in the solid, boundary-layer combustion dynamics, and transient gasdynamics in the chamber. Mathematical models for these important subsystems have been established, and techniques for solving these mathematical problems have been described.

It has been shown that the thermal transients in the solid can be best understood by introducing two timescales, the well-known diffusion timescale and the faster surface timescale. The coupling of these timescales during transients produces interesting behavior of the regression rate. The cases that are worth mentioning are the overshooting phenomenon during throttling transients and the phase lead and amplification for the forced oscillatory response. It has been shown that the phase lead is critical to produce a mechanism that results in the low-frequency instabilities commonly observed in hybrid rockets. Finally, it is important to state that the thermal lag system has been determined to be stable by itself.

For the boundary-layer combustion dynamic modeling, we first modified the classical regression rate expression for the case of quasi-steady gas-phase combustion but allowed for the transient heat transfer in the solid. This resulted in an expression for the wall heat flux in terms of the oxidizer mass flux and the regression rate. The reverse coupling of the heat flux and the regression rate is induced by the blocking effect. In the second part of the treatment, the quasi-steady assumption has been relaxed by introducing a phase lag for the boundary-layer combustion delays. A scaling expression for this delay has been adapted from turbulent boundary-layer literature.

In the next step of the development, the thermal lag and the boundary-layer combustion models have been coupled to obtain the TC coupled system. It has been shown that the TC coupled system could produce low-frequency instabilities with finite boundary-layer combustion delays. It has also been determined that three key ingredients to produce these unstable oscillations are the blocking effect, the phase character behavior of the thermal lag system, and the boundary-layer delay time.

The TC coupled system takes the oxidizer mass flux as the input and yields the regression rate as the output. To relate the more observable parameters of the motor, such as chamber pressure, to the known input variables, such as the oxidizer mass flow rate, a gasdynamic model has been introduced. The particular model discussed in this chapter resolves the filling/emptying dynamics and longitudinal acoustic modes of the chamber. It has been shown that this gasdynamic model by itself or when coupled to the boundary-layer combustion transients (with a delay term) is always stable. However, when it is integrated to the TC coupled system to produce the TCG coupled system, the low-frequency instabilities, predicted by the TC coupled system, would show as chamber pressure oscillations. This indicates the importance of the phase-lead character of the thermal transients in the solid in the mechanism that is producing the low-frequency oscillations.

The following conclusions can be drawn from the results of the TCG coupled model:

1) A plausible mechanism that generates low-frequency chamber pressure oscillations is suggested. The physical transient model of the motor is presented in a mathematical formalism that allows one to estimate the expected oscillation frequency. The amplitude of the oscillations cannot be determined by this linear model.

2) The oscillation frequency estimated by the model is in very good agreement with the motor test data from several programs using three distinct oxidizers,

several fuel formulations, and a wide range of motor dimensions and operating conditions. We suggest the following equation as a universal scaling law for the primary hybrid oscillation frequency:

$$f = 0.234\left(2 + \frac{1}{O/F}\right)\frac{G_o RT_{\text{av}}}{LP_c} \tag{62}$$

where $RT_{\text{av}} = 6.38 \times 10^5\,(\text{m/s})^2$ for GOX/LOX systems and $RT_{\text{av}} = 4.47 \times 10^5\,(\text{m/s})^2$ for low-energy oxidizers systems such as N_2O.

3) This mode of instability is common to all kinds of hybrids: liquefying or conventional fuels, liquid, or gaseous oxidizers. It is reasonable to believe that this low-frequency mode is present in every hybrid system to some extent. Some motors are more unstable compared to others because these motors possess more disturbances to excite the TC coupled oscillations. For example, the oxidizer injector configuration or precombustion chamber geometry affects the scale and the frequency of the disturbances that would excite the commonly observed low-frequency mode. For this reason, the design of the fore end of the motor has been critical in controlling the stability of the system.

4) Even though the linear theory very successfully predicts the oscillation frequency of the chamber pressure, it fails to establish an estimation process for the amplitude of the oscillations. The theory predicts an unlimited growth of the oscillations. In reality, the amplitude of the chamber pressure fluctuations will be limited by nonlinear effects that are not covered in the linearized TCG coupled theory.

5) It has been shown that the longitudinal acoustic oscillations that commonly coexist with the low-frequency oscillations can be generated by the excitation induced by the nonlinear waveforms of the low-frequency chamber disturbances. In short, it is plausible that high-frequency acoustic modes are driven by the low-frequency oscillations.

Estimating the amplitude of the pressure oscillations and developing schemes to minimize (and eventually eliminate) them is one of the most important practical aspects of a stability theory. Thus one of the key directions for future research is to extend the theory to account for the nonlinear phenomena that take place in the motor and to better understand the dynamic interactions between the fundamental hybrid combustion scheme and the disturbances that excite the instability modes. Another area of interest is to develop the feed system and the oxidizer atomization/vaporization models and to integrate them with the existing TCG coupled system in order to predict the transient behavior of a liquid fed hybrid rocket. Finally it would be desirable to modify the transient theory to understand the effects of variations on the classical hybrid scheme. Two of these promising schemes are the hybrid systems utilizing nano-sized metal powders as fuel additives and systems with high intensity swirl injection of the oxidizer. Both of these variations change the hybrid combustion process to some extent and it is expected that they would also alter the stability character of the combustion system.

Acknowledgements

Part of this work was carried out under cooperative agreements NAG3-2615 with the NASA Glenn Research Center and agreements NCC2-1172 and NCC2-1300 with the NASA Ames Research Center.

References

[1] Williams, F. A., "Grain Design and Throttling of Hybrid Rocket Motors," *Chemical Engineering Progress Series*, Vol. 62, No. 61, 1965, pp. 86–94.

[2] Gutrie, D. M., and Wolf, R. S., "Non-Acoustic Combustion Instability in Hybrid Rocket Motors," Report No. 91-24250, Carnarillo, CA, 1991.

[3] Boardman, T. A., Carpenter, R. L., and Claflin, S. E., "A Comperative Study of the Effects of Liquid-Versus Gaseous-Oxygen Injection on Combustion Stability in 11-inch-Diameter Hybrid Motors," AIAA Paper 97-2936, July 1997.

[4] Dijkstra, F., Korting, P., and van der Berg, R., "Ultrasonic Regression Rate Measurement in Solid Fuel Ramjets," AIAA Paper, 90-1960, 1990.

[5] Marxman, G. A., Wooldridge, C. E., and Muzzy, R. J., "Fundamentals of Hybrid Boundary Layer Combustion," *Progress in Astronautics and Aeronautics*, Vol. 15, 1964, pp. 485–522.

[6] Boardman, T. A., Brinton, D. H., Carpenter, R. L., and Zolods, T. F., "An Experimental Investigation of Pressure Oscillations and Their Suppression in Subscale Hybrid Rocket Motors," AIAA Paper 95-2689, July 1995.

[7] Boardman, T. A., Carpenter, R. L., Goldberg, B. E., and Shaeffer, C. W., "Development and Testing of 11- and 24-Inch Hybrid Motors Under the Joint Government/Industry IR&D Program," AIAA Paper 93-2552, June 1993.

[8] Karabeyoglu, M. A., Zilliac, G., Cantwell, B. J., DeZilwa, S., and Castellucci, P., "Scale-up Tests of High Regression Rate Paraffin-based Hybrid Rocket Fuels," *Journal of Propulsion and Power*, Vol. 20, No. 6, Nov.–Dec. 2004, pp. 1037–1045.

[9] Greiner, B., and Frederick, R. A., Jr., "Hybrid Rocket Instability," AIAA Paper, 93-2553, June 1993.

[10] Wooldridge, C., Marxman, G. A., and Kier, R., "Investigation of Combustion Instability in Hybrid Rockets," NASA CR-66812 Final Rept., 1969.

[11] Wooldridge, C., and Marxman, G. A., "Combustion Instability and the Role of Chemical Kinetics in Hybrid Combustion," AIAA Paper 68-498, 1968.

[12] Brown, R. S., and Muzzy, R. J., "Linear and Nonlinear Pressure Coupled Instability of Solid Propellants," *AIAA Journal*, Vol. 8, No. 8, June 1970, pp. 1492–1500.

[13] Greiner, B., and Frederick, R. A., Jr., "Experimental Investigation of Labscale Hybrid Instability," AIAA Paper, 94-2878, 1994.

[14] Jenkins, R. M., and Cook, J. R., "A Preliminary Analysis of Low Frequency Pressure Oscillations in Hybrid Rocket Motors," AIAA Paper 95-2690, July 1995.

[15] Karabeyoglu, M. A., "Transient Combustion in Hybrid Rockets," Ph.D. Dissertation, Stanford Univ., Dept. of Aeronautics and Astronautics, Stanford, CA, Aug. 1998.

[16] Beckstead, M. W., and Price, E. W., "Nonacoustic Combustion Instability," *AIAA Journal*, Vol. 5, No. 11, Nov. 1967, pp. 1989–1996.

[17] Price, E. W., Rice, D. W., and Crump, J. E., "Low-Frequency Combustion Instability of Solid Rocket Propellants," NOTS-TP-3524 Technical Progress Rept. to U.S. Naval Ordanance Test Station, China Lake, CA, July 1964.

[18] Williams, F. A., *Combustion Theory*, Addison–Wesley, New York, NY, 1965, pp. 365–441.
[19] Crocco, L., and Cheng, S. I., "Theory of Combustion Instability in Liquid Propellant Rocket Motors," AGARDograph 8, Butterworths Scientific Publications. London, 1956, pp. 25–72.
[20] Culick, F. E. C., and Yang, V., "Combustion Instabilities in Liquid Rockets," *Progress in Astronautics and Aeronautics*, Vol. 169, 1995, pp. 3–37.
[21] Karabeyoglu, M. A., and Altman, D., "Dynamic Modeling of Hybrid Rocket Combustion," *Journal of Propulsion and Power*, Vol. 15, No. 4, 1999, pp. 562–571.
[22] Altman, D., and Humble, R., "Hybrid Rocket Propulsion Systems," *Space Propulsion Analysis and Design*, McGraw-Hill, New York, NY, 1995, pp. 365–441.
[23] Landau, H. G., "Heat Conduction in Melting Solid," *Quarterly Journal of Applied Mathematics*, Vol. 8, 1950, pp. 81–94.
[24] Karabeyoglu, M. A., Altman, D., and Bershader, D., "Transient Combustion in Hybrid Rockets," AIAA Paper 95-2691, July 1995.
[25] Esker, D. R., and Brewster, M. Q., "Laser Pyrolysis of Hydroxyl-Terminated Polybutadiane," *Journal of Propulsion and Power*, Vol. 12, No. 2, 1996, pp. 296–301.
[26] Nachbar, W., and Williams, F. A., "On the Analysis of Linear Pyrolysis Experiments," *Ninth Symposium on Combustion*, Combustion Institute, Pittsburgh, PA, 1963, pp. 345–357.
[27] Kumar, R. N., and Stickler, D. B., "Polymer Degradation Theory and Pressure Sensitive Hybrid Combustion," *Thirteenth Symposium on Combustion*, Combustion Institute, Pittsburgh, PA, 1970, pp. 1059–1072.
[28] Fodor, G., *Laplace Transforms in Engineering*, Akademiai Kiado, Budapest, Hungary, 1965, pp. 127–193.
[29] Cannon, R. H., *Dynamics of Physical Systems*, McGraw-Hill, New York, NY, 1967, pp. 374–416.
[30] Arfken, G., *Mathematical Methods for Physicists*, Academic Press, New York, NY, 1985, pp. 794–853.
[31] Horton, M. D., Bruno, P. S., and Graesser, E. C., "Depressurization Induced Extinction of Burning Solid Propellant," *AIAA Journal*, Vol. 2, No. 2, pp. 292–297.
[32] Marxman, G. A., "Combustion in the Turbulent Boundary Layer on a Vaporizing Surface," *Tenth Symposium on Combustion*, Combustion Institute, Pittsburgh, PA, 1965, pp. 1337–1349.
[33] Marxman, G. A., "Boundary Layer Combustion in Propulsion," *Eleventh Symposium on Combustion*, Combustion Institute, Pittsburgh, PA, 1967, pp. 269–289.
[34] Parikh, P. G., Jayaraman, R., Reynolds, W. C., and Carr, L. W., "Transient Response of a Turbulent Boundary Layer," ASME FED-Vol. 12, American Society of Mechanical Engineers, New York, 1984, pp. 31–42.
[35] Schlichting, H., "*Boundary Layer Theory*," McGraw-Hill, 1955, Chap. 21.
[36] Wooldridge, C., and Muzzy, R. J., "Internal Ballistic Consideration in Hybrid Rocket Design," *AIAA Journal of Spacecraft*, Vol. 4, No. 2, Feb. 1966, pp. 255–262.
[37] Karabeyoglu, M. A., De Zilwa, S., Cantwell, B. J., and Zilliac, G., "Transient Modeling of Hybrid Rocket Low Frequency Intabilities," *Journal of Propulsion and Power*, Vol. 21, No. 6, Nov.–Dec. 2005, pp. 1107–1117.
[38] Moelwyn-Hughes, E. A., *Physical Chemistry*, 2nd rev. ed., Pergamon, Oxford, 1961, Chap. 6.

[39] Karabeyoglu, M. A., Cantwell, B. J., and Stevens, J., "Elevation of Homologous Series of Normal Alkanes as Hybrid Rocket Fuels," 41st AIAA/ASME/SAE/ASEE Joint Propulsion Conference and Exhibit, Tucson, AZ, July 2005.

[40] Pucci, J. M., "The Effects of Swirl Injector Design on Hybrid Flame-Holding Combustion Instability," AIAA Paper 2002-3578, July 2002.

[41] Jeans, J., *Science and Music*, Dover, New York, 1968, pp. 130–137.

This page intentionally left blank

Chapter 10

Metals, Energetic Additives, and Special Binders Used in Solid Fuels for Hybrid Rockets

G. A. Risha*
Pennsylvania State University, Altoona, Pennsylvania, 16601
and
B. J. Evans,† E. Boyer,‡ and K. K. Kuo§
Pennsylvania State University, University Park, Pennsylvania, 16802

I. Introduction

RELATIVELY low mass and linear regression rates of solid fuels have been among the major drawbacks of classical hybrid rocket engine technology due to low density, inertness of conventional solid fuels, and the diffusion-controlled combustion process. The thermal degradation in the pyrolysis process of inert polymeric fuels has been considered to be one of the key processes occurring in hybrid rocket engines and solid-fuel ramjet engines [1]. The fuel-surface regression rate generated by this process is a very important design and performance parameter and is strongly affected by the operating conditions and the composition and thermophysical properties of the solid fuel. In addition, fluid dynamic, heat-transfer, and combustion processes in these solid-fuel systems are characterized by complex interactions involving numerous physical phenomena, simultaneously taking place in the combustion chamber and the fuel grain. These complex interactions include solid-fuel pyrolysis; metal vaporization for metallized solid fuels; oxidizer atomization and vaporization; gas-phase species mass diffusion; mixing and combustion between the fuel-rich and oxidizer-rich species; turbulent flow with mass addition; conductive, convective, and radiative energy transfer; and time-varying

*Assistant Professor, Division of Business and Engineering.
†Research Assistant, Department of Mechanical and Nuclear Engineering.
‡Research Associate, Department of Mechanical and Nuclear Engineering.
§Distinguished Professor, Department of Mechanical and Nuclear Engineering.

flow-channel configuration. Considering these complex processes, one must be aware of the advantages and impact of each viable performance enhancement technique on the physical and thermal properties of the solid fuel or the oxidizer. For example, although high-energy oxidizers contribute more energy to the propulsion system, they may produce chlorine-containing products preventing the reactant combination from being considered "green." Moreover, increasing the reactivity of the conventional solid fuel by replacing hydroxyl-terminated polybutadiene (HTPB) with a more energetic binder component such as glycidyl azide polymer (GAP) begins to transition the solid fuel from a highly inert one to a fuel-rich solid propellant, thus directly compromising the inherently safe nature of classical hybrid rocket propulsion systems.

Until now, regression rates of conventional solid fuels, for example, HTPB, have typically been an order of magnitude lower than solid propellants, thus requiring a relatively large fuel-surface area to produce a desired thrust level [2]. Despite the slower polymeric solid-fuel regression rates, hybrid rocket propulsion systems have many major advantages over conventional solid- and liquid-propellant rockets, especially in view of the recent growing emphases on improved safety, higher density impulse, low development and production costs, minimal environmental impact, on–off operational capability, thrust modulation, and greater controllability for rocket engines [3, 4]. With these advantages, it is of great interest to improve solid-fuel technology as well as to explore new advanced energetic fuel ingredients that can be constituents of future generation solid fuels.

Why is it imperative to advance solid-fuel technology? Solid-fuel grains are much more ductile than solid-propellant grains and, thus, are less likely to be damaged, therefore, significantly lowering the probability of catastrophic motor failure, which is the highest priority for manned space missions. The exhaust products are much more environmentally friendly than the toxic exhaust of most solid-propellant rockets, which produce chlorine-containing product species. The inherent safety of hybrid rocket technology is predominately because the solid-fuel grain is usually an inert polymer such as HTPB. Thus, adding oxidizer or improving the binder with a more energetic material is not so attractive and may cause the so-called inert fuel to possess propellant-like characteristics. However, the inertness of solid fuel adversely affects propulsive performance requiring further investigation and mitigation of inferior burning rates of solid fuels compared to solid propellants. In hybrid systems, performance can be increased by either energizing the solid fuel or increasing oxidizer reactivity: both have pros and cons. It has been proven in previous research studies dating back to 1956 that the presence of chemically reactive species such as metal particles considerably accelerates the pyrolysis process of many polymers [5–7]. The thermal degradation rate enhancement of a polymer surface in contact with oxygen or air is thought to be caused by 1) absorption of oxygen by the solid, which changes the structure of polymer chains and alters the decomposition mechanism; 2) heterogeneous exothermic reactions at the surface, which may involve energetic materials embedded in the solid fuel; and 3) heat transfer from the diffusion flame zone governed by gas-phase reactions between the fuel-pyrolysis products and the surrounding oxidizer species. Thermoanalytical studies [using thermal gravimetric analysis (TGA), differential thermal analysis (DTA), and differential scanning calorimetry (DSC) techniques] involving the thermal pyrolysis of polybutadiene binders in air or oxygen have revealed a strong enhancement of the first-stage exothermic decomposition, which comprises cyclization, crosslinking,

and partial depolymerization [8–12]. The effect of pressure on heat feedback to the fuel surface, and thereby on the regression rate, is influenced by many factors: 1) the kinetics of gas-phase and heterogeneous chemical reactions, 2) the radiative heat transfer from the condensed-phase products in the flame zone and core flow, and 3) the diffusion rate of reactive oxidizing species to the flame zone and to the fuel surface. Marxman and Gilbert [13], Marxman et al. [14], and Marxman [15] contended that in certain situations the kinetic rates of chemical reactions may affect or even control the regression rate of the solid fuel. These phenomena can be affected directly by the presence of energetic additives in the solid fuel.

Generally, performance enhancement techniques of hybrid-propulsion systems can be broken down into three possible categories: 1) adding energetic particles into the solid-fuel grain, 2) replacing the virtually inert HTPB binder with more energetic polymers, for example, GAP, and/or 3) substituting liquid oxygen (LOX) with more energetic and dense liquid oxidizers such as hydroxyl ammonium perchlorate (HAP) or hydroxyl ammonium nitrate (HAN). The energetic particles may have special coatings to increase their reactivity and energy release rate during their ignition and combustion processes. However, the use of energetic binders or high-density liquid oxidizers may subject the system to undesirable effects, such as processing, handling and environmental issues, and higher cost. Therefore, from the aforementioned advantages and shortcomings of enhancement techniques, a desirable way to increase solid-fuel properties and performance is to introduce energetic particles into the fuel so that the inherent safety of the overall system is not compromised. The focus of this chapter is to provide information regarding the uses of metallized solid fuels and gas generants for military, commercial, and private applications while discussing pioneering work and experimental evidence of the practicality of advanced solid fuels for these applications. Some of the other performance-enhancing techniques are covered in greater detail elsewhere in this book.

A. Conventional Solid Fuels

During the past 60 years, an abundance of metallized and nonmetallized solid-fuel formulations have been the subject of investigations for both hybrid and solid-fuel ramjet (SFRJ) propulsion systems. In addition, polymeric fuels have been extensively used as binders in solid-propellant systems, gas-generation systems, ducted rockets, and even amateur rocketry, and so understanding the nature of individual components, for example, binder or solid fuel, of the fuel/oxidant combination can assist in the explanation of the complex processes found in solid-propellant combustion studies [16–19]. These solid fuels ranged from wood, rubber, plastic, salami, and graphite, to organic waste [20]. Table 1 lists physical and thermodynamic properties of several common fuels and binders used in solid fuels and solid propellants such as solid-fuel density, melting and boiling temperatures, oxygen balance, and heat of formation.

Early performance studies of nonmetallized inert polymers date back to the 1950s with the works of Schultz and Dekker [21] and Chaiken et al. [22], who studied the decomposition of polymethylmethacrylate (PMMA) and polystyrene (PS). The degradation of PMMA and PS in a chemically reactive environment was addressed experimentally by McAlevy and Hansel [6]. Throughout the years, with the emergence and wide use of polybutadiene-based polymers as baseline

Table 1 Physical and thermodynamic properties of selected solid fuels/polymeric binders[a]

Binder name	Chemical formula	ρ, g/cm^3	T_{melt}, °C	T_{boil}, °C	Oxygen balance, %	ΔH_f^o, kJ/mol
Hydroxyl-terminated polybutadiene (HTPB)	$C_{10}H_{15.4}O_{0.07}$	0.92	241	——	−323.26	−51.88
Glycidyl azide polymer (GAP)	$C_3H_5N_3O$	1.29	>200	——	−121.09	142.26
Polyethylene glycol (PEG)	C_2H_4O	1.13	4–8	>300	−181.59	−195.02
Polymethyl methacrylate (PMMA)	$C_5H_8O_2$	1.19		——	−191.77	−430.53
Polyurethane (PU)	$C_{10}H_{18.711}N_{0.273}O_{3.294}$	1.00	222	250	−213.29	−679.06
3,3–Bis(azidomethyl)oxetane (BAMO)	$C_5H_8N_6O$	1.22	——	67	−123.69	518.82
Polybutadiene/acrylnitrile (PBAN)	$C_{10}H_{14.588}N_{0.416}O_{0.875}$	0.98	——	——	−273.33	75.94
Pentaerythritol tetranitrate (PETN)	$C_5H_8N_4O_{12}$	1.78	143	180	−10.12	−538.90
Polyethylene (PE)	$(C_2H_4)_n$	0.94	120–130	——	−342.19	−53.81
Polypropylene glycol (PPG)	$C_{10}\ H_{20.195}O_{3.431}$	1.00	——	——	−218.39	−725.92
Carboxyl-terminated polybutadiene (CTPB)	$C_{10}H_{14.958}O_{0.194}$	0.92	280–350	——	−315.67	−9.71
Polystyrene (PS)	$(C_6H_5CHCH_2)_n$	1.12	240	——	−307.23	37.24

[a]Fraunhofer Institut für Chemische Technologie (ICT) database, 2001.

solid propellant and hybrid binders/fuels, the thermal degradation and pyrolysis of HTPB and carboxyl-terminated polybutadienes (CTPB) became the subject of study for many researchers in the propellant development field. Other polymers studied included polybutadiene–acrylic acid (PBAA), polybutadiene–acrylonitrile (PBAN), polyurethane (PU), and other materials such as fluorocarbons by Bouck et al. [9]. HTPB has been employed in many laboratory-scale hybrid engines, commercial and military solid fuels, and even the recent Ansari X Prize winner SpaceShipOne [23].

B. Solid-Fuel Additives

In the mid-1950s, interest in metal combustion was first stimulated in solid propellants when it was found that the addition of aluminum particles substantially increased propellant performance [24–27]. Combustion of metals is of great interest due to its inherent advantages such as damping of pressure oscillations by condensed-phase products and increase in specific impulse I_{sp} and propellant density. Metals and boron (where, for simplicity, boron will be considered with metallic materials even though it is not a true metal) possess desirable combustion characteristics such as high heats of combustion or energy release and good physical properties such as high density [27, 28]. Figure 1 shows relative heats of combustion with oxygen for various metals on both a gravimetric basis and volumetric basis. In comparison with HTPB, most of the energetic fuels showed higher volumetric heat of combustion. Therefore, the inclusion of metal particles materials in solid fuels provides not only higher energy release (corresponding to increased flame temperature and increased specific impulse), but also increased

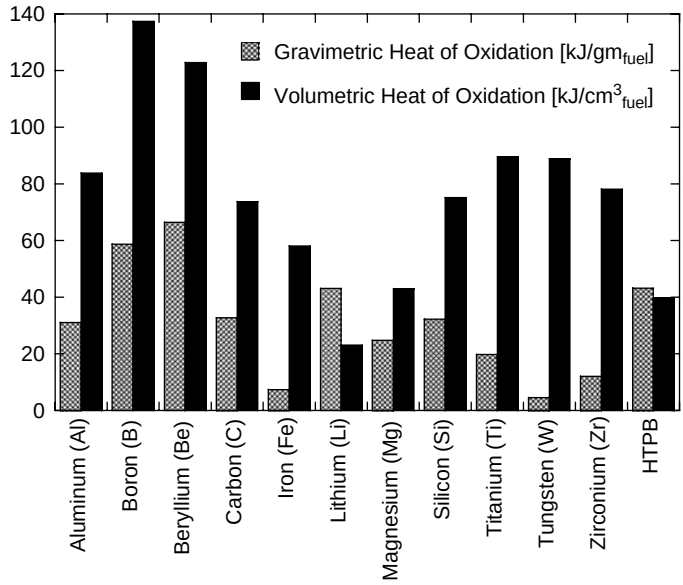

Fig. 1 Comparison of heats of combustion with oxygen (heat of oxidation) of several fuels.

Table 2 Physical and thermodynamic properties of common fuels and their final oxides[a]

	Virgin material properties			Gravimetric heat of oxidation,	Volumetric heat of oxidation,		Final oxide properties			
Fuel	ρ, g/cm^3	T_{melt}, °C	T_{boil}, °C	kJ/gm$_{fuel}$	kJ/cm^3	Final oxide	ρ, g/cm^3	T_{melt}, °C	T_{boil}, °C	ΔH_f°, kJ/mol
Aluminum (Al)	2.70	660	2467	31.1	83.9	Al_2O_3(s)	3.97	2054	3800	−1676
Boron (B)	2.34	2077	2550	58.7	137.0	B_2O_3(s)	2.46	450	2065	−1273
Beryllium (Be)	1.85	1287	2468	66.5	123.0	BeO(s)	3.01	2530	3900	−609
Carbon (C)	2.25	3652	N/A	32.8	73.8	CO_2(g)	1.98×10^{-3}	−56.6	−78.5	−394
Iron (Fe)	7.86	1535	2750	7.39	58.1	Fe_2O_3(s)	5.24	1462	——	−826
Lithium (Li)	0.534	181	1342	43.2	23.0	Li_2O(s)	2.013	>1700	——	−598
Magnesium (Mg)	1.74	649	1107	24.7	43.0	MgO(s)	3.58	2832	3260	−601
Silicon (Si)	2.33	1412	3217	32.3	75.2	SiO_2(s)	2.20	1723	2590	−904
Titanium (Ti)	4.50	1663	3358	19.7	89.6	TiO_2(s)	4.26	1830–1850	2500–3000	−939
Tungsten (W)	19.35	3407	5660	4.59	88.8	WO_3(s)	7.16	1473	——	−838
Zirconium (Zr)	6.49	1852	4377	12.0	78.1	ZrO_2(s)	5.60	2677	——	−1098
HTPB	0.92	241	——	43.3	39.8	——	——	——	——	——

[a]ICT database, 2001.

density impulse, which is important for volume-limited propulsion systems. Table 2 shows thermodynamic and physical properties of several energetic additives. From the gravimetric standpoint, that is, mass basis, beryllium has the highest heat of oxidation among the potential energetic additives. However, beryllium oxide is a highly toxic species preventing it from being a viable candidate. Volumetrically, boron yields the highest heat of oxidation, but difficulties with its ignition and incomplete combustion to form species other than B_2O_3 as final products present obstacles to its adoption. Aluminum seems to be the best choice based on its thermal properties, ease of processing, and relatively low cost. However, the existence of Al_2O_3 as an inert oxide layer on the external surface of the particle is undesirable and hard to avoid. The amount of active aluminum in the particle depends on the manufacturing process and storage conditions. Fortunately, the oxide layer is brittle and can form many cracks when the Al particle expands during heating, allowing pure aluminum to react with oxidizer.

In the 1960s, the U.S. Air Force made a significant effort to develop hybrid rockets as a viable alternative to liquid and solid rocket propulsion systems [29]. This effort was perhaps the earliest documented program to employ a metallized solid fuel in a hybrid rocket motor. In the first phase of the program, a small payload hybrid rocket propulsion system for the Sandpiper target drone was developed. The solid fuel consisted of 90% PMMA and 10% of powdered magnesium dispersed throughout the grain. The liquid oxidizer was 25% nitric oxide and 75% nitrogen tetroxide, better known as MON-25 [20, 29]. Additional metals that were considered were aluminum, magnesium, boron, zirconium, and beryllium. These materials were usually in powdered form and were processed like other granular ingredients into the solid fuel.

The sizes of these particles traditionally used in the early development of hybrid rockets and SFRJs were usually on the order of micrometers, with the smallest being 2–5 μm. The greater energy release from the oxidation of the metal particles substantially increased the regression rate compared to nonmetallized solid fuels. With this apparent benefit in mind and recent advances in nanotechnology, nanosized particles possess the ability to release the energy in a shorter time and closer distance from the regressing fuel surface. There are many direct advantages for incorporating nanosized particles into solid fuels and fuel-rich propellants such as 1) shorter ignition delay, 2) shorter burning time based on the consideration of the d^2 law (e.g., a factor of 10 decrease in diameter results in a reduction of 100 in burn time), 3) more complete combustion in volume-limited propulsion systems, 4) higher particle specific surface area enhancing the rate of heat transfer, and 5) greater flexibility in designing new energetic fuel/propellants with desirable physical properties.

Despite all of the desirable characteristics of nanosize particles, they do possess some undesirable characteristics. As already mentioned, aluminum particles generally have an oxide layer, which makes the particle less reactive until the oxide layer is removed. In addition, the oxide weight percentage increases for smaller particles and can be greater than 50 wt % in some cases. Also, as the particles become smaller, the solid-fuel grain processing becomes very difficult due to high viscosity of the fuel mixture. Additives other than those already mentioned can also be added to control the physical properties of the solid fuel, for example, carbon black

can increase the opacity. Other additives can include Escorez® and guanidinium azo–tetrazolate (GAT) for increasing fuel density and flame temperature [30], carbon nanotubes to increase reactivity and solid-fuel density, as well as stabilizers. Some hybrid engines available commercially for amateur rocketry also include special ingredients to enhance the visual effect of the launch [31, 32].

II. Metallized Polymeric and Nonpolymeric Solid Fuels

The use of metallized solid fuels for hybrid rocket propulsion systems has been the subject of investigation for more than 40 years. The large amount of energy that is released during the combustion process by metal additives makes them beneficial for enhancing the propulsive performance of solid fuels. Specifically, the ability to ignite and fully combust the metal additive in the near-surface region increases the heat release and, thus, the heat transferred back to the solid-fuel surface from the combustion zone. The result of the increased heat transfer to the solid fuel is an increase in the rate of decomposition of the fuel, which results in an increase in the linear-regression rate and thrust generation.

Though serious effort has been made to investigate metallized solid fuels for use in propulsion systems, the Sandpiper target missile and the Lockheed Martin/NASA-developed sounding rocket are the only flight vehicles that have used metallized solid-fuel formulations [29, 33].

The Sandpiper target missile solid fuel consisted of 10 wt % magnesium in a PMMA binder. The system combined a boost phase that produced nominal thrust of 500 lbf and a sustain phase that allowed a thrust level to be selected by adjusting a mechanical orifice valve. Sustain thrust levels were varied from approximately 100 to 240 lbf dependent on the flight altitude and Mach number of the intended mission. The U.S. Air Force at Eglin Air Force Base completed three test flights with this missile system within a three-month period starting in December 1967. The Sandpiper system reached a maximum altitude of 78,000 ft and a Mach number of 2.5 during powered flights lasting 5 min. The end result of the 1.5-year program was the demonstration of a low-cost, adjustable thrust hybrid rocket motor.

The hybrid sounding rocket (HYSR) program conducted jointly by Lockheed Martin and NASA Marshall Space Flight Center (MSFC) operated between 1999 and 2002. During this time period, the research and development goal focused on the replacement of current two- and three-stage sounding rockets with a single-stage propulsion system. The solid-fuel formulation used consisted of an HTPB-based binder containing a relatively high level of aluminum addition. Little information on the solid-fuel and the system performance is available in public literature. Successful flight testing of the system was completed on 18 December 2002 producing approximately 60,000 lbf of vacuum thrust. Further details of the design and development of this system is provided in Chapter 14.

Most research has incorporated metal additives in polymeric-based solid fuels, though recent efforts have considered the addition of metal additives to nonpolymeric paraffin-based solid fuels as well. The addition of various types of metals, for example, LiH, Al, B, B_4C, W, Mg, etc., has been considered in fuel formulations by various researchers. Results show that differences in shapes and sizes have a significant effect in the enhancement of propulsive performance and combustion efficiency. Early research considered the addition of micrometer-sized additives

to the baseline solid fuels; advancements in nanosized particle production in the mid-to-late 1990s shifted the focus of research to the use of nanosized particles in fuel formulations. The ignition and the burnout time of single particles are primarily governed by the initial size of the particle, according to the d^2 law for spherical particle burning. The greatly reduced ignition and combustion times associated with nanosized particles provides more complete combustion within volume-limited propulsion systems.

With the exception of the preceding hybrid rocket propulsion systems, research of metallized solid fuels has since been completed predominantly at a laboratory scale. As mentioned earlier, metallized solid-fuel formulations have included a wide variety of additives with a wide variety of sizes and morphology. The following sections cover a comprehensive review of the work completed over the previous 40 years of particle addition for enhancement of the solid-fuel performance.

A. Lithium-Based Particle Additives in Solid Fuels

The use of lithium-based particles for addition to solid fuels for increased energy release is based on their status as alkali metals, which are extremely reactive due to the one electron in their outer shell. Though lithium is highly reactive, the volumetric heat of oxidation is relatively low compared to more traditional particles, for example, Al, B, and B_4C. Two research programs that used lithium-based particle addition were conducted in the mid-1960s. The first of these two studies is the work of Smoot and Price [34], who used lithium hydride (LiH) in variable amounts in a butyl rubber binder with a fluorine/oxygen (FLOX) oxidizer. The second study conducted by Osmon [35], used lithium–aluminum hydride (LiAlH) in a polyethylene (PE) binder and 90% hydrogen peroxide (H_2O_2) as the oxidizer.

The work of Smoot and Price, conducted at the then Lockheed Propulsion Company, consisted of a series of 139 laboratory-scale test firings in a 6-in. (15.2-cm) two-dimensional slab motor configuration. Fuel formulations ranging from pure butyl rubber to 10 wt % butyl rubber and 90 wt % LiH were evaluated with various oxidizer combinations from pure oxygen to pure fluorine. Operating chamber pressures were varied from 21 to 156 psia (0.15 to 1.08 MPa) through nozzle throat diameter variation. Average regression rate data for the test series were determined from the average of five measurements along the length of the fuel grain. The focus of their research was to gain understanding as to what particle loading percentage would provide substantial increase of the solid-fuel regression rate and whether the increase was proportional to the percent particle addition. Although the operating conditions of their work, that is, oxidizer flux, are far outside the practical range of interest for operation of practical hybrid systems, it still provides useful insight into the behavior of highly loaded solid-fuel formulations.

Figure 2 is a reproduction of the data presented by Smoot and Price [34] for variable LiH addition and variable oxidizer combinations. The oxidizer was adjusted to contain the required amount of oxygen to form carbon monoxide from the carbon in the binder, with the rest of the oxidizer being fluorine. The fuel was varied from pure butyl rubber up to 90 wt % LiH with 10 wt % binder. For this series of tests, the nominal chamber pressure was approximately 60 psia (0.41 MPa). Results showed that the addition of up to 50 wt % LiH gave minimal increase in the regression rate for oxidizer flux values up to 0.04–0.05 $\text{lbm/in.}^2 \cdot \text{s}$ (28–35 $\text{kg/m}^2 \cdot \text{s}$). Above this

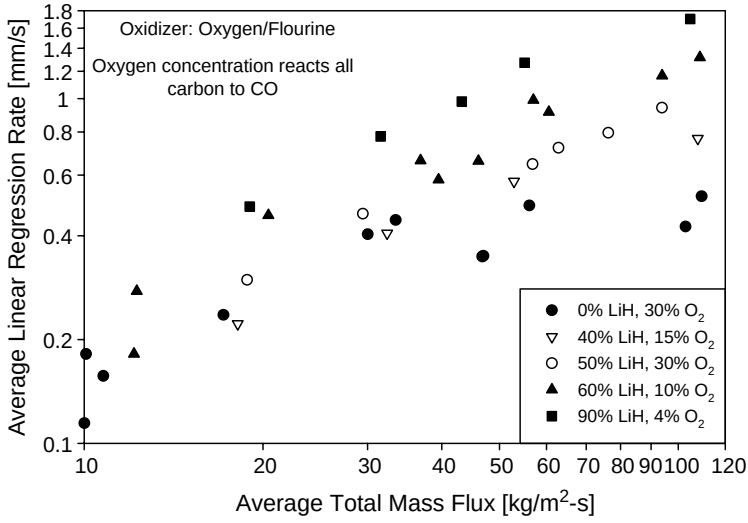

Fig. 2 Effect of percent of LiH on regression rate of butyl-based solid fuels. (From Smoot and Price [34].)

oxidizer mass flux range, a strong divergence is observed from the 0.8 power-law dependence on mass flux, as expected from classical theory for the baseline butyl rubber. In this higher mass flux regime, the regression rate was shown to be a strong function of the operating pressure and the fuel composition, while being less dependent on the total mass flux. The transition to the pressure-dependent burning region in the high mass flux regime was speculated to be the transition from diffusion-controlled combustion to kinetics-controlled combustion. As claimed by Smoot and Price, the mass flux level of transition to pressure-dependent combustion and sensitivity of a solid fuel to pressure was also shown to be dependent on the percent addition of LiH. With increased loading density of LiH to the solid fuel, the transitional level increases and the pressure sensitivity decreases in the pressure-dependent regime.

At approximately the same time as the work of Smoot and Price, Osmon, of the then Northrop Norair, conducted experiments using LiAlH particle addition in a PE binder [35]. The oxidizer/fuel combination evaluated experimentally consisted of 90% H_2O_2 liquid oxidizer and 95 wt % LiAlH in a 5 wt % PE binder solid-fuel formulation. Nominal chamber pressures from 120 to 404 psia (0.83 to 2.79 MPa) with average oxidizer flux levels ranging from 0.08 to 0.25 $\text{lbm/in.}^2 \cdot \text{s}$ (56 to 176 $\text{kg/m}^2 \cdot \text{s}$) were evaluated in a test series consisting of six tests. A single-port, center-perforated motor was used in this series of tests with a nominal length of 20 in. (51 cm).

Average regression rates between 0.0691 in./s (1.76 mm/s) and 0.111 in./s (2.82 mm/s) were measured using a weight-based determination of a nominal final port diameter. As discussed by Osmon [35], the upstream portion of the fuel grain regressed significantly more than the downstream. In the range of 1.5–4 in. from the head end, the fuel grain demonstrated significantly more erosion than at

downstream locations. Osmon attributed this increase to the expansion of the H_2O_2 during the decomposition process. With use of the pressure–time trace data and the assumption of constant C^* during the test, instantaneous regression rate values were obtained and correlated to the oxidizer mass flux and chamber pressure. The exponent on the oxidizer mass flux and pressure were both 0.4. The results of this should be viewed skeptically because the assumption of constant C^* is unjustified.

B. Aluminum-Based Particle Additives in Solid Fuels

Aluminum is one of the most researched additives for solid-fuel formulations. Many researchers have considered the addition of aluminum to both traditional polymeric binders and recently to nonpolymeric binders, that is, paraffin solid fuel. The main advantages of aluminum are the relatively high heat of oxidation (31.1 kJ/gm), relatively high density (2.7 g/cm^3), and ease of ignition in the hot combustion environment of the rocket motor chamber. These properties make aluminum an attractive additive for increasing the performance of a propulsion system, especially a volume-limited system.

In the mid-1960s, United Technology Corporation (UTC) of Sunnyvale, California investigated the application of a prepackaged hybrid-propulsion system for application to tactical missile systems for the U.S. Air Force [36]. The final fuel selections for application and further evaluation contained ammonium perchlorate (AP). Even though final selections were based on the nonsustaining combustion characteristic of the fuel formulation, these formulations are not included here because they are not pure hybrid systems. During the solid-fuel formulation selection process of the 18-in.- (45.7-cm-) diameter motor development project and an earlier U.S. Air Force contract, a few tests were conducted on fuel formulations that did not contain solid oxidizer in the fuel matrix. In total, eight tests were conducted with aluminum in the fuel matrix (Table 3). Three fuel/oxidizer combinations were evaluated: 1) 30% R-45 polymer/20% Al/50% triaminoquanidine azide–hydrazine azide (THA) with red-fuming nitric acid (RFNA) oxidizer, 2) 30% R-45 polymer/20% Al/50% THA with LOX oxidizer, and 3) 35% 3812 QX polymer/20% Al/45% tetraformaltrisazine (TFTA) with a 75%/25% mixture of ClF_5/ClO_3F for the oxidizer. The fuels were evaluated in either a 5-in.- (12.7-cm-) diam motor (combinations 1 and 2) or a 3.5-in.- (8.89-cm-) diam motor (combination 3). Unfortunately, no specific data are given on the fuel-grain geometry, and, therefore, no average oxidizer mass flux data are available for comparison of regression rates. Also included in Table 3 are results from tests of non-metallized fuels that contained the high-nitrogen compound THA, for comparison with metallized fuel test results. The first two tests presented in Table 3 were completed in the fuel evaluation and selection process for the 18-in.- (45.7-cm-) diam hybrid rocket motor, the end of project deliverable item [36], and were completed in a 5-in.- (12.7-cm-) diam motor. The remaining six tests conducted with metallized solid-fuel formulations are presented along with effective baseline formulations using similar oxidizers, including LOX and inhibited red-fuming nitric acid (IRFNA). The baseline fuel contains 50 wt % THA, which is the same weight percentage as in the metallized-fuel formulation.

In the mid-1970s, Lips of the German Research and Development Institute for Air and Space Travel (DFVLR) conducted a series of experiments considering

Table 3 Aluminized solid-fuel combustion test results of UTC [36]

Fuel composition	Oxidizer composition	Chamber pressure, psia	Oxidizer flow rate, lbm/s	Average regression rate, in./s	Burn time, s	Motor diameter, in.
35% QX/ 20% Al/ 45% TFTA	75% ClF_5/25% ClO_3F	533.0	0.62	0.034	9.95	3.5
35% QX/ 20% Al/ 45% TFTA	75% ClF_5/25% ClO_3F	600.0	0.62	0.039	8.96	3.5
30% R-45/ 20% Al/ 50% THA	LOX	72.8	0.40	0.031	15.18	5
30% R-45/ 20% Al/ 50% THA	LOX	108.4	0.61	0.035	8.40	5
30% R-45/ 20% Al/ 50% THA	LOX	209.0	1.23	0.076	5.92	5
50% R-45/50% THA	LOX	30.0	0.58	0.017	19.81	5
50% R-45/50% THA	LOX	71.0	0.59	0.024	18.80	5
50% R-45/50% THA	LOX	270.0	0.59	0.038	17.88	5
50% R-45/50% THA	LOX	337.0	0.56	0.037	16.11	5
30% R-45/ 20% Al/ 50% THA	RFNA	556.0	0.94	0.130	4.85	5
30% R-45/ 20% Al/ 50% THA	RFNA	272.0	0.94	0.104	4.90	5
30% R-45/ 20% Al/ 50% THA	RFNA	730.0	0.92	0.134	4.10	5
50% R-45/50% THA	IRFNA	950.0	0.60	0.160	1.52	2
50% R-45/50% THA	IRFNA	835.0	0.60	0.160	2.61	2
50% R-45/50% THA	IRFNA	864.0	0.60	0.160	2.51	2
50% R-45/50% THA	IRFNA	920.0	0.60	0.160	2.06	2

highly aluminized solid fuels (60–80% Al) with FLOX oxidizer [37–39]. The specific objectives of the research were the evaluation of 1) binder composition, 2) metal type, 3) metal-loading concentration, and 4) oxidizer composition. Two motors were used in the evaluation of solid-fuel formulations. The first motor was a transparent slab motor, used for the evaluation of the preceding four variables, and the second was a 13.8-in.- (35.0-cm-) long, 7.1-in.- (18.0-cm-) outer-diameter, single-port center-perforated fuel grain. An active splash block was installed upstream of the fuel grain, and a modular mixing and reaction plenum was located in the aft end section of the fuel grain.

The polymer type used in the binder was evaluated through a series of tests in which the aluminum content, oxidizer composition, chamber pressure, and initial oxidizer mass flux were held constant. The binders evaluated were PU, CTPB–acrylonitrile (CTBN) copolymer, PBAA copolymer, polyisobutylene (PIB), and polyimide (PI). All fuels grains contained 60 wt % aluminum and the oxidizer was FLOX-40 (40% F_2/60% O_2, both in liquid form). The initial oxidizer mass flux was set to be 65.1 $kg/m^2 \cdot s$. Typical results of the experiments are shown in Table 4, where the regression rates were calculated as an average of the burned web over the aft one-third of the fuel-grain length since uneven burning of the fuel surface was observed over the length of the fuel grain. The issue arises from the incomplete vaporization of the oxidizer before interaction with the boundary layer causing impingement on the surface of the solid fuel.

As observed, the use of CTBN exhibits the highest regression rate in this set of tests, closely followed by PBAA. These two polymers exhibited a char layer on the solid-fuel surface due to the decomposition process of the polymer. The thermal decomposition process of the individual polymers was also studied. Onset of decomposition for both polymers occurs at relatively low temperatures from the exothermic bond-breaking –C=C– and –C≡C–. Breakage of these bonds evolves gaseous and carbonaceous fragments, leaving behind the char layer as observed. Similar observations were also made for the decomposition of HTPB fuel, which was not considered in the regression rate portion of the study, but is a commonly used binder.

The effect of the metal additive type was evaluated using 60 wt % metal additive in a PU binder. The oxidizer was again FLOX-40 with initial G_{ox} values of either 65.1 or 73.6 $kg/m^2 \cdot s$. The metal additives considered were Al, Si, B, 97% Al/3% Mg, 50% Al/50% Mg, and pure Mg. Typical results of the regression rate behaviors of the fuels are presented in Table 5. The regression rates of Al, Si, B, and

Table 4 Effect of binder type on regression rate [37]

Propellant combination		$r_{b,av}$,
Fuel	Oxidizer	mm/s
60% Al/40% PU	FLOX-40	0.64
60% Al/40% CTBN	FLOX-40	0.85
60% Al/40% PBAA	FLOX-40	0.76
60% Al/40% PIB	FLOX-40	0.39
60% Al/40% PI	FLOX-40	0.31

Table 5 Effect of metal additive type on regression rate [37]

Propellant combination		$r_{b,\mathrm{av}}$,	$G_{\mathrm{ox},i}$,
Fuel	Oxidizer	mm/s	kg/m$^2\cdot$s
60% Al/40% PU	FLOX-40	0.64	65.1
60% Si/40% PU	FLOX-40	0.61	65.1
60% B/40% PU	FLOX-40	0.58	65.1
60% AlMg-3/40% PU	FLOX-40	0.62	73.6
60% AlMg-50/40% PU	FLOX-40	0.73	73.6
60% Mg/40% PU	FLOX-40	0.74	73.6

3% Mg-coated Al are very similar. In addition to solely the material variation, the particle size was also evaluated as a portion of the study. Aluminum distributions with particle sizes from less than 32 μm to 200–250 μm were evaluated with no distinct effect on the regression rates. The lack of measured changes in regression behavior for different metal types and sizes was not addressed in detail in the study.

The metal-loading effect was also evaluated for aluminum-loading concentrations between 40 and 80 wt %. Typical regression rates are presented in Table 6. A 36% increase in the regression rate is observed between the 40% aluminized fuel and the 60% aluminized fuel. Replacing 10% of the binder with carbon particles provides approximately a 10% increase in the linear regression rate. The increase in regression rate with the increasing amounts of aluminum shows that at least a portion of the aluminum is being combusted in the near solid-fuel surface region and is contributing to the amount of heat being supplied to the surface. In the case of 80% aluminum loading, the slight decrease compared to the combined Al and C addition case and very mild increase compared to the 60% Al case show that the additional aluminum is not releasing sufficient energy in the near-surface region to affect the regression behavior, and therefore, the combustion process in the near-surface region is not as efficient at the lower loading conditions. Low efficiency can be the effect of two causes: 1) The slightly lower F_2 content of the oxidizer in this case causes the combustion to occur over a larger distance, or 2) the aluminum is agglomerating on the surface significantly before removal and does not combust as efficiently.

Table 6 Effect of weight percentage of metal particle additive on solid fuel regression rate [37]

Propellant combination		$r_{b,\mathrm{av}}$,	$G_{\mathrm{ox},i}$,
Fuel	Oxidizer	mm/s	kg/m$^2\cdot$s
40% Al/60% PU	FLOX-40	0.47	73.6
60% Al/40% PU	FLOX-40	0.64	65.1
60% Al/10% C/30% PU	FLOX-40	0.70	65.1
80% Al/20% PU	FLOX-30	0.66	65.1

Table 7 Oxidizer composition effect on regression rate of metallized solid fuel.

Propellant combination		$r_{b,\mathrm{av}}$,	$G_{\mathrm{ox},i}$,
Fuel	Oxidizer	mm/s	kg/m$^2\cdot$ s
60% Al/40% PU	O_2	0.30	73.6
60% Al/40% PU	FLOX-40	0.64	65.1
60% Al/40% PU	FLOX-90	0.86	65.1
60% Al/40% PU	F_2	0.90	65.1

The consideration of oxidizer composition used PU grains loaded with 60% Al at initial oxidizer mass fluxes of 65.1 kg/m$^2\cdot$ s. The resulting regression rates were significantly increased as the F_2 content increased, as seen in Table 7. The strong dependence of regression rate on F_2 content was attributed to the product evolution of F_2 and Al. The major product species is AlF_3, which sublimates at 1550 K and, therefore, will not accumulate on the surface of the reacting aluminum particle as in the case of O_2 reacting with Al, that is, Al_2O_3 accumulation. The second contributing factor is the higher heat of combustion associated with F_2 and Al (4.3 kcal/mol) compared to O_2 and Al (3.8 kcal/mol). Testing was also conducted by Lips [37–39] in a non-transparent axisymmetric motor for evaluation of selected fuel formulations. Results of testing the 60% Al/40% PU with FLOX-40 and 80% Al/20% PU with FLOX-90 are shown in Fig. 3. The resulting curve fits for the

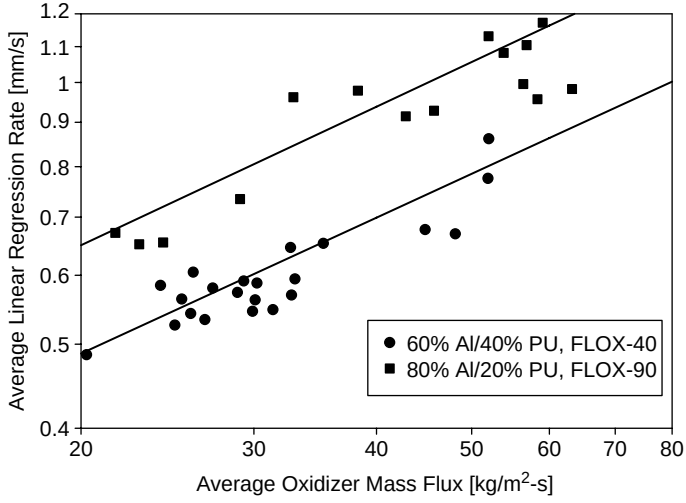

Fig. 3 Variation of regression rate with $G_{\mathrm{ox,av}}$ for two aluminized solid-fuel formulations. (From Lips [37].)

two fuel formulations are

$$r_b = 0.045\, G_{\mathrm{ox,av}}^{0.53}\text{: 80\% Al/20\% PU with FLOX-90} \tag{1}$$

$$r_b = 0.034\, G_{\mathrm{ox,av}}^{0.52}\text{: 60\% Al/40\% PU with FLOX-40} \tag{2}$$

The regression rate is increased by ~34% on average when evaluated at the two extremes of the average oxidizer mass flux measured. The increase in aluminum concentration and the increase in F_2 content both contribute to the increase in regression rate observed.

Efficiencies for the center-perforated series of test firings were studied through the use of a modular mixing device followed by a reaction chamber located at the aft end of the solid-fuel grain. The mixing device was a disk made of pyrolytic graphite that had three holes in it. The purpose was to mix the very oxidizer-rich core flow with the very fuel-rich boundary-layer region before introduction into the reaction chamber. Fuel grains loaded with 60 wt % Al that did not have a mixing device installed and had a small reaction chamber demonstrated very low C^* combustion efficiency and I_{sp} efficiency, 75% and 67%, respectively. Installation of the mixing device and increasing the reaction chamber free volume increased the efficiencies dramatically, reaching levels of 92% for C^* combustion efficiency and 90% for I_{sp} efficiency. Higher percentage aluminum (80 wt %) cases demonstrated lower efficiencies than the tests involving 60 wt % Al, even when combusted with a higher F_2 content oxidizer. The increase in aluminum content does increase the mass burning rate and thus thrust generation, but decreases the efficiency of combustion and thrust generation. This is predominantly due to two-phase flow losses and inefficient combustion of the aluminum particles within the combustion chamber.

During the early-to-mid 1990s, researchers at the Jet Propulsion Laboratory and Cohen Professional Services actively researched the addition of aluminum particles to HTPB-based solid fuels in a two-dimensional slab motor configuration [40–42]. Average oxidizer mass flux values of 7–35 $\mathrm{kg/m^2 \cdot s}$ based on the head end hydraulic diameter were used. Fuel formulations included a baseline HTPB fuel and two HTPB-based solid fuels containing 40 wt % Al/30 wt % spherical coal particles with aluminum mean particle size from 40 to 95 μm. As the fuel surface regressed, a surface melt layer that contained aluminum, coal, and binder was formed that then progressed into flakes and would periodically detach from the burning surface and become entrained into the combustion zone. The ejection of aluminum agglomerates was also observed; agglomerations on the order of 1 mm in diameter and larger were observed in the combustion region. This result was independent of the mean particle size contained in the solid fuel. The other major observation made of the regressing surface appearance is the transition from a melt layer-to-flake formation on the fuel surface at lower oxidizer mass fluxes to a continuous generation of carbonaceous ash at higher oxidizer mass fluxes [40]. This occurrence can be related to the decomposition of the HTPB occurring in a very fast manner due to the increased surface heat flux, and the ash residue is the solid-phase decomposition products and possibly results from the desorption process of the fragments of HTPB fuel at the regressing surface. This situation is the result of the physical removal of solids from the surface being the rate-limiting process in the regression of the surface.

The average regression rate was evaluated in two different test series: 1) the effect of the particle size and 2) the effect of a one-slab vs two-slab motor configuration. The particle size was shown to have no direct effect on the regression rate. Though particle sizes differed from 40 to 95 μm average diameter, no difference in agglomeration and removal were seen in post-test grain analysis. The similarity in regression rates also shows that these two particle sizes combust and release their energy at approximately the same distance from the surface and thus provide similar heat flux values to the surface. The one-slab vs two-slab motor configurations resulted in a significant difference in the measured linear regression rates. As seen in Fig. 4, the single-slab configuration exhibited a lower regression rate than the twin-slab configuration of approximately 40%. This is in contrast to the baseline HTPB case in which a similar series of experiments were conducted and showed no discernable difference in regression rates. The differences in the metallized cases show the importance of the radiation heat transfer in the overall heat transfer to the solid-fuel surface. The other interesting trend is the decreased dependence of the regression rate on the oxidizer mass flux. At the condition of low oxidizer mass flux ($<12\,\mathrm{kg/m^2 \cdot s}$) the convective heat transfer, which is dependent on the oxidizer flow velocity, is less important and the importance of radiative heat transfer to the solid fuel is noted.

In a later work by the same authors [41], a modeling effort was made to simulate the average regression rates of metallized HTPB fuels. Two sets of data and model predictions were presented for cases of 170- and 200-psia (1.17- and 1.38-MPa) average chamber pressures. At a chamber pressure of 200 psia (1.38 MPa), the model was shown to predict quite accurately the empirical data. At the lower chamber pressure, the model overpredicted the regression rate. The overprediction reached a maximum of approximately 8% and decreased as the total mass flux level increased. The authors attributed this to more efficient combustion of aluminum

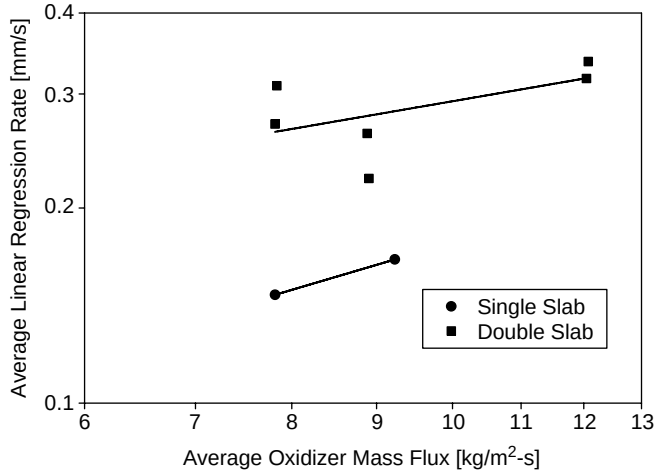

Fig. 4 Effect of single vs double slab configuration on regression of metallized HTPB solid fuel [41].

particles at a higher total flux level. The data presented do not exhibit a power law nature at the lower total flux levels, thus, exhibiting the high levels of radiative heat flux in this region. The result is a pressure dependence of mass burning rate, due to the high levels of radiative heat transfer, relatively low chamber pressures, and relatively low oxidizer mass flux levels. This effect, which was also observed by Smoot and Price [34], is expected to decrease as the total flux is increased and the regression behavior enters a region in which the convective heat transfer is dominant again.

Work conducted by George et al. [43] during the late 1990s evaluated the effect of aluminum addition and fuel-grain geometry on regression behavior. Baseline HTPB solid fuels were evaluated along with metallized grains containing 19.67 wt % Al with an average particle size of 28 μm. The fuel-grain length was evaluated for four cases total (160, 250, 400, and 545 mm) and two cases in the metallized fuel tests (250 and 400 mm). The initial inner diameter was either 12 or 20 mm. Oxidizer mass flux levels varied from approximately 50 to 500 $\mathrm{kg/m^2 \cdot s}$ at chamber pressures ranging from 174 to 290 psia (1.2 to 2.0 MPa). Data reduction was completed to determine the spatially averaged regression rate from the pressure–time trace recorded during the test. The drawback of this methodology is the assumption of a constant value of combustion efficiency throughout the test duration. The major advantage is the increase in data available for regression rate behavior analysis. Two of the results obtained from the post-test analysis are values of the instantaneous regression rate (spatially averaged) and an average combustion efficiency value. Determined combustion efficiency values for metallized grains had a value of 89% compared to 93% for pure HTPB fuels. The power-law curve fits that were obtained for the aluminized-fuel grains were

$$r_{b,\mathrm{av}} = 1.4 \times 10^{-5} G_{\mathrm{ox,av}}^{0.93} \quad L_g = 250\,\mathrm{mm}, \qquad d_{p,i} = 12\,\mathrm{mm} \tag{3}$$

$$r_{b,\mathrm{av}} = 1.3 \times 10^{-5} G_{\mathrm{ox,av}}^{0.89} \quad L_g = 400\,\mathrm{mm}, \qquad d_{p,i} = 20\,\mathrm{mm} \tag{4}$$

As is demonstrated by the curve-fit coefficients, there is very little dependence on the grain length. The authors did not discuss the reasoning behind this behavior, but it is observed that at this modest scaling ($d_{p,i} = 12$–20 mm and $L_g = 250$–400 mm) there is not a noticeable effect on the regression rate level of the aluminized solid fuel.

The research of metallized solid-fuel formulations at Pennsylvania State University (PSU) has occurred over the duration of two major research initiatives. The first of these research programs was conducted under the sponsorship of the NASA MSC between 1994 and 1996. The second research program was conducted under the sponsorship of the U.S. Navy and has been operating since 2000.

Studies performed under the NASA program were conducted in a windowed, two-dimensional slab geometry hybrid rocket engine using gaseous oxygen (GOX) as the oxidizer [44–47]. The system utilized a real-time X-ray radiography system for obtaining the solid-fuel surface location throughout the duration of the combustion test. To determine the effects of solid-fuel additives on the combustion behavior of HTPB-based solid fuels, three types of particles were added to the solid fuels: 1) carbon black (~75 nm), 2) ultrafine aluminum (UFAL), also called

Alex® (100–150 nm), and 3) conventional Al (5–15 μm). Tests were conducted at average oxidizer mass fluxes ranging from 140 to 390 $kg/m^2 \cdot s$ and nominal chamber pressures from 210 to 1300 psia (1.45 to 8.96 MPa). The slab motor housed two solid-fuel grains 23 in. (58.4 cm) in length and 3 in. (7.62 cm) wide.

The evaluation of UFAL was conducted by adding a specified amount of particles (4, 12, or 20%) to one of the solid-fuel slabs, while the other slab was pure HTPB to allow the direct measurement in the same test of the increase in solid-fuel regression rate for both formulations. Figure 5 shows the effect of UFAL addition on the time- and space-averaged regression rate and the mass burning rate. At a particle addition of 20 wt % of UFAL, a maximum increase in the regression rate of ∼43% was seen, which corresponds to a mass burning rate increase of ∼70%. The time-averaged regression rates measured along the axial distance of the slab demonstrated a much higher regression rate than those of the pure HTPB slab. Ignition and combustion of the UFAL particles in the near-surface region provides significantly more heat feedback to the solid-fuel surface and, thus, generate a higher regression rate than the nonmetallized case. The addition of conventional micrometer-sized aluminum particles also demonstrated increase in regression rate compared to baseline HTPB, but not to the same degree as nanosized particle addition. Micrometer-sized aluminum particle addition at 20 wt % demonstrated a 12% increase in the regression rate, compared to the 40% increase gained through the same weight percent of Alex aluminum particles. The increase in regression rate for solid fuels with micrometer-sized aluminum particles was attributed to the increase in radiative heat transfer to the surface as well as an increase in flame temperature. The additional increase in solid fuels containing nanosized Alex particles can be attributed to the higher rate of exothermic reactions in the near surface region [44–47].

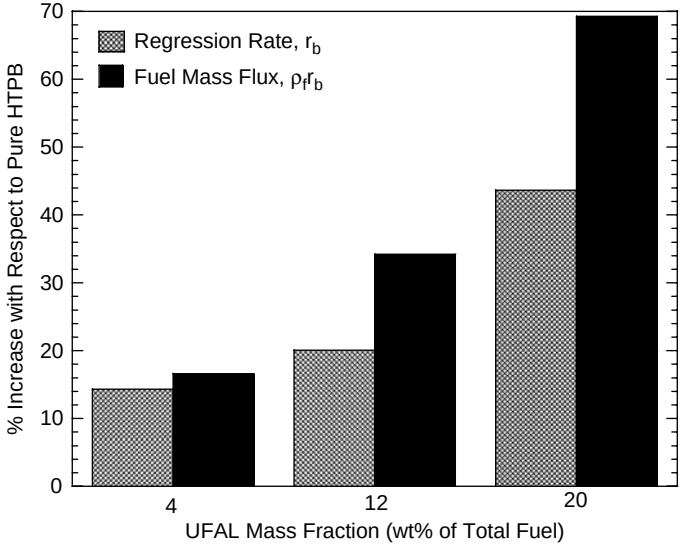

Fig. 5 Effect of UFAL particle addition on regression and mass-burning rates [53].

The second series of hybrid rocket engine combustion studies was conducted in two center-perforated hybrid rocket engines at PSU. The first, called the long-grain center-perforated (LGCP) hybrid rocket engine, is a traditional steel-cased engine that is capable of housing 16-in.- (40.6-cm-) long cartridge-loaded fuel grains [48–54]. The small amount of mass required per fuel grain makes this engine ideal for particle evaluation. The LGCP engine also has the capability of operating with either GOX or N_2O, allowing a performance comparison between two oxidizers. A more thorough discussion of the LGCP engine setup is given by Risha et al. [50]. The second center-perforated engine used for fuel evaluation is the X-ray transparent casing (XTC) hybrid rocket engine [55–58]. This engine is approximately three times the size of the LGCP and uses a thick-walled paper phenolic tube for the motor case allowing for instantaneous imaging of the solid-fuel surface through the use of a real-time X-ray radiography system. It also has the capability to install diagnostics at any given axial location. Both hybrid rocket engines have the capabilities of thrust measurement and pressure measurements at the head end and aft end of the motor. Temperature measurements of the regressing fuel surface have also been made in the XTC engine using fine-wire thermocouples installed in the fuel grain. Further details of the XTC engine design are given by Evans et al. [55].

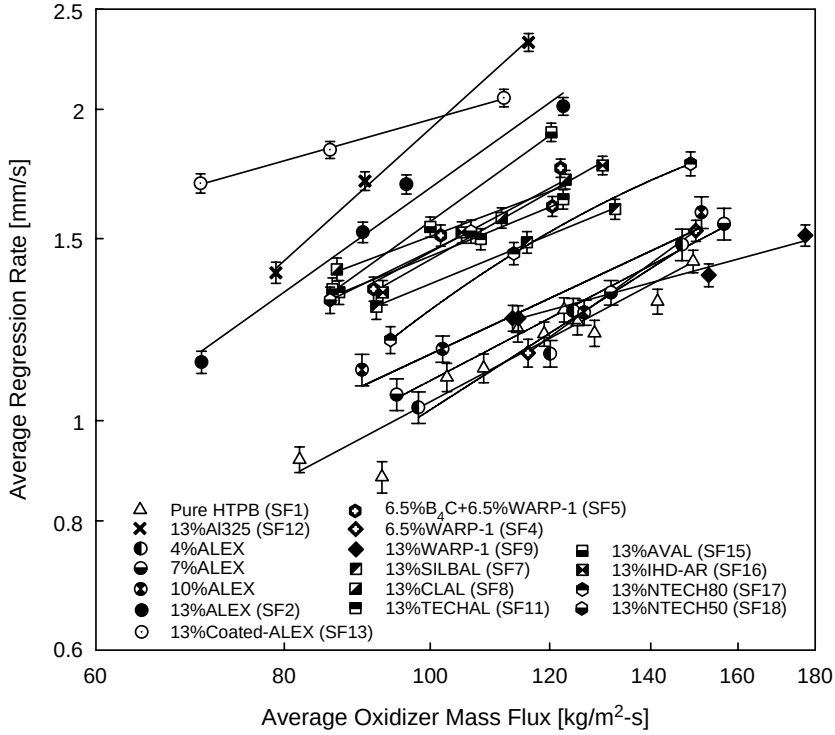

Fig. 6 Comparison of aluminized solid-fuel regression rate behaviors [56, 62].

The addition of nanosized additives was considered using the LGCP engine with comparisons to traditional micrometer-sized aluminum-particle-containing fuel, baseline HTPB solid fuel, and baseline paraffin solid fuel. A total of 19 different aluminized HTPB-based fuel formulations were evaluated using this engine, producing a wealth of information on the differences in combustion behavior. Figure 6 presents a comparison of the average regression rates for these formulations, and information on the particles used is given in Table 8, which will be discussed in more detail later. From a thermodynamic standpoint, the energy increase in a system due to the addition of the same weight percentage of aluminum should be independent of the particle type added. However, these results show that the regression rates and combustion efficiencies measured are highly dependent on the particle type and manufacturer. Among the 19 formulations, the two that demonstrated the largest increase in regression rates are solid fuel 12 (SF12 containing 13% micrometer-sized Al particles) and solid fuel 13 (SF13 containing 13% Viton-A coated Alex® Al particles). An increase of 123% in regression rate over pure HTPB fuel formulations is demonstrated by SF13 at an average oxidizer flux of 112 $kg/m^2 \cdot s$ [51]. SF12 was the only formulation that contained micrometer-sized aluminum, thereby providing a comparison of performance between micrometer-sized and nanosized particles in the same engine configuration. Solid fuels containing Viton-A coated Alex® aluminum particles (SF13) demonstrated similar regressionrate enhancement in magnitude compared to SF12, but the slope of the regression rate of SF12 is much steeper implying that the performance is affected less by the changing oxidizer-to-fuel ratio during the combustion event. As is seen in Fig. 6, fuels containing coated Alex® particles (SF13) exhibit a higher regression rate than those containing uncoated Alex® particles (SF2). The fluorinated compound coating the aluminum particles can lead to rapid ignition and more complete combustion as will be discussed further when considering the efficiencies.

Figure 6 also shows a series of motor firings to investigate the effect of the percent Alex® aluminum particle on propulsive performance that was conducted in the LGCP engine. Five formulations were evaluated that contained either 4, 7, 10, 17, or 20% aluminum. Fuels loaded with 17 or 20% aluminum demonstrated strong combustion instability and are not included in Fig. 6. The periodic nature of observed plume jet oscillations was believed to be the result of the periodic shedding of material from the surface and subsequent reaction in the combustion chamber. The values for 4–10% loading demonstrate a consistent increase in the regression rate over the baseline fuel. It was decided that based on the available data a loading of 13% demonstrated a limit of stable combustion [54]. This result is also expected to be highly dependent on the engine geometry and solid-fuel grain geometry and may occur at different levels of loading percentage for different engines.

Evaluation of nitrous oxide as an oxidizer was considered in a recent series of studies in the LGCP engine. The test series allowed the comparison between two different oxidizers (nitrous oxide and GOX) on propulsive performance. A series of tests was conducted considering the addition of 13% Silberline® aluminum flakes to an HTPB fuel. The regression rate results are presented in Fig. 7. As expected, the regression rate is lower when N_2O is the oxidizer than when GOX is used. Similar trends are seen in the slopes for both oxidizers, whether it is pure HTPB or aluminized fuel. An increase of 15% in the regression rate is measured

Table 8 Summary of published, measured, and calculated physical properties of energetic nanosized particles [52]

Particle I.D.	Distributor	Average diameter,[a] nm	Average diameter,[b] nm	Specific surface area, m^2/g	Active content, wt %		Average oxide layer thickness, nm	ρ_{eff}, g/cm^3	Remarks
					KOH[c]	TGA			
Alex®	Argonide Corporation	100–150	160	13.3[d]	84.8	84.4	3.1	2.84	Al particles
WARP-1	CMPI[e]	70	68	27.5[a]	49.2	51.0	5.3	3.20	Al particles
SILBAL	Silberline	50–200 thick	——	——	88.8	86.2	4.6[f]	2.83	Al flakes
CLAL	NAWC[g]-China Lake	50–200 thick	——	——	61.8	69.0	4.6[f]	3.00	Viton-A coated SILBAL flakes
TECHAL	Technanogy	46	45	44.4[a]	58.1	67.2	2.0	3.02	Al particles
B_4C	CMPI	120	——	13[a]			——	2.54	B_4C particles
Cat-B_4C	CMPI	120	——	13[a]			——	2.54	catalyzed B_4C
Boron	SB Boron Corp.	<150	82	31.0[a]	N/A	74.7	3.8	2.37	Boron particles
Coated Alex®	NAWC–China Lake	100–150	160	13.3[a]	N/A	84.4	3.1	2.84	Viton-A coated Alex®

IHD-AR	NSWC[h]–Indian Head	80	41	50.0[a]	N/A	76.3	1.3	2.92	Al particles quenched in Ar
IHD-HE	NSWC–Indian Head	——	26	70.0[a]	N/A	43.9	3.1	3.29	Al particles quenched in He
NTECH-80	Nanotechologies	80	102	20.0[d]	N/A	74.0	2.5	2.95	Al particles
NTECH-50	Nanotechologies	50	54	36.0[d]	N/A	61.0	3.1	3.09	Al particles
AVAL	Aveka, Inc.	30–40	23	75.0[a]	N/A	33.5	2.9	3.43	Al particles
Coated-Boron	NAWC-China Lake	<150	82	31.0[a]	N/A	74.7	3.8	2.37	Viton-A coated boron
Valimet H-2	——	——	——	——	98.6	N/A	——	——	Al standard powder

[a]Manufacturer-supplied data.
[b]Derived from specific surface area data.
[c]Potassium hydroxide (KOH) hydrolysis method.
[d]Brunauer, Emmett, and Teller (BET) measurements made at PSU.
[e]Ceramic Materials Processing, Inc. (CMPI).
[f]Flake was assumed to be elliptical in shape with uniform thickness.
[g]Naval Air Warfare Center (NAWC).
[h]Naval Surface Warfare Center (NSWC).

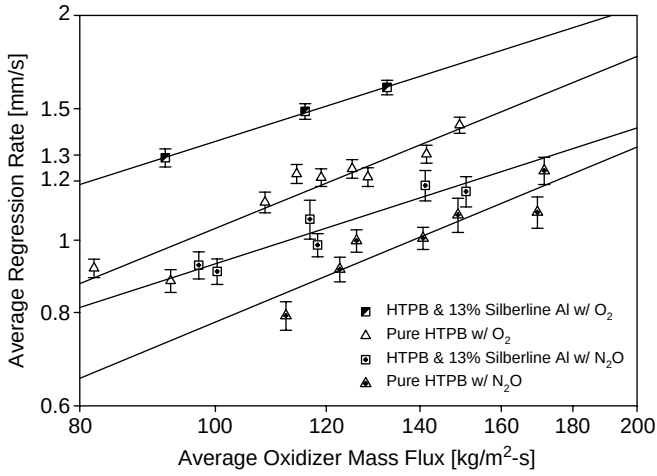

Fig. 7 Comparison of average regression rates of GOX and N_2O oxidizers [54].

for aluminized fuels when N_2O is used, compared to an increase of 20% that was measured for the same fuel formulation when GOX was used [49]. Silberline® aluminum flakes increase the burning rate of the fuel with N_2O toward burning rates seen by the baseline HTPB fuel used with GOX, thereby offsetting the drawback in performance of using N_2O oxidizer, but still benefiting from the ease of storage capabilities of N_2O.

Paraffin-based solid fuels containing aluminum flakes have also been tested by Evans et al. [56–58]. The measured average regression rate data of these tests are presented in Fig. 8 and compared to those of two other paraffin-fuel

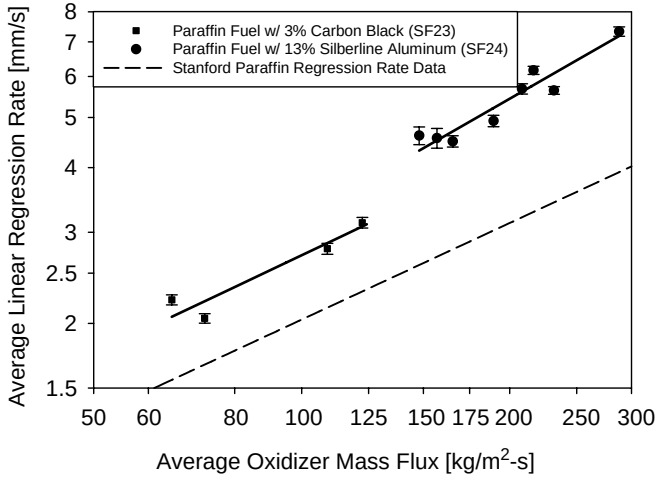

Fig. 8 Average regression rate data for paraffin-based solid-fuel formulations [56].

formulations: one with 3 wt % carbon black particles from PSU and the other with paraffin solid-fuel used by Karabeyoglu et al. [59] of Stanford University. The Stanford data curve fit has the same slope as the PSU data for non-aluminized paraffin fuel; however, the regression rates of the PSU data are higher due possibly to the difference in processing techniques and the slight difference in fuel formulations. The difference in surface energy release resulting from the amount and size of carbon black powder may significantly contribute to the measured differences in the regression rates.

It is immediately noticeable that there is a significant increase in the average regression rates of solid fuels containing nanosized aluminum flakes. When the curve fit for the 3 wt % carbon black baseline paraffin fuel formulation is extrapolated to the $G_{ox,av}$ value of 190 $kg/m^2 \cdot s$, an increase of $\sim$30% is seen for the formulations containing 13 wt % Silberline aluminum particles. An increase of about 60% is observed for the difference between the aluminized paraffin and the Stanford University curve-fit results. It is conjectured that, due to the Kelvin–Helmholtz type of surface instability wave (as determined by Oran and Boris [60]) formed on the molten-fuel layer on the free surface of the solid fuel, the aluminum particles are able to become encapsulated in the molten paraffin and leave the solid-fuel surface as droplets are stripped. This is in contrast to HTPB-based solid fuels containing similar aluminum particles in which the particles collected on the free surface until sufficient aerodynamic forces act on the particle agglomerates to entrain them in the flow. The resultant power-law curve-fit coefficients for all solid-fuel formulations are presented in Table 9. In Table 9 the coefficients provided are correlated with average oxidizer mass flux (G_{ox}) in kilograms per meter squared per second using the conventional power law for mass burning rate in kilograms per second and linear regression rate in millimeters per second as shown by

$$\dot{m}_b = A \cdot G_{ox,av}^n \tag{5}$$

$$r_b = B \cdot G_{ox,av}^m \tag{6}$$

The difference in regression and mass burning rates between fuel formulations containing different particles extends to the C^* combustion efficiency and I_{sp} efficiency as well. The efficiencies for HTPB-based solid-fuel formulations are presented in Table 10. Solid fuels containing Viton-A coated Alex (SF13) exhibited higher combustion efficiency than that of the uncoated (SF2). The fluorinated compound (Viton-A) is believed to facilitate in the ignition process and burned more efficiently than the uncoated particles. Solid fuel SF12 demonstrated a significantly lower C^* efficiency than that of SF13, showing the more complete combustion of the nanosized particles than the traditional micrometer-sized particles within the combustion chamber. The highest specific impulse efficiency also corresponds to SF13, with a maximum value of 86%. The specific impulse efficiencies of the micrometer-sized particle containing fuels were significantly lower, with a maximum value of 78%. It is evident from the reported data that the coating of aluminum particles with Viton-A leads to more complete combustion. C^* and I_{sp} efficiencies are consistently higher when a coating is applied.

The preceding results lead to the conclusion that the removal of the particles from the solid-fuel surface, ignition of the particles, and complete combustion of the particles in the near-surface region is highly dependent on the particle type.

Table 9 Power-law correlation parameters for linear-regression and mass-burning rates [48, 49, 57]

Solid fuel	Solid fuel additive	Mass-burning rate parameters		Linear-regression rate parameters	
		A, kg/s	n	B, mm/s	m
SF1	Pure HTPB	89.960×10^{-5}	0.627	0.05410	0.647
SF2	13% Alex	11.111×10^{-5}	1.171	0.01395	1.040
SF4	6.5%WARP-1	5.817×10^{-5}	1.200	0.00744	1.062
SF5	6.5%WARP-1 +13%B_4C	25.842×10^{-5}	0.954	0.04011	0.780
SF7	13%SILBAL	8.804×10^{-5}	1.155	0.0870	0.596
SF8	13%CLAL	20.267×10^{-5}	1.017	0.12038	0.549
SF9	13%WARP-1	3.676×10^{-3}	0.359	0.19220	0.396
SF11	13%TECHAL	6.911×10^{-5}	1.246	0.09159	0.599
SF12	13%Al325	2.164×10^{-5}	1.571	0.00444	1.318
SF13	13%C-Alex	22.896×10^{-5}	1.084	0.29384	0.412
SF15	13%AVAL	0.1287×10^{-5}	2.137	0.01250	1.048
SF16	13%IHD-AR	1.169×10^{-5}	1.584	0.03197	0.826
SF17	13%NTECH-80	6.694×10^{-5}	1.213	0.02568	0.848
SF18	13%NTECH-50	22.614×10^{-5}	0.986	0.05538	0.710
SF23	Paraffin with 3% carbon	1.436×10^{-3}	0.739	0.14630	0.634
SF24	Paraffin with 13% SILBAL	9.507×10^{-3}	0.554	0.09401	0.766
——	4%Alex	6.126×10^{-5}	1.171	0.01579	0.907
——	7%Alex	24.972×10^{-5}	0.886	0.03444	0.751
——	10%Alex	25.373×10^{-5}	0.900	0.04739	0.699
——	Pure HTPB with N_2O oxidizer	1.894×10^{-3}	0.322	0.02160	0.778
——	13% SILBAL with N_2O oxidizer	2.705×10^{-3}	0.292	0.05750	0.604

A variety of standard particle characterization techniques were applied to the 15 types of particles examined in the PSU study as displayed in Table 8. Trends in propulsive performance, that is, regression rate and mass burning rate, in general matched trends in particle characteristics, that is, active content and surface area, but there were some significant exceptions, such as Aveka's ultrafine aluminum particles. Results of the PSU study indicated that there is still much more to understand regarding the correlation between physical properties and the measured combustion performance [52].

Studies conducted in the XTC engine allowed the evaluation of the solid fuels characterized in the LGCP hybrid rocket motor under a different motor geometry. The effects of a modest scaling of geometric dimensions ($\sim$3:1 initial port diameter) were evaluated and showed a decrease in the average regression rate (Fig. 9) [57]. An average decrease was determined based on average oxidizer mass fluxes of 100, 200, and 300 kg/m$^2 \cdot$ s, showing a decrease of $\sim$13% for pure HTPB grains. The decrease in regression rate was attributed to the decrease in heat transfer due to the larger port diameter. When SF7 (HTPB containing 13 wt % SILBAL)

Table 10 C^* combustion efficiencies and I_{sp} efficiencies for HTPB-based solid fuels [48]

Solid fuel	Additive, by wt %	C^* combustion efficiency, %	I_{sp} efficiency, %
SF1	None	72–91	73–88
SF2	13%Alex	77–89	59–72
SF4	6.5%WARP-1	73–81	47–54
SF5	6.5% B_4C/ and 6.5%WARP-1	71–80	51–68
SF7	13%SILBAL	72–80	65–68
SF8	13%CLAL	83–85	61–64
SF9	13%WARP-1	69–89	81
SF11	13%TECHAL	81–94	70–80
SF12	13%Al-325	81–85	71–78
SF13	13%C-Alex	88–92	71–86
SF15	13%AVAL	87–98	75–82
SF16	13%IHD-AR	73–78	68–73
SF17	13%NTECH-80	80–90	74–77
SF18	13%NTECH-50	76–87	77–78

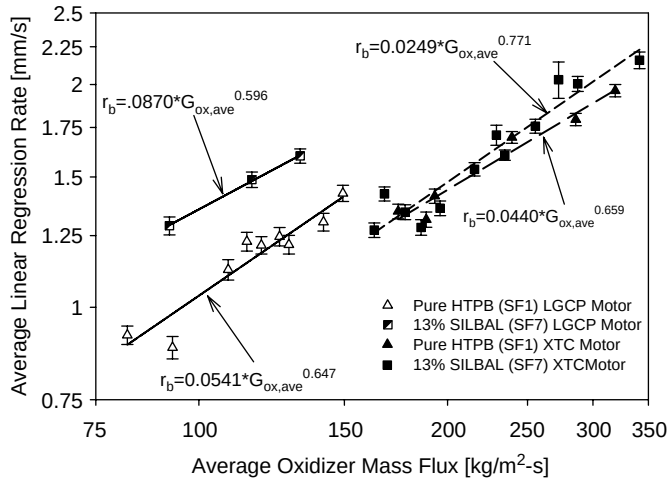

Fig. 9 Comparison of average regression rate data of pure HTPB fuel and metallized HTPB fuel containing 13 wt % Silberline® Al flakes obtained from XTC rocket motor [56, 57].

was evaluated in the XTC hybrid rocket engine, the measured regression rates lay almost on top of the curve for the baseline HTPB (SF1) also evaluated in the XTC motor, as seen in Fig. 9. Because SF7 demonstrated an ∼60% increase in regression rate in the smaller LGCP engine, besides the geometric scaling effect

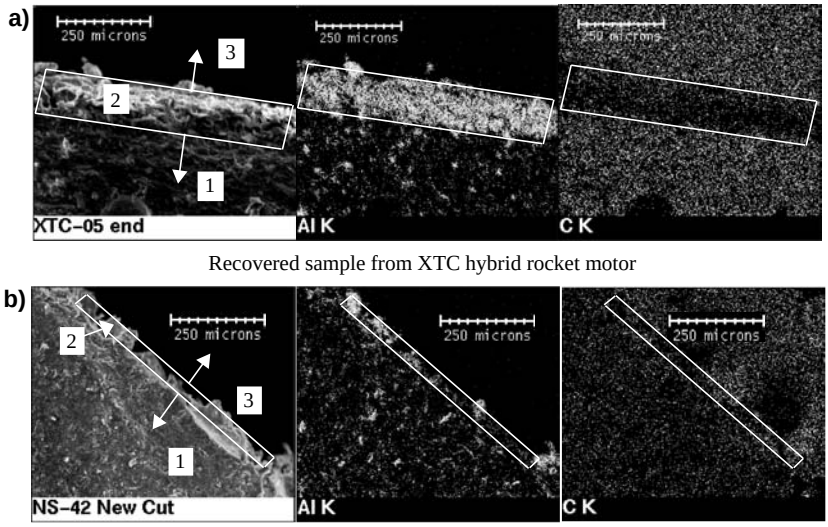

Fig. 10 Melt layer of typical HTPB-based solid fuel with Silberline Al flakes: 1) chemically undisturbed solid-fuel region, 2) melt-layer region, and 3) boundary-layer region [57].

there must be other physical or chemical mechanisms causing this drastic reduction in burning rate. It was speculated that the geometry of the aluminum flakes inhibits the efficient removal of particles from the solid-fuel surface. Particles with different morphologies can help to alleviate this problem.

Utilizing scanning electron microscopy (SEM) in combination with energy dispersive x-ray spectroscopy (EDS), the fuel surface behavior for SF7 was analyzed for recovered grains from both engines. Figure 10 shows the SEM micrographs (lower right) and the elemental maps for aluminum (lower left), carbon (upper left), and oxygen (upper right) for tests conducted in the XTC (Fig. 10a) and LGCP engines (Fig. 10b). From the SEM/EDS figures, the approximate melt-layer thickness of the XTC sample is 110 μm. The corresponding melt-layer thickness of the recovered sample from the LGCP motor is approximately 30 μm. The XTC test also contained a 25-μm thermocouple embedded in the fuel grain to measure the thermal wave profile and surface temperature during the test firing. The resultant temperature–time trace obtained is shown in Fig. 11 with the coordinate axis transformed to the distance from the burning surface by the average regression rate data, where $x = 0$ is defined as the fuel surface. The three regions corresponding to the SEM/EDS photographs are shown in Fig. 11. The thickness of the plateau region corresponds very closely to the observed melt-layer thickness from the SEM/EDS analysis. The ineffective particle removal from the surface does not allow the particles to release their energy in an efficient manner.

A common observation in XTC tests conducted with SF7 is the occurrence of a bump in the pressure–time trace that can last from 1 to 3 s, depending on the engine operating conditions. In long-duration tests, two bumps have been observed,

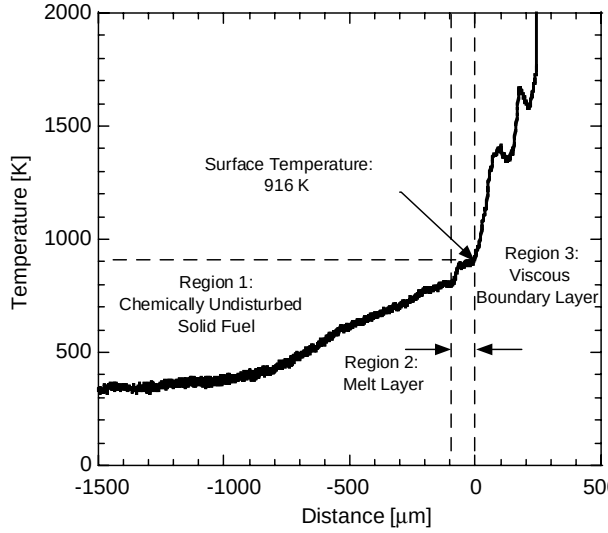

Fig. 11 Temperature–time trace measured by 25-mm thermocouple cast in solid-fuel grain of test XTC-05-SILBAL-13 with observed melt layer [56].

though the second is not nearly as strong as the first. When the spectrogram of the pressure signal is analyzed, a low-frequency oscillation centered on approximately 40 Hz (±5–10 Hz is common though) is observed at the same time. It is hypothesized that the pressure oscillation observed corresponds to the thick, highly aluminized melt layer on the surface, which can be detached from the fuel surface and enter the combustion zone as a relatively large piece. This can also explain the lack of regression rate increase observed in these solid-fuel formulations because the large highly aluminized pieces are not efficiently burnt in the combustion chamber.

With use of a real-time X-ray radiography system coupled with an X-ray transparent chamber casing, instantaneous regression rate data were also measured in the XTC engine allowing the determination of burning behavior over the duration of a combustion event. Traditionally, the average regression rate behavior has been shown to correlate well with the average oxidizer mass flux in a power-law nature if the chamber pressure is maintained in the appropriate range. The instantaneous regression behavior was deduced for both HTPB-based and paraffin-based solid fuels containing 13 wt % Silberline® aluminum. The instantaneous oxidizer mass flux was then determined from the measured oxidizer mass flow rate and the instantaneous port diameter. Figure 12 shows two different tests for each fuel formulation operated at different initial oxidizer mass fluxes. As is seen, the instantaneous regression rate does not correlate in a power-law nature with the instantaneous oxidizer mass flux because the data on the log–log plot in Fig. 12 do not follow a straight-line relationship. Consideration was also paid to the correlation with instantaneous total mass flux, showing similar lack of correlation to a power-law description.

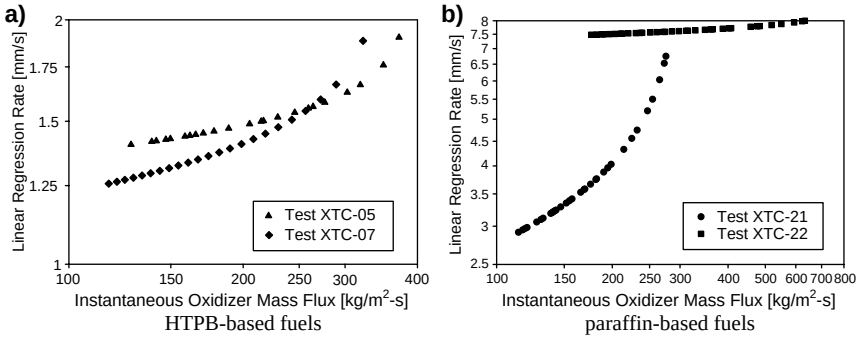

Fig. 12 Dependency of instantaneous regression rate of aluminized fuels on instantaneous oxidizer mass flux [56].

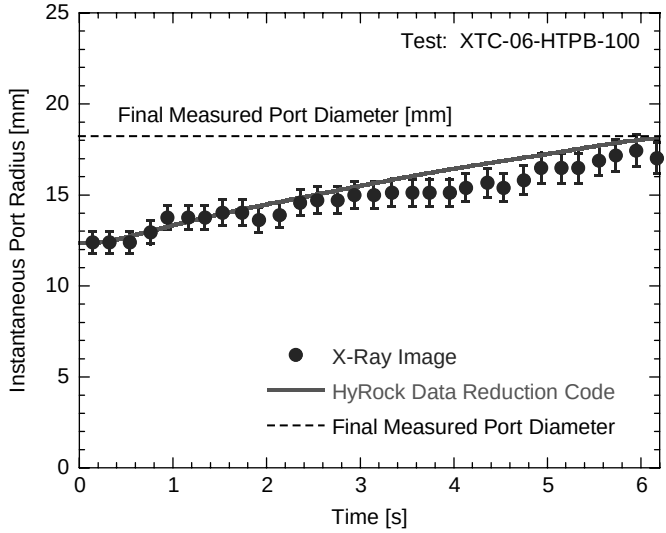

Fig. 13 Comparison of instantaneous port radius between X-ray movie and calculated results from data reduction code [48].

For a baseline solid fuel (SF1) case, the instantaneous regression rates obtained from the X-ray movie were compared to the instantaneous regression rate results obtained from the HyRock data reduction code [48] for validation. The superimposed results are shown in Fig. 13. The X-ray image data agreed very well with the HyRock code results for each axial location. The dashed line in Fig. 13 represents the measured final diameter of the solid-fuel grain, which also agreed well with both the X-ray image data and the HyRock code results.

C. Boron-Based Particles Additives in Solid Fuels

The other major category of particle additive that has been investigated by researchers is boron-based particles. These include a high-purity boron, whether coated or uncoated, and boron carbide. Both particles types have been given significant attention due to the very high gravimetric heat of oxidation of boron (58.7 kJ/gm). The major issue to be resolved with boron is inability to ignite and fully combust the particles within the rocket engine. This leads to poor combustion efficiencies that draw from the propulsive performance of the system. Many studies have been conducted in this area; several selected cases are reviewed here. The combustion of boron has also been the subject of great focus for the application to solid-fuel ramjet systems. Similarities between hybrid rocket engines and solid-fuel ramjets allow for the extension of results from either field to be applied qualitatively to the other.

As another portion of the U.S. Air Force sponsored study [36], researchers at UTC investigated the use of boron as a solid-fuel additive as well. As already mentioned, the addition of AP was considered in many of the fuel-rich propellant formulations considered, but these cases are excluded here because the grains are essentially solid propellant rather than solid fuel. In total, seven hybrid rocket engine firings were conducted in their 3.5-in.- (8.89-cm-) diam evaluation engine without AP content. The binder used was either R-45 or 3812 QX, depending on the formulation. Six fuel-propellant combinations were evaluated and are presented along with measured regression rates in Table 11. As in the case of the aluminized solid-fuel tests, no data regarding the initial or final port diameters were provided; thus, no explicit relationship between oxidizer mass flux and regression rate can be presented. Again, the test durations are also included so that an educated guess of the average oxidizer mass flux can be made, assuming that the initial port diameters are the same between grains evaluated in the same engine.

The use of boron and boron carbide containing solid-fuel formulations for SFRJ application has been studied extensively at the Israel Institute of Technology [61–64]. As mentioned earlier, the complete combustion of boron or boron-carbide-containing solid fuels is a continuing problem associated with SFRJ applications. The use of aft burners where bypass air is mixed with the partially reacted fuel/air mixture is one means of increasing the propulsive efficiency. The other means of increasing the efficiency considered is the application of a coating such as Mg, Ti, or fluorocarbons to help in the ignition process. Through the use of a two-dimensional slab motor with a high-speed camera, the regression behavior of B_4C/Mg-containing fuels was captured [61]. Two fuel-grain configurations were considered: 1) A small piece of metallized fuel was imbedded in a grain of nonmetallized PMMA fuel and 2) the entire slab was metallized. Visually acquired information relating to the ejection of mass from the surface was similar between the two fuel configurations. The ejection of mass from the surface was observed to occur predominantly through two means. The first is the ejection of a nonburning fuel piece. A relatively large mass is removed from the surface and travels at a low trajectory, which was usually below the diffusion flame layer. This form of mass removal appeared to be the result of local breaking between the surface layer and the subsurface layer. The second form of ejection is the periodic burst of particles into the flowfield, which occurs at locations where glowing was observed

Table 11 Boron-containing solid-fuel combustion results of UTC [36]

Fuel composition	Oxidizer composition	Chamber pressure, psia	Oxidizer flow rate, lbm/s	Average regression rate, in./s	Burn time, s	Motor diameter, in.
50%R-45/ 50% B	ClF_3	490.0	0.29	0.019	9.70	3.5
55% R-45/ 27% B/ 18% TFTA	ClF_3	1175.0	0.30	——	0.90	3.5
50% QX/ 20% B/ 30% TFTA	75% ClF_5/ 25% ClO_3F	220.0	1.28	0.012	13.95	3.5
50% QX/ 20% B/ 30% TFTA	75% ClF_5/ 25% ClO_3F	270.0	0.66	0.011	12.60	3.5
46.89% QX/ 22.60% B/ 30.51% TFTA	75% ClF_5/ 25% ClO_3F	275.0	0.66	0.011	15.77	3.5
44.99% QX/ 18.34% B/ 36.67% TFTA	75% ClF_5/ 25% ClO_3F	295.0	0.66	0.014	12.75	3.5
35% QX/ 20% B/ 45% TFTA	75% ClF_5/ 25% ClO_3F	600.0	0.30	——	10.50	3.5

before the ejection. It was postulated that local impingement of oxidizer from the freestream due to large-eddy mixing led to reaction at the surface layer. The evolved gases due to degradation of the bulk material would lead to local pressure buildup and eject the particles in many directions. The relatively high speed of particle ejection, on the order of meters per second, can introduce the particles into high-oxygen-concentration regions while they are still quite hot helping the ignition and combustion process. These two mass removal processes were initially demonstrated for B_4C in an HTPB binder, but were later shown to be relatively independent of the binder, oxidizer, or catalysts added [62].

Further study of these findings showed the usefulness of using a bypass air system for the combustion of boron or boron-carbide particles in a more efficient manner [63, 64]. Without use of bypass air, the ignition and combustion of boron or boron carbide in an SFRJ is highly dependent on the ejection velocity and trajectory from the fuel surface. As shown by Gany and Netzer [61], the ejection of particles from the surface is somewhat random and unpredictable. If the particles take a long time to ignite, the available oxidizer species in the bypass air and subsequent reaction chamber allow for more complete combustion of the particles, thus releasing more of the chemical energy.

Work at the Naval Postgraduate School by Natan and Netzer [65] and Nabity et al. [66] considered solid-fuel formulations containing high concentrations of boron-carbide particles. The effect of the bypass air split ratio, grain length, and air flux levels on combustion efficiency have all been investigated. A 2.5-in.- (64-mm-) coaxial dump, axisymmetric motor was employed in the studies to evaluate the effects individually. The metallized-fuel grains consisted of 50% B_4C/5% Mg/45% HTPB. A reaction vessel was provided at the aft end region of the fuel grain allowing mixing of the bypass air with the partially burned products. Another test configuration used a windowed section in place of the bypass air inlet. This test rig setup was used in the evaluation of equivalence ratio (through variation of grain length) and inlet airflow conditions. A particle analyzer was positioned at the aft end section of the fuel grain to analyze the effect of the various parameters on the particle size distribution. Increasing the grain length, and thus increasing the equivalence ratio, showed a wider distribution of particle sizes. This was attributed to the increased recirculation zone that was present from the shorter grains. The length of the diffusion flame in the shear layer was also shorter in these cases, resulting in less chance of particle ignition. The variation of the air mass flow rate resulted in a decrease in the combustion efficiency. The diffusion flame moves closer to the surface of the fuel grain as the air flux is increased, thus reducing the chance of particles being ejected from the surface at the proper velocity to ignite within the diffusion flame. The effect of the bypass air was evaluated from 0 to 42% of the total flow rate. The efficiency consistently increased from 36 to 85% over the range of bypass split ratios considered.

As part of the hybrid rocket solid-fuel formulation studies conducted at PSU, boron and boron-carbide-containing solid-fuel formulations were also evaluated [48, 51, 53]. In total, seven different boron or boron-carbide-containing fuel formulations were evaluated in the LGCP engine and showed varying results. The measured regression rate behavior as a function of the average oxidizer mass flux is presented in Fig. 14. With the exception of the catalyzed B_4C, all fuel formulations demonstrate a higher linear regression rate at all oxidizer mass fluxes considered.

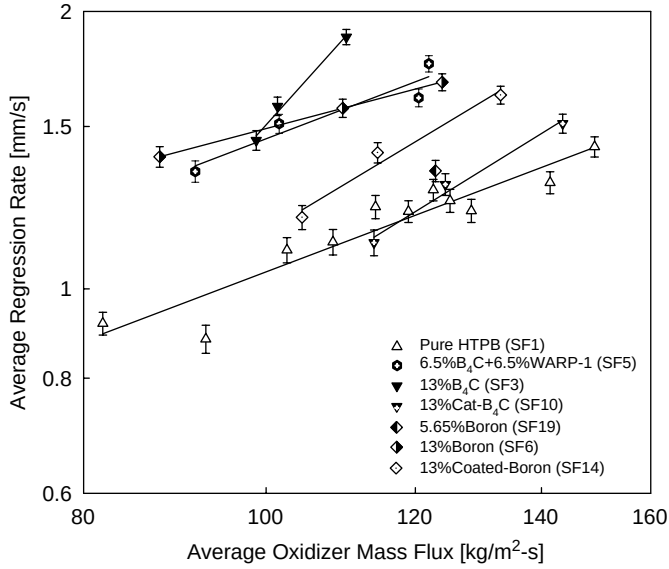

Fig. 14 Comparison of boron and B_4C containing solid-fuel regression rates [48].

The largest increase in regression rate measured was for fuel-type SF3, which contained 13% B_4C particles, with an increase of 108% when considering an average oxidizer mass flux of 112 $kg/m^2 \cdot s$. The resulting power-law curve-fit parameters for the presented fuel formulations are given in Table 12.

Differences in the regression and mass burning rates are also observed in the combustion and specific impulse efficiencies. The efficiency data measured are

Table 12 Mass burning rate and linear-regression rate power-law curve-fit parameters [48]

Solid fuel	Solid fuel additive	Mass-burning rate parameters		Linear regressions-rate parameters	
		A, kg/s	n	B, mm/s	m
SF1	Pure HTPB	89.960×10^{-5}	0.627	0.0541	0.647
SF3	13%B_4C	3.663×10^{-9}	3.413	4.286×10^{-5}	2.273
SF5	6.5%B_4C/ and 6.5%WARP-1	25.482×10^{-5}	0.954	0.04011	0.780
SF6	13%Boron	14.528×10^{-5}	1.090	0.12381	0.541
SF10	13%Cat-B_4C	0.1252×10^{-5}	1.999	0.00282	1.266
SF14	13%C-Boron	4.344×10^{-7}	2.271	0.00401	1.230

Table 13 C^* and I_{sp} efficiency results of boron and boron-carbide-containing fuels [48]

Solid fuel	Additive, by wt %	C^* combustion efficiency, %	I_{sp} efficiency, %
SF1	None	72–91	72–88
SF3	13%B_4C	60–81	50–84
SF5	6.5%B_4C/ and 6.5%WARP-1	71–80	51–68
SF6	13%BORON	78–81	63–69
SF10	13%Cat-B_4C	76–82	64–71
SF14	13%C-Boron	76–81	69–76
SF19	5.65%Boron	83	83

presented in Table 13 along with the baseline pure HTPB-fuel formulation. The values of both the C^* and I_{sp} efficiencies are lower than those that were observed for aluminized solid-fuel formulations, which are consistent with the findings presented earlier for other boron-based particle-containing solid fuels. Specific impulse efficiency values reveal that significant losses are occurring, presumed to be the result of unburned particles leaving the nozzle and two-phase flow losses. Fuel formulation SF19, presented in Table 13, contains only 5.65% by weight of boron particles, but contains a molar equivalent of 13 wt % aluminum. The higher measured C^* and I_{sp} efficiencies for this fuel show that boron burns more effectively in lower weight concentrations in the LGCP hybrid rocket engine.

III. Gas Generator and Specialized Solid Fuels

In a classical hybrid rocket configuration, liquid oxidizer is injected at the head end of the motor and flows through ports in a solid-fuel grain. Heat feedback to the solid-fuel grain from diffusion flames causes fuel regression. Some packaging and efficiency improvements may be realized if the combustion is staged, using a gas generator as part of the system, combined with a secondary combustion chamber. This may be implemented in a variety of ways. One of the most common designs is to mix a limited percentage of solid oxidizer into the fuel grain, generating fuel-rich gas when burned. Additional gaseous or liquid oxidizer can be injected either upstream to flow through ports in the gas generator, or downstream in a secondary combustion chamber. Another method is to generate a partially reacted oxidizer-rich hot gas to flow through a solid-fuel grain. This technique was used in NASA's Peroxide Hybrid Upper Stage (PHUS) Program [67]. Other novel designs including oxidizer flow through a fluidized bed containing a large number of small fuel grains or pellets to generate fuel-rich gas can also be envisioned [68, 69]. Although these concepts appear to contravene the basic hybrid rocket concept of physical separation of fuel and oxidizer for safety, in some cases it can be advantageous for the propulsion system to adopt these novel designs.

In many ways, a gas generator hybrid rocket can be considered to be similar to a SFRJ or ducted rocket, differing only in the source of oxidizer. Much of the research and literature available on SFRJ systems may provide insight to the design and operation of gas generator hybrid systems and some were discussed in

the preceding section. However, in the interests of brevity and clarity, the scope of the discussion here is limited to self-contained rocket systems only.

Perhaps the simplest design is to use a fuel-rich solid-propellant grain with either forward or aft injection of oxidizer. This design offers some advantages over a conventional arrangement, such as lower flame temperature, simpler grain geometry for higher regression rates [70] (and, hence, higher thrust), and greater throttling ratios (thrust ratios up to 20:1) [71].

Because the fuel-rich solid propellant does not have to be optimized for single-component performance, a wide variety of solid oxidizers and fuel formulations can be considered, including the ubiquitous AP and HTPB. Other oxidizers such as ammonium nitrate [72], triaminoguanidine nitrate (TAGN) [73], or nitramines [74] have also been studied. Energetic polymers such as GAP are also well suited for use in a fuel-rich solid propellant.

Similarly, many different oxidizers can be considered in a system design. The use of dense liquid oxidizers such as HAN solution (90% in H_2O) [75] or white fuming nitric acid [76] with an AP/HTPB grain have been demonstrated at laboratory scale.

Possibly the largest scale demonstration of the gas generator hybrid concept was NASA's PHUS project. This project used a catalyzed 90% hydrogen peroxide gas generator system with aft end injection. There were 11- and 24-in. motors tested using a fuel formulation made up of 60% AP in a matrix of HTPB, polyether (PPG) or a mixture of the two [77]. Although containing oxidizer, the fuel-rich propellant mixture hazard was evaluated as Department of Transportation (DOT) class 1.4C, retaining the inherent inertness of a solid-fuel grain. The 10,000-lbf (44,500-N) thrust motors were designed to operate at 200 psia (1.38 MPa) with a vacuum specific impulse greater than 310 s. Test results showed that the larger diameter motor generally performed better than the smaller one, with very stable operation ($+/-$ 1% pressure variation) and high combustion efficiency ($>$98%). Regression rates of about 0.06 in./s (1.5 mm/s) were observed at 200 psi (1.38 MPa) with a pressure exponent of 0.3 for the fuel-rich solid propellant using a mixture of HTPB and PPG binders. Burning rate and combustion stability of the fuel-rich solid propellant were found to be sensitive to AP particle size and L^* at very low oxidizer flow rates [78].

IV. Environmental Aspects

Although not directly impacting propulsion system performance, environmental aspects must be considered in light of regulatory requirements and secondary consequences of both production and operation. In the evaluatation of the environmental impacts of a potential launch system, the responsible U.S. government agency [Office of the Associate Administrator for Commercial Space Transportation (AST)] considers three categories: atmospheric, noise, and other impacts. Atmospheric impacts can include degradation of air quality, acid rain, ozone depletion, and global warming. Noise is judged by the effect of acoustic energy on humans, animals, and structure, whereas the final category encompasses effects on water, land, and biological systems [79]. Atmospheric or other effects can also be generated during the manufacturing process.

Table 14 Typical exhaust products from different propulsion systems [78]

Solid propellant	Liquid hydrocarbon	Hypergolic propellant	Cryogenic (LOX/LH2)	Hybrid
HCl	CO_2	CO_2	H_2O	CO
Al_2O_3	CO	CO	H_2	CO_2
CO	H_2	NO_x		H_2
N_2	H_2O	N_2		NO_x
CO_2	OH^-	H_2O		H_2O
NO_x	NO_x	H_2		OH
Cl^-				
H_2O				

Environmental impact on the atmosphere by a propulsion system can be evaluated by the exhaust products released during operation. Typical product species of either high concentration or high environmental impact generated by different types of propulsion systems are shown in Table 14.

In the troposphere, the most environmentally significant species are HCl, Al_2O_3, NO_x, and CO_2 [79]. Here, hybrids have an obvious advantage over traditional solid boosters, due to the lack of chlorine released from AP oxidizer. The amount of alumina or other metal oxide released may be comparable or less, depending on the type and fraction of additive to the solid fuel. Although highly desirable from an energetic standpoint, the use of beryllium is obviously ruled out for any terrestrial-based system because of the high toxicity of the oxide [80]. NO_x levels also vary with the fuel and oxidizer choice; the use of N_2O oxidizer can be expected to generate significantly more NO_x than that from the use of LOX.

Stratospheric impact is from potential climate disruption, that is, greenhouse gas effect trapping heat in the atmosphere, and depletion of the ozone layer. Combustion products that are either direct or indirect contributors to the greenhouse effect include CO, CO_2, H_2O, and NO_x [79]. Because fuels used for solid-propellant binders, many liquid engines, and hybrids are hydrocarbon based, direct comparisons between the systems are not possible; instead the type and total mass of propellants need to be evaluated. Ozone depletion is mainly caused by the photochemical reactions with chlorine-containing compounds, and so here hybrid rockets have a significant advantage over conventional solid-propellant systems. In both cases, the overall effect of emissions from rocket engines is nearly insignificant compared to industrial sources [79]. Higher altitude (mesosphere and ionosphere) effects are currently not well understood, but no significant long-term effect is expected [79].

Because most noise from a rocket is generated by the interaction of the supersonic exhaust jet with the surrounding atmosphere, it should scale most closely with motor or engine size and thrust and be less dependent on the type of system generating the thrust. Other factors affecting the noise impact of a launch system, such as trajectory, are also not directly related to the propellant and propulsion system choice.

Environmental effects on water, land, and biological systems can be considered mainly from the dispersal of the ground cloud formed during launch or

from propellant scattered in an accident [79]. Hybrid propellants currently being considered contain no chlorine compounds that either release HCl during normal operation or can leach into the local water in the case of an explosion. In fact, most hybrid propellants and additives are essentially nontoxic, resulting in minimal local environmental impact in the case of an accident. The physical separation of fuel and oxidizer also serves to reduce the probability of an accident generating propellant release.

Hybrid rockets are generally considered green [81]. Although very few vehicles have been launched using hybrid rocket propulsion at the time of publication, the available regulatory documents support this view. The environmental assessment for operation of Scaled Composites' SpaceShipOne during its test and Ansari X Prize flights resulted in a "Finding of No Significant Impact" [82], and one for test firing a 250,000-lb thrust motor at NASA Stennis Space Center (SSC) concluded the temporary releases of CO_2, CO, and NO_x would "not affect the local community and [would] have minimal impact at the SSC site" [83].

V. Summary and Conclusions

The inherent safety of hybrid rocket technology is predominately due to the fact that the solid fuel grain is usually inert. However, solid fuel inertness adversely affects propulsive performance, which requires further investigation and mitigation of inferior burning rates of solid fuels compared to solid propellants. Solid-fuel grains are much more ductile than solid-propellant grains and, thus, are less likely to be damaged, therefore, significantly lowering the probability of catastrophic motor failure, which is the highest priority for manned space missions. The exhaust products are much more environmentally friendly than the toxic exhaust of solid-propellant rockets, which produce chemicals such as chlorine. Propulsive performance of hybrid rocket engines and SFRJs reverts back to the characteristics of the solid fuel itself. Polymeric fuel thermal degradation, also known as the fuel-surface regression rate of the inert solid fuel, is considered to be one of the key processes during combustion in these systems. The regression behavior of a solid fuel is strongly affected by the operating conditions and the composition and thermophysical properties of the solid fuel.

In the past, regression rates of conventional solid fuels, for example, HTPB, have typically been an order of magnitude lower than solid propellants, thus, requiring a relatively large fuel-surface area to produce a given thrust level. Interest in metal combustion was first stimulated in solid propellants in the mid-1950s, when it was found that the addition of aluminum particles substantially increased propellant performance. The attractiveness of metals is that while still being a fuel, when integrated in to the solid fuel they provide high heats of combustion, good physical properties, for example, increased solid-fuel density, and increased flame temperature, thereby increasing specific impulse and energy release. Moreover, as ingredients, metals are easily mixed in the polymeric resin because they are usually in powdered form and are processed like other granular ingredients into the solid fuel. Common metals used in these systems are aluminum (most popular), magnesium, boron, and zirconium.

Although a serious effort has been made to formulate metallized solid fuels for use in propulsion systems, the Sandpiper target missile and the Lockheed

Martin/NASA-developed sounding rocket are the only flight vehicles that have utilized metallized solid-fuel formulations. Thus, research of metallized solid fuels has since been completed predominantly at a laboratory scale. In most of the investigations, three of the classical fuels, lithium, aluminum, and boron, have been studied by researchers throughout the world: Lithium, being highly reactive, possesses a relatively low heat of combustion compared to other classical fuels; aluminum, having both a high heat of combustion and being easily ignitable, carries an inert oxide shell that has to be removed for continued oxidation; and boron has very high heat of combustion but major difficulty in ignition. It has been demonstrated that the inclusion of the metal particles in the solid-fuel grain whether nano- or micrometer-sized enhances the linear and mass burning rate of the solid fuel. With the recent advances in energetic particles, it is believed that metallized solid fuels can decrease the performance gap between solid propellants and solid fuels, while maintaining solid fuel's inherent safety and inertness.

References

[1] De Wilde, J., "A Fuel Pyrolysis Model for Combustion Calculations," AIAA Paper 91-1868, 27th AIAA/SAE/ASME/ASEE Joint Propulsion Conference, Sacramento, CA, June 1991.

[2] Hybrid Steering Committee, "Hybrid Rocket Propulsion: Report of an AIAA Workshop," Washington, DC, July 1995.

[3] Knuth, W. H., Chiaverini, M. J., Gramer, D. J., and Sauer, J. A., "Experimental Investigation of a Vortex-Driven High-Regression Rate Hybrid Rocket Engine," AIAA Paper 98-3348, 34th AIAA/ASME/SAE/ASEE Joint Propulsion Conference, Cleveland, OH, July 1998.

[4] Kuo, K. K., "Importance and Challenges of Hybrid Rocket Propulsion Beyond Year 2000," Invited von Kármán Lecture *Proceedings of the 37th Israel Annual Conference on Aerospace Sciences*, 1997, pp. II-1–II-31.

[5] Grassie, N., *Chemistry of High Polymer Degradation Processes*, Interscience, New York, 1956.

[6] McAlevy, R. F., III, and Hansel, J. G., "Linear Pyrolysis of Thermoplastics in Chemically Reactive Environments," *AIAA Journal*, Vol. 3, No. 2, 1965, pp. 244–249.

[7] Hansel, J. G., and McAlevy, R. F., III, "Energetics and Chemical Kinetics of Polystyrene Surface Degradation in Inert and Chemically Reactive Environments," *AIAA Journal*, Vol. 4, No. 5, 1966, pp. 841–848.

[8] Cheng, J. T., Ryan, N. W., and Baer, A. D., "Oxidative Decomposition of PBAA Polymer at High Heating Rates," *Twelfth Symposium (International) on Combustion*, Combustion Inst., Pittsburgh, PA 1969, pp. 525–532.

[9] Bouck, L. S., Baer, A. D., and Ryan, N. W., "Pyrolysis and Oxidation of Polymers at High Heating Rates," *Fourteenth Symposium (International) on Combustion*, Combustion Inst., Pittsburgh, PA, 1973, pp. 1165–1176.

[10] Thomas, T. J., and Krishnamurthy, V. N., "Thermogravimetric and Mass-Spectrometric Study of the Thermal Decomposition of PBCT Resins," *Journal of Applied Polymer Science*, Vol. 24, No. 8, 1979, pp. 1797–1808.

[11] Ninan, K. N., Krishnan, K., Rajeev, R., and Viswanathan, G., "Thermoanalytical Investigations on the Effect of Atmospheric Oxygen on HTPB Resin," *Propellants, Explosives, Pyrotechnics*, Vol. 21, No. 4, 1996, pp. 199–202.

[12] Chen, J. K., and Brill, T. B., "Chemistry and Kinetics of Hydroxyl-Terminated Polybutadiene (HTPB) and Diisocynate-HTPB Polymers During Slow Decomposition and Combustion-like Conditions," *Journal of Combustion and Flame*, Vol. 87, Nos. 3–4, 1991, pp. 217–232.

[13] Marxman, G. A., and Gilbert, M., "Turbulent Boundary Layer Combustion in the Hybrid Rocket," *Ninth Symposium (International) on Combustion*, Combustion Inst., Pittsburgh, PA, 1963, pp. 371–383.

[14] Marxman, G. A., Wooldrige, C. E., and Muzzy, R. J., "Fundamentals of Hybrid Boundary-Layer Combustion," *Heterogeneous Combustion*, edited by H. G. Wolfhord, I. Glassman, and L. Green, J., Vol. 15, Progress in Astronautics and Aeronautics, Academic Press, New York, 1964, pp. 485–522.

[15] Marxman, G. A., "Combustion in the Turbulent Boundary Layer on a Vaporizing Surface," *Tenth Symposium (International) on Combustion*, Combustion Inst., Pittsburgh, PA, 1965, pp. 1337–1349.

[16] Cohen, N. S., Fleming, R. W., and Derr, R. L., "Role of Binders in Solid Propellant Combustion," *AIAA Journal*, Vol. 12, No. 2, 1974, pp. 212–218.

[17] Kishore, K., "Comprehensive View of the Combustion Models of Composite Solid Propellants," *AIAA Journal*, Vol. 17, No. 11, 1979, pp. 1216–1224.

[18] Beck, W. H., "Pyrolysis Studies of Polymeric Materials Used as Binders in Composite Propellants: A Review," *Combustion and Flame*, Vol. 70, No. 2, 1987, pp. 171–190.

[19] Fong, C. W., and Hamshere, B. L., "The Mechanism of Burning Rate Catalysis in Composite HTPB–AP Propellant Combustion," *Combustion and Flame*, Vol. 65, No. 1, 1986, pp. 61–69.

[20] Altman, D., "Hybrid Rocket Development History," AIAA Paper 91-2515, 27th AIAA/ASME/SAE/ASEE Joint Propulsion Conference, Sacramento, CA, June 1991.

[21] Schultz, R. D., and Dekker, A. O., "The Absolute Thermal Decomposition Rates of Solids–Part 1. The Hot-Plate Pyrolysis of Ammonium Chloride and the Hot-Wire Pyrolysis of Polymethylmethacrylate (Plexiglas 1A)," *Fifth Symposium (International) on Combustion*, Combustion Inst., Pittsburgh, PA, 1955, pp. 260–267.

[22] Chaiken, R. F., Andersen, W. H., Barsh, M. K., Mishuk, G. M., and Schultz, R. D., "Kinetics of the Surface Degradation of Polymethylmethacrylate," *Journal of Chemical Physics*, Vol. 32, No. 1, 1960, pp. 141–146.

[23] David, L., "Space ShipOne Wins $10 Million Ansari X Prize in Historic 2nd Trip to Space," <http://www.space.com/missionlaunches/xprize2_success_041004.html> [retrieved 1 Dec. 2006].

[24] Melcher, J. C., Burton, R. L., and Krier, H., "Combustion of Aluminum Particles in Solid-Rocket Motor Flows," *Solid Propellant Chemistry, Combustion, and Motor Interior Ballistics,* edited by V. Yang, T. B. Brill, and W.-Z. Ren, Progress in Astronautics and Aeronautics, Vol. 185, AIAA, Reston, VA, 2000, pp. 723–747.

[25] Glassman, I., *Combustion*, 3rd ed., Academic Press, San Diego, CA, 1996.

[26] Bucher, P., Ernst, L., Dryer, F. L., Yetter, R. A., Parr, T. P., and Hanson-Parr, D. M., "Detailed Studies of the Flame Structure of Aluminum Particle Combustion," *Solid Propellant Chemistry, Combustion, and Motor Interior Ballistics,* edited by V. Yang, T. B. Brill, and W.-Z. Ren, Progress in Astronautics and Aeronautics, Vol. 185, AIAA, Reston, VA, 2000, pp. 689–722.

[27] Price, E. W. and Sigman, R. K., "Combustion of Aluminized Solid Propellants," *Solid Propellant Chemistry, Combustion, and Motor Interior Ballistics,* V. Yang, T. B. Brill,

and W.-Z. Ren, Progress in Astronautics and Aeronautics, Vol. 185, AIAA, Reston VA, 2000, pp. 663–687.

[28] Price, E. W., "Combustion of Metallized Propellants," *Fundamentals of Solid Propellant Combustion*, edited by Kuo, K. K. and Summerfield, M., Progress in Astronautics and Aeronautics, Vol. 90, AIAA, New York, 1984, pp. 479–513.

[29] Mead, Jr., F. B., "Early Developments in Hybrid Propulsion Technology at the Air Force Rocket Propulsion Laboratory," AIAA Paper 95-2946, 31st AIAA/ASME/SAE/ASEE Joint Propulsion Conference, San Diego, CA, July 1995.

[30] Wright, A. M., Dunn, L., Alford, B., and Patton, J., "A Thrust and Impulse Study of Guanidinium Azo-Tetrazolate as an Additive for Hybrid Rocket Fuel," AIAA Paper 99-2538, 39th AIAA/ASME/SAE/ASEE Joint Propulsion Conference, Los Angeles, CA, June 1999.

[31] "HyperTEK Hybrid Rocket Propulsion Systems," <http://www.hypertekhybrids.com/manual.pdf> [retrieved 1 Dec. 2006].

[32] "Contrail Rockets Product 2," <http://contrailrockets.com/Products/prod02.htm> [retrieved 1 Dec. 2006].

[33] Arves, J., Gnau, M., Joiner, K., Kearney D., McNeal, C., and Murbach, M., "Overview of The Hybrid Sounding Rocket (HYSR) Project," AIAA Paper 2003-5199, 39th AIAA/ASME/SAE/ASEE Joint Propulsion Conference, Huntsville, AL, July 2003.

[34] Smoot, L. D., and Price, C. F., "Regression Rates of Metalized Hybrid Fuel Systems," *AIAA Journal*, Vol. 4, No. 5, 1966, pp. 910–915.

[35] Osmon, R. V., "An Experimental Investigation of a Lithium Aluminum Hydride–Hydrogen Peroxide Hybrid Rocket in *Aerospace Chemical Engineering*," edited by D. J. Simkin, Chemical Engineering Progress Symposium Series, Vol. 62, No. 21, American Institute of Chemical Engineers, New York, NY, 1966, pp. 92–102.

[36] Vickland, C. W., *Experimental Investigation of Prepackaged Hybrid Propulsion Systems*, United Technology Center, Interim Rep. AFRPL-TR-66-268, Sunnyvale, CA, 1 March 1967.

[37] Lips, H. R., "Metal Combustion in High Performance Hybrid Rocket Propulsion Systems," AIAA Paper 76-640, 12th AIAA and SAE Propulsion Conference, Palo Alto, CA, July 1976.

[38] Lips, H. R., "Heterogeneous Combustion of Highly Aluminized Hybrid Fuels," *AIAA Journal*, Vol. 15, No. 6, 1977, pp. 777–778.

[39] Lips, H. R., "Experimental Investigation on Hybrid Rocket Engines Using Highly Aluminized Fuels," *Journal of Spacecraft*, Vol. 14, No. 9, 1977, pp. 539–545.

[40] Strand, L. D., Ray, R. L., Anderson, F. A., and Cohen, N. S., "Hybrid Rocket Fuel Combustion and Regression Rate Study," AIAA Paper 92-3302, 28th AIAA/ASME/SAE/ASEE Joint Propulsion Conference, Nashville, TN, July 1992.

[41] Strand, L. D., Ray, R. L., and Cohen, N. S., "Hybrid Rocket Combustion Study," AIAA Paper 93-2412, 29th AIAA/ASME/SAE/ASEE Joint Propulsion Conference, Monterey, CA, June 1993.

[42] Strand, L. D., Jones, M. D., Ray, R. L., and Cohen, N. S., "Characterization of Hybrid Rocket Internal Heat Flux and HTPB Fuel Pyrolysis," AIAA Paper 94-2876, 30th AIAA/ASME/SAE/ASEE Joint Propulsion Conference, Indianapolis, IN, June 1994.

[43] George, P., Krishnan, S., Varkey, P. M., Ravindran, M., and Ramachandran, L., "Fuel Regression Rate Enhancement Studies in HTPB/GOX Hybrid Rocket Motors," AIAA Paper 98-3188, 38th AIAA/ASME/SAE/ASEE Joint Propulsion Conference, Cleveland, OH, July 1998.

[44] Chiaverini, M. J., "Regression Rate and Pyrolysis Behavior of HTPB-Based Solid Fuels in a Hybrid Rocket Motor," Ph.D. Dissertation, Pennsylvania State Univ., University Park, PA, Sept. 1997.

[45] Chiaverini, M. J., Serin, N., Johnson, D., Lu, Y. C., Kuo, K. K., and Risha, G. A., "Regression Rate Behavior of Hybrid Rocket Solid Fuels," *Journal of Propulsion and Power*, Vol. 16, No. 1, 2000, pp. 125–132.

[46] Chiaverini, M. J., Serin, N., Johnson, D. K., Lu, Y. C., and Kuo, K. K., "Instantaneous Regression Behavior of HTPB Solid Fuels Burning with GOX in a Simulated Hybrid Rocket Motor," *Challenges in Propellants and Combustion 100 Years After Nobel*, edited by K. K. Kuo, Begell House, New York, 1997, pp. 719–733.

[47] Chiaverini, M. J., Kuo, K. K., Peretz, A., and Harting, G. C., "Regression-Rate and Heat, Transfer Calculations for Hybrid Rocket Combustion," *Journal of Propulsion and Power*, Vol. 17, No. 1, 2001, pp. 99–110.

[48] Risha, G. A. "Enhancement of Hybrid Rocket Combustion Performance Using Nano-Sized Energetic Particles," Mechanical Engineering Ph.D. Dissertation, Pennsylvania State Univ. University PA, Park, Aug. 2003.

[49] Favorito, N. A., "Development and Testing of a Nitrous Oxide Feed System for an Experimental Hybrid Rocket Motor," Mechanical Engineering M.S. Thesis, Pennsylvania State Univ., University Park, PA, Dec. 2005.

[50] Risha, G. A., Ulas, A., Boyer, E., Kumar, S., and Kuo, K. K., "Combustion of HTPB-Based Solid Fuels Containing Nano-Sized Energetic Powder in a Hybrid Rocket Motor," AIAA Paper 2001-3535, 37th AIAA/ASME/SAE/ASEE Joint Propulsion Conference, Salt Lake City, UT, July 2001.

[51] Risha, G. A., Boyer, E., Wehrman, R. B., and Kuo, K. K., "Performance Comparison of HTPB-Based Solid Fuels Containing Nano-Sized Energetic Powder in a Cylindrical Hybrid Rocket Motor," AIAA Paper 2002-3576, 38th AIAA/ASME/SAE/ASEE Joint Propulsion Conference, Indianapolis, IN, July 2002.

[52] Risha, G. A., Boyer, E., Evans, B., Kuo, K. K., and Malek, R., "Characterization of Nano-Sized Particles for Propulsion Applications," *Synthesis, Characterization and Properties of Energetic/Reactive Nonmaterials*, Materials Research Society Symposium – Proceedings, Vol. 800, Material Research Society, Dec. 2003, pp. 243–254.

[53] Risha, G. A., Evans, B., Boyer, E., Wehrman, R. B., and Kuo, K. K., "Nano-Sized Aluminum, and Boron-Based Solid-Fuel Characterization in a Hybrid Rocket Engine," AIAA Paper 2003-4593, 39th AIAA/ASME/SAE/ASEE Joint Propulsion Conference, Huntsville, AL, July 2003.

[54] Favorito, N. A., "The Effect Of Varying Percentages of Aluminum Nano-Particles Powder in a Hybrid Rocket," B.S., in Mechanical Engineering Honors Thesis, Pennsylvania State Univ., University Park, Aug. 2003.

[55] Evans, B., Risha, G. A., Favorito, N., Boyer, E., Wehrman, R. B., Libis, N., Kuo, K. K., "Instantaneous Regression Rate Determination of a Cylindrical X-Ray Transparent Hybrid Rocket Motor," AIAA Paper 2003-4592, 39th AIAA/ASME/SAE/ASEE Joint Propulsion Conference, Huntsville, AL, July 2003.

[56] Evans, B., Favorito, N. A., Boyer, E., Risha, G. A., Wehrman, R. B., and Kuo, K. K., "Characterization of Nano-Sized Energetic Particle Enhancement of Solid-Fuel Burning Rates in an X-Ray Transparent Hybrid Rocket Engine," AIAA Paper 2004-3821, 40th AIAA/ASME/SAE/ASEE Joint Propulsion Conference, Fort Lauderdale, FL, July 2004.

[57] Evans, B., Favorito, N. A., Boyer, E., and Kuo, K. K., "Characterization of Solid Fuel Mass-Burning Enhancement Utilizing an X-ray Translucent Hybrid Rocket Motor," 6th International Symposium on Special Topics in Chemical Propulsion, Santiago, Chile, March 2005.

[58] Evans, B., Favorito, N. A., and Kuo, K. K., "Analysis of Solid Fuel Burning-Rate Enhancement Techniques in a Hybrid Rocket Motor," AIAA Paper 2005-3909, 41st AIAA/ASME/SAE/ASEE Joint Propulsion Conference, Tucson, AZ, July 2005.

[59] Karabeyoglu, M. A., Zilliac, G., Cantwell, B. J., DeZilwa, S., and Castellucci, P., "Scale-Up Tests of High Regression Rate Liquefying Hybrid Rocket Fuels," AIAA Paper 2003-1162, 41st Aerospace Sciences Meeting and Exhibit, Reno, NV, Jan. 2003.

[60] Oran, E. S., and Boris, J. P., *Numerical Simulation of Reactive Flows*, Elsevier Science, New York, NY, 1987, pp. 216–518.

[61] Gany, A., and Netzer, D. W., "Combustion Studies of Metallized Fuels for Solid Fuel Ramjets," *Journal of Propulsion and Power*, Vol. 2, No. 5, 1985, pp. 423–427.

[62] Gany, A., "Combustion of Boron-Containing Fuels in Solid Fuel Ramjets," *Combustion of Boron-Based Solid Propellants and Solid Fuels*, edited by K. K. Kuo and R. Pein, Begell House, New York, 1993, pp. 91–112.

[63] Natan, B., and Gany, A., "Effects of Bypass Air on Boron Combustion in Solid Fuel Ramjets," *Journal of Propulsion and Power*, Vol. 9, No. 1, 1993, pp. 155–160.

[64] Natan, B., and Gany, A., "Combustion Characteristics of a Boron-Fueled Solid Fuel Ramjet with Aft-Burner," *Journal of Propulsion and Power*, Vol. 9, No. 5, 1993, pp. 694–701.

[65] Natan, B., and Netzer, D. W., "Experimental Investigation of the Effect of Bypass Air on Boron Combustion in a Solid Fuel Ramjet," *Combustion of Boron-Based Solid Propellants and Solid Fuels*, edited by K. K. Kuo and R. Pein, Begell House, New York, 1993, pp. 427–437.

[66] Nabity, J. A., Lee, T., Natan, B., and Netzer, D. W., "Combustion Behavior of Boron Carbide Fuel in Solid Fuel Ramjets," *Combustion of Boron-Based Solid Propellants and Solid Fuels*, edited by K. K. Kuo and R. Pein, Begell House, New York, 1993, pp. 287–302.

[67] "Rocket Propulsion Testing," <https://rockettest.ssc.nasa.gov/ssc_ptd/projects_h202_phus.htm> [retrieved 1 Dec. 2006].

[68] Akiba, R., Nakajima, T, and Nagata, H., "A New Era of the Hybrid Rocket," *Journal of Space Science and Technology*, Vol. 16, No. 2, 2000, pp. 1–5.

[69] Shin, S., Aoki, Y., Nagata, H., Kudo, I., Akiba, R., and Kubota, I., "Preliminary Study for Staged Combustion Hybrid Rocket," *22nd International Symposium on Space Technology and Science*, Japan Society for Aeronautical and Space Sciences, Tokyo, Japan, 2000, pp. 116–120.

[70] Osherov, A., and Natan, B., "The Starting Transient in a Gas-Generator Hybrid Rocket Motor," *Propellants, Explosives, and Pyrotechnics*, Vol. 25, No. 5, 2000, pp. 260–270.

[71] DeRieux, E. T., "Solid-Hybrid Propulsion," *Astronautics*, Vol. 7, No. 3, 1962, pp. 30–31, 72.

[72] Miyata, K., and Frederick, R. A., Jr., "Ammonium Nitrate-Based Solid Fuel Gas Generator for Gas Hybrid Rockets," AIAA Paper 96-3254, 32nd AIAA/ASME/SAE/ASEE Joint Propulsion Conference, Lake Buena Vista, FL, 1996.

[73] Eisele, S., Volk, F., and Menke, K., "Gas Generator Materials Consisting of TAGN and Polymeric Binders," *Propellants, Explosives, and Pyrotechnics*, Vol. 17, No. 4, 1992, pp. 155–160.

[74] Eisenreich, N., Krause, H. H., Pfeil, A., and Menke, K., "Burning Behavior of Gas Generators with High Boron Content," *Propellants, Explosives, and Pyrotechnics*, Vol. 17, No. 4, 1992, pp. 161–163.

[75] Yano, Y., "Combustion Characteristics of a Small-Scale, Tactical Hybrid Rocket Propulsion System," AIAA Paper 2001-3538, 34th AIAA/ASME/SAE/ASEE Joint Propulsion Conference, Salt Lake City, UT, July 2001.

[76] Takashita, Y., and Teramoto, Y., "Study of Gas-Hybrid Rocket (I)–Nitric Acid/AP-Composite-Gas-Generator," *Journal of the Japan Explosives Society*, Vol. 57, No. 4, 1996, pp. 135–141.

[77] Markopolous, P., and Abel, T., "Development and Testing of a Peroxide Hybrid Upper Stage Propulsion System," AIAA Paper 2001-3243, 34th AIAA/ASME/SAE/ASEE Joint Propulsion Conference, Salt Lake City, UT, July 2001.

[78] Lund, G. K., Starrett, W. D., and Jensen, K. C., "Development and Lab-Scale Testing of a Gas Generator Hybrid Fuel in Support of the Hydrogen Peroxide Hybrid Upper Stage Program," AIAA Paper 2001-3244, 34th AIAA/ASME/SAE/ASEE Joint Propulsion Conference, Salt Lake City, UT, July 2001.

[79] *Volume 1: Programmatic Environmental Impact Statement for Licensing Launches*, Office of the Associate Administrator for Commercial Space Transportation (AST), Federal Aviation Administration, Dept. of Transportation, 24 May 2001; also <http://www.faa.gov/about/office_org/headquarters_offices/ast/licenses_permits/media/volume1-PEIS.pdf> [retrieved 1 Dec. 2006].

[80] *Beryllium Oxide Material Data Safety Sheet*, Alfa Aesar, A Johnson Mathey Company, Inc., Ward Hill, MA, May 10, 2004.

[81] Baker, A. M, Heywood, M., and Newlands, R., "The Hybrid Engine as a Green Propulsion Unit for Amateur Rockets," *Proceedings of the First International Conference on Green Propellants for Space Propulsion*, ESA Publ. Div., Noordwijk, The Netherlands, 2001, pp. 327–334.

[82] *Finding of No Significant Impact*, Office of the Associate Administrator for Commercial Space Transportation (AST), Federal Aviation Administration, Dept. of Transportation, Federal Register, Vol. 69, No. 38, 26 Feb. 2004, pp. 9007–9014.

[83] *Environmental Assessment for the 250K Hybrid Motor Test Project*, NASA John C. Stennis Space Center, Stennis Space Center, MI, Nov. 1998.

Chapter 11

Hydrogen Peroxide, Hydroxyl Ammonium Nitrate, and Other Storable Oxidizers

Stephen Heister*
Purdue University, West Lafayette, Indiana 47907
and
Eric Wernimont†
General Kinetics Inc., Huntington Beach, California 92649

I. Introduction

ALTHOUGH liquid oxygen is in many respects the ideal oxidizer, its cryogenic nature makes it unsuitable for many applications. The plumbing and feed systems are complicated dramatically when using this fluid because provisions for boiloff and potential geysering must be included and cryogenic valves and pumps must be used for fluid control. In many military and space applications, oxidizer storability is desired, if not required, under mission constraints. For these reasons, there has always been ample motivation for study and development of hybrid rockets using storable oxidizers. Efforts dating back over the past 40 years have included study of such liquids/fluids as nitrogen tetroxide, nitric acid [and its variants red-fuming nitric acid (RFNA) and inhibited RFNA (IRFNA)], hydrogen peroxide (HP), hydroxyl ammonium nitrate (HAN), nitrous oxide, and other energetic liquids. Whereas there have been limited efforts on reverse hybrids using solid oxidizers and storable liquid fuels, these configurations are generally undesirable due to reduced safety and performance as compared to the traditional scheme. Gaseous oxygen is another storable oxidizer of note, but its poor density relegates it mainly to use in laboratory and ground demonstrations [1–6].

Table 1 summarizes some of the physical properties of these storable oxidizers. Nitric acid is particularly attractive for applications demanding low temperatures within the operating range due to its very low freezing point. Nitrogen tetroxide

*Professor, School of Aeronautics and Astronautics.
†Operations Manager.

has seen numerous uses in the liquid propulsion community; its hypergolicity with hydrazine-based fuels makes it particularly attractive for storable bipropellant applications. However, its very high vapor pressure and the toxicity of the vapor are becoming of greater concern in the present day, and its application for future programs appears to be somewhat limited. The corrosivity of nitric acid also is cause for reduced interest in this oxidizer in the present environment. HP is currently available in rocket grade aqueous solutions at both the 90 and 98% level. The interest in low-toxicity propellants has led to an increased interest in this oxidizer. Similarly, HAN has received increased attention of late because it provides a high-density, low-toxicity alternative. Although there are various formulations under consideration, data are provided for HAN in a 95% aqueous solution.

There are also significant developments under way with systems using nitrous oxide. Because it is of low toxicity, the high vapor pressure actually becomes a desirable feature for this fluid, thereby permitting the use of self-pressurizing tankage. This feature is a substantial simplification because it eliminates the need for a separate pressurization system. The fluid is seeing use in hobbies rockets [7] and as a rocket augmentation system on the SpaceshipOne vehicle [8] currently under development by Scaled Composites.

Of the alternatives noted in Table 1, HP, HAN, and nitrous oxide are receiving the most attention in the current research environment. For these reasons, our discussion in this chapter will primarily focus on these fluids.

Note that most of the flight-testing and the limited production programs of the past have all used storable oxidizers. Sounding rocket programs dating back to the 1960s [9] in ONERA used RFNA with a nylon-based fuel, and early Swedish efforts employed nitric acid and a polybutadiene- (PB-) based fuel. During the same time, United Technologies Corporation developed a target drone dubbed Sandpiper. This vehicle, which employed MON-25 (25%NO/75% N_2O_4) and a magnesium-loaded Poly-methyl metacrylate (PMM) fuel grain had six successful flights in the late 1960s. A growth version of the drone, High Altitude Supersonic Target (HAST), used IRFNA/PB/PMM propellants and had many successful flights. The Firebolt target drone of the 1980s was a further development of this technology.

Table 1 Physical properties at ambient pressure/temperature of storable oxidizers used in hybrid propulsion developments

Oxidizer	Specific gravity	Freezing point, °F	Boiling point, °F	Vapor Pressure, psi	Heat of formation cal/g
Nitric acid	1.549	−42	181	0.39	−658
Nitrogen tetroxide	1.44[a]		70	14.8	−50.9
90% HP	1.39	11.3	286	0.066	−1440
98% HP	1.43	27.5	299	0.043	−1340
95% HAN	1.68	5	338	<0.002	−940
Nitrous oxide	1.98[a]		−126	582	443

[a]Liquid density at conditions above vapor pressure.

II. Propellant Performance Comparisons

Table 2 shows a comparison of the performance (estimated using one-dimensional equilibrium thermochemistry) of various storable oxidizer combinations with the cryogenic option liquid oxygen (LOX). Table 2 includes the optimal oxidizer/fuel (O/F) ratio; fuel, oxidizer, and bulk densities, ρ_f, ρ_{ox}, and ρ_b; and specific impulse I_{sp}, and density impulse $\rho_b I_{sp}$ for several propellant combinations. Most hybrid testing of late has employed hydroxyl-terminated polybutadiene (HTPB) as a fuel. Polyethylene (PE) and, most recently, dicyclo–pentadiene (DCPD) have been burned, although differences in fuel do not generally contribute to large differences in specific impulse. In general, Table 2 indicates that LOX is a superior oxidizer if I_{sp} is the only consideration. However, the storable oxidizers enjoy significant advantages in bulk density and thereby provide competitive or superior amounts of impulse on a per unit volume basis, as indicated in the far right column in Table 2. Because the storable oxidizers tend to optimize at high O/F ratios, the size of the high-pressure combustion chamber containing the fuel is minimized.

In addition, the monopropellant characteristics of hydrogen peroxide (HP) and HAN provide substantial system-level advantages over LOX-based systems [10–13]. For example, a small catalyst bed can be employed to provide turbine drive gases for pump-fed configurations, thereby eliminating the need for a separate liquid bipropellant gas-generator system that would be required when using LOX. A recent study [11] of a Titan-class strapon booster was conducted, and the system schematics are shown in Fig. 1, which demonstrates the simplifications in the plumbing system. For the LOX-based system, a separate tank is required to house fuel or an alternate monopropellant (HP assumed in Fig. 1) for turbine-drive gas-generation purposes. The inclusion of an additional fluid not only increases system complexity, but can also have dramatic effects on system costs because procurement, storage, and delivery systems must be provided for each fluid in the system.

In the subject design study [11], the higher bulk density of the HP/PE system led to a smaller overall booster size despite the increased propellant load associated with the I_{sp} disadvantage as compared with LOX. The overall size comparison is shown in Fig. 2. The study also showed that the HP/PE system offered over a

Table 2 Performance comparison for several storable propellant combinations with LOX/HTPB, $P = 1000$ psi, sea-level expansion

Propellant combination	Optimal O/F	ρ_f, g/cm^3	ρ_{ox}, g/cm^3	ρ_b, g/cm^3	I_{sp}, s	$\rho_b I_{sp}$, g · cm^3
LOX/HTPB	2.3	0.92	1.14	1.06	298.4	316
90% HP/PE	7.8	0.90	1.39	1.31	266.1	348
98% HP/PE	7	0.90	1.43	1.33	275.7	367
98% HP/DCPD	6.2	1.01	1.43	1.35	277.5	375
95% HAN/HTPB	9.6	0.92	1.68	1.56	251.1	392
N_2O/HTPB	7.4	0.92	1.98	1.74	266.4	463

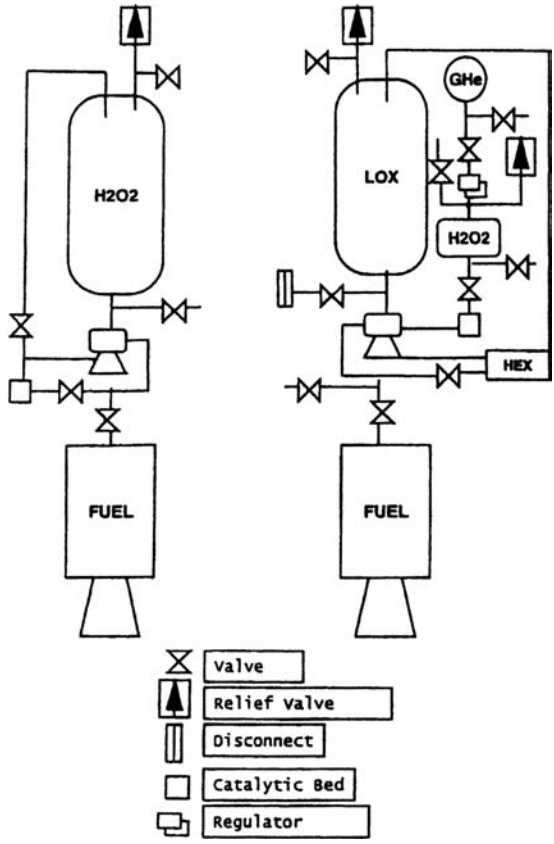

Fig. 1 Engine cycle comparisons for large pump-fed hybrid rocket booster.

20% savings in inert weight as compared to the LOX/HTPB system due to the enhanced bulk density and simplicity of the system. Boiloff issues, tank insulation requirements, and other factors all play a role in determining the optimal fluid for a given application. For these reasons, the system-level issues need careful evaluation in comparing cryogenic and storable oxidizer systems.

Prior efforts have largely focused on HTPB as a fuel. Although HTPB is an excellent binder for solid rocket motors where grain cracks are a safety hazard, hybrids are virtually unaffected by grain cracks. The major disadvantage that HTPB has is driven by a cost issue. The expensive nature arises because HTPB is a crosslinked material and a specialty chemical. Because it is a crosslinked material, the manufacturing method typically used is batch casting. Batch casting necessitates expensive tooling and a substantial curing time. Use of such tooling also requires considerable time in tooling preparation as well as assembly and disassembly.

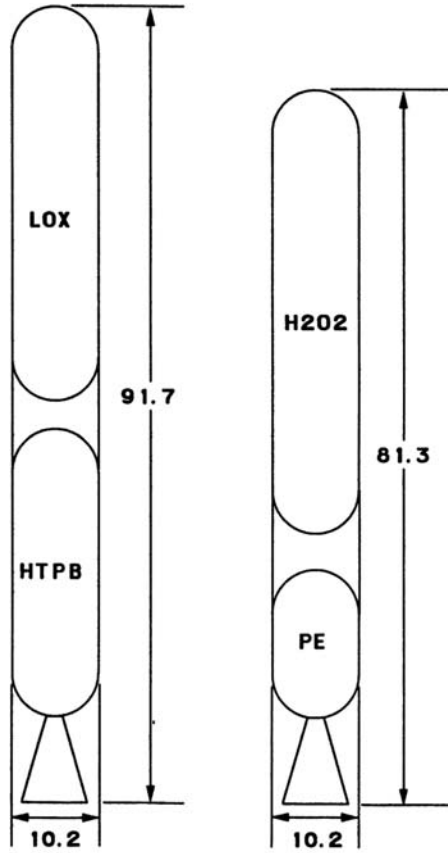

Fig. 2 Design study results comparing size of LOX/HTPB and HP/PE hybrid rocket boosters.

In contrast, PE is a thermoplastic, which is commonly produced as a final product via extrusion from a die in a continuous process. Hence, PE only requires that it be cooled and then length cut for a finished fuel grain. For these reasons, PE should make a more inexpensive fuel than HTPB. This manufacturing simplification may be accomplished without a performance loss because the theoretical performance of HTPB and PE are virtually identical. Although some previous researchers of hybrid motors used PE, most of that research seemed to focus on the use of high-density polyethylene (HDPE). Similar arguments hold for paraffin-based fuels currently under development [14].

Most recently, DCPD has been evaluated for application as a hybrid rocket fuel [15–17]. This material has interesting characteristics in that it is hydrophobic and permits encapsulation of energetic ingredients that may react with water or oxygen in the air. Configurations have been investigated to encapsulate both lithium aluminum hydride (LAH) and lithium hexa–hydrido aluminate

(LHA), energetic metal hydrides that are reactive with oxygen and water vapor in air.

III. Prior Work Using HP, HAN, and N_2O Oxidizers

There has been relatively little published work on HAN and N_2O-oxidized hybrids. Basic performance attributes and advantages of HAN were discussed by Ramohalli and Dowler [18]. Thiokol Corporation has obtained a patent on a gas-generator concept utilizing HAN-type compounds as oxidizers [19]. There was some basic work done by American Rocket Corporation (AMROC) in the 1980s and early 1990s, but this has not been released in the open literature. Our understanding is that the current nitrous hybrid manufacturer, Space Dev Corporation, has rights to these data.

For these reasons, the bulk of the discussion here will be focused on HP-oxidized hybrids because there is a substantial amount of published literature on this oxidizer.

There has been previous interest by two research groups using the propellant combination of HP/PE. Pugibet and Moutet [20] at ONERA published results from a laboratory-scale program at total mass flux levels between 0.06 and 0.13 lbm/(in.$^2 \cdot$ s) for chamber pressures of 150–400 psia. The other major contribution is the work of Moore and Berman [21], Moore and Cooper [22], and Moore et al. [23, 24] at General Electric Company (GE) in the mid-1950s. The GE tests are at the total mass flux levels of between 0.35 and 1.0 lbm/(in.$^2 \cdot$ s) at chamber pressures from 350 to 600 psia (200 to 100 lbf). In the mid-1960s, Osmon [25] used HP oxidizer with pressed grains of lithium aluminum hydride ($LiAlH_4$) powder as fuel. Osmon's experiments are in the oxidizer mass flux range of 0.08–0.3 lbm/(in.$^2 \cdot$ s) at chamber pressures between 120 and 400 psia (100 and 220 lbf). Note that both the GE group and Osmon used silver screen catalytic beds to decompose the HP before entering the combustion chamber. (Decomposition methods are discussed in Section V.) In the tests conducted by Pugibet and Moutet [20], an atomized spray into the motor was used, ignited by a catalytic surface coating of the fuel. The posttest of Pugibet and Moutet's fuel grains show that there is a difference of fuel regression in the region where liquid HP may impinge on the grain. The GE motors showed very uniform fuel regression in the axial direction, whereas Osmon's fuel regressed similar to that of the Pugibet and Moutet grains. It is likely that the Osmon catalytic bed allowed liquid HP through, giving the fuel regression noted. The incomplete HP decomposition may not have been noted because the fuel selected is slightly hypergolic and would have decomposed the HP on contact. Fuel regression correlations of the form

$$r = \alpha G^{\beta} P_c^{\gamma} \tag{1}$$

are typically sought in accordance with the limited theory available for combustion of this nature. Table 3 shows the fuel regression rate correlations provided by the aforementioned researchers. Classical theory [26] suggests that in a turbulent diffusion-dominated regime the regression rate should be independent of chamber pressure and a function of total mass flux G to the 0.8 power ($\beta = 0.8$ and $\gamma = 0$). Evident from Table 3 is the historical nonconformity to such a stipulation.

Table 3 Summary of correlation exponents for HP hybrids

Reference	β	γ	Comment
Moore and Berman [21]	0.45	0.0	90% HP/PE
Osmon [25]	0.4	0.4	90% HP/95% $LiAlH_4$ (G_{ox})
Pugibet and Moutet [20]	0.5	0.52	96% HP/CTPB

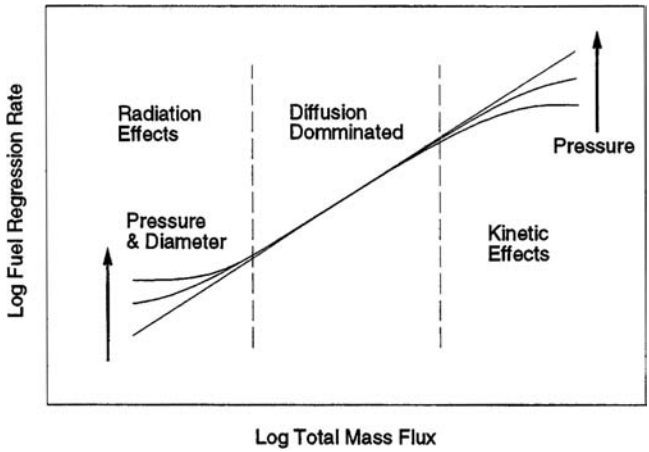

Fig. 3 Qualitative perspective of fuel regression vs total mass flux.

In general, the fuel regression rate may not be purely diffusion dominated [27]. In such a case, the fuel regression rate becomes affected by the pressure at the extreme lower and upper ends of total mass flux. Figure 3 shows this general trend as stipulated by Wooldridge and Marxman [26] and as observed by authors using gaseous oxygen (GOX) oxidizer systems [1, 28]. It is possible that the work of Pugibet and Moutet [20] and that of Osmon [25] both reside in the radiation effects area of fuel regression rate curve. The GE data suggest a strong pressure dependence, although the testing is at high mass fluxes, which may be in the diffusion-dominated regime.

The following sections provide recent results obtained during extensive testing at Purdue University. Over 100 successful tests were conducted using the HP/PE combination and 22 successful tests using HP/DCPD with and without lithium hydride additives.

IV. Recent HP/PE Experience

We can trace the use of the HP in hybrid motors to the mid-1950s when Moore and Berman [21], Moore and Cooper [22], and Moore et al. [23, 24] used H_2O_2 with PE. There were two researchers in the 1960s, Osmon [25], using H_2O_2 with lithium aluminum hydride, and Pugibet and Montet [20], using H_2O_2 with

carboxyl-terminated polybutadiene (CTPB). Although the early investigators were quite successful, interest waned (most probably due to the search for higher energy propellants during this era), and essentially no published work exists for a three decade period beginning in the mid-1960s. Current requirements for lower cost, nontoxic propulsion systems have motivated a renewed interest in H_2O_2. Recent efforts have been undertaken at Purdue University [29–31] and the U.S. Air Force Academy [32]. This section will focus on the data generated at Purdue University and will be compared to the prior investigators.

A. Test Program

The test program was formulated to maximize the amount of information available to actually design a HP/PE hybrid. For this reason, many different parameters were studied, none of which were studied in great detail. Most parameters were investigated across a range of total mass port flux levels, allowing determination of fuel regression rate influence. The entire test program involved firing 12 different series of motors, with each series dedicated to examination of a specific parameter. A total of 100 firings were conducted in association with these test series, which are summarized in Table 4. The following sections will discuss results obtained from the bulk of these tests. Testing accomplished using radial-flow geometry (test series C in Table 4) is reported in elsewhere [33]. All other tests used a single center-perforated fuel grain with regulated pressure-fed 85–88% H_2O_2 (highly stabilized 30–50 ppm of standard H_2O_2 stabilizers) liquid injected along the centerline of the motor at the head end of the motor. The liquid H_2O_2 was injected using a standard cone injector that reacted with a consumable catalytic bed (see Sec. V).

Table 4 Test series summary

Series	Purpose	Number of motors	Test parameters
A	System verification	12	$Pc \sim 100$ psia; $G \sim 0.25$–0.35 lbm/(in.$^2 \cdot$ s); 85% HP Interox; high-density PE
B	Broader flux	12	$G \sim 0.15$–0.35 lbm/(in.$^2 \cdot$ s); 3 times at 80% HP Interox
C	Radial flow motor	20	Proof of concept; eight ignition tests
D	PE types	11	LDPE; UHMW
E	Higher mass flux, *Pc*	8	Flight weight, LDPE; proof of combustion
F	New HP vendor	5	Air Liquid 85% HP
G	Increase *Pc*	5	$Pc \sim 200$ psia
H	Lengthen aft combustion	4	Increase by 2 and 4 in.
I	Action time study	4	Two at 6 and 9 s each
J	Increase *Pc*	5	$Pc \sim 400$ psia
M	Increase mass flux	10	$G \sim 0.35$–1.0 lbm/(in.$^2 \cdot$ s)
Y	Ignition behavior	4	Visual observation, polymethyl methacrylate (PMMA) fuel

As indicated in Table 4, a broad range of tests were conducted over the 12 test series. Unfortunately, we were unable to maintain a consistent HP vendor over the three-year study. Although some differences in fluid were noted [34], they were generally minor. In addition, we experimented with several different throat materials before arriving at a suitable option, which was used throughout test series D–Y. Early efforts were aimed at optimizing fuel-grain length to obtain O/F ratios near the 7.5 value, which tends to maximize specific impulse for these propellants. Many of the later tests actually achieved fairly low mixture ratios (in the 5–6 range) because fuel regression rates exceeded our estimates. A complete list of all test conditions along with greater test apparatus detail may be found by Wernimont [34] and will not included here in the interest of brevity.

B. Fuel Properties

Substantial efforts were expended in quantifying combustion behavior for various PE formulations including low-density PE (LDPE), HDPE, and ultra-high molecular weight (UHMW) materials. To accomplish this, PE rod was purchased from a local vendor for testing in the given experimental apparatus. The rod stock was then machined to the desired length and port diameter. Because the PE purchased was an off-the-shelf item, it was necessary to determine the characteristics of the PE fuel after purchase. Fuel density was determined by measuring both volume and weight of a precisely machined cylindrical sample. For tracking purposes, each lot purchased is assigned a dash number, corresponding to the purchase order number. According to vendor naming, a single lot of HDPE, UHMW, as well as three separate lots of LDPE were purchased. Based on the density determined for the purchased LDPE, it seems that this material is more accurately a mid-density-PE (MDPE) made by copolymerization with little branching, with the exception of LD-149, which seems to be a branched low-density material. Based on density, it also seems likely that the HDPE is made from the Ziegler–Natta process. Initial firings were conducted with HDPE, but once it was determined LDPE had potential for slightly higher fuel regression and combustion efficiency, it was used for the remainder of tests.

Differential scanning calorimeter (DSC) data were taken for the PE materials fired in the test program to obtain a rough idea of the melt-layer behavior and the depolymerization process. All of the DSC data shown are taken with a 70°C 5-min isotherm followed by a 10°C/min ramp to 550°C under inert gaseous nitrogen purge. Over this temperature range, all of the PE material exhibited the same general characteristics of endothermic melting and depolymerization. Typically DSC data are used to determine material specific heat as a function of temperature, however these data will be used as an indicator of general behavior. The data provided are weight normalized heat flow for sample sizes between 1 and 3 g. The material for DSC testing is collected during machining for the samples used to determine density described earlier.

Figure 4 shows the DSC response for the three types of LDPE fired in the test program. As can be seen from Fig. 4, the melting temperatures for the LDPE materials are between 110 and 130°C. Figure 4 also shows depolymerization beginning at approximately 350°C and finishing at roughly 470°C. During the depolymerization regime, sample temperature is sufficient to break the bonds in the polymer, at

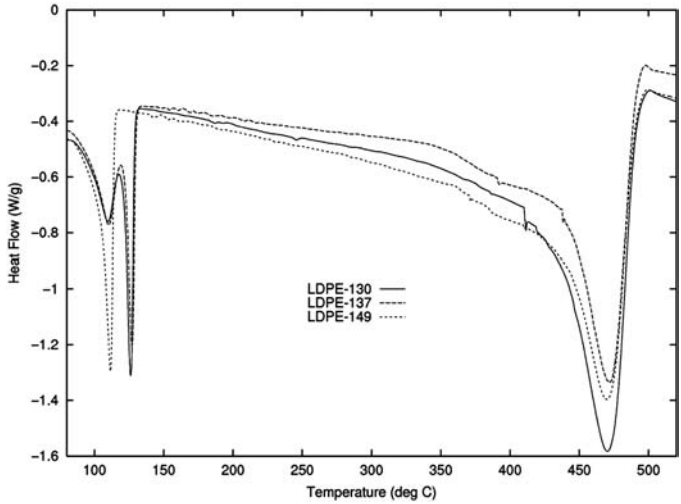

Fig. 4 DSC response for LDPE material tested at 10°C/min.

which point the melted material becomes a short-chain molecule, which is gaseous at ambient pressure. This depolymerization process continues as the temperature is increased until the entire polymer has become gaseous. Figure 5 shows the melt transitions for LDPE, UHMW and the HDPE tested in the motors fired.

The degree of polymer crystallinity corresponds directly to the integrated amount of endothermic behavior exhibited during melting (assuming identical polymer chemistry). PE material characteristics of percent crystallinity and melt temperature are given in Table 5 [35–37].

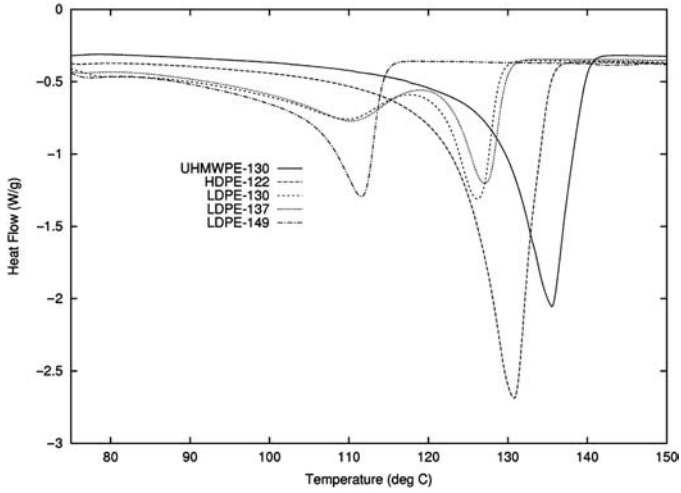

Fig. 5 DSC melt response for PE materials tested at 10°C/min.

Table 5 Crystallinity and melt temperatures of PE fuels

Material	Crystallinity, %	Melt temperature, °C
LDPE	45–55	106–111
LLDPE	25–75	125
UHMWPE	45	132
HDPE	85	125–132

Figure 5 shows that the crystallinity is greatest for HDPE, followed by UHMW and the LDPEs in that order. By the comparison of the expected melt temperatures from Table 5 and those measured from DSC, an interesting conclusion can be drawn. It seems that LDPE-149 is actually a completely branched LDPE, whereas LDPE-130 and LDPE-137 are LLPDEs with some branching. The branching for LDPE-130 and LDPE-137 can be seen as that portion of their melt behavior at 110°C. This information also corroborates with that obtained from the density information. Crystallinity information from the DSC also suggest that the LLDPEs (LDPE-137 and LDPE-130) are on the lower end of the typical range for LLDPEs, which would imply a certain degree of branching as exhibited by the double endothermic event. The difference in the melt behavior of the LDPEs will become important to the behavior of the fuel surface during combustion.

Figures 6 and 7 show the depolymerization behavior of the materials used in the test program (UHMW-130, HDPE-122, LDPE-130, LDPE-137, and LDPE-147). Information in this regime is better illustrated by thermogravimetric analysis;

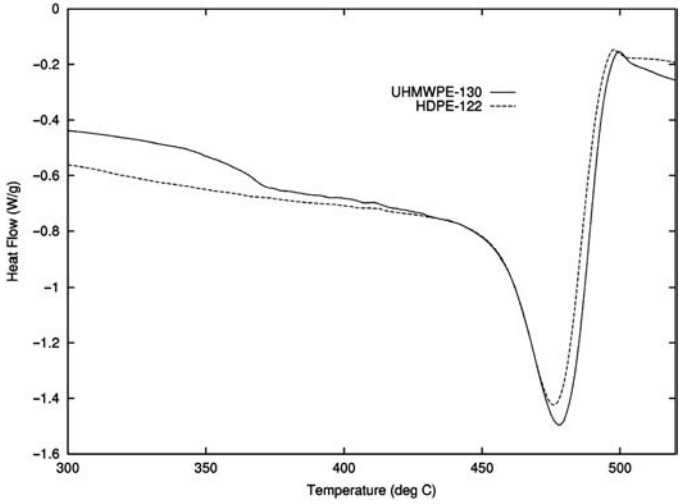

Fig. 6 DSC depolymerization response at 10°C/min for HDPE-122 and UHMWPE-130.

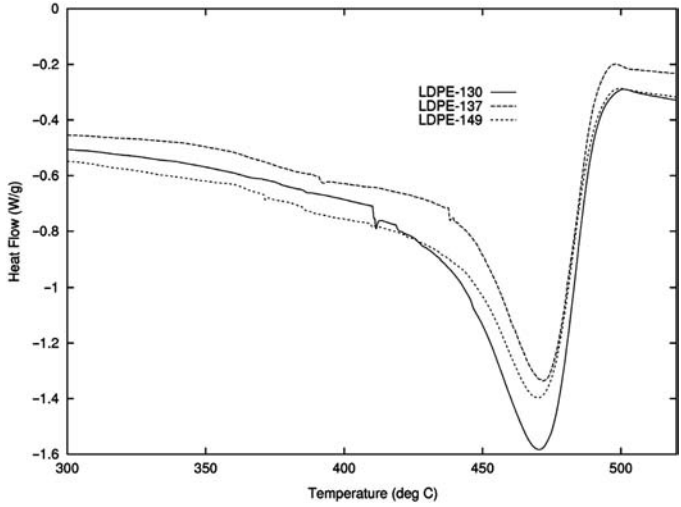

Fig. 7 DSC depolymerization response for LPDE at 10°C/min.

however, DSC does provide some rough information. The first conclusion drawn from Figs. 6 and 7 is that the temperature and the amount of energy required for complete depolymerization is approximately the same for all of the materials. This is to be expected because the basic chemistry involved in depolymerization of the PE is roughly the same. However, UHMW-130 appears to have some material other than PE entrained because a portion of this material gasifies around 370°C. Another DSC was run under identical conditions for UHMW but stopped and allowed to cool at 400°C. This partly decomposed UHMW is observed to have a slight brown surface and a 7% weight loss from initial conditions. It is unknown if the observed weight loss is a material other than PE that is entrained in the UHMWPE for easier manufacture. Other materials may have been added to the UHMW for manufacturing purposes because UHMW is highly viscous as a melt and must be processed differently than other classes of PE.

V. Consumable Ignition Device

Probably the greatest challenge in creating a workable hybrid-propellant combination lies in the development of an ignition concept that provides a rapid and reproducible rise in chamber pressure and thrust. In the past, secondary injection of pyrofouric fluids, electric ignition sources, torches, and catalytic ignition systems have been used in hybrid rockets. With the exception of the catalytic system, all of these concepts require additional hardware and/or fluids to support ignition of the motor. For this reason, the catalytic concept was pursued through the use of a consumable catalytic bed (CCB) [38].

The CCB is inserted into a pocket that was machined into the forward end of the fuel grain. No special ignition sequence was used in any of the testing, the engine was literally “slam started” by opening the main fire valve, which

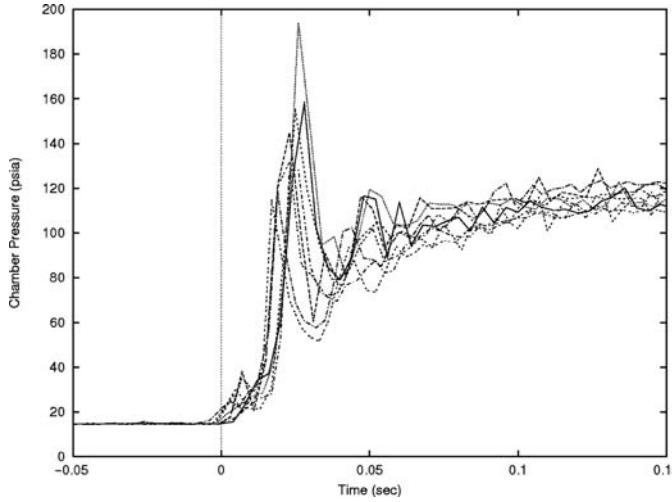

Fig. 8 Typical motor ignition traces, D-series testing.

provides maximum HP flow. As HP comes into contact with the surface of the CCB, it is decomposed. If the HP is at sufficient concentration, the decomposition products are at a temperature such that autoignition of the fuel occurs. As the HP flow continues, the CCB is consumed. If the CCB is sized properly, there will be enough energy in the combusting fuel grain to support thermal decomposition of the HP injected after CCB consumption; that is, the device operates for a small fraction of the test duration.

Figure 8 highlights a group of typical ignition transients obtained with the use of 85% HP with a CCB in the D-series tests. This collection shows that the CCB is repeatable and produces rapid ignition transients. The peaks at approximately 30 ms represent a pressure overshoot due to increased oxidizer mass flow when the oxidizer valve is first opened. Because there is no cavitating venturi in the fluid system, the oxidizer mass flow is governed strictly by pressure differential. Consequently, initial fluid flow is greatest for the first 20 ms before the chamber pressure has a chance to climb to its steady-state value. As can be seen from Fig. 8, steady-state combustion has been achieved in 50 ms.

VI. HP/PE Test Results

Because the CCB device contributed a nonnegligible amount of mass and energy during our test burns, which typically varied between 5 and 20 s we were forced to improve on the data reduction methodology that had typically been used by hybrid rocket experimentalists. Average regression rates and port total flux levels from a given test firing are obtained from an integral reconstruction of the entire chamber pressure history with the CCB and inerts flows taken into account. When this process is used, the entire regression rate and mass flux histories may be reconstructed from the measured time-dependent data. A complete description

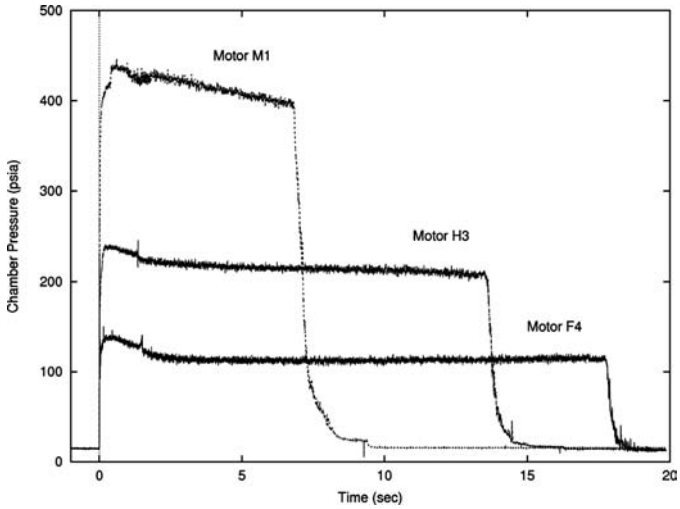

Fig. 9 Measured chamber pressure histories for motors F4, H3, and M1 at average pressures about 100, 200, and 400 psi, respectively.

of the methodology, which will be used throughout this work, is provided by Wernimont and Heister [39].

Reliable ignition and combustion was demonstrated over a range of initial oxidizer fluxes $0.1 < G_{ox} < 1.2\,\text{lbm}/(\text{in.}^2 \cdot \text{s})$ and chamber pressures $100 < Pc < 400$ psia during the testing with 85% HP. A few tests were conducted with 80% HP, but reliable ignition and combustion could not be achieved using the injector and CCB design implemented in these tests. We believe that one could design a device to operate at these lower concentrations with an improved injector (with smaller droplet sizes) and CCB designs. Our injector produced droplets that were quite large; 350-μm volumetric mean diameter is reported by the manufacturer.

Typical chamber pressure histories obtained during the test program are shown in Fig. 9. Overall, the combustion obtained was very smooth as evidenced by the low amount of noise in the pressure signals. Typical unsteadiness in the pressure signals was of the order of 1–2% (zero-to-peak) of the mean pressure in this test program. Sharp tailoffs were always observed in the testing; action times were determined using a bisector technique commonly used in solid rocket data reduction. The spike in motor F4 and H3 traces in the interval $1 < t < 2$ s is attributed to ejection of small portions of the CCB through the nozzle. In the M1 pressure trace, a slight increase in Pc is observed after the main ignition event. This behavior may be attributed to increased oxidizer flow rate due to a change in injector discharge coefficient.

A. Regression Rate Behavior

Although there were test series dedicated to assessing the influence of PE type on fuel regression and combustion, the bulk of the measurements were obtained using LDPE fuel. A compilation of these measurements is provided in Fig. 10,

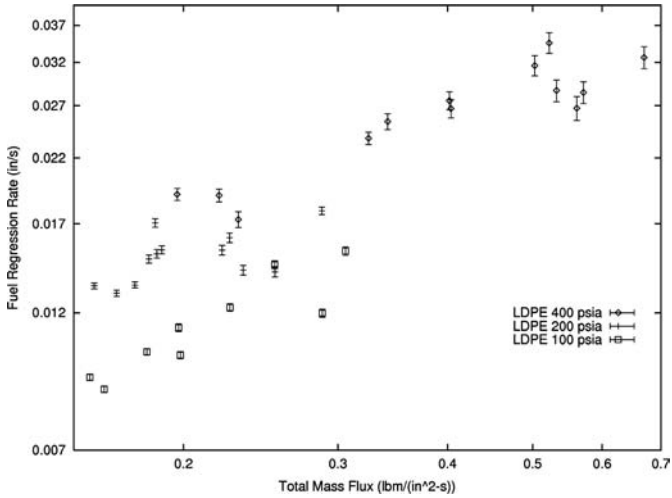

Fig. 10 LDPE fuel regression data showing effect of pressure; values are average fuel regression rate and average total mass flux.

which highlights dependence of regression rate on flux level and chamber pressure. Whereas the low-pressure (100-psi) data appear to behave a classical regression law ($r \sim G^{n}$) consistent with turbulent convection-dominated behavior, the higher-pressure results show a distinct insensitivity to port total mass flux G in the range $0.1 < G < 0.3\,\text{lbm}/(\text{in.}^2 \cdot \text{s})$. In this lower flux region, regression rates at the higher pressures tested (200 and 400 psia) are as much as 75% greater than those at low pressures. The data are consistent with a radiation-based regression law that has been theorized, but infrequently observed for low mass flux conditions.

In fact, this behavior is ideal because regression rates would no longer be influenced by changes in port geometry (either shape or size). For the booster application, design studies [11] indicate an optimal mass flux level of about $0.4\,\text{lbm}/(\text{in.}^2 \cdot \text{s})$ assuming a classical regression law, $r \sim G^{0.8}$. Presumably, designers could make use of this desirable behavior (flux insensitivity) for other applications as well.

To compare the data from this test program with that of previous researchers, we performed correlations assuming a classical, mass flux-dominated regression behavior. Although this approach is not warranted for the higher pressure results, it does permit gross comparisons with results of other researchers who made similar assumptions. The resulting correlations are presented in Table 6. Note that for the low-pressure data the exponent of 0.78 is in close agreement with theory assuming a turbulent convective-dominated behavior. The exponent is reduced at the higher pressures due to the radiative-dominated behavior.

The correlations from Table 6 are compared with those obtained by other researchers in Fig. 11. Previous researchers using HP [20–25] had also noted deviations from turbulent diffusion-dominated regression ($G^{0.8}$). Previous researchers,

Table 6 LDPE/85% HP fuel regression flux correlations

Correlation, in./s	Average *Pc*, psia	Average *G* total, lbm/in.$^2 \cdot$ s
$0.040G^{(0.78)}$	100	0.1–0.3
$0.035G^{(0.52)}$	200	0.1–0.3
$0.041G^{(0.49)}$	400	0.2–0.7

however did not test at low pressure (100 psia) where turbulent diffusion dominated behavior was noted in this test series. Previous research efforts with HP do show a total mass flux exponential dependence similar to that explainable with radiation-driven regression. It is evident from Fig. 11 that this appears to be true, independent of fuel selection, and is provided only to show the trends in exponent of total mass flux. Although other researchers have shown fuel regression for HP-oxidized systems to differ from turbulent diffusion-dominated behavior, the Purdue study is the first to show experimentally the shift to radiation-dominated behavior.

Figure 12 shows the combustion efficiency vs the characteristic chamber length L^* for the motors tested. For our purposes, L^* is calculated as the combustor volume aft of the fuel grain and forward of the throat divided by the throat area. This parameter is often used in the liquids industry to design a motor for acceptable ($>95\%$) combustion efficiency. This parameter is specific to propellant combination, but for comparison to liquid oxygen and ethyl alcohol, L^* values are between 40 and 120 in. [40]. Figure 12 shows that efficiency gains are derived from increased L^*

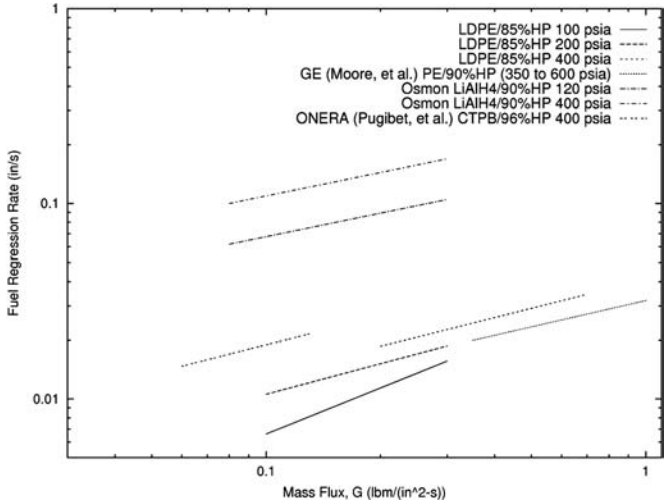

Fig. 11 Comparison of HP investigators' regression rate measurements.

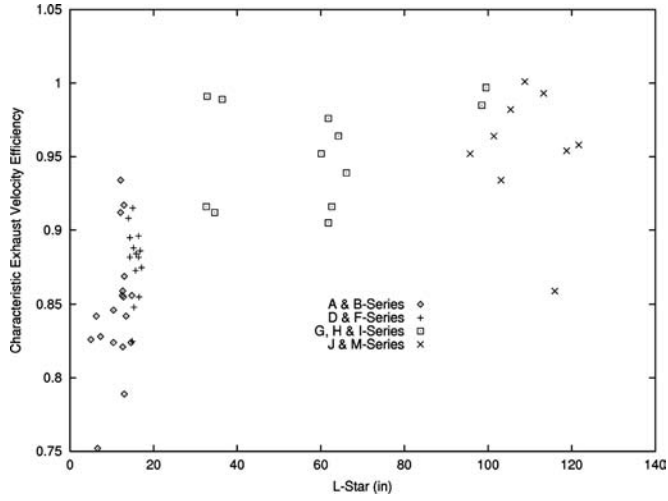

Fig. 12 Effect of L^* on C^* efficiency with inerts.

as is generally the case. Figure 12 suggests that L^* values as low as 40 in. may provide sufficient aft combustion volume for efficiencies above 90%.

B. Combustion Stability Behavior

Overall, the level of combustion oscillations was observed to be below 3.5% zero-to-peak of mean throughout the testing program. Figure 13 shows a typical waterfall plot for motor F4. A slight tendency for nonacoustic combustion oscillations up to a frequency of approximately 70 Hz is noted. Comparison with behavior in other motors suggests that the higher frequency (acoustic) portion may account for roughly 1.5% zero-to-peak chamber pressure response. Although the Fig. 13

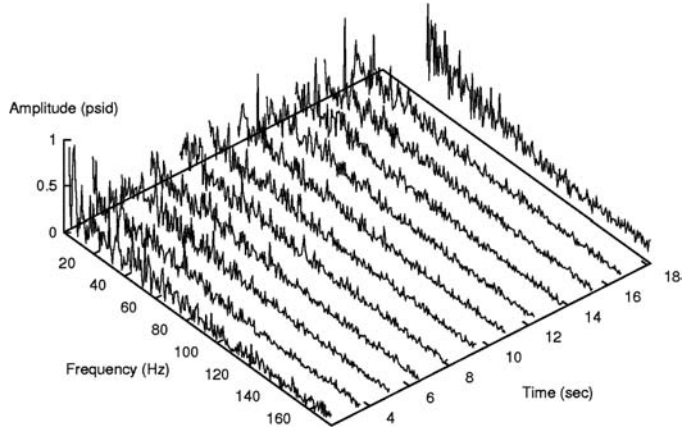

Fig. 13 Waterfall plot of chamber pressure for motor F4.

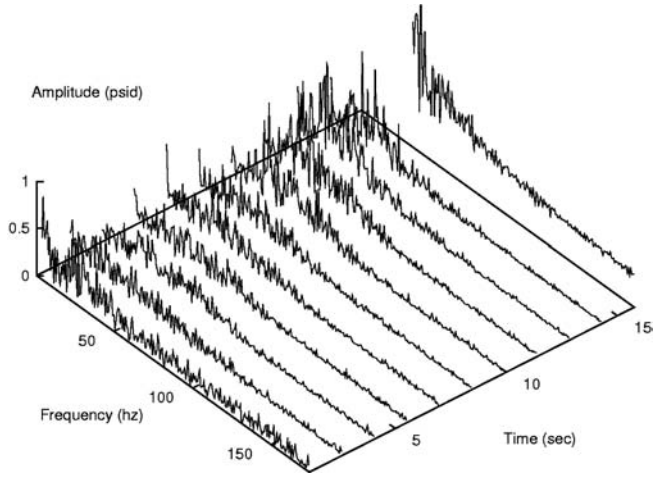

Fig. 14 Waterfall plot of chamber pressure for motor G3.

motor F4 waterfall plot shows no preferred waveform for this propellant combination, later motors do have preferred oscillatory waveforms. As an example, Fig. 14 shows the waterfall plot for motor G3, which has a preferred waveform at roughly 20–35 Hz with amplitude of around 0.75 psi, differential (psid) zero-to-peak. Three other motors, G4, I4, and M3, exhibited similar responses to that of motor G3. Other motors, J3, G5, and J5, exhibited a preferred waveform at roughly 65–80 Hz with an amplitude of around 0.5 psid zero-to-peak.

C. Post-fire Fuel Grains

Some of the fuel grain carcasses were cut along the axis of symmetry to help determine which posttest spatial average method to use in final port diameter calculation. This also provided a means of fuel carcass examination for other interesting information. The length scale shown with the provided figures is in inches closest to the motor carcass.

Figure 15 shows the aft portion of the motor D10 fuel grain. This motor operated at an average chamber pressure of approximately 100 psia and used LDPE (LD-137). As can be seen from Fig. 15, the internal port diameter appears smooth with no

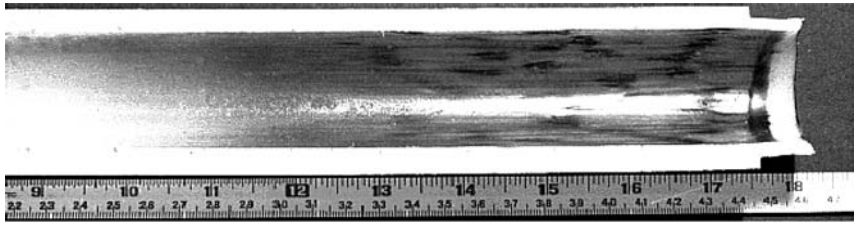

Fig. 15 Aft portion of motor D10 postfire fuel grain, flow direction from left to right.

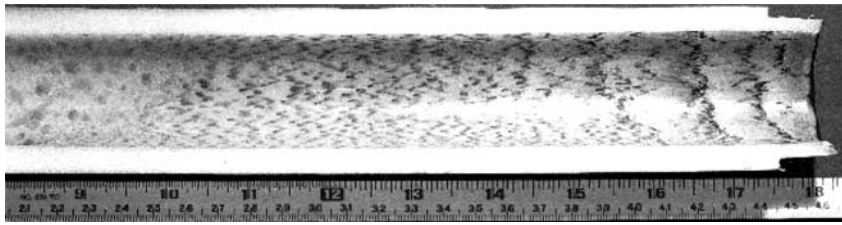

Fig. 16 Aft portion of motor D7 postfire fuel grain.

great difference in total fuel regression noted along the length. Figure 16 shows the aft portion of the motor D7 fuel grain. This motor operated at conditions identical to that of motor D10 including initial port diameter. The only difference between the two tests is that motor D7 used UHMW-130 instead of LD-137. As can be seen from Figs. 15 and 16, the UHMW material appears to collect charred material in a more distinct pattern going aft. In the last ~8 in. of fuel grain, the pattern becomes progressively more distinct. In the last ~2 in., a rough pattern appears every $\frac{3}{4}$ in. The difference in postfire fuel surface between motors D7 and D11 is probably a result of the depolymerization process. The UHMW-130 exhibited a partial polymer breakdown at ~375°C as opposed to complete depolymerization at ~475°C for the LDPE-137 (see Figs. 3 and 4).

Figure 17 shows the aft portion of the motor H3 fuel grain. This motor operated at an average chamber pressure of approximately 200 psia and used LD-137, which is the same material used in motor D10. Figure 17 shows that the increase in chamber pressure has a strong influence on the character of the final fuel port surface. This motor behavior is representative of all of the motors fired in the ~200 psia chamber pressure regime. As can be seen from Fig. 17, the port is smooth on the forward end and transitions into a wave pattern much more distinguishable than that observed in D7 (UHMW, ~100 psia). The last ~6 in. of the fuel carcass exhibit distinct waves that are approximately $\frac{3}{4}$ in. apart. Motor H3 and D10 are fired at identical flux levels, but the surface conditions shown for both are representative of other motors fired at identical pressure conditions. The reduced data shown in Fig. 10 suggest that the fuel regression behavior at higher chamber pressures (200 and ~400 psia) is both radiation and diffusion controlled rather than just diffusion controlled. These two heat transfer modes must permit greater energy transfer to

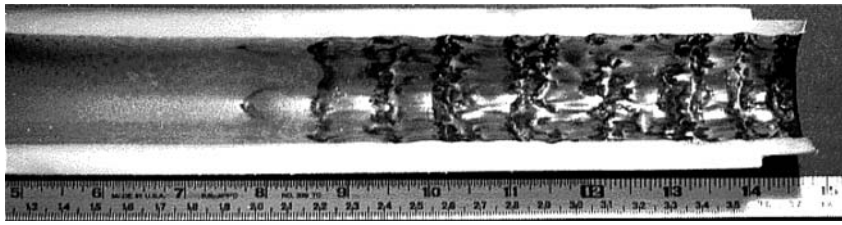

Fig. 17 Aft portion of motor H3 postfire fuel grain.

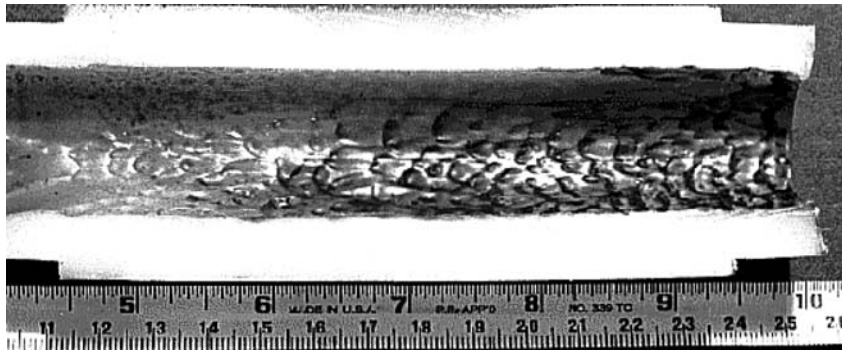

Fig. 18 Aft portion of motor M3 postfire fuel grain.

the solid material, in which case a thicker melt layer may develop, which may in turn flow and form the wavelike fuel surface condition.

Figures 18 and 19 show the aft portion of the M3 and M4 fuel grains, respectively. These motors are fired at identical operating conditions of ~400 psia chamber pressure as well as flux and initial port diameter. The only difference between these two motors is the LDPE type. Motor M3 is fired with LD-137 and motor M4 is fired with LD-149. As can be seen from Fig. 18 (LD-137), the increased chamber pressure again strongly influenced the inner port diameter surface. Figure 18 shows that there is again a transition port length, where upstream the fuel surface is smooth. The aft ~4.5 in. of fuel surface is rough with surface pitting (wavelike behavior in both axial and circumferential directions) in contrast to the repeating axial wave pattern experienced in the ~200 psia motors. This surface pitting is not observed in motor M4 as seen in Fig. 16. In fact, the surface of motor M4 is quite smooth. This is true for all of the motors fired with LD-149 in the M series (the only series fired with LD-149), whereas those fired with LD-137 experienced the random pocketing on the fuel surface. The only possible conclusion for this difference in posttest fuel surface is the melt behavior of the

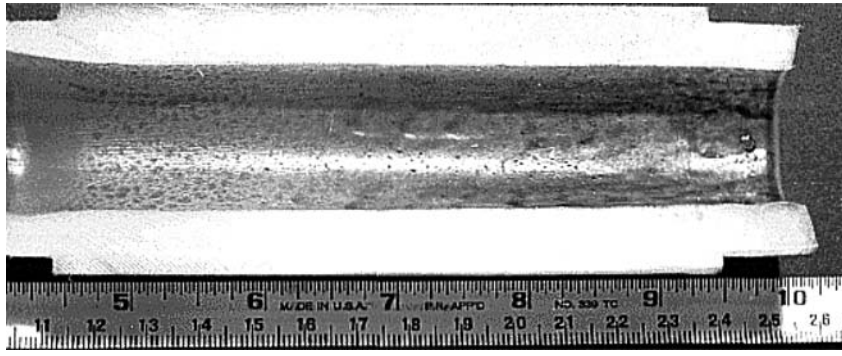

Fig. 19 Aft portion of motor M4 postfire fuel grain.

different materials. Material LD-149 exhibited a single-melt temperature in DSC testing (Fig. 2), whereas LD-137 had a double-melt temperature. It seems possible that the double-melt temperature permitted flow of the lower temperature melt layer before it could be depolymerized. The limited data from the M-series tests are insufficient to determine if these two materials experienced distinctly different fuel regression. However, the bulk fuel regression data do suggest that the two materials exhibit similar behavior.

VII. HP/DCPD Experience

A series of tests have recently been conducted to investigate combustion of HP with dicyclo-pentadiene (DCPD) fuels with and without LAH loadings. The DCPD fuel has the useful attributes of being hydrophobic and capable of encapsulating reactive ingredients such as LAH for long-term storage. Because LAH decomposes when exposed to atmospheric oxygen and moisture, these characteristics are particularly desirable. In theory, there are significant performance enhancements achievable using DCPD/LAH-loaded fuel grains as noted in the performance predictions shown in Fig. 20.

DCPD is an energetic, low-toxicity hydrocarbon that has potential as a propellant in liquid and solid applications, as well as in hybrids. Figure 21 shows the

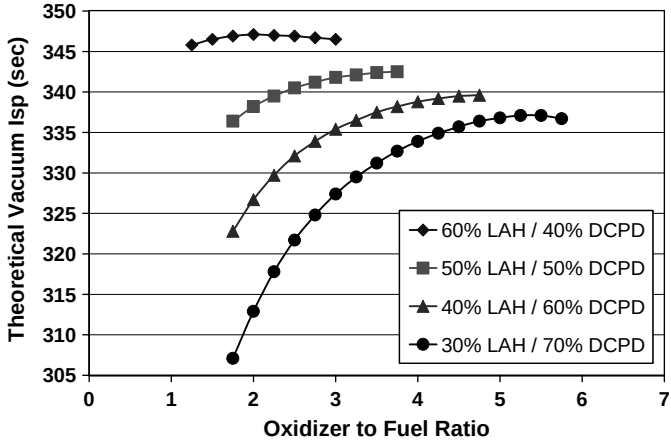

Fig. 20 Theoretical vacuum I_{sp} vs O/F ratio at varying LAH/DCPD loadings, $Pc = 1000$ psi and expansion ratio = 50.

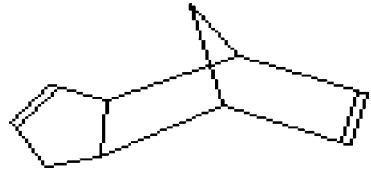

Fig. 21 DCPD monomer molecule.

Table 7 Physical characteristics of DCPD monomer

Characteristic	Value
Molecular formula	$C_{10}H_{12}$
Molecular weight	132.21 g/mole
Density	1.01 g/cm^3
Boiling point	170.1°C
Freezing point	33.65°C
Heat of formation	52.36 kcal/mole

molecular structure of the molecule. Table 7 presents physical data of the DCPD liquid monomer molecule.

As it polymerizes, DCPD undergoes ring opening metathesis polymerization. A ruthenium-based catalyst opens one of the cyclic rings of the monomer molecule and joins the molecule to an adjacent molecule. The polymerization is exothermic and produces 23.86 kcal of heat per mole of polymerized DCPD. The unaltered polymerization process is quite rapid. Gelation of the liquid DCPD can occur a few minutes after the addition of the catalyst, with the complete polymerization occurring in less than 1 h. The polymerization process can be accelerated or slowed by the addition of specified compounds. The speed of the polymerization determines the hardness of the polymer and the temperature of the exotherm. A faster curing time increases the hardness of the polymer and the temperature of its exotherm. The initial fluid temperature also affects the speed of the polymerization because the warmer the fluid, the faster the DCPD begins to gel. In this research, an inhibitor, triphenyl phosphine (TPP), is used to control the curing process and fuel-grain hardness. Five hardness levels were considered, varying from no use of TPP to 0.01–0.04 g of TPP/64 g of DCPD. More details on the manufacturing process used for the experiments is provided by Corpening [17].

A. LAH

LAH is a metal hydride, which, in addition to its use as a propellant, is used as a reducing agent and is being investigated as a source of hydrogen for fuel cells. It is a highly reactive compound, being both air and moisture sensitive. LAH reacts vigorously with water and is ignited by highly concentrated HP, burning with a distinctive red flame. LAH is also somewhat unstable in that it decomposes around 165°C, producing hydrogen gas. Table 8 presents physical data of LAH. Because of its sensitivity to air and moisture, LAH must be handled in a dry, inert atmosphere.

B. Test Apparatus

The combustion chamber was fabricated from schedule-40, 1.5-in. steel pipe. Figure 22 provides a schematic of the chamber indicating placement of fuel grain, a paper phenolic insulator, a silica/carbon phenolic nozzle, and a CCB [38] ignition system. Early tests of the chamber utilized a phenolic nozzle, whereas later tests employed a water-cooled nozzle design as shown in the schematic (Fig. 23). A

Table 8 Physical characteristics of LAH

Characteristic	Value
Molecular formula	$LiAlH_4$
Molecular weight	37.96 g/mole
Density	0.92 g/cm^3
Melting point	Decomposes around 165°C
Heat of formation	−26.2 kcal/mole

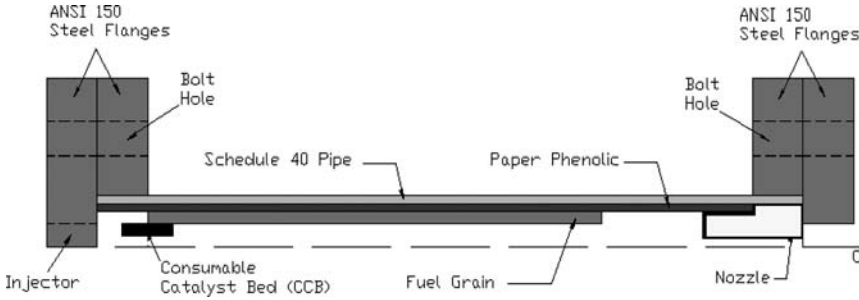

Fig. 22 Side cutaway view of hybrid engine design.

hollow cone swirl atomizer was employed to deliver the oxidizer at cone angles between 70 and 88 deg.

C. Test Results

A total of 22 tests were conducted in three distinct test series. Seven firings were conducted in series A to investigate the effect of TPP loading on grain hardness and combustion/regression characteristics at a fixed design mass flux of 0.6 lb/s · in^2. A total of nine firings were conducted in series B to investigate the effect of LAH loading between 20 and 50% of the fuel grain mass. Six firings were conducted

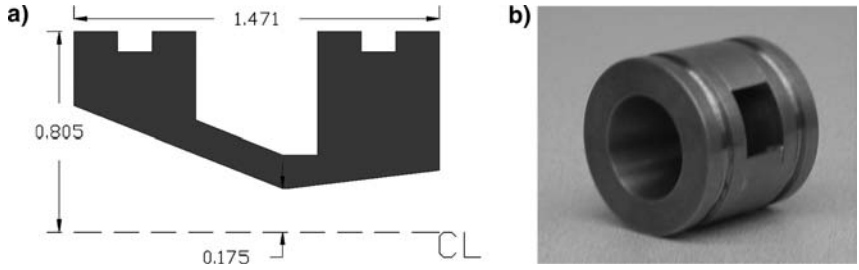

Fig. 23 Copper water-cooled nozzle, dimensions in inches; various throat diameter parts constructed to permit flux variations in testing: a) cutaway and b) image.

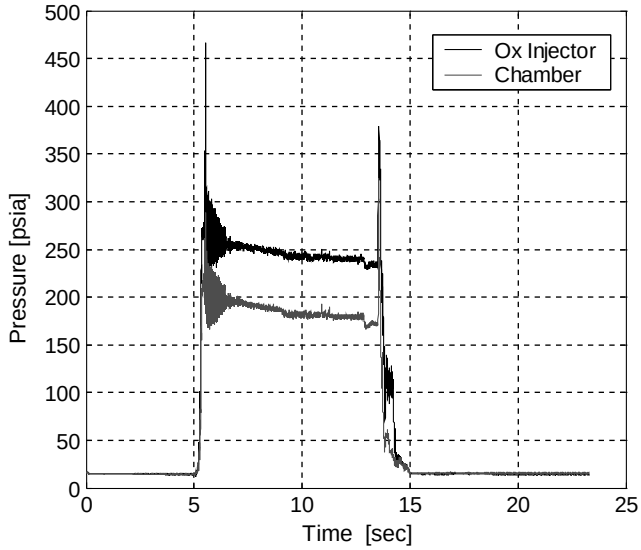

Fig. 24 Typical unfiltered system pressure data series A, test 2, using DCPD-only fuel grain.

in series C to evaluate DCPD regression dependence on flux level over a range of design flux levels from 0.2 to 0.7 $\mathrm{lb/s \cdot in^2}$. All testing was conducted at a target chamber pressure of 200 psi. Figure 24 shows a typical injector/chamber pressure trace from test series A. The spike at test onset is a water hammer effect on the pressure transducer, and the spike at test end is due to oxidizer depletion and nitrogen purge flowing through the engine.

Figure 25 shows the chamber pressure during engine ignition by the CCB. There is a significant noise level during the CCB consumption, higher than the noise observed during 80–90% peroxide tests of Wernimont [34]. A typical fast fourier transform (FFT) of the *Pc* data is shown in Fig. 26 with the attendant waterfall plot shown in Fig. 27. There are distinct peaks at 2.5 and 100 Hz and another smaller peak at 160 Hz. The 2.5- and 100-Hz activity is predominantly limited to the ignition event; no organized activity at any appreciable level is observed subsequent to CCB burnout. Calculations show that these frequencies correspond closely to bulk mode oscillations attributable to the filling of the CCB cavity and the chamber itself. Noise levels after ignition drop dramatically, and the combustion process is quite smooth. Combustion c^* efficiencies ranged from 90 to 98% during the series A testing.

The ballistic reconstruction technique of Wernimont and Heister [39] was used to reduce all test data. Figure 28 shows the integral averaged regression data for the five 98% RGHP/DCPD tests (solid line). The small dashed line represents data from HP/PE results reported in the preceding section. Finally, the large dashed line represents a typical regression rate correlation for GOX/HTPB [40]. Note that the regression rate correlations for the DCPD and PE tests use total mass flux, whereas

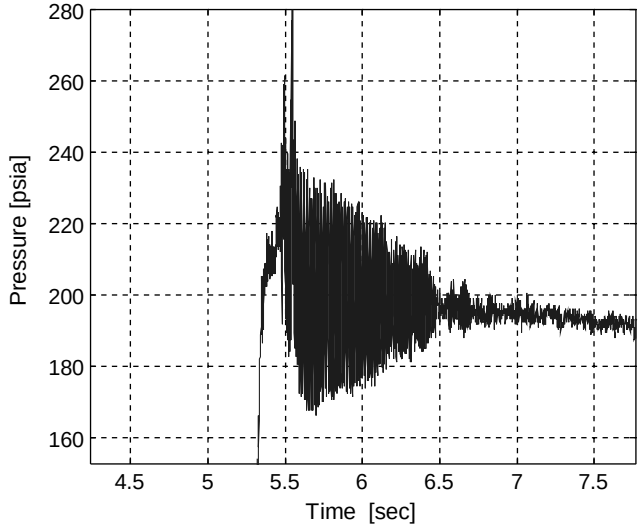

Fig. 25 Chamber pressure during CCB burn (engine ignition) from series A, test 2, DCPD-only fuel grain.

the correlation for GOX/HTPB uses only oxidizer mass flux. The increased energy associated with the 98% HP and the characteristics of the DCPD fuel provide regression rates comparable to the LOX/HTPB combination. Based on the limited flux range tested in this series, the regression rate correlation was $r \approx 0.065G^{0.19}$,

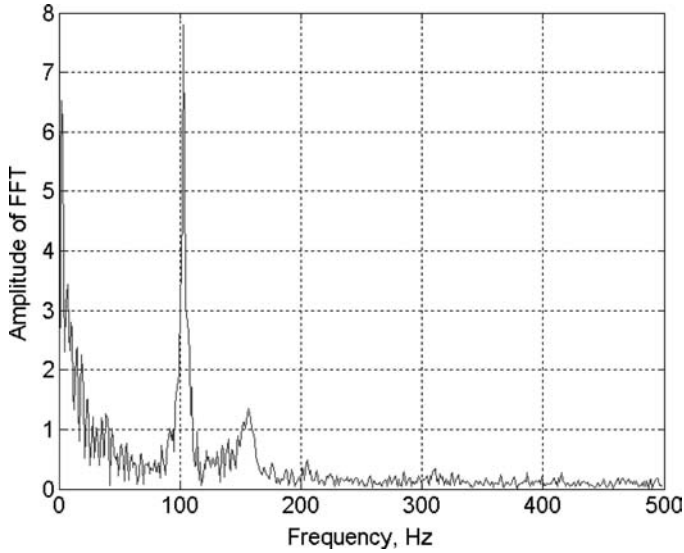

Fig. 26 FFT during ignition for series A, test 2.

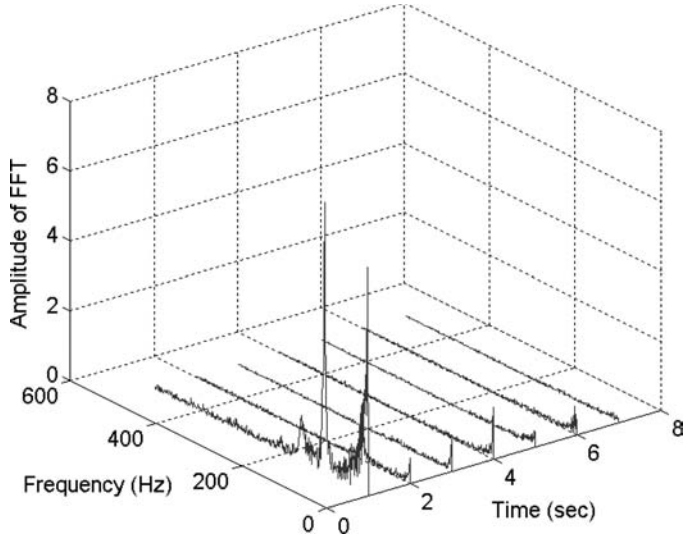

Fig. 27 Chamber pressure FFT waterfall plot for series A, test 2.

showing a very weak flux dependence relative to diffusion-dominated theory. This result is similar to the HP/PE data in that a radiation effect could be important with this propellant combination.

Test series B consisted of fuel grains with DCPD as the binder and a metal hydride additive, lithium aluminum hydride ($LiAlH_4$ or LAH), at various loadings.

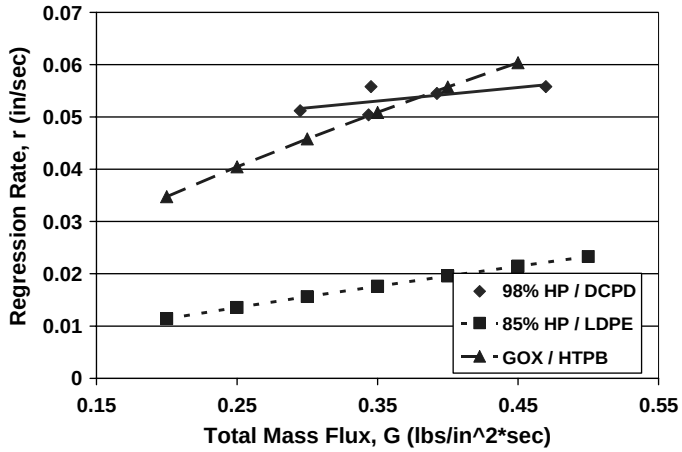

Fig. 28 Compilation of series A regression rate data and comparison with HP/PE experiments and GOX/HTPB regression rates.

Previous work conducted by Osmon [25] used 95% LAH with 5% PE in mechanically pressed grains. Therefore, the work herein differs from that of Osmon because of the different binder, lower LAH loadings, and the casting and curing process for the fuel grains. Series B results were disappointing in that very poor combustion efficiencies, ranging from 63 to 81%, were obtained. Osmon measured c^* efficiencies in the 80–86% range, and one test was able to replicate this level of performance and shows regression increase over pure DCPD grains. The relatively low-pressure levels employed in the testing may explain the poor combustion results. Because the LAH/DCPD fuel grains were formulated and cast without the use of vacuum loading, the process was time consuming and it was difficult to maintain completely nonreacted fuel specimens. This may have contributed to the low combustion efficiency from these firings. There were no visible gas pockets within any of the fuel grains, leading one to believe there were no gas releasing reactions occurring during the cure process. The L^* values based on the aft mixing volume and throat area ranged from 95 to 125 in. so that the aft mixing length is believed to have been sufficient. Further testing of the raw LAH by Swift Enterprises, Ltd. (after firing all LAH/DCPD fuel grains), has shown that the material used is 96% in the bulk LAH with the other 4% believed to be an oxide layer. This seems to be the most definitive cause for the drastically low combustion efficiencies and also explaining the small sparklike substances seen exiting the nozzle during LAH/DCPD testing.

Figures 29 and 30 provide system pressures during the firing and during the ignition transient for a typical series B firing. There seems to be significantly less noise during ignition for this propellant combination; the cause of the noise level

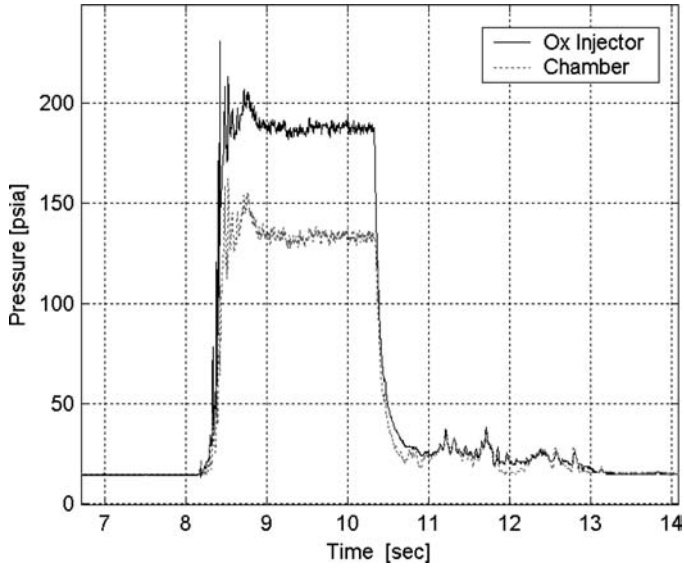

Fig. 29 Unfiltered system pressure data from series B, test 13, 40% LAH/60% DCPD.

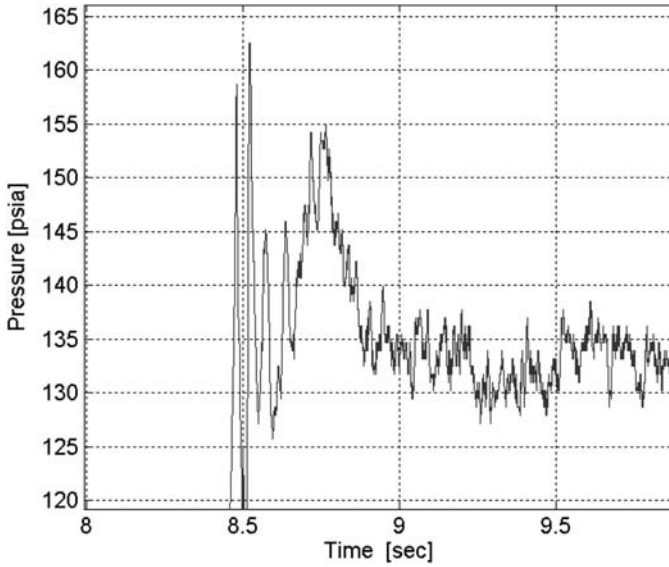

Fig. 30 Chamber pressure during engine ignition from series B, test 13, 40% LAH/60% DCPD.

change is not known at this time. Similar performance to the pure DCPD results is noted for the remainder of the firing.

Test series C incorporated pure DCPD grains with a new lot of cure catalyst and a fixed TPP loading. The combustion results for this series were also somewhat disappointing with c^* efficiencies ranging from 76 to 86%. Although manufactured with the same TPP loading as some series A grains, the series C grains were much harder and less pliable. A likely explanation was a variation in the ruthenium-based catalyst used to cure the DCPD. For series A, the ruthenium catalyst had been improperly sealed and, therefore, degraded over time. The catalyst used to make the DCPD grains for series C was properly sealed and stored; therefore, little-to-no degradation occurred. The result of this was that the fuel grains from series A were softer, even at the same TPP loading than those of series C. When the fuel grains of series A were cast using the poor catalyst, the reaction took longer, and therefore, the grains were softer. This then led to a misconception in softness based solely on TPP loading because it was assumed there were no difficulties with the catalyst. Therefore, using the proper catalyst for series C with the same TPP loading led to harder fuel grains.

The measured injector and chamber pressures in series C all resembled results from the series A testing. Regression data from series A and C are provided in Fig. 31. The fit of these data, excluding tests 21 and 22, yields $r \approx 0.0753G^{0.352}$, also pointing to the lower exponent that seems to be characteristic of HP hybrid combustion. This regression equation does not include the effects of tests 21 and 22 that were conducted at high flux levels and relatively small port size and aft-mixing length [17]. Note that the data are of tenuous use in that the associated

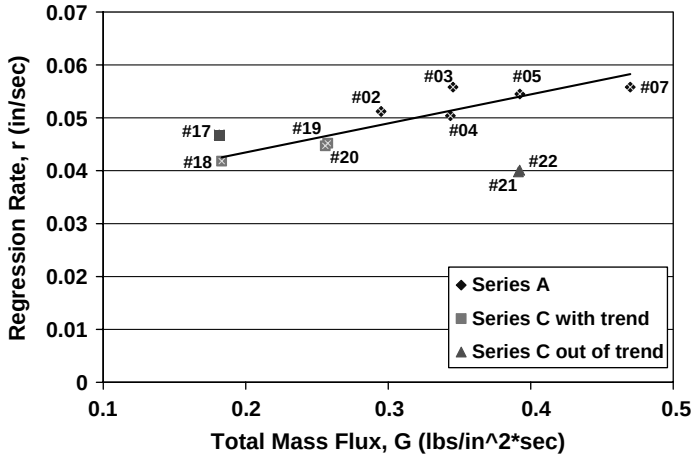

Fig. 31 Regression rate vs mass flux from series A and C, pure DCPD grains.

combustion was quite poor due to the suboptimal TPP loading associated with the series C catalyst.

VIII. Conclusions

Storable oxidizers have a long history of use in hybrid rocket applications. The advantages of storability, high-density impulse, and high O/F operation provide system-level simplifications for many applications. In addition, the monopropellant characteristics of some of the alternative storable oxidizers can provide substantial system-level advantages. Combustion with storable oxidizers has been most studied using nitric acid and HP, but substantial work has been undertaken with nitrous oxide and to a lesser extent HAN and its derivative formulations. Regression behavior and combustion efficiency are similar to that obtained using LOX. Storable oxidizers continue to provide an attractive alternative for many hybrid-propulsion missions.

References

[1] Chiaverini, M. J., Serin, N., Johnson, D. K., Lu, Y. C., Kao, K. K., and Risha, G. A., "Thermal Pyrolysis and Combustion of HTPB-Based Solid Fuels for Hybrid Rocket Motor Applications," AIAA Paper 96-2845, 32nd AIAA/ASME/SAE/ASEE Joint Propulsion Conference, Lake Buena Vista, FL, July 1996.

[2] Strand, L. D., Ray, R. L., Anderson, F. A., and Cohen, N. S., "Hybrid Rocket Fuel Combustion and Regression Rate Study," AIAA Paper 92-3302, 28th AIAA/ASME/SAE/ASEE Joint Propulsion Conference, Nashville, TN, July 1992.

[3] Ramohalli, K., and Yi, J., "Hybrids Revisited," AIAA 20th Joint Propulsion Conference, July 1990, p. 11.

[4] Greiner, B., and Fredrick, R. A., Jr., "Experimental Investigation of Labscale Hybrid Instability," AIAA Paper 94-2878, 30th AIAA/ASME/SAE/ASEE Joint Propulsion Conference, Indianapolis, IN, June 1994.

[5] Greiner, B., and Frederick, R. A., Jr., "Results of Labscale Hybrid Rocket Motor Investigation," AIAA Paper 92-3301, 28th AIAA/ASME/SAE/ASEE Joint Propulsion Conference, Nashville, TN, July 1992.
[6] Vanmeter, M., "Experimental Investigation of Hybrid Rocket Combustion Instabilities," M.S. Thesis, School of Aeronautics and Astronautics, Purdue Univ., LaFayette, IN, Aug. 2002.
[7] <http://www.magnumrockets.com/hypertek.html> 10 Aug. 1997.
[8] Macklin, F., Grainger, C., Veno, M., and Benson, J., "New Applications for Hybrid Propulsion," AIAA Paper 2003-5202, 39th AIAA/ASME/SAE/ASEE Joint Propulsion Conference, Huntsville, AL, July 2003.
[9] Altman, D., "Hybrid Rocket Development History," AIAA Paper 91-2515, 27th AIAA/ASME/SAE/ASEE Joint Propulsion Conference, Sacramento, CA, June 1991.
[10] Vonderwell, D. J., Murray, I. F., and Heister, S. D., "Optimization of Hybrid Rocket Engine Fuel Grain Design," AIAA Paper 94-3144, 30th AIAA/ASME/SAE/ASEE Joint Propulsion Conference, Indianapolis, IN, June 1994.
[11] Ventura, M., and Heister, S. D., "Hydrogen Peroxide as an Alternative Oxidizer for a Hybrid Rocket Strap-on Booster," *Journal of Propulsion and Power*, Vol. 11, No. 3, 1995, pp. 562–565.
[12] Clapp, M. B., and Hunter, M. W., "A Single Stage to Orbit Rocket with Non-Cryogenic Propellants," AIAA Paper 93-2285, June 1993.
[13] Schoonover, P. L., Crossley, W. A., and Heister, S. D., "Application of a Genetic Algorithm to the Optimization of Hybrid Rockets," *Journal of Spacecraft and Rockets*, Vol. 37, No. 5, 2000, pp. 622–629.
[14] Karabeyoglu, M. A., Zilliac, G., Castellucci, P., Urbanczyk, P., Stevens, J., Inalhan, G., and Cantwell, B. J., "Development of High-Burning-Rate Hybrid-Rocket-Fuel Flight Demonstrators," AIAA Paper 2003-5196, 39th AIAA/ASME/SAE/ASEE Joint Propulsion Conference, Huntsville, AL, July 2003.
[15] Humble, R. W., "Fuel Performance Enhancements for Hybrid Rockets," AIAA Paper 2000-3437, 36th AIAA/ASME/SAE/ASEE Joint Propulsion Conference, Huntsville, AL, July 2000.
[16] Corpening, J., Heister, S. D., Palmer, K., and Rusek, J. J., "Combustion of Advanced Non-Toxic Hybrid Propellants," AIAA Paper 2003-4595, 39th AIAA Joint Propulsion Conference, Huntsville, AL, 2003.
[17] Corpening, J., "Experiments on Combustion of Advanced Hybrid Rocket Fuels Using Hydrogen Peroxide Oxidizer," M.S. Thesis, School of Aeronautics and Astronautics, Purdue Univ., LaFayette, IN, May 2004.
[18] Ramohalli, K, and Dowler, W., "A Helping HAN for Hybrid Rockets," *Aerospace America*, Jan. 1995, pp. 20–21.
[19] Biddle, R. A., and Sutton, E. S., "Highly Soluble, Non-Hazardous Hydroxylammonim Salt Solutions for use in Hybrid Rocket Motors," U.S. Patent 4,527,389, 9 July 1985.
[20] Pugibet, M., and Moutet, H., "On the Use of Hydrogen Peroxide as Oxidizer in Hybrid Systems," *La Recherche Aerospatiale*, No. 132, 1969, pp. 15–31 (translation NASA, TTF-13034, May 1970).
[21] Moore, G. E., and Berman K., "A Solid–Liquid Rocket Propellant System," *Jet Propulsion*, Vol. 26, No. 11, 1956, pp. 965–968.
[22] Moore, G. E., and Cooper, F. M., "Propellant System," U.S. Patent 2791883, May 14, 1957.

[23] Moore, G. E., Driscoll, D. H., and Berman, K., "A Hybrid Rocket Propellant System: 90-Percent Hydrogen Peroxide/Solid Fuel; Part II," Technical Rept. R53A0509, General Electric, Schenectady, NY, July 1954.

[24] Moore, G. E., Driscoll, D. H., and Berman, K., "A Hybrid Rocket Propellant System: 90-Percent Hydrogen Peroxide/Solid Fuel; Part I," General Considerations, General Electric, Technical Rept. R52A0516, Schenectady, NY, July 1954.

[25] Osmon, R. V., "An Experimental Investigation of a Lithium Aluminum Hydride–Hydrogen Peroxide Hybrid Rocket," *Aerospace Chemical Engineering*, Vol. 62, No. 61, 1966, pp. 92–102.

[26] Wooldridge, C. E., and Muzzy, R. J., "Internal Ballistic Considerations in Hybrid Rocket Design," *Journal of Spacecraft*, Vol. 4, No. 2, 1967, pp. 225–261.

[27] Kosdon, F. J., and Williams, F. A., "Pressure Dependence of Nonmetalized Hybrid Fuel Regression Rates," *AIAA Journal*, Vol. 5, No. 4, 1967.

[28] Estey, P., Altman, D., and McFarlane, J., "An Evaluation of Scaling Effects for Hybrid Rocket Motors," AIAA Paper 91-2517, 27th AIAA/ASME/SAE/ASEE Joint Propulsion Conference, Sacramento, CA, June 1991.

[29] Wernimont, E. J., and Heister, S. D., "Performance Characterization of Hybrid Rockets Using Hydrogen Peroxide Oxidizer," AIAA Paper 95-3084, July 1995.

[30] Wernimont, E. J., and Heister, S. D., "Progress in Hydrogen Peroxide Oxidized Hybrid Rocket Experiments," AIAA Paper 96-2696, 32nd AIAA/ASME/SAE/ASEE Joint Propulsion Conference, Lake Buena Vista, FL, July 1996.

[31] Wernimont, E. J., and Heister, S. D., "Experimental Study of Chamber Pressure Effects in a Hydrogen Peroxide-Oxidized Hybrid Rocket," AIAA Paper 97-2801, 33rd AIAA/ASME/SAE/ASEE Joint Propulsion Conference, Seattle, WA, July 1997.

[32] Humble, R., and Sandfry, R., "HYSTAR Hybrid Rocket Program at the United States Air Force Academy," AIAA Paper 97-2797, 33rd AIAA/ASME/SAE/ASEE Joint Propulsion Conference, Seattle, WA, 1997.

[33] Caravella, J. R., Heister, S. D., and Wernimont, E. J., "Characterization of Fuel Regression in a Radial Flow Hybrid Rocket," *Journal of Propulsion and Power*, Vol. 14, No. 1, 1998, pp. 51–56.

[34] Wernimont, E. J., "Experimental Study of Combustion in Hydrogen Peroxide Hybrid Rockets," Ph.D. Dissertation, School of Aeronautics and Astronautics, Purdue Univ., West Lafayette, IN, Aug. 1997.

[35] Schwartz, S. S. and Goodman, S. H., *Plastics Material and Processing*, Van Nostrand Reinhold, New York, NY, 1982.

[36] Richardson, T. L., *Industrial Plastics: Theory and Practice*, 2nd ed., Delmar, New York, NY, 1989.

[37] Kroschwitz, J. I. (ed.), *Concise Encyclopedia of Polymer Science and Engineering*, Wiley, New York, NY, 1990.

[38] Wernimont, E. J., Meyer, S. E., and Ventura, M. C., "A Hybrid Motor System with a Consumable Catalytic Bed, A Composition of the Catalytic Bed and A Method of Using," U.S. Patent Application 08/623,937, filed 28 March 1996.

[39] Wernimont, E. J., and Heister, S. D., "Reconstruction Technique for Reducing Hybrid-Rocket Combustion Test Data," *Journal of Propulsion and Power*, Vol. 15, No. 1, 1999, pp. 128–136.

[40] Sutton, G. P., and Biblarz, O., *Rocket Propulsion Elements*, 7th ed., Wiley, New York, 2001, pp. 597–607.

This page intentionally left blank

Chapter 12

Similarity and Scaling Effects in Hybrid Rocket Motors

Alon Gany*
Technion—Israel Institute of Technology, Haifa 32000, Israel

Nomenclature

a = droplet acceleration; constant
C_F = thrust coefficient
c_p = specific heat at constant pressure
c^* = characteristic velocity
D = port diameter
d = droplet diameter
F = thrust
G = mass flux
g = standard gravity acceleration
h = heat transfer coefficient
I = impulse
I_{sp} = specific impulse
k = droplet evaporation rate constant; chemical kinetic constant
L = combustor (fuel grain) length
L_v = heat of vaporization or gasification
M = Mach number
m = mass
$\dot{m}$ = mass flow rate
Nu = Nusselt number
n = exponent
O/F = oxidizer-to-fuel mass ratio
Pr = Prandtl number
p = pressure
$\dot{q}$ = heat-transfer rate

*Professor, Lena and Ben Fohrman Chair in Aeronautical Engineering, Faculty of Aerospace Engineering; Head, Sylvia and David I.A. Fine Rocket Propulsion Center. Fellow AIAA.

R = specific gas constant
Re = Reynolds number
$\dot{r}$ = fuel regression rate
T = temperature
t_b = burning time
u = axial gas velocity
v = droplet velocity
α = exponent
λ = heat-conduction coefficient
μ = viscosity
ρ = density
τ = characteristic time

Subscripts

b = burning
c = average properties at the end of combustor
ch = chemical
drop = droplet
f = flame; fuel
hole = injector hole
i = initial
ig = ignition
in = injector
ℓ = liquid
ox = oxidizer
pen = penetration
res = residence
s = solid fuel
w = wall

I. Introduction

THE objective of this study is to present a similarity analysis and an experimental investigation to determine the conditions under which a laboratory-scale hybrid rocket motor should be tested to simulate firings of a full-scale system and to define the relevant scaling rules in hybrid propulsion. The research combines the means for better understanding of the fundamental phenomena along with saving time, effort, and costs in the development of full-scale hybrid-propulsion systems.

The hybrid motor comprises some unique features that differ fundamentally from those of other rocket engines. Typically, it consists of a cylindrical polymeric solid-fuel grain having a single- or multiport shape, placed in the combustor and burned with an oxidizer flowing through its ports. As a result, a gas-phase diffusion flame is established between the fuel gasification products and the oxidizer within the port flow boundary layer developing over the condensed surface. Typical hybrid motor geometry and the main combustion and flow characteristics are presented in Fig. 1. The fundamentals of hybrid combustion were studied by Marxman and Gilbert [1], Wooldridge and Muzzy [2], and Marxman [3], followed by many

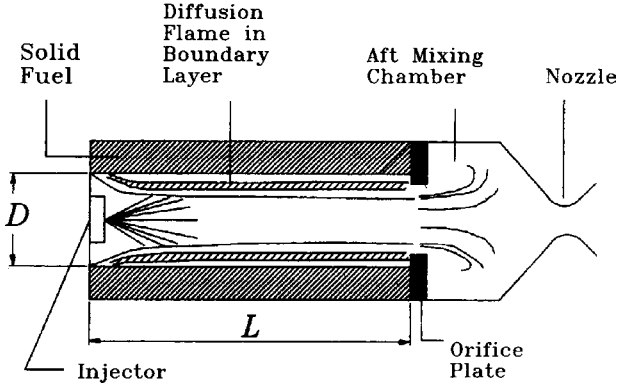

Fig. 1 Single-port hybrid rocket combustor schematic.

others, and reviewed in text books [4–6]. While giving quite good insight, those studies revealed complex phenomena affected by fuel and oxidizer combination, geometry, and size, as well as flow and operating conditions.

Typically, the development of hybrid rockets and the prediction of their characteristics have generally been based on simplified empirical methods and correlations. Consequently, different aspects might have been overlooked or masked, and the predictions have often been unsatisfactory, particularly for scaling purposes, where available data have been mainly applicable to the individual system tested.

The use of empirical correlations with many parameters and constants might involve misinterpretation of the true physical processes and, hence, erroneous predictions when extrapolating to unstudied ranges. The comprehensive study by Estey et al. [7] is a good example: It includes useful data and discussions and many different correlations, attempting to account for different aspects including scale effects. However, it demonstrates the limitations of parametric correlations aimed at extrapolation to different scales. Wooldridge and Muzzy [2], Chiaverini et al. [8], Evans et al. [9], George et al. [10], Carmicino and Russo-Sorge [11], and others have noticed the effect of the hybrid combustor size (mainly port diameter) on the fuel regression rate $\dot{r}$, showing, in general, that $\dot{r}$ tends to decrease with increasing port diameter (for the same mass flux). However, this effect has not been correlated in a way that enables prediction for different-size motors.

This author's view is that scaling rules between systems under consideration can and should be appropriately derived for conditions preserving similarity. In this respect, the present chapter raises a new conceptual approach to hybrid rocket motor testing for scaling purposes.

The main idea associated with similarity analysis is that, by identifying the appropriate similarity rules of the dominant, controlling processes, one can predict the likely results of a test in a system of a certain scale by way of the interpretation of data obtained from another experiment (in a different-scale system). In other words, one can define the conditions under which a laboratory-scale model system should be tested to simulate the behavior of a full-scale (or prototype) system.

Namely, the idea is not to replace experiments by an absolute theory, but to extend correctly and use available test data to untested systems of a different size range.

True similarity implies that the different processes occurring in two different-scale systems are of similar fashion. Namely, the values of the operating variables such as temperature, pressure, velocity, or concentrations in one system should be linearly related to those at the corresponding points of the other system. As was stated by Spalding [12], who dealt with general combustion systems, a complete combustion modeling that will fulfill the similarity rules of every process and effect is practically impossible. Hence, we actually seek a partial modeling that will preserve the rules of the most significant phenomena and provide reliable indication of the main trends. Such an analysis uses relatively simple concepts, and it concentrates on the dominant aspects, rather than on detailed mathematical modeling. Detailed discussion and guidelines on similarity and scaling in chemically reacting systems is presented by Rosner [13]. A number of similarity studies have been conducted in the field of airbreathing propulsion: Stewart [14] and Stewart and Quigg [15] investigated gas turbine combustors, Hottel et al. [16] studied liquid-fuel ramjet combustors, whereas Ben-Arosh and Gany [17] applied a comprehensive theoretical and experimental study to the solid fuel ramjet (SFRJ) combustor. Gany [18] proposed a detailed theoretical similarity model for the scaling of hybrid motors. At that time, no data from experiments directly aimed at similarity and scale analysis were available. Thus, the analysis was supported by data from the literature. Nevertheless, an experimental study aimed at validating the theoretical analysis was conducted later on by Swami and Gany [19] revealing good agreement.

The approach in the present study is to examine each individual process to assess its relative significance and to find out what should be the operating conditions that would preserve similarity of that process in a different-scale system. One can then determine the common conditions that satisfy the similarity rules of the most important individual processes, thus yielding the best practical approximation of the overall similarity of the system. The resulting rules are then applied for predicting scale effects, and experimental data are used to examine and validate the theory.

II. Analysis

A. Geometry

In general, an obvious similarity requirement is a geometric similarity. It means preserving constant ratio between linear dimensions in different motors. If the motor port diameter D is used to represent the scale, then L can be used to represent the motor (fuel grain) length,

$$L \propto D \tag{1}$$

One may use a single-port laboratory motor to simulate a multiple-port full-scale motor. Geometric similarity has been required and applied in similitude analysis of different combustors [14–19], although certain component processes may, in some specific cases, be simulated for systems whose dimensions are not scaled by the same proportion [12].

In the case of the hybrid motor combustor, the geometry directly affects the general flowfield pattern; thus, geometric similarity is a basic requirement. The developing boundary layer, which significantly affects the burning characteristics, is dominant within the combustor, along the solid-fuel grain, whereas the aft mixing chamber represents another flow zone (Fig. 1). Note, however, that unlike in other combustor types, the port diameter of the hybrid combustor increases during the combustion process as a result of the fuel regression, causing some deviations from the initial dimension proportions as well as from the scaling factor.

B. Transport Phenomena

Transport phenomena are of major significance in the overall flow and combustion process in hybrid rocket motors. They affect the flow pattern, boundary layer, heat transfer to the surface, diffusion, mixing, and flame characteristics. Hybrid motors are characterized by a turbulent internal flow with dominant boundary-layer effects. Hence, the most significant parameter that dominates the flow and transport phenomena is Reynolds number *Re*. Similarity of those features can be achieved by requiring the same Reynolds number at corresponding cross sections of the related motors,

$$Re = \rho u D/\mu = \text{const} \tag{2}$$

C. Heating Regime

Similarity of heating regime requires constant ratio between the heat transfer to the wall and the overall heat generation, that is, the rate of heat addition to the flow. The heat transfer in hybrid combustors is mainly attributed to turbulent forced convection with minor contribution of radiation. This is the case for polymeric-fuel grains, which are considered the main subject of the present research. (For metallized fuels, radiation may play a more significant role in the heat transfer process.) Accounting for the fact that both the burning surface and the flow cross-sectional area are proportional to D^2, one obtains

$$h\left(T_f - T_w\right) D^2 \propto \rho u D^2 c_p \left(T_c - T_i\right) \tag{3}$$

where T_i is the initial temperature, T_c is the final average temperature at the end of the motor, T_f is the flame temperature, and T_w is the wall (surface) temperature. The left-hand-side term in Eq. (3) represents the heat transfer to the wall (taking into account that $L \propto D$), whereas the right-hand-side term stands for the rate of heat generation (the rate of heat addition to the flow).

If similarity of the temperature field is maintained, which also implies similar physical properties in corresponding points in the flowfield, then Eq. (3) implies constancy of Nusselt number, $Nu = hD/\lambda$. In the characteristic combustor regime, this requirement is fulfilled by the constancy of Reynolds (and Prandtl) numbers, since $Nu = f(Re, Pr)$; for example, in a fully developed turbulent pipe flow,

$$Nu = 0.023\, Re^{0.8}\, Pr^{0.33} \tag{4}$$

and $Pr = \mu c_p/\lambda$ represents a combination of physical properties.

The diffusion flame nature of the combustion process in hybrid motors emphasizes the significance of constancy of Reynolds number in corresponding sections as a result of the domination of physical processes and properties vs chemical aspects.

D. Chemistry Aspects

Similarity of chemical kinetics requires similarity of the temperature and species concentration fields. This requirement is particularly significant, considering the highly nonlinear nature of the Arrhenius-type gas-phase chemical kinetic constant, $k = A\exp(-E/R_0T)$. Because of the establishment of a diffusion flame, which tends to take place at the location of stoichiometric oxidizer to fuel O/F ratio, T_f is basically close to the adiabatic flame temperature at this O/F ratio (somewhat less because of heat losses) and is not a direct function of the overall O/F ratio.

Different fuel and oxidizer combinations exhibit different stoichiometric O/F ratios and different heats of combustion. In addition, the supply rate of fuel gases (directly related to the solid-fuel regression rate) is inversely proportional to the heat of gasification or decomposition of the solid fuel. When the complexity of the process is considered, an obvious requirement of the present model would be the use of the same fuel and oxidizer combination as well as constant overall oxidizer to fuel ratio

$$O/F = \text{const} \tag{5}$$

Note, however, that in contrast to liquid-fuel combustors, where the fuel flow is a controllable variable, it is not directly controlled in the hybrid combustor, and the validity of the requirement of the same O/F is yet to be proved.

Some specific aspects may yield additional requirements. Characteristic chemical reaction time of hydrocarbon fuels is known to be inversely proportional to pressure, $\tau_{\text{ch}} \propto 1/p$. A similar trend is exhibited by the ignition delay time τ_{ig}. On the other hand, residence time can be approximated by $\tau_{\text{res}} \propto D/u$. Constancy of the ratio $\tau_{\text{res}}/\tau_{\text{ch}}$ leads to

$$(pD)/u = \text{const} \tag{6}$$

which is also known to fulfill similarity of flameholding characteristics.

Satisfying Eq. (6) along with constant Reynolds number would yield

$$pD = \text{const} \tag{7}$$

as well as a similar velocity field.

It is worth noting that the so-called pD scaling [expressed by Eq. (7)] is one of the most useful scaling techniques for airbreathing combustors [12, 14–16] and has also been proven to yield good results for SFRJ combustors [17]. However, in spite of the similarities between SFRJ and hybrid motors, one should carefully evaluate the significance and relevancy of pD scaling to hybrid propulsion.

E. Compressibility

Maintaining similarity of compressibility effects is expressed by constancy of Mach number in corresponding points. With $M = u/\sqrt{\gamma RT}$, such a requirement would be fulfilled for simultaneous existence of similarity of velocity and temperature fields.

F. Liquid Phase and Injector Characteristics

Classical hybrid motors consist of the injection of an oxidizer in either gaseous or liquid form. When a liquid oxidizer is used, its special characteristics should be considered in the light of their effects on the overall combustion process.

1. Droplet Life Time

Droplet life time (or burning time) is mainly a result of its evaporation time. To maintain similarity between systems of different scales, one should require that the droplet evaporation/burning (life) time τ_{drop} be proportional to the combustor residence time τ_{res}. Generally, droplet lifetime can de derived from the d^2-consumption law, yielding

$$\tau_{\text{drop}} = d^2/k \tag{8}$$

where d is the droplet initial diameter and k is the burning rate constant. Because the combustor residence time is $\tau_{\text{res}} = L/u$, the requirement for $\tau_{\text{drop}}/\tau_{\text{res}} = \text{const}$ in similar systems yields

$$ud^2/kL = \text{const} \tag{9}$$

Now, the droplet burning rate constant k is known to have a weak dependence on pressure, which can be approximated by

$$k \propto p^{\alpha} \tag{10}$$

with α of the order of $\frac{1}{4}$. Substituting Eq. (10) in Eq. (9) for $\alpha = 1/4$ gives

$$ud^2/p^{1/4}L = \text{const} \tag{11}$$

as was also the conclusion of Stewart [14] for droplet combustion. Note that when combining the geometric similarity as well as constancy of Reynolds number to Eq. (11) one obtains

$$d^2/p^{5/4}D^2 = \text{const} \tag{12}$$

which yields the desired proportion between droplet size, combustor dimension, and operating pressure when scaling hybrid combustors

$$d \propto D \cdot p^{\frac{5}{8}} \tag{13}$$

One can further show that if pD constancy exists, the result is

$$d \propto p^{-\frac{3}{8}} \tag{14}$$

or

$$d \propto D^{\frac{3}{8}} \tag{15}$$

For large (long) motors, droplet lifetime may not have a great effect. However, in laboratory-scale motors, droplet size and lifetime may be quite significant.

2. Spray Momentum and Penetration

Spray momentum has some effect on the flow structure and droplet penetration due to injection. The characteristic penetration distance can be derived from the droplet size and injection velocity v_{in}. Approximating the droplet drag coefficient by $C_D = 24/Re_{\text{drop}}$ where

$$Re_{\text{drop}} = \rho|v - u|d/\mu \tag{16}$$

one obtains the droplet deceleration at the initial stage, where $u \approx 0$,

$$a = 18\mu v_{\text{in}}/\rho_\ell d^2 \tag{17}$$

The characteristic penetration distance is defined as $L_{\text{pen}} = v_{\text{in}}^2/2a$. Requiring for similarity the same proportion between the penetration distance and the motor length, one obtains

$$v_{\text{in}} d^2/D = \text{const} \tag{18}$$

This relationship may impose constraints on the pressure drop Δp over the injector. Because $v_{\text{in}} \propto \sqrt{\Delta p}$, then

$$\Delta p \propto D^2/d^4 \tag{19}$$

Introducing the similarity requirement for droplet lifetime [Eq. (13)] where $Re = \text{const}$, one obtains

$$\Delta p \propto D^{-2} p^{-2.5} \tag{20}$$

In cases fulfilling the pD similarity condition (14) and (15), Δp would vary according to

$$\Delta p \propto p^{-0.5} \tag{21}$$

$$\Delta p \propto D^{0.5} \tag{22}$$

Note, however, that the pressure drop itself affects the droplet size: Higher Δp usually causes smaller droplet size. Thus, the situation would be generally better for larger motors. In addition, typically spray momentum and penetration distance would be less significant than droplet lifetime.

3. Injector

The constancy of Reynolds number as a similarity requirement yields the mass flow rate proportion

$$\dot{m} \propto D \tag{23}$$

which, for the same O/F ratio, means also

$$\dot{m}_{ox} \propto D \tag{24}$$

When a multihole, for example, shower head, injector is used, one may ask whether the number of injector holes can be retained when scaling the system. In certain cases the injector hole diameter may be proportional to the droplet size. In such cases,

$$\dot{m}_{hole} \propto vd^2 \tag{25}$$

When the penetration similarity criterion (18) is maintained, Eq. (25) becomes

$$\dot{m}_{hole} \propto D \tag{26}$$

This is exactly the same proportion of the overall flow rate. Hence, in cases described by Eq. (25), preserving spray penetration similarity would also preserve the number of injector holes.

III. Model Discussion

Best fulfillment of similarity requirements would be obtained for the following conditions: 1) geometric similarity; 2) same fuel and oxidizer combination; 3) same Reynolds number at corresponding sections; 4) same value of pD in model and prototype; 5) requiring droplet diameter in proportion to $Dp^{5/8}$, for conditions fulfilled by item 4, the droplet diameter should be scaled according to $d \propto D^{\frac{3}{8}}$; and 6) scaling of injector pressure drop according to $\Delta p \propto D^{-2}p^{-2.5}$, for conditions fulfilled by item 4, the requirement becomes $\Delta p \propto D^{0.5}$.

Under these conditions, equality of O/F ratio, Prandtl number, and Mach number would also take place.

At this point one should evaluate the relative significance of the listed requirements, seeking a partial similarity modeling that will preserve the most significant phenomena and indicate the main trends in actual systems. Such consideration would point out whether any of the listed similarity requirements may be relaxed for practical scaling purposes. The six given requirements will now be examined one by one:

1) In general, the geometry requirement should be kept, otherwise the systems will not be really similar. Nevertheless, the sensitivity of fuel regression rate predictions to small deviations in this parameter may be within satisfactory limits. Hence, if it is only for the regression rate, some deviation of the motor length from the scale factor may be tolerated. On the other hand, the overall O/F ratio as well

as performance parameters, for example, c^*, I_{sp}, F, are quite sensitive to the L/D ratio.

2) Same fuel and oxidizer are mandatory. It would be very difficult to interpret test results of different combinations.

3) It appears that because of the greater significance of the physical processes than chemical aspects in the hybrid system, for example, diffusion flame characteristics, turbulent transport phenomena, droplet dynamics, and combustion, Reynolds number is the most significant similarity operating parameter. Constancy of Reynolds number in systems under similarity conditions implies

$$GD = \text{const} \tag{27}$$

$$\dot{m}/D = \text{const} \tag{28}$$

Since

$$\dot{m} = \dot{m}_{ox}[(1 + O/F)/(O/F)] \tag{29}$$

and $O/F = \text{const}$ under similarity conditions, one obtains the following [see also Eqs. (23) and (24)]:

$$G_{ox}D = \text{const} \tag{30}$$

$$\dot{m}_{ox}/D = \text{const} \tag{31}$$

4) Constancy of pD is a very strong requirement that has been found to be the major similarity condition in airbreathing combustors. Its main implication is in keeping similarity of chemistry aspects in gas-phase reactions (and, in addition similarity of Mach number). Here, pD scaling is supposed to result in the same combustion efficiency. However, because physical rather than chemical aspects dominate the hybrid combustor processes, this requirement may be relaxed, provided that a) requirement 3, that is, the same Reynolds number, is fulfilled; b) the pressure is sufficiently high, so that chemical kinetics are much faster than physical transport, for example, diffusion; and c) an aft mixing chamber would take care of completing the gas-phase chemical reactions. Indeed, most investigators have not noticed any pressure effects at regular operating pressures, and only at low pressures or at very high mass fluxes regression rate sometimes seems to exhibit some pressure dependence [2–7, 20, 21]. It is assumed here that a pure polymeric fuel is used. If some oxidizer is incorporated in the fuel grain, then one may expect certain pressure effects.

5) This droplet diameter requirement is irrelevant if the system employs a gaseous oxidizer. When the oxidizer is in liquid form, this requirement is mainly intended to ensure proper operation of small motors by seeking smaller oxidizer droplets. The requirement may be relaxed for low-heat-of-evaporation oxidizers such as liquid oxygen (LOX) (or when the spray consists of very small droplets), but may be quite significant for small motors operating with high-heat-of-evaporation oxidizers, for example, nitric acid, hydrogen peroxide, whose droplets lifetime is relatively long. Calculations conducted by Gany et al. [22] for a 1-m-long hybrid combustor revealed that whereas the former complete their evaporation at a short

Table 1 Boiling temperature and heat of evaporation of selected oxidizers

Oxidizer	Boiling point at 20 atm, K	Heat of evaporation, J/kg
O_2	134	2.14×10^5
N_2O_4	384	4.15×10^5
RFNA[a] ($85\%HNO_3 + 15\%N_2O_4$)	456	5.76×10^5
H_2O_2	550	13.89×10^5

[a]Red fuming nitric acid.

distance relative to the combustor length, the latter may be only partially evaporated at the end of the fuel grain. Properties affecting evaporation rate of several liquid oxidizers are summarized in Table 1.

6) This requirement is again relevant only for liquid and not gaseous oxidizer. Penetration distance seems to be of small significance unless one deals with very small motors. Gany [23] showed that injected droplets of typical sizes approach the surrounding gas velocity after a relatively short distance. One can conclude that this similarity requirement may be relaxed without affecting the overall process significantly.

In summary, the minimum and most significant operating conditions that maintain the most dominant similarity parameters and should be kept when scaling hybrid rocket motors are as follows: geometric similarity, namely, $L \propto D$; same fuel and oxidizer combination; scaling the oxidizer flow rate in proportion to the length scale (port diameter), that is,

$$\dot{m}_{ox} \propto D \qquad \text{or} \qquad G_{ox} \propto D^{-1}$$

IV. Theoretical Model Predictions

Maintaining the preceding mentioned three main operating conditions, one would expect the following relations between parameters of different-scale systems.

A. Fuel Regression Rate

The regression rate $\dot{r}$ is the most significant internal ballistics parameter of hybrid motors. In common polymeric fuels, it is dominated by convective heat transfer to the wall and by the heat of gasification of the fuel according to

$$\dot{r} = \dot{q}_w/(\rho_s L_v) \tag{32}$$

(For metallized fuels, radiation effect may not be negligible, whereas for liquefying fuels such as paraffin, additional effects should be taken into account.)

For dominant convective heat transfer,

$$\dot{q}_w = h(T_f - T_w) \tag{33}$$

For similar temperature fields and equal T_f, T_w, and gas properties, one obtains the same Nusselt number, which can be expressed as follows:

$$Nu \propto Re^n Pr^{0.33} \tag{34}$$

With Prandtl number $Pr = \text{const}$ (because of the equal gas properties) and relating h to Nusselt number Nu, one can show that

$$\dot{r} \propto G^n D^{n-1} \tag{35}$$

When operating under similarity conditions, one does not have to assume the most appropriate value of n, nor does one have to have information on possible variations along the grain or whether or not the boundary layer is fully developed. With $GD = \text{const}$, the result would anyway be expected as

$$\dot{r}D = \text{const} \tag{36}$$

or

$$\dot{r} \propto 1/D \tag{37}$$

Note, that under similarity conditions with $GD = \text{const}$ and $\dot{r}D = \text{const}$, the ratio between the perpendicular mass flux from the gasifying fuel at the wall $\rho_s \dot{r}$ and main axial flow mass flux G remains constant, implying similarity of blowing effect on the heat transfer (see Marxman and Gilbert [1]).

B. Oxidizer/Fuel Ratio

The oxidizer/fuel ratio is defined as

$$O/F = \dot{m}_{\text{ox}}/\dot{m}_f \tag{38}$$

According to the similarity analysis, $\dot{m}_{\text{ox}} \propto D$. The fuel flow rate,

$$\dot{m}_f = \rho_s \dot{r} A_b \tag{39}$$

Because the burning surface $A_b \propto D^2$ and the regression rate $\dot{r} \propto D^{-1}$, one expects that under similarity conditions

$$\dot{m}_f \propto D \tag{40}$$

This result indicates that the overall O/F ratio is expected to remain the same for hybrid systems under similarity conditions. As already stated, constant O/F is an important, but not directly controlled factor in keeping with other similarity parameters.

C. Energetic Performance and Thrust

For equal O/F, the theoretical characteristic velocity should not change, that is,

$$c^* = \text{const} \tag{41}$$

As regards the theoretical specific impulse, it can be expressed by

$$I_{\text{sp}} = C_F c^*/g \tag{42}$$

and is supposed to stay approximately the same,

$$I_{\text{sp}} \approx \text{const} \tag{43}$$

except for slight variations in C_F resulting from variations in operating pressure.

Thrust would roughly scale with motor size,

$$F \tilde{\propto} D \tag{44}$$

as a result of the correlation $F = C_F c^* \dot{m}$.

Because the fuel grain mass is scaled according to

$$m_f \propto D^3 \tag{45}$$

then, with $O/F = \text{const}$ (implying overall propellant mass is also proportional to D^3) and $I_{\text{sp}} \approx \text{const}$, the overall motor impulse is expected to scale according to

$$I \tilde{\propto} D^3 \tag{46}$$

D. Burning Time

Fuel regression during the burning process causes continuously increasing deviation from the initial geometric proportions of the hybrid combustor. Thus, systems that initially maintain similarity conditions may violate the scaling rules during the overall process. The problem can be minimized by either conducting short experiments or by scaling the combustion time appropriately. Because $\dot{r}$ is proportional to D^{-1} and

$$D = D_0 + 2\dot{r}t_b \tag{47}$$

then, for maintaining the same geometric proportions between the model and prototype systems over the burning time, the firing test duration should be scaled according to

$$t_b \propto D^2 \tag{48}$$

This is an important operating result that should be accounted for when performing firing tests. Its implications will be further discussed later. Note that Eq. (48) also reveals the overall burning time of different systems under similarity conditions.

E. Combustion Efficiency

As mentioned before, combustion efficiency in hybrid motors is affected to a large extent by the aft mixing chamber. In principle, the mixing chamber should be scaled according to *pD* scaling. However, if this condition is not maintained, one should use a large enough aft mixing chamber to obtain satisfactory combustion efficiency in all tests.

V. Experimental Research and Validation of Theory

Numerous available test data of hybrid motor firings have been reviewed to compare them to the theory. No parametric investigation purposefully oriented toward maintaining similarity of operating conditions when testing different-scale motors has been found. Nevertheless, over the ranges tested, a number of systems reported in the literature were found to maintain the most significant similarity conditions, namely, geometric similarity, same fuel and oxidizer combination, and $GD = \text{const}$ or $G_{ox}D = \text{const}$. These test results from the literature will be presented first, yielding a limited but valuable comparison to theory with regard to one of the main parameters: dependence of regression rate $\dot{r}$ on port diameter D for systems preserving similarity.

Nevertheless, to obtain a more comprehensive database, a special test program aimed at studying scale effects under similarity conditions was conducted by Swami and Gany [19]. Its description and results will then follow.

A. Comparison to Data from the Literature

Table 2 presents experimental results obtained from three test programs employing different systems as regards size range, operating conditions, and oxidizer/fuel combination: gaseous oxygen plus polymethylmethacrylate (PMMA) (Wooldridge and Muzzy [2]), gaseous oxygen plus hydroxyl-terminated polybutadiene (HTPB) (Ramohalli et al. [24]), and liquid hydrogen peroxide plus polyethylene (PE) (Wernimont and Heister [25]). The data have been grouped for each propellant combination in more or less equal GD or $G_{ox}D$ values to examine the resulting $\dot{r}D$ values, which are predicted by the present similarity/scaling theory to remain constant under these conditions. Note that in none of these test series has the chamber pressure been scaled according to the theoretical similarity requirement ($pD = \text{const}$). As was mentioned before, pressure does not seem to play any significant role in the ranges tested. This fact justifies relaxing the similarity requirement of constancy of pD (requirement 4), as was already discussed.

The data of Table 2 have been used to examine the theory both for gaseous oxidizer and for liquid oxidizer systems. Figure 2, which presents the dependence of regression rate $\dot{r}$ on port diameter D, demonstrates an excellent agreement between the present theory and data of Wooldridge and Muzzy [2] on hybrid motors employing gaseous oxygen plus PMMA at different $G_{ox}D$ levels. Figure 3 exhibits a similar comparison between the present theoretical model and test results of Wernimont and Heister [25] from a hybrid system employing liquid H_2O_2 plus PE. In this case, many individual test points of more or less equal GD level closely

Table 2 Summary of experimental results preserving *GD* scaling

Oxidizer	Fuel	D, cm	L, cm	L/D	G, g/s · cm^2	$\dot{r}$, mm/s	GD, g/s · cm	$\dot{r}D$, mm^2/s	Ref.	Comments
O_2(g)	PMMA	5.1	51	10	56	2.0	286	102	[2]	Data points were reduced from experimental correlation. Pressure = 500 psia G = oxidizer mass flux
		10.2	102	10	28	0.97	286	99		
		20.3	203	10	14	0.51	286	104		
		5.1	51	10	14	0.76	71.5	38.8		
		10.2	102	10	7	0.38	71.5	38.8		
		20.3	203	10	3.5	0.18	71.5	36.5		
		5.1	51	10	2.8	0.20	14.3	10.2		
		10.2	102	10	1.4	0.97	14.3	9.9		
		20.3	203	10	0.7	0.05	14.3	10.2		
O_2(g)	HTPB	1.3			10.5	0.84	13.4	106	[24]	Wide spread of test points. Pressure: 45–200 psia G = oxidizer mass flux
		2.5			5.3	0.53	13.4	135		
		3.8			3.5	0.22	13.4	106		
$H_2O_2(\ell)$	PE	1.8	36.6	20.1	21.5	0.34	39.1	6.1	[25]	Actual experimental points. Pressure: 74–92 psia G = total mass flux in this set
		1.9	36.6	19.2	21.6	0.30	41.5	6.0		
		2.2	36.6	16.6	18.2	0.28	40.2	6.3		
		2.2	19.5	8.8	17.5	0.27	39.1	6.1		
		2.2	26.5	11.9	18.0	0.26	40.0	6.0		
		2.5	36.8	14.6	15.2	0.21	38.6	5.4		
		2.6	36.8	14.4	15.1	0.23	39.0	6.0		
		3.2	36.3	11.5	12.9	0.18	40.9	5.8		

g = gas, ℓ = liquid.

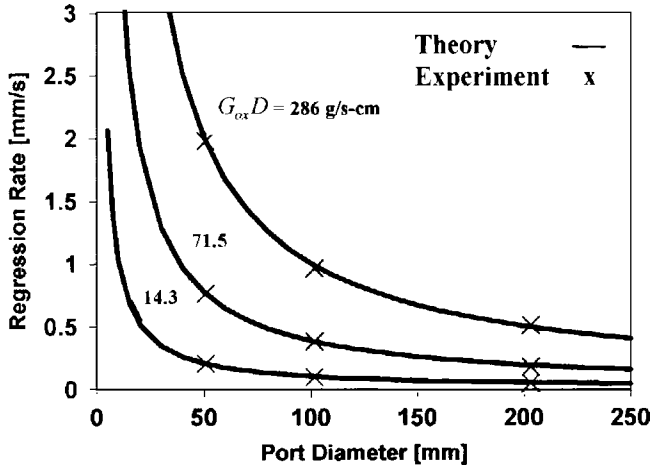

Fig. 2 Regression rate $\dot{r}$ vs port diameter D for hybrid motors maintaining similarity of operating conditions: present theory and data of Wooldridge and Muzzy [2] on GOX+PMMA systems at different $G_{ox}D$ levels.

agree with the theoretical curve. The tests by Wernimont and Heister [25] did not generally preserve constant L/D ratio. As discussed before, it is obvious though that the L/D ratio has only a minor effect on the average fuel regression rate (unless extremely short grains are used).

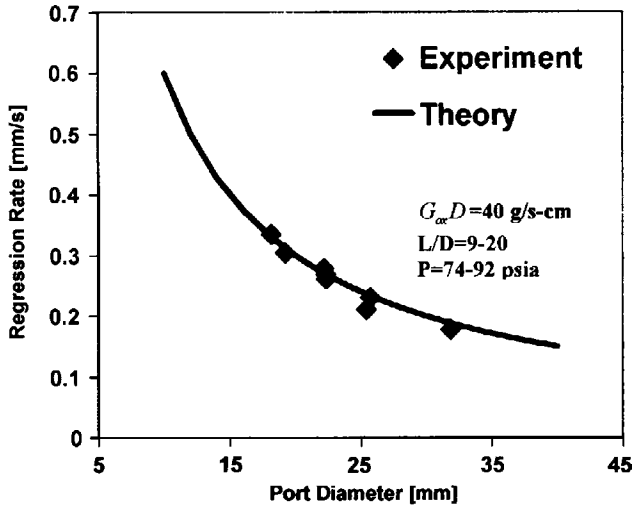

Fig. 3 Regression rate $\dot{r}$ vs port diameter D for hybrid motors scaled under similarity conditions: present theory and test results of Wernimont and Heister [25] for liquid H_2O_2 + PE system.

B. Comprehensive Experimental Similarity/Scaling Research

As mentioned before, because of the limited test data in the literature that could be related to systems scaled under similarity conditions, we conducted a focused test program to examine a wide scope of the similarity and scaling theory and to form a comprehensive database [19].

A schematic of the test facility with the motor and its associated control units is presented in Fig. 4. To permit the use of different size motors, the test facility was built as a modular unit. PMMA (Plexiglas®) was used as the fuel grain, and gaseous oxygen (GOX) was used as an oxidizer in all of the tests. The fuel grain was placed after the oxygen inlet at the head end and ended before the aft mixing chamber. The other end of the aft mixing chamber was attached to a converging nozzle assembly. The ignition of the motor was achieved by injecting a small amount of ethylene in the inlet oxygen flow for about 300 ms and igniting the resulting oxygen/ethylene mixture using a spark plug. After ignition, the ethylene flow and spark plug were turned off. The whole setup was mounted on a thrust stand. During the tests, the oxygen and ethylene flow rates (measured by choked nozzles in their supply lines), motor and aft mixing chamber pressures, and the thrust were continuously recorded.

Motors having initial port diameters of 7.5, 10, 15, 23, 34, and 40 mm, that is, fivefold diameter ratio, approximately, and initial geometric proportions, length-to-port diameter ratio, $L/D = 10$, were tested. The chamber pressure was always higher than 25 bar in all of the tests.

The average fuel regression rate was calculated from the overall mass loss and the burn time. In general, average values of the different parameters recorded during the motor operation, including the motor port diameter, were used to represent the experimental results. Motor test duration was scaled linearly with motor initial port diameter, that is, $t_b \propto D$, up to a maximum value of 16 s for motors of initial port diameter equal to or higher than 34 mm. This was a compromise between the desire for the same relative final port diameter, which requires burn time in proportion to D^2, and the negative aspects resulting from too long burn times and relatively large variations from the initial dimensions and proportions.

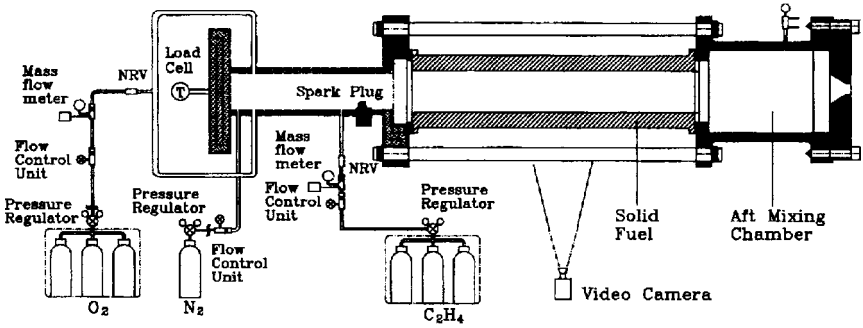

Fig. 4 Hybrid rocket test setup (after Swami and Gany [19]).

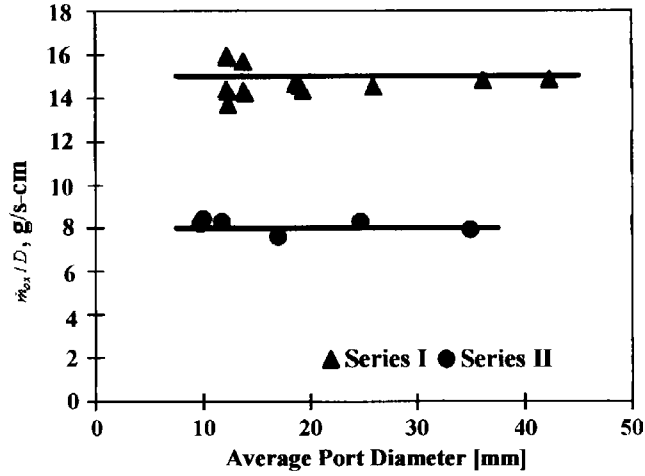

Fig. 5 Actual test conditions showing approximately constant $\dot{m}_{ox}/D$ over range of port diameters for each test series.

Two test series, series I at approximately constant value of $\dot{m}_{ox}/D = 15$ ($\pm 10\%$) g/s · cm ($G_{ox}D = 19$ g/s · cm) and series II at $\dot{m}_{ox}/D = 8$ ($\pm 10\%$) g/s · cm ($G_{ox}D = 10$ g/s · cm), were carried out, as shown in Fig. 5. Figure 6 shows a comparison between the theoretical and experimental variations of the regression rate with motor port diameter. The test results agree very well with the theoretical prediction of $\dot{r} \propto D^{-1}$ [Eq. (37)], validating the similarity model.

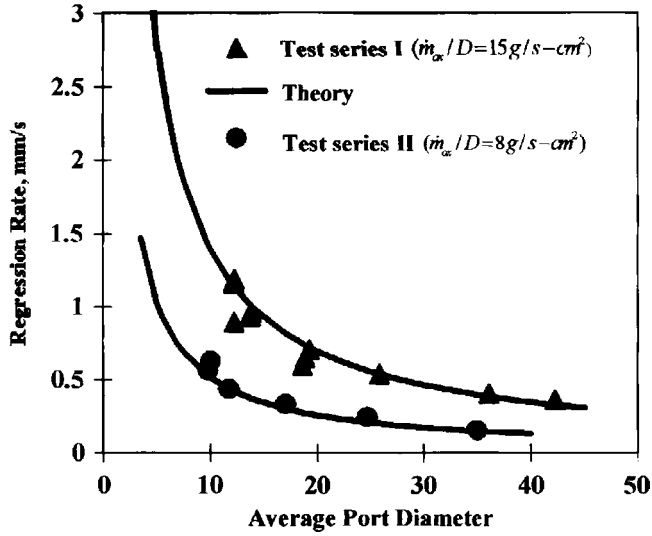

Fig. 6 Regression rate variation with combustor port diameter, test series I and II.

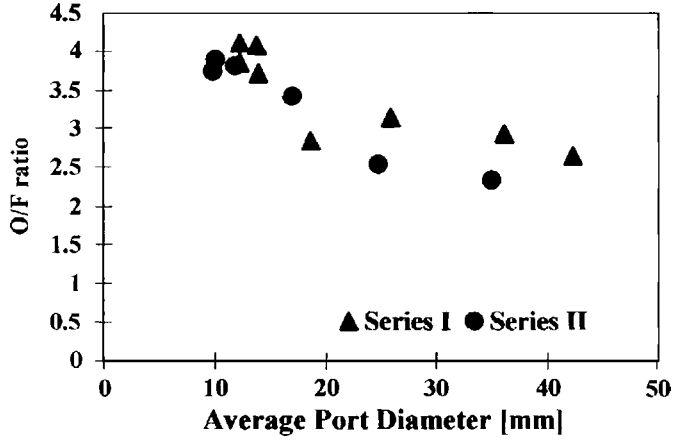

Fig. 7 Experimental results of O/F ratio vs combustor port diameter.

In Fig. 7, experimental results of overall oxidizer/fuel O/F mass ratio vs motor port diameter are shown for the two test series. The stoichiometric O/F ratio for the oxygen PMMA system is 1.92. One can see that in all of the cases the motor operated at O/F values higher than the stoichiometric value.

In both of the test series, the oxidizer/fuel ratio seems to be fairly constant within the typical experimental spread for the larger average port diameters (>15 mm) with somewhat higher values at smaller port diameters. A constant O/F ratio is predicted by the model (for constant L/D) and serves as an important similarity parameter. The increased values of O/F ratio found for port diameters smaller than 15 mm are attributed to the relatively large change in L/D ratio from its initial value in smaller port diameter motors, leading to somewhat smaller average L/D

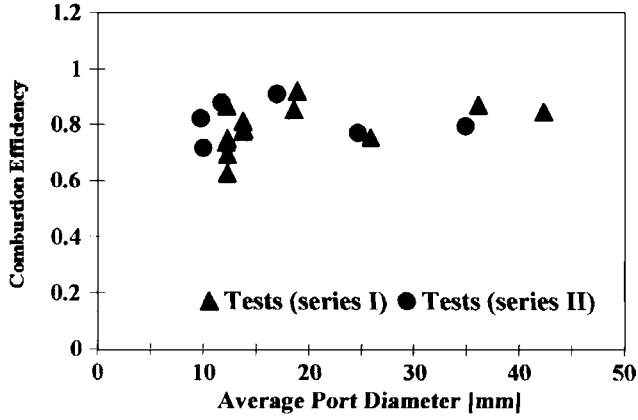

Fig. 8 Combustion efficiency test data vs port diameter.

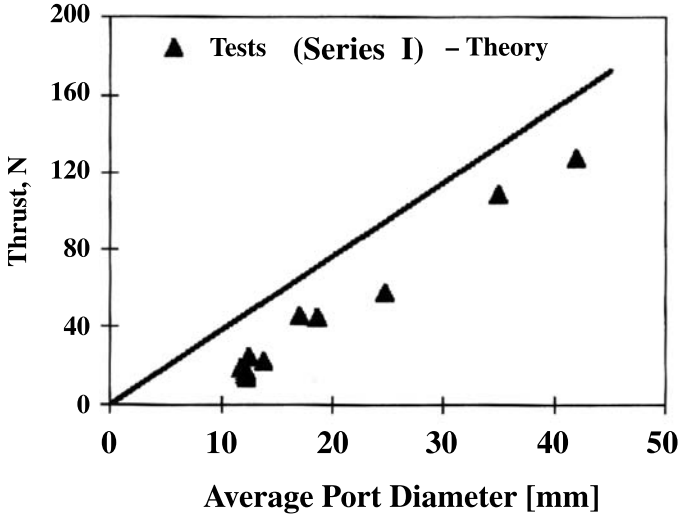

Fig. 9 Motor thrust vs port diameter, test series I, $\dot{m}_{ox}/D = 15$ g/s · cm.

ratios and, hence, lower fuel flow rates, implying higher O/F ratios in these cases. Also note that, in general, the O/F ratio in the second test series (which is of the smaller oxygen flow rate) tends to be somewhat lower (by about 20%) than in the first test series. This behavior results from the fuel regression rate dependence on $\dot{m}_{ox}$, which is typically smaller than linear dependence.

Combustion efficiency is defined in terms of the ratio between the experimental and theoretical [26] values of combustor's characteristic velocity c^*. The test results are summarized in Fig. 8, revealing pretty constant combustion efficiency (typically

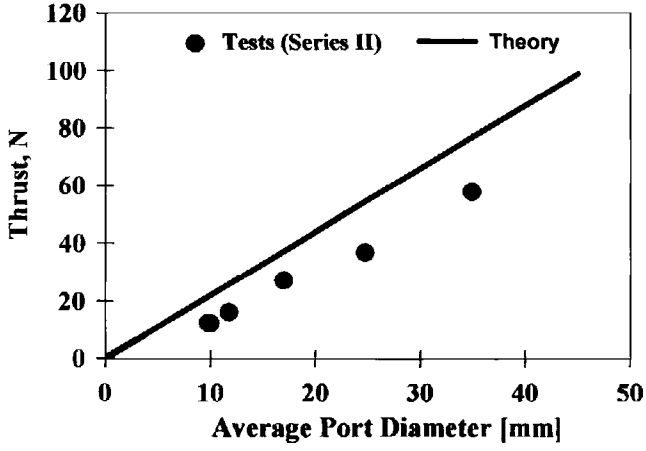

Fig. 10 Motor thrust vs port diameter, test series II, $\dot{m}_{ox}/D = 8$ g/s · cm.

of the order of 80–90%) for the entire range in both series. Somewhat lower values of combustion efficiency were obtained in certain tests particularly for the smaller port diameters. These results may be attributed to the higher relative heat losses in the smaller motors.

The variation of motor thrust with port diameter is presented in Fig. 9 for series I and in Fig. 10 for series II. Figures 9 and 10 both show almost linear approximation for the entire range as predicted by Eq. (44). Comparing the experimental values of the thrust with the theoretical values (calculated on the basis of theoretical c^* and C_F), one can see a similar trend. The lower experimental values of the thrust are because of the lower experimental values of the characteristic velocity c^* as indicated by the combustion efficiency data (Fig. 8), as well as because of flow losses, lowering the C_F values.

VI. Conclusion

The message of this study is that scaling of hybrid rocket motors should be done under appropriate similarity conditions.

A similarity analysis has defined the scaling rules in hybrid propulsion and the operating conditions under which a laboratory-scale motor has to be tested to predict the likely behavior of a full-scale motor.

The most significant scaling rules are the following: 1) maintaining geometric similarity, 2) using the same oxidizer and fuel combination, and 3) scaling the oxidizer flow rate $\dot{m}_{ox}$ in proportion to the port diameter D (resulting in maintaining the same value of $G_{ox}D$ and GD).

Under such conditions, the different-scale systems are predicted to yield inverse proportion between $\dot{r}$ and D, constancy of O/F, c^* (and approximately I_{sp}), and approximately linear proportion between F and D.

The excellent agreement between theory predictions and experimental data both from the literature and from the present tests supports the validity of the theory and indicates the important role that it can play in the development of hybrid rocket motors.

References

[1] Marxman, G. A., and Gilbert, G. M., "Turbulent Boundary Layer Combustion in the Hybrid Rocket," *Ninth Symposium (International) on Combustion*, Combustion Inst., Pittsburgh, PA, 1963, pp. 371–383.

[2] Wooldridge, C. E., and Muzzy, R. J., "Internal Ballistic Considerations in Hybrid Rocket Design," *Journal of Spacecraft and Rockets*, Vol. 4, No. 2, 1967, pp. 255–262.

[3] Marxman, G. A., "Boundary Layer Combustion in Propulsion," *Eleventh Symposium (International) on Combustion*, Combustion Inst., Pittsburgh, PA, 1967, pp. 269–289.

[4] Seifert, H. S., "Hybrid Rocket Theory and Design," *Jet, Rocket, Nuclear, Ion and Electric Propulsion: Theory and Design*, edited by W. H. T. Loh, Springer-Verlag, New York, 1968, Chap. 7, pp. 332–355.

[5] Altman, D., and Humble, R., "Hybrid Rocket Propulsion Systems," *Space Propulsion Analysis and Design*, McGraw-Hill, New York, 1995, pp. 365–441.

[6] Boardman, T. A., Holzman, A. L., and Sutton, G. P., "Hybrid Propellant Rockets," *Rocket Propulsion Elements*, edited by G. P. Sutton and O. Biblarz, 7th ed., Wiley, New York, 2001, Chap. 15, pp. 579–607.

[7] Estey, P., Altman, D., and McFarlane, J., "An Evaluation of Scaling Effects for Hybrid Rocket Motors," AIAA Paper 91-2517, 27th AIAA/SAE/ASME/ASEE Joint Propulsion Conference, Sacramento, CA, June 1991.

[8] Chiaverini, M. J., Serin, N., Johnson, D. K., Lu, Y. C., Kuo, K. K., and Risha, G. A., "Regression Rate Behavior of Hybrid Rocket Solids Fuels," *Journal of Propulsion and Power*, Vol. 16, No. 1, 2000, pp. 125–132.

[9] Evans, B., Favorito, N. A., and Kuo, K. K., "Study of Solid Fuel Burning-Rate Enhancement Behavior in an X-Ray Translucent Hybrid Rocket Motor," AIAA Paper 2005-3909, 41st AIAA/SAE/ASME/ASEE Joint Propulsion Conference, Tucson, AZ, July 2005.

[10] George, P., Krishnan, S., Varkey, P. M., Ravindran, M., and Ramachandran, L., "Fuel Regression Rate Enhancement Studies in HTPB/GOX Hybrid Rocket Motors," AIAA Paper 98-3188, 34th AIAA/SAE/ASME/ASEE Joint Propulsion Conference, Cleveland, OH, July 1998.

[11] Carmicino, C., and Russo-Sorge, A., "Role of Injection in Hybrid Rockets Regression Rate Behavior," *Journal of Propulsion and Power*, Vol. 21, No. 4, 2005, pp. 606–612.

[12] Spalding, D. B., "The Art of Partial Modeling," *Colloquium on Modeling Principles*, *Proceedings of the Ninth Symposium (International) on Combustion*, Combustion Inst., Pittsburgh, PA, 1963, pp. 833–843.

[13] Rosner, D. E., *Transport Processes in Chemically Reacting Flow Systems*, Dover, Mineola, NY, 2000, Chap. 7, pp. 405–454.

[14] Stewart, D. C., "Scaling of Gas Turbine Combustion Systems," *AGARD Selected Combustion Problems II*, Butterworth Science, London, 1956, pp. 384–413.

[15] Stewart, D. C., and Quigg, G. C., "Similarity Scale Effects in Ramjet Combustors," *Proceedings of the Ninth Symposium (International) on Combustion*, Combustion Inst., Pittsburgh, PA, 1963, pp. 907–922.

[16] Hottel, H. C., Williams, G. C., Jensen, W. P., Tobey, A. C., Burrage, P. M. R., "Modeling Studies of Baffle-Type Combustors," *Proceedings of the Ninth Symposium (International) on Combustion*, Combustion Inst., Pittsburgh, PA, 1963, pp. 923–935.

[17] Ben-Arosh, R., and Gany, A., "Similarity and Scale Effects in Solid Fuel Ramjet Combustors," *Journal of Propulsion and Power*, Vol. 8, No. 3, 1992, pp. 615–623.

[18] Gany, A., "Scale Effects in Hybrid Motors Under Similarity Conditions," AIAA Paper 96-2846, 32nd AIAA/SAE/ASME/ASEE Joint Propulsion Conference, Lake Buena Vista, FL, July 1996.

[19] Swami, R. D., and Gany, A., "Analysis and Testing of Similarity and Scale Effects in Hybrid Rocket Motors," *Asta Astronautica*, Vol. 52, No. 8, April 2003, pp. 619–628.

[20] Smoot, L. E., and Price, C. F., "Pressure Dependence of Hybrid Fuel Regression Rates," AIAA Journal Vol. 5, No. 1, 1967, pp. 102–106.

[21] Kosdon, F. J., and Williams, F. A., "Pressure Dependence of Nonmetallized Hybrid Fuel Regression Rates," *AIAA Journal*, Vol. 5, No. 4, 1967, pp. 774–778.

[22] Gany, A., Timnat, Y. M., and Wolfshtein, M., "Two-Phase Flow Effects on Hybrid Combustion," *Acta Astonautica*, Vol. 3, 1976, pp. 241–263.

[23] Gany, A., "Theoretical Investigation of a Hybrid Rocket Motor Employing Liquid Oxidizer," D.Sc. Dissertation, Faculty of Aerospace Engineering, Technion—Israel Inst. of Technology, Haifa, Israel, July 1975.

[24] Ramohalli, K., Bates, R., Jones, M., Wygle, B., and Yi, J., "Some Recent Results From a Program in Hybrids at The University of Arizona," AIAA Paper 95-2945,

31st AIAA/SAE/ASME/ASEE Joint Propulsion Conference, San Diego, CA, July 1995.

[25] Wernimont, E. J., and Heister, S. D., "Performance Characterization of Hybrid Rockets Using Hydrogen Peroxide Oxidizer," AIAA Paper 95-3084, 31st AIAA/SAE/ASME/ASEE Joint Propulsion Conference, San Diego, CA, July 1995.

[26] Cruise, D. R., "Theoretical Computations of Equilibrium Compositions, Thermodynamic Properties and Performance Characteristics of Propellant Systems (PEP Code)," Naval Weapons Center, Rept. NWC-TP-6037, China Lake, CA, April 1979.

This page intentionally left blank

Chapter 13

Large-Scale Hybrid Motor Testing

George Story*
NASA, Marshall Space Flight Center, Alabama 35812

Nomenclature

C^* = Characteristic exhaust velocity
I_{sp} = Specific impulse

I. Introduction

HYBRID rocket motors can be successfully demonstrated at a small scale virtually anywhere. There have been many suitcase-sized portable test stands assembled for demonstration of hybrids. They show the safety of hybrid rockets to the audiences. These small show motors and small laboratory-scale motors can give comparative burn rate data for development of different fuel/oxidizer combinations; however, questions that are always asked when hybrids are mentioned for large-scale applications are how do they scale and has it been shown in a large motor? To answer those questions, large-scale motor testing is required to verify the hybrid motor at its true size.

The necessity to conduct large-scale hybrid rocket motor tests to validate the burn rate from the small motors to application size has been documented in several places [1–3]. Comparison of small-scale hybrid data to that of larger scale data indicates that the fuel burn rate goes down with increasing port size, even with the same oxidizer flux. This trend holds for conventional hybrid motors with forward oxidizer injection and hydroxyl-terminated polybutadiene- (HTPB-) based fuels. Although the reason this is occurring would make a great paper, or study, or thesis, it is not thoroughly understood at this time. Potential causes include that, because hybrid combustion is boundary layer driven, the larger port sizes reduce the interaction (radiation, mixing, and heat transfer) from the core region of the port.

This chapter focuses on some of the large, prototype-sized testing of hybrid motors. The largest motors tested have been American Rocket Company's

*Engineer, Solid and Hybrid Propulsion Systems.

(AMROC's) 250,000-lbf thrust motor at Edwards Air Force Base and the Hybrid Propulsion Demonstration Program's 250,000-lbf thrust motor at NASA Stennis Space Center. Numerous smaller tests were performed to support the burn rate, stability, and scaling concepts that went into the development of those large motors.

II. Background: Why Hybrids?

Hybrids, considered part solid- and part liquid-propulsion system, have been caught in the middle of development goals of the various NASA and military programs. Solid rocket motor technology has matured due to the advantages of design simplicity, on-demand operational characteristics, and moderately low cost. The reliability of solids, given minimal maintenance requirements, made them the ideal system for military applications. On the other hand, liquid rocket engine technology has matured due to their higher specific impulse (I_{sp}) over solids and variable control thrust capability.

Before 2004, hybrid rockets have been used in only one flight-production application (Teledyne Ryan AQM-81A Firebolt Supersonic Aerial Target). Their recent successful application to a manned-flight demonstration (Burt Rutan's SpaceShipOne) may suggest that advantages have been overlooked in some potential applications, and hybrids may be getting renewed interest. Hybrid rockets inherently combine the safety features of a liquid-propulsion system (throttle, shutdown, restart) while deriving the cost and operational benefits of a solid-propulsion system. Specific details regarding these advantages include the following:

1) *Handling*—Virtually all hybrids fuels are considered inert [class 1.4c propellant, zero trinitrotuluene (TNT) equivalent], that is, they can be transported via normal shipping techniques with no additional safety requirements. This is a significant benefit when compared to traditional solids, where any processing is considered a hazardous operation and special handling considerations must be observed.

2) *Casting*—Classical hybrid motors can be cast in light industrial facilities employing the techniques used in traditional solid-propellant casting. Hybrids are largely insensitive to cracks and defects in the propellant, but gross disturbances in the flow from air bubbles cast in the fuel (voids) can cause problems during hot-fire operations.

3) *Simplicity*—Hybrid rockets are more complex than solids due to the need for an oxidizer delivery system, with an associated oxidizer tank pressurization system and pump if necessary. Although hybrids are more complex than solids, they use only one fluid system, which make them less complex than liquid-bipropellant systems (liquid rocket engines).

4) *Throttling*—Hybrids can be throttled by increasing the oxidizer flow rate via varying the opening of the oxidizer valve in a pressure-fed system or speeding the pump in a pump-fed system. Because the fuel regression rate is a function of the oxidizer flux, lowering the oxidizer flow rate lowers the fuel regression rate and resultant thrust level.

5) *Restart*—Hybrid motors can typically be ignited many times, until the fuel grain is consumed or the nozzle and other components are past their design-life limits.

6) *Performance*—The I_{sp} of an HTPB/liquid oxygen (LOX) rocket is equivalent to a rocket propellant-1 (RP-1)/LOX engine and significantly higher than a solid rocket motor [4]. Other fuel and oxidizer combinations yield higher and lower performance values, with different system issues to work with [5]. To a certain extent, performance can be tailored utilizing fuel additives or other propellant modifications to meet specific requirements.

7) *Cost*—The handling and casting process costs should be significantly lower than that of a solid, with no oxidizer in the fuel and, therefore, lower safety concerns. Because there is only one liquid propellant used, the system costs should be significantly less than that of a liquid system.

III. High-Energy Hybrid Space Engines

Space propulsion systems typically use solid rockets, with relatively low I_{sp} but high-density impulse or LOX/hydrogen systems with high I_{sp} but lower density impulse. In the 1960s, NASA decided to investigate hybrid rockets to see if a high I_{sp} and high-density system could be developed [6].

NASA selected United Technologies Corporation (UTC) to perform a series of investigations devoted to high-energy space engines. One concept was based on the use of the very energetic reaction between lithium and fluorine, two elements at the opposite ends of the Mendeleev periodic table. The lithium was incorporated into an HTPB binder and the fluorine was mixed with oxygen to create FLOX, optimizing the performance of the system [6].

To satisfy conductivity restrictions of the binder and avoid melting of the lithium, an eventual composition incorporating a combination of lithium and lithium hydride was finally developed for the propulsion system shown in Fig. 1. This throttleable system burned smoothly and exhibited very high performance. Its ground performance converted to vacuum I_{sp}, with an area ratio of 40:1, would be in excess of 400 s. This firing is shown in Fig. 2, which appeared on the cover of the 26 January 1970 issue of *Aviation Week and Space Technology* [6].

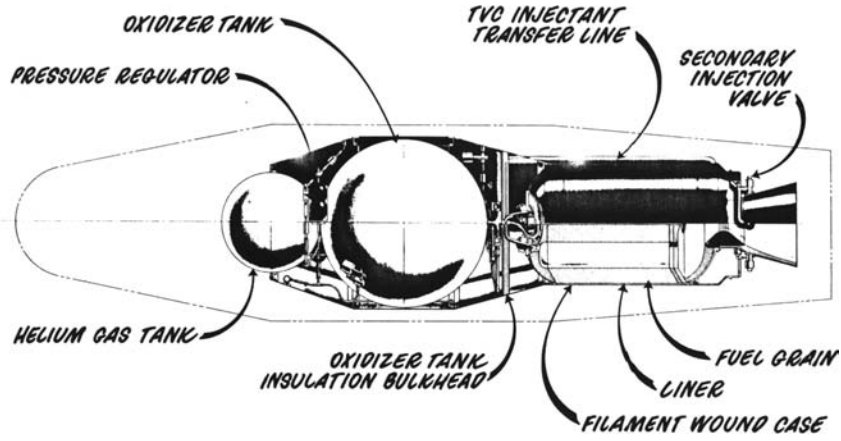

Fig. 1 UTC hybrid upperstage concept [6].

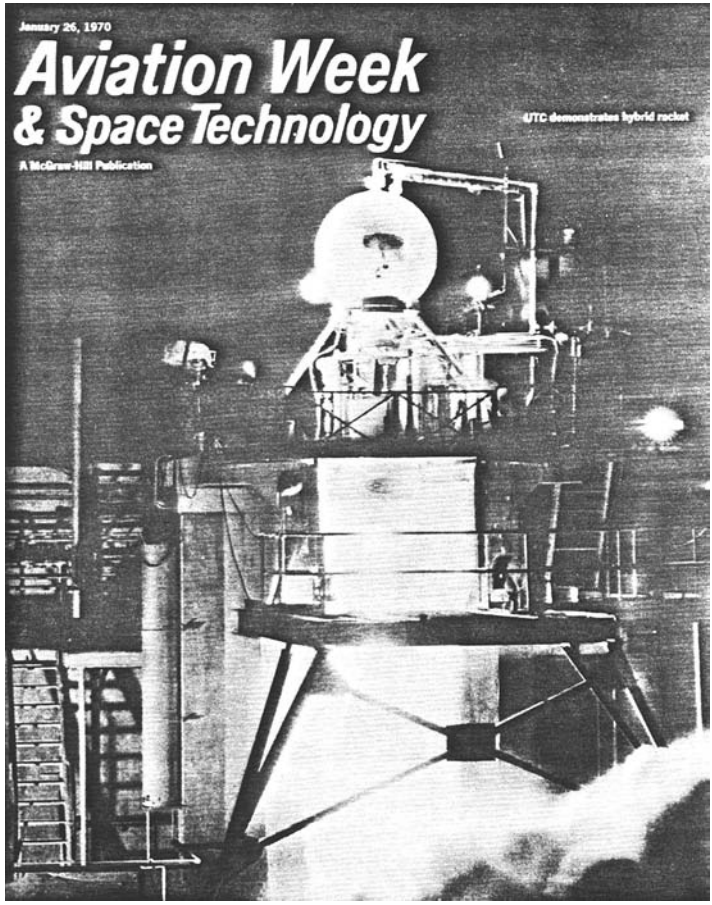

Fig. 2 UTC hybrid firing [6].

IV. AMROC Experience

AMROC was for years the leader in hybrid rocket development. Their dream was a low-cost commercial vehicle for entry into space. During the time AMROC was financially solvent, they did exciting work on a large range of sizes of hybrid rocket motors. They published numerous hybrid papers to generate interest in hybrids; however, they still kept their trade secrets close. The AMROC intellectual property rights and data were eventually sold to Space Dev, who are currently pursuing hybrids.

A. AMROC Combustion Stability at 75,000-Pounds Force Thrust

Initial development activity at AMROC targeted a 75,000-lbf thrust motor for suborbital payload delivery on the single engine test (SET) launch vehicle.

During the development of the 75,000-lb thrust H-500 motor, AMROC used three sizes of test motors [7]:

1) *Small scale*—The small scale motors were ~18 in.-diam motors producing 10,000-lb thrust. These small-scale motors were used for fuel formulation, insulation, and other materials for compatibility testing. There were 19 of these motors built and fired.

2) *Half scale*—The half-scale motors were ~36-in.-diam motors producing 33,000-lb thrust. These motors were used to test different concepts and issues in multiport grain development. There were three of these motors built and fired.

3) *Full scale*—The full-scale motors were ~51-in.-diam motors producing 75,000-lb thrust. These were tested in heavy-weight cases and in flight-weight composite cases. There were 12 of these motors built; one was a manufacturing pathfinder and the remainder were fired. Details of the tests run in each configuration is shown in Table 1 [7].

AMROC found nonacoustic instability (NAI) during the development of a large-scale hybrid rocket motor. The frequencies of the oscillations were related to the fill/flush time of the combustion chamber. The observed frequencies were similar to, though slightly higher than, those predicted by solid rocket motor correlations. The magnitude of the oscillation was governed by the oxidizer feed system and injector characteristics [7].

Stability problems were first encountered by AMROC during the 33,000-lbf motor firings. Because their 10,000-lbf motors were relatively immune to instabilities, AMROC reasoned that the physical mechanisms driving the oscillations were enhanced at larger scale. Therefore, solving the stability problem at half-scale would not guarantee that the full-scale motor to be free of oscillation. AMROC

Table 1 AMROC 75,000-lbf motor development testing [7]

Motor	First firing	No. of firings	Comments
H-001	4 Dec. 1986	4	33,000-lbf motor
H-002	17 Feb. 1987	3	33,000-lbf motor
H-003	21 April 1987	4	Last 33,000-lbf motor
H-004	14 Oct. 1987	5	First 75,000-lbf motor
D-001	18 April 1988	6	Fiberglass motor case
H-005	23 Dec. 1987	5	
H-006		0	Manufacturing pathfinder, not fired
H-007	28 June 1988	3	
H-008	26 July 1988	5	
H-009	2 Sept. 1988	1	First full-duration firing
H-010	25 Oct. 1988	6	
H-011	19 Dec. 1988	1	
H-012	13 March 1989	1	
H-013	18 April 1989	1	
DF-1	11 July 1989	3	Qualification test motor
DF-2	5 Oct. 1989	1	SET-1 flight motor

decided to work on the stability problems using the larger 75,000-lbf motor. A series of tests were performed using the 75,000-lbf motor to identify the cause of and eliminate the combustion oscillations [7].

AMROC identified inadequate LOX vaporization as the major cause of NAI. This points out the need for either a precombustion (vaporization) chamber upstream of the combustion ports to allow for adequate gasification of the LOX or injecting the oxidizer in gaseous form. For liquid injection, reduced droplet size was more important than low axial velocity in increasing droplet vaporization. Splashblocks, defined as sacrificial fuel surface areas downstream of the LOX injector, were used to increase the residence time in the vaporization chamber and found to be effective in suppressing NAI. AMROC found that the required area of forward-facing surface was 13% of the total motor cross-sectional area [7].

AMROC demonstrated their theories on the qualification test motor (DF-01), which employed the enhanced techniques to suppress NAIs. Changes from early full-scale motors included 1) increased venturi pressure drop to increase feed system capacitance, 2) decreased injector manifold volume to reduce injector capacitance, 3) increased injector pressure drop to reduce droplet size, and 4) use of splashblocks to increase effective droplet residence time.

With these modifications, the qualification test motors met all requirements for combustion stability [7].

B. AMROC 250,000-Pounds Force Motor Development

After the failed launch of SET-1 on 5 October 1989, which was built around the 75,000-lbf hybrid motor (Fig. 3), AMROC reevaluated the market and started to design a larger, 250,000-lbf hybrid rocket motor for a different sized launch vehicle [8].

The first full-scale H-250,000-lbf development motor (DM-01) was designed and produced in just 10 months in 1992 (Fig. 4). This effort required the development of multiple components: a 74-in.-diam, 386-in.-long graphite/epoxy motor

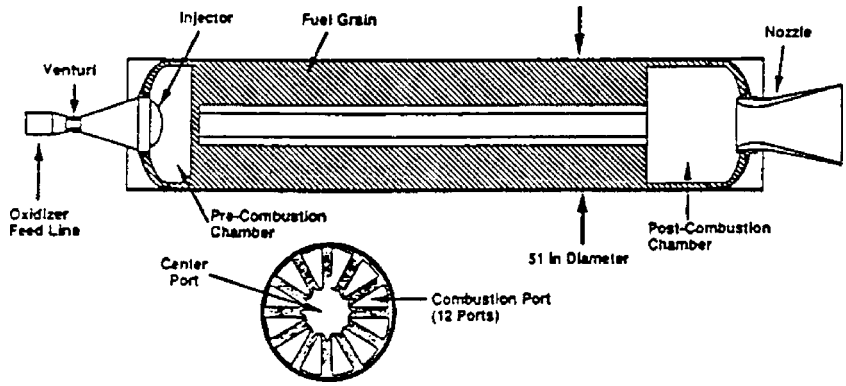

Fig. 3 AMROC 75,000-lbf hybrid motor [7].

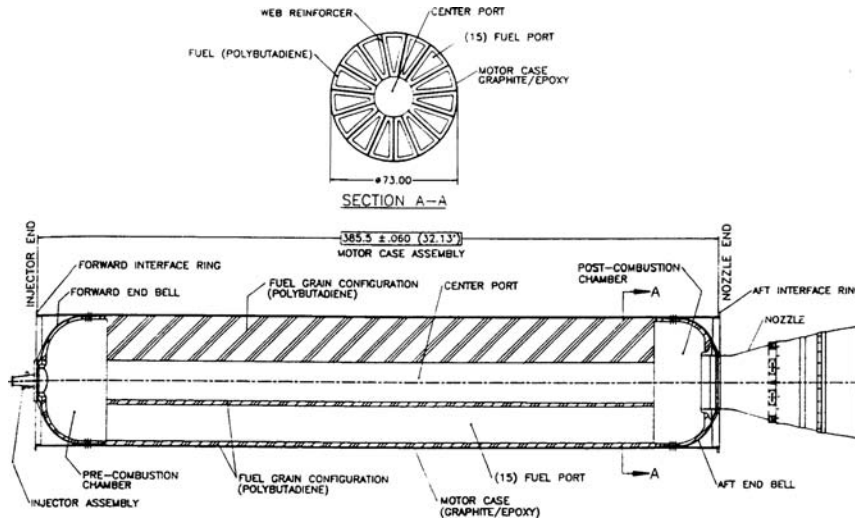

Fig. 4 AMROC DM-01 250,000-lbf hybrid motor [8].

Table 2 H-250,000-lbf design parameters [8]

Parameter	Value
Average vacuum thrust, lbf	257,000
Average vacuum specific impulse, s	280
Total vacuum impulse, lbf · s	18,500,000
Average chamber pressure, psia	400
Burn time, s	72

case; a 9:1 area ratio silica/phenolic nozzle; a 400,000-lbf thrust horizontal test stand; composite port molds; motor casting fixtures; fuel mixers; and motor manufacturing procedures. The total project duration, from initial design to the completion of testing, was 13 months [8]. The design parameters are given in Table 2.

C. Test Results

The DM-01 motor was tested in a series of four static firings. The first burn was successfully conducted on 22 January 1993. The second burn was successfully completed on 17 February 1993. The third burn was successfully conducted on 11 March 1993. After the third burn, the exit cone had excessive wear, and so part of it was cut off before the next test rather than having it fail during test 4. That lowered the nozzle expansion ratio and the thrust. On 24 March 1993, the fourth burn prematurely ended when the case failed [8]. The motors were relatively stable and performance data are shown in Table 3.

Table 3 AMROC 250,000-lbf DM-01 test results [8]

	Burn			
Parameter	1	2	3	4
Thrust, lbf	216,900	231,900	215,400	214,800
Fuel mdot, lbm/s	357	351	339	310
LOX mdot, lbm/s	569	600	619	587
I_{sp}, s	234	244	225	239
O/F ratio	1.59	1.71	1.82	1.89
Chamber pressure, psia	412	419	378	369
Nozzle area ratio	8.33	8.00	7.61	3.70
Throat area, in.^{2}	364	381	402	418
Vacuum thrust, lbf	257,000	272,300	255,800	235,200
Vacuum I_{sp}, s	278	286	267	262

The second motor (DM-02) was also developed and fired successfully as part of the Hybrid Technology Option Project [9]. However, the motor was only fired once. After the firing of DM-02, AMROC discovered that the motor had problems with the manufacturing processes that formed the case insulation and discontinued the testing on that hardware. With investor monies running low, they began to refocus on smaller scale hybrids to investigate fuel and combustion issues. AMROC found it more cost effective to test the motors at NASA Stennis Space Center than at Edwards Air Force Base or their own test facilities [10].

D. AMROC 10,000-Pound Force at NASA Stennis Space Center

AMROC used 10,000-lb thrust LOX/polybutadiene hybrid rocket motors for research and development work. A number of these motors were tested at NASA's Component Test Facility at NASA Stennis Space Center. These motors have led to advances in combustion stability and material selection for use on AMROC's 250,000-lb thrust hybrid rocket motors. Among the demonstrations conducted, there was a pump-fed hybrid motor. AlliedSignal Aerospace had been developing high-reliability, low-cost cryogenic turbopumps based on their foil bearing technology. This was the first application of a turbopump-fed hybrid rocket motor. The AlliedSignal foil bearing LOX turbopump and AMROC's hybrid rocket motor were brought together and tested at NASA Stennis Space Center (SSC) in October 1994 with the first test of the pump-fed hybrid rocket motor in November 1994 [10].

The hybrid motor consisted of a HTPB fuel cast directly into the motor case in a "double-D" two-port configuration (Figs. 5 and 6). Some of the motor design parameters may be found in Table 4. The fuel was composed of HTPB, an isocyanate curative, and small quantities of additives to achieve the desired mechanical properties. The injector was a shower head configuration. Some of the stable test data are shown in Fig. 7.

The test stand configuration for the motor (shown in Fig. 8) included a cavitating venturi. The cavitating venturi in Fig. 8 is the unlabeled device between the hybrid motor and the valve designated MV42. A cavitating venturi is a proven critical piece of hardware to isolate the hybrid motor oscillations from the liquid oxidizer feed

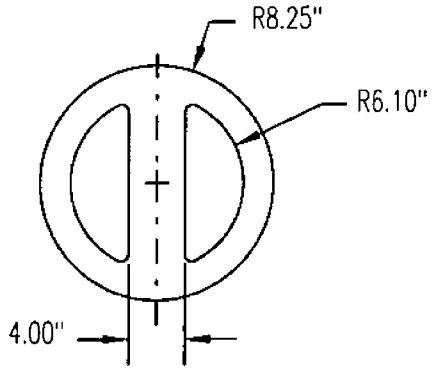

Fig. 5 AMROC 10,000-lbf double d motor [10].

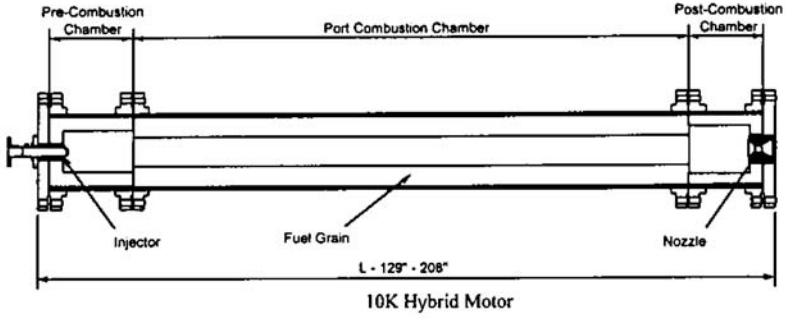

Fig. 6 AMROC 10,000-lbf hybrid motor [10].

Table 4 10,000-lbf turbopump motor configuration [10]

Parameter	Value
Fuel formulation	DM-02
Maximum chamber pressure	500 psia
Initial oxidizer mass flux	0.5 $\frac{\text{lb}_\text{m}}{(\text{s} \cdot \text{in.}^2)}$
Injector pressure drop	90 psid
Postcombustion chamber L^*	250 in.
Precombustion chamber length	20 in.

system, ensuring no oscillations on pressure-fed systems [7]. These tests, although demonstrating a turbopump and the hybrid motor together for the first time, did not prove that a cavitating venturi was necessary for a turbopump driven system. However, it may be desirable from the turbopump operation conditions. A cavitating

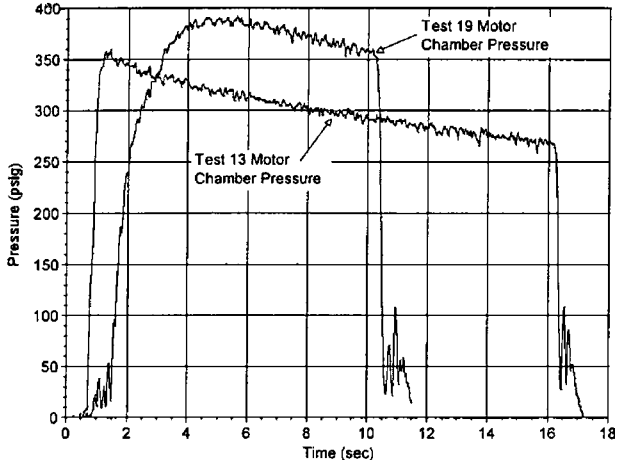

Fig. 7 AMROC turbopump data [10].

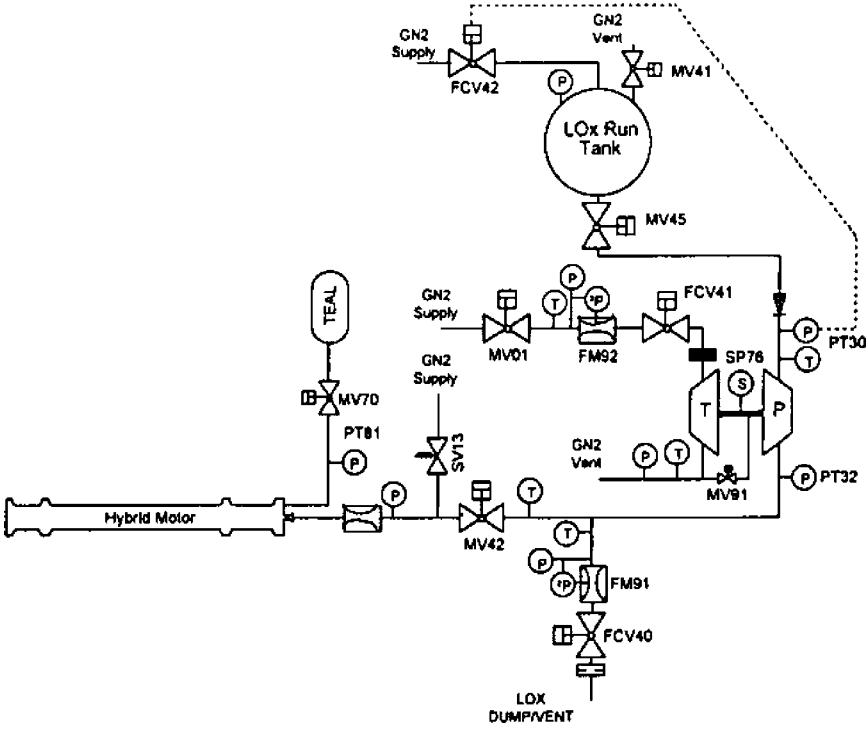

Fig. 8 SSC test arrangement for AMROC turbopump [10].

venturi requires a certain minimum pressure drop across it, and whereas a turbopump could probably provide that pressure rise, the pump might be smaller if that extra pressure rise was not required. However, in a turbopump-driven system, it may be better to have a steady back pressure behind the oxidizer pump, provided by the cavitating venturi, to keep the changes in motor pressure from affecting the speed of the pump. Without a cavitating venturi between the turbopump and the motor, as the motor pressure dropped over time, the turbopump would tend to spin faster with the reduced back pressure, increasing the oxidizer flow or requiring greater system control to keep it from spinning more.

V. Hybrid Propulsion Demonstration Program 250,000-Pounds Force Hybrid Motor

The Hybrid Propulsion Demonstration Program (HPDP) program was formed to mature hybrid propulsion technology to a readiness level sufficient to enable commercialization for various space launch applications [11, 12]. Participants in HPDP have included Allied Signal Aerospace; The Boeing Company, Rocketdyne Division; Environmental Aeroscience Corporation; Lockheed Martin; Thiokol; UTC-Chemical Systems Division; and NASA [Marshall Space Flight Center (MSFC) and SSC]. The goal of the HPDP was to develop and test a 250,000-lb vacuum thrust hybrid booster to demonstrate hybrid propulsion technology and enable manufacturing of large hybrid boosters for current and future space launch vehicles. The HPDP has successfully conducted four tests of the 250,000-lb thrust hybrid rocket motor at NASA SSC. Figure 9 shows the HPDP 250,000-lbf thrust motor 2, test 3, and Fig. 10 its layout.

A. 11-Inch and 24-Inch Motor Testing at MSFC

There has been significant testing of hybrid motors at MSFC in the 11-in. and 24-in. diameter with gaseous oxygen (GOX) and LOX. That testing, from the Joint Industry Research and Development (JIRAD) program, the Large Scale Solid Rocket Combustion Simulator Program, and other programs, all fed into the HPDP program [13–16]. This subscale work continued during the development of the HPDP 250,000-lbf thrust motor and provided the basis for many of the design features of the larger motor.

B. 250,000-Pound Force Thrust Hybrid Test Motor

Table 5 lists the 250,000-lbf hybrid motor design requirements. Details of the injector, fuel grain, and nozzle design are given by Boardman et al. [11, 12]. A photograph of a pretest aft end of the grain is shown in Fig. 11.

C. Head End Designs

To address the combustion stability concerns that had been found in the development of large-scale hybrid rockets [7, 17, 18], the HPDP consortium came up with two ways to try to control the combustion instability: a passive technique, with no moving parts (employed on motor 1) and an active approach, using heat addition from the forward end (employed on motor 2).

1. Motor 1 Design Basis and History

The motor 1 head design was based on previous solid-fuel ramjet stability historical data, with the creation of "a stable zone of hot, recirculating, combustion gases ahead of the establishment of the primary combustion zone" [19]. Several of these concepts were designed and subscale tested with GOX in the 11-in.-diam motor, which was ignited with an oxygen hydrogen torch. "All oxidizer dump plenum configurations that produced flow recirculation of combustion gas at the leading edge of the diffusion flame sheet resulted in stable operation. Configurations that did not produce such flow structures exhibited unstable combustion"[19]. Testing with LOX in the 11-in.-diam hybrid motor produced similar stability results. "The comparison showed that flow field features which reduced or eliminated acoustic oscillation in motors using gaseous-oxygen injection were also required to stabilize combustion in liquid-oxygen-injected motors" [19]. This testing evaluated the effects of short and long fuel-lined vaporization chambers with different flameholding concepts: fuel fin, flameholder, and fuel inhibitor. The LOX was injected with either a solid cone or axial injector. The combination of the long fuel-lined vaporization chamber with the fuel fin and the solid cone injector had the lowest average nonacoustical oscillation amplitude percentage and also had the highest vaporization chamber heat output. The following determination was made by Boardman et al. [20]:

> Fuel fins are effective in both short and long vaporization chambers in reducing the average instability level associated with liquid-oxygen injection. This is most likely

Fig. 9 HPDP 250,000-lbf thrust motor 2, test 3 [3].

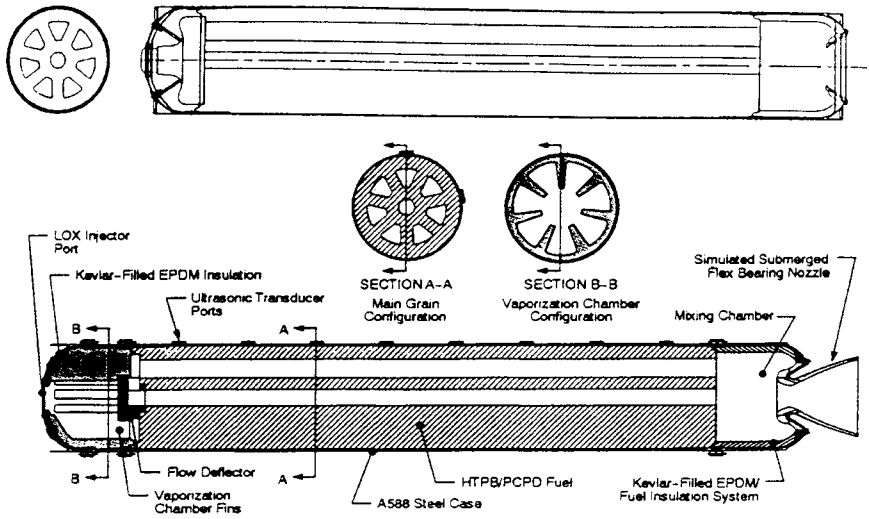

Fig. 10 Layout of 250,000-lbf HPDP hybrid motor layout [3].

because of the combustion port, spanwise, hot-gas recirculation zone behind the fuel fin and flame from combustion on the fin surface entering the combustion port. Incorporation of fuel fins appears to offer a viable means of scaling a combustion oscillation suppression method to larger liquid oxygen based motors.

This work supported the concept that became the bases for the design of the motor 1 head end.

Testing with the 24-in.-diameter LOX motor was started in parallel with the 11-in.-diameter GOX motor testing to support the ramjet combustion stability concepts [21]. Testing was conducted with domed-shaped vaporization chambers with varying length fins and no fins. Carpenter et al. [21] had no conclusions listed on the effect of fins; however, they did support previous AMROC conclusions stating that the oxidizer feed system must be decoupled from the motor oscillations. This decoupling was implemented by moving the cavitating venturi, which regulates the liquid oxygen flow, from well upstream of the injector to right before the injector. A well-designed cavitating venturi speeds the fluid to the point where the local fluid pressure is less than the vapor pressure of the fluid and the fluid flashes, and then the flow rate is controlled by the vapor pressure, not the downstream pressure. This effectively eliminated the feed system coupling of the oscillations with the motor oscillations [7]. Subsequent HPDP testing of the 24-in.-hybrid motor evaluated the effect of the centerport on combustion efficiency [16, 22]. These tests showed the effect of the centerport on the motor combustion, by blocking the centerport with a fuel plug or making a tortuous path to the centerport by use of a fuel flow port deflector. Blocking the centerport lead to more stable motors compared to unblocked centerport motors, but the centerport open motors were within the $+/-2.5\%$ stability band HPDP requirements. The $+/-2.5\%$ stability band was an indicator of the stability, based on the pressure variations vs a 1-s

Table 5 Design parameters 250,000-lbf motor [3]

Parameter	Value
Maximum vacuum thrust	250,000 lbf (1,112,055 N)
Average vacuum specific impulse	280 s
C^* efficiency	98%
Maximum operating pressure	900 psia (61.2 atm)
Average chamber pressure	750 psia (51.0 atm)
Burn time	80 s
LOX flow rate	600 lbm/s (272.2 kg/s)
Oxidizer flux level	0.64 lbm/sec/in.^{2} (0.045 kg/s · cm^2)
Port length	380 inch (9.65 m)
Length-to-diameter ratio	35.3
Fuel/oxidizer	HTPB[a]/LOX

[a]HTPB and polycyclopentadiene (PCPD) with no metal additives.

Fig. 11 Pretest 250,000-lbf HPDP motor ports [3].

moving average of the low-speed chamber pressure. The final motor of that 24-in.-diam series incorporated a flat-topped fuel flow deflector, a fuel lined vaporization chamber with fins, and a nozzle throat designed to provide a chamber pressure of 900 psi. According to Jones et al. [16] this configuration of motor

> showed that altering conditions in the center port provided a more stable motor with high combustion efficiencies. Results from the incorporation of the fuel flow deflector also indicate that a more uniform regression along the length of the grain was obtained. These data resulted in the incorporation of the fuel deflector into the first 250K-lbf motor.

2. Motor 2 Design Basis and History

The motor 2 head end design was also influenced greatly by historical data, initially being based on data from the AMROC. During the late 1980s and early 1990s, AMROC was the leader in hybrid technology. Some of their combustion stability experience is listed in a patent [23] and a paper on combustion stability [7]. Based on AMROC's published documentation [23], hybrid combustion instability was thought to be caused by several reasons:

> One of the causes of erratic performance is the flow of unvaporized liquid oxidizer, which disrupts the normally stable boundary layer combustion process. Ideally, during combustion a combustion zone is formed in the boundary layer at the interface of the vaporizing fuel flow and the vaporized oxidizer, within the momentum boundary layer and is the source of the heat flow to the surface of the solid fuel to maintain fuel vaporization. As unvaporized liquid oxidizer is distributed along the surface of the solid propellant (grain), the temperature of the forward reaction mixture is reduced, thus the efficient combustion area is developed toward the aft end of the rocket. As the pressure differences within the combustion area increase, the hot reaction products move forward into the area of low pressure and temperature, then aft again, producing a series of low frequency oscillations along the length of the grain. This results in erratic combustion and unstable thrust. Thus, it is essential for stable hybrid rocket engine performance that there is a consistent boundary layer over the entire solid propellant.

Another large cause of combustion stability AMROC documented included feed system coupling with the hybrid combustion. This they addressed by a cavitating venturi just upstream of the LOX injector [7]. The AMROC suggested correction of the boundary-layer problem is to inject a phyrophoric liquid into the oxidizer stream to vaporize the oxidizer before entry into the combustion zone [23]:

> The hypergolic fluid is injected in an amount sufficient to vaporize all of the liquid oxygen. The flow rate can be readily calculated from the temperature of the liquid oxidizer and the flow rate of the oxidizer. For example, a hybrid engine using liquid oxygen and a trialkyl aluminum pryogolic fluid, a flow rate of about 0.1% by weight of the liquid oxidizer is sufficient to vaporize all the oxidizer. Flow rates higher than 5% by weight of the oxidizer are unnecessary and can lead to unstable burning. Usually the flow rate is from about 0.5 to 3.0% by weight of the oxidizer.

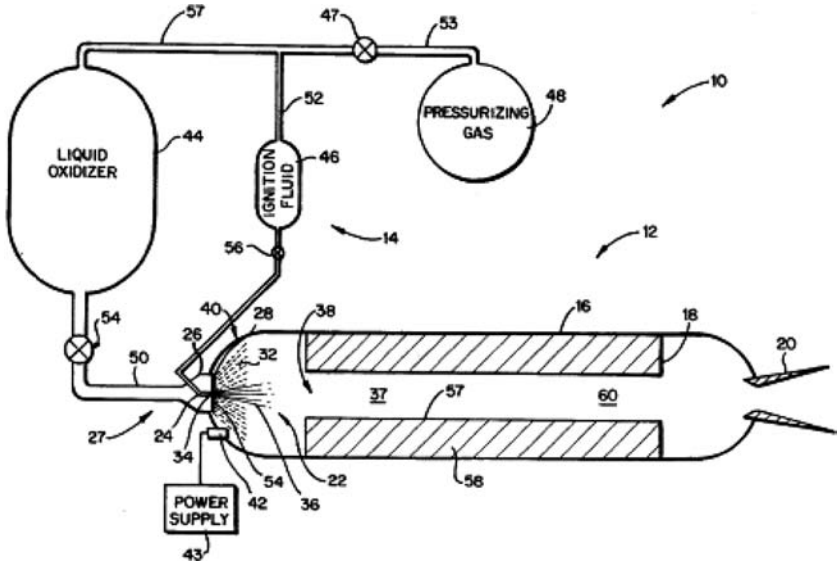

Fig. 12 U.S. Patent 5582001 motor layout: 32) LOX spray, 34) ignition fluid injector, 36) ignition fluid spray, and 26) LOX injector.

To support the claims in AMROC's patent, Bradford et al. [23] included test data from a series of tests, using the configuration shown in Fig. 12:

> Hybrid engines were constructed incorporating a polybutadiene solid grain and utilizing a casing containing a precombustion zone as shown in [Fig. 12]. Liquid oxygen was utilized as the liquid oxidizer and triethyl aluminum (TEAL) as the hypergolic fluid. One engine (Example 1) [Fig. 13, H8#1] was operated with TEAL only injected during initial start ups. Two other engines (Example 2 and 3) [Fig. 13, H8#2 and H8#3] were operated with the TEAL injected continuously. Example 4 [Fig. 14] was a test burn lasting 70 seconds with TEAL continuously injected. Figure 13 shows three short test firings; Example 1 [Fig. 13, H8#1] shows the aft port pressure during a time when TEAL was not injected. Both Example 2 and Example 3 [Fig. 13, H8#2 and H8#3] show the aft port pressure, under identical conditions, while TEAL was being injected. Example 1 shows the low frequency harmonics (oscillations) of hybrid rocket engines that have been reported in the literature while Example 2 and 3 show that said low frequency harmonics have been eliminated.

Figure 14 shows motor plot 2 with TEAL flowing through the entire burn.

These AMROC conclusions were also somewhat supported by HPDP testing with LOX on the 11-in. motor. This series of motors was ignited by triethylaluminum/triethylborane (TEA/TEB), which is a mixture of pyrophoric liquids. According to Boardmen et al. [20],

The heat input from the TEA/TEB combustion is approximately 3,600 Btu/sec, substantially exceeding that available from steady-state combustion of fuel in the vaporization chamber. Heat required to vaporize liquid oxygen is approximately 90 Btu/lbm, or approximately 400 Btu/sec at average motor liquid-oxygen flow rates. Thus the heat available from TEA/TEB combustion is well in excess of that necessary

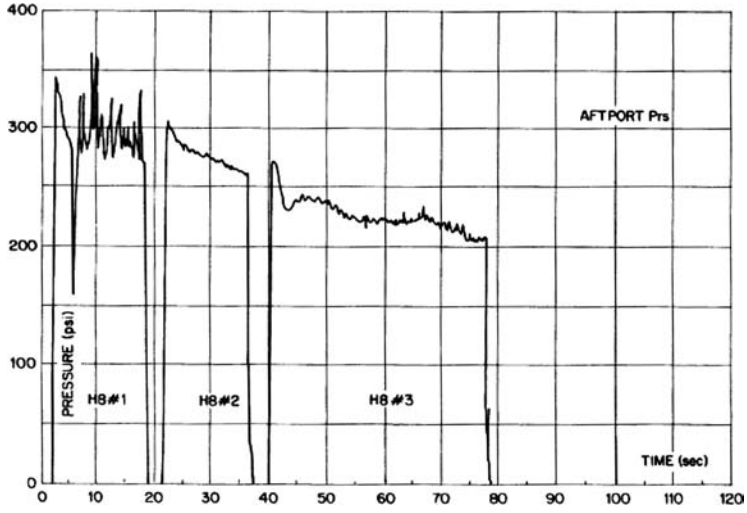

Fig. 13 U.S. Patent 5582001 motor plot 1, effect of TEAL addition on chamber pressure; H8#1 no TEAL and H8#2 and H8#3 TEAL on.

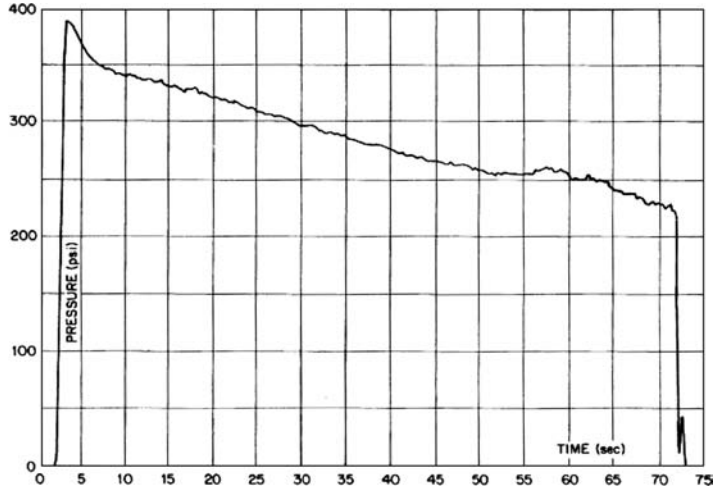

Fig. 14 U.S. Patent 5582001 motor plot 2, TEAL flowing the entire burn.

> to vaporize the liquid oxygen. Examination of motor pressure data indicates that the effect of TEA/TEB combustion on stability appears to be significant in some cases and less so in others.

Motor 2's vaporization chamber design (and motor 1's) came from the inherent safety consideration and argument between a safe, solid inert hybrid fuel with a zero TNT equivalency requiring a pyrophoric liquid to start it and make it operate in a stable condition. The special care needed to handle the pyrophoric liquid had raised a question of the handling safety of the whole system. Also, members of the consortium had come to doubt if motor 1 would be stable, and so it was decided to test a concept where the ignition and the stabilizing heat would come from a hybrid motor itself instead of a pyrophoric liquid. Motor 1 retained the pyrophoric liquid for ignition purposes only.

Additional testing was conducted on the 11-in. and 24-in.-diam LOX motors to evaluate this concept. Jones et al. [16] discuss the results of the 11-in. motor ignition system and the 24-in. motor vaporization system testing. Testing of both sized motors was performed to see if small hybrids could start large hybrids and if the heat could keep it stable. Startup was smooth, and combustion stability was increased compared to motors without this active heat source. The success of this testing led to the incorporation of the hybrid "heater motors" into the 24-in. Large Subscale Quad Port Test Series. Jones et al. [16] report

> On test HP24-8020, the (GOX feed to the heater motor) system was terminated at T+11 seconds which caused the motor to go unstable .... The test confirmed the hypothesis, as shown in multiple 11- and 24-inch tests series, that the flame anchoring in the head-end of a hybrid motor is essential for motor stability.

The conclusion that heat addition was necessary was also supported by the 11-in.-diam GOX testing for passive techniques for combustion stability. An interesting footnote to that work was the conclusion that "heat released from combustion of hydrogen gas in the dump plenum at an estimated mixture ratio of 120 also stabilized combustion in configurations that were otherwise clearly unstable." This conclusion was also used in the design and development of motor 2 [19].

Two HPDP tests [22] show the effect of fins and no fins on multiport hybrid motors. These motors were tested with the same conical injector. The motor having fins in the forward dome had more fuel regress (19.64 lbm) than that of the motor dome without the fins (4.24 lbm), even if corrected for the burn time differences ($\sim$18 vs $\sim$8 s). However, that additional head end fuel regression did not result in an increased motor C^* efficiency (both yielded 98%) or combustion stability, as judged by the chamber pressure average oscillation divided by average pressure (1.60 vs 1.60%). The conclusion that can be drawn from Tables 4, 6, and 12 of Story and Jones [22] is that the impingement of LOX on the head end fuel fins can cause it to erode, but that additional fuel flow may not contribute to combustion stability or an increased C^* efficiency.

The motor 2 head-end design that was eventually built and tested was similar to the patented design [24] (Figs. 10 and 15). The design incorporated heater motors to start the main motor and provide heat to vaporize the LOX for combustion

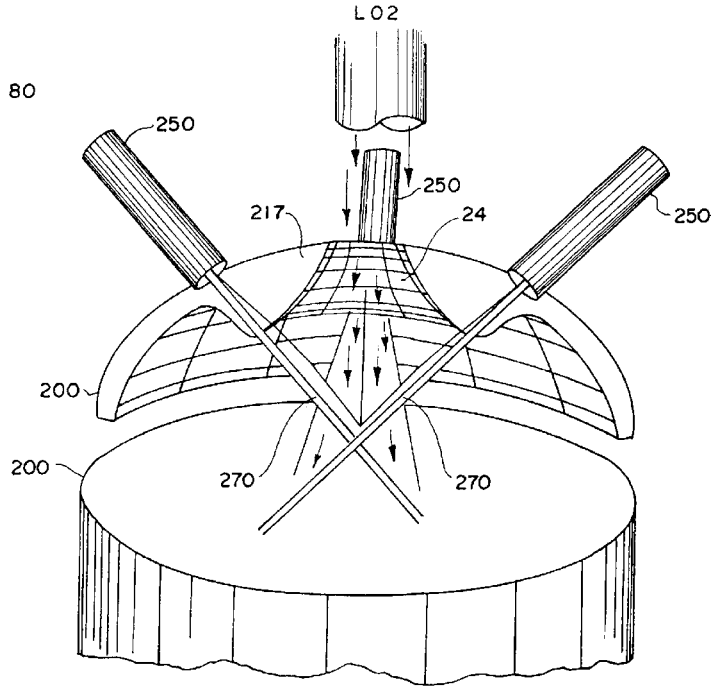

Fig. 15 U.S. patent 5794435, stable-combustion oxidizer vaporizer for hybrid rockets: 200) hybrid fuel, 250) small hybrid motors, 270) small hybrid motor exhaust gas flow, and arrows LOX flow.

stability. An axial injector was designed for motor 2 in as much as motor 1 used a conical spray pattern injector, and AMROC's patent [23] indicated that LOX impingement on the burning fuel surface could be a cause of the instability. The head end also incorporated a recirculation area in the front end, where gaseous oxidizer would theoretically recirculate and burn the head end fuel, generating even more heat.

D. Ballistic Tests

1. Motor 1, Test 1

Motor 1, test 1 was the first of the 250,000-lbf hybrids tested at NASA and was conducted on 9 July 1999. This was the passive combustion stability design employing fins in the head end and a flow deflector over the centerport (Fig. 10). It was lit by TEA/TEB and exhibited unstable behavior (Fig. 16). Because of an external TEA/TEB system fire, the test conductors terminated the test prematurely. There was minor scorching of some of the TEA/TEB ignition system components, however, no damage to the test stand. Calculations have shown that the requested TEA/TEB flow rate to motor was supplied even though some TEA/TEB escaped to the atmosphere. Subsequent testing of the TEA/TEB ignition system indicated

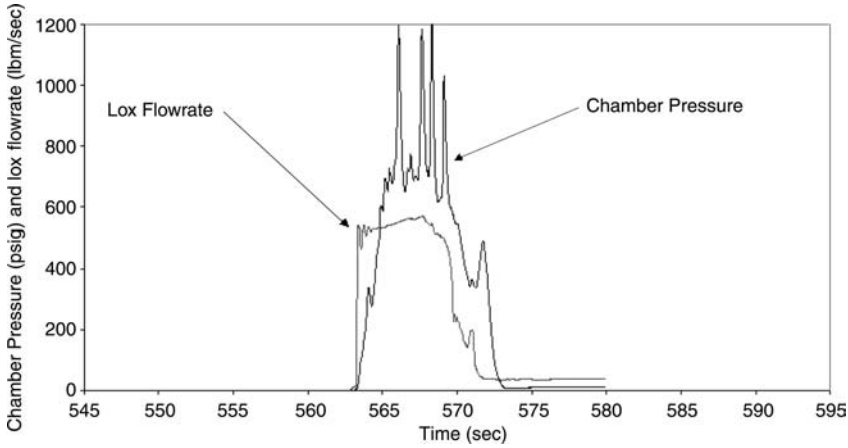

Fig. 16 HPDP 250,000-lbf motor 1, firing 1 [3].

failed pressure transducer diaphragms, which were overpressured due to water hammer effect, causing the TEA/TEB to leak. Once the TEA/TEB, a phyrophoric liquid, came in contact with air, it burned.

2. Motor 2, Test 1

Motor 2, test 1 was the first test of the active combustion stability system, with embedded heater motors in the head end. The ignition system consisted of two banks of small gaseous hybrid motors embedded in the forward dome of the motor. The test was conducted on 13 August 1999. Ignition was smooth, and combustion was stable (Fig. 17). A small pressure blip that occurred during the

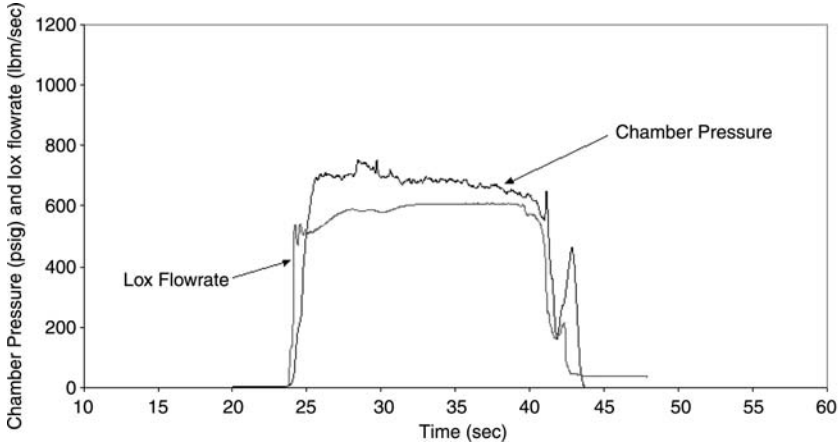

Fig. 17 HPDP 250,000-lbf motor 2, firing 1 [3].

first few seconds of the test was believed to be from the backlighting of one bank of the gaseous hybrid motors in the head end. Pretest checks indicated that the ignition system of one of the banks of gaseous hybrid motor was shorted out.

3. Motor 2, Test 2

Motor 2, test 2 was a refiring of the motor 2, test 1 hardware, except the nozzle from motor 1, test 1 was used. The test was conducted on 9 September 1999. The nozzles, by design, were refurbished between each test, and the nozzle from motor 1, test 1 was available and had eroded less than the nozzle from motor 2, test 1.

Motor 2, test 2 ignited smoothly; however, large pressure oscillations were encountered during the burn (Fig. 18). It is believed the small gaseous hybrid heater motors, as they burned (where the ports got bigger and the flux dropped, which shifted the O/F), produced less heat to provide the amount necessary for LOX vaporization and hold to the flame at a fixed location to establish combustion stability.

4. Motor 2, Rework

Because the small gaseous hybrids for heater motors had burned till they were no longer able to provide a sufficient heat source and/or flameholding device, they were drilled out and recast in a slightly different configuration.

5. Motor 2, Test 3

Motor 2, test 3 was reassembled using the refurbished nozzle from motor 2, test 1. The test was conducted on 17 January 2002 and exhibited a smooth ignition and steady pressure trace (Fig. 19). The small pressure disturbances/blips are believed to be from ejecta. Parts of the recasting of the head end were found posttest outside the motor.

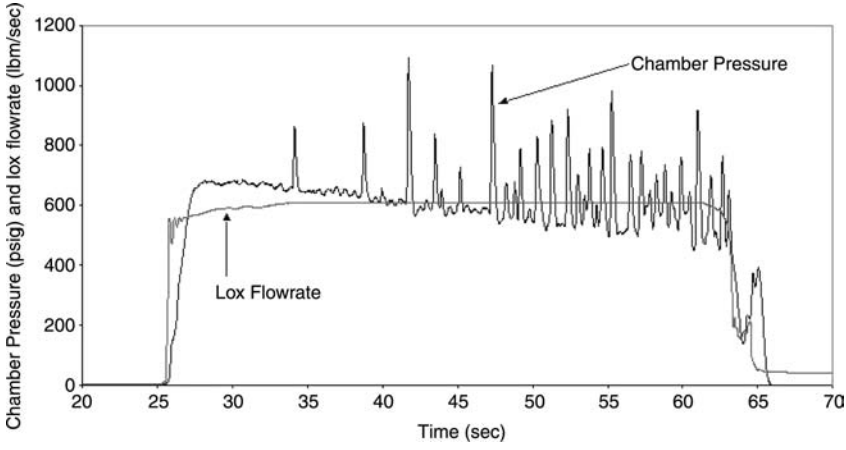

Fig. 18 HPDP 250,000-lbf motor 2, firing 2 [3].

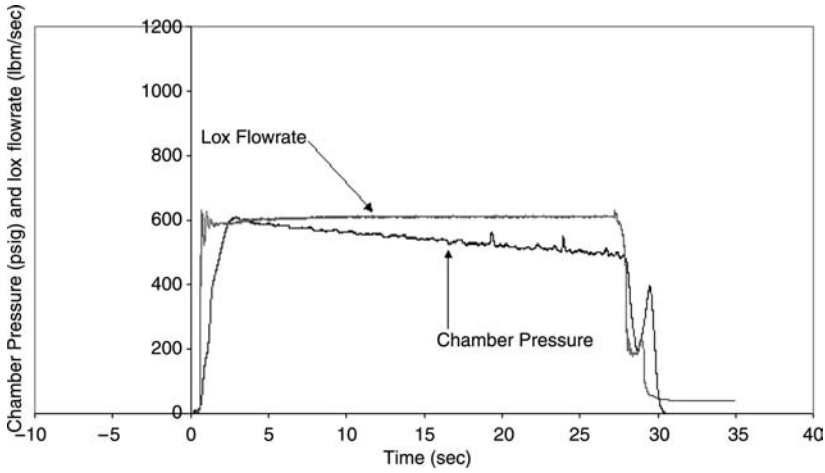

Fig. 19 HPDP 250,000-lbf motor 2, firing 3 [3].

Motor weights were calculated by three techniques during the 250,000-lbf program. The first technique was to weigh the components or, sometimes, the assembled motor on a truck scale (at MSFC and/or SSC). The second technique was use of a system called the bore crawler. It used mechanical arms and fingers to measure the port geometry pre- and posttest. Data from that technique were provided by Park et al. [25]. A third technique was developed that used a laser to map the port area. The laser was pulled through the individual ports pre- and posttest, and the area of the ports at those locations were calculated. From that information the motor weights were calculated. The data from the laser technique, indicating the port shape, are shown in Fig. 20.

Average regression rate data of the ports per test are shown in Figs. 21–23. There was a significant difference between the three weighing techniques, with the maximum percentage differences of techniques near 10%. This has lead to some uncertainty in the performance calculations. Another possible contributor to

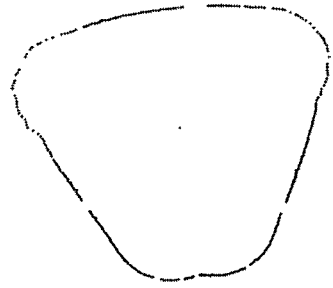

Fig. 20 Laser port mapping sample, pretest port [3].

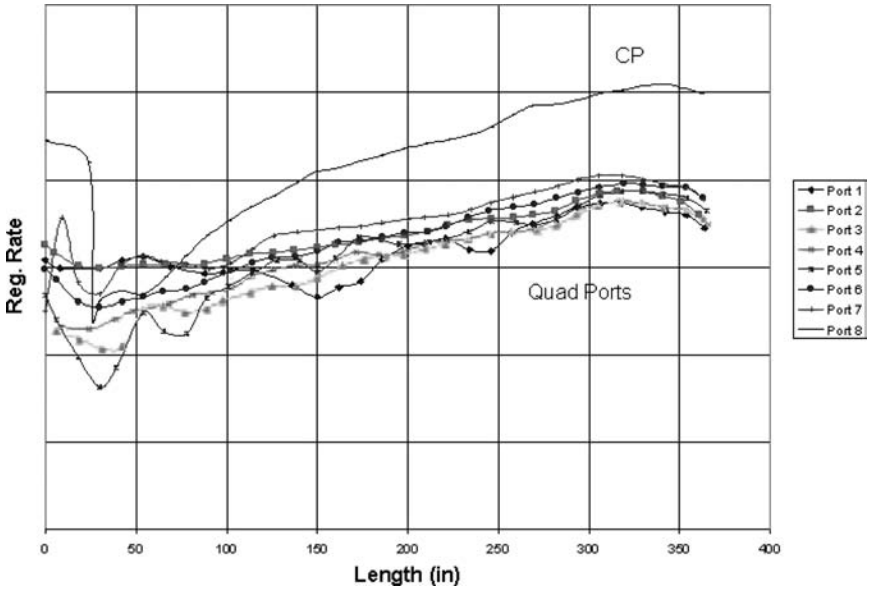

Fig. 21 HPDP 250,000-lbf motor 2, test 1 regression rates (center port and quad ports) [3].

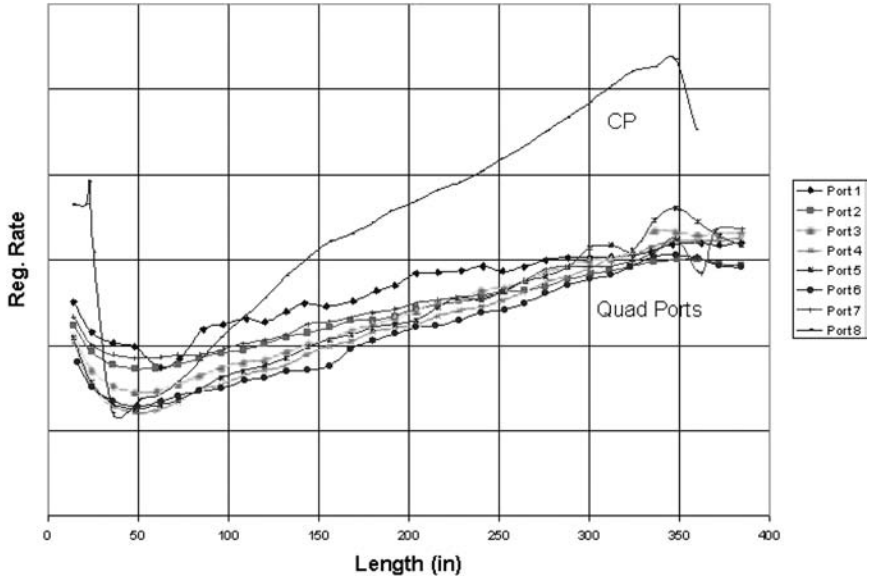

Fig. 22 HPDP 250,000-lbf motor 2, test 2 regression rates (center port and quad ports) [3].

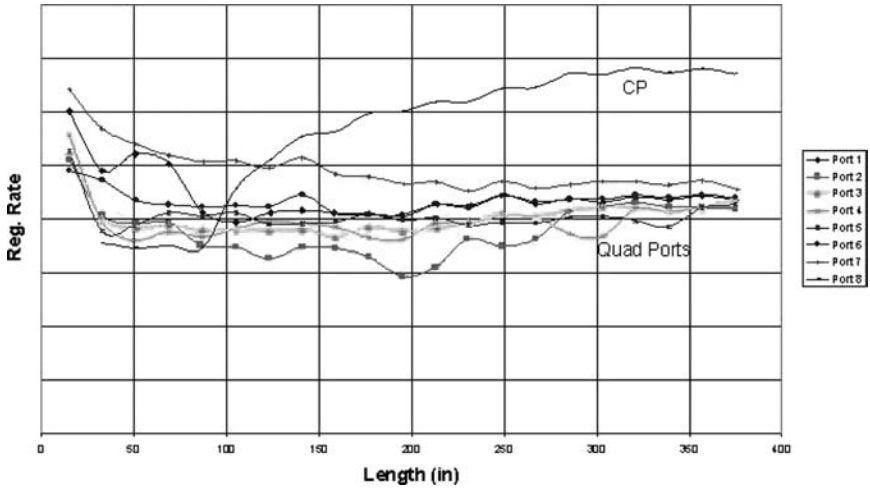

Fig. 23 HPDP 250,000-lbf motor 2, test 3 regression rates (center port and quad ports) [3].

the uncertainty in the performance calculations is that the cavitating venturi was never calibrated.

C^* data from theoretical calculations with $PC = 600$ psia are shown in Fig. 24. The test O/F and I_{sp}/C^* calculations are from HPDP final report [26] with laser mapping of centerport weights.

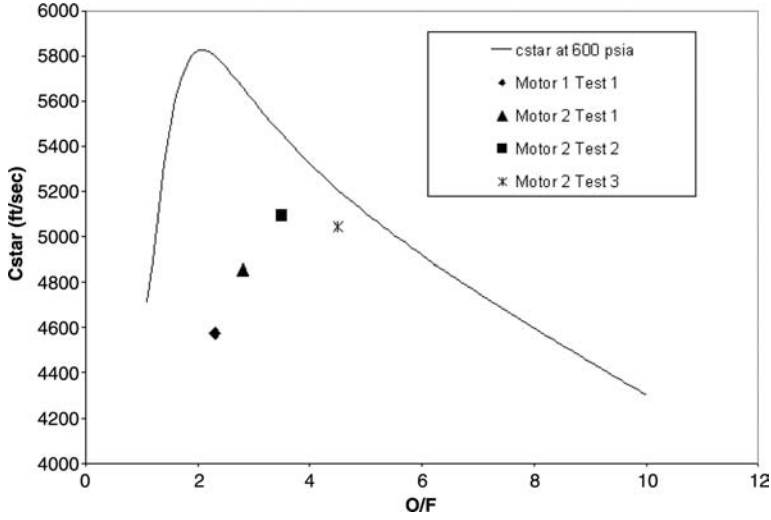

Fig. 24 Theoretical C^* vs data [3].

E. Performance Analyses

The global performance calculations for the motors are shown in Table 6. The high O/F ratios for the motor 2 tests can be attributed to two things: scale up from small hybrid rocket motor burn rates and the typical shift in O/F seen in hybrid motors. The 250,000-lbf hybrid was designed based on a motor with a hydraulic port diameter of 2. The hydraulic port diameter of the 250,000-lbf motor ports was on the order of four times as large. Subsequent testing of the three-quarter-scale motor, a large single-port quad motor, in the HPDP program provided a clue as to what would happen: an expected 30% reduction in fuel regression rate [2]. Other work comparing small ports regression rates extrapolated to larger ports showed an error in the regression rates greater than 10% [1]. Reduction in the fuel flow rate affects the O/F, chamber pressure, and thrust.

Stability of the tests can clearly be seen in the spectrograms of the test data Figs. 25–28. The spectrograms show the power spectral densities over time, with the amplitude at the right representing the logarithmic magnitude of the oscillations. The tests where the heater motors provided stability are easily recognizable. Another way to look at the stability is shown in Figs. 29–31, which show the filtered composite normalized by average pressure. The bandpass filter is between 5 and 500 Hz to remove the nonacoustic response. The oscillations upstream of the injector show the noise from the cavitating venturi. The two pressure blips in motor 2, test 3, which are believed to be ejecta, show up quite well. The unstable nature of motor 2, test 2 is also quite evident in Fig. 30, with the rms excursions denoting an excitation in acoustic activity concurrent with the low-frequency events.

F. General

A multiple-port grain configuration was used in 250,000-lbf hybrid motors due to the low fuel regression rate requiring a large surface area to generate the fuel flow necessary for desired thrust level. The head end and the aft end attached to each side of the main fuel grain represent a precombustion chamber for heating and vaporizing LOX and a mixing chamber for completing the reaction of unburned fuel with oxidizer, respectively. One explanation for the chamber pressure oscillations

Table 6 Average motor performance parameters [3]

		Motor 2		
Parameter	Motor 1, test 1	Test 1	Test 2	Test 3
Thrust, vacuum, lbf	177136.9	186336.9	210065.5	195989.4
I_{sp} vacuum	250.0	248.6	276.9	263.9
I_{sp} vacuum efficiency	0.77	0.78	0.90	0.92
C^*	4,576.3	4,855.9	5,092.9	5,044.2
C^*%	78.7	84.9	93.5	97.6
Global O/F	2.3	2.8	3.5	4.5
Duration, s	7.9	18.6	38.9	28.0
Chamber pressure, psia	594	625	600	542

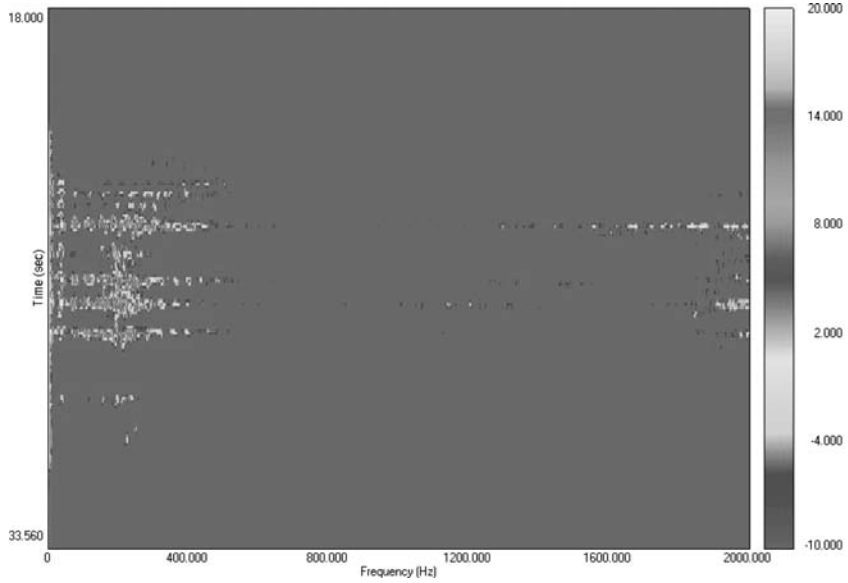

Fig. 25 Motor 1, test 1 Fwd *PC* spectrogram [3].

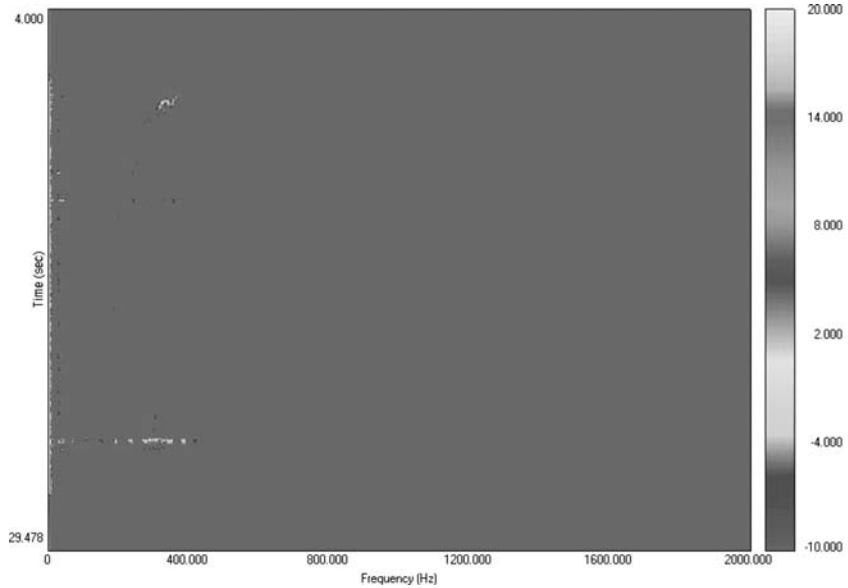

Fig. 26 Motor 2, test 1 Fwd *PC* spectrogram [3].

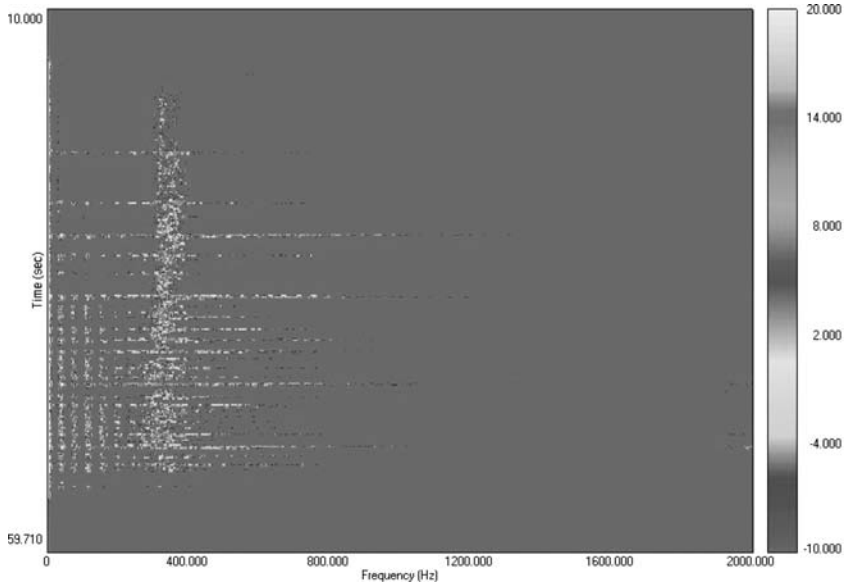

Fig. 27 Motor 2, test 2 Fwd *PC* spectrogram [3].

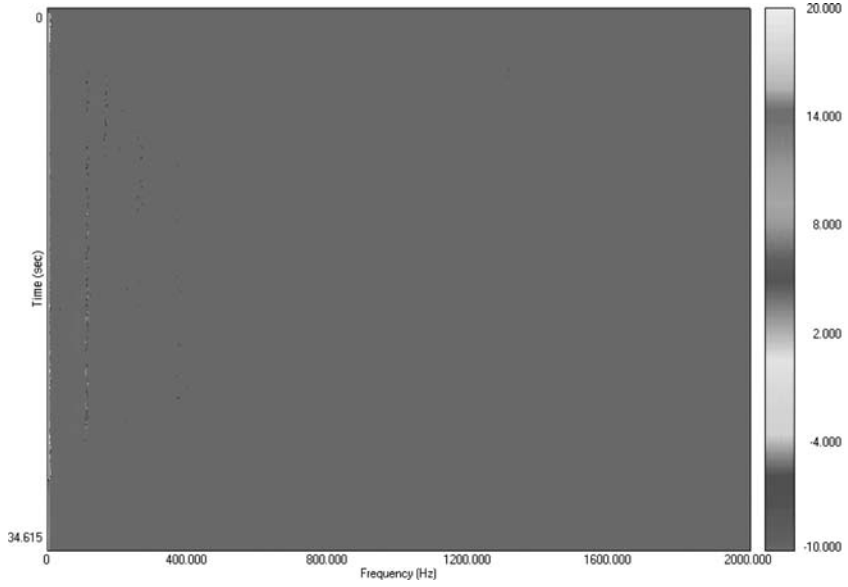

Fig. 28 Motor 2, test 3 Fwd *PC* spectrogram [3].

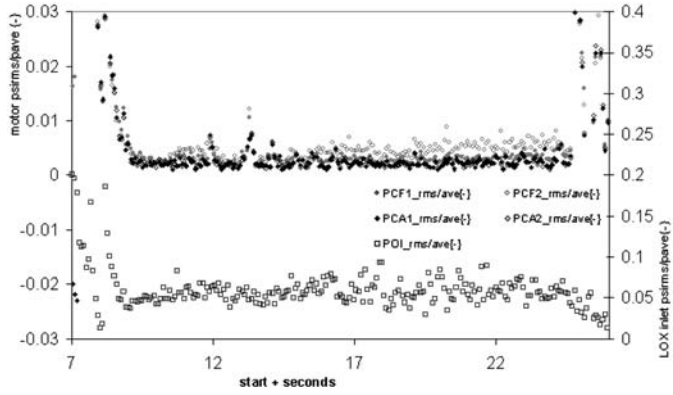

Fig. 29 Filtered composites normalized by average pressure, motor 2, test 1 [3].

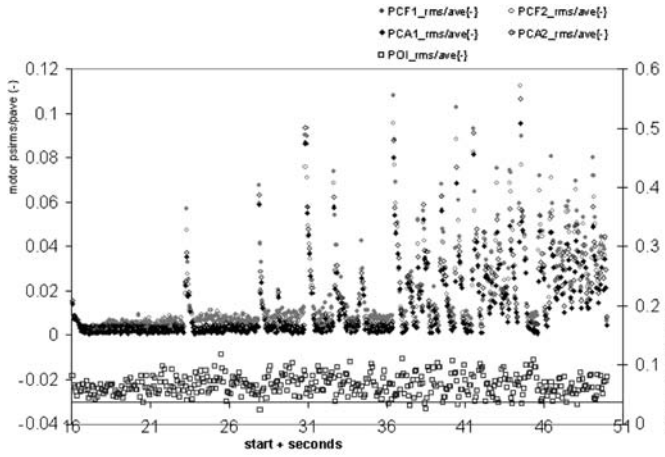

Fig. 30 Filtered composites normalized by average pressure, motor 2, test 2 [3].

that occurred in motor 1, test 1 and motor 2, test 2 may be because of different fuel regression rates in the multiple chambers (quad ports and centerport) that resulted from uneven LOX distribution, incomplete vaporization of LOX at lower temperature, and incomplete combustion in the mixing chamber. The operation of the heater motors in motor 2, tests 1 and 3 seems to have corrected for these phenomena. However, incomplete reaction of fuel with oxidizer in the ports and in the aft mixing chamber may have lowered the motor combustion efficiency in all of the motors.

To prevent unstable combustion in hybrid motors, flow and combustion conditions under the lower temperature of LOX and very oxidizer-rich environment at the forward end of the fuel grain need to be precisely determined to establish

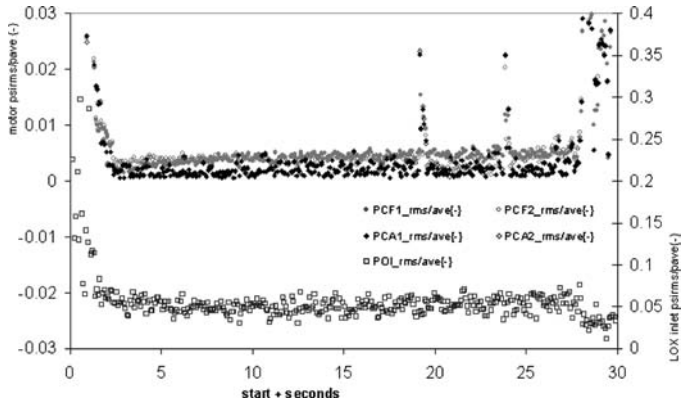

Fig. 31 Filtered composites normalized by average pressure, motor 2, test 3 [3].

a proper flame front, which keeps the motor stable. A proper flame front was demonstrated using the hybrid heater motors on motor 2, tests 1 and 3.

G. Performance

Motor performance in terms of the C^* efficiency yields 78–97%, whereas in terms of vacuum I_{sp} yields 77–92%. The low C^* efficiency implies that the fuel that was released from the grain did not burn completely, which may have been due to poor mixing of the oxidizer-rich and fuel-rich areas of the gasses in the motor. The I_{sp} efficiency was lowered by the C^* efficiency issues, as well as the low pressure due to the lower than expected fuel regression rate. Based on the bore crawler data, the amount of fuel regression in motor 1 indicates severe difference from each port [25]. The amount of regressed fuel of the quad ports vary from 155 to 220 lbm with the centerport of 112 lbm, which is equivalent to the minimum regression of the quad ports after compensation of the cross-sectional area ratio. The low regression of the centerport in motor 1 is believed to be because of the existence of the flow deflector, causing a tortuous path for the LOX to take. In contrast, in motor 2, fuel regression in the centerport exceeds the maximum regression in the quad ports, implying a larger amount of oxidizer flowing through the centerport than the quad ports. Motor 2's axial injector directs the LOX directly toward the centerport.

H. Pressure

Motor pressure–time characteristics in Figs. 16–19 exhibited both stable and unstable combustion, especially large-amplitude pressure oscillation in the motor 1 test and the second test of motor 2. The averaged chamber pressures of motor 1 and motor 2 lie between 542 and 625 psia, far less than the designed average pressure of 750 psia at LOX flow rate of 600 lbm/s, as given in Table 5. In the motor 1 test and the second test of motor 2, severe chamber pressure fluctuations (spikes) were noticed throughout the tests. Relatively small pressure peaks at the ending period are due to the onset of gaseous nitrogen for shutdown. In motor 1, test 1 and motor 2, test 2, each pressure spike using the high-speed data acquisition system

(12,500 data/s) revealed similar characteristics of pressure buildup and discharge processes. Magnitude of the spikes are generally close to the theoretical maximum operating pressure level, although some surged as much as twice the mean pressure. Decrease in pressure timewise is expected, due to the throat erosion, lower flux level, as the ports open up with subsequent lower fuel regression rates changing the O/F ratio.

I. C^*

One of the ballistic parameters that quantifies motor performance is C^*, a characteristic velocity shown in Fig. 32. The ratio of actual C^* to the theoretical maximum C^* from the industry standard thermochemistry code represents motor efficiency. The C^* efficiency in Fig. 32 indicates that a significant amount of fuel has not released all of its energy inside of the motor as previously experienced [27], as shown in Fig. 24. Also, the C^* efficiency seems to be higher in the motors with motor with higher O/F ratios. These phenomena have been observed in single-port subscale motors [28]. Possible causes in the 250,000-lbf hybrid may be that the same mixing in the aft end of a motor may cause more combustion in an oxidizer-rich environment or that the lower flux levels provided more reaction time in the ports and mixing chamber.

J. Regression Rate

Direct measurement of the port circumferences was attempted using both mechanical (crawler) and laser measuring devices to calculate the amount of fuel regressed. Figure 20 shows a typical prefire quad-port configuration and Figs. 21–23 show the average fuel regression rate of individual ports of motor 2 acquired by the laser device. Notice that the regression profiles of the quad ports are not

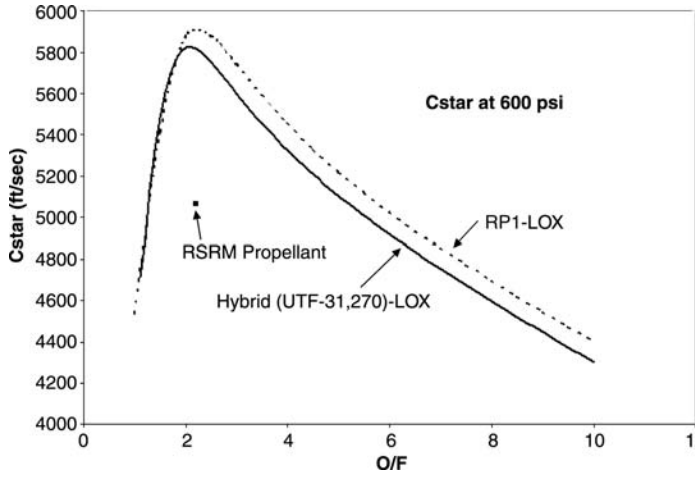

Fig. 32 Theoretical C^* performance of UTF-31,270 with LOX [3].

coincident with the result from the crawler [25]. Also, note that direct impingement of oxidizer flow increases regression rate at the port as shown in Figs. 21–23.

In general in motor 2, the regression rate increases monotonically lengthwise except in the third test where the rate for the quad ports stay relatively in constant. From this result, it is obvious to consider dependency of the LOX flux level, motor length, and port diameter in a fuel regression correlation.

K. Stability

A hybrid motor differs fundamentally in terms of combustion behavior compared with solid and liquid rockets in that the O/F ratio has an axial dependency. Historically, both acoustic instabilities and NIAs related to the motor geometry were encountered during the development of a large-scale hybrid rocket motor. It is believed that the relatively cold flow of oxidizer in the head end causes pressure oscillation; thus, methods of adequate LOX vaporization, reduced droplet size, and use of flow deflector were introduced to suppress combustion instabilities [7]. Significant effort was made to evaluate combustion instability during the hybrid motor development in terms of vortex shedding [18] and diffusion flame movement [29], but the complexity of the multiphase diffusion flame combustion dynamics in the turbulent reacting flow has not been fully disclosed yet.

From the instability point of view, it is not clear from Figs. 21–23 that, excluding deviation in the quad ports, significant difference in the regression rate at the centerport from those at the quad ports in the second test leads to unstable combustion because motor 2, tests 1 and 3 were stable.

Variation of local O/F ratio in the combustion chambers may be a key factor for determining hybrid motor stability. In addition, the multiport with a one head end LOX injector configuration having pressure variation between combustion ports from the uneven distribution of oxidizer could be an additional source for the instability by developing pressure oscillation in the tangential mode at the port entrance. The centerports in motor 1 and motor 2 are examples of the uneven distribution cases. The apparent local O/F ratio in the centerport of motor 1 seems lower than the optimum value from the entrance leading to a fuel-rich condition through the entire port length. It could be a result of the flow deflector. In contrast to motor 1, the centerport (CP) of motor 2 has much higher oxidizer level at the inlet, allowing a continuous increase of the fuel regression rate downstream with the ongoing advantage of higher temperature. Even an excessive amount of LOX at the inlet might cause the port entrance to be under two-phase combustion.

AMROC apparently experienced the same situation with different regression rates in the CP and outer port and designed around it, because their large-scale motors used only quad ports and blocked the CP. The blocked CP also acted as a splashblock, which increased the residence time in the forward chamber [7, 18].

A possible cause for pressure fluctuation in these motors is the difference of the fuel regression rate between the upstream and the downstream in the chamber and/or continuous throat erosion. A traveling wave in the combustion chamber disturbs turbulent mean flowfield characteristics in the ports, which enhances mixing of unburned fuel and oxidizer in a periodic fashion and the fuel regression rate by enhanced heat transfer to the fuel. From this point, the gas filling and discharging sequence is being unbalanced until the chamber pressure reaches the

maximum operating status. Continuous fuel regression and throat erosion disrupts the continuity by discharging more gases, resulting in lowering the chamber pressure. This single-port combustion phenomenon, along with the interaction with the other ports in a multiport design, could have lead to the instability caused in motor 1, test 1 and motor 2, test 2.

L. Nozzle

It was obvious that the reaction of carbon in the throat with hot oxygen in the exhausting gases accelerated the throat erosion. Real-time erosion rate of the throat is not available because only pre- and postmeasurements were conducted. The results showed a higher erosion rate than predicted from the early subscale test data, with low O/F ratios [30]. However, later subscale tests with the same material indicated a similar erosion rate [16]. Different characteristics of the gas flow from the individual combustion ports caused irregular throat erosion aligned with the ports. This has been seen before in tests with multiport grains [30] and was expected.

Figure 33 shows thrust vs chamber pressure ratio for motor 2 as an indirect indication of the throat erosion characteristics. The slope of the curve in Fig. 33 correlates with nozzle erosion rate. Note that discontinuities in the second test are due to the pressure peaks, where instantaneous changes of the thrust coefficient, a dependent parameter on chamber pressure, occurred. Ignoring the discontinuities, throat erosion rate remains relatively constant, excluding the transient period of initial heating and charring at the beginning stages.

M. HPDP 250,000-Pounds Force Conclusions

Motor 1's passive design was unstable. This does not imply that all hybrids of this size will require an active heat source in the front end of a hybrid, but this one was unsuccessful in achieving stable performance. Motor 2 was stable during tests 1 and 3, but drastically unstable in test 2. The concept to add heat in the head end of the motor worked, but the design solution tested could not provide stability for the full 80-s duration. Another design solution will have to be worked for future full-duration testing.

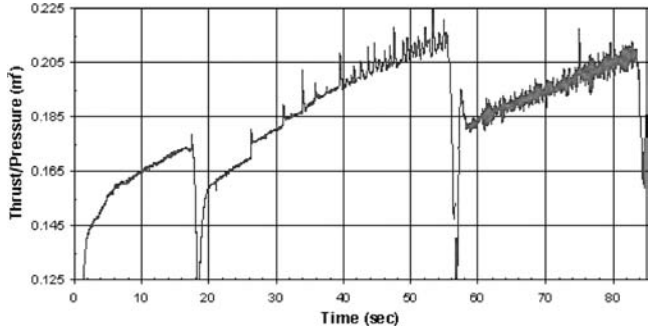

Fig. 33 Motor 2 tests, thrust/pressure [3].

Scaleup from small hybrids to large hybrids, as demonstrated by the achieved regression rates and lower than expected chamber pressures, was not done effectively on this program. Scaleups should be made from the largest port data possible.

The nozzle material selected for this program eroded greater than the design parameters.

HPDP 250,000-lbf testing, in some fashion, should continue. The I_{sp} and stability observed in these tests provide an incentive to further improve this simple rocket system. Motor 1's grain has been fired for only 8 s, and there have been several suggestions put forward for additional testing.

VI. Scaled Composites SpaceShipOne

In 2004, a small hybrid rocket-powered, privately developed spaceship was released from an airplane and flew to the edge of space. This vehicle was developed to win the X Prize and had to be flown twice within two weeks. Although the size of SpaceShipOne's hybrid is not necessarily large in terms of thrust, its test setup and integration into the vehicle were shown to be novel and ingenious. In a test-what-you-fly mantra, Scaled Composites built a portable test stand that contained the flight oxidizer tank as well as the hybrid motor, in the inflight configuration (Fig. 34). This allowed the propellant weights to be weighed directly on the test stand, using sensors built into the device. This was especially necessary due to

Fig. 34 Scaled Composites test trailer [data available at http://www.scaled.com].

the use of nitrous oxide as an oxidizer. Nitrous oxide properties are not as well documented as those of LOX or even hydrogen peroxide, and the weight of the oxidizer tank and contents is a good way to keep track of the flow rates.

Several items of interest include the following:

1) The motor case is directly tied into the oxidizer tank, with the plumbing inside the tank (Fig. 35). This reduces the need for an additional structure to carry the load from the motor through the tank. Also, it reduces the expansion/contraction issues with oxidizer loading, even though those should be minimal with room-temperature nitrous oxide.

2) The motor case and nozzle overwrap is a one piece item, with fewer leak paths due to fewer connection points.

3) The hybrid had a cutoff system in case of hybrid motor burn through. A fiber optic wire was wrapped around the motor case, and if it was broken/burnt through during the flight, the oxidizer valve was to be commanded shut and the thrust terminated, increasing the safety of the system.

4) It was also reported that to prove the insulation system was tolerant to the fuel burning irregularly, one motor case was fired for twice the normal 80-s burn time, with no burn throughs.

The basic sizing and design of the oxidizer tank and hybrid motor configuration was designed by Tim Pickens working directly for Scaled Composites.

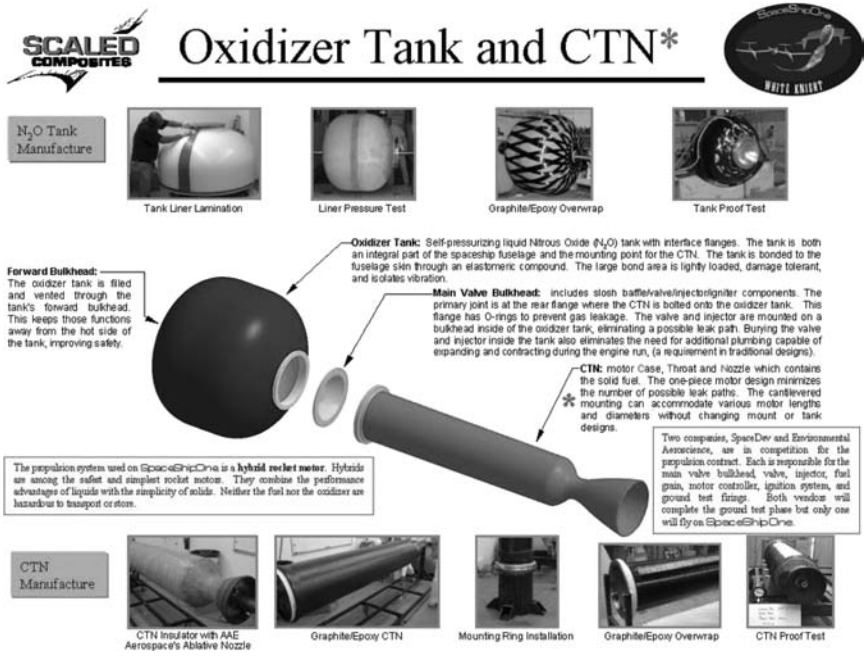

Fig. 35 Scaled Composites hybrid motor [data available at http://www.scaled.com].

The specifics of the interior configuration (number of ports, fuel type, and ignition system) of the hybrid motor were designed and proposed by two competing companies with experience in hybrid rocket motor testing and development: Environmental Aerosciences Corporation (eAc) and Space Dev. Space Dev had previously purchased the rights to AMROC technologies, patents, and test data. eAc had been a participant in the development and flight of the HPDP N_2O/HTPB sounding rockets launched out of NASA Wallops Flight Facility in 1996 and 1997. The internal configurations of the motors were slightly different; eAc proposed a single-port design and SpaceDev proposed a four-port design [31]. After a series of ground tests on the test trailer, Scaled Composites awarded the contract to Space Dev, and their motors have been flown on all the SpaceShipOne flights leading to winning the X prize.

VII. Lockheed Martin/Defense Advanced Research Projects Agency Falcon Testing

A large hybrid rocket motor was successfully test fired 21 January 2005 on the U.S. Air Force Research Laboratory's Test Stand 2-A on the ridge overlooking Edwards Air Force Base dry lake bed and surrounding California's Mojave Desert (Fig. 36). The test ran for the planned 60-s duration, and an initial review of the data indicates that test objectives were met.

A second version of the motor was fired for 120 s on 10 June 2005. The second fuel grain was designed such that the 120-s test firing represented over 170 s of runtime for the flight configuration.

Fig. 36 Lockheed Martin Falcon Test 21 Jan. 2005.

The hybrid motors that were tested are full-scale versions of an upperstage motor and measure 11 ft in length and 5 ft in diameter. Besides the thrust size of this motor, ~23,500 lb of thrust, and long duration, another item of interest about this testing is that the test was the first to fire a multiport, multirow hybrid motor [Lockheed Martin press releases]. Although the details of this configuration have not been publicly released, the change in configuration might represent a step forward in the technology from the documented previous large-scale hybrid testing.

These tests supported the Defense Advanced Research Projects Agency (DARPA)/U.S.Air Force/NASA Falcon Program, which was a 36-month long Phase II effort to develop and demonstrate an affordable and responsive space lift launcher capable of placing a small satellite, weighing 1000 lb, into a circular orbit of 100 mile.[†]

VIII. Lockheed Martin's Planned Fuel Expulsion

One of the potential shortcomings of hybrid rockets is the residual fuel left remaining in a motor after the burn and the potential failure modes of a multiport web breaking off and damaging the nozzle or plugging the throat. Previous design solutions have been shown to increase the fuel strength by web stiffeners [32], overbuild the web thickness to eliminate the concern by intentionally leaving the residual web overly thick (which works well for ballistic motors and HPDP 250,000-lbf), or just overdesign the system to account for the residual fuel. The problem with these solutions is it does not optimize the hybrid for a flight configuration because the motor has to accelerate that inert residual fuel mass. An optimal solution would be that the fuel remain in place and continue burning until it was wafer thin.

Lockheed Martin investigated the fuel expulsion issue, at what point would the fuel fail, and how best to deal with it. A structural model was developed based on a beam model, using pressure differences between the ports as the loading of the beam. Because the pressure in individual ports is difficult to model, an approximation was made that the difference between the forward and aft chamber pressure could be the limiting case for the port-to-port differential pressure. That fuel structural model was integrated into a ballistics code, where once a piece of fuel got to where it would analytically fail and would break off, it no longer contributed to the ballistic performance of the motor. They performed two tests of a 10-in.-diam hybrid motor: one with a low tensile strength fuel and another with a higher tensile strength fuel. The low tensile strength fuel failed at a residual web thickness of approximately 1 in., and the effect was visible in the pressure trace. The high tensile strength fuel lasted much longer in the burn and started breaking at a web thickness of approximately 0.155 in. Because of the noise in the pressure trace, it is difficult to determine when the fuel broke loose, but the implications of the testing are clear: A high tensile fuel may permit the web thickness to remain intact in the motor longer and break off only when the parts are small, allowing hybrid rockets to burn to almost depletion on the fuel side, increasing the system

[†]Data available at http://www.darpa.mil/body/news/2004/falcon_ph2_tbpdf.

performance by lowering the inert weight, and lowering the risk of the potential fuel failure modes because the fuel segments are so small [33].

IX. Conclusions

Hybrid motors have been demonstrated at large sizes with good success. These successes and the inherent safety and simplicity of hybrids have lead hybrids to be the propulsion system of choice for a privately developed manned application.

AMROC's experience with the DM-01 demonstrates that a large-scale hybrid can be designed, fabricated, and tested in 13 months. SpaceShipOne's hybrid motor was also developed, integrated with the flight system, and flown in just a few years. Manufacturing processes to develop and build hybrid rocket motors are available and ready to use.

Scaleup from small hybrids to large hybrids, as demonstrated by the achieved regression rates and lower than expected chamber pressures, was not done effectively on the HPDP 250,000-lbf program. Burn rates, derived from multiport motors with port hydraulic diameters of 2, were used to design the HPDP motor, without any adjustment for port size. The designed HPDP 250,000-lbf port diameters were on the order of four times as large as the motor from which the burn rate came, without any verification of those burn rates at near the final size until much too late in the program. Inaccurate predictions of regression rate on the large-scale data, based on subscale data, show up in higher than planned oxidizer-to-fuel ratios and result in lower chamber pressure and thrust values. The HPDP 250,000-lbf missed the regression rates by $\sim$30% and, therefore, missed the target pressures and thrust values. However, on AMROC's large motors, the scaleup was done effectively: Small-scale burn rates were tested on larger, full-sized biport motors, which allowed the burn rates to be adjusted before the final design of the full-scale multiport motor. For conventional hybrids with forward oxidizer injection, scaleups should be made from the largest port data possible. Testing of hybrids should be as close to the flight size as possible to understand the possible lower regression rates and stability issues that appear in larger motors.

AMROC lead the way in solving the NAI combustion stability concerns associated with large-scale hybrid rockets. They successfully demonstrated a solution with the stable DM-01 and DM-02 firings. HPDP demonstrated that the similar combustion stability could be obtained with heat addition from the forward end provided by smaller hybrid motors.

Most large-scale hybrids have been tested with pressure-fed systems. Pressure-fed systems have been employed successfully on the hybrid flight systems (Firebolt, SpaceShipOne). Larger flight systems may need to be powered by pump-fed systems. AMROC, AlliedSignal Aerospace, and NASA SSC have demonstrated that hybrids can have stable combustion with a pump-fed LOX system at a meaningful thrust and flow level.

There is still work that needs to be completed on large-scale hybrids to make hybrids more competitive. The oxidizer-rich hybrid combustion products have shown to have higher than expected erosion rates on some of the traditional solid rocket motor throat materials. Lower throat erosion would lead to an increase in the performance of the motors and, therefore, is an area that needs to be investigated further. Another concern that needs to be addressed further is lowering the

residual burnout mass of hybrid motors: A solution has been demonstrated at a representative scale, with high tensile fuel that remains in place until web is very thin, that shows promise. Analytical tools need to be developed to predict the fuel regression rates as the combustion ports are scaled up in size; currently this must be done empirically.

Hybrid motors at the 250,000-lbf size have demonstrated that they can be stable at or near the design thrusts and pressures by both HPDP and AMROC testing. Subsequent designs should reap the lessons learned from those programs and lead to a stable and efficient hybrid rocket motor design for large-scale applications.

References

[1] Estey, P., Altman, D., and McFarlane, J., "An Evaluation of Scaling Effects for Hybrid Rocket Motors," AIAA Paper 91-2517, 27th AIAA/SAE/ASME/ASEE Joint Propulsion Conference, Sacramento, CA, June 1991.

[2] Yee, S. M., and Shaeffer, C. W., "Fuel Regression Characteristics in Two Hybrid Motor Configuration," AIAA Paper 97-3079, 33rd AIAA/SAE/ASME/ASEE Joint Propulsion Conference, Seattle, WA, 1997.

[3] Story, G., Zoladz, T., Arves, J., Kearney, D., Abel, T., and Park, O., "Hybrid Propulsion Demonstration Program 250K Hybrid Motor," AIAA Paper 2003-5198, 39th AIAA/SAE/ASME/ASEE Joint Propulsion Conference, Huntsville, AL, 2003.

[4] Weyland, H. H., "Hybrid Rocket Motor Fuel Studies," AIAA Paper 97-3077, 33rd AIAA/SAE/ASME/ASEE Joint Propulsion Conference, Seattle, WA, July 1997.

[5] Estey, P., and Whittinghill, G., "Hybrid Rocket Motor Propellant Selection Alternatives," AIAA Paper 92-3592, 28th AIAA/SAE/ASME/ASEE Joint Propulsion Conference, Nashville, TN, July 1992.

[6] Altman, D., "Hybrid Rocket Propulsion, Prospects for the Future," AIAA Paper, AIAA Annual Meeting and Technical Display, Long Beach, CA, May 1981.

[7] Guthrie, D. M., and Wolf, R. S., "Non-Acoustic Combustion Instability in Hybrid Rocket Motors," AIAA Paper, 26th AIAA/SAE/ASME/ASEE Joint Propulsion Conference, Orlando, FL, July 1990.

[8] Estey, P. N., McFarlane, J. S., Kniffen, R. K., and Lichatowich, J., "Large Hybrid Rocket Testing Results," AIAA Paper 93-4279, AIAA Space Programs and Technologies Conference, Huntsville, AL, Sept. 1993.

[9] Estey, P., "Hybrid Technology Option Project: A Cooperative Effort for Tomorrow's Space Transportation," AIAA Paper 94-4503, AIAA Space Programs and Technologies Conference, Huntsville, AL, Sept. 1994.

[10] McFarlane, J. S., Saville, M. P., and Nunez, S. C., "Testing of a 10,000 lbf Thrust Hybrid Rocket Motor with a Foil Bearing Lox Turbopump," AIAA Paper 95-2941, 31st AIAA/SAE/ASME/ASEE Joint Propulsion Conference, San Diego, CA, July 1995.

[11] Boardman, T. A., Abel, T. M., Claflin, S. E., and Shaffer, C. W., "Design and Test Planning for a 250-KLBF Thrust Hybrid Rocket Motor under Hybrid Propulsion Demonstration Program," JANNAF Propulsion and Joint Subcommittee Meeting, 9–13 Dec. 1996.

[12] Boardman, T. A., Abel, T. M., Claflin, S. E., and Shaeffer, C. W., "Design and Test Planning for the 250-klbf Thrust Hybrid Rocket Motor Under the Hybrid Propulsion Demonstration Program," AIAA Paper 97-2804, 33rd AIAA/SAE/ASME/ASEE Joint Propulsion Conference, Seattle, WA, 1997.

[13] Kliger, J. J., "JIRAD 11-inch Hybrid Motor Test Program," Thiokol Corp. Rept. TR 10197, Promontory, UT, July 1993.
[14] Boardman, T. A., Kliger, J. J., and Abel, T. A., "Solid Rocket Combustion Simulation Using a Hybrid Fuel Approach," 31st JANNAF Combustion Subcommittee Meeting, Oct. 1994.
[15] Abel, T. M., Carpenter, R. L., Claflin, S. A., Crawford, J. T., and Holt, D. M., "SRM Simulation and Hybrid Propulsion Testing at the Marshall Space Flight Center," AIAA Paper 95-2944, 31st AIAA/SAE/ASME/ASEE Joint Propulsion Conference, San Diego, CA, July 1995.
[16] Jones, M. D., Abel, T. M., and Weeks, D. J., "Subscale Hybrid Rocket Motor Testing at the Marshall Space Flight Center in Support of the Hybrid Propulsion Demonstration Program (HPDP)," AIAA Paper 97-2800, 33rd AIAA/SAE/ASME/ASEE Joint Propulsion Conference, Seattle, WA, July 1997.
[17] McFarlane, J. S., "10,000 lbf Thrust Hybrid Motor Testing at Stennis Space Center, A Hybrid Motor Testbed," AIAA Paper 96-2694, 32nd AIAA/SAE/ASME/ASEE Joint Propulsion Conference, Lake Buena Vista, FL, July 1996.
[18] McFarlane, S., Kniffen, J., and Lichatwich, J., "Design and Testing of AMROC's 250,000 lbf Thrust Hybrid Motor," AIAA Paper 93-2551, 29th AIAA/SAE/ASME/ASEE Joint Propulsion Conference, Monterey, CA, June 1993.
[19] Boardman, T. A., Brinton, D. H., Carpenter, R. L., and Zoladz, T. F., "An Experimental Investigation of Pressure Oscillations and Their Suppression in Subscale Hybrid Rocket Motors," AIAA Paper 95-2689, 31st AIAA/SAE/ASME/ASEE Joint Propulsion Conference, San Diego, CA, July 1995.
[20] Boardman, T. A, Carpenter, R. L., and Claflin, S. E., "A Comparative Study of the Effects of Liquid Versus Gaseous-Oxygen Injection on Combustion Stablitiy in 11-Inch-Diameter Hybrid Motors," AIAA Paper 97-2936, 33rd AIAA/SAE/ASME/ASEE Joint Propulsion Conference, Seattle, WA, July 1997.
[21] Carpenter, R. L., Boardman, T. A., Claflin, S. E., and Harwell, R. J., "Hybrid Propulsion for Launch Vehicle Boosters—A Program Status Update," AIAA Paper 95-2688, 31st AIAA/SAE/ASME/ASEE Joint Propulsion Conference, San Diego, CA, 1995.
[22] Story, G. T., and Jones, H. S., "Distribution of Liquid Oxygen in the Head End of a Multi-Port Hybrid Motor," AIAA Paper 97-2935, 33rd AIAA/SAE/ASME/ASEE Joint Propulsion Conference, Seattle, WA, July 1997.
[23] Bradford, M. D., Kniffen, R. J., and McKinney, B. C., "Hybrid Rocket Combustion Enhancement," U.S. Patent 5582001, 10 Dec. 1996.
[24] Jones, H. S., "Stable-Combustion Oxidizer Vaporizer for Hybrid Rockets," Lockheed Martin, U.S. Patent 5794435, Bethesda, MD, 18 Aug. 1998.
[25] Park, O. Y., Bryant, C. T., and Carpenter, R. L., "Performance Analyses of HPDP 250K Hybrids," AIAA Paper 2000-3544, 2000.
[26] "HPDP Final Report Package December 1999—Final Test Report," Lockheed Martin Astronautics, Huntsville Operations, Huntsville AL, Dec. 1999.
[27] Arves, J. P., and Jones, H. S., "A Standardized Technique for Evaluating Hybrid Rocket Motor Performance," AIAA Paper 97-2933, 33rd AIAA/SAE/ASME/ASEE Joint Propulsion Conference, Seattle, WA, July 1997.
[28] Karabeyoglu, M. A., Zilliac, G., Cantwell, B. J., DeZilwa, S., and Castelluci, P., "Scale-Up Tests of High Regression Rate Liquefying Hybrid Rocket Fuels," AIAA Paper 2003-647, 39th AIAA/SAE/ASME/ASEE Joint Propulsion Conference, Huntsville, AL, July 2003.

[29] Arves, J. P., Jones, H. S., and Wygle, B. S., "Flame Position and Surface Heating as a Factor in Hybrid Rocket Performance," AIAA Paper 96-3093, 32nd AIAA/SAE/ASME/ASEE Joint Propulsion Conference, Lake Buena Vista, FL, July 1996.

[30] Boardman, T. A., Carpenter, R. L., Goldburg, B. E., and Shaeffer, C. W., "Development and Testing of 11- and 24-Inch Hybrid Motors under the Joint Government/Industry IR&D Program," AIAA Paper 93-2552, 29th AIAA/SAE/ASME/ASEE Joint Propulsion Conference, Monterey, CA, June 1993.

[31] Dornheim, M. A., "Hybrid Matched to Spaceship Goals," *Aviation Week and Space Technology*, Vol. 158, No. 16, 21 April 2003.

[32] McKinney, B. C., and Kniffen, R. J., "Hybrid Rocket Motor Solid Fuel Grain," American Rocket Co., U.S. Patent 5,339,625, 23 Aug. 1994.

[33] Kearney, D. A., and Geiman, W. W., "Accounting for Planned Fuel Expulsion by Hybrid Rockets," AIAA Paper 2005-3546, 41st AIAA/SAE/ASME/ASEE Joint Propulsion Conference, Tucson, AZ, July 2005.

Chapter 14

Flight Testing of Hybrid-Powered Vehicles

George Story*
NASA, Marshall Space Flight Center, Alabama 35812

and

Joe Arves†
Lockheed Martin, New Orleans, Louisiana

I. Introduction

HYBRID rocket powered vehicles have had a limited number of flights. In 2004, Scaled Composites had a successful flight that put a manned vehicle in a trajectory that peaked at over 62 miles high, the edge of space. The profile was flown twice in two weeks to win the X-Prize. This endeavor successfully demonstrated a hybrid rocket used in a manned launch system. Hybrids have also been used in a number of one time launch attempts: Single-Engine Test-1 Launch Vehicle (SET-1), Hybrid Sounding Rocket (HYSR), and Hybrid Propulsion Demonstration Program (HPDP). Hybrids have also been developed for use and flown in target drones.

II. Background

A. Pacific Rocket Society

The Pacific Rocket Society was conducting tests and flight of hybrid rockets in the mid-1940s. The most successful of these units, where the propellants consisted of liquid oxygen (LOX) with a rubber fuel, was successfully tested in June 1951, reaching an altitude estimated to be about 30,000 ft [1].

*Engineer, Solid and Hybrid Propulsion Systems.
†Chief Engineer, Hybrid Propulsion Systems.

B. ONERA and Volvo-Flygmotor

The following description was reported by Altman [1]:

> During the early 1960s, two European organizations became interested in sounding rockets based on storable propellants utilizing nitric acid. These organizations were ONERA in France and Volvo–Flygmotor in Sweden. Both organizations conducted their investigations for about 10 years. ONERA developed a hybrid sounding rocket based on an amine fuel and nitric acid [2] which was 6.3 in. in diam and 130 in. long, weighing 165 lbs. The motor was throttleable over a 5/1 range to optimize performance. Its first successful flight occurred in 1964 and these flights continued over a three year period eventually reaching altitudes in excess of 100 km (over 10 times the altitude reached by the Pacific Rocket Society about 15 years earlier).

C. United Technology Center's Sandpiper/High Altitude Supersonic Target/Firebolt

Also in the early 1960s, United Technology Center and Beech Aircraft, under a U.S. Air Force contract, began work on a target drone vehicle based on a storable propellant combination composed of inhibited red fuming nitric acid (IRFNA) as an oxidizer and Plexiglas®-based fuel. The layout of this motor is shown in Fig. 1 [1, 3].

Originally called the Sandpiper and later the High Altitude Supersonic Target (HAST), the vehicle experienced a series of successful propulsion flights. It was designed to be aircraft launched and to fly horizontally at several altitudes and Mach numbers (up to 5) for ranges in excess of 100 miles. Its thrust duration was 300 s and was throttlable on demand over an 8:1 range. The vehicle itself was a modified 180-in.-long version of the U.S. Navy AQM-37A liquid-bipropellant rocket-powered target missile, with slight modifications.

This work later became the Firebolt target missile system, which was under development by Teledyne Ryan. It used the hybrid-propulsion system as originally demonstrated in the Sandpiper Program. The engine, built by the Chemical Systems Division (CSD) of United Technology, was throttleable between 0.53 kN (120 lb) and 5.3 kN (1200 lb). A ram air turbine compressor, with an inlet below the center fuselage, pressurized the IRFNA oxidizer before it was delivered to the thrust chamber and also provided electrical power for the missile. After air launch at about Mach 1.5 from an F-4 aircraft, the hybrid rocket could propel the XAQM-81A to speeds greater than Mach 4 at altitudes of 30,000 m (100,000 ft). The

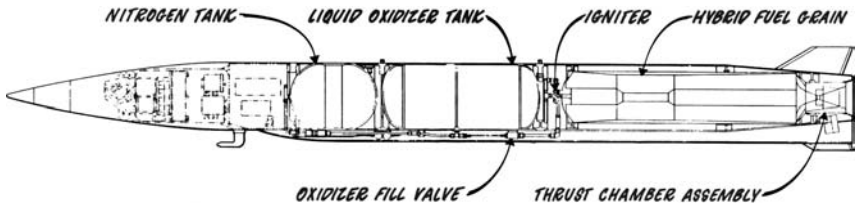

Fig. 1 Firebolt hybrid rocket target vehicle [1].

Firebolt could fly a preprogrammed course and/or respond to guidance commands from the ground. The parachute recovery system allowed either a soft landing or a midair retrieval. The propulsion system was also tested at the U.S. Air Force Rocket Propulsion Laboratory (AFRPL), with different fuel/oxidizer combinations [3, 4]. The Firebolt completed its evaluation period in 1984; however, no production contract was ever given.

D. Starstruck's Dolphin

Starstruck's Dolphin was a prototype vehicle developed to become a sounding rocket and to develop the technology for a planned follow on vehicle called Constellation. The planned Constellation was to be a four-stage vehicle to get a payload of ~3200 lb into elliptical geosynchronous transfer orbit. The Dolphin was a 51-ft-long, 42-in.-diam recoverable booster, powered by a 35,000-lbf thrust hybrid rocket. The payload would be 1000 lbm to 125-mile altitude. The hybrid rocket was developed and tested in Carson City, Nevada. Douglas Ordahl was the bridge person from the hybrid work conducted at United Technologies CSD to the work conducted at Starstruck. Ordahl was the former head of hybrid propulsion at CSD.

Water launch was selected to reduce the cost required for launch by eliminating the launch pad, to increase the orbital insertion options by being mobile, and to get around government restrictions on launch from land. However, the decision to perform water launches came with a price.

The launch procedure for the Dolphin was fairly straightforward. The Dolphin was filled with LOX, slid off the boat, and floated horizontally in the water. A weight, attached to the aft end of rocket, was dropped into the water and pulled the rocket upright. The nitrogen tanks were pressurized in the water, and the vehicle was ready for launch.

On the first launch attempt, on 6 February 1984, travel-loosened fittings in the nitrogen system which were used to actuate the valves were leaking. Because the vehicle was designed for water launch, access ports were not designed to reduce the number of water entry points. When an access port was made, by grinding open the intertank, a fire started on some electronic circuits. The positive spin on the event is that it demonstrated the safety of hybrid rockets: No secondary fires from the fuel occurred onboard.

The second launch attempt, on 30 March 1984, had a leak into the electronics, which allowed salt water to contact with the electronics and caused the vehicle to shift into abort mode.

The third attempt, on 3 August 1984, was semisuccessful. Agreements were made to launch the vehicle in protected (less choppy) waters near a military base on an island. Because of the prelaunch restrictions, the planned firing was only to be 15 s for a planned apogee of 8000 ft, to keep the vehicle from being able to reach populated land, which was ~10 miles from the launch area. The vehicle reached full thrust of 35,000 lbf thrust at 0.5 s into the launch. The vehicle, due to the ocean rocking, came out of the water at a 5-deg angle and was successfully vectored to vertical by the liquid injection thrust vector control (TVC) system (Fig. 2, Wade [5]). However, a TVC valve stuck closed, and the vehicle began to pitch over. Thrust was terminated via telemetry at 14 s into the launch, apogee was

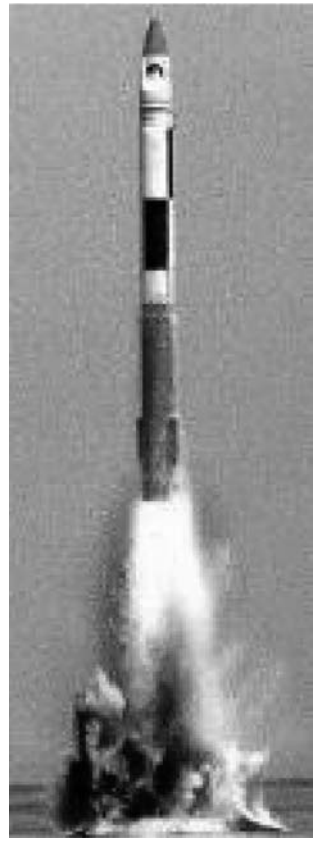

Fig. 2 Starstruck Dolphin launch [5].

2300 ft at 16 s, and water impact occurred at 28 s. The launch proved hybrids can be safely terminated.

In October of 1984, Starstruck was restructured, and eventually the program was dissolved [6–8].

E. American Rocket Company

Former members of the Starstruck company formed a new company called the American Rocket Company (AMROC) in 1985. AMROC was dedicated to the development of the hybrid rocket for space-launch vehicles [9]. A 75,000-lb motor was developed at AMROC, which was designated H-500 (Fig. 3). The first firing was on 14 October 1987. The motor completed qualification tests on 11 July 1989.

The H-500 flight motor was designed to be used on the SET-1 launch vehicle (Fig. 4). SET-1 was to be a suborbital vehicle that carried two payloads. The launch vehicle (schematically shown in Fig. 4) was developed in 9 months for under $5 million. The SET-1 vehicle development included 1) guidance and

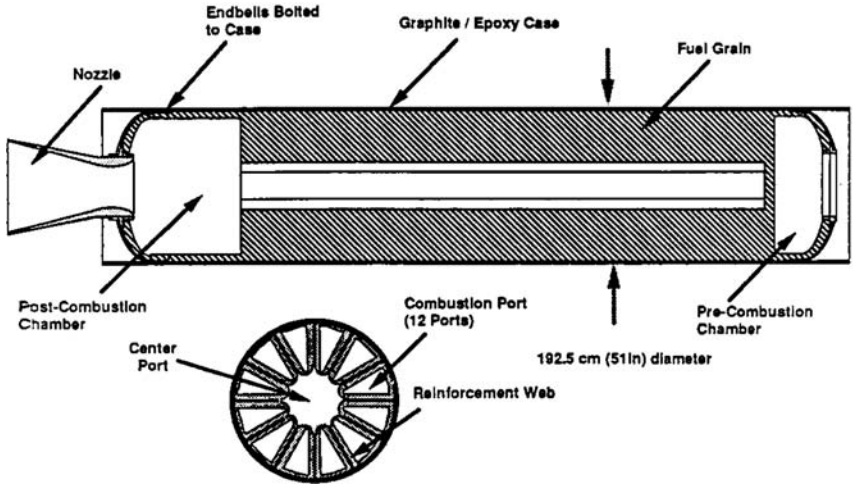

Fig. 3 AMROC H-500 hybrid motor [10].

control, telemetry, transponder, power distribution, control electronics and instrumentation; 2) hydrogen peroxide liquid injection TVC system; 3) nonfragmenting flight termination system; 4) catalytic heated helium pressurization system; 5) monopropellant hydrogen peroxide roll control system, 6) launch pad, transport and ground support operations and equipment; 7) integrated two payloads, Massachusetts Institute of Technology (MIT) Space Systems Laboratory payload and a Department of Defense (DoD) payload; and 8) range documentation, safety qualification, and environmental approvals for the Vandenberg Air Force Base launch [10].

On 5 October 1989, an attempt to launch the SET-1 was made by AMROC (Fig. 5). At the ignition command, the main liquid valve failed to open completely

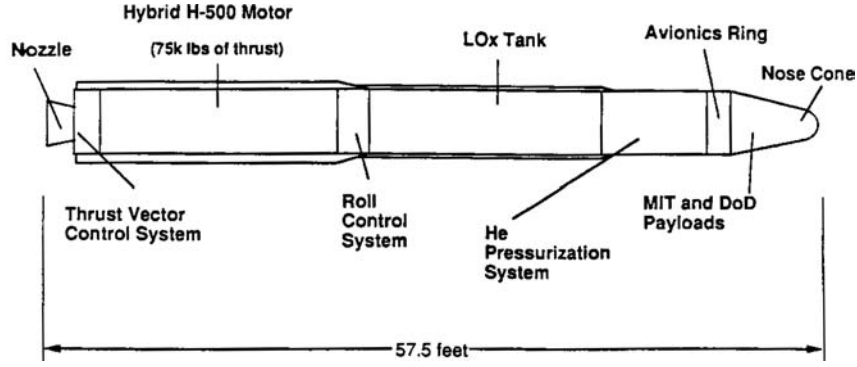

Fig. 4 AMROC SET-1 launch vehicle [10].

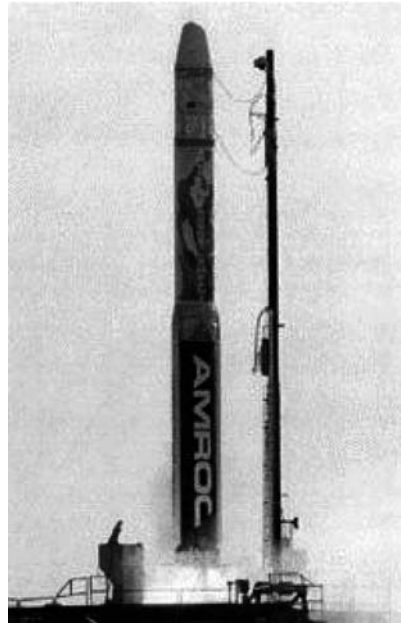

Fig. 5 AMROC SET-1 launch attempt [5].

due to moisture that had frozen the valve. Without the full flow of oxygen, the motor developed insufficient thrust for liftoff. Unfortunately, the guidance and control system was issuing automatic commands for a pre-planned pitch maneuver. This resulted in the dumping of a large quantity of hydrogen peroxide liquid injection thrust vector fluid into the nozzle. The hydrogen peroxide began decomposing when it came into contact with the hot flame bucket below the vehicle, which produced oxygen that mixed and ignited with the fuel-rich exhaust gasses coming from the motor. The resulting fire in the flame bucket engulfed the vehicle. The aft skirt of the motor case was consumed, and the vehicle fell over. The top two-thirds of the vehicle suffered only minor damage, and the avionics were intact [10].

As far as AMROC could tell, all of the vehicle systems worked as designed except for the LOX valve. There was less than $1000 damage to the U.S. Air Force launch pad. The launch failure was not a fundamental problem with the hybrid rocket motor. In fact, the safety and nonexplosive nature of the hybrid motor was proven conclusively [10].

F. HPDP Sounding Rocket Flights from Wallops Island

A series of four hybrid sounding rockets were successfully launched as part of the HPDP. These flights demonstrated a safe nonpyrophoric/nonpyrotechnic ignition sequence, inexpensive component manufacturing techniques, simple launch operations, and a quick launch turnaround time.

This work was performed under HPDP, which included NASA/Marshall Space Flight Center (MSFC), Lockheed Martin, Environmental Aeroscience Corporation

(eAc), Pratt and Whitney Chemical Systems Division, Allied Signal, Boeing North American Rocketdyne Division, and Thiokol.

The sounding rocket (Fig. 6, eAc Website [11]) objectives included the following:

1) Design, fabricate, and launch a series of hybrid sounding rockets, and recover at least one proof-of-concept demonstration vehicle.
2) Demonstrate a safe, nonpyrotechnic/nonpyrophoric hybrid ignition technique.
3) Perform analysis on the recovered flight vehicle to determine the effects of flight on hybrid-propulsion systems and the vehicle.

To fulfill these sounding rocket objectives, a series of four rocket flights using a nitrous oxide (N_20)/hydroxyl-terminated polybutadiene (HTPB) propellant combinations was proposed to demonstrate hybrid propulsion. The first two sounding rocket flights would be low-altitude checkout flights in which the hybrid-propulsion flight system and launch pad operations would be evaluated. The last two flights would be high-altitude flights that utilized a similar vehicle to that which was used in low-altitude flights. At least one of the high-altitude flights would have to be recovered to examine the effects of flight on the hybrid-propulsion systems.

The N_2O sounding rocket project was divided into five separate development phases:

1) Develop a hybrid motor to achieve an altitude of 20 n miles. This stage of the project included the design, fuel-grain modifications, nozzle development, and subscale motor testing using facility-supplied N_2O. Inexpensive techniques

Fig. 6 HPDP sounding rocket [11].

for manufacturing and testing hybrid motor components were also developed. The motor consisted of an annular injector, a 40-in. long fuel grain and a 1.75-in.-diam glass phenolic nozzle with an expansion ratio of 5.2. N_2O was chosen as the oxidizer because it is safe, inexpensive, and noncryogenic. N_2O also has a high vapor pressure at ambient temperatures that allows two-phase storage and efficient oxidizer delivery through a self-pressurizing process. Therefore, an oxidizer tank pressurization system is not needed, which greatly simplifies the launch vehicle.

2) Design a low-cost, flightlike oxidizer tank. The tank was constructed of Al 6062 and was welded using a proprietary process developed by eAc. Each flight oxidizer tank was proof tested to 1.5 times the maximum allowable working pressure of 700 psig. One tank was burst tested to evaluate the material properties and the weld process. Tank design included development of a fill/vent system that would interface with the existing motor design and the Wallops Flight Facility (WFF). The fill and drain system used a valveless approach, which is similar to the Hypertek system that is commercially available.

3) Test the integrated system on a vertical test stand. These tests incorporated the flight tank, ignition system, and motor configuration that would be used on the low-altitude flights. These tests offered an excellent opportunity to demonstrate the fill/vent process and to qualify the function of the rail release mechanism. With this system, the ignition and proper operation of the motor can be verified before release.

4) Checkout the vehicle at Goddard Space Flight Center (GSFC) facility and the two low altitude launches. This was a complete review of the system, including joint tests, evaluation of mass properties, and static balance tests. Data from these tests were fed into the models to predict flight performance. Once the low-altitude vehicle was thoroughly reviewed, the vehicle was transported to the launch rail on Wallops Island. The first low-altitude sounding rocket was launched with a partial oxidizer load and achieved 24,780 ft with no operational anomalies. The second low-altitude vehicle, which had been previously checked out, was transported to the same rail and launched within 90 min of the first low-altitude launch. This proved to be a successful demonstration of the simple, safe, launch pad operation characteristics of hybrid launch vehicles.

5) Launch of the high-altitude rockets was preceded by some changes to the fuel-grain and injector design. The first vehicle achieved an altitude of approximately 120,000 ft and landed within 1.5 sigma of the predicted target point. The second vehicle achieved an altitude of approximately 110,000 ft and was successfully recovered. Postflight examination of the vehicle indicated no damage to the hardware due to the flight. The fuel grain and nozzle exhibited the same regression and erosion characteristics that were measured on the static tests [12, 13].

The program met all of its planned objectives:

1) A N_2O vehicle was designed, fabricated, and launched in a series of hybrid sounding rocket flights, and one proof of concept demonstration vehicle was recovered.

2) The flight vehicles' hybrid motors were ignited with a safe, nonpyrotechnic/non-pyrophoric ignition technique.

3) The recovered flight vehicle was inspected, and the fuel grain and nozzle performed the same in flight as in the ground testing that proceeded the flights.

Another unwritten objective was accomplished: It got hybrids flying again. One issue with hybrid flight concepts/designs presented to various potential customers is, "do you have any flight data?" This series moved hybrids in the right direction [13].

III. Lockheed Martin HYSR Project

A large-scale hybrid rocket was successfully launched from the NASA WFF on 18 December 2002 as a technology demonstration for hybrid propulsion and related subsystems. The HYSR Program started in 1999. The overall goal of the program was to develop a single-stage propulsion system capable of replacing existing two- and three-stage sounding rockets, with additional objectives to demonstrate the required technology for the launch of a large-scale hybrid sounding rocket booster, to demonstrate the positive attributes of hybrid propulsion, to demonstrate two hybrid-based subsystems, and to advance the technology readiness level of hybrid propulsion. The hybrid rocket had a propellant combination of LOX and HTPB and produced approximately 60,000 lb of vacuum thrust. The three-year technology demonstration program was a collaborative effort between NASA and Lockheed Martin and had a total budget under $6 million, which was a combination of Lockheed Martin and NASA funding. The program advanced technology readiness level and performance of hybrid propulsion [14].

A. Introduction

To satisfy the program objectives, a plan was implemented that included static testing of heavyweight test articles, verification of the various components and subsystems, prototype testing of a flight weight test article, and a flight demonstration of the hybrid vehicle. The static testing of the hybrid motor and subsystems would occur at NASA Stennis Space Center (SSC) and the flight demonstration would occur at NASA WFF.

The HYSR team was composed of personnel from five different centers. Lockhead Martin Michoud Operations was responsible for the design, analysis, and fabrication of the test articles, flight vehicle, and ground support equipment. NASA SSC was responsible for test stand fabrication, static testing, and data acquisition during testing. NASA WFF was responsible for the flight analysis, flight and ground safety at the range, propellants, launch support, and vehicle/payload tracking. NASA MSFC was responsible for program oversight and to provide funding for the testing at SSC and the flight activities at WFF. NASA Ames Research Center (ARC) would provide a payload and nosecone for the flight.

Before the flight demonstration, three tasks were defined to qualify the propulsion system at SSC. Task A contained the static testing of the hybrid motor design within a heavyweight case using facility-supplied oxidizer and pressurant. Task B contained oxidizer expulsion system testing from a heavy-weight LOX and helium tank that was similar to the flight design. Task C would couple a flight-weight oxidizer pressurization system with a hybrid motor to demonstrate a

full-duration static test that incorporated all of the propulsion subsystems. The vehicle configuration used in task C was intended to be as close as possible to the flight configuration that could still be tested within the existing facilities at NASA SSC.

B. Task A: Heavy-Weight Motor Testing

Task A testing took place from February to September 2000 at NASA SSC's E-3 Complex. Four full-scale motors were tested to gain fuel regression, stability, and performance data to validate the fuel-grain design for the HYSR. The fuel that was cast into the motor cases was a mixture of HTPB and high percentage of aluminum to optimize the delivered energy of the system. The motor case center segment had five penetrations equally spaced around the circumference of the motor with weldolets used for pass-through Swagelok^{TM} connectors. These penetrations were used to route the gaseous oxygen to the Lockheed Martin patented staged combustion system (U.S. Patent 5,794,435), which is used for ignition and maintaining combustion stability throughout flight. Figure 7 shows the motor case used for task A testing.

There were two center segment fuel-grain configurations tested in task A due to a redesign that was necessary after test 2. The initial fuel-grain design incorporated 10 quadrilateral ports around a single circular centerport. After the first two tests, it was determined that the initial design flux (total mass flow rate divided by the port cross-sectional area) was too aggressive, and the port size was increased for future tests to correct this problem. Figure 8 shows a completed heavy-weight motor with the facility thrust adapter bolted to the forward dome.

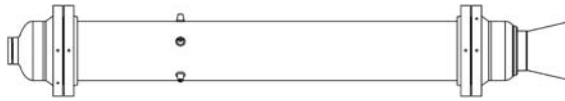

Fig. 7 HYSR Heavy-weight motor case used for task A testing [14].

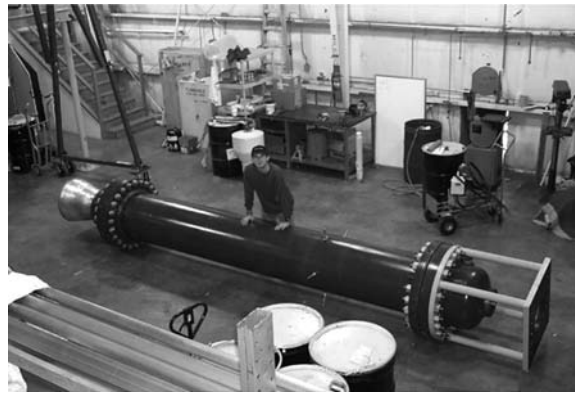

Fig. 8 HYSR completed heavy-weight motor assembly [14].

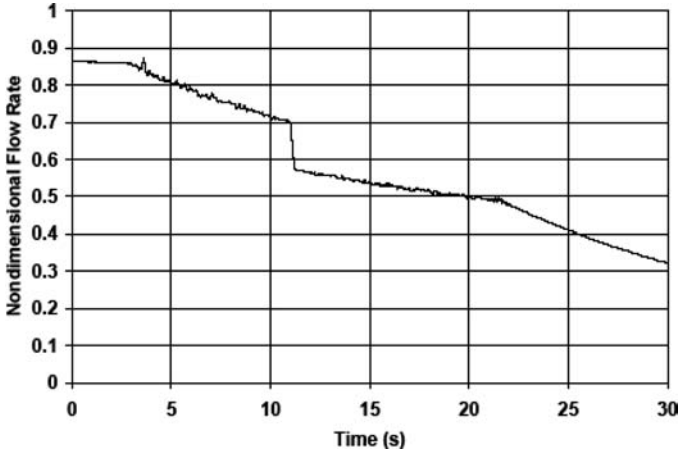

Fig. 9 LOX flow rate vs time for test 4 [14].

The LOX flow rate from the 6-ft-diam facility tank for task A, test 4 is shown in Fig. 9. A planned LOX throttle was demonstrated by initially opening both LOX line ball valves to achieve the maximum flow rate, and at 8 s into the burn, one of the ball valves was closed to reduce the total LOX flow rate. The LOX flow rate decreases in time to simulate the LOX flow rate expected in the flight vehicle.

Figure 10 is a plot of the vacuum thrust from test 4 of the heavy-weight motor test series. The motor was tested for approximately 20 s with a planned throttle at 8 s into the burn. The vacuum thrust is regressive vs time due to the reduction in propellant flow rate vs time and, to a lesser effect, nozzle erosion. The increase

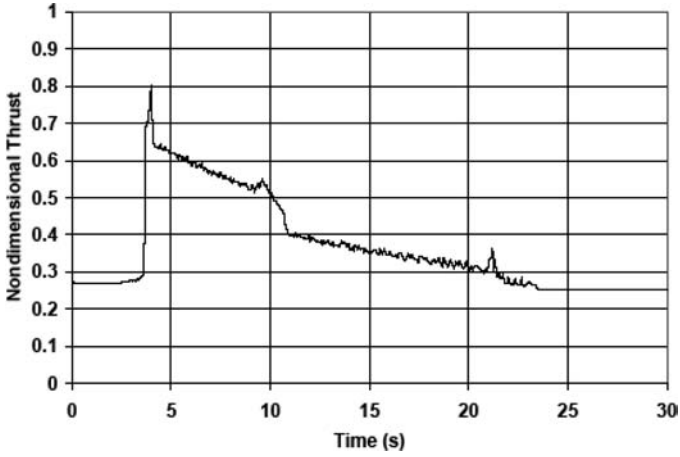

Fig. 10 Vacuum thrust vs time for test 4 [14].

in thrust during the ignition transient was caused by solid fuel being ejected from the motor. The fuel failed due to high loading and weak fuel tensile strength. After the HYSR program, Lockheed Martin investigated how fuel failures occur and developed a possible solution to that problem for future hybrids [15].

Other than the initial ignition transient, the motor performed within a $\pm 2.5\%$ stability band around the mean value. The motor also demonstrated a high C^* and I_{sp} efficiency.

C. Task B: Oxidizer Expulsion Testing

The oxidizer expulsion tests were established as a proof of concept and systems refinement exercise for the Lockheed Martin patented heated helium pressurization system (U.S. Patent 5,722,232). The testing took place between 13 September 1999 and 12 January 2000 at NASA SSC's E Complex.

Figure 11 is a schematic of the heated helium pressurization system. Helium, initially at cryogenic temperature and moderate pressure, is stored within a spherical tank located at the top of the LOX tank. The system is started by igniting a small-diameter hybrid heater, and the combustion is sustained with a low flow rate of gaseous oxygen. The exhaust products of the hybrid heater are mixed with helium to create an inert mixture of pressurant. The helium mixture flows through a minimal surface area heat exchanger in the helium tank to attempt to minimize the helium residual. The pressurant enters the LOX tank through a stainless steel diffuser, which disperses the flow into the ullage. The helium-exhaust constituent mixture provides a high-energy pressurant that forces the LOX into the hybrid motor. Storing helium at cryogenic temperatures and then heating the pressurant before it enters the oxidizer tank provides a volumetrically and thermodynamically efficient stored gas system. The mole fraction of the helium in the pressurant gas is greater than 94%, an environment in which no combustion is possible.

Figure 12 is the calculated LOX flow rate from the test tank. The flow rate was calculated using the cavitating venturi flow equation, which is dependent on the upstream temperature, upstream pressure, and venturi throat area. The throttle step that occurs at approximately 10 s in Fig. 12 is calculated by simply reducing the

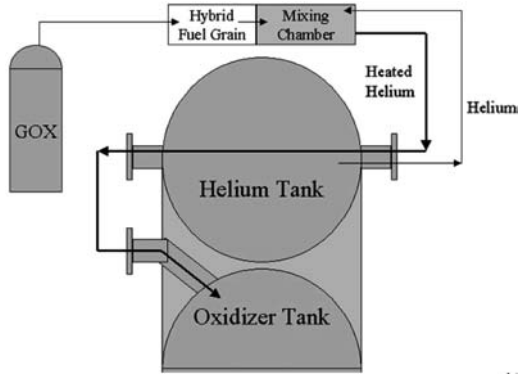

Fig. 11 Schematic of heavy-weight heated helium system [14].

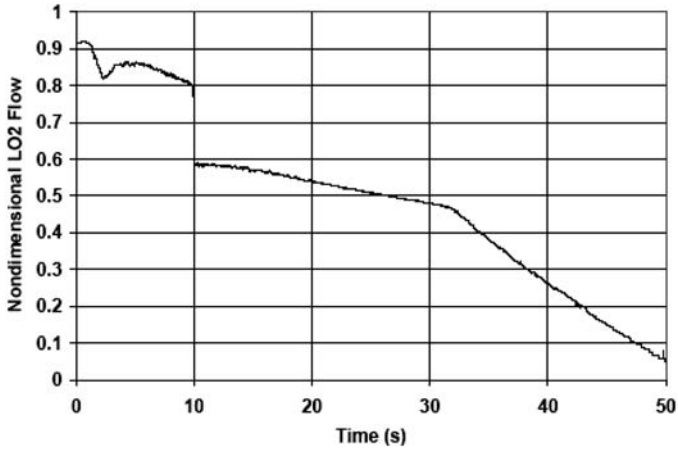

Fig. 12 Calculated LOX flow rate for task B; data after 33 are suspect for reasons discussed in the text [14].

available area from both venturis to the area of the primary venturi. This step does not actually happen as sharply as shown in Fig. 12. The actual reduction of flow can be best evaluated by the reduction in thrust during the motor test. Also, the calculated flow rate after 33 s is not valid. It was evident from the video recordings that the liquid flow ended at this time. The calculated flow after 33 s is artificially high because the pressurant has the same temperature and pressure as the LOX. (The equation does not recognize the difference.)

D. Task C: Integrated Testing

The purpose of the integrated testing was to measure the performance of a prototype flight article to support flight trajectory and dispersion analysis before the actual flight. The flight-weight hardware and tooling were designed and manufactured at the Michoud Assembly Facility, and the testing was conducted at NASA SSC. The helium tank, LOX tank, and motor case are the three primary flight-type structures fabricated for this testing. These components were fabricated in the flight configuration with the exception of the payload adapter, which was not welded to the helium tank, and the forward dome of the motor case had a solid section around the circumference of the dome to interface with the thrust adapter on the test stand. The helium pressurization and gaseous oxygen staged combustion subsystems would incorporate flight weight components, but not in the identical flight configuration.

Unfortunately, the assembled rocket could not be tested vertically within the given budget and schedule constraints. To fit within the existing E-3 facility at NASA SSC, the LOX tank was positioned vertically and the hybrid motor would have to be tested in the horizontal position so that sea-level thrust could be measured. This meant that a 90-deg elbow had to be placed between the vertical LOX

Fig. 13 Integrated test firing [14].

tank and the horizontal hybrid motor. This test configuration eliminated the possibility to evaluate the performance of the components enclosed within the intertank compartment, as well as the umbilical feed system.

The integrated test was performed on 24 July 2001. Motor ignition and the subsystems performed as predicted. The testing was manually aborted after the throttle sequence due to a burn through 3 in. aft of the forward insulation. The data collected from the testing were adequate to advance toward the flight phase of the program. Figure 13 shows the motor firing during the integrated test.

E. Flight Activities

A rationale to proceed to flight was submitted to Lockheed Martin management, NASA WFF, and NASA MSFC. The probable cause of the motor burn through was identified, and the problem could be corrected by insulating the entire motor case. Multiple oxidizer expulsion and several heavy-weight ground tests were performed and the test data correlated with predictions. With the proper range safety measures in place, proceeding to flight would be less expensive and time consuming than performing an additional ground test. Based on the existing data and proposed corrective actions, it was decided to proceed to flight. Figure 14 is a photograph of the loading of the assembled vehicle onto the launch rail at NASA WFF.

The payload of the HYSR sounding rocket was provided by NASA ARC and consisted of several suborbital aerodynamic reentry experiments and ballast. The despin section was provided by Lockheed Martin. The objective for this flight was to develop a unique axial ejection technique for multiple reentry bodies and to

Fig. 14 Assembled vehicle at the launch site [14].

develop the means for testing lifting entry concepts over an ocean range. The ease with which experiments can be performed and integrated, based in part on modular data acquisition/transmission systems, led to it being referred to conceptually as a wind-tunnel-in-the-sky.

A number of dry runs and "wet runs" were performed at the launch rail before the launch of the HYSR to establish the loading timeline, to verify umbilical separation, and to validate the flightworthiness of the system. These dry and wet runs included erecting the launcher, pressurizing the system, loading with cryogens, cycling valves, deriving fill and conditioning times, and cycling the disconnect valves. These demonstration tests revealed a number of issues that had to be resolved before flight. Most of the problems involved components that were not in the flight configuration during the ground demonstration. These components had to be retrofitted or repaired after a separate series of laboratory testing. On 12 August 2002, the final wet run test was performed with no major issues. Figure 15 shows the HYSR during a wet run.

On the final launch attempt, the LOX and helium tanks were loaded in under 60 min. The LOX tank was prepressurized to 745 psig at T−10 s, and the ignition sequence was commanded. After three years of development, the HYSR was launched from WFF on 18 December 2002 at 0615 hrs EST. Figure 16 shows the vehicle shortly after ignition.

After an analysis of the flight data, it was concluded that the vehicle achieved an altitude of approximately 42 km, impacted 65 km downrange, and had a time of flight of 213 s. The initial acceleration of the vehicle from the rail was approximately 6.1 *g*, which was determined from high-speed video of the vehicle on the launch rail. The burn time of the motor was approximately 33.4 s, and the timed despin and payload ejection events occurred as planned. Although the performance was lower than predicted, the factors that reduced the altitude could be explained and performance could be recovered in future missions.

Fig. 15 HYSR in vertical configuration during testing [14].

Fig. 16 HYSR launch [14].

The HYSR flight results proved to be extremely promising. The timer and ejection events appeared to work adequately. Data were acquired for all three experiments. The basic data/transmission system that was identical on the waverider and linear aerobrake worked very well. The flight also provided a unique opportunity to test a unique payload retrieval system for eventual water recovery [14].

IV. Fredericksburg Launches

Fredericksburg High School (FHS) in Texas attained national recognition in 2000 with the successful design, fabrication, and flight of a hybrid sounding rocket. The 23-ft, 470-lb rocket, Redbird 9-H, (Fig. 17), flew to over 35,000 ft, an altitude record for a U.S. high school. This launch from the U.S. Army's White Sands

Fig. 17 Redbird 9H setup for launch [16].

Fig. 18 Redbird 10H sounding rocket [17].

Missile Range surpassed a prior year's milestone, which had established FHS as the first U.S. high school to achieve transonic flight when its vehicle accelerated to 833 mph [16]. FHS's program has other motors in the pipeline to be launched [17] (Fig. 18).

V. Scaled Composites: SpaceShipOne

The Ansari X Prize was a contest with a $10 million reward for the first commercial company to get 3 people to 62 n miles high and repeat within 2 weeks. Scaled Composites built a two-stage airplane to win the prize with the second-stage plane powered by a N_2O/HTPB hybrid rocket. The first-stage airbreathing plane, called the White Knight, was designed to carry the second stage to ~50,000 ft before its separation from the second stage, SpaceShipOne. SpaceShipOne's N_2O/HTPB motor was then ignited and fired for ~80 s.

With an airplane-based system, Scaled Composites could perform an airplane-type test program, incrementally testing the flight regions (Fig. 19). Scaled Composites performed its first captive carry of SpaceShipOne under White Knight on 20 May 2003. This test, and a subsequent test on 29 July 2003, demonstrated that the combined vehicles did not demonstrate any unexpected aerodynamic interactions. The first glide test of SpaceShipOne was 7 August 2003, with much of the subsonic handling capabilities of the system verified (Fig. 20). On the seventh glide test, the N_2O valve and propulsion system was given a full check out by cold-flowing N_2O out the motor. The first powered flight, on 17 December 2003, consisted of a 15-s burn of the hybrid motor. This short-duration burn enabled SpaceShipOne to achieve Mach 1.2 and an apogee of 67,800 ft. This flight was the first privately developed rocket vehicle to reach Mach 1. On 8 April 2004, the hybrid motor was fired for 40 s, lofting the vehicle to an apogee of 105,000 ft with a maximum powered velocity of Mach 1.6. Inching closer to a full-duration burn, the next flight on 13 May 2004 had a hybrid motor burn of 55 s, which reached Mach 2.5 at shutdown and achieved an apogee of 211,400 ft. Another milestone was achieved: The first commercial astronaut flight over 100 km (328,000 ft) occurred on 21 June 2004. This flight had a 76-s burn, powering SpaceShipOne to Mach

Fig. 19 White Knight carrying SpaceShipOne [24].

Fig. 20 Separation of White Knight from SpaceShipOne [24].

2.9 and an apogee of 328,491 ft. The pilot experience approximately $3\frac{1}{2}$ min of weightlessness near apogee [18].

The first X Prize flight occurred on 29 September 2004. With a pilot and the equivalent weight of two passengers, the hybrid motor was fired for 77 s, propelling SpaceShipOne to Mach 2.92 and a final apogee of 337,700 ft. This flight had a dramatic right-hand roll at 190 deg/s that was believed to be caused by a lack of symmetry in the hybrid motor thrust with a very low angle of attack. The spin was slowed slightly with the use of aerodynamic controls to 140 deg/s, and eventually the reaction control system was exercised to stop the roll [18].

The second X Prize flight occurred on 4 October 2004 and won the X Prize of $10 million. The hybrid motor was fired for 83 s and reached Mach 3.09 at shutdown. The vehicle reached an apogee of 367,500 ft and exceeded the maximum altitude achieved by the X-15. This flight also experience $3\frac{1}{2}$ min of weightlessness. The flight-test program encompassed 13 months and 17 flights with 6 rocket-powered tests [18]. The flight was an historic event and NASA Administrator Sean O'Keefe recognized it in a statement [19]:

> Not unlike the first U.S. and Soviet space travelers in 1961, and China's first successful spaceflight last October, these private citizens are pioneers in their own right. They are doing much to open the door to a new marketplace offering the experience of weightlessness and suborbital space flight to the public.

Marion Blakey, Administrator of the Federal Aviation Administration (FAA) was on hand for the launch, "This was not only a historic flight, the standards of safety that were set here today are going to go on to ensure that there's going to be lots of tourists out there that'll enjoy it. We'll be partner with you on it." Blakey awarded pilot Binnie his commercial astronaut wings. The launch team also received a call from President George Bush to express his congratulations [20].

The hybrid motors worked (Fig. 21) and performed their missions as designed; however the first X Prize launch hybrid motor experienced some combustion instabilities

> This can be heard in the X Prize flight videos as a high-pitched noise. In the videos, visible shuddering which shakes pilot Mike Melville back and forth also indicates nitrous oxide feed problems. This would result from low pressure in the oxide tanks at the end of the engine burn. Nitrous oxide is the oxidizer for the engine's solid propellant [21].

The second X Prize hybrid motor also had some minor problems that need to worked on for future systems: "Partway up some moderate chugging pulsations were seen in the exhaust plume, and he reported feeling vibration at that point. Combustion instability is fairly normal for hybrids and on SpaceShipOne chugging can occur when the liquid nitrous oxide oxidizer runs out, leaving only gas" [22].

Scaled Composites developed multiple unique and innovative parts for this record-breaking hybrid flight system.

1) The choice of N_2O allows the system to be self-pressurizing. N_2O has a high vapor pressure, which allows a blowdown system. This simplifies the design greatly.

2) SpaceShipOne is completely built around the hybrid motor and oxidizer tank. The tank is bonded to the inside of the airframe.

Fig. 21 SpaceShipOne's hybrid motor firing [24].

3) The N_2O valves were inside the oxidizer tank. This eliminates leak paths and allows the hybrid motor case to bolt directly to the oxidizer tank, simplifying structural loads.

4) The hybrid motor included a composite case, with a silica phenolic liner and a carbon fiber epoxy over wrap. Scaled Composites designed the motor case, the nozzle, and the oxidizer tank.

5) The case had burn through sensors built into the motor on the interior and exterior of the motor case, so that if any unusual burning occurred, the N_2O valve could be closed and turn the motor off.

6) The motor during development was fired for twice the scheduled burn duration to check the motor silica phenolic insulation system. There were no burn throughs.

7) The hybrid motor/grain design was competed between two companies with two different motor designs, with a series of test motors fired with the test oxidizer tank. Both eAc and SpaceDev opted to use HTPB, but with different proprietary mixes. Also eAc choose a single-port design and SpaceDev chose a quad-port design. SpaceDev was chosen to build cast the hybrid grains for the flight vehicles, and eAc's design for some of the oxidizer system plumbing and valves was also incorporated into the flight vehicle [23, 24].

The choice of hybrid rockets for the first privately funded manned-space-flight launch visualizes the advantages of hybrids: safety, simplicity and performance. It bodes well for the use of hybrids in future applications, manned and unmanned.

VI. Recent Developments

A. Lockheed Martin/Defense Advanced Research Projects Agency/NASA Falcon

Falcon is a joint Defense Advanced Research Projects Agency (DARPA)/NASA/U.S. Air Force small launch vehicle (SLV) program to develop and demonstrate an affordable and responsive space lift capability: one that can quickly launch a small satellite into low Earth orbit. Under the award agreement, Lockheed Martin conducted a phase IIa preliminary design and development effort to mature its hybrid launch vehicle design. Lockheed Martin has fired two upper-stage hybrids in support of a phase IIa contract. The goal of the Falcon SLV program is to develop and demonstrate an affordable and responsive space lift capability [25, 26]. The Lockheed Martin vehicle concept is shown in Fig. 22 [27]. Unfortunately, a follow on contract for this promising concept was not awarded.

B. Virgin Galactic

Virgin Galactic, a company established by Richard Branson's Virgin Group, is developing space tourism by creating a vehicle (Fig. 23) based on the Scaled Composite's SpaceShipOne. The vehicle will be reusable and take suborbital

Fig. 22 Lockheed Martin Falcon SLV [27].

rides and will continued to be powered by hybrid rockets [28]. Virgin Galactic is redesigning the hybrid rocket because the new vehicle will be larger and "because SpaceShipOne's (SS1) engine had low- and high-frequency combustion instability" [21].

Fig. 23 Virgin Galactic space tourism vehicle [28].

C. Space Dev Dream Chaser

In 2005, Space Dev announced a hybrid-based launch concept called the Dream Chaser (Fig. 24). This six-passenger vehicle could be used separately as a suborbital vehicle or as part of a larger booster system to get it to orbit [29, 30].

D. United Technologies Corporation Reusable Space Access Launch Vehicle System

U.S. patent 6,726,154 details a 1.5-stage symbiotic hybrid architecture (Fig. 25) and an integrated propulsion system: a reusable upper stage with strapon hybrid combustion chambers. All of the engines, hybrids and liquids, would fire off the pad, and once the hybrids burned out, they would be jettisoned. The oxidizer

Fig. 24 SpaceDev Dream Chaser [29].

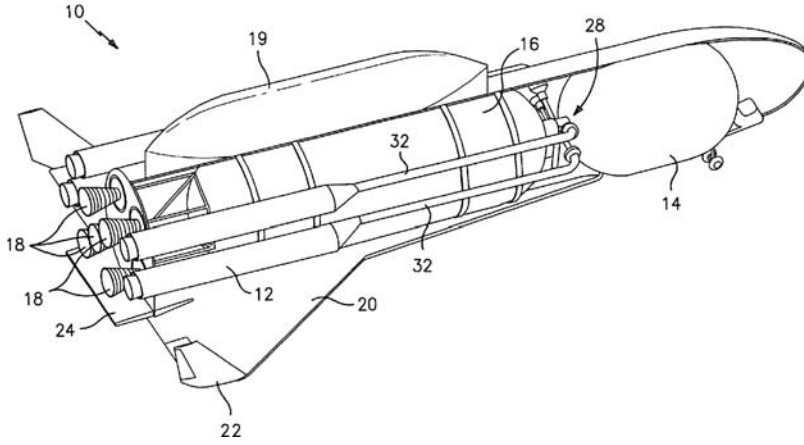

Fig. 25 U.S. Patent 6,726,154 reusable space access launch vehicle system.

for the hybrids would be contained in the main vehicle. The potentially high-cost components of a hybrid rocket, oxidizer pumps, tanks, and pressurization systems, could be reused again as part of the main vehicle. The empty motor cases and nozzles would be jettisoned. This concept was evaluated in the NASA Space Launch Initiative (SLI) trade studies.

E. Space Dev's Streaker Family

Space Dev has made announcements of its Streaker family (Fig. 26, Table 1) of N_20/HTPB-based rockets [31, 32], but has since removed mention of the concept from its website. It may have become a subset of the DreamChasers system, or been dropped entirely.

F. Partially Developed But Never Flown AMROC Aquila

After the unsuccessful launch attempt of SET-1, AMROC reevaluated the launch market and saw a niche for a larger vehicle based on a larger 250,000-thrust hybrid motor. AMROC started marketing the vehicle before testing the hybrid rocket.

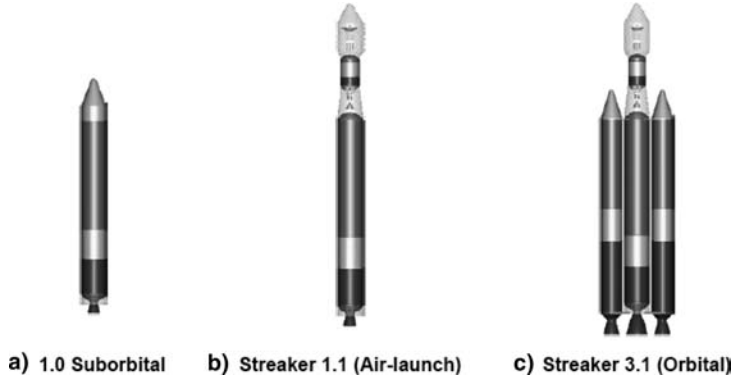

Fig. 26 SpaceDev Streaker Launch family [32].

Table 1 Space Dev Streaker Launch family

Configuration	Stage 1	Stage 2	Stage 3	Terminal	100 n mile, 28.5 deg	460 n mile, SSO
Streaker 1.0	None	CCB	None	None	N/A	Demonstration
Streaker 1.1 M	C-17	CCB	HUS	MoTV	260 lb	115 lb
Streaker 1.1	C-17	CCB	HUS	None	N/A	CAV launch
Streaker 3.0	2 CCB	CCB	None	None	N/A	CAV launch
Streaker 3.1	2 CCB	CCB	HUS	MoTV	1260 lb	660 lb
Streaker 5.1	4 CCB	CCB	HUS	MoTV	2110 lb	1190 lb

CCB - Common Core Booster.
HUS - Hybrid Upper Stage.
CAV - Common Aero Vehicle.
MoTV - Maneuvering Orbital Transfer Vehicle.

In January 1992, AMROC successfully completed the first development tests of the H-1500 hybrid-propulsion system with 225,000 lbf (1000 kN) of thrust. Several H-1500 hybrid motors would have been clustered together to provide boost propulsion for the Aquila launch vehicle.

The Aquila launch vehicle (LV) was to be a ground-launched, four-stage, hybrid-propulsion based launch vehicle capable of delivering up to 3200 lbm (1450 kg) payloads into a 100-n mile (185-km) circular orbit at a 90-deg inclination. The key features of the Aquila LV are shown in Fig. 27. These features include the

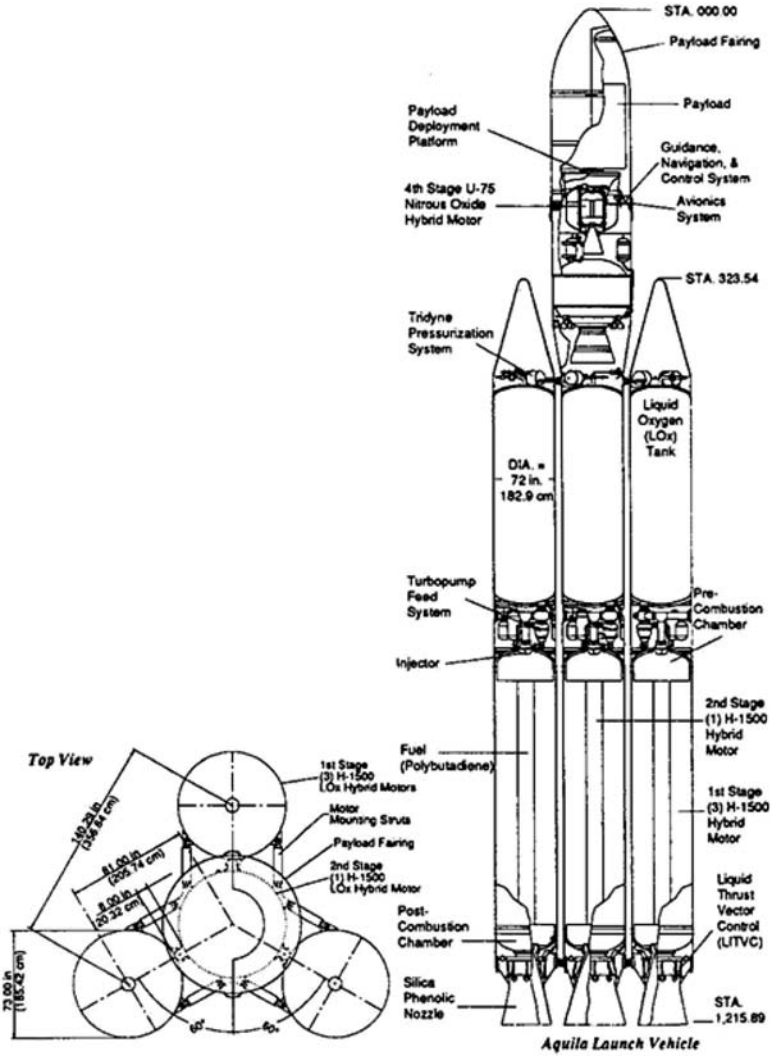

Fig. 27 AMROC Aquila Vehicle [33].

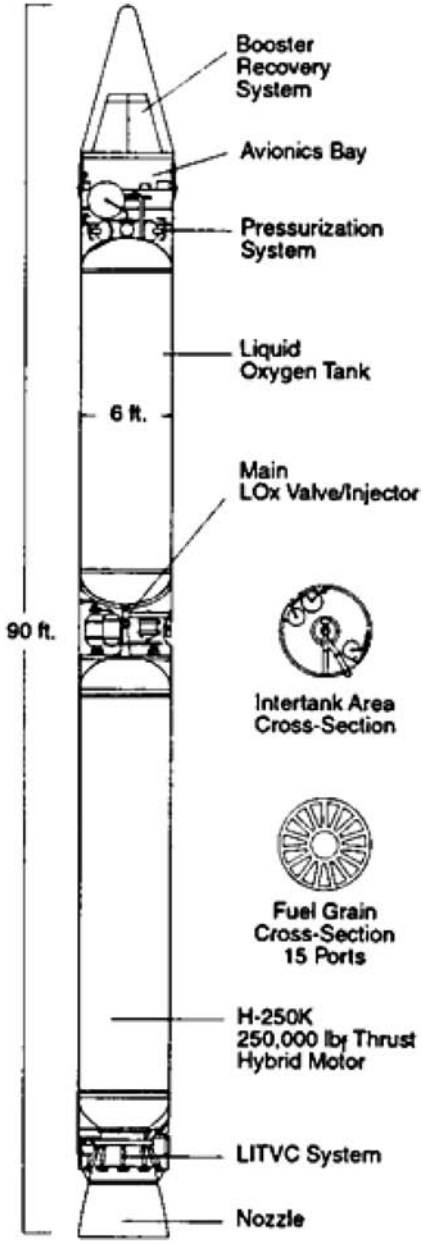

Fig. 28 AMROC HyFLYER [34].

following: a high-accuracy inertial guidance, navigation, and control system; H-1500 hybrid motor for first- and second-stage propulsion; an ORBUS 21S solid rocket motor for third-stage propulsion; a U-75 hybrid motor for upper-stage propulsion and maneuvering; and a 94-in. (239-cm) diam payload fairing for single or multiple payloads [33].

The third stage was to be an off-the-shelf United Technologies Corporation CSD ORBUS 21S solid rocket motor. The Aquila fourth-stage motor was to be an AMROC pressure-fed U-75 N_20/HTPB hybrid motor [33]. This N_20/HTPB motor was a predecessor to the hybrid used on SpaceShipOne, because Space Dev purchased AMROC's intellectual property, including designs and test data.

AMROC had decided to pursue the HyFLER as a step to the Aquilia vehicle. The HyFLYER was a suborbital vehicle based on a single H-1500 motor. AMROC tested two H-1500 (250, 000 thrust) motors and several versions on a N_2O hybrid before the company folded.

G. Partially Developed But Never Flown AMROC HyFLYER

A joint industry/government team had been formed to develop, build, and fly the HyFler sub-orbital LV powered by a 250,000-lb thrust hybrid rocket motor. The project called the Hybrid Technology Option Project (HyTOP) was cofunded by government and industry and will result in the first demonstration of a large-scale hybrid rocket motor. The team of AMROC, Martin Marietta Manned Space Systems, and United Technologies CSD have formed an industrial partnership to conduct the HyTOP effort with ARPA, NASA, and the U.S. Air Force [34].

HyTOP was meant to be a stepping stone from the hybrid technology research and development to the commercialization of hybrid rockets. The HyFLYER (Fig. 28) was to be the first flight test of the 250,000 motor. Later, larger vehicles were to be based on this core, with multiple boosters strapped together. AMROC had financial troubles during this development, became insolvent, and the vehicle was never finished.

VII. Hybrid Strapon Concepts

Whereas hybrid vehicles have been proposed and some flown, arguably the best niche for hybrid rockets is in a strap on application for a liquid booster. The relative immaturity of the technology has led hybrids to be overlooked as strapons for liquid systems. Hopefully future hybrid development will provide this opportunity for hybrids.

A. Space Shuttle Redesigned Solid Rocket Motor (RSRM) Replacements

After Space Shuttle *Challenger*, NASA took a second look at hybrid rockets, with the end application to be the replacement of space shuttle solid rocket motors. Several teams of companies examined hybrid rockets for this application, with some results being gas generator hybrids and some being conventional hybrids and the necessary development needed for the system of choice. However, these system studies [35–38] were not followed with a development program due to the decision to purse an advanced solid rocket motor.

In 2001, NASA was looking at different boost options for the space shuttle and included hybrids as one of the alternatives [39].

B. AMROC Titan and Delta Strapon Sizing Studies

In 1992, AMROC investigated upgrading the current launch vehicles of that time by replacing the solid strapons with hybrids:

> Currently both the Delta and Atlas are using solid rocket motors to augment thrust during the boost phase to increase the payload capability beyond that of the core vehicle. The use of hybrid rocket motors will increase this payload capability another increment. This is primarily due to the fact that the hybrid motor can be throttled deeper than the solid and the hybrid has a higher ISP [40].

In the case of the Delta LV, according to AMROC estimates, the use of four 260,000-lb thrust motors (H-1800s) would have allowed for a payload mass increase of 500 lb to geostationary transfer orbit (GTO). At that time, the Delta used nine Graphite Epoxy Motor (GEM) solid motors as strapon boosters [40].

In the case of the Titan II, an increase of 6000 lb to low Earth orbit could have been accomplished with the use of two 500,000-lbf LOX/HTPB strapon boosters. AMROC calculations showed that this was a benefit of approximately 1000 lb over a solution using 10 Castor IV strap-ons [40].

Similar gains could be shown analytically by using hybrids as strapons for the Atlas II vehicle where the capability to throttle the hybrid significantly can be used to reduce the structural loads on the core vehicle (see Fig. 29) [40].

C. Lockheed Martin Optimization Study for Atlas IIAR

An optimization technique was developed by Lockheed Martin and applied to the Atlas IIAR to show the effects of hybrids as strapons to the core vehicle [41]. A solid rocket industry standard code, Solid Prediction Program, was converted for analysis of hybrid rocket motors and developed into a subroutine for a Lockheed Martin developed vehicle synthesis tool, FASTPASS [42]. The following conclusion was reached by Markopoulos et al. [41]:

> Analyses indicate a significant potential for payload increases with the addition of hybrid rocket boosters to the Atlas Family of Launch Vehicles. As an example, both pressure-fed and pump-fed hybrid rocket motors were synthesized along with an Atlas IIAR to deliver 10,500 lb of payload to a geosynchronous transfer orbit.

The baseline Atlas IIAR is quoted in the analysis as being able to deliver 8600 lb to GTO [41].

D. AMROC Next Generation Launch System (NGLS) Strapon Sizing Studies

In the early 1990s, alternatives were being looked at to boosting NASA payloads to orbit by other than the space shuttle.

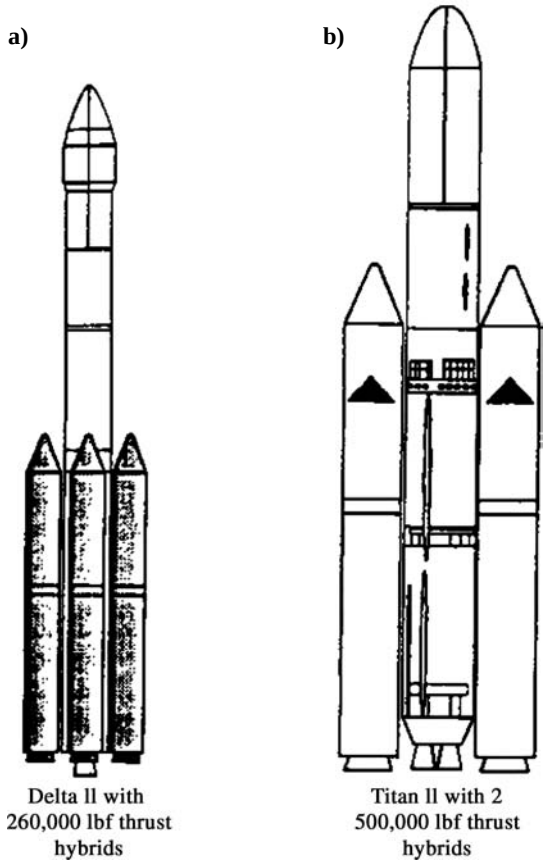

Fig. 29 AMROC strapons on Delta and Titan [40].

Currently, national planners are involved with the analysis and design of the Next Generation Launch Vehicle. During the latest studies of the proposed Spacelifter launch vehicle, a core vehicle was proposed that would utilize strap-on boosters to provide a wide range of payload capability into low Earth orbit. In such a scenario, a hybrid rocket motor provides the premier design option for the strap-on booster due to the hybrid's inherent safety, operational flexibility and low cost. Strap on booster designs are presented that meet the mission goals of 20,000 to 50,000 pounds to low earth orbit [43].

By the use of a modified version of AMROCs 250,000-thrust motor to a longer burn time and higher thrust motor (see Fig. 30, Table 2), a family of LVs were proposed based on a LOX hydrogen core vehicle (see Fig. 31). Another twist to the concept is to save the LOX/hydrogen core vehicle and just cluster seven of the larger 280,000-thrust hybrid motors fed from a single LOX tank (Fig. 32).

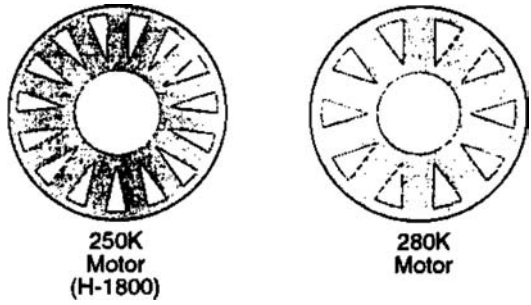

Fig. 30 Motor fuel grain configuration comparison.

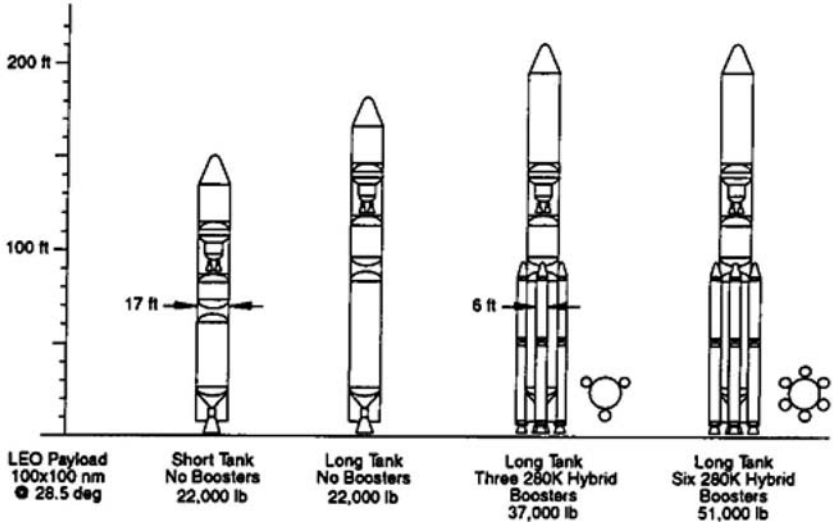

Fig. 31 AMROC NGLS-type core with hybrid strapons [43].

Table 2 AMROC NGLS strapon hybrid motor sizing [43]

Parameter	250,000 Motor H-1800	250,000 Motor	Difference, %
Diameter, in.	73	73	—
Length, ft	30	45	+50
Thrust (sl), lb	236,000	277,000	+17
Burn time, s	72	114	+58
Propellant weight, lb	66,500	122,100	+84
No. of Ports	15	10	−33
Hydraulic Diameter, in.	8.4	10.1	+20

sl, sea level.

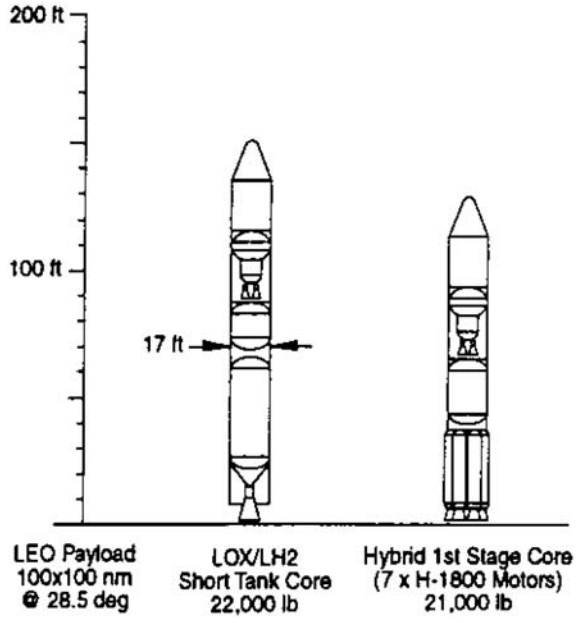

Fig. 32 AMROC NGLS-type vehicle with hybrid first stage [43].

E. AMROC National Launch System and Personnel Launch System with Hybrid Rockets

In 1992, two new space transportation concepts were being investigated in the United States. One, the National Launch System (NLS), was being proposed to launch unmanned payloads. Another, the Personnel Launch System (PLS), was a small spacecraft designed exclusively for personnel transport. Consideration was given to launching the PLS using an element of the NLS booster. The demanding requirements for crew safety and safe return after abort indicated that the PLS may be better served by a launcher optimized for crew safety, leaving the NLS to be optimized for its unmanned cargo carrying load. The unique safety characteristics of hybrid propulsion could have been invaluable in this manned launch role [44].

All forms of rocket propulsion can claim the potential for high reliability. Increased reliability generally is accompanied by increased complexity and inspection requirements. Mission reliability is not, however, the most critical factor where manned systems are concerned. The paramount issue in manned system planning is not how likely a failure is, but what are the consequences of a failure if it occurs [44].

With conventional solid- and liquid-propulsion systems, to ensure crew safety and minimize the likelihood that catastrophe will occur, considerable effort is spent on maximizing system reliability. In addition, complex and often troublesome health monitor systems are required to give advanced warning of impending

failure. This is necessary to allow time for emergency escape systems to carry personnel to a safe distance, away from potentially life threatening explosive blast waves [44].

With hybrid propulsion systems, you start with a noncatastrophic system. Effort may still be expended to maximize system reliability and, therefore, mission success, but the consequences of catastrophic failure associated with other propulsion systems are not present. Where crew safety is at stake, safe hybrid may be the only defensible technology for use in primary propulsion applications [44].

Based on the PLS requirements shown in Fig. 33 and Table 3, a hybrid launcher was sized to get it to a low Earth orbit. The system size is shown in Fig. 34, with specifications listed in Table 4 [44]. Additional sizing was done with the same core vehicle to get the payload information shown in Fig. 35.

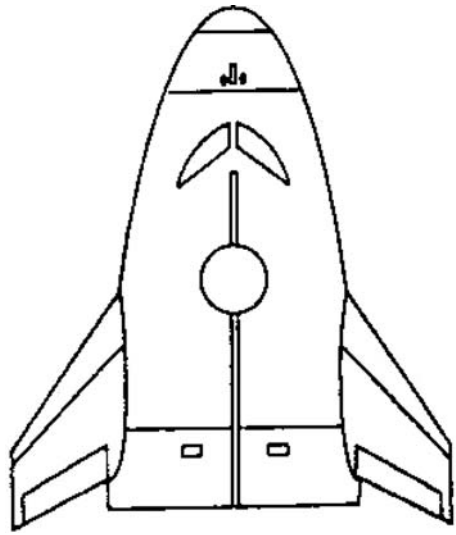

Fig. 33 AMROC PLS upper-stage vehicle [44].

Table 3 PLS mass summary

Parameter	Value, lb
Empty weight	17,335
Useful load	3,370
Propellant	4,067
Gross weight	24,772
Abort/escape system	9,770

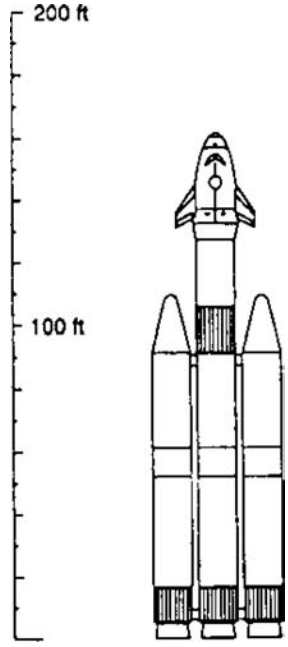

Fig. 34 AMROC PLS launcher configuration [44].

Table 4 AMROC PLS launcher system sizing [44]

Parameter	Value
Booster module (first- and second-stage motors)	
Propellant weight	400,000 lb
Burnout weight	65,100 lb
Takeoff weight	465,100 lb
Average I_{sp} (vacuum)	300 s
Diameter	144 in
Length overall	112 ft
Average thrust (vacuum)	1,400,000 lbf
Third stage	
Propellant weight	100,000 lb
Burnout weight	16,100 lb
Takeoff weight	116,100 lb
Average I_{sp} (vaccum)	322 s
Diameter	144 in
Length overall	34 ft
Average thrust (vacuum)	168,000 lbf
Payload to 35 × 220 n mile 28.5-deg inclination orbit	25,300 lb
Gross vehicle takeoff weight	1,536,700 lb

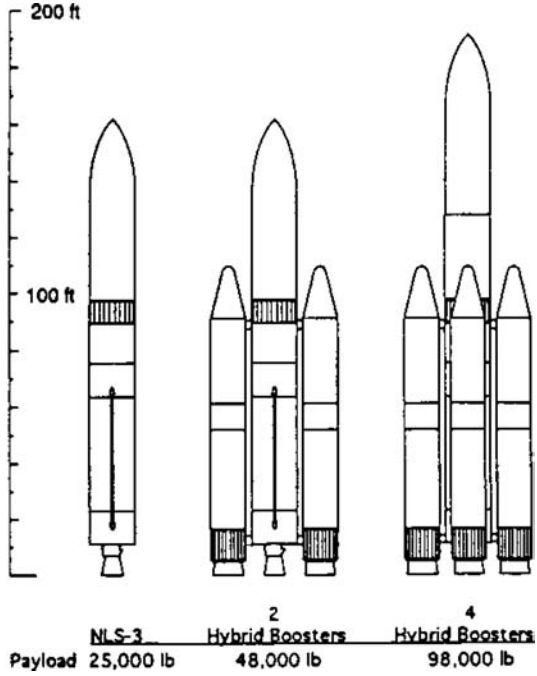

Fig. 35 AMROC PLS launcher system sizing payload [44].

F. Thiokol Strapons for Single-Stage Vehicles

Many single-stage-to-orbit (SSTO) and reusable LV (RLV) configurations were being evaluated as potential means of reducing payload delivery cost to low Earth orbit (LEO) in 1994. Solid or hybrid boosters can provide thrust augmentation as a means to increase conveniently and economically the capability or reduce

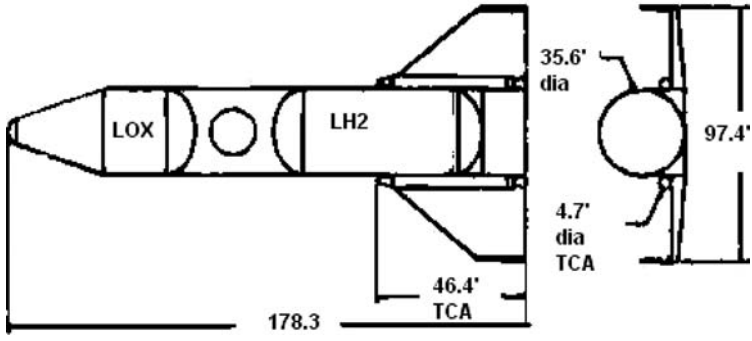

Fig. 36 Thiokol single-stage vehicle with strapon hybrids [45].

Table 5 Thiokol hybrid strapons

Parameter	Value
Diameter, in.	56.0
Length, in.	599.3
Fuel weight, lb	20,500.0
LOX weight, lb	52,500.0
TCA weight, lb	30,700.0
Total weight, lb	83,729.1
Mass fraction	0.877
Average vacuum thrust, lbf	469,200
Specific impulse, s	291.3
Total impulse, lbm · s	20,905,400.0
Burn time, s	44.6
Average mixture ratio	2.6
Average pressure, psi	1,002.0

the overall size of a baseline SSTO vehicle to more effectively and economically capture the majority of the overall mission model. With this in mind, strapon boosters (solid and hybrid) were designed to allow the basic size of the SSTO to be reduced to better target the high traffic portion of the mission model and also to capture larger payloads. Simple operational concepts for increasing the performance of the boosters were developed that are consistent with the rapid turn around philosophy of the SSTO vehicle. Solid and hybrid propulsion were shown to have been an effective method of thrust augmentation for the SSTO mission [45].

The solid and hybrid strapons were sized to increase the vehicle payload from 25,000 lbm to 50,000 [45]. The hybrid strapons were fed from the vehicle main oxidizer tank and sized as shown in Table 5.

The analysis showed the promise of hybrid strapons as a means to augment the booster launch capabilities.

VIII. Conclusions

The Firebolt was a hybrid rocket-based supersonic target system that got through production and development and was demonstrated with several successful flights propelling the vehicle to ∼Mach 4, but did not get production funding for an operational system.

AMROC developed SET-1 as a suborbital launch system and the motor and other subsystems functioned well in component tests. However, on the brink of launching, but the vehicle did not launch due to frozen condensation on the LOX valve not allowing the LOX valve to open fully, keeping the motor on the pad. SET-1's unfortunate failure on the pad proved the safety of hybrids: Damage to the test stand and payload were minimal. AMROC studied many hybrid rocket-based concepts and were in development of the HyFlyer vehicle when they shut down.

The HPDP's N_2O/HTPB-based sounding rockets were successfully launched out of Wallops Island, with a maximum altitude of ∼120,000 ft. They demonstrated

quick turnaround, safe nonpryogenic ignition, and upon recovery of the rocket, the flight effect on the motor was determined to be the same as the ground testing.

Lockheed Martin's HYSR program's successful launch demonstrated several patented concepts that could be used on future hybrid systems. A staged combustion system was used for ignition and motor combustion stability. A heated helium pressurization system was employed for minimizing the weight of pressure-fed propulsion systems by heating the ullage gas and pressurant tank. Although the vehicle did not perform as well as predicted, the issues that caused the lower than expected performance were identified and can be corrected in future applications.

Hybrid rockets have been successfully propelled a privately financed manned vehicle to the edge of space in a historic series of flights: first privately funded rocket vehicle to break Mach 1, first privately funded vehicle to reach 62 n miles high, and then first to be able to do it twice in two weeks. Scaled Composite's selection of a N_2O/HTPB-based hybrid motor system for SpaceShipOne indicates that a hybrid motor's advantages of safety, simplicity, and cost will be returned to for larger, more complex systems.

Multiple studies have been done with hybrid rockets in the past. Replacing the space shuttle solid rocket motors was looked at as an option. Strapon replacements for expendable LVs Atlas and Delta have been considered. Boost augmentation for proposed SSTO vehicles have been examined. These studies all indicated that hybrids had some advantages for their vehicle configuration over the current strapons or other proposed strapons.

Hybrid-based vehicles have been proposed, sized, and studied for multiple payloads and applications: NLS and Next Generation Vehicle requirements. These studies showed some advantages over the proposed systems. These requirements were never met, and the systems were never produced.

However, there are new LVs being proposed, where hybrids are potential players. Space Dev is studying hybrids for the Dream Chaser vehicle, Lockheed Martin was developing the Falcon vehicle for DARPA and the U.S. Air Force. NASA is currently investigating concepts for a space shuttle replacement: Hybrids should be discussed if strapon rockets are needed.

Hybrid rocket motors have made limited progress into the world of LVs because of the low technical maturity and flight history of hybrids prohibiting the investment into the necessary development. Recent demonstrations of hybrids have raised the technology readiness levels of hybrid rockets. Sizing studies have shown that a hybrid LV or hybrid-augmented vehicle could be developed and carry significant payload, if the technology is ready. The HYSR flight and SpaceShipOne have advanced the maturity of hybrids, hopefully to the point of making hybrids a viable candidate for future vehicle systems.

References

[1] Altman, D., "Hybrid Rocket Propulsion, Prospects for the Future," AIAA Paper, AIAA Annual Meeting and Technical Display, Long Beach, CA, May 1981.

[2] Salmon, M., "ONERA Hybrid Rocket for Scientific Probes," World Aerospace Systems, May 1968, p. 5.

[3] Mead, F. B., Jr., and Bornhorst, B. R., "Certification Tests of A Hybrid Propulsion System for the Sandpiper Target Missile," U.S. Air Force Rocket Propulsion Lab., Rept. AFRPL-TR-69-73, June 1969.

[4] Parsch, A., "Teledyne Ryan AQM-81," <http://www.astronautix.com/lvs/firebolt.htm>.
[5] Wade, M., <http://www.astronautix.com/lvs/dolphin.htm>.
[6] O'Lone, R. G., "Bay Area Firms Pursue Booster Designs," *Aviation Week and Space Technology*, 25 June 1984.
[7] "Starstruck Launches Prototype Dolphin Rocket in First Flight," *Aviation Week and Space Technology*, 13 Aug. 1984.
[8] "Starstruck Management is Reorganized," *Aviation Week and Space Technology*, 22 Oct. 1984.
[9] "Getting Into The Launch Business: The Amroc Story, Part 1," <http://www.spacearium.com/article.php?story=20040512060105553&query=SET-1> [12 May 2004].
[10] Kniffen, R. J., McKinney, B., and Estey, P., "Hybrid Rocket Development at the American Rocket Company," AIAA Paper 90-2762, 26th AIAA/ASME/SAE/ASEE Joint Propulsion Conference, Orlando, FL, July 1990.
[11] Environmental Aeroscience Corporation (eAc) website, <http://www.hybrids.com/gallery.html>.
[12] Arves, J. P., Jones, H. S., Kline, K., Smith, K., Slack, T., and Bales, T., "Development of a N2O/HTPB Sounding Rocket," AIAA Paper 97-2803, 33rd AIAA/ASME/SAE/ASEE Joint Propulsion Conference, Seattle, WA, July 1997.
[13] Arves, J. P., Jones, H. S., Kline, K., Smith, K., Slack, T., and Bales, T., "Overview of Hybrid Sounding Rocket Program," AIAA Paper 97-2799, 33rd AIAA/ASME/SAE/ASEE Joint Propulsion Conference, Seattle, WA, July 1997.
[14] Arves, J., Gnau, M., Joiner, K., Kearney, D., McNeal, C., and Murbach, M., "Overview of the Hybrid Sounding Rocket (HYSR) Project," AIAA Paper 2003-5199, 39th AIAA/ASME/SAE/ASEE Joint Propulsion Conference, Huntsville, AL, July 2003.
[15] Kearney, D. A., and Geiman, W. W., "Accounting for Planned Fuel Expulsion by Hybrid Rockets," AIAA Paper 2005-3546, 41st AIAA/ASME/SAE/ASEE Joint Propulsion Conference, Tucson, AZ, July 2005.
[16] *Aerospace America*, Dec. 2000.
[17] Arnecke, S., Houseal, S., Landis, J., and Williams, B., "Flight of the Redbirds," AIAA Paper 2005-4090, 41st AIAA/ASME/SAE/ASEE Joint Propulsion Conference, Tucson, AZ, July 2005.
[18] Scaled Composites website, "Teir One Private Manned Space Program," <http://www.scaled.com/projects/tierone/logs-WK-SS1.htm>.
[19] "NASA Administrator Lauds Successful Human Space Flight," NASA Press Release 04-199, 21 June 2004.
[20] David, L., "SpaceShipOne Wins $10 Million Ansari X Prize in Historic 2nd Trip to Space," <http://www.space.com/missionlaunches/xprize2_success_041004.html> [4 Oct. 2004].
[21] Coppinger, R., "SS2 Faces Major Design Decisions," Flight Global, <http://www.flightglobal.com/Articles/2005/11/15/Navigation/177/202884/SS2+faces+major+design+decisions.html> [15 Nov. 2005].
[22] Dornheim, M. A., "SpaceShipOne Won," *Aviation Week and Space Technology*, Vol. 161, No. 14, 10 Oct. 2004, pp. 34–36.
[23] Dornheim, M. A., "Hybrid Matched to Spaceship Goals," *Aviation Week and Space Technology*, Vol. 158, No. 16, 21 Apr. 2003, p. 69.
[24] Scaled Composites Website, "Tier One Private Manned Space Program-Gallery," <http://www.scaled.com>.

[25] "Lockheed Martin Successfully Test Fires Second Falcon Small Launch Vehicle Hybrid Motor," Lockheed Martin Press Release, <http://www.lockheedmartin.com/wms/findpage.do?dsp=fec&ci=16895&rsbci=Ø&fti=112&ti=Ø&sc=400> [16 June 2005].

[26] "DARPA, Air Force Kick-Off Falcon Phase II Small Launch Vehicle Effort," DARPA News Release, <http://www.darpa.mil/body/news/2004/falcon_ph2_t1.pdf> [5 Sept. 2004].

[27] Lockheed Martin Michoud image gallery of Hybrid Propulsion, <http://www.lockheedmartin.com/wms/findPage.do?dsp=fec&ci=16347&rsbci=15260&fti=0 & ti=0&sc=400>.

[28] Virgin Galactic Website, <http://www.virgingalactic.com>.

[29] Space Dev Website, <http://www.spacedev.com>.

[30] Benson, J., "Safe and Affordable Human Access to LEO," AIAA Paper 2005-6758, Space 2005, Long Beach, CA, Aug. 2005.

[31] Macklin, F., Grainger, C., Veno, M., and Benson, J., "New Applications for Hybrid Propulsion," AIAA Paper 2003-5202, 39th AIAA/ASME/SAE/ASEE Joint Propulsion Conference, Huntsville, AL, July 2003.

[32] Williams, G., Macklin, F., Sarigul-Klijn, M., Sarigul-Klijn, N., and Benson, J., "Almost There: Responsive Space," Paper RS2-2004-8000, 2nd Responsive Space Conf., 19–22 April 2004.

[33] Estey, P. N., and Flittie, K. J., "AQUILA: The Next Generation Launch Service for Small Satellites," AIAA Paper 92-1844, 14th AIAA International Communication Satellite Systems Conference, Washington, DC, March 1992.

[34] Estey, P., "Hybrid Technology Option Project: A Cooperative Effort for Tommorrow's Space Transportation," AIAA Paper 94-4503, AIAA Space Programs and Technologies Conference, Huntsville, AL, Sept. 1994.

[35] Friedman, B., Kobayashi, A., Culver, D., Barnette, B., Hoffman, L., Strickfaden, B., and Hansen, C., "Hybrid Propulsion Technology Program," Contact NAS8-37775, Final Report, Aerojet Solid Propulsion, Aerojet TechSystems, Martin Marietta Aerospace, Sacramento, CA, Jan. 1990.

[36] "Hybrid Propulsion Technology Program," Contract NAS8-37776, Final Rept., Atlantic Research Corp., Virginia Propulsion Division, Jan. 1990.

[37] Jenson, G. E., Holzman, A. L., Leisch, S. O., Keilback, J., Parsley, R., and Humphrey, J., "Hybrid Propulsion Technology Program," Final Rept., Contract NAS8-37778, Chemical Systems Div., United Technologies, San Jose, CA, Jan. 1990.

[38] Schuler, A. L., and Wiley, D. R., "Hybrid Propulsion Technology Program," Contact NAS8-37777, Final Report, General Dynamics Space Systems Division, Thiokol Corporation, San Diego, CA, Nov. 1989.

[39] Sackheim, R., Ryan, R., and Threet, E., "Survey of Advanced Booster Options for Potential Shuttle-Derivative Vehicles," AIAA Paper 2001-3414, 37th AIAA/ASME/SAE/ASEE Joint Propulsion Conference, Salt Lake City, UT, July 2006.

[40] Estey, P. N., and Hughes, B. G. R., "The Opportunity for Hybrid Rocket Motors in Commercial Space," AIAA Paper 92-3431, 28th AIAA/ASME/SAE/ASEE Joint Propulsion Conference, Nashville, TN, July 1992.

[41] Markopoulos, P., Szedula, J. and Abel, T., "Application of Hybrid Rocket Boosters to Launch Vehicle Systems," AIAA Paper 1997-2934, 33rd AIAA/ASME/SAE/ASEE Joint Propulsion Conference, Seattle, WA, July 1997.

[42] Szedula, J. A., "FASTPASS: A tool for Launch Vehicle Synthesis," AIAA Paper 96-4051, 6th NASA and ISSMO Symposium & Multidisciplinary Analysis and Optimization, Bellevue, WA, Sept. 1996.

[43] Flittie, K. J., and McKinney, B., "Hybrid Booster Strap-ons for the Next Generation Launch System," AIAA Paper 93-2269, June 1993.

[44] McKinney, B. C., "The Application of Large Scale Hybrids to NLS and Future Personal Launch Vehicles," AIAA Paper 92-3304, 28th AIAA/ASME/SAE/ASEE Joint Propulsion Conference, Nashville, TN, July 1992.

[45] Allen, B. D., Sauvageau, D. R., and Joyner, C. R., "Reusable Launch Vehicle Design Flexibility," AIAA Paper 94-4499, AIAA Space Programs and Technologies Conference, Huntsville, AL, Sept. 1994.

This page intentionally left blank

Chapter 15

Challenges of Hybrid Rocket Propulsion in the 21st Century

Kenneth K. Kuo*

Pennsylvania State University, University Park, Pennsylvania 16802

and

Martin Chiaverini†

Orbital Technologies Corporation, Madison, Wisconsin 53711

Nomenclature

A = area
B = blowing parameter
C_f = skin-friction coefficient
c_p = constant-pressure specific heat
D = diameter
E_a = activation energy
f_m = fuel/air mixture ratio
G = mass flux ρu
H = heat of reaction
h = port height
k = rate constant
Le = Lewis number
N_p = particle number density
O/F = oxidizer-to-fuel mass ratio
P = pressure
Pr = Prandtl number
Q = heat flux

*Distinguished Professor of Mechanical Engineering, Department of Mechanical and Nuclear Engineering, Propulsion Engineering Research Center.

†Principal Propulsion Engineer.

R = gas constant
Re_D = Reynolds number based on diameter
Re_x = Reynolds number based on length
R_u = universal gas constant
$\dot{r}$ = regression rate
St = Stanton number
T = temperature
t = time
u = velocity
w = web thickness
x = axial location
Y = mass fraction
α = coefficient defined in Eq. (42) used in Eq. (41)
γ = ratio of specific heats
ΔH = total heat for pyrolyzing solid fuel from its initial temperature T_i
ε = emissivity
θ = ratio of average flame temperature $T_{f,\text{av}}$ to surface temperature T_s
κ = absorption coefficient
μ = viscosity
ρ = density
σ = Stefan–Boltzmann constant

Subscripts

conv = convective
e = boundary-layer edge
f = fuel
fl = flame
g = gas
o = oxidizer
rad = radiative
w = wall
x = axial
0 = no blowing case on the fuel surface
∞ = freestream

I. Introduction

A. Background

TO facilitate the discussion in the challenging areas and method of future hybrid rocket developments, some background materials are introduced in this section, even though there are other chapters describing various features of hybrid rockets. The term hybrid rocket is defined by Sutton [1] and classified into various types in Chapter 1 of this volume [2]. As commonly known, most chemical rockets require two reacting media: a fuel and an oxidizer to burn and release thermal energy in the combustion chamber. When both reacting media are liquids, the

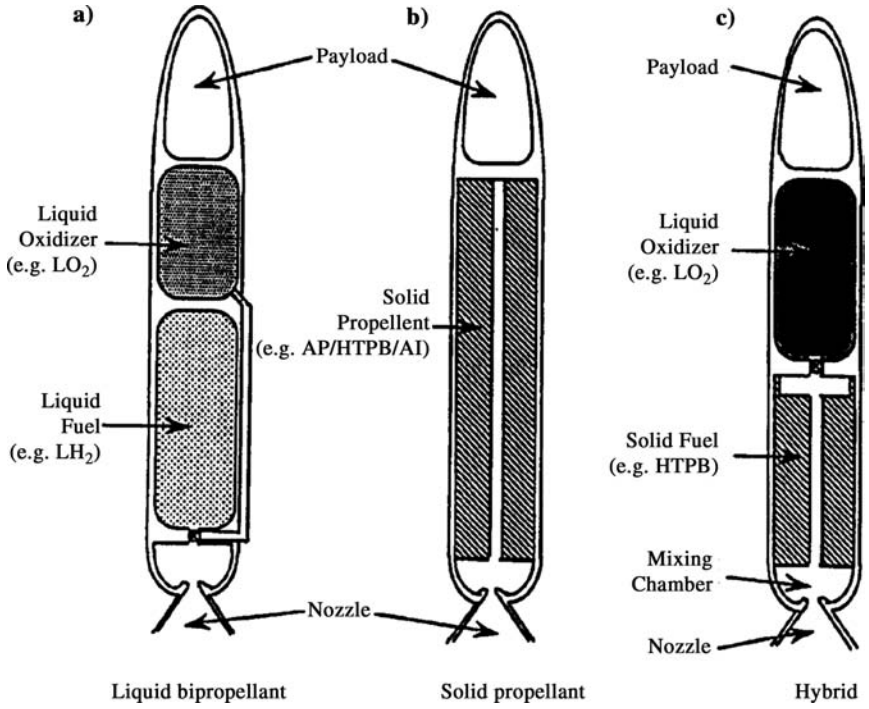

Fig. 1 Three types of chemically-powered rockets.

rocket is called a liquid-bipropellant rocket, or simply, a liquid-propellant rocket. Liquid oxygen (LO_2 or LOX), liquid flourine (LF_2), nitrogen tetroxide (N_2O_4), and nitric acid (HNO_3) are commonly used liquid oxidizers in liquid-propellant rockets, whereas liquid hydrogen (LH_2), methane (CH_4), and hydrazine (N_2H_4) are often employed as liquid fuels. When both reacting components are solids in the form of either a premixed homogeneous propellant or a physically combined heterogeneous propellant, the rocket is called a solid-propellant rocket. In the case of a homogeneous solid propellant, nitrocellulose (NC) is commonly mixed and crosslinked with nitroglycerin (NG) to form a double-based propellant with both ingredients serving as fuel and oxidizer; NG serves as the oxider-rich ingredient and NC as the slightly fuel-rich one. A commonly used heterogeneous rocket propellant consists of ammonium perchlorate (AP) as the solid oxidizer and hydroxyl-terminated polybutadiene (HTPB) as the solid fuel. The AP particles are held together physically in a binder matrix of HTPB without chemical bonding at the particle/binder interfaces [1, 3]. When one component is liquid and the other one is solid, the rocket is called a hybrid rocket. This third type of chemical rocket propulsion system represents a type of amalgam of the liquid- and solid-propellant rockets, yet it has important and distinguishing features common to neither of the two other systems. Figure 1 illustrates the basic differences between the liquid-propellant, solid-propellant, and hybrid rocket systems.

The concept of hybrid rocket propulsion is not new; it was first introduced around 1937 in Russia by Andrussow according to Green [4]. In the interest of

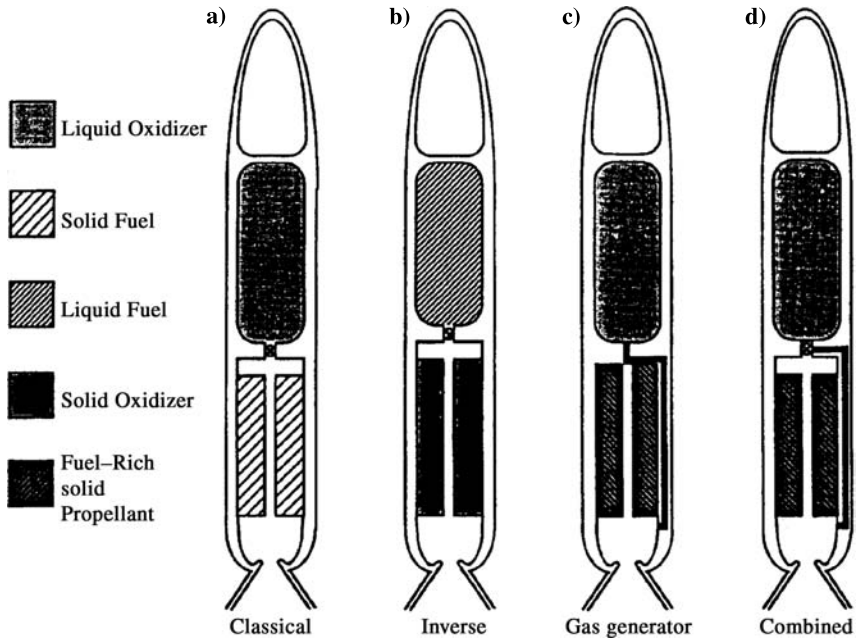

Fig. 2 Various types of hybrid rockets.

discussion convenience, classification of various types of hybrid rockets are given here and shown in Fig. 2. The classical hybrid rocket configuration is of great interest for various applications; it consists of a solid-fuel grain cast into the combustion chamber and a separate tank containing a liquid oxidizer such as LOX. The oxidizer can be fed into the ports of the fuel grain in the combustion chamber either by gas pressure or by a pump system. In this configuration, the liquid oxidizer is injected into the head end of the solid-fuel grain through a precombustion chamber, which serves to vaporize the oxidizer and allows it to enter the combustion ports in a more uniform manner than a liquid spray jet. The pyrolyzed gaseous fuel and oxidizer mix and react along the length of the fuel grain and undergo final mixing in the aft combustion chamber. The hot product gases are then expelled from the nozzle to generate thrust.

The inverse hybrid motor shown in Fig. 2 works in much the same manner as the classical hybrid except that a liquid fuel and a solid oxidizer react to form the combustion products. In the gas-generator type of hybrid rocket, the solid fuel is loaded with a small amount of solid oxidizer, forming a fuel-rich solid-propellant grain. Oxidizer is then injected into the afterburner section to mix and burn with the fuel-rich gases generated by the solid grain. Finally, the combined type shown in Fig. 2d has both aspects of the classical and gas-generator types of hybrid motors because the oxidizer is injected into both the head end of the fuel grain and the aft mixing chamber. Other configurations, such as an inverse gas generator using solid oxidizer and liquid fuel, are also possible [4]. Of all of the design concepts shown in Fig. 2, the classical hybrid rocket has received the most attention, and therefore, it is used as the main configuration for discussion in this chapter. More

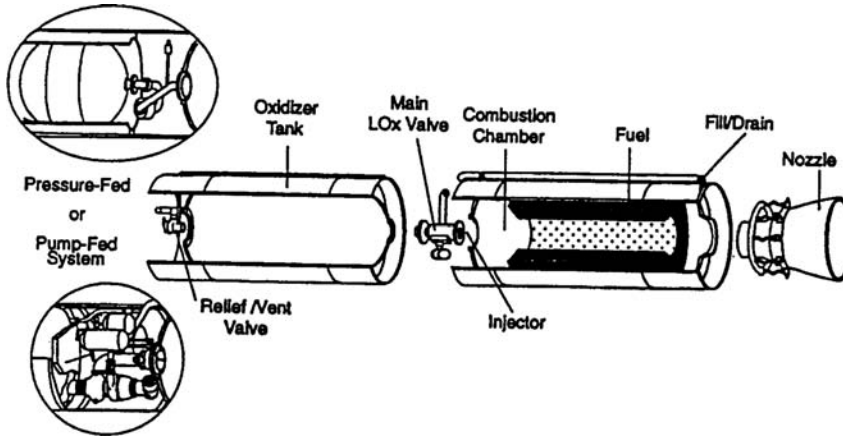

Fig. 3 Major components of a classical hybrid rocket motor. (From Estey et al. [5].)

details of the classical hybrid propulsion system adapted from Estey and Hughes [5] are shown in Fig. 3.

B. Specific Advantages and Disadvantages of Hybrid Rockets

In view of the distinct features of separately stored fuel and oxidizer in different physical states and controlled motor operation, classical hybrid propulsion systems offer several important advantages over their liquid and solid rocket counterparts; these advantages make them attractive alternatives for commercial, military, and scientific applications. The following listed advantages are commonly recognized in the propulsion community:

1) Hybrid rocket motors are very safe during fabrication, storage, testing and operations, with minimal explosion or detonation hazard.
2) They have stop-start–restart capabilities.
3) Hybrid rockets have higher specific impulse than solid rockets and higher density impulse than liquid rockets.
4) There is minimal environmental impact with hybrid rocket launches.
5) The propulsion system cost is much lower than those of solid and liquid rocket propulsion systems.
6) Hybrid rockets have high reliability (half the pumps and plumbing of liquid-propellant engines; stronger than solid-propellant grains, and much less sensitive to cracks and debonds).
7) There is greater maneuverability with controlled thrust profiling on demand over a wide range of operating conditions.

In the following paragraphs, the major advantages just listed are described in more detail with comparisons to solid- and liquid-propulsion systems.

The inverse hybrid motor shown in Fig. 2 works in much the same manner as the classical hybrid except that a liquid fuel and a solid oxidizer react to form the combustion products. Generally, the classical hybrid requires a total liquid mass to

solid mass ratio ranging from 2 to 7, whereas the inverse configuration has a mass ratio of about 0.5 [3] and, in some special cases, as low as 0.1. In the gas-generator version, the solid fuel is loaded with a small amount of solid oxidizer, forming a fuel-rich solid-propellant grain. Oxidizer is then injected into the afterburner section to mix and burn with the fuel-rich gases generated by the solid grain. Finally, the combined type shown in Fig. 2d has both aspects of the classical and gas-generator types of hybrid motors because the oxidizer is injected into both the head end of the fuel grain and the aft mixing chamber. Other configurations, such as an inverse gas generator using solid oxidizer and liquid fuel, are also possible [3]. Laboratory-scale cryogenic hybrids using frozen solid fuel such as ethylene and n-pentane have also been tested [4]. Of all of the design concepts shown in Fig. 2, the classical hybrid rocket has received the most attention, and therefore, it is used as the main configuration for discussion in this chapter. More details of the classical hybrid propulsion system adapted from Estey and Hughes [5] and Kuo [6] are shown in Fig. 3.

1. Improved Safety

First, unlike solid-propellant rockets, hybrid rockets are much less sensitive to cracks and imperfections in the solid-fuel grain. Even though the oxidizer and combustion product gases can penetrate into crack cavities, reactions in the cavity regions are limited and unable to generate any significant local pressurization and grain damage. In contrast to hybrid solid-fuel grain, once the solid-propellant grain is cast into either a segment or a monolithic grain, it constitutes a major hazard for catastrophic energy release and requires exhaustive precautionary measures in all phases of storage assembly, transportation, stacking, and prelaunch preparation. Therefore, hybrid rockets are much safer than solid-propellant rockets [2, 6].

Unlike liquid fuels, such as highly volatile and reactive hydrogen, solid fuels are not hazardous for storage and transportation. Hybrid rockets are indeed much safer than liquids during the latter stages of prelaunch operations when the vehicle is fueled and during all flight phases. In liquid-bipropellant systems, leakage of propellants or structural failures due to mishandling or excess loads, whether on the launch pad or inflight, could lead to a catastrophic conflagration if the leakage or failure results in a fuel/air fire or mixing of the fuel and oxidizer. On the contrary, there is much lower probability for any violent energy release hazard involved in the event of leakage or structural failure in the hybrid's liquid oxidizer system.

These safety features represent the most desirable and distinguishing characteristics of hybrid rockets. Their safety characteristics will definitely have a strong impact for reducing future propulsion hazards to the payload of unmanned missions, launch facilities, and manned flights.

2. Greater Operability and Reduced Servicing Requirements

Compared to liquid rockets, the relative simplicity of hybrid rockets offers important benefits in prelaunch operations due to their fewer components and operational steps, for example, all liquid-fuel-related operations are eliminated. This is a significant advantage for booster applications.

Although more complex than solid rockets, hybrid rockets offer significant operational advantages. Hybrid fuel without oxidizer present is inert, whereas

solid-propellant motors contain large masses of hazardous propellant and, therefore, require considerably greater care and attention during all ground handling. Hybrid motors can employ a monolithic grain that eliminates the need for stacking operations, can be operated in a "holddown" mode for pre-launch checkout, and can be shut down if necessary. They can be shut down in the event of a mission abort at any time during their thrusting period. Because hybrids can be throttled, they allow operational flexibility and permit accurate closed-loop thrust tailoring, which is especially important during periods of high dynamic pressure or maneuvering for trajectory corrections. Hybrids offer the same controllability, shutdown, and restart benefits as liquids with simpler prelaunch and launch operations.

3. High Propulsion Performance

In terms of propulsion performance, the theoretical vacuum specific impulse performance of LOX/HTPB hybrids exceeds 360 s [7]. This is considerably higher than the best of all solid-propellant rockets (about 320 s). The I_{sp} of the hybrid rocket compares very closely with the LOX/RP combination used in many liquid propellant boosters and core engines, as shown in Fig. 4. Some hybrid motors, using cryogenic liquids and fuels with light metal additives, can deliver better performance than the best liquid propellants, (that is, over 460 s). Also, the density impulse of typical classical hybrid rockets is in the range of 300–520 $g \cdot s/cm^3$, which is higher than that of liquid propellant rockets (in the range of 100–430 $g \cdot s/cm^3$). In comparison with solid-propellant rockets, although hybrid rockets have significantly higher specific impulse, their density impulse is lower. This imposes constraints on certain volume-limited applications. However, it is important to consider the greater operability of hybrid rockets in comparison with the solid rockets, which may offset their lower density impulse characteristics for some applications.

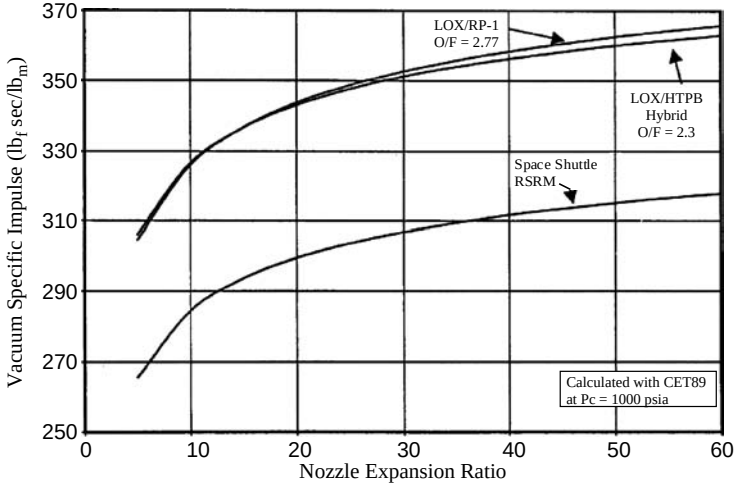

Fig. 4 Performance comparisons of hybrids, liquids, and solids. (From Kuo [6].)

Table 1 Exhaust emissions from typical liquid, hybrid, and solid rocket engines

Species	LO_2/RP-1, lbm/s per 10^5-lb thrust [8]	Hybrid, lbm/s per 10^5-lb thrust [8]	Solid, lbm/s per 10^5-lb thrust [8]
H_2O	81.1	64.1	31.3
CO_2	93.6	103.9	11.7
CO	134.8	137.0	79.8
HCl	——	——	69.9
Al_2O_3	——	——	100.0
H_2	4.5	3.0	6.9
H	0.1	0.0	0.1
OH	0.0	0.1	0.1
N_2	——	1.2	29.0

4. Minimal Environmental Impact

In general, rocket launchers can have four types of effects on the atmosphere, including stratospheric ozone depletion, acid rain, reduction of local air quality due to dispersion of toxic compounds, and global warming. According to Hawk and Grey as cited by Chiaverini et al. [8], space launches are a negligibly small contributor to all of these effects relative to other natural and anthropogenic sources. Nevertheless, they believe that there will soon be regulatory demands to reduce atmospheric pollution by rocket launches to a minimum. At present, the most important effluents affecting the atmosphere are the chlorine and aluminum used in solid propellants. The nitrogen in certain storable liquid propellants and in solid-propellant ingredients also contributes to some extent to acid rain, ozone depletion, and generation of nitrogen oxides.

The effluents of typical hybrids (excluding afterburning in the exhaust plume) calculated by Hawk and Grey are compared with those of liquid-propellant and solid-propellant space boosters in Table 1. Note that hybrids generate roughly the same product species distribution as oxygen hydrocarbon liquid boosters, whereas solid-propellant effluents are rich in hydrogen chloride, aluminum oxide, and nitrogen. Hybrid rockets with nonmetalized fuels can have environmentally clean exhaust without hydrogen chloride and aluminum oxide and other undesirable product species. Therefore, hybrid rockets are at least as ecologically benign as liquid rockets and definitely have less environmental impact than solid rockets.

5. Relatively Low System Cost

Generally speaking, life-cycle costs of any propulsion system consist of nonrecurring costs [including 1) research, development, testing, and evaluation (RDT&E) and 2) system procurement] and recurring costs for operations and support. According to the AIAA Workshop Report [7], hybrid RDT&E costs are likely to fall between those of new liquids and solids because they depend largely on system complexity. However, compared with solids, the hybrid's lower hazard risk will tend to reduce or eliminate the additive costs associated with the handling of hazardous propellants and complete motor assemblies loaded with

them. Also, the ability to stop and restart hybrid rocket tests and inspect the test motors between firings should introduce cost savings by reducing the number of test motors required to obtain desired data.

For expendable launchers, solid-propellant rockets are much cheaper (by about 30–50%) than the equivalent liquid systems. The higher cost of liquid rockets is mainly due to their much higher hardware costs because the typical oxygen hydrocarbon propellants themselves cost about one order of magnitude less than solid propellants, for example, \$0.2–\$0.5 per kg vs about \$2–\$3 per kg for solids. For hybrids, the propellant cost will approach that of liquid rockets, whereas their hardware costs (especially for pressurized rather than pump-fed designs) are likely to approach those of solids and, in fact, may even turn out to be lower than solids because of the aforementioned benefits associated with the manufacturing and handling of less hazardous material and assemblies. Hence, expendable hybrid rockets are likely to be less expensive to manufacture than either liquids or solids.

For reusable boosters, procurement and production costs depend heavily on the number of times a rocket engine is reused. The procurement costs of hybrids relative to liquid- or solid-propellant rockets are not yet clear. Operational costs of hybrids are likely to fall below those of both liquids and solids. They are operationally simpler to prepare for launch than liquids and less prone to delays due to equipment failures or prelaunch test and checkout anomalies. A comparison of cost drivers for hybrid-, liquid-, and solid-propulsion systems [7] is shown in Table 2. It is quite obvious that hybrids have many advantages over the other two propulsion systems from the cost point of view. It also appears that the life-cycle cost of a new hybrid booster is likely to be significantly lower than that of either a new liquid-propellant booster or a new solid-propellant booster.

6. Disadvantages of Hybrid Rockets

There are several disadvantages of hybrid rockets associated with their performance. Most of these disadvantages are currently being addressed by various groups and will hopefully be overcome in the future. These are discussed in the

Table 2 Cost drivers for hybrid-, liquid-, and solid-propulsion systems (Kuo [6] with modifications)

Cost implication	Hybrid	Liquid	Solids
Operations	√[a]		
Environmental impact	√	√	
Operational flexibility	√	√	
Toxicity	√		
Manufacturing costs	√		
Operational safety	√		
Flight safety	√		
Operational simplicity			√
Existing database	**?**	√	√

[a]Check mark denotes advantage.

"Major Challenges in Hybrid Propulsion" section. The major disadvantages are as follows:

1) Combustion efficiencies of hybrid rockets (typically 93–98%) are slightly lower than those of liquid-propellant or solid-propellant rockets.
2) The density impulse of hybrid rockets is usually lower than that of solid-propellant rockets, thereby resulting in larger volumes.
3) Some fuel "slivers" could remain in the combustion chamber at the end of motor operation; therefore, the effective solid-fuel mass fraction is slightly reduced in the hybrid motor.
4) Oxidizer-to-fuel mass ratio can vary during hybrid motor operation, resulting in slight variations in specific impulse.
5) The regression rates of commonly used solid fuels in classical hybrids are relatively low in comparison with solid propellants; this shortcoming imposes constraints on the fuel-grain design.
6) At the present time, the predictive analytical models and numerical codes have not yet reached a highly matured stage, partly due to the lack of experimental data for model validation and also due to the lack of certain realistic input information (such as fuel decomposition rates and mechanisms as a function of surface temperature).

7. Why the Hybrid Propulsion System Has Not Been Developed to Its Full Maturation

It is quite clear from the preceding discussions that hybrid-propulsion systems have many advantages (and limited disadvantages) over existing solid-propellant and liquid-propellant propulsion systems. This raises the obvious question as to why hybrid rockets are not in widespread use and have not been fully developed. The following reasons may explain the current situation.

1) From the standpoint of launch-readiness and simplicity, solid-propellant rockets are generally ready and reliable for launching, especially for military applications.
2) From the performance point of view, liquid-propellant rockets have high specific impulse; therefore, they have been preferred for civil space launch applications.
3) Liquid oxidizers are restricted on many battle ships, and this regulation restricts the possibility for launching missiles powered by hybrid rockets.
4) Experts in the chemical propulsion field tend to be sharply divided, with their experience in either liquids or solids.
5) Scaling laws have not been completely investigated for hybrid rockets (though work in this area is progressing).
6) Unlike the burning rate of solid propellants, the solid-fuel regression rate depends on many parameters. Historically, there has been a lack of basic understanding of the solid fuel combustion processes under either simulated or actual motor operating conditions. Usually, the support for the research portion of a hybrid program is a very small fraction of the overall motor development program. In view of lack of financial support, research studies in this subject area suffer greatly, are

usually conducted in very narrow scopes, and, therefore, can not reach the desired stage for systematic planning and broad coverage.

7) There is a lack of long-term national programs, as well as international collaboration activities in the development of hybrid rockets. However, this trend is expected to change due to many attractive features of hybrid rockets. Also, many commercial companies appear to be in favor of hybrid rocket development, based on recent activities at Scaled Composites, Space Propulsion Group (SPG), Space Dev, Lockheed Martin, ORBITEC, and similar programs.

C. Combustion Processes Involved in the Hybrid Rockets

As mentioned earlier, the classical hybrid motor configuration is used for this discussion because it is the most broadly adopted one for various applications. There are numerous physicochemical processes occurring in the combustion chamber, which consists of a vaporization chamber in the fore end, a solid-fuel-grain section, and an aft-end mixing chamber connected to the exit nozzle. The vaporization chamber is sometimes called the precombustion chamber and the aft-end mixing chamber is also called the postcombustion chamber, as shown in Fig. 5, the American Rocket Company (AMROC) H-1800 hybrid rocket. To simplify the description of many important and intricate processes, three lists of pertinent processes involved in each major component of the hybrid rocket motor are given:

1) *Precombustion chamber*—a) injection of pyrophoric igniter material or actuation of an ignition device; b) atomization of liquid oxidizer spray jet; c) thermal heating and pyrolysis of solid fuel; d) rapid chamber pressurization at the onset of ignition due to the igniter discharge; e) quenching of a fraction of fuel surface caused by impingement of cold-liquid ligaments and droplets; f) advancement of pyrolysis front over all exposed fuel surfaces and flame anchoring near certain locations; g) penetration of vaporized and liquid oxidizer streams into the ports of solid-fuel grain; h) fuel surface regression due to pyrolysis and the associated contour variations; and i) combustion of vaporized fuel in oxidizer-rich environment.

2) *Solid-fuel-grain section*—a) thermal heating and pyrolysis of solid fuel; b) desorption of polymer fragments from the pyrolyzing fuel surfaces; c) diffusion of

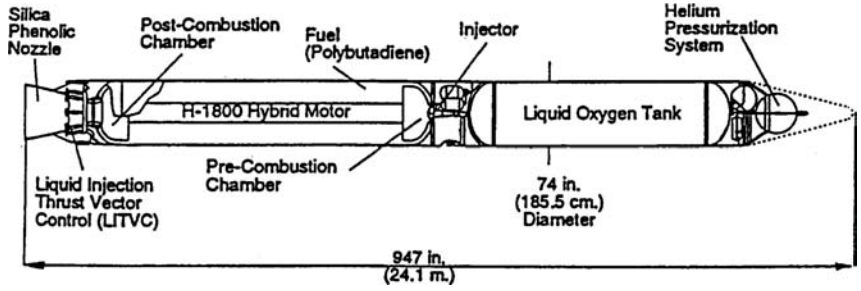

Fig. 5 AMROC H-1800 hybrid rocket. (From Estey et al. [5].)

fragmented fuel species toward the flame zone; d) formation of boundary-layer-like shear flow near surface regions of the solid-fuel grain; e) diffusion of unburned oxidizer to the pyrolyzing fuel surfaces and engagement in heterogeneous reactions; f) propagation of the pyrolysis front spreading over exposed fuel surfaces; g) fuel surface regression due to continued heating from the turbulent diffusion flame; h) increase of axial mass flux along the port of the fuel grain due to mass addition; i) acceleration of the bulk flow in the axial direction; j) Reduction of axial mass flux as port area increases in the later stage; k) grain deformation in response to any unbalanced forces due to onset of ignition, pressure excursion, etc.; l) nonuniformity of burning in a noncircular port of multiport grains; m) toward the

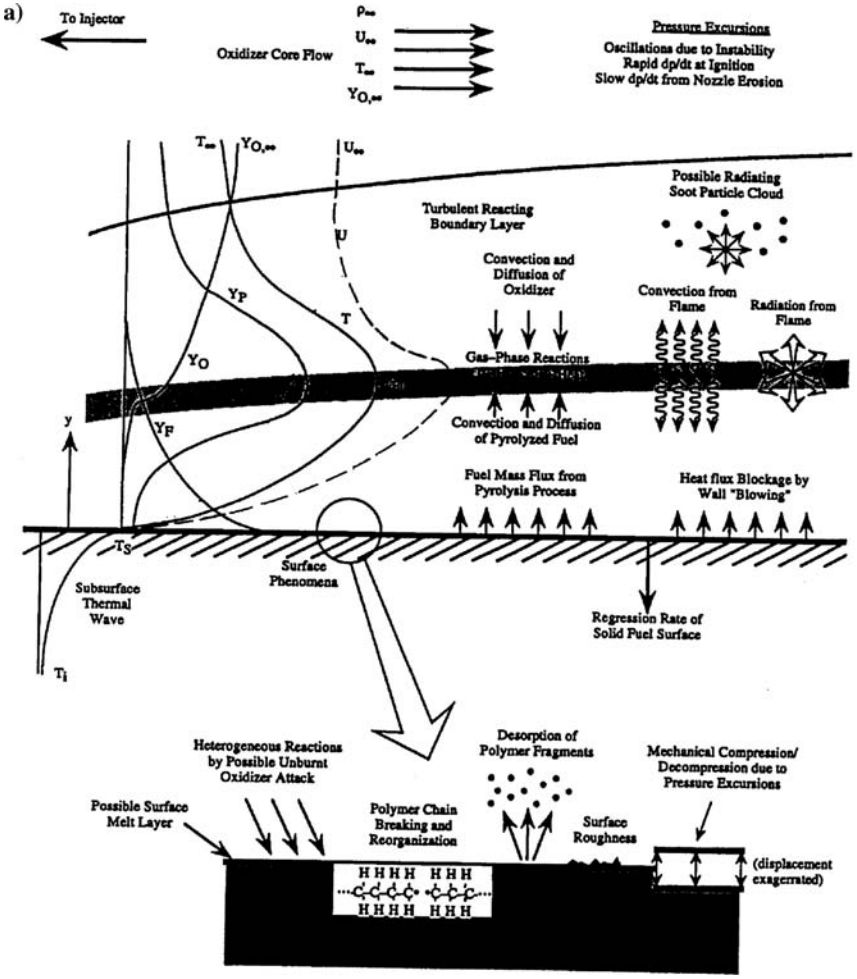

Fig. 6 Physical processes involved in hybrid rocket combustion.

end of burn, grain integrity associated with the support of thin webs for multiport grains; n) damping or amplification of any combustion disturbances or instability waves; and o) potential ejection of unburned sliver residues.

3) *Postcombustion chamber*—a) mixing of jet streams from all solid-fuel ports; b) heating of thermal insulation material; c) continued chemical reactions between any unreacted fuel- and oxidizer-rich species; d) exhausting product gases, soot, and any other condensed-phase particles from the nozzle; e) damping or amplification of any combustion disturbances or instability waves; and f) erosion of nozzle throat.

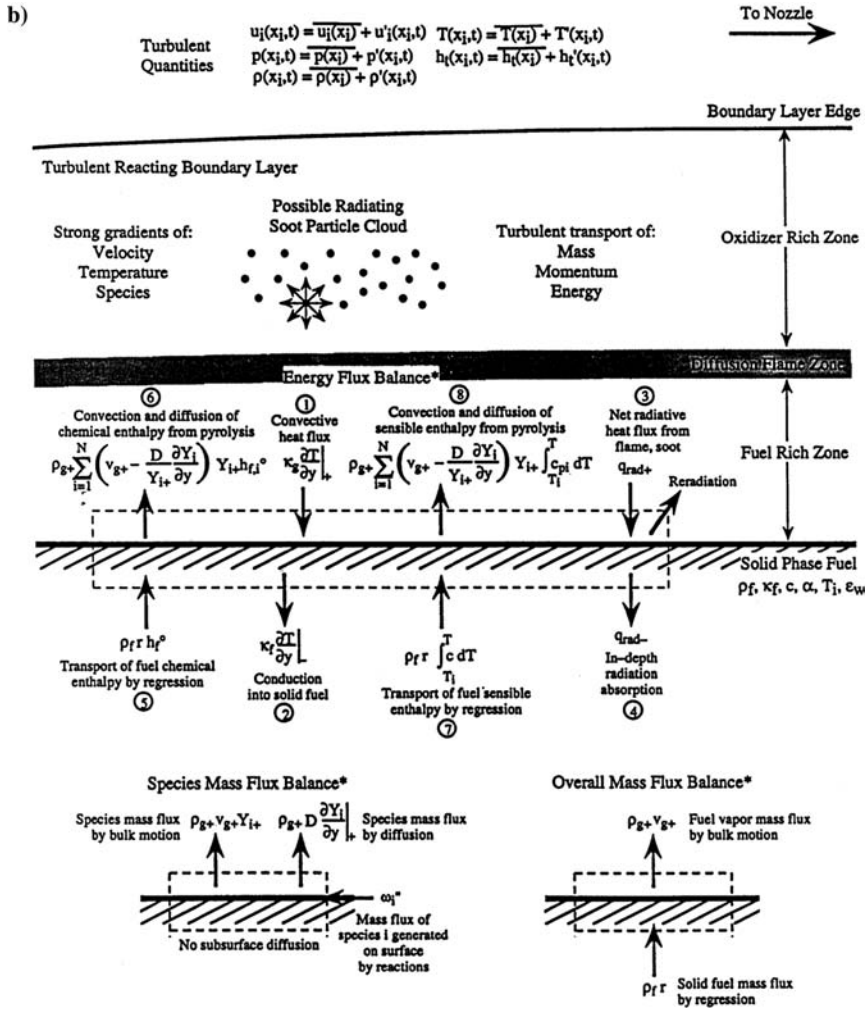

Fig. 6 Continued.

In addition to the preceding list, Fig. 6 also shows many important hybrid combustion processes. A chemically reacting shear layer develops over the solid-fuel surface due to the reaction between the injected oxidizer from the head-end region of the motor and the pyrolyzed fuel fragment species. The reacting shear flow has boundary-layer behavior especially in the region before the fully developed station. The boundary layer over most portions of the solid-fuel grain is turbulent. The turbulent boundary layer is characterized by strong velocity, temperature, and species gradients normal to the surface; mass, momentum, and energy transport are dominated by turbulent eddy motions and fluctuations. Near the fuel surface, many complicated physicochemical processes can occur sequentially and/or simultaneously. The major processes include 1) melt-layer formation by liquefaction, 2) polymer chain breaking and reorganization in the heated zone of the solid fuel, 3) heterogeneous reactions between the polymer fragments and oxidizers diffused across the gaseous diffusion flame, 4) desorption of polymer fragments and mass diffusion and advection of pyrolyzed fuel species in the transverse direction into the shear layer, 5) formation of surface ripples and bumps due to the interaction of the shear flow with pyrolyzing surface material, and 6) surface displacement due to mass loss and mechanical compression/decompression associated with chamber pressure variation. It is quite obvious that the surface regression rate is affected by these many intricate physicochemical processes. This could be one of the reasons why the hybrid-propulsion system has not been developed to its full maturation.

II. Major Challenges in Hybrid Rocket Propulsion

Many challenges still exist in the development of future high-performance hybrid rockets. These challenges can be divided into three areas, as follows: 1) continuation in the development of energetic fuels and oxidizers while acquiring more in-depth understanding of their ignition and combustion behavior, 2) improvements in the design and operation of highly reliable hybrid rocket motors with great operational flexibilities, and 3) attainment of strong and continuous support from rocket propulsion policy makers and program managers to recognize the importance and advantages of this type of propulsion system. Some of specific topics for performance enhancement and design considerations are discussed next. Suggestions to overcome the anticipated obstacles are also addressed with each item.

A. Development of Energetic Solid Fuels and Oxidizers and Enhancement of Solid-Fuel Regression Rates

First is selection of oxidizers that are nontoxic, high density, high energy, and self-pressurizing. The self-pressuring feature is highly beneficial because the pumping system can be eliminated or partially replaced. This can significantly reduce the parasitic weight of the propulsion unit. Depending on the mission application, noncryogenic oxidizer is easier to store and handle.

Second, to enhance the regression rate of HTPB type of solid fuels, ultrafine metal or metal hydride powders could be added. These special additives can not only increase the linear regression rate of the solid fuels but also increase the density impulse of the hybrid rocket. The enhancement of linear regression rate of several families of HTPB-based solid fuels has been demonstrated by Chiaverini et al. [8] and Risha et al. [9].

Third, paraffin types of solid fuels studied by Karabeyoglu [10] and Evans et al. [11] have demonstrated substantially higher linear regression rates than the HTPB solid fuel. The finding of suitable stiffener for the paraffin type of fuel is a very important task to use the fuel grain to support the structure of the hybrid motor. Suitable processing technique for uniformly dispersing energetic metal particles in the laboratory scale paraffin fuel grain has been developed by Evans et al. [11]. The technique has to be extended to the prototype-scale solid-fuel grains.

Fourth, synthesis and processing of new types of energetic solid-fuel grains should be developed to have desirable regression rates, mechanical and thermal properties for ignition and combustion in rocket motor operating environment, as well as for long-term storage.

Last, compatibility of the selected energetic fuel compounds with the oxidizer-rich fluid must be studied and their combustion performance must be optimized.

B. Measurement of Solid-Fuel Regression Rate as a Function of Operating Conditions

First for hybrid rockets, depending on the grain design, the average solid fuel regression rate could be quite different from the instantaneous regression rate. It is important to measure the instantaneous regression rate as a function of the motor operating conditions. Direct measurement of instantaneous regression rate can be performed using nonintrusive measurement techniques. For example, ultrasonic pulse–echo methods and real-time x-ray radiography techniques can be very helpful.

Second, characterization of regression behavior of a given solid fuel in subscale instrumented motors would be beneficial for determination of operating condition dependency. This procedure can also reduce the development costs for introducing a new fuel into the hybrid motor. The measured regression rate data can be used for model development and validation. Once validated, the model and computer code can be used for scale-up simulations.

Third, embedding ultrafine break wires at different depths of the solid fuel grain could also provide useful information on the regression pattern and the thermal wave behavior of the fuel grain. Subsurface temperature profile measurement near the surface of the pyrolyzing solid fuel could give very useful information about the heat flux into the unburned subsurface zone and the instantaneous surface temperature. The effect of in-depth radiation absorption can also be studied with this type of measurement.

Fourth, it is useful to consider the solid-fuel pyrolysis mechanism and associated chemical kinetics at various surface temperatures so that the solid-fuel regression rate can be linked directly with the surface temperature and the local oxidizer concentration. This would provide essential information for accurate numerical simulations using computation fluid dynamic codes. Conducting pyrolysis experiments with well-controlled surface temperatures could be very helpful. Flash pyrolysis of HTPB was conducted by Arisawa and Brill [12, 13] to determine the decomposition products of HTPB. Flash pyrolysis of uncured R-45M, the pre-polymer of HTPB, was performed under various heating rates, temperatures (ranging from 450 to 609°C), and pressures in an argon environment.

According to them, using R-45M rather than cured HTPB is justified because during rapid thermal decomposition, such as occurs in a hybrid rocket motor, the urethane bonds between the crosslinking agent (such as Isonate 143L), and the prepolymer cleave first. The HTPB acts like an uncured polymer when it decomposes. Chen and Brill's T-Jump/Fourier Transform Infrared (FTIR) spectroscopy was used to determine the gaseous pyrolysis products [14]. There were 13 gaseous products, representing about 70% of the mass of the original sample, identified in the study (Fig. 7). Of these 13 products, 95–98% of the measured masses were attributed to 6 major products: butadiene (BD), ethylene (ET), trans-butadiene oligomer (t-BDO), 4-vinyl 1-cyclohexene (4-VCH), 1,5-hexadiene (1,5-HD), and cyclopentane (CP). Chen and Brill [14] reached several important conclusions in their study. First, at $p \sim 2$ atm and $515 < T < 560$°C, the pyrolysis of polybutadiene compounds was dominated by bulk-phase reactions in the polymer, such as bond breaking and polymer chain reorganization. However, for lower pressures ($p < 2$ atm) and higher, temperatures ($560 < T < 609$°C), or for even higher pressures ($p = 11$ atm) at all temperatures ($T > 465$°C), the rate of gaseous product evolution was controlled by formation and desorption of higher molecular weight fragments from the fuel surface (Fig. 6). Chen and Brill [14] stated that the temperature at which transition between controlling mechanisms (from bulk-phase kinetics to desorption kinetics) occurs corresponds to the temperature where the bulk-phase pyrolysis reactions probably reach their maximum rate. This temperature is a function of pressure with higher pressures corresponding to lower transition temperatures. Therefore, for modeling the combustion processes of rockets containing HTPB, the kinetics of desorption from the surface should be used instead of the bulk-phase chemical decomposition kinetics.

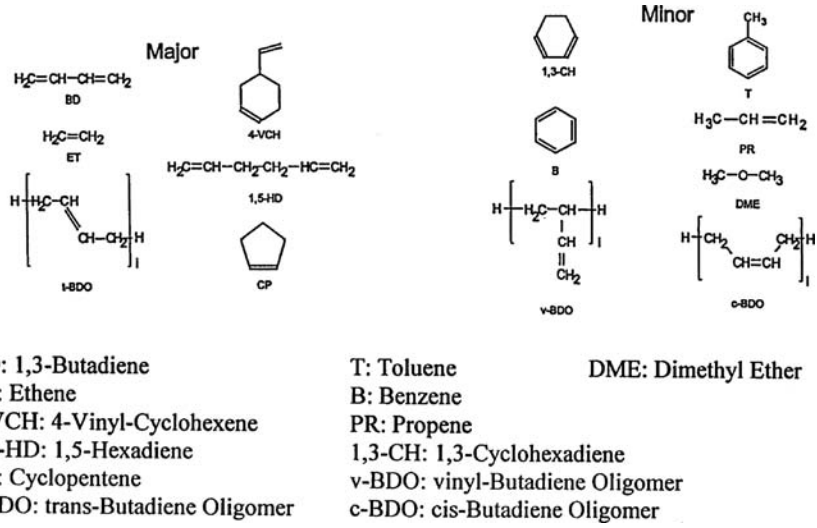

Fig. 7 Identification of 13 major gaseous products from decomposition of HTPB. (From Arisawa and Brill [12].)

Chiaverini et al. [15] performed pyrolysis study of various HTPB-based solid fuels under conductive heating using a hot metal cylinder under well-controlled surface temperatures. Many HTPB solid fuels showed abrupt change of activation energies at certain surface temperatures (Fig. 8). In agreement with the findings of Arisawa and Brill [12, 13] and Chen and Brill [14], the activation energy at higher surface temperatures is much lower due to the physical desorption of high molecular fragments. The relative molar concentrations of a HTPB-based fuel at 500–800°C were obtained by Chiaverini et al. [15] and are given in Table 3. It is quite obvious that the pyrolysis products are highly dependent on the surface temperature. This implies that the gas-phase diffusion flame of the solid fuel can depend strongly on the burning surface temperature of the solid fuel. The local solid-fuel regression rate is dominated by the local energy feedback from the adjacent diffusion flame, which is in turn depending on the gaseous oxidizer concentration and turbulence level in flame zone. This kind of complex interdependent condition is far more complicated than the solid-propellant combustion situation. For the latter, the burning rate is usually a function of the chamber pressure, and in some cases, the erosive burning condition can be also important. In the hybrid rocket motor, the regression rate of the solid fuel is always highly dependent on the local flowfield structure, heat-transfer rates, and the energy release processes. Thus, the functional form is far more complicated and should be characterized.

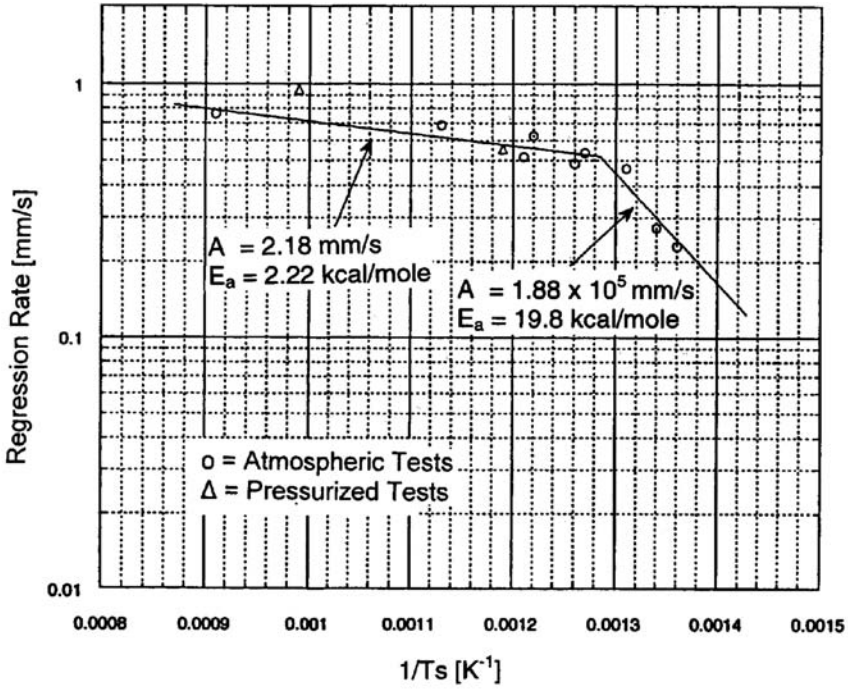

Fig. 8 Arrhenius plot of an HTPB-based solid fuel (SF5) with change of activation energy around $T_s = 780$ K. (From Chiaverini et al. [15].)

Table 3 Pyrolysis products of an HTPB-based solid fuel (SF5) and molar concentrations[a]

Species M_i	Relative molar concentrations of pyrolysis products at various temperatures, %			
	500°C	600°C	700°C	800°C
Ethene, C_2H_4	——	12.65	14.49	29.93
Propene, C_3H_6	——	4.56	7.38	11.94
1,3-Butadiene, C_4H_6	78.70	53.36	44.70	11.05
3-Pentene-1-Yne, C_5H_6	——	11.29	18.36	14.27
Cyclopentene, C_5H_8	——	3.92	——	——
Benzene, C_6H_6	——	4.89	10.41	13.63
Toluene, C_7H_8	——	——	4.66	5.22
4-Vinyl-Cyclohexene, C_8H_{12}	21.30	9.33	——	——
Styrene, C_8H_8	——	——	——	2.49
Indene, C_9H_8	——	——	——	6.04
Naphthalene, $C_{10}H_8$	——	——	——	5.43

[a]From Chiaverini et al. [15].

C. Correlation Development for Solid-Fuel Regression Rates

To predict the performance of a hybrid motor, the most influential parameter to be determined is the instantaneous regression rate of the solid fuel at any specific location of the motor. Various correlations have been developed for regression rate determination. Some of them are based on heat/mass-transfer-dominated concepts, and others emphasize the effect of chamber pressure on chemical kinetics and flame structure. More recently, polymer decomposition processes were studied under different heating rates, and they are believed to have significant influence on the solid-fuel regression rate. Correlations are, therefore, categorized into three groups, which are described in the following paragraphs.

1. Regression Rate Models Based on Heat and Mass Transfer Mechanism

Regression rate correlations based on heat and mass transfer from the flame to the fuel surface appear to be the most popular approach. Several historical studies are presented with comments on their limitations and drawbacks.

Bartel and Rannie's analysis. Perhaps the earliest analysis to consider most of the essential features of hybrid combustion was that of Bartel and Rannie as cited by Green [4]. Bartel and Rannie considered the one-dimensional axial flow of air through a tube of fuel. Turbulent air enters the tube of diameter D with a velocity U_0, density ρ_0, pressure p_0, and stagnation temperature T_0. Carbon was used for the solid fuel. They believed that the diffusion or transport of oxygen to the fuel surface was the controlling mechanism of the fuel regression process. They assumed that the mass addition due to fuel burning was negligible in comparison to the axial air mass flux along the tube. By examining the rate of heat added to

the gas flowing through an elemental cross section, they obtained the following expression:

$$m_f'' = (C_f G f_m/2)\exp(-2C_f x/D) \tag{1}$$

where m_f'' is the local mass burning rate of fuel per unit area ($=\rho_f \dot{r}$), C_f the friction coefficient on the fuel surface, G the average mass flux along the tube, f_m the fuel/air ratio of the reaction, x the distance along the tube from the entrance, and D the tube inner diameter. They also used the well-known pipe flow correlation of friction coefficient with Reynolds number: $C_f = 0.046\,Re_D^{-0.2}$. When this expression is substituted into Eq. (1), a $G^{0.8}$ dependency is obtained, because Reynolds number Re_D can be written as GD/μ. According to this expression, the fuel burning rate decreases exponentially with axial position along the tube, which is not adequate for the full length of the hybrid motor grain because the accumulative mass addition effect is quite significant in increasing the local mass flux in the downstream portion.

Emmons' analysis. Emmons as cited by Green [4] also obtained a solution for the boundary-layer combustion of a gaseous oxidizer flowing over a solid-fuel surface. He assumed a laminar flame zone of finite thickness in the boundary layer. He then transformed the energy, momentum, and species equations into the Blasius-type equations by assuming unity Prandtl, Lewis, and Schmidt numbers. His analysis yielded

$$m_f'' = \rho_e u_e Y(B)/Re_x^{1/2} \tag{2}$$

where $Y(B)$ is a function of the heat ratio defined as the ratio of the sum of chemical and thermal energy of unit mass of the oxidizer core flow to the sum of thermal energy required to bring a unit mass of solid fuel from its initial temperature to the surface temperature and to convert it from solid phase to the gas phase, that is,

$$B = [(Co_e - Co_s)\Delta H_r/n_o + c_p(T_e - T_s)]/[L + c_s(T_s - T_i)] \tag{3}$$

where Co is the oxidizer concentration, ΔH_r the heat of reaction per mass of fuel, n_o the O/F ratio, T the temperature, L the heat of phase change, c_p the specific heat of the gas, and c_s the specific heat of the solid; subscript e indicates the outer edge of the boundary layer and subscripts s and i represent the surface and initial conditions, respectively. For the range of $0.5 < B < 5$, Emmons found

$$m_f'' = \rho_e u_e[0.18 + \log_{10}(B + 0.7)]/Re_x^{1/2} \tag{4}$$

where $\rho_e u_e = G$. Notice from this expression that m_f'' is proportional to $G^{0.5}$ due to the assumed laminar nature of the flow. The boundary layer involved in practical hybrid systems is mostly turbulent due to the destabilizing influence of mass injection at the solid surface as well as the high Reynolds number of the oxidizer flow.

Peck and Houser's analysis. Peck and Houser [16] made a useful contribution with their measurement of the instantaneous regression rate of a cylindrical hybrid-fuel grain of several polymeric fuels burning with gaseous oxygen (GOX). They burned cylindrical solid fuels of varying total length having an initial inner diameter of 2.54 cm. Most tests were conducted with polymethylmethacrylate (PMMA plexiglas) as the solid fuel. The instantaneous regression rates were deduced at several axial positions at various flow rates, using an interrupted burning technique. Peck and Houser found that the instantaneous inner radius of the combustor port followed the sum of two power laws of time. However, their correlation has no physical significance to the interpretation of the phenomena of hybrids. They also made no attempt to account for the surface heatup time just following ignition. Peck and Houser showed experimentally that the local regression rate decreases with time due to an increase in port area (corresponding decrease in port mass flux) and increases with axial distance due to an increase in mass flux from fuel addition. Furthermore, they showed that the measured fuel surface temperatures by the embedded thermocouples were the same for both translucent fuel grains and opaque fuel grains processed with carbon black additive, implying a negligible amount of in-depth radiation absorption in the subsurface region.

Marxman, Gilbert, Wooldridge, and Muzzy's analysis. Probably the most influential heat-transfer correlation of hybrid combustion was developed by Marxman and Gilbert [17] and Marxman et al. [18]. According to their postulation, a flame sheet is established in the boundary layer, which separates the boundary layer into two zones: one zone is above the flame, where the temperature and velocity gradients are opposite in the transverse direction, and the other zone is below the diffusion flame, where these gradients are in the same direction. These trends are represented qualitatively in Fig. 6. The upper zone is oxidizer-rich whereas the lower zone is fuel-rich. The flame occurs at a position where the concentrations of reactants are sufficient for combustion to occur [17]. Because Marxman and Gilbert believed that heat transfer from the flame to the fuel surface was the controlling mechanism of hybrid combustion, they applied an energy flux balance from the gaseous flame zone to the fuel surface including the heated region of the solid fuel to obtain an expression for the fuel regression rate. Their energy balance led to the following equation:

$$\rho_f \dot{r} \Delta H = Q_w \tag{5}$$

where ρ_f is the solid-fuel density, $\dot{r}$ the regression rate, Q_w the heat flux to the wall including both convective and radiative fluxes, and ΔH the total energy required to heat the solid fuel from its initial temperature to the surface temperature and to decompose and vaporize a unit mass of fuel.

To derive a useful equation for the regression rate from Eq. (5), Marxman and Gilbert [17] made several important simplifications to the problem. First, they assumed that the boundary-layer flow was turbulent over most of its length due to the destabilizing effect of fuel injection at the surface. Second, they reasoned that Reynolds analogy and unity Lewis and Prandtl numbers ($Le = Pr = 1$) hold in both the upper and lower boundary-layer zones, but not necessarily in the flame sheet itself. Third, they assumed that the velocity profile in the boundary layer

is unaffected or only slightly affected by the presence of wall blowing and combustion, so that the standard friction coefficient for a turbulent boundary layer remains valid. By employing these assumptions, they obtained an equation for the regression rate given by

$$\dot{r} = CGRe_x^{-0.2}(St/St_0)(u_e/u_c)(h_f - h_w)/(\rho_f \Delta H) \tag{6}$$

where C is a function of the mainstream Mach number, St the Stanton number, St_0 the Stanton number in the absence of blowing, u_e the velocity at the edge of the boundary layer, u_c the velocity at the flame, h_f the stagnation enthalpy at the flame temperature, and h_w the enthalpy at the wall in the gas phase. The ratio of Stanton numbers, St/St_0, represents the fraction of heat transferred to the surface by convection when compared to the case with no blowing. This ratio may be lower than 0.2 [17]. The velocity ratio, u_e/u_c, is determined by the flame position in the boundary layer. When radiative heat transfer is also important, for the case of metalized fuels [18], an additional term may be added to the right side of Eq. (6):

$$\dot{r}_{\text{rad}} = \sigma \varepsilon_w(\varepsilon_g T_f^4 - \alpha_g T_w^4)/(\rho_f \Delta H) \tag{7}$$

where σ is the Stefan–Boltzmann constant, ε_w the emissivity of the wall, ε_g the emissivity of the gas at the flame temperature T_f, and α_g the absorptivity of the gas at the wall temperature T_w.

Marxman et al. [18] presented methods to obtain some of the factors comprising the right side of Eq. (6), which are not known a priori for a given hybrid system. Using the integral technique of boundary-layer theory, they show that the velocity ratio may be obtained from

$$u_c/u_e = [(O/F)(h_f - h_w)/\Delta H]/\{Y_{\text{OX}e} + [(O/F) + Y_{\text{OX}e}](h_f - h_w)/\Delta H\} \tag{8}$$

where O/F is the oxidizer-to-fuel mass ratio and $Y_{\text{OX}e}$ is the mass fraction of oxidizer in the free-stream core flow, which, for a hybrid motor using GOX as the oxidizer, would equal unity. Marxman et al. assumed that O/F ratio and the $(h_f - h_w)/\Delta H$ factor are independent of axial position and remain constant for a given oxidizer/fuel combination. The Stanton number ratio was found to be

$$St/St_0 = 1.2B^{-0.77} \tag{9}$$

for $5 \leq B \leq 100$, where B is the blowing parameter, defined by

$$B \equiv (\rho v)_w/[\rho_e u_e(C_f/2)] \approx (u_e/u_c)(h_f - h_w)/\Delta H \tag{10}$$

When the Prandtl number is equal to 1 and the radiation term in Eq. (7) is negligible, the B parameter can be approximated by the last expression given in Eq. (10). The mass transfer number B is a very important parameter in hybrid combustion. It represents both the similarity parameter for a boundary layer with injection and a thermodynamic parameter of the system. When $B =$ constant and $Le = 1$, the velocity, species concentration, and enthalpy profiles are similar everywhere in the turbulent boundary layer [18]. It is useful to note that the range of B, as defined in Eq. (10), for most hybrid systems is ranging from 5 to 20, and in this range,

the best exponent for Stanton number vs B correlation found by Netzer [19] and suggested by Altman [20] is -0.68, namely,

$$St/St_0 = B^{-0.68} \tag{11}$$

Although the difference between this exponent and -0.77 given in Eq. (9) seems to be small, according to Altman, it means that the effect of ΔH on solid fuel regression rate is about 40% stronger.

Marxman et al. [18] reduced their regression rate equation (6) to a simplified form by combining Eqs. (6), (9), and (10), thus, obtaining

$$\rho_f \dot{r} = \left[0.036\, GB^{0.23} Re_x^{-0.2}\right] \propto \left[B^{0.23} G^{0.8} x^{-0.2}\right] \tag{12}$$

for hybrid motor combustion with no radiative heat transfer. Again, specifying the oxidizer/fuel combination essentially fixes B. They explain that, because B is raised to a small power, even large changes in $(h_f - h_w)$ or ΔH produce only minor changes in the regression rate. The physical reasoning behind this observation is that, in the analysis of Marxman et al., the regression rate of the solid fuel is coupled tightly to the aerodynamics of the reacting boundary-layer flow. Increasing $(h_f - h_w)$, for example, would tend to increase the regression rate. However, the increase in fuel mass addition creates stronger blowing and blockage of the convective heat transfer to the surface. This effect tends to decrease the regression rate. Therefore, the fuel regression rate depends primarily on G, the total mass flux. Because G at any axial location x depends on both the oxidizer flow entering the combustion port as well as all fuel pyrolyzed upstream of this location, the local regression rate, thus, depends on the regression rate at all upstream locations. In addition, G decreases as the port area increases during burning. Therefore, one expects the regression rate to increase with axial position along the fuel grain, while decreasing with time.

For systems with nonnegligible radiative heat transfer effect to the fuel surface, such as in the case of a solid-fuel grain loaded with metal powder additives, one must find a blowing parameter due to radiative heat transfer, B_{rad}. For this parameter, Marxman et al. obtained

$$B_{\text{rad}}/B = 1 + (Q_{\text{rad}}/Q_{\text{conv}})(B_{\text{rad}}/B)^{0.77} \tag{13}$$

where

$$Q_{\text{conv}} = 0.036\, G\Delta H (Gx/\mu)^{-0.2} B^{0.23} \tag{14}$$

$$Q_{\text{rad}} = \sigma \varepsilon_w (\varepsilon_g T_f^4 - \alpha_g T_w^4) \tag{15}$$

whereas B remains as defined earlier. Estimating B_{rad}/B as $\exp(1.3 Q_{\text{rad}}/Q_{\text{conv}})$ (which is approximately true over a wide range of $Q_{\text{rad}}/Q_{\text{conv}}$), they obtained a modified version of Eq. (6),

$$\dot{r} = [Q_{\text{conv}} \exp(-Q_{\text{rad}}/Q_{\text{conv}}) + Q_{\text{rad}}]/(\rho_f \Delta H) \tag{16}$$

which accounts for the increase in regression rate due to radiative heat transfer. This equation reduces to Eq. (6) if $Q_{\text{rad}} = 0$. Note from Eq. (16) that an increase in radiative heat transfer results in a decrease in convective heat transfer due to the corresponding increase in mass blockage. If $Q_{\text{rad}} = Q_{\text{conv}}$, then r increases by about 35% over that for $Q_{\text{rad}} = 0$.

In a later paper, Muzzy [21] provided an excellent summary of some of the major implications of the heat-transfer-rate-dominated model developed by Marxman and Gilbert [17] and Marxman et al. [18]. He emphasized several important findings:

1) Based on the mass blockage effect, the regression rate depends only weakly on the enthalpy difference between the flame and the fuel surface; thus many different types of solid fuels have similar regression rates. For the same reason, the burning rates of hybrid-fuel grains are not sensitive to their initial temperatures.

2) The regression rate depends strongly on port geometry. A change in regression rate at an upstream position can influence those along the entire length of the fuel grain because local regression rate depends on those at all upstream positions. This implies that optimal hybrid motor design requires a thorough understanding of internal ballistic behavior.

3) Only strong radiation sources can significantly increase the regression rate. Weak radiative transfer to the surface, on the order of 50% of the convective heat transfer, results in a small (about 10%) net increase in regression rate [21].

2. *Other Analyses Including Gas-Phase Thermal Radiation*

Estey et al. [22] also considered the effects of thermal radiation on regression rate of solid fuels. They employ a radiative flux term of the form

$$Q_{\text{rad}} = \sigma T_g^4 (1 - \mathrm{e}^{-\kappa PD}) \tag{17}$$

which is similar to that suggested by Muzzy [21]. The parameter κ represents the gas-phase absorption coefficient. The term in parentheses in Eq. (17) is the emissivity of the gas phase, which increases as the product of pressure and diameter (or hydraulic diameter) increases due to the nature of the inverse exponential function. Marxman et al. [18] stated that for a plexiglass/oxygen system the gas-phase emissivity is about 0.02. Altman concluded that the addition of a radiative heat-transfer term for metal-particle-loaded fuels improves empirical correlations, whereas for pure hydrocarbon fuels the classical convective heat transfer equation worked best.

Strand et al. [23] also provided a treatment of radiative heat transfer. They considered radiation from both the gas and a soot particle cloud that forms shortly after ignition. For the gas-phase contribution, Strand et al. used Eq. (17), but also included an empirical expression for κ as a function of pressure,

$$\kappa = 9.33 \times 10^{-4} - 6.19 \times 10^{-6} P + 1.79 \times 10^{-8} P^2 \tag{18}$$

which was obtained from radiation measurements of a high-energy nonmetalized solid propellant, where P was measured in pounds per square inch gauge. The

thermal radiation emanating from the particle cloud was represented by

$$Q_{\text{rad,cloud}} = \sigma T_g^4 (1 - \mathrm{e}^{-a_p N p}) \tag{19}$$

where N_p is the particle number density and a_p a multiplier constant. The product $a_p N_p$ depends on the weight fraction of the radiating particles and appears to be difficult to evaluate [23]. In contrast to the previous researchers mentioned, Strand et al. concluded that particle radiation from powdery soot is a significant source of energy driving solid-fuel regression. Also, they stated that variations in gas radiation with pressure and O/F ratio should be accounted for in future works. Experimentally, they found that radiative heat flux accounted for about 30% of the total heat flux, which represents a much higher percentage than those found by other researchers. However, it should be noted that the Strand et al. motor operated at a relatively low pressure (up to 2.2 MPa) and low oxidizer mass flux (up to 105.7 $\mathrm{kg/m^2 \cdot s}$ or 0.15 $\mathrm{lb_m/in.^2 \cdot s}$).

In contrast to the Strand et al. findings, Salita [24] stated that neither gas-phase radiation nor radiation from soot particles should be important in hybrid combustion of both metalized and pure hydrocarbon fuels. According to Salita, soot particles may not appear in hybrids because of the highly oxidative core flow. In addition, the boundary layer along a large fraction of the fuel grain is relatively thin so that the radiation from the flame zone should have very low emissivity. Experimental verification of this postulation is required for the future model and/or fuel regression rate correlation development for the hybrid rocket motors.

3. *Pressure-Dependent Regression Rate Analyses*

The effect of pressure on regression rate has been studied by several researchers, including Stickler and Kumar [25] and Rastogi and Deepak [26], who attributed the pressure effect to oxidizer attack on the solid-fuel surface, and Kosdon and Williams [27], who used thickening of the gas-phase reaction zone based on finite-rate kinetics to explain pressure dependency. Miller [28] assumed that the pressure dependency was caused by second-order gas-phase reactions. One of the most influential pressure-dependent studies was conducted by Smoot and Price [29, 30] in the mid-1960s, and is discussed as follows.

Smoot and Price's analysis. Smoot and Price [29, 30] performed over 150 experiments with a laboratory-scale slab burner and developed a theory of hybrid regression rate by extending the work of Moutet and Barrere [31] to include the effects of condensed-phase species at the wall. Like previous researchers, Smoot and Price also found that the regression rate should theoretically depend on $G^{0.8}$.

Smoot and Price performed experiments using solid fuels of butyl rubber, polybutadiene-acrylic acid (PBAA) copolymer, and polyurethane (PU). They varied the oxidizer composition from 100% fluorine to 100% oxygen. As expected, Smoot and Price found that average regression rates were higher when a larger ratio of fluorine to oxygen was used as the oxidizer. They also discovered that at low total mass fluxes ($<$49.3 $\mathrm{kg/m^2 \cdot s}$ or 0.07 $\mathrm{lb_m/in.^2 \cdot s}$) the average regression rates of the butyl rubber solid-fuel slabs followed the $G^{0.8}$ law. However, at higher total mass fluxes, the regression rate became essentially independent

of mass flux, but strongly dependent on total operating pressure. This trend was observed for butyl rubber burning with 100% fluorine. At relatively low operating pressures (<1 MPa), the regression rates always fell below those predicted by the $G^{0.8}$ relationship. Increases in pressure cause the regression rate to be closer to the predicted values using the heat-transfer theory. At 7 MPa, the $G^{0.8}$ line was reached. It is useful to note that for practical hybrid rocket motors the operating pressure would most likely be above 3.5 MPa, much higher than those used by Smoot and Price in their experiments [29].

Smoot and Price defined three different regions of regression rate dependence. In the low mass flux region, the regression rate was controlled entirely by the rate of heat transfer and depends on $G^{0.8}$. For the medium mass flux region, the regression rate depended on both flow rate and pressure, with increasing pressure causing increasing regression rate at constant mass flux. In this region,

$$\dot{r} = (aG^{0.8}bp^n)/(aG^{0.8} + bp^n) \tag{20}$$

where p is the motor chamber pressure and a, b, and n are empirical constants. In the third region, the regression rate depends solely on operating pressure, such that $\dot{r} = ap^n$, like a solid-propellant burning rate expression. This region corresponds to high mass fluxes [29]. Note that there is a discrepancy between their results and the general trend described by Muzzy, shown in Fig. 9. This discrepancy was noticed and discussed by Smoot and Price.

Smoot and Price [32] also studied the regression rate behavior of solid fuel grains with lithium hydride (LiH) as an additive to butyl rubber. They varied the solid fuel composition from 100% butyl rubber to 90% LiH and the oxidizer composition from 100% fluorine to 100% oxygen. Smoot and Price found that in the relatively low total mass flux regime ($G < 28.2\,\mathrm{kg/m^2 \cdot s}$ or $0.04\,\mathrm{lbm/in.^2 \cdot s}$), the average regression rate increased significantly with LiH only if the amount of LiH in the grain was greater than about 50% [32]. This is the same region where they found 100% butyl rubber grains to regress according to the $G^{0.8}$ law, as discussed earlier. At higher mass flux levels, where the operating pressure influenced the regression rate, the solid-fuel regression rate displayed much more sensitivity to the LiH mass fraction. Smoot and Price postulated that the observed change in regression

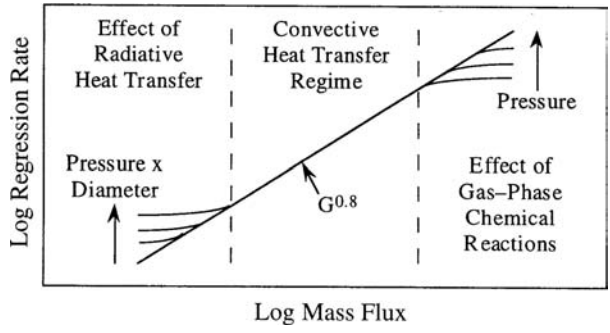

Fig. 9 Regimes of regression rate dependency on mass flux and pressure. (From Muzzy [21].)

rate due to LiH mass fraction sensitivity must be associated with the transition from one controlling mechanism to the other. They also found that increasing the percentage of LiH reduced the pressure dependence. One of the challenges we are facing in the advancement of future hybrid rocket motors is that we must study this kind of transition in controlling mechanism for specific fuel/oxidizer combinations adopted for their propulsion systems.

Smoot and Price suspected that either gas-phase oxidizer-fuel reactions or heterogeneous reactions between oxidizer and solid fuel at the fuel surface were responsible for the dependence of regression rate on pressure [30]. After performing a series of experiments varying the fluorine partial pressure independently, they found that the solid-fuel regression rates depended significantly on the partial pressure of fluorine, but not on the total pressure. They eventually concluded that oxidizer diffusion to the fuel surface and subsequent first-order heterogeneous reactions were responsible for the pressure dependence, and derived the following equation:

$$P_{o\infty}/(\rho_f \dot{r}) = \{33P_\infty (x/\mu)^{0.2} Sc^{2/3} * [\exp(B\lambda) - 1]/G^{0.8} B\lambda\} + 1/k \qquad (21)$$

where $P_{o\infty}$ is the partial oxidizer pressure in the freestream in pounds per square inch absolute, P_∞ the total freestream pressure, Sc the Schmidt number, λ the weight fraction of gaseous products from fuel decomposition, and k a kinetic rate constant. Note that even though Smoot and Price's work was exhaustive, their test conditions were outside the range of practical hybrid rocket applications; both flow rates and pressures were about one order of magnitude lower than those of actual motors.

Marxman, Wooldridge, and Muzzy's analysis. Marxman et al. [18] also studied the effect of pressure on regression rate. They showed that heterogeneous reactions at the solid-fuel surface could not by themselves account for the pressure sensitivity observed by Smoot and Price. Marxman et al. attributed regression rate pressure dependency to finite-rate gas-phase and heterogeneous reactions occurring in the turbulent boundary layer. To account for the pressure dependency, they derived the following equation:

$$\dot{r}/\dot{r}_\infty = (2t_m/t_r)^{0.5} \{1 - t_m/t_r[1 - \exp(-(t_r/t_m))]\}^{0.5} \qquad (22)$$

where $\dot{r}_\infty$ is the reference state regression rate calculated from the heat-transfer based analysis, using Eq. (12) or Eq. (16), t_r a characteristic reaction time, and t_m a characteristic mixing time. The value of t_m/t_r can be approximated by

$$t_r/t_m = C_1 G^{0.8} x^{-0.2}/P \qquad (23)$$

where C_1 is an empirical constant that depends on the particular fuel-oxidizer combination.

Muzzy's analysis. In his review article [21], Muzzy states that for nonradiative systems with large values of t_r/t_m, that is, low pressures and/or high G values, Eqs. (12), (22), and (23) can be combined to give

$$\dot{r} = C_2 P^{0.5} G^{0.4} x^{-0.1} \qquad (24)$$

in the region where chemical kinetics are an important factor in determining regression rate. Notice from Eq. (24) that when kinetics are important, the regression rate has a weaker dependency on total mass flux G than that predicted by the heat-transfer-rate-dominated model, where r is proportional to $G^{0.8}$.

Figure 9 summarizes the important results discussed in the preceding sections. At medium mass fluxes, the regression rate is dominated by the convective heat-transfer rate and theoretically follows Eq. (6) or Eq. (12). In this regime, neither radiation nor kinetics influences the regression rate. At very high mass fluxes and low-pressure conditions, the dependency of the gas-phase reaction rates on pressure can have a significant effect on regression rate. When the motor pressure is lower than a threshold value, the regression rates will be lower than those predicted by convective heat-transfer analysis because the gas-phase reaction rates become relatively slow compared to the heat-transfer rate. As pressure increases, the regression rate increases to approach the convectively predicted value.

Pressure has the opposite effect on the other end of the mass flux spectrum. At low mass fluxes, the effect of gas-phase radiation becomes important. Because of the complicated interactions between mass blowing from the fuel surface and convective plus radiative heat transfer to the fuel surface, only a strong radiation source can significantly influence the regression rate at low mass fluxes. In the low mass flux regime, the effect of radiation becomes apparent because the heat flux due to convection is reduced in relative magnitude. As the product of pressure and motor inner diameter, pD, increases, the effect of radiation becomes more prominent at a given mass flux. The pD term gives a measure of the gas optical density as described by Hottel [33] and Incropera and DeWitt [34]. When product of pD is high, the gas emits thermal radiation more efficiently and the regression rate increases to higher values than predicted by simple convective model.

In spite of the fact that the basic dependency of t_r/t_m on G and P is known from previous studies, accurate determination of the characteristic reaction time t_r and the characteristic mixing time t_m is difficult to achieve. We must have suitable kinetic mechanism with accurate rates for evaluating the characteristic reaction time. We also should have detailed flowfield structure to calculate the characteristic mixing time. These are challenges for further development in the hybrid rocket motor analysis.

4. Comprehensive Instantaneous Regression-Rate Correlation Development

Chiaverini et al. [35] correlation. A high-pressure, windowed, slab-geometry hybrid motor was designed and used by Chiaverini et al. [35] for conducting an experimental investigation on the combustion and pyrolysis behavior of HTPB-based solid fuels burning with GOX. Their laboratory-scale motor had operating conditions similar to those of subscale and full-scale motors with respect to GOX mass flux and pressure. A real-time x-ray radiography/image processing system and an ultrasonic pulse–echo measurement system were both used to obtain instantaneous solid-fuel regression rates at various axial locations. Fuel temperature measurements were made using an array of 25-μm fine-wire embedded thermocouples. The regression rates were found to be dependent on entrance and injector effects in the upstream region. The local regression rates displayed a dependence on axial location in the downstream region. In addition, a location of minimum

regression rate was found to exist on the fuel slab and to move downstream with time. Radiative heat transfer was found to influence the regression rate at lower mass flux levels. Chiaverini et al. [35] found that the relationship between regression rate and mass flux shows the existence of at least two regimes: One follows the convectively controlled regression rate behavior, and the other is influenced by radiation at low mass flux levels. The description of their correlation is given in Chapter 2 of this volume and, thus, not repeated here. For a 2D slab motor, the convective and radiative heat flux terms, Q_{conv} and Q_{rad}, can be expressed in the following forms:

$$Q_{\text{conv}} = aG^n x^{n-1} B^{0.23} \Delta H \tag{25}$$

$$Q_{\text{rad}} = \sigma T_{\text{fl}}^4 (1 - \mathrm{e}^{-kPh}) \tag{26}$$

In Eq. (25), n should theoretically be equal to 0.5 for laminar flow and 0.8 for turbulent flow. In Eq. (26), h represents the instantaneous channel height between the fuel slab surfaces, a parameter similar to the hydraulic diameter. When Eqs. (25) and (26) were substituted into Eq. (16), the following regression rate expression was obtained:

$$\dot{r} = c_1 G_o^n x^m \left(\frac{c_2[1 - \exp(-\kappa Ph)]}{G_o^n x^{n-1}} + \exp\left\{ \frac{-c_2[1 - \exp(-\kappa Ph)]}{G_o^n x^{n-1}} \right\} \right) \tag{27}$$

where $c_1 = aB^{0.23}/\rho_f$ and $c_2 = \sigma {T_{\text{fl}}}^4/(aB^{0.23}\Delta H)$. In Eq. (27), the mass flux at the motor inlet, G_o, is used in the correlation development. Additionally, the x^m term is allowed to differ from its theoretical expression of x^{n-1} to account for axial dependency not predicted by convective heat-transfer theory. After the substituting of $Re_x = G_o x/\mu$ into Eq. (27) and rearranging, a dimensionless form was obtained,

$$\frac{\rho_f \dot{r}}{G_o} = a_1 Re_x^{n-1} \left(\frac{x}{L}\right)^{m-n+1} \times \left\{ \frac{a_2[1 - \exp(-\kappa Ph)]}{G_o Re_x^{n-1}} + \exp\left[\frac{-a_2[1 - \exp(-\kappa Ph)]}{G_o Re_x^{n-1}} \right] \right\} \tag{28}$$

The parameters c_1, c_2, m, n, and k in the correlation were determined through a least-squares analysis. The values of these parameters for both the laminar and turbulent portions of data are tabulated in Table 4. It is quite evident that the correlation well represents the data because almost all of the data lie within $a \pm 5\%$

Table 4 Correlation parameters for Eq. (27)

	Parameter				
Data	c_1	c_2	n	m	k
Laminar	0.1165	6.632	0.50	0.313	17.13
Turbulent	0.0158	84.389	0.90	0.344	17.13

error band. The n value for the laminar portion is 0.5, and for the turbulent portion it is 0.9, which is slightly higher than the theoretical value of 0.8. The use of G_o instead of the local flux G in the correlation could account for this difference. G_o is more convenient than G because it is the controlled oxidizer mass flux, whereas G has to be integrated at every spatial location.

Chiaverini et al. [35] also found that the addition of ultra-fine aluminum powders (Alex® powder, manufactured in Russia by exploding thin aluminum wires in an argon environment) can significantly increase both regression rates and mass burning rates, $\rho_f \dot{r}$, in comparison to cured pure HTPB. The Alex powder used by them had a mean particle size around 180 nm. Figure 5 of Chapter 10 by Risha et al. [9] in this volume shows the increase in regression and mass burning rates with weight percent of Alex powder. With an Alex weight fraction of 20%, the regression rate increased by about 40%, whereas the mass burning rate increased by almost 70% over that of pure HTPB. This increase is significant because low regression rates are sometimes cited as a drawback of hybrid rocket motors. Based on observations of the different surface structures of recovered slabs of pure HTPB and HTPB with added Alex, the primary mechanism of regression enhancement is believed to be associated with aluminum particle reaction-induced heat release near the solid-fuel surface [36]. However, the addition of Alex particles may also increase the effective radiative heat flux to the fuel surface. Through fine-wire thermocouple measurements, pyrolyzing fuel surface temperatures for pure HTPB were found to be between 930 and 1190 K, depending on operating conditions. The activation energy of the HTPB fuel was determined to be around 11.5 kcal/mol. This agreement with Arisawa and Brill's data [12] suggests that there is a strong linkage between the heat- and mass-transfer-dominated mechanism and the polymer decomposition mechanism; the overall pyrolysis rate of a solid fuel should also be governed by formation and desorption of high molecular weight fragments from the fuel surface as a result of thermal heating.

Evans et al. [11] correlation. Following the work of Chiaverini et al. [35, 36], a cylindrical x-ray translucent casing (XTC) hybrid rocket motor was designed and tested for obtaining the instantaneous regression rate data of several different solid fuels by Evans et al. [11]. The deduced instantaneous burning behavior of pure HTPB fuel formulations exhibited very close agreement with the correlation analysis developed by Chiaverini et al. [35] for their 2D slab motor, except that the leading coefficient in the correlation was considered as a function of oxidizer mass flow rate in the cylindrical motor. It was found that the instantaneous values of O/F ratio has a profound effect on radiative-to-convective heat flux ratio and modified blowing parameter, which is more suitable to be used in the evaluation of the Stanton number ratio, St/St_0, required for the regression rate correlation. All visual data of the instantaneous solid-fuel web thicknesses were analyzed at the aft end of the solid-fuel grain and correlated as a power-law function of time according to

$$r(t) - r_0 = a(t - t_{\text{ign}})^n \qquad \text{or} \qquad \dot{r}(t) = a \cdot n(t - t_{\text{ign}})^{n-1} \tag{29}$$

A data analysis, based on Chiaverini et al. was first utilized for correlating the measured instantaneous regression rates with the flow conditions. Tests conducted

with HTPB-based solid fuels (with and without 13 wt% Silberline® aluminum particles) were analyzed using this method. The proposed dimensionless form of the fuel regression rate by Chiaverini et al. takes the following form:

$$\rho_f \dot{r}/G_{\text{tot}} = 0.0155\, Re_D^{-0.2}\,(St/St_0)\, B\theta^{0.6} \left\{1.3\left(q''_{\text{rad}}/q''_{\text{conv}}\right)^{0.75} + \exp\left[-1.3\left(q''_{\text{rad}}/q''_{\text{conv}}\right)^{0.75}\right]\right\} \tag{30}$$

where G_{tot} is the total mass flux, St is the Stanton number with surface blowing, the subscript 0 corresponds to the case of no surface blowing, θ is defined as ratio of the average flame temperature $T_{f,\text{av}}$ to the surface temperature T_s, q''_{rad} is the radiative heat flux to the surface, and q''_{conv} is the convective heat flux to the surface. To determine the burning surface temperature, the pyrolysis law in the Arrhenius form suggested by Chiaverini et al. [15] for HTPB fuel was utilized,

$$T_S = -\left[E_a/R_u \ln\left(\dot{r}/A\right)\right] \tag{31}$$

where the suggested activation energy $E_a = 4.91$ kcal/mol and the preexponential factor $A = 11.04$ mm/s were adopted in the data reduction analysis.

An energy flux balance at the surface of the solid fuel was analyzed to determine the total heat flux to the surface of the solid fuel,

$$q''_{\text{total}} = q''_{\text{rad}} + q''_{\text{conv}} = \rho_f \dot{r}\left(\sum_i Y_i \Delta H^o_{f,i} - \Delta H^o_{f,\text{HTPB}}\right) + \rho_f \dot{r}\left(\sum_i Y_i \int_{T_{\text{ref}}}^{T_s} c_{p,i}\, \mathrm{d}T\right) \tag{32}$$

Note that the mole fractions of the chemical species from the HTPB fuel were analyzed by Chiaverini et al. [15] as a function of surface temperature in their conductive pyrolysis study. The mass fractions in Eq. (32) were deduced from their measured mole fraction values. The summation symbols in Eq. (32) were performed over all of the species present in the pyrolysis product mixture leaving the fuel surface. The c_p values of the product species as functions of temperature and enthalpy of formation data were obtained elsewhere [37–40].

The radiative component of the heat flux for pure HTPB fuel was determined from the soot particles present in the reaction zone. Based on the data of Strand et al. [23], soot accounts for approximately 80% of the total radiant heat flux in the system. The following correlation was used to express the soot radiation flux:

$$q''_{\text{rad,soot}} = \sigma T_g^4 \left(1 - \mathrm{e}^{-\kappa_s}\right) \tag{33}$$

The gas-phase radiation was considered to be negligible in comparison with the soot radiation in the study of Chiaverini et al. [41]; therefore, it was neglected in the analysis of Evans et al. [11]. In the measurements of Strand et al. [23], the flame temperature was found to be slightly lower than the adiabatic flame temperature of ~3400 K. Because of this, a gas temperature T_g of 95% of the adiabatic flame temperature was used for radiation calculation. The exponent κ_s in

Eq. (33) was assumed to not vary significantly with chamber pressure but depend strongly on the O/F ratio in the following form [41]:

$$\kappa_s = 0.51 - 0.113 \times O/F \tag{34}$$

The convective heat flux in Eq. (32) can be determined from the difference of the total and radiative heat fluxes. The ratio of the radiative to convective heat flux can also be determined.

The blowing parameter B in Eq. (30) is defined in Eq. (10). This blowing parameter physically represents the ratio of the vertically injected mass flux to the horizontal mass flux based on values at the edge of the boundary layer. In Eq. (10), the subscript e represents properties evaluated at the edge of the boundary layer and the skin friction coefficient C_f corresponds to the condition with mass addition from the wall. The ratio of the skin-friction coefficient with blowing to that without blowing, as suggested by Marxman [42] was determined by

$$C_f/C_{f0} = \ln(1+B)/B \tag{35}$$

Substituting of Eq. (35) into Eq. (10) and solving for B yields

$$B = \exp\{\rho_f \dot{r}/[\rho_e u_e (C_{f0}/2)]\} - 1 \tag{36}$$

When ρ_e is assumed the bulk density of the products and u_e is assumed the maximum velocity in the cylindrical port, the product $\rho_e u_e$ can be rewritten as

$$\rho_e u_e = G_{\text{tot}}/0.849 \tag{37}$$

based on turbulent velocity profile in pipe flow. When the well-known Reynolds–Colburn analogy is used for nonunity Prandtl numbers and the definition of Stanton number for turbulent pipe flow, the nonblowing skin friction coefficient is related to the Reynolds number according to

$$C_{f0}/2 = 0.023\, Re_D^{-0.2} \tag{38}$$

Equation (36) can now be evaluated to determine the blowing parameter B. The effect of radiation can be significant on the blowing parameter as suggested by Marxman [42]. The modified blowing number as presented by Chiaverini et al. [41] takes the form

$$B_{\text{mod}} = B \cdot \exp(q''_{\text{rad}}/q''_{\text{conv}}) \tag{39}$$

The relationship between the blowing parameter B and the Stanton number ratio given by Marxman and Gilbert [17] then becomes

$$\left(\frac{St}{St_0}\right)_{\text{mod}} = \left[\frac{\ln(1+B_{\text{mod}})}{B_{\text{mod}}}\right]^{\frac{4}{5}} \times \left\{\left(1 + \frac{13B_{\text{mod}}}{10} + \frac{4B_{\text{mod}}^2}{11}\right) \Bigg/ \left[(1+B_{\text{mod}})\left(1+\frac{B_{\text{mod}}}{2}\right)^2\right]\right\}^{\frac{1}{5}} \tag{40}$$

which is valid for blowing numbers from 1 to 200, covering a broad range of test conditions. For comparison purposes, Stanton number ratios were evaluated using both the modified and the unmodified blowing parameters. It was found by Evans et al. [11] that the regression rate calculated by using the modified relationship for St/St_0 is much closer to the measured results (within $\pm 4.5\%$ agreement). The modified correlation by Evans et al. is given by Eq. (41), in which θ is the temperature ratio of T_f/T_s. According to Venkateswaran and Merkle's numerical simulation for a hybrid rocket system [43] used by Chiaverini et al. [41], a variation in the bulk temperature from 91 to 97% of the adiabatic flame temperature occurred across the reaction zone of the solid fuel. Based on their results, an average flame temperature of 94% of the adiabatic flame temperature was selected in the evaluation of θ,

$$\rho_f \dot{r}/G_{\text{tot}} = 0.023\alpha Pr^{-2/3} Re_D^{-0.2} \left(St/St_0\right)_{\text{mod}} B_{\text{mod}}\, \theta^{0.6} \times \left\{1.3\left(q''_{\text{rad}}/q''_{\text{conv}}\right)^{0.75} + \exp\left[-1.3\left(q''_{\text{rad}}/q''_{\text{conv}}\right)^{0.75}\right]\right\} \tag{41}$$

The leading coefficient (0.0155) of Eq. (30) proposed by Chiaverini et al. [41] is the combination of a constant (0.02952) calculated from the coefficient (0.023) in the skin-friction relationship for in turbulent pipe flow, Reynolds analogy, and the assumption of Prandtl number equal to 0.7, as well as a least-squares curve-fit coefficient α (determined to be 0.524). Based on the least-squares fit of the instantaneous regression rate data, Evans et al. [11] found that the new α values ranged from 0.470 to 0.625. The α values for nonmetalized HTPB solid fuels were correlated with their oxygen mass flow rate and a linear dependence was determined as

$$\alpha = 0.6351\dot{m}_{\text{ox}} + 0.4144 \tag{42}$$

where $\dot{m}_{\text{ox}}$ is given in kilograms per second. Essentially, the previous coefficient of 0.0155 has been replaced by $0.023\alpha Pr^{-2/3}$. For metalized HTPB solid fuels, the α value was found to be independent of $\dot{m}_{\text{ox}}$ and is equal to a constant $= 0.524$. The replacement of 0.0155 by $0.023\alpha Pr^{-2/3}$ is still valid, and Eq. (41) is suitable for both the metalized and nonmetalized HTPB-based solid fuels. Therefore, Eq. (41) represents the latest fuel regression rate correlation for HTPB-based solid fuels. Similar correlations must also be developed for different types of solid fuels before they are extensively used in future hybrid rocket propulsion systems. This kind of correlations is much more complex than $r_b = aP^n$ type of expression for solid-propellant burning rate. This is because the combustion processes of solid fuels in the convective stream of oxidizers are highly complicated and can be influenced by many parameters given in the Eq. (41).

From the microthermocouple measurements by Evans et al. [11], the surface temperature of the metalized HTPB fuel was found to be very close to the melting temperature of Al due to the accumulation of particles on the regressing fuel surface. This accumulation also caused the fuel regression rate to be decreased for the conditions with larger port area. Analysis of the visual data obtained from the real-time x-ray radiography system during XTC hybrid rocket motor firings was conducted for the three different solid fuels, including the baseline nonmetallized

HTPB fuel, the metallized HTPB-based solid fuels, and the metallized paraffin-based solid fuels. The time variation of the instantaneous regression rate of the paraffin fuel was found to depend strongly on the oxidizer flow conditions and the initial grain geometry. Characterization of the surface temperatures of different solid fuels will also be necessary to advance future hybrid rocket systems.

D. Suppression of Combustion Instabilities

The following list of considerations should be given to suppress any combustion instabilities in future hybrid rocket motors.

1) Decoupling the acoustic communication between the oxidizer feed-line system and the combustion chamber is necessary to eliminate one source of instability.
2) Develop methods for suppressing instabilities in the low-frequency, non-acoustical ranges for transverse, longitudinal, and tangential pressure waves.
3) Lining of the precombustion chamber with a solid-fuel layer, as well as providing compartments in the fore end of the hybrid motor could eliminate and reduce the transverse mode(s) of oscillations.
4) Injector design for the oxidizer spray should be compatible with the detailed grain configuration in the precombustion chamber and the major portion of the solid-fuel grain.
5) Providing flame-holding solid-fuel surfaces near the precombustion chamber is also critical to eliminate the oscillation of the pyrolysis front in the upstream portion of the solid-fuel grain.
6) Grain geometry design has to incorporate the experience and knowledge gained in combustion instability studies.
7) Modeling and numerical simulation should include the simulation of possible combustion instabilities caused by either acoustic or nonacoustic types of oscillations.

E. Improvement of Combustion Efficiency and Fuel/Oxidizer Utilization

The following list of considerations should be given to increase the combustion efficiency and improving higher percentage of fuel/oxidizer utilization in future hybrid rocket motors.

1) In case liquid oxidizer is used, the injection patterns of the liquid oxidizer should be well designed and controlled to be highly compatible with the geometric structure of the fuel grain.
2) Concepts to increase volumetric loading of solid fuel should be applied to future fuel-grain designs.
3) Ignition systems should be suitably designed for liquid oxidizers to react efficiently with solid fuel; their impact on performance should be considered in the propulsion system design.
4) Technical problems with multiport design associated with large motors (such as solid-fuel grain integrity, web support systems, centerport burning, acceleration

effects on thin webs toward the later stage of burn, etc.) should be addressed in the motor design.

5) If needed, injection of a portion of vaporized oxidizer into the aft-end post-combustion chamber could be helpful in the combustion of certain unburned fuel species as well as for throttling purposes. One has to deal with the impact of O/F shift problem as well as accounting for the delivered performance.

6) It is useful to optimize mixing chamber geometry and the contour of the submerged nozzle, so that the flow residence time is adequate to ensure high combustion efficiency.

7) Additives for enhancing gas-phase reaction kinetics should be helpful for certain fuel/oxidizer combinations.

8) Grain geometry optimization should be considered in the design process to decrease the sliver mass fraction to a minimum.

9) Pressuring system should be designed for controlling the flow rate from the oxidizer tank, for example, N_2O can self-pressurize the oxidizer tank (U.S. Patent 5,722,232), which is an attractive feature for simplifying the design of the oxidizer supply system.

10) As suggested by Story and Arves [44], burn through of the forward insulation materials should be avoided. Use of burn through sensors can help to turn the motor off under emergency conditions. Insulation material development and advancement could also help solving the burn through problem.

F. Scaling Law Development Considerations

This is a very important area because various experimental evidence has shown the difference in the regression rates of the same solid-fuel burned in different-sized hybrid motors, for example, results shown by Evans et al. [11] and Risha et al. [10]. Although scaling law development for hybrid rockets may be more challenging than that for solid- and liquid-propellant rockets, it is highly beneficial to consider it for reducing the cost of development by studying the smaller scale system and then expand the design to a larger system. In the scaling law consideration, the motors of different sizes must have geometric similarity; also the same oxidizer/fuel combination must be used for comparing the combustion phenomena in the motor or for simulation of certain localized phenomena. The dynamic similarity is extremely important by keeping the Reynolds number the same for both the laboratory scale and the prototype scale. The scaling effects were considered by Gany [45, 46] as well as by Venkateswaran and Merkle [43] for hybrid rockets. Useful information on scaling laws is also available by Altman [20] and Estey et al. [22]. However, significant progress in this area is still needed. The following list of considerations should be given in the development of appropriate scaling laws for future hybrid rocket motors. Detailed discussions of the scaling law are given by Gany [45] in Chapter 12 in this volume. Therefore, the discussion covered here is limited.

1) It would be useful to follow the guidelines developed by Spalding [47] and Rosner [48] for general similarity analysis in chemically reacting flow systems.

2) The most logical way to conduct scaling-law development for the hybrid system should be based on parametric study of comprehensive numerical codes that are capable of simulating combustion processes in several different-sized motors.

To the present, such models and codes do not exist and should be developed in the future. This point is discussed further in Sec. II.G.

3) Many different timescales and length scales should be considered in the scaling-law development. The timescales include mixing time for fuel and oxidizer species, chemical reaction times associated with gas-phase reactions and surface heterogeneous reactions, ignition delay time, thermal-wave propagation time in the solid fuel after the ignition event, flow residence time, and pressure wave propagation times. The characteristic lengths involve shear flow momentum and thermal boundary-layer thicknesses, port size, length of the fuel grain, nozzle throat size, mixing length, average turbulent eddy size, etc.

4) Scaling effects should be studied, not only for predicting solid-fuel regression rates, but also for simulation of combustion instability behavior corresponding to different-sized motors.

G. Minimization of Nozzle Erosion

1) The nozzle erosion characteristics for hybrids are generally different from those of solids because the chemical composition of product gases flowing through the nozzle depends on the throttling process. The time-dependent nature of the combustion product is partly caused by the changing of the F/O ratio when the port area of the solid-fuel grain is enlarging as the burning time is advanced. Specially formulated high-temperature ablative materials should be developed to resist erosion under oxidizer-rich environments, in case the motor is designed to operate under such conditions.

2) It would be advantageous to utilize a portion of liquid oxidizer as a coolant to the nozzle so that the degree of erosion can be reduced.

3) Nozzle erosion under high oxidizer flow rates must be addressed in the design consideration, as well as mitigation of nozzle throat erosion rate.

H. Development of Comprehensive Models and Numerical Codes

There have been three major research activities in the computational fluid dynamics (CFD) simulation of hybrid motor combustion processes, conducted by Sankaran [49] Venkateswaran and Merkle [43, 50], Farmer et al. [51], and Liang et al. [52]. Venkateswaran and Merkle's work was performed in close coordination with the companion experimental program conducted by Chiaverini et al. [15, 35, 53] with detailed descriptions given in a report to NASA by Kuo et al. [54] and Merkle and Venkateswaran [55]. The computational modeling was tailored to the 2D slab-motor configuration used by the experimental team. The model for the gas phase comprised a standard Navier–Stokes solver coupled to chemical species and turbulence transport equations. The chemical kinetics model includes five chemical species, namely, C_4H_6 (which was considered to be the pyrolysis product of the HTPB fuel), O_2, CO, CO_2 and H_2O. Following Westbrook and Dryer's suggestion [56], the combustion of gaseous hydrocarbon fuels with oxygen was a simplified two-step reaction mechanism, that is,

$$C_4H_6 + 3\tfrac{1}{2}O_2 \longrightarrow 4CO + 3H_2O \qquad \text{(R1)}$$

$$CO + \tfrac{1}{2}O_2 \longrightarrow CO_2 \qquad \text{(R2)}$$

For the solid-phase pyrolysis, the Arrhenius equation developed by Chiaverini et al. [57] was employed. The standard k–ε model [58] with additional low Reynolds number terms for near wall effects [59] was employed for modeling the turbulence. Radiation heat transfer was represented by a simplified emission model [60]. The gas phase was treated as a purely emitting medium. The following approximation, which is appropriate in the limit of optically thin media, was used in the computation:

$$Q_{\text{rad,thin}} = \sum_{i,j} \left[4\sigma k_{ij} T_{ij}^4 / J_{ij} \right] F_{ij\to k} \tag{43}$$

where $1/J_{ij}$ is the volume of the (i,j)th cell and $F_{ij\to k}$ is the view factor of the cell with respect to the k grid location on the fuel-slab surface. Summing up the contributions from all the cells in the computational domain yielded the total radiative flux incident on a given axial location along the fuel surface, which was employed in the interfacial energy balance. Detailed energy and species mass flux balances were conducted at the solid–gas interface to determine the burning rate and surface temperature. The coupled set of governing equations was solved using an implicit time-marching method [61, 62].

Detailed comparisons were made between the computational predictions and experimental data (Fig. 10). This shows the comparison of the predicted and measured regression rates for three separate test runs [53]. The time-averaged GOX mass flux for tests 8, 11, and 9 were 105, 165, and 210 $\text{kg/m}^2\cdot\text{s}$, respectively. The experimental results represent time-averaged regression rate data over the whole test, whereas the computations show the results midway through the burn, which should represent an approximate average regression rate. Fairly good agreement

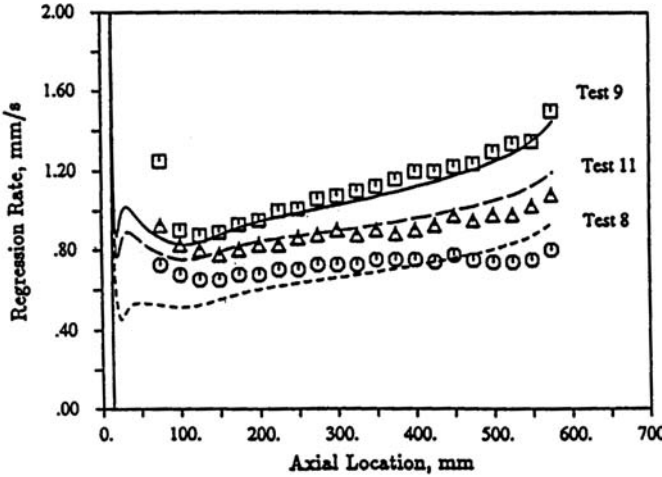

Fig. 10 Comparisons of computed regression rates midway through burn with measured average regression rates for tests 8, 11, and 9 [53] at $G = 100$, 165, and 210 $\text{km/m}^2\cdot\text{s}$, respectively. (From Vankateswaran and Merkle [43].)

can be observed over a major portion of the fuel slab. More important, the relative change in the regression rate as a function of the oxidizer flow rate is quite well predicted. Furthermore, both the experiments and the calculations show a faster regression rate near the aft end. The greatest discrepancy is near the leading edge of the fuel slab, where transition from laminar to turbulent flow may impact the comparisons. The energy budgets at the fuel surface revealed that convection was the dominant mode of heat transfer, whereas radiation accounted for about 10–25% of the total heat flux. The predicted fuel surface temperatures and pressure–time traces are in good agreement with the measured data.

A set of predicted temperature and velocity contours corresponding to three times (near the start of burn, midway in burn, and end of burn) during a test with a GOX mass flux at 165 $kg/m^2 \cdot s$ is shown in Fig. 11. In Fig. 11, the grid size in the y coordinate is exaggerated by a factor of 10 for clarity. The temperature contours in Fig. 11a show a peak temperature of 3500 K, which is roughly representative of the flame location. The flame is seen to start very near the surface near the leading edge of the fuel slab, where the oxidizer and pyrolyzed fuel first come into contact. Farther downstream, the flame moves outward as the oxidizer is consumed. The velocity contours in Fig. 11b show that the gases accelerate rapidly because of the expansion of the hot products associated with exothermic heat release by combustion and mass addition by fuel pyrolysis. Note that the boundary-layer thickness grows very quickly near the upstream end because of the displacement effect introduced by the flame as well as mass addition effect. Figure 11b also reveals that the acceleration effects become weaker as combustion progresses. Decay of flow velocity with respect to time is largely associated with the widening flow channel height. The reduction of flow velocity near the end of the burn also causes the convective heat flux to drop, thereby producing lower surface regression rate during the late stage of the test.

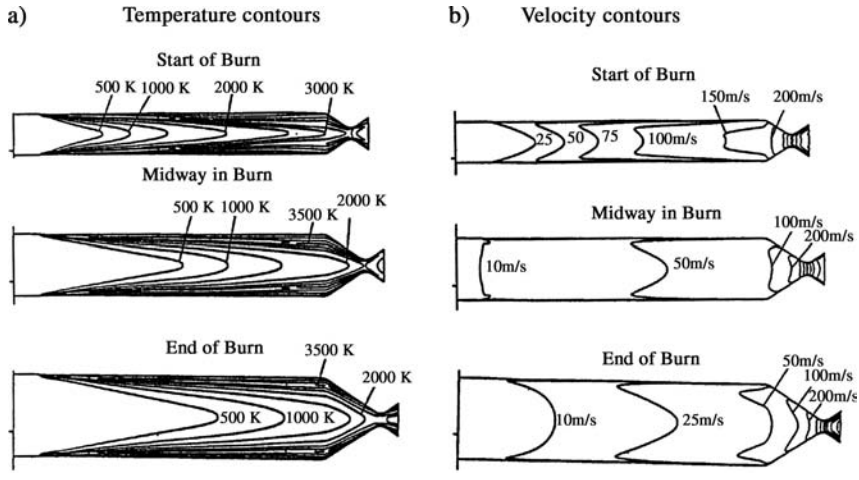

Fig. 11 Computed temperature and velocity contours at three stages in the burn. (From Venkateswaran and Merkle [43].)

Venkateswaran and Merkle [43] also extended their numerical simulation to the axisymmetric case to study size scaleup relationships. Results demonstrated that detailed CFD analyses can play a useful role in the understanding of hybrid combustion and in the design of hybrid combustors. The work of Farmer et al. [51] is quite similar to that of Venkateswaran and Merkle [43], except that their consideration of solid-fuel pyrolysis is slightly more complicated by including various hydrocarbons in a single-step forward reaction. In brief, these models still lack a detailed thermal pyrolysis reaction mechanism for realistic consideration of chemical kinetics and mass diffusion of fragmented fuel species. Pyrolysis studies, such as Arisawa and Brill [12], McCreedy and Keskkula [63], Lengellé et al. [64], Lu and Kuo [65], and many others reviewed by Beck [66], would be useful for the construction of pyrolysis models for numerical simulations.

The CFD analysis of Liang et al. [52] was focused on the simulation of certain aspects of the 24-in. Joint Independent Research and Development (JIRAD) hybrid rocket motor behavior. The work was carried out using the GALACSY algorithm multiphase combustion code, which consists of a comprehensive set of droplet dynamic submodels for the atomization and evaporation processes. In a large portion of their work they still utilized the GOX as the oxidizer instead of LOX jet spray interaction with the fuel surfaces. They found that the recirculating flow pattern in the precombustion chamber is important for stabilizing the diffusion flame above the surface of the solid fuel. Even though some of the results are quite interesting, the current capability of the existing codes is still believed to be far from conducting highly realistic simulation of internal ballistics of hybrid motor using liquid oxidizers.

A list of suggested considerations for model formulation and numerical code development is given next.

1) To improve predictive capability, future models should include more realistic turbulent combustion simulations, spray jet breakup and atomization phenomena, and detailed fuel pyrolysis processes. A pertinent work on thermal decomposition of polybutadiene, conducted by McCreedy and Keskkula [63], revealed a very complicated decomposition mechanism (Fig. 12). According to them, the condensed-phase decomposition process involved both endothermic and exothermic processes; the former includes chain scission and depolymerization steps, the latter include crosslinking and cyclization reactions. For solid fuels containing multiple ingredients, the thermal decomposition processes are even more complicated than the one shown in Fig. 12. More extensive studies in this area are needed to advance the understanding of the fuel decomposition process to include key reaction steps in model formulation and solution.

2) In recent years, substantial progress in spray atomization and combustion has been made by many researchers and is summarized in two books edited by Kuo [67, 68]. Many useful theoretical modeling and numerical simulations can be incorporated into future model and code developments for hybrid engines.

3) Numerical simulation can also help to interpret many complicated physicochemical phenomena such as combustion instabilities, nozzle erosion, and solid-fuel grain deformation and surface regression.

4) Combustion processes occurring in noncircular port crosssections of multiport fuel-grain configurations should also be considered in the numerical simulation.

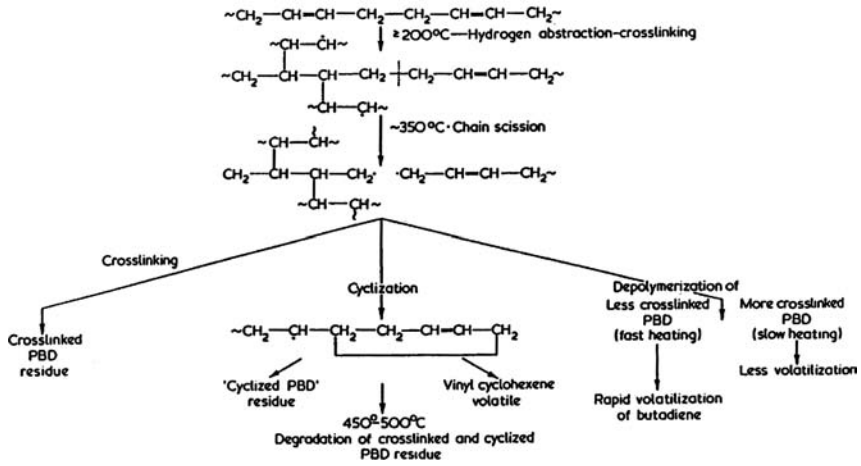

Fig. 12 Thermal decomposition mechanism of polybutadiene. (From McCreedy and Keskkula [62].)

I. Special Propulsion System Design Considerations

To achieve high-performance propulsion system design for hybrid rockets, the following list of considerations could be highly beneficial.

1) It would be important to achieve the reusable oxidizer supply and control system for repeating flights of hybrid motor. It is beneficial to design and construct such system for the reusable shuttle system.

2) Use of hybrid rocket as strapon booster for liquid or solid rockets (core vehicles) to increase the payload, for example, Atlas IIAR from 8600 lb to geosynchrono transfer orbit (GTO) to 10,500 lb of payload. Based on the inherent safety, operational flexibility, and low-cost features of hybrid rocket motors, the increase of payload is expected to be achievable in the near future.

3) Restart-function operation and control are highly attractive features, which can be achieved without much difficulty in hybrid-propulsion systems.

4) Flame holding at the head end of the motor is important to establish stable combustion in hybrid rocket motors using LOX/HTPB reactant systems.

5) Design of the precombustion chamber of LOX system is necessary to achieve sufficient evaporation of LOX droplets so that the reliable ignition and stable combustion can be ensured.

6) Unevenness of the LOX jet entering different ports (quad and centerports) could introduce a nonuniform fuel burning out situation. Therefore, the design of the oxidizer jets should provide a good match between different ports for the case of multiport fuel grains.

7) O/F variations along the fuel grain can lead to uneven amount of fuel regression; thus, this effect must be considered in the motor design. A detailed analysis and predictive code could be highly useful in this regard.

8) Solid-fuel formulation, selection of the reacting oxidizer, and suitable grain design are important steps to avoid the occurrence of low surface regression rate situation.

9) To achieve high reliability of hybrid rocket system for space propulsion mission, especially for manned flight, it is useful to consider one-piece design of case, throat, and nozzle (CTN).

III. Future Applications of Hybrid-Propulsion Systems

It is anticipated that hybrid-propulsion systems could be utilized in many applications, including large-scale boosters for space launchers, upper-stage orbital control purposes, and tactical and strategic missile systems. In the applications for large space-launch boosters, manned vehicles could be held on the pad during engine runup to verify propulsion system operation before launch because hybrid motors (or engines) have zero TNT equivalency [7]. Hybrid engines have mission abort capability to preserve crew safety during all stages of the flight profile. All engines should be able to be shut down in the event of a noncatastrophic failure. In addition, hybrids can minimize environmental impact as discussed in detail earlier. Furthermore, the operational cost for both manned and unmanned space launchers would be significantly reduced for hybrid propulsion systems. Hence hybrids could become the boosters of choice in the 21st century for a large fraction of the world's space launchers.

Hybrid rockets should also benefit upper stages by incorporating apogee and perigee kick-motor functions into a single motor for use in all low-orbit launchers and also incorporating deorbit propulsion for low Earth orbit satellites. Many already mentioned advantages of hybrids are also beneficial to upper-stage use. These include 1) higher specific impulse than either storable liquids or solids (especially when metal additives such as aluminum, aluminum hydride, aluminum–lithium, beryllium, or beryllium hydride are used in the solid fuels), 2) relatively high propellant density, 3) restart and throttling capability, 4) safe manufacturing, and 5) relatively low cost.

For tactical missile applications, the gas-generator type of hybrids offers a number of advantages over conventional solid-propellant motors. When fuel-rich solid propellants are used, the weapon systems are much less vulnerable to fires or mechanical impact and, therefore, possess the characteristics of insensitive munitions. Their throttling capability also enables hybrids to serve as smart propulsion systems. Other advantages (including their higher specific impulse, lower sensitivity to storage and ambient operating temperatures, insensitivity to fuel-grain flaws, and the ability to tailor their signatures) will also make hybrids attractive for missile applications in the 21st century.

IV. Summary and Conclusions

In comparison with the existing solid- and liquid-propellant rockets, numerous advantages of hybrid-propulsion systems have been identified. These include 1) improved operational safety, 2) greater operability and reduced servicing requirements, 3) higher propulsion performance, 4) minimal environmental impact, 5) relatively low system cost, and 6) greater reliability. Based on the current technology, there are still several disadvantages, which can be overcome in the future. These disadvantages include 1) slightly lower combustion efficiency than solids and liquids, 2) lower density impulse than solids, 3) total fuel utilization less than 100%, 4) varying oxidizer-to-fuel mass ratio during hybrid motor operation,

5) relatively low regression rate of existing solid fuels, and 6) less mature development than solids and liquids in terms of basic research, engineering design, and flight demonstration.

To stimulate future research and development in hybrid propulsion, many suggestions are provided for nine major challenges. These are 1) development of energetic solid fuels and oxidizers and enhancement of solid-fuel regression rates, 2) measurement of solid-fuel regression rate as a function of operating conditions, 3) correlation development for solid-fuel regression rates, 4) suppression of combustion instabilities, 5) improvement of combustion efficiency and fuel/oxidizer utilization, 6) scaling-law development considerations, 7) minimization of nozzle erosion, 8) development of comprehensive models and numerical codes, and 9) special propulsion system design considerations.

Recent hybrid research and development efforts in the United States have been characterized by close cooperation among government laboratories, industry, and academia. This kind of arrangement is very helpful for maximizing opportunities to share costs in manufacturing, laboratory and test facilities, and skills and, thereby, will benefit hybrid development. The policy should be continued to efficiently advance the state of the art in hybrid propulsion. Technical maturity in hybrid rocket is urgently needed for the enhancement of future propulsion systems.

V. Recommendations for Future Research and Development

To follow the spirit of von Kármán [69] in his influence and impact to the great advancement in the aerospace industry, the following recommendations are specifically made to propulsion field policy makers and program managers to ensure that they realize the importance of the following points.

1) It is vital to establish long-term commitment among government, industry, and academia. Development work and research investigations have to be conducted in parallel even in the late stage of the rocket motor development work. There are new problems continuously being encountered in motor development. Academic research facilities are usually equipped with advanced diagnostic instrumentation and possess skillful numerical simulation capabilities for solving complicated problems such as hybrid combustion.

2) It is important to educate and produce well-trained young engineers and scientists to face many challenges that, still exist in the hybrid-propulsion field.

3) Stronger international collaboration should be encouraged and implemented.

4) Development cost can be reduced with close cooperation between industry and academia.

5) Nonengineering policy makers should give technical personnel the chance for the required cost estimation and adequate time to accomplish any major projects.

It is the wish of the authors that this chapter will stimulate continued support for successful development of many reliable hybrid propulsion systems for the benefit of mankind.

Acknowledgments

K. K. Kuo would like to take this opportunity to thank NASA, Naval Sea Systems Command (NAVSEA), and Naval Surface Warfare Center, Indian Head for supporting his hybrid research work at Pennsylvania State University (PSU). Based on these previously funded projects, he gained useful knowledge in the hybrid propulsion area. He would like to acknowledge the invitation by the Organizing Committee of the 37th Israel Annual Conference on Aerospace Sciences for him to prepare and deliver the von Kármán Lecture on Hybrid Rocket Propulsion. A portion of this chapter is extracted from his von Kármán Lecture material. The support and encouragement of Roger Harwell of NASA Marshall Space Flight Center and Marion D. Kitchens of NASA Headquarters (HQ) are highly appreciated. Similarly, the support of Richard Bowen of NAVSEA, Carl Gotzmer, and Nancy Johnson of Indian Head are greatly acknowledged. William Escher of NASA HQ also authorized our use of NASA Jet Propulsion Laboratory, California Institute of Technology's test motor, in addition to our slab and cylindrical motors. He would also like to acknowledge Jerry Grey of AIAA for inviting him to serve as one of the participants in the 1995 AIAA Workshop on Hybrid Propulsion. Through this activity, he gained a great deal of hybrid motor program development information, some of which is summarized in this chapter. We would like to thank Arie Peretz of RAFAEL, Israel, for his participation in several hybrid projects. Thanks to many participants at the High Pressure Combustion Laboratory of PSU for their contributions to hybrid rocket studies; these include Grant A. Risha, Frank Y. C. Lu, George C. Harting, Eric Boyer, Brian Evans, Nick A. Favorito, David K. Johnson, Brian Wehman, and Nadir Serin of TUBITAK, Turkey.

References

[1] Sutton, G., *Rocket Propulsion Elements: An Introduction to the Engineering of Rockets*, 6th ed., Wiley, New York, NY, 1992, Chapter 1.

[2] Altman, D., and Holzman, A., "Overview and History of Hybrid Rocket Propulsion," *Fundamentals of Hybrid Rocket Combustion and Propulsion*, Progress in Astronautics and Aeronautics, edited by M. Chiavernini and K. K. Kuo, Vol. 218, AIAA, Reston, VA, 2006, Chap. 1.

[3] Kuo, K. K., and Summerfield, M. (eds.), *Fundamentals of Solid-Propellant Combustion*, Progress in Astronautics and Aeronautics, Vol. 90, 1984, pp. 1–891.

[4] Green, L., "Introductory Considerations on Hybrid Rocket Combustion," *Heterogeneous Combustion*, Progress in Astronautics and Aeronautics, edited by H. G. Wolfhard, I. Glassman, and L. Green Jr., Academic Press, New York, 1964, p. 451.

[5] Estey, P. N., and Hughes, B. G. R., "The Opportunity for Hybrid Rocket Motors in Commercial Space," AIAA Paper 92-3431, 28th AIAA/SAE/ASME/ASEE Joint Propulsion Conference, Nashville, TN, July 1992.

[6] Kuo, K. K., "Importance and Challenges of Hybrid Rocket Propulsion beyond Year 2000," *Proceedings of the 37th Israel Annual Conference on Aerospace Sciences*, Invited von Kármán Lecture, Omanuth Press Ltd, Haifa, Israel, 1997, pp. II-1–II-31.

[7] "Hybrid Rocket Propulsion," AIAA Workshop, Report, Washington, DC, July 1995.

[8] Chiaverini, M. J., Serin, N., Johnson, D. K., Lu, Y. C., and Kuo, K. K., "Instantaneous Regression Behavior of HTPB Solid Fuels Burning with GOX in a Simulated Hybrid

Rocket Motor," *Challenges in Propellants and Combustion 100 Years After Nobel*, edited by K. K. Kuo et al., Begell House, New York, NY, 1997, pp. 719–733.

[9] Risha, G. A., Evans, B., Boyer, E., and Kuo, K. K., "Metals, Energetic Additives, and Special Binders Used in Solid Fuels for Hybrid Rockets," *Fundamentals of Hybrid Rocket Combustion and Propulsion*, edited by M. Chiaverini and K. K. Kuo, Vol. 218, AIAA, Reston, VA, Progress in Astronautics and Aeronautics, 2006, Chap. 10.

[10] Karabeyoglu, A., "Combustion Instability and Transient Behavior in Hybrid Rocket Motors," *Fundamentals of Hybrid Rocket Combustion and Propulsion*, edited by M. Chiaverini and K. K., Kuo, Progress in Astronautics and Aeronautics, Vol. 218, AIAA, Reston, VA, 2006, Chap. 9.

[11] Evans, B., Favorito, N. A., and Kuo, K. K., "Study of Solid Fuel Burning-Rate Enhancement Behavior in an X-ray Translucent Hybrid Rocket Motor," AIAA Paper 2005-3909, 41st AIAA/ASME/SAE/ASEE Joint Propulsion Conference, Tucson, AZ, July 2005.

[12] Arisawa, H., and Brill, T. B., "Flash Pyrolysis of Hydroxyl-Terminated Polybutadiene (HTPB) I: Analysis and Implications of the Gaseous Products," *Combustion and Flame*, Vol. 106, No. 1/2, 1996, pp. 131–143.

[13] Arisawa, H., and Brill, T. B., "Flash Pyrolysis of Hydroxyl-Terminated Polybutadiene (HTPB) II: Implications of the Kinetics to Combustion of Organic Polymers," *Combustion and Flame*, Vol. 106, No. 1/2, 1996, pp. 144–154.

[14] Chen, J. K., and Brill, T. B., "Chemistry and Kinetics of Hydroxyl-terminated Polybutadiene (HTPB) and Diisocyanate-HTPB Polymers during Slow Decomposition and Combustion-like Conditions," *Combustion and Flame*, Vol. 87, No. 3/4, 1991, pp. 217–232.

[15] Chiaverini, M. J., Harting, G. C., Lu, Y. C., Kuo, K. K., Peretz, A., Jones, H. S., Wygle, B. S., and Arves, J. P., "Pyrolysis Behavior of Hybrid-Rocket Solid Fuels Under Rapid Heating Conditions," *Journal of Propulsion and Power*, Vol. 15, No. 6, 1999, pp. 888–895.

[16] Houser, T. J., and Peck, M. V., "Research in Hybrid Combustion," *Heterogeneous Combustion*, edited by H. G. Wolfhard, I. Glassman, and L. Green Jr., Progress in Astronautics and Aeronautics, Vol. 15, AIAA, New York, NY, 1964, pp. 559–581.

[17] Marxman, G. A., and Gilbert, M., "Turbulent Boundary Layer Combustion in the Hybrid Rocket," *Ninth International Symposium on Combustion*, Academic Press, New York, 1963, pp. 371–383.

[18] Marxman, G. A., Wooldridge, C. E., and Muzzy, R. J., "Fundamentals of Hybrid Boundary Layer Combustion," *Heterogeneous Combustion*, Progress in Astronautics and Aeronautics, Vol. 15, Academic Press, New York, 1964, pp. 485–521.

[19] Netzer, D. W., "Hybrid Rocket Internal Ballistics," Chemical Propulsion Information Agency, CPIA Publ. 222, Jan. 1972, pp. 1–45.

[20] Altman, D., "Hybrid Rocket Propulsion Systems," *Space Propulsion Analysis*, edited by R. W. Humble, G. N. Henry, and W. J. Larson, McGraw-Hill, New York, NY, 1996, Chap. 7.

[21] Muzzy, R. J., "Applied Hybrid Combustion Theory," AIAA Paper 72–1143, Joint Propulsion Specialist Conference, New Orleans, LA, Nov./Dec. 1972.

[22] Estey, P. N., Altman, D., and McFarlane, J. S., "An Evaluation of Scaling Effects for Hybrid Rocket Motors," AIAA Paper 91-2517, 27th AIAA/ASME/SAE/ASEE Joint Propulsion Conference, Sacramento, CA, June 1991.

[23] Strand, L., Jones, M. D., Ray, R. L., and Cohen, N. S., "Characterization of Hybrid Rocket Internal Heat Flux and HTPB Fuel Pyrolysis," AIAA Paper 94-2876, 30th AIAA/ASME/SAE/ASEE Joint Propulsion Conference, Indianapolis, IN, June 1994.

[24] Salita, M., "Comparison of Four Boundary Layer Solutions for Fuel Regression Rate in Classical Hybrid Rocket Motors," AIAA Paper 91-2520, 27th AIAA/ASME/SAE/ASEE Joint Propulsion Conference, Sacramento, CA, June 1991.

[25] Stickler, D. B., and Kumar, R. N., "Polymer-Degradation Rate Control of Hybrid Rockets," MIT Rep. Accession No. N72-13735, Massachusetts Inst. of Technology, Cambridge, MA, Sept. 1970.

[26] Rastogi, R. P., and Deepak, D., "Pressure Dependence of Hybrid Fuel Burning Rate," *AIAA Journal*, Vol. 14, No. 7, 1976, pp. 988–990.

[27] Kosdon, F. J., and Williams, F. A., "Pressure Dependence of Nonmetalized Hybrid Fuel Regression Rate," *AIAA Journal*, Vol. 5, No. 4, 1967, pp. 774–777.

[28] Miller, E., "Hybrid Rocket Combustion Regression Rate Model," *AIAA Journal*, Vol. 4, No. 4, 1966, pp. 752–753.

[29] Smoot, L. D., and Price, C. F., "Regression Rates of Nonmetalized Hybrid Fuel Systems," *AIAA Journal*, Vol. 3, No. 8, 1965, pp. 1408–1413.

[30] Smoot, L. D., and Price, C. F., "Pressure Dependence of Hybrid Fuel Regression Rates," *AIAA Journal*, Vol. 5, No. 1, 1967, pp. 102–106.

[31] Moutet, A., and Barrere, M., "Contribution a l'Etude de la Combustion dans les Fusées a Lithergol ou Hybrides," *Advances in Aeronautical Sciences*, Pergamon Press, New York, 1961, pp. 465–495.

[32] Smoot, L. D., and Price, C. F., "Regression Rates of Metalized Hybrid Fuel Systems," *AIAA Journal*, Vol. 4, No. 5, 1966, pp. 910–915.

[33] Hottel, H. C., "Radiant-Heat Transmission," *Heat Transmission*, edited by W. H. McAdams, 3rd ed., McGraw–Hill, New York, 1954, pp. 55–125.

[34] Incropera, F. P., and DeWitt, D. P., *Fundamentals of Heat and Mass Transfer*, 4th ed., Wiley, New York, 1996, Chaps. 12 and 13, pp. 633–782.

[35] Chiaverini, M. J., Serin, N., Johnson, D., Lu, Y. C., Kuo, K. K., and Risha, G. A., "Regression Rate Behavior of Hybrid Rocket Solid Fuels," *Journal of Propulsion and Power*, Vol. 16, No. 1, 2000, pp. 125–132.

[36] Chiaverini, M. J., Serin, N., Johnson, D. K., Lu, Y. C., and Kuo, K. K., "Instantaneous Regression Behavior of HTPB Solid Fuels Burning with GOX in a Simulated Hybrid Rocket Motor," *Challenges in Propellants and Combustion 100 Years After Nobel*, edited by K. K. Kuo, T. B. Brill, R. A. Pesce-Rodriguez, A. R. Mitchell, J. Covino, S. K. Chan, A. Peretz, N. K. Gunners, S. T. Thynell, and S. H. Chan, Begell House, New York, NY, 1997, pp. 719–733.

[37] Kee, R. J., Rupley, F. M., and Miller, J. A., "The Chemkin Thermodynamic Data Base," Sandia Technical Rep. SAND87-8215B, UC-4, Sandia National Labs, Livermore, CA, April 1994.

[38] Burcat, A., and McBride, B. "1997 Ideal Gas Thermodynamic Data for Combustion and Air-Pollution Use," Technion Aerospace Engineering, TAE Rep. 804, June 1997.

[39] Richter, H., Benish, T. G., Mazyar, O. A., Green, W. H., and Howard, J. B., "Formation of Polycyclic Aromatic Hydrocarbons and Their Radicals in a Nearly Sooting Premixed Benzene Flame," *Proceedings of the Combustion Institute*, The Combustion Institute, Pittsburgh, PA, Vol. 28, Part II, 2000, pp. 2609–2618.

[40] Sumathi, R., Carstensen, H.-H., and Green, W. H., "Reaction Rate Prediction via Group Additivity Part 1: H Abstraction from Alkanes by H and CH3," *Journal of Physical Chemistry*, Vol. A 105, 2001, pp. 6910–6925.

[41] Chiaverini, M. J., Kuo, K. K., Peretz, A., and Harting, G. C., "Regression-Rate and Heat-Transfer Correlations for Hybrid Rocket Combustion," *Journal of Propulsion and Power*, Vol 17, No. 1, 2001, pp. 99–110.

[42] Marxman, G. A., "Combustion in the Turbulent Boundary Layer on a Vaporizing Surface," *Tenth Symposium (International) on Combustion*, The Combustion Institute, Pittsburgh, PA, 1965, pp. 1337–1349.

[43] Venkateswaran, S., and Merkle, C. L., "Size Scale-Up in Hybrid Rocket Motors," AIAA Paper 96-0647, 34th AIAA Aerospace Sciences Meeting, Reno, NV, Jan. 1996.

[44] Story, G., and Arves, J., "Flight Testing of Hybrid-Powered Vehicles," *Fundamentals of Hybrid Rocket Combustion and Propulsion*, edited by M. Chiaverini, and K. K. Kuo, Progress in Astronautics and Aeronautics, Vol. 1XX, AIAA, Reston, VA, 2006, Chap. 14.

[45] Gany, A., "Similarity and Scale Effects in Hybrid Rocket Motors," *Fundamentals of Hybrid Rocket Combustion and Propulsion*, edited by M. Chiaverini and K. K., Kuo, Progress in Astronautics and Aeronautics, Vol. 1XX, 2006, Chap. 12.

[46] Gany, A., "Scale Effects in Hybrid Motors Under Similarity Conditions," AIAA Paper 96-2846, July 1996.

[47] Spalding, D. B., "The Art of Partial Modeling," *Ninth International Symposium on Combustion*, Academic Press, New York, NY, 1963, pp. 833–843.

[48] Rosner, D. E., *Transport Processes in Chemically Reacting Flow Systems*, Butterworth, Stoneham, MA, 1986, Chap. 7, pp. 405–454.

[49] Sankaran, V., "Computational Fluid Dynamics Modeling of Hybrid Rocket Flowfields Combustion," *Fundamentals of Hybrid Rocket Combustion and Propulsion*, edited by M. Chiaverini and K. K., Kuo, Progress in Astronautics and Aeronautics, Vol. 1XX, AIAA, Reston, VA, 2006, Chap. 8.

[50] Venkateswaran, S., and Merkle, C. L., "Combustion Processes in Hybrid Rocket Engines," *Thirteenth Workshop for Computational Fluid Dynamic Applications in Rocket Propulsion and Launch Vehicle Technology*, NASA 3332, Vol. 2, 1995, pp. 1313–1336.

[51] Farmer, R. C., Cheng, G. C., and Mersch, T. H., "Analysis of Steady and Unsteady Hybrid Combustion," 1996 JANNAF Propulsion and Joint Subcommittee Meetings, CPIA Publication 650, Vol. II, 9–13 Dec. 1996, pp. 485–500.

[52] Liang, P.-Y., Ungewitter, R., and Claflin, S., "Combustion Processes in Hybrid Rocket Engines," *Thirteenth Workshop for Computational Fluid Dynamic Applications in Rocket Propulsion and Launch Vehicle Technology*, NASA 3332, Vol. 2, 1995, pp. 1337–1348.

[53] Chiaverini, M., Harting, G., Lu, Y. C., and Kuo, K., "Fuel Decomposition and Boundary Layer Combustion Processes of Hybrid Rocket Motors," AIAA Paper 95-2686, 31st AIAA/ASME/SAE/ASEE Joint Propulsion Conference, San Diego, CA, July 1995.

[54] Kuo, K. K., Lu, Y. C., Chiaverini, M. J., Johnson, D. K., Serin, N., and Risha, G. A., "Fundamental Phenomena on Fuel Decomposition and Boundary-Layer Combustion Processes with Applications to Hybrid Rocket Motors," Part 1, Final Rept. NASA, Contract NAS8-39945, 30 June 1996.

[55] Merkle, C. L., and Venkateswaran, S., "Fundamental Phenomena on Fuel Decomposition and Boundary-Layer Combustion Processes with Applications to Hybrid Motors," Part 2, Final Rept. NASA Contract NAS8-39945, 30 June 1996.

[56] Westbrook, C. K., and Dryer, F. L., "Simplified Reaction Mechanisms for the Oxidation of Hydrocarbon Fuels and Flames, *Combustion Science and Technology*, Vol. 27, 1981, pp. 31–43.

[57] Chiaverini, M. J., Serin, N., Johnson, D. K., Lu, Y. C., and Kuo, K. K., "Thermal Pyrolysis and Combustion of HTPB-Based Solid Fuels for Hybrid Rocket Motor Applications," AIAA Paper 96-2845, 32nd AIAA/ASME/SAE/ASEE Joint Propulsion Conference, Lake Buena Vista, FL, July 1996.

[58] Jones, W. P., and Launder, B. E., "The Prediction of Laminarization with a Two-Equation Model of Turbulence," *International Journal of Heat and Mass Transfer*, Vol. 15, 1972, pp. 301–314.

[59] Chien, K., "Predictions of Channel and Boundary Layer Flows with a Low-Reynolds-Number Turbulence Model," *AIAA Journal*, Vol. 20, No. 1, 1982, pp. 33–38.

[60] Siegel, R., and Howell, J. R., *Thermal Radiation Heat Transfer*, 3rd ed., Hemisphere, New York, NY, 1992, pp. 1–1072.

[61] Choi, Y.-H., and Merkle, C. L., "The Application of Preconditioning to Viscous Flows," *Journal of Computational Physics*, Vol. 105, 1993, pp. 207–223.

[62] Venkateswaran, S., Deshpande, M., and Merkle, C. L., "The Application of Preconditioning to Reacting Flow Computations," A95-3650109-34 12th AIAA Computational Fluid Dynamics Conference, Washington, DC, 1995, pp. 306–316.

[63] McCreedy, K., and Keskkula, H., "Effect of Thermal Crosslinking on Decomposition of Polybutadiene," *Polymer*, Vol. 20, 1979, pp. 1155–1159.

[64] Lengellé, G., Fourest, B., Godon, J. C., and Guin, C., "Condensed Phase Behavior and Ablation Rate of Fuels for Hybrid Propulsion," AIAA Paper 93-2413, 29th AIAA/ASME/SAE/ASEE Joint Propulsion Conference, Monterey, CA, June 1993.

[65] Lu, Y. C., and Kuo, K. K., "Thermal Decomposition Study of Hydroxyl-Terminated Polybutadiene (HTPB) Solid Fuel," *Thermochimica Acta*, No. 275, 1996, pp. 181–191.

[66] Beck, W. H., "Pyrolysis Studies of Polymeric Materials Used as Binders in Composite Propellants: A Review," *Combustion and Flame*, Vol. 70, No. 2, 1987, pp. 171–190.

[67] Kuo, K. K. (ed.), *Recent Advances in Spray Combustion: Spray Atomization and Drop Burning Phenomena, Vol. I*, Progress in Aeronautics and Astronautics, Vol. 166, AIAA, Reston, VA, 1996, pp. 1–517.

[68] Kuo, K. K. (ed.), *Recent Advances in Spray Combustion: Spray Combustion Measurements and Model Simulation, Vol. II*, Progress in Aeronautics and Astronautics, Vol. 171, AIAA, Reston, VA, 1996, pp. 1–467.

[69] von Kármán T., and Edson, L., *The Wind and Beyond*, Little, Brown and Co., Boston, 1967, pp. 1–376.

Index